

# 2010

## Solid-State Sensors, Actuators, and Microsystems Workshop

Greeting from the Chair

Committees

Acknowledgements

Table of Contents

Author Index

Keyword Index

Copyright

[www.hh2010.org](http://www.hh2010.org)



Sponsored by the  
Transducer Research Foundation, Inc.

Additional grant support provided:  
National Institute of Standards and Technology (NIST), CMMI and ECCS Divisions  
of the National Science Foundation (NSF), Sandia National Laboratories,  
Transducer Research Foundation, and U.S. Army Research Laboratory

Hilton Head Workshop  
June 6 - 10, 2010 • Hilton Head, South Carolina  
Editors: David J. Monk and Kimberly L. Turner

TRF Catalog Number: 10TRF-0001  
Library of Congress Control Number: 2010926577  
ISBN Number: 0-9640024-8-5  
ISSN: 1539-2058 (Print) • ISSN: 1539-204X (Electronic)  
DOI: 10.31438/trf.hh2010.0

# Greetings from the General Chair

Welcome to the 2010 Solid State Sensors, Actuators, and Microsystems Workshop; the fifteenth in the biannual series of regional meetings that alternate with the International Transducers Conference. This meeting will offer an open atmosphere of discussion, collaboration and interaction, which has been its hallmark since the beginning in 1984. We'll see new ideas and new methods, hear about exciting applications and meet new colleagues. We'll also hear about progress on ongoing ideas/open problems and applications and renew relationships with old friends. The combination of ideas, opportunities and relationships has always been the objective of this meeting and we've worked hard to continue in this tradition.

The Workshop schedule remains organized around single session oral presentations with several poster presentations. Dave Monk has assembled and led a strong and opinionated program committee through a paper selection process resulting in the program published in this digest. Oral papers were selected on the basis of high quality content and likely broad interest to the meeting audience. Poster papers were selected on the basis of high quality as well, and for their probable high interest to a subset of the meeting attendees. The poster papers will be introduced by their authors using a "shotgun" session that has been popular at past meetings. We've also included Late News Oral and Late News Poster papers based on a selection process that occurred in mid-March. The program committee is to be congratulated for their efforts in reading, studying, ranking, debating, re-ranking, and selecting from the nearly 300 submitted abstracts.

We also have significant unscheduled time for informal discussions among friends and colleagues. Technical brainstorming, collaborative ideas, job offers and business plans are usually topics for these breaks. We hope the relaxed environment here on the ocean helps to stimulate such interaction and creativity.

Several changes have been introduced this year in an attempt to keep the meeting fresh. Prior to 2008, admission to the meeting was limited to those who were affiliated with an institution located in the Americas. Following the change in 2008, we have continued soliciting abstract submissions and registrations from all previous alumni, regardless of the location of their current affiliation. This change recognizes that many of us have the opportunity to develop our careers in locations throughout the world and this experience can be an important factor in a meeting such as this. In addition, we have something new and exciting planned for the period formally known as the "Rump Session." Make sure you attend to test your knowledge about the field of MEMS, maybe learning something new, and enjoying time with your colleagues and friends, new and old.

A tremendous "thank you" goes to Dave and the entire Technical Program Committee for their efforts in creating this program. Additionally, this year, we had two folks working tirelessly on the development side of the meeting. James Walker served as Chair for Commercial Support. He brought new and innovative ideas to the meeting, and at the time this went to press, had lined up 19 Exhibitors/Sponsors. This year, each organization that purchased a table display will have the opportunity to display a poster in the Wednesday Open Poster/Commercial Poster Session as well. Clark T.-C. Nguyen served as the Chair for Student Support, and did an outstanding job garnering support for student attendees. These are valuable and essential features of the Hilton Head Workshop, and I am most thankful to have had outstanding people taking the lead on these tasks.

Thanks also goes to the Transducers Research Foundation, NIST and Sandia National Laboratory for their continued support of travel for presenting student authors, thus enabling the meeting to continue the invigoration of our community with young talent, new ideas, and enthusiasm for the future of our community. Mark Allen has continued to provide excellent support of the local arrangements and thanks to Mehran Mehregany for his oversight of our finances. Katharine Cline and her team at Preferred Meeting Management, Inc. are to be given special thanks for all of their hard work in pulling this meeting together and for making it run so smoothly. The work they do "behind the scenes" to make this meeting special is difficult to comprehend and our community and our meeting would suffer without them.

This meeting of course, belongs to all of you, thank you for your support. I would appreciate hearing your opinion regarding the changes that have been made this year as well as your suggestions for changes to future meetings so we can keep this meeting special. As well I sincerely hope you all have a great time.

Kimberly L. Turner  
General Chair

# Organizing Committee

## General Chair

Kimberly L. Turner  
University of California, Santa Barbara, USA

## Technical Program Chair

David J. Monk  
Freescale Semiconductor, Inc., USA

## Treasurer

Mehran Mehregany  
Case Western Reserve University, USA

## Commercial Support and Exhibition

James Walker  
Demont & Breyer Patent Law, USA

## Student Travel Support

Clark Nguyen  
University of California, Berkeley, USA

## Local Arrangements

Mark G. Allen  
Georgia Institute of Technology, USA

# Technical Program Committee Members

David Arnold  
University of Florida, USA

Amy Herr  
University of California, Berkeley, USA

Stephen Bart  
Analog Devices, USA

Michael Huff  
MEMS Exchange, USA

Jonathan Bernstein  
Draper Laboratory, USA

Hal Jerman  
Coherent, USA

Sunil Bhave  
Cornell University, USA

Tina Lamers  
Avago Technologies

Stephen Casalnuovo  
Sandia Laboratories, USA

Markus Lutz  
SiTime, USA

Abhi Chavan  
Corvenits, Inc., USA

David J. Monk  
Freescale Semiconductor, USA

Eugene Chow  
Palo Alto Research Center, USA

Michael Post  
National Research Council of Canada, CANADA

Hemant Desai  
MEMSIC, USA

Beth Pruitt  
Stanford University, USA

Bruno Frazier  
Georgia Institute of Technology, USA

Mark Shannon  
University of Illinois, Urbana-Champaign, USA

Luc Fr chet  
Universit  de Sherbrooke, CANADA

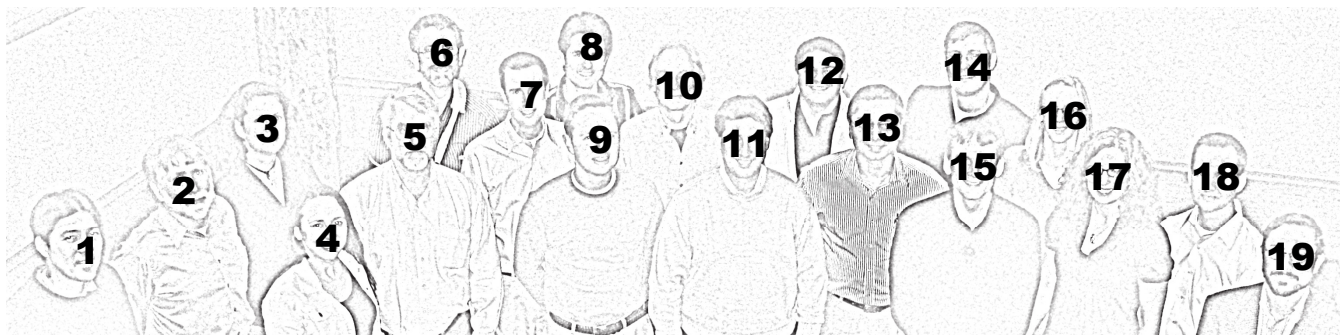
Andrei Shkel  
DARPA, USA

Jonathan Hammond  
RFMD, USA

Kimberly L. Turner  
University of California, Santa Barbara, USA

Peter Hartwell  
Hewlett Packard, USA

# Technical Program Committee



- 1 – Eugene Chow
- 2 – Stephen Casalnuovo
- 3 – Beth Pruitt
- 4 – Amy Herr
- 5 – Hal Jerman
- 6 – Jonathan Bernstein
- 7 – David Arnold
- 8 – Luc Frechette
- 9 – Jonathan Hammond
- 10 – Michael Post

- 11 – Dave Monk (Technical Program Chair)
- 12 – Sunil Bhawe
- 13 – Abhi Chavan
- 14 – Markus Lutz
- 15 – Mark Shannon
- 16 – Tina Lamers
- 17 – Kimberly L. Turner (General Chair)
- 18 – Peter Hartwell
- 19 – Stephen Bart

not pictured: Hemant Desai, Bruno Frazier, Michael Huff, and Andrei Shkel

# Acknowledgements

Special acknowledgement to the Transducer Research Foundation, Inc., National Institute of Standards and Technology (NIST), CMMI and ECCS Divisions of the National Science Foundation (NSF), Sandia National Laboratories, and U.S. Army Research Laboratory for their educational grant funding support of this Workshop.

## Exhibitors and Benefactors

We gratefully acknowledge the support of this Workshop from the following companies and institutions as of the printing of May 7, 2010:

**Brewer Science, Inc.**

**Coventor, Inc.**

**DeMont & Breyer**

**Freescale Semiconductor**

**Integrated Sensing Systems (ISSYS), Inc.**

**IntelliSense**

**Journal of Micromechanics and Microengineering**

**MEMS and Nanotechnology Exchange**

**MEMS Investor Journal**

**MEMSCAP Inc.**

**Okmetic Inc.**

**Polytec, Inc.**

**Primaxx, Inc.**

**Sandia National Laboratories**

**Silex Microsystems**

**Springer**

**Tegal Corporation**

**Tousimis**

**XACTIX, Inc.**

# Table of Contents

Scroll to the title and select a **Blue** link to open a paper. After viewing the paper, use the bookmarks to the left to return to the beginning of the Table of Contents.

---

## Sunday, June 6, 2010

6:00 p.m.-  
9:00 p.m.      **Registration and Welcome Reception**

## Monday, June 7, 2010

7:00 a.m.      **Breakfast**

7:45 a.m.      **Welcome and Introduction**  
Kimberly L. Turner, *University of California, Santa Barbara, USA*  
David J. Monk, *Freescale Semiconductor, Inc., USA*

### Invited Speaker I

Session Chair: D.J. Monk, *Freescale Semiconductor, USA*

8:15 a.m.      **BOSCH DRIE SHAPING MEMS - HISTORY, APPLICATIONS  
AND FUTURE DIRECTIONS** ..... 1  
*Franz Laermer and A. Urban*  
*Robert Bosch GmbH, GERMANY*

### Session 1 - Sensors and Actuators

Session Chair: M. Lutz, *SiTime, USA*

9:00 a.m.      **COMPOSITE POLYSILICON-PLATINUM LATERAL  
NANO-ELECTROMECHANICAL RELAYS** ..... 7  
R. Parsa<sup>1</sup>, S. Chong<sup>1</sup>, N. Patil<sup>1</sup>, K. Akarvardar<sup>2</sup>, J. Provine<sup>1</sup>, D. Lee<sup>1</sup>, D. Elata<sup>3</sup>,  
S. Mitra<sup>1</sup>, H.-S.P. Wong<sup>1</sup>, and R.T. Howe<sup>1</sup>  
<sup>1</sup>*Stanford University, USA*, <sup>2</sup>*SEMATECH, USA*, and  
<sup>3</sup>*Technion – Israel Institute of Technology, ISRAEL*

9:25 a.m.      **3-D MICROMACHINED SPHERICAL SHELL RESONATORS WITH  
INTEGRATED ELECTROMAGNETIC AND ELECTROSTATIC  
TRANSDUCERS** ..... 11  
S.A. Zotov, I.P. Prikhodko, A.A. Trusov, and A.M. Shkel  
*University of California, Irvine, USA*

9:50 a.m. **NEAR FIELD PHOTOTHERMAL ANNEALING FOR RAPID LASER PRINTING OF METALLIC MICRO AND NANO STRUCTURES** ..... 15  
F. Xiao, T.H. Wu, and P.Y. Chiou  
*University of California, Los Angeles, USA*

10:15 a.m. **Break and Tabletop Exhibits**

**Session 2 - Microfluidics and Chemical Sensors**

Session Chair: H. Jerman, *Coherent, Inc., USA*

10:40 a.m. **A RESETTABLE HIGH-DENSITY MICROFLUIDIC PARTICLE TRAPPING SYSTEM** ..... 19  
R.D. Sochol, B. Lüthi, K. Iwai, M. Dueck, L.P. Lee, and L. Lin  
*University of California, Berkeley, USA*

11:05 a.m. **IN-PLANE MODE RESONANT CANTILEVERS AS LIQUID-PHASE CHEMICAL SENSORS WITH PPB RANGE LIMITS OF DETECTION** ..... 23  
L.A. Beardslee<sup>1</sup>, K.S. Demirci<sup>1</sup>, Y. Luzinova<sup>1</sup>, J.J. Su<sup>1</sup>, B. Mizaikoff<sup>3</sup>, S. Heinrich<sup>2</sup>,  
F. Josse<sup>2</sup>, and O. Brand<sup>1</sup>  
<sup>1</sup>*Georgia Institute of Technology, USA*, <sup>2</sup>*Marquette University, USA*, and  
<sup>3</sup>*University of Ulm, GERMANY*

11:30 a.m. **SECOND EIGENMODE OPERATION OF SUSPENDED MICROCHANNEL RESONATORS FOR HIGH PRECISION FLOW-THROUGH MASS SENSING** ..... 27  
J. Lee and S.R. Manalis  
*Massachusetts Institute of Technology, USA*

12:00 p.m. **Poster/Oral Session – Preview Presentation 1**  
Session Chair: S. Bart, *Analog Devices, Inc., USA*

1:00 p.m. **Networking Lunch**

2:30 p.m. **Poster/Oral Session 1 – Contributed and Late News**  
- 4:00 p.m. Session Chairs: D. Arnold, *University of Florida, USA*, T. Lamers, *Avago Technologies, USA*,  
and A.M. Shkel, *DARPA, USA*  
***Contributed Posters and Late News Posters for Session 1***

4:00 p.m. **Poster/Oral Session 2 – Contributed and Late News**  
- 5:30 p.m. Session Chairs: J. Bernstein, *Draper Laboratory, USA* and E. Chow, *Palo Alto Research Center, USA*  
***Contributed Posters and Late News Posters for Session 2***

## Tuesday, June 8, 2010

7:30 a.m. **Breakfast**

### Invited Speaker II

Session Chair: M. Shannon, *University of Illinois, Urbana-Champaign, USA*

8:15 a.m. **METALS IN MICROFLUIDICS - COUPLING PLASMONICS, ELECTRON TRANSFER AND NANOFUIDICS IN A MONOLITHIC STRUCTURE** ..... 30  
S.P. Branagan, N. Contento, and Paul W. Bohn  
*University of Notre Dame, USA*

### Session 3 - Surface Fluidics

Session Chair: M. Shannon, *University of Illinois, Urbana-Champaign, USA*

9:00 a.m. **NOVEL THREE-DIMENSIONAL SURFACE MICROFLUIDICS ENABLED BY UNCONVENTIONAL FLUIDIC INTERFACES** ..... 33  
L.F. Hong and T.R. Pan  
*University of California, Davis, USA*

9:25 a.m. **EWOD MICRODEVICES FOR SYNTHESIS OF <sup>18</sup>F-LABELED TRACERS FOR POSITRON EMISSION TOMOGRAPHY (PET)** ..... 37  
S. Chen, H. Ding, G.J. Shah, R.M. van Dam, and C.-J. Kim  
*University of California, Los Angeles, USA*

9:50 a.m. **MANIPULATION OF LIQUID SPREADING ON ASYMMETRIC NANOSTRUCTURED SURFACES** ..... 41  
K.-H. Chu, R. Xiao, M.E. Alf, K.K. Gleason, and E.N. Wang  
*Massachusetts Institute of Technology, USA*

10:15 a.m. **Break and Tabletop Exhibits**



**Session 4 - Physical Sensors**  
Session Chair: A. Chavan, *Corventis, Inc., USA*

10:40 a.m.	<b>LORENTZ FORCE MEMS MAGNETOMETER</b> .....	<b>45</b>
	M.J. Thompson and D.A. Horsley <i>University of California, Davis, USA</i>	
11:05 a.m.	<b>AN INTRAOCULAR PRESSURE SENSOR BASED ON A GLASS REFLOW PROCESS</b> .....	<b>49</b>
	R.M. Haque and K.D. Wise <i>University of Michigan, USA</i>	
11:30 a.m.	<b>A 15 ATM. PRESSURE SENSOR UTILIZING MICRODISCHARGES IN A 1.6 mm<sup>3</sup> CERAMIC PACKAGE</b> .....	<b>53</b>
	S.A. Wright, H.A. Zipperian, and Y.B. Gianchandani <i>University of Michigan, USA</i>	
11:55 a.m.	<b>SUBNANOWATT MICROBUBBLE PRESSURE TRANSDUCER</b> .....	<b>57</b>
	C.A. Gutierrez and E. Meng <i>University of Southern California, USA</i>	
12:20 p.m. - 2:00 p.m.	<b>Networking Lunch</b>	
7:00 p.m. - 9:00 p.m.	<b>Banquet</b>	

## Wednesday, June 9, 2010

7:30 a.m. **Breakfast**

### Invited Speaker III

Session Chair: S. Bhave, *Cornell University, USA*

8:15 a.m. **DEVELOPMENT OF HIGH-PERFORMANCE, HIGH-VOLUME  
CONSUMER MEMS GYROSCOPES** ..... 61

Joe Seeger, M. Lim, and S. Nasiri

*InvenSense, Inc., USA*

### Session 5 - Resonators/Filters

Session Chair: S. Bhave, *Cornell University, USA*

9:00 a.m. **PARALLEL LATTICE FILTERS UTILIZING ALUMINUM  
NITRIDE CONTOUR MODE RESONATORS** ..... 65

K.E. Wojciechowski and R.H. Olsson III

*Sandia National Laboratories, USA*

9:25 a.m. **STABLE OSCILLATION OF MEMS RESONATORS BEYOND  
THE CRITICAL BIFURCATION POINT** ..... 70

H.K. Lee, J.C. Salvia, S. Yoneoka, G. Bahl, Y.Q. Qu, R. Melamud,

S. Chandorkar, M.A. Hopcroft, B. Kim, and T.W. Kenny

*Stanford University, USA*

9:50 a.m. **THERMO-ELECTRO-MECHANICAL MODELING OF HIGH  
FREQUENCY THERMALLY ACTUATED I<sup>2</sup>-BAR RESONATORS** ..... 74

A. Rahafrooz and S. Pourkamali

*University of Denver, USA*

10:15 a.m. **Break and Tabletop Exhibits**

## Session 6 - Chemical/Bio Systems

Session Chair: L. Frechette, *Université de Sherbrooke, CANADA*

- 10:40 a.m. **A MICROFABRICATED COMPREHENSIVE TWO-DIMENSIONAL GAS CHROMATOGRAPHY SYSTEM** ..... 78  
S. Reidy, S.-J. Kim, K. Beach, B. Block, E.T. Zellers, K. Kurabayashi, and K.D. Wise  
*University of Michigan, USA*
- 11:05 a.m. **A HIGH POWER DENSITY MEMS MICROBIAL FUEL CELL** ..... 82  
S. Choi, H. Lee, Y. Yang, B.E. Rittmann, and J. Chae  
*Arizona State University, USA*
- 11:30 a.m. **BIOMIMETIC SUPERHYDROPHOBIC SURFACES USING VIRAL NANOTEMPLATES FOR SELF-CLEANING AND DROPWISE CONDENSATION** ..... 86  
M. McCarthy<sup>1</sup>, R. Enright<sup>1,2</sup>, K. Gerasopoulos<sup>3</sup>, J.N. Culver<sup>3</sup>, R. Ghodssi<sup>3</sup>, and E.N. Wang<sup>1</sup>  
<sup>1</sup>*Massachusetts Institute of Technology, USA*, <sup>2</sup>*University of Limerick, IRELAND*, and <sup>3</sup>*University of Maryland, USA*

12:00 p.m. **Networking Lunch**  
- 1:30 p.m.

## Session 7 - Late News Oral

Session Chair: B. Frazier, *Georgia Institute of Technology, USA*

- 1:30 p.m. **BULK METALLIC GLASS NANOWIRES FOR USE IN DIRECT ALCOHOL FUEL CELL** ..... 90  
M. Carmo<sup>1</sup>, S. Ding<sup>1</sup>, G. Kumar<sup>1</sup>, K. Sun<sup>2</sup>, J. Schroers<sup>1</sup>, and A.D. Taylor<sup>1</sup>  
<sup>1</sup>*Yale University, USA* and <sup>2</sup>*University of Michigan, USA*
- 1:45 p.m. **DETACHMENT LITHOGRAPHY: FABRICATION OF 3D MICROSTRUCTURES AND GUIDED-ASSEMBLY OF NANOMATERIALS** ..... 92  
J. Yeom<sup>1,2</sup> and M.A. Shannon<sup>1</sup>  
<sup>1</sup>*University of Illinois, Urbana-Champaign, USA* and <sup>2</sup>*Cbana Labs Inc., USA*
- 2:00 p.m. **ELECTROTHERMAL MICROCANTILEVER WITH INTEGRATED SOLID-STATE HEATER-THERMOMETER AND NPN BACK-TO-BACK DIODES** ..... 94  
P. Fletcher, B. Bhatia, Y. Wu, M. Shannon, and W. King  
*University of Illinois, Urbana-Champaign, USA*
- 2:15 p.m. **HYBRID BIOMIMETIC DIRECTIONAL MICROPHONE FOR THE FULL SPACE SOUND SOURCE LOCALIZATION** ..... 96  
C.C. Chen, Y.C. Chen, K.-Y. Lin, and Y. T. Cheng  
*National Chiao Tung University, TAIWAN*

2:30 p.m.	<b>SELF-ASSEMBLING SINGLE CELLS ACROSS MICROPOSTS: FIRST AXIAL FORCE MEASUREMENTS IN IMMATURE CARDIOMYOCYTES</b> .....	<b>98</b>
	R.E. Taylor, K. Kim, and B.L. Pruitt <i>Stanford University, USA</i>	
2:45 p.m.	<b>TEMPERATURE-STABLE HIGH-Q ALN-ON-SILICON RESONATORS WITH EMBEDDED ARRAY OF OXIDE PILLARS</b> .....	<b>100</b>
	R. Tabrizian, G. Casinovi, and F. Ayazi <i>Georgia Institute of Technology, USA</i>	
3:00 p.m.	<b>Poster/Oral Session – Preview Presentation 2</b>	
- 3:30 p.m.	Session Chair: A. Herr, <i>University of California, Berkeley, USA</i>	
5:00 p.m.	<b>Poster/Oral Session 3 – Contributed Posters</b>	
- 6:30 p.m.	Session Chairs: H. Desai, <i>MEMSIC, USA</i> and M. Huff, <i>MEMS Exchange, USA</i> <b><i>Contributed Posters for Session 3</i></b>	
6:30 p.m.	<b>Poster/Oral Session 4 – Commercial &amp; Open Posters</b>	
- 8:00 p.m.	Session Chairs: B. Frazier, <i>Georgia Institute of Technology, USA</i> and M. Post, <i>National Research Council of Canada, CANADA</i> <i>Papers not included in the Technical Digest.</i>	
8:00 p.m.	<b>Rump Session</b>	
- 9:30 p.m.	Session Chairs: P. Hartwell, <i>Hewlett-Packard Laboratories, USA</i> and B. Hardy, <i>MEMSCAP Inc., USA</i>	

## Thursday, June 10, 2010

7:30 a.m. **Breakfast**

### Invited Speaker IV

Session Chair: S. Casalnuovo, *Sandia National Laboratories, USA*

8:15 a.m. **MICROFLUIDIC DELIVERY OF NANOMEDICINE:  
THE LITTLE DROP OF FLUID THAT COULD** ..... 102  
Abraham P. Lee, A.T.-H. Hsieh, A. Tovar, and K. Hettiarachchi  
*University of California, Irvine, USA*

### Session 8 - Bio Analysis

Session Chair: S. Casalnuovo, *Sandia National Laboratories, USA*

9:00 a.m. **DISCONTINUOUS NANOPOROUS STRUCTURES ENABLE  
LOW-POWER ELECTROPHORETIC IMMUNOASSAYS OF  
SERUM PROTEIN BIOMARKERS** ..... 106  
C. Hou and A.E. Herr  
*University of California, Berkeley, USA*

9:25 a.m. **PHARMASAT: DRUG DOSE DEPENDENCE RESULTS FROM  
AN AUTONOMOUS MICROSYSTEM-BASED SMALL  
SATELLITE IN LOW EARTH ORBIT** ..... 110  
A.J. Ricco<sup>1</sup>, M. Parra<sup>1</sup>, M. Piccini<sup>1</sup>, D. Ly<sup>1</sup>, D. Niesel<sup>2</sup>, M. McGinnis<sup>2</sup>, A. Kudlicki<sup>2</sup>,  
J.W. Hines<sup>1</sup>, L. Timucin<sup>1</sup>, C. Beasley<sup>1</sup>, R. Ricks<sup>1</sup>, M. McIntyre<sup>1</sup>, C. Friedericks<sup>1</sup>,  
M. Henschke<sup>1</sup>, R. Leung<sup>1</sup>, M. Diaz-Aguado<sup>1</sup>, C. Kitts<sup>3</sup>, I. Mas<sup>3</sup>, R. Rasay<sup>3</sup>,  
E. Agasid<sup>1</sup>, E. Luzzi<sup>1</sup>, K. Ronzano<sup>1</sup>, D. Squires<sup>1</sup>, and B. Yost<sup>1</sup>  
<sup>1</sup>NASA Ames Research Center, USA, <sup>2</sup>University of Texas Medical Branch, USA, and  
<sup>3</sup>Santa Clara University, USA

9:50 a.m. **AUTOMATED PROTEIN IMMUNOBLOTTING BY  
PHOTOPATTERNING OF POLYACRYLAMIDE  
GEL IN TWO-DIMENSIONAL MICRODEVICE** ..... 114  
M. He and A.E. Herr  
*University of California, Berkeley, USA*

10:15 a.m. **Break and Tabletop Exhibits**

## Session 9 – Actuators

Session Chair: J. Hammond, *RFMD, USA*

- 10:40 a.m. **RADIAL THERMOELECTRIC GENERATOR MODULES FOR IN-LINE POWER GENERATION FROM HOT GAS STREAMS** ..... 118  
I. Boniche and D.P. Arnold  
*University of Florida, USA*
- 11:05 a.m. **ELECTROLYSIS-BASED INCHWORM ACTUATORS** ..... 122  
L. Giacchino and Y.-C. Tai  
*California Institute of Technology, USA*
- 11:30 a.m. **NANOENERGETIC SILICON AS A THRUST ACTUATOR FOR JUMPING MICROROBOTS** ..... 126  
L.J. Currano<sup>1</sup>, W.A. Churaman<sup>1</sup>, J. Rajkowski<sup>2</sup>, C.J. Morris<sup>1</sup>, and S. Bergbreiter<sup>2</sup>  
<sup>1</sup>*U.S. Army Research Laboratory, USA* and <sup>2</sup>*University of Maryland, USA*
- 11:55 a.m. **PARAMETER SWEEP STRATEGIES FOR SENSING USING BIFURCATIONS IN MEMS** ..... 130  
C.B. Burgner<sup>1</sup>, K.L. Turner<sup>1</sup>, N.J. Miller<sup>2</sup>, and S.W. Shaw<sup>2</sup>  
<sup>1</sup>*University of California, Santa Barbara, USA* and <sup>2</sup>*Michigan State University, USA*
- 12:20 p.m. **Networking Lunch and Workshop Adjourns**  
- 2:00 p.m.

**Poster/Oral Session 1**  
**Contributed and Late News**  
Monday, June 7  
2:30 p.m. - 4:00 p.m.

**Bio-Inspiration and Biomedical Devices**

- P1 **3D NEURAL PROBES WITH COMBINED ELECTRICAL AND CHEMICAL INTERFACES** ..... 134  
Y. Li, J. John, X. Zhang, J. Zhang, J.A. Loeb, and Y. Xu  
*Wayne State University, USA*
- P2 **LARGE AREA SPRAYING OF TERAHERTZ MATERIALS ON FREE-STANDING BIOCOMPATIBLE SILK FILMS** ..... 138  
H. Tao<sup>1</sup>, J. Amsden<sup>2</sup>, A. Strikwerda<sup>1</sup>, K. Fan<sup>1</sup>, D.L. Kaplan<sup>2</sup>, F.G. Omenetto<sup>2</sup>,  
R.D. Averitt<sup>1</sup>, and X. Zhang<sup>1</sup>  
*<sup>1</sup>Boston University, USA and <sup>2</sup>Tufts University, USA*
- P3 **POLYCRYSTALLINE DIAMOND-ON-POLYMER MICROELECTRODE ARRAYS FOR MECHANICALLY-FLEXIBLE NEURAL INTERFACING** ..... 142  
A. Hess, D. Sabens, H.B. Martin, and C.A. Zorman  
*Case Western Reserve University, USA*

**Gas Sensors**

- P4 **MICROCANTILEVER ARRAY SENSORS USING NANOPOROUS METAL-ORGANIC FRAMEWORKS (MOFs) FOR GAS DETECTION** ..... 146  
J.-H. Lee<sup>1</sup>, R.J. Houk<sup>2</sup>, J.A. Greathouse<sup>2</sup>, M.D. Allendorf<sup>2</sup>, and P.J. Hesketh<sup>1</sup>  
*<sup>1</sup>Georgia Institute of Technology, USA and <sup>2</sup>Sandia National Laboratories, USA*
- P5 **POROUS SILICON RESONATOR FOR SENSITIVE VAPOR DETECTION** ..... 150  
Y. Hwang, F. Gao, and R.N. Candler  
*University of California, Los Angeles, USA*

**Microfluidics**

- P6 **A MICROFLUIDIC PLATFORM FOR THE FLUIDIC ISOLATION AND OBSERVATION OF CELLS CHALLENGED WITH PATHOGENS** ..... 154  
C.D. James<sup>1</sup>, M.W. Moorman<sup>1</sup>, B.D. Carson<sup>1</sup>, J. Joo<sup>2</sup>, C.S. Branda<sup>1</sup>, R.P. Manginell<sup>1</sup>,  
J. Lantz<sup>3</sup>, R. Renzi<sup>1</sup>, A. Martino<sup>1</sup>, and A.K. Singh<sup>1</sup>  
*<sup>1</sup>Sandia National Laboratories, USA, <sup>2</sup>University of Tennessee, USA, and <sup>3</sup>GAITS, USA*
- P7 **A MONOLITHIC EWOD CHIP BY SURFACE MICROMACHINING** ..... 158  
W.C. Nelson and C.J. Kim  
*University of California, Los Angeles, USA*

P8	<b>AN ESCHERICHIA COLI CONCENTRATOR USING MAGNETIC PARTICLES IN A MICROFLUIDIC CHANNEL FOR THE URINARY TRACT INFECTION (UTI) APPLICATION</b> .....	162
	Y. Yang, S. Kim, and J. Chae <i>Arizona State University, USA</i>	
P9	<b>LOW PRESSURE DROP MICRO PRECONCENTRATORS WITH A COBWEB TENAX-TA FILM</b> .....	166
	B. Alfeeli <sup>1,2</sup> and M. Agah <sup>1</sup> <sup>1</sup> <i>Virginia Polytechnic Institute and State University, USA and</i> <sup>2</sup> <i>Kuwait Institute for Scientific Research, KUWAIT</i>	
P10	<b>LUMPED-ELEMENT ANALYSIS OF AN ELECTROSTATIC SQUEEZE-FILM MEMS DROPLET EJECTOR</b> .....	170
	E.P. Furlani <sup>1</sup> , H.V. Panchawagh <sup>1</sup> , and T.L. Sounart <sup>2</sup> <sup>1</sup> <i>Eastman Kodak Company, USA and</i> <sup>2</sup> <i>Sandia National Laboratories, USA</i>	
P11	<b>SURFACE MEDIATED FLOWS IN GLASS NANOFLUIDIC DEVICES</b> .....	174
	S. Prakash and M.B. Karacor <i>Ohio State University, USA</i>	
P12	<b>THREE-DIMENSIONAL TIME RESOLVED MEASUREMENTS OF CHARGED QUANTUM DOTS IN NANOCONFINED CHANNELS USING TOTAL INTERNAL REFLECTION FLUORESCENCE MICROSCOPY (TIRFM)</b> .....	178
	T.M. Wynne and S. Pennathur <i>University of California, Santa Barbara, USA</i>	

### **Modeling, Characterization, Fabrication and Materials**

P13	<b>A HYBRID TECHNOLOGY FOR Pt-Rh AND SS316L HIGH POWER MICRO-RELAYS</b> .....	182
	F.M. Ozkeskin and Y.B. Gianchandani <i>University of Michigan, USA</i>	
P14	<b>A STUDY ON NONLINEAR DYNAMICS OF MEMS INERTIAL SENSOR UNDER OVERLOAD CONDITIONS</b> .....	186
	D. Lin, T. Miller, and K. Suryanarayanan <i>Freescale Semiconductor, Inc., USA</i>	
P15	<b>AN SPM-BASED CONTACT TESTER FOR STUDY OF MICROCONTACTS</b> .....	190
	L. Chen <sup>1</sup> , Z.J. Guo <sup>2</sup> , N. Joshi <sup>1</sup> , H. Eid <sup>1</sup> , G.G. Adams <sup>1</sup> , and N.E. McGruer <sup>1</sup> <sup>1</sup> <i>Northeastern University, USA and</i> <sup>2</sup> <i>University of Pennsylvania, USA</i>	
P16	<b>ATOMIC LAYER DEPOSITED ALUMINA FOR USE AS AN ETCH BARRIER AGAINST XENON DIFLUORIDE ETCHING</b> .....	194
	G.L. Smith <sup>1</sup> , R.G. Polcawich <sup>1</sup> , J.S. Pulskamp <sup>1</sup> , T. Waggoner <sup>2</sup> , and J.F. Conley, Jr. <sup>2</sup> <sup>1</sup> <i>US Army Research Laboratory, USA and</i> <sup>2</sup> <i>Oregon State University, USA</i>	



P17	<b>CONTACT GEOMETRY EFFECTS ON FRICTION IN MEMS PROBE ARRAYS</b> .....	198
	W.S. Smith <sup>1</sup> , P.G. Hartwell <sup>2</sup> , R.G. Walmsley <sup>2</sup> , and T.W. Kenny <sup>1</sup> <i><sup>1</sup>Stanford University, USA and <sup>2</sup>HP Labs, USA</i>	
P18	<b>FABRICATION OF MULTIPLE HEIGHT MICROPROBES USING UV LITHOGRAPHY ON TIMED-DEVELOPMENT-AND-THERMAL-REFLOWED PHOTORESIST</b> .....	202
	J.K. Kim, H.C. Ahn, X. Cheng, K.-T. Kim, G.-H. Kim, and Y.K. Yoon <i>University at Buffalo, The State University of New York, USA</i>	
P19	<b>HIGH CURRENT PROPERTIES OF A MICROSPRING CONTACT FOR FLIP CHIP PACKAGING</b> .....	206
	B. Cheng <sup>1,2</sup> , E.M. Chow <sup>1</sup> , D. DeBruyker <sup>1</sup> , I. Shubin <sup>3</sup> , J. Cunningham <sup>3</sup> , A. Chow <sup>3</sup> , J. Shi <sup>3</sup> , M. Griere <sup>3</sup> , and K.F. Bohringer <sup>2</sup> <i><sup>1</sup>Palo Alto Research Center, Inc., USA, <sup>2</sup>University of Washington, USA, and <sup>3</sup>Oracle, USA</i>	
P20	<b>LITHOGRAPHICAL PATTERNING AND CARBONIZATION OF ELECTROSPUN SU-8 NANOFIBERS FOR A HIGH CAPACITY ELECTRODE</b> .....	210
	G.-H. Kim, G.J. Kim, and Y.-K. Yoon <i>University at Buffalo, The State University of New York, USA</i>	
P21	<b>OHMIC CONTACT WITH ENHANCED STABILITY TO POLYCRYSTALLINE SILICON CARBIDE VIA CARBON INTERFACIAL LAYER</b> .....	214
	F. Liu, B. Hsia, D.G. Senesky, C. Carraro, A.P. Pisano, and R. Maboudian <i>University of California, Berkeley, USA</i>	
P22	<b>ONE MASK ONE EXPOSURE IN-SITU MAGNETIC ACTUATOR FABRICATION METHOD</b> .....	218
	S.E. Chung, J. Kim, S. Min, L.N. Kim, and S. Kwon <i>Seoul National University, KOREA, SOUTH</i>	
P23	<b>SELF-POWERED ION GAUGE AND SELF-POWERED ION PUMP</b> .....	222
	Y. Lu and A. Lal <i>Cornell University, USA</i>	
P24	<b>VERTICAL PILLAR ARRAYS AS PLASMON NANOCAVITIES</b> .....	226
	M. Bora, B.J. Fasenfest, E.M. Beheymer, A.S.-P. Chang, H.T. Nguyen, J.A. Britten, C.C. Larson, and T.C. Bond <i>Lawrence Livermore National Lab, USA</i>	

## Physical and Optical Sensors and Devices

- P25 **A BIAxIAL MICROMIRROR FOR ANGULAR AND DEPTH SCANNING IN OPTICAL COHERENCE TOMOGRAPHY (OCT)** ..... 230  
U. Izhar<sup>1</sup>, B.S. Ooi<sup>2</sup>, and S. Tatic-Lucic<sup>1</sup>  
<sup>1</sup>*Lehigh University, USA and*  
<sup>2</sup>*King Abdullah University of Science and Technology (KAUST), SAUDI ARABIA*
- P26 **ACOUSTIC TRANSDUCERS BUILT ON EDGE-RELEASED MEMS STRUCTURES** ..... 234  
S.-J. Chen, Y.K. Choe, and E.S. Kim  
*University of Southern California, USA*
- P27 **FABRICATION AND ELECTRICAL CHARACTERIZATION OF MICROSCALE DIELECTRIC BARRIER DISCHARGE DEVICES** ..... 238  
J.C. Zito and D.P. Arnold  
*University of Florida, USA*
- P28 **INTEGRATED VERTICAL PARALLEL PLATE CAPACITIVE HUMIDITY SENSOR** ..... 242  
N. Lazarus and G.K. Fedder  
*Carnegie Mellon University, USA*
- P29 **MICROMACHINED MULTIFUNCTIONAL PIEZOELECTRIC T-BEAM TRANSDUCERS** ..... 246  
Z. Zhang, K. Mateti, C.D. Rahn, and S. Tadigadapa  
*Pennsylvania State University, USA*
- P30 **PIEZORESISTIVE MICROCANTILEVERS FROM ULTRANANOCRYSTALLINE DIAMOND** ..... 250  
N.L. Privorotskaya<sup>1</sup>, H. Zeng<sup>2</sup>, J.A. Carlisle<sup>2</sup>, R. Bashir<sup>1</sup>, and W.P. King<sup>1</sup>  
<sup>1</sup>*University of Illinois, Urbana-Champaign, USA and*  
<sup>2</sup>*Advanced Diamond Technologies, USA*
- P31 **THIN SILICON MEMS CONTACT-STRESS SENSOR** ..... 254  
J. Kotovsky<sup>1</sup>, A.C. Tooker<sup>1</sup>, and D.A. Horsley<sup>2</sup>  
<sup>1</sup>*Lawrence Livermore National Lab, USA and* <sup>2</sup>*University of California, Davis, USA*

## Late News

- P32 **A FULLY-PASSIVE WIRELESS MICROFABRICATED NEURO-RECORDER** ..... 258  
H.N. Schwerdt, W. Xu, S. Shekhar, A. Abbaspour-Tamijani, B.C. Towe, and J. Chae  
*Arizona State University, USA*
- P33 **NOVEL METHOD OF PROTECTING AND CONNECTING CMOS CHIPS ENABLES NETWORKED PACING LEADS** ..... 260  
R. Azevedo, B. Costello, J. Frank, M. Jensen, T. Thompson, and M. Zdeblick  
*Proteus Biomedical, Inc, USA*

P34	<b>NUMERICAL MODELING AND EXPERIMENTAL VERIFICATIONS OF SINGLE-STEP, DEPOSITION-FREE, HERMETIC SEALING USING SILICON MIGRATION</b> .....	<b>262</b>
	R. Kant and H. Choo <i>Lawrence Berkeley National Laboratory, USA</i>	
P35	<b>SILICON MICROMACHINING TECHNIQUES FOR SUBMILLIMETER WAVE APPLICATIONS</b> .....	<b>264</b>
	C. Lee, B. Thomas, G. Chattopadhyay, A. Peralta, R. Lin, C. Jung, and I. Mehdi Jet Propulsion Laboratory, USA	

**Poster Session 2**  
**Contributed and Late News**  
Monday, June 7  
4:00 p.m. - 5:30 p.m.

**Bio-Inspiration and Biomedical Devices**

- P36 **A MONOLITHIC MICRO DEVICE FOR GLUCOSE-RESPONSIVE INSULIN DELIVERY** ..... 266  
J. Chen, C.R. Gordijo, M. Chu, X.Y. Wu, and Y. Sun  
*University of Toronto, CANADA*
- P37 **MANDUCA SEXTA OLFACTORY NEURAL INTERFACE** ..... 270  
C.J. Shen, A. Ramkumar, A. Lal, and R.F. Gilmour  
*Cornell University, USA*
- P38 **SENSING SINGLE CELL CONTRACTILITY UTILIZING MOIRE FRINGES** ..... 274  
X.Y. Zheng<sup>1</sup>, H. Surks<sup>2</sup>, and X. Zhang<sup>1</sup>  
<sup>1</sup>*Boston University, USA* and <sup>2</sup>*Tufts Medical Center, USA*

**Gas Sensors**

- P39 **MICROFABRICATED GAS CHROMATOGRAPH FOR SUB-PPB DETERMINATIONS OF TCE IN VAPOR INTRUSION INVESTIGATIONS** ..... 278  
H.W. Chang, S.K. Kim, T. Sukaew, F. Bohrer, and E.T. Zellers  
*University of Michigan, USA*

**Microfluidics**

- P40 **A MICROMACHINED CLOG-FREE EJECTOR FOR LONG-TERM RELIABLE HYDROGEL PRINTING** ..... 282  
R. Almeida and J.W. Kwon  
*University of Missouri, USA*
- P41 **CHARACTERIZATION OF COLLOIDAL SYSTEMS IN A STANDALONE PZT-GLASS CAPILLARY MICROFLUIDIC ULTRASONIC TWEEZER** ..... 286  
M.K. Araz and A. Lal  
*Cornell University, USA*
- P42 **ELASTOMERIC RESERVOIR FOR MEMS-BASED TRANSDERMAL DRUG DELIVERY SYSTEMS** ..... 290  
C.T. Smith<sup>1</sup>, P. Wei<sup>1</sup>, M. Mojarrad<sup>2</sup>, M. Chiappetta<sup>2</sup>, B. Ziaie<sup>1</sup>, and M.P. Rao<sup>3</sup>  
<sup>1</sup>*Purdue University, USA*, <sup>2</sup>*Eli Lilly & Company, USA*, and <sup>3</sup>*University of California, Riverside, USA*

P43	<b>FLOW RATE INSENSITIVE THERMAL CONDUCTIVITY DETECTOR</b> .....	294
	B.C. Kaanta <sup>1</sup> , H. Chen <sup>2</sup> , and X. Zhang <sup>1</sup> <i><sup>1</sup>Boston University, USA and <sup>2</sup>Schlumberger Doll Research, USA</i>	
P44	<b>NANOPARTICLE SEPARATION AND METROLOGY BY THREE-DIMENSIONAL NANOFLUIDIC SIZE EXCLUSION</b> .....	298
	S.M. Stavis, J. Geist, and M. Gaitan <i>National Institute of Standards and Technology, USA</i>	
P45	<b>PLANAR PHOSPHOLIPID MEMBRANES IN MICROFLUIDICS ENABLING KINETICS STUDIES OF CERAMIDE CHANNELS</b> .....	302
	C. Shao, M. Colombini, and D.L. DeVoe <i>University of Maryland, USA</i>	

### **Modeling, Characterization, Fabrication and Materials**

P46	<b>A LARGE-SCALE FLEXIBLE MOLDING TECHNOLOGY FOR PRODUCING BIOMIMETIC DRY ADHESIVES IN MULTIPLE MATERIALS USING A COMMERCIAL ACRYLIC MASTER</b> .....	304
	D.E. Sameoto <sup>1</sup> and C. Menon <sup>2</sup> <i><sup>1</sup>University of Alberta, CANADA and <sup>2</sup>Simon Fraser University, CANADA</i>	
P47	<b>APPLICATION OF MILLISECOND PULSED LASER WELDING IN MEMS PACKAGING</b> .....	308
	P. Bozorgi, C.B. Burgner, Z. Yie, C. Ding, K.L. Turner, and N.C. MacDonald <i>University of California, Santa Barbara, USA</i>	
P48	<b>CHARACTERIZATION OF THE COMPLETE STRESS STATE IN THIN FILM CMOS LAYERED MATERIALS</b> .....	312
	F. Fachin <sup>1</sup> , M. Varghese <sup>2</sup> , S.A. Nikles <sup>2</sup> , and B.L. Wardle <sup>1</sup> <i><sup>1</sup>Massachusetts Institute of Technology, USA and <sup>2</sup>MEMSIC Inc., USA</i>	
P49	<b>DERIVING A SIMULATION MODEL OF A SINGLE 40-KHZ CMUT CELL FROM IMPEDANCE AND INTERFEROMETER MEASUREMENTS</b> .....	316
	I.O. Wygant <sup>1,2</sup> , M. Kupnik <sup>1</sup> , and B.T. Khuri-Yakub <sup>1</sup> <i><sup>1</sup>Stanford University, USA and <sup>2</sup>National Semiconductor, USA</i>	
P50	<b>ELECTRICAL CHARACTERIZATION OF PECVD SILICON CARBIDE FOR APPLICATION IN MEMS VAPOR HF SACRIFICIAL RELEASE</b> .....	320
	L. Chen <sup>1</sup> , T. Lee <sup>2</sup> , C. Regan <sup>1</sup> , F. Sammoura <sup>1</sup> , C. Tsau <sup>1</sup> , M. Mehregany <sup>2</sup> , K. Nunan <sup>1</sup> , and K. Yang <sup>1</sup> <i><sup>1</sup>Analog Devices Inc., USA and <sup>2</sup>Case Western Reserve University, USA</i>	

P51	<b>GROWTH OF HIGHLY C-AXIS ORIENTED ALN FILMS ON 3C-SIC/SI SUBSTRATE</b> .....	324
	C.-M. Lin <sup>1</sup> , W.-C. Lien <sup>1</sup> , T.-T. Yen <sup>1</sup> , V.V. Felmetsger <sup>2</sup> , D.G. Senesky <sup>1</sup> , M.A. Hopcroft <sup>3</sup> , and A.P. Pisano <sup>1</sup> <sup>1</sup> University of California, Berkeley, USA, <sup>2</sup> Tegal Corporation, USA, and <sup>3</sup> Hewlett-Packard Laboratories, USA	
P52	<b>HIGH PERMEABILITY PERMALLOY FOR MEMS</b> .....	328
	M. Glickman <sup>1</sup> , T. Niblock <sup>2</sup> , J. Harrison <sup>1</sup> , I.B. Goldberg <sup>1</sup> , P. Tseng <sup>1</sup> , and J.W. Judy <sup>1</sup> <sup>1</sup> University of California, Los Angeles, USA and <sup>2</sup> Magzor, Inc., USA	
P53	<b>MICROFABRICATED QUASIPERIODIC OPTICAL DIFFRACTION APERTURE ARRAYS FOR THE NANOMETROLOGY OPTICAL RULER IMAGING SYSTEM</b> .....	332
	N. Yoshimizu, A. Lal, and C.R. Pollock Cornell University, USA	
P54	<b>PACKAGING OF LARGE LATERAL DEFLECTION MEMS USING A COMBINATION OF FUSION BONDING AND EPITAXIAL REACTOR SEALING</b> .....	336
	M. Messana, A.B. Graham, S. Yoneoka, R.T. Howe, and T.W. Kenny Stanford University, USA	
P55	<b>PDMS AND SILICON MICROMECHANISMS IN A MONOLITHIC PROCESS</b> .....	340
	A. Gerratt, I. Penskiy, and S. Bergbreiter University of Maryland, USA	
P56	<b>TIME EVOLUTION OF RELEASED HOLE ARRAYS INTO MEMBRANES VIA VACUUM SILICON MIGRATION</b> .....	344
	J. Provine <sup>1</sup> , N. Ferralis <sup>2</sup> , A.B. Graham <sup>1</sup> , M.W. Messana <sup>1</sup> , R. Kant <sup>3</sup> , R. Maboudian <sup>2</sup> , T.W. Kenny <sup>1</sup> , and R.T. Howe <sup>1</sup> <sup>1</sup> Stanford University, USA, <sup>2</sup> University of California, Berkeley, USA, and <sup>3</sup> University of California, San Francisco, USA	
P57	<b>VERY-HIGH-ASPECT-RATIO MICRO METAL STRUCTURES OF NON-STRAIGHT PATTERNS</b> .....	348
	G. Sun <sup>1</sup> , X. Zhao <sup>2</sup> , and C.-J. Kim <sup>1</sup> <sup>1</sup> University of California, Los Angeles, USA and <sup>2</sup> Nankai University, CHINA	

### Physical and Optical Sensors and Devices

P58	<b>100 NM THICK ALUMINUM NITRIDE BASED PIEZOELECTRIC NANO SWITCHES EXHIBITING 1 MV THRESHOLD VOLTAGE VIA BODY-BIASING</b> .....	352
	N. Sinha <sup>1</sup> , Z. Guo <sup>1</sup> , V.V. Felmetsger <sup>2</sup> , and G. Piazza <sup>1</sup> <sup>1</sup> University of Pennsylvania, USA and <sup>2</sup> Tegal Corporation, USA	

P59	<b>A PLANAR, INTEGRATED TOTAL INTERNAL REFLECTION SENSOR FOR BIOFOULING DETECTION</b> .....	<b>356</b>
	K.H. Nam <sup>1,2</sup> , W. Choi <sup>3</sup> , J. Yeo <sup>4</sup> , S.H. Ko <sup>4</sup> , and L. Lin <sup>1</sup> <i><sup>1</sup>University of California, Berkeley, USA, <sup>2</sup>Ewha Womens University, KOREA, <sup>3</sup>LG Innotek, KOREA, SOUTH, and <sup>4</sup>Korea Advanced Institute of Science and Technology (KAIST), KOREA, SOUTH</i>	
P60	<b>AN ALUMINUM NITRIDE PIEZOELECTRIC MICROPHONE FOR AEROACOUSTIC APPLICATIONS</b> .....	<b>360</b>
	M.D. Williams, B.A. Griffin, A. Ecker, J. Meloy, and M. Sheplak <i>University of Florida, USA</i>	
P61	<b>LOW-COST THERMAL MEMS GYROSCOPE</b> .....	<b>364</b>
	A.M. Leung <i>Simon Fraser University, CANADA</i>	
P62	<b>PASSIVE WIRELESS DIRECT SHEAR STRESS MEASUREMENT</b> .....	<b>368</b>
	J. Sells, V. Chandrasekharan, H. Zmuda, M. Sheplak, and D.P. Arnold <i>University of Florida, USA</i>	
P63	<b>REAL-TIME HERMITICITY DETECTION USING TITANIUM DIOXIDE THIN FILM RESISTORS AS BOTH OXYGEN AND PRESSURE SENSORS</b> .....	<b>372</b>
	F. Sammoura and K. Yang <i>Analog Devices Inc., USA</i>	
P64	<b>WICKING OPTIMIZATION FOR THERMAL COOLING - WITH A TITANIUM BASED FLAT HEAT PIPE SYSTEM</b> .....	<b>376</b>
	C. Ding, P. Bogorzi, M. Sigurdson, C.D. Meinhart, and N.C. MacDonald <i>University of California, Santa Barbara, USA</i>	

#### Late News

P65	<b>A WIRELESS-ENABLED RADIATION DETECTOR USING MICROMACHINED STEEL AND GLASS ELEMENTS IN A TO-5 PACKAGE</b> .....	<b>380</b>
	C.K. Eun and Y.B. Gianchandani <i>University of Michigan, USA</i>	
P66	<b>BIOINSPIRED WATER-ENHANCED ACCELERATION SENSING USING ARTIFICIAL HAIRCELL SENSOR</b> .....	<b>382</b>
	H. Hu and C. Liu <i>Northwestern University, USA</i>	
P67	<b>HETERODYNED ELECTROSTATIC TRANSDUCTION OSCILLATORS EVADE LOW FREQUENCY NOISE ALIASING</b> .....	<b>384</b>
	G. Bahl <sup>1</sup> , J. Salvia <sup>1</sup> , H.K. Lee <sup>1</sup> , R. Melamud <sup>2</sup> , B. Kim <sup>3</sup> , R.T. Howe <sup>1</sup> , and T.W. Kenny <sup>1</sup> <i><sup>1</sup>Stanford University, USA, <sup>2</sup>SiTime Corporation, USA, and <sup>3</sup>Sandia National Laboratories, USA</i>	

P68	<b>HIGH ASPECT RATIO TRANSMISSION LINES MICROMACHINED IN SILICON WITH LARGE THERMAL OXIDE DIELECTRICS .....</b>	<b>386</b>
	S.T. Todd, J.E. Bowers, and N.C. MacDonald <i>University of California, Santa Barbara, USA</i>	
P69	<b>LOW TEMPERATURE QUALITY FACTOR SCALING OF GHz FREQUENCY SILICON RESONATORS .....</b>	<b>388</b>
	E. Hwang and S.A. Bhave <i>Cornell University, USA</i>	
P70	<b>TWO DEGREE OF FREEDOM PZT MEMS ACTUATED FLAPPING WINGS WITH INTEGRATED FORCE SENSING .....</b>	<b>390</b>
	J.S. Pulskamp, G.L. Smith, R.G. Polcawich, C.M. Kroninger, and E.D. Wetzel <i>U.S. Army Research Laboratory, USA</i>	



**Poster/Oral Session 3**

**Contributed**

Wednesday, June 9

5:00 p.m. - 6:30 p.m.

**Actuators**

- P71 **A STUDY OF MICROMACHINED DISPLACEMENT PUMPS FOR VACUUM GENERATION** ..... 392  
H. Zhou, V. Sharma, H. Li, and M.A. Schmidt  
*Massachusetts Institute of Technology, USA*
- P72 **A WIRELESSLY CONTROLLED SHAPE-MEMORY-ALLOY MEMS GRIPPER MICROFABRICATED USING AN ELECTROPLATING-BASED BONDING PROCESS** ..... 396  
M.S. Mohamed Ali<sup>1,2</sup> and K. Takahata<sup>1</sup>  
<sup>1</sup>*University of British Columbia, CANADA* and <sup>2</sup>*Universiti Teknologi Malaysia, MALAYSIA*
- P73 **CMOS-MEMS 8-BIT MEMDAC NANOPositionER WITH INTEGRATED POSITION SENSING AND DIGITAL CONTROL** ..... 400  
N. Sarkar and R. Mansour  
*University of Waterloo, CANADA*
- P74 **HIGH-SPEED AXIAL-FLUX PERMANENT MAGNET MICROMOTORS WITH ELECTROPLATED WINDINGS** ..... 404  
F. Herrault, P. Galle, and M.G. Allen  
*Georgia Institute of Technology, USA*
- P75 **SINGLE-LAYER ELASTOMERIC OUT-OF-PLANE ACTUATOR WITH ASYMMETRIC SURFACE PROFILE** ..... 408  
T. Maleki, G. Chitnis, A. Panja, and B. Ziaie  
*Purdue University, USA*

**Biological Diagnostics, Systems, and Analysis**

- P76 **A CHEMOMECHANICAL NANOMACHINE FOR SENSING AND ACTUATION BASED ON A BIASED BROWNIAN RATCHET ARCHITECTURE** ..... 412  
G. Lavella<sup>1</sup>, R. Morfino<sup>2</sup>, and M.M. Maharbiz<sup>1</sup>  
<sup>1</sup>*University of California, Berkeley, USA* and <sup>2</sup>*Polytechnic University of Turin, ITALY*
- P77 **DISPOSABLE IMMUNOASSAY CHIPS FOR HIV MONITORING IN RESOURCE-CONSTRAINED ENVIRONMENTS** ..... 415  
C.-F. Chen<sup>1,2</sup>, J. Liu<sup>1</sup>, E. Wong<sup>3</sup>, C.-C. Chang<sup>2</sup>, I. Hewlett<sup>3</sup>, and D.L. DeVoe<sup>1</sup>  
<sup>1</sup>*University of Maryland, USA*, <sup>2</sup>*National Taiwan University, TAIWAN*, and <sup>3</sup>*U.S. Food and Drug Administration, USA*

P78	<b>FAST AND MINIMALLY-INVASIVE TUMOR MARGIN DETECTION USING A NOVEL MICROMACHINED “SIDE-VIEWING” OIDS PROBE</b> .....	418
	C.-C. Chang <sup>1</sup> , A. Garcia-Urbe <sup>1</sup> , J. Zou <sup>1</sup> , L.V. Wang <sup>2</sup> , B. Banerjee <sup>3</sup> , and J. Kuczynski <sup>3</sup> <sup>1</sup> Texas A&M University, USA, <sup>2</sup> Washington University, St. Louis, USA, and <sup>3</sup> University of Arizona College of Medicine, USA	
P79	<b>HUMAN TEAR FLUID DIAGNOSTIC ASSESSMENT ENABLED BY MICROFLUIDIC PROTEIN ELECTROPHORESIS</b> .....	422
	K. Karns, A. Denisin, and A.E. Herr <i>University of California, Berkeley, USA</i>	
P80	<b>ISOELECTRIC FOCUSING – MULTIPLEXED REVERSED PHASE LIQUID CHROMATOGRAPHY – MALDI-TOF MASS SPECTROMETRY IN A MICROVALVE-INTEGRATED POLYMER CHIP</b> .....	426
	J. Liu <sup>1</sup> , C.-C. Chen <sup>1</sup> , C.-C. Chang <sup>2</sup> , and D.L. DeVoe <sup>1</sup> <sup>1</sup> University of Maryland, USA and <sup>2</sup> National Taiwan University, TAIWAN	
P81	<b>MICROFABRICATED SUBSTRATES FOR THE REMOTE GENERATION OF PRECISION FORCES ON SINGLE CELLS VIA INTRACELLULAR MAGNETIC FLUORESCENT NANOPARTICLES</b> .....	428
	P. Tseng, J.W. Judy, and D. Di Carlo <i>University of California, Los Angeles, USA</i>	
P82	<b>ON-CHIP PCR WITH FREE-STANDING PARYLENE CHANNEL</b> .....	431
	P. Satsanarukkit, H. Lo, Q. Quach, and Y.C. Tai <i>California Institute of Technology, USA</i>	
P83	<b>STRETCHABLE TACTILE SENSING SKIN FOR INTELLIGENT PROSTHETIC LIMBS</b> .....	435
	S. Zhao, H. Hu, and C. Liu <i>Northwestern University, USA</i>	
P84	<b>THE CAPTURE AND 3-D CULTURE OF VIABLE CIRCULATING TUMOR CELLS USING HIGH OPEN-FACTOR PARYLENE-C/HT MEMBRANE FILTERS</b> .....	439
	B. Lu <sup>1</sup> , T. Xu <sup>2</sup> , A. Goldkorn <sup>2</sup> , and Y.C. Tai <sup>1</sup> <sup>1</sup> California Institute of Technology, USA and <sup>2</sup> University of Southern California, USA	

## **Power Generation and Management**

P85	<b>ALL-SOLID-STATE 3-D RECHARGEABLE LITHIUM BATTERIES WITH SILICON ROD STRUCTURED ELECTRODE</b> .....	443
	J. Wang, J.E. Trevey, S.H. Lee, and V.M. Bright <i>University of Colorado, USA</i>	

- P86 **HIGHLY EFFICIENT IONIC WIND-BASED COOLING MICROFABRICATED DEVICE FOR MICROCHIP COOLING APPLICATIONS** ..... 447  
A. Ongkodjojo, R.C. Roberts, A. Abramson, and N.C. Tien  
*Case Western Reserve University, USA*
- P87 **MATERIAL DISTRIBUTION DESIGN FOR A PIEZOELECTRIC ENERGY HARVESTER DISPLAYING GEOMETRIC NONLINEARITY** ..... 451  
M.A. Philippine, C.-F. Chiang, J. Salvia, C.M. Jha, S. Yoneoka, and T.W. Kenny  
*Stanford University, USA*
- P88 **MICROMACHINED THICK-FILM COPPER POWER INDUCTORS AND TRANSFORMERS FOR INTEGRATED POWER CONVERTERS** ..... 455  
C.D. Meyer<sup>1,2</sup>, S.S. Bedair<sup>1</sup>, B.C. Morgan<sup>1</sup>, and D.P. Arnold<sup>2</sup>  
<sup>1</sup>*U.S. Army Research Laboratory, USA* and <sup>2</sup>*University of Florida, USA*

### **Resonant Devices**

- P89 **ACOUSTIC RESONANCE IN AN INDEPENDENT-GATE FINFET** ..... 459  
D. Weinstein<sup>1</sup> and S.A. Bhave<sup>2</sup>  
<sup>1</sup>*Massachusetts Institute of Technology, USA* and <sup>2</sup>*Cornell University, USA*
- P90 **CAPACITIVE-PIEZO TRANSDUCERS FOR HIGHER Q CONTOUR-MODE ALN RESONATORS AT 1.2 GHZ** ..... 463  
L.-W. Hung and C.T.-C. Nguyen  
*University of California, Berkeley, USA*
- P91 **CAPACITIVELY TRANSDUCED MICROMECHANICAL RESONATORS WITH SIMULTANEOUS LOW MOTIONAL RESISTANCE AND Q > 70,000** ..... 467  
M. Akgul, B. Kim, Z. Ren, and C.T.-C. Nguyen  
*University of California, Berkeley, USA*
- P92 **GHZ RANGE NANOSCALED ALN CONTOUR-MODE RESONANT SENSORS (CMR-S) WITH SELF-SUSTAINED CMOS OSCILLATOR** ..... 471  
M. Rinaldi, C. Zuniga, C. Zuo, and G. Piazza  
*University of Pennsylvania, USA*
- P93 **Q AMPLIFICATION IN GALLIUM NITRIDE THICKNESS-MODE FILTERS USING ACOUSTOELECTRIC EFFECT** ..... 475  
V.J. Gokhale, Y. Shim, V.A. Thakar, and M. Rais-Zadeh  
*University of Michigan, USA*
- P94 **QUALITY FACTOR SENSITIVITY TO CRYSTALLOGRAPHIC AXIS MISALIGNMENT IN SILICON MICROMECHANICAL RESONATORS** ..... 479  
A.K. Samarao and F. Ayazi  
*Georgia Institute of Technology, USA*

- P95 **SENSITIVITY ENHANCEMENT USING PARAMETRIC AMPLIFICATION IN A RESONANT SENSING ARRAY** ..... 483  
Z. Yie<sup>1</sup>, K.L. Turner<sup>1</sup>, N.J. Miller<sup>2</sup>, and S.W. Shaw<sup>2</sup>  
*<sup>1</sup>University of California, Santa Barbara, USA and <sup>2</sup>Michigan State University, USA*
- P96 **VACUUM ENCAPSULATED RESONATORS FOR HUMIDITY MEASUREMENT** ..... 487  
R.G. Hennessy, M.M. Shulaker, R. Melamud, N. Klejwa, S.A. Chandorkar, B.S. Kim,  
J. Provine, T.W. Kenny, and R.T. Howe  
*Stanford University, USA*

# BOSCH-DRIE SHAPING MEMS – HISTORY, APPLICATIONS AND FUTURE DIRECTIONS

*Franz Laermer<sup>1</sup> and Andrea Urban<sup>2</sup>*

<sup>1</sup>Robert Bosch GmbH, Corporate Research Microsystems, Stuttgart, Germany

<sup>2</sup>Robert Bosch GmbH, Engineering Sensor Process Technology, Reutlingen, Germany

## ABSTRACT

Deep Reactive Ion Etching (DRIE) is virtually shaping the MEMS-field. The basic technology originally developed at Bosch is free from the design restrictions and compatibility problems related to the old wet-etching technology which was based on potassium hydroxide (KOH-) solution. The technology has enabled a wide range of new devices like the inertial sensors for acceleration and yaw rate detection, pressure sensors for mid- to high-pressure applications, MEMS microphones, micro-mirrors and quite recently also timing devices fabricated in silicon. These products conquered both the automotive application area, and later on also the consumer field. From the surface-near micromachining of the early development stages, DRIE is nowadays heading towards a true 3D-microstructuring. Pressure sensors, microphones and micromirrors represent first examples of this trend, but also packaging applications like DRIE-structured silicon caps, functionalized silicon carrier substrates for intelligent systems-in-package, and through-silicon vias (TSV's) for chip-stacking and new chip-integration concepts are receiving increasing attention.

This paper leads from the early development phase targeting first high-volume products, to the development of advanced high-rate etching solutions targeting today's new and challenging product families.

## INTRODUCTION

Precise and reproducible microstructuring technologies are the key to the fabrication of arbitrarily shaped silicon devices, e.g. sensors and actuators. From the very beginning of MEMS, device performance features were closely linked to the limitations of the microstructuring technology, which was at the time mostly wet etching in KOH and other alkaline solutions. This technology was suitable for the fabrication of comparatively simple devices like pressure and mass-flow sensors, where etching of rectangular grooves with tilted (111)-sidewalls from the wafer backside was sufficient to produce the required membranes at the wafer frontside, but when it came to more complex geometries, KOH-etching was no longer a good choice. The etching behaviour is selective on crystal orientation, with fast etching crystal planes like (100) or (110), and slowly etching crystal planes like (111) which normally appear as the structural sidewalls. Corner compensation techniques are often required for non-convex geometries, which significantly restrict design flexibility and depend on process time thus reducing process control.

It became obvious that new microstructuring techniques were needed to overcome the design restrictions and the compatibility problems involved with KOH in a semiconductor infrastructure. The capability to produce arbitrarily shaped geometries in silicon was recognized as a true enabler for MEMS devices of enhanced functionality. Plasma etching was already well-established in IC-manufacturing, and it was also well known that plasma was offering enhanced flexibility with regards to etchable geometries. However, low etching speed (<1  $\mu\text{m}/\text{min}$ ), rapid mask erosion during the etch (selectivities < 15:1), and achievable etching depths of only some  $\mu\text{m}$ 's made it inapplicable to the MEMS specific needs. A significant enhancement of the

existing plasma etching technology to meet the MEMS requirements was achieved by the introduction of the "BOSCH-DRIE" plasma process, which was embraced by the MEMS community as the answer to their long-felt needs.

The "BOSCH-process" provided the high etching-speed and mask selectivities needed at that time (>2 $\mu\text{m}/\text{min}$  and >100:1, respectively), compatibility to standard photoresist masking, IC technology and IC factory infrastructure, as well as vertical sidewalls and minimum critical dimension loss to ensure good reproducibility and high accuracy of critical devices.

## PROCESS TECHNOLOGY

Dependent on process chemistry, etching-speed is closely related to the concentration of radical species or of charged species, the so-called ions, or to both of them. Chlorine or bromine dominated process chemistries do not etch silicon spontaneously at room temperature, at least not at significant rate, for lack of activation energy to keep the etching reaction progressing, and for the need to remove reaction products of low volatility from the wafer surface. The driving factor behind the latter mechanisms is an energetic ion flow to the wafer surface to provide both activation energy and reaction product removal to/from the local etching areas, which requests for large ion concentration or ion density in the plasma as generated e.g. from an ECR-source [1]. Perpendicular directionality of the ion impact onto the wafer surface is the source of anisotropy of the etch, since ions preferentially hit the bottom compared to the sidewalls of a trench. As a consequence, the bottom of a trench etches much faster than the sidewalls in this case. In addition to the intrinsically anisotropic characteristics of a chlorine or bromine etching chemistry, sidewall passivation may be added by deposited sidewall films on a molecular scale, or by oxidation or nitrification of the sidewall surfaces on an atomic scale to improve or tailor profile accuracy and evolution. With ion-impact being the rate-limiting factor, massive ion energy flow is needed to achieve an increase in etch-rate. The latter however accelerates mask material erosion as well. As a general tradeoff, selectivity and critical dimension control are diminishing with a more aggressive ion bombardment for higher etch-rate. This is typical for a situation of an ion-induced etching reaction.

In contrast to the halogens of lower reactivity like chlorine and bromine, fluorine-based chemistry is characterized by an immediate and spontaneous reaction of the fluorine radicals with silicon atoms, once absorbed onto the silicon surface. The reaction products are silicon fluorides, predominantly  $\text{SiF}_4$ , which shows a high volatility and readily leaves the surface without further assistance. At room temperature, no activation energy beyond thermal energies is needed to induce the reaction which is a purely chemical etch. Yielding highly volatile reaction products, no removal mechanism is required to clear the etch bottom from reaction products at room temperature. As a consequence, application of an energetic ion flow to the surface is generally not creating anisotropy of the etch profiles nor accelerating the etching speed significantly. Etching proceeds at any unprotected silicon surface with no preferential orientation, making the etching

profiles highly isotropic. As a particular advantage of the purely chemical etching nature of the fluorine radicals, selectivities may reach extremely high values, and photoresist masking is feasible. Etching speed scales with the amount of fluorine radicals reaching the silicon surface, which requests for a large density of chemically active species rather than ions generated in the plasma. Higher etching-speed from larger fluorine radical concentration levels is not conflicting with photomask stability, as long as the wafer temperature is maintained within certain borders (<100°C).

In MEMS-applications, high anisotropy is a must and directionality needs to be introduced somehow into the etch, except for sacrificial release processes where lateral underetching of fabricated structures is on target and isotropy is welcome. In principle, several options exist to reach anisotropic etching behaviour:

1. Ion-induced reaction mechanism
2. Non-volatile reaction products, which need ion-assistance to clear them off the surface
3. Sidewall passivation by reaction of additives with silicon on an atomic level
4. Sidewall passivation by deposition of thin films on a molecular level

Option 1 is the situation typical for chlorine and bromine based chemistries, see e.g. [1]. It is not applicable to fluorine chemistry (see comparison in [2]).

Option 2 is contributing to the anisotropy of chlorine and bromine etches (together with option 1). It also contributes to the anisotropy of fluorine-based etches at cryogenic temperatures (-100°C and below) [3].

Option 3 is in principle applicable to all halogen chemistries and consists of silicon surface oxidation or nitrification by the appropriate additives like oxygen, nitrogen and/or nitrous oxides. For chlorine and bromine chemistries, this option is often used in combination with 1 to tailor profile details. For fluorine chemistry, this option is relevant for most of the anisotropy observed in cryogenic dry etching (see above), and for the anisotropy achieved in the so-called “black silicon method” [4] at room-temperature. At room-temperature, sufficient stability of the protective layer on the sidewall surface is achieved only for a large excess of the additive gas compared to the fluorine supply gas (sulfur hexafluoride, SF<sub>6</sub>) which is at the cost of etching-speed. At cryogenic temperature, stability of sidewall passivation is increasing and additive gas flow can be reduced to levels more economic with regards to etching-rate [5].

Option 4 is applicable to all halogen chemistries. In older chlorine or bromine based etches, using chlorocarbons (eg. CCl<sub>4</sub>), chlorofluorocarbons (CCl<sub>2</sub>F<sub>2</sub>), bromocarbons (CBr<sub>4</sub>), bromofluorocarbons (CF<sub>3</sub>Br) or bromochlorocarbons (CCl<sub>2</sub>Br<sub>2</sub>) as halogen supply gases, sidewall polymer films were building up from the monomers left behind after splitting off a halogen radical as an etching species. For fluorine chemistries, fluorocarbons (CF<sub>4</sub>, C<sub>2</sub>F<sub>6</sub>, CHF<sub>3</sub>, C<sub>4</sub>F<sub>10</sub>, C<sub>4</sub>F<sub>8</sub>) also split in the plasma into fluorine radicals and remaining monomers, which may or may not build-up polymeric sidewall protective films depending on the amount of excess fluorine. The more excess fluorine available, the faster the achievable etching speed (which depends on free fluorine radical concentration), however the lower the tendency to build up a protective sidewall film. In addition, recombination between fluorine radicals and unsaturated monomers eliminates active species pairwise, and competes with etching silicon and protective sidewall polymer buildup, respectively. This makes a “mixed process” consisting of fluorine delivering and polymer forming

compounds like mixtures of SF<sub>6</sub> and C<sub>4</sub>F<sub>8</sub> both inefficient and difficult to control.

The “Bosch process” overcomes these limitations by generating a high-density plasma remote and decoupled from the wafer combined with a sophisticated etching and passivation scheme, and a low energetic ion impact onto the wafer. Etch and passivation steps are alternating each other separated in the time domain and are controlled independently from each other [6].

During the etching steps, sulfur hexafluoride (SF<sub>6</sub>) readily delivers fluorine radicals after excitation of gas molecules by electron impact from the plasma. During the passivation steps, an unsaturated fluorocarbon gas is excited in the plasma to generate polymer-forming monomers which build up teflon-like protective sidewall films. From a number of potentially suitable fluorocarbons, octafluorocyclobutane (C<sub>4</sub>F<sub>8</sub>) was found to be the best choice.

The discontinuous nature of the process overcomes a number of general problems involved with anisotropic etching: pairwise extinction of etching fluorine radicals and passivating polymer-forming monomers by gas-phase recombination is avoided by separating them in the time-domain. This is of particular importance for the plasma source area itself where high concentration levels of both species are generated and the recombination losses would be strong. Outside the source area, in a more diluted state, the situation is less critical. It was shown by the authors that if separation is maintained mainly for the plasma source, process performance still remains high even with species mixing below the plasma source in the downstream area under conditions of so-called ultrafast gas-pulsing [7].

The nature of the passivating teflon-like polymer requires only low-energetic ion impact during the subsequent etching step for its complete removal from the etching floor. For the low ion energies needed, photoresist and SiO<sub>2</sub>-mask erosion remains very small yielding the high selectivity values needed from the application side.

As a side-effect resulting from the sequence of etching and passivation steps, some sidewall scalloping occurs typically on the order of some 10 nm's. Although undesired in some applications e.g. in the optical domain, sidewall scalloping reduces the risk of silicon spikes formation on the trench floor. In any plasma process of high anisotropy and selectivity, particles or residues of all kind act as micromasks which may yield corresponding silicon patterns if they endure etching long enough. In the “Bosch-process”, micromasks smaller than the scallop-sizes are undercut and extinguished from the surface before leaving their imprint in the silicon. Only if their size is exceeding a critical dimension limit beyond what the process can tolerate (undercut), they will cause undesired patterns on the trench floor.

## EQUIPMENT TECHNOLOGY

From the etch-rate target of several μm/min, it is clear that a high-density plasma source with species densities on the order of 10<sup>12</sup>...10<sup>14</sup> cm<sup>-3</sup> in the plasma generation zone is needed to meet the challenge. In addition, in a pressure regime of several Pa (Pascal) it is easier to reach the required densities of chemically active species, however requesting the plasma source to remain in a high-density plasma mode. In 1990, the only high-density high-pressure plasma source available was the microwave surfatron at 2.45 GHz excitation frequency [8], [9]. Later on, inductively coupled plasma (ICP) sources made their way into the equipment industry, most of them powered at 13.56 MHz radio frequency. Both types of sources show astonishingly similar key performance features. Should plasma source power levels in future exceed 5 kWatts for the extremely high etch-rate conditions, the question

may be raised again whether the microwave magnetron-powered or the RF-powered plasma source is the better option on a longer term. Microwave technology enables virtually unlimited power levels at a very low cost, for reasons of the high-volume production of magnetrons for industrial and commercial heating applications which is driving down prices per kWatt output power to very low levels. In addition, microwave equipment with waveguides, tuning studs, circulator, beam splitters and water load can bear practically any reflected power levels without suffering damage or instability of plasma operation. These facts make it worthwhile to keep a close eye on this potential alternative to the inductively coupled plasma sources as of today. The microwave surfatron or similar constructions may potentially come back in the form of “plasma boosters” upstream of an ICP-source, to generate just huge amounts of neutral radicals in a “chemical reactor”, with the ICP source below adding a homogeneous ion distribution of low-temperature and low-plasma potential to provide directionality in the etching reaction [10].

Today’s dominating plasma source in the equipment industry is the inductively coupled plasma (ICP)-source. The following schematic diagrams are showing three types of ICP-sources: The first one (Fig. 1) which is sometimes also called “transformer coupled plasma” (TCP) is using a planar coil on top of a dielectric window for generation of the plasma. Plasma generation is at relatively close distance to the wafer, which limits applicable power levels (and achievable etching-rates) in a “Bosch”-type process: for power levels above 1 kWatt, hot electrons from the dense plasma are causing etch profile distortions which are correlated with the soft sidewall passivation film. The advantage of this configuration is the uniform plasma potential and charge distribution over the wafer surface, which keeps asymmetric tilting of etched sidewalls extremely small. For the fabrication of micromachined gyroscopes with out-of-plane mode for the detection of Coriolis forces, this is highly beneficial for the reduction of cross-coupling between base vibration mode and detection mode (see later in this paper).

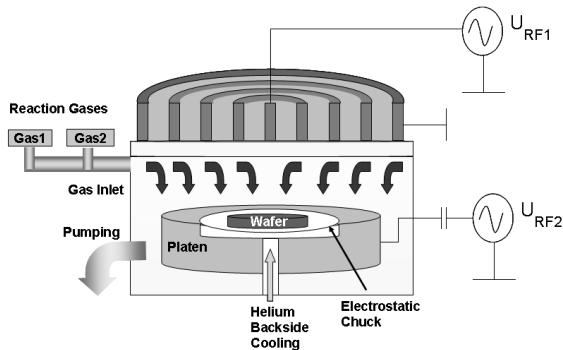


Fig. 1: Inductively coupled plasma source with planar RF coil for uniform excitation of the plasma. He-gas serves for cooling the wafer, a second RF generator is biasing the substrate electrode for accelerating ions from the plasma towards the wafer.

The second type of inductive source (Fig. 2) is using a RF coil wound around a dielectric vessel. The plasma is excited inside the vessel, where chemically active species and ions are generated at a high density. This is the classical ICP configuration. Plasma excitation is non-uniform, with denser plasma regions close to the driving coil near the dielectric wall, whilst plasma excitation towards the center of the reactor is comparatively weak, following

the magnetic field distribution created by the inductive coil (compare Biot-Savart’s-equation for field distribution calculation). The drawback is that process gas flowing through the center of the vessel is excited only comparatively weakly, and large amounts of more or less unexcited process gas are diluting the active species created in the boundary area, which is at the cost of overall rate. Either the reactor vessel is designed for “small diameter” (equivalent to high surface-to-volume ratio) to direct most of the process gas through high-density areas near the dielectric walls, or as an alternative, liners etc. are introduced into the reactor center to prevent process gases from flowing through the areas of only weak excitation. In general, in an ICP-tool the wafer is more remote from the plasma excitation zone. The diffusion or drift zone between plasma generation and substrate position allows the plasma to cool down efficiently before reaching the wafer, which enables also high plasma power levels on the order of 3...5 kWatts. As a major drawback, plasma potential and ion current distribution are less uniform, yielding asymmetric tilting of etched sidewall profiles (outer sidewalls of etched structures show more negative slopes than inner sidewalls) which has a negative impact on the performance e.g. for gyroscopes with out-of-plane detection mode.

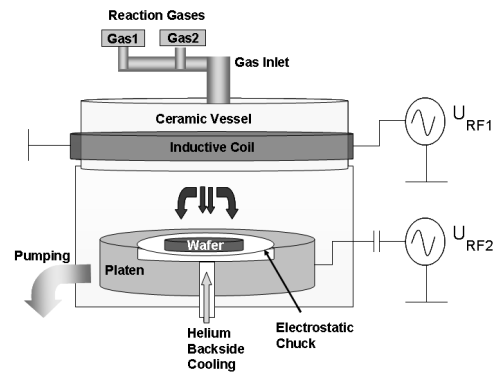


Fig. 2: Classical ICP-tool with inductive coil wound around dielectric vessel. The wafer is located downstream from the source, separated by a drift zone for plasma cooling and homogenization of species distribution.

A solution to overcome this drawback is depicted in Fig.3: A magnetic ion collimator is placed between the plasma source exit and the wafer position. Some magnetic enhancement of the plasma discharge itself takes place, boosting the source efficiency to some extent. Most importantly, magnetic fields of opposing signs counter-act as lenses acting onto the charged particles which are drifting down from the source region towards the wafer, tailoring spatial plasma potential and ion current distributions [11].

As the one alternative, uniformity of the plasma potential distribution in the sheath close to the wafer location can be targeted for optimization. With a proper adjustment of the DC currents to the magnetic coils for best plasma sheath potential homogeneity, profile tilting can be reduced to the low levels as compared to the configuration shown in Fig. 1, yielding similarly high performance for the types of gyroscopes with out-of-plane detection mode regarding undesired mode coupling (see below).

Uniformity of etching depth is another matter of increasing concern for growing wafer sizes, e.g. from 6” to 8” diameter. A typical phenomenon on etched wafers is a rate increase from wafer center to edge, the problem getting the more severe the larger the wafer sizes. One of the reasons for higher etching speed at the

wafer border compared to the wafer center is an enhancement of etching species concentration because there is no more silicon consuming the fluorine radicals outside of the wafer boundaries. This phenomenon might potentially be compensated by placing a “dummy-load” in the form of a silicon or carbon absorber ring of appropriate width around the wafer. Absorber solutions like that are not appreciated in a manufacturing environment, since they are non-adjustable (except by changing their geometries), reduce the overall etching-rates, and introduce a consumable to the reactor design which represents a serious particle source as well.

An additional reason for the rate increase from wafer center to edge is an enhancement of the ion current drawn to the wafer boundaries as compared to the wafer center: the dielectric surface of the substrate electrode surrounding the wafer area is less attractive to charges from the plasma sheath than the wafer itself, the latter having a more direct connection to the biasing radio-frequency power and a lower impedance towards the plasma. The attempt to reach impedance matching between the wafer and its surroundings by introducing e.g. a metal or a conductive layer covered by a tailored dielectric shield again leads to an optimization problem for mechanical parameters like geometries and layer thicknesses, which is not appreciated as a good manufacturing solution either.

The second alternative to make use of the magnetic collimator depicted in Fig. 3 is for optimizing its spatial filtering characteristics to the charged particles on their way to the wafer for targeting a best-as-possible etch-rate distribution. Adjusting the currents through the collimating electromagnets to redirect ion flow away from the wafer border areas and focus more towards the wafer center can be applied to compensate the rate increase from center to edge and to achieve an optimized etch-rate uniformity. Etch-rate variation of +/- 1% (min-max) is possible for an open silicon area of 20 % on a 6”-wafer, which represents a typical silicon load situation in MEMS. Note that the optimized collimator adjustments for best profile uniformity (smallest asymmetric profile “tilting”) are in general significantly different from those for best etch-rate uniformity. This trade-off between different optimization targets requires compromising with respect to the individual application, to focus on optimizing its most critical specification parameters and give away on others.

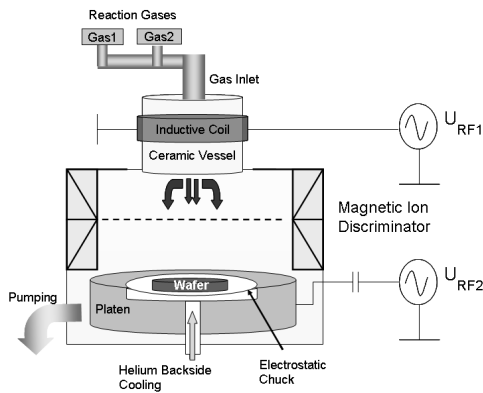


Fig. 3: ICP-source with adjustable magnetic ion collimator for homogenization of profile forms over the wafer, or alternatively, for optimized uniformity of the etch-rate distribution over the wafer.

The notching phenomenon well-known for high-aspect ratio trenches is more predominant for the high-density inductively coupled plasma as compared to the low-density RIE conditions,

with ion densities being typically by 2-3 orders of magnitude higher than for the RIE sources. Notching appears as a consequence of charging in high-aspect ratio trenches, when the etch reaches a dielectric interface and overetching takes place [12], [13], [14]. Positive ions (kations) accumulate at the dielectric trench floor, and strong electrical fields build up between the floor and the sidewalls of the trench. As a consequence, incoming kations are re-directed towards the sidewalls, away from the positive charges already trapped at the trench floor. Notches cut deeply into the structures where re-directed ions are bombarding the sidewalls. Uncontrolled sidewall attack corrupts mechanical properties of functional devices and represents a serious reliability problem, and a particle source in manufacturing, which makes this phenomenon highly undesirable. Since electrical charges are at the origin of notching, reduction of charging is the key to its elimination.

An advanced pulsing scheme involving both the substrate bias power [15] and the plasma source power [16] yields efficient discharge and notch suppression capabilities, even under strong overetch conditions.

As long as the substrate is powered, negative DC-bias effectively repels negative ions (anions), and only positive ions (kations) and electrons are able to reach the wafer. Since electrons have only little directionality and can be easily deflected, they reach the wafer surface but hardly make it to the dielectric bottom of high-aspect ratio trenches: for discharging their dielectric floors, electrons are inefficient candidates. During phases with bias power off, the substrate loses its repulsive character towards negative ions (anions) which can then reach the wafer surface. Due to their higher mass and directionality, anions are well appropriate for effectively neutralizing accumulations of positive charges even in high-aspect ratio trenches. As an additional effort to increase available amounts of anions, the plasma source power is pulsed together with substrate bias pulsing, switching off the plasma discharge periodically. At each plasma shutdown, during afterglow phases, strong anion peaks are generated. Pulsing frequencies are on the order of 60-100 Hz and several kHz for the substrate electrode and for the plasma source power, respectively.

## ENABLING NEW SENSOR DEVICES

In the following section, some sensor devices introduced to the MEMS field by Bosch are discussed. The first product development was for a surface-micromachined capacitive type accelerometer for automotive applications, see Fig. 4. The sensor is fabricated from a 10 μm thick epitaxial polysilicon layer on top of a sacrificial oxide, with a thin buried polysilicon layer underneath used for electrical interconnections [17].

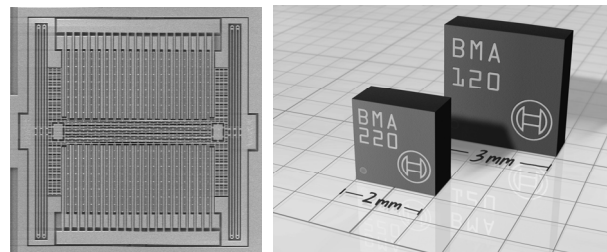


Fig 4: Single-axis acceleration sensor made from 10 μm thick epitaxially deposited polysilicon by “Bosch-DRIE” (left). The world’s smallest triaxial acceleration sensor in 2\*2\*1 mm<sup>3</sup> package size (right) launched recently as a product.



High aspect-ratio comb capacitors serve to detect deflections of the seismic mass in response to acceleration. The comb capacitor area is where the anti-notching capabilities of the plasma etching process come into play to assure quality of the safety-critical devices. A first product was introduced to the automotive market in early 1997 for passenger retention systems like the airbag. Later on, follow-up generations of different types of accelerometers for low-g as well as multi-axial sensitivity were brought to the market. Starting from 2004, also the consumer area has been addressed by low-cost and strongly miniaturized triaxial acceleration sensors. Quite recently, Bosch started supplying the world's smallest triaxial accelerometers mainly for cell-phone applications, with a package size of only  $2 \times 2 \times 1 \text{ mm}^3$ .

After a first generation of gyroscopes [18] fabricated from bulk- and surface-micromachining, a surface-micromachined gyroscope [19], [20] was launched in year 2000 mainly for car navigation and roll-over protection systems, see Fig. 5. This sensor consists of a pseudo-vibrating structure in a rotary oscillation mode, driven electrostatically through high-aspect ratio comb structures. Angular rotation around an axis in the chip-plane yields a periodic out-of-plane torsional vibration of the oscillating mass, as a reaction to Coriolis forces, which is detected capacitively by capacitor plates made from the thin buried polysilicon layer underneath the structure. The measured signal amplitude is proportional to applied angular rate. Profile control of the tether beams carrying the vibrational structure is crucial: any profile deviations from vertical (in particular "asymmetric profile tilting"), give rise to unwanted mode coupling between planar base vibration and out-of-plane detection modes: the so-called "quadrature" component is a serious performance-limiting factor in all gyroscopes sharing a configuration of a planar base vibration mode and an out-of-plane detection mode. Here the considerations described before for tailoring a homogeneous plasma potential distribution over the sheath close to the wafer are of a high relevance to key performance features of the gyroscope.

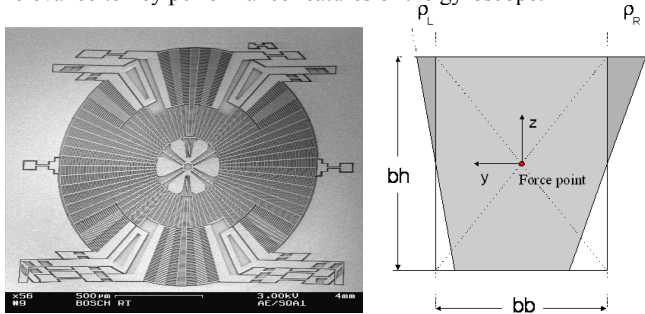


Fig.5: Surface-Micromachined Gyroscope of the rotational type (left). Profile asymmetries ("asymmetric tilting", right) yield undesired mode-coupling and must be avoided.

In 2005, a new generation of surface-micromachined gyroscopes of the linear-linear vibrating type was launched for automotive anti-skidding systems (electronic stability program, ESP), see Fig. 6. One motion mode is excited into a periodic linear vibration by electrostatic forces from a comb-drive, with an orthogonal linear motion mode used for detection of Coriolis-forces resulting from angular velocity. With both orthogonal modes used for drive and detect being planar modes, and detection performed by a second set of comb capacitors, the sensitivity axis for angular rotation is out-of-plane [21]. With the detection mode being chosen as an out-of-plane vibration mode, also in-plane angular rotation speed is detectable by polysilicon capacitor plates underneath the structures. Again, for the latter configuration,

mode-coupling between in-plane and out-of-plane vibration modes is a performance-limiting factor. Asymmetric profile tilting as the major cause for the "quadrature" component must be avoided by providing a homogeneous plasma sheath potential distribution over the wafer. Aside from automotive applications in car safety systems, surface-micromachined gyroscopes are receiving increasing attention also from the consumer side, e.g. for image-stabilization in digital cameras. Combining devices with different detection modes and sensitivity axis into a single chip enables multi-sensors for triaxial yaw rate detection, similar to the accelerometer case. Potential applications for multiaxial yaw rate sensors are navigation systems in handheld devices.

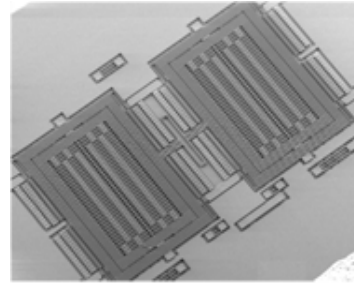


Fig. 6: Surface-micromachined Gyroscope of the linear type. Combining several devices of different sensitivity axis into a multi-chip yields multiaxial (triaxial) yaw rate sensors.

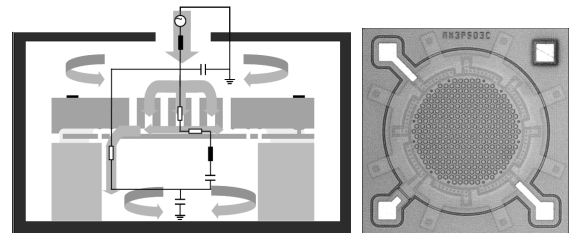


Fig. 7: Schematic cross-section of a MEMS microphone illustrating a reduced network model for electromechanical simulation (left), and an IR transmission picture from the top of the microphone chip (right).

New applications in the consumer electronics field which depend on through-wafer etches are MEMS-microphones, MEMS micromirrors for pico-projectors and the through-silicon-vias (TSV's) for area-saving chip-stacking and bare-die mounting technologies.

For fabrication of MEMS-microphones, a cavern must be etched through the whole wafer thickness to provide the acoustic volume – or sound access-hole – to the sound-pressure sensitive membrane. In addition, the counter-electrode to the membrane-capacitor needs perforation or "vent-holes" to adjust for the correct damping of the acoustic membrane. Fig. 7 shows a schematic cross-section of a MEMS microphone developed at Bosch [22], including a reduced network model for description of its electromechanical behavior, and a picture of the microphone chip itself taken by infrared microscopy from the top. The IR-magnification shows the perforated frontplate, the membrane and its fixation by tether beams underneath the frontplate, and the electrical contact pads. The fabrication technology is the same established process as used for the production of the inertial sensors, with through-wafer backside trenching added for

generation of the acoustic cavity. Particular requirements for the DRIE through-wafer etching step are high-etching speed on the order of 10  $\mu\text{m}/\text{min}$  or higher to keep process time reasonably short and within economic limits, and good uniformity of the etching speed over the wafer to keep performance parameters within tight specifications.

Fig 8a and 8b illustrate a schematic process flow for TSV contacts fabrication to an integrated pressure sensor of Advanced Porous Silicon Micromachining-technology (APSM, see [23], [24]). TSV's are etched into the silicon and covered by a dielectric insulation layer deposited to the sidewalls. After opening the dielectric bottom to the metal 1 contact layer of the frontside circuit, the TSV's are either filled with copper by electroplating, or a thin-film metal is conformally coated onto the sidewalls. Contact areas are structured subsequently on the wafer backside. Chips like that can either be directly soldered onto PCB's as bare dice, or stacked on top of other electronic chips, like microcontrollers, multiplexers, memories or RFID for minimum area consumption.

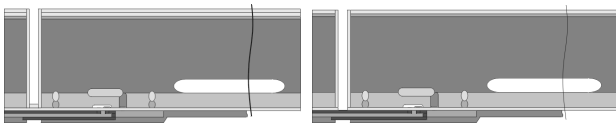


Fig 8a: Process flow for fabrication of TSV's: High aspect ratio trenches are etched and passivated by insulating dielectrics (left). The bottom oxide is opened to metal 1 contacts of the IC (right).



Fig 8b: Trenches with insulated sidewalls are refilled with copper by electroplating (left scheme), and cross-section through refilled test-structures in the middle, or sputter-coated with a metal thin-film, and the metal structured into backside contacts for chip-stacking and bare-die mounting (right scheme).

For etching the deep silicon vias, parameter ramping is often a good choice to use for adapting the process to the increasing aspect ratio of the vias with process progress [25]. This enables a good control of profile evolution, with regards to the needs for subsequent conformal coating and refill of the trenches.

## SUMMARY

The "Bosch process" is enabling new micromachining processes and MEMS designs for enhanced device functionalities [26]. Today DRIE is mature technology: pull from the application side has replaced technology push. A lot of development work is still invested from equipment suppliers into improving etch-rate, mask-selectivity, profile control and uniformity as well as suppression of notching for ever higher aspect ratios, both targeting hardware and process. Applications are defining their specific needs and DRIE has to fulfill the individual device specifications. Driven by new applications and the innovation pace from the consumer electronics area, "Bosch-DRIE" technology will continue shaping MEMS into the future.

## CONTACT

Franz Laermer  
Robert Bosch GmbH, P.O. BOX 106050, DE-70049 Stuttgart  
Tel: +49-711-811-7671, franz.laermer@de.bosch.com

## REFERENCES

- [1] Sung, K.T., and Pang, S.W., 39<sup>th</sup> National Symposium of the American Vacuum Society, Chicago, Illinois (USA), (1993), 1206-1210
- [2] Tian, W.-C., Weigold, J.W., Pang, S.W., J. Vac. Sci. Tech. B18, (2000), 1890
- [3] Bartha, J.W., J. Greschner, M. Puech and P. Mauquin, Journal of Microelectronic Eng. 27, (1995), 453-456
- [4] H. Jansen, M. d. Boer, R. Legtenberg, M. Elwenspoek, Journal Micromech. and Microeng. 5, (1995), 115-120
- [5] Jansen, H., M. de Boer, H. Wensink, B. Kloeck, M. Elwenspoek, Microelectron. Journal 32, (2001), 769-777
- [6] F. Laermer and A. Schilp, German Patent DE-4241045 (26.5.94), US-Pat. #5,501,893 (26.3.96)
- [7] F. Laermer and A. Urban, Eur.Pat. EP-1554747 (30.8.06)
- [8] B. Charlet, L. Peccoud, T. Dupeux, SFV-CIPG Antibes France 183 (1987)
- [9] B. Charlet, L. Peccoud, Eur. Pat. EP-0359777 (29.07.92)
- [10] F. Laermer and A. Schilp, WO 01/88950
- [11] V. Becker, K. Breitschwerdt, F. Laermer, A. Schilp, US-Pat. #6,709,546 (23.3.04), #7,094,706 (22.8.06)
- [12] T. Nozawa, T. Kinoshita, T. Nishizuka, A. Narai, T. Inoue, A. Nakaue, 1994 Dry Process Symposium I-8, (1994), 37-41
- [13] T. Kinoshita, M. Hane, J. P. McVittie, J. Vac. Sci. Technol. B 14, (1996), 560-565
- [14] G. S. Hwang, K. P. Giapis, J. Vac. Sci. Technol. B15, (1997), 70-87  
G.S. Hwang, K.P. Giapis, Japanese Journal Applied Phys. 37, (1998), 2291-2301
- [15] F. Laermer and A. Schilp, US-Pat. #6,926,844 (9.8.05)
- [16] F. Laermer, US-Pat. #7,361,287 (22.4.08)
- [17] M. Offenberger, F. Laermer, B. Elsner, H. Muenzel and W. Riethmueller, Proc. Transducers'95, Stockholm, Sweden, (1995), 589-592
- [18] M. Lutz, W. Golderer, J. Gerstenmeier, J. Marek, B. Maihoefer, S. Mahler, H. Muenzel, U. Bischof, Proc. Transducers'97, Chicago, (1997), 847-850
- [19] R. Schellin, A. Thomae, M. Lang, W. Bauer, J. Mohaupt, G. Bischopink, L. Tanten, H. Baumann, H. Emmerich, S. Pintér, J. Marek, K. Funk, G. Lorenz, and R. Neul, Advanced Microsystems for Autom. Applications 99, Berlin, Germany (1999), 239
- [20] K. Funk, H. Emmerich, A. Schilp, M. Offenberger, R. Neul, F. Laermer, Proceedings MEMS'99, Orlando, FL, (1999), 57-60
- [21] U.-M. Gómez, B. Kuhlmann, J. Classen, W. Bauer, C. Lang, M. Veith, E. Esch, J. Frey, F. Grabmaier, K. Offterdinger, T. Raab, H.-J. Faisst, R. Willig, R. Neul, Proc. Transducers'05, Seoul, (2005), 184-187
- [22] C. Leinenbach, K. van Teeffelen, F. Laermer, H. Seidel, Proc. IEEE-MEMS'2010, HongKong (2010), 659-662
- [23] G. Lammel, S. Armbruster, C. Schelling, H. Benzel, J. Brasas, M. Illing, R. Gampp, V. Senz, F. Schaefer, S. Finkbeiner, Proc. Transducers'03, Boston (2003), 35-36
- [24] S. Armbruster, F. Schaefer, G. Lammel, H. Artmann, C. Schelling, H. Benzel, S. Finkbeiner, F. Laermer, P. Ruther, O. Paul, Proc. Transducers'03, Boston (2003), 246-249
- [25] J. Hopkins, H. Ashraf, J. K. Bhardwaj, A. M. Hynes, I. Johnston, and J. N. Shepherd, Materials Research Soc. Symp. Proceedings 546, (1999), 63
- [26] Stephen D. Senturia, Microsystem Design, Kluwer Academic Publ., 2<sup>nd</sup> ed., (2001), 71

# COMPOSITE POLYSILICON-PLATINUM LATERAL NANO-ELECTROMECHANICAL RELAYS

R. Parsa, S. Chong, N. Patil, K. Akarvardar<sup>1</sup>, J. Provine, D. Lee, D. Elata<sup>2</sup>, S. Mitra, H.-S. P. Wong, R. T. Howe  
 Center for Integrated Systems, Dept. of Electrical Engineering, Stanford University, Stanford, CA 94305  
<sup>1</sup>SEMATECH, Albany, NY, USA <sup>2</sup>Technion – Israel Institute of Technology, Haifa, Israel

## ABSTRACT

This paper reports the fabrication and performance of laterally actuated, polysilicon-platinum composite nanoelectromechanical (NEM) relays. Laterally actuated relays are defined in a single lithography step, enabling symmetric electrode and beam structures. The platinum coating serves as the conducting contact material and can also provide a local routing layer. Decoupling mechanical and electrical properties of the NEM relay allows independent optimization of each property. The NEM relays exhibited less than 3k $\Omega$  contact resistance and can operate for 10<sup>8</sup> cycles in room ambient.

## INTRODUCTION

In advanced CMOS technology nodes, the minimum static power dissipation is limited by finite subthreshold slope and gate leakage. NEM relays are promising devices for low power logic applications due to zero leakage current, infinite subthreshold slope, and scalable actuation voltage [1,2]. SRAM cells [3] and FPGA blocks, where low switching speed and limited number of cycles are acceptable [4], are two attractive near-term applications for NEM relays.

Polysilicon has been characterized extensively as a structural material for MEMS devices and is known to be an excellent elastic material for mechanical structures. However, it is not well suited for electrical contacts, due to the formation of native oxide on the surface of polysilicon when exposed to oxygen. Passing current through contacting polysilicon surfaces requires a high applied voltage between the two sides of the contact to break through the native oxide. The resulting high field modifies the surface of the contact after every switching event, causing variations in the device characteristics. Furthermore, the device performance degrades rapidly due to contact degradation, in-use stiction, or particle attraction.

Although all-metal switches usually mitigate the problem of native oxide formation and require smaller applied voltages across the contact to pass current; their long-term mechanical reliability has yet to be demonstrated. Ruthenium switches showed functionality with low biases across the contact and survived up to about 2x10<sup>6</sup> cycles in a sealed probe station at room pressure [5]. TiN switches actuated in oil demonstrated significant reliability improvement over operation in air ambient [6,7]. Tungsten switches fabricated via Atomic Layer Deposition (ALD) were operated at biases less than 1V across the contact [8]. AlN switches utilizing piezoelectric actuation have also been recently demonstrated [9].

MEMS structures with metal coating have been demonstrated for various RF, optical and sensing applications. Detailed studies on various metal alloys as the electric contact for MEMS switches have been published in the past [10]. Large vertically actuated switches with metal-coated contacts covered with a thin dielectric [11] have shown more than 10<sup>9</sup> cycle lifetimes in N<sub>2</sub> ambient. Functionality of basic circuit elements have been demonstrated by relays fabricated via this method [1]. In this work, we use composite laterally actuated relays consisting of a polysilicon beam with Pt-coated sidewalls, which allows the mechanical and electrical contact reliability issues to be decoupled.

## PRINCIPLE OF OPERATION

A prototypical three terminal relay consists of three parts: 1) a deflecting beam (or source), which forms the channel for current flow; 2) an actuating gate electrode, which exerts force to the beam and determines the state of the switch; and 3) a drain electrode, which contacts the beam in the on state. Fig. 1a shows a five terminal device with one beam, two symmetrical gates and drains placed on each side of the beam in an on state configuration.

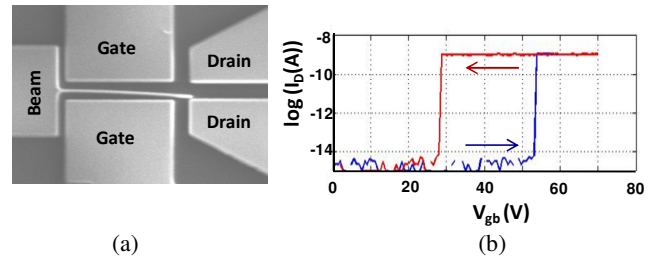


Figure 1. (a) SEM of a five terminal NEM relay with 14.2 $\mu$ m-long beam and (b) its hysteretic I-V characteristic. Due to the symmetry of the structure, identical I-V characteristics were observed when actuating to each side.

When  $|V_{gate}-V_{beam}|$  ( $V_{gb}$ ) is applied, the electrostatic force attracts the beam toward the gate, which is balanced by the elastic force of the deflected beam. Beyond the pull-in voltage ( $V_{gb}>V_{PI}$ ), elastic forces can no longer balance the electrostatic force, and the beam collapses toward the gate until contact is made at the drain. Since pull-in is achieved at an unstable state, the voltage at which the beam disconnects from the drain (pull-out voltage,  $V_{PO}$ ) is smaller than  $V_{PI}$ , resulting in a hysteretic characteristic (Fig. 1b).

## DESIGN AND FABRICATION

In designing lateral NEM relays, multiple parameters such as beam width ( $t$ ), beam length ( $L$ ), beam-to-gate gap ( $g_0$ ), beam-to-drain gap ( $d$ ), beam-drain overlap ( $L_d$ ), drain-to-gate space ( $S_{gd}$ ), and beam-gate overlap ( $L_g$ ), are considered as shown in Fig. 2.

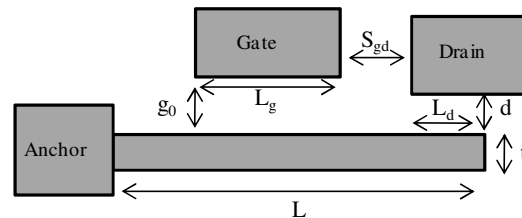


Figure 2. Schematic of a three terminal NEM relay and design parameters.

$V_{PI}$  and  $V_{PO}$  can be controlled by adjusting the physical dimensions of the NEM relays. According to the 1-D parallel plate model [12],  $V_{PI}$  and  $V_{PO}$  are estimated as:

$$V_{pi} = \sqrt{\frac{8kg_0^3}{27\epsilon WL}}, \quad V_{po} = \sqrt{\frac{2k}{\epsilon WL}g_{min}^2(g_0 - g_{min})}, \quad k = \frac{2EWt^3}{3L^3} \quad (1)$$

where  $k$  is the spring constant of the beam depending on its geometry and material,  $E$  is the Young's modulus of the beam material,  $\epsilon$  is the permittivity of the ambient enclosing the relay, (e.g. vacuum or oil), and  $g_{min}$  is the minimum gap between gate and beam when beam is pulled in. In this model the fringing field effect is neglected. Further, it is assumed that the actuation electrode overlaps the entire length of the beam. It is important to allocate sufficiently large  $S_{gd}$  to ensure the beam does not touch the gate after connecting to the drain. Unfortunately, for a fixed  $L$  increasing  $S_{gd}$  increases the actuation voltage due to the reduction in  $L_g$ , the length over which electrostatic force is exerted. Adequate amount of  $L_d$  is required to ensure the beam touches the drain when pulled in.

It can be seen in Eq. (1) there are several parameters that can be adjusted to tune  $V_{pi}$  such as the spring constant of the beam ( $k$ ) [13], dielectric constant ( $\epsilon$ ) [7], and actuation gap ( $g_0$ ). One possible method of reducing  $g_0$  is to deposit a material on the beam and electrode sidewalls. Although the increase in the beam width stiffens it, the decrease in the electrode gap dominates and leads to a decrease in the actuation voltage when the desired coating material with adequate thickness is used (Fig. 3).

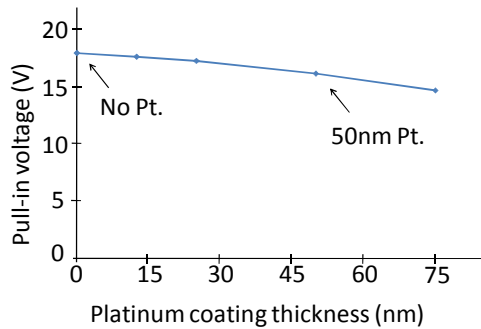


Figure 3. Pull-in voltage calculation vs. deposited sidewall metal on a 24 $\mu$ m-long, 600nm-wide polysilicon beam with 500nm-wide actuation gap.

SEM images showing actuation of the device and the process steps for fabrication of the NEM relay are provided in Fig. 4a and 4b, respectively.

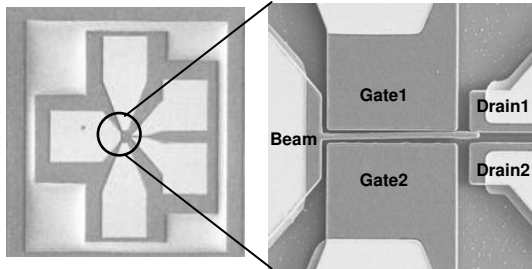


Figure 4a. SEM images showing actuation of a 5-terminal polysilicon switch coated with platinum on the sidewalls and selected top surfaces. Beam length=16 $\mu$ m, beam-drain overlap=2 $\mu$ m, gate-drain space=2 $\mu$ m, beam-to-gate gap=600nm, beam-to-drain gap=500nm.

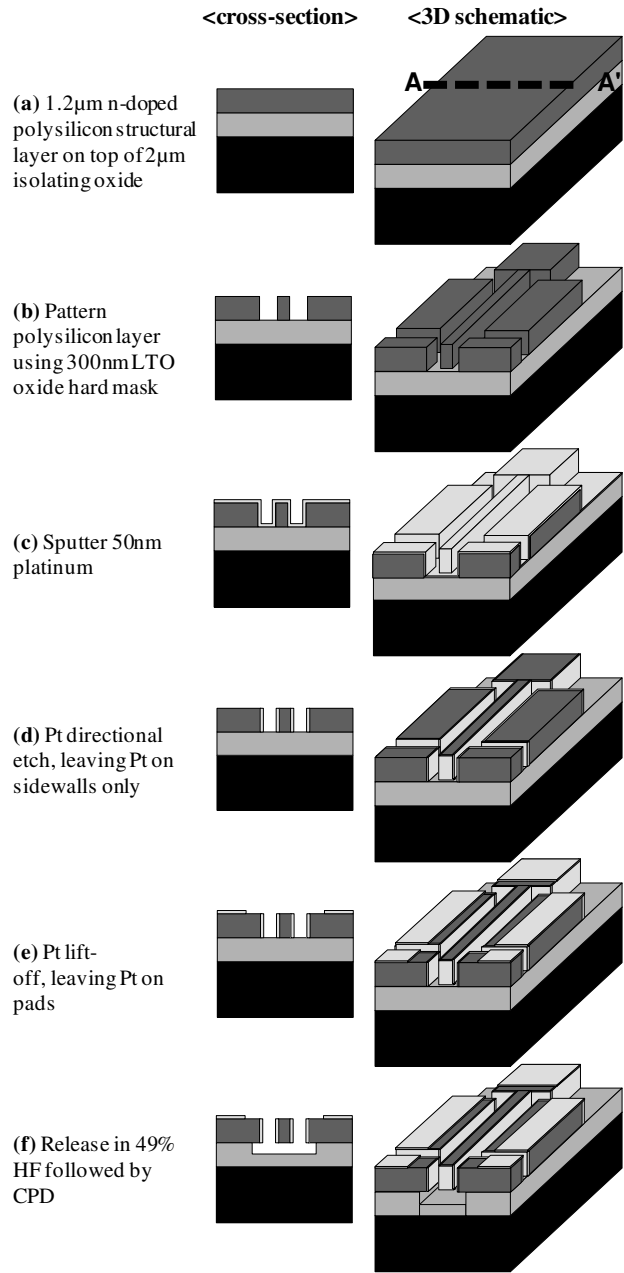


Figure 4b. 3D and 2D cross section view (taken along A-A' at all steps) of process flow used in fabrication of polysilicon relays with Pt sidewall coating (not drawn to scale).

First, a 2 $\mu$ m-thick oxide is deposited at 400 $^{\circ}$ C to serve as both the sacrificial layer and insulating layer between the device layer and Si wafer. Next a 1.2 $\mu$ m-thick layer of phosphorous-doped polysilicon is deposited at 580 $^{\circ}$ C as the structural layer and annealed at 1075 $^{\circ}$ C for 30sec. To assist in obtaining a vertical etch profile, 300nm oxide is deposited at 400  $^{\circ}$ C to serve as a hard mask for etching the polysilicon. This oxide is patterned using an i-line stepper at its 500nm resolution limit and then etched by RIE (250 mTorr, 50 sccm CHF<sub>3</sub>, 20 sccm CF<sub>4</sub>, 100 sccm Ar). The patterns are transferred to the polysilicon device layer by another RIE step (12 mTorr, 25 sccm Cl<sub>2</sub>, 140 sccm HBr, 3 sccm O<sub>2</sub>). A 50nm Pt layer is sputtered on the wafer followed by an anisotropic argon

sputter etch (12.5 mTorr, 100W, 15 sccm Ar, 8 minutes) of the platinum to remove the Pt film from the bottom and top surfaces, leaving the sidewalls intact. Openings on the pads are patterned via conventional optical lithography. This step is followed by evaporation of 50nm thick platinum. The undesired platinum is removed via liftoff, leaving the metal on top of the pads only. The process is completed by releasing the devices in 49% HF followed by a critical point drying (CPD) step to avoid release stiction. Fig. 5 shows an SEM of the beam and electrode coverage by the deposited platinum after release.

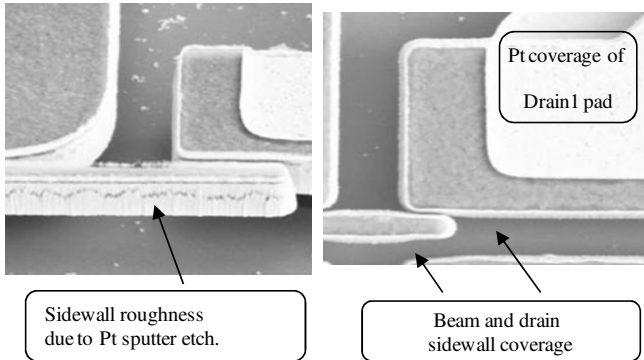


Figure 5. SEM image of polysilicon switch showing a continuous path from the beam-drain contact point to the top of the pad which will be probed.

## RESULTS

Contact resistance was extracted by measuring the drain-to-beam current after pull-in under different drain biases. When tested in room-ambient immediately after the CPD step, the relays had a contact resistance of less than 3k $\Omega$ , for drain biases ranging from 10mV to 1V (Fig. 6). In contrast, polysilicon NEM relays without coating had G $\Omega$ -range contact resistance with drain biases ranging from 3V to 5V. The Pt-coated relay's contact resistance is in the desired range for such relays because the mechanical delay typically is higher than RC delays [2]. Too low of a contact resistance will cause significant current flow after the switch closes and could cause overheating.

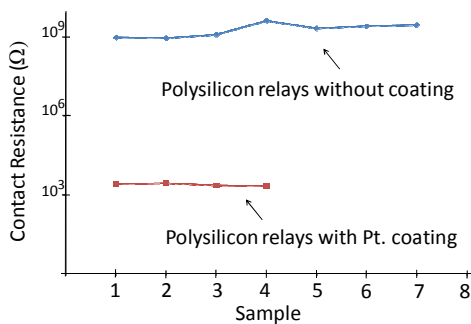


Figure 6. Pt-coated relays show 100X reduction in contact resistance ( $0.01V < V_D < 1V$ ) in comparison to non-coated relays ( $3V < V_D < 5V$ ). Devices were tested in room ambient immediately following release and drying.

The platinum film coating the beam and sidewalls reduces the actuation gap  $g_0$ , which lowers the pull-in voltage of the relays as expected (Fig 7). Another method to reduce the actuation voltage is changing the environment surrounding the relay and increasing the dielectric constant of the material in the gap between the gate and the beam. Actuating fabricated switches in oil reduced the

actuation voltage by a factor close to  $(\epsilon_{oil}/\epsilon_{air})^{0.5}$  and yields sharper pull-in and pull-out (Fig. 8). Repeated measurements of the same relay in oil yielded consistent actuation and contact characteristics.

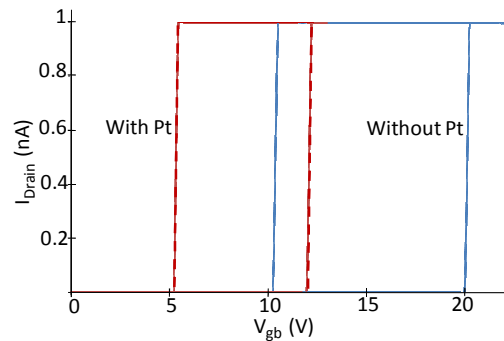


Figure 7. Experimental data showing reduced pull-in bias of a 22.5 $\mu$ m-long polysilicon beam via 50nm Pt deposition. Compliance limit is set to 1nA.

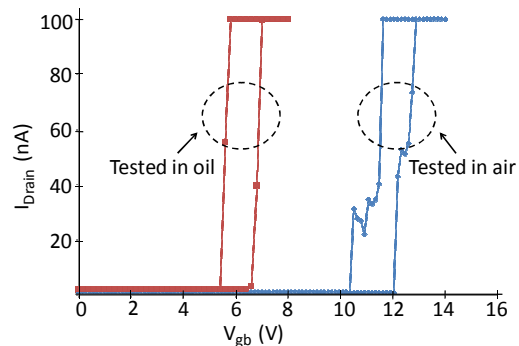


Figure 8. Pull-in and pull-out characteristics of 23.5 $\mu$ m-long Pt coated polysilicon switch in air and oil. Actuation bias is reduced in oil due to higher dielectric constant (1.8) of oil. Compliance limit is set to 100nA.

To observe the effect of electrical stress, contact-and-hold procedures were performed in room ambient on several coated NEM relays by passing up to 1 $\mu$ A current while in contact.

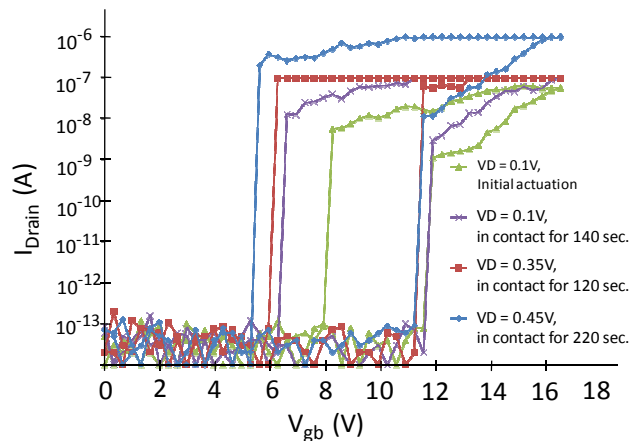


Figure 9. Hold in contact characteristics of a 23.5 $\mu$ m-long Pt coated polysilicon beam showing reliable pull-in and pull-out after being in contact for more than 8min. The relay passes  $\sim 0.25$ mC with drain biases of 0.1V, 0.35V, and 0.45V (with current compliances of 0.1 $\mu$ A, 0.1  $\mu$ A, and 1  $\mu$ A, respectively).

No in-use stiction was observed during room-ambient operation. Reliable pull-in and pull-out were achieved after the beam was in contact with the drain for more than 8 minutes, with drain biases of 0.1V to 0.45V, corresponding to approximately 0.25mC of charge passing through the contact (Fig. 9). An increase in contact resistance after many contacts was observed.

The NEM relay used for the contact-and-hold test (Fig. 9) was also subjected to cycling tests. Since the device was stored in dry nitrogen ambient for two days, first a pull-in and pull-out test was performed to ensure that the device is still functional. To cycle the device, the beam was connected to 0V and drain to 100mV with a current compliance of 100nA on both terminals. The gate was then pulsed from 0V to 16.5V. The pulse had a rise and fall time of 100nsec. A few pulses of 1Hz with duty cycle of 50% were applied multiple times to ensure the functionality of the device and setup. Next the frequency was changed to 250kHz and the current on the beam and drain was monitored. Analytical calculations of the fundamental resonant frequency for this relay yield a value of 860kHz. Due to sampling limitations, currents were recorded every 5sec. Device survived over  $10^8$  switching cycles (Fig. 10).

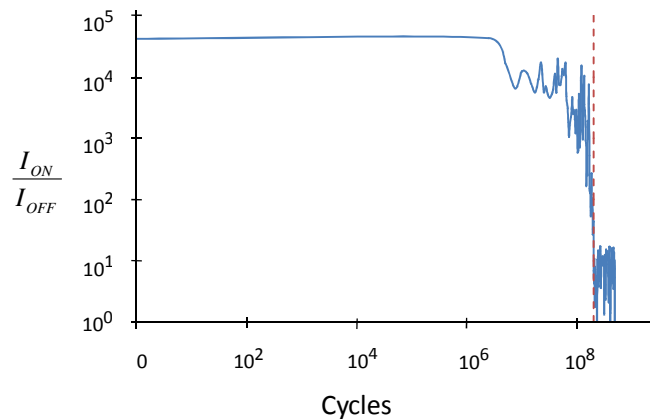


Figure 10. Endurance data operated in room ambient showing more than  $10^8$  cycles with  $I_{on}/I_{off} > 10^3$ .

A sharp decrease of  $I_{ON}/I_{OFF}$  after  $2 \times 10^8$  cycles was observed. Hot switching of the relay after the contact-and-hold test could have caused the thin platinum coating to be damaged. Asperity size changes due to the test affects the contact resistance. Pull-in and pull-out test after completing  $5 \times 10^8$  cycles showed the device was not functional. Testing of more devices in air, dry nitrogen, and oil environment will help to get a better understanding of the degradation mechanisms.

## CONCLUSION

Laterally actuated NEM relays consisting of platinum-coated polysilicon composite beams were fabricated and demonstrated to have  $< 3k\Omega$  contact resistance and to operate for over  $10^8$  switching cycles in room ambient conditions. The need for a single structural material having both proper electrical and mechanical properties has been eliminated through the use of the composite lateral relay design.

## ACKNOWLEDGEMENT

Fabrication work was performed at the Stanford Nanofabrication Facility (a member of the National Nanotechnology Infrastructure Network) supported by the NSF under Grant ECS-9731293, its lab members, and the industrial

members of the Stanford Center for Integrated Systems. This work was supported by the DARPA MTO program “Nano Electro Mechanical Computers (NEMS)” (Contract number: NBCH 1090002, Program manager: Dr. T. Akinwande). The authors would like to thank Nathan Klejwa, Scott Lee, Chen Chen, and Vivian Feig for helpful discussions.

## REFERENCES

- [1] F. Chen, M. Spencer, R. Nathanael, C. Wang, H. Fariborzi, A. Gupta, H. Kam, V. Pott, J. Jeon, T.-J. King Liu, D. Markovic, V. Stojanovic, and E. Alon, “Demonstration of Integrated Micro-Electro-Mechanical Switch Circuits for VLSI Applications”, IEEE ISSCC 2010, pp. 150-152.
- [2] K. Akarvardar, D. Elata, R. Parsa, G. C. Wan, K. Yoo, J. Provine, P. Peumans, R. T. Howe, and H.-S. P. Wong, “Design Considerations for Complementary Nanoelectromechanical Logic Gates”, IEDM 2007, pp. 299-302.
- [3] S. Chong, K. Akarvardar, R. Parsa, J.-B. Yoon, R. T. Howe, S. Mitra, and H.-S. P. Wong, “Nanoelectromechanical (NEM) Relays Integrated with CMOS SRAM for Improved Stability and Low Leakage”, ICCAD 2009, pp. 478-484.
- [4] C. Chen, R. Parsa, N. Patil, S. Chong, K. Akarvardar, J. Provine, D. Lewis, J. Watt, R. T. Howe, H.-S. P. Wong, and S. Mitra, “Efficient FPGAs using Nanoelectromechanical Relays”, ACM Intl. Symp. FPGA 2010, pp. 273-282.
- [5] D. A. Czapslewski, G. A. Patrizi, G. M. Kraus, J. R. Wendt, C. D. Nordquist, S. L. Wolfley, M. S. Baker, and M. P. de Boer “A Nanoelectromechanical Switch for Integration with CMOS Logic”, Journal of Micromechanics and Microengineering, vol. 19, 2009.
- [6] W. W. Jang, J.-B. Yoon, M.-S. Kim, J.-M. Lee, S.-M. Kim, E.-J. Yoon, K. H. Cho, S.-Y. Lee, I.-H. Choi, D.-W. Kim, and D. Park, “NEMS switch with 30 nm-thick beam and 20 nm-thick air-gap for high density non-volatile memory applications”, Solid State Electronics 2008, pp. 1578-1583.
- [7] J.-O. Lee, M.-W. Kim, S.-D. Ko, H.-O. Kang, W.-H. Bae, M.-H. Kang, K.-N. Kim, D.-E. Yoo, and J.-B. Yoon, “3-T Nanoelectromechanical Switching Device in Insulating Liquid Media for Low Voltage Operation and Reliability Improvement”, IEDM 2009, pp. 227-230.
- [8] B.D. Davidson, S.M. George, and V.M. Bright, “Atomic layer deposition (ALD) Tungsten nanoelectromechanical transistors”, Proc. IEEE MEMS 2010, pp. 424-427.
- [9] N. Sinha, T. Jones, Z. Guo, and G. Piazza, “Demonstration of low voltage and functionally complete logic operations using body-biased complementary and ultra-thin AlN piezoelectric mechanical switches”, Proc. IEEE MEMS 2010, pp. 751-754.
- [10] R. A. Coutu, Jr, P. E. Kladitis, K. D. Leedy, and R. L. Crane, “Selecting metal alloy electric contact materials for MEMS switches”, Journal of Micromechanical Microengineering, 2004, 1157-1164.
- [11] H. Kam, V. Pott, R. Nathanael, J. Jeon, E. Alon, and T.-J. King Liu “Design and Reliability of a Micro-Relay Technology for Zero-Standby-Power Digital Logic Applications”, IEDM 2009, pp. 809-812.
- [12] V. Kaajakari, Practical MEMS, Small Gear Publishing, 2009.
- [13] D. Lee, W. S. Lee, J. Provine, J.-O. Lee, J.-B. Yoon, R. T. Howe, S. Mitra, and H.-S. P. Wong, “Titanium Nitride Sidewall Stringer Process for Lateral Nanoelectromechanical Relays”, Proc. IEEE MEMS 2010, pp. 456-459.

# 3-D MICROMACHINED SPHERICAL SHELL RESONATORS WITH INTEGRATED ELECTROMAGNETIC AND ELECTROSTATIC TRANSDUCERS

S.A. Zotov, I.P. Prikhodko, A.A. Trusov\*, A.M. Shkel

MicroSystems Laboratory, Mechanical and Aerospace Engineering, University of California, Irvine, CA, USA

## ABSTRACT

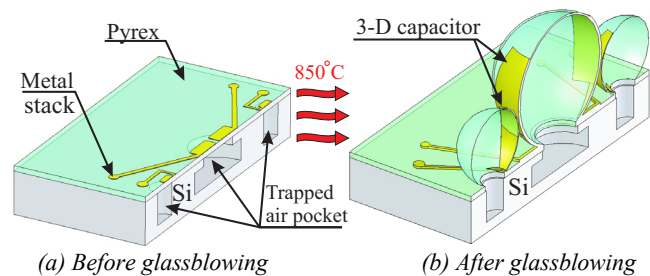
This paper presents a new paradigm for design and fabrication of 3-D spherical shell resonators. The approach uses pressure and surface tension driven plastic deformation (glassblowing) on a wafer scale as a mechanism for creation of inherently smooth and symmetric 3-D resonant structures with integrated electrodes. Feasibility of the new approach was demonstrated by fabrication and characterization of Pyrex glass spherical shell resonators with millimeter scale diameter and average thickness of 10-20  $\mu\text{m}$ . Integrated 3-D metal electrodes were used to actuate the two dynamically balanced 4-node wineglass modes. For 1 MHz glass-blown resonators, the relative frequency mismatch  $\Delta f/f$  between the two degenerate wineglass modes was measured as 0.63 % without any trimming or tuning. The intrinsic manufacturing symmetry and high aspect ratio transducer architectures of the proposed technology may enable new classes of high performance 3-D MEMS for communications and navigation applications.

## INTRODUCTION

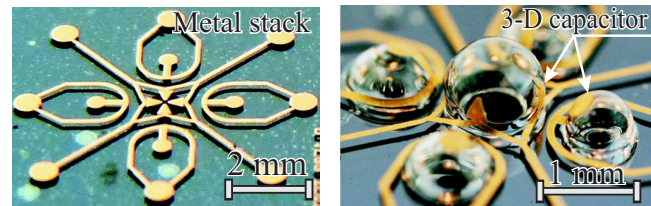
Miniature resonators are required for a range of applications, including signal processing, timing, frequency control, and inertial sensing [1]. A wide array of surface and bulk fabrication technologies for silicon MEMS resonators has been developed over the past decades with several commercial silicon resonators currently entering the consumer electronics market. Conventional planar technologies for MEMS resonator fabrication rely on photolithography and silicon DRIE which provide relative fabrication tolerances on the order of 1 %. The fabrication imperfections, surface roughness, DRIE induced scalloping and footing, as well as aspect ratio limitations present challenges in device symmetry, frequency specification and matching, quality factor maximization, and further device miniaturization without performance sacrifice. These factors motivate the investigation of alternative, non-planar architectures and technologies for resonant MEMS with simultaneously increased symmetry and aspect ratios.

This paper explores the hypothesis that plastic deformation driven by surface tension and pressure, or glassblowing [2], may serve as an enabling mechanism for wafer-scale fabrication of highly smooth and symmetric 3-D spherical shell resonators. The proposed micromachining approach consists of 1) bonding a Pyrex glass wafer on a silicon substrate with pre-etched cavities 2) patterning of flat metal features on the silicon-on-glass substrate 3) heating the wafer stack above the softening point of glass. The induced plastic deformation of the metal-on-glass stack creates 3-D spherical shells with integrated metal electrodes, Fig. 1 and 2.

Operation of continuous, dynamically balanced wineglass modes in 3-D axisymmetric shells provides increased robustness to fabrication imperfections. In conventional planar mass-spring type resonators, linear sensitivity of the natural frequency  $f$  to fabrication imperfections is governed by  $\Delta f/f \propto (3/2) \Delta w/w$ , where  $w$  is the nominal suspension beam width and  $\Delta w$  is the associated fabrication tolerance. In contrast, variation  $\Delta w$  of the nominal shell thickness  $w$  appears only as a second order term in the relative frequency mismatch  $\Delta f/f \propto (3/4) (\Delta w/w)^2$  for a spherical shell resonator operated in a balanced wineglass mode [3]. This paper presents the glassblowing approach to 3-D shell resonator fabrication and reports experimental characterization.



(a) Before glassblowing (b) After glassblowing  
Figure 1: Conceptual schematic of 3-D spherical shell resonator fabrication using wafer-scale metal-on-glass stack glassblowing.



(a) Before glassblowing (b) After glassblowing  
Figure 2: Photographs of fabricated 3-D spherical shell resonators with integrated electrostatic transducers.

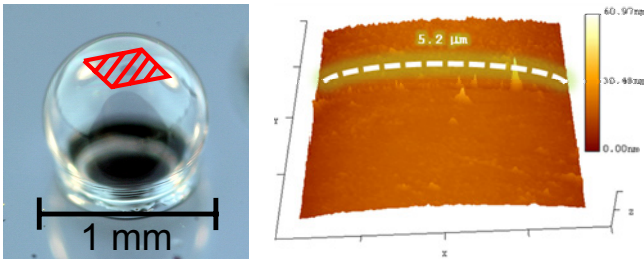
## GLASS-BLOWN SHELL AS VIBRATORY ELEMENT

Fabrication of 3-D resonant shells relies on wafer-scale glassblowing, which was previously developed for creation of extremely smooth and symmetric spherical cells for chip-scale atomic devices [4]. The process starts by hermitically bonding a 100  $\mu\text{m}$  thick Corning Pyrex 7740 glass wafer to a silicon wafer with an array of 0.5 mm diameter cylindrical cavities etched 0.8 mm deep, Fig. 1(a). The wafer stack is then heated above the 850  $^{\circ}\text{C}$  softening point of Pyrex glass. Above this temperature, the viscosity of glass reduces, and the expansion of the air trapped inside the pre-etched silicon cavities causes the flat glass to be blown into spherical shapes, Fig. 1(b).

## Surface Quality of Glass-Blown Spheres

Surface roughness is a known performance limiting effect in microscale resonators. Development of surface tension driven glassblowing process is expected to provide surface roughness improvement compared to the conventional fabrication processes based on etching. To investigate this hypothesis experimentally, several glass-blown shells were characterized using an Agilent Nano R2 Atomic Force Microscope (AFM). The initial average surface roughness of the Pyrex 7740 wafer before glassblowing was measured as 0.48 nm over a  $(5.2 \mu\text{m})^2$  area. The average surface roughness after the fabrication was measured as 0.85 nm on the outer shell surface. This translates into the overall 1 ppm figure of merit relative to the 0.9 mm diameter of the shell, Fig. 3. The uncertainty of both AFM measurements was on the order of  $\pm 0.2$  nm. The final shell roughness is comparable to the initial glass roughness before the fabrication. Further reduction in shell roughness can be achieved by controlling the level of impurities and contaminants in the nitrogen atmosphere of the glassblowing furnace.

To compare the glassblowing technology with conventional surface micromachining, the same set of measurements was



(a) 0.9 mm glass-blown shell  
 $5.2 \times 5.2 \mu\text{m}$  measured area  
 (b) Measurement of 0.85 nm  
 average roughness.

Figure 3: Glass shell surface roughness measured with an atomic force microscope. Relative roughness measurement is 1 ppm.

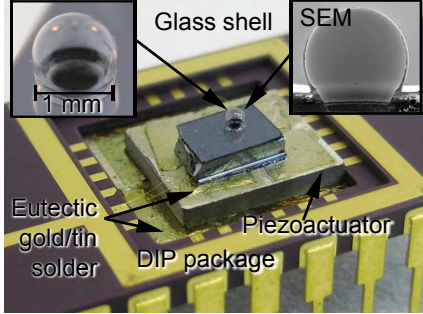


Figure 4: Photograph of a packaged glass-blown shell bonded to a piezoelectric actuator for structural mode characterization.

performed on a sidewall of a silicon resonator defined by DRIE using Unaxis Versaline VL-7339. Surface defects were measured as 17 nm over the same area, equivalent to 167 ppm roughness relative to the 100  $\mu\text{m}$  beam thickness. This comparison demonstrates the potential of the glassblowing technology to produce high aspect ratio 3-D resonators with very low surface roughness.

### Non-Contact Characterization of Resonant Modes

Inherent fabrication symmetry and measured low surface roughness suggest that glass-blown spheres can serve as high quality resonant structures with superior degree of isotropy. This section investigates the resonant properties of fabricated spheres using non-contact characterization methods facilitated by a Laser Doppler Vibrometer (LDV). For the experiment, a 3-D shell die was eutectically bonded to a piezoelectric (PZT) plate actuator and packaged using a ceramic DIP package, Fig. 4. The PZT was chosen for the preliminary experiments for simple excitation of multiple order vibratory modes in spatial 3-D structures. A Polytec OFV5000 single-point LDV was used to directly measure velocities of points on the vibrating shell surface in real time.

Finite Element Modeling (FEM) of the glass-blown shell with a 0.9 mm diameter and a 10  $\mu\text{m}$  average thickness predicted that dynamically balanced 4-node wineglass modes occur at the resonant frequencies of 1.271 MHz  $\pm 0.3\%$ . For the experimental characterization, the packaged glass-blown shell was mounted on a rotary stage in focus of the LDV, Fig. 5. The PZT substrate was driven with 1 V AC at frequencies ranging from 1.25 to 1.29 MHz. In order to measure velocity as a function of the angular position on the shell (longitude), a scan was performed by rotating the packaged device with respect to the stationary LDV beam in 15° increments of longitude. Fig. 6 shows frequency responses of the glass-blown shell at several locations in the equatorial plane. The measurement reveals a 0.63% relative frequency mismatch  $\Delta f/f$  between the two theoretically degenerate wineglass modes.

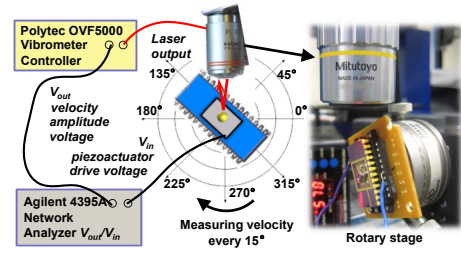


Figure 5: Schematic of the experimental testbed for dynamic characterization of glass-blown shells as mechanical elements.

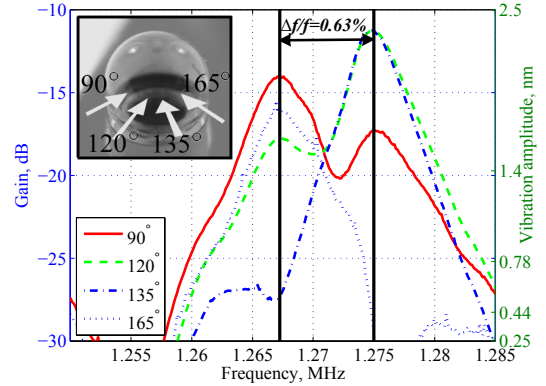


Figure 6: Measured frequency responses corresponding to the 4-node wineglass modes, revealing mismatch  $\Delta f/f$  of only 0.63%.

Next, we analyzed the mode-shapes corresponding to the two resonant frequencies and compared them to the theoretical 4-node wineglass velocity distributions. Velocity amplitudes were measured at 24 equally spaced points along the shell equator and plotted in polar coordinates, Fig. 7. As expected from FEM, the elastic wave patterns exhibit 4 points with zero displacement, which is a characteristic property of a 4-node wineglass mode [1]. The relative spatial orientation between the two 4-node wineglass velocity patterns is defined by the principal axes of elasticity. For a fixed latitude  $\theta$  cross section, the radial displacement  $r$  of an order  $m$  vibratory mode is a function of time  $t$  and longitude angle  $\varphi$  [5]:

$$r(\varphi) = P_n^m(\cos\theta) \sin(m\varphi + m\varphi_0) \cos(\omega t),$$

where  $P_n^m(\cdot)$  is the associated Legendre function and  $\omega$  is the vibration frequency. The experimental velocity amplitude maps measured at the equator for  $m = 2$  mode were fitted to this analytical model, revealing  $\varphi_0 = 27^\circ$  angle between the principal axes of elasticity, Fig. 7. The non-contact characterization using off-chip actuation revealed isotropy and principal axis alignment on par with the state-of-the-art planar silicon MEMS [1], calling for the development of integrated on-chip transducers.

### TRANSDUCER INTEGRATION

Integration of electromagnetic and electrostatic transducers with the glass-blown spherical resonators requires definition of conductive traces and electrodes on the curved 3-D surfaces of the spherical structures. Conventional methods such as line-of-sight metal deposition using a shadow mask are not practical due to the aspect ratio limitations.

### 3-D Metal Fabrication

Instead of patterning metal conductors on the curved surface of already glass-blown spherical structures, the explored fabrication approach relied on definition of metal features prior to the glassblowing step, Fig. 8(a). The flat metal features are deposited on top of the Pyrex substrate using, for instance,



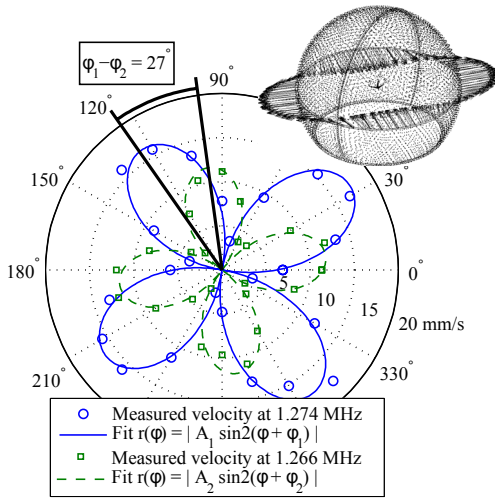


Figure 7: Measured velocity distribution along the equator of a spherical shell excited into 4-node wineglass modes by PZT.

conventional lift off procedure. When the bonded Pyrex-Si wafer stack with patterned metal structures is heated above the 850 °C softening point of glass, spherical glass structures with integrated 3-D metal electrodes and traces are created, Fig. 8(b).

The main practical challenge of the proposed technique was devising a metal stack that is ductile enough to plastically deform together with the glass substrate during the glassblowing step. At the same time, the metal conductor should be resistant to degradation during the high-temperature treatment. The initial approach of using a stack of 0.5  $\mu\text{m}$  Au and 0.05  $\mu\text{m}$  Cr proved intricate due to the partial segmentation of the continuous traces during the plastic deformation phase of the glassblowing step. This limitation was overcome after multiple design iterations by introducing an intermediate 0.8  $\mu\text{m}$  thick layer of ductile Cu between the Cr adhesion layer and the Au corrosion resistant top layer. Fig. 1(b) and 8(b) show fabricated samples containing glass-blown spherical shells with integrated 3-D metal electrodes and traces, formed from a flat Pyrex glass wafer with patterned Cr-Cu-Au metal stack.

### Design of Integrated Transducers

Successful fabrication of the patterned metal features on the surface of glass-blown spherical structures allowed for the integration of electromagnetic and electrostatic transducers. The explored architecture for on-chip electromagnetic transducers utilizes 3-D metal traces on the surface of a glass-blown shell, Fig. 8. The metal trace was patterned as a folded coil to account for the stretching of the metal trace during the plastic deformation of the glass shell. The final 3-D geometry of the shell and metal electrodes was defined by the glassblowing step, which created a 20  $\mu\text{m}$  wide 3-D metal trace across a spherical resonant shell of 1.3 mm diameter, Fig. 8(b).

For the generation of magnetic field a pair of millimeter-scale 0.5 Tesla permanent magnets was bonded to the die on opposite sides of the glass-blown shell, Fig. 9. When a current is passed through the metal trace on the spherical shell, a distributed Lorentz force is generated which is used to excite mechanical response of the spherical shell. While electromagnetic actuation is commonly used in micro- and nano-scale resonators [6], its drawback is the demanding requirement for strong magnetic fields (on the order of 1 Tesla), which are usually achieved by using external permanent magnets or superconductive coils.

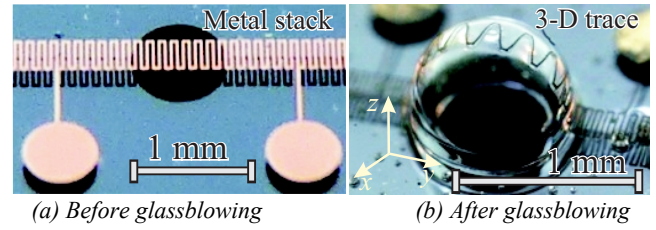


Figure 8: Photographs of a continuous 20  $\mu\text{m}$  wide, 130  $\Omega$  metal trace fabricated on a glass-blown spherical shell structure.

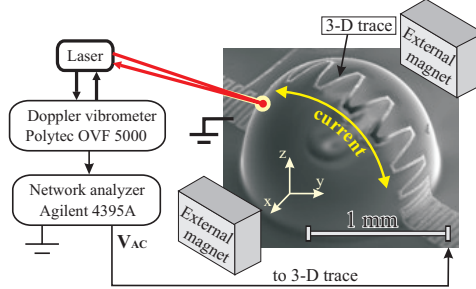


Figure 9: Schematic of the experimental testbed for on-chip electromagnetic excitation of glass-blown resonant shells.

The 3-D metal fabrication technology was also used to implement electrostatic transducers integrated with glass-blown spherical resonators. The idea behind the design of the 3-D capacitors for electrostatic transduction is to form a large-area, high aspect ratio capacitor between the resonant shell and stationary electrodes supported by satellite spherical structures, Fig. 1 and 2. The diameter of the implemented central resonant shell was approximately 1.3 mm, while the satellite smaller shells were of 0.85 mm in diameter.

### ON-CHIP TRANSDUCER CHARACTERIZATION

Feasibility of the 3-D spherical glass-blown resonators with integrated transduction was experimentally demonstrated by driving the central resonant shell into mechanical resonance.

#### Electromagnetic Actuation

Operation of the 3-D electromagnetic transducers was characterized experimentally using a spherical shell with integrated 20  $\mu\text{m}$  wide, 130  $\Omega$  metal trace running across the shell, Fig. 8. An AC actuation current of 0.2 mA was passed through the metal trace in presence of a 0.5 Tesla magnetic field generated by the two millimeter scale permanent magnets, Fig. 9. A Lorentz force on the order of 0.5  $\mu\text{N}$  was generated to actuate vibrations of the glass-blown shell. The mechanical response of the shell was measured using the LDV. Frequency response characterization revealed a 687 kHz resonance corresponding to a rocking mode of shell vibrations, Fig. 10. While this experiment demonstrated operational 3-D electromagnetic resonators with an integrated actuator, requirement for relatively high currents and magnetic fields motivated the investigation of alternative transduction approaches.

#### Electrostatic Actuation

Performance of the integrated 3-D electrostatic transducers was characterized using a fabricated prototype with 4 discrete capacitors formed between the central resonant shell and the smaller satellite structures, Fig. 1(b). Unlike the previous electromagnetic architecture, the electrostatic design ensures selective excitation of the 4-node wineglass modes which provides inherent rejection of common mode accelerations and has potential

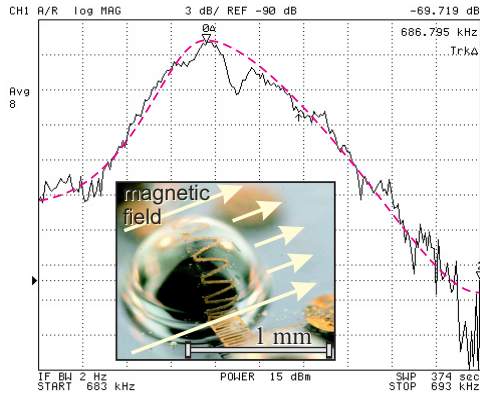


Figure 10: Measured frequency response of a glass-blown shell actuated with an on-chip 3-D magnetic transducer.

for high quality factor and low phase noise operation [1]. To excite vibrations of the central shells, a combination of DC and AC voltages was applied across the driving capacitors, Fig. 11. Mechanical response of the electrostatically excited resonator was characterized by measuring velocities at 36 equally spaced locations along the shell equator using the LDV. A 4-node wineglass mode of vibration was identified at 943.7 kHz. This resonant frequency differs from 1.27 MHz previously observed using PZT due to the increased diameter of the shell with integrated metal (1.3 mm compared to 0.9 mm).

Velocity amplitude data for the shell equator vibrating at 943.7 kHz was collected and plotted in polar coordinates to analyze the mode-shape in more detail, Fig. 12. The measurement data shows a characteristic pattern of a wineglass mode with 4 nodes and 4 points of maximum velocity amplitude. Analysis of the velocity phase data revealed 4 regions of 180° alternating phase, confirming the 4-node wineglass mode. The experiments demonstrate feasibility of integrated 3-D capacitors for transduction of dynamically balanced wineglass modes in glass-blown spherical shell resonators.

## CONCLUSIONS

A new technology for fabrication of 3-D spherical shell MEMS resonators with integrated electromagnetic and electrostatic transduction was developed and experimentally demonstrated. The fabrication approach takes advantage of plastic deformation driven by pressure and surface tension forces (glassblowing) to create smooth and symmetric, high aspect ratio 3-D structures. The axisymmetric 3-D shell architectures demonstrate surface roughness on the order of 1 ppm and provide inherent robustness to fabrication imperfections. Without any trimming or tuning of the natural frequencies, a 1 MHz shell resonator demonstrated a 0.63% frequency mismatch between two degenerate wineglass modes, on par with the state-of-the-art planar silicon MEMS. Even though the presented results are the initial steps toward mature dynamic 3-D MEMS, we believe the approach may lead to high precision devices with high aspect ratio architectures, efficient low noise transduction, increased stability, and reduced energy dissipation. The approach may lead to a new class of inertial instruments and truly exploiting the physics of 3-D elastic waves on micro-scale.

## ACKNOWLEDGEMENTS

This work was supported by the National Science Foundation grant CMMI-0928999. Design, modeling, and characterization was performed in the UCI Microsystems Laboratory. The authors

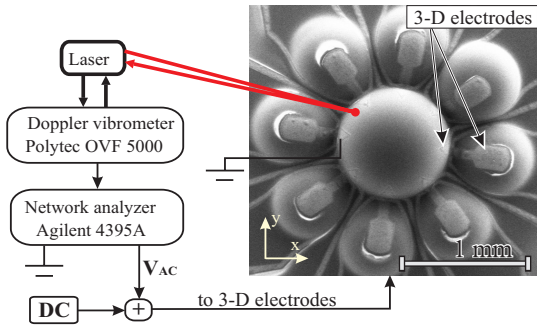


Figure 11: Schematic of the experimental testbed for on-chip electrostatic excitation of glass-blown resonant shells.

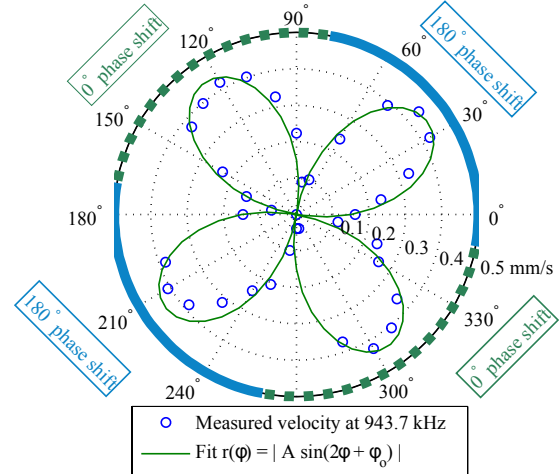


Figure 12: Measured velocity amplitude and phase distribution along the equator of a spherical shell vibrating in a 4-node wineglass mode excited by on-chip capacitive transducers.

would like to acknowledge the UCI Integrated Nanosystems Research Facility and Materials Characterization Center.

## REFERENCES

- [1] C. Nguyen, "MEMS Technology for Timing and Frequency Control," IEEE Trans. Ultrasonics, Ferroelectrics and Frequency Control, vol. 54, no. 2, pp. 251-270, Feb. 2007.
- [2] E. J. Eklund, A. M. Shkel, "Glass Blowing on a Wafer Level," IEEE JMEMS, vol. 16, no. 2, pp. 232-239, 2007.
- [3] E. J. Loper, D. D. Lynch, K. M. Stevenson, "Projected Performance of Smaller Hemispherical Resonator Gyros," Proc. Position Location and Navigation Symposium, 61-64, 1986.
- [4] E. J. Eklund, A. M. Shkel, S. Knappe, E. Donley, J. Kitching, "Glass-blown Spherical Microcells for Chip-Scale Atomic Devices," Sensors and Actuators A: Physical, Vol. 143, Issue 1, pp. 175-180, 2008.
- [5] F. I. Niordson, "Free Vibrations of Thin Elastic Spherical Shells," Int. J. Solids Structures, vol. 20, pp. 667-687, 1984.
- [6] A. N. Cleland, M. L. Roukes, "Fabrication of High Frequency Nanometer Scale Mechanical Resonators from Bulk Si Crystals," Appl. Phys. Lett., vol. 69, no. 18, pp. 2653-2655, 1996.

## CONTACT

\* A.A. Trusov, tel: +1-949-824-6314; atrusov@uci.edu.

# NEAR FIELD PHOTOTHERMAL ANNEALING FOR RAPID LASER PRINTING OF METALLIC MICRO AND NANO STRUCTURES

Fan Xiao<sup>1\*</sup>, Ting-Hsiang Wu<sup>2</sup>, and Pei Yu Chiou<sup>1</sup>

<sup>1</sup>Department of Mechanical and Aerospace Engineering, University of California at Los Angeles, USA

<sup>2</sup>Department of Electrical Engineering, University of California at Los Angeles, USA

## ABSTRACT

We report on a rapid near field photothermal printing (NPTP) approach for fabricating metallic micro- and nano-structures guided by flexible and transparent polymer molds. The optical energy of nanosecond laser pulse is spatially redistributed by a PDMS phase-shifting mask, resulting in selective gold melting in light intensity enhanced areas. The melted gold migrates to cold areas and forms desired structures after cooled down. Using NPTP, We have demonstrated rapid laser printing of periodic Au nanowire array with a 320 nm linewidth, nanosphere arrays with 400 nm in diameter, and non-periodic structures on both glass and PDMS substrate across a 1 mm<sup>2</sup> area with few laser pulses.

## INTRODUCTION

Metallic micro and nanostructures have wide applications in solar cell harvesting[1], plasmonic devices[2], color filters[3], and biomedical fields such as metallic particle guided gene delivery[4], photothermal therapy[5], and biosensors[6]. Methods for fabricating metallic nanostructures are versatile, ranging from chemical synthesis, electron beam lithography, ion beam lithography, nanoimprint lithography (NIL)[7], and laser induced dewetting processes. Among them, laser induced dewetting process is considered as an economical method for rapid and large area fabrication.

To future guide laser induced dewetting and self-organization processes, two types of methods have been proposed, including using pre-patterned substrates[8], and spatially shaping the projected laser patterns[9, 10]. Linearly polarized pulse laser intrinsically induces spatially periodic energy density distribution and Multi-beam Interference Lithography (MIL) utilizes at least two laser beams to redistribute periodic energy density at the metallic film surface. They both belong to the later type and allow low cost and rapid fabrication of two-dimensional nanowires and nanoparticles on a continuous thin metallic film. Using nanosecond laser pulses, MIL based photothermal annealing techniques are capable of direct laser printing of periodic metallic nanostructures from thin metal films coated on various types of substrates including glass, silicon, and polymer[11]. However, both of them are limited to fabricating periodic structures with simple shapes.

Here, we propose a rapid laser printing technology capable of fabricating both periodic and non-periodic micro- and nano-scale metallic structures using near field photothermal printing (NPTP) guided by a transparent phase-shifting mask. The schematic process using NPTP to fabricate periodic nanoparticles is illustrated in Fig 1. A laser pulse with uniform spatial light intensity passing through a PDMS phase-shifting mask redistributes its optical energy in space and forms a non-uniform light intensity profile at the interface of this PDMS mask and the underlying gold thin film. The laser pulses shaped by the PDMS phase-shifting mask selectively heat up and melt the gold film in areas with high light intensity. Due to instability of a molten gold film on a glass substrate, the molten film, driven by surface tension, quickly migrates to cold areas. The shape evolution of the molten film is controlled by surface tension of molten gold, laser pulse energy,

duration, and pulse number. Since the formation of these gold nanostructures needs only one to few laser pulses, it has the potential for rapid, large-scale nanofabrication by scanning laser pulses across a large area. Furthermore, since the local shape of a PDMS mold determines the near field light pattern, NPTP has the potential for fabricating arbitrary shape of 2D metal nanostructures by designing the PDMS phase-shifting mask.

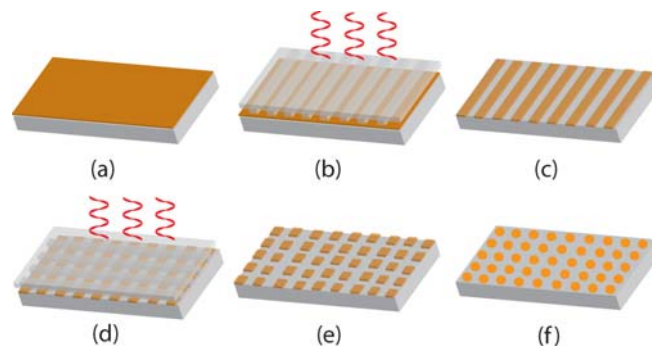


Figure 1: Schematic of NPTP processes. (a) A thin gold film is coated on a glass slide; (b) A 1-D grating PDMS mold is placed on top of a gold thin film and irradiated by pulsed laser; (c) Gold nanowires form after exposure; (d) Rotate the PDMS mold and repeat the above processes (b); (e) Isolated gold squares form; (f) Gold squares bead up and form nanospheres after flood laser exposure.

## SIMULATION AND EXPERIMENTAL RESULTS

Fig. 2 shows the simulated light intensity distribution near a periodic PDMS mold and a gold thin film using the finite difference time domain (FDTD) method. The incident light is TE polarized with a wavelength of 532 nm. Fig. 2(a) shows the grating pattern on the PDMS mold with a periodicity of 5/3  $\mu\text{m}$  and positioned in contact with a 10 nm gold film on a glass substrate. Fig 2(b) shows electric field redistribution during propagation through the grating structure. The incident uniform laser pulse is affected by the periodic PDMS grating structure, resulting in non-uniform profile. The total energy density distribution on the metal surface is plotted in Fig 2(c). The optical energy is strongly modified and shows a peak right underneath the grating tip and a valley between adjacent grating protuberances. Assume there is a threshold incident energy fluence for metal melting, by adjusting the pulse energy, gold thin film near the strong light intensity regions above the threshold is selectively melted while gold film near the low energy regions remain solid. Due to high surface tension of molten film, the molten gold migrates to the cold areas at a speed over 200m/s[12]. After it quickly cools down, film rupture is expected to be observed.

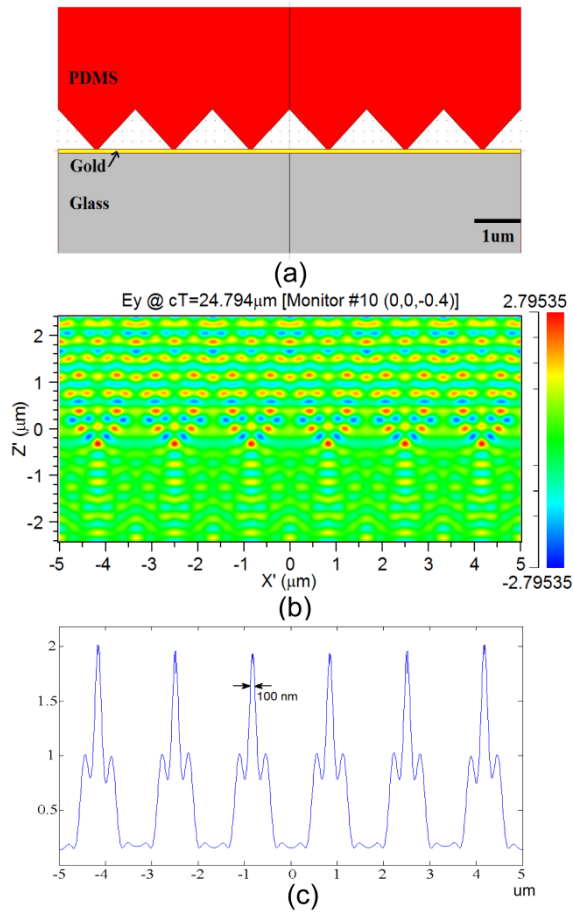


Figure 2: (a) PDMS/Au/Glass structure in Rsoft simulation; (b) FDTD Simulated electric field distribution during propagation through the grating structure; (c) Total energy density redistribution on the gold surface.

In the experiment, a Q-switched Nd:YAG pulse laser with a pulse width of 6 ns and a wavelength of 532 nm is applied. A 1 nm Ti/10 nm gold thin film is deposited on a 100 μm thick glass substrate by electron-beam evaporation. A PDMS mold with 5/3 μm spacing grooves is simply a replica of a plane ruled reflection grating with 34° nominal blaze angle and 600 grooves/mm (10RG600-1850-2, Newport Corp).

To fabricate the PDMS phase-shifting mold, a 3 mm thick PDMS layer is first cured on top of a silicon wafer to provide a mechanical support for molding. A thin PDMS layer is then spin coated on the thick PDMS base. Before it is cured, the grating structure is placed on top of this thin PDMS film for molding. This process is carried out in vacuum to drive out the bubbles trapped between the grating and the PDMS. The PDMS mold is peeled off from the grating structure after it is cured.

Fig. 3 demonstrates the NPTP processes for fabricating a 1D gold nanowire array, 2D nanosquare and nanosphere arrays. During laser annealing process, the PDMS phase-shifting mold is generally positioned on the Au thin film without applying any external mechanical pressure. In Fig. 3(a), separated gold wires are formed after illuminating two laser pulses with a fluence of 80 mJ/cm<sup>2</sup>. Smaller line width can be achieved by increasing the laser fluence such that a wider melting zone can be achieved. However, the laser

fluence should also be kept smaller enough so that the peak intensity regions do not evaporate, which causes re-deposition of Au residues on the PDMS mold. The narrowing can also be achieved by increasing the pulse number. By rotating the PDMS mold by 90° and followed by another three laser pulsing, gold nanowires are cut into squares (Fig 3(b)). More laser pulses or larger fluence is used in wire-cutting to achieve the same rupture due to the thicker nanowires compared to the initial continuous film. The shape of these isolated 2D nanosquares can evolve into 3D nanospheres by flood laser pulsing with a fluence of 150 mJ/cm<sup>2</sup>. Molten metal squares ball up due to surface tension driven shape evolution and form nanospheres with smooth surface. Fig. 3(c) and 3(d) show the SEM images of two types of periodic gold nanospheres arrays. The latter formed by rotating the PDMS grating mold with 120°, with isolated diamonds formation before flood exposure. The periodicity of the nanospheres in two dimensions can also be different by using different grating periodicity in the two sequential exposures. A 6 mJ laser pulse utilized in this experiment is able to cover a print area of 1 mm<sup>2</sup>. Large print area can be accomplished by scanning the light beams across the phase shift mask.

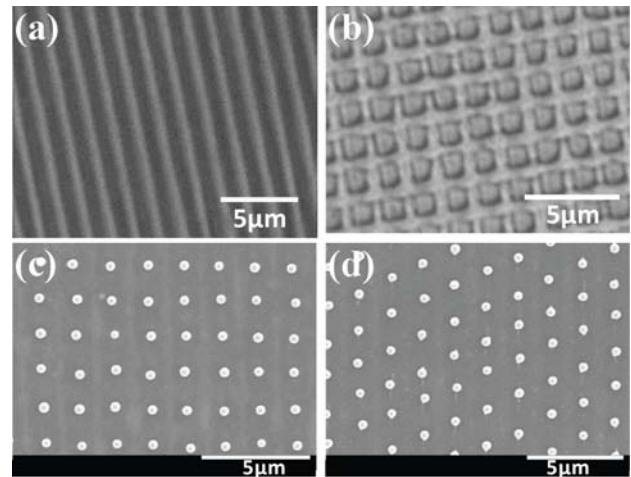


Figure 3: Photothermal annealed periodic nanostructures (line-line and particle-particle spacing is 5/3 μm). (a) gold nanowires; (b) 1×1 μm<sup>2</sup> gold square before flood exposure; (c) 400 nm diameter gold nanospheres form orthogonal array after flood exposure; (d) hexagonal gold nanosphere array.

Since NPTP utilizes near field optical patterns to generate local heating to induce metal dewetting, the fabricated structures are not limited to periodic patterns. Any arbitrary shape of patterns can be fabricated by designing the phase shifting masks. Fig. 4 demonstrates photothermal annealing of few example patterns using NPTP. The PDMS phase shifting mold used here is designed by ourselves and fabricated by replicating a patterned photoresist master mold on a silicon wafer. All patterns in Fig. 4 are obtained by a single laser pulse. The metallic structure formed is determined by reconstructed optical energy distribution after passing through the phase-shifting mold, resulting in not exact one-to-one mapping compared to the phase-shifting pattern. By properly designing the PDMS phase-shift mask, holes, rings, triangles, crosses, squares, meshes, and more complex shape of structures can be achieved.

Plastic and polymer are two common types of materials used as flexible substrates in electronics and photonic applications. The

melting temperature of these materials is usually much lower than the melting temperature of metals and semiconductors. Pulse laser annealing is a commonly applied technology in electronic industry to obtain high quality polycrystalline film since it minimizes heating to the underlining substrates and is compatible with the low thermal budget of these low melting temperature substrates. In NPTP, the pattern formation process takes place within  $1\mu\text{s}$ , so it also permits laser printing on substrates that have low thermal budget. Shown in Fig. 5 is NPTP printing of a 100nm thick gold thin film coated on a flexible PDMS substrate.

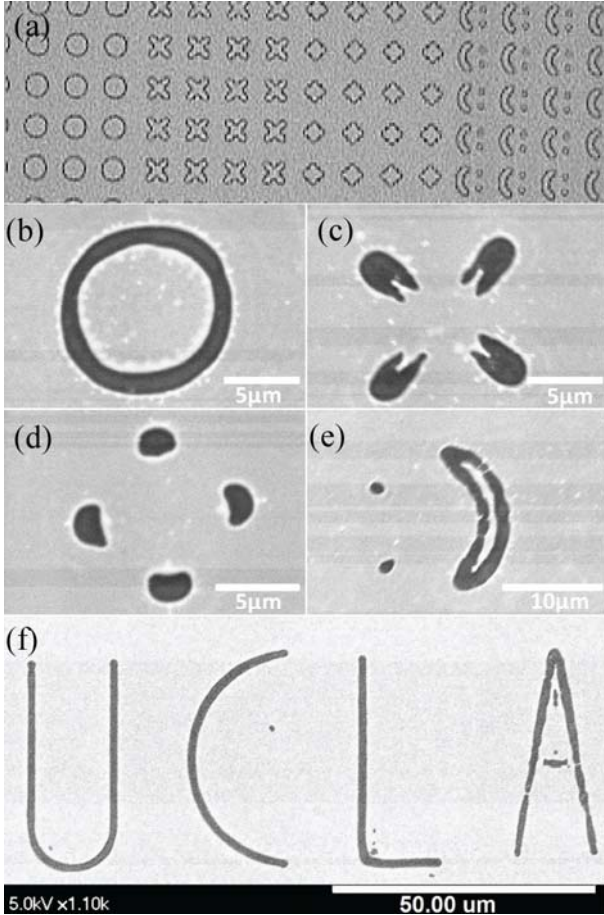


Figure 4: NPTA printing of arbitrary metallic structures (a) PDMS phase-shifting mask used to print arbitrary patterns; (b)-(e) arbitrary metallic patterns printed using NPTP corresponding to the phase-shifting patterns in (a); (f) "UCLA" pattern with smallest line width of  $1\mu\text{m}$ ;

## DISCUSSION AND CONCLUSION

The possible damage of PDMS phase-shifting mold is considered. One possible cause is contamination due to redeposition of evaporated metal. The laser pulse has a spatial Gaussian profile. In order to achieve large area fabrication, the maximum energy in the center of the laser spot can become high enough to evaporate the metal. By controlling the incident laser energy, the evaporation of metal can be avoided. The pulse laser annealing process takes place within  $1\mu\text{s}$ , so the burning of PDMS due to hot molten metal underneath is negligible.

The printing resolution of NPTP is mainly limited by two factors including near field optical field distribution resolution and the thermal diffusion length in the thin film. The former is controlled by the phase-shifting pattern on PDMS mold and incident laser energy fluence. Simulation shows that given the same periodicity, different phase-shifting pattern results in similar redistribution profile constituting of interlaced peaks and valleys, but in aspects of peak-valley ration and FWHM, the modulation of light still shows difference. By applying different energy fluence, the width above the melting threshold is different, which induces the primary melting of the metal film. From the simulation result shown in Fig. 2(c), a 100 nm wide optical heating line can be produced using near field phase shifting mold with a 532 nm wavelength light beam. However, this narrow heating area is broadened quickly in the lateral direction by thermal diffusion in the gold thin film during pulse duration (6 nsec). The thermal diffusion length in a 10 nm thick gold film is 870 nm (estimated by  $L = (Dt)^{1/2}$  where  $D$  is the thermal diffusion coefficient on a 2D thin film and  $t$  is the pulse duration 6 nsec), which means the heat quickly diffuses to the adjacent area where the optical energy absorbed is under the melting threshold, and makes wider area melt. To increase the printing resolution of NPTP, laser pulses with shorter pulse duration can be used to reduce the thermal diffusion length.

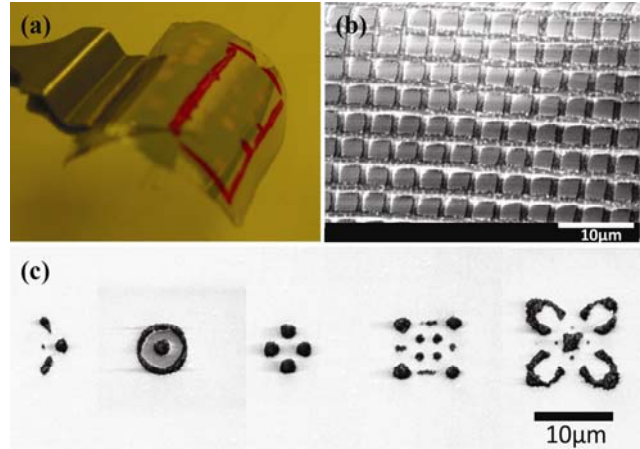


Figure 5: NPTA printing of metallic patterns on thin PDMS substrate; (a) PDMS substrate with thin gold layer on top of it; (b) Gold square array on PMDS; (c) Arbitrary metallic structures on PMDS.

To conclude, we have demonstrated a near field photothermal printing method for rapid laser printing of metallic micro and nanostructures, such as nanowires, nanosquares, and nanospheres and other arbitrary patterns. It utilizes laser induced dewetting and self-organization processes guided by spatially shaped light patterns between a phase shifting mask and the printed metal thin film. The rapid laser pulsing, metal dewetting, and shape evolution processes promise NPTP a high speed printing technology for fabricating metallic nanostructures.

## ACKNOWLEDGEMENT

This project is supported in parts by the NSF grants CBET-0853500 and NSF ECCS-0901154.

## REFERENCE

- [1] Law, M., et al., Nanowire dye-sensitized solar cells. *Nature materials*, 2005. 4(6): p. 455-459.
- [2] Righini, M., et al., Parallel and selective trapping in a patterned plasmonic landscape. *Nature Physics*, 2007. 3(7): p. 477-480.
- [3] Laux, E., et al., Plasmonic photon sorters for spectral and polarimetric imaging. *Nature Photonics*, 2008. 2(3): p. 161-164.
- [4] Wu, T.H., et al., Image patterned molecular delivery into live cells using gold particle coated substrates. *Opt. Express*, 2010. 18: p. 938-946.
- [5] Cho, M.H., et al., Designed fabrication of multifunctional magnetic gold nanoshells and their application to magnetic resonance imaging and photothermal therapy. *Angewandte Chemie (International ed. in English)*, 2006. 45(46): p. 2138344.
- [6] Alivisatos, P., The use of nanocrystals in biological detection. *Nature Biotechnology*, 2004. 22(1): p. 47-52.
- [7] Cui, B., C. Keimel, and S.Y. Chou, Ultrafast direct imprinting of nanostructures in metals by pulsed laser melting. *Nanotechnology*, 2010. 21: p. 045303.
- [8] Xia, Q. and S.Y. Chou, The fabrication of periodic metal nanodot arrays through pulsed laser melting induced fragmentation of metal nanogratings. *Nanotechnology*, 2009. 20: p. 285310.
- [9] Kaganovskii, Y., H. Vladomirsky, and M. Rosenbluh, Periodic lines and holes produced in thin Au films by pulsed laser irradiation. *Journal of Applied Physics*, 2006. 100: p. 044317.
- [10] Nishioka, K. and S. Horita, Periodic arrays of submicron Si and Ni dots on SiO<sub>2</sub> fabricated using linearly polarized Nd:YAG pulsed laser. *Applied Physics A: Materials Science & Processing*, 2008. 91(2): p. 235-240.
- [11] Moon, J.H., J. Ford, and S. Yang, Fabricating three-dimensional polymeric photonic structures by multi-beam interference lithography. *Polymers for Advanced Technologies*, 2006. 17(2): p. 83-93.
- [12] Bischof, J., et al., Dewetting modes of thin metallic films: Nucleation of holes and spinodal dewetting. *Physical review letters*, 1996. 77(8): p. 1536-1539.

## CONTACT

\* Fan Xiao, tel: +1-310-880-1399; michille521@gmail.com

# A RESETTABLE HIGH-DENSITY MICROFLUIDIC PARTICLE TRAPPING SYSTEM

Ryan D. Sochol<sup>1\*</sup>, Barthélemy Lüthi<sup>1</sup>, Kosuke Iwai<sup>1</sup>, Megan Dueck<sup>2</sup>, Luke P. Lee<sup>2</sup> and Liwei Lin<sup>1</sup>

<sup>1</sup>Department of Mechanical Engineering

<sup>2</sup>Department of Bioengineering

Berkeley Sensor and Actuator Center, University of California, Berkeley, USA

## ABSTRACT

Microfluidic bead-based microarrays offer an ideal platform for chemical and biological applications, such as bio-molecule detection, diagnostics and drug screening. Despite the numerous advantages inherent to dynamic bead-based microfluidic arrays, current microparticle trapping methods remain limited in terms of trapping density and device resettability. Here we present a simple, resettable microparticle arraying system by utilizing geometric designs in microfluidics to manipulate microscale hydrodynamics. Under forward fluidic flow, arrays of individual 15  $\mu\text{m}$  diameter microbeads immobilize in designated trapping positions between microposts. Under backward fluidic flow, the arrayed microbeads release rapidly to reset the microfluidic device.

## INTRODUCTION

### Dynamic Microarrays

There are two fundamental classes of microarrays: static and dynamic microarrays. Static microarrays consist of bio-molecules or chemicals immobilized on a static substrate [1]. Alternatively, dynamic microarrays consist of bio-molecules or chemicals immobilized on mobile substrates, such as microparticles (e.g. microbeads) [2]. Dynamic microarrays offer a superior platform compared to static microarrays due to several advantages, including faster reaction times due to larger surface areas of the microparticles, reduced background noise, and the ability to ‘mix-and-match’ particles corresponding to different screenings [3-5]. Also, the constant mixing of solutions and particulate substrates in

microfluidic channels results in faster reaction kinetics compared to the diffusion-based mixing of static systems. One caveat of particulate-based microfluidic platforms is that the microparticles must be visualized for signal detection (e.g. via flow cytometry). However, for systems that preclude expensive, high-maintenance flow cytometry equipment, alternative technologies are required to immobilize microparticles for signal detection.

### Microparticle Trapping Techniques

Microfluidic particulate arraying methods provide an effective alternative to flow cytometry for bio-molecule detection applications [6]. Currently, there are a limited number of passive, hydrodynamic techniques for immobilizing microparticles [7-10]. For example, to immobilize cells, Khademhosseini et al. use microwells for cell docking [8], while Di Carlo et al. integrate elevated U-shaped ‘weir’ trapping structures into a microfluidic system [9]. In terms of microbeads, Kim et al. use microfilters composed of micropillars to immobilize microbeads [10]. Although the aforementioned techniques enable the immobilization of microparticles in microfluidics, they lack the ability to achieve high-density arrays of individual microparticles (i.e. without particle-particle contact). To independently array microparticles (i.e. one particle per trap), Tan et al. employ a ‘trap-and-release’ microfluidic system, and have demonstrated effective trapping of microbeads [3] and hydrogel-encapsulated cells [11]. To further improve microparticle trapping density of individual microparticles, we have previously presented a hydrodynamic

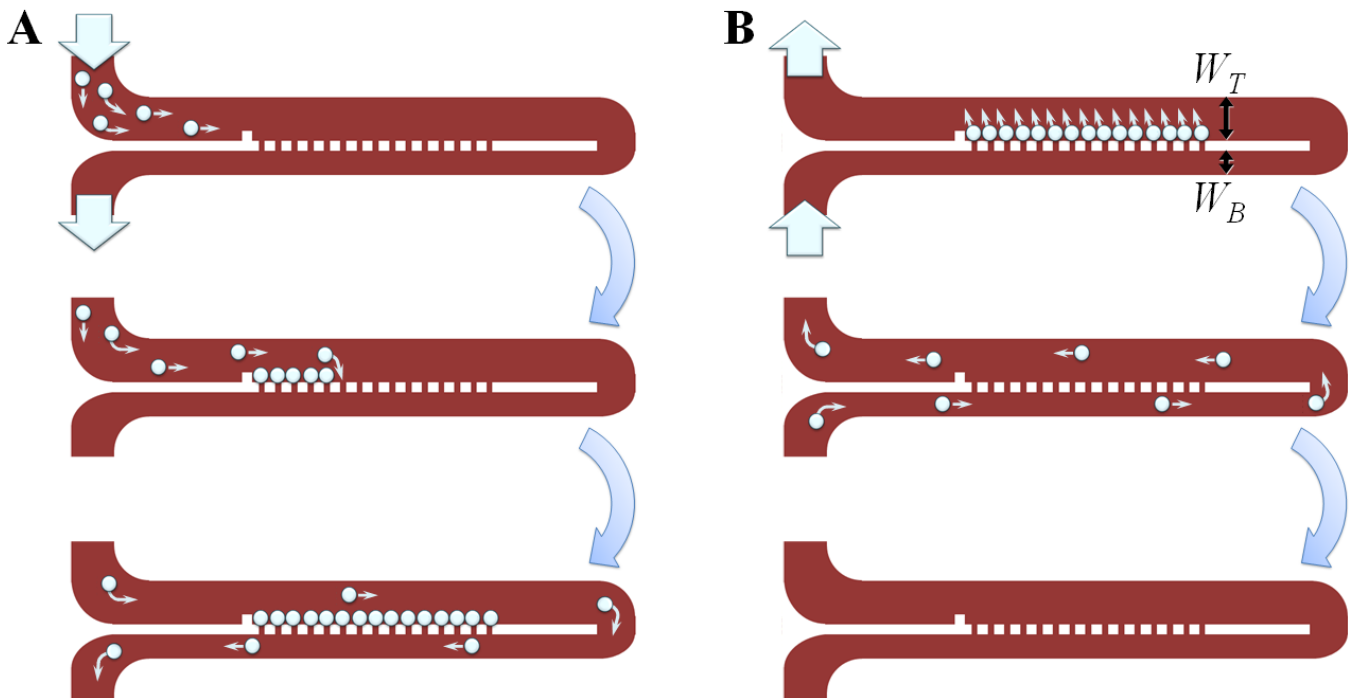


Figure 1: Conceptual illustrations of Resettable Micropost Array Trapping ( $\mu\text{PAT}$ ). (A) Under forward fluidic flow, microparticles array at the designated trapping sites between microposts. (B) Under backward fluidic flow, microparticles release to reset the microarray.  $W_T$  and  $W_B$  denote the top width and the bottom width, respectively.

microbead trapping technique [12]. However, these techniques are limited in terms of device resettability. If resettability cannot be achieved, a new device is required for each particulate-based microarray run, which greatly increases the cost, time and labor associated with these dynamic microarray techniques.

### Microparticle Release Techniques

Simultaneously achieving both high-density arrays of microparticles as well as microdevice resettability has remained a significant challenge [11-13]. Complex techniques have been implemented to release microparticles from trapping sites. For release during forward flow rates, lasers have been used to heat aluminum plates in order to generate microbubbles [3, 11]. As the bubble increases in size, the microparticle is displaced from the trapping site and re-enters the main fluid flow. This technique is ideal for releasing individual microparticles of interest; however, thermal bubble generation is inefficient for resetting an entire microarray (i.e. with thousands of arrayed microparticles). Furthermore, the trapping sites downstream from the released microparticle must be occupied; otherwise the particle will be re-trapped in a vacant downstream trap [3, 11]. For release during backward (alternatively reverse) flow rates, pneumatic valves have been employed to prevent the immobilization of particles at the backs of the original trapping sites to facilitate the release of microparticles [14]. Similarly, accurately placing microfeatures can also redirect microparticles for release during backward flow [13]. In contrast to the prior techniques, here we show that by tuning simple geometric microfluidic designs, both high-density particle trapping and device resettability can be accomplished.

## MICROPOST ARRAY TRAPPING ( $\mu$ PAT)

### Microbead Trapping

The  $\mu$ PAT technique consists of arrays of rectangular microposts which direct flow between the microposts to resolve trapping sites (Fig. 1A). Microbead trapping occurs under forward fluidic flow rates. Initially, flow between the microposts in the upstream area have lower fluidic resistance, which facilitates the transportation and immobilization of microbeads at the designated trapping sites. When microbeads immobilize at each trapping location, flow is diverted from the occupied trap, yielding increased flow rates to the remaining vacant sites. This process continues until beads are immobilized at all of the trapping sites, which redirects fluid flow, and therefore additional microbeads, to the next array of traps (Fig. 1A).

### Microbead Release

Microbeads release under backward fluidic flow rates to reset the microfluidic device. Resettability is achieved through modifying two simple dimensions – the top width ( $W_T$ ) and the bottom width ( $W_B$ ). Initially, the microbeads are released from the trapping sites. When the microbeads enter other arrays of traps, the microbeads bypass all of the traps instead of re-arraying at the bottom side of the traps. By directing microbeads to an outlet location, the device can be reset for additional experiments with new sets of microbeads, thereby enabling the use of a single microdevice for multiple bead-based experiments.

## DESIGN

The foundation of resettable  $\mu$ PAT is that for an equivalent input flow rate,  $W_T$  and  $W_B$  can be tuned to control both the trapping mode and the resetting mode for an array. Specifically, the microchannel widths must be optimized to ensure that microbeads ultimately: (i) immobilize in the designated trapping

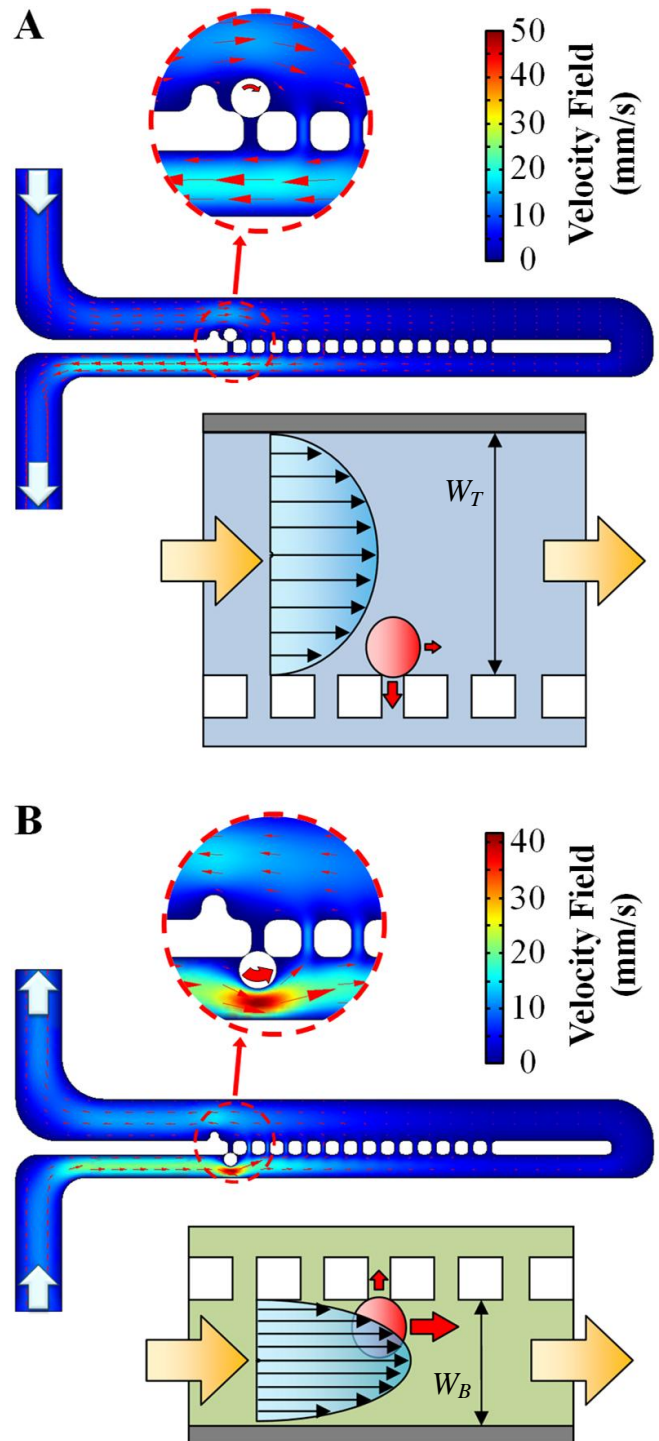


Figure 2: Two-dimensional COMSOL Fluid Velocity Field Simulations and Conceptual Schematics of Fluidic Forces on Microbeads for Resettable  $\mu$ PAT. (A) Trapping Case. (B) Resetting Case.  $W_T$  and  $W_B$  denote the top width and the bottom width, respectively. The magnitude of the input velocity is  $7.83 \times 10^{-3}$  m/s for both cases.

sites for the trapping mode, and (ii) bypass the back (bottom) sides of the trapping sites for the resetting mode. For the trapping case,  $W_T$  must be high enough such that the fluid flow bypassing a trapped bead does result in the bead being displaced from the trap



(Fig. 2A). However, if  $W_T$  is too high, microbeads will not bypass the occupied trapping sites and instead array on top of previously trapped beads, resulting in bead-bead contact. For the resetting case,  $W_B$  must be minimized to increase the fluidic forces in the microchannel to prevent microbeads from immobilizing at the back sides of trapping sites (Fig. 2B). However, the minimization of  $W_B$  is limited by the polydispersity of the microbeads. Additionally, altering either microchannel width directly impacts the overall flow pattern. Thus, in order to optimize the  $\mu$ PAT system to achieve both modes, both  $W_T$  and  $W_B$  must also be tuned with respect to each other.

## FABRICATION

The resettable  $\mu$ PAT systems can be manufactured using a number of high-aspect ratio microfabrication techniques to fabricate devices in a material of choice (e.g., glass, polymers, etc.). For this study, the  $\mu$ PAT systems were fabricated via standard photolithography and soft lithography methods. Briefly, an 18  $\mu$ m layer of SU-8 negative photoresist was spin-coated onto a clean Si wafer. Using a photomask, the  $\mu$ PAT and microchannel patterns were UV exposed onto the layer of photoresist via contact photolithography. The wafer was then developed to become a positive master for the micromolding process. Next, the silicone elastomer, polydimethylsiloxane (PDMS), was mixed at a 10:1 ratio and poured onto the master. After curing of the PDMS, the elastomer was removed from the master. Individual devices were cut and then punched with holes at inlet and outlet locations. Glass slides were washed in successive dishes of Acetone, Isopropanol and DI water, while the PDMS devices were washed in successive dishes of Isopropanol and DI water. The glass slides and PDMS devices were dried with a Nitrogen gun, and then exposed to UV ozone. Lastly, the PDMS devices were thermally bonded to the glass slides. For the current  $\mu$ PAT system, the microposts were 15  $\mu$ m in width and length, and 18  $\mu$ m in height.

## RESULTS

Resettable  $\mu$ PAT was achieved as microbeads immobilized at the designated trapping sites under forward fluidic flow rates, and released from the trapping sites to reset the microarray under backward fluidic flow rates (Fig. 3). Experimental results for  $\mu$ PAT resettability corresponding to differing dimensions of  $W_T$  and  $W_B$  are shown in Figure 4A. For cases where  $W_B$  was too high (i.e.  $W_B \geq 30 \mu$ m), microbeads ultimately immobilized at the back of the trapping sites when the flow was reversed (Fig. 4). However, one of the results of decreasing  $W_B$  is that the fluidic shear stress at the edge of microbeads located at the back of the trapping sites can be increased (Fig. 2B). By reducing  $W_B$ , microbeads were transported in the direction of the shear stress, ultimately bypassing the potential trapping sites located at the back sides of the traps to reset the microdevice (Fig. 3 and Fig. 4A). This also provides insight into the observation that for cases with higher fluid flow rates, and therefore higher fluidic shear stresses, device resettability was enhanced (Fig. 4). By adjusting  $W_T$  and  $W_B$  such that  $W_T = 45 \mu$ m and  $W_B = 25 \mu$ m, 100% device resettability was accomplished (Fig. 3 and Fig. 4A).

## CONCLUSIONS

In this work, we have successfully demonstrated our novel resettable hydrodynamic microparticle immobilization technique –  $\mu$ PAT – for achieving: (i) high-density and high-throughput arraying of microbeads, and (ii) microarray resettability for a microfluidic device. High-density trapping enables the acquisition of high numbers of data points (i.e. immobilized microparticles)

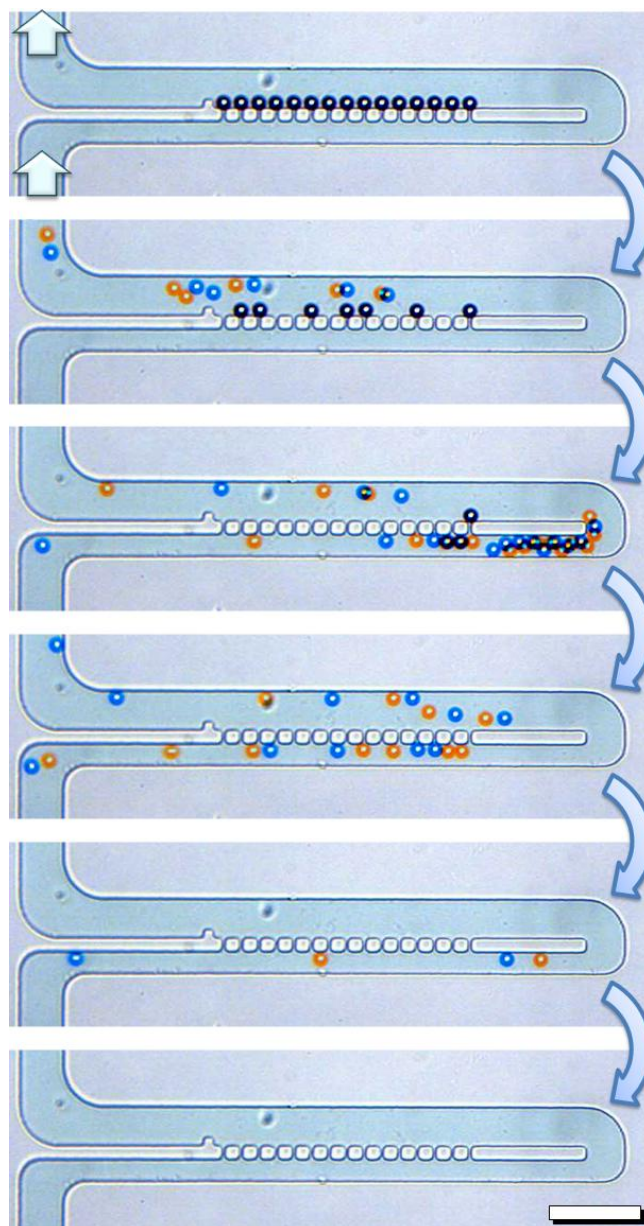


Figure 3: Sequential Micrographs of  $\mu$ PAT Resetability. Under backward fluidic flow, microparticles release to reset the microarray. Scale Bar = 100  $\mu$ m

from a single experiment, without sacrificing device ‘real-estate.’ Microdevice resettability is particularly advantageous since multiple bead-based experiments can be run using a single microfluidic device, thereby significantly reducing the costs, time and labor associated with fabricating multiple devices. Here we tune simple geometric dimensions in microfluidics to array and immobilize microbeads under forward fluidic flow rates, and release the microbeads to reset the arrays under backward fluidic flow rates. While the current system was designed to array 15  $\mu$ m diameter microbeads, the  $\mu$ PAT technique offers a scalable methodology for trapping and releasing particles of any size. Thus, for chemical and biological applications, such as biomolecule detection, diagnostics and drug screening, where dynamic particulate-based microfluidic platforms are ideal, our system offers a simple, yet powerful technique for realizing resettable, high-density microparticle arraying.

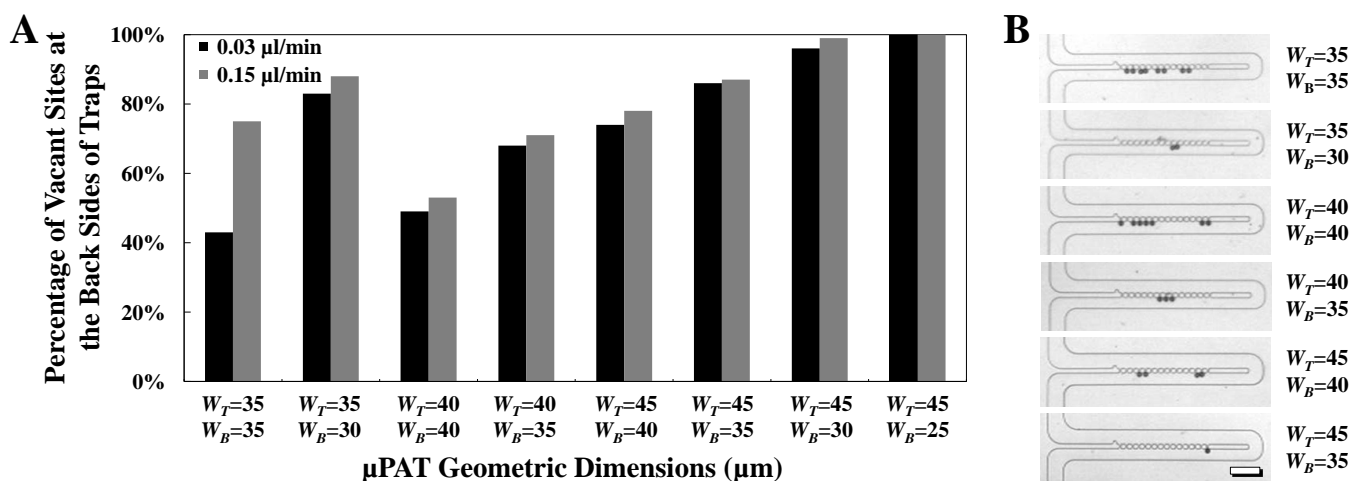


Figure 4: Microdevice Resettability. (A) Percentage of vacant sites located at the back (bottom) sides of trapping sites during backward fluid flow rates of 0.03  $\mu\text{l/min}$  (black) and 0.16  $\mu\text{l/min}$  (gray) for  $\mu\text{PAT}$  with differing geometric dimensions. 100% = Full Microdevice Resettability. (B) Microphotos of microbeads immobilized at the back sides of trapping sites during backward fluid flow rates for  $\mu\text{PAT}$  with differing geometric dimensions.  $W_T$  and  $W_B$  denote the top width and the bottom width, respectively. Scale Bar = 100  $\mu\text{m}$

#### ACKNOWLEDGEMENTS

The authors would like to acknowledge Joanne C. Lo, Paul Lum, Grégoire B. Rouelle, Ben P. Casavant, Armon Mahajerin, Adrienne Higa, Brian Sosnowchik, Liwei Lin Lab, Luke P. Lee Lab (BioPOETS), and the Biomolecular Nanotechnology Center (BNC) for their help, guidance and support.

#### REFERENCES

- [1] W. H. Robinson, C. DiGennaro, W. Hueber, B. B. Haab, M. Kamachi, E. J. Dean, S. Fournel, D. Fong, M. C. Genovese, H. E. N. de Vegvar, K. Skrinier, D. L. Hirschberg, R. I. Morris, S. Muller, G. J. Pruijn, W. J. van Venrooij, J. S. Smolen, P. O. Brown, L. Steinman, and P. J. Utz, "Autoantigen microarrays for multiplex characterization of autoantibody responses," *Nature Medicine*, vol. 8, pp. 295-301, 2002.
- [2] H. Noda, Y. Kohara, K. Okano, and H. Kambara, "Automated bead alignment apparatus using a single bead capturing technique for fabrication of a miniaturized bead-based DNA probe array," *Analytical Chemistry*, vol. 75, pp. 3250-3255, 2003.
- [3] W. H. Tan and S. Takeuchi, "A trap-and-release integrated microfluidic system for dynamic microarray applications," *Proceedings of the National Academy of Sciences of the United States of America*, vol. 104, pp. 1146-1151, 2007.
- [4] X. B. Zuo, X. H. Yang, K. M. Wang, W. H. Tan, and J. H. Wen, "A novel sandwich assay with molecular beacon as report probe for nucleic acids detection on one-dimensional microfluidic beads array," *Analytica Chimica Acta*, vol. 587, pp. 9-13, 2007.
- [5] J. K. K. Ng and W. T. Liu, "Miniaturized platforms for the detection of single-nucleotide polymorphisms," *Analytical and Bioanalytical Chemistry*, vol. 386, pp. 427-434, 2006.
- [6] J. Y. Du, P. Bernasconi, K. R. Clauser, D. R. Mani, S. P. Finn, R. Beroukhim, M. Burns, B. Julian, X. P. Peng, H. Hieronymus, R. L. Maglathlin, T. A. Lewis, L. M. Liau, P. Nghiemphu, I. K. Mellingshoff, D. N. Louis, M. Loda, S. A. Carr, A. L. Kung, and T. R. Golub, "Bead-based profiling of tyrosine kinase phosphorylation identifies

SRC as a potential target for glioblastoma therapy," *Nature Biotechnology*, vol. 27, pp. 77-83, 2009.

- [7] J. Nilsson, M. Evander, B. Hammarstrom, and T. Laurell, "Review of cell and particle trapping in microfluidic systems," *Analytica Chimica Acta*, vol. 649, pp. 141-157, 2009.
- [8] A. Khademhosseini, J. Yeh, G. Eng, J. Karp, H. Kaji, J. Borenstein, O. C. Farokhzad, and R. Langer, "Cell docking inside microwells within reversibly sealed microfluidic channels for fabricating multiphenotype cell arrays," *Lab on a Chip*, vol. 5, pp. 1380-1386, 2005.
- [9] D. Di Carlo, L. Y. Wu, and L. P. Lee, "Dynamic single cell culture array," *Lab on a Chip*, vol. 6, pp. 1445-1449, 2006.
- [10] D. N. Kim, Y. Lee, and W. G. Koh, "Fabrication of microfluidic devices incorporating bead-based reaction and microarray-based detection system for enzymatic assay," *Sensors and Actuators B-Chemical*, vol. 137, pp. 305-312, 2009.
- [11] W. H. Tan and S. Takeuchi, "Dynamic microarray system with gentle retrieval mechanism for cell-encapsulating hydrogel beads," *Lab on a Chip*, vol. 8, pp. 259-266, 2008.
- [12] R. D. Sochol, A. Mahajerin, B. P. Casavant, P. Singh, M. Dueck, L. P. Lee, and L. Lin, "Bead-immobilized molecular beacons for high throughput SNP genotyping via a microfluidic system," *2009 IEEE 22nd International Conference on Micro Electro Mechanical Systems. MEMS 2009*, pp. 304-7, 2009.
- [13] K. Iwai, T. Wei-Heong, and S. Takeuchi, "A resettable dynamic microfluidic device," *2008 21st IEEE International Conference on Micro Electro Mechanical Systems - MEMS '08*, pp. 649-52, 2007.
- [14] K. Iwai and S. Takeuchi, "A dynamic microarray with pneumatic valves for selective trapping and releasing of microbeads," in *2009 IEEE 22nd International Conference on Micro Electro Mechanical Systems. MEMS 2009: Ieee*, 2009, pp. 371-374.

#### CONTACT

\*Ryan D. Sochol, tel: +1-410-935-8971; rsochol@gmail.com

# IN-PLANE MODE RESONANT CANTILEVERS AS LIQUID-PHASE CHEMICAL SENSORS WITH PPB RANGE LIMITS OF DETECTION

L.A. Beardslee<sup>1</sup>, K.S. Demirci<sup>1</sup>, Y. Luzinova<sup>1</sup>, J.J. Su<sup>1</sup>, B. Mizaikoff<sup>3</sup>, S. Heinrich<sup>2</sup>, F. Josse<sup>2</sup>, O. Brand<sup>1</sup>

<sup>1</sup>Georgia Institute of Technology, Atlanta, Georgia, USA

<sup>2</sup>Marquette University, Milwaukee, Wisconsin, USA

<sup>3</sup>University of Ulm, Ulm, Germany

## ABSTRACT

To reduce fluid damping in liquids and improve the detection limit in liquid-phase chemical sensing applications, resonant cantilever sensors vibrating in their *in-plane* rather than out-of-plane resonant mode have been fabricated and tested, resulting in measured Q-factors up to 70 in water (up to 4,000 in air) and detection limits in the ppb range for polymer-coated cantilevers exposed to volatile organics in water. In-plane vibrations were thermally excited and detected using piezoresistors arranged in a Wheatstone bridge configuration. The special U-shaped layout of the piezoresistive Wheatstone bridge based on diffused silicon resistors ensures an output signal for the in-plane modes, but suppresses out-of-plane modes, thus enabling stable closed-loop operation of the resonant sensors at the desired first in-plane mode's frequency.

## INTRODUCTION

The current state of the art for detecting trace contaminants in water involves field sampling and the use of laboratory instruments, such as liquid and gas chromatography, mass spectrometry, or optical spectroscopic techniques for analysis. Generally, these technologies are not appropriate for in-field use or use by first responders because of their cost and complexity of operation. However, miniaturized versions of such laboratory equipment, in particular micro gas chromatography ( $\mu$ GC) systems [1] and fiber-based IR sensors [2] have made substantial progress in recent years. Both of these technologies show promise for analyzing complex samples in the field, yet both systems are still fairly complex. For targeted detection of a few analytes of interest in a fluid sample, microfabricated chemical sensors and in particular sensor arrays can offer a simple, low-cost alternative. Among possible sensing schemes, mass-sensitive transducers, which sense the analyte mass, have gained interest in recent years. Cantilever-based sensors [3,4] are of particular interest because of their ease of manufacture, and thus are considered here.

Traditionally, cantilevers have been used in either their torsional or out-of-plane flexural modes for resonant sensing applications. The main advantage of using the out-of-plane mode is that it is the lowest-frequency cantilever mode (assuming that the cantilever width is larger than the cantilever thickness) and, thus, is generally the easiest to excite and detect. Resonant silicon cantilevers vibrating in an out-of-plane flexural mode have been successfully employed for chemical sensing in air [5, 6] with the cantilevers typically exhibiting quality factors (Q-factors) around 1,000 in air. The dependence of the Q-factor (measured in air) of the fundamental out-of-plane flexural mode on the cantilever geometry has been investigated in detail in [7].

However, in case of liquid operation, the out-of-plane mode is less desirable because of considerable (i) fluid damping (and associated low quality factors) and (ii) mass loading due to the acceleration of the surrounding liquid. Experimental data show quality factors in liquid to be typically around 10 and a reduction of the resonance frequency from the "in-air" to the "in-water"

value of up to 50% [8]. For mass-sensitive (resonant) chemical sensors, the limit of detection is typically defined as three times the ratio of the short-term frequency stability, i.e. the minimal resolvable frequency change, and the sensor sensitivity. While the reduced Q-factor directly impacts the frequency stability, the added fluid mass generally reduces the sensor sensitivity, and it is thus challenging to build robust cantilever-based mass-sensitive chemical sensors with low detection limits for liquid operation.

One promising approach to mitigate damping from fluids in liquid sensing applications has been demonstrated in [9] by creating a fluid channel inside the resonator itself, so that the device can be operated in air or even vacuum, gives considerably improved quality factors compared to liquid operation. The disadvantage of this implementation is both the associated more complex fabrication sequence, and the fact that the resonators with embedded fluid channels currently rely on an external detection scheme using optical measurement setups that do not readily lend themselves to embedded applications. A second approach involves using shear wave acoustic devices, such as the well-known quartz crystal microbalance. While the use of such acoustic wave devices typically yields excellent limits of detection [10], they rely on piezoelectric transducers and their fabrication is typically not compatible with integrated circuit processes.

In the present work, we explore the use of the *first in-plane flexural mode* of a simple cantilever to address the discussed challenges of liquid-phase chemical sensing using a resonant sensor platform and demonstrate ppb-range detection limits for volatile organic compounds (VOC) in water. Thereby, the improved detection limit stems from both the lower mass loading by the fluid and the improved quality factors in liquid. In addition, mechanical characterization data is presented, which highlights the higher quality factors and also reduced mass loading effects found for these cantilevers.

## CANTILEVER DESIGN AND FABRICATION

Cantilevers with widths ranging from 45 $\mu$ m to 90 $\mu$ m and lengths ranging from 200 $\mu$ m to 1000 $\mu$ m were fabricated and characterized (see Figure 1a). The devices were fabricated and released using a CMOS-compatible bulk micromachining process that is presented elsewhere [11]. The cantilevers feature integrated resistive structures for electrothermal excitation and piezoresistive detection of the first in-plane flexural mode (see Figure 1b). Thermal excitation is favored for liquid operation because it can generate large actuation forces, which are needed to overcome the considerable viscous drag of the surrounding fluid.

A Wheatstone bridge configuration with the four piezoresistors in a U-shaped layout is chosen for vibration detection. Thereby, the placement of the resistors allows for suppression of both the thermal signal from the excitation resistors and also the signals created by torsional and out-of-plane flexural modes. This way, the first in-plane flexural mode generates the strongest detection signal, even though its resonance frequency is several times higher than that of the first out-of-plane mode for the device dimensions investigated in this work. The excitation

resistors are located close to the clamped edge of the cantilever to minimize the static temperature elevation of the cantilever during operation. The excitation resistors run along the cantilever side to maximize the resulting bending moment. During normal device operation only one of the two resistors is powered with an ac voltage superimposed on a dc bias voltage.

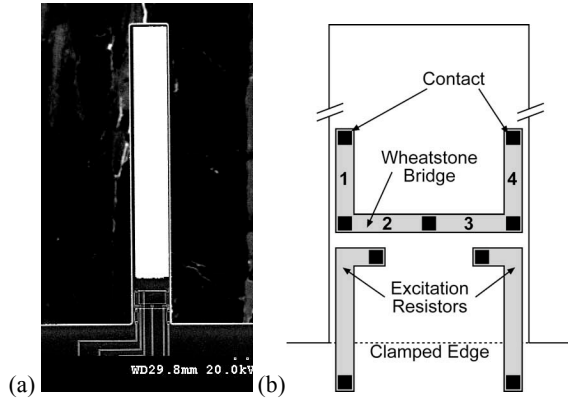


Figure 1: (a) SEM photograph of 60  $\mu\text{m}$  wide and 400  $\mu\text{m}$  long cantilever (coated with gold for biochemical sensing applications); (b) schematic layout of heating resistors and U-shaped piezoresistive Wheatstone bridge.

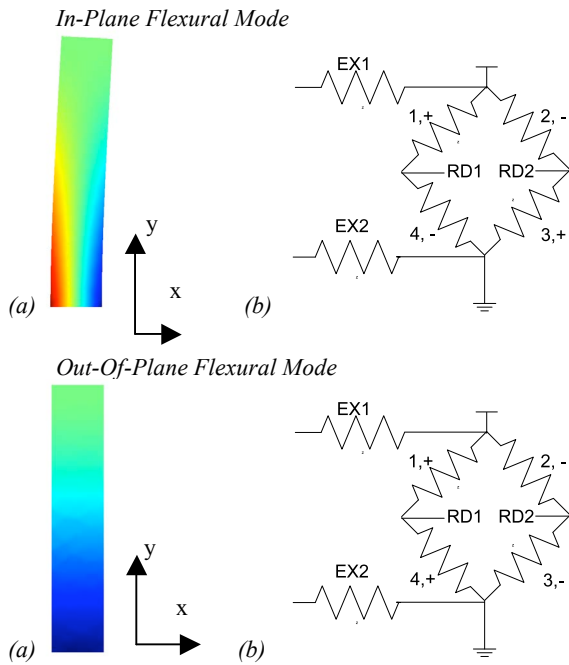


Figure 2: (a) Distribution of the bending stress component  $\sigma_y$  in  $y$ -direction as simulated using the FEM software COMSOL for a 75 $\mu\text{m}$  wide and 400 $\mu\text{m}$  long cantilever vibrating in the first out-of-plane and the first in-plane resonance mode; (b) Signs of the expected resistance change of the piezoresistors (see Fig. 1) in case of the first out-of-plane and the first in-plane mode, assuming that resistor 1 experiences a positive resistance change. RD1 and RD2 represent the bridge output terminals, and EX1 and EX2 denote the two excitation resistors.

The resistor placements were chosen by examining the symmetry of the longitudinal stress component in the cantilever's flexural vibration modes. Figure 2 compares the simulated stress on the cantilever surface in  $y$ -direction, i.e. along the cantilever length, of the first in-plane and the first out-of-plane flexural mode. The resistors were placed and connected in a way that the resistance changes associated with the in-plane mode result in a bridge output signal, while the resistance changes associated with the out-of-plane mode yield a largely suppressed output signal. Using  $p$ -type piezoresistors aligned along the  $[110]$  directions, the longitudinal and transverse piezoresistive coefficients have similar magnitude but opposite sign [12], and the in-/out-of-plane flexural mode shapes result in the characteristic resistance changes highlighted in Figure 2.

## SENSOR PACKAGING

For liquid testing the resonators were packaged using acrylic manifolds fabricated on a stereolithography tool (see Figure 3). The manifolds were glued into 28-pin DIL (Dual-In-Line) packages, which allows for electrical connection to the die via wire-bonding. An acrylic ring was glued to the surface of the die, and silicone gaskets were used to seal the bottom of the die to the lower manifold and to seal the top manifold (which screws into the thermoplastic inserts on the DIL package) to the glued-on ring, thus creating a flow cell. For chemical sensing experiments the flow cell allows a sample to flow from top to bottom through the micromachined opening in the sensor chip. For mechanical characterization in liquid, a drop of water was simply placed on the area enclosed by the ring and allowed to percolate through the bulk micromachined opening, immersing the cantilever.

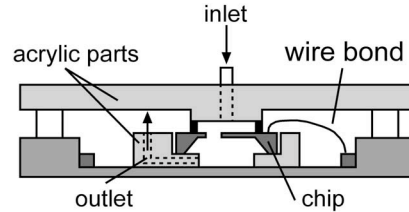


Figure 3: Schematic cross-section of packaging concept with fluid flow through the etch opening in the sensor chip (top to bottom).

For chemical measurements a thicker surface protection was needed to protect the aluminum lines on the device surface from corrosion during liquid operation. The passivation used in this work consisted of three layers of pulse-deposited PECVD silicon oxide followed by PECVD silicon nitride. The total thickness of the passivation stack was 1.2 $\mu\text{m}$ . The PECVD depositions were done consecutively without removing the wafer from the processing chamber. In addition, the tool used had a load lock, which helps to lower the amount of contamination in the deposition chamber.

## RESULTS

### Physical Testing

Twenty different cantilever sizes were tested in air and water. The length and width of each cantilever was different, but they were all approximately 12 $\mu\text{m}$  thick. Figure 4 shows the quality factor of the first in-plane flexural mode as a function of its resonance frequency. As expected if shear forces are dominating the fluid damping, the  $Q$ -factor increases roughly with the square root of the resonance frequency.  $Q$ -factors as high as 67 were measured for a 200 $\mu\text{m}$  long and 90 $\mu\text{m}$  wide cantilever, which

represents a considerable improvement over published data in the range of 10-20 for the out-of-plane mode in liquid [8]. As evidence of reduced mass loading effects by the surrounding fluid, the cantilevers utilizing the first in-plane flexural mode show a frequency drop of around 10% upon immersion in liquid, compared to frequency drops of the order of 50% for the out-of-plane mode.

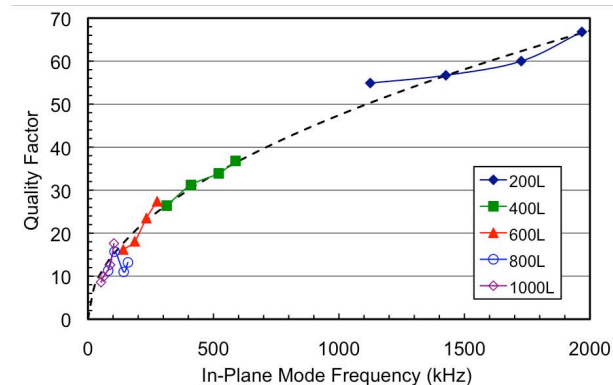


Figure 4: Quality factor in water as a function of in-plane mode frequency in water. For each length, cantilevers with a width of 45, 60, 75 and 90  $\mu\text{m}$  were measured. The lowest frequency in each group corresponds to the narrowest cantilever, and the frequency increases with each increasing width. The dashed line represents a square-root dependence of  $Q$  with frequency.

### Chemical Testing

To create mass-sensitive chemical sensors, polymer layers were deposited on 75 $\mu\text{m}$  wide, 400 $\mu\text{m}$  long, and 6.3 $\mu\text{m}$  thick cantilevers that also had a 3000  $\text{\AA}$  gold layer on their surface (see Figure 1a). The polymer layer absorbs analyte from the environment, thus increasing the mass of the resonator. The polymers were spray-coated using an air brush on both sides of the cantilever. A 0.3 $\mu\text{m}$  thick PIB (polyisobutylene) film was used on each side of one cantilever, while another cantilever was coated with 2 $\mu\text{m}$  of EPCO (ethylene-propylene copolymer) on each side. HMDS was used as an adhesion promoter.

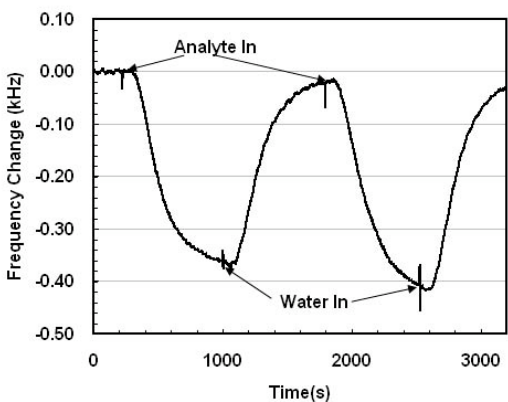


Figure 5: Response of EPCO-coated cantilever to two subsequent exposures to a 5ppm tetrachloroethylene solution. The resulting sensitivity is approx. 75Hz/ppm. The measured short-term frequency stability is approx. 1Hz. The frequency spikes observed during measurement are due to pressure effects resulting from pump switching.

For testing, a system with two syringe pumps was used, with the pumps connected to the flow cell using a three-way T. PEEK tubing was used to make all connections. One syringe pump was filled with analyte solution (the analyte was kept constantly stirring for at least half an hour before use to ensure a uniform solution) another was filled with water, which was used to desorb the analyte from the polymer film.

Periodically, analyte solution was injected into the flow cell causing the frequency to decrease and then finally reach a stable level, at which point water was injected to desorb the analyte from the polymer film. As an example, Figure 5 shows the sensor response of the EPCO-coated resonator, i.e. the measured frequency change versus time for two subsequent injections of a 5ppm tetrachloroethylene solution. The resulting sensor sensitivity is approximately 75Hz/ppm at the in-plane resonance frequency of 426kHz.

As stated above, the limit of detection (LOD) for a mass-sensitive (resonant) sensor can be estimated from

$$\text{LOD} = 3 \frac{\Delta f_{\min}}{S} \quad (1)$$

where  $S$  is the sensitivity in [Hz/ppm] and  $\Delta f_{\min}$  is the short-term frequency stability in [Hz], measured in this work using the Allan variance method. Both the PIB and EPCO-coated devices tested had a frequency stability of approximately 1Hz for a gate time of 4 sec. This way, the LOD of the EPCO-coated cantilever for tetrachloroethylene is estimated to be 45ppb. Limits of detection for several other analytes dissolved in water are summarized in Figure 6 as obtained from measured sensitivity and Allan variance data using Eq. (1).

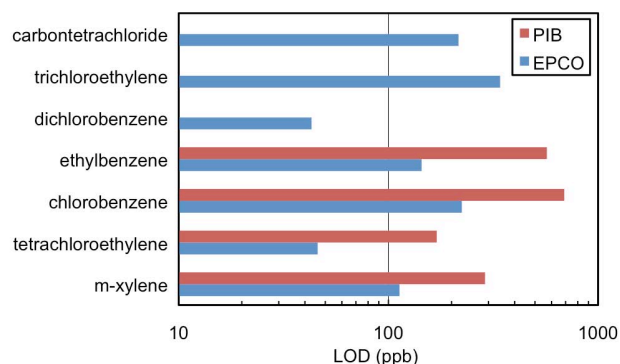


Figure 6: Limit of detection (LOD) for example analytes as obtained from experimental sensitivity and frequency stability data for 400 $\mu\text{m}$  by 75 $\mu\text{m}$  by 6.3 $\mu\text{m}$  cantilevers coated on both sides with either 2 $\mu\text{m}$  EPCO or 0.3 $\mu\text{m}$  PIB.

The presented liquid measurements not only give low limits of detection, they were also found to be highly repeatable and consistent over several analyte concentrations. A calibration curve was constructed for tetrachloroethylene by measuring four different concentrations in duplicate using both EPCO and PIB as sensitive layers. The resulting curves with error bars (see Figure 7) show that the response of the cantilever is linear, and consistent across several different concentrations. The error bars in Figure 7 are mostly within the size of the symbols and we typically found less than 5% difference between measurements at the same concentration.

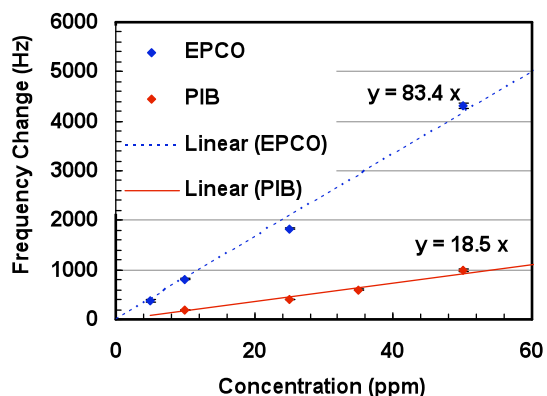


Figure 7: Measured frequency change of EPCO (blue symbols) and PIB-coated (red symbols) cantilevers as a function of the tetrachloroethylene concentration in water. The lines are linear fits to the measurement data according to the equation given in the graph.

Further improvements in the presented sensing system are possible. First, the sensitivity can be improved by using shorter cantilevers with higher resonance frequencies. Figure 8 shows *simulated* frequency changes for a 2% change in the density of a 4 $\mu\text{m}$  polymer layer on top of 12 $\mu\text{m}$  thick cantilevers with different dimensions. The simulations were done using eigenmode analysis in COMSOL. In combination with the results shown in Figure 4, we find that in-plane mode cantilevers with higher frequency, i.e. shorter and wider cantilevers, exhibit a higher sensitivity and a higher quality factor (and, thus, potentially better frequency stability). In addition, the effect of the cantilever thickness needs to be explored. While thinner cantilevers will yield a higher chemical sensitivity, thicker cantilevers generally exhibit higher Q-factors due to their increased inertia.

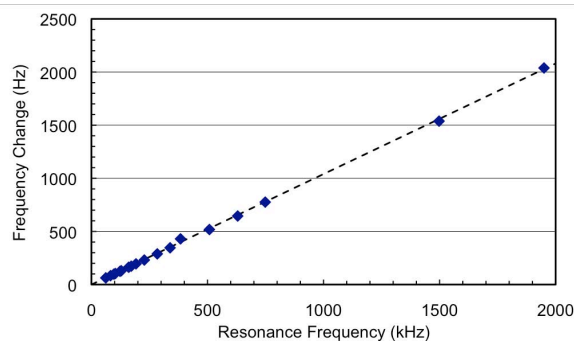


Figure 8: Simulated change of resonance frequency of polymer-coated 12 $\mu\text{m}$  thick silicon cantilevers to a 2% change in the polymer density as a function of the resonance frequency of the cantilever; each symbol corresponds to a cantilever with different lateral dimensions; the polymer thickness was assumed to be 4 $\mu\text{m}$  with a density of 840 kg/m<sup>3</sup>. Using tetrachloroethylene/EPCO with a partition coefficient of  $\approx 1300$  as an example, the 2% density change would stem from a  $\approx 8\text{ppm}$  analyte concentration in the surrounding liquid.

## CONCLUSION

In-plane mode cantilevers were fabricated and tested as liquid chemical sensors for volatile organics in water. The devices presented here yield ppb range limits of detection for common organic pollutants in water, which approaches detection limits needed for water quality monitoring [13]. Compared to other chemical sensor approaches, the cantilevers used in this work have the advantage that their fabrication process is CMOS compatible and that they use integrated excitation and detection schemes. They can be manufactured using the same tool set and similar processing as integrated circuits, resulting in a small footprint even in array format and, thus, allowing them to be used in embedded or handheld devices.

## ACKNOWLEDGEMENTS

The authors would like to thank the staff of the Georgia Tech Nanotechnology Research Center for their help. This work has been funded in part by the National Science Foundation under award ECCS-0824017.

## REFERENCES

- [1] G. Serrano, H. Chang, E.T. Zellers, "A micro gas chromatograph for high-speed determination of explosive vapors", *Transducers and Eurosensors 15<sup>th</sup> International Conference Solid State Actuators and Microsystems* (2009), pp. 1654-1657.
- [2] B. Mizaikoff, "Mid-IR fiber optic sensors", *Analytical Chemistry*, 75, 258A (2003).
- [3] P. S. Waggoner, H. G. Craighead, "Micro- and nanomechanical sensors for environmental, chemical, and biological detection", *Lab on a Chip*, 7, 1238 (2007).
- [4] K. M. Goeders, J. S. Colton, L. A. Bottomley, "Microcantilevers: sensing chemical interactions via mechanical motion", *Chemical Reviews*, 108, 522 (2008).
- [5] D. Lange, C. Hagleitner, A. Hierlemann, O. Brand, H. Baltes, "Complementary metal oxide semiconductor cantilever arrays on a single chip: mass-sensitive detection of volatile organic compounds", *Analytical Chemistry*, 74, 3084 (2002).
- [6] A. R. Krause, C. Van Neste, L. Senesac, T. Thundat, E. Finot, "Trace explosive detection using photothermal deflection spectroscopy", *Journal of Applied Physics*, 103, 094906 (2008).
- [7] K. Naeli, O. Brand, "Dimensional considerations in achieving large quality factors for resonant silicon cantilevers in air", *Journal of Applied Physics*, 105, 014908 (2009).
- [8] C. Vancura, Y. Li, J. Lichtenberg, K. U. Kirstein, A. Hierlemann, F. Josse, "Liquid-phase chemical and biological detection using fully integrated magnetically actuated complementary metal oxide semiconductor resonant cantilever sensor systems", *Analytical Chemistry*, 79, 1646 (2007).
- [9] T. P. Burg, M. Godin, S. M. Knudsen, W. Shen, G. Carlson, J. S. Foster, K. Babcock, S. R. Manalis, "Weighing of biomolecules, single cells and nanoparticles in fluid", *Nature*, 446, 4517 (2007).
- [10] Z. Li, Y. Jones, J. Hossenlopp, R. Cernosek, F. Josse, "Analysis of liquid-phase guided shear horizontal acoustic wave sensors", *Analytical Chemistry*, 77, 1175 (2005).
- [11] J. H. Seo, O. Brand, "High Q-factor in-plane mode resonant microsensors platform for gaseous/liquid environment", *IEEE J. Microelectromechanical Systems*, 17, 483 (2008).
- [12] S. Senturia, *Microsystem Design*, Springer, New York, 2001.
- [13] <http://www.epa.gov/safewater/contaminants/index.html>.

# SECOND EIGENMODE OPERATION OF SUSPENDED MICROCHANNEL RESONATORS FOR HIGH PRECISION FLOW-THROUGH MASS SENSING

J. Lee and S.R. Manalis\*

Department of Biological Engineering, Massachusetts Institute of Technology, Massachusetts, USA

## ABSTRACT

An intrinsic uncertainty in particle mass sensing with the suspended microchannel resonator (SMR) results from variation in a particle's position near the free end of the resonator. To circumvent this error without modifying the resonator geometry, we employ the second flexural bending mode of the SMR which exhibits additional frequency shift peaks while particles pass over antinodes. The antinode peaks have the attractive property that they are insensitive to the lateral position of the particle within the microchannel. We measure polystyrene beads with the first and second modes. For 3  $\mu\text{m}$  diameter beads, the second mode sensing at antinodes improves the coefficient of variation (CV) in buoyant mass from 1.76 to 1.05 % for population measurements and from 1.40 to 0.53 % for a single particle trapped.

## INTRODUCTION

Although the SMR has a  $\sim 1$  femtogram resolution in a 1 Hz bandwidth and can weigh single nanoparticles and cells as they transit the embedded microchannel [1], the particle flow path near the tip of the SMR is uncertain (Fig. 1(a)) and this variation can reduce precision of the mass measurement. This position dependent error can broaden the mass histogram of a population of particles and introduce uncertainty during single particle trapping where the mass of single particle is measured repeatedly [2]. Employing doubly clamped resonators, hydrodynamic particle focusing, or particle trapping at predefined mechanical structures could reduce this measurement uncertainty. However these strategies either require fabricating new SMR structures and fluidic interfaces or may reduce the measurement throughput. In this work, we show that the position dependent error can be eliminated in existing SMR structures without sacrificing throughput by utilizing higher order flexural bending modes.

## THEORY

When a point mass is deposited on a vibrating cantilever, the resulting change in resonant frequency depends strongly on the location of the added mass. From the Euler-Bernoulli beam equation, displacement at a position normalized by the cantilever length is given by:

$$u_n\left(\frac{x}{L}\right) = \frac{A_n}{2} \left[ \cosh\left(\frac{\lambda_n x}{L}\right) - \cos\left(\frac{\lambda_n x}{L}\right) \right] - B(\lambda_n) \left[ \sinh\left(\frac{\lambda_n x}{L}\right) - \sin\left(\frac{\lambda_n x}{L}\right) \right] \quad (1)$$

$$B(\lambda_n) = (\cosh(\lambda_n) + \cos(\lambda_n)) / (\sinh(\lambda_n) + \sin(\lambda_n))$$

where  $x$  is the position from the clamped base,  $L$  is the cantilever length,  $A_n$  is the tip amplitude, and  $\lambda_n$  is the eigenvalue for the  $n^{\text{th}}$  flexural bending modes; 1.8751, 4.6941, 7.8548, and 10.996 are eigenvalues for the first four bending modes, respectively [3]. Using this mode shape shown in Fig. 1(b) (top) and applying the Rayleigh-Ritz theorem which equates the time averaged kinetic energy and strain energy at resonance, the relative resonance frequency shift of the cantilever is estimated by

$$\left(\Delta f/f\right)_n = -1 + \left(1 + u_n(x/L)^2 \cdot \Delta m/m_{\text{eff}}\right)^{-0.5} \quad (2)$$

where  $A_n=1$  (normalized mode shape),  $f$  is the resonance frequency, and  $m_{\text{eff}}$  is the effective mass of the cantilever when there is no particle [4]. Figure 1(b) shows mode shapes and relative resonance frequency shifts for the first four flexural bending modes when 2

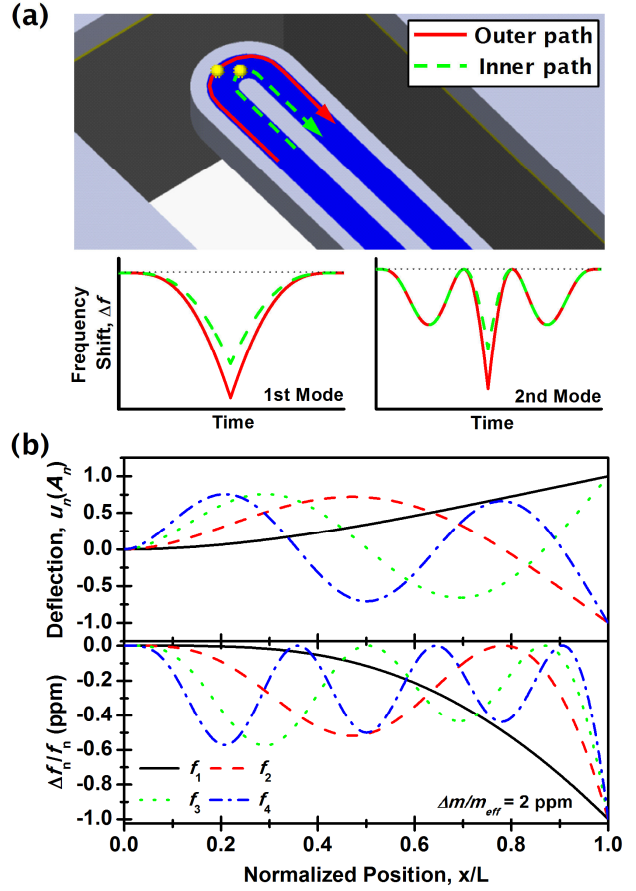


Figure 1: (a) A particle may transit anywhere between the inner and outer channel wall. A particle that makes a U-turn near the inner wall results in a smaller frequency shift than if it turns near the outer wall. (b) Mode shape and resonance frequency shift upon point mass loading on a cantilever as a function of the position of the added mass normalized by the cantilever length. For a cantilever that resonates at its  $n^{\text{th}}$  ( $n \geq 1$ ) flexural bending mode, there are  $2n-1$  peaks in the frequency shift measured during a single particle transit (one peak at the free end and  $2n-2$  peaks at antinodes).

parts-per-million (ppm) of mass is added at various positions along the cantilever.

When a particle transits the U-shaped embedded microchannel of the SMR, there are  $2n-1$  frequency shift peaks at the  $n^{\text{th}}$  flexural bending mode. As shown in Fig. 1(a), a particle flowing through the microchannel can travel along random paths. In the most extreme cases, the particle can be positioned at the inner and outer edges of the microchannel. Since  $\Delta m/m_{\text{eff}}$  in equation (2) is much less than unity, the maximum position-dependent error is estimated by

$$\left(\frac{f_i - f_o}{f - f_m}\right) \approx \frac{u_n(x_i/L)^2 - u_n(x_o/L)^2}{u_n(x_m/L)^2} \quad (3)$$

where, the subscripts  $i$ ,  $o$ , and,  $m$  denote particle positions at the inner edge, the outer edge, and the midpoint of the channel, respectively. The maximum position error is  $\sim 11\%$  for a  $210\ \mu\text{m}$  long SMR used in first mode sensing. However, the frequency shift measured at antinodes is nearly insensitive to the lateral position of the particle in the channel (see Fig. 1(a) for comparison of the first and second mode sensing).

## RESULTS AND DISCUSSIONS

To date, only the fundamental mode of the SMR has been utilized and higher vibration modes have yet to be explored. For microcantilevers, it has been shown that performance in a viscous medium can be improved by operating them at higher modes since their quality factors increase with mode number [5]. However this is not always the case for vacuum packaged SMRs since the mechanisms that give rise to viscous loss are different.

SMR devices used in this work are  $406\ \mu\text{m}$  long,  $28.5\ \mu\text{m}$  wide, and  $12\ \mu\text{m}$  thick, and their channel cross-sections are  $7.9 \times 8\ \mu\text{m}^2$ . Figure 2 shows that resonance frequencies of the first, second, and third flexural bending modes decrease linearly with increasing fluid density as expected. Interestingly, the quality factor of each mode exhibits non-monotonic behaviors which decrease or increase with increasing viscosity (Fig. 3). The local minimum in the plot of quality factor vs. viscosity occurs at higher viscosities as the mode number rises. Observed non-monotonic trends may be explained with the theory for the first mode [6] but the effects of compressibility in the fluid become increasingly important for higher modes since the resonance frequency increases. Detailed theoretical investigation considering the effects of compressibility is currently underway. In addition, the quality factors of higher modes are significantly lower than that of the first mode when the

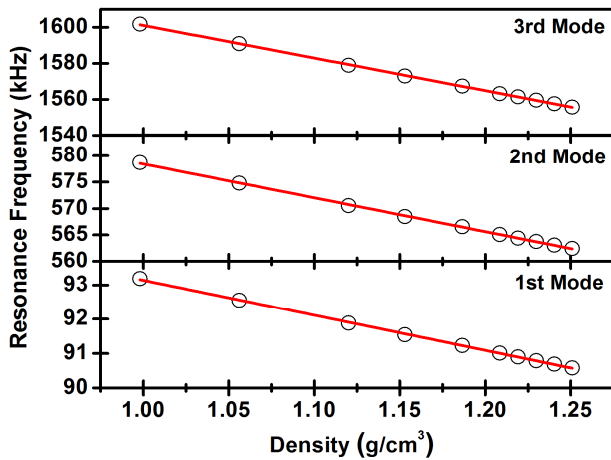


Figure 2: Resonance frequencies of the first, second, and third flexural bending modes are linear functions of fluid density. Density was varied by mixing glycerol with water in different ratios (24 ~ 96%).

Table 1: Dimensions (length ( $l$ ), width ( $w$ ), and thickness ( $t$ )) and resonant characteristics of 5 existing SMRs. Resonance frequencies ( $f$ ), quality factors ( $Q$ ), and mass resolutions ( $\delta m$ ) are measured with each SMR filled with water.

#	$l$ ( $\mu\text{m}$ )	$w$ ( $\mu\text{m}$ )	$t$ ( $\mu\text{m}$ )	$f_1$ (kHz)	$Q_1$	$f_2$ (kHz)	$Q_2$	$\delta m_{1,1\text{kHz}}$ (fg)	$\delta m_{1,1\text{Hz}}$ (fg)	$\delta m_{2a,1\text{kHz}}$ (fg)	$\delta m_{2a,1\text{Hz}}$ (fg)	$f_2$ feedback
1	210	33	7	209.9	12,064	1297.5	4,798	10.2	0.24	37.7	0.29	O
2	210	33	12	384	5,880	2311	1,760	14.1	0.71	—	—	X
3	321	57	19	231	2,270	1396	810	113.7	4.6	—	—	X
4	406	28.5	7	54.7	23,447	340.2	9,080	90.8	6.5	30.5	2.0	O
5	406	28.5	12	93.2	10,742	578.7	3,023	48	0.7	35	5.4	O

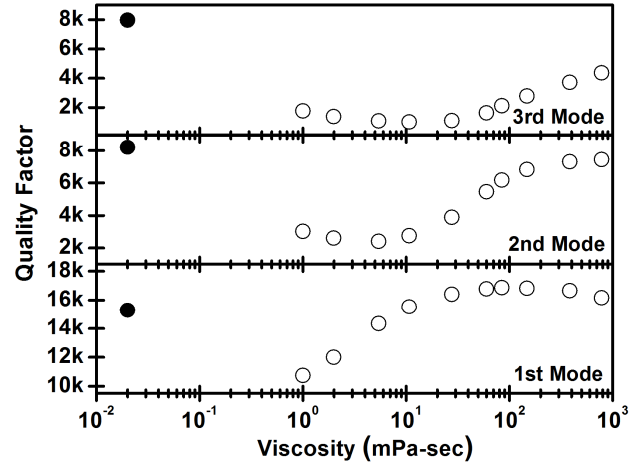


Figure 3: Quality factors of the first, second, and third flexural bending modes are highly non-monotonic functions of fluid viscosity. Viscosity was varied by mixing glycerol with water in different ratios (24 ~ 96%). Solid circles represent quality factors of dry SMRs filled with air.

SMR is filled with water ( $Q_1=10,742$ ,  $Q_2=3,023$ , and  $Q_3=1,760$ ). One potential drawback of higher mode sensing is that the reduced quality factor may result in a lower mass resolution. Thus, there is a tradeoff between mass resolution and precision that should be considered for a given application of the SMR.

We successfully operated the SMR in feedback mode with the first and second modes, however we found that feedback was not stable for higher order modes. This may be due to the increased stiffness as the mode number rises. In a 1 kHz bandwidth, frequency noises measured were 0.439 and 0.142 ppm for the first and second modes, respectively. While SMRs used in this work exhibit lower frequency noise with the second mode than with the first mode, this is not a universal characteristic. Three out of five different SMR designs allow feedback operation in both the first and second modes however only two out of the three designs exhibit better mass resolution with the second mode (Table 1). This indicates that there are preferable designs for higher mode operations and that the structures used in this work may not be optimal.

Monodispersed particles would be ideal for evaluating the performance of 2<sup>nd</sup> mode sensing since dispersity may overshadow the position-dependent error. Typical CVs of commercially available NIST size standard beads are 1~2 % in diameter (3~6 % in volume or mass) which are comparable to the position-dependent error. We therefore used a dynamic single particle trapping method where alternating pressure between bypass channels maintains a single particle in the suspended microchannel for repeated measurements [2]. Figure 4 shows resonance frequency shifts of the first and second modes as a nominally  $4.17\ \mu\text{m}$  diameter



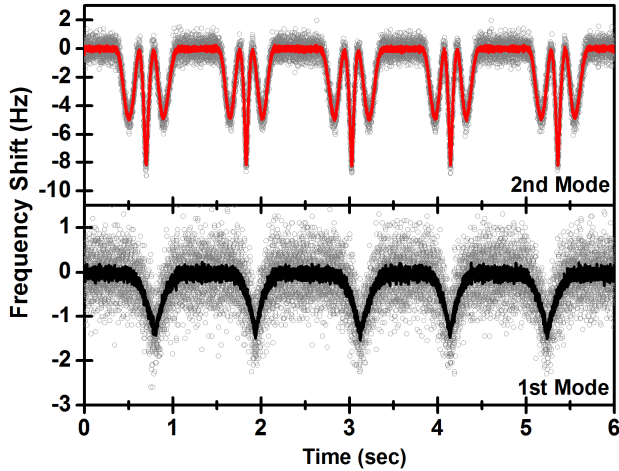


Figure 4: Frequency shift vs. time for a nominally  $4.17 \mu\text{m}$  diameter polystyrene bead that is repeatedly measured. Gray dots show raw data sampled at 2 kHz, and black (first mode) and red (second mode) solid lines show data smoothed with the Savitzky-Golay filter ( $n=12$ , 3<sup>rd</sup> order).

polystyrene bead (NT21N, Bangs Laboratories) repeatedly transits the suspended microchannel. As expected from theory, the first mode sensing exhibits one peak near the tip and the second mode sensing exhibits three peaks per every trapping cycle.

Following calibration with  $4.17 \mu\text{m}$  diameter beads, we measured a population of  $3 \mu\text{m}$  diameter polystyrene beads (4203A, Thermo Scientific) and trapped a single particle drawn from the same population for about 1 hr. Figure 5 shows histograms of the relative frequency shift for the first mode tip, second mode tip, and second mode antinode sensing. For both population and trapping measurements, the second mode antinode sensing when the left and right antinode peaks are averaged offers the lowest CV ( $\Delta f_{2,a}$  (avg)).

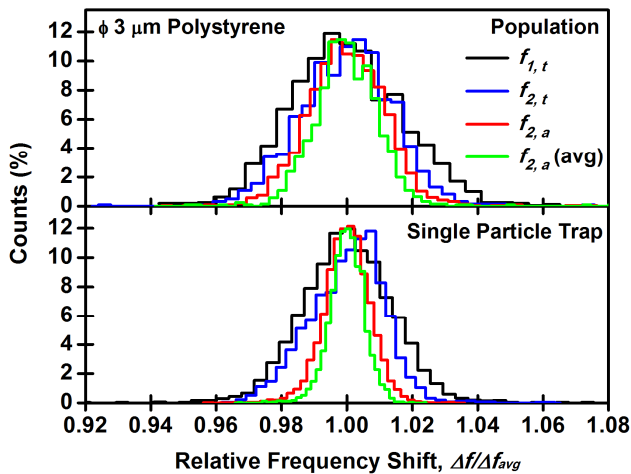


Figure 5: Histograms of relative frequency shifts for nominally  $3 \mu\text{m}$  diameter polystyrene particles (population) and repeated measurements of a particle drawn from the same population (single particle trapping). Subscripts 1 and 2 denote mode number and subscripts  $t$  and  $a$  denote tip and antinode, respectively. The second mode sensing at antinodes generates the narrowest histogram for both population and trapping measurements when frequency shifts at the left and right antinodes are averaged.

Table 2: A summary of the first and second flexural mode sensing characteristics for population and trapping measurements with  $3 \mu\text{m}$  diameter polystyrene beads.

Mode		$\mu$ (Hz)	$\sigma$ (Hz)	CV (%)
Population	$\Delta f_{1,t}$	0.590	0.010	1.76
	$\Delta f_{2,t}$	3.258	0.047	1.45
	$\Delta f_{2,a}$	1.962	0.024	1.24
	$\Delta f_{2,a}$ (avg)	1.962	0.021	1.05
Trapping	$\Delta f_{1,t}$	0.584	0.008	1.40
	$\Delta f_{2,t}$	3.281	0.032	0.99
	$\Delta f_{2,a}$	1.957	0.014	0.70
	$\Delta f_{2,a}$ (avg)	1.957	0.010	0.53

Detailed results are summarized in Table 2. Interestingly, the second mode tip sensing also exhibits narrower dispersion than the first mode tip sensing for both population and single particle trapping although theory predicts more error with the second mode. The mass resolution in a 1 kHz bandwidth is 48, 35, and 21 fg for the first mode tip, second mode antinode, and second mode tip sensing, respectively.

## CONCLUSIONS

This paper reports promising characteristics of the higher eigenmode operation of suspended microchannel resonators for flow-through mass sensing. Existing SMR devices can be operated at their second flexural bending modes to achieve high precision mass sensing and, in some cases, provide improved mass resolution.

## REFERENCES

- [1] T. P. Burg, M. Godin, S. M. Knudsen, W. Shen, G. Carlson, J. S. Foster, K. Babcock, and S. R. Manalis, “Weighing of biomolecules, single cells and single nanoparticles in fluid”, *Nature*, **446**, 1066 (2007).
- [2] M. Godin, F. F. Delgado, S. Son, W. H. Grover, A. K. Bryan, A. Tzur, P. Jorgensen, K. Payer, A. D. Grossman, M. W. Kirschner, and S. R. Manalis, “Using buoyant mass to measure the growth of single cells”, *Nature Method*, accepted for publication.
- [3] A. N. Cleland, *Foundations of Nanomechanics: from solid-state theory to device applications*: Springer, 2003.
- [4] S. Dohn, W. Svendsen, A. Boisen, and O. Hansen, “Mass and position determination of attached particles on cantilever based mass sensors”, *Review of Scientific Instruments*, **78**, 103303 (2007).
- [5] T. Braun, M. K. Ghatkesar, N. Backmann, W. Grange, P. Boulanger, L. Letellier, H. Lang, A. Bietsch, C. Gerber, and M. Hegner, “Quantitative time-resolved measurement of membrane protein-ligand interactions using microcantilever array sensors”, *Nature Nanotechnology*, **4**, 179 (2008).
- [6] T. P. Burg, J. E. Sader, and S. R. Manalis, “Nonmonotonic Energy Dissipation in Microfluidic Resonators”, *Physical Review Letters*, **102**, 228103 (2009).

## CONTACT

\*S.R. Manalis, tel: +1-617-253-0632; [scottm@media.mit.edu](mailto:scottm@media.mit.edu)

# METALS IN MICROFLUIDICS - COUPLING PLASMONICS, ELECTRON TRANSFER AND NANOFUIDICS IN A MONOLITHIC STRUCTURE

S.P. Branagan<sup>1</sup>, N. Contento<sup>1</sup>, and P.W. Bohn<sup>1,2\*</sup>

<sup>1</sup>Department of Chemical and Biomolecular Engineering, University of Notre Dame, Notre Dame, Indiana, USA

<sup>2</sup>Department of Chemistry and Biochemistry, University of Notre Dame, Notre Dame, Indiana, USA

## ABSTRACT

Present work details the characterization of engineered metallic features in several micro/nanofluidic structures. Three distinct analytical applications for these nanoporous structures are targeted: (1) molecular reactivity of surface-immobilized enzymes under confinement (2) plasmonically active sensing elements supporting enhanced optical transmission (3) fabrication of metallic structures for *in situ* monitoring of electron transfer reaction products. Two generally applicable Au/polymer structures are introduced, including Au nanocapillary array membranes (NCAMs) and Au embedded annular nanoband electrodes (EANEs).

## INTRODUCTION

The ultimate goal of this program is to establish intelligent control of molecular transport in space and time at small length scales – enabling the construction of materials and structures that can sense molecular characteristics, e.g. size, charge, molecular shape, etc., then generate control signals that control transport based on those characteristics. Specifically, these experiments seek to manipulate, (separate, isolate, react, detect) low-mass samples with the same precision and level of control currently possible with bench-scale samples by combining microfluidic and nanofluidic structures under the rubric of integrated microfluidics.

These nanofluidically mediated interactions frequently require metallic elements in the flow path, thereby making it possible to realize plasmonic sensing, electrokinetic fluid switching and electrochemical transformations in a single integrated architecture. To effect these electrochemical transformations, a layer of Au is incorporated within the nanofluidic feature. Two of these structures are the Au nanocapillary array membrane (NCAM), and the Au embedded annular nanoband electrode (EANE). These NCAMs can be used to support plasmonic sensing via enhanced optical transmission, while maintaining compatibility with electrokinetic transport. EANEs, meanwhile, can be used to effect heterogeneous electron transfer events at very high efficiency inside the nanopore during electrokinetic pumping.

## MOLECULAR REACTIVITY UNDER CONFINEMENT

A key practical reason for pursuing small scale architectures is the characteristic gain in reaction rate. Most enzymatic reactions in free solution are diffusion limited; this represents a transport-imposed upper bound, regardless of the intrinsic capability of the enzyme species. Previously published work<sup>1</sup> studied the behavior of enzymes geometrically-confined to the inside surface of a nanometer-scale pore. Horseradish peroxidase (HRP) catalyzes the oxidation of a fluorogenic substrate, Amplex Red (AR), to fluorescent resorufin in the presence of H<sub>2</sub>O<sub>2</sub>. Figure 1 depicts two configurations of surface-immobilized HRP, where the enzyme can be bound to either (A) a planar surface in a microchannel or (B) the interior of cylindrical nanopores as part of an integrated micro/nanofluidic structure. In both cases, the immobilized HRP

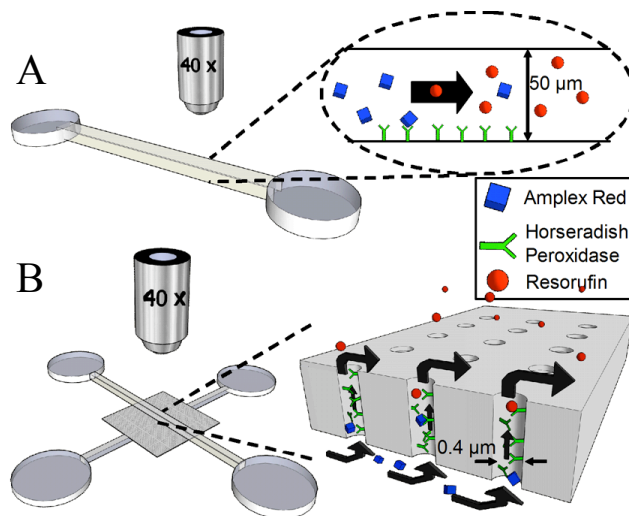


Figure 1: Schematics of planar-surface immobilized HRP reaction formats (A) single microchannel system, HRP immobilized on one planar surface (B) 3-dimensional micro/nanofluidic system with HRP immobilized on the interior nanopore walls. In all figures, chemical species are coded as: Amplex Red (blue) HRP (green), and Resorufin (red)

under confinement was characterized and compared to finite

element simulations of a modified Eley-Rideal mechanism to bracket the value of the initial reaction velocity. Initial reaction velocities were estimated to be  $\geq 5$  times higher in microchannel, and  $\geq 20$ -fold higher in the nanopores than for the same enzyme in macroscale fluid solution (see Table 1).

Table 1: Comparison of enzyme-to-substrate ratios and initial rates for various enzyme reaction geometries

	[E] / [S] ratio	Initial rate / $\mu\text{M min}^{-1}$
Free solution (literature) <sup>2</sup>	$\sim 0.001$	1.8
Planar surface in microchannel	$\sim 0.001$	12
Nanopore array (experiment)	100	36
Nanopore array (simulation)	-	15 - 60

It is worth noting that the nanopore experiments exhibit a very different enzyme: substrate ratio ( $[E]/[S] \sim 100$ ) compared to the same reaction in fluid solution ( $[E]/[S] \sim 0.001$ ), however the total mass of enzyme molecules was similar. Therefore, we attribute the gain in reactivity to two factors, both related to confinement: (1) the high aspect ratio nanopore that constrains the diffusive boundary layer, greatly reducing the substrate-to-site diffusion time, and (2) the increase in  $[E]/[S]$  ratio in the femtoliter-size nanopore volume. These hypotheses as to the mechanistic origins of the improved reaction rate, however, require a more advanced detection strategy than *ex situ* fluorescence microscopy.

This challenge leads to one of the major motivations for pursuing metallic features in nanofluidic structures: the potential for electrochemical characterization *in situ*. The past decade has brought major advances in nanoelectrochemistry in parallel with improved fabrication techniques. Au is an attractive metal for incorporation into microfluidics primarily due to surface functionalization via the wide range of Au-thiol chemistries. Previous work by our group has pursued Au-functionalized nanopore membranes in a variety of configurations, three of which are shown in Figure 2.

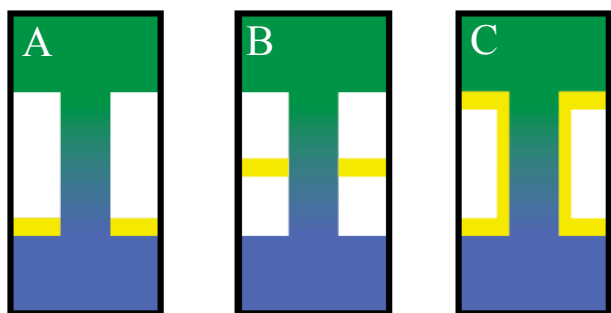


Figure 2: Au-polymer nanopore configurations (A) Au on one side of a nanocapillary array membrane (Au NCAM) (B) Au contained within an embedded annular nanoband electrode (EANE) (C) fully covered Au membrane

The key electrical advantage of Au, i.e. its excellent conductivity, also presents unique challenges for electrokinetic transport. Typically, the electrical current path electroosmosis ways through all-polymer nanofluidic devices will drive and/or electrophoresis through the solution, thereby constituting an effective means of driving nanofluidic transport. Incorporating a Au feature offers a parallel, low-resistance pathway which shorts out electrokinetic transport, often leading to unpredictable charge accumulation/depletion effects, and ultimately undesirable Faradaic reactions. Work by our group has probed these issues in detail, and has illuminated a number of strategies for successful injection across Au-functionalized nanopores of the types shown in Figure 2<sup>3, 4</sup>. Injection traces for each of these geometries are shown in Figure 3.

## METALS IN MICROFLUIDICS SUPPORTING OPTOFLUIDIC SENSING

Another important application of metals in microfluidic structures is plasmonic sensing of surface-bound analytes. Beyond the commercially available surface plasmon resonance biosensors, much work over the past decade has pursued enhanced optical transmission (EOT) through nanoporous metallic features<sup>5, 6</sup>. Previously published work detailed a new technique for mapping

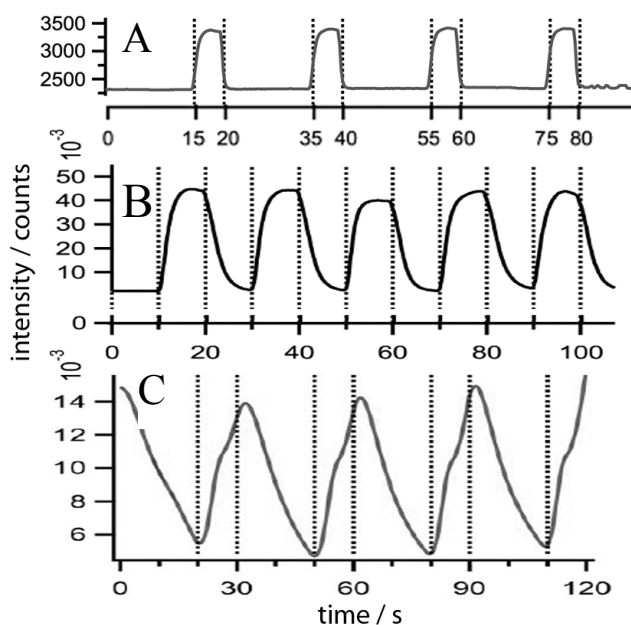


Figure 3: Injections across Au/polymer nanofluidic membranes (A) electrokinetic injections across a one-sided Au-polymer NCAM (B) electrokinetic injections across an EANE (C) pressure-driven flow across a fully coated Au/polymer membrane

enhanced optical transmission through integrated optofluidic nanopore arrays<sup>7</sup>. This technique, illustrated in Figure 4, involves monochromatic illumination and two microscope objectives. The first objective condenses the light to form a linearly polarized wavefront at the plane of the sample, at which the nanopore array is sensitive to both the wavelength,  $\lambda$ , and the angle (via the in-plane wavevector component  $k_x = (2\pi/\lambda) \cdot \sin \theta$ ). The second objective, of higher numerical aperture (NA), collects the transmitted EOT image and maps the spectral information onto different coordinates on the CCD. Figure 4(B) shows just such an EOT image of the nanopore array, including the distinctive vertical bands of illumination, where different regions of the nanopore array transmit at varying efficiencies. During chemical sensing, these vertical bands shift with characteristic changes in the local refractive index, enabling label-free transduction of surface-bound chemical species. This technique is applicable to any of the published EOT-based detection formats<sup>8-10</sup>, and represents a much faster route to characterize the full spectrum of plasmonic resonant shifts.

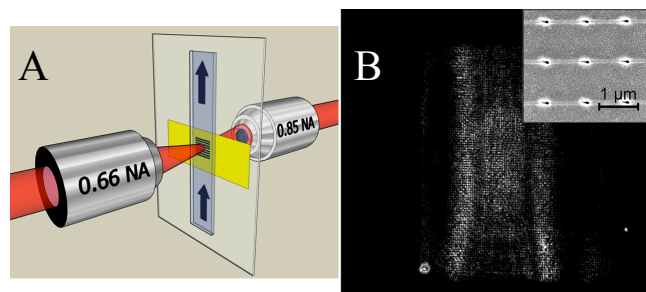


Figure 4: Wavevector resolved spectroscopic imaging of enhanced optical transmission (EOT) (A) schematic of the optical technique with nanopore-array and microchannel in the sample plane of the EOT microscope (B) EOT image of a  $100 \times 100 \mu\text{m}$  pore array, with corresponding SEM close up (inset)

## IN SITU NANOELECTROCHEMISTRY FOR ELECTRON TRANSFER REACTIONS

As discussed in Section II, nanoelectrochemistry offers one important strategy for reaction monitoring *in situ*. Current work pursues a novel micro/nanofluidic structure (Figure 5). This structure is fabricated out of glass (top microchannels) while the bottom nanochannels are fabricated in hard polydimethylsiloxane elastomer (h-PDMS)<sup>11</sup>. This structure supports simultaneous electrochemical and fluorescence monitoring of nanopore reactors. Current work pursues vanillyl-alcohol oxidase and D-amino acid oxidase families of enzyme pairs, and sarcosine oxidase (SO) specifically. Here, the SO incorporates a covalently-bound FAD/FADH<sub>2</sub> cofactor, which cycles between active and inactive states which can be followed through the cofactor (FAD) fluorescence, while the product generation is monitored electrochemically (H<sub>2</sub>O<sub>2</sub>). Since many different oxidase/oxidoreductase enzymes share these common characteristics, this structure enables access to a wide range of enzymatic reactions<sup>12</sup>.

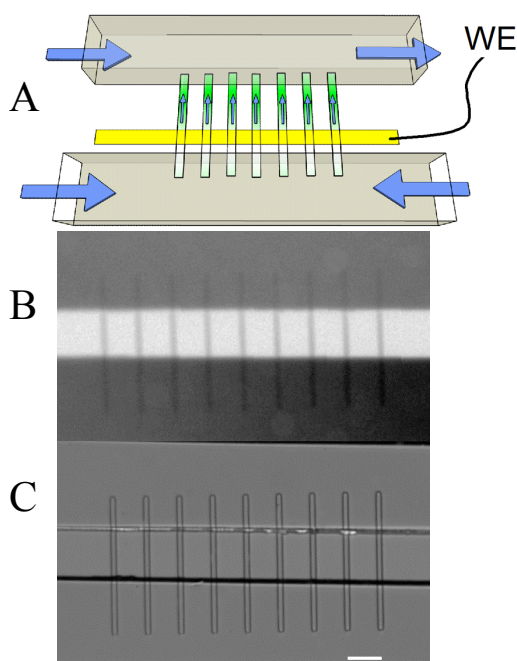


Figure 5: Nanochannel reactors coupled to an *in situ* working electrode (A) schematic showing location of working electrode and flow paths (B) fluorescence micrograph of nanochannel reactors (no electrode) (C) brightfield micrograph of the same structure.

## CONCLUSIONS

Integrating metallic features into three-dimensional microfluidic-nanofluidic architectures offers one approach to many of the most interesting challenges in integrated microfluidics. Direct transduction of chemical reactions near an EANE, for example, provides the most direct measurement yet of nanoscale electron transfer reaction *in situ*. Similarly, the fundamental reactivity of enzyme species may be examined through simultaneous electrochemical and optical detection. Lastly, label-free sensing via optofluidic coupled EOT enables an attractive route for transduction of chemical products within subwavelength nanoporous structures. These on-chip analysis techniques

represent an advancement towards the next generation of small-scale, lab-on-a-chip style analytical devices.

## ACKNOWLEDGEMENTS

This work was supported by the Department of Energy through grant DE FG02 07ER15851, and by the Army Corps of Engineers through contracts W9132T-07-2-0003 and W9132T-10-2-0010.

## REFERENCES

- [1] Z. Wang, T. L. King, S. P. Branagan and P. W. Bohn, *Analyst*, 2009, **134**, 851-859.
- [2] G. H. Seong, J. Heo and R. M. Crooks, *Anal Chem*, 2003, **75**, 3161-3167.
- [3] A. Piruska, S. Branagan, D. M. Cropek, J. V. Sweedler and P. W. Bohn, *Lab on a Chip*, 2008, **8**, 1625-1631.
- [4] A. Piruska, S. P. Branagan, A. Minnis, Z. Wang, D. M. Cropek, J. V. Sweedler and P. W. Bohn, *Lab on a Chip*, 2010, DOI: 10.1039/b924164g.
- [5] T. W. Ebbesen, H. J. Lezec, H. F. Ghaemi, T. Thio and P. A. Wolff, *Nature*, 1998, **391**, 667-669.
- [6] H. F. Ghaemi, T. Thio, D. E. Grupp, T. W. Ebbesen and H. J. Lezec, *Phys Rev B*, 1998, **58**, 6779-6782.
- [7] S. P. Branagan and P. W. Bohn, *Opt Express*, 2009, **17**, 18995-19005.
- [8] J. M. Yao, M. E. Stewart, J. Maria, T. W. Lee, S. K. Gray, J. A. Rogers and R. G. Nuzzo, *Angew Chem Int Edit*, 2008, **47**, 5013-5017.
- [9] N. H. Mack, J. W. Wackerly, V. Malyarchuk, J. A. Rogers, J. S. Moore and R. G. Nuzzo, *Nano Lett*, 2007, **7**, 733-737.
- [10] A. De Leebeeck, L. K. S. Kumar, V. de Lange, D. Sinton, R. Gordon and A. G. Brolo, *Anal Chem*, 2007, **79**, 4094-4100.
- [11] H. Schmid and B. Michel, *Macromolecules*, 2000, **33**, 3042-3049.
- [12] D. P. H. M. Heuts, N. S. Scrutton, W. S. McIntire and M. W. Fraaije, *Febs J*, 2009, **276**, 3405-3427.

## CONTACT

\*P.W. Bohn, tel: +1-574-631-1835; pbohn@nd.edu

# NOVEL THREE-DIMENSIONAL SURFACE MICROFLUIDICS ENABLED BY UNCONVENTIONAL FLUIDIC INTERFACES

Lingfei Hong<sup>1,2</sup>, and Tingrui Pan<sup>1\*</sup>

<sup>1</sup>Department of Biomedical Engineering, University of California, Davis, California, USA

<sup>2</sup>School of Instrumentation Science and Optoelectronics Engineering, Beihang University, Beijing, China

## ABSTRACT

Surface microfluidics, offering unique flow characteristics and addressing intrinsic interfacial problems encountered in microfluidic systems, becomes an attractive alternative to the conventional closed-channel counterparts. Moreover, the planar structure in surface microfluidics enables simple microfabrication, while the open-surface platform allows direct fluidic operations and easy surface modification. In the paper, we first present novel three-dimensional microfluidic manipulations utilizing the unique flexible gas-liquid interface on surface microfluidic platform. The surface-micropatterned triple lines, defining the gas/liquid/solid interfacial boundaries, play an important role in determining the microflow profile. Specifically, the distinct elastic gas-liquid interface enables time-dependent (capacitive) and three-dimensional (deformable) operations of the flow, in contrast to the primary linear (resistive) nature of conventional microfluidics. Spatiotemporally dependent flow patterns on the planar microfluidic surfaces have been theoretically analyzed and experimentally controlled. Utilizing the distinct flow characteristics, new surface microfluidic functionalities, such as microflow regulation and flow rate-controlled switching, have been established. Furthermore, 3D surface microfluidic networks have been fabricated by fluidic connection of two independent planar surfaces, and microflow multiplexers with two-level flow-switching have been successfully devised to illustrate its potential in digital microfluidics.

## INTRODUCTION

Microfluidics has been widely employed in chemical and biological analyses over the past decades [1-2]. Constructed by a wide variety of microfabrication techniques, microfluidic devices serves an attractive alternative to conventional fluidic systems and offers desirable features, including miniature amount of reagents, accelerated reaction speed and efficiency, and integratable-processing capability. Basic fluidic functions, e.g., mixing, pumping, and switching, have all been implemented by a number of active and passive fluidic designs [3-7]. However, a large majority of microfluidic devices, which utilizes the closed-channel configuration and requires spatial confinement of flow, usually involves complex multilayer microfabrication and packaging of the fluidic conduits. Moreover, any gas-liquid interface (e.g., bubble trapping) in microscale channel could present unexpected hurdles to microfluidic operations, which becomes further problematic with dimension down-scaling.

Surface microfluidics, an effective alternative to addressing the aforementioned issues encountered in conventional microfluidics, has received increasing attention from microfluidic community recently [8-10]. Enabled by the latest advances in interfacial sciences and surface chemistry, planar microfluidic pathways are defined lithographically by the contrast of interfacial energies instead [11-14]. The boundaries among solid/liquid/gas phases, known as triple line, serve as virtual borders of fluid flow. Majority of surface microfluidic devices, also known as surface directed channels, are established by confining flow between two surfaces of identical micropatterns with wettability contrast to the substrates [11-12, 14-15]. The similar concept is first

demonstrated in a two-immiscible microfluidic system in a closed channel configuration [15]. Further investigations focus on different micropatterning techniques of wettability contrast. A variety of micromachining techniques have been successfully demonstrated to define hydrophilic patterns on hydrophobic substrates or hydrophobic patterns on hydrophilic substrates, including direct writing by retrofitted pen [14, 16], photolithography [11, 17], lift-off [4, 12], inkjet printing [18-19], microplasma writing [13], and deposition [20]. In comparison with the existing surface patterning methods, our group has previously developed a one-step photopatterning technique to achieve ultrahigh contrast wettability on a wide variety of surfaces. Using a photosensitive superhydrophobic nanocomposite formula (with water contact angle  $>165^\circ$ ), surface microfluidics has been established on single planar substrate using the superhydrophobic micropatterns, which comes with one unrestricted elastic gas-liquid interface [9, 21]. The complete open-surface platform permits direct environmental access, flexible fluidic operations and simple surface modification, while the single planar structure of surface microfluidics enables one-step microfabrication without packaging or alignment.

Considering the substantial fluidic differences between surface and closed-channel flows, more in depth microfluidic analysis is of essential importance to the emerging direction. Furthermore, the distinct elastic gas-liquid boundary could potentially enable novel spatiotemporal control of the fluid due to the presence of fluidic compliance (capacitance) and pressure-dependent resistance, which is usually negligible in conventional system. In this paper, we present analytical and experimental investigation of surface microfluidics with emphasis on the spatiotemporal manipulation of the elastic gas-liquid interface. The planar fluidic circuits are defined by the interfacial triple lines of microfabricated superhydrophobic structures on hydrophilic substrate. Moreover, the elastic gas-liquid boundary adds vertical dimension and thereby lateral compliance to the laminar microflow, analogous to stray capacitance in electronic circuits, and therefore, the pressure gradient not only propels the fluid but controls the cross-sectional profile of the flow. In addition, the compliance of the interface introduces temporal dependence of the fluidic field. Based on the unique three-dimensional and time-dependent flow characteristics, new microfluidic operations have been achieved through the interfacial manipulation, including microflow regulation and flow rate-controlled switching. Furthermore, 3D surface microfluidic networks have been fabricated by fluidic connection of two independent planar surfaces, and microfluidic multiplexers with three-level flow-switching have been successfully devised to illustrate its potential in digital microfluidics.

Figure 1 shows a prototype of a surface microfluidic device with parallel 3D spiral flows. As can be seen, it consists of two micropatterned superhydrophobic substrates placed face-to-face with a spacer. Colored fluids are directed by the surface guided microchannels on one side and connected through miniature vertical capillary bridge towards the other side. Running up-and-down between the top and bottom surfaces, the streams develop into 3D spiral flow patterns without intercepting with each other.

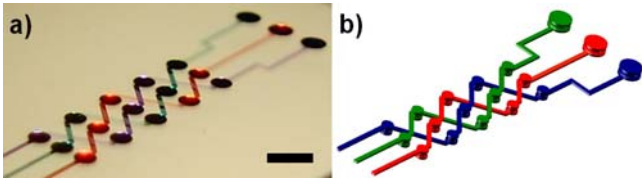


Figure 1: (a) Prototype of a surface microfluidic device with parallel spiral flows along with (b) schematic illustration of unintercepted 3D flow streams. (Scale bar: 2mm)

## THEORETICAL ANALYSIS

As aforementioned, elastic boundary of the gas-liquid interface in surface microfluidics introduces lateral fluidic compliance/capacitance as well as pressure-dependent resistance, unlike its closed-channel counterpart, and therefore, the linear flow-pressure relationship (i.e., Poiseuille's equation) is no longer valid. To analyze surface microfluidic networks, a lumped-element equivalent model has been developed. Similar to the transmission line theory, the distributed-parameter network is used to describe the resistive and capacitive nature of the fluidics in an infinitesimal length. More complicatedly, resistance ( $R$ ) and capacitance ( $C$ ) of the surface microfluidic network is flow-dependent or pressure-dependent (i.e., resistance and capacitance vary with flow rate or pressure). For example, in a straight microchannel, flow through the resistive solid-liquid boundary generates pressure gradient. At the meanwhile, deformed by the induced pressure change, the elastic gas-liquid interface accommodates fluidic accumulation and alters the cross-sectional area. As a consequence, the flow resistance is adaptively modified by the influx. Figure 2(a) represents a general lumped-element model of a fluidic component using distributed parameters.

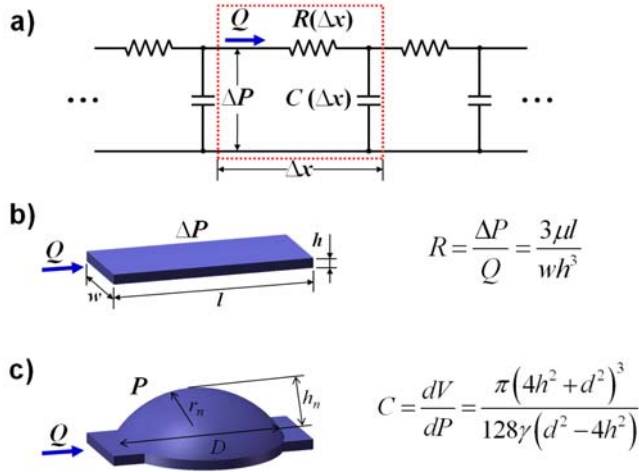


Figure 2: (a) A general lumped-element model describing a surface microfluidic component with both distributed resistive and capacitive elements, (b) the resistive model of a straight channel with unaltered boundary, (c) the capacitive model of a circular reservoir with deformable interface.

More importantly, despite the complex nature of surface flow, the pressure/flow dependence can be applied to tailor the resistive and capacitive characteristics of individual fluidic components. In general, at low flow rate (with small pressure drop), straight microchannels can be approximated as primarily resistive elements as long as the deformation of the gas-liquid interface is insignificant. Thus, the fluidic resistance of a microchannel with one unaltered but frictionless boundary can be calculated according

to the classic laminar flow theory  $R = \frac{3\mu l}{wh^3}$ , where  $\mu$  is the

dynamic viscosity of the fluid,  $l$ ,  $w$ , and  $h$  are the length, width and height of the microchannel, respectively. In contrast, the profile of a circular reservoir with relative high surface-to-volume ratio is subject to even a slight pressure change, which deforms the gas-liquid interface into a spherical dome with the radius of curvature predicted by Laplace equation  $1/r = \Delta P/2\gamma$  ( $\gamma$  is the fluidic surface tension). As a result, under small surface flow, the reservoir behaviors major capacitive characteristics, which can be expressed as

$$C = \frac{dV}{dP} = \frac{\pi(4h^2 + d^2)^3}{128\gamma(d^2 - 4h^2)}$$

where  $h$  is the height of accumulated liquid, and  $d$  is the diameter of the reservoir. Figure 2 (b) and (c) show the geometrical design parameters used to determine the resistive (microchannel) and capacitive (reservoir) flow elements, respectively.

Incorporating the distinct capacitive and resistive characteristics into surface microfluidic design, novel fluidic operations (e.g., first-order or higher-order pressure-flow responses) can be implemented. Furthermore, the frictionless, deformable and capacitive gas-liquid interface enables 3D manipulation of the fluid. More specifically, microflow regulation, consisting of resistive microchannels and a capacitive reservoir, exhibits the first-order fluidic response, analogous to the first-order  $RC$  circuit. The flexible but geometrically confined interface can function as a pressure-limiting unit to restrict the maximal flow passing through. Furthermore, by connecting two first-order fluidic circuits with separate cutoff frequencies, flow rate-controlled switching can be implemented using vertical expansion of the flexible interface. Both operations will be demonstrated and characterized in the following section as unique fluidic functions enabled by surface microfluidic networks.

## EXPERIMENTAL METHODS

All planar microfluidic structures are fabricated by photopatterning a superhydrophobic nanocomposite as previously reported [9], in which polytetrafluoroethylene (PTFE) nanoparticle filler (Microdispers-200, Polyscience, Inc.) with extremely low chemical energy and nanotopology is embedded in a photopatternable SU-8 polymer matrix (SU-8 2050, MicroChem Corp.). The surface micromachining began with spin-coating a thick SU-8 photoresist layer (of  $30\mu\text{m}$  thick) onto an acid-cleaned glass substrate. Subsequent to soft bake and selective UV-exposure, the superhydrophobic nanocomposite material, dissolved in an ethanol solution, is spray-coated onto the exposed SU-8 layer as a uniform thin film (of  $2\mu\text{m}$  thick). Followed by Isopropyl alcohol/DI water rinsing and blow drying, the substrate was immersed in SU-8 developer to form micropatterns with extreme wettability. To establish 3D microfluidic networks, two microfabricated planar fluidic substrates are placed face-to-face with a spacer and fluidic connected through miniature capillary bridges of the capacitive elements (reservoirs). In addition, the height of the spacer is adjusted according to different fluidic functions to be implemented.

Both DI water and aqueous-based color dyes (Waterman Paris) are used to conduct the fluidic evaluation. Inflow is directly injected to the inlet reservoir/channel from a computer-programmable syringe pump (KD Scientific). The inlet pressure is determined by the fluidic curvature at the injection reservoir (i.e., hydraulic pressure). The outlet reservoir of a relatively large footprint is to provide zero pressure reference and insensitive to the

volume change. The overall fluidic profile is screened through a horizontally placed digital stereomicroscope. The maximal flow rate is assessed at the steady-state condition for microflow regulation.

## RESULTS AND DISCUSSION

To demonstrate the unique spatiotemporal (i.e., three-dimensional and time-dependent) characteristics of surface microfluidics, two functional 3D microfluidic devices, a microflow regulator and a flow rate-controlled switch, have been fabricated and characterized. Using a capacitive fluidic element, the microflow regulator is able to limit the maximal flow through as well as to provide first-order fluidic damping. Whereas the flow rate controlled switch comprises two  $RC$  circuits in series, of which each stage has individual spatiotemporal response to different fluidic waveforms. Incorporating fluidic switches into 3D surface microfluidic networks, a microfluidic multiplexer has been devised with individual addressable microchannels using pulsed fluidic waveforms.

### Microflow Regulation

Microflow regulators, providing dynamic control of microflow characteristics (e.g. flow rates and flow patterns), usually include active controlling unit or specific structural design, which involves multistep microfabrication and packaging [22-23]. In surface microfluidics, the spatiotemporal dependence of fluidic circuits enables a unique flow-limiting mechanism, that is, the maximal driven pressure is geometrically dependent. A flow passing through a circular reservoir with a primary pressure-dependent capacitance connected to a more resistive surface microchannel. The flow rate established by the pressure head in the reservoir can be determined by the radius of curvature of the accumulated fluid in the reservoir. According to Laplace equation, a smaller radius of curvature leads to a higher pressure across the gas-liquid interface. Therefore, the maximal pressure head is achieved when the fluid forms a hemi-spherical dome shape (i.e., the radius of curvature equal to that of the reservoir). The growing hemi-spherical dome with decreasing pressure head would lead to positive feedback with mechanical instability, and eventually overflow to superhydrophobic surface.

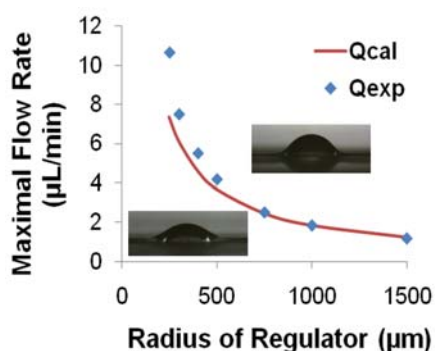


Figure 3: Experimental and computational results of the maximal flow rates in the flow-regulating reservoirs with different radii. The inserted snapshots indicate the steady state of the two regulators with 1mm and 2mm diameters' reservoirs, respectively.

To investigate the microflow regulation, the controlling reservoirs with different sizes from 500 $\mu\text{m}$  to 3mm in diameter are connected to a straight microchannel with constant resistance (of 200 $\mu\text{m}$  in width, 40 $\mu\text{m}$  in depth, and 2cm in length). Figure 3 shows the experimental measurements in comparison with the computational results of the maximal flow rates in the flow-

regulating reservoirs with different radii. As can be seen, the results are well matched in the large reservoir configurations; however, a slight divergence from theoretical predictions has been observed in small reservoirs, where the stray capacitance and deformed interface of the microchannel contribute to additive fluidic conductance. The inserts in Figure 3 show the steady state liquid profile on circular reservoirs with diameters of 1mm (bottom left) and 2mm (top right). In 1mm-diameter one, the liquid height change in the channel which is comparable with that in the reservoir, should be considered when doing the calculations.

### Flow Rate-Controlled Switching

Combining the flexible surface microfluidic network with capillary bridges, a flow rate-controlled switch is devised. As mentioned previously, the vertical expansion of gas-liquid interface of a capacitive element (reservoir) can be adjusted by the magnitude of inflow. By connecting two capacitive-resistive units in series, flow rate-dependent activation can be achieved. As shown in Figure 4, in two circular reservoirs with different diameters, the height of liquid dome can be dynamically controlled by the injection flow rate. That is at lower injection rate, fluid goes directly through the first reservoir (closer to the injection end) towards the second one (the far end) and accumulate there; while injecting at higher rate, most of the liquid builds up inside the first reservoir due to the aforementioned flow regulation. As a result, it is capable of addressing individual capillary bridge contact between the bottom and top substrates using different pulsed fluidic waveform, which serves as flow-activated switch function in the open fluidic circuits. Figure 4 illustrates individual activation of capillary bridge contacts based on two capacitive elements (reservoir) with different radii by controlling pulsed-flow rate. The pulsed flow can selectively control fluidic accumulation and thereby connect the capillary bridge between two fluidic circuits of the top and bottom substrates. Once the liquid bridge is formed, the flow rate can be reduced to a much lower level to maintain the continuous fluidic connection, from which the pulsed flow can be further used to control the next stage of fluidic function.

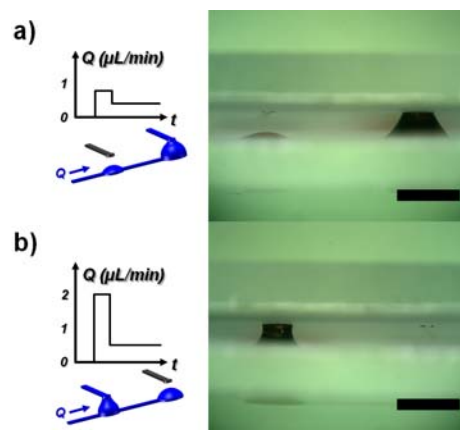


Figure 4: Microscopic illustrations of pulsed-flow switching along with applied pulsed flow waveforms (scale bars: 1mm).

Furthermore, based on the same principle demonstrated in pulsed-flow switch, a microfluidic multiplexing function can be implemented. Figure 5 shows the microfluidic multiplexer built on a 3D surface fluidic network. Under corresponding excitation flow pulses, the selected microchannel is individually activated. The multiplexer network can be easily extended to multistage configuration, while the simple pulse activation illustrates its potential in digital microfluidics. More sophisticated 3D surface fluidic operations are currently under investigation.

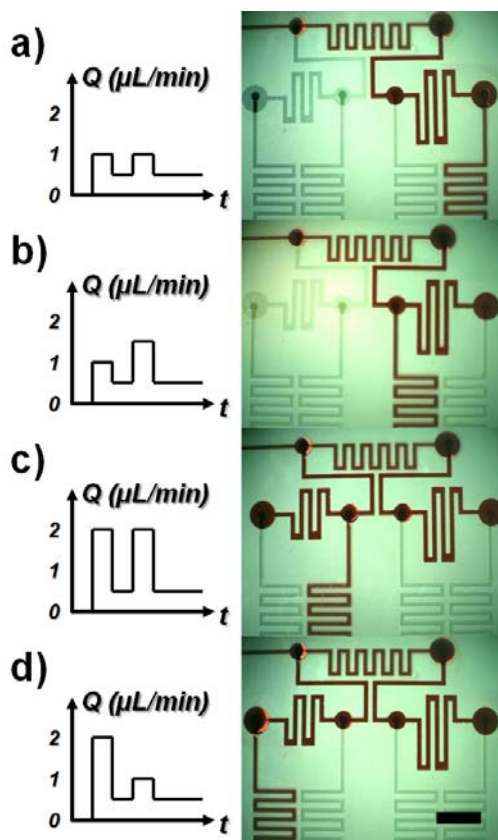


Figure 5: Demonstration of two-stage flow switching in a 3D microfluidic network with different switching-flow pulses (scale bar: 2mm).

## CONCLUSION

By introducing a novel flexible frictionless gas-liquid interface, the surface microfluidic networks enable novel spatiotemporal fluidic manipulations on the planar surfaces, micropatterned by the nanocomposite material with extreme wettability. Detailed theoretical analysis, using the lumped-element model, establishes both basic capacitive (circular reservoir) and resistive (straight microchannel) elements in the open fluidic platform. Further employing the deformable interface of a capacitive element, unique surface microfluidic functions have been implemented, i.e., microflow regulation and flow-rate controlled switching. Microflow regulator provides the functions of maximal flow restriction and fluctuation elimination, while the flow-rate controlled switching allows spatial activation of a specific path according the fluidic waveform. Furthermore, microfluidic multiplexers integrated with three-level flow-switching have been successfully devised, in which fluidic pulse signals can digitally activate individual microchannels. In summary, surface microfluidics, governed by distinct gas-liquid and solid-liquid interfaces, opens new possibilities to maneuver microflow in three-dimensional and time-dependent fashions, which can be further explored in digital and biomedical microfluidic applications.

## ACKNOWLEDGEMENT

This work is in part supported by the National Science Foundation (Award Numbers: ECCS-0846502 and CMMI-0944353), University of California, Davis, and China Scholarship Council (CSC). I would like to thank the Transducer Research

Foundation and National Institute of Standards and Technology, Boulder for the travel support to the conference.

## REFERENCES

- [1] D. J. Beebe *et al.*, "Physics and applications of microfluidics in biology," *Annu Rev Biomed Eng*, 4, 261, 2002.
- [2] G. M. Whitesides, "The origins and the future of microfluidics," *Nature*, 442, 368, 2006.
- [3] D. Therriault *et al.*, "Chaotic mixing in three-dimensional microvascular networks fabricated by direct-write assembly," *Nat Mater*, 2, 265, 2003.
- [4] M. J. Swickrath *et al.*, "Modulating passive micromixing in 2-D microfluidic devices via discontinuities in surface energy," *Sensor Actuat B*, 140, 656, 2009.
- [5] W. Gu *et al.*, "Computerized microfluidic cell culture using elastomeric channels and Braille displays," *Proc. Natl. Acad. Sci. USA*, 101, 15861, 2004.
- [6] G. M. Walker *et al.*, "A passive pumping method for microfluidic devices," *Lab Chip*, 2, 131, 2002.
- [7] M. A. Unger, H. P. Chou, T. Thorsen *et al.*, "Monolithic microfabricated valves and pumps by multilayer soft lithography," *Science*, 288, 113, 2000.
- [8] B. D. Piorek *et al.*, "Free-surface microfluidic control of surface-enhanced Raman spectroscopy for the optimized detection of airborne molecules," *Proc. Natl. Acad. Sci. USA*, 104, 18898, 2007.
- [9] L. Hong, and T. Pan, "Photopatternable Superhydrophobic Nanocomposites for Microfabrication," *J. Microelectromech. Syst*, 1, 2010.
- [10] M. Zimmermann *et al.*, "Capillary pumps for autonomous capillary systems," *Lab Chip*, 7, 119, 2007.
- [11] B. Zhao *et al.*, "Principles of surface-directed liquid flow in microfluidic channels," *Anal. Chem.*, 74, 4259, 2002.
- [12] S. Bouaidat *et al.*, "Surface-directed capillary system; theory, experiments and applications," *Lab Chip*, 5, 827, 2005.
- [13] J. West *et al.*, "Microplasma writing for surface-directed millifluidics," *Lab Chip*, 7, 981, 2007.
- [14] M. Watanabe, "Surface-directed channels filled with organic solvents," *Lab Chip*, vol. 9, no. 8, pp. 1143, 2009.
- [15] B. Zhao *et al.*, "Surface-directed liquid flow inside microchannels," *Science*, 291, 4, 2001.
- [16] P. Lam *et al.*, "Surface-tension-confined microfluidics," *Langmuir*, 18, 948, 2002.
- [17] J. S. H. Lee *et al.*, "Electrokinetic flow in a free surface-guided microchannel," *J Appl Phys*, 99, 2006.
- [18] M. Watanabe, "Microfluidic devices easily created using an office inkjet printer," *Microfluid Nanofluid*, 8, 403, 2010.
- [19] S. Y. Yang *et al.*, "Integration of a surface-directed microfluidic system with an organic electrochemical transistor array for multi-analyte biosensors," *Lab Chip*, 9, 704, 2009.
- [20] H. Gau *et al.*, "Liquid morphologies on structured surfaces: From microchannels to microchips," *Science*, 283, 46, 1999.
- [21] L. Hong, and T. Pan, "Surface microfluidics fabricated by superhydrophobic nanocomposite photoresist," in MEMS 2010, Hongkong, 2010.
- [22] B. Z. Yang *et al.*, "A planar compliance-based self-adaptive microfluid variable resistor," *J Microelectromech S*, 16, 411, 2007.
- [23] W. Xu *et al.*, "A vapor based microfluidic flow regulator," *Sensor Actuat B*, 142, 355, 2009.

## CONTACT

\*Tingrui Pan, tel: +1-530-754-9508; [tingrui@ucdavis.edu](mailto:tingrui@ucdavis.edu)



# EWOD MICRODEVICES FOR SYNTHESIS OF $^{18}\text{F}$ -LABELED TRACERS FOR POSITRON EMISSION TOMOGRAPHY (PET)

Supin Chen<sup>1\*</sup>, Huijiang Ding<sup>2,3</sup>, Gaurav J. Shah<sup>4</sup>, R. Michael van Dam<sup>1,2,3</sup>, and Chang-Jin "CJ" Kim<sup>4</sup>

<sup>1</sup>Biomedical Engineering Department, <sup>2</sup>Department of Molecular and Medical Pharmacology,

<sup>3</sup>Crump Institute for Molecular Imaging, <sup>4</sup>Mechanical and Aerospace Engineering Department  
University of California, Los Angeles (UCLA), Los Angeles, CA 90095

## ABSTRACT

We demonstrate the drying (i.e., removing water content) of cyclotron-produced [ $^{18}\text{F}$ ]fluoride solutions and synthesis of 2- [ $^{18}\text{F}$ ]fluoro-2-deoxy-D-glucose ([ $^{18}\text{F}$ ]FDG) and 1- [ $^{18}\text{F}$ ]fluoro-4-nitrobenzene ([ $^{18}\text{F}$ ]FNB) as example tracers on an electrowetting-on-dielectric (EWOD) platform using multifunctional electrodes (for heating, temperature sensing, and EWOD driving). This is an important step toward the development of an affordable, universal synthesizer for imaging tracers used in Positron Emission Tomography (PET).

## INTRODUCTION

Positron Emission Tomography (PET) is a highly sensitive type of noninvasive functional medical imaging for specific and quantitative measurement of biochemical activity in patients for diagnosis of cancer or Alzheimer's, monitoring of cancer treatment, visualization of immune responses, and many other clinical and research applications [1], [2]. It requires the administration of a chemical tracer labeled with a positron-emitting isotope, such as fluorine-18 ( $^{18}\text{F}$ ). We report the development of a droplet microfluidic device for synthesis of  $^{18}\text{F}$ -labeled PET tracers, based on electrowetting-on-dielectric (EWOD) technology enhanced with localized on-chip heating capability.

Microfluidics in general is attractive for PET tracer synthesis, because shorter reaction times reduce radioisotope decay and typical radiolabeling reactions produce only nanograms of tracer [3]. However, EWOD presents additional advantages: (1) With no tubes and discrete pumps, the overall system is simple and compact, easier to clean, and more reliable [4]. (2) Microfluidic sequences are configured on a generic chip electronically (i.e., no hardware adjustment needed), allowing synthesis of a variety of tracers with one system. This is a stark contrast to the current state of the art, in which system setup must be adjusted for different types of probe synthesis. (3) Our chip is made open to operate in air (i.e., not oil-filled), enabling effective evaporations for exchange of solvents, which is critical for many radiosyntheses that are water-sensitive but begin with cyclotron-produced [ $^{18}\text{F}$ ]fluoride in [ $^{18}\text{O}$ ]H<sub>2</sub>O. (4) The chip surface is more chemically inert and thermally stable (vs. PDMS, polycarbonate). The resulting system enjoys enormous reductions in the size and weight of radiation shielding (typically lead), and cost (below \$5K expected vs. the conventional \$50K-\$250K). Currently, although over 1400 PET labeling compounds have been published in literature [5], only several are available to imaging centers by commercial radiopharmacies. As an affordable and flexible synthesizer, this chip would empower final users to produce tracers of their choice locally on-demand, eventually making PET imaging as readily available as CT and MRI.

We have demonstrated the drying (i.e., removing water content) of [ $^{18}\text{F}$ ]fluoride solutions – the most critical step in synthesis of most  $^{18}\text{F}$ -labeled radiotracers – using an EWOD chip with multifunctional electrodes, which allow heating and temperature sensing as well as the electrowetting actuation. Two  $^{18}\text{F}$ -labeled radiotracers were reliably synthesized. The first, 1- [ $^{18}\text{F}$ ]fluoro-4-nitrobenzene ([ $^{18}\text{F}$ ]FNB), is used to label various

antibodies and peptides. The second, 2- [ $^{18}\text{F}$ ]fluoro-2-deoxy-D-glucose ([ $^{18}\text{F}$ ]FDG), is a labeled-sugar that is the most important PET tracer and commonly used in the diagnosis and monitoring of cancer [6].

## DEVICE AND EXPERIMENTS

### EWOD Device Fabrication

Assisted by multifunctional (heating, temperature sensing, and EWOD driving) electrodes developed for MADLI sample preparation [7] our new device performs drying and reaction steps for radioactive tracer production. Instead of the etched hydrophilic patterns of [7], we used a circular resistor pattern enclosed by the EWOD electrode (Figure 1c) for centering residue from evaporating droplets. Hydrophilic patterns were avoided because, unlike the MALDI case, droplets must be moved after reactions are completed. Many radiolabeling reactions require low vapor pressure solvents, which presented the main challenge. These solvents could not be stored in a sealed device due to the need to remove water during evaporation steps. Instead, solvents were loaded in the EWOD chip at their time of use.

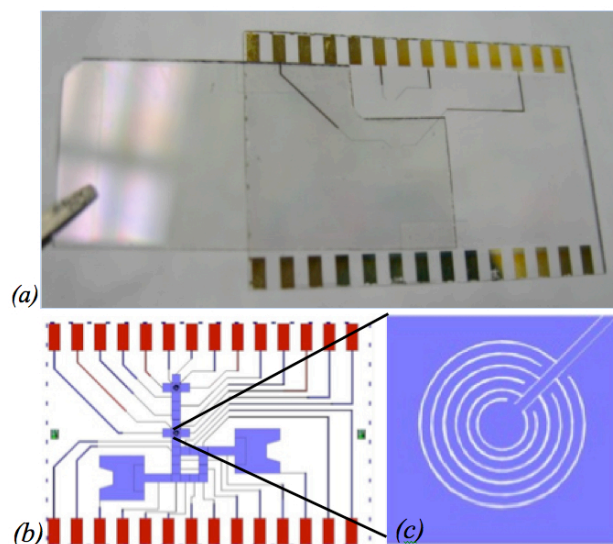


Figure 1: EWOD chip for probe synthesis. (a) with cover plate on, (b) device layout, and (c) heater layout.

Device fabrication is shown in Figure 2. 700  $\mu\text{m}$  thick glass wafers coated with 140 nm ITO (TechGophers Inc.) were covered with 20/200 nm of evaporated Cr/Au. Gold and ITO layers were etched to form heaters, EWOD electrodes, connection lines, and contact pads. 1  $\mu\text{m}$  PECVD silicon nitride was deposited as a dielectric, and 1  $\mu\text{m}$  of Cytop<sup>®</sup> was spin-coated and annealed at 200  $^{\circ}\text{C}$  to make the surface hydrophobic. A cover plate was prepared from 700  $\mu\text{m}$  thick glass coated with 150 nm ITO (Delta Technologies Inc.) to serve as a ground electrode for electrowetting. The cover plate was coated with thinner layers of PECVD silicon

nitride (100 nm) and Cytop<sup>®</sup> (100 nm). The cover plate was spaced and bonded to the EWOD substrate using 100  $\mu\text{m}$  thick double-sided tape (3M Inc.).

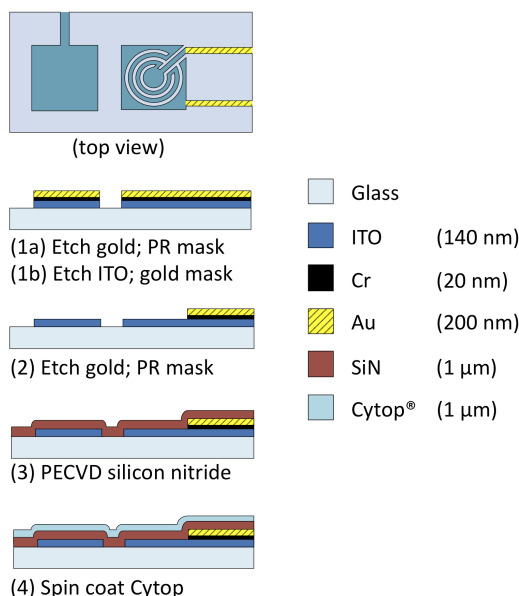


Figure 2: Process flow to fabricate EWOD substrate.

### Solution Preparation

Acetonitrile (MeCN), anhydrous dimethyl sulfoxide (DMSO), Kryptofix 2.2.2, mannose triflate, potassium carbonate ( $\text{K}_2\text{CO}_3$ ) and hydrochloric acid (HCl) were purchased from Sigma-Aldrich, and 1,4-dinitrobenzene was purchased from Acros Organics. No-carrier-added [ $^{18}\text{F}$ ]fluoride ion, obtained from the UCLA Cyclotron and Radiochemistry Center, was produced in an RDS-112 cyclotron (Siemens). Aqueous [ $^{18}\text{F}$ ]fluoride ion was treated with  $\text{K}_2\text{CO}_3$  and Kryptofix 2.2.2, a phase-transfer agent to a final concentration of 56 mM  $\text{K}_2\text{CO}_3$ , 112 mM Kryptofix 2.2.2 in MeCN and water (5:1 v/v). For preparation of [ $^{18}\text{F}$ ]FNB, a solution of 1,4-dinitrobenzene (20 mg/mL) was used. For preparation of [ $^{18}\text{F}$ ]FDG, solutions of mannose triflate (50 mg/mL) and HCl (1N) were used. For radio-TLC running buffers for [ $^{18}\text{F}$ ]FNB and [ $^{18}\text{F}$ ]FDG, we used dichloromethane/hexane (1:1 v/v) and MeCN/water (95:5 v/v), respectively.

In addition, solvents commonly used for radiotracer synthesis were tested for EWOD compatibility. Repeatable movement, splitting, and merging of droplets was accomplished with MeCN, DMSO, DMF, MeOH,  $\text{K}_2\text{CO}_3$  (1 M), HCl (1 N), and NaOH (1 N) with voltages below 90  $V_{\text{rms}}$  and frequencies ranging 0-20 kHz.

### Device Actuation

Multifunctional electrodes were connected to a switch to alternate between EWOD actuation and temperature control. Voltage and current applied to the electrodes were controlled by a LabVIEW program, which sequenced EWOD actuation using a digital I/O device (DAQPad 6507, National Instruments) and performed PID control over heating with a DC source meter (Model 2400, Keithley Instruments).

## RESULTS AND DISCUSSION

### Synthesis of 1-[ $^{18}\text{F}$ ]fluoro-4-nitrobenzene ([ $^{18}\text{F}$ ]FNB)

Figure 3 illustrates radiosynthesis of [ $^{18}\text{F}$ ]FNB. It is produced by a one-step reaction of dried [ $^{18}\text{F}$ ]fluoride with the precursor

dinitrobenzene in DMSO. On chip, this is accomplished by loading a water/MeCN droplet with  $^{18}\text{F}$ ,  $\text{K}_2\text{CO}_3$ , and Kryptofix. The droplet is moved by EWOD to a heater electrode (Figure 4a) and heated at  $105^\circ\text{C}$  for 3 minutes (Figure 4b). Next, an azeotropic drying step is repeated 3 times, in which an MeCN droplet is loaded, moved to the heater electrode (Figure 4c), and heated at  $105^\circ\text{C}$  for 3 minutes (Figure 4d). A droplet of dinitrobenzene in DMSO is then loaded and moved to the same heater along a different pathway to avoid cross-contamination (Figure 4e). The droplet is subsequently heated to  $120^\circ\text{C}$  for 3 minutes for radiolabeling reaction (Figure 4f).

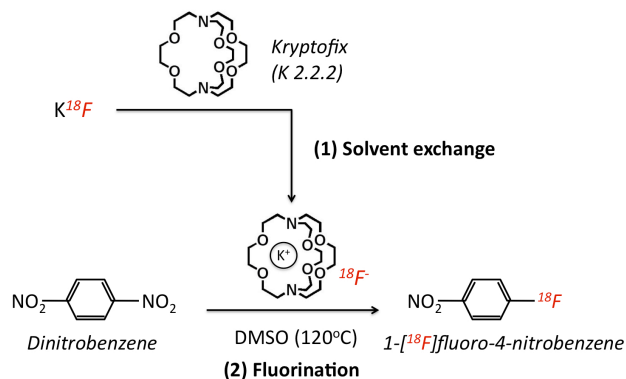


Figure 3: Synthesis of 1-[ $^{18}\text{F}$ ]fluoro-4-nitrobenzene.

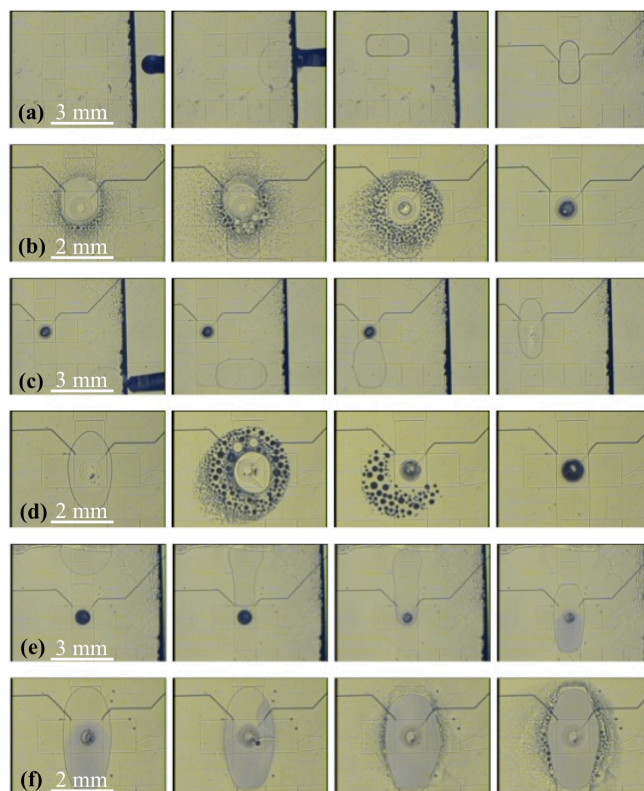


Figure 4: Synthesis process to produce [ $^{18}\text{F}$ ]FNB on EWOD: (a) loading and movement of  $^{18}\text{F}$  droplet, (b) heating of  $^{18}\text{F}$  droplet ( $105^\circ\text{C}$ , 3 min), (c) loading and movement of acetonitrile, (d) heating of acetonitrile ( $105^\circ\text{C}$ , 3 min), (e) loading of dinitrobenzene droplet, (f) heating of dinitrobenzene droplet ( $120^\circ\text{C}$ , 3 min).

Probe synthesis on EWOD device is analyzed by removing the cover plate and transferring the product droplet with a capillary onto a thin-layer chromatography (TLC) plate. [ $^{18}\text{F}$ ]FNB is separated from free fluoride by TLC with a running buffer of 90% MeCN and 10% H<sub>2</sub>O. Composition of radioactive components is then measured with a radio-TLC scanner (miniGITA Star, Raytest). Conversion to desired product, [ $^{18}\text{F}$ ]FNB, averaged  $78 \pm 12\%$  (n=8 runs) with results ranging as high as 96% as shown in Figure 5.

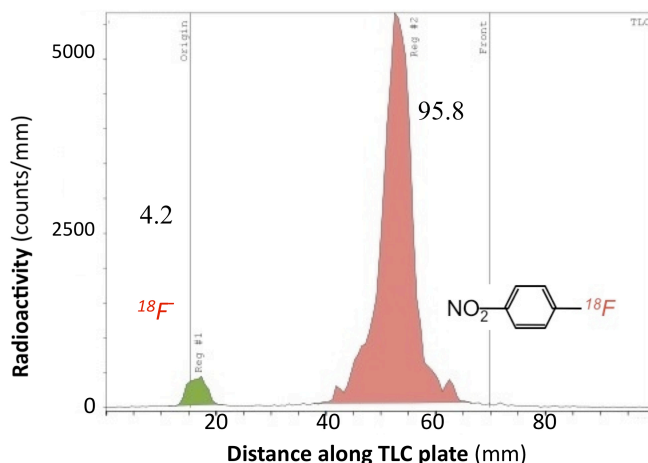


Figure 5: Radio-TLC results showing product purity after on-chip drying and reaction to produce [ $^{18}\text{F}$ ]FNB. The left peak represents unbound [ $^{18}\text{F}$ ]fluoride. The right peak represents the desired product, [ $^{18}\text{F}$ ]FNB.

### Synthesis of 2- $^{18}\text{F}$ fluoro-2-deoxy-D-glucose ( $^{18}\text{F}$ ]FDG)

Figure 6 illustrates radiosynthesis of [ $^{18}\text{F}$ ]FDG, a two-step reaction. The first step is a fluorination reaction in which the precursor manose triflate in MeCN is labeled with dried [ $^{18}\text{F}$ ]fluoride to produce a fluorinated intermediate, 2- $^{18}\text{F}$ fluoro-1,3,4,6-tetra-O-acetyl-d-glucose ([ $^{18}\text{F}$ ]FTAG). The second step is a deprotection reaction in which HCl is added to remove the acetyl protecting groups.

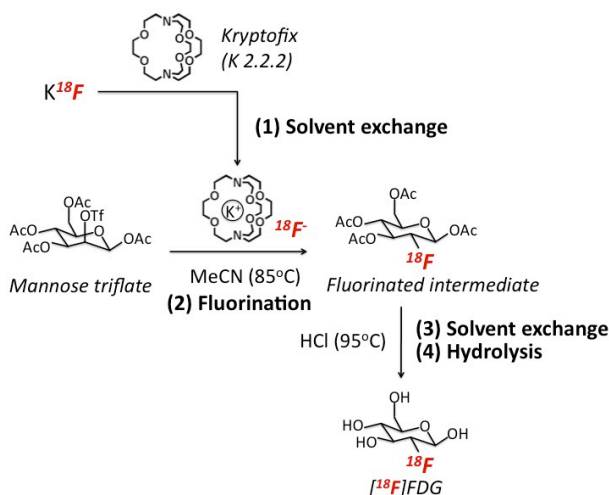


Figure 6: Synthesis of 2- $^{18}\text{F}$ fluoro-2-deoxy-D-glucose ( $^{18}\text{F}$ ]FDG).

The [ $^{18}\text{F}$ ]FDG synthesis process using EWOD is shown in Figure 7. After loading of fluoride, azeotropic drying, shown in Figure 7b, is repeated 6 times using acetonitrile to ensure residual water will not interfere with fluorination reaction. Fluorination reaction is accomplished by loading a precursor droplet of mannose triflate in acetonitrile. The precursor droplet is moved to the fluoride and heated to 85 °C for 5 minutes (Figure 7c). During the fluorination reaction, more acetonitrile droplets are added to maintain a liquid phase during reaction. Fluorination is followed by solvent evaporation and hydrolysis (Figure 7d). A 1  $\mu\text{L}$  droplet of 1 N HCl was added 3 times over the 5 minute deprotection reaction to replenish the droplet as it evaporated. If a more constant acid concentration is desired, water droplets can be added instead.

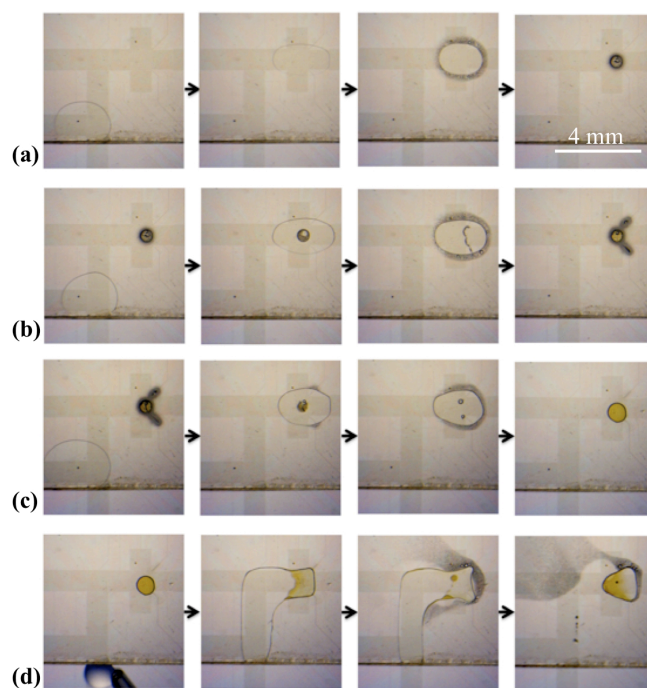


Figure 7: Synthesis process on EWOD: (a) loading of  $^{18}\text{F}$  droplet at cover plate edge, droplet movement to heating site, and evaporation of  $^{18}\text{F}$  droplet by resistive heating (105°C, 3 min), (b) loading of acetonitrile droplet at cover plate edge, droplet movement to heating site, and evaporation by heating (105°C, 3 min), (c) loading of mannose triflate droplet at cover plate edge, droplet movement to heating site, and heating for radiolabeling reaction (85°C, 5 min), (d) loading of HCl droplet at cover plate edge, droplet movement to heating site, and heating of droplet to remove protecting groups (95°C, 5 min).

Product was recovered with a capillary after removing the cover plate, and  $^{18}\text{F}$ -labeled compounds were separated by TLC and measured with a radio-TLC as was done for analysis of [ $^{18}\text{F}$ ]FNB synthesis. As shown by the example result in Figure 8, conversion to desired product was high (84.9%).

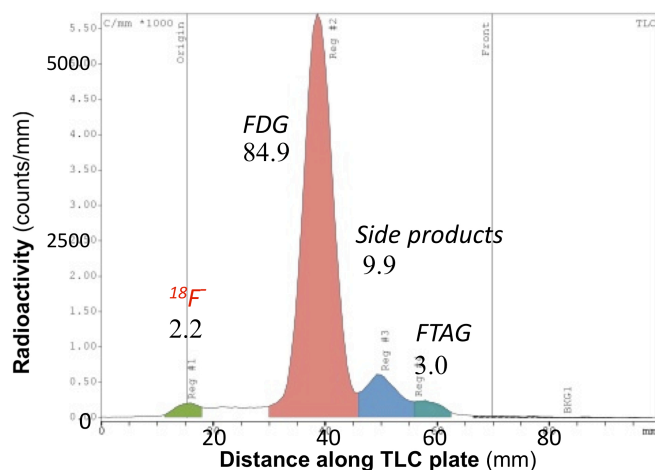


Figure 8: Radio-TLC results showing crude product purity after on-chip drying and reaction to produce [ $^{18}\text{F}$ ]FDG. The left peak represents unreacted [ $^{18}\text{F}$ ]fluoride. The second peak from the left shows 84.9% of the radioactivity incorporated into the desired product, [ $^{18}\text{F}$ ]FDG. The rightmost peak represents the intermediate compound. The third peak from the left represents side products from incomplete hydrolysis.

## CONCLUSION

We have demonstrated the synthesis of 1- [ $^{18}\text{F}$ ]fluoro-4-nitrobenzene ([ $^{18}\text{F}$ ]FNB) and 2- [ $^{18}\text{F}$ ]fluoro-2-deoxy-D-glucose ([ $^{18}\text{F}$ ]FDG) from cyclotron-produced  $^{18}\text{F}$  radioisotope solutions using an EWOD device with multifunctional electrodes for heating. Greater quantities of radioactive tracers can be produced for imaging by handling larger concentrations of  $^{18}\text{F}$  droplets or running processes in parallel. Future work will be towards automating droplet loading to the chip and developing a more generic synthesizer EWOD chip for the production of additional PET tracers.

## ACKNOWLEDGMENT

This work was supported in part by the National Cancer Institute (Caltech NanoSystems Biology Cancer Center, grant number 68D-1079964) as well as the Industry-University Cooperative Research Program and Sofie Biosciences, Inc. (UC Discovery Grant number bio08-129095). We would like to thank Prof. Nagichettiar Satyamurthy and the staff of the UCLA Cyclotron and Radiochemistry Center for providing [ $^{18}\text{F}$ ]fluoride, Prof. Kwang-Fu Clifton Shen and his lab for use of their lead shielding and analytical equipment, and Mr. Wyatt Nelson for developing a PID temperature control program.

## REFERENCES

- [1] M.E. Phelps, "Positron emission tomography provides molecular imaging of biological processes," *Proceedings of the National Academy of Sciences of the United States of America*, 97, 16, pp. 9226-9233, 2000.
- [2] C. G. Radu, C. J. Shu, E. Nair-Gill, S.M. Shelly, J.R. Barrio, N. Satyamurthy, M.E. Phelps, and O.N. Witte, "Molecular imaging of lymphoid organs and immune activation by positron emission tomography with a new [ $^{18}\text{F}$ ]-labeled 2'-deoxycytidine analog," *Nature Medicine*, 14, 7, pp. 783-788, 2008.
- [3] A. M. Elizarov, "Microreactors for radiopharmaceutical synthesis," *Lab on a Chip*, 9, 10, pp. 1326-1333, 2009.
- [4] J. Gong and C.-J. Kim, "All-electronic droplet generation on-chip with real-time feedback control for EWOD digital microfluidics," *Lab on a Chip*, 8, 6, pp. 898-906, 2008.
- [5] R. Iwata, "Reference book for PET radiopharmaceuticals," [http://kakuyaku.cyric.tohoku.ac.jp/public/Reference\\_Book\\_2004.pdf](http://kakuyaku.cyric.tohoku.ac.jp/public/Reference_Book_2004.pdf).
- [6] C.-C. Lee, G. Sui, A. Elizarov, C.J. Shu, Y.S. Shin, A.N. Dooley, J. Huang, A. Daridon, P. Wyatt, D. Stout, H.C. Kolb, O.N. Witte, N. Satyamurthy, J.R. Heath, M.E. Phelps, S.R. Quake, and H.R. Tseng, "Multistep synthesis of a radiolabeled imaging probe using integrated microfluidics," *Science*, 310, 5755, pp. 1793-1796, 2005.
- [7] W. Nelson, I. Peng, J. A. Loo, R.L. Garrell, and C.-J. Kim, "An EWOD droplet microfluidic chip with integrated local temperature control for multiplex proteomics." *Proceedings of IEEE International Conference on Micro Electro Mechanical Systems*, Sorrento, Italy, January 2009, pp. 280-283.

## CONTACT

\*Supin Chen, tel: +1-310-825-3977; supinchen@ucla.edu

# MANIPULATION OF LIQUID SPREADING ON ASYMMETRIC NANOSTRUCTURED SURFACES

K.-H. Chu<sup>1\*</sup>, R. Xiao<sup>1</sup>, M.E. Alf<sup>2</sup>, K.K. Gleason<sup>2</sup> and E. N. Wang<sup>1</sup>

<sup>1</sup>Department of Mechanical Engineering, and <sup>2</sup>Department of Chemical Engineering, Massachusetts Institute of Technology, Cambridge, Massachusetts, USA

## ABSTRACT

We demonstrate the manipulation of liquid spreading on asymmetric nanostructured surfaces using electrowetting. Asymmetric nanopillar arrays were fabricated with diameters of 500 to 750 nm and deflection angles of 3 to 52 degrees using deep reactive ion etching and angled metal deposition process on silicon. Droplets can achieve uni-directional, asymmetric, and nearly symmetric spreading behaviors with various applied electric potentials on asymmetric nanostructured surfaces. A theory based on an energy argument is also developed to predict the spreading behaviors and shows excellent agreement with experimental results. This work shows that we can manipulate liquid spreading in a single direction on-demand, which suggests new opportunities to tailor advanced nanostructures to achieve active control of complex flow patterns for various microfluidic and thermal applications.

## INTRODUCTION

The manipulation of liquid spreading is important for a broad range of microfluidic, biological, and thermal management applications [1-3]. Engineered surfaces have received significant interest to enable control of liquid behavior, such as varying the liquid film thickness [4] and the final wetted shape [5]. By utilizing groove geometries and patterned surface chemistries, elongated droplets with distinct contact angles in the orthogonal directions have also been achieved [6,7]. In all of the previous studies, however, the spreading behavior on these engineered surfaces is symmetric [4-7]. Furthermore, dynamic control of spreading behavior has not yet been demonstrated.

In this work, we present the design of asymmetric nanostructures that can not only be used to achieve uni-directional spreading [8], but also to actively control the directionality of liquid spreading with applied electric potentials. The asymmetric nanopillars can introduce energy barriers on more than one axis, which allows the liquid to propagate in a single preferred direction and pin in all others. However, with the application of electric potential, the spreading directionalities can change depending on the magnitude of potential difference by decreasing the energy barriers in different directions.

## FABRICATION

Asymmetric nanopillars were fabricated using MEMS processing on silicon with diameters ranging from 500 to 750 nm, spacings of 3.5  $\mu\text{m}$ , and heights of 9 to 10  $\mu\text{m}$ . The pillars were patterned using projection lithography, and etched in silicon with deep reactive ion etching (DRIE). A thin gold film was subsequently deposited onto one side of the pillars with an electron beam evaporator. The residual stress between the two materials caused the pillars to deflect. The thickness of the gold film controlled the deflection angle.

Fig. 1 shows scanning electron micrographs (SEMs) of three representative asymmetric nanopillar arrays with deflection angles,  $\phi$ , (as defined in the Fig. 1 inset) ranging from 7°-25°. A Cartesian coordinate system is defined for convenience, as shown in Fig. 1, where the pillars deflect in the positive X (+X) direction. After the fabrication, we conformally coated the nanopillars with a polymer

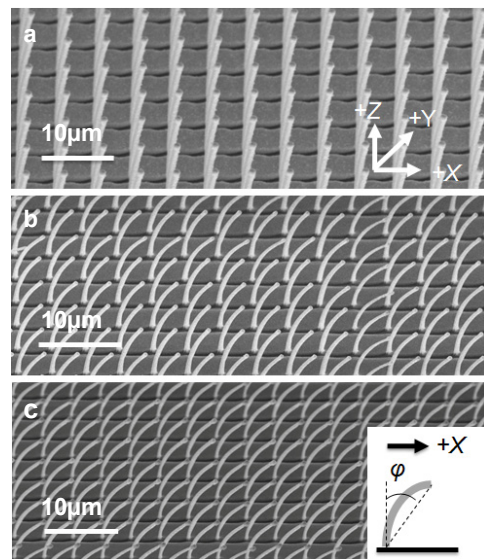


Figure 1: Scanning electron micrographs (SEMs) of fabricated asymmetric nanostructured surfaces with 500-750 nm pillars and deflection angles of a) 7°, b) 12° and c) 25°. Schematic in inset defines the deflection angle,  $\phi$ .

layer using an initiated chemical vapor deposition (iCVD) process [9,10]. The deposited polymer allowed controlled investigations of the effect of geometry on liquid spreading behavior. Different polymers were used in the experiments to tailor the surface energy of nanostructures, such that the effect of surface properties on spreading behavior could also be studied. In addition, the polymer served as the dielectric layer for electrowetting experiments.

## UNI-DIRECTIONAL SPREADING

### Phenomenon

When a water droplet is deposited on a typical periodic nanostructured hydrophilic surface, the droplet spreads in all directions (Fig. 2a). Asymmetric nanostructures, on the other hand, can introduce local energy barriers *via* geometry in different directions, so that in some cases, uni-directional spreading is achieved. For example, when the same droplet shown in Fig. 2a is placed on the deflected nanopillar array with a deflection angle of 12°, the liquid spreads only in the +X direction (Fig. 2b). Fig. 3 shows time-lapse images of the side and top view of such uni-directional spreading behavior. The images demonstrate that the liquid droplet propagates primarily in the +X direction while the contact line pins in both the -X direction and along the Y-axis. To investigate the spreading behavior further, we studied the liquid film propagating ahead of the droplet within the nanopillars, as indicated by the arrow in Fig. 3b.

### Theory and Model

We found that the behavior of the liquid film was well-correlated with the behavior of the macroscopic droplet, *i.e.* the liquid film propagation determines the direction of the

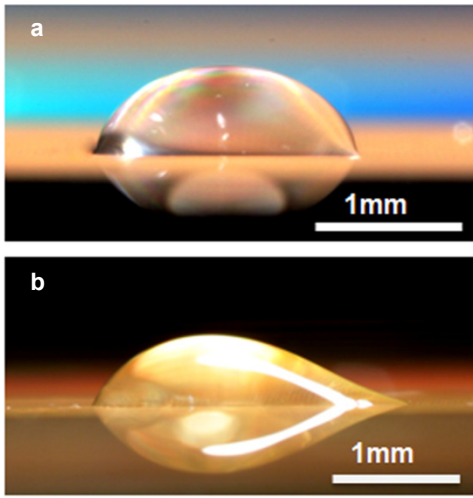


Figure 2: Spreading behaviors and droplet shapes on typical symmetric nanostructured surfaces and the asymmetric nanostructured surfaces fabricated in this work. **a)** 1  $\mu\text{L}$  water droplet symmetrically spreads on typical vertical nanopillars. **b)** The same droplet spreads uni-directionally on asymmetric nanostructures with a  $12^\circ$  deflection angle. The scale bars in the insets are  $10\ \mu\text{m}$ .

macroscopic droplet spreading. To explain the uni-directional liquid film propagation, we developed a simple two-dimensional geometric model. The asymmetric pillars were simplified as slanted rectangles in the 2D model, as shown in the Fig. 4. The model assumes that the liquid film propagate only if the contact line is able to reach the next row of pillars. In addition, when liquid film propagates, the local contact angle of the liquid cannot be smaller than  $\theta_{eq}$  according to Young's Equation [5] due to the fact that  $\theta_{eq}$  is the lowest energy state. Therefore,  $\theta_{eq}$  of the liquid must be equal to or smaller than a critical angle defined as  $\theta_{cr}$  shown in the Fig. 4. Because the film propagates at the height of the pillars, then  $\theta_{cr} = \tan^{-1}(H_{eff}/l_{eff})$ , where  $H_{eff}$  and  $l_{eff}$  are the effective height of the pillars and spacing between pillars, respectively. Thus, the critical angle in the  $+X$  direction is given by

$$\theta_{cr,+x} = \tan^{-1} \frac{(H/l) \cos \varphi}{1 - (H/l) \sin \varphi} \quad (1)$$

where  $H$  and  $l$  are the actual height and spacing between the pillars, respectively, and  $\varphi$  is the pillar deflection angle. Similarly, for the case of liquid film propagation in the  $-X$  direction, the critical angle is given by

$$\theta_{cr,-x} = \tan^{-1} \frac{(H/l) \cos \varphi}{1 + (H/l) \sin \varphi} \quad (2)$$

If  $\theta_{cr} > \theta_{eq}$ , then the liquid film propagates within the nanopillars, otherwise, the liquid film pins.

To study the spreading behavior and validate the theoretical model, a series of experiments were conducted. We used DI water and DI water with surfactants (Triton X-100 with concentrations ranging from 0.01% to 0.00125% by volume) on the polymer (*poly*(cyclohexyl methacrylate-*co*-divinyl benzene)) coated surface with an equilibrium contact angle of  $80^\circ$  (DI water). On this surface, surfactants were necessary to decrease the equilibrium contact angle in order to satisfy the condition for imbibition [11], which is the condition in which the liquid can start to spread.

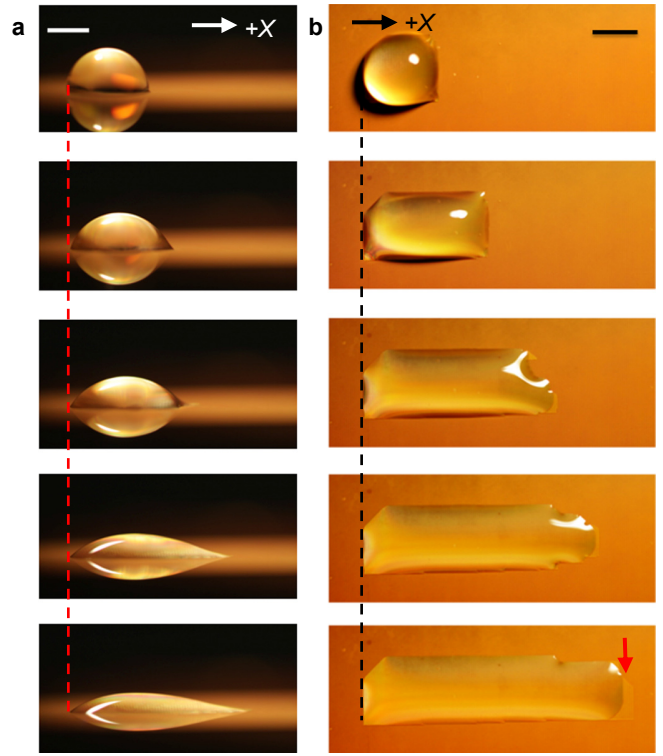


Figure 3: Time-lapse images of uni-directional spreading of a liquid droplet. **a)** Side view and **b)** top view of a  $1\ \mu\text{L}$  droplet of DI water with 0.002% by volume of surfactant spreading on a surface with pillar diameters of 500-750 nm, spacings of  $3.5\ \mu\text{m}$ , and heights of  $10\ \mu\text{m}$  deflected at  $12^\circ$  as shown in Fig. 2. The initial location of the droplet contact line in the  $-X$  direction is indicated by the dotted lines, where the contact line stays pinned throughout the spreading process. The liquid film propagates in front of the macroscopic droplet as highlighted by the arrow in **b**. The scale bars are 1 mm.

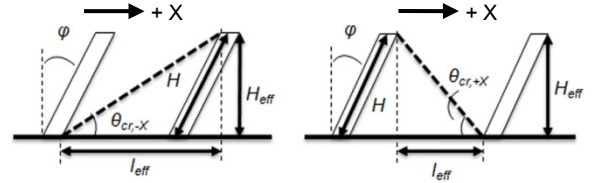


Figure 4: Schematics explaining the geometries for the developed model that determines the critical angle,  $\theta_{cr,-x}$  and  $\theta_{cr,+x}$  to initiate spreading in both  $-X$  (top) and  $+X$  (bottom), respectively. The parameters  $H$ ,  $H_{eff}$ ,  $l_{eff}$ , and  $\varphi$  are the pillar height, effective height, effective distance between pillars, and pillar deflection angle.

Fig. 5 depicts the experimental results of uni-directional spreading and the theoretical curves based on the geometric model. The model is plotted for the case  $\theta_{cr} = \theta_{eq}$  in both  $+X$  and  $-X$  where the  $H/l$  ratio is 2.87 ( $H = 10\ \mu\text{m}$ ) for different pillar deflection angles and equilibrium contact angles. The region bounded by  $\theta_{cr,-x}$  and  $\theta_{eq} = 65^\circ$  (*i.e.*, the imbibition condition) indicates the parameter space (in blue) that allows uni-directional spreading. The square symbols ( $\square$ ) indicate experiments in which the liquid film propagates only in the  $+X$  direction, whereas the circles ( $\circ$ ) are experiments where the film propagates directionally (in  $+X$  and  $-X$ ). The triangles ( $\Delta$ ) show instances where the spreading is

nearly uni-directional, *i.e.*, the film propagates in  $-X$  but the propagation rate was at least five times slower than in  $+X$ . The crosses ( $\times$ ) represent experiments where the film does not propagate at all due to the imbibition condition.

### CONTROL OF SPREADING BEHAVIOR

In the previous studies, we tailored the polymers to ensure that the imbibition condition can be satisfied to achieve uni-directional spreading [8]. In the subsequent step of this work, we studied the effect of an applied electric potential across the droplet and the surface, to achieve on-demand control of spreading directionalities. Electrowetting is a well-known phenomenon that involves modifying the wettability and the contact angle of a liquid (electrolyte) on the surface using an electric potential [2,12,13]. The effect due to electrowetting on contact angle based on a thermodynamic model is given by [13]

$$\theta = \cos^{-1} \left( \cos \theta_{eq} + \frac{\epsilon_0 \epsilon_d}{2d\gamma_{lv}} V^2 \right) \quad (3)$$

where  $\theta$  is the contact angle under electrowetting effect,  $\epsilon_0$  is vacuum permittivity,  $\epsilon_d$  is relative permittivity of the dielectric layer,  $d$  is the thickness of the dielectric layer,  $\gamma_{lv}$  is surface tension of the liquid, and  $V$  is the applied electric voltage. In the experiments, we used 0.1 M NaCl solution on the surfaces coated with another polymer (*poly(N-isopropylacrylamide-co-di(ethylene glycol) divinylether)*). The liquid (NaCl solution) on the polymer coated surfaces has an equilibrium contact angle,  $\theta_{eq}$ , of  $66^\circ$  and the contact angle with electrowetting can be calculated based on equation (3). However, to predict  $\theta$ , the relative permittivity of the polymer,  $\epsilon_d$ , needs to be determined, which is dependent on the frequency of the applied voltage. In this work, we used experiments to determine the relationship between the droplet contact angle and applied voltage,  $V$ , as shown in Fig. 6.

A droplet of 0.1 M NaCl solution deposited on asymmetric nanostructured surfaces initially remains static due to the imbibition condition. With electrowetting, the contact angle of the liquid decreases, and the liquid starts to spread when the imbibition condition is satisfied. In the presence of asymmetric nanostructures, when the applied potential is sufficient to satisfy the imbibition condition, the liquid will spread uni-directionally as shown in Fig. 7a. An example case is shown with an applied voltage of  $V=1.5$  V, which causes the initially static droplet to spread in only the  $+X$ , direction (Fig. 7b). Furthermore, by changing the magnitude of the electric potential, different droplet spreading directionalities can be achieved. As the voltage is increased to  $V=2.1$  V, the liquid unpins in  $-X$  and spreads bi-directionally. The spreading, however, is asymmetric; the rate is three times faster in  $+X$  as compared to  $-X$  (Fig. 7c). Moreover, with increasing applied  $V$ , the asymmetry decreases. In the case of an applied  $V > 2.5$  V, the liquid spreading is nearly symmetric, *i.e.* the rates in  $+X$  and  $-X$  are approximately equal (Fig. 7d).

We further conducted a series of experiments with different pillar deflection angles and the contact angles,  $\theta$ , associated with the applied potentials. The experimental results is also overlaid with the model for uni-directional spreading and plotted in Fig. 8 for the case  $\theta_{cr} = \theta$  where the  $H/l$  ratio is 2.57. In Fig. 8, the square symbols ( $\square$ ) indicate experiments in which the liquid propagates only in the  $+X$  direction. The triangles ( $\Delta$ ) shows the spreading is bi-directional asymmetric, while circles ( $\circ$ ) show experimental results of nearly bi-directional symmetric liquid spreading. The crosses ( $\times$ ) represent experiments where the liquid does not spread at all due to the imbibition condition.

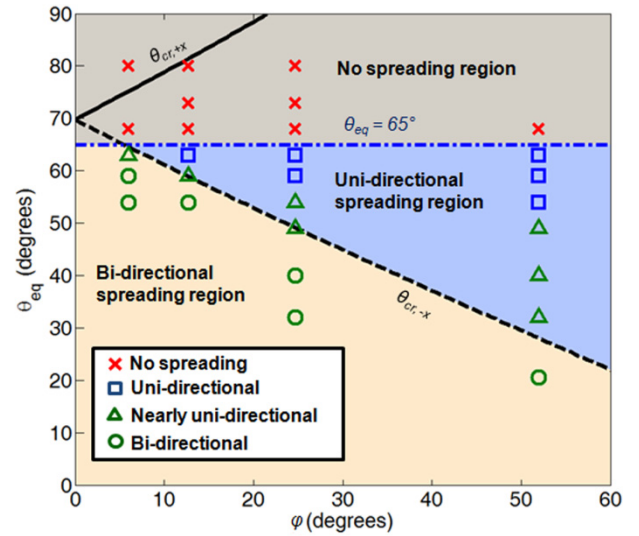


Figure 5: Experimental results and the theoretical curves predicting uni-directional liquid spreading. The squares ( $\square$ ), circles ( $\circ$ ), triangles ( $\Delta$ ), and crosses ( $\times$ ) show experimental results of uni-directional, bi-directional, nearly uni-directional, and no liquid propagation, respectively. The theoretical curves based on the proposed model are shown for  $\theta_{eq} = \theta_{cr}$  with varying deflection angles,  $\phi$ , for  $H/l = 2.87$ . The center region (blue) bound by  $\theta_{cr,-x}$  and  $\theta_{eq} = 65^\circ$  represents the parameter space that leads to uni-directional liquid spreading.

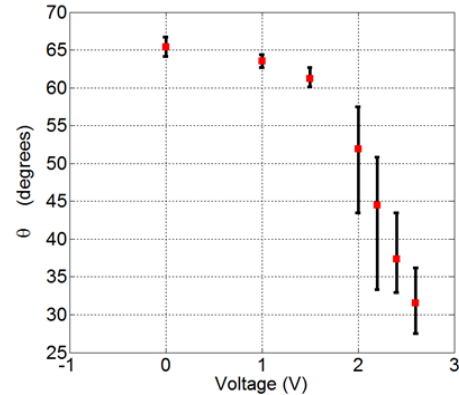


Figure 6: Relationship between the contact angles of the droplet,  $\theta$ , with varying applied voltage,  $V$ .

Despite the simplifications in the proposed model, the experiments and model show excellent agreement. The proposed 2-D model can well predict spreading behaviors because the liquid equilibrates along the Y-axis faster than along the X-axis thereby causing liquid propagation primarily along the X-axis for these fabricated geometries.

### CONCLUSION

Asymmetric nanostructured surfaces were fabricated that can achieve uni-directional liquid spreading. With electrowetting, various spreading behaviors on the nanostructured surfaces have been demonstrated. A combined study of experiments and modeling shows the effect of nanopillar geometry and surface energy on spreading behavior. The study provides design guidelines to tune the droplet behavior from uni-directional to

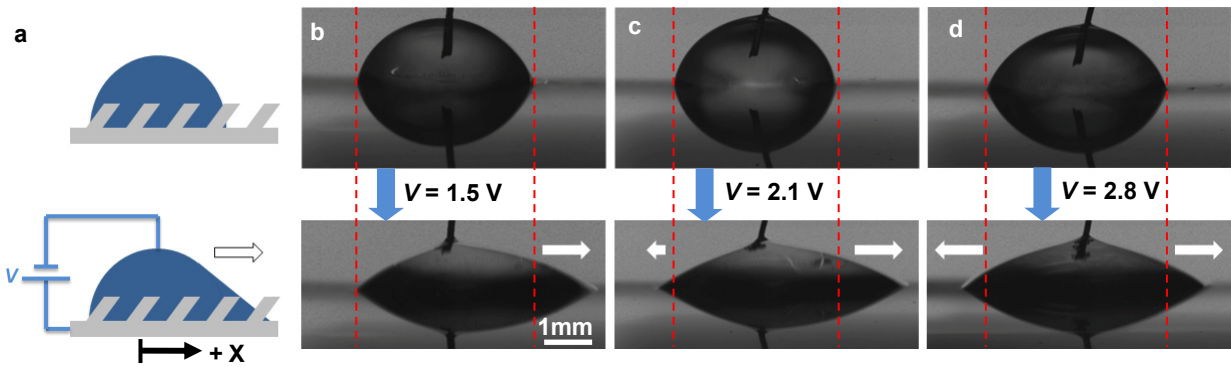


Figure 7: Manipulation of spreading behavior with water droplets on asymmetric nanostructured surfaces by electrowetting. **a)** Schematic shows experimental setup where an initially static symmetric droplet spreads only to the right (+X direction) with an applied potential  $V$ , which represents results shown in **b)**. **b)** With  $V=1.5$  V, the droplet spreads uni-directionally (in +X). **c)** With  $V=2.1$  V, the droplet spreads bi-directionally (in +X and -X), but asymmetrically where the rate is at least three times faster in +X than in -X. **d)** With  $V=2.8$  V, the droplet spreads bi-directionally, but the rates are comparable in +X and -X. The red dotted lines highlight the initial positions of the droplets on both sides, and the white arrows highlight the spreading rates and directions.

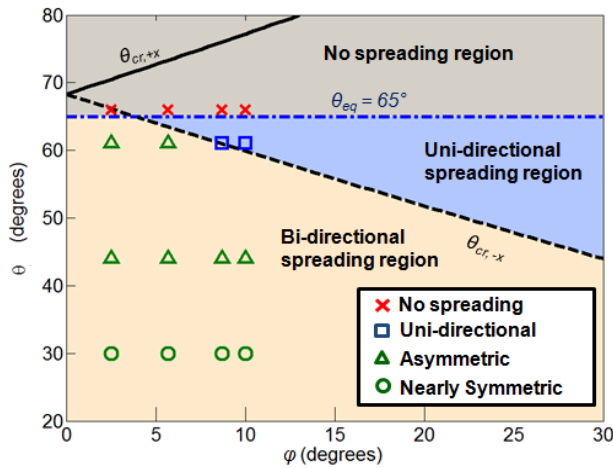


Figure 8: Experimental results overlaid with model predictions for different deflection angles,  $\phi$ , for  $H/l = 2.57$ , and contact angles,  $\theta$ , obtained from the applied voltages,  $V$ . The crosses ( $\times$ ), squares ( $\square$ ), triangles ( $\triangle$ ), and circles ( $\circ$ ) show experimental results of no spreading, uni-directional, bi-directional asymmetric, and nearly bi-directional symmetric liquid spreading, respectively.

bi-directional asymmetric or symmetric spreading using both nanostructure design and applied electric fields. These results suggest exciting opportunities to achieve real-time control of wetting behavior.

## ACKNOWLEDGEMENT

The authors gratefully acknowledge funding support from the National Science Foundation (under Award EEC-0824328), the DARPA Young Faculty Award, and the Northrop Grumman New Faculty Innovation Grant. The authors would also like to acknowledge the Intel Higher Education Grant for a generous computer donation, and the MIT Microsystems Technology Lab.

## REFERENCES

- [1] D Quéré, “Non-sticking Drops”, Rep. Prog. Phys., 68, 2495–2532 (2005).
- [2] T. N. Krupenkin, J. A. Taylor, T. M. Schneider, and S. Yang, “From Rolling Ball to Complete Wetting: The Dynamic

- Tuning of Liquids on Nanostructured Surfaces” Langmuir, 20, 3824-3827 (2004).
- [3] C. W. Extrand, S. I. Moon, P. Hall, and D. Schmidt, “Superwetting of Structured Surfaces”, Langmuir, 23, 8882-8890 (2007).
- [4] R. Xiao, K.-H. Chu, and E. N. Wang, “Multilayer Liquid Spreading on Superhydrophilic Nanostructured Surfaces”, Appl. Phys. Lett., 94, 193104 (2009).
- [5] L. Courbin, E. Denieul, E. Dressaire, M. Roper, A. Ajdari, and H. A. Stone “Imbibition by polygonal spreading on microdecorated surfaces”, Nature Mater., 6, 661-664 (2007).
- [6] J. Y. Chung, J. P. Youngblood, and C. M. Stafford, “Anisotropic Wetting on Tunable Micro-wrinkled Surfaces”, Soft Matter, 3, 1163-1169 (2007).
- [7] J. Drelich, J. L. Wilbur, J. D. Miller, and G. M. Whitesides, “Contact Angles for Liquid Drops at a Model Heterogeneous Surface Consisting of Alternating and Parallel Hydrophobic Hydrophilic Strips”, Langmuir, 12, 1913-1922 (1996).
- [8] K.-H. Chu, R. Xiao, and E. N. Wang, “Uni-directional liquid spreading on asymmetric nanostructured surfaces”, Nature Mater., accepted (2010)
- [9] S.H. Baxamusa, S.G. Im, and K.K. Gleason, “Initiated and oxidative chemical vapor deposition: a scalable method for conformal and functional polymer films on real substrates” PCCP, 11, 5227-5240 (2009).
- [10] M.E. Alf, A. Asatekin, M.C. Barr, S.H. Baxamusa, H. Chelawat, G. Ozaydin-Ince, C.D. Petruczok, R. Sreenivasan, W.E. Tenhaeff, N.J. Trujillo, S. Vaddiraju, J. Xu, and K.K. Gleason. “Chemical Vapor Deposition (CVD) of conformal, functional, and responsive polymer films”, Adv. Mater., 21, 1-35 (2009).
- [11] J. Bico, C. Tordeux, and D. Quéré, “Rough Wetting”, Europhys. Lett., 55, 214-220 (1999).
- [12] E. N. Wang, M.A. Bucaro, J.A. Taylor, P. Kolodner, J. Aizenberg, and T. Krupenkin, “Droplet mixing using electrically tunable superhydrophobic nanostructured surfaces”, Microfluid Nanofluid, 7, 137–140 (2009).
- [13] F. Mugele, and J.-C. Baret, “Electrowetting: from basic to applications”, J. Phys., 17, R705-R774 (2005).

## CONTACT

\*K.-H. Chu, tel: +1-617-253-2198; khchu@mit.edu



# LORENTZ FORCE MEMS MAGNETOMETER

M.J. Thompson and D.A. Horsley\*

Mechanical and Aerospace Engineering, University of California, Davis, California, USA

## ABSTRACT

This paper describes a MEMS Lorentz-force navigation magnetometer whose fabrication is fully compatible with existing foundry processes used to manufacture MEMS inertial sensors. The magnetometer is shown to have a Brownian-noise limit and corresponding angular resolution of 3.4 nT/rt-Hz, 0.03 degrees/rt-Hz when operated at 25 mTorr and 62 nT/rt-Hz, 0.56 degrees/rt-Hz when operated at ambient pressure. To achieve Brownian-limited performance at atmospheric pressure parametric amplification was performed which amplifies the Lorentz force 40% more than the Brownian noise force and increases the field sensitivity of the device up to 82.5-fold.

## INTRODUCTION

### Compass Magnetometers

MEMS Lorentz force magnetometers are advantageous over other magnetometers because they are free from hysteresis, require no specialized materials and can be monolithically integrated with other MEMS inertial sensors. MEMS Z-axis Lorentz force magnetometers have achieved resolutions of 200 nT/ $\sqrt{\text{Hz}}$  using foundry fabrication [1]. The device presented here, shown in Fig. 1, was earlier shown when operated at atmospheric pressure, to have an electronic noise-limited resolution of 1  $\mu\text{T}/\sqrt{\text{Hz}}$  with a natural frequency ( $f_n$ ) of 8468 Hz and a quality factor ( $Q$ ) of 48.8 [2]. To improve the performance of this device parametric amplification is utilized to increase the field sensitivity and secondly the device is operated in a 25 mTorr vacuum, so that the device becomes Brownian noise limited.

### Parametric Amplification

Parametric amplification increases the force to displacement transduction of the sensor by modulating the mechanical spring constant at twice the natural frequency. Previous work on parametrically amplified Lorentz force magnetometers showed how the Lorentz and Brownian noise forces are both amplified and the amplification acts like increasing the quality factor ( $Q$ ) of the MEMS resonator [3].

## DESIGN AND OPERATION

### Fabrication

The device, shown in Fig. 1, was fabricated using the MEMSCAP SOIMUMPS foundry process with a 10  $\mu\text{m}$  device layer. The device is a resonant force sensor, which detects the displacement resulting from Lorentz force on current-carrying flexures. The current is modulated at the device's natural frequency ( $f_n$ ) to maximize the force sensitivity, given by  $Q/k$ , where  $k$  is the mechanical stiffness [2]. Differential capacitors convert the motion of the device to an electrical output through JFET buffers.

### Lorentz force

The beams on the folded flexure springs are the Lorentz force actuators [2,3]. A Lorentz force is applied to the shuttle when the current-carrying beams of the flexures are in a magnetic field. Folded flexure beams are advantageous because they prevent stress caused from constrained expansion due to ohmic heating [2].

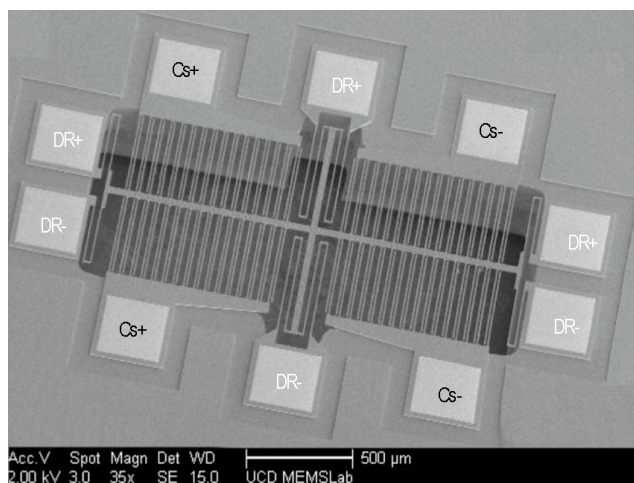


Figure 1. SEM of the magnetometer with three folded flexures used as Lorentz force actuators ( $Dr+$ ,  $Dr-$ ) and differential capacitive displacement detection ( $Cs+$ ,  $Cs-$ ).

### Parametric Design

Parametric amplification requires the mechanical spring constant to vary at twice the natural frequency and be phase locked with the excitation or drive input. In MEMS resonators, the non-linear parallel plate capacitance is equivalent to a voltage controlled, negative spring stiffness [3]. To achieve parametric amplification, an AC voltage at twice the natural frequency ( $2f_n$ ) is applied across the capacitors. For this device, the AC voltage ( $f_c$ ) is applied to the MEMS shuttle and DC voltage ( $V_b$ ) is applied to the other side of the capacitor through the JFET bias resistor.

### Electrical Circuit

To create the current for the Lorentz force actuators, a voltage modulated at the natural frequency ( $f_n$ ) is applied to the top of the flexure ( $Dr+$ ) and the inverse is applied to the bottom of the flexure ( $Dr-$ ). This creates the required current but also creates a zero voltage node where the flexures join the shuttle. To control the voltage on the shuttle a signal is applied equally to the top and bottom of the flexure ( $f_c$ ). The motion is detected using displacement dependant differential parallel plate capacitors ( $Cs+$ ,  $Cs-$ ). The output from the detection capacitors are buffered with high input impedance JFET's.

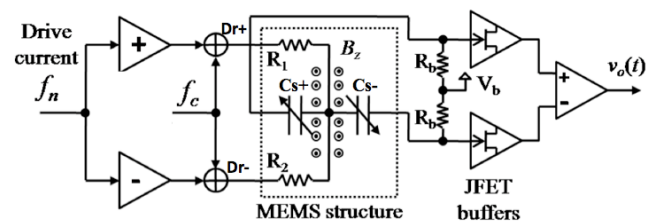


Figure 2. Electrical circuit for sensor drive and electronic detection.

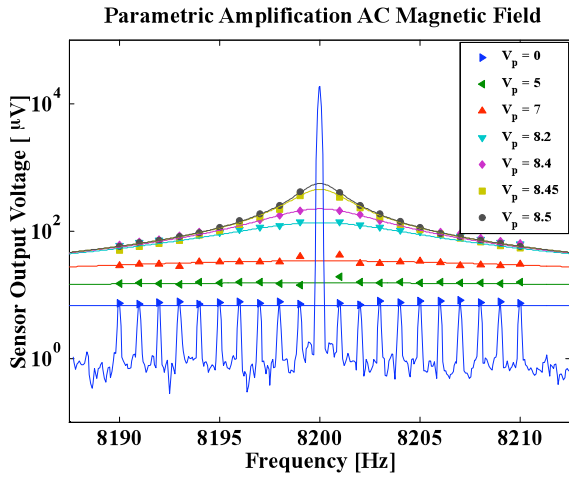


Figure 3. Sensor response at various pump voltages to 40  $\mu\text{T}$  magnetic field signals. The tone at 8.2 kHz is capacitive feedthrough. With  $V_p = 0$ , the sensitivity is constant over the 30 Hz measurement span, whereas at  $V_p = 8.5\text{V}$  the 3 dB bandwidth is  $\sim 1\text{ Hz}$ .

## EXPERIMENTS

Unless otherwise stated, the voltage bias is fixed at 18.6 V and the flexure current is 2.67 mA. The device has  $f_n = 8200\text{Hz}$  and  $Q = 48.8$  while operated in atmospheric conditions. The device was placed on top of an electromagnet. The electromagnet applied 10 test signals from 1 Hz to 10 Hz in 1 Hz increments with a 40  $\mu\text{T}$  amplitude.

### Parametric Amplification of the Lorentz Force

The 10 test signals appear as sidebands around the drive frequency (8.2 kHz) of the device as shown in Fig. 3. The full spectrum is shown for no parametric excitation. Capacitive feedthrough of the excitation signal at  $f_n$  (8.2 kHz) corrupts the measurement at DC field but has no effect on the AC test signals. As the parametric pump is increased the figure tracks the response of the 10 test signals. To measure the increase in transduction, a second-order transfer function was fit to each frequency response by choosing an effective  $Q_{\text{eff}}$  [3]. The increase in  $Q$  is shown in Fig. 4 as a function of the applied parametric voltage and agrees well with the analytical model. At the highest pump voltage ( $V_p = 8.5\text{ V}$ ), the sensitivity is increased 82.5-fold, conferring an effective  $Q_{\text{eff}}$  of 4026. As parametric amplification is increased the bandwidth of the device decreases with the original bandwidth of 85 Hz shrinking to 1 Hz for a parametric gain of 82.5.

### Parametric Amplification of Brownian and Lorentz Forces

The parametric voltage was set to give a parametric gain of 20 shown in Fig. 5. The full spectrum and a second-order data fit applied to the 10 signal peaks are shown. To measure the Brownian noise response the drive signal was turned off, so that the device was only excited by the parametric pump signal. The spectrum of the sensor output was averaged and a second-order fit applied. The fit obtained from the Lorentz force test tones was 40% greater (20) than the fit obtained from the Brownian noise force (14) for the same parametric pump excitation. This can be explained by a phenomenon called noise squeezing [4]. Noise squeezing occurs because parametric amplification is phase sensitive, with the in-phase signal being amplified and the in-quadrature signal being attenuated. The Lorentz current drive is phase locked with the parametric signal to achieve maximum

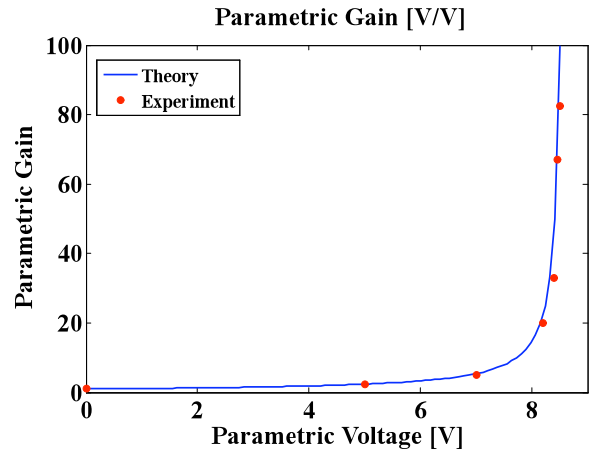


Figure 4. Parametric gain versus pump voltage amplitude.

amplification. However, the Brownian noise is white noise and spans over all phases; thus, the in-phase component is amplified and the in-quadrature component is attenuated. This fact leads to a reduction in the average noise amplification.

### Noise Squeezing

The amplitude and phase time history of the sensor output is recorded in Fig. 5 with and without parametric amplification. When the device is not being parametrically amplified the in-phase and in-quadrature components of the noise are equal in amplitude and Johnson noise from the bias resistor  $R_b$  dominates the response, shown in Fig. 2. When the device is parametrically excited, the output noise distribution becomes elliptical. The elliptical shape is caused by the phase sensitive amplification, noise squeezing, of the Brownian noise force. The in-phase component of the Brownian noise force is amplified while the out-of-phase component is attenuated. However, the attenuation of the out-of-phase component is not measured here because the Johnson noise dominates. Fig. 5 demonstrates how parametric amplification increases the force to displacement transduction so that the sensor can measure the Brownian noise force and becomes Brownian noise limited.

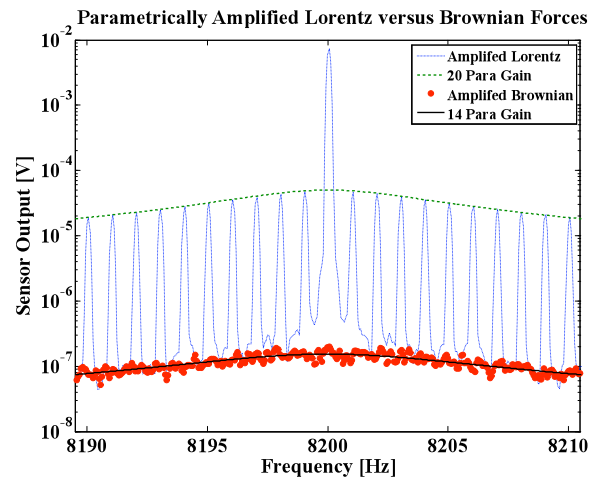


Figure 5. The spectrum and second-order fit for the device with the pump signal fixed at 8.3 V with the drive signal on, to measure the Lorentz force response, and with the drive off, to measure the Brownian noise response.

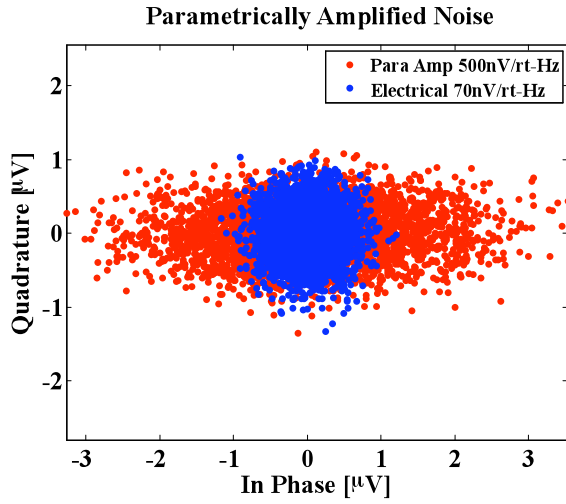


Figure 6. Time history of the amplitude and phase of the sensor output for no excitation and for an 8.4 V parametric excitation.

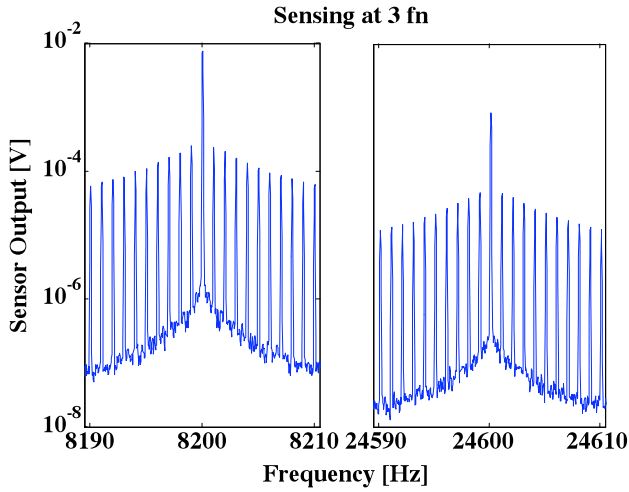


Figure 7. Sensor output at  $f_n$  (8.2 kHz) and at  $3f_n$  (24.6 kHz).

### Sensing at $3f_n$

The detection of DC magnetic fields is corrupted by the drive to sense capacitive feedthrough, which results in the large peak at 8.2 kHz in Fig.'s 3, 5 and 7. One method to bypass feedthrough is to drive and sense at different frequencies. The parametric pump signal applied to the MEMS shuttle causes the sense motion signal at  $f_n$  to be mixed with the parametric signal at  $2f_n$ . This mixing creates two extra signals, one at  $f_n$  and one at  $3f_n$ . The signal at  $f_n$  is 90 degrees phase shifted from the sense signal at  $f_n$  and adds 2.6% to the final amplitude and a 12 degree phase shift. The response of the magnetometer is shown at  $f_n$  (8.2 kHz) and at  $3f_n$  (24.6 kHz) in Fig. 7. The peak at 8.2 kHz is 50% larger than the peak at 24.6 kHz indicating that the peak at 8.2 kHz is dominated by capacitive feedthrough. The experiment does not introduce any DC magnetic field with the electromagnet but there is an ambient magnetic field of 60  $\mu\text{T}$ . The peak at 24.6 kHz corresponds to an equivalent DC magnetic field of 2.4 mT – the source of this peak is discussed below.

### DC Transfer Characteristic

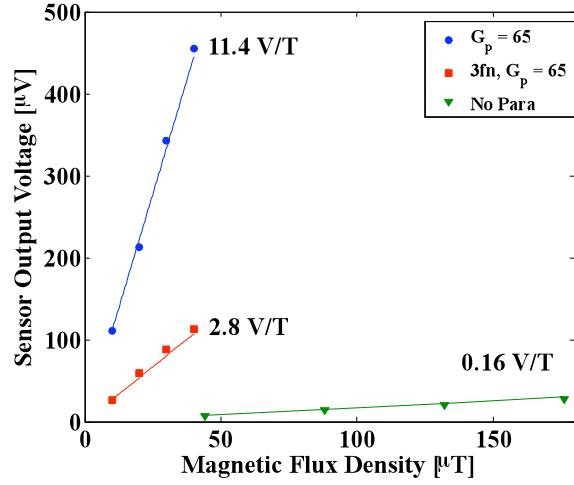


Figure 8. Transfer characteristic measured with and without parametric amplification demonstrating linear response.

### Linearity

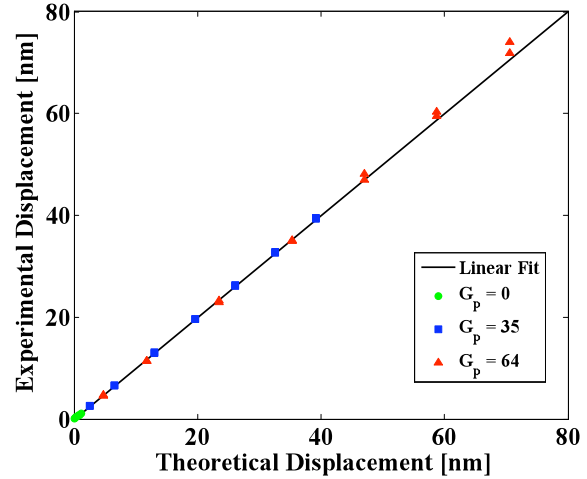


Figure 9. Linear theoretical versus experimental displacement for a 1 Hz input signal.

### Sensitivity

The magnetic field transfer characteristic of the device is shown in Fig 8. The device is tested without parametric amplification, with 65 fold parametric amplification sensing at  $f_n$  and 65 fold parametric amplification at  $3f_n$ . If the device is not parametrically amplified the field sensitivity is 0.16 V/T. The field sensitivity of the device for a parametric gain of 65 is 11.4 V/T and 2.8 V/T when measured at  $f_n$  and  $3f_n$ , respectively.

### Sensor Linearity

The dominant non-linearity in the device comes from the motion detection capacitors. This non-linearity is exploited to achieve parametric amplification but it also limits the sensor's output linearity. Since the onset of nonlinearity is determined by displacement, the maximum field input for linear response depends on the parametric gain. Fig. 9 shows the theoretical versus experimental displacement of the sensor for different parametric gains. For a maximum displacement of 46 nm and a parametric gain of 65-fold the maximum linear field sensitivity is 68  $\mu\text{T}$ .

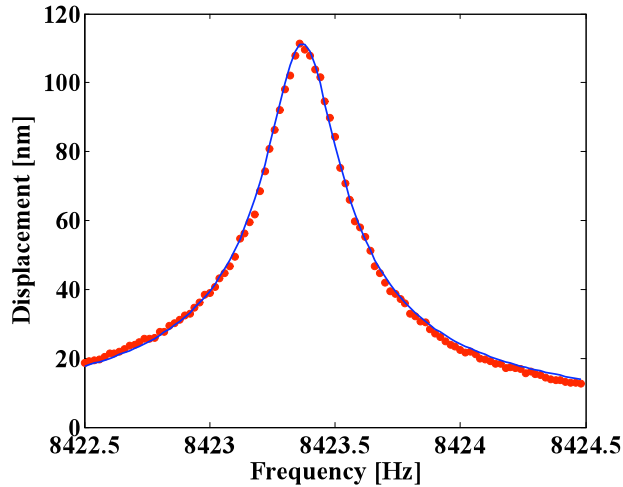


Figure 10. Magnetometer frequency response in a vacuum of 25 mTorr, a 97 mTesla DC magnetic field, drive current of 500 nA and a capacitive bias of 2.5 V.

## EXPERIMENTS IN A VACUUM

An alternative method to increase the magnetometer's  $Q$  is to operate the device in a 25 mTorr vacuum. Increasing  $Q$  has a two-fold benefit of lowering the Brownian noise floor and increasing the sensitivity. Most resonant MEMS devices are operated in a vacuum for the aforementioned reason.

### Frequency Response

The sensor's frequency response is shown in Fig. 10 when measured in a DC magnetic field of 97 mT by sweeping the frequency of the flexure current. The device was driven with a 500 nA current and the capacitors were biased with 2.5 V. The device has a natural frequency of 8423.4 Hz and a quality factor of 31,000. If this device was operated with a 2.67 mA current then the device would have a Brownian noise limit of 3.4 nT/ $\sqrt{\text{Hz}}$ .

### Brownian Noise measurement

The Brownian noise spectrum is measured with a 5 V bias applied across the MEMS structure and zero flexure current, shown in Fig. 6, with a 14 pm/ $\sqrt{\text{Hz}}$  equivalent electronic noise floor and a Brownian noise peak of 26 pm/ $\sqrt{\text{Hz}}$ . The Brownian noise peak is equivalent to a resolution of 3.4 nT/ $\sqrt{\text{Hz}}$  when operated with a 2.67 mA flexure current which, in comparison with operation at atmospheric pressure, is a 25-fold improvement over the parametrically amplified (62 nT/ $\sqrt{\text{Hz}}$ ) experiment and 295-fold improvement over the electronically limited (1  $\mu\text{T}/\sqrt{\text{Hz}}$ ) experiment.

## DISCUSSION

The peak at  $3f_n$  (24.6 kHz) shown in Fig. 5 is not due to capacitive feedthrough or DC magnetic field. It is believed that a small residual AC voltage is present on the shuttle due to unbalanced flexure resistances resulting from small fabrication variations. The force created from the electrostatic actuation between the shuttle and the sense capacitors would also be parametrically amplified, corrupting the DC field measurement. To minimize this electrostatic force each flexure requires separate voltage adjustment to account for the mismatched resistances.

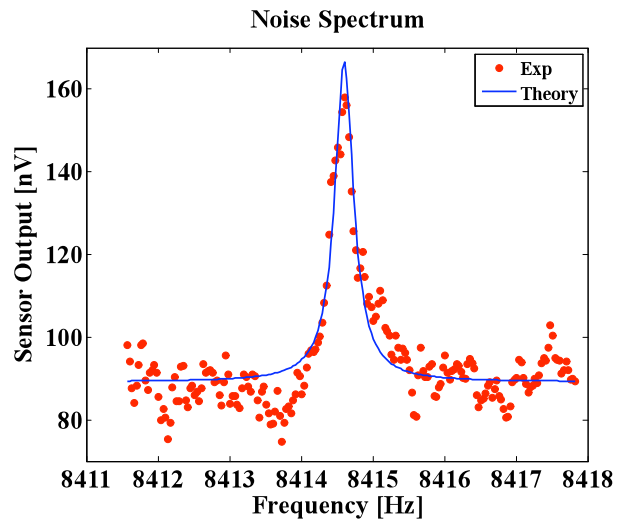


Figure 11. Noise measurement in a 25 mTorr vacuum with a 5 V capacitive bias.

## CONCLUSION

Through this paper we have studied two methods for improving the 1  $\mu\text{T}/\sqrt{\text{Hz}}$  resolution of a Lorentz force magnetometer.

Operating the device at atmospheric pressure, parametric amplification was performed which improves the performance in three ways. First, the force to displacement sensitivity was increased up to 85 fold. Secondly, the force sensitivity of the MEMS structure was increased until the sensor became Brownian noise limited, rather than electronic noise limited. Thirdly, the Lorentz force sensitivity was increased 40% more than the Brownian force sensitivity due to noise squeezing. For a drive current of 2.67 mA and a minimum parametric gain of 10-fold the sensor has a noise resolution of 62 nT/ $\sqrt{\text{Hz}}$ .

Alternatively the device was operated in a 25 mTorr vacuum where the device has a resolution of 3.4 nT/ $\sqrt{\text{Hz}}$  for a 2.67 mA drive current.

## ACKNOWLEDGEMENT

This work was supported by NSF CAREER award ARRA CMMI-0846379.

## REFERENCES

- [1] H. Emmerich and M. Schofthaler, "Magnetic field measurements with a novel surface micromachined magnetic-field sensor," *IEEE Trans. Electron Dev.*, 47(5), pp. 972-977, (2000).
- [2] M.J. Thompson and D.A. Horsley, "Resonant MEMS magnetometer with capacitive read-out," *Proc. IEEE Sensors 2009*, Christchurch, NZ, 992, (2009).
- [3] M.J. Thompson and D.A. Horsley, "Parametrically-amplified MEMS magnetometer," *Proc. 15th Int. Conf. Solid-State Sensors Actuators & Microsystems (Transducers 2009)*, Denver, Colorado, 1194, (2009).
- [4] D. Rugar and P. Grutter, "Mechanical parametric amplification and thermomechanical noise squeezing," *Phys. Rev. Lett.*, 67(6), pp. 699-672, (1991).

## CONTACT

\*D.A. Horsley tel +1 530 752-1778; dahorsley@ucdavis.edu

# AN INTRAOCULAR PRESSURE SENSOR BASED ON A GLASS REFLOW PROCESS

R. M. Haque and K. D. Wise

Engineering Research Center for Wireless Integrated MicroSystems (WIMS)  
The University of Michigan, Ann Arbor, MI 48109-2122 USA

## ABSTRACT

This paper presents an intraocular pressure sensor fabricated using a new process that reflows glass into DRIE-etched silicon cavities to form three-dimensional microstructures. The capacitive pressure sensor is formed using a 4 $\mu$ m thick boron etch-stopped silicon diaphragm having dimensions of 0.85mm x 1.65mm. The sensor operates in touch-mode with a linear response and sensitivity of 26fF/mmHg, resolving better than 1mmHg over a 650-850mmHg dynamic range. Vertical silicon feedthroughs in the glass provide electrical access to the sensor. This pressure sensor is part of an intraocular microsystem being developed for monitoring the eye pressure of patients diagnosed with glaucoma.

## INTRODUCTION

Glaucoma is the second-leading cause of blindness, affecting over 68 million people worldwide. Intraocular pressure is important in detecting and treating this disease, but its measurement involves equipment typically found in a hospital or doctor's office, limiting the frequency of measurements and complicating treatment. A number of implantable intraocular pressure sensors have been reported recently [1-3], but many of the reported devices have been excessively invasive or may be large enough to partially occlude the field of view in low-light situations. A compact, highly-integrated intraocular microsystem (Fig. 1) is being developed that will record pressure every 15 minutes, transmitting the stored data to the outside world once a day on demand. The microsystem will contain an ultra-low-power microcontroller [4], power source, capacitive pressure sensor, and wireless interface, all housed in a parylene-coated glass package. The use of a glass substrate ensures sensor hermeticity, enhances antenna performance, and allows photovoltaic energy scavenging. Vertical feedthroughs in the glass provide electrical connections to the pressure sensor and to the antenna, which are mounted on the external surfaces of the intraocular package.

The pressure sensor component of the full microsystem is described in this work, with a specific focus on a newly developed fabrication technique. Boron doping defines the diaphragm thickness, while vertical interconnects made of highly-doped silicon provide electrical connections to the plates of the capacitive sensor. The pressure sensor exhibits a linear response when operating in touch-mode, where the sensor is constantly in contact with the bottom plate. Changes in pressure change the contact area rather than gap, resulting in the linear response. While stiction effects are present, they do not significantly degrade the required resolution of the device. The vacuum-referenced sensor operates with a dynamic range of 650mmHg to 850mmHg to accommodate changes in ambient pressure, such as pressurized cabins of an airplane or travel to higher elevations. The external readout module will record atmospheric pressure and compensate for these changes when the intraocular pressure is transferred from the implanted microsystem. Intraocular pressure typically varies between 8 and 50mmHg, with the onset of glaucoma defined as a pressure value above 21mmHg relative to ambient. A resolution of 1mmHg is used for standard tonometric methods, such as Goldmann applanation, in the doctor's office.

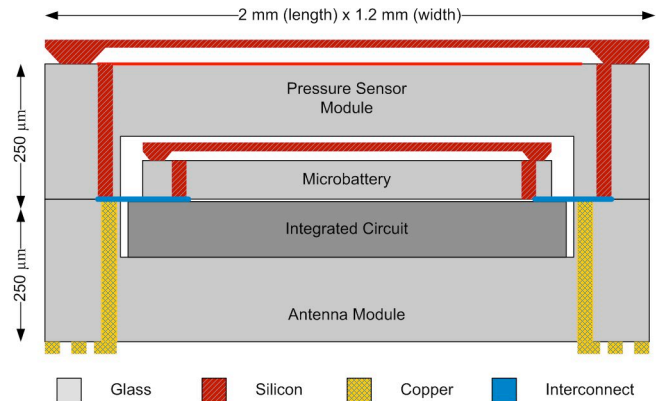


Fig. 1: A complete intraocular microsystem, demonstrating vertical interconnects and glass packaging of the components.

Accessing the internal plate of hermetically-sealed capacitive pressure sensors is an important issue in designing these devices, and in the past, such sensors were implemented using lateral feedthroughs employing polysilicon or eutectic metal access leads [5-6]. The device used in this work uses vertical connections through the glass to simplify electrical access to the capacitor and keep the leads totally within the sealed implantable package. This also helps minimize the overall size of the device.

## FABRICATION PROCESS

### Glass Reflow

Since glass is difficult to micromachine with precision, a new wafer-level glass-in-silicon process (Fig. 2) has been developed. In this process, a highly-doped silicon wafer (p-type, <0.01 $\Omega$ -cm) is etched 250 $\mu$ m deep using DRIE, forming a mold. After anodically bonding in vacuum (Suss SB6e) to a standard 500 $\mu$ m-thick borosilicate glass wafer (Plan Optik), the silicon-glass sandwich is heated above the glass transition temperature, causing the glass to reflow into the mold as shown in Fig. 2, step 2. Optimization of the reflow temperature, reflow time, and mask design rules ensures appropriate glass filling and flow. For this process, heating above 750 $^{\circ}$ C for a period of 8 hours was sufficient to achieve complete glass filling, as shown in Fig. 3.

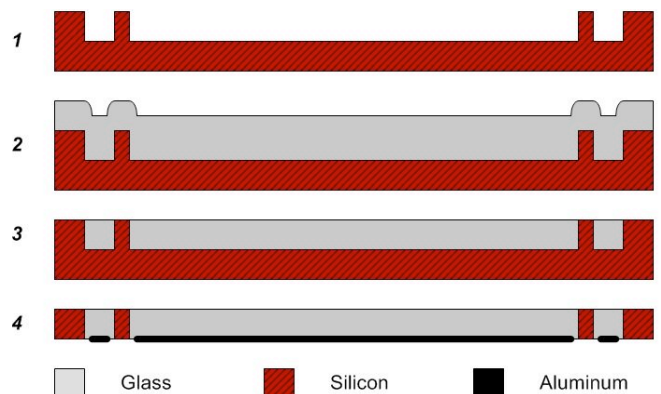


Fig. 2: Process flow for forming glass-in-silicon wafers with integrated feedthroughs.

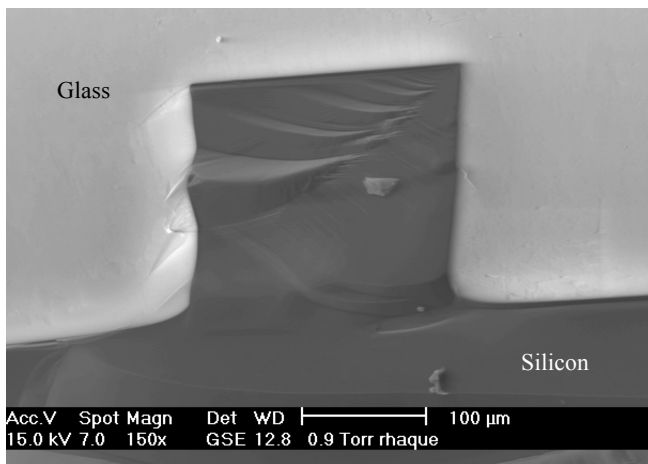


Fig. 3: Cross-section of the glass reflow process showing complete glass filling of a cavity in the silicon. The lighter colored region is glass, while the lower, darker region, is silicon.

The planarization and polishing shown in Fig. 2, step 3, was accomplished with an IPEC chemical mechanical polishing (CMP) tool with double platens. One platen is dedicated to conventional polishing with slurry while the other platen was retrofitted with a special diamond-embedded pad (Trizact, 3M). Lapping on the diamond pad planarizes the glass until it is flush with the surface of the silicon. The surface can then be polished on the other pad while flowing slurry specifically designed for oxides. The silicon is simultaneously polished in this step as well, although at a slightly slower rate than the glass. For later process steps such as anodic bonding, this polishing step is absolutely critical. Wafers that have some surface roughness or high spots will not adequately bond, and any roughness can serve as a source of potential leaks.

In the final processing step, the silicon is lapped from the back side in a similar fashion to the process used on the front side until the glass regions are exposed. A second CMP step can be used to polish the back side of the wafers if double-sided polished glass-in-silicon wafers are desired. Mounting the wafer on a carrier is essential for this thinning step.

Although similar processes have been reported [7-8], this is the first time such a glass-in-silicon process is thought to have been demonstrated at the wafer level. The completed glass-in-silicon wafer can be further processed using conventional fabrication techniques. Although the 100mm wafers are only 250 $\mu$ m thick after thinning, they are robust enough to survive conventional spin-rinse driers and process steps such as liftoff. Fig. 4 shows a completed 100mm glass-in-silicon wafer.

### Pressure Sensor Design and Fabrication

The capacitive pressure sensor is fabricated using the dissolved-wafer process as shown in Fig. 5. The sensor is designed with a nominal 15 $\mu$ m zero-pressure gap, defined using a KOH (45% at 85 $^{\circ}$ C) recess etch into a standard p-type silicon wafer (Fig. 5, step 1). Two boron-doping steps are then used to produce etch-stops that set the device dimensions. A deep boron diffusion sets the eventual rim thickness at 15 $\mu$ m. This is followed by a shallow boron diffusion that sets the diaphragm thickness at 4 $\mu$ m. The lateral dimensions of the diaphragm are lithographically set at 0.85mm x 1.65mm. A 150nm-thick silicon dioxide layer is thermally grown over the surface of the diaphragm to protect against shorts when the plates touch. As is well known, the pressure sensitivity of capacitive pressure sensors is a strong function of the gap spacing, diaphragm thickness, lateral

dimensions, and internal diaphragm stress [9]. The lateral dimensions are controlled to better than 1 $\mu$ m by lithography, while the diaphragm thickness is set by the etch-stop to within about  $\pm 0.2\mu$ m. Diaphragm stress is also highly reproducible with the use of a thermal oxide adding compressive stress to the diaphragm. A modified oxide-nitride stack or an oxynitride film could also be used to set the stress as desired. The gap is more widely variable, however, and as in most pressure sensors, individual calibration is required to meet the demands of the intraocular application. For this system, this will be accomplished in the embedded processor of the intraocular microsystem.

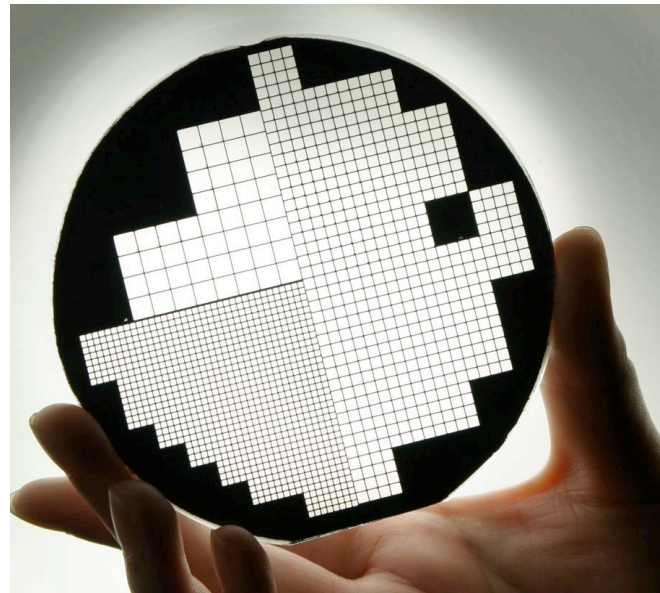


Fig. 4: A completed glass-in-silicon 100mm-diameter wafer.

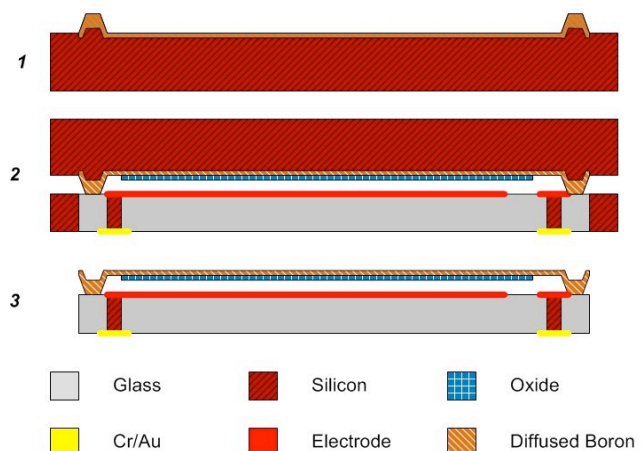


Fig. 5: Dissolved-wafer process flow for the intraocular pressure sensor. Step 2 shows the bonding of a silicon diaphragm wafer with a glass-in-silicon wafer.

The glass-in-silicon wafer serves as the substrate to which the diaphragm rim is bonded. A thin stack of titanium, platinum, and gold is patterned using liftoff to serve as the electrical contact within the pressure sensor cavity. Each vertical silicon feedthrough is electrically connected to the two different capacitive plates in this single masking step. One forms the bottom electrode on the glass surface, while the other provides a connection to the highly-doped boron diaphragm, forming the upper electrode.

With the diffusions and the diaphragm oxide in place, the diaphragm wafer and the glass-in-silicon wafer are aligned and anodically bonded (Suss MA-6/BA-6 and SB6e) together using a 1.5 $\mu\text{m}$ -thick aluminum sacrificial spacer (on the glass-in-silicon wafer, as shown in Fig. 2, step 4) to distribute the electrical field and prevent unintended shorts. After bonding, a chromium/gold stack (Fig. 5, step 2) is deposited and defined using liftoff to make ohmic contacts to the feedthroughs and protect them during subsequent processing. The wafers are then placed in an ethylenediamine pyrocatechol (EDP) etch to remove the lightly-doped silicon and perform die separation (Fig. 5, step 3). The overall die size is approximately 1.2mm x 2mm. The glass is 250 $\mu\text{m}$  thick and provides appropriate interconnects to the sensing plates for the capacitor. Fig. 6 shows several completed intraocular pressure sensors on a U.S. penny, while Fig. 7 shows an SEM profile view of one of the devices.



Fig. 6: Completed intraocular pressure sensors on a US penny, showing the electrical contacts on the back of the devices and the vacuum-sealed silicon diaphragm on the front. The diaphragm size is 0.85mm x 1.65mm.

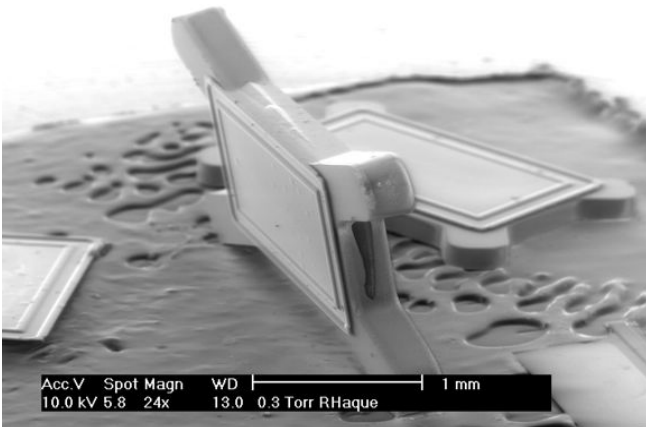


Fig. 7: An SEM view showing the profile of a released pressure sensor. The silicon sensor rim is 15 $\mu\text{m}$  thick, and supports a 4 $\mu\text{m}$ -thick diaphragm. The glass is approximately 250 $\mu\text{m}$  thick.

### PRESSURE SENSOR PERFORMANCE

The pressure sensors were designed and simulated using COMSOL to estimate appropriate diaphragm dimensions. Depending on the dimensions chosen, the device can operate in either the typical non-touching (gap-sensitive) mode or in the

touching (area-sensitive) mode. In either case, the glass substrate serves as an overpressure stop. Fig. 8 shows the simulated deflection for diaphragm thicknesses of 4 $\mu\text{m}$  and 5 $\mu\text{m}$ , ignoring any overpressure stop. The large variation in deflection with only a one-micron change in diaphragm thickness is quite clear.

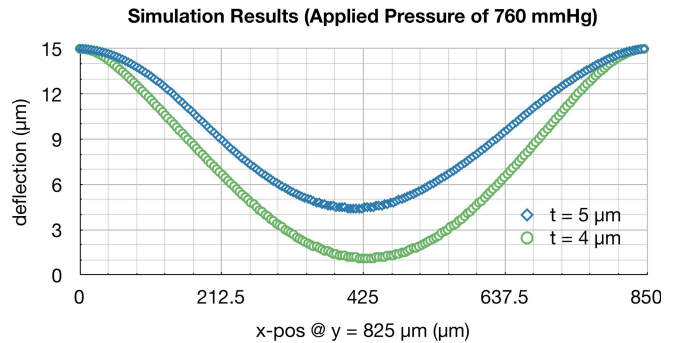


Fig. 8: Simulated deflection of a 0.85mm x 1.65mm diaphragm for two values of diaphragm thickness. No overpressure stop is included.

All capacitance measurements were made using an HP4284A LCR meter operating with a sampling rate of 1MHz. The silicon diaphragm serves as one plate of the capacitance with the electrode on the glass as the other plate. Fig. 9 shows the overall measured capacitance versus pressure characteristic for pressures below an atmosphere. The two regions of operation are clearly visible. Below about 450mmHg the plates do not touch and the response is highly non-linear, characteristic of gap-sensitive sensors. Above this level, the plates touch, and the response becomes linear.

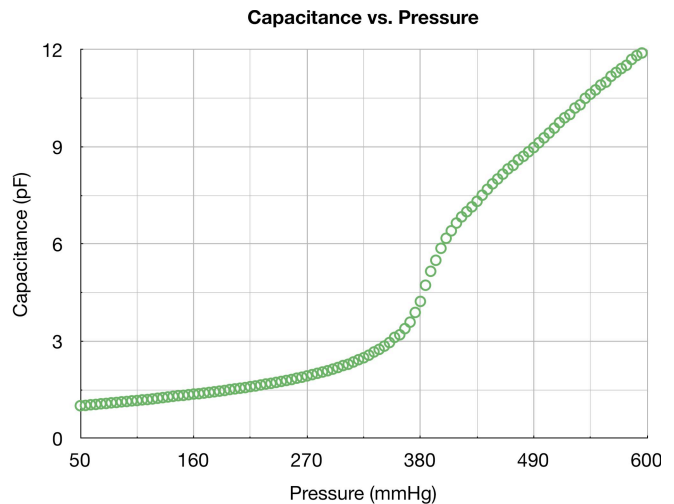


Fig. 9: Measured pressure versus capacitance characteristic of an intraocular pressure sensor, showing touch-mode operation above about 450 mmHg.

The capacitance versus pressure characteristic was next measured in an externally-regulated pressure chamber. In order to evaluate the possible effects of stiction, the applied pressure was swept from 750mmHg down to 550mmHg, then slowly increased to 850mmHg, and then returning again to 750 mmHg. Although some hysteresis can be detected, presumably due to stiction at the interface between the oxide-coated diaphragm and the sensing electrode on the glass, after correction the estimated maximum error due to these effects should fall within the 1mmHg resolution

required in this application. Fig. 10a shows the response of the pressure sensor with a detail view around 750 mmHg shown in the plot of Fig. 10b. The pressure sensitivity is 26fF/mmHg.

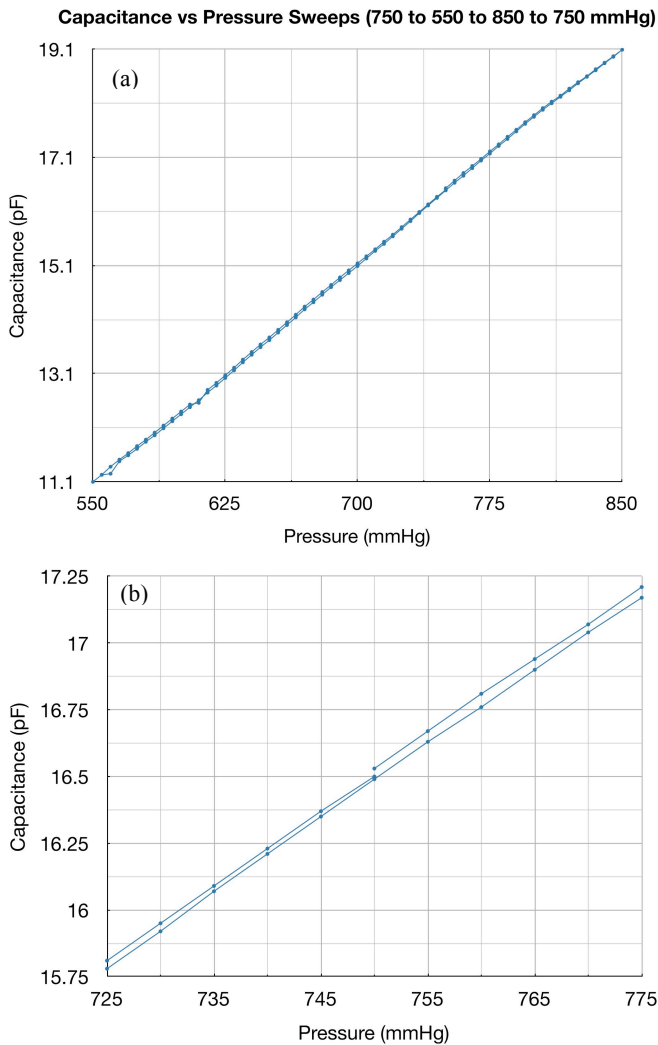


Fig. 10: (a) Measured capacitance versus pressure while cycling pressure from 750 to 550 to 850 and back to 750 mmHg; (b) close-up view around 750 mmHg.

The 100 $\mu$ m-diameter silicon feedthrough resistances were measured to be about 2.2 $\Omega$ , in good agreement with the calculated resistance of approximately 3.2 $\Omega$  for 0.01 $\Omega$ -cm bulk resistivity silicon. Fig. 11 is a photo of a glass-in-silicon wafer used for electrical testing. These wafers have electrical pads on one side of the wafer and metal interconnects in various patterns on the other.

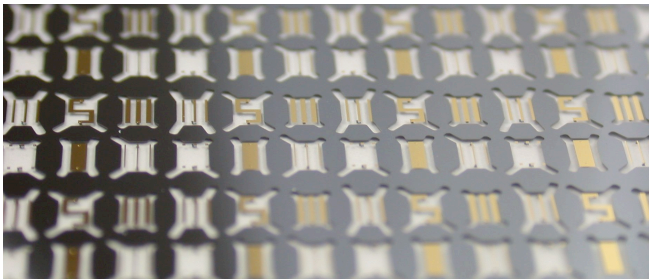


Fig. 11: A photo of die used for electrical testing of feedthroughs.

## CONCLUSION

This paper presents a new process for creating high-aspect-ratio glass microstructures and has demonstrated the process with the design and fabrication of a pressure sensor for an intraocular microsystem. The pressure sensor operates in touch-mode with a sensitivity of 26fF/mmHg and linear response. Hysteretic effects are present, but deemed acceptable for the intraocular application and the expected operation of the microsystem.

The simple and robust glass-in-silicon process may be useful in a wide range of new devices, especially those benefiting from a transparent substrate, vertical feedthroughs, electrical isolation, thermal isolation, or complex die shapes. The process is currently being used for several aspects of the intraocular microsystem, including the pressure sensor, the embedded microbattery, and the antenna.

## ACKNOWLEDGEMENTS

The work described here was supported primarily by the Engineering Research Centers Program of the National Science Foundation under Award Number ECE-9986866 and by a gift from Ms. Polly Anderson.

## REFERENCES

- [1] P-J. Chen, D. C. Rodger, S. Saati, M. S. Humayun, and Y-C Tai, "Microfabricated Implantable Parylene-Based Wireless Passive Intraocular Pressure Sensors," *IEEE J. Microelectromech. Syst.*, 17, pp. 1342-1351, December 2008.
- [2] K. Stangel, S. Kolnsberg, D. Hammerschmidt, B. J. Hosticka, H. K. Trieu, and W. Mokwa, "A Programmable Intraocular CMOS Pressure Sensor System Implant," *IEEE J. Solid-St. Circuits*, 36, pp. 1094-1100, July 2001.
- [3] E. Y. Chow, S. Chakraborty, W. JU. Chappell, and P. P. Irazoqui, "Mixed-Signal Integrated Circuits for Self-Contained Sub-Cubic Millimeter Biomedical Implants," *IEEE Int. Sol-St. Circuits Conf.*, pp. 236-237, February 2010.
- [4] M. Seok, S. Hanson, Y.-S. Lin, Z. Foo, D. Kim, Y. Lee, N. Liu, D. Sylvester, and D. Blaauw, "The Phoenix Processor: A 30pW Platform for Sensor Applications," *IEEE Symp. On VLSI Circuits*, pp. 188-189, 2008.
- [5] A. V. Chavan and K. D. Wise, "Batch-Processed Vacuum-Sealed Capacitive Pressure Sensors," *IEEE Journal of MicroElectroMechanical Systems*, pp. 580-588, December 2001.
- [6] A. DeHennis and K. D. Wise, "An All-Capacitive Sensing Chip for Absolute Pressure, Temperature, and Relative Humidity," *IEEE International Conference on Solid-State Sensors and Actuators (Transducers '03)*, Boston, pp. 1860-1863, June 2003.
- [7] P. Merz, H. J. Quenzer, H. Bernt, B. Wagner and M. Zoberbier, "A Novel Micromachining Technology for Structuring Borosilicate Glass Substrates," *IEEE Int. Solid-State Sensors and Actuators Conf.*, 2003, pp. 258-261.
- [8] C-W. Lin, et al., "Implementation of Silicon-on-Glass MEMS Devices with Embedded Through-Wafer Silicon Vias using the Glass Reflow Process for Wafer-Level Packaging and 3D Chip Integration", *J. Micromech. Microengr.*, vol. 18, 2008.
- [9] S. T. Cho, K. Najafi, and K. D. Wise, "Internal Stress Compensation and Scaling in Ultrasensitive Silicon Pressure Sensors," *IEEE Transactions on Electron Devices*, 39, pp. 836-842, April 1992.

## CONTACT

R. M. Haque: rhaque@umich.edu



# A 15 ATM. PRESSURE SENSOR UTILIZING MICRODISCHARGES IN A 1.6 mm<sup>3</sup> CERAMIC PACKAGE

Scott A. Wright, Heidi A. Zipperian, and Yogesh B. Gianchandani  
Engineering Research Center for Wireless Integrated MicroSystems (WIMS)  
University of Michigan, Ann Arbor, MI, USA

## ABSTRACT

This paper reports a high-pressure sensor that utilizes differential measurements of pulsed DC microdischarge currents. The microdischarges are created between three photochemically-patterned metal foil electrodes – two cathodes and one anode – within a gas-filled capsule. The external pressure deflects a diaphragm, which also serves as one cathode, varying the inter-electrode spacing. This changes the differential current between the two competing cathodes. The electrodes are fabricated from Ni foil, and separated by dielectric spacers within a micromachined glass cavity. The structures are enclosed within 1.6 mm<sup>3</sup> ceramic surface-mount packages. Devices with 25- $\mu$ m-thick nickel diaphragms reinforced with 75- $\mu$ m-thick epoxy provide a sensitivity of 2,864 ppm/psi (42,113 ppm/atm.).

## INTRODUCTION

Microscale pressure sensors are potentially useful for mining and subterranean exploration if they can withstand high pressures and temperatures. A variety of optical and electrical microstructures have been proposed for these and various high-pressure and high-temperature applications. Fabry-Perot and other interferometers have been fabricated on the ends of fiber optic cables using a diaphragm to modulate a cavity thickness [1]. A microscale sensor has been fabricated using this technology to measure temperature and pressure [2]. Another sensing technology uses Bragg gratings, which are photo inscribed into fibers and used to trace wavelength shifts caused by strain (or pressure, displacement) and temperature changes [3]. A miniature bulk-modulus-based fiber Bragg grating sensor has been explored for pressure and temperature measurements in petroleum boreholes [4]. Piezoresistive pressure sensors with diaphragms made from silicon carbide [5], and more recently even Si [6], have been reported that can also operate at elevated temperatures. Sapphire membranes have also been used in this context [7].

Microdischarges, or microplasmas, are miniature plasmas created in gases between electrodes and are used for on-chip chemical sensing and other applications. A discharge-based approach to pressure sensing is of interest because of the wide dynamic range and temperature immunity of the transduction method. Devices utilizing microdischarges are well suited for high temperature operation as the electrons have average thermal energies exceeding 3 eV (34,815 K) [8] away from the cathode. Ions have thermal energies exceeding 0.03 eV above ambient (644 K) in a 23°C (296 K) ambient environment.

The target pressure range of these sensors is 1-15 atm. These microdischarge-based pressure sensors operate by measuring the deflection of a diaphragm electrode resulting from an external pressure. The diaphragm serves as a cathode and when deflected, the distance between the anode and the deflected diaphragm is affected, altering the current distribution of microdischarges between two cathodes with pressure. Microdischarge-based pressure sensors are fundamentally different than ion gauges, which are not effective at atmospheric pressure because the small mean free path of the created ions, 20-65 nm, makes them difficult to detect at the collector [9].

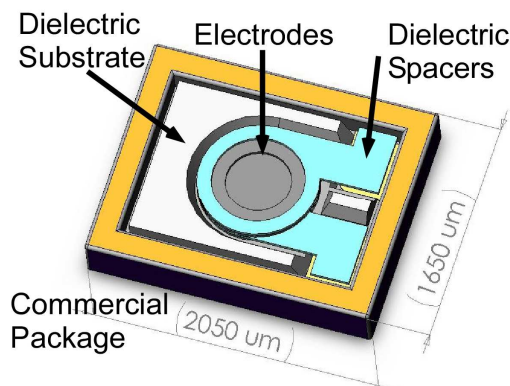


Figure 1: Schematic of device contained within a commercial Kyocera Package.

A microdischarge-based pressure sensor that exploits the variation, with pressure, of the mean free path of gas molecules was previously reported [10]. It uses an unsealed structure fabricated and operated in clean gas environments up to 2.5 atm. and 1,000°C.

This paper describes microdischarge-based microscale pressure sensors that utilizes sealed ceramic packages with a deflecting diaphragm-cathode, a stationary cathode, and an anode. These sensors are laboratory tested in an oil environment. The active volume of these devices is 0.057 mm<sup>3</sup>, which is  $\approx$ 10x smaller than previously reported microdischarge-based pressure sensors, while the targeted pressure range is  $\approx$ 6x higher. Instead of a multi-cathode arrangement, multiple anodes may be used; however, anode current shows very high dependence on encapsulated gas pressure [11]. This high sensitivity results in relatively small dynamic ranges, thereby limiting the utility of multi-anode configurations.

## DESIGN AND OPERATION

A pressure sensor consists of two electrodes enclosed within a commercial package with a dielectric substrate and spacers as shown in Fig. 1. (The third diaphragm electrode seals the package.) A dielectric Pyrex substrate is used within the package to maintain the position and spacing between the electrodes and diaphragm. Each electrode has a single lead for electrical contact to a package feedthrough. Dielectric spacers are used between electrodes to maintain inter-electrode spacing and provide electrical isolation. A microdischarge chamber exists in the center of the package, in a through-hole. A single disk-shaped anode electrode serves as the bottom of the chamber while the center electrode (cathode 1) is torus-shaped, allowing the discharges to exist between the bottom anode and both cathodes. The top cathode is disk-shaped as well, confining the discharges.

The encapsulated microdischarge-based sensors operate by measuring changes in current distribution of pulsed DC microdischarges between an anode and two cathodes. The distal diaphragm cathode (cathode 2) deflects due to external pressure,

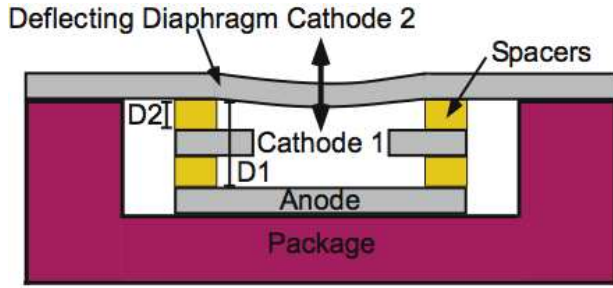


Figure 2: Conceptual image of sensor operation showing the anode, the proximal stationary torus-shaped cathode 1, and the distal diaphragm, cathode 2.

changing the inter-electrode spacing (Fig. 2). To determine the pressure causing this deflection, it is first necessary to separately determine the current in the two cathodes. These current components are denoted as  $I_1$  in the proximal stationary torus-shaped cathode (cathode 1) and  $I_2$  in cathode 2. The differential current, expressed as a fraction of the total peak current,  $(I_1 - I_2) / (I_1 + I_2)$ , is treated as the sensor output. At lower pressures cathode 2 is less deflected and more current flows through cathode 1, while at higher pressures more current flows through the deflected cathode 2. The readout is thus a displacement measurement for the diaphragm-electrode. An important benefit of using a differential output that is expressed as a fraction of the total is that the exact magnitudes are less important than fractional changes.

The gas pressure in the sealed cavity remains relatively constant because the cavity volume remains relatively unchanged by the diaphragm displacement. The high external pressure causes a great deal of initial displacement and additional pressure variations cause only small displacement changes. These changes can be measured directly using the microdischarge current distribution, but do not alter the internal package pressure significantly. Thus measurements of the internal package pressure are less sensitive than measurements of the diaphragm displacement.

Finite element analysis (ANSYS<sup>®</sup>) is used for diaphragm design, considering spacer compression and diaphragm deflection. Options range from 25- $\mu\text{m}$ -thick nickel foil for high sensitivity to cold-rolled 125- $\mu\text{m}$ -thick stainless steel for very-high pressure operation. The maximum achievable pressure with diaphragms of specified thicknesses and materials are outlined in Table 1.

Table 1: FEA analysis was performed using ANSYS<sup>®</sup> software to determine the maximum measurable pressure of sensors utilizing various diaphragms.

Material	Thickness ( $\mu\text{m}$ )	Deflection ( $\mu\text{m}$ )	Max. Stress (MPa)	Max. Pressure (psi)
Nickel	25	0.63	59	100-200
304 SS	25	2.4	215	400-500
60% Hardened 304 SS	125	7.3	1,027	20,000

To control power consumption and parasitic heating in the pressure sensors, pulsed DC microdischarges are used, as opposed to constant DC discharges. A computer controlled, single ended, transformer coupled, gate drive circuit creates the pulses. A current limiting ballast resistor is used in series with the anode, and 100- $\Omega$  resistors are used in series with each cathode to measure current.

The basic operation of a DC microdischarge in a sensor is driven through electron and ion transport. The electrons are drawn towards the anode, whereas the positive ions are drawn to the two separate cathodes forming positively charged sheaths around them. Upon cathode impact, the energetic ions eject high energy secondary electrons from the cathodes, which sustain the microdischarges by ionizing additional neutral molecules and continuing the breakdown process. The current in each cathode is composed of a combination of positive ions impacting the cathodes from the microdischarges and secondary electrons ejected from the cathodes upon ion impact. Further away from the cathodes, the current is carried primarily by the faster moving electrons, which cannot reach the cathodes because of surrounding sheaths.

Sensor characteristics such as the sensitivity, pressure dynamic range, and temperature dynamic range depend on a variety of dimensional parameters, including inter-electrode spacing, electrode diameter, and the cathode thickness. (Cathode thickness effects sheath sizes as well as electrode positioning). The sensors are designed to function with an applied voltage of 500 V; altering the voltage results in different sensitivities. A sealed sensor is shown in Fig. 3(a), with a visible bond ring. A scanning electron microscope image of the components within a sensor is shown in Fig. 3(b).

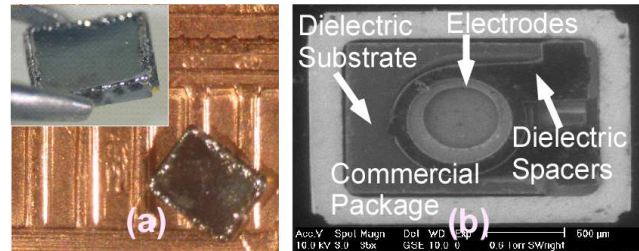


Figure 3: (a) Photograph of pressure sensor on a penny with a laser-welded diaphragm. (b) SEM image of the sensor illustrating the stacked electrode and dielectric spacer layers.

## FABRICATION

The sensors are formed by stacking bulk-metal electrodes and dielectric spacers within a dielectric substrate. This substrate is then enclosed in a commercial package by bonding a metal diaphragm to the top of the package, as shown in Fig. 4.

The package used for the sensor is designed for crystal oscillators and has external dimensions of 2.05x1.65x0.5 mm<sup>3</sup> (Kyocera, Japan). The package has two internal feedthroughs with internal gold-coated contact pads, which are used for the anode and cathode 1. A third gold-coated contact pad on the rim makes electrical contact to cathode 2, the diaphragm lid.

Within the packages a 175- $\mu\text{m}$ -thick-Pyrex substrate maintains the position of the electrodes and dielectric spacers. The sidewalls of this substrate and the recessed area in the center are formed using a micro abrasive jet (MAJ) process, also known as powder abrasive blasting (Bullen Ultrasonics, Eaton OH). The substrates are formed from Schott D263 borosilicate glass due to its

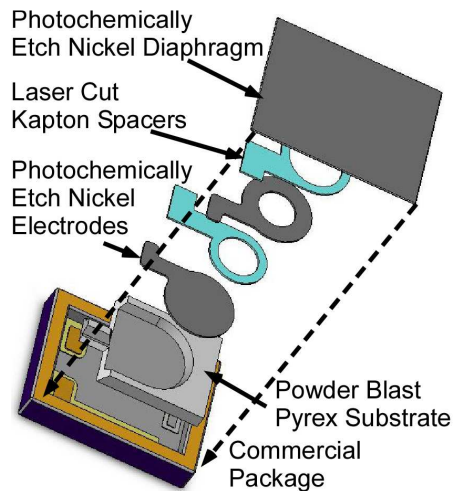


Figure 4: Component integration illustrating stacked electrode/spacer structure within a commercial package before diaphragm attachment.

machinable and dielectric properties. The MAJ process is used because it allows a 100  $\mu\text{m}$  deep recess to be etched into the center of the substrate, in which the microdischarge chamber is housed.

The 25- $\mu\text{m}$ -thick-bulk-foil electrodes have outer diameters of 800  $\mu\text{m}$  and are patterned from nickel for several reasons. Primarily it is robust, inexpensive, easily machinable by micro-electro-discharge machining and photochemical etching, and has a sufficient secondary emission coefficient (i.e. secondary electrons created per incident ion) in a nitrogen ambient.

The electrodes are lithographically patterned and etched from nickel foil using photochemical machining. This process involves coating a thin sheet of metal with photoresist, exposing the resist, and spraying the sheet with a chemical etchant to dissolve the exposed metal. The exposed metal is completely removed, leaving through-holes in the sheet, and the resist is stripped (ChemArt Company, Lincoln RI).

The 25- $\mu\text{m}$ -thick-dielectric torus-shaped spacers serve to electrically isolate the electrodes from one another and from the diaphragm, and to allow microdischarges to be created in the center through-holes. They also define the inter-electrode spacing. Kapton is used due to its dielectric properties and ability to withstand 400°C temperatures without significant dielectric loss. The spacers are laser cut from a Kapton sheet for precision (Tech-Etch, Plymouth MA).

Electrical contact is made between the nickel electrodes and the gold contact pads of the package by conductive silver epoxy. The epoxy also serves to physically secure the electrodes.



Figure 5: Test set-up used to apply high pressure oil to the sensor.

The diaphragm electrode is bonded to the package using laser welding or solder bonding. When solder bonding, a Sn/Pb foil bond ring is used between the package and diaphragm. These bonding procedures hermetically seal the device within the package. The diaphragm rests on the electrode/spacer stack to strictly define the maximum inter-electrode spacing.

## RESULTS AND DISCUSSION

Pressure sensors were fabricated and tested at pressures up to 15 atm. (200 psi) in dielectric oil. Compressed nitrogen was used to pressurize the oil at lower pressures while a hydraulic jack (Fig. 5) was used at higher pressures. Pulses 1 ms in duration with 500 V were applied. The applied voltage pulses resulted in current pulses through each cathode. The transient current peaks were approximately 100-200  $\mu\text{s}$  in duration, with amplitudes of 5-50 mA (25  $\mu\text{J}$  per pulse), varying with pressure.

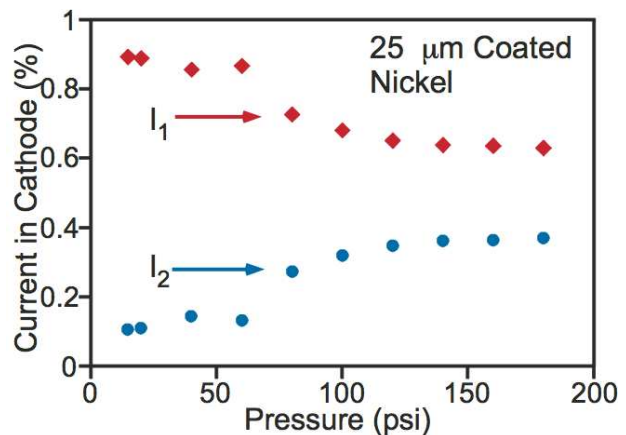


Figure 6: Current distribution between cathodes 1 and 2 in a sensor with a 25- $\mu\text{m}$ -thick nickel diaphragm coated with a 75- $\mu\text{m}$ -thick epoxy layer. Each data point is the average of 100 measurements.

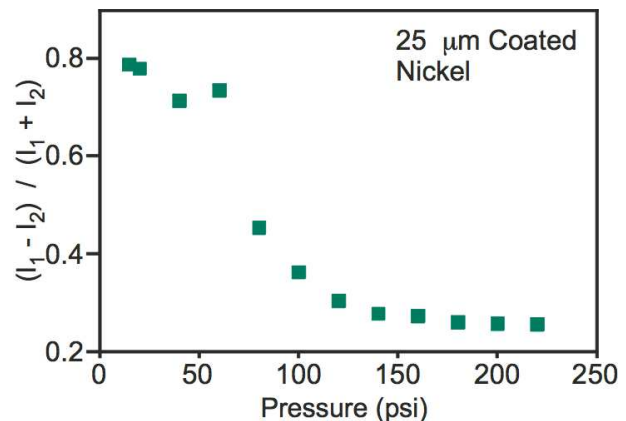


Figure 7: Sensor output as a function of pressure in a sensor with a 25- $\mu\text{m}$ -thick nickel diaphragm coated with a 75- $\mu\text{m}$ -thick epoxy layer. Each data point is the average of 100 measurements. Pressure was measured up to 15 atm.

Pressure was determined by measuring the difference between the fractional current in each cathode. Figure 6 shows the fractional current distribution between cathodes 1 and 2 in a sensor

with a 25- $\mu\text{m}$ -thick nickel diaphragm coated with a 75- $\mu\text{m}$ -thick epoxy layer as a function of pressure. This sensor provided a sensitivity of 2,864ppm/psi (42,113ppm/atm.) and operated up to 15 atm. (Fig. 7).

## CONCLUSIONS

Encapsulated microdischarge-based pressure sensors have demonstrated an ability to measure pressures up to 15 atm. within oil environments. By utilizing different diaphragm materials and thicker diaphragms, the sensors are expected to operate up to 20,000 psi, as experienced in petroleum exploration and pumping. The electrical nature of the readout avoids an intermediate transduction step that is common to many sensors. The discharge-based transduction provides a large readout that does not require local amplification, although it does require a high voltage (pulsed) power source. The small volume occupied by the sensors could be useful for embedded systems and portable applications.

## ACKNOWLEDGMENTS

This work was supported primarily by the Advanced Energy Consortium. The authors acknowledge guidance on testing methods from Dr. J. Shah of Schlumberger Corporation.

## REFERENCES

- [1] R. Fielder, K. Stingson-Bagby, M. Palmer, "State of the art in high-temperature fiber optic sensors," *SPIE*, 5589(1), pp. 60-69, 2004
- [2] D. Abeysinghe et al., *J. Micromech. and Microeng.*, 12(3) pp. 229-235, 2002.
- [3] T. Li, Z. Wang, Q. Wang, X. Wei, B. Xu, W. Hao, F. Meng, S. Dong, "High pressure and temperature sensing for the downhole applications," *SPIE*, 6757(1), pp. 1-7, 2007.
- [4] Y. Zhao, Y. Liao, S. Lai, *IEEE Photonics Technology Letters*, 14(11), pp. 1584-1586, 2002.
- [5] A. Ned, R. Okojie, A. Kurtz, "6H-SiC pressure sensor operation at 600°C," *HITEC*, Albuquerque, NM, pp. 257-260, 1998.
- [6] S. Guo, H. Eriksen, K. Childress, A. Fink, M. Hoffman, *IEEE MEMS*, Tucson, AZ, Jan. 2008, pp. 892-895.
- [7] S. Fricke, A. Friedberg, T. Ziemann, E. Rose, G. Muller, D. Telitschkin, S. Ziegenhagen, H. Seidel, U. Schmidt, "High temperature (800°C) MEMS pressure sensor development including reusable packaging for rocket engine applications," *MNT for Aerospace Applications, CANEUS*, pp. 5p, 2006.
- [8] M. Kushner, "Modeling of microdischarge devices: Plasma and gas dynamics," *J. Phys. D: App. Phys.*, 38(11), pp. 1633-1643, 2005.
- [9] C. Edelmann, "Measurement of high pressures in the vacuum range with the help of hot filament ionization gauges," *Vacuum*, 41(7-9), pp. 2006-2008, 1990.
- [10] S. Wright, Y. Gianchandani, *J. Microelectromechanical Sys.*, 18(3) pp. 736-743, 2009.
- [11] C. Wilson, Y. Gianchandani, R. Arslanbekov, V. Kolobov, A. Wendt, "Profiling and modeling of dc nitrogen microplasmas," *J. Appl. Phys.*, 94(5), pp. 2845-2851, 2003.

# SUBNANOWATT MICROBUBBLE PRESSURE TRANSDUCER

C. A. Gutierrez\* and E. Meng

University of Southern California, Los Angeles, California, USA

## ABSTRACT

We present the first all-Parylene microbubble pressure transducer ( $\mu$ BPT). The  $\mu$ BPT utilizes an electrolytically generated microbubble ( $\mu$ B), trapped in a Parylene microchamber, for pressure sensing. Pressure-induced bubble size variation is detected by electrochemical impedance measurement. Real-time hydrostatic pressure measurement with excellent sensitivity ( $-10.7 \Omega/\text{psi}$ ,  $\pm 0.1 \text{ psi}$ ) up to 1.8 psi and tracking of internal pump pressure in a MEMS-based implantable drug delivery system were achieved. The transduction method and device format uniquely leverage the surrounding liquid environment, obviating the need for hermetic or special packaging techniques for sensing in wet environments. Arrayed  $\mu$ BPTs are biocompatible, fabricated on flexible substrates, ultra-miniature (200  $\mu\text{m}$  diameter, 10  $\mu\text{m}$  thick), and can be operated at very low power ( $\leq \text{nW}$ ) making them especially attractive for *in vivo* pressure measurement applications.

## INTRODUCTION

It is known that gas bubbles respond to external pressure [1] but few efforts exploit this phenomena for sensing. At frequencies below resonance (55 kHz for a bubble of 50  $\mu\text{m}$  radius [2]), microbubbles respond instantaneously to pressure variations. Using microelectromechanical systems (MEMS) technology, miniature devices which can precisely produce, localize, and measure bubble response at very small scales can be fabricated. Polymer-based MEMS fabrication technology in combination with microbubble dynamics are leveraged here to introduce a new class of pressure transducer with unique capabilities.

State-of-the-art ultra-miniature pressure sensing technologies generally occupy 400-500  $\mu\text{m}$  diameter footprints. Our unique electrochemical-based pressure sensing technique does not utilize conventional diaphragm-based pressure transduction, enabling significant reductions in overall footprint, materials processing costs, and power consumption. Electrochemical impedance-based sensing can be accomplished at nanowatt power levels, making this attractive for wireless and implantable applications. Previously, pressure measurements within a microfluidic channel were demonstrated using  $\mu$ B-based transduction [3], however this approach utilized rigid substrate materials and thus was not amenable to wide application (e.g. sensing small pressure variations *in vivo*). Here, Parylene C is featured as both the flexible substrate and structural material; this combination enables a novel sensor configuration capable of controlling bubble generation, localization, and transduction in a completely released and portable device compatible with diverse liquid environments. In particular, these features address the unmet need for robust *in vivo* pressure sensors. Our  $\mu$ B pressure sensing approach eliminates the need for hermetic packaging (for operation in wet environments) and the exclusive use of polymer materials reduces cost, adds mechanical flexibility, and facilitates integration for medical applications.

## THEORY

### Microbubble Dynamics

The response of suspended bubbles to changes in ambient pressure is well studied with regard to bubble dynamics and mass diffusion processes across the gas-liquid interface. The fundamental dynamics of a suspended bubble fixed in an unbounded incompressible viscous liquid are governed by the

Rayleigh-Plesset equation [4]:

$$r\ddot{r} + \frac{3}{2}\dot{r}^2 = \frac{1}{\rho} \left( p_g - p_\infty - \frac{2\sigma}{r} - \frac{4\mu}{r} \dot{r} \right) \quad (1)$$

where  $r$  is the bubble radius (dots denote time-derivative),  $p_g$  and  $p_\infty$  are the pressure in the gas at the bubble wall and ambient pressure far away from the bubble (infinite distance),  $\sigma$  is surface tension,  $\mu$  is fluid viscosity, and  $\rho$  is fluid density.

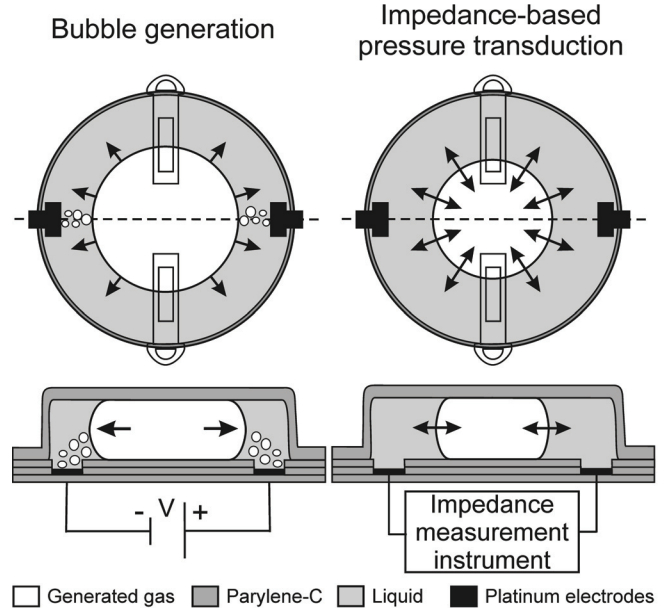


Figure 1: (Left) Electrolytic generation and growth of a bubble within a fluid-filled Parylene microchamber. (Right) Bubble size instantaneously responds to variations in external pressure and is tracked through measurement of solution impedance. Two electrodes are located at the periphery of the chamber and shown in black. Top row = top view, bottom row = cross-sections.

Under the condition that the pressure oscillation frequency is much smaller than the bubble resonant frequency and neglecting any interfacial mass transfer effects, a simple assumption is that the gas follows a polytropic law of compression with a polytropic exponent  $b \approx 1$  at low frequency [4]:

$$p_g = p_i \left( \frac{r_0}{r} \right)^b \quad (2)$$

where  $r_0$  and  $p_i$  are initial bubble radius and equilibrium gas pressure inside the bubble, respectively. From Eq. 1, the following pressure-radius relationship is obtained:

$$p_\infty = p_i \left( \frac{r_0}{r} \right)^b - \frac{2\sigma}{r} \quad (3)$$

The pressure-radius bubble response can therefore be estimated by Eq. 3, which describes the balance of forces acting on the bubble. For a given number of gas molecules produced by

electrolysis and a non-varying surface tension, bubble size is a direct and instantaneous measure of ambient pressure (Figure 1).

If one now considers the bubble behavior over larger time scales, the effects of mass transfer at the bubble liquid interface become significant. The bubble will dissolve in the presence of an under-saturated liquid as a consequence of diffusion across the bubble-liquid interface. Bubble dissolution rate in an under-saturated solution was derived by Epstein and Plesset [1]:

$$\frac{dr}{dt} = \frac{k(c_s - c_\infty)}{\rho_\infty + 2\tau/3r} \left( \frac{1}{r} + \frac{1}{(\pi kt)^{1/2}} \right) \quad (4)$$

where  $k$  is the coefficient of diffusivity of the gas in the liquid,  $c_s$  and  $c_\infty$  are the saturation concentrations of gas in the liquid at the bubble surface and in the bulk,  $\rho_\infty$  the density of gas in the bubble with a gas-liquid interface of zero curvature, and  $\tau$  is the modified surface tension. The mass-diffusion processes taking place across the bubble-liquid interface play a significant role in the behavior of gas bubbles because they may ultimately determine the presence or absence of bubbles in a liquid. These processes are governed by Henry's law, which establishes a connection between the partial pressure of a gas acting on a liquid surface,  $p_g$ , and the equilibrium (or saturation) concentration of gas in the liquid:

$$c_s = ap_g \quad (5)$$

$a$  is a constant characteristic of the particular gas-liquid combination and is a function of temperature. If the ambient pressure is fixed and equal to  $p_\infty$ , then it is clear that unless the gas concentration  $c$  at the bubble surface satisfies Eq. 5, the bubble will not be in equilibrium, and will either grow or shrink according to whether  $c > c_s$ , or  $c < c_s$ . Mass transfer driven bubble dissolution is a slow process; typical values for bubbles of radius  $\sim 100 \mu\text{m}$  are estimated to be on the order of  $\sim 0.1 \mu\text{m}/\text{sec}$  [4].

### Liquid Impedance-based Transduction

The underlying principle of impedance-based transduction is the measurement of solution resistance. The electrode-electrolyte interface has been well studied and characterized [5, 6] and is simply modeled as shown in Figure 2 below:

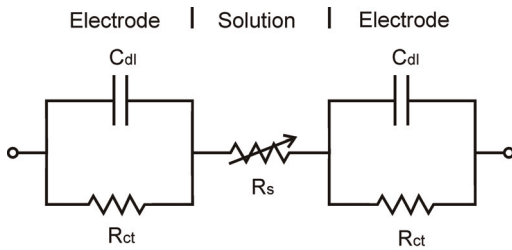


Figure 2: Electrical equivalent circuit for the electrode-electrolyte interface (Randles model).

where  $C_{dl}$ ,  $R_{ct}$ , and  $R_s$  are the double-layer capacitance, charge transfer resistance, and solution resistance, respectively. By applying a small alternating current at a sufficiently high frequency (typically  $>1 \text{ kHz}$ ), the parallel components are shorted through  $C_{dl}$ , and  $R_s$  dominates the measured impedance. The solution resistance is a function of ionic concentration, distance between the electrodes, and cross-sectional area of electrolyte between the electrodes. A trapped  $\mu\text{B}$  acts as an insulating sphere in the conductive incompressible electrolyte between the electrodes. Therefore, monitoring  $\mu\text{B}$  size variations, through measurement of

electrolyte impedance (resistance), is a direct measure of external pressure variations.

## METHODS

### Materials and Fabrication

The transducer features an all-Parylene construction (substrate and structural material) which provides flexibility and biocompatibility for medical and *in vivo* applications. Electrodes and traces are formed from thin film platinum. No further materials were utilized nor were any hermetic sealing or encapsulation techniques required. This “wet” sensor is open to and filled by the surrounding aqueous liquid (via fluidic access ports) which serves as the electrolyte (Figure 3). Isolation of the sensor from the environment is therefore not necessary. Added costs and complexities associated with hermetic packaging are avoided.

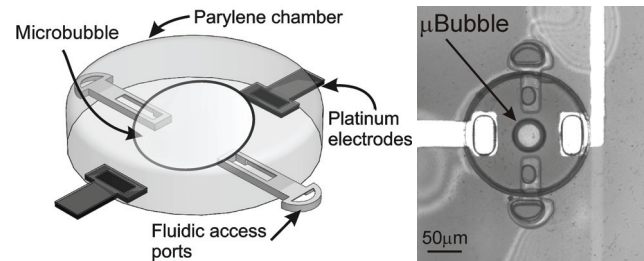


Figure 3: (Left) Model of pressure transducer. (Right) Optical micrograph of actual device ( $200 \mu\text{m}$  diameter) with a bubble.

Fabrication techniques were previously reported [7]. Briefly, platinum electrodes ( $2000 \text{ \AA}$ ) were deposited and patterned on a Parylene coated ( $10 \mu\text{m}$  thick) soda lime wafer ( $1 \text{ mm}$  thick) followed by a  $1 \mu\text{m}$  thick Parylene insulation layer. A  $2 \mu\text{m}$  sacrificial photoresist layer then formed the fluidic access ports followed by a second Parylene deposition step ( $2 \mu\text{m}$  thick). A  $10\text{-}12 \mu\text{m}$  sacrificial photoresist layer was then spun-on and patterned to establish the chamber height and diameter ( $200\text{-}300 \mu\text{m}$ ). The chamber structure was enclosed by a final of  $4.2 \mu\text{m}$  Parylene layer, followed by opening of access port vias by oxygen plasma.

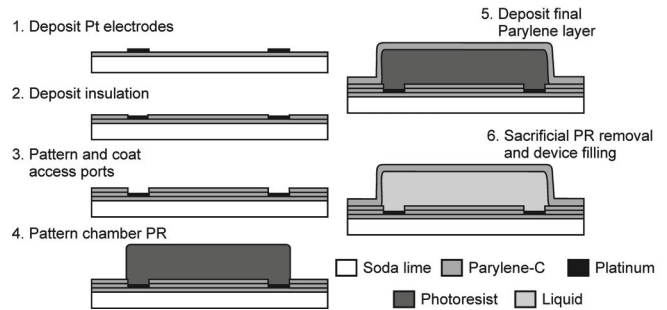


Figure 4: Fabrication process flow for a single transducer. Cross-section taken through electrodes.

Following removal of sacrificial photoresist by immersion in acetone and isopropyl alcohol, chambers were simultaneously filled at the wafer-level by passive soaking in a bath of the desired electrolyte solution. The chamber design allows the ionic conductive path to be constrained within in the chamber interior. This enables the measurement solution resistance in a known geometry and minimizes the potential for cross talk between arrayed sensors. Test dies containing several  $\mu\text{BPTs}$  were

fabricated. In addition, a  $\mu$ BPT array integrated at the tip of flexible Parylene cable was fabricated and completely released from the substrate to form a pressure probe.

### Experimental Setup

The devices were filled with deionized (DI) water or 1x phosphate buffered saline (PBS) as the electrolyte. A microbubble was electrolytically generated within the chamber by applying a DC current pulse (typically 1  $\mu$ A, 5 s for DI water). Device impedance was monitored using a LabVIEW-interfaced Analog Devices Impedance Converter (AD5933) calibrated using an Agilent Precision LCR meter (1  $V_{pp}$ , 5 kHz). A calibrated pressure source metered external hydrostatic pressure applied to  $\mu$ BPTs housed in a testing jig. A series of pressure steps were applied up to 1.8 psi while impedance was monitored.

## RESULTS AND DISCUSSION

### Hydrostatic Pressure Measurement

Measurement of hydrostatic pressure variations was performed. Impedance measurements exhibited excellent resolution up to 1.8 psi (Figure 5).

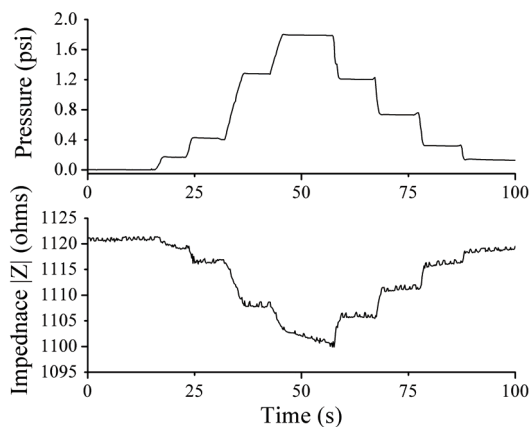


Figure 5: (Top) Profile of applied hydrostatic pressure from calibrated pressure source. (Bottom) The measured impedance response (1x PBS) from the  $\mu$ BPT to the applied pressure profile.

Measurements were obtained within 100 seconds of bubble formation; minimal change in bubble volume occurred over this time. Some measurement drift was observed at maximum pressure (1.8 psi) and was attributed to mass transport-driven bubble dissolution at this elevated pressure. Stable measurements were most easily obtained at pressures below 2 psi (13.9 kPa). A calibrated sensor response of  $-10.7 \Omega/\text{psi}$  was obtained by a best fit linearization and clearly demonstrates pressure tracking capability (Figure 6). Pressure measurement resolution was estimated to be  $\pm 0.1$  psi (689.4 Pa). It was possible to detect pressure variations with excitation amplitudes of only 100 mV, 10 nA ( $\sim 1$  nW); detection at lower excitation amplitudes was also possible but not characterized here. When DI water was used as the electrolyte, a solution resistance of several megohms was typically observed making it possible to realize sub-nanowatt device operation. The bubble generation phase does require somewhat higher power levels but these are typically in the microwatt range and only a few seconds in duration. Although a device configuration open the surrounding environment is desirable the integration of liquid entrapment structures, such as a Parylene-based stiction valve, can provide a means for the entrapment of a particular electrolyte

within the device while it is operated in a different medium [8]. This capability, combined with the small size and polymer construction, makes this technology amenable to low power applications such as implantable wireless pressure monitoring.

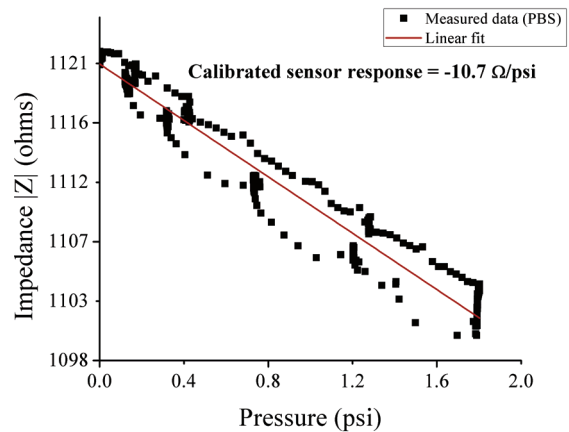


Figure 6: Impedance-pressure plot generated from data in Fig. 5

### Drug Delivery Pump Pressure Measurement

For practical applications, an array of  $\mu$ BPTs was fabricated on the tip of a flexible Parylene cable. This allowed placement of transducers in an environment of choice (Figure 7).

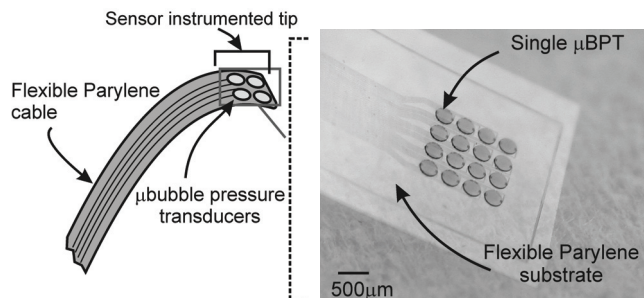


Figure 7: (Left) Drawing of  $\mu$ BPT array positioned at the tip of a flexible Parylene cable. (Right) Optical micrograph of array.

Practical pressure sensor operation was demonstrated in the real-time tracking of internal pressure in an electrolysis pump utilized in a MEMS drug delivery system [9]. Unlike conventional transducers, the small form factor and flexibility of the  $\mu$ BPT array made possible its integration within the polymer-based drug delivery pump to assess internal pressurization conditions. The  $\mu$ BPT array was placed in contact with fluid in the pump chamber. (Figure 8). Pump ON/OFF states were clearly detected and calibrated pressure measurements agree well with previously reported data measured with a conventional silicon pressure transducer [9] (Figure 9).

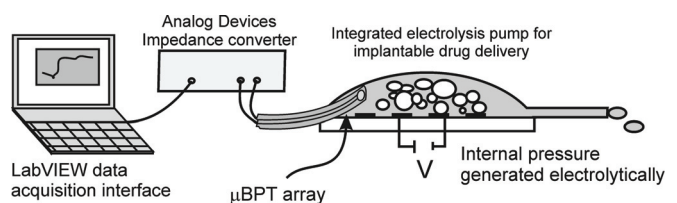


Figure 8: Experimental setup for monitoring intra-pump pressure produced via electrolysis.

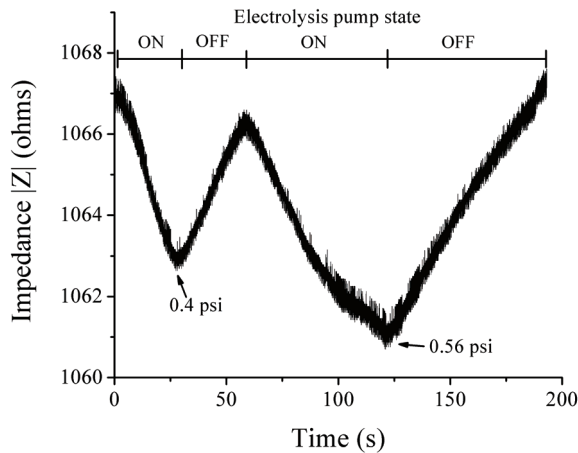


Figure 9: Impedance response to electrolysis pump activation/deactivation cycles (5mA pump current). Calibrated measurement of pressure ( $-10.7 \Omega/\text{psi}$ ) are shown at two points.

### Static Bubble Approximation

According to Faraday's law, the number of gas molecules in an electrolytic gas bubble is determined by the total charge transferred during electrolysis:

$$\Delta Q = nzF \quad (6)$$

where  $z$  is the total charge associated with the formation of a single gas molecule,  $F$  is the Faraday constant, and  $n$  is moles of gas molecules. The electrochemical reaction of electrolytic bubble generation was thoroughly studied in [10]. It was shown that  $\text{H}_2$  and  $\text{Cl}_2$  gases are the main products of electrolysis of a NaCl aqueous solution with negligible byproducts. In practice, the gas composition of the bubble is nearly all hydrogen, due to the lower standard potential required for hydrogen gas evolution. Additionally, the solubility of hydrogen is about three orders of magnitude lower than for  $\text{Cl}_2$ .

Once the bubble is formed, the slow diffusion-limited dissolution process maintains an approximately constant bubble size for a period of time ( $\sim 20$  min), and is dependent on the kinetics and solubility of the gas/liquid interface. There are several factors enabling the use of a slowly shrinking bubble to measure pressure. Generally, smaller bubbles will have higher surface tension and therefore higher internal pressures which serves to speed up the dissolution according to Eq 1. The surface to volume ratio also increases with decreasing bubble size. Finally, it is known that platinum acts as a catalyst and can increase the recombination rate significantly.

In this device, the exposure of the platinum electrodes is limited to the periphery and there is essentially no contact between the recombining gas and the electrodes, thereby minimizing any catalytic effect. In addition, the bubble is compressed due to the fixed chamber height and is forced to expand only in lateral directions. This effectively reduced the surface to volume ratio over which bubble dissolution can occur by limiting mass transport processes to the edges of the bubble. In other words, the top and bottom surfaces of the bubble, which are in contact with the chambers top and bottom surfaces, do not contribute significantly to the mass transport process. These factors taken together give rise to longer bubble lifetimes allowing their use as quasi-constant pressure sensors over short to medium time scales ( $\sim 15$ - $20$  min). Over larger time scales, the measurement of pressure via bubble dissolution rate is also possible and was previously demonstrated

[3]. Other electrolyte-gas combinations can be utilized, such as ethylene glycol or alcohols, which may provide insoluble conditions for entrapped gases for applications requiring long term constant-volume  $\mu\text{B}$  transduction capability.

### CONCLUSION

We have designed and fabricated a Parylene-based pressure transducer utilizing a unique liquid-impedance transduction technique. Response of a bubble to external pressure variations is harnessed to electrochemically monitor pressure. The sensor operates in communication with the surrounding liquid environment (either DI water or PBS), thereby eliminating the need for hermetic packaging. Preliminary sensor characterization indicates a sensing resolution of  $\pm 0.1$  psi over a 0-2 psi range.

### ACKNOWLEDGEMENTS

This work was funded in part by the Engineering Research Centers Program of the NSF under Award Number EEC-0310723, an NSF CAREER Award (ECS-0547544), and the Bill and Melinda Gates Foundation (CG). The authors would like to thank Dr. Donghai Zhu, Mr. Connor McCarty, Ms. Roya Sheybani and the members of the USC Biomedical Microsystems Laboratory for their assistance.

### REFERENCES

- [1] P. S. Epstein and M. S. Plesset, "On the stability of gas bubbles in liquid-gas solutions," *J. Chem. Phys.*, vol. 18, pp. 1505-1509, 1950.
- [2] B. Ran and J. Katz, "The response of microscopic bubbles to sudden changes in ambient pressure," *J. Fluid Mech.*, vol. 224, pp. 91-115, 1991.
- [3] D. A. Ateya, A. A. Shah, et al., "Impedance-based response of an electrolytic gas bubble to pressure in microfluidic channels," *Sensors and Actuators A*, vol. 122, pp. 235-241, 2005.
- [4] M. S. Plesset and A. Prosperetti, "Bubble dynamics and cavitation," *Ann. Rev. Fluid Mech.*, vol. 9, pp. 145-185, 1977.
- [5] J. E. B. Randles, "Kinetics of rapid electrode reactions," in *Proc. Discussions of the Faraday Society 1947*, pp. 11-19.
- [6] H. L. Helmholtz, "Studien uber electriche grenzschichten," *Annalen der Physik und Chemie*, vol. 7, 1879.
- [7] C. A. Gutierrez, C. McCarty, et al., "An Implantable All-Parylene Liquid-Impedance based MEMS Force Sensor," in *Proc. IEEE MEMS 2010*, Hong Kong, China, pp. 600-603.
- [8] C. A. Gutierrez and E. Meng, "Improved Self-Sealing Liquid Encapsulation in Parylene Structures by Integrated Stackable Annular-Plate Stiction Valve," in *Proc. IEEE MEMS 2010*, Hong Kong, China, pp. 524-527.
- [9] P.-Y. Li, R. Sheybani, et al., "A Parylene Bellows Electrochemical Actuator," *Microelectromechanical Systems, Journal of*, vol. 19, pp. 215-228, 2010.
- [10] S. Z. Hua, F. Sachs, et al., "Microfluidic actuation using electrochemically generated bubbles," *Anal. Chem.*, vol. 74, pp. 6392-6396, 2002.

### CONTACT

\*C. A. Gutierrez., tel: (213) 821 3949; cagutier@usc.edu



# DEVELOPMENT OF HIGH-PERFORMANCE, HIGH-VOLUME CONSUMER MEMS GYROSCOPES

*J. Seeger, M. Lim, and S. Nasiri*  
InvenSense, Inc., Sunnyvale, California, USA

## ABSTRACT

This paper discusses the challenges and success factors for creating the world's first integrated MEMS gyroscopes for the consumer electronics market. A disruptive MEMS processing platform called Nasiri-Fabrication is described which has enabled Motion Processing applications, creating the largest and fastest growing MEMS sensors market segment. The paper also presents the design challenges and methodology behind the creation of the world's smallest and best performing consumer grade gyroscope.

## INTRODUCTION

InvenSense was founded in April 2003 by Steve Nasiri, a seasoned MEMS veteran, with a unique combination of entrepreneurial success and MEMS sensor manufacturing expertise. The company was started on the principle that commercialization of silicon gyros requires a thorough understanding of all aspects of sensor production including MEMS fabrication, design, backend operations, and high volume production. Moreover these critical aspects must be mutually optimized to be universally adopted in the cost sensitive, high volume, consumer electronics market.

During the first year, the company was self funded by Steve Nasiri and employed a series of consultants to help develop its business plan and core intellectual property (IP). InvenSense cemented its disruptive fabrication platform recognizing that it has inherent cost, size, and performance advantages that can revolutionize the way MEMS products are manufactured. This technology was deeply rooted in the founder's past activities and his general expertise in volume production and MEMS fabrication. The fabrication platform is now known as Nasiri-Fabrication.

MEMS gyroscopes were identified as a product with huge potential in both automotive and consumer markets. InvenSense focused on consumer electronics (CE) because the market requires small size and low-cost which Nasiri-Fabrication can inherently address. Initially, the company targeted image stabilization for digital still cameras. This feature was becoming increasingly important as the resolution of the digital cameras steadily grew and the camera size was reduced requiring single handed operation. InvenSense succeeded in filing four of its core patents, fine tuning its business plan, and creating the blueprint of its first dual-axis gyroscope. The focus on the consumer market resonated with the VC community and InvenSense received its first funding of \$8M in April of 2004, while operating from the founder's kitchen table.

From the inception, the market strategy, design, and fabrication converged to develop an extremely low cost and highly manufacturable gyro satisfying the CE market requirements. The first generation dual-axis MEMS gyroscope started production in 2006 and shipped to several Japanese DSC camera makers. The second generation gyroscope went into production in 2008, and largely due to the success of the Nintendo Wii Motion Plus, over 50 million units were shipped. In early 2010, InvenSense announced the world's first Motion Processing Unit™ (MPU), featuring the industry's first 3-axis gyroscope with embedded Digital Motion Processor™ (DMP) hardware accelerator for 6-axis sensor fusion.

Today the consumer market is the single largest market for MEMS sensors. Every portable consumer electronics device is

moving toward the integration of Motion Processing™ technology. InvenSense, as reported by iSuppli, is now recognized as the number one supplier of gyroscopes for the CE market and as the innovation leader in MEMS.

At the time InvenSense was founded, there were several companies either developing or already producing gyroscopes for the automotive and consumer markets. Some used MEMS, while others used quartz or piezoceramics. InvenSense not only has been able to enter the market but has validated motion processing capability by addressing the key challenges of developing a gyroscope for the consumer market: low cost, high reliability, high performance, and fast time-to-market. Meeting these challenges required an experienced leadership team with knowledge spanning the core fabrication and design IP, as well as operations, test, packaging, applications and marketing. This paper presents the InvenSense core technical IP including Nasiri-Fabrication and MEMS design.

## NASIRI-FABRICATION

The foundation for building the InvenSense line of inertial sensors is the Nasiri-Fabrication platform. It is a unique platform that is ideal for developing a low-cost gyroscope and other MEMS devices. It addresses the components that influence cost, size, and performance. The key attributes of the Nasiri-Fabrication are the use of single crystal silicon, wafer level integration with CMOS electronics, and a cost effective wafer level packaging technique.

The process flow is described in Figure 1. Only six masks are required to produce the integrated and hermetically sealed gyroscope. The device mask, which defines the MEMS structure, is the only critically dimensioned mask. Eutectic bonding between a germanium layer deposited on the MEMS and the top aluminum layer on the CMOS simultaneously creates multiple interconnects and a hermetic seal for thousands of devices per wafer. This one simple step addresses both the electrical integration and the packaging of thousands of sensors and is the cornerstone of Nasiri-Fabrication. The manufacturing uses commercially available equipment with standard off-the-shelf processes making the process easily scalable and portable to multiple foundries.

The process seamlessly integrates MEMS and CMOS and avoids the complex process interdependencies of other integrated platforms. This allows the IC design to use the best CMOS technology nodes to add features and to lower costs as needed. The process also allows circuits under the MEMS outside the small cavity areas. This maximizes the available CMOS area and minimizes the wiring parasitics between the MEMS structure and interface circuits. The top layer of CMOS aluminum provides electrodes for actuation and sensing of the MEMS structure. Unlike two-chip MEMS platforms, in which the routing to the sensor uses the MEMS layers, all signal routing in Nasiri-Fabrication is done using the CMOS substrate, leveraging the low resistance, compact metal routing capability of the multi-metal CMOS process. Electronic shielding is enabled, routing congestion is reduced, and signal fidelity is preserved. The AlGe contacts between the MEMS and CMOS support differential capacitive sense structures due to the compact size of the contacts and its demonstrated reliability. InvenSense has leveraged this capability to make over 100 contacts to capacitance sensing comb structures

per chip.

The all-silicon construction avoids problems caused by thermal mismatch of materials. Using a bulk silicon device layer allows for thicker MEMS structures (20-100 $\mu\text{m}$ ) which provides inherently better noise and sensitivity due to larger masses, larger capacitances, and higher frequencies for operation outside of the audio range. MEMS designers have the flexibility of choosing the thickness for optimal performance, which is not easily achieved in a surface micromachining processes.



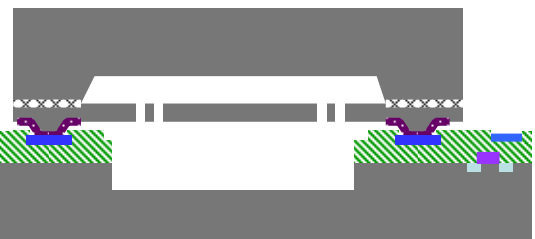
(a) The engineered silicon on insulator (ESOI) wafer is formed starting with a standard silicon handle wafer etched with simple targets for backside alignment (mask 1); followed by oxidation and cavity etch (mask 2). A second wafer is fusion bonded to the handle wafer and subsequently thinned to define the device layer thickness.



(b) The MEMS wafer is completed by etching the device layer to form standoffs (mask 3) that define the seal ring, the electrical contacts to CMOS, and the vertical gap between the CMOS and MEMS; depositing and patterning a germanium layer (mask 4) over standoffs; and patterning (mask 5) and deep reactive ion etching the device layer to form the mechanical structure.



(c) A standard CMOS wafer is fabricated by an independent foundry, and cavities (mask 6) can be etched into the CMOS wafer, if needed for larger clearance under moving MEMS structures.



(d) The MEMS wafer is bonded to the CMOS wafer using AlGe eutectic bonding between the Al on the CMOS and the Ge on the MEMS wafer. After bonding, a portion of the MEMS wafer is removed by conventional dicing saw cuts to expose the CMOS wire bond pads.

Figure 1: Simple six mask Nasiri-Fabrication process flow.

The resonating MEMS device is encapsulated and hermetically sealed in a vacuum environment. The vacuum level is controlled during the bonding process. Getters are not required to maintain the vacuum because the seal is hermetic and the materials used in the process do not outgas. This point is actually

more important than first may be realized. Damping is one of the key functional parameters that affects the proof-mass velocity and gyro bias. Achieving a stable and constant damping factor, which is a direct function of the vacuum, is critical. Adding getters to maintain a vacuum over the product lifetime does not guarantee a constant vacuum or hermeticity, and hence builds in a reliability problem, particularly in humid environments.

Wafer level integration of MEMS, electronics and micro packaging addresses the widely recognized high cost of package and test associated with MEMS devices. Each die is fully encapsulated and is packaged using standard, low-cost QFN packages, as shown in Figure 2. Furthermore, the bonded wafer has full functionality, allowing each die to be tested at wafer probe. Wafer level testing provides mapping information for timely feedback to the foundries for improved process control, and provides device level traceability. Use of conventional high speed testers at the wafer probing level reduces the test costs associated with custom testers needed for sensitivity calibration of packaged parts.



Figure 2: Fully functional, hermetically sealed, 3-axis gyroscope and standard QFN package.

## GYROSCOPE DESIGN

Nasiri-Fabrication provides a platform well-suited for gyroscope design. The process provides controlled vacuum, thick structures, low parasitics, and built-in reliability. Nonetheless, the gyroscope design challenges are formidable. The design must work within the process: it must be robust against inherent process variations and against the package stresses brought on by low-cost packaging. The design must meet the consumer market demands of cost, size, performance, and reliability and the design must meet the rapid development time required to be the first in the market. The key to meeting these challenges has been to comprehend the fundamental issues in gyroscopes and properly design the integrated system to compensate for the error sources. This was achieved by developing good simulation capabilities and structured design flows. While this already existed for the IC industry, this was relatively new for the MEMS industry.

## Mechanical Architecture

MEMS vibratory gyroscopes measure rotation rate by vibrating a proof-mass and sensing the Coriolis force caused by angular velocity. Beyond the goal of making a vibrating structure that gives rise to a Coriolis force, the true goals of the gyro transducer are to minimize the error sources that corrupt the Coriolis signal and to simplify the IC architecture. The former is achieved by a design that minimizes Brownian noise, rejects external vibrations, survives shock, rejects package stresses, and minimizes cross-axis sensitivity. The latter is achieved by a design that has high transducer sensitivity, minimal quadrature, carefully designed resonant modes, and minimal parasitic capacitance.

All InvenSense X- and Y-axis gyroscopes are based on

coupled dual-mass (tuning fork) proof-masses that are driven out-of-plane and generate Coriolis forces in-plane, as shown in Figure 3. The vibration mode consists of a five-mass system. The two proof-masses translate out-of-plane coupled together through lever arms connected to three separate torsion plates. The torsion plates are mounted on springs that act as pivot points, which is the key to achieve vertical motion using thick silicon. Aluminum electrodes on the IC are located under the torsion plates forming parallel-plate electrodes that can exert torque on the torsion plates for actuation and detect the torsion plate angle for feedback to resonate and provide amplitude control.

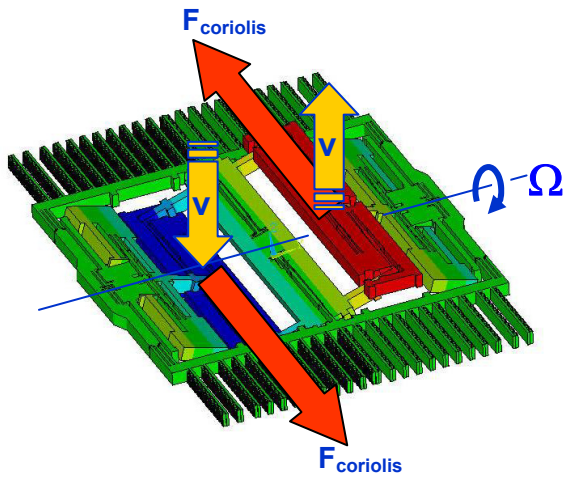


Figure 3: X-axis gyroscope driven mode

The coupled mass system is essential for rejecting external vibrations because the design is fully balanced and therefore does not move in response to linear acceleration. However, the first generation gyroscopes, which operated in the 12 kHz to 15 kHz range, were found to respond to acoustic interference. Later generation gyros were designed to operate in the 25 kHz to 30 kHz range to avoid interference from sound and other ambient sources of noise found in consumer applications.

The key to reducing size has been to improve the Coriolis sensing system. In the first generation sensors, the three torsion plates were connected to a sensing frame. The sensing frame was suspended such that it could only rotate. The Coriolis forces from the proof-masses created a torque that rotated the ring in plane. Motion of the ring was detected by capacitive combs. The full scale angular rate in image stabilization generated merely  $\sim 1\text{\AA}$  of mechanical deflection of the sensing frame. Sensing the deflection required lots of capacitive combs and low-noise electronics.

In the next generation InvenSense introduced patented “dual-mode sensing,” in which the two outer torsion plates are anchored to the substrate, and the center torsion plate is flexibly connected to the sense frame. By flexibly connecting the drive system and sense system, two resonant modes are created, and the drive resonant frequency is in the middle. This introduced several benefits including lower sensitivity variation as well as 2x higher mechanical sensitivity. The design improvement resulted in smaller MEMS that met the same performance with higher resonant frequency to avoid the audio range. In the third and current generation, the sense frame was further optimized into a four-bar linkage. The Coriolis torque moves the four-bar linkage which is sensed in-plane using capacitive electrodes, as shown in Figure 4. The four-bar linkage has lower inertia than the corresponding rigid frame structure of the past. This generation

also anchors the structure at two points which minimizes sensitivity to any stress associated with conventional QFN plastic packages.

InvenSense introduced a Z-axis gyroscope in 2009. It consists of two proof-masses that are resonated in-plane as shown in Figure 5. The proof-masses are flexibly coupled and resonate in a differential mode. The proof-masses can move in two directions but the actuation structures are constrained to move only in the drive direction. The Z-axis gyroscope also uses dual-mode sensing. The proof-masses are flexibly coupled to the sense frame and the resulting Coriolis torque moves the sense frame similar to the X and Y gyroscopes. In this manner, the Z-axis gyroscope is able to leverage the entire sense-system mechanics and electronics developed for the X-and-Y sensor. In fact, the first generation Z-gyro simply replaced the Y-gyro drive masses with proof-masses that are driven in-plane, enabling rapid development.

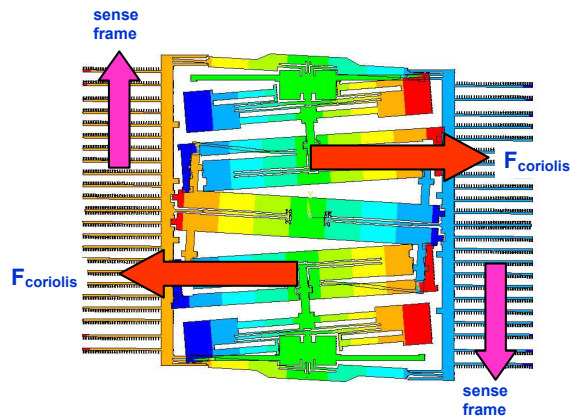


Figure 4: X-axis gyroscope sense frame first resonant mode

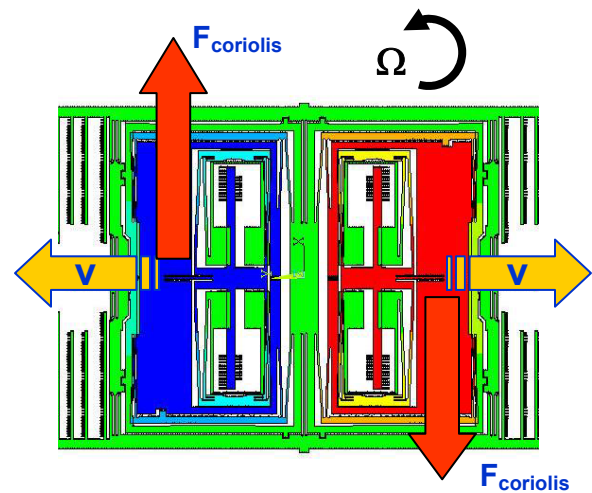


Figure 5: Z-axis gyroscope driven mode

### IC Architecture

The gyro signal path is the core of the MPU-3000. Shown in Figure 6, it includes a drive-loop that vibrates the structure at resonance, a sense path that detects the motion caused by Coriolis acceleration, a synchronous demodulator that recovers the rotation signal, and an ADC that provides digital output to the motion processor.

The IC architecture was chosen for the balance of noise, power, and size to meet the market requirements. The charge-

pump provides high signal gain for the low-noise, continuous time signal path. The drive-loop consists of a capacitive position sensing stage followed by a simple 90° phase shift to oscillate the MEMS structure at resonance.

The IC also compensates for transducer variation and imperfections. For example, the trans-capacitance value in the drive-loop and sense path amplifiers are programmable and can be written to on-chip, non-volatile memory during factory trim to compensate for both etching and vertical gap variations. The patented feedthrough (FT) cancellation block, is a programmable capacitor that is used to reduce the undesired quadrature signal. Amplitude control circuitry maintains constant vibration amplitude as the damping varies due to process and temperature variation. The digital signal path provides means for offset temperature compensation that can be factory programmed.

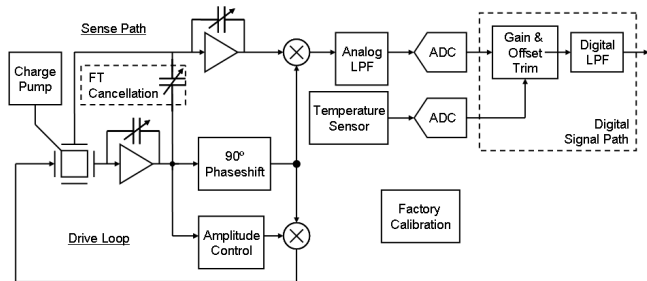


Figure 6: Single-axis gyroscope signal path electronics

## RESULTS

InvenSense has met the challenges of the consumer market, introducing the world's first dual-axis gyroscope in 2006 and new generations of smaller size products at lower cost regularly ever since, as shown in Table 1. The commercialization of multiple products with millions of gyros ships are a testament of successful integration of the core IP of Nasiri-Fabrication and design.

In the current generation gyroscope, the MPU-3000 shown in Figure 7, the MEMS size per axis is one-half the size of the first generation; the CMOS area per axis is one-third of the first generation. The process has migrated from 0.5µm CMOS to 0.18µm and is being built on a 200 mm line.

Characterization of this product shows that the goals of small-size and high performance have been achieved in a standard plastic package. The sensitivity variation is better than 4% over a temperature span of 145°C as shown in Figure 8. The Allan variance plot in Figure 9 indicates an angle random walk of 0.016deg/√s and a bias instability of better than 0.01%/s at 10s.

## CONCLUSION

InvenSense entered the consumer market for gyroscopes in 2006 based on Nasiri-Fabrication and novel dual-axis gyroscope design. The fabrication platform has been proven to be reliable, low-cost, and suited for high volume production. The gyroscope design has met the market needs for size, cost and performance culminating with nearly 100 million units shipped. Continuing design innovation to reduce size, improve performance, and integrate additional sensors has earned InvenSense the technological leadership. InvenSense has enabled the motion processing market, with expected demand to reach over one billion units annually by 2015. InvenSense is preparing to meet this exciting demand by increasing capacity and to continually introduce high value products.

Table 1: InvenSense gyroscope product history

Product	IDG-1000	IDG-600	IXZ-600	MPU-3000	
MP Date	2006	2008	2009	2010	
Gyro Axes	X/Y	X/Y	X/Z	X/Y/Z	
Package	6x6x1.4 QFN	5x4x1.2 QFN	5x4x1.2 QFN	4x4x0.9 QFN	mm <sup>3</sup>
Die Size	12.2	7.4	7.4	6.7	mm <sup>2</sup>
MEMS Area	4.1	2.8	2.8	2.9	mm <sup>2</sup>
CMOS technology	0.5um	0.35um	0.35um	0.18um	
Output	Analog	Analog	Analog	Digital	

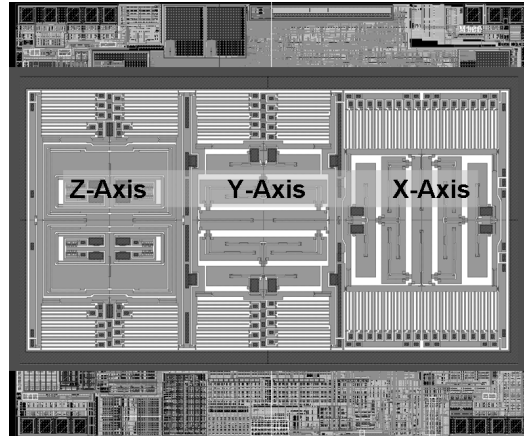


Figure 7: MPU-3000, 3-Axis gyroscope in 2.8mm x 2.4mm

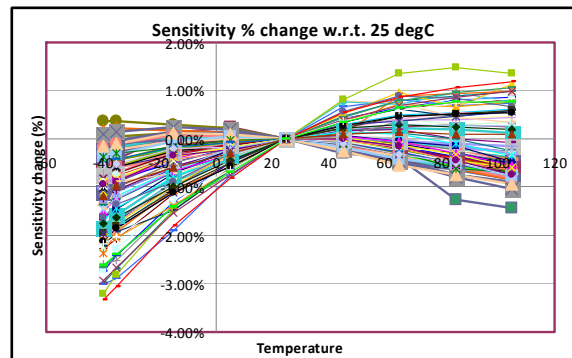


Figure 8: MPU-3000, sensitivity variation of 30 units (90 axes) from -40°C to 105°C.

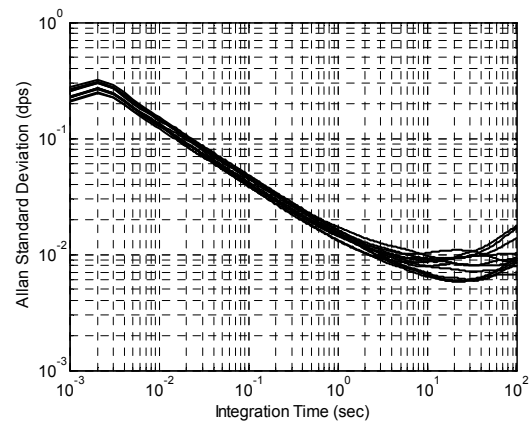


Figure 9: MPU-3000, Allan deviation for 4 units (12 axes)

# PARALLEL LATTICE FILTERS UTILIZING ALUMINUM NITRIDE CONTOUR MODE RESONATORS

K. E. Wojciechowski\*, and R. H. Olsson III

Sandia National Laboratories, Albuquerque, NM, USA

## ABSTRACT

In this work we describe a new parallel lattice (PL) filter topology for electrically coupled AlN microresonator based filters. While 4<sup>th</sup> order, narrow percent bandwidth (0.03%) parallel filters based on high impedance (11 kΩ) resonators have been previously demonstrated at 20 MHz [1], in this work we realize low insertion loss PL filters at 400-500 MHz with termination impedances from 50 to 150 Ω and much wider percent bandwidths, up to 5.3%. Obtaining high percent bandwidth is a major challenge in microresonator based filters given the relatively low piezoelectric coupling coefficients,  $k_t^2$ , when compared to bulk (BAW) and surface (SAW) acoustic wave filter materials.

## INTRODUCTION

Wide percent (> 1 %) bandwidth filters are needed to achieve the high data rates in applications ranging from CDMA base station transceivers to WiMAX and GSM. These require large percent bandwidth at intermediate frequencies or IF frequencies (~70-900 MHz). Typically wide bandwidths are achieved at low IF frequencies with SAW devices using Lithium Niobate, LiNbO<sub>3</sub>, or Lithium Tantalate, LiTaO<sub>3</sub> as the filter material. These materials are used because of their high  $k_t^2$  allowing for low insertion loss (IL). Unfortunately they are not easily integrated with CMOS or other semiconductor technologies. In addition, SAW and BAW technologies result in large devices at these frequencies for a low motional impedance. The motional impedance per unit area, of a SAW/BAW device, is dependent on frequency due to the direct relationship between wavelength,  $\lambda$ , of the acoustic wave and electrode spacing. As a result transduction efficiency is dependent on the wavelength, and as  $\lambda$  increases the effective transduction coefficient decreases for SAW and BAW devices. This results in large devices at IF frequencies which have significant insertion loss (-20 dB) in the pass band [2]. It should be noted that BAW or film bulk acoustic wave devices (FBARs) at low IF frequencies are difficult to manufacture and have high insertion loss because they require film thickness that are on the order of 10's of microns (wavelength/2 or  $\lambda/2$ ).

Aluminum Nitride (AlN) contour mode resonators transduced with the  $d_{31}$  piezoelectric coefficient have a motional impedance (per unit area) that is independent of device frequency as the acoustic wave in the material is orthogonal to the electric field used to induce it [3]. Hence this form of transduction (dependent on AlN film thickness not wavelength) can result in much smaller filters with similar or lower insertion loss (across a wide range of IF frequencies) than can be achieved with SAW and BAW resonators of equal size.

While SAW filters can create high order filter responses with a single device (advantage SAW), multiple AlN resonators (similar to BAW) must be employed to achieve similar performance. For instance high order ladder or lattice filters can be implemented using multiple resonators. For filter topologies consisting of individual resonators (ladder, lattice) the achievable percent bandwidth of the filter is directly proportional to the separation of the series,  $f_s$ , and parallel resonances,  $f_p$ , of the resonators used in the filter [4]. For BAW resonators this is directly related to the  $k_t^2$  of the material. This is a direct consequence of the transduction mechanism used in these devices. i.e. the resulting capacitance,  $C_o$ ,

of the piezoelectric transducer is in parallel with the mechanical resonance. For these devices  $k_t^2$  is proportional to the ratio of  $C_x$ , the resonator motional capacitance to  $C_o$ . Or equivalently it is proportional to the ratio ( at resonance  $\omega = \omega_s = 2\pi f_s$  ), of the impedance  $Z_o = 1/(\omega C_o)$ , to the motional resistance of the resonator,  $R_x$ .

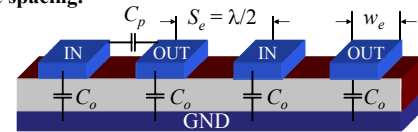
$$k_t^2 \approx \frac{d_{ij}^2}{\epsilon_i S_{jj}} \propto \frac{C_x}{C_o} \propto \frac{Z_o}{R_x} \quad (1)$$

$$f_p = f_s \sqrt{1 + \frac{C_x}{C_{ft}}}, \text{ for BAW } C_{ft} = C_o \quad (2)$$

Where  $d_{ij}$  is the piezoelectric coefficient,  $\epsilon_i$  is the effective permittivity of the piezoelectric material in the  $i$  direction and  $S_{jj}$  is the mechanical compliance. It is well known, (2), that the separation of the  $f_p$  and  $f_s$  is related to the ratio of  $C_x/C_o$  in BAW devices. This is because the feed through or the capacitance in parallel with the mechanical resonator,  $C_{ft}$ , is equal to  $C_o$ . Hence material properties dictate this separation.

In AlN contour mode resonators use of the  $d_{31}$  coefficient enables the decoupling of the relationship between material property  $k_t^2$  and the separation between the series and parallel resonance.

- a) **Top only transduction (TOT).  $w_e$  = electrode width, and  $S_e$  = electrode spacing.**



- Top electrode ■ Bottom electrode ■ Piezoelectric Film (AlN)

- b) **Electrical model for TOT.**

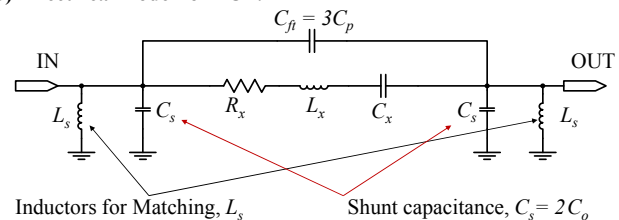


Figure 1: a) Cross section of a TOT AlN overtone resonator. b) electrical equivalent model.

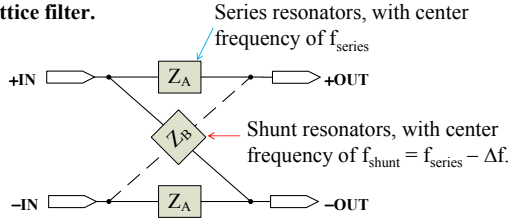
This is achieved by: 1) Using top only transduction (TOT) by arranging the drive and sense electrodes such that the resulting transduction capacitance,  $C_o$ , is a shunt capacitance to ground at the inputs and outputs of the resonator (figure 1a). Therefore reducing the capacitance,  $C_{ft}$ , which is in parallel with the mechanical resonance. This increases the separation of the series and parallel resonance. 2) The shunt capacitance,  $C_s$ , can be resonated out with matching networks consisting of integrated or off-chip inductors (figure 1b). This recovers insertion loss resulting from this configuration. Conversely, capacitance in

parallel with the mechanical resonance,  $C_{fs}$ , cannot be easily removed with matching networks, especially without compromising the low frequency filter rejection.

To summarize the main advantages of AIN contour mode resonators based filters at IF frequencies are: 1) Frequency independent motional impedance which enables small size compared to SAW and FBAR for a given IL. 2) Increased separation between series and parallel resonance enabling wide percent bandwidth filters to be implemented exceeding the material limit set by  $k_t^2$  (Maximum bandwidth = 1.2% for a  $k_t^2 = 2.4\%$  in our case) [5]. 3) Multiple resonators with closely spaced center frequencies, required to design wide bandwidth filters, can be realized with good accuracy using AIN contour mode resonators. These advantages enable a new parallel lattice filter topology which can be used to achieve high percentage bandwidth filters at IF frequencies.

## PARALLEL LATTICE FILTERS

### a) Basic lattice filter.



### b) Lattice filter implemented with an inverting element. A transformer in this case.

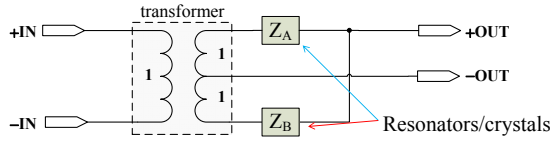


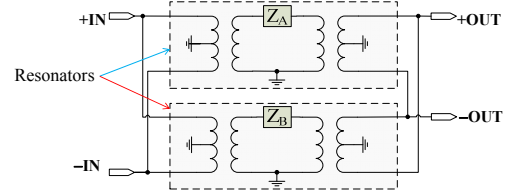
Figure 2: a) Basic lattice filter with series and shunt resonators with impedances,  $Z_A$  and  $Z_B$  respectively. b) Alternative implementation of a lattice [4]. Note that this is equivalent to an  $L/2$  section in a ladder filter [4].

As was mentioned above, PL filter topology is particularly well suited for implementation with AIN contour mode resonators as they provide key technological advantages which enable parallelization of lattice networks: small feed through capacitance (large separation between  $f_s$  and  $f_p$ ), multiple frequency resonators on a single chip, and low impedance resonators [3]. In addition, AIN contour mode resonators provide the ability to perform signal inversion. This removes the need for external inversion required to implement a lattice filter. Finally the PL lattice topology reduces overall filter insertion loss by placing resonators in parallel instead placing them in series as is done with ladder filters.

Consider the basic lattice filter in figure 2a. Alternatively this filter can be implemented using two resonators with the addition of an inversion. In figure 2b a transformer (external to the resonators) is added to provide signal inversion [4]. The lattice in figure 2a has also been implemented using active circuitry to provide the inversion [1]. The lattice filters in this work implement a lattice utilizing topologies in figure 1a, 3a and 3b. Note that the lattices are implemented with electrically coupled resonators and the resonators provide the necessary inversions, hence there is no need for active circuitry. The basic lattice filter shown in figure 2a has a lower and upper limit on its achievable percent bandwidth. This limit is set by resonator Q or 3dB bandwidth, desired termination

impedance, and desired insertion loss. As the series and shunt frequencies are moved closer together the range of frequency where the output responses of the two resonators add constructively shrinks. As a result a narrow pass band can be achieved at the cost of insertion loss.

### a) Fully differential lattice using 2 AIN fully differential resonators.



### b) Balun lattice filter using 2 AIN balun resonators.

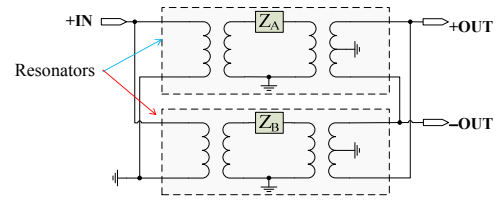


Figure 3: Schematics of electrically coupled AIN resonator based lattice filters. a) Fully differential and b) Balun lattice filters.

For narrow bandwidths increasing resonator area may not be sufficient to overcome the loss. Conversely, as the series and shunt resonances in a lattice are moved apart pass band ripple becomes large and the termination impedances required to flatten the filter response may become unacceptably large. As a result the 3dB bandwidth,  $f_{3dB}$ , of the resonators, sets a practical upper limit on filter bandwidth ( $BW_{3dB} = 2 \times f_{3dB}$ ) for a two frequency (single lattice) filter (figures 2a,b and 3a,b). Note this limit is approximate and depends on the termination impedance requirements as well. Larger bandwidths can be achieved with a single lattice as long as resonator impedance can be made small enough (increase resonator size) to meet ripple and IL specifications for a given termination. Essentially the 3 dB bandwidth of the resonators can be increased through Q loading.

The alternative to reducing resonator impedance in a single lattice, is to place multiple lattice filters in parallel. One method of doing so is to equally divide the bandwidth into  $2 \times N$  frequencies where  $N$  is the number of lattice filters in parallel. Each lattice having two frequencies,  $f_{series}$ , and  $f_{shunt}$  (figure 2a).

$$BW_{3dB} \cong \frac{2N}{2N-1} \Delta f \quad (3)$$

$$f_{series}(k) = f_{center} + \frac{\Delta f}{2} - (k-1) \times \frac{\Delta f}{2N-1}, \quad k \text{ odd} \quad (4)$$

$$f_{shunt}(k) = f_{center} + \frac{\Delta f}{2} - (k-1) \times \frac{\Delta f}{2N-1}, \quad k \text{ even} \quad (5)$$

The approximate 3dB filter bandwidth is given by (3). Note  $\Delta f$  is the spacing between the maximum and minimum resonator frequencies. Equations (4-5) calculate the series and shunt frequencies for each of the  $N$  lattice filters. Where  $k$  is an integer representing the  $k^{th}$  lattice filter ( $k = 1$  to  $N$ ), and  $f_{center}$  is the desired center frequency of the overall filter response. Figure 4 shows the relationship between filter shape factor and  $N$ .

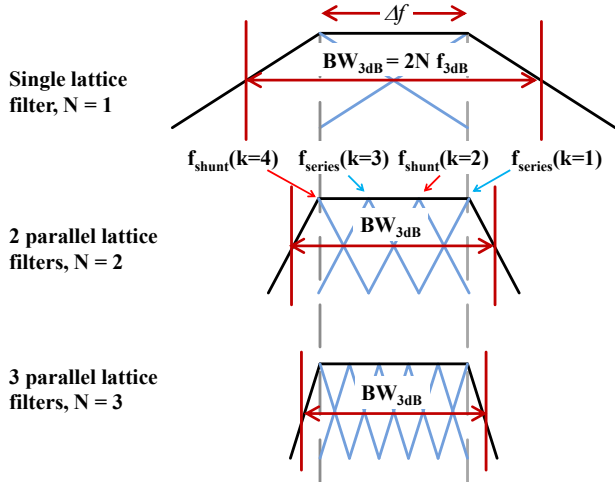


Figure 4: Conceptual diagram depicting how parallel lattice filters (parallel resonators) can be used to obtain a wide bandwidth filter response.

As the number parallel stages is increased the filter shape factor improves. This is because as  $N$  increases each individual resonators loaded  $Q$ ,  $Q_{loaded}$ , increases ( $f_{3dB}$  decreases). Therefore increasing  $N$  improves filter shape factor. However, increasing  $Q_{loaded}$  requires an increase in individual resonator impedance (at resonance),  $R_x$ , with respect to the termination impedance,  $R_T$  (6). It was found through simulation that equations (6-8) yield a low ripple response. Where,  $Q_{unloaded}$  is the unloaded  $Q$  of the resonator and  $Q_{loaded}$  is the loaded  $Q$  of a single resonator with input and output terminations of  $R_T$ . From (7-8) it can be seen that the differential filter insertion loss increases with  $N$ .

$$\frac{I}{Q_{loaded}} = \frac{I}{Q_{unloaded}} \left( 1 + \frac{2R_T}{R_x} \right) = \frac{\Delta f}{Nf_{center}} \quad (6)$$

$$R_x = \frac{2R_T}{\frac{\Delta f}{N} \frac{Q_{unloaded}}{f_{center}} - 1} \quad (7)$$

$$IL_{filter} \cong 20 \log \left( \frac{R_T}{R_x + R_T} \right) \quad (8)$$

Figure 5 shows the results of a model implemented in GENESYS<sup>TM</sup> to illustrate the tradeoff between shape factor and insertion loss of the PL filter architecture. This was done for  $f_{center} = 465$  MHz,  $\Delta f = 22$  MHz,  $R_T = 50 \Omega$  and  $Q_{unloaded} = 600$ . The resonators frequencies were calculated using (4-5) and their impedances were calculated using (7). Also it was assumed the shunt capacitance was zero for purposes of this illustration. Hence filter insertion loss is optimistic in this example. For  $N > 1$  the resonators at the band edges (maximum and minimum values of  $f_{series}$  and  $f_{shunt}$ ) have been scaled to increase their impedance by a factor 1.5. It was found through simulation that this reduced pass band ripple. Finally as  $N$  is increased ripple also increases. Ripple, due to increasing  $N$ , could possibly be reduced by scaling more than two resonator impedances in the filter. This added degree of freedom has not yet been investigated. Finally it should be noted that the design equations (3-8), are empirical and are not necessarily optimal.

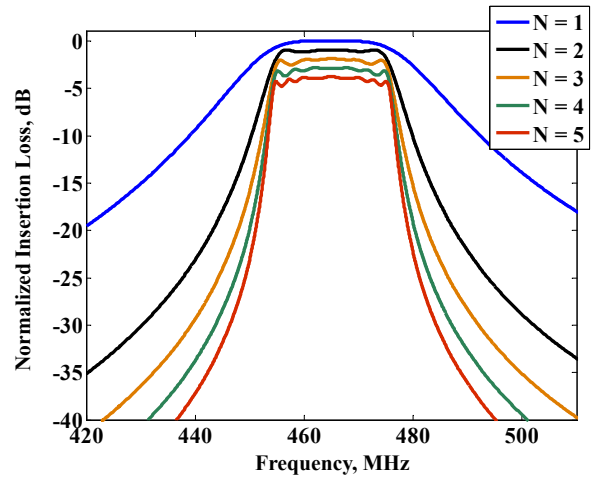


Figure 5: This illustrates the tradeoff between filter shape factor and insertion loss as  $N$ , filter order, is increased. All filter responses are normalized to  $N = 1$  case.

### EXAMPLE FILTER DESIGN

Three filters were designed in this work (Filters 1-3 in tables 1-2). The first consisted of placing two ( $N = 2$ ) basic lattice filters (figure 2a) in parallel. The second filter is derived from two parallel balun lattices (figure 3a) and the third filter has three ( $N = 3$ ) differential lattice filters in parallel. In this section we will discuss the design of the third filter in greater detail. Figure 6 shows the block diagram and physical layout for the differential lattice filter design.

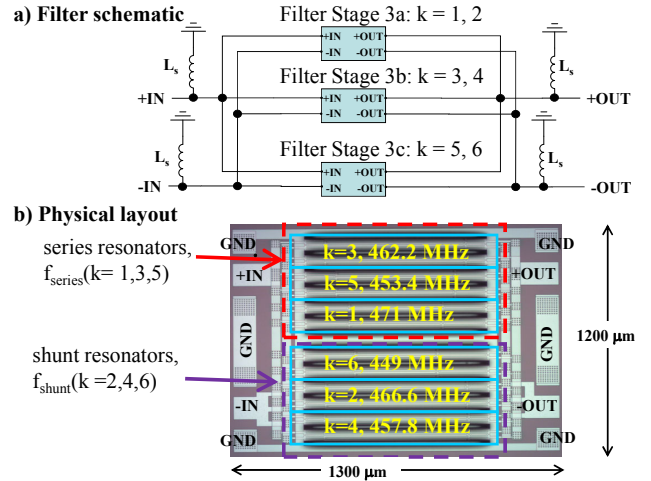


Figure 6: a) 23 MHz parallel lattice filter schematic and b) Photograph of the filter. The blue boxes denote two identical differential resonators.

The design parameters for this filter are listed in table 1. The filter was to target an insertion loss of -9 dB or better with a termination impedance of 150 ohms. Its center frequency was to be 460 MHz with a 5%, 3 dB bandwidth (24 MHz). The six individual resonator frequencies were calculated using equations (4-5) with  $N = 3$ ,  $\Delta f = 22$  MHz, and  $f_{center} = 460$  MHz. For this filter each single frequency differential resonator was implemented using two parallel 6<sup>th</sup> overtone devices (6 electrodes).

Table 1: Target filter parameters

Filter #	Filter	Target Center Frequency (MHz)	Target 3dB Bandwidth (MHz)	Number of parallel lattices ( $N$ )	Target Insertion Loss (dB)	Target Ripple (dB)	Target $R_T$ ( $\Omega$ )	Designed $\Delta f$ (MHz)	Designed $R_x$ ( $\Omega$ )
1	5 MHz Lattice	480	5	2	-3	< 1	< 200	5	25
2	1.2 MHz Balun lattice	490	1.2	2	-9	< 1	< 200	1.2	50
3	23 MHz Differential Lattice	460	23	3	-9	< 1	< 200	22	38.5

Table 2: Measured filter parameters

Filter #	Filter	Measured Center Frequency (MHz)	Measured 3 dB Bandwidth (MHz)	Measured Insertion Loss (dB)	Ripple (dB)	$R_T$ ( $\Omega$ )	20 dB Shape factor	$L_s$ ( $Q=20$ ) (nH)	$C_s$ per port (pF)
1	5 MHz Lattice	478	5.1	-2.9	1.7	50	2.7	19.7	5.64
2	1.2 MHz Balun lattice	494	1.6	-8.8	$\sim 0$	50	3.6	N/A	+IN: 3.6 $\pm$ OUT: 7.1
3	23 MHz Differential Lattice	465	24.7	-11.7	2.0	150	1.4	8	10.3

Each resonator (figure 7a) was designed to have an impedance of  $2 \times R_x$ . When placed in parallel they provide a resistance of  $R_x$ . At the time of design a differential resonator model had not yet been developed. Therefore the filter was modeled in GENESYS™ using three basic lattice filter stages in parallel (figure 6a). Filter stage 3a ( $k=1,2$ ) is the topmost filter in figure 6a. Filter stages 3b ( $k=3,4$ ) and 3c ( $k=5,6$ ) are directly below.

a) Differential resonator physical layout



b) Diagram of differential resonator.

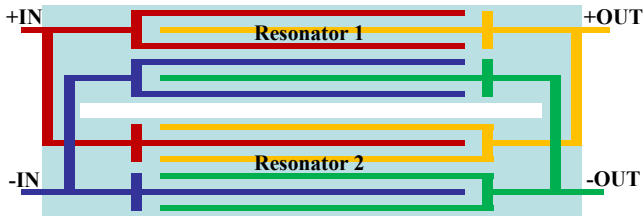


Figure 7: a) Two identical differential resonators placed in parallel. b) Mirrored layout used to match the input and output impedances of the filter.

The resonator impedance,  $R_x$ , was scaled in the RF modeling software until the desired pass band response was obtained. Note that equations (5-7) were not developed at the time however the

value of  $R_x$  (table 1) found through simulation agrees well with the value predicted by (7) assuming an unloaded Q between 600 and 700. In addition a shunt inductor,  $L_s$ , (figure 6a) was used to remove the shunt capacitance at the filter inputs and outputs. Since both  $R_x$  and  $C_s$  scale with resonator area,  $L_s$  must be scaled as well. Ultimately IL is limited by the Q of  $L_s$  as this dictates how well the shunt capacitance can be resonated out. Finally, to obtain resonator center frequencies in small steps of 4.4 MHz around 460 MHz is difficult by changing only resonator electrode spacing. This is due to the manufacturing grid used to make the photolithographic masks for the top electrode. It sets the minimum allowed increment in the electrode spacing ( $\lambda/2$ ). Hence wavelength must be an integer multiple of eight times the grid size, (9). Hence for a given grid size and material speed,  $c_m$ , all possible frequencies can be calculated using  $f_{\text{center}} = c_m / \lambda$ . Where lambda is given by (9).

$$\lambda = 8 \times \text{grid size} \times M, \quad M \in \text{Integers} \quad (9)$$

For a material speed of 8700 m/s, a grid size of 5 nm,  $M = 472$  yields a center frequency of 460.81 MHz. Incrementing or decrementing  $M$  by one changes the center frequency by approximately 1 MHz. However, incrementing  $M$  to obtain exactly 4.4 MHz is not possible and the error can be quite large. As a result we have adopted a method of varying electrode width,  $w_e$  (figure 1), for fine tuning of resonator center frequency.

## EXPERIMENTAL RESULTS

As was mentioned in the previous section, several filters were designed, fabricated and tested. The target and measured filter parameters are given in tables 1 and 2. It should be pointed out that impedance matching networks at the input and output ports were used to reduce ripple for the 5 and 23 MHz bandwidth filters. This was done in a RF simulation tool using the filters measured s-



parameters. The matching network consisted of four shunt inductors,  $L_s$ , each having a Q of 20. In addition the port impedances were increased to 150  $\Omega$  for the 23 MHz filter. Figure 8 shows the measured results (after matching in GENESYS™) for the three filters. The basic lattice and balun lattice models agreed well with the simulated results (dashed lines in figure 8). However, the differential lattice filter (23 MHz) did not. It was discovered that this difference was due to a modeling oversight. The model did not capture the differential resonator. Instead, it consisted of three basic lattice filters with single input/output resonators. Hence, it did not fully capture the interaction between differential resonators. A new model with differential resonators was developed which agreed well with the 23 MHz filter performance. Interestingly, the modeling error indicates two possible ways of improving the filters performance. First, by using the basic lattice topology instead of the differential lattice. Second, it was found (through simulation) that by balancing the number of resonator input and output electrodes for each port (+IN, -IN, +OUT, -OUT) the differential lattice filter performance is similar to the original model (figure 8).

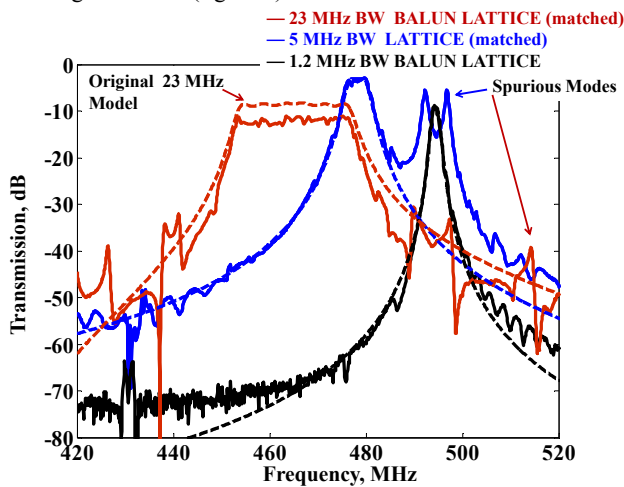


Figure 8: Measured Transmission of lattice filters. RED: 5.3 % BW at 463.5 MHz. BLUE: 1 % BW at 478 MHz. BLACK: 0.24 % BW at 494 MHz. Measured with AGILENT E5071C using SOLT calibration. All terminated with 50 ohms except 23 MHz BW filter (Table 2). Dashed lines show transmission predicted by models.

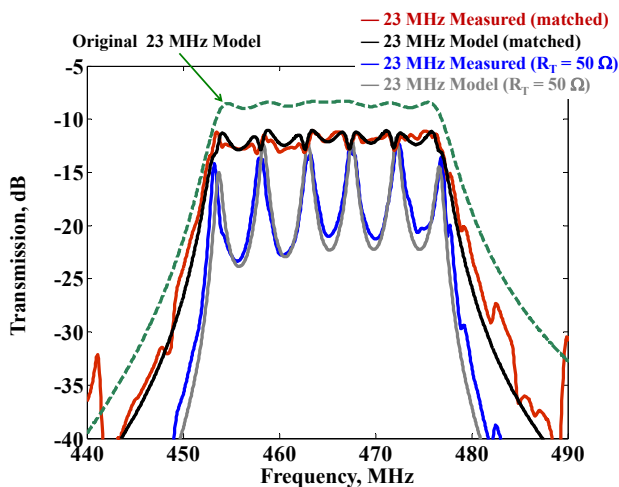


Figure 9: Comparison between original, (dashed green), and new 23 MHz filter models, (black and grey) with fully differential resonators and measured data (red and blue).

Figure 9 shows the results of the new model. There is close agreement with the modeled and measured results once the differential resonators were fully modeled. There is a large amount of ripple in the pass band of the 23 MHz filter when compared to the original model (figure 8). We believe the cause of the ripple is due to the use of unbalanced differential resonators.

Finally, the 5MHz basic lattice in figure 8 has very significant spurious modes in the measured transfer function. We are currently investigating methods to remove or minimize these modes. We also observed spurious modes outside the filter band of the other filters, however, they are not as severe (figure 8).

## CONCLUSIONS

This work demonstrates three different filters based on the parallel lattice topology. The PL filter topology uses parallel electrically coupled lattice networks to achieve a wide bandwidth filter response. It is particularly well suited for implementation with AIN contour mode resonators as they provide key technological advantages which enable parallelization of lattice networks: small feed through capacitance, multiple frequency resonators on a single chip, and single-ended-to-differential conversion. We have demonstrated 1 % bandwidth filters with insertion losses as low as -2.9 dB at 500 MHz. In addition, > 5% bandwidth filters have been achieved exceeding the  $k_r^2$  limit. To the best of our knowledge this is the first demonstration of the parallel lattice filter topology.

## ACKNOWLEDGEMENTS

The authors would like to thank the Microelectronics Development Laboratory staff at Sandia National Laboratories including Melanie Tuck, Jim Stevens and Craig Nakakura for AIN process development. This work was partially supported by Rockwell Collins, and we would like to acknowledge Bob Newgard, Chris Conway and Dr. Bob Potter of Rockwell Collins for that support. Sandia National Laboratories is a multiprogram laboratory operated by the Sandia Corporation, Lockheed Martin Company, for the United States Department of Energy's National Nuclear Security Administration under contract DE-AC04-94AL85000.

## REFERENCES

- [1] M. U. Demirci, C. T.-C. Nguyen, "Single-resonator fourth-order micromechanical disk filters," 18th IEEE International Conference on Micro Electro Mechanical Systems, 2005, pp. 207-210, 2005.
- [2] TriQuint data sheet for 479.5 MHz SAW filter, Part # 855271, www.triquint.com.
- [3] R. H. Olsson III, K. E. Wojciechowski, M. R. Tuck, J. E. Stevens and C. D. Nordquist, "Multi-Frequency Aluminum Nitride Micro-Filters for Advanced RF Communications," Government Microcircuit Applications and Critical Technology Conference, March 2010, In-Press.
- [4] A. I. Zverev, Handbook of Filter Synthesis, John Wiley & Sons, New York, 1967.
- [5] G. Piazza, "Piezoelectric Aluminum Nitride Vibrating RF MEMS for Radio Front-End Technology", P.h.D. Thesis, Department of Electrical Engineering and Computer Science, University of California, Berkeley, 2005, p 69.

## CONTACT

\*K. E. Wojciechowski, tel: +1-505-284-0034; kwojcie@sandia.gov

# STABLE OSCILLATION OF MEMS RESONATORS BEYOND THE CRITICAL BIFURCATION POINT

H.K. Lee<sup>1\*</sup>, J.C. Salvia<sup>2†</sup>, S. Yoneoka<sup>1</sup>, G. Bahl<sup>2</sup>, Y.Q. Qu<sup>1</sup>, R. Melamud<sup>1‡</sup>,  
S. Chandorkar<sup>1</sup>, M.A. Hopcroft<sup>1‡</sup>, B. Kim<sup>1\*</sup>, and T.W. Kenny<sup>1</sup>

<sup>1</sup>Department of Mechanical Engineering, Stanford University, Stanford, California, USA

<sup>2</sup>Department of Electrical Engineering, Stanford University, Stanford, California, USA

## ABSTRACT

MEMS resonators have many useful features, but they can suffer performance limitations because of the limited linear range of motion of their micromechanical elements. Operation beyond the critical bifurcation limit is believed to cause significant instabilities and is generally discouraged [1]. However, the stability criterion for closed-loop oscillators differs from that for open-loop observation [2], thereby enabling operation of stable oscillators beyond the limit dictated by critical bifurcation. This paper describes the use of phase-controlled oscillators to prove stable operation beyond the critical bifurcation limit, which can directly improve the power handling capabilities of many micromechanical oscillators.

## INTRODUCTION

MEMS resonators are considered as the next generation frequency reference because of their miniaturization-friendly characteristics [3]. Frequency references are an essential component of electronic devices, and quartz crystal-based references (quartz resonators) have dominated the market. Although quartz resonators have many advantages, they have become a bottleneck in the miniaturization of electronic devices because the process of manufacturing them is hard to integrate with the current semiconductor fabrication processes. However, MEMS resonators can be batch fabricated with a standard semiconductor fabrication process. Therefore, they have the potential to provide micro-scale frequency references at a low cost. Hence, they tend to be more adequate for frequency references in miniaturized electronics.

The power handling performance of MEMS resonator-based oscillators is of great interest since phase noise, which is one of the important characteristics of a frequency reference, often scales inversely with carrier power. Even though MEMS resonators offer many promising attributes, the phase noise performance of MEMS resonator-based oscillators needs to improve for use in radio communications. Since the phase noise, especially the far-from-carrier phase noise, decreases with larger carrier power, researchers have developed various methods to enhance the power handling capacities of MEMS resonator-based oscillators [4,5]. Agarwal et al. utilized the balance between the electrical softening effect and the mechanical stiffening effect to attain larger power handling in linear resonators [4].

Although larger vibration amplitude would be favorable for power handling performance, nonlinearities arise in most MEMS resonators, and the onset of critical bifurcation is believed to set the limit [1]. Since the output current from a MEMS resonator is proportional to the mechanical vibration amplitude, we can achieve larger power handling by increasing the range of motion of the micromechanical elements. However, the maximum range of motion has not been exploited because of the belief of the instability at large amplitude [1]. Most MEMS resonators have nonlinearities that arise when the vibration amplitude is large, and

they cause the amplitude dependent frequency change, also called the Duffing or A-f effect, and this phenomenon is well understood [2,6]. If the amplitude becomes larger than the critical bifurcation point, multiple amplitude solutions exist for some driving frequencies, as shown in Figure 1, where resonators can lose stability. Open-loop observation of the amplitude-frequency (A-f) curve of resonators using a network analyzer reinforced this idea. When a resonator operates in the nonlinear regime, part of the A-f curve is unobservable in open-loop measurement because of instability in the vicinity of the critical bifurcation point. In addition, designers often associate the idea of instability in open-loop observation with instability in closed-loop system [1]. Thus, the critical bifurcation point has constrained the maximum vibration amplitude of MEMS resonator-based oscillators.

The stability criteria for the open-loop system cannot be directly applied to the closed-loop system since they have different driving conditions. While a network analyzer sets a driving frequency during an open-loop measurement, the feedback circuit in a closed-loop oscillator sets a phase between the input and output of a resonator. Because of this difference, the stability condition of a closed-loop system differs from that for an open-loop system; a resonator within a closed-loop system is stable in any amplitude and frequency condition, regardless of the critical bifurcation [2]. In order to experimentally demonstrate stable operation of MEMS resonator-based oscillators beyond the critical bifurcation point, we utilized a phase-controlled oscillator to measure A-f points that constitute the A-f curve.

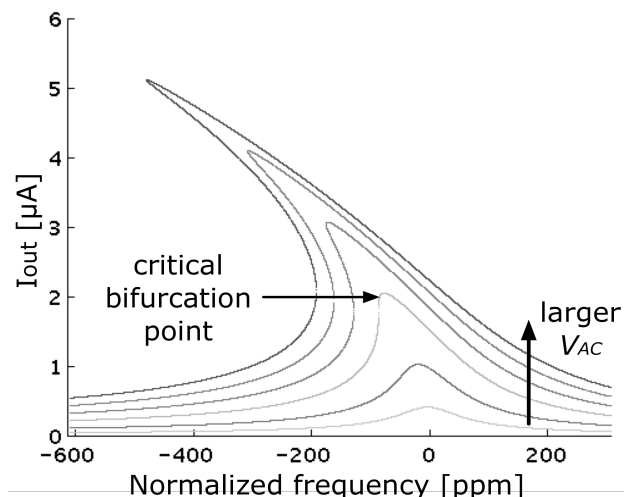


Figure 1: Theoretical amplitude-frequency (A-f) curves of a resonator at various driving conditions. When an A-f curve is below the critical bifurcation point, the frequency-to-amplitude relation is a one-to-one function. However, when an A-f curve is above the critical bifurcation point, the frequency-to-amplitude relation becomes one-to-many for some frequencies.

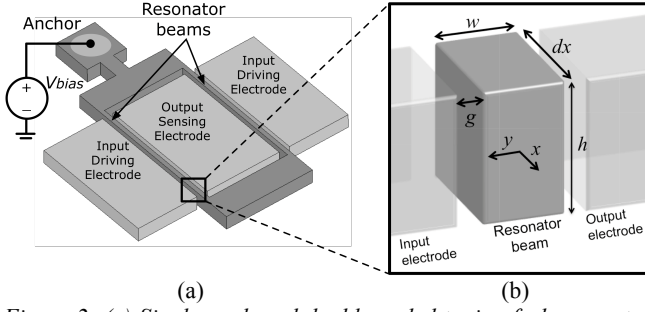


Figure 2: (a) Single-anchored double-ended tuning fork resonator for this study. (b) Differential element of a resonator beam.  $x$  is the longitudinal direction, and  $y$  is the direction of beam displacement.  $h$  is the height of the beam,  $w$  is the width of the beam, and  $g$  is the size of the transduction gap.

## THEORY

### Flexural Mode Beam Resonator

We used single-anchored double-ended tuning fork (SA-DETF) type flexural mode silicon resonators for this study. We have fabricated MEMS resonators by using the ‘epi-seal’ process introduced in [7]. Among many types of resonators that can be realized under the ‘epi-seal’ process, DETF type resonators have shown reliable performance [8]. In addition, single-anchored resonators experience only the electrical softening effect in the first order [5]; thus, they go into the nonlinear regime easily and predictably. Therefore, SA-DETF resonators are appropriate for this study. Figure 2a shows the SA-DETF resonator that we used for the experiment. The beams are  $200 \mu\text{m}$  long,  $6 \mu\text{m}$  wide, and  $20 \mu\text{m}$  thick. The transduction gap is  $1.5 \mu\text{m}$ . The resonant frequency of the resonator is about  $1.33 \text{ MHz}$ .

We operate resonators by using electrostatic actuation and sensing, and the nonlinearity arises from the electrostatics. For actuation, we apply the bias voltage ( $V_{bias}$ ) to the resonant beams, and supply a stimulus AC signal ( $v_{AC}$ ) to the input electrodes. In order to detect the output signal by using capacitive sensing, we virtually ground the output electrode. Then, the net electrostatic force on a differential element (Fig. 2b) is given as follows:

$$f_{ES}(x,t) = \frac{\epsilon_0 h}{2} \left[ \frac{(V_{bias} - v_{AC}(t))^2}{(g - v(x,t))^2} - \frac{V_{bias}^2}{(g + v(x,t))^2} \right] \quad (1)$$

where  $\epsilon_0$  is the vacuum permittivity,  $v$  is the beam displacement in  $y$ -direction, and  $f_{ES}$  is position and time dependent electrostatic force for unit length of the beam. If we combine equation 1 with the force balance equation of the differential element, we get

$$\rho_{mass} \frac{\partial^2 v}{\partial t^2} + c \frac{\partial v}{\partial t} = -B \frac{\partial^4 v}{\partial x^4} + f_{ES}(x,t) \quad (2)$$

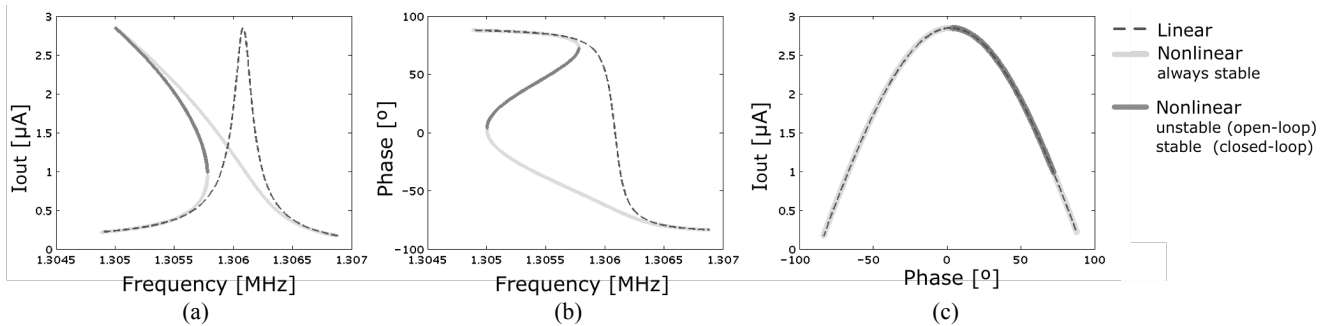


Figure 4: Theoretical amplitude-frequency-phase relation when a resonator is in the nonlinear regime (solid lines). The same relation when nonlinearities are not considered is also drawn for comparison (dashed lines). Entire solid lines are stable, thus observable, from closed-loop observation with a phase-controlled oscillator. However, parts of solid lines are unstable from open-loop observation.

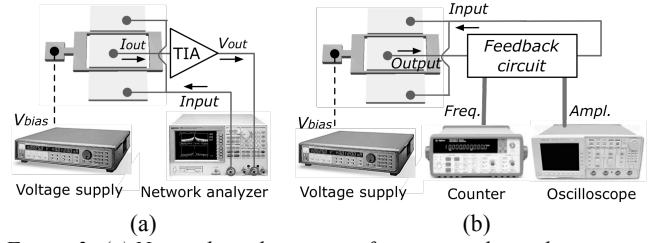


Figure 3: (a) Network analyzer setup for an open-loop observation. Voltage supply sets bias voltage ( $V_{bias}$ ), and trans-impedance amplifier (TIA) converts output current to voltage. (b) Oscillator setup for a closed-loop observation.

where  $\rho_{mass}$  is the mass per unit length,  $c$  is the damping coefficient, and  $B$  is the bending stiffness. Since the electrostatic force term in equation 2 is nonlinear with respect to  $v$ , as shown in equation 1, the resonator system described in equation 2 is a nonlinear system.

In order to estimate the nonlinear behavior of a resonator, we use an approximate method. First, we approximate the electrostatic force term in equation 2 by using the Taylor series expansion with the assumption of small  $v$ .

$$f_{ES}(x,t) \approx \frac{\epsilon_0 h V_{bias}}{g^2} \left[ v_{AC}(t) + \frac{2V_{bias}}{g} v(x,t) + \frac{4V_{bias}}{g^3} v(x,t)^3 \right] \quad (3)$$

After that, we can estimate the vibration amplitude and the resonant frequency at each of driving amplitudes by using the harmonic balance method [6].

### Stability Criterion for Each Driving Condition

An open-loop system and a closed-loop system have totally different driving conditions. Figure 3a shows a resonator within the open-loop system. A network analyzer in the open-loop system provides  $v_{AC}$  with a given frequency and measures the response at that frequency, and it obtains the A-f curve of a resonator by measuring at many frequency values. In short, the network analyzer sets a driving frequency. A resonator within a closed-loop system appears in Figure 3b. Unlike the network analyzer in the open-loop system, a feedback circuit in the closed-loop system determines a phase between the output current, or equivalently  $v$ , and  $v_{AC}$ . Although the circuit usually sets  $v_{AC}$  to lag  $v$  by  $90^\circ$  for the maximum vibration amplitude, other values of phase still can be used.

The stability conditions for both systems differ since they have different driving conditions, and stability is always guaranteed in a closed-loop system. With regard to the stability criterion for an open-loop system and a closed-loop system, Yurke et al. demonstrated rigorous mathematical derivation [2]. Besides,

we can develop intuition for the result of [2] from the frequency-amplitude-phase relation of a resonator in the nonlinear regime. Figure 4 contrasts the nominal frequency-amplitude-phase relation of a resonator that is in the nonlinear and the linear regimes. In the nonlinear case, the frequency-to-amplitude relation, shown in Figure 4a, is one-to-many for some frequencies. Therefore, the amplitude of a resonator is indeterminate for those driving frequencies, and this phenomenon causes instability in the open-loop system that sets a driving frequency. In addition, part of the A-f curve of a resonator in the nonlinear regime is unobservable because of the instability. However, the phase-to-amplitude and the phase-to-frequency relations are always a one-to-one function regardless of the nonlinearity, as shown in Figure 4b-c. For any given phase, a unique amplitude-frequency solution exists. Therefore, instability does not occur in the closed-loop system that sets an input-to-output phase rather than a driving frequency. Thus, the entire A-f curve becomes observable and stable oscillation above the critical bifurcation point becomes possible in a closed-loop oscillator.

### THE EXPERIMENTAL SETUP

We can measure a resonator's nonlinear A-f curve from a closed-loop system simply by implementing the phase-controlled feedback circuit. From the preceding section, we know that stable oscillation is possible at any driving condition when a resonator is in a closed-loop system. However, the closed-loop oscillator with a fixed input-to-output phase can give us only one frequency and amplitude pair that corresponds to a phase. In other words, we can measure one A-f point in the entire A-f curve by utilizing the fixed-phase closed-loop system. Since we need to measure the entire A-f curve that comprises multiple A-f points, we need to be able to access multiple A-f points using a closed-loop system. Therefore, a closed-loop system with controllable phase is necessary for this study.

We built an experimental setup with a minor modification to a standard feedback circuit to incorporate a phase shifter for phase controllability, as shown in Figure 5. The phase shifter stage allows manual control of the feedback circuit's phase in two stages in order to provide wide phase range. Automatic level control including a variable gain amplifier maintains the input driving voltage,  $v_{AC}$ . After the modification, the feedback circuit was integrated to the closed-loop system shown in Figure 3b. An oscilloscope monitors the output of the trans-impedance amplifier to estimate the output current amplitude, and a frequency counter measures the frequency of oscillation. Then, we used the experimental setup to measure the A-f points that constitute the A-f curve, including operation points that are not accessible to ordinary fixed-phase oscillators.

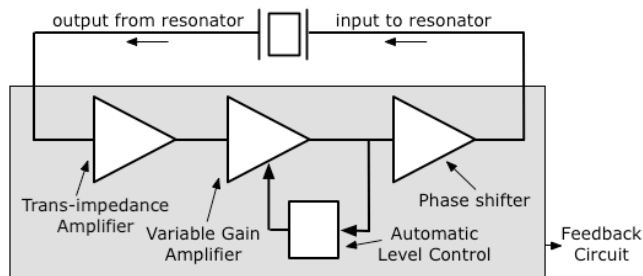


Figure 5: Circuit diagram of the phase-controlled feedback circuit. The trans-impedance amplifier (TIA) converts current to voltage. The variable gain amplifier and automatic level control maintain the drive amplitude ( $v_{AC}$ ), and the phase shifter sets the phase.

### RESULTS

We measured the A-f characteristic of the resonator, shown in Figure 1a, at several  $V_{bias}$  and  $v_{AC}$  conditions by using the phase-controlled closed-loop system. Since we wanted to measure the output current around the critical bifurcation as well as the maximum achievable output current in the system, we decided to use many  $V_{bias}$  and  $v_{AC}$  values: 45 V and 60 V for  $V_{bias}$ , and 0.18 V, 0.30 V, and 0.42 V for  $v_{AC}$  amplitude. We manually changed the input-to-output phase of the feedback circuit shown in Figure 3b, and measured amplitude and frequency values at various phase values. The measured nonlinear A-f curves appear in Figure 6.

We demonstrated stable oscillation of the resonator above the critical bifurcation point, and improved the power handling by exploiting the nonlinear regime. We could obtain nonlinear A-f curves, which appear in Figure 6, from the closed-loop system. Thus, we experimentally proved the stability of a resonator in the nonlinear regime. In addition, Figure 7 shows a time-domain waveform at the highest current amplitude. Since the waveform is stable, we can further state the stability above the critical

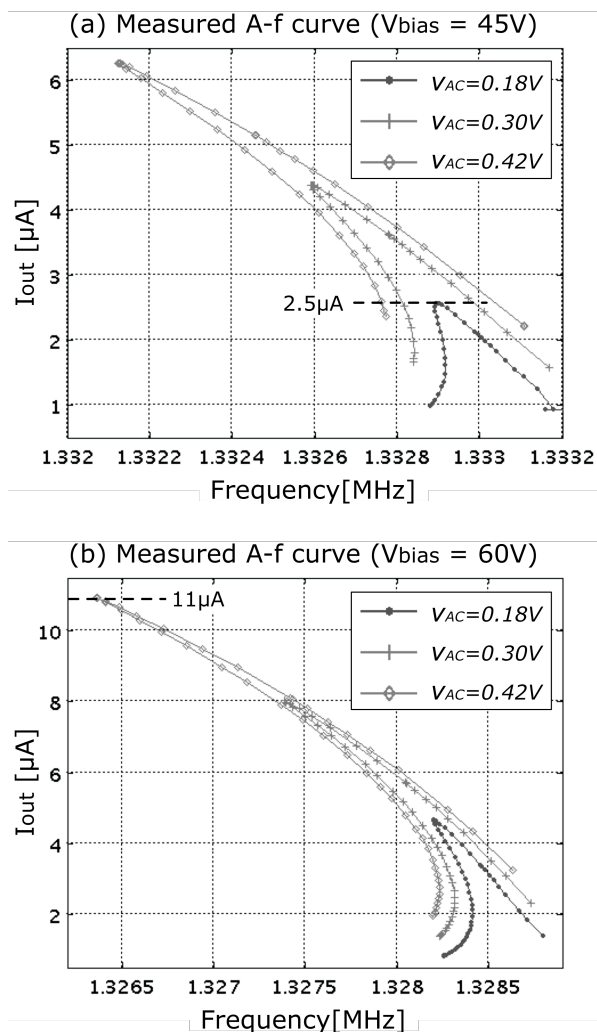


Figure 6: Measured A-f curves using the phase-controlled feedback circuit for 3 different values of  $v_{AC}$  and 2 different values of  $V_{bias}$ . Numerous phase values are used for each driving condition to measure A-f points (points with a marker) that constitute an A-f curve. More nonlinear frequency shift is observed at larger  $V_{bias}$  and  $v_{AC}$  values.

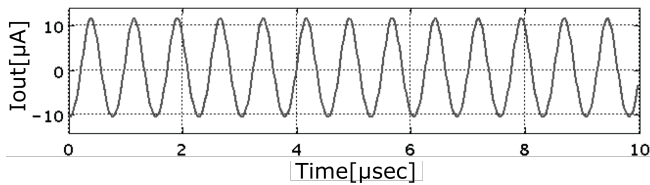


Figure 7: The output waveform of a resonator, which is converted from the output waveform of the trans-impedance amplifier of the feedback circuit (Fig.5), when the resonator is at the operating point with the highest current amplitude on Figure 6. Stable oscillation much above the critical bifurcation point is shown to be possible.

bifurcation point. In terms of the power handling improvement, we can compare the bottommost curve of Figure 6a and the uppermost curve of Figure 6b. The bottommost curve shows the A-f curve just above the critical bifurcation point and the uppermost curve shows the A-f curve with the largest power handling from this experiment. Comparing the peak current amplitude of two curves, we can notice that the peak of the uppermost curve is 4.4 times larger than that of the bottommost curve. In other words, the power handling performance improves by almost 20x by exploiting the nonlinear regime.

## CONCLUSIONS

In this study, we demonstrate stable oscillation of MEMS resonator-based oscillators beyond the critical bifurcation point. Considering that the maximum drive limit has not yet been determined, there is still further room for improvement of the current handling, thereby the power handling. In addition, the critical bifurcation point has constrained the resonator design optimization process [1,5]. Since it is no longer valid constraint, we now have more degrees of freedom in the design of MEMS resonators. Thus, we may design resonators with improved performance. Also, we can utilize the phase-controlled feedback circuit as a measurement tool to observe the nonlinear A-f characteristic of MEMS resonators. Since a part of nonlinear A-f curve is unobservable in open-loop observation with a network analyzer, the experimental setup in this study provides a better nonlinear characterization method. Therefore, it allows more capable analysis of nonlinear behaviors of MEMS resonators.

Future study will include the research on other limiting factors and on the phase noise performance. Although the critical bifurcation does not limit the vibration amplitude, it is highly probable that other mechanisms such as pull-in [9] limit the amplitude. Therefore, we will investigate other limiting mechanisms for the ultimate power handling performance. In addition, research on the phase noise performance in the nonlinear regime is ongoing since it is suspected that nonlinearities may worsen phase noise even if the power handling is improved [10].

## ACKNOWLEDGEMENTS

This work was supported by DARPA HERMIT (ONR-N66001-03-1-8942), the Bosch Palo Alto Research and Technology Center, the Samsung Scholarship, the National Science Foundation Graduate Fellowship, and the National Users Network facilities funded by the National Science Foundation under award ECS-9731294. The authors would especially like to thank Clark Nguyen, Amit Lal, and Andrei Shkel for their DARPA HERMIT program management.

† currently at SiTime Corporation, Sunnyvale, CA, USA

‡ currently at Hewlett-Packard Laboratories, Palo Alto, CA, USA

• currently at Sandia National Laboratories, Albuquerque, NM, USA

## REFERENCES

- [1] V. Kaajakari, T. Mattila, A. Oja, and H. Seppä, "Nonlinear Limits for Single-Crystal Silicon Microresonators", *Journal of Microelectromechanical Systems*, 13, 5 (2004).
- [2] B. Yurke, D.S. Greywall, A.N. Pargellis, and P.A. Busch, "Theory of Amplifier-Noise Evasion in an Oscillator Employing a Nonlinear Resonator", *Physical Review A*, 51, 5 (1995).
- [3] C.T.-C. Nguyen, "MEMS Technology for Timing and Frequency Control", *IEEE Transactions on Ultrasonics, Ferroelectrics, and Frequency Control*, 54, 2 (2007).
- [4] M. Agarwal, S.A. Chandorkar, R.N. Candler, B. Kim, M.A. Hopcroft, R. Melamud, C.M. Jha, T.W. Kenny, and B. Murmann, "Optimal Drive Condition for Nonlinearity Reduction in Electrostatic Microresonators", *Applied Physics Letters*, 89, 214105 (2006).
- [5] M. Agarwal, *Nonlinearities and Phase Noise in Electrostatically-Transduced-MEMS-Resonator Based Oscillators*, Ph.D. dissertation at Stanford University, California, 2007.
- [6] C. Hayashi, *Nonlinear Oscillations in Physical Systems*, Princeton University Press, New Jersey, 1985.
- [7] R.N. Candler, M.A. Hopcroft, B. Kim, W.-T. Park, R. Melamud, M. Agarwal, G. Yama, A. Partridge, M. Luts, and T.W. Kenny, "Long-Term and Accelerated Life Testing of a Novel Single-Wafer Vacuum Encapsulation for MEMS Resonators", *Journal of Microelectromechanical Systems*, 15, 6 (2006).
- [8] B. Kim, R.N. Candler, M. Hopcroft, M. Agarwal, W.-T. Park, and T.W. Kenny, "Frequency Stability of Encapsulated MEMS Resonator", *Sensors and Actuators, A: Physical*, 136, 125 (2007).
- [9] A.H. Nayfeh, M.I. Younis, E.M. Abdel-Rahman, "Dynamic Pull-In Phenomenon in MEMS Resonators", *Nonlinear Dynamics*, 48, 153 (2007).
- [10] V. Kaajakari, J.K. Koskinen, and T. Mattila, "Phase Noise in Capacitively Coupled Micromechanical Oscillators", *IEEE Transactions on Ultrasonics, Ferroelectrics, and Frequency Control*, 52, 12 (2005).

## CONTACT

\*H.K. Lee, tel: +1-650-796-9882; hyungkyu@stanford.edu

# THERMO-ELECTRO-MECHANICAL MODELING OF HIGH FREQUENCY THERMALLY ACTUATED I<sup>2</sup>-BAR RESONATORS

Amir Rahafrooz and Siavash Pourkamali

Department of Electrical and Computer Engineering, University of Denver, Denver, CO, USA

## ABSTRACT

This work presents development of a comprehensive electrical equivalent model for thermally actuated high frequency MEMS resonators with piezo-resistive readout and verification of the model with experimental results. We have previously demonstrated experimentally that as opposed to the general presumption, thermal actuation could be a very suitable mechanism for actuation of high frequency (VHF, UHF and higher) resonators and it becomes more powerful as the resonator dimensions are shrunk down [1]. Here, a combination of analytical, finite element and numerical analysis has been carried out to further justify this argument and allow prediction and optimization of the behavior of such resonators. It is demonstrated that thermal-piezoresistive nanomechanical resonators in the GHz frequency range, can provide motional conductance as high as 1mA/V with static power consumptions in the order of a few  $\mu$ W.

## INTRODUCTION

As a promising emerging technology for the next generation integrated frequency references, electronic filters, and resonant sensors, micromechanical resonators have been the center of significant attention over the past few years [2-6]. A wide variety of high frequency micro and nanoscale electromechanical resonators have been developed, most of which use piezoelectric [3,4] or electrostatic (capacitive) [5,6] electromechanical transduction. Piezoelectric micro-resonators require deposition of piezoelectric and metal thin films generally resulting in lower quality factors and frequency and quality control issues. In case of capacitive resonators, the weak electromechanical coupling leads to the need for deep submicron transduction gaps, associated with excessive squeezed film damping when operating in air (e.g. for sensory applications), fabrication challenges, and power handling limitations.

Thermal actuation is another well known mechanism that can be implemented at microscale without any fabrication challenges or the need for inconvenient material integration. It also has great properties such as large actuation force, low operating voltage and simplicity of design and integration. On the downside, power consumption and high body temperature of such actuators could limit their application in some cases. Furthermore, thermal actuators are usually considered and referred to as slow actuators only suitable for DC or very low-frequency applications. Consequently, although thermally actuated micromechanical resonant devices with frequencies in the hundreds of kHz have been utilized for chemical [7] or physical [8] sensory applications, there has been very little study on utilization of thermal actuation in high frequency resonant devices. In our previous work [1] we demonstrated thermally actuated resonators with frequencies as high as 61MHz (Fig. 1) using resonant structures usually referred to as I<sup>2</sup>-Bulk Acoustic wave Resonators (I<sup>2</sup>-BARs), or dog-bone resonators [5]. It was also briefly argued and shown experimentally that as opposed to the capacitive and piezoelectric actuators, for which actuator surface area is imperative for maintaining the required actuation force and output signal amplitude, thermal actuators become more powerful as the resonator dimensions are scaled down into the nanoscale to reach higher resonant frequencies.

In this work a comprehensive electrical equivalent model for thermally actuated high frequency MEMS resonators with piezo-resistive readout is developed and verified using the experimental results. The main goal is to study the transduction behavior of thermally-piezoresistive I<sup>2</sup>-BAR resonators with nanoscale dimensions operating in the GHz range. The model confirms that as the resonator dimensions are shrunk down the performance of thermally actuated resonators improves and higher or similar current gains can be achieved while consuming smaller DC power. Also this model paves the way to further optimize the resonator dimensions and structures.

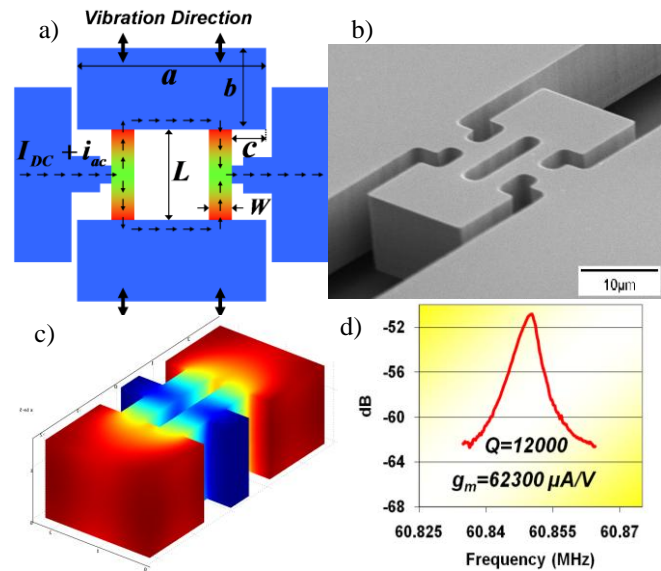


Figure 1: a) Top view schematic diagram of a thermally actuated I<sup>2</sup>-BAR showing the current flow through the structure; b) SEM view of a fabricated 61MHz 15µm thick I<sup>2</sup>-BAR; c) Finite element modal analysis of the in-plane resonant mode of the structure (Red and blue show the maximum and minimum vibration amplitudes respectively); d) A measured resonance peak from the same device.

## THERMO-ELECTRO-MECHANICAL MODELING

I<sup>2</sup>-BARs can be thermally actuated by applying a combination of DC and AC voltages between their two pads. This results in an alternating ohmic loss component with the same frequency as the input AC signal in the structure:

$$P_{ac} = \frac{2V_{dc}v_{ac}}{R_A} \quad (1)$$

where  $R_A$  is the electrical resistance of the thermal actuators and  $V_{dc}$  and  $v_{ac}$  are the DC and AC actuation voltages. The resulting temperature fluctuations in the thinner extensional bars in the middle of the structure actuate the structure in its in-plane resonant mode. The same pillars also act as piezoresistors modulating the DC current passing through them due to the alternating stress at resonance. Therefore, the overall input to output transfer function of the system can be divided into three sub-systems of thermal, mechanical and electrical nature as shown in Fig. 2a.

Figure 2b shows the equivalent electrical circuits of the thermal subsystem. The thermal equivalent circuit consists of a capacitance and a resistance representing the thermal capacitance and thermal resistance of the thermal actuators resulting in the following small signal electrical to thermal transfer function:

$$H_{th}(s) = \frac{T_{ac}}{v_{ac}} = \frac{2V_{dc}R_{th}}{R_A(1 + R_{th}C_{th}s)} \quad (2)$$

where  $T_{ac}$  is the fluctuating temperature amplitude,  $R_{th}$  and  $C_{th}$  are the effective thermal resistance and capacitance of the actuator, and  $s=j\omega$  is the Laplace transform parameter.

The force generated by the resulting thermal stress can be calculated as:

$$F = 2\alpha T_{ac}AE \quad (3)$$

Where  $\alpha$  is the thermal expansion coefficient of the thermal actuator structural material,  $A$  is the thermal actuator cross sectional area, and  $E$  is the Young's modulus of the thermal actuator along its length. The coefficient "2" has been added since there are two actuator beams in each resonator contributing to the actuation force.

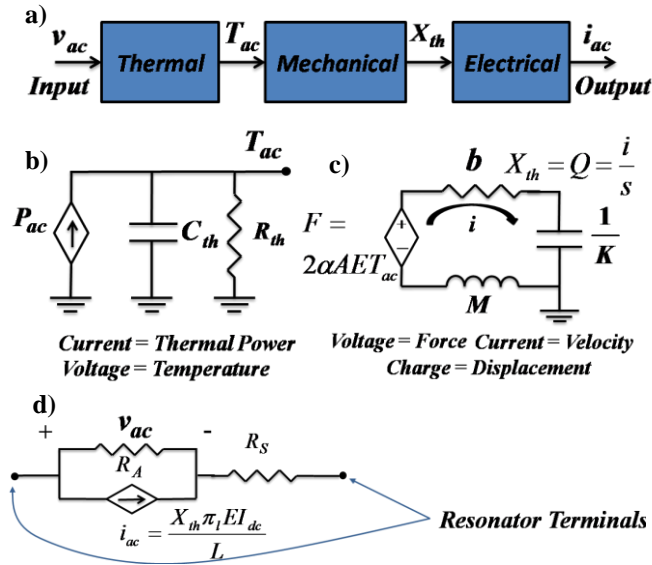


Figure 2: a) Block-diagram demonstration of the thermo-electro-mechanical model of the resonator that can be divided into three sub-systems of thermal, mechanical and electrical nature; b) Equivalent electrical circuit for the thermal sub-systems; c) Equivalent electrical circuit for the mechanical sub-systems; d) Equivalent electrical circuit for the electrical sub-system.

In the equivalent electrical circuit of the mechanical subsystem shown in Fig. 2c, the voltage source represents the thermally generated mechanical force, and the inductor, capacitor, and resistor represent the effective mechanical mass, stiffness, and damping of the resonator respectively. Consequently, current represents velocity and charge ( $Q = \int i dt$ ) represents displacement. Therefore:

$$X_{th}(s) = Q(s) = \frac{i(s)}{s} = \frac{F}{(Ms^2 + bs + K)} \quad (4)$$

where  $M$ ,  $K$  and  $b$  are the effective mechanical mass, spring constant and damping coefficient of the structure,  $X_{th}$  is the

elongation amplitude of the thermal actuator. Replacing the actuation force from Eq. 3 into Eq. 4 results in the following transfer function for the mechanical subsystem:

$$H_m(s) = \frac{X_{th}(s)}{T_{ac}} = \frac{2\alpha AE}{(Ms^2 + bs + K)} \quad (5)$$

The undamped resonance frequency of the resonator is  $\omega_0 = \sqrt{K/M}$  and its intrinsic quality factor is  $Q = M\omega_0/b$ . At the resonance frequency, the mechanical stiffness and mass in the mechanical transfer function cancel each other out and  $H_m$  is simplified to:

$$H_{m,res} = \frac{X_{th}(s)}{T_{ac}} \Big|_{s=j\omega_0} = \frac{2\alpha AEQ}{Mj\omega_0^2} = \frac{2\alpha AEQ}{jK} \quad (6)$$

where  $j = \sqrt{-1}$  showing that the mechanical displacement is lagging behind the temperature (and force) fluctuations by  $90^\circ$ , which is typically the case for mechanical resonators at resonance. The displacement, which is the output of the mechanical subsystem, causes a change in the resistivity of the thermal actuators due to the piezoresistive effect:

$$r_{ac} = R_A \pi_l E \frac{X_{th}}{L} \quad (7)$$

where  $\pi_l$  is the longitudinal piezoresistive coefficient of the actuator beams,  $r_{ac}$  is the amplitude of the actuator resistance fluctuations, and  $L$  is the length of the thermal actuators. Since a DC bias voltage is applied to the thermal actuators, this change in resistance modulates the current in the actuators:

$$i_{ac} = \frac{r_{ac}}{R_A} I_{dc} \quad (8)$$

Therefore, the transfer function of the electrical subsystem (Fig. 2d) will be as follows:

$$H_e = \frac{i_{ac}}{X_{th}} = \frac{\pi_l EI_{dc}}{L} \quad (9)$$

Finally, the overall transfer function that relates the AC motional current to the AC input voltage is the product of the three transfer functions of the thermal, mechanical and electrical subsystems:

$$H_T = \frac{i_{ac}}{v_{ac}} = H_{th} H_m H_e = \frac{4\alpha AE^2 I_{dc}^2 \pi_l}{L(Ms^2 + bs + K)} \frac{R_{th}}{(1 + R_{th}C_{th}s)} \quad (10)$$

At resonance:

$$H_T \Big|_{s=j\omega_0} = \frac{4\alpha E^2 \pi_l Q A I_{dc}^2}{KLj} \frac{R_{th}}{(1 + R_{th}C_{th}s)} \quad (11)$$

If  $\omega \gg \tau_{th}^{-1} = (R_{th}C_{th})^{-1}$ , which is usually the case for the resonator dimensions in this work,  $H_T$  simplifies to:

$$H_T \Big|_{s=j\omega_0} = g_m = 4\alpha E^2 \pi_l Q \frac{A I_{dc}^2}{KLC_{th}\omega_m} \quad (12)$$

The transfer function in Eq. 12 can be referred to as small signal voltage to current gain, or motional conductance ( $g_m$ ) of the resonator at its resonance frequency.

**Resonator Equivalent Electrical Circuit:** For the single-port I<sup>2</sup>-BAR resonators demonstrated in [1], where the same thermal actuators also act as piezoresistive sensors, the physical resistance of the resonator connects the input and output of the resonators. Therefore, the equivalent electrical circuit includes a resistance  $R_A + R_s$  connected between the two terminals of the resonator, which is the overall resistance in the current path between the two pads of the resonator.  $R_s$  is the parasitic resistance in the current path which is not part of the actuators (mostly support beams). In parallel to the static resistance of the actuators, there needs to be a series RLC combination with the values shown in Fig. 3 that represents the mechanical resonant behavior of the structure.

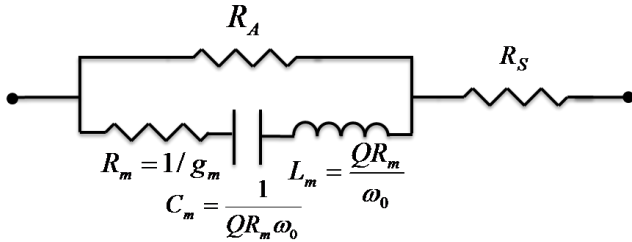


Figure 3: overall equivalent electrical circuit for one-port thermally actuated resonators with piezo-resistive readout.

**Calculation of Actuator Thermal Capacitance:** To calculate the  $g_m$  of a thermal-piezoresistive I<sup>2</sup>-BAR, which is the most important parameter to be extracted from the model; all the parameters except the effective thermal capacitance of the actuators ( $C_{th}$ ) are known for every set of resonator dimensions. Due to the distributed nature of the thermal parameters including thermal generator (resistance of the structure), thermal capacitance and thermal conductance, analytical derivation of the effective equivalent values for the thermal parameters could be quite complicated. Therefore, COMSOL finite element analysis was used to analyze the AC thermal behavior of the actuators and calculate the fluctuating temperature amplitude ( $T_{ac}$ ) at different points along the length of the actuator beams (Fig. 4). The mean value of the small signal temperature amplitudes at different points along the actuators is the effective temperature fluctuation amplitude for the actuator.

If  $\omega \gg \tau_{th}^{-1} = (R_{th} C_{th})^{-1}$ , i.e. the thermal time constant of the actuator is much larger than the mechanical time constant of the resonator, which is generally the case for the resonator dimensions in this work,  $C_{th}$  can be calculated using the value of ( $T_{ac}$ ) obtained from the finite element analysis and a rearranged and simplified version of Eq. 2:

$$C_{th} = \frac{I_{dc} I_{ac} R_A}{T_{ac} \omega_m} \quad (13)$$

## RESULTS

In order to verify the validity of the derived models, several measurement results for I<sup>2</sup>-BAR resonators with different dimensions were compared to the values predicted by the model (Table 1). There is a good agreement between the measured and calculated  $g_m$  values for most of the data points. Considering the several possible sources of error the discrepancies between measurement and calculations seem to be quite justified. Some of the major sources of error include errors in calculation of the motional conductance from the logarithmic measured transmission data (from the network analyzer) and de-embedding the parasitic resistances, uncertainty in resistivity and other physical properties

of the structural material (e.g. piezoresistive coefficient) and dimensions, as well as changes in the material properties at elevated temperatures.

To further emphasize and demonstrate our hypothesis of thermal actuation becoming more suitable for higher frequency resonators, two scaled down versions of the resonator of Fig. 1 with resonant frequencies of 900MHz and 2.1GHz were analyzed using the developed model. As shown in Table 1, similar  $g_m$  as the 61MHz resonator can be achieved for the higher frequency resonators with significantly reduced DC bias current and power consumptions. Table 1 also includes examples of improved resonator dimensions for further minimization of resonator power consumptions in the GHz range.

It is desirable to maximize the resonator motional conductance ( $g_m$ ) (for improved signal to noise ratio) with minimal power consumption. Therefore, a figure of merit for the resonators has been defined as the ratio of the resonator  $g_m$  to the overall DC power consumption and  $Q$  of the resonator:

$$F.M. = \frac{g_m}{Q \cdot P_{DC}} = 4\alpha E^2 \pi_1 \frac{A}{K L C_{th} \omega_m (R_A + R_s)} \quad (14).$$

As clearly seen in Table 1, resonator figures of merit clearly increase for similar resonators (same structural aspect ratios) as the resonator dimensions are shrunk down.

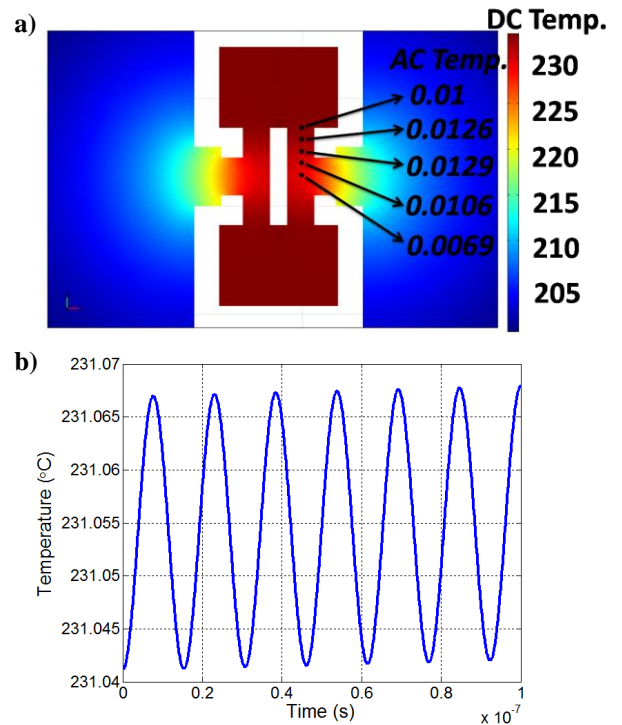


Figure 4: a) COMSOL finite element thermal analysis of the resonator of Figure.1 by applying DC and AC currents of 60mA and 5mA respectively. The color code shows static temperature of the structure resulting from the DC bias current, and the numbers show temperature fluctuation amplitude ( $T_{ac}$ ) of different points along the actuator; b) time domain temperature variations of a point in the middle of the thermal actuator showing  $T_{ac}$  of  $\sim 0.01^\circ\text{C}$ .



Table 1. Measurement and simulation results for thermal-piezoresistive  $I^2$ -BARs with different dimensions.

Scale Factor	Resonator Dimensions ( $\mu\text{m}$ )						Measured/Assumed Parameters				Calculated Parameters				
							Current (mA)	Q. Factor	Freq. (MHz)	$g_m$ (mA/V)	Power (mW)	$R_A$ ( $\Omega$ )	$g_m$ (mA/V)	F.M. ( $10^{-3}/V^2$ )	Power ( $\mu\text{W}$ ) @ $g_m=1$ (mA/V)
1X	274	30	67	31	4	10	16.8	29000	7.94	5.73	3.60	3.49	8.00	0.767	449
							40.5	37000	7.75	61.2	20.9	3.49	63.81	0.825	327
0.7X	193	21	47	22	2.7	10	26	24000	10.87	22.6	9.82	3.67	24.90	1.06	394
							30.5	16000	10.63	24.3	13.5	3.67	24.43	1.13	553
0.5X	144	16	35	16	2	10	21.3	12000	13.94	12.8	6.52	3.60	13.18	1.69	494
							30.2	7000	13.78	22.2	13.1	3.60	16.00	1.74	818
1X	80	53	16	64	17.4	10	55	28500	15.89	4.72	39.2	6.80	4.26	0.038	9191
							80	29000	15.65	17.5	82.8	6.80	9.60	0.040	8629
							50	10800	15.91	1.30	32.4	6.80	1.33	0.038	24346
							90	10900	15.73	9.30	105	6.80	4.50	0.039	23313
0.5X	39	25	8.5	32	8.5	10	20	29000	31.18	0.683	5.60	6.96	1.31	0.081	4276
							65	38500	30.72	24.2	59.2	6.96	19.21	0.084	3080
							30	11000	31.17	0.581	12.6	6.96	1.12	0.081	11264
							70	12000	30.9	6.17	68.6	6.96	6.82	0.083	10059
1X	22	15	4.4	18	5	15	60	14000	61.64	16.5	18.0	2.34	17.3	0.686	1041
							100	12000	60.85	62.3	50.0	2.34	42.8	0.713	1169
							60	7500	61.65	9.76	18.0	2.34	9.26	0.685	1945
							100	7700	61.11	37.5	50.0	2.34	27.1	0.704	1845
0.0723X	1.59	1.08	0.39	1.3	0.36	1.08	4.67	14000	900	-	1.57	32.6	17.3	7.87	90.7
0.5X Act.*							2.24	14000	904.5	-	0.378	32.6	17.3	32.7	21.8
0.25X Act.*							1.09	14000	905.7	-	0.0908	32.1	17.3	136	5.25
0.031X							1.99	14000	2100	-	0.667	79.1	17.3	18.5	38.6
0.5X Act.*	0.68	0.46	0.14	0.28	0.075	0.46	0.961	14000	2111	-	0.161	79.1	17.3	76.8	9.30
0.25X Act.*							0.475	14000	2113	-	0.0404	80.2	17.3	306	2.33
= data obtained under atmospheric pressure															

\* To improve the resonator figure of merit (lower power consumptions while maintaining the same  $g_m$ ), the actuator beams have been shrunk down in these devices while keeping the same size for the rectangular masses on their two ends.

## CONCLUSIONS AND FUTURE WORK

A comprehensive electrical equivalent model for thermally actuated high frequency  $I^2$ -BARs was derived and verified using measurement results. A good agreement between the measurement data and theoretical calculations was demonstrated. As the model predicts and measurement data confirms, relatively high motional conductances can be maintained for such resonators by consuming orders of magnitude less power as their dimensions are shrunk down into the nanoscale. Based on the analysis in this work, thermal actuation of nanoscale resonators with frequencies in the GHz range is theoretically feasible and the power consumption for such devices will be in the few  $\mu\text{W}$  range.

The model also provides the capability to further optimize the thermal-piezoresistive resonators to achieve stronger electro-thermo-mechanical coupling (higher  $g_m$ ), with lower power consumption.

## ACKNOWLEDGEMENTS

This work was supported by National Science Foundation under grants #0839951 and #0800961.

## REFERENCES

[1] A.Rahafrooz, A.Hajjam, B.Tousifar, and S.Pourkamali, "Thermal actuation, a suitable mechanism for high frequency electromechanical resonators," IEEE MEMS 2010.

[2] C. Nguyen, "MEMS technology for timing and frequency control," IEEE Trans. Ultrasonics, Ferroelectrics and Frequency Control, vol. 54, no. 2, pp. 251-270, Feb. 2007.

[3] B. P. Harrington, and R. Abdolvand, "Q-enhancement through minimization of acoustic energy radiation in micromachined lateral-mode resonators," Transducers 2009, pp. 700-703.

[4] M. Rinaldi, C. Zuniga, C. Zuo, and G. Piazza, "Ultra-thin Super High Frequency two-port ALN contour-mode resonators and filters," Transducers 2009, pp. 577-580.

[5] G.K. Ho, K. Sundaresan, S. Pourkamali and F. Ayazi, "Low impedance, highly tunable, I2-resonators for temperature compensated reference oscillators," MEMS'05, pp. 116-120.

[6] S. Pourkamali, et al, "Low-Impedance VHF and UHF Capacitive Silicon Bulk Acoustic-Wave Resonators—Part II," IEEE Transactions on Electron Devices, Volume 54, Issue 8, Aug. 2007, pp. 2024-2030.

[7] J. H. Seo and O. Brand, "High Q-Factor In-Plane-Mode Resonant Microsensor Platform for Gaseous/Liquid Environment," JMEMS 2008, Vol. 17, issue 2, pp. 483-493.

[8] A. Hajjam, J.C. Wilson, A. Rahafrooz, and S.Pourkamali, "Fabrication and characterization of resonant aerosol particle mass sensors," IEEE MEMS 2010.

## CONTACT

Siavash Pourkamali, 2390 S. York St., Denver, Colorado, USA, Phone: +1-303-871-2471, Email: spourkam@du.edu

# A MICROFABRICATED COMPREHENSIVE TWO-DIMENSIONAL GAS CHROMATOGRAPHY SYSTEM

Shaelah Reidy, Sung-Jin Kim, Katharine Beach, Bruce Block, Edward T. Zellers, Katsuo Kurabayashi, and Kensall D. Wise

Engineering Research Center for Wireless Integrated MicroSystems  
The University of Michigan, Ann Arbor, MI 48105

## ABSTRACT

This paper reports a thermally-modulated comprehensive two-dimensional chromatography system. A static stationary-phase coating process using non-polar polydimethylsiloxane (PDMS) and polar polytrifluoropropylmethylsiloxane (PTFPMS) produced a resolution of 14,425 and 5,800 theoretical plates, respectively, using an air carrier in 3m columns. With a meso-scale thermal modulator between a 3m-long PDMS-coated first-column and a 0.25m-long PTFPMS-coated second column and working from -25°C to 200°C with 100ms peak widths, a 10-component mixture of alkanes and ketones was separated. Replacing the meso-scale modulator with a microfabricated device operating between -30°C and 250°C (with heating/cooling rates of 3000°C/s and -570°C/s), heptane and 2-hexanone were separated with a 7s modulation period. They would co-elute from a one-dimensional system.

## INTRODUCTION

Gas chromatography (GC) is the most widely-used technique for separating, identifying, and quantifying volatile and semi-volatile organic compounds (VOCs and SVOCs), which are of concern in areas such as indoor and ambient air quality, climate change (global warming), industrial emissions control, and breath analysis. Measurements of these pollutants are essential to assessing the sources, sinks, and transport pathways of these compounds as well as their effects on the environment and its inhabitants.

The Engineering Research Center for Wireless Integrated MicroSystems (WIMS) at the University of Michigan is working to develop a completely microfabricated gas chromatograph for environmental monitoring. The microsystem uses preconcentration, separation, and gas sensing technologies that were developed by members of the WIMS  $\mu$ GC team. The system is designed for autonomous operation using ambient air as the carrier gas and a microfabricated pump to drive the separation. This microsystem is shown in Fig. 1. All of the system components have been achieved [1-4] and are capable of separating complex mixtures of VOCs with sub-ppb detection limits [5,6]. The separation of air-phase petroleum hydrocarbons utilizing a 3m-long microcolumn operating into a flame ionization detector is also shown in Fig. 1. Temperature programming is effective in these microfabricated components because of their very low mass and can speed up separations by more than an order of magnitude.

When analyzing highly-complex mixtures of 30-50 volatile organic compounds, achieving the required resolving power and avoiding co-elutions is a continuing challenge for one-dimensional separation systems. Since its invention over a decade ago, comprehensive two-dimensional gas chromatography (2D-GC, GCxGC) has been developed to separate and analyze complex mixtures (e.g., petroleum, flavors, environmental pollutants, breath biomarkers, and, in this case, extraterrestrial atmospheres). GCxGC employs two coupled columns of different selectivity, as in Fig. 1, but adds a modulator between the columns and subjects the entire sample to a two-dimensional separation. As effluent emerges from the primary column, it is collected and then rapidly

re-injected to produce sharp chemical pulses that are rapidly separated by the second column. The results can be displayed using the two orthogonal retention-time axes of the columns. The horizontal separation plane displays the time output of the first-dimension column, and the vertical plane shows the much faster elutions from the second. Usually, the first column is coated with a non-polar stationary phase and the second with a polar phase. This

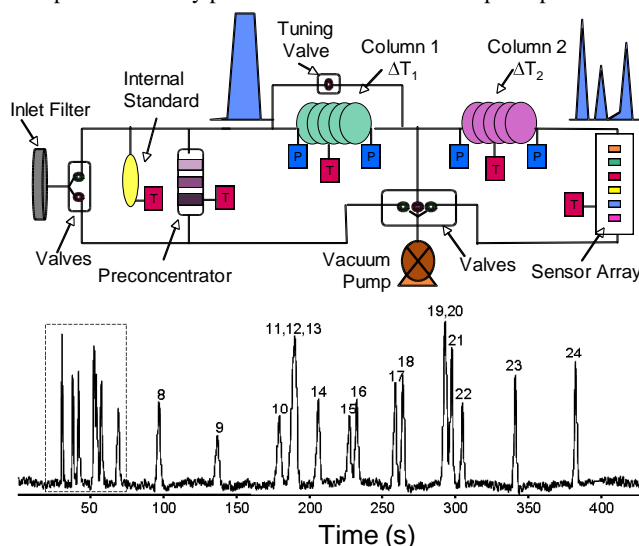


Fig. 1: Block diagram of a microfabricated chromatography-based gas analyzer (above), and a chromatogram showing the separation of air-petroleum hydrocarbons which utilizes the microcolumns.

combination allows components to be independently separated, first according to their volatility and then according to their polarity. In comparison to conventional one-dimensional gas chromatography, GCxGC has a much higher peak capacity because the available peak capacity is the product of the peak capacity of both dimensions. Other advantages of GCxGC include enhanced detectability due to analyte refocusing, true background around resolved peaks, and more reliable identification due to the use of two retention times and well-ordered bands of compound groups. The most important instrumental component in GCxGC is the modulator. Modulation is required to transfer the sample from the first (primary) column to the second column. The modulator continuously traps, focuses, and then re-mobilizes components eluting from the primary column, acting as a continuous injector for the secondary column. There are two classifications of modulators: pneumatic and thermal.

## GCxGC SYSTEM DESIGN

The GCxGC system consisted of a 3m-long nonpolar (PDMS-coated) first-dimension column, a thermal modulator, and a 0.50m-long polar (PTFPMS or polyethylene glycol (PEG)) second-dimension column. The first-dimension column provides

the primary separation of the sampled mixture based on volatility. This column is connected to the modulator, which is a two-stage device that traps and releases the compounds as it cycles repeatedly from low to high temperature. Two modulators have been used. The first was a meso-scale device formed from a 10cm-long 0.18mm-id PDMS-coated section of stainless-steel tubing and divided into two separately-heated sections, cycling between  $-25^{\circ}\text{C}$  and  $200^{\circ}\text{C}$ . The second was a microfabricated modulator ( $\mu\text{TM}$ ) [7,8] cycling from  $-35^{\circ}\text{C}$  to  $250^{\circ}\text{C}$ . The first and second stages of the  $\mu\text{TM}$  consisted of meander-line boron-doped-Si microchannels 4.2cm and 2.8cm long, respectively, with cross-sectional dimensions of  $250\mu\text{m}$  (w) x  $140\mu\text{m}$  (h) and having a wall thickness of  $30\mu\text{m}$ . Both modulators were coated with PDMS and were heated from a resting temperature provided by a cold chamber or thermoelectric cooler. Since movement of the analytes through the system is strongly dependent on temperature, decreasing the temperature essentially stops the movement of analyte while increasing the temperature rapidly increases it.

Modeling was done to determine the optimum column dimensions. Using Spangler's equation [9] for the height equivalent to a theoretical plate (H), which is a measure of column efficiency, the expected column performance was explored as a function of the linear column velocity. The resulting Golay plots are shown in Fig. 3 for 3m-long first-dimension column cross-sections of  $150\mu\text{m}$  (w) x  $240\mu\text{m}$  (d) and for  $158\mu\text{m}$  (w) x  $310\mu\text{m}$  (d). The latter dimensions were used for the final  $\mu\text{GC}$  reported here. The minimum H defines the optimum operating point for the column. The second-dimension columns were fabricated in 10cm and 25cm lengths ( $46\mu\text{m}$  wide and  $170\mu\text{m}$  deep). By chamfering the corners of columns there is about a 20% improvement in column performance. Fig. 3 illustrates this improvement by the decrease in plate height (H).

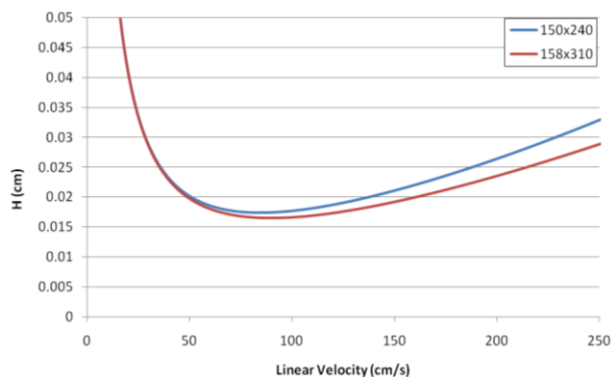


Fig. 2: Theoretical Golay plot of the improvement in column performance by increasing the column dimensions.

## FABRICATION

The separation columns have a square spiral geometry to minimize surface area (Fig. 4). The 3m-long primary column has a die size of  $3.2\text{cm}$  x  $3.2\text{cm}$ ; the 25cm-long second column is  $1.5\text{cm}$  x  $1.5\text{cm}$  in size. Both are fabricated on 100mm silicon wafers using DRIE. A 4mm silicon rim around the column allows attachment of the fluidic connection lines and electrical connections to on-chip heaters and temperature sensors formed using  $250\text{\AA}/500\text{\AA}$  Ti/Pt on the back of the silicon wafer. Two large heaters are patterned on the back side of the column to suppress any temperature gradients. The high thermal conductivity of silicon helps to ensure temperature uniformity over the surface area of the column. After the channel etch, the wafer is capped with an anodically-bonded Pyrex 7740 wafer at  $400^{\circ}\text{C}$  with

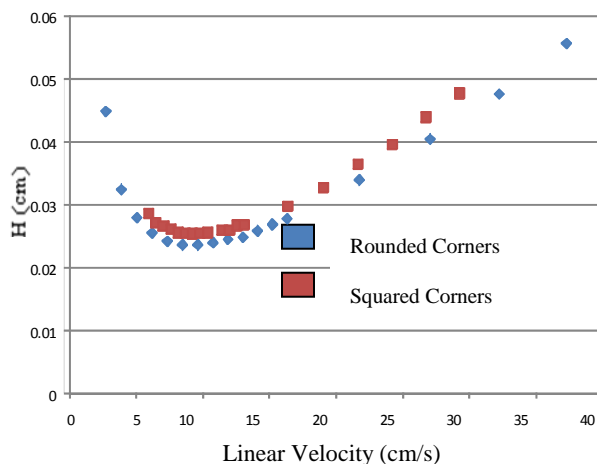


Fig. 3: Column performance versus linear velocity for rounded and square corner geometries.

a force of  $\sim 200\text{N}$ . A two-step DRIE process is used to etch the column inlet/outlet ports  $380\mu\text{m}$  deep x  $380\mu\text{m}$  wide to accommodate  $250\mu\text{m}$  (i.d.) connection capillaries and reduce pressure restrictions. Fig. 4 shows the columns along with an SEM cross-section. Fig. 5 shows the center portion of a 3m column.

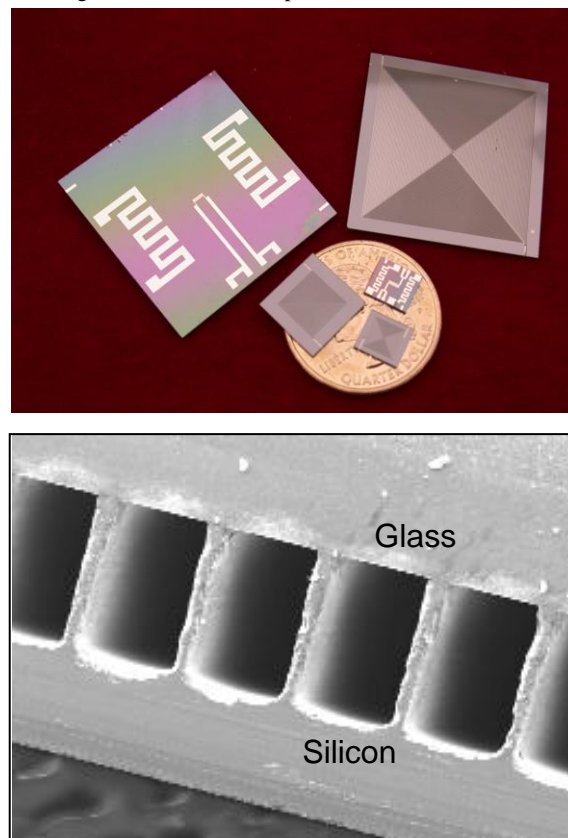


Fig. 4: 2D-GC columns (3m, 25cm, and 10cm) having optimized dimensions on a U.S. quarter, with heaters and sensors to allow closed-loop temperature program on their back surfaces.

The  $\mu\text{TM}$  [7,8] had a similar structure. Its channels were sealed with anodically-bonded Pyrex, 40 or  $100\mu\text{m}$  thick. Microheaters and temperature sensors made of Ti/Pt were patterned on the Pyrex. Microfabricated Si spacers were used to



Fig. 5: Top view of the center portion of a 3m-long microcolumn.

create a 22-63 $\mu\text{m}$  air gap between the  $\mu\text{TM}$  and the top of the thermoelectric cooler and were precisely aligned with a microscope and bonded with an epoxy adhesive onto the Pyrex membrane. Then the  $\mu\text{TM}$  was mounted on a printed circuit board with ultrasonically-bonded wire used for electrical connections. A thin layer of thermally conductive paste was used to ensure good thermal contact between the spacers and the thermoelectric cooler. With a height gauge, the  $\mu\text{TM}$  with spacers was manually aligned and bonded to the cooling unit. Finally, a custom-made chamber was used to seal the  $\mu\text{TM}$ . Further details on modulator performance and design considerations have been discussed in detail. [7,8]

The complete GC x GC microsystem consists of the two microcolumns, the thermal modulator, a commercial thermoelectric cooler, four transfer-line heaters, and associated electronics; it is assembled on a custom printed circuit board measuring 5cm x 12.5cm x 7.5cm and shown in Fig. 6.

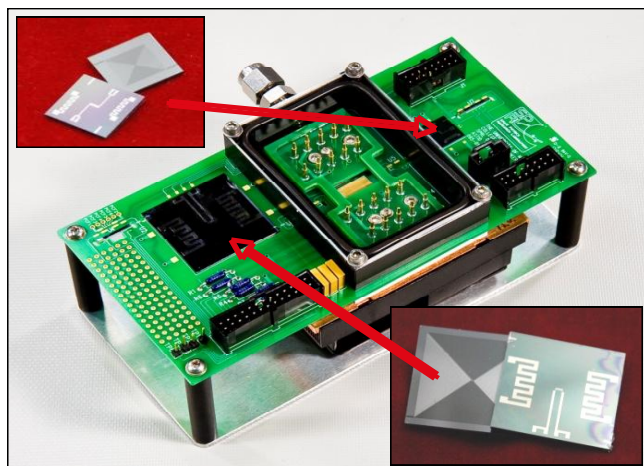


Fig. 6: The GCxGC system, with insets of the first-dimension column (bottom right) and the second-dimension column (top left).

## TEST RESULTS

The columns were coated in a static process producing a stationary-phase thickness of about 0.15 $\mu\text{m}$ . Polydimethylsiloxane and either polytrifluoropropylmethylsiloxane (PTFPMS) or polyethylene glycol (PEG) were used for the non-polar and polar phases, respectively, producing a resolution of 14,425 and 5,800 theoretical plates, respectively, using an air carrier in 3m columns.

Using 3m- and 0.25m- long PDMS and PTFPMS microcolumns, a GCxGC microsystem was first implemented using the

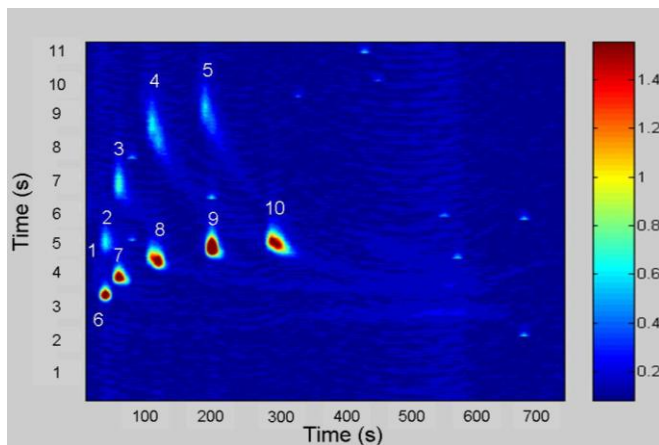


Fig. 7: A two-dimensional contour plot of a 10-component GCxGC separation using 3m- and 0.25m-long microcolumns and a two-stage thermal modulator. Alkanes are separated primarily by the first column (x-axis) and the ketones are separated primarily by the second column (y-axis). Color reflects peak height on the FID.

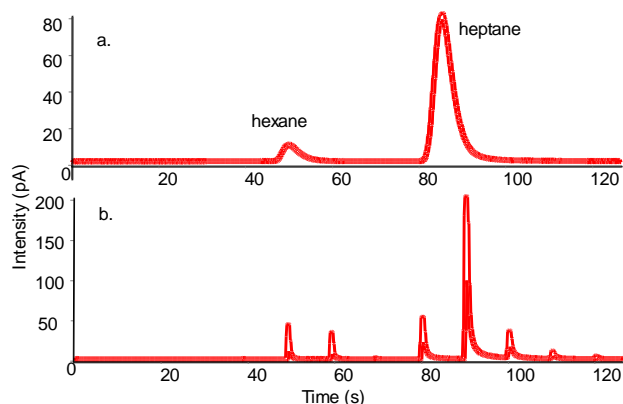


Fig. 8: Separation of hexane and heptane with the modulator off (a) and on (b) with fused silica capillaries as separation columns and the microfabricated thermal modulator.

meso-scale modulator described above. Modulation was between -25 $^{\circ}\text{C}$  and 200 $^{\circ}\text{C}$  within a few hundred milliseconds. Fig. 7 shows a two-dimensional separation of a 10-component mixture of alkanes ( $\text{C}_6\text{-C}_{10}$ ) and ketones ( $\text{C}_3\text{-C}_7$ ).

The  $\mu\text{TM}$  was first tested using fused silica capillaries with the same cross-sectional areas as the microcolumns. Fig. 8a shows the separation of hexane and heptane with the modulator in the flow path but not operating, while Fig. 8b shows a modulated separation of the same two compounds. The modulation period was 10s with a 1s offset between the two stages. The microcolumns were then integrated into the system and additional separations were performed. Fig. 9a shows the modulation of a single peak. The modulation period was 10s and the modulated peak width is 217ms. Fig. 9b shows the separation of heptane and 2-hexanone, with a modulation period of 7s. These two peaks co-elute from a one-dimensional separation but are clearly separated in the two-dimensional plane.

Since the modulator obtains more slices with a wider analyte band, an additional 3m non-polar column was coated and used as a first dimension column. This allowed an increase in the inlet pressure while utilizing the same volumetric flow rate. The

increase in pressure increased the linear velocity in the second dimension column, reducing the second-dimension analysis time. The separation of three normal alkanes ( $C_7$ ,  $C_8$ , and  $C_9$ ) from two alcohols that co-elute was obtained as shown in Fig. 10.

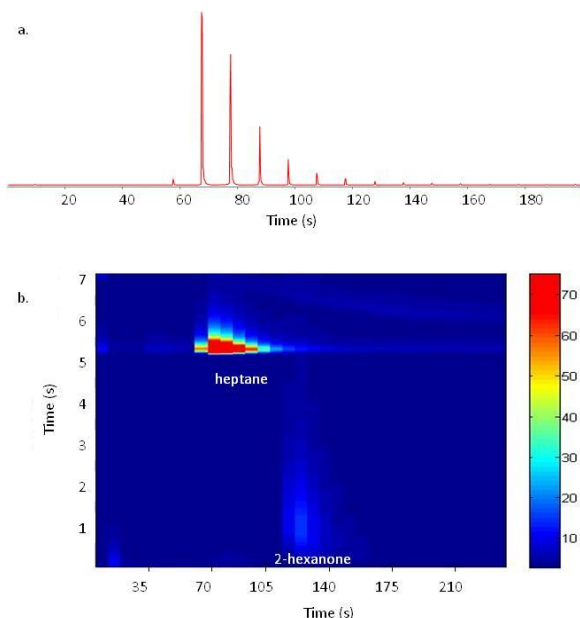


Fig. 9: a) Modulated peak with microfabricated first- and second-dimension columns and a microfabricated thermal modulator. b) Separation of heptanes and 2-hexanone on microfabricated GCxGC system. The peaks would co-elute in a one-dimensional separation.

This separation shows the many benefits of GCxGC separations. The nonpolar alkanes align toward the bottom and the more polar alcohols separate more on the second dimension column. The alcohols are also at much lower concentration than the alkanes but are easily distinguished from the other peaks as well as the baseline.

## CONCLUSIONS

There are many benefits to GCxGC separations compared to one-dimensional systems, including increased detection, structured chromatograms to aid in peak identification, and an increase in peak capacity. All of these benefits are critical for the development of field-portable systems. This is the first reported thermally-modulated microfabricated GCxGC system. With continued development such systems will be key in identifying complex VOC mixtures outside of the laboratory environment.

## ACKNOWLEDGMENTS.

This work was supported by NASA/ASTID under the grant No. NNG-06GA89G and by the National Science Foundation under Award Number EEC-0096866. The authors would also like to thank Robert Gordenker and Brendan Casey for their support.

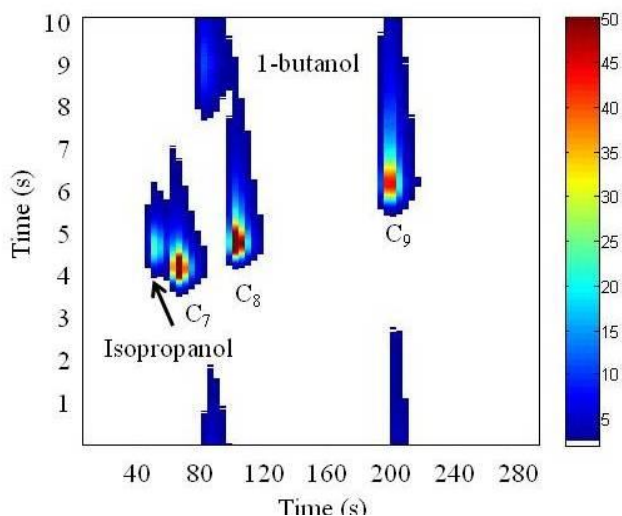


Fig. 10: Separation of five compounds, three normal alkanes, and two alcohols, using a 6m-long first-dimension column and 0.25m-long second-dimension column.

## REFERENCES

- [1] Agah, M.; et al. "High-Speed MEMS-based Gas Chromatography," Displays, Sensors, and MEMS, San Francisco, CA, Nov. 2004.
- [2] H. Kim, et al., "A Micropump-Driven High-Speed MEMS Gas Chromatography System," *Int. Conf. on Solid-State Sensors, Actuators, and Microsystems (Transducers'07)*, Lyon, France, pp. 1505-1508, June 2007.
- [3] E. T. Zellers, et al., "An Integrated Micro-Analytical System for Complex Vapor Mixtures," *Int. Conf. on Solid-State Sensors, Actuators, and Microsystems (Transducers'07)*, Lyon, France, pp. 1491-1496, June 2007.
- [4] M. Agah and K. D. Wise, "PECVD-Oxynitride Gas Chromatographic Columns," *Digest IEEE Electron Devices Meeting*, Washington, DC, pp. 311-314, December 2005.
- [5] C.-J. Lu, et al., "First Generation Hybrid MEMS Gas Chromatograph," *Lab On A Chip*, 5, 1123-1131 (2005).
- [6] G. Serrano, H. Chang, E. T. Zellers, A micro gas chromatograph for high-speed determinations of explosive vapors, *Proc. Transducers '09*, Denver, Colorado, USA, June 21-25, 2009, pp. 1654-1657.
- [7] S. J. Kim, et al., "Microfabricated Thermal Modulator for Comprehensive Two-Dimensional Gas Chromatography: Design, Thermal Modeling, and Preliminary Testing," *Lab on a Chip*, 2010, in press, DOI: 10.1039/C001390K
- [8] S.-J. Kim, et al., "A Miniaturized Robust High-Speed Thermal Modulator for Comprehensive 2D Gas Chromatography," *IEEE Conf. on MicroElectroMech. Systems*, Hong Kong, January 2010 pp. 124-127.
- [9] G. E. Spangler, "Height Equivalent to a Theoretical Plate Theory for Rectangular GC Columns" *Anal. Chem.*, 70, pp. 4805, 1998.

Contact: Shaelah Reidy, sreidy@umich.edu

# A HIGH POWER DENSITY MEMS MICROBIAL FUEL CELL

S. Choi<sup>1</sup>, H.-S. Lee<sup>2</sup>, Y. Yang<sup>1</sup>, B.E. Rittmann<sup>2</sup>, and J. Chae<sup>1\*</sup>

<sup>1</sup> School of Electrical, Computer and Energy Engineering, Arizona State University, Tempe, Arizona, USA

<sup>2</sup> Center for Environmental Biotechnology, Biodesign Institute, Arizona State University, Tempe, Arizona, USA

## ABSTRACT

We report a microfabricated microbial fuel cell (MFC) that produces a high power density using a *Geobacteraceae*-enriched mixed bacterial culture. The MFC features 4.5- $\mu\text{L}$  anode/cathode chambers defined by 20- $\mu\text{m}$ -thick photo-definable polydimethylsiloxane (PDMS). The short proton diffusion length (20  $\mu\text{m}$ ) in the anode lowers electrolyte resistance and consequently enhances power generation. A maximum current density of 16.3  $\text{mA}/\text{cm}^2$  and power density of 2.3  $\text{mW}/\text{cm}^2$  are achieved. The start-up time is only 2 days for maximum current generation. The MFC was operated under semi-continuous flow conditions, and L-cysteine was added in order to chemically scavenge the dissolved oxygen in the anode chamber.

## INTRODUCTION

Microbial fuel cell (MFC) is an electrochemical device that converts organic substrates into electricity through microbial catabolism. Since the first microfabricated MFC in 2002 [1], interest in MEMS (Micro-Electro-Mechanical systems) MFCs has grown not only for miniaturized power sources [2-6], but for the studies of individual microorganism behavior [7, 8]. When it comes to the usefulness in studies of microbes, the MEMS MFCs have many advantages to characterize a small number of, or even a single, bacterial electron transfer due to the micro-sized electrode that can be in the size of individual microorganism. For miniaturized power sources, MEMS technology may be a potential solution to increase the power density in miniature MFCs by increasing the specific surface area, anode area divided by volume of the anode compartment. For example, Siu *et al.* presented a microfabricated polydimethylsiloxane (PDMS) MFC with embedded micropillar electrodes to increase the specific surface area up to 144  $\text{cm}^{-1}$  [4]. Nevertheless, earlier MEMS MFCs had low power output [1-5, 7], short life time [1-4] and long start-up time [6], which are unacceptable for a practical portable power source. Those limitations were mainly due to the following two factors. First, the bacteria used in these MEMS MFCs (*Saccharomyces cerevisiae* or *Shewanella oneidensis MR-1*) are not efficient for generating high power density, as they require mediators to transfer electrons from donor substrate to the anode [1-5, 7]; *Saccharomyces cerevisiae* are unable to produce shuttling compounds, demanding exogenous mediators for current generation. The exogenous-mediator MFCs are impractical because of costs and mediator toxicity [9]. Second, high internal resistance in the micro-sized MFCs caused a substantial loss of power generation. A long distance between the anode and cathode can increase ohmic resistance, the main form of internal resistance [10], causes slow start-up and decreases power density [5, 10]. Siu *et al.* microfabricated a 100- $\mu\text{m}$ -thick PDMS gasket that was manually assembled between anode and cathode; however, it is extremely hard to manually manipulate such a thin PDMS film to assemble the fuel cell [4]. Qian *et al.* reported a batch-fabricated MEMS technology to give short electrode spacing using a 100- $\mu\text{m}$ -thick SU-8 spacer in a micro-scale MFC [5]. They accelerated the start-up period and showed long-term sustainability of power generation. However, their approach still had low power density at 15  $\mu\text{W}/\text{cm}^2$  (0.15  $\mu\text{W}/\text{cm}^2$ ), which is even lower than that of the MFC using *Saccharomyces cerevisiae* [4, 5].

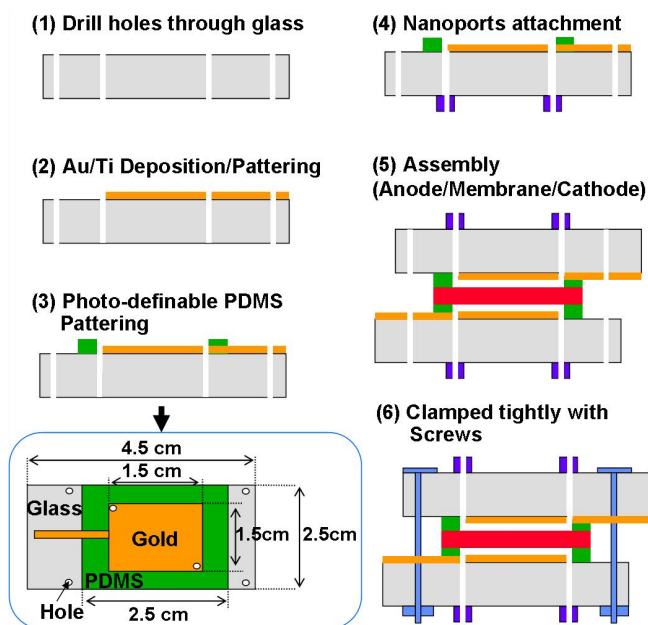


Figure 1: Schematic of the fabrication process

In this work, we report the possibilities of a micro-sized MFC as a power source by enhancing the power generation. We used *Geobacteraceae*-enriched mixed bacterial cultures to obtain high current, since these are anode-respiring bacteria (ARB) that produce a conductive biofilm matrix [11, 12]. We designed the MEMS MFC to have a short proton-transfer distance and a high specific surface area ( $500 \text{ cm}^{-1}$ ) to lower the internal resistance by using photo-definable PDMS, which increase the power density and decrease the start-up time.

## MATERIALS AND METHODS

### Device fabrication and assembly

Fig. 1 shows the fabrication process of the MFC. We cut two glass substrates (VWR International 75 mm x 25 mm x 1 mm) to 45 mm x 25 mm and mechanically drilled with six holes on each substrate: one inlet, one outlet, and four screws. The glass substrates were then coated with Ti/Au (20 nm/200 nm) by e-beam evaporator and patterned to define the electrodes (1.5 cm x 1.5 cm) using a lift-off process. After that, we spin-coated photo-definable PDMS (WL-5150, Dow corning) at 750 rpm for 30 sec. This PDMS layer was used for a spacer and the thickness of the layer can be controlled by the spin speed. The PDMS layer was prebaked at 110  $^{\circ}\text{C}$  for 120 sec. prior to UV exposure (3000  $\text{mJ}/\text{cm}^2$ ) through a negative photo-mask. Following the exposure, the substrate was baked at 150  $^{\circ}\text{C}$  for 180 sec. and agitated in WL-9653 developer (Dow corning) for 30 sec. Finally, the PDMS-coated substrates were cured at 180  $^{\circ}\text{C}$  for 1 hr. The thickness of the PDMS was measured as 20  $\mu\text{m}$ , corresponding to the depth of the anode/cathode chamber. The patterned PDMS defined a 4.5- $\mu\text{L}$  volume for each (anode or cathode) chamber. The inlet and outlet of the microfluidic channel were accessed

from the back side of the substrates via nanoports (10-32 Coned assembly, IDEX Health & Science) and connected with fluidic tubing (outer diameter: 0.0625 inch, inner diameter: 0.002 inch, 1548, IDEX Health & Science). We used CMI 7000 (Membranes international Inc.) as cation exchange membrane (CEM) to permit only cation transport needed to maintain electroneutrality in both chambers. The CEM surface area was 1.7 cm x 1.7 cm. To assemble the dual-chamber MFC, we sandwiched the CEM between the anode and cathode chamber and clamped them with four screws (Fig 1 & Fig 2). The MFC was operated at 30°C.

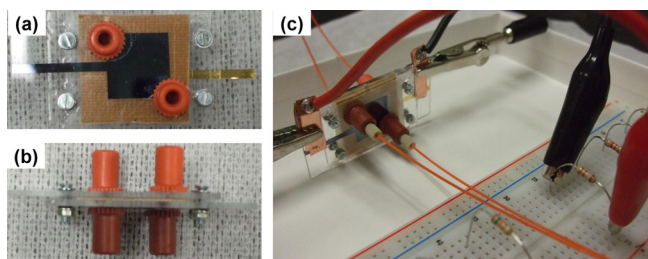


Figure 2: (a) Device top view (b) side view (c) experiment setup for monitoring of the MFC power generation

### Inoculum

The inoculum was obtained from an acetate-fed MFC mother reactor inoculated originally with a mixture of activated sludge and anaerobic digester sludge. 16S-rRNA gene clone libraries on the inoculum showed *Geobacter sulfurreducens*-enriched mixed bacterial culture [11]. Acetate was the sole electron donor present in the anode chamber at 25 mM in mineral medium. The composition of the mineral medium was (per L of deionized water):  $\text{KH}_2\text{PO}_4$  1680 mg,  $\text{Na}_2\text{HPO}_4$  12,400 mg,  $\text{NaCl}$  1600 mg,  $\text{NH}_4\text{Cl}$  380, 5 mg EDTA, 30 mg  $\text{MgSO}_4 \cdot 7\text{H}_2\text{O}$ , 5 mg  $\text{MnSO}_4 \cdot \text{H}_2\text{O}$ , 10 mg  $\text{NaCl}$ , 1 mg  $\text{CO}(\text{NO}_3)_2$ , 1 mg  $\text{CaCl}_2$ , 0.001 mg  $\text{ZnSO}_4 \cdot 7\text{H}_2\text{O}$ , 0.001 mg  $\text{ZnSO}_4 \cdot 7\text{H}_2\text{O}$ , 0.1 mg  $\text{CuSO}_4 \cdot 5\text{H}_2\text{O}$ , 0.1 mg  $\text{AlK}(\text{SO}_4)_2$ , 0.1 mg  $\text{H}_3\text{BO}_3$ , 0.1 mg  $\text{Na}_2\text{MoO}_4 \cdot 2\text{H}_2\text{O}$ , 0.1 mg  $\text{Na}_2\text{SeO}_3$ , 0.1 mg  $\text{Na}_2\text{WO}_4 \cdot 2\text{H}_2\text{O}$ , 0.2 mg  $\text{NiCl}_2 \cdot 6\text{H}_2\text{O}$ , and 1 mg  $\text{FeSO}_4 \cdot 7\text{H}_2\text{O}$ . The initial pH in the anode chamber was  $7.5 \pm 0.1$  [11]. 2.5 g/L L-cysteine was added in the anolyte to scavenge the dissolved oxygen in the anode chamber. The catholyte was 100 mM potassium ferricyanide and 100 mM phosphate buffer in which the initial pH was adjusted at  $7.5 \pm 0.2$  with 0.1 M NaOH. Anolyte and catholyte solutions were continuously from a syringe pump at the speed of 1.5  $\mu\text{L}/\text{min}$ .

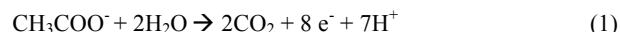
### Measurement setup

We measured the potential between the anode and cathode by a DAQ/68 data acquisition system (National Instrument) and recorded them every 1 min via LabVIEW (National Instrument). An external resistor was connected between electrodes of the MFC to close the circuit. We calculated the current through the resistor via ohm's law and the output power via  $P=V \times I$ . Current and power density were calculated based on the anode area (2.25  $\text{cm}^2$ ) or anode chamber volume (4.5  $\mu\text{L}$ ), respectively. The MFC system was closed with a 150- $\Omega$  external load. Inoculum and catholyte were injected to fill the 4.5- $\mu\text{L}$  anode/cathode chamber by a syringe pump, and then the ends of tubing were sealed with silicone for biofilm formation at fed-batch mode.

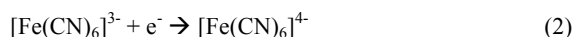
### MFC operation

With acetate being the substrate to the anode of the MFC,

protons, electrons, and  $\text{CO}_2$  are the metabolic products of the ARB reaction, as shown in Equation (1). Electrons are transferred to the anode via the conductive matrix that the ARB forms and flow to the cathode through the external electrical circuit.



Protons released by the ARB reaction travel through CEM towards the cathode. At the cathode, potassium ferricyanide,  $[\text{Fe}(\text{CN})_6]^{3-}$ , captures the electrons (Equation (2)) and the cycle is completed.



## RESULTS AND DISCUSSION

### Current generation

After we filled the anode chamber with inoculum and L-cysteine, the open circuit voltages (OCV) in batch- and continuous-mode were 346 mV and 745 mV in 20 hours, respectively (data not shown). The substantial drops of OCV in batch-mode could be attributed to  $\text{O}_2$  intrusion into the anode chamber.  $\text{O}_2$  can abiotically react with the anode when anode potential is negative enough to reduce  $\text{O}_2$  into  $\text{H}_2\text{O}$ , which can significantly reduce OCV. In addition,  $\text{O}_2$  in the anode chamber is a strong electron sink for the bacteria, which divert electron flow to  $\text{O}_2$  oxidation instead of to current. Macro-sized MFCs also are adversely affected by  $\text{O}_2$  intrusion into the anode, but the MEMS MFC is more sensitive to the presence of  $\text{O}_2$  intrusion because even small rates of  $\text{O}_2$  intrusion can divert significant electron flow when the system size is so small. Therefore, we added L-cysteine to reduce any  $\text{O}_2$  entering the anode and operated MEMS MFC in semi-continuous flow conditions.

As shown in Fig 3, transient current generation was observed as soon as the inoculum including L-cysteine was injected. After we confirmed that the current increased to 0.5  $\mu\text{A}$ , 5 hours after the injection of the inoculum, we fed fresh anolyte (a mixture of 25 mM acetate and 2.5 g/L L-cysteine in mineral medium) and catholyte solutions continuously to each chamber at 1.5  $\mu\text{L}/\text{min}$ . Current increased to 50  $\mu\text{A}$  in approximately 5 hours after the continuous feed of anolyte/catholyte. Once the current dropped to baseline due to the depletion of the solution in the 1-mL feeding syringe, we re-injected fresh anolyte/catholyte into both chambers, and the current increased to a peak value of 63.7  $\mu\text{A}$  (14.2  $\text{mA}/\text{cm}^3$ ) in 2 days. The maximum current was 66.7  $\mu\text{A}$  (14.8  $\text{mA}/\text{cm}^3$ ) in the third cycle.

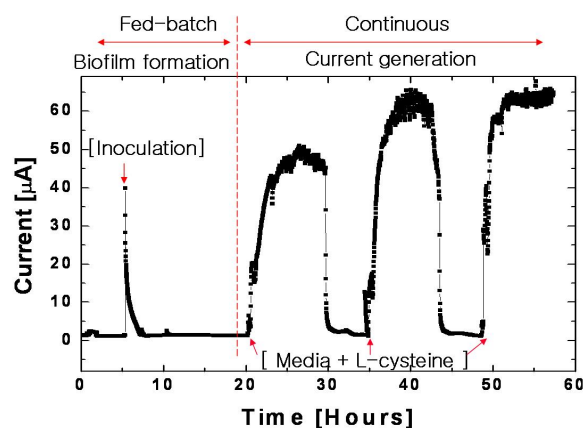


Figure 3: Current produced from the MEMS MFC with a 150 $\Omega$  load

Repeated cycles of anolyte/catholyte addition showed good reproducibility of current generation. The current became stable and increased as the cycle was repeated. This reproducible current generation indicates that ARB oxidized acetate and transferred acetate electrons to the anode in the MEMS MFC. The current increase with operation cycles supports that the ARB attached to the gold anode and proliferated. Thus, one main factor for the rapid current generation was that the *Geobacter sulfurreducens*-enriched culture created its own conductive biofilm [12].

The results in Fig. 3 show that our MEMS MFC exhibited a significantly shorter start-up time compared to macro-sized MFCs. We believe that mitigation of O<sub>2</sub> intrusion by L-cysteine and a high specific surface area (500 cm<sup>2</sup>) of the anode increased ARB biofilm formation on the anode surface and led to fast start-up.

### Polarization curve and power output

The voltage responses to different loads are shown in Fig. 4. OCV of 687 mV was regained immediately upon load removal. We derived the polarization curve and power output from values of Fig. 4 and show them in Fig. 5. The maximum power output and current were 10.5 μW and 73 μA, respectively. The maximum current and power density per volume of anode chamber were 16.3 mA/cm<sup>3</sup> and 2.3 mW/cm<sup>3</sup>, respectively.

Table 1 compares our output results with the literature [3-7]. We report the volumetric power density for micro-sized MFCs up to now; previous reports of volumetric power densities were only 0.34 to 32 μW/cm<sup>3</sup>. The main contributor for such high volumetric power density is the large specific surface area (500 cm<sup>2</sup>) in our MEMS MFC, compared to other MFCs [4-7]. Having high specific surface area allows high power density per unit volume. Yet, specific surface area is not the only parameter to determine the power density. A prior micro-sized MFC having similar specific surface area (510 cm<sup>2</sup>) only produced 2.3 μW/cm<sup>3</sup> [3], orders of magnitude less than our maximum power density.

Another important factor for highest volumetric maximum power density is a small energy loss (voltage term), described by Equation (4).

$$E_{Device} = OCV - IR_{int} = I(R_a + R_m + R_c + R_e) \quad (4)$$

where  $R_a$ ,  $R_m$ ,  $R_c$  and  $R_e$  are anodic, membrane, cathodic and electrolyte resistance, respectively [14].  $R_e$  can be expressed by:

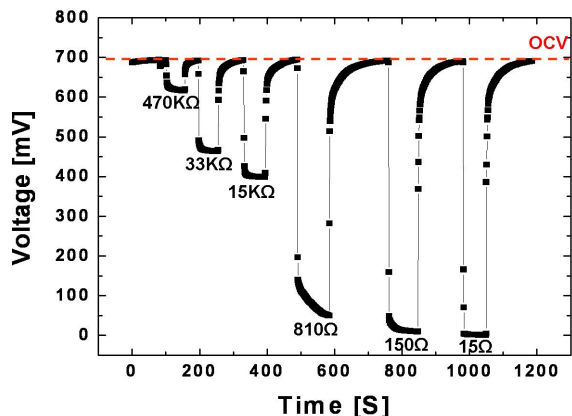


Figure 4: Voltage response to different load resistors

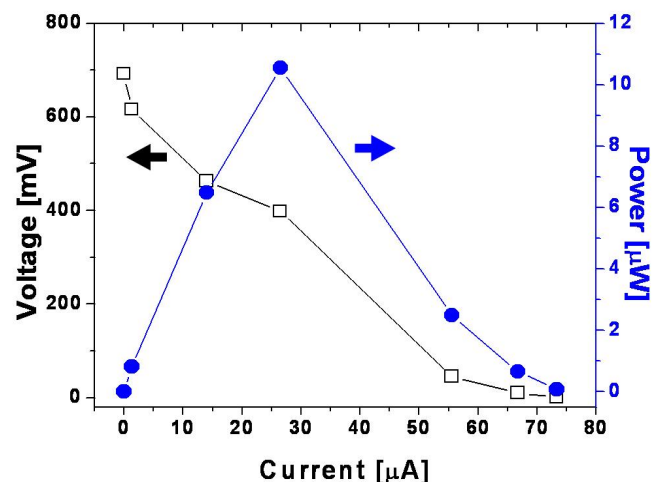


Figure 5: Polarization curve (black square) and power output (blue circle) measured as a function of current

Table 1: Summary of microfabricated MFCs in literature

Biocatalyst	Operation	Anode mediator / Anolyte / Catholyte	Anode / Area [cm <sup>2</sup> ]	Cathode / Area [cm <sup>2</sup> ]	Membrane Area [cm <sup>2</sup> ]	Space; anode to membrane	Anode volume [cm <sup>3</sup> ]	Specific surface area [cm <sup>-1</sup> ]	Max. Power (Current)	Start-up Time	Power density		Ref.
											P <sub>S</sub> (μW/cm <sup>2</sup> ) <sup>e</sup>	P <sub>V</sub> (μW/cm <sup>3</sup> )	
<i>Saccharomyces cerevisiae</i>	Fed-batch	Yes / Glucose / [Fe(CN) <sub>6</sub> ] <sup>3-</sup>	Au/0.12 (0.51) <sup>e</sup>	Au/0.51	1	80 μm	0.001	510	2.3 nW (15 μA) under 10 Ω	NA <sup>d</sup>	0.019	2.3	[3]
<i>Saccharomyces cerevisiae</i>	Fed-batch	Yes / Glucose / [Fe(CN) <sub>6</sub> ] <sup>3-</sup>	Au/1.2 (2.16) <sup>e</sup>	Au/1.2	1.2	100 μm	0.015	144	0.48 μW (36 μA) under 1KΩ	NA <sup>d</sup>	0.4	32.1	[4]
<i>Shewanella oneidensis</i> MR-1	Fed-batch	No / TSB <sup>a</sup> / [Fe(CN) <sub>6</sub> ] <sup>3-</sup>	Au/0.38	Carbon Cloth /0.38	0.38	1.2 cm	0.154	2.5	143.3 nW (0.6 μA) under 20 KΩ	NA <sup>d</sup>	0.377	0.93	[7]
<i>Shewanella oneidensis</i> MR-1	Fed-batch	No / TSB <sup>a</sup> / [Fe(CN) <sub>6</sub> ] <sup>3-</sup>	Au/0.15	Carbon Cloth /0.4	0.15	100 μm	0.0015	100	23 nW (0.8 μA) under 40 KΩ	2 Days	0.15	15	[5]
<i>Geobacter Sulfurreducens</i>	Continuous	No / Acetate / Fe(CN) <sub>6</sub> <sup>3-</sup>	Au/0.01	Coiled Au wire /1	0.5	NA <sup>d</sup>	0.35	0.03	0.12 μW (0.6 μA) under 330 KΩ	10 Days	12	0.343	[6]
<b>Mixed Bacterial culture<sup>b</sup></b>	<b>Continuous</b>	<b>No / Acetate + L-cysteine / Fe(CN)<sub>6</sub><sup>3-</sup></b>	<b>Au/2.25</b>	<b>Au/2.25</b>	<b>2.25</b>	<b>20 μm</b>	<b>0.0045</b>	<b>500</b>	<b>10.5 μW (26 μA) under 15 KΩ</b>	<b>2 Days</b>	<b>4.67</b>	<b>2333</b>	<b>This Work</b>

<sup>a</sup>Tryptone soya broth; <sup>b</sup>*Geobacteraceae*-enriched culture; <sup>c</sup>Effective surface area;

<sup>d</sup>Not Available; <sup>e</sup>Calculation based on geometric surface area



$$R_e = \frac{l}{A \cdot K} \quad (5)$$

where  $l$  is the distance (cm) and  $A$  is the cross-sectional area (cm<sup>2</sup>) over which the ionic conduction occurs, and  $K$  is the specific conductivity ( $\Omega \cdot \text{cm}$ )<sup>-1</sup> of the electrolyte [15]. Our electrode distance was 0.048 cm (membrane thickness 457  $\mu\text{m}$  + spacer 20  $\mu\text{m}$ ), the conductivity of our medium was 0.017 ( $\Omega \cdot \text{cm}$ )<sup>-1</sup>, and the cross sectional area of the membrane was 2.25 cm<sup>2</sup>. Therefore, we computed  $R_e$  as only 1.26  $\Omega$ , and energy loss by electrolyte resistance was as small as 32  $\mu\text{V}$  ( $26 \mu\text{A} \times 1.26 \Omega$ ) at the maximum volumetric power density 2333  $\mu\text{W}/\text{cm}^3$ . Resistance of CEM is 20  $\Omega$  ( $45.1 \Omega \cdot \text{cm}^2$  ( $R_m \cdot A$ ) divided by anode surface area 2.25 cm<sup>2</sup>) in phosphate buffer medium [14]. We estimated the energy loss by membrane resistance as 520  $\mu\text{V}$  ( $20 \Omega \times 26 \mu\text{A}$ ); thus, overall ohmic energy losses were only 555  $\mu\text{V}$  for the maximum current density, which is negligible compared to the total energy losses 289 mV, OCV 687 mV – 398 mV (at the maximum power output) in Fig 5. These analyses indicate that electrode energy losses were the main energy bottleneck for our MEMS MFC.

Using the polarized curve in Fig 5, we estimated internal resistance ( $R_{\text{ini}}$ ) from the point where the MFC polarization curve exhibited a near-linear drop (ohmic losses): from 10  $\mu\text{A}$  to 60  $\mu\text{A}$ . Linear fitting of the curve yielded a  $R_{\text{ini}}$  value of  $\sim 10 \text{ k}\Omega$ , which includes  $R_a$ ,  $R_c$ ,  $R_m$ , and  $R_e$ . The sum of  $R_m$  and  $R_e$  only is 21.3  $\Omega$ , and, therefore, electrode resistance ( $R_a + R_c$ ) is computed at 9980  $\Omega$ . The linear-fitting approach is consistent to the early analysis that electrode energy losses are the main energy-barrier in the MEMS MFC.

## CONCLUSION

We demonstrated that a microfabricated MFC utilizing a *Geobacter sulfurreducens*-enriched biofilm can give high power density. To achieve the high power density, we utilized a very thin photo-definable PDMS spacer patterned to define 4.5- $\mu\text{L}$  anode/cathode chambers. The maximum current density of 16.3 mA/cm<sup>2</sup> and power density of 2.3 mW/cm<sup>2</sup> were by far the highest among all previously reported MEMS MFCs, and this was due to the high anode specific surface area, efficient ARB of *Geobacter sulfurreducens* capable of creating a conductive biofilm, elimination of O<sub>2</sub> exposure, and low ohmic losses. Moreover, the start-up time was only 2 days for maximum current generation.

## REFERENCES

- [1] M. Chiao, K.B. Lam, Y. Su, and L. Lin, "A miniaturized microbial fuel cell," Technical Digest of the 2002 Solid-State Sensors and Actuators Workshop, Hilton Head Island, SC, pp. 59-60.
- [2] M. Chiao, K.B. Lam, and L. Lin, "Micromachined Microbial Fuel Cells," Proceedings of 16<sup>th</sup> IEEE International Conference on Micro Electro Mechanical Systems (MEMS) 2003, Kyoto, Japan, (2003), pp.383-386.
- [3] M. Chiao, K.B. Lam, and L. Lin, "Micromachined microbial and photosynthetic fuel cells," J. Micromech. Microeng., 16, 2547 (2006).
- [4] C. Siu, and M. Chiao, "A Microfabricated PDMS Microbial Fuel Cell," J. Microelectromech. Syst., 17, 1329 (2008).
- [5] F. Qian, M. Baum, Q. Gu, and D. E. Morse, "A 1.5  $\mu\text{L}$  microbial fuel cell for on-chip bioelectricity generation," Lab on a Chip, 9, 3076 (2009).
- [6] E.A. Parra, and L. Lin, "Microbial fuel cell based on electrode-exoelectrogenic bacteria interface," Proceedings of

- 22<sup>nd</sup> IEEE International Conference on Micro Electro Mechanical Systems (MEMS) 2009, Sorrento, Italy, (2009), pp.31-34.
- [7] H. Hou, L. Li, Y. Cho, P. de Figueiredo, and A. Han, "Microfabricated Microbial Fuel Cell Arrays Reveal Electrochemically Active Microbes," PLOS one, 4, e6570, (2009).
- [8] E.A. Parra, A. Higa, C.R. Buie, J.D. Coates, and L. Lin, "Real-time biocatalyst loading and electron transfer via microfabricated transparent electrode," Proceedings of 23<sup>rd</sup> IEEE International Conference on Micro Electro Mechanical Systems (MEMS) 2010, Hong Kong, (2010), pp.1183-1186.
- [9] D.R. Lovely, and K.P. Nevin, "Electricity Production with Electrocigens," Chapter 23, Bioenergy, ASM Press, Washington, DC, USA, 2008.
- [10] H. Liu, S. Cheng, and B.E. Logan, "Power generation in fed-batch microbial fuel cells as a function of ionic strength, temperature, and reactor configuration," 3 Environ. Sci. Technol., 9, 5488, (2005).
- [11] H. S. Lee, P. Parameswaran, A. Kato-Marcus, C.I. Torres, and B.E. Rittmann, "Evaluation of energy-conversion efficiencies in microbial fuel cells (MFCs) utilizing fermentable and non-fermentable substrates," Water Research, 42, 1501, (2008).
- [12] C.I. Torres, A.K. Marcus, H.S. Lee, P. Parameswaran, R. Krajmalnik-Brown, and B.E. Rittmann, "A kinetic perspective on extracellular electron transfer by anode-respiring bacteria," FEMS Microbiol Rev., 34, 3, (2010).
- [13] Z. He, J. Kan, Y. Wang, Y. Huang, F. Mansfeld, and K.H. Nealson, "Electricity production coupled to ammonium in a microbial fuel cell," Environ. Sci. Technol., 43, 3391, (2009).
- [14] F. Harnisch, U. Schroder, and F. Scholz, "The suitability of monopolar and bipolar ion exchange membranes as separators for biological fuel cells," Environ. Sci. Technol., 42, 1740, (2008).
- [15] Y. Fan, E. Sharbrough, and H. Liu, "Quantification of the internal resistance distribution of microbial fuel cells," Environ. Sci. Technol., 42, 8101, (2008).

## CONTACT

\*J. Chae, tel: +1- 480-965-2082; Junseok.Chae@asu.edu

# BIOMIMETIC SUPERHYDROPHOBIC SURFACES USING VIRAL NANOTEMPLATES FOR SELF-CLEANING AND DROPWISE CONDENSATION

M. McCarthy<sup>1\*</sup>, R. Enright<sup>1,2</sup>, K. Gerasopoulos<sup>3</sup>, J.N. Culver<sup>3</sup>, R. Ghodssi<sup>3</sup>, and E.N. Wang<sup>1</sup>

<sup>1</sup>Massachusetts Institute of Technology, Cambridge, Massachusetts, USA

<sup>2</sup>University of Limerick, Limerick, Ireland, <sup>3</sup>University of Maryland, College Park, Maryland, USA

## ABSTRACT

We report the fabrication and characterization of biomimetic superhydrophobic surfaces synthesized using self-assembly and metallization of the *Tobacco mosaic virus* (TMV) onto micropillar arrays. A novel biofabrication process was used to accurately recreate the hierarchical surface structures of the lotus leaf (*Nelumbo nucifera*) and has provided key insights into the role of both nanoscale and microscale features on water repellency of aquatic and wetland plant leaves under droplet impact. The biomimetic surfaces have been demonstrated to be robust, where droplets rebound with impact velocities greater than 4.3 m/s. Additionally, there is a two-fold increase in the steady state condensation heat transfer coefficient across the biomimetic surfaces as compared to planar ones.

## INTRODUCTION

Superhydrophobic surfaces, with static contact angles greater than 150° and droplet hystereses less than 10°, resist wetting and exhibit self-cleaning properties. Such properties are ideal for coatings on buildings, solar cells, and textiles, as well as drag reduction and increased heat transfer *via* drop-wise condensation [1,2]. In nature, a wide array of wetland and aquatic plant leaves exhibit self-cleaning properties and resist wetting upon the impact of rainfall. Due to the abundance of water, these wetland plants do not rely on the intake of moisture through their leaves to hydrate. In fact, their superhydrophobic properties are a necessity for survival. Shedding water from the surface dramatically increases the uptake of CO<sub>2</sub> for photosynthesis, and these self-cleaning abilities reduce the formation of bacteria and fungi that would otherwise thrive in such hot moist climates [3,4]. Significant efforts have focused on mimicking the naturally occurring structures of the lotus leaf, which demonstrates superhydrophobic self-cleaning properties [4]. However, existing fabrication methods have limited the ability to accurately mimic both the surface structures and resulting water-repellent behavior of the lotus under droplet impact.

In this work, a novel method for creating biomimetic hierarchical surfaces based on the *Tobacco mosaic virus* (TMV) is implemented to study the role of length scales on the anti-wetting behavior of superhydrophobic surfaces. The TMV is a plant virus, measuring 300 nm in length and 18 nm in diameter, which is benign to humans and can be genetically engineered to have enhanced binding properties. The use of the TMV for the synthesis of biomimetic water-repellent surfaces has several specific advantages over existing techniques. Specifically, the existence of functional groups enables self-assembly and directed patterning over a wide range of materials (metals, ceramics and polymers) and geometries [5].

## FABRICATION

Biomimetic surfaces inspired by the lotus leaf have been fabricated using self-assembly and metallization of the *Tobacco mosaic virus* onto micropillar arrays. A photo-definable negative resist (SU-8 10, Microchem) was spin-coated to a thickness of

15 μm on a silicon wafer and exposed to create micropost arrays. The wafer was then diced into individual 2 cm x 2 cm die. The die were placed in a phosphate buffer solution (pH 7) containing the TMV at a concentration of 0.1 mg/mL and allowed to incubate overnight where the virus self-assembled on the exposed silicon and SU-8 surfaces. After TMV assembly, the surface-exposed cysteines of the virus were activated with a palladium catalyst in a solution prepared by mixing a palladium salt with phosphate buffer. The samples were then coated with nickel in an electroless plating solution in which they were immersed for 3-5 minutes. The catalyst solution was prepared by dissolving 29 mg of NaPdCl<sub>4</sub> in 10 mL of DI water. The nickel plating solution was prepared by mixing 0.6 g NiCl<sub>2</sub>, 0.45 g Glycine, 1.5 g Na<sub>2</sub>B<sub>4</sub>O<sub>7</sub>, 0.77 g DMAB and 25 mL of DI water and stirring until solution turns to pH 7.

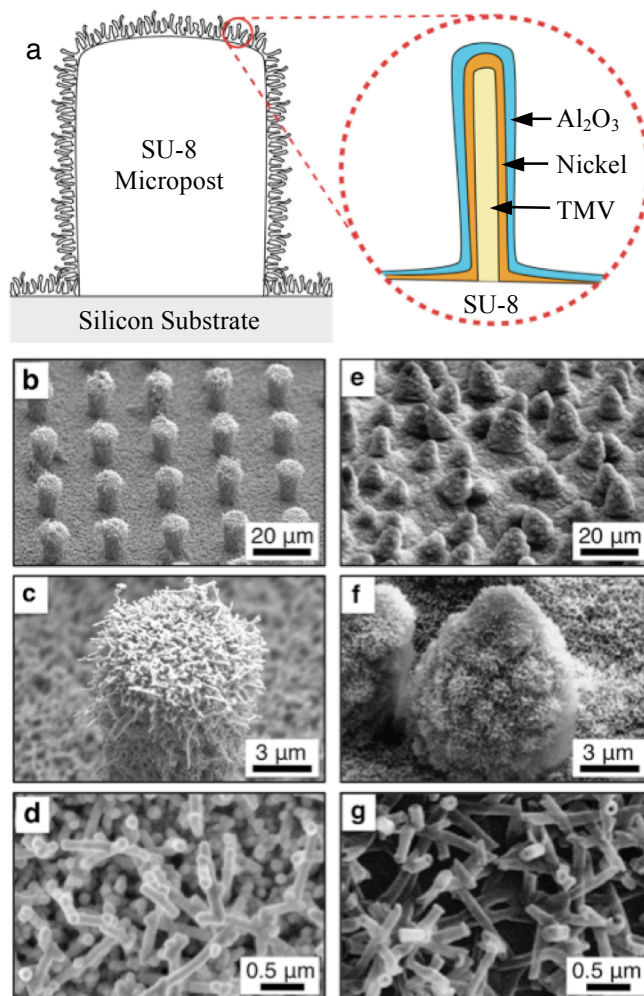


Figure 1: (a) Cross sectional schematic of the hierarchical surface structures and a direct comparison of (b-d) the biomimetic surfaces with (e-g) the naturally occurring lotus leaf [3].

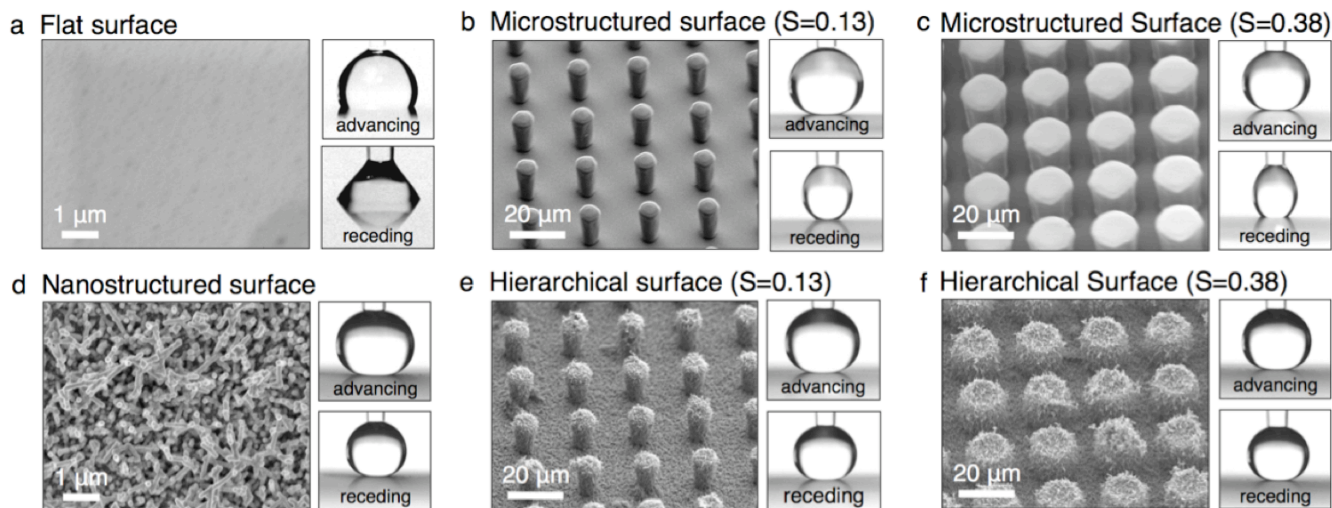


Figure 2: SEM images of experimentally characterized surfaces and optical images of their advancing and receding contact angles. (a) Flat surface, (b,c) microstructured surfaces with 15  $\mu\text{m}$  tall posts spaced 20  $\mu\text{m}$  apart with diameters and solid fractions of (b)  $d = 8 \mu\text{m}$ ,  $S = 0.13$  and (c)  $d = 14 \mu\text{m}$ ,  $S = 0.38$ , (d) nanostructured surface, and (e,f) hierarchical surfaces with 15  $\mu\text{m}$  tall posts (with nanostructures) spaced 20  $\mu\text{m}$  apart with diameters and solid fractions of (e)  $d = 8 \mu\text{m}$ ,  $S = 0.13$  and (f)  $d = 14 \mu\text{m}$ ,  $S = 0.38$ .

After metallization, the surfaces were functionalized through atomic layer deposition (ALD) of  $\text{Al}_2\text{O}_3$  followed by vapor-phase deposition of silane to achieve superhydrophobic properties. A uniform 15 nm thick  $\text{Al}_2\text{O}_3$  was deposited, which also provides a conformal coating to the nanoscale features of the virus. A silane monolayer was formed onto the  $\text{Al}_2\text{O}_3$  surface at room temperature with the samples exposed to vapor-phase (Tridecofluoro-1,1,2,2-Tetrahydrooctyl)-1-Trichlorosilane for 40 minutes.

Figure 1(a) shows a cross-sectional schematic of the resulting micro- and nano-scale surface structures while Fig. 1(b-g) provides a side-by-side comparison of the biomimetic and naturally occurring surfaces at various length scales. As can be seen, self-assembly of the TMV provides consistent and conformal coverage of the polymer microstructures. This is particularly important for the current work, where not only the scale of the nanostructure is well mimicked, but also the shape and orientation, resulting in surfaces that closely resemble the lotus leaf. This has implications on both the physics of water-repellency as well as the viability of this nanomanufacturing technique for large-scale production.

Figure 2 shows the six surfaces fabricated for the current work. Flat surfaces both with (Fig. 2(d)) and without (Fig. 2(a)) viral nanostructures, as well as microstructured (Fig. 2(b,c)) and hierarchically structured (Fig. 2(e,f)) surfaces with two different solid fractions, have been synthesized and experimentally characterized. The solid fraction of the surfaces is calculated as  $S = \pi d^2 / 4L^2$ , where  $d$  and  $L$  are the pillar diameter and center-to-center spacing, respectively.

## CHARACTERIZATION

Droplet contact angle measurements and droplet impingement imaging were obtained using a high-speed camera (Phantom v7.1, Vision Research) and image-processing software (ImageJ). A micropump and controller (Micro4 Syringe Pump, World Precision Instruments) was used to dispense and control water droplets.

### Contact Angle Measurements

Superhydrophobic surfaces are defined as those with static contact angles greater than  $150^\circ$ , contact angle hystereses of less than  $10^\circ$ , and roll-off tilt angles typically less than  $2^\circ$ . Contact angle hysteresis is defined as the difference between the advancing

and receding contact angles, and the roll-off tilt angle is the angle of a tilted surface at which a droplet will roll off. These three values are inter-related and collectively used to determine a surface's ability to demonstrate self-cleaning behavior.

Static contact angle measurements were obtained by applying single 10  $\mu\text{L}$  droplets to the sample surface and evaluating the apparent contact angle using image processing software. Advancing and receding contact angles were measured by increasing and decreasing the volume of a droplet on the sample surfaces while capturing images (Fig. 2). The nanostructured and hierarchical surfaces demonstrated roll-off angles below the accuracy of the measurement capabilities ( $< 0.25^\circ$ ), and at no time during the testing of these surfaces could a droplet be maintained in static equilibrium. Accordingly, the static contact angle for nanostructured and hierarchical surfaces was taken to be the average of the advancing and receding contact angles. This is an acceptable approximation as the contact angle hysteresis is smaller than the accuracy of the measurement method. Results for static contact angle and contact angle hysteresis are shown in Fig. 3, for each fabricated sample. Both the nanostructured and hierarchical surface are superhydrophobic with static contact angles over  $170^\circ$  and hystereses less than  $2^\circ$ .

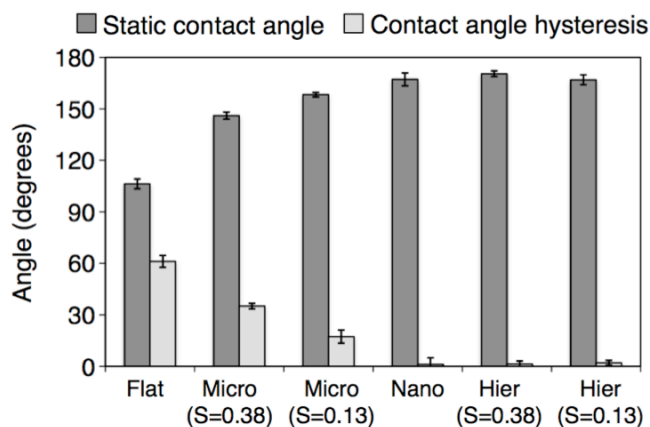


Figure 3: Experimental results of static contact angle and contact angle hysteresis for each fabricated sample shown in Fig. 2.

These results raise interesting questions about the need for hierarchical structures in superhydrophobic water-resistant surfaces. If superhydrophobicity can be achieved with nanoscale features alone, why do self-cleaning aquatic and wetland plant leaves invariably have hierarchical surface structures [3]? The answer lies in the role of each length scale on water-repellency under droplet impact.

### Droplet Impact Wetting

The relationship between contact angle and surface roughness is predicted by the theories of Cassie and Baxter, and Wenzel [5]. Cassie and Baxter's theory governs the behavior of static droplets resting on top of the surface roughness. Vapor pockets are present underneath the liquid resulting in a composite liquid-vapor-solid interface. In Wenzel's model, the droplet has completely penetrated the roughness and no vapor pockets are present. A droplet in the Wenzel state pins to the surface structures and resists droplet motion. While the Cassie state is statically stable, a droplet can be forced into the Wenzel state by overcoming an energy barrier that exists between the two states [5]. This transition from Cassie to Wenzel can occur during droplet impact and will be destructive to self-cleaning properties, making the dynamics of impingement crucial for robust self-cleaning surfaces. Accordingly, the wetting of superhydrophobic surfaces under droplet impact has been experimentally investigated.

To study the role of dual length scales on droplet impingement, 10  $\mu\text{L}$  droplets (2.7 mm diameter) were dropped from heights of 0.5-100 cm on each sample, resulting in impact velocities of 0.2 - 4.3 m/s. High speed imaging of droplet impacts on various surfaces are shown in Fig. 4. Figure 5(a) shows the critical impact velocity,  $V_C$ , at which wetting of a surface is first observed. At speeds higher than this value, the droplet (or some fraction of the droplet) remains attached, signifying a transition to the Wenzel state. Figure 5(b) shows the critical kinetic energy,  $E_C$ , of the droplet at which transition is first observed, defined as

$$E_C = 0.5mV_C^2 \quad (1)$$

where  $m$  is the mass of the droplet.

The microstructured surfaces wet at relatively low critical velocities while the nanostructured surface transitions to a wetted state at 2.7 m/s. Figure 4(a,b) shows high-speed images of droplets impacting microstructured ( $S=0.38$ ) and nanostructured surfaces above their critical velocities. Transition is seen for both; a large pinned droplet remains on the microstructured surface for a velocity of 2.1 m/s, and a small pinned droplet remains on the nanostructured surface for a velocity of 4.3 m/s.

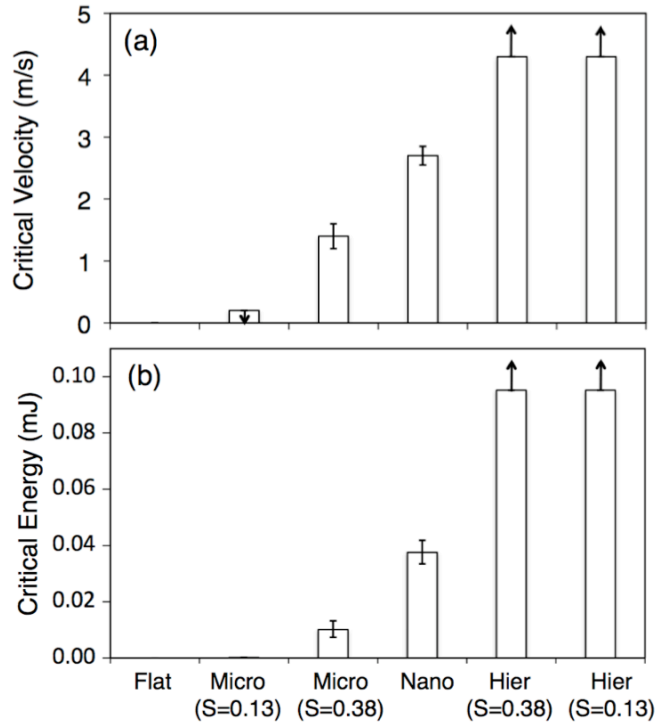


Figure 5: Droplet impact wetting results showing (a) the critical impact velocity,  $V_C$ , and (b) the critical impact energy,  $E_C$ , required to wet each fabricated surface structure.

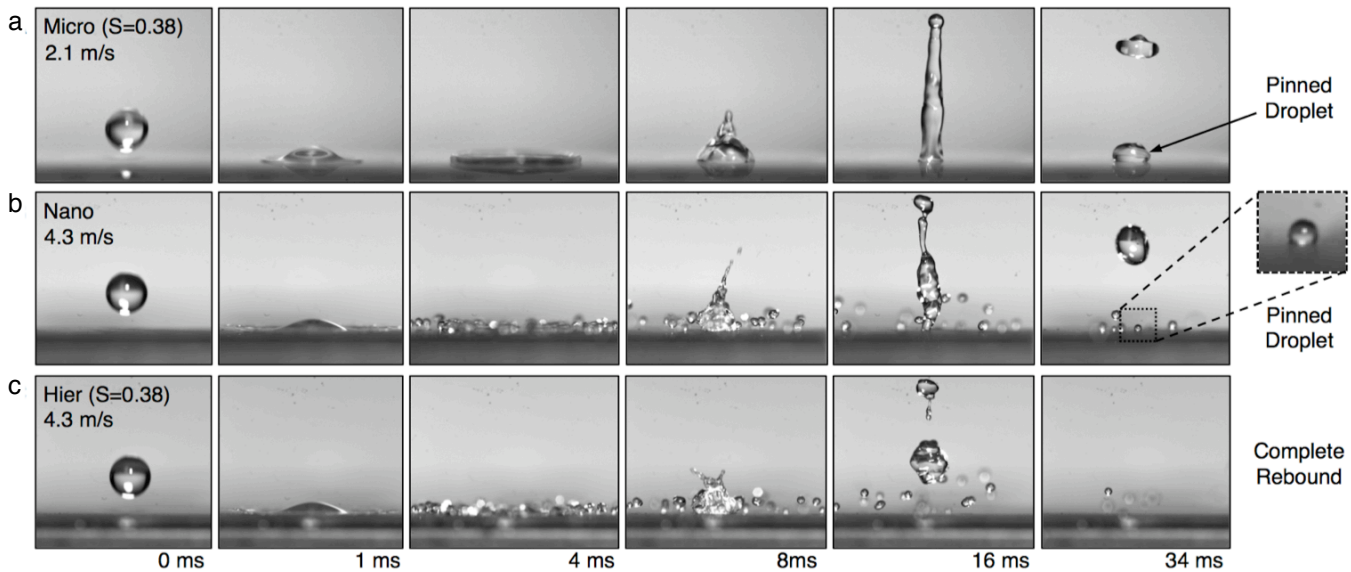


Figure 4: High-speed imaging of 10  $\mu\text{L}$  droplets impacting (a) the microstructured surface with a solid fraction of  $S=0.38$  and an impingement velocity of 2.1 m/s, showing a large portion of the droplet wetted to the surface and partial rebound, (b) the nanostructured surface with a velocity of 4.3 m/s showing partial wetting and break-up into satellite droplets, and (c) the hierarchical surface with a solid fraction of  $S = 0.38$ , showing complete rebound and break-up into satellite droplets.

The hierarchical surface shows complete rebound and break-up of the impinging droplets for all achievable speeds (Fig. 4(c)). While the critical velocities of the hierarchical surfaces have not been determined, it can be seen that the critical kinetic energy for the hierarchical transition is notably higher than the sum of its nano and microscale components (Fig. 5(b)). For the maximum speed considered (4.3 m/s), the critical kinetic energy for hierarchical transition is shown to be at least twice as large as the sum of its components.

These counterintuitive results can be explained by considering the effects of compressibility on the impact pressure of impinging droplets. As a spherical droplet impacts a perfectly flat surface, a compressible no-flow region is generated in the droplet, resulting in large pressures associated with the compressed fluid [7]. This compressibility event occurs over a circular area on the order of tens of microns for millimeter-scale droplets falling at terminal velocities [7]. This critical length scale is identically matched by the microscale component of hierarchical structures found in aquatic and wetland plants and suggests that each length scale plays a distinct role in water repellency under droplet impact. It is proposed here that the microstructures have a destructive effect on the generation and propagation of the large pressures associated with compression, while the nanostructures provide a large anti-wetting Laplace pressure resisting transition to a wetted state.

### Dropwise Condensation

In addition to biomimetic self-cleaning behaviors, robust superhydrophobic surfaces can be implemented for the enhancement of condensation heat transfer rates. During the condensation process, water vapor changes phase into liquid on a sub-cooled surface. The liquid water forming on this surface results in an increased thermal resistance between it and the condensing vapor, which can greatly reduce the heat transfer coefficient of the process. Superhydrophobic surfaces are promising for the realization of drop-wise condensation heat transfer, where the condensing liquid does not wet the interface but instead forms into small droplets that roll off of the surface. This eliminates the existence of an insulating water film and has the potential to increase heat transfer coefficients by a factor of ten.

The condensation heat transfer performance of the hierarchical structures was evaluated by exposing the surface to a jet of water vapor while controlling the backside temperature using a thermoelectric module and active cooling. Figure 6 shows a sample being tested at a 45° incline, while Fig. 7 shows preliminary experimental results for the hierarchical and flat surfaces. A two-fold increase in heat transfer coefficient was observed for the superhydrophobic surfaces as compared to flat samples with identical surface chemistries.

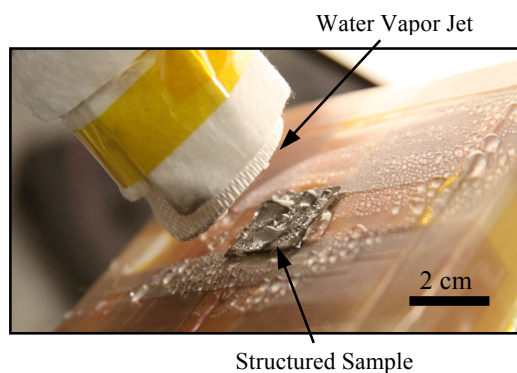


Figure 6: Image of the condensation process across a structured sample subject to a jet of condensing water vapor.

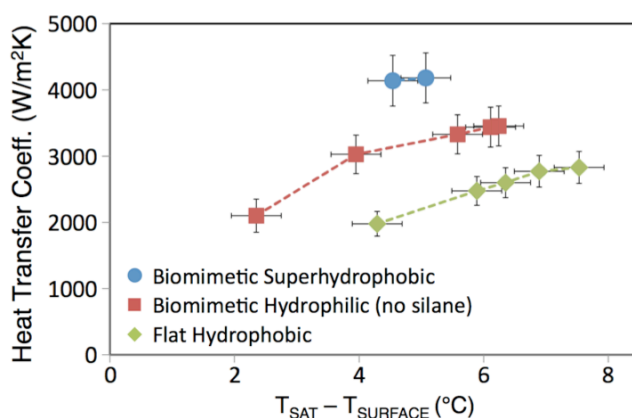


Figure 7: Experimental results of condensation heat transfer coefficient as a function of sub-cooling temperature.

### CONCLUSIONS

Biomimetic surfaces inspired by the hierarchical structures of the lotus leaf have been fabricated using self-assembly and metallization of the *Tobacco mosaic virus* onto micropillar arrays. Wetting properties of the biomimetic superhydrophobic surfaces were evaluated through contact angle measurements, droplet impingement testing, and drop-wise condensation heat transfer studies. Static contact angles of over 170° and contact angle hystereses of less than 2° have been achieved. While surface hierarchy has little effect on the wetting of static droplets, it has been shown that hierarchical structures play an important role in water repellency under droplet impact. In addition, a two-fold increase in condensation heat transfer coefficient has been achieved with biomimetic surfaces as compared to flat surfaces.

By investigating the wetting mechanisms of biological structures, deeper insights into the design of high-performance thermal-fluidic systems can be gained. This work serves as a basis for developing robust superhydrophobic structures for self-cleaning surfaces, drop-wise condensation heat transfer, and drag reduction in both microscale and macro scale applications.

### REFERENCES

- [1] X. Feng, *et al.*, “Design and Creation of Superwetting and Antiwetting Surfaces”, *Advanced Materials*, 18, 3063 (2006).
- [2] J. Boreyko, *et al.*, Self-Propelled Dropwise Condensate on Superhydrophobic Surfaces”, *Phys. Rev. Letters*, 103, 184501 (2009).
- [3] K. Koch, *et al.*, “Multifunctional Surface Structures of Plants: An Inspiration for Biomimetics”, *Prog. in Mat. Science* 54, 137 (2009).
- [4] A. Solga, *et al.*, The Dream of Staying Clean: Lotus and Biomimetic Surfaces”, *Bioinspiration and Biomimetics*, 2, S126 (2007).
- [5] K. Gerasopoulos, *et al.*, “Biofabrication Methods for the Patterned Assembly and Synthesis of Viral Nanotemplates”, *Nanotechnology*, 21, (2010).
- [6] A. Lafuma, *et al.*, “Superhydrophobic States”, *Nature Mat.*, 2, (2003).
- [7] O.G. Engel, “Damage Produced by High-Speed Liquid-Drop Impacts”, *J. Appl. Phys.* 44, 692 (1973).

### CONTACT

\*M. McCarthy, tel: +1-617-253-6401, mattmcc@mit.edu

# BULK METALLIC GLASS NANOWIRES FOR USE IN DIRECT ALCOHOL FUEL CELL

Marcelo Carmo<sup>1a</sup>, Shiyun Ding<sup>1b</sup>, Golden Kumar<sup>1b</sup>, Kai Sun<sup>2</sup>, Jan Schroers<sup>1b</sup> and André D. Taylor<sup>1a\*</sup>

<sup>1a</sup>Chemical Engineering Department,  
<sup>1b</sup>Mechanical Engineering Department  
Yale University, New Haven, CT, USA

<sup>2</sup>Department of Materials Science and Engineering – The University of Michigan, Ann Arbor, MI, USA

## ABSTRACT

A key issue for direct alcohol fuel cells is its meager performance due to poor efficiency and durability of the catalysts. Developing a new class of materials that can outperform conventional catalysts during long-term operation is of critical importance. Here we report for the first time a nanoimprinting approach using Pt<sub>57.5</sub>Cu<sub>14.7</sub>Ni<sub>5.3</sub>P<sub>22.5</sub> bulk metallic glass (BMG) to create a new class of high performance nanowire catalyst. Accelerated durability tests reveal that BMG nanowires maintain their electrochemical surface area in comparison to conventional Pt/C catalysts. BMGs represent a new class of high performance fuel cell catalysts that are CMOS compatible.

## INTRODUCTION

Micro fuel cells were once championed as viable alternatives over existing battery technology for portable electronic devices. However, a key remaining issue is the meager performance of these devices due to poor efficiency and durability of the catalysts [1]. The poor durability of the commercial platinum supported on carbon black (Pt/C) catalyst is reflected by a significant loss of platinum electrochemical surface area (ECSA) over time during fuel cell operation [2]. The mechanisms for the loss of platinum ECSA (Fig. 1) have been discussed [2] and can be summarized as; corrosion of the carbon support, platinum dissolution and platinum nanoparticle agglomeration.

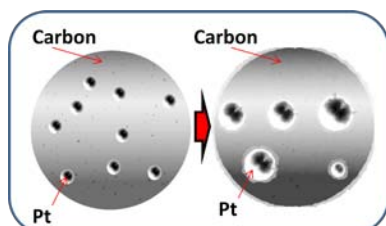


Figure 1 – Conventional Pt/C catalysts suffering from nanoparticles agglomeration and dissolution over long term operation.

Developing a new class of materials that can circumvent Pt-based anode poisoning (loss of efficiency/performance) and the agglomeration or dissolution (durability issue) of supported catalysts during long-term operation is of critical importance (Fig. 1). Here we report for the first time a CMOS compatible approach using Pt<sub>57.5</sub>Cu<sub>14.7</sub>Ni<sub>5.3</sub>P<sub>22.5</sub> bulk metallic glass (BMG) [3] to create a new class of high performance nanowire fuel cell catalyst. These BMG nanowires materials have the potential to eliminate the degradation pathways described above. Since these catalysts do not require a support, the support corrosion problem is eliminated; BMG nanowires are also less vulnerable to dissolution during fuel cell operation than the Pt/C nanoparticles. Additionally, the BMGs have an anisotropic morphology that can improve mass transport and catalyst utilization [4].

## RESULTS AND DISCUSSION

Accelerated fuel cell durability comparisons reveal that BMG nanowires maintain their electrochemical surface area (ECSA) in comparison to conventional Pt/C catalysts (Fig. 2). In fact, the

BMG ECSA showed a slight increase whereas the commercial Pt/C catalyst lost about 35% after 1000 cycles. This loss can be attributed to the agglomeration and dissolution of platinum nanoparticles (Fig. 1), while the increase in ECSA for the BMG represents an alloy improvement described by an increase in the Pt surface area as the copper in the BMG dissolves [5].

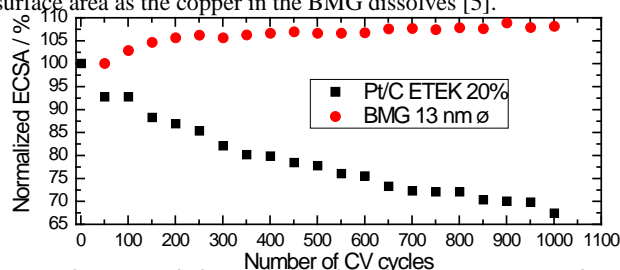


Figure 2 - Loss of electrochemical surface area (ECSA) of BMG 13nm and Pt/C (E-TEK) catalysts with number of CV cycles in nitrogen-purged 0.5 molL<sup>-1</sup> H<sub>2</sub>SO<sub>4</sub> solution at room temperature (0.05–1.2 V vs. RHE, sweep rate 50 mVs<sup>-1</sup>). The BMG catalyst maintains performance after 1000 cycles while the conventional E-TEK catalyst decreases by ~35%.

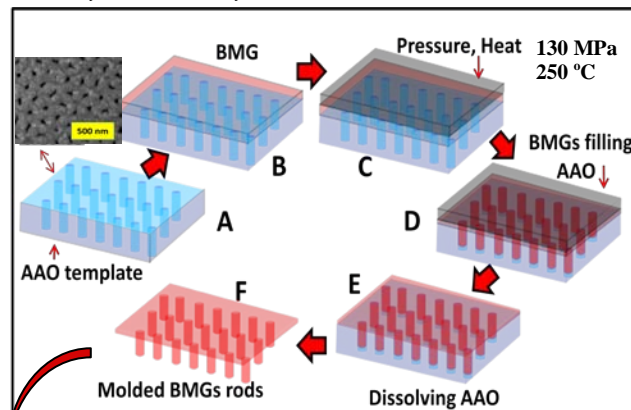


Figure 3 – Schematic synthesis of BMG nanowires.

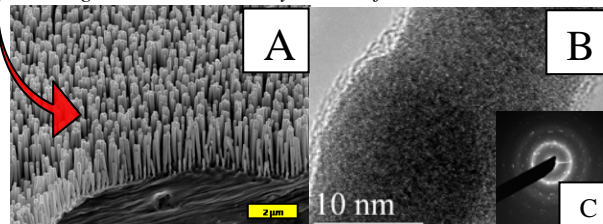


Figure 4 – A) Scanning Electron Microscopy (SEM), B) Transmission Electron Microscopy (TEM) and C) Selected Area Electron Diffraction (SAED) images for BMG nanowires.

BMGs are a subset of glass forming alloys that can be easily vitrified and formed into relatively large amorphous sections [3]. The absence of crystallites, grain boundaries and dislocations in the amorphous structure of bulk metallic glass results in a homogeneous and isotropic material down to the atomic scale, which displays very high strength, hardness, elastic strain limit and

corrosion resistance. Because of their accommodation to dimensions at multiple length scales, BMGs can be formed into high catalyst surface areas without the need for a high surface area support. The BMG nanowire fabrication sequence (Fig. 3) allows the diameter of nanowires to be controlled from ca. 100 nm to 10 nm (Fig. 4) with an aspect ratio up to 200:1 [4]. These length scales are very close to conventional fuel cell supported catalyst particles dimensions and can easily be synthesized inside of a micro fabrication foundry, differentiating this process from existing complex catalyst synthesis techniques. The BMG is heated (250 °C) into the super cooled liquid region where it softens and under applied pressure (130 MPa) can be thermoplastically imprinted (Fig. 3c) so that the BMG fills the nanopores (Fig. 3d). We note that the diameters of the BMG nanowires can be made even smaller dependent upon the template dimensions [3]. The alumina (AAO) template is dissolved in KOH solution (Fig. 3e) to isolate the nanowires. Fig. 4 shows the a) SEM and b) TEM image of the BMGs. The uniform vertical nanowires are well-isolated and parallel to one another. The selected area diffraction (SAED) image (Fig. 4c) suggests a polycrystalline Pt structure with a complete alloy formation, however, we are currently investigating whether the e-beam could influence the crystallinity of the BMG. Noble metal alloys have shown enhanced performance over conventional Pt/C catalysts [5, 6], however, traditional thin film sputtering or e-beam evaporation cannot form the high surface areas needed for the electrochemical reactions [5, 7, 8]. Nanowires synthesized from organometallic precursors suffer from complex synthesis and low throughput/reproducibility (size control) [7]. Fig. 5a illustrates the CO oxidation for several electrodes used for this study: pure Pt, BMG flat surface, and BMG nanowires (x length and diameters ranging from 100 down to 13 nm.). The BMG nanowires have a higher  $\text{CO}_{\text{ads}}$  tolerance due to a higher onset potential for CO oxidation.

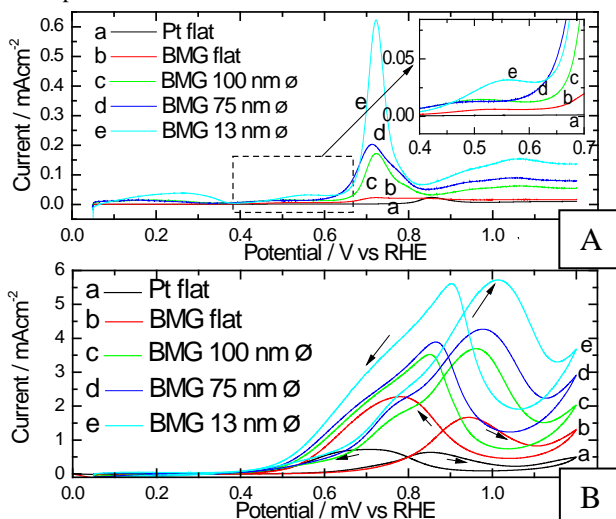


Figure 5 – A) CO stripping illustrates a higher performance for adsorbed CO oxidation for BMGs over pure Pt. The wire diameters illustrate the higher surface area (performance) of the smaller diameter wires in the same fixed area and wire length. B) Ethanol 1.0 molL<sup>-1</sup> oxidation illustrating a superior catalyst performance of BMG materials for direct ethanol fuel cells in comparison to pure Pt. Electrolyte: 0.5 molL<sup>-1</sup> H<sub>2</sub>SO<sub>4</sub> solution at room temperature, sweep rate 50 mVs<sup>-1</sup>.

This suggests that BMG nanowires are not as susceptible to self-poisoning (due to CO generation from the alcohol electro-oxidation step) as pure platinum. Electrochemical characterizations show a higher ethanol activity for BMG nanowires (Fig. 5b).

The nanowires become more active at higher potentials ( $E > -0.2$  V) and demonstrate higher alcohol oxidation current densities than the BMG flat disc and pure Pt disc. The Pt-enriched nature of the outer surface enables all surface sites of the BMG nanowires to be highly conductive. This is conducive to the reaction kinetics on the catalyst surfaces, and hence may result in an enhancement in the electrochemical activity (Fig. 6).

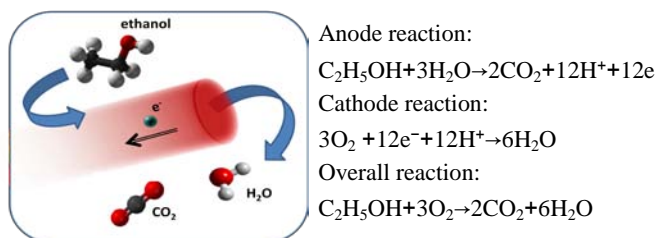


Figure 6 – Ethanol oxidation over bulk metallic glass (BMG) nanowire.

The electronic and strain effects may also play a major role in the activity enhancement. The enhanced activity for the alcohol oxidation Pt based BMGs with respect to pure Pt can also be ascribed to the synergetic effect of Cu and Ni oxides [1].

## CONCLUSIONS

We have shown experimentally that the alcohol oxidation reaction activity and stability of fuel cell electrodes could be enhanced through the application of BMGs. BMG nanowires surpass the performance of conventional Pt/C catalysts. BMG nanowires created via nanoimprinting **represent a new class of high performance fuel cell catalyst materials that are CMOS process compatible**. On-going efforts are underway to integrate these materials into our previously described micro fuel cell architecture [8]. The performance can be further optimized through its chemical composition and structure to address a wide range of functionalities. The ability to form these materials into very high surface areas opens up a new range of possibilities for next-generation electrochemical devices and sensors.

## REFERENCES

- [1] K Kinoshita, Electrochemical oxygen technology, Wiley Inc., New York, 1992.
- [2] P.J. Ferreira, et al., "Instability of Pt/C Electrocatalysts in PEMFC - A Mechanistic Investigation", Journal of the Electrochemical Society, 152, A2256, (2005).
- [3] G. Kumar, H.X. Tang, J. Schroers, "Nanomoulding with Amorphous Metals", Nature, 457, 868 (2009).
- [4] J. Shroers, N. Paton, "Amorphous Metal Alloys Form like Plastics", Advanced Materials & Processes, 164, 61, (2006).
- [5] P. Mani, R. Srivastava, P. Strasser, "Dealloyed Pt-Cu Core-Shell Nanoparticle Electrocatalysts for Use in PEMFCs", Journal of Physical Chemistry C, 112, 2770 (2008).
- [6] M. Carmo, et al., "Alternative Supports for the Preparation of Catalysts for PEMFCs: The Use of Carbon Nanotubes", Journal of Power Sources, 142, 169, (2005).
- [7] J.T. Hu, T.W. Odom, C.M. Lieber, "Chemistry and Physics in One Dimension: Synthesis and Properties of Nanowires and Nanotubes", Accounts of Chemical Research, 32, 435, (1999).
- [8] A.D. Taylor, et al., "Nanoimprinted Electrodes for Micro Fuel Cell Applications" Journal of Power Sources, 171, 218, (2007).

## CONTACT

\*André D. Taylor, tel: (203) 432-2217; [andre.taylor@yale.edu](mailto:andre.taylor@yale.edu)

# DETACHMENT LITHOGRAPHY: FABRICATION OF 3D MICROSTRUCTURES AND GUIDED-ASSEMBLY OF NANOMATERIALS

Junghoon Yeom<sup>1,2,\*</sup> and Mark A. Shannon<sup>1,2,\*\*</sup>

<sup>1</sup>Department of Mechanical Science and Engineering, University of Illinois, Urbana, Illinois, USA

<sup>2</sup>Cbana Labs Inc., Champaign, Illinois, USA

## ABSTRACT

We present a versatile technique to create arrays of micrometer-size patterns of photosensitive polymers like photoresists (PRs) on the surface of soft stamps and to transfer these patterns to planar, curved, and porous substrates. A PR film was patterned through detachment lithography, utilizing the difference in adhesion to induce the fracture in the film. Various 3D structures were fabricated on glass cylinders as well as flat Si substrates. The detached patterns were printed on a nanoporous membrane, facilitating the guided assembly of nanomaterials.

## MAIN TEXT

Photolithography, despite its dominance in the industries of microelectronics and MEMS for patterning photoresists (PRs), finds a limitation in adapting to curved or 3D substrates due to its reliance on projection optics and the limited depth of focus [1]. Among many recent developments, micro-contact printing ( $\mu$ CP) has received considerable attentions to provide a low-cost microfabrication technique as well as produce patterns on complex geometries [2]. The  $\mu$ CP process, however, is normally used to pattern self-assembled monolayers or organic molecules, not PRs that have high molecular weights.

Our approach to the  $\mu$ CP patterning of PRs is to bring a PR film spin-coated on a flat PDMS stamp into intimate contact with a rigid mold with protruding features, and then remove the stamp to pick up the portions of the film that are not in contact (Fig. 1) [3]. This subtractive method for patterning, called detachment lithography (DL), utilizes the mechanical fracture in the film, in which the shear stress for fracture is provided by the difference in adhesion between the mold/film and film/stamp interfaces [4]. The DL process can be harnessed in two ways: i) the detached PR patterns on the stamp can be subsequently printed onto the substrates (right, Fig. 1) and ii) the PR films transferred onto the Si mold remain photochemically active and can be used to form 3D microstructures (left, Fig. 1).

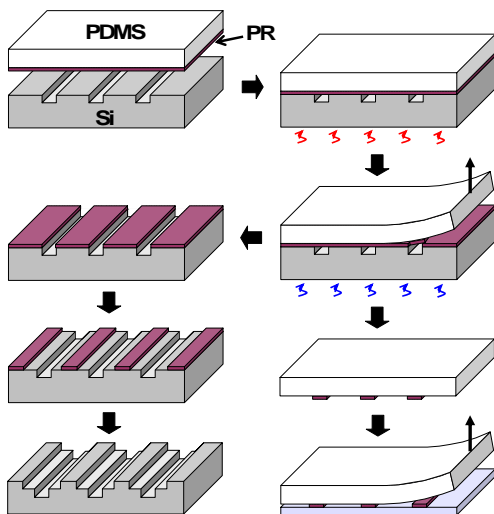


Figure 1: A schematic of the DL process flow.

A thin film of PR (0.5–3  $\mu$ m) was spin-coated on the flat PDMS stamp, and then the film on the stamp was brought into conformal contact with the pre-patterned Si mold. After annealing, the stamp-PR-mold stack was placed on a cold Al block, and the stamp was removed from the mold in a fast peeling speed ( $> 10$  cm/s). The regions of the PR film in contact with the protruded parts of the mold were detached, leaving the opposite patterns of the PR on the stamp. The fast removal of the stamp at reduced temperature increased the adhesion between the stamp and film, improving the detachment yield. On the other hand, when the detached film on the stamp was transferred to a receiving substrate, the stamp was removed from the substrate at much slower peeling and an elevated temperature. Thus, the yield of the DL process and ensuing transfer was significantly improved using the kinetically and thermally adjustable adhesion of the elastomeric stamp.

Figure 2(a-b) shows the SEM images of the various detached PR patterns that were printed on the glass slides. The adhesion of the transferred PR films was strong enough to withstand subsequent etching or liftoff process. When a glass cylinder was rolled across the surface of the stamp, the PR patterns were transferred from the stamp to the rod surface (Fig. 2c). The thicker PR patterns were also transferred to the etched Si substrate, demonstrating the feasibility of creating free-standing microstructures (Fig. 2d). The minimum feature size attained via the DL process depends on the film thickness, molecular weight, and process parameters (peeling speed and temperature) [5]. For S1805 of 0.56  $\mu$ m in thickness, as small as 5- $\mu$ m lines separated by 5- $\mu$ m could be detached and transferred. The completeness of detachment was investigated with XPS and micro Raman spectroscopy. The element scan from XPS showed no residual PR from the detached region, and Raman signal for PR was not detected from the PDMS stamp after detachment.

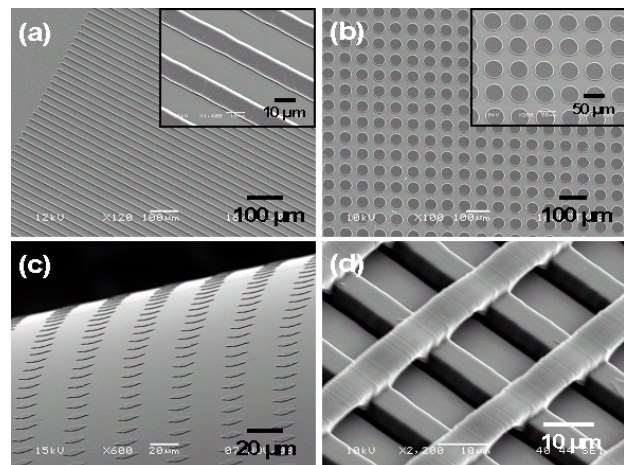


Figure 2: The detached PR patterns are transferred to planar, curved, and protruded substrates. SEM images of 0.85- $\mu$ m-thick PR S1805 are shown for an array of (a) 10  $\mu$ m lines separated by 20  $\mu$ m, (b) 50  $\mu$ m circles separated by 20  $\mu$ m printed on glass slides, (c) 10 x 10  $\mu$ m squares transferred on a glass cylinder of 6 mm in dia., and (d) 7  $\mu$ m lines tenting over the etched patterns.



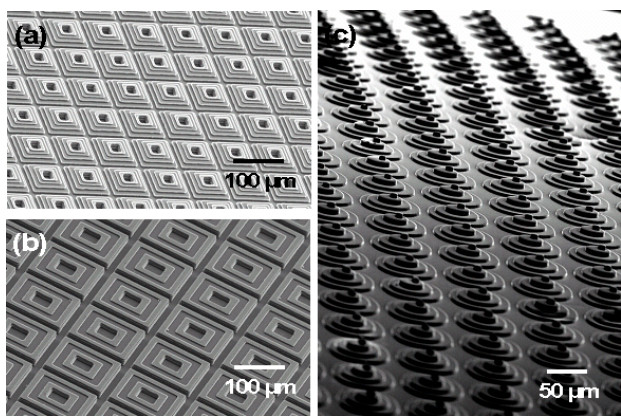


Figure 3: SEM images of an array of (a-b) 4-level Si microstructures using DRIE etching with the transferred PR as a mask, (c) multilevel PDMS microstructures molded from the Si microstructures and bonded onto a glass cylinder.

The transferred PR films on the Si mold in Fig. 1 remain photochemically active and can be patterned using standard photolithography. PR 1518 was transferred only to the top surface of the pre-etched Si, and the transferred film was uniform across the 5-cm wafer area. After exposure and development, the patterned PR served as an etch mask, and the already-etched Si substrate was further etched using DRIE to form Si multilevel structures (Fig. 3a-b). These 3D structures are difficult to be fabricated because non-uniform coating of PR is generated when spin-coated or sprayed. The smallest features in the 3D structures we fabricated were as small as 2-μm, and the submicron 3D structures could be generated if the proper masks were available. The 3D structures on the curved surface were also created by the PDMS molded from the multilayer Si structures and bonded on a glass rod (Fig. 3c).

Another challenging substrate to be patterned is a porous membrane. If the PR solution is spin-coated or sprayed, the PR would flow into the pores, making it difficult to be exposed and developed. Moreover, many porous substrates are fragile and delicate, and the lamination with dry photoresist films may damage the porous membrane or substrate. With the DL process, the PR patterns picked up by the stamp can be printed onto the porous membrane without damaging or plugging the pores.

As a proof-of-a-concept, the detached PR patterns were transferred to the anodized aluminum oxide (AAO) membrane (Fig. 4a). The utility of the patterned porous membrane was demonstrated when various nanomaterials in solution were vacuum-filtered through the membrane [6]. The nanomaterials would deposit only on the windows of the patterned membrane, which may represent a facile, robust, and inexpensive assembly method of nanomaterials. The single-walled carbon nanotubes and latex particles of ~1 μm in solutions were assembled in the patterned AAO membrane as shown in Fig. 4b and c, respectively.

#### ACKNOWLEDGEMENT

The authors acknowledge the financial support from the NANO-CEMMS at the University of Illinois, which is funded by National Science Foundation under Grant DMI-0328162. We also thank the travel support from Cbana Labs Inc.

#### CONTACT

\*J. Yeom; jungyeom@illinois.edu,

\*\*M.A. Shannon; mshannon@illinois.edu

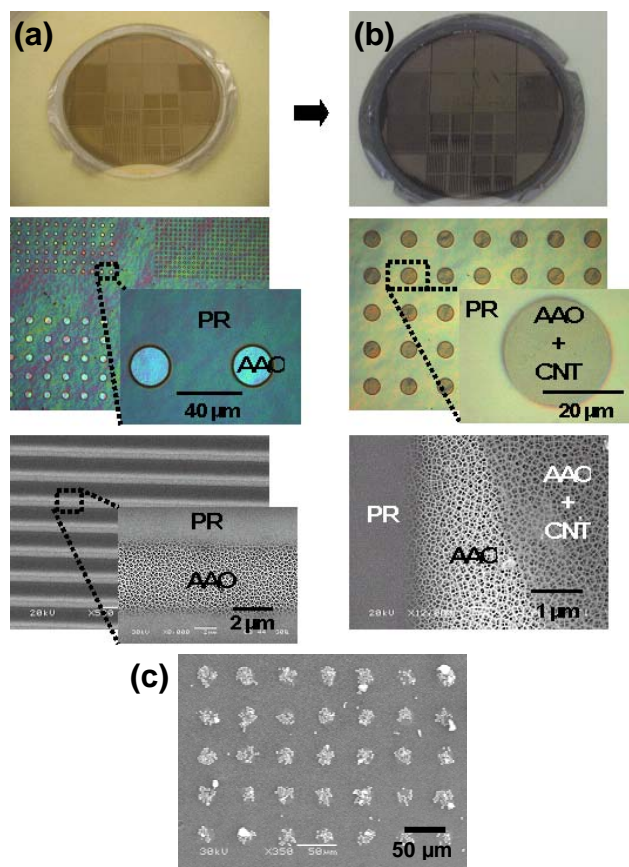


Figure 4: (a) the detached PR patterns transferred to a 220 nm anodized aluminum oxide (AAO) filter substrate, (b) single-walled carbon nanotubes (SWCNT) suspended in 1% SDS solution were vacuum-filtrated over the patterned AAO membrane, and (c) a SEM image of an array of 1 μm latex beads filtrated over the patterned AAO membrane.

#### REFERENCES

- [1] R.J. Jackman, J.L. Wilbur, and G.M. Whitesides, "Fabrication of Submicrometer Features on Curved Substrates by Microcontact Printing", *Science*, 269, 664-666 (1995)
- [2] Y. Xia and G.M. Whitesides, "Soft Lithography", *Angewandte Chemie International Edition*, 37, 5, 550-575 (1998)
- [3] J. Yeom and M.A. Shannon, "Detachment Lithography of Photosensitive Polymers: A Route to Fabricating Three-dimensional Structures", *Advanced Functional Materials*, 20, 2, 289-295 (2010)
- [4] J.-H. Choi, D. Kim, P.J. Yoo, and H.H. Lee, "Simple Detachment Patterning of Organic Layers and its Application to Organic Light-emitting Diodes", *Advanced Materials*, 17, 2, 166-171 (2005)
- [5] M.A. Meitl, Z.-T. Zhu, V. Kumar, K.J. Lee, X. Feng, Y.Y. Huang, I. Adesida, R.G. Nuzzo, and J.A. Rogers, "Transfer Printing by Kinetic Control of Adhesion to an Elastomeric Stamp", *Nature Materials*, 5, 1, 33-38 (2006)
- [6] J.H. Oh, H.W. Lee, S. Mannsfeld, R.M. Stoltenberg, E. Jung, Y.W. Jin, J.M. Kim, J.-B. Yoo, and Z. Bao, "Solution-Processed, High-performance n-Channel Organic Microwire Transistors", *Proceedings of the National Academy of Sciences*, 106, 15, 6065-6070 (2009)

# ELECTROTHERMAL MICROCANTILEVER WITH INTEGRATED SOLID-STATE HEATER-THERMOMETER AND NPN BACK-TO-BACK DIODES

Patrick C. Fletcher, Bikram S. Bhatia, Yan Wu, Mark A. Shannon, and William P. King\*

Department of Mechanical Science and Engineering, University of Illinois, Urbana, Illinois, USA

## ABSTRACT

This paper reports the integration of both electrical and thermal elements into an atomic force microscope (AFM) cantilever, where the electrode and heater-thermometer are electrically isolated by an NPN back-to-back diode. The electrothermal (ET) cantilever can be self-heated to more than 400°C while the tip voltage can be measured or controlled independent of tip temperature, up to 10 volts. To our knowledge, this is the first microcantilever to have a solid-state junction and heater integrated near a tip.

## INTRODUCTION

Microcantilevers with integrated heaters [1] can be used to control nanometer-scale temperature fields for data storage [2], nano-manufacturing [3], and materials analysis [4]. However, such probes are not well suited for nanoelectronic measurements, as they cannot independently control temperature and measure or apply electric potential. We report an electrothermal AFM cantilever which combines the functions of heated and electrically-conductive AFM cantilever tips.

## DESIGN

The microcantilever consists of doped single-crystal silicon and has three legs serving as electrical paths to the cantilever free end. The cantilever free end has an N-type heater, N+-type tip, and region of P+-doped silicon that electrically isolates these two functional regions. The N<sup>+</sup>P<sup>+</sup> junction is a Zener diode whereas the P<sup>+</sup>N junction is a standard diode. While the heater and electrode are electrically isolated, heat conduction between the two devices allows tip temperature control.

The key challenge in designing the cantilever was the integration of a high-quality NPN junction at the cantilever free end. The dopant distributions are critical to device performance and depend upon device thickness and diffusion process parameters. The dopant must diffuse through the thickness of the cantilever (1.5 μm) to avoid current leakage, but this process also narrows the P+-type region (5 μm) and risks current leakage at the top of the NPN junction. Fig. 1 (a) shows the doped NPN junction near the cantilever free end and Figs. 1 (b)-(d) shows simulation results for the doping concentrations near the NPN junction for the process used, which balances these competing requirements.

## RESULTS

Fig. 2 shows the cantilever fabrication process, which begins with an N-type silicon-on-insulator wafer doped with 10<sup>18</sup> atoms/cm<sup>3</sup> antimony. We fabricate sharp silicon tips and define the cantilever using DRIE etching down to the SiO<sub>2</sub> layer. Next, the cantilever legs are doped N+-type to 10<sup>20</sup> atoms/cm<sup>3</sup> with antimony ion implantation and a short initial diffusion. Similarly, the P+-type regions are doped to 10<sup>19</sup> atoms/cm<sup>3</sup> with boron ion implantation and the critical diffusion. The cantilever is released with a backside etch through the handle wafer and a hydrofluoric acid etch. One 4" wafer yields ≈300 devices with >90% yield. Fig. 3 shows micrographs of a fabricated cantilever and cantilever tip.

We characterized the cantilever electrical and thermal properties. Fig. 4 shows the current-voltage (I-V) characteristics for a back-to-back diode device using a current controlled sweep

across the solid-state heater and the NPN junction. The NPN isolation region is a Zener diode (N<sup>+</sup>P<sup>+</sup>) and a standard diode (P<sup>+</sup>N) facing away from each other. Breakdown voltages across

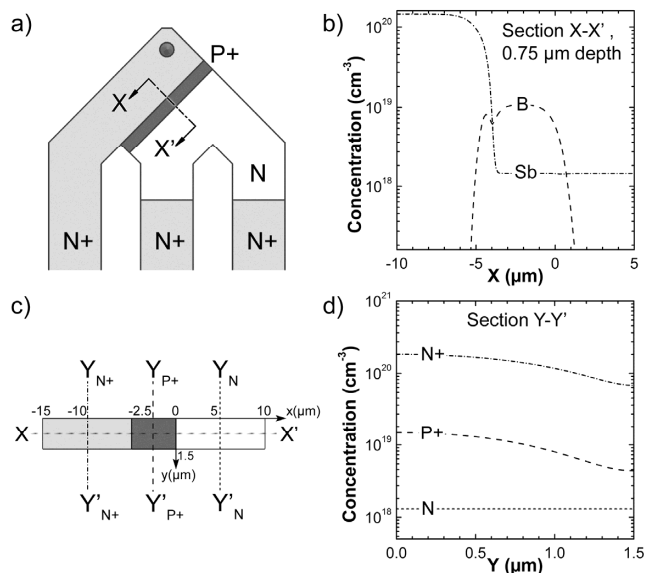


Figure 1. (a) Cantilever design with doping as indicated. (b) Simulation results of lateral and vertical doping concentrations for the NPN junction. A cross-section of the NPN junction is shown in (c), with the lateral X-X' doping concentrations shown in (b) and the vertical Y-Y' doping concentrations shown in (d). Target concentrations for the N<sup>+</sup>, P<sup>+</sup>, and N-type regions are 10<sup>20</sup>, 10<sup>19</sup>, and 10<sup>18</sup> atoms/cm<sup>3</sup>, respectively.

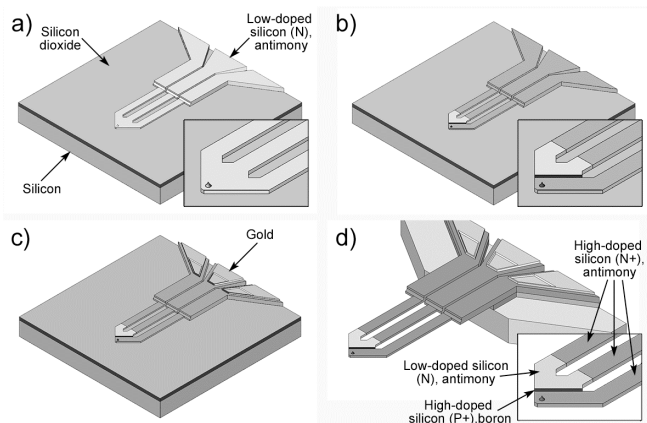


Figure 2. Fabrication process for NPN junction electrothermal cantilever. (a) Starting with an antimony-doped SOI wafer, we form and sharpen the tip using oxidation sharpening and define the cantilever shape using deep-reactive ion etching (DRIE), (b) then selectively dope the cantilever N+-type with antimony and P+-type with boron. (c) Electrical connections are formed with sputtered gold and the cantilever is released (d) with backside DRIE and an HF etch to remove the sacrificial SiO<sub>2</sub>.

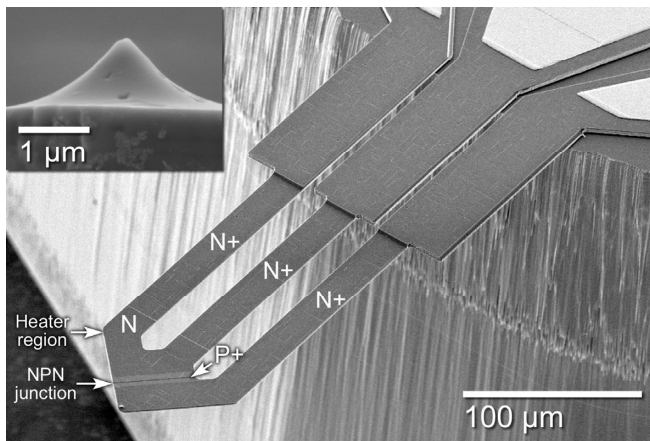


Figure 3. Single-crystal doped silicon microcantilever with integrated solid state heater and electrode using NPN doping to form back-to-back diodes.

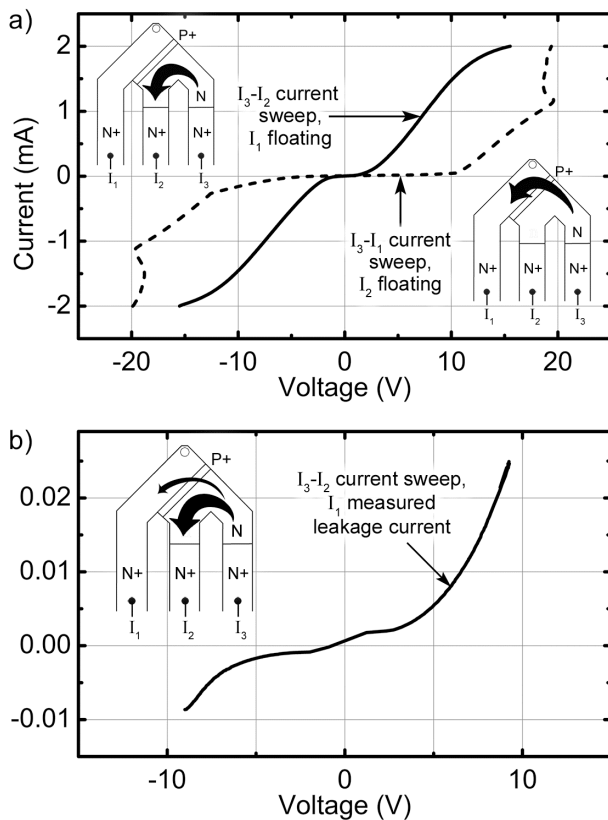


Figure 4. Current-controlled current-voltage electrical characterization of an NPN junction ET cantilever. (a) The solid line shows a current sweep across the N-type heater region and the dashed line shows a current sweep across the NPN region. Diode breakdown occurs at  $\pm 10$  volts and thermal runaway occurs at  $\pm 20$  volts. (b) The solid line shows the leakage current at I1 while the heater temperature is ramped using  $-2$  mA to  $2$  mA across I3 - I2. Note the magnitude of the y-axis in comparison to the swept current, indicating current leakage two orders of magnitude lower than heater current.

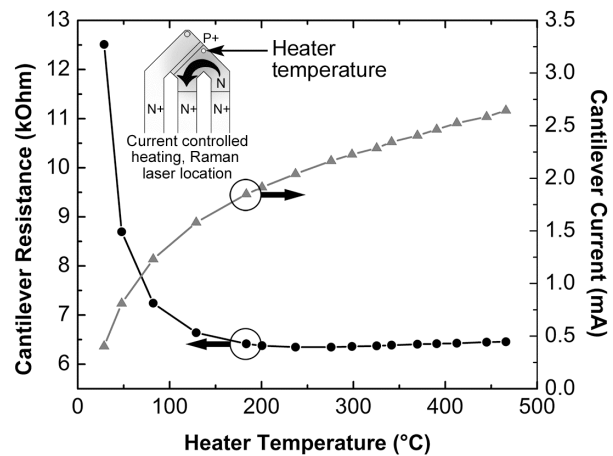


Figure 5. Raman spectroscopy temperature calibration at the heater apex and cantilever tip for the NPN junction ET cantilever. The diode design has a  $30^\circ\text{C}$  temperature difference between the tip and heater at a heater temperature of  $466^\circ\text{C}$ .

the back-to-back diodes are  $\pm 10$  volts, indicated by the sudden increase in leakage current in Fig. 4 (a). Thermal runaway in the heater region occurs at about  $\pm 20$  volts.

Fig. 4 (b) shows that leakage current is nearly zero during static heater operation at  $450^\circ\text{C}$ , up to the breakdown voltage of about  $\pm 10$  volts. Current flow is impeded in forward and reverse directions for the back-to-back diode design, and hysteresis is not observed during current-controlled I-V measurements. Current leakage is two orders of magnitude lower than heater current during heater operation between  $-2$  mA and  $2$  mA.

Laser Raman spectroscopy calibrated the heater temperature during electrical excitation in air, with no electrode bias voltage. Fig. 5 shows this data, where the heater operates at  $>400^\circ\text{C}$  with  $40$  mW of dissipated power.

## CONCLUSION

We report an AFM cantilever having an NPN junction device integrated into the cantilever free end, which combines the functions of heated and electrically-conductive AFM cantilever tips. Such a device facilitates combined nanoscale electronic and thermal measurements. These microcantilevers make it possible to measure temperature-dependent electronic properties of a surface or induce electro-thermal modifications to a surface with nanometer-scale resolution.

## REFERENCES

- [1] J. Lee, T. Beechem, T. L. Wright *et al.*, *JMEMS*, vol. 15, pp. 1644-1655, Dec, 2006.
- [2] P. Vettiger, *et al.*, "The "millipede" - Nanotechnology entering data storage," *IEEE Transactions on Nanotechnology*, vol. 1, pp. 39-55, Mar 2002.
- [3] W. K. Lee, *et al.*, "Maskless Nanoscale Writing of Nanoparticle-Polymer Composites and Nanoparticle Assemblies using Thermal Nanoprobes," *Nano Letters*, vol. 10, pp. 129-133, 2009.
- [4] J. Lee, *et al.*, "Electrical and Thermal Coupling to a Single-Wall Carbon Nanotube Device Using an Electrothermal Nanoprobe," *Nano Letters*, vol. 9, pp. 1356-1361, 2009.

## CONTACT

\*W.P. King, telephone: ++1-217-244-3864; wpk@illinois.edu

# HYBRID BIOMIMETIC DIRECTIONAL MICROPHONE FOR THE FULL SPACE SOUND SOURCE LOCALIZATION

C. C. Chen\*, Y. C. Chen, Keng-Yu Lin, and Y. T. Cheng

Microsystems Integration Laboratory, Department of Electronics Engineering & Institute of Electronics, National Chiao Tung University, Hsinchu, Taiwan, ROC.

## ABSTRACT

The paper presents a hybrid biomimetic directional microphone with a central floating pivot support by hybridizing the supersensitive ears of the parasitoid fly with the flexibility of the clover stalk. By introducing the mIIDpA, the mIPD, and the sensing region, the presented design with the state-of-the-art characteristics of mIIDpA 2.7dB/mm<sup>2</sup> and mIPD 155° has shown a highly potential application for the sound source localization with full space sensitivity. Excellence match between theoretical calculation and measurement results indicates the accuracy of the presented model and about 30% net diaphragm displacement improvement.

## INTRODUCTION

It has been a challenge using a miniature microphone to realize sound source localization due to diminutive interaural level difference and time difference [1]. Several developed biomimetic MEMS microphones still exhibited several deficiencies, such as the trade-off of structural sensitivity and rigidity and the increase of process complexity with optical readout integration [1,2,4]. Among them, the biomimetic microphone using a central pivot-supported (CP-S) design [3] has drawn lots of attention due to the characteristics of simple fabrication process, easy sensing circuit implementation, and good directional identification as well as signal sensing ability. However, the asymmetrical beam structure, shown in Fig. 1 (a), would lead to an undesired deformation that might cause device failure or the degradation of device sensitive and directional abilities. In order to overcome this dilemma, we present a new symmetrical beam structure. By hybridizing the supersensitive ears of the parasitoid fly with the flexibility of the clover stalk, as shown in Fig. 1 (b) and (c), the structurally coupled mechanism of the central floating support reveals two unique design merits: (1) fourfold rotation axial symmetry of the central beams effectively compensates the undesired deformation due to the gravity and the residual stresses for maintaining diaphragm rigidity, and (2) the central floating joint makes the sensing diaphragm more flexible for higher sound sensitivity and directivity.

For fair comparison, two microphones with the hybrid and CP-S designs both having the same structure parameters listed in Table 1 are fabricated using a three-layer copper electroplating process [5] respectively to validate device performance. Measured resonant frequencies of the hybrid and CP-S designs are about 10 and 12 KHz, respectively, close to the CoventorWare simulation [6] shown in Fig. 2 (a). Better directivity and larger net displacement in the polar plot shown in Fig. 2 (b) reveal that the hybrid design has a superior ability in sound source localization, i.e. about 36% sensitivity and 34% directivity improvements in comparison with that of the CP-S design. Figure 3 shows measured acoustic responses of the hybrid microphone applied with 80dB sound waves in frequency domain and it evidences that the hybrid design has well-performance at 200Hz with significant phase difference. Figure 4 shows the diaphragm displacements of the two kinds of microphones driven by a 80dB and 200Hz sinusoidal sound wave located at  $(r, \theta, \varphi) = (24\text{cm}, 37^\circ, 0^\circ)$ .

Meanwhile, by considering the motion equation of the microphone diaphragm, the corresponding displacement in the steady state of the ipsi- (+) and contralateral (-) membranes can

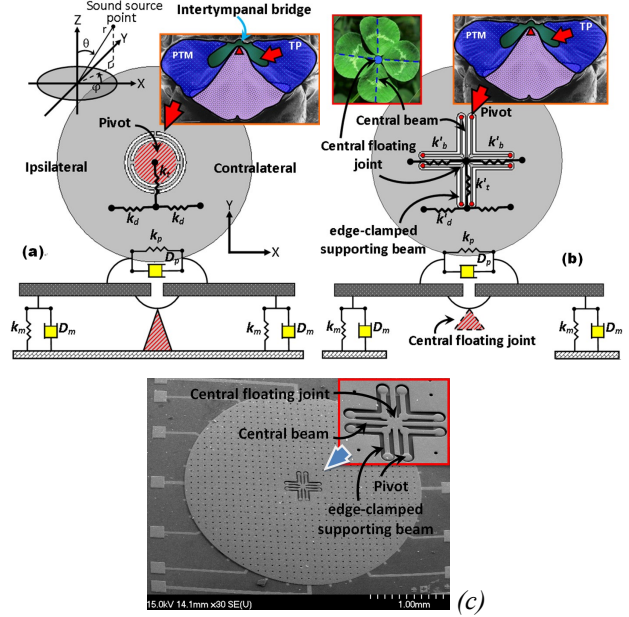


Figure 1: (a) Schemes of the conventional CP-S design with coordinate parameters  $(r, \theta, \varphi)$ . (b) Scheme of the hybrid biomimetic microphone with central floating gimbal design. (c) The SEM photograph of the hybrid microphone.

be expressed by the linear combination of the displacements of translational and rocking modes:

$$Z_{\pm} = \frac{P(t) \cdot \pi(a^2 - c^2)}{m} \times \left\{ \frac{\cos(\omega\tau/2)\sin(\omega t + \frac{\varphi_t}{2})}{\sqrt{(\omega_r^2 - \omega^2)^2 + (2\omega_r\eta_r\omega)^2}} \pm \frac{\sin(\omega\tau/2)\cos(\omega t + \frac{\varphi_r}{2})}{\sqrt{(\omega_r^2 - \omega^2)^2 + (2\omega_r\eta_r\omega)^2}} \right\} \quad (1)$$

where  $P(t)$ ,  $a$ ,  $c$ ,  $m$ ,  $\tau$ ,  $\varphi_t$  and  $\varphi_r$ ,  $\omega$ ,  $\omega_r$  and  $\omega_r$ , and  $\eta_t$  and  $\eta_r$  are the sound pressure, the diaphragm radius, the radius of central support, the mass of the diaphragm, the time delay factor, the translational- and rocking-mode phases, the operating frequency, the translational- and rocking-mode resonant frequencies, and the translational- and rocking-mode damping ratios, respectively. The theoretical model for elaborating the dynamic response is likewise verified by experimental measurements depicted in Fig. 4. Excellence match between calculation and measurement results indicates the accuracy of presented model and about 30% net diaphragm displacement improvement. Additionally, the performances of a biomimetic microphone can be also strictly compared using two mechanical indicators, the mechanical interaural intensity difference per area (mIIDpA) and the mechanical interaural phase difference (mIPD) [1], which can be obtained as follows:

$$\text{mIIDpA} = \left[ 20 \log_{10} \frac{|Z_{\text{ipsi}}|}{|Z_{\text{contra}}|} \right] / \pi(a^2 - c^2), \quad \text{mIPD} = \angle \frac{Z_{\text{contra}}}{Z_{\text{ipsi}}} \quad (2)$$

Table 1: Dimension parameters of the hybrid and CP-S design

Hybrid design	
Radius of diaphragm ( $a$ )	1500 $\mu$ m
Thickness of diaphragm ( $T$ )	5 $\mu$ m
Length of edge-clamped supporting beam ( $L$ )	250 $\mu$ m
Length of central beam ( $L$ )	250 $\mu$ m
Width of beam ( $W$ )	15 $\mu$ m
Spacing between beams	15 $\mu$ m
CP-S design	
Radius of diaphragm ( $a$ )	1500 $\mu$ m
Thickness of diaphragm ( $T$ )	5 $\mu$ m
Radius of CP region ( $c$ )	225 $\mu$ m
Radius of ring	270 $\mu$ m
Width of ring	30 $\mu$ m
Length of beam ( $L$ )	30 $\mu$ m
Width of beam ( $W$ )	30 $\mu$ m

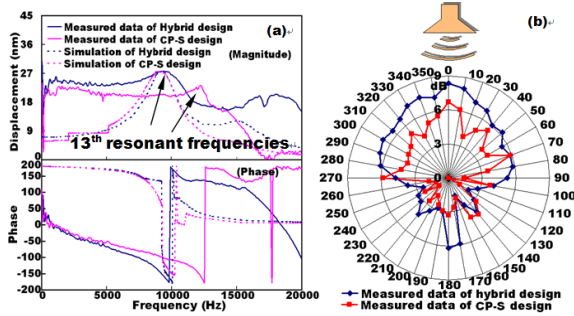


Figure 2: Comparison of (a) the frequency spectrum and (b) the logarithmic polar patterns of net diaphragm displacements between the hybrid and CP-S design.

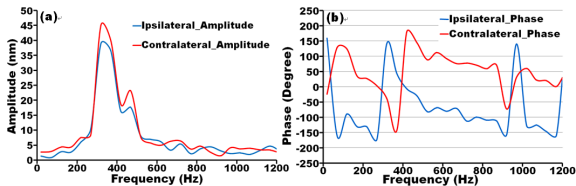


Figure 3: Acoustic responses of hybrid design in frequency domain in terms of (a) amplitudes and (b) phases of ipsilateral and contralateral of diaphragm, respectively.

For instance, the ipsi- and contralateral membranes move in opposite directions with equal amplitudes must have the mIIDpA and mIPD with the values of near 0 dB/mm<sup>2</sup> and 180°, respectively. Table 2 shows the comparisons in terms of nature frequencies and mechanical performances between the parasitoid fly [2], the conventional designs [1,3,4] and the new structure. The presented hybrid design with the state-of-the-art characteristics of mIIDpA 2.7dB/mm<sup>2</sup> and mIPD 155° has shown a highly potential application for the sound source localization with full space sensitivity.

In summary, we develop a hybrid biomimetic microphone with a central floating pivot support. Better acoustic sensitivity and directivity can be realized theoretically and experimentally. The hybrid structure can not only inherit the advantages from conventional CP-S design, but also promote sound source localization sensitivity for MEMS microphones with a potential application for hearing aid devices [1].

## REFERENCES

- [1] H. J. Liu, M. Yu, and X. M. Zhang, "Biomimetic optical directional microphone with structurally coupled diaphragms," Applied Physics Letters, 93, 243902-1 (2008).
- [2] H. Liu, L. Currano, D. Gee, B. Yang, and M. Yu, "Fly-Ear

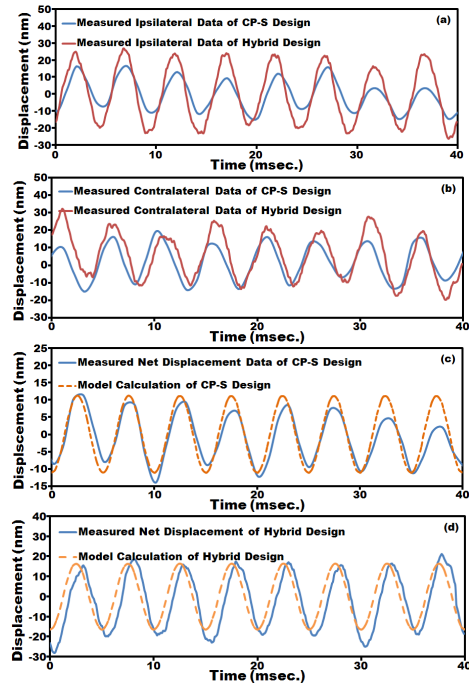


Figure 4: Measured (a) ipsilateral and (b) contralateral results of hybrid and CP-S design, respectively. Comparison of model and net displacement are of (c) CP-S and (d) hybrid design, respectively.

Table 2: Comparisons in terms of nature frequencies and mechanical performances.

Comparison	First translational mode frequency	First rocking mode frequency	mIIDpA (dB/ mm <sup>2</sup> )	mIPD (deg)	Full space sensing
Parasitoid fly [2]	31KHz	7.1KHz	10.0	80	Yes
Ref. [1]	2.0KHz	1.2KHz	0.5	95	No
Ref. [3]	0.7KHz*	0.2KHz*	2.7	135	Yes
Ref. [4]	2.0KHz	X	10.5	X	No
New design	1.8KHz*	0.7KHz*	2.7	155	Yes

\* : theoretical derivation; X: not available

- Inspired Acoustic Sensors for Gunshot Localization," Proc. of SPIE, 7321, 73210A-1 (2009).
- [3] N. Ono, A.Satio, and S. Ando, "Design and experiments of bio-mimicry sound source localization sensor with gimbal-supported circular diaphragm," Conference on Solid State Sensors, Actuators and Microsystems, Boston (2003), pp.935-938.
- [4] W. Cui, B. Bicen, N. Hall, S. A. Jones, F. L. Degertekin, and R. N. Miles, "Optical Sensing Inadirectional Memsmicrophone Inspired by the Ears of the Parasitoid Fly, Ormia Ochracea," Proc. IEEE MEMS, 614 (2006).
- [5] Y. C. Chen, C. C. Chen, Wen Hao Ching and Y. T. Cheng, "Design and Fabrication of High Performance Biomimetic Microphone Using Oxalis-Like Sensing Diaphragm for Sound Localization," APCOT Digest, 1B2-1(2008).
- [6] CoventorWare, <http://www.coventor.com/>, version 2008.

## CONTACT

\*C. C. Chen, Tel: +886-3-5712121  
#54223; [gettgod.ee92g@nctu.edu.tw](mailto:gettgod.ee92g@nctu.edu.tw)

# SELF-ASSEMBLING SINGLE CELLS ACROSS MICROPOSTS: FIRST AXIAL FORCE MEASUREMENTS IN IMMATURE CARDIOMYOCYTES

R.E. Taylor\*, K. Kim, and B.L. Pruitt

Mechanical Engineering, Stanford University, Stanford, CA, USA

## ABSTRACT

We have designed and fabricated a novel silicone-based tool to enable measurement of force-generation by single immature heart cells. This tool combines micropost arrays with a sacrificial layer process to permit the self-assembly of developing cardiomyocytes across wide spread microposts. Here we report the first axial force-generation measurements of neonatal rat cardiomyocytes. This technique has critical utility for tissue engineers in evaluating immature phenotypes.

## INTRODUCTION

Measurements of single immature heart cell mechanics has not been possible using the same axial methods that enable adult cardiomyocyte (CM) force-generation characterization.<sup>1,2,3</sup> Current methods rely on the persistent elongated shape of isolated adult CMs and are not compatible with immature heart cells due to the spherical phenotype in dissociated, immature cells or stem cells. However, there is also a need to assay force generation in immature or stem cell derived CMs throughout development to create functional, active cardiac grafts.

Here we present a novel technique that enables such force measurements for the first time by combining microfabricated, force-sensing platforms with a cell-culture sacrificial layer technique. We fabricate PDMS-based devices and self-assemble single immature CMs across pairs of wide spread microposts. This low cost technique achieves massively parallel cell testing with the desired 2-point axial cell loading configuration and force fidelity with potentially higher adhesion strength than gold-standard carbon-fiber methods adult CM techniques (and without glue!).

## THEORY AND CALIBRATION

Euler beam theory is suitable for modeling the small displacements of these high aspect ratio posts (Figure 1a). The elastic modulus,  $E$ , must be known to perform these calculations.

$$F = \frac{3E\pi r^4}{4H^3} \Delta x \quad (1)$$

Due to batch modulus variation, we instead calibrate our PDMS by deflecting the microposts with a characterized piezoresistive microcantilever.<sup>4</sup> Deviations from classical beam theory due to substrate deformation and viscoelastic effects as well as modulus variability are mitigated by this calibration (see Figure 1b and 1c).<sup>5,6</sup> We calibrated 10 microposts and found  $E = 1.23 \pm 0.19$  MPa and an average beam stiffness of  $k = 0.0472 \pm 0.0074$  N/m (Table 1).

Table 1: Modulus of elasticity, effective post stiffness, and peak force generation based upon calibration results.

Calibration and Measurements	
Effective post stiffness, $k$	$0.0472 \pm 0.0074$ N/m
PDMS modulus of elasticity, $E$	$1.23 \pm 0.19$ MPa
Peak cell force generation, $F$	$23.8 \pm 6.0$ nN

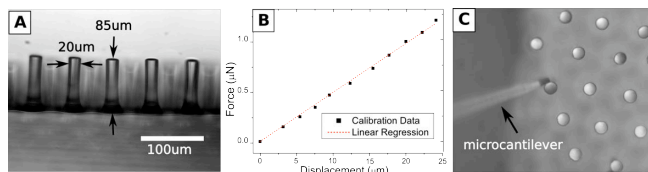


Figure 1: (A) Cylindrical posts are  $20\mu\text{m}$  in diameter and  $85\mu\text{m}$  tall. Scale bar represents  $100\mu\text{m}$ . (B) For small displacements force is linearly proportional to displacement. (C) Post stiffnesses are calibrated with piezoresistive microcantilevers.

## METHODS AND RESULTS

The overall process flow (Figure 2) consists of four steps: post fabrication, sacrificial layer deposition, protein/cell deposition, and dissolution of sacrificial layer.

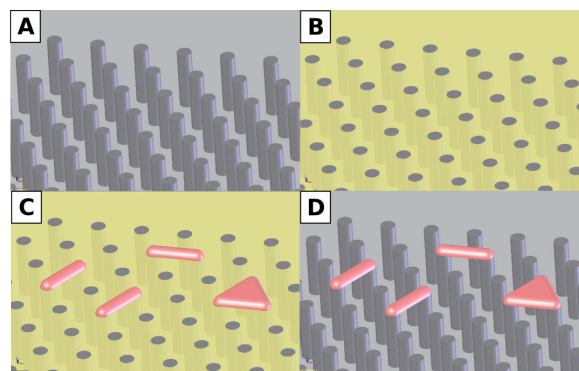


Figure 2: (A) Seeding begins with an mPAD array that is (B) flooded with PNIPAAm to yield a smooth surface. Next, (C) cells spread across the flat surface of posts and sacrificial polymer, and (D) after 4-72 hours of attachment substrates are cooled to dissolve the PNIPAAm leaving cells suspended across posts.

### Post Fabrication

Micropost array detectors (mPADs) made of polydimethylsiloxane (PDMS, Sylgard 184) consist of  $20\mu\text{m}$  diameter by  $85\mu\text{m}$  high posts in a hexagonal array with  $60\mu\text{m}$  spacing (Figure 2). mPADs are fabricated according to the protocol used by Tan et al.<sup>7</sup>

### Sacrificial Layer

The thermo-responsive polymer poly(N-isopropylacrylamide) (PNIPAAm, Polysciences) is used as a sacrificial layer.<sup>8</sup> Posts are inverted on a soft 40:1 PDMS backing layer and flooded with 1% aqueous PNIPAAm. Here we take advantage of the aqueous solution repulsion from the hydrophobic-hydrophobic stack to prevent PNIPAAm from coating the tops of the posts. Devices are evaporated overnight and the backing is peeled the next morning (Figure 3).

### Cell Seeding

For all protein and cell coating steps, care is taken to judiciously maintain substrate temperature at  $37^\circ\text{C}$  to avoid

PNIPAAm dissolution. Specific protein patterning is unnecessary since cells preferentially attach to the microposts. Devices are coated in 0.1% gelatin solution for 1 hr followed by cell seeding and attachment for 2-3 days.

### Dissolve PNIPAAm

When cells are adhered for testing, the devices are cooled to room temperature (~1 hour) to dissolve the PNIPAAm and release the posts (Figure 4).

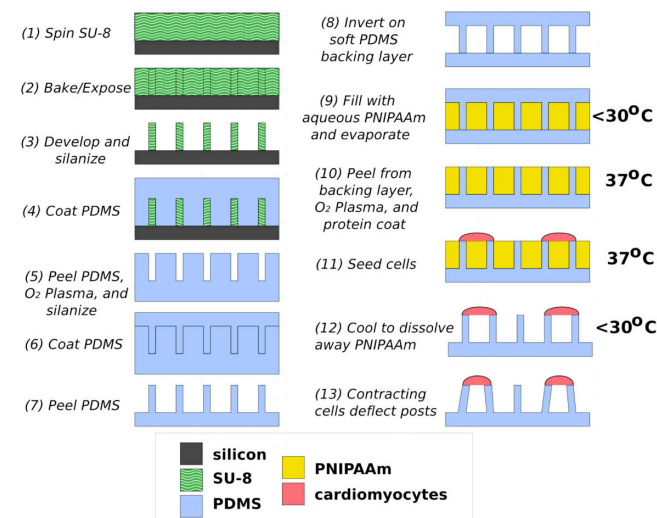


Figure 3: PDMS microposts are created by double-molding an SU-8 master post array. PDMS mPADs are inverted on a 40:1 PDMS backing layer creating a tight hydrophobic temporary bond. The sandwiched layers are filled with an aqueous 1% PNIPAAm solution. Once the PNIPAAm evaporates, the backing is peeled leaving a flat device with exposed post surfaces for subsequent cell attachment. Cells preferentially attach to the posts and therefore spread across posts without the need for protein patterning. Cooling causes the PNIPAAm to dissolve and leave behind single suspended cells.

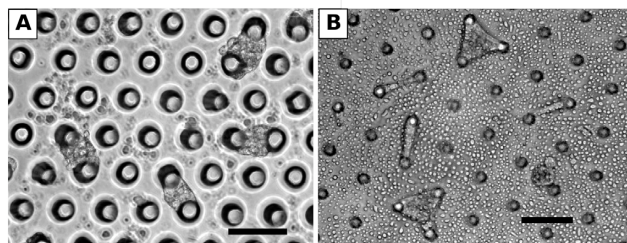


Figure 4: Beating cells successfully suspended across posts tend to take a linear form across two posts or a triangular form across three posts. Scale bar represents 100 $\mu\text{m}$ . Cells that do not spread across posts remain associated with posts nonetheless (B, lower right).

### Cell measurements

Cells are paced at 0.5Hz and 1Hz with a biphasic square wave of 15-25V (IonOptix Myopacer). Phase contrast microscopy video of cell contractions provides deflection data for force calculations (Figure 5). The peak force generated by rat neonatal cardiomyocytes is  $23.8 \pm 6.0$  nN (n=8). To our knowledge, such measurements have not been reported nor were possible before.

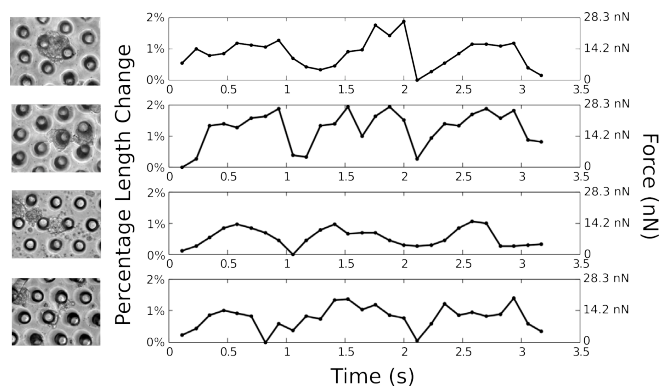


Figure 5: Percentage of cell length change and equivalent force generation vs time for four representative cells.

### ACKNOWLEDGMENTS

This work has been performed with support from the following: NSF CAREER Award ECS-0449400, NSF EFRI-CBE 0735551, CIRM RC1-00151-1, NIH R21 HL089027, and Stanford Bio-X Grants. Microcantilevers were fabricated at the Stanford Nanofabrication Facility, which is supported by the NSF under grant 9731293.

### REFERENCES

- [1] G. Iribe, M. Helmes, and P. Kohl, "Force-length relations in isolated cardiomyocytes subjected to dynamic changes in mechanical load," *Am. J. Physiol. Heart Circ.*, 292, (2007) pp. H1487-H1497.
- [2] G. Lin, S. J. Pister, K.P. Roos, "Surface Micromachined Polysilicon Heart Cell Force Transducer," *JMEMS*, 9, 1(2000) pp. 9-17.
- [3] S. Yin, X. Zhang, C. Zhan, J. Wu, J. Xu, and J. Cheung, "Measuring single cardiac myocyte contractile force via moving a magnetic bead," *Biophys. J.*, 88, 2(2005) pp. 1489-1495.
- [4] S-J. Park, M.B. Goodman, and B.L. Pruitt. "Analysis of nematode mechanics by piezoresistive displacement clamp," *PNAS*, 104, 44(2007) pp. 17376-17381.
- [5] I. Schoen, W. Hu, and V. Vogel, "Substrate Contributions in Elastic Pillar Arrays: Correction of Cellular Force Measurements", *Biophysical Journal*, 98, 3 (2010) p. 336a.
- [6] I. Lin, K. Ou, Y. Liu, K. Chen, and X. Zhang, "Viscoelastic characterization and modeling of polymer transducers for biological applications," *Journal of Microelectromechanical Systems*, 18, 5(2009) pp. 1087-1099.
- [7] J.L. Tan, J. Tien, D.M. Pirone, D.S. Gray, K. Bhadriraju, and C.S. Chen, "Cells lying on a bed of microneedles: an approach to isolate mechanical force," *PNAS*, 100, 4(2003) pp. 1484-1489.
- [8] J.Z. Xi, J.J. Schmidt, and C.D. Montemagno, "Self-assembled microdevices driven by muscle", *Nat. Mater.*, 4, (2005) pp. 180-184.

### CONTACT

\*R.E. Taylor, rebeccat@stanford.edu

# TEMPERATURE-STABLE HIGH-Q ALN-ON-SILICON RESONATORS WITH EMBEDDED ARRAY OF OXIDE PILLARS

R. Tabrizian, G. Casinovi, and F. Ayazi

Georgia Institute of Technology, Atlanta, Georgia, USA

## ABSTRACT

This paper reports on a new temperature compensation technique for high- $Q$  AlN-on-Silicon bulk acoustic wave resonators. A uniform array of silicon dioxide ( $\text{SiO}_2$ ) pillars are formed in the silicon body of the resonator to generate a composite resonator with a near-zero temperature coefficient of frequency (TCF). At a resonance frequency of 24MHz, a total frequency drift of 90 ppm over the temperature range of  $-20^\circ\text{C}$  to  $100^\circ\text{C}$  was measured while  $Q$  exceeded 10,000 at all temperatures. This compensation technique is applicable to bulk acoustic resonators with thick silicon substrate that demonstrate high  $Q$  as well as good power handling and linearity.

## INTRODUCTION

AlN-on-Silicon resonators are characterized by low insertion loss and a high  $Q$  [3]. However, a major drawback of silicon resonators is in their high TCF, which is in the range of  $-20$  to  $-30$  ppm/ $^\circ\text{C}$  for uncompensated resonators [1] [2]. In order to compensate for this large negative TCF, a layer of a material with positive temperature coefficient of elasticity (typically  $\text{SiO}_2$ ) can be added to the resonator stack [1-3]. However, in order to achieve full temperature compensation in length-extensional resonators, the thicknesses of the  $\text{SiO}_2$  and Si layers should be comparable. This creates several problems, given that a relatively thick layer of silicon (20-60  $\mu\text{m}$ ) is required in AlN-transduced resonators to achieve a high  $Q$  as well as good power handling and linearity. One problem is that the addition of a comparably thick  $\text{SiO}_2$  layer will result in a considerable drop in the device  $Q$ . Secondly, a thick  $\text{SiO}_2$  layer makes the fabrication process challenging. In order to address these challenges, we present a new method of passive material compensation. Instead of adding a thick layer of oxide, a uniform array of  $\text{SiO}_2$  pillars are formed in the silicon body of the resonator to generate a composite structure with a near zero TCF. The pillars are formed by filling square-shaped trenches etched in the body of the resonator with high-temperature LPCVD  $\text{SiO}_2$ . In contrast to oxide-compensated capacitive resonators, the presented resonators do not require a DC electric field for operation and are hence immune from dielectric charging effects that cause frequency drift [4].

## RESONATOR DESIGN

A silicon resonator with a two-dimensional array of uniformly distributed oxide pillars can be modeled as a network of series and parallel finite-mass springs. Figure 1 shows a typical array of oxide pillars and its equivalent mass-spring network model.

The equivalent mass and stiffness of the springs, which determine the resonance frequency of the system and its variation with temperature, depend on the distribution and configuration of the oxide pillars. Assuming a totally uniform pattern, the overall amount of oxide required to fully compensate the negative TCF of the silicon resonator can be estimated from the following equation:

$$\frac{1}{2} \left( \frac{\rho_{ox}^{1/2} E_{si}^{1/2}}{\rho_{si}^{1/2} E_{ox}^{1/2}} + \frac{E_{ox}}{E_{si}} \right) \left( \frac{TCE_{ox}}{TCE_{si}} \right) \left( \frac{V_{ox}}{V_{si}} \right) = -1 \quad (1)$$

Here  $V_{ox}$  and  $V_{si}$  are the overall volume of oxide pillars and silicon in the resonator,  $E_{ox}$  and  $E_{si}$  are Young's Modulus and  $\rho_{ox}$  and  $\rho_{si}$  are density of oxide and silicon respectively.

ANSYS simulations were used to adjust the dimensions and distribution of the oxide pillars and the thickness of the top oxide layer in order to achieve zero TCF over the desired range of temperature at a specific resonance frequency.

## RESONATOR FABRICATION

To fabricate the resonators, trenches with slightly tapered sidewalls are first etched into the device layer of an SOI wafer and subsequently filled with LPCVD  $\text{SiO}_2$  deposited at  $850^\circ\text{C}$ . A smooth top surface is obtained by short wet etching and subsequent deposition of  $\text{SiO}_2$ . A nearly smooth surface is required for the deposition of Mo electrodes and high-quality AlN. The rest of the fabrication process is similar to the one reported in [3] with some minor modifications. Figure 2 shows an SEM picture of a fabricated temperature-stable 24MHz resonator with uniformly distributed array of oxide pillars.

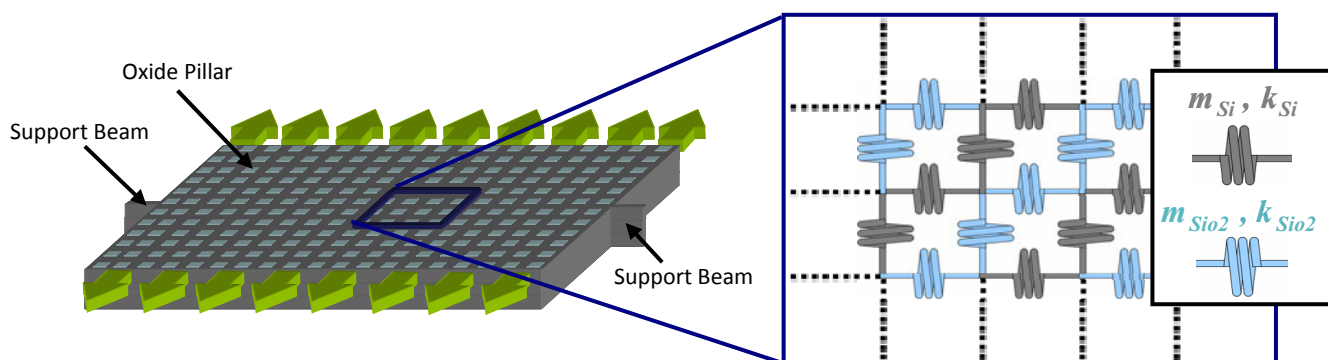


Figure 1: A typical array of oxide pillars in resonator and simplified equivalent mass-spring model. Arrows show resonance direction.



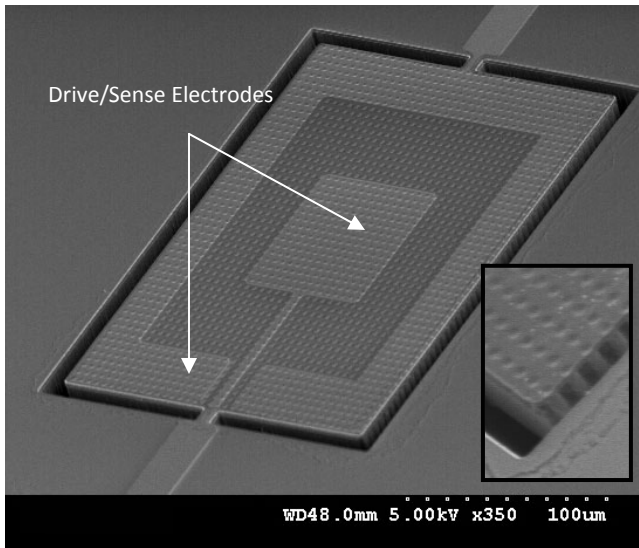


Figure 2: SEM picture of a temperature compensated 24MHz resonator with  $\text{SiO}_2$  pillars. Inset shows the oxide pillars.

### CHARACTERIZATION RESULTS

Figure 3 is the measured frequency response of the temperature stable resonator of Figure 2 showing very high  $Q$ .

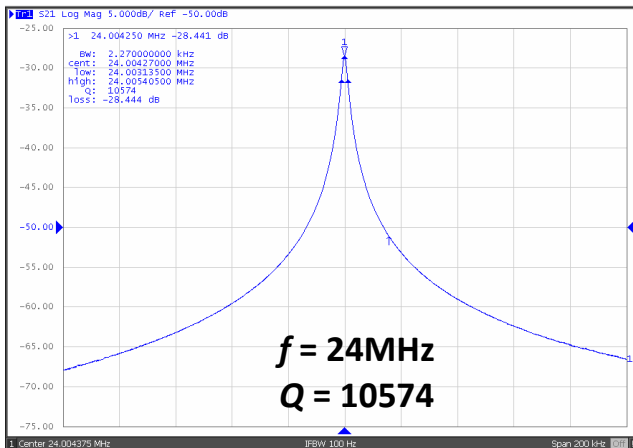


Figure 3: Frequency response of the 24MHz temperature compensated resonator of Figure 2.

Figure 4 shows the temperature characteristics of three identical samples of compensated 24MHz resonators from across the wafer with a  $1.4 \mu\text{m}$  of surface LPCVD oxide layer deposited between a  $20 \mu\text{m}$  layer of silicon body and Mo/AlN/Mo layers. A resonance frequency drift of 90-180 ppm over the range  $-20^\circ\text{C}$  to  $100^\circ\text{C}$  was measured for these three samples while  $Q$  exceeded 10,000 at all temperatures (in vacuum). Figure 5 shows the temperature characteristic of  $Q$  for the resonator of Figure 2.

### ACKNOWLEDGMENT

This work has been supported by Integrated Device Technology, Inc.

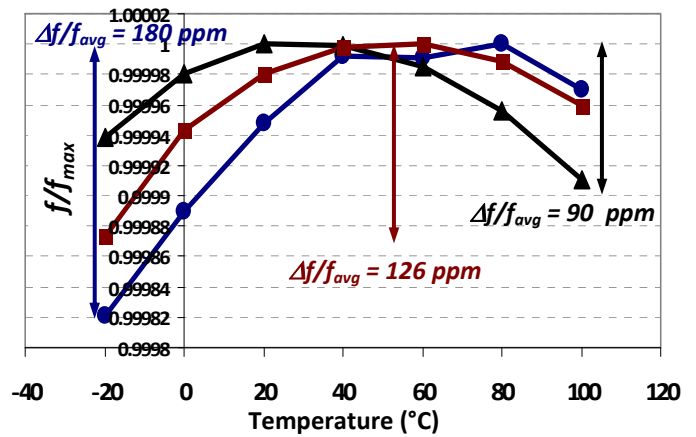


Figure 4: Temperature characteristic of three 24MHz temperature compensated AlN-on-Si resonators with oxide pillars.

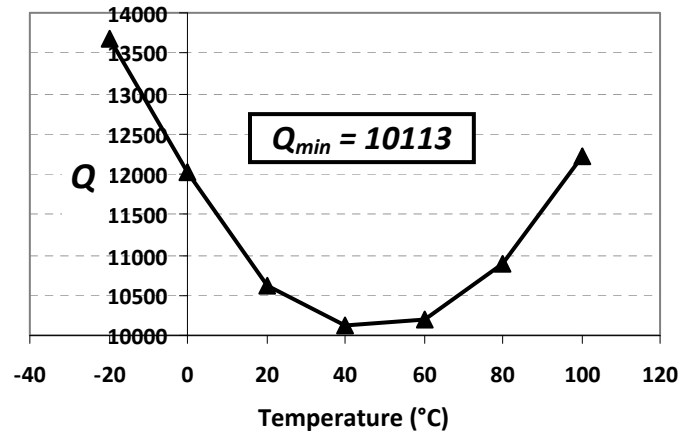


Figure 5: Temperature characteristic of  $Q$  for the resonator of Figure 2.

### REFERENCES

- [1] F. Ayazi, "MEMS for Integrated Timing and Spectral Processing," Invited Paper, Proc. IEEE Custom Integrated Circuits Conference (CICC 2009), Sept. 2009, pp. 65-72
- [2] R. Abdolvand, H. Miri Lavasani, and F. Ayazi, "A Low Voltage Temperature-Stable Micromechanical Piezo Oscillator," Tech. Digest of the 14th International Conference on Solid State Sensors, Actuators and Microsystems (Transducers'07), Lyon, France, June 2007, pp. 53-56.
- [3] W. Pan and F. Ayazi, "Thin-Film Piezoelectric-on-Substrate Resonators with Q Enhancement and TCF Reduction," Tech. Digest of 23rd IEEE International Conference on Micro Electro Mechanical Systems (MEMS 2010), Hong Kong, January 24 - 28, 2010, pp. 104-107
- [4] G. Bahl et al, "Observation of fixed and mobile charge in composite MEMS resonators", Solid-State Sensors, Actuators, and Microsystems Workshop, Hilton Head 2008, Hilton Head, SC, USA, pp 102-105

### CONTACT

R.Tabrizian, tel: +1-404-259-7322; [Roozbeh@gatech.edu](mailto:Roozbeh@gatech.edu)  
F. Ayazi, [ayazi@gatech.edu](mailto:ayazi@gatech.edu)

# MICROFLUIDIC DELIVERY OF NANOMEDICINE: THE LITTLE DROP OF FLUID THAT COULD

Abraham P. Lee<sup>1,2</sup>, Albert T.-H. Hsieh<sup>1</sup>, Armando Tovar<sup>1</sup>, and Kanaka Hettiarachchi<sup>1</sup>

<sup>1</sup>Department of Biomedical Engineering,

<sup>2</sup>Department of Mechanical & Aerospace Engineering

DARPA/Industry Micro/nano Fluidics Fundamentals Focus (MF3) Center

University of California at Irvine, 3120 Natural Sciences II, Irvine, CA 92697-2715, U.S.A.

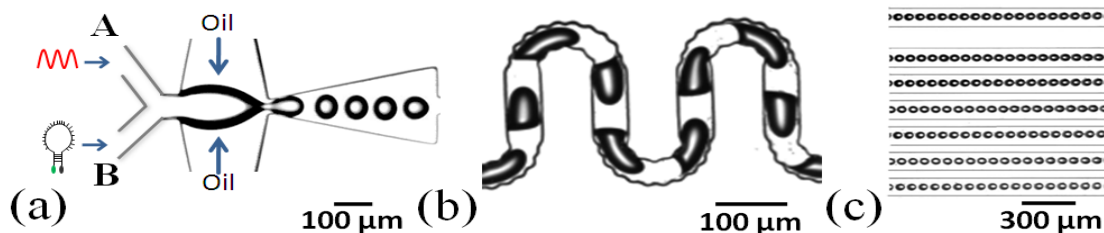
## ABSTRACT

Medicine as we know it is a series of standard procedures (check-ups, sample collection, lab tests, drugs, and treatment) that are generally stand alone with little to no connectivity between the different “stations”. However, these medical stations are starting to converge in tiny fluid drops delivered by microfluidic chips. Over the years, lab-on-a-chip devices have demonstrated strong potential for rapid detection and point-of-care diagnostics. These devices are capable of detection and manipulation at the cellular and molecular level with high throughput. More recently, digital “droplet” microfluidic chips have shown promise to “nanomanufacture” the “magic bullet”, hybrid micro/nano particles that incorporate imaging, detection, diagnostics, and targeted delivery of drugs for advanced therapies. I will introduce three active microfluidic “nanomedicine” platforms in my lab: DNA analysis and detection, protein serodiagnostics to screen antibodies, and an acoustically active lipospheres for ultrasound imaging and drug delivery.

## DNA HYBRIDIZATION DETECTION

The monodispersed picoliter microfluidic droplet generation system developed by our group and others [0] can serve as a promising micro-reactor for biological and chemical

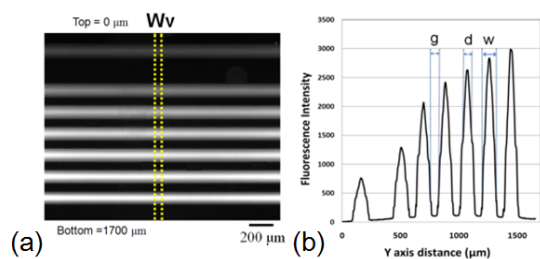
assays. It employs pressure-driven flow to inject aqueous solutions into aqueous immiscible solutions and form picoliter microdroplets. The biological or chemical reagents are all encapsulated in microdroplets and each droplet is isolated by the immiscible liquid (e.g. mineral oil), thus greatly reducing sample contamination on the microchannel side walls and eliminating reagent dispersion problems. The system is useful not only for DNA sample identification, but also for quantitative analysis. The liquid-liquid reaction rate of DNA hybridization in homogeneous liquid is about 40-fold faster than the hybridization rate in a solid-liquid interface [0]. Hence, it is advantageous to improve the DNA sample/sensing probe hybridization rate using this technique rather than the conventional immobilized-probe approach. Compared to conventional microfluidics with continuous laminar flows, the microdroplet allows rapid mixing among reagents in droplet [0]. The microdroplet formation system that we developed is capable of generating over five hundred monodisperse droplets per second with a size deviation of less than two percent [0]. However, because of the fundamental differences between the microdroplet generation system and other conventional techniques, a liquid-liquid reaction based DNA sensing probe is needed to conduct DNA detection in microdroplets.



**Fig. 1** The merged A and B streams are broken off by side streams and form microdroplets. (a) Consecutive micrographs of droplet generation. The generation time is 2.66 ms/droplet. (b) DNA and MB are rapidly mixed in sawtooth edged U-shaped channel (c) Picoliter droplets moving in hybridization region [0].

In order to achieve rapid DNA detection in homogeneous liquid phase with single nucleotide mismatch sensitivities, we used molecular beacon (MB) as the DNA sensing probe in the microdroplets [0]. The target DNA and MB were all encapsulated in monodispersed picoliter droplet emulsions to reduce sample volume and to enhance the DNA detection efficiency. In our paper [0], we demonstrate a fast DNA sample and mutant detection in a few seconds, and evaluate dynamic MB-DNA duplex formation using Label-Free DNA Analysis in Microdroplet (LFDAM) system. The more stable the MB-DNA

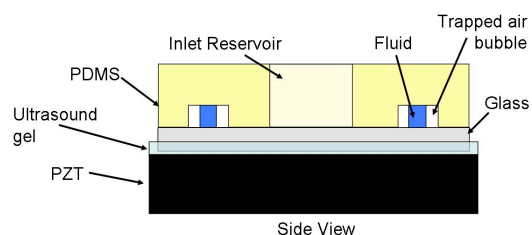
duplex, the stronger the MB fluorescence restored. The measured fluorescence intensity is directly proportional to sample concentration, droplet volume, droplet generation rate, and fluorescence acquisition time. Figure 1 illustrates (a) the microfluidic droplet generation device, (b) the mixing serpentine channel, and (c) a snapshot of the droplets travelling in the microchannels. Figure 2 illustrates the gradual increase in fluorescent intensity as the droplets travel in the microchannels and more time is lapsed so the MB-DNA duplex has a chance to reach equilibrium.



**Fig. 2** The dynamic binding reaction of target DNA with MB can be observed from the fluorescence change of MB inside droplet. (a) The horizontal average-multiple-line-scan method is used to measure the fluorescence intensity. The yellow dash line represents the fluorescence analysis from the top to the bottom of an image. (b) The measured result shows that the MB fluorescence gradually increases downstream in the LFDAM [0].

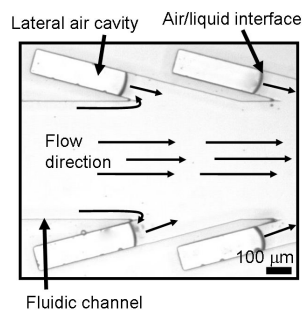
### ANTIBODY SERODIAGNOSTICS ASSAYS

A novel microfluidic actuator is designed around the use of trapped air bubbles in lateral cavities and the resultant acoustic streaming generated from an outside acoustic energy source [0,0]. This actuator is simple to fabricate, integrate, and operate in a compact portable configuration. The orientation of the lateral cavities to the main microchannel is used to control the bulk fluid motion within the device and the first order flow generated by the oscillating bubble is used to develop a pumping platform that is capable of driving fluid within a chip. The device is fabricated using traditional soft lithography. [0] One of the main advantages of using the LCAT platform is the simple fabrication needed for integration into existing chips. The LCATs are designed within the same layer as the main microchannel and only the single lithography step needed for the main microchannels is required to fabricate both channel features and the LCATs. The device is operated by placing it on top of an external acoustic energy source. The operation of the device can be seen in Fig. 3 where a PZT is coated with ultrasound gel to enhance acoustic energy transfer through the bottom substrate of the chip.



**Fig. 3** Schematic of Acoustic Bubble-Array Micromixer

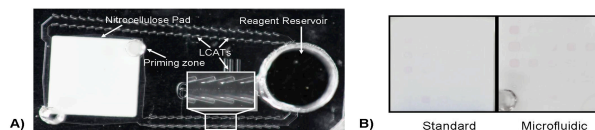
The demonstration of the pumping capabilities of the LCAT platform is done using cavities oriented at  $15^\circ$  to the main channel. The orientation of the cavities utilizes the first order oscillatory flow from the air/liquid interface to produce a net flow away from the cavity interface. The design can be seen in Fig.4, where the trapped air bubble can be seen within the lateral cavity and the two cavities are oriented at a shallow angle ( $15^\circ$ ) to the main microchannel.



**Fig. 4** LCAT pumping design with cavities at  $15^\circ$  angles.

This pump is integrated into a recirculation immunoassay device for enhanced antibody-antigen binding through fluid flow for convection-limited transport. The device is designed to continuously deliver the analyte over a binding region. The recirculation assay device has the advantages of allowing high flow rates for increased binding efficiency while maintaining a low fixed volume. In traditional microfluidic flow through devices, the higher flow rates lead to larger volume consumption during operation. The operation of the device is performed using a protein spotted nitrocellulose pad that is bound with gold-conjugated secondary antibodies for optical confirmation of binding.

To determine the effectiveness of a recirculation assay platform (Fig. 6a) [0], it is compared to a traditional assay where gold conjugated antibodies (goat anti-human IgG (H&L)) are delivered over a protein spotted nitrocellulose pad for 15 minutes. The comparison shown in Fig. 6B shows an increase in spot intensity using the microfluidic recirculation platform compared to the traditional benchtop assay where  $50 \mu\text{L}$  is incubated within a well plate for the same amount of time. The simulation and experimental results showed good agreement for antigen site binding.



**Fig. 5** (a) Image of colorimetric immunoassay chip. (b) Comparison of standard and microfluidic 1 OD gold-conjugated secondary antibody delivery.

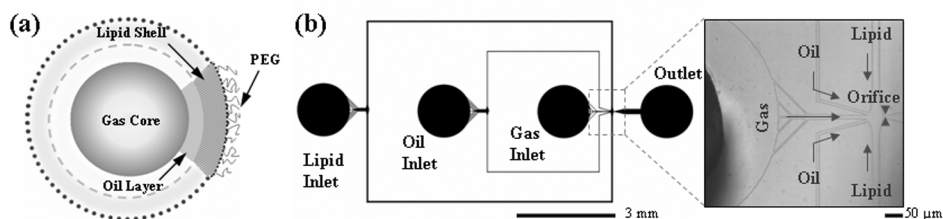
### MULTILAYER MICROPARTICLES FOR NANOMEDICINE (MMN)

The utilization of acoustically active lipospheres (AALs) (Fig. 6a) capable of delivering bioactive substances at high concentrations in the lipid-oil complex has been reported [0,0]. The oil layer is capable of carrying highly hydrophobic drugs such as the chemotherapeutic drug Paclitaxel, which is currently delivered to cancer patients intravenously. Paclitaxel can be dissolved at high concentrations (70 mg/ml) in the lipid-oil complex of the AALs [0]. Such vehicles can provide an alternative method of delivery of therapeutic drugs that have poor oral bioavailability.

The commonly used production technique of mechanical shaking creates a highly polydisperse microbubble population, with varying amounts of oil within many of the microbubble vehicles. Thus, the drug dosages within each vehicle are also

not consistent. Microfluidic chambers provide an ideal platform for the controlled production of monodisperse double emulsions [0] and microbubble contrast agents [0] with a much smaller size

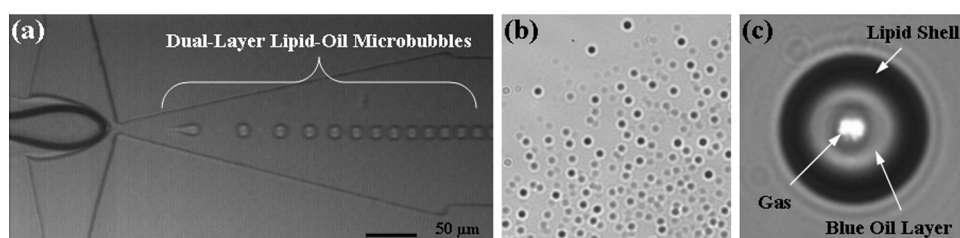
distribution. Our device (Fig. 6b) combines two hydrodynamic flow-focusing regions together and features expanding nozzle geometry to generate gas-filled dual-layer lipospheres.



**Fig. 6** (a) Schematic of an AAL and (b) PDMS-based microfluidic flow-focusing device

Microfluidic generated lipospheres are visible in brightfield (Fig. 7b), and the inner blue layer confirms the existence of the additional triacetin oil layer (Fig. 7c). The outer

DSPC lipid shell stabilizes the vehicle and the inner triacetin oil layer can contain dissolved therapeutics. The gas interior makes the vehicle acoustically active to ultrasound pulses.



**Fig. 7** (a) Production by flow-focusing and (b) generated AALs. (c) Close-up of AAL

Microbubble size and production rate are highly prone to downstream pressure conditions. The large viscosity difference between the oil and gas makes the production of dual-layer lipospheres particularly challenging. Channel geometry in addition to the liquid and gas flow rates are the main factors used to control the liposphere sizes.

Paclitaxel is a poorly water soluble drug and its large size prevents it from being accommodated within the phospholipid bilayers in liposomes. In a dual-layer vehicle, a high volume fraction of the oil phase can be used and paclitaxel exhibits good solubility in triacetin. The production method will enable more precise dosages of drug to be delivered. Conjugating a cyclic-RGD peptide to the shell due to over-expression of  $\alpha\beta3$  integrin in the tumor blood vessel endothelium is a possibility for targeted delivery.

The issue of creating long-lasting dual-layer microbubble lipospheres for drug delivery in microfluidic systems poses interesting studies concerning the impact of device geometry and scale, flow parameters, and the synergy between shell, internal components, and surrounding medium on the stabilization.

With microfluidics technology, we can produce monodisperse dual-layer microbubbles in a suitable size range for oral drug delivery or direct injection into the circulation (10 $\mu$ m or less). The composition makes them ultrasonically active and able to carry a large and precise drug payload to the target site. On-going and immediate experiments are to demonstrate drug loading in the manufactured dual-layer vehicles, *in vitro* targeted delivery to cancer cells, *in vivo* biodistribution animal studies, and to demonstrate that the drug Paclitaxel can remain, or be slowly released over time.

## CONCLUSIONS

Microfluidic droplet interfaces can deliver a broad range of nanomedicine applications, including the detection of biomolecules (e.g. DNA), the diagnostics of antibodies specific to infectious diseases, and the targeted therapy for cancer and other diseases with molecular markers. The microfluidic chips generate monodisperse fluid volumes and controlled fluid motion that form integration modules for future healthcare solutions.

## REFERENCES

- [1] Shia-Yen Teh, Robert Lin, Lung-Hsin Hung, and Abraham P. Lee, "Droplet Microfluidics", Lab on a Chip, vol. 8 (2), pp. 198-220, 2008.
- [2] Gao, Y., L. K. Wolf, et al. (2006). "Secondary structure effects on DNA hybridization kinetics: a solution versus surface comparison." Nucleic Acids Res. 34(11): 3370-3377.
- [3] Tice, J. D., H. Song, et al. (2003). "Formation of droplets and mixing in multiphase microfluidics at low values of the Reynolds and the capillary numbers." Langmuir 19(22): 9127-9133.
- [4] Tan, Y. C., J. S. Fisher, et al. (2004). "Design of microfluidic channel geometries for the control of droplet volume, chemical concentration, and sorting." Lab Chip 4(4): 292-298.
- [5] Abraham P. Lee, "Microfluidic Cellular and Molecular Detection for Lab-on-a-Chip Applications", the 31st Annual International Conference of the IEEE Engineering in Medicine and Biology Society, Minneapolis, Minnesota, USA, 2-6 September, 2009.

- [6] Albert T. Hsieh, Patrick J. Pan, Abraham P. Lee, "Rapid label-free DNA analysis in picoliter microfluidic droplets using FRET probes", *Microfluidics and Nanofluidics*, vol. 6 (3), pp. 391-401, 2009.
- [7] Armando R. Tovar, Algimantas Jasinskas, Philip L. Felgner, and Abraham P. Lee "Microfluidic 5-Step Colorimetric Immunoassay with On Chip Pumping", The Thirteenth International Conference on Miniaturized Systems for Chemistry and Life Sciences (uTAS 2009) ICC Jeju, Jeju, Korea, November 1-5, 2009
- [8] Armando Tovar, Maulik Patel, and Abraham P. Lee, "Acoustic cavity transducers for the manipulation of cells and biomolecules",
- [9] Whitesides, G. M. et. al., « Soft lithography in biology and biochemistry,» *Annual Review of Biomedical Engineering*, 3, 335-373, 2001.
- [10] Yuen, P.K. et al, "Microfluidic Devices for Fluidic Circulation and Mixing Improve Hybridization Signal Intensity on DNA Arrays," *Lab on a Chip*, 3, 46-50, 2003.
- [11] Kanaka Hettiarachchi, Esra Talu, Marjorie L. Longo, Paul A. Dayton, Abraham P. Lee, "Manufacture of Dual-Layer Microbubble Lipospheres as Drug Delivery Vehicles in Microfluidic Devices", The Eleventh International Conference on Miniaturized Systems for Chemistry and Life Sciences (uTAS 2007), p.191-193, Paris, France, October 7-11, 2007
- [12] Evan C. Unger, Thomas P. McCreery, Robert H. Sweitzer, Veronica E. Caldwell, and Yunqiu Wu, "Acoustically Active Lipospheres Containing Paclitaxel: A New Therapeutic Ultrasound Contrast Agent," *Investigative Radiology*, Vol. 33, pp. 886-892 (1998).
- [13] M. J. Shortencarier, P. A. Dayton, S. H. Bloch, P. A. Schumann, T. O. Matsunaga, and K. W. Ferrara, "A method for radiation-force localized drug delivery using gas-filled lipospheres," *IEEE Trans Ultrason Ferroelectr Freq Control*, Vol. 51, pp. 822-831 (2004).
- [14] T. Nisisako, S. Okushima and T. Torii, "Controlled formulation of monodisperse double emulsions in a multiple-phase microfluidic system," *Soft Matter*, Vol. 1, pp. 23-27 (2005).
- [15] K. Hettiarachchi, E. Talu, M. L. Longo, P. A. Dayton, and A. P. Lee, "On-chip generation of microbubbles as a practical technology for manufacturing contrast agents for ultrasonic imaging," *Lab Chip*, Vol. 7, pp. 463-468 (2007).

# DISCONTINUOUS NANOPOROUS STRUCTURES ENABLE LOW-POWER ELECTROPHORETIC IMMUNOASSAYS OF SERUM PROTEIN BIOMARKERS

Chenlu Hou and Amy E. Herr\*

University of California, Berkeley, CA 94720, USA

## ABSTRACT

To realize low-power electrophoretic immunoassays for protein biomarkers, we introduce discontinuous nanoporous structures photopatterned within microfluidic channels as separation matrices. The discontinuous cross-linked gels enhance analyte mobility differences, therefore reducing the required electrophoretic separation length and electrical potential to complete biomarker detection. An optimized mask-based fabrication protocol is introduced to eliminate protein exclusion and “destacking” dispersion near the pore-size discontinuity. Using the optimized sieving matrix, concurrent quantitation of C reactive protein (CRP) and tumor necrosis factor – alpha (TNF- $\alpha$ ) were developed. Both protein species are important in host inflammatory and infection response. The ultra-short separation distance electrophoretic immunoassay reported here provides flexibility in field-portable diagnostic instrument design by relaxing electrical potential requirements and providing multiplexing capabilities.

## INTRODUCTION

Commercially available lateral flow assays – including home pregnancy tests – provide simple “yes/no” readouts. The non-quantitative readouts from such “test strips” cannot provide an accurate representation of complex physiological conditions. Adapting laboratory-grade diagnostic assays for clinical or near-patient settings would therefore enable rapid clinical decision making, effective disease treatment and containment, and assessment of treatment efficacy.

Many types of assays capable of quantifying protein biomarkers have been developed and employed for clinical diagnostics. To isolate biomarkers of interest, surface-based biosensors require surface immobilization of a capture probe and multiple washing steps. On the other hand, electrophoretic immunoassays rely on effective electrophoretic separation of a probe (antibody) from the larger immune-complex (probe bound to target protein biomarker) in which the magnitude of immune-complex formation reflects target biomarker concentration. Elimination of surface immobilization and washing steps not only simplifies assay implementation and reduces reagent consumption, but also renders the assay format reusable and appropriate for continuous monitoring. When implemented with microfluidic technology, electrophoretic immunoassays can be automated and integrated with upstream sample preparation.

Yet, a major limitation to point-of-care use of electrophoretic immunoassays centers on the need for high electric fields (100s V/cm) applied across centimeters of separation length. Thus, a reduction in the required separation length would, in turn, reduce applied electrical potential (voltage) constraints, while allowing high electric field strength operation.

Our group and others have improved electrophoretic immunoassay performance by fabricating nanoporous sieving matrices within microfluidic separation channels [1]. The sieving matrices enhance mobility differences among analytes, thus reducing the separation distance required for resolving the immune complex. In particular, photopolymerization yields cross-linked polyacrylamide (PA) gels with control over characteristics such as

gel pore-size and pore-size distribution. Our previous reports utilized cross-linked polyacrylamide separation gels with moderate gradients in sieving pore-size to complete immunoassays in 1 mm [2].

We now introduce microchip nanoporous discontinuous gels as an electronic alternative to performance-limited test strips, encompassing both low-power consumption and quantitative biomarker measurement. Our multi-analyte assays build on a new design strategy that obviates cumbersome, expensive high-voltage power supplies currently required for electrophoresis. The approach significantly reduces electrophoretic immunoassay power consumption (mW to  $\mu$ W); consequently, conventional- or solar-battery power is an option for portable operation including quantitative global health, military, and clinical diagnostics.

## EXPERIMENTAL

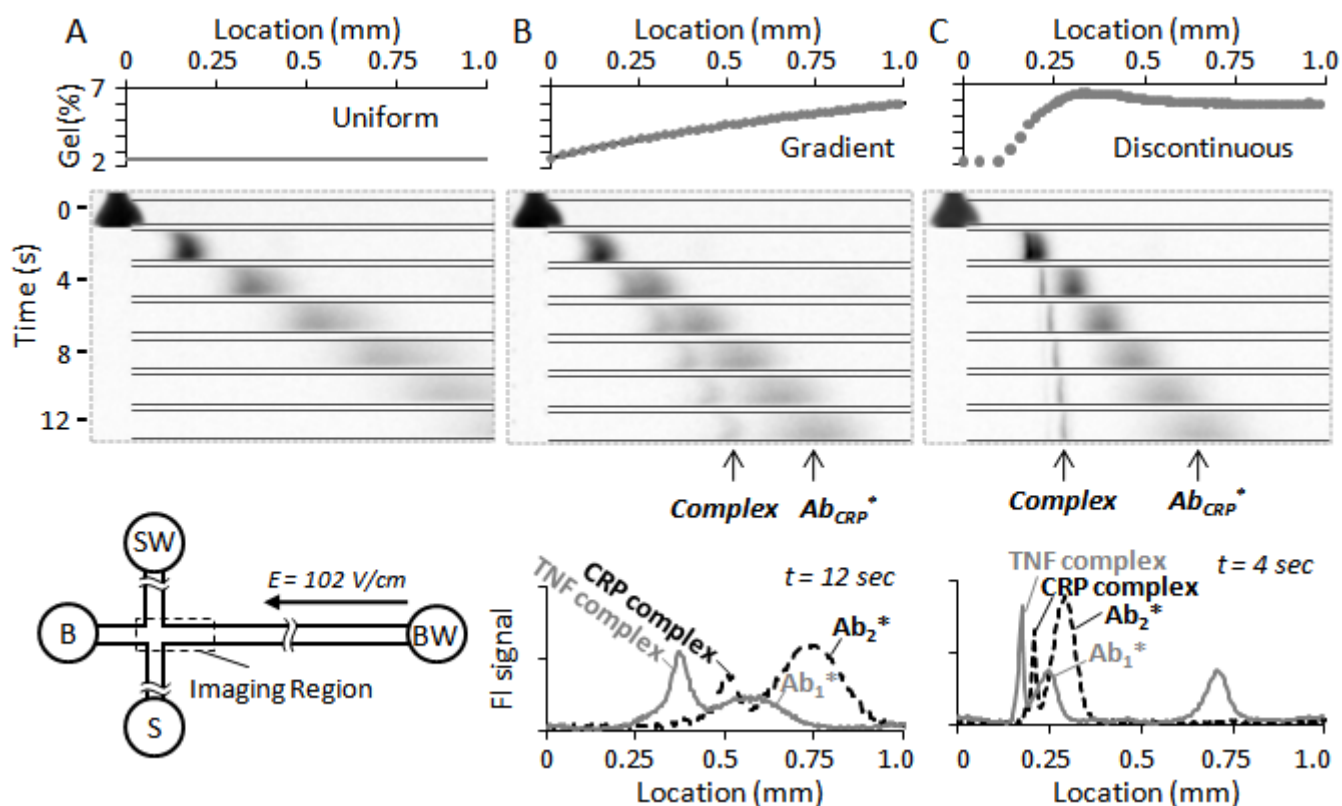
### Gel Fabrication

Three separation gel formats were fabricated within microfluidic channel networks as shown in Figure 1A and used to optimize electrophoretic assay performance: 1) uniform pore-size gels, 2) large-to-small pore-size gradient gels, and 3) discontinuous pore-size gels. For all three formats, the microfluidic channels were coated with a self-assembled silane monolayer, which provides covalent linkage of the PA gel to the channel walls. Gel precursor solutions of appropriate acrylamide concentration (indicated as %T) were prepared by diluting 30% (w/v) acrylamide/bis-acrylamide stock solution with 1x Tris-glycine electrophoresis buffer to a total volume containing 0.2% (w/v) VA-086 photoinitiator. Following vigorous sonication and degassing, precursor solutions were introduced into the channels via capillary action. Photopatterning of uniform pore-size gels and decreasing pore-size gradient gels has been previously reported by our group and others [1, 3].

To create a large-to-small pore-size discontinuity in the separation channel, a chip filled with high %T precursor solution was aligned to a transparency mask exposing the separation channel to UV illumination from an Olympus IX-50 microscope equipped with a mercury arc lamp and an UV objective. Further details on exposure conditions to optimize the discontinuous gel structure for separation are included in the Results and Discussion section. Following the first exposure, unpolymerized high %T gel precursor solution in the loading channel was flushed out and replaced with low %T precursor solution via pressure driven flow, followed by flood exposure of the entire chip to a UV lamp. As a result, the loading channel was filled with large pore-size gel and a large-to-small pore-size discontinuity was located in proximity to the injection junction in the separation channel.

### Gel Pore-size Characterization

To characterize effective pore-size of discontinuous gels along the separation axis, electrophoretic mobility of a model analyte (anti-C reactive protein antibody) was obtained as a function of migration distance from separation images captured on an Olympus IX-70 microscope equipped with a CCD camera. Mobility measurement of the same model analyte on five uniform pore-size PA gels yields a calibration curve between apparent



**Figure 1. Polymer photopatterning enables unprecedented efficiency ( $< 5s$ ,  $< 500 \mu m$ ) in electrophoretic immunoassays for two protein inflammation markers (CRP, TNF- $\alpha$ ).** The spatially varying gel pore-size is shown on the top panel, as determined by  $Ab_{CRP}^*$  mobility. For display clarity, CCD images from the CRP assay with red fluorescence are shown in grayscale for the first 12 s of the separation (middle panel). Gradient gel fluorescence intensity profiles are shown at 12 s of separation for the 2-color concurrent assays (B, bottom panel). The concurrent assays achieve similar separation resolution on the discontinuous gel at 4 s of separation (C, bottom panel).  $E = 102 V/cm$ . Sample contains 16 nM CRP and 22 nM TNF- $\alpha$ .

electrophoretic mobility and gel composition (%T):  $\log(\text{mobility}, \text{cm}^2/V/s) = -0.111(T) - 3.71$  ( $R^2 = 0.974$ ). The calibration curve is used to extract effective gel pore-size along the separation axis for discontinuous gels as well as gradient pore-size gels.

### Protein Samples and Assay Setup

For multi-analyte assays, affinity reagents toward different analytes were labeled with spectrally distinct fluorophores: anti-CRP antibody was labeled with Alexa Fluor 568 dyes with red fluorescence and anti-TNF- $\alpha$  antibody was labeled with Alexa Fluor 488 dyes with green fluorescence. Samples containing fluorescently labeled antibodies and target analytes were mixed and incubated in plastic tubes previously coated with a 5% (w/v) bovine serum albumin (BSA) solution. The BSA coating minimizes non-specific adsorption of protein samples onto the tube walls. For assay development, the chip was sandwiched between an in-house machined manifold and an aluminum frame for fluid introduction. The SW, B, BW reservoirs were filled with Tris-glycine native buffer and a 5  $\mu L$  protein sample was introduced to the S reservoir. Sample injection and separation was initiated by applying voltage through platinum electrodes inserted in each reservoir.

## RESULTS AND DISCUSSION

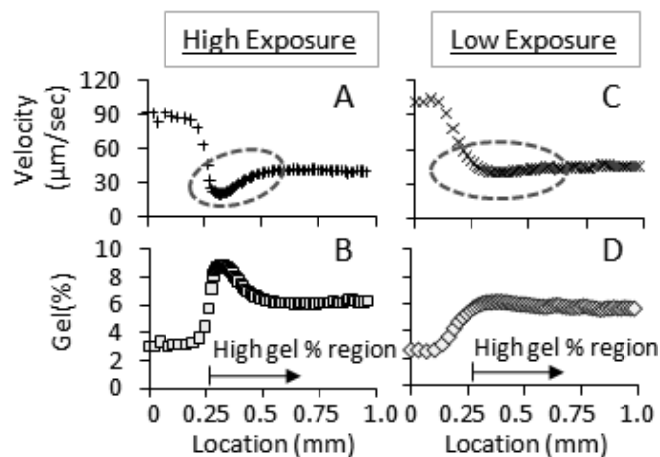
Electrophoretic immunoassay is complete when the antibody (probe) peak is resolved from the immune complex peak. The

separation is quantified as the separation resolution (SR). SR is defined as the ratio of peak-to-peak separation distance ( $\Delta L$ ) to peak width ( $4\sigma$ ). Assuming uniform electric field and electrophoretic mobility for simplicity, the peak-to-peak distance between the immune complex and free antibody is directly proportional to the mobility difference between the two species:  $\Delta L = (\Delta\mu/\mu_{Ab})L_{Ab}$ . Both mobility ( $\mu$ ) and differential mobility ( $\Delta\mu/\mu$ ) are dependent on PA gel composition according to the Ferguson relationship:  $\mu = \mu_0 10^{-K \cdot T}$ . Here  $K$  is the migration retardation coefficient. As the immune complex has a larger retardation coefficient than the antibody due to its larger size, decreasing gel pore-size by increasing  $T$  yields an increased peak-to-peak distance ( $\Delta L$ ) and increased SR at a given migration distance. However, practical assay implementation requires large pore-size gels in the loading channel to allow unbiased introduction of immune complexes. A 2.5%T large pore-size loading gel was chosen as PA has been observed to fail to cross-link at  $\leq 2\%T$ . Through photopolymerization, we achieve control over gel pore-size and pore-size distribution in the separation channel for optimal assay performance.

Figure 1A illustrates the uniform large pore-size gels did not resolve immune complex from antibody probe within the first mm of separation length. In comparison, introduction of a gradual 2.5%T-to-8%T pore-size gradient in the separation channel (Figure 1B) yields CRP assay completion in 925  $\mu m$  at 12.2 s. Use of the gradient gel yielded separation of anti-TNF antibody from immune

complex in 850  $\mu\text{m}$  at 14.5 s. While the gradient gel notably enhanced the mobility difference between the antibody and complex compared to the uniform large pore-size gels, effective separation of Ab\* from CRP complex was not achieved until the proteins migrated into a pore-size region with  $T > 4\%$ . Therefore, increasing the slope of the pore-size gradient, or, equivalently, locating a small pore-size region proximal to the injection junction would result in a more compact device for electrophoretic immunoassays.

Thus, we introduce a nanoporous “step discontinuity” in the separation matrix that yields the shortest separation distances reported to date. Using the nanoporous discontinuity, two-color immunoassays for key inflammation biomarkers (CRP and TNF- $\alpha$ ) require a separation length of just 350  $\mu\text{m}$  versus 10 cm in standard capillary formats typically used for these inflammatory markers. Under full-field imaging mode, quantitation was completed in 4 s on a discontinuous gel with an equivalent separation gel pore-size of 6%T (Figure 1C). An  $\text{SR} \geq 1$  was achieved for CRP in a separation length of 330  $\mu\text{m}$  while an  $\text{SR} \geq 1$  for TNF was achieved in a separation length of 310  $\mu\text{m}$ . For the discontinuous gel demonstrated here, an applied electric field strength of 100 V/cm would require less than 3.5 V across the required separation length, which is a significant reduction of electrical potential requirement for electrophoretic immunoassays.

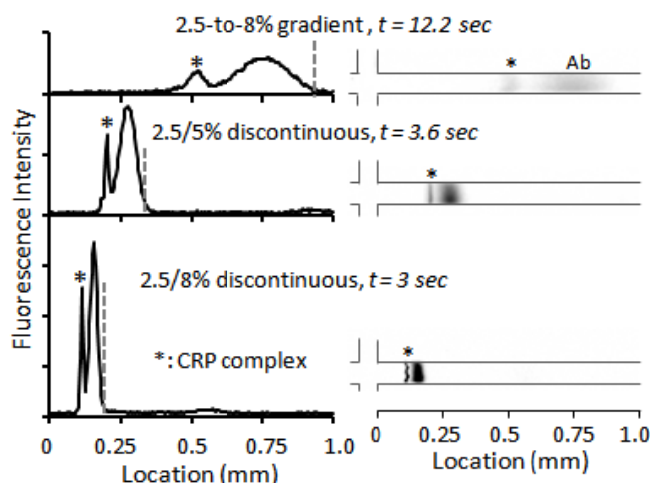


**Figure 2. Controlling photopatterning illumination power offers improved control over pore-size at discontinuity.** Protein tracer exhibits more uniform velocity aft of discontinuity on 2.5/5%T gel fabricated at  $7.5 \text{ mW/cm}^2$  exposure (C, D) vs.  $\sim 600 \text{ mW/cm}^2$  (A, B). Both gels were fabricated with 5% precursor solution in the first exposure. Loading gel (2.5%T) fabrication conditions were the same in both cases.

To achieve the desired performance, we have overcome non-idealities that stymied previous attempts by our group and others at discontinuous gel fabrication, namely: (1) exclusion of large proteins [1] and (2) “destacking” of analyte bands during separation [4]. Initial discontinuous gel fabrication using the mercury arc lamp and UV objective as the exposure source yielded a non-ideal pore-size distribution near the discontinuity as revealed by analyte mobility tracking (Figure 2A-B). Exposing a separation channel filled with 5%T precursor solution resulted in an apparent pore-size of 9%T at the discontinuity. The reduced pore-size acted to exclude the larger immune complexes. Additionally, the apparent pore-size increased from that of a 9%T to that of a 6%T gel during the first 300  $\mu\text{m}$  aft of the gel discontinuity. The pore-size increase resulted in “de-stacking” of analyte bands, negatively

impacting separation resolution. We address the performance-degradation by controlling exposure intensity (Fig 2C-D). Illumination power was reduced by inserting metallic-coated neutral density filters in the light path between the mercury arc lamp and the UV objective. With the modified partial-illumination setup and an optimized exposure time of 3.3 min, a more uniform pore-size separation gel can be observed after the interface. An effective pore-size of 6%T near the interface allowed free migration of the immune complexes.

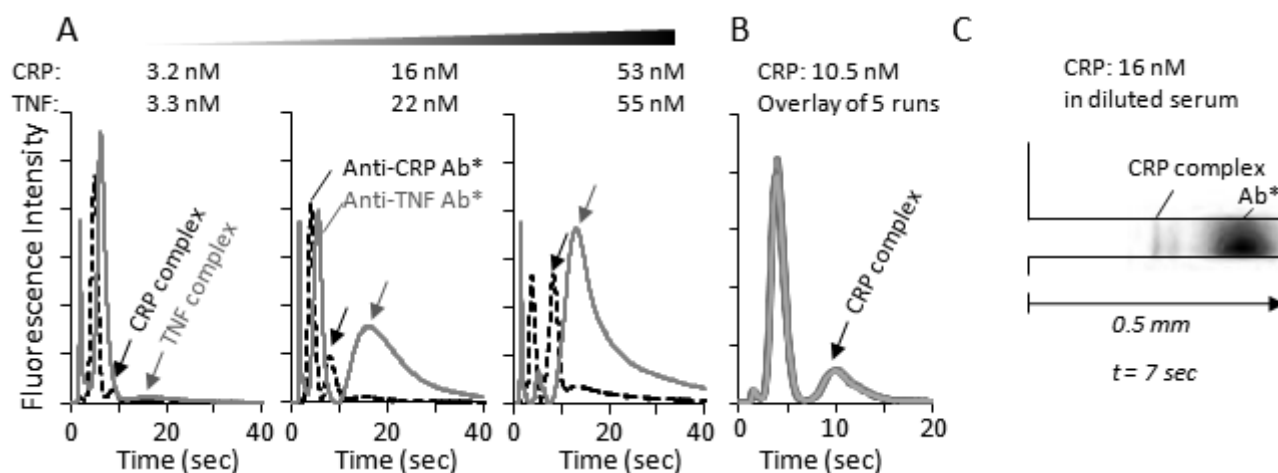
With the optimized fabrication protocol, a 2.5/5%T discontinuous gel allows completion of a CRP immunoassay with a nearly 3x reduction in separation length and assay duration compared to a 2.5%T-to-8%T gradient gel (Figure 3). A 2.5/8%T discontinuous gel further reduces separation lengths to  $< 200 \mu\text{m}$  (Fig 3, bottom panel). The 2.5/8%T discontinuity excluded the CRP immune complex while allowing antibody migration, thus maximizing the mobility difference ( $\Delta\mu/\mu$ ). A secondary performance benefit offered by the discontinuous gels is the ability to “stack” proteins, hence improving signal-to-noise ratio and detection sensitivity. The “stacking” effect stems from the slowed migration of the protein analytes across the large-to-small pore-size discontinuity. Compared to the 2.5%T-to-8%T gradient gel, the 2.5/5%T discontinuous gel achieved nearly 4 times improvement in the signal-to-noise ratio whereas 8 times improvement was observed on the 2.5/8%T discontinuous gel (Figure 3, left panels).



**Figure 3. Tuning pore-size of discontinuity achieves baseline resolution in short separation length (indicated by grey dashed line).** Channel fluorescence intensity profiles for separation resolution  $\geq 1$  are shown on the left for three separation gel formats whereas corresponding CCD separation images are shown on the right. Sample contains 16 nM CRP.

Although the 2.5/8%T discontinuous gel resulted in the shortest separation length using full-field imaging for detection, the expense and size of scientific-grade CCD cameras makes PMT or photodetector based single-point detection a preferred method for point-of-care instruments. Under single point detection, assay duration is largely determined by the slowly migrating proteins. If using a 2.5/8%T discontinuous gel, the immune complexes could take an infinitely long time to reach the single point detector due to physical exclusion by the small pore-size gels. Therefore, the 2.5/5%T discontinuous gel was chosen for single-point detection studies as both TNF- $\alpha$  and CRP immune complexes could enter the separation gel.





**Figure 4. Inflammation biomarker assay performed on discontinuous gel is quantitative (A) and reproducible (B).** (A) Electropherograms generated on discontinuous gel chip with incubates containing CRP = 3.2 nM/TNF = 3.3 nM, CRP = 16 nM/TNF = 22nM, CRP = 53 nM/TNF = 55 nM. (B) Electropherograms from the 1<sup>st</sup>, 3<sup>rd</sup>, 5<sup>th</sup>, 7<sup>th</sup>, 9<sup>th</sup> run over a 20 min period are overlaid. (C) illustrates CRP measurement performed in diluted serum.

Simultaneous quantitation of TNF- $\alpha$  and CRP were performed on the 2.5/5%T discontinuous gel. Red and green fluorescence collected just 270  $\mu$ m downstream of the injection junction was spectrally demultiplexed via bandpass filters followed by PMT detection (Figure 4A). Both CRP and TNF- $\alpha$  assays are quantitative, with increasing biomarker concentration resulting in increased complex peak areas and a commensurate decrease in free antibody. In contrast to surface-immobilized biosensors, continuous monitoring is feasible via sequential injections and separations. For ten sequential CRP assays conducted over a 20 min period (Figure 4B), the analyte migration times exhibited a %RSD less than 2.5%. The %RSD for the SR was 1.0% and the antibody-to-complex peak height ratio exhibited a 2.7% RSD. The reproducibility performance is expected because polyacrylamide gels suppress non-specific adsorption and the separation gel pore-size was optimized for unrestricted migration of analytes of interests. Detection of CRP in diluted human serum was demonstrated in 7 s within 500  $\mu$ m of separation length; analysis of additional samples is underway (Fig 4C).

## CONCLUSIONS

With the introduction of discontinuous nanoporous gels, electrophoretic immunoassays are now amenable to low voltage (< 9 V) operation while maintaining high electric fields (> 100 V/cm) due to the ultra-short separation lengths (< 0.5 mm). Demonstrated here for two inflammatory markers (including CRP in human serum), the assay formats are adaptable for other protein biomarkers through tuning sieving matrix pore-size to match target analyte mobilities. Our current efforts focus on revisions to chip designs to realize portable diagnostic instruments and assessment of clinical samples for translation to near-patient environments.

## ACKNOWLEDGEMENTS

The authors thank the Hellman Family Faculty Award at UC Berkeley for generous financial support, as well as Caliper Life Sciences for glass chip and equipment support. The authors thank Ms. Kelly Karns and Dr. Mei He for assistance. C. Hou is a National Science Foundation Graduate Research Fellow. A. E. Herr is a DARPA young faculty awardee and Alfred P. Sloan Research fellow in chemistry.

## REFERENCES

- [1] A. E. Herr, D. J. Throckmorton, A. A. Davenport, and A. K. Singh, "On-chip native gel electrophoresis-based immunoassays for tetanus antibody and toxin," *Analytical Chemistry*, vol. 77, pp. 585-590, Jan 2005.
- [2] C. Hou and A. E. Herr, "Multiplexed analysis of inflammation biomarkers using spectrally-encoded on-chip electrophoresis," in *Transducer 2009*, Denver, CO, 2009, pp. 1574-1577.
- [3] C. T. Lo, D. J. Throckmorton, A. K. Singh, and A. E. Herr, "Photopolymerized diffusion-defined polyacrylamide gradient gels for on-chip protein sizing," *Lab on a Chip*, vol. 8, pp. 1273-1279, Aug 2008.
- [4] S. Yang, J. K. Liu, C. S. Lee, and D. L. Devoe, "Microfluidic 2-D PAGE using multifunctional in situ polyacrylamide gels and discontinuous buffers," *Lab on a Chip*, vol. 9, pp. 592-599, 2009.

## CONTACT

\*Amy E. Herr, tel: +1-510-6663396; aeh@berkeley.edu

# PHARMASAT: DRUG DOSE DEPENDENCE RESULTS FROM AN AUTONOMOUS MICROSYSTEM-BASED SMALL SATELLITE IN LOW EARTH ORBIT

A.J. Ricco<sup>1\*</sup>, M. Parra<sup>1</sup>, M. Piccini<sup>1</sup>, D. Ly<sup>1</sup>, D. Niesel<sup>2</sup>, M. McGinnis<sup>2</sup>, A. Kudlicki<sup>2</sup>, J.W. Hines<sup>1</sup>,  
L. Timucin<sup>1</sup>, C. Beasley<sup>1</sup>, R. Ricks<sup>1</sup>, M. McIntyre<sup>1</sup>, C. Friedericks<sup>1</sup>, M. Henschke<sup>1</sup>, R. Leung<sup>1</sup>, M. Diaz-Aguado<sup>1</sup>,  
C. Kitts<sup>3</sup>, I. Mas<sup>3</sup>, R. Rasay<sup>3</sup>, E. Agasid<sup>1</sup>, E. Luzzi<sup>1</sup>, K. Ronzano<sup>1</sup>, D. Squires<sup>1</sup>, B. Yost<sup>1</sup>

<sup>1</sup>Small Spacecraft Division, NASA Ames Research Center, Moffett Field, California, USA

<sup>2</sup>University of Texas Medical Branch, Galveston, Texas, USA

<sup>3</sup>Santa Clara University, Santa Clara, California, USA

## ABSTRACT

We designed, built, tested, space-qualified, launched, and downlinked bioanalytical data from PharmaSat, the first fully autonomous outer-space pharmaceutical dose-response bioanalytical system on a free-flying satellite. PharmaSat tracks microorganism culture population density and metabolic activity in 48 microwells via 3-color optical absorbance. Its 5.1-kg total mass includes solar cells, integrated spacecraft “bus” module (power/batteries/control/communications), and a sealed containment vessel housing the biofluidic, optical, thermal, and sensor subsystems. Data were obtained from all subsystems over several days following nutrient introduction to initiate growth of *Saccharomyces cerevisiae*, followed by challenges with three dose levels of an antifungal agent.

## INTRODUCTION

Long-term spaceflight affects living organisms. Data for mammals are consistent with immune stress, decreased bone density, muscle atrophy, and slowed wound healing. For cells and microorganisms in culture, absence of gravity means thermal gradients do not cause convection as on Earth, potentially altering mass transport that influences nutrient delivery and waste removal. For all living organisms, rates of damage from high-energy radiation increase measurably outside the shielding of Earth’s magnetosphere. In microbes, rates and extent of growth vary, and pathogen virulence has been reported to change [1]. Astronauts can contract infections; effective treatment may involve changes in therapy

relative to terrestrial afflictions, particularly if microbes respond differently to antimicrobials.

PharmaSat was developed to conduct a low-cost *in-situ* outer-space study of the efficacy of a widely-used antifungal (AF) drug, voriconazole, against a common, well-studied “model organism,” the fungus *S. cerevisiae* (brewer’s yeast).

Integrated bioreactors have flown on manned spacecraft [2-4]; they require humans to initiate experiments, record data, and collect/prepare samples for return to Earth for characterization [2]. Our fully autonomous microsystems [5] obviate the

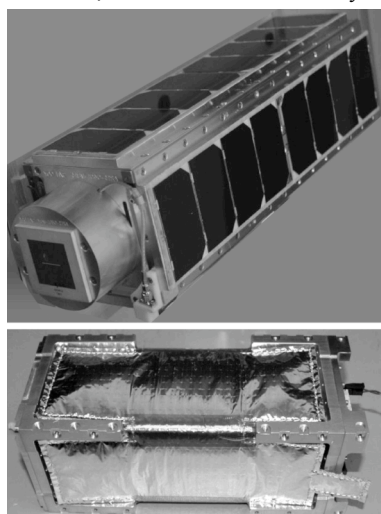
cost and other limitations of human-tended space biological experiments while expanding the range of launch opportunities.

On May 19, 2009, the 5.1-kg PharmaSat spacecraft launched as a secondary payload aboard a Minotaur I rocket from Wallops Flight Facility, Virginia. This “hitchhiker” approach to space science offers much lower launch costs (about \$40,000/kg) than dedicated space biology missions, but can add operational constraints: PharmaSat was delivered for test and launch-vehicle integration nearly 7 weeks before launch; no power was available for thermal control prior to deployment in space, although temperature was maintained between 4 and 37 °C. As an add-on payload, PharmaSat was mounted, using a vibration-damping fastener, to the Minotaur I upper-stage rocket motor; calculations predicted < 5 °C temperature increase inside the pressure vessel containing the biofluidic subsystem during the short burn time of this motor.

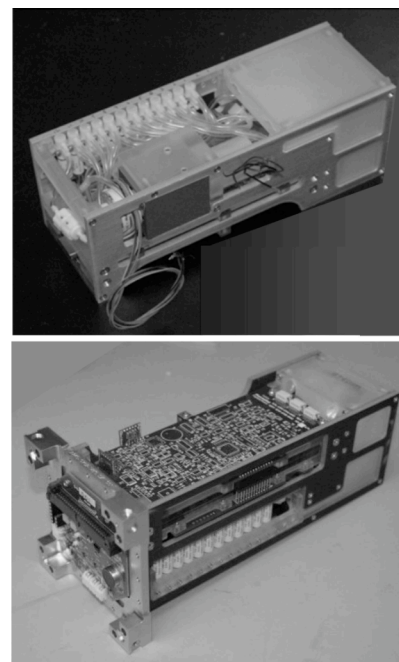
About 20 min after launch, PharmaSat was spring-ejected into low-Earth orbit (460 km elevation) as a free-flying satellite. It functioned nominally; within days, results from the PharmaSat microgravity 48-microwell drug-dose-dependence experiment were telemetered to Earth ([http://www.nasa.gov/mission\\_pages/smallsats/pharmasat/main/index.html](http://www.nasa.gov/mission_pages/smallsats/pharmasat/main/index.html)). Leveraging multiple micro and miniature technologies, PharmaSat is the first fully autonomous outer-space pharmaceutical dose-response analytical system. Here we report its design, development, and the spaceflight and ground-control experimental results from this integrated bioanalytical system.

## DESIGN AND CONSTRUCTION

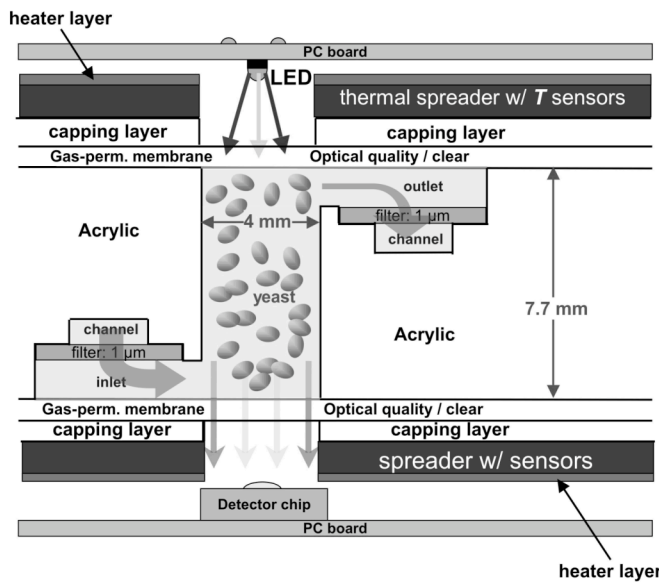
PharmaSat’s 5.1 kg mass comprises a structure approximately 10 x 10 x 35 cm, Figure 1, including triple-junction solar cells; patch antenna for 2.4-GHz communication; mechanical structure; spacecraft power, processor, communications, and control system (collectively, the “bus”); and the experimental containment vessel, internal



**Figure 1:** Integrated PharmaSat free-flying satellite (~35 cm long, 5.1 kg) with solar panels, patch antenna on near end (top); payload frame and insulation-wrapped pressure vessel (bottom) containing the integrated culturing and bioanalytical system.



**Figure 2:** Two views of PharmaSat integrated payload (which slides inside the pressure vessel shown in Figure 1). It includes fluidic, optical, thermal, sensor, and electronics subsystems.



**Figure 3:** Microfluidic, optical, and thermal cross section of one of 48 wells; each contains 100  $\mu\text{L}$  and has integral 1.2- $\mu\text{m}$  filter membranes at inlet and outlet to confine the yeast. RGB LED and detector pair at opposite ends of each well measure 3-color transmittance. Patterned Kapton heaters plus aluminum thermal spreaders give  $< 0.3\text{ }^\circ\text{C}$  temperature uniformity across the card.

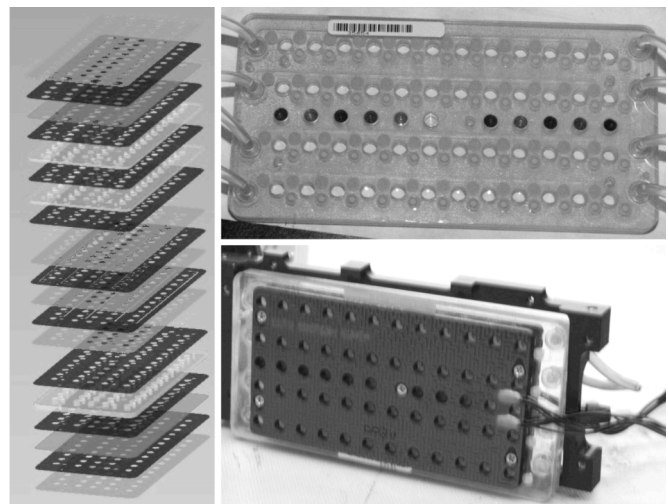
volume 1.2 L (Figures 1, 2), which houses the bio/fluidic, optical, thermal, sensor, and payload electronics subsystems (Figure 2). Magnetic rods passively orient the satellite, aiming its long axis and hence antenna toward Earth's N magnetic pole when the spacecraft is above the northern hemisphere. Magnetic hysteresis rods damp "wobble" in spacecraft motion by dissipating energy when they move in Earth's magnetic field.

### Fluidic SubSystem

The PharmaSat fluidic card (cross section: Figure 3) includes forty-eight 100- $\mu\text{L}$  culture wells, 4 mm diameter x 7.8 mm deep, and 11 solid-state reference wells. 9-mm pitch along rows and 9- and 13.5-mm spacing between rows allow card optical analysis with standard multiwell plate readers. The card was fabricated by Micronics, Inc. from laser-cut poly(methylmethacrylate) layers (Figure 4) laminated with pressure-sensitive adhesive interlayers supported on (poly(ethylene terephthalate)) carrier films. Four independent sets of manifolded fluidic inlets and outlets with 1.2- $\mu\text{m}$  nylon fiber membrane filters (Sterlitech) supply nutrients and antifungal agent to the four 12-well banks containing the yeast.

Covering tops and bottoms of the fluidic cards is a 51- $\mu\text{m}$ -thick layer of optical-quality poly(styrene) (PS), which provides gas permeability for  $\text{CO}_2$  and  $\text{O}_2$  exchange. Cards were fabricated without a top cover layer, sterilized using ethylene oxide, off-gassed in vacuum for 2 weeks at 55  $^\circ\text{C}$ , and stored in sterile bags.

Inoculation of biowells with microorganisms and fluid filling of fluid storage bags, tubing, channels, and wells are carried out under sterile conditions prior to payload integration. To prepare a card for laboratory or flight experiments, solid-state colored optical reference elements are placed in the eleven "dry" wells. Each biowell is inoculated with 10  $\mu\text{L}$  of dormant *S. cerevisiae* culture, to provide a final density of 5 – 10  $\times 10^5$  /mL, with care to avoid wetting filter membranes. To help eliminate gas bubbles, wells and channels are purged with  $\text{CO}_2$ . The open wells are then covered by a second PS film. Channels and inoculated biowells are next filled with thoroughly vacuum-degassed sterile water; any

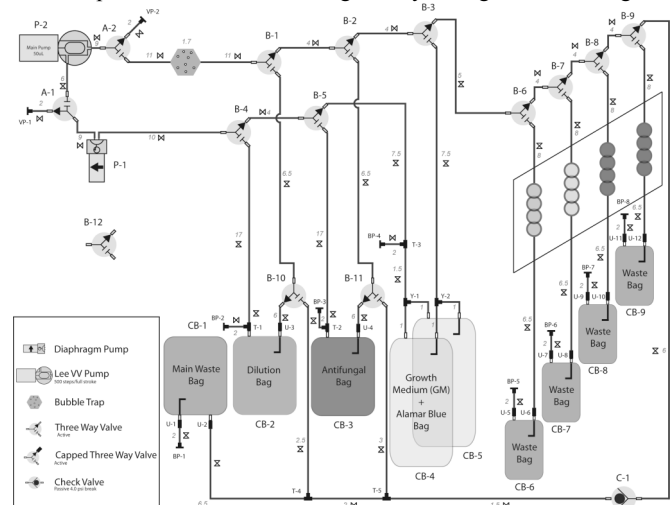


**Figure 4:** Exploded view of fluidic card showing laser-cut acrylic and PSA layer stack (left). Completed card (upper right) shows 4 banks of 12 wells each and 11 reference wells (colored, along center line). A pair of patterned Kapton heater films with aluminum spreader plates (bottom) sandwiches the fluidic card.

remaining  $\text{CO}_2$  bubbles dissolve gradually as stasis medium flows through the wells and channels.

The fluid-delivery-and-dosing system, Figure 5, comprises 14 solenoid-operated valves (The Lee Co.); a piston-type metering pump (Lee) and a diaphragm-based pump (KNF Neuberger); a bubble trap (developed in-house); nine medical-grade fluoro-polymer bags (American Fluoroseal) for growth medium, viability dye, antifungal agent, and waste; and medical-grade connecting tubing (Sanipure 60 tubing, Saint-Gobain Performance Plastics).

The fluidics card and system maintain the micro-wells in a bubble-free state for 5 – 7 weeks after loading and assembly, despite the permeability of the covering membranes to water vapor. This issue was mitigated by filling the waste bag for



**Figure 5:** Block diagram of fluid delivery and dosing system. The variable-volume (VV) metering pump makes precise dilutions of the antifungal agent for delivery at 3 concentrations. The diaphragm pump provides higher flow rates for circulation and mixing. Each bank of 12 wells has a dedicated waste bag, while the growth medium, antifungal agent, dilution, and mixing bags are common.

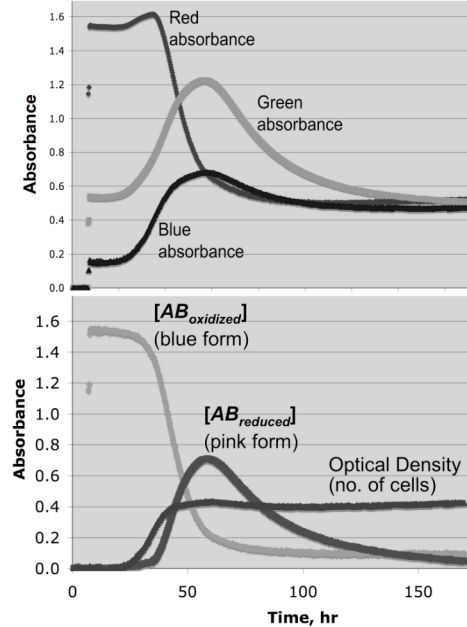
each well bank with several mL of stasis buffer maintained at a low “back pressure”, replacing water lost to evaporation and preventing bubble formation. Evaporation was also mitigated by the sealed pressure vessel, the internal air volume (< 0.4 L) of which was humidified to near saturation by evaporation from the fluidic card.

### Optical, Thermal, and Sensor SubSystems

Each of the 48 fluidic and 11 solid-state reference wells has a dedicated optical sub-assembly (Figure 3), comprised of a 3-color LED (Lite-On) providing illumination bands at 470, 525, and 615 nm with 26, 35, and 18 nm spectral half-widths, respectively, and an intensity-to-frequency ASIC (Texas Advanced Optoelectronic Solutions) providing > 5 decades of digital output. Only a single LED wavelength band at a single well is energized at once, eliminating any possibility of optical crosstalk.

The optical system measures organism growth in two ways: optical density changes due to light scattering by the yeast cells, which is directly proportional to cell number [6], and color change of a “viability” dye, alamar blue (AB), which is deliberately added to the growth medium. AB changes from blue (oxidized form) to pink (reduced form) when enzymes generated by metabolic processes in cells act upon it [7]. AB’s blue form has its absorbance maximum at 600 nm, the pink at 570 nm. To first order, the red LED tracks the concentration of oxidized AB, the green is sensitive to the pink form, and the blue, where neither pink nor blue forms of the dye absorbs particularly strongly, responds mainly to light scattering by the yeast cells.

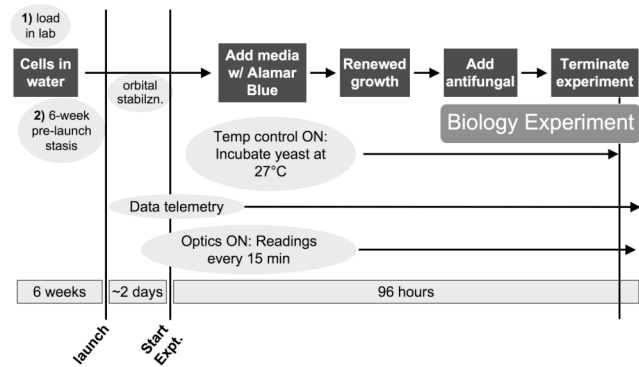
The match of the three LED bands to the three optical parameters of interest is, unfortunately, imperfect. We measured optical absorbance “cross terms”, finding the three most important of them to be (1) absorption of the blue band by the blue form of AB (10% of its absorbance at 615 nm); (2) absorption of the blue band by the pink form of AB (29% of its absorbance at 525 nm); (3) absorption



**Figure 6:** Three-color absorbance of one microwell of growing yeast measured with the PharmaSat optical system. **Top:** As-measured absorbances, corrected for known absorbance of initial concentration of blue form of alamar blue. **Bottom:** Absorbances after correction for “cross terms”, resulting in absorbances of the two forms of AB and the optical density due to light scattering by the yeast cells.

of the green band by the blue form of AB (35% of its absorbance at 615 nm). Figure 6 shows uncorrected absorbances (top) and absorbances after correction for the optical cross terms (bottom), allowing reasonably accurate estimation of cell number and the concentrations of AB in its oxidized and reduced forms.

The thermal system utilizes a pair of custom Kapton-film heaters (Minco) mated with 3-mm-thick black-anodized Al plates (mini-



**Figure 7:** Operational timeline for PharmaSat space experiment.

mizing light reflections) as thermal spreaders sandwiching the fluidic card (Figure 3). A “bang-bang” controller operated by the system microcontroller provides temperature stability of < 0.3 °C. Average power consumption by the thermal systems was ~ 2 W to maintain the card at the 27 °C growth temperature while in orbit.

Sensors in the pressure vessel include six for temperature (Analog Devices) distributed over the thermal spreaders to monitor fluidic card temperature and provide the control signal; a micro-machined pressure transducer (Motorola); and a thin-film capacitive humidity sensor (Sensirion). In the spacecraft bus, acceleration is monitored in 3 axes by MEMS accelerometers (Silicon Designs); a PIN diode (Hamamatsu) monitors radiation flux.

### RESULTS FROM ORBIT AND GROUND CONTROLS

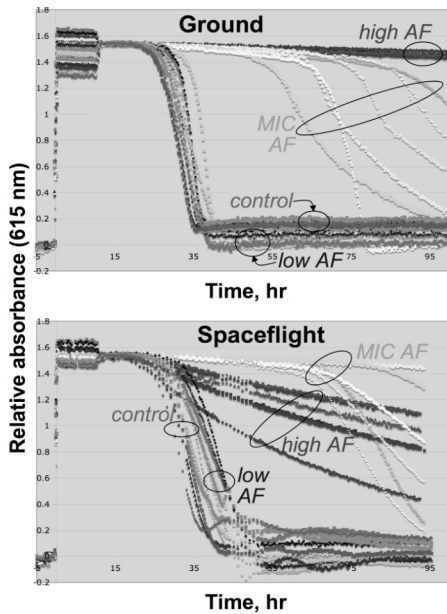
Figure 7 shows the operational timeline for the PharmaSat space experiment. Nearly 7 weeks after integration with the rocket, PharmaSat launched on May 19, 2009; it was deployed 20 min later. Radio contact was established within hours and its orbit passively stabilized. Orbital trajectory puts PharmaSat in sunlight ~ 2/3 and darkness ~ 1/3 of each 97-min orbit. Li-ion batteries in the bus are charged by the solar panels, providing uninterrupted power.

Following stabilization (gravity < 10<sup>-3</sup> xg, calculated from variations in currents from the 4 solar panels), some 47 hr after orbital deployment, PharmaSat changed the temperature of the fluidic card from ambient (~ 6 – 16 °C, depending on the phase of orbit) to 27 °C. With temperature stabilized, *S. cerevisiae* (strain: BY4743) growth was initiated 3.6 hr later in all 48 wells by pumping in a 3x exchange of RPMI-1640 nutrient medium (as in [8], omitting phenol red) containing alamar blue viability dye (10% of stock), one 12-well bank at a time, displacing the stasis buffer.

Meaningful measurements of AF dose dependence require the antifungal agent to be introduced when the yeast are growing stably but prior to the culture reaching high density, when the AF generally becomes ineffective. Because growth rate in the microgravity environment was not known in advance, growth progress was monitored by telemetry; based on initial growth rates, AF was administered approximately 12 hr after initial RPMI introduction.

Using an identical satellite system in the ground laboratory, housed in a thermal chamber to mimic temperatures reported from the satellite, and with *S. cerevisiae* loaded from the same prepared cultures within two days of the flight loading of yeast, a “delayed synchronous” ground control experiment was conducted in order to meaningfully compare ground and space results.

Figure 8 compares the results from the ground-control experiment (top) with the spaceflight results, telemetered from orbit (bottom). The data shown here are corrected absorbances of alamar blue throughout the growth and challenge process in its oxidized form, as measured using the red LED and after correction for “cross terms” described above. After initial growth, a growth medium/AF



**Figure 8:** Terrestrial (top) and spaceflight (bottom) growth curves for *S. cerevisiae* at 27 °C in RPMI growth medium as a function of voriconazole antifungal concentration. 6 wells are tracked for each condition: “Control” includes no AF; “low AF”, “MIC”, and “high AF” correspond to 0.13, 0.50, and 2.0 µg/mL concentrations of voriconazole, respectively. (Circles and ellipses indicate sets of growth curves for each labeled condition).

= 6 independent microwells, which were initially loaded with yeast corresponding to an approximate optical density (OD) of 0.1.

Because the delay between loading the organisms and deployment in space could not be predicted exactly (weather and other factors can, and do, cause launch delays), the remaining 6 wells of each bank of 12 were loaded with yeast at an OD of 0.2: in the event that insufficient organisms survived the stasis period in the OD = 0.1 groups of wells, the OD = 0.2 wells were included to provide an extra 100% population margin for initiating growth. Because AF dose dependence tests are typically more reliable at lower yeast population densities, the successful and stable growth of all 24 wells containing the OD = 0.1 cultures led us to choose those data for our initial ground/flight comparisons.

Figure 9 analyzes AF = 0 yeast growth rates by two measures, both of which indicate slower growth ( $p < 0.04$ ) in space’s microgravity environment than on Earth. In a significant gravitational field, even small thermal gradients, as might, for example, be caused by the on/off cycling of the fluidic card heater, can result in thermal convection in an otherwise quiescent culture (due to fluid density differences). In contrast, in microgravity conditions, fluid density differences do not drive convection. Thus, it may be the case that the yeast grow more slowly in space because the transport of nutrients to the cells and/or the transport of waste products away from the cells is slower, being driven solely by diffusion, than on Earth where convection can play a role in mass transport.

Figure 8 shows that the “low AF” condition, AF = 0.13 µg/mL, does not significantly affect growth parameters relative to zero AF. Thus, spaceflight growth is slower by about the same relative factor at this low AF concentration as in the absence of AF.

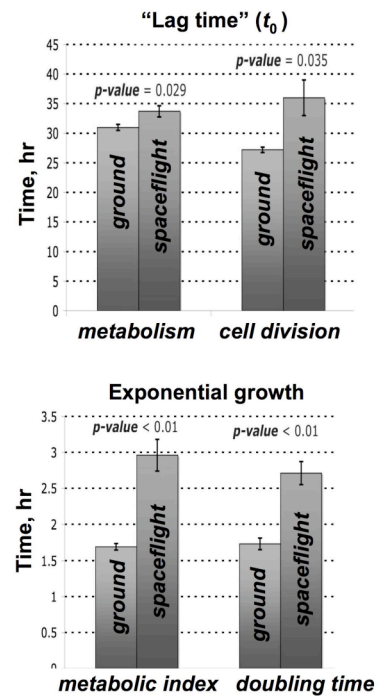
At the MIC, both ground and spaceflight data show significant spread in the 9 growth curves for AF = 0.5 µg/mL. This was ex-

pected, as the growth rates with the antifungal near its MIC are very sensitive to small differences in concentration, temperature, and other parameters. Interestingly, the spaceflight data show roughly the same slowing of growth at the MIC as they do at the zero and low AF concentrations.

At high antifungal concentrations (AF = 2.0 µg/mL), an interesting difference is observed: as expected, terrestrial data show near-total inhibition of growth. In space, however, Figure 8 reveals significant metabolic activity, as measured by the decrease in [AB] with time for all 6 wells. We speculate that diffusion-only mass transport may allow yeast to continue limited metabolic activity at higher AF concentrations in space than on Earth. If verified (ultimately in animal models), this could have significant implications for the treatment of fungal infections in the space environment.

pected, as the growth rates with the antifungal near its MIC are very sensitive to small differences in concentration, temperature, and other parameters. Interestingly, the spaceflight data show roughly the same slowing of growth at the MIC as they do at the zero and low AF concentrations.

At high antifungal concentrations (AF = 2.0 µg/mL), an interesting difference is observed: as expected, terrestrial data show near-total inhibition of growth. In space, however, Figure 8 reveals significant metabolic activity, as measured by the decrease in [AB] with time for all 6 wells. We speculate that diffusion-only mass transport may allow yeast to continue limited metabolic activity at higher AF concentrations in space than on Earth. If verified (ultimately in animal models), this could have significant implications for the treatment of fungal infections in the space environment.



**Figure 9:** Comparison of “lag time” before yeast growth begins (top) and the time constant of the exponential growth phase (bottom) for ground and spaceflight measurements with zero antifungal agent concentration.

## REFERENCES

- [1] J.W. Wilson, C.M. Ott, ..., and C.A. Nickerson, “Space Flight Alters Bacterial Gene Expression and Virulence and Reveals a Role for Global Regulator Hfq,” *PNAS*, 104, 16299 (2007).
- [2] T.G. Hammond, F.C. Lewis, T.J. Goodwin, *et al.*, “Gene Expression in Space,” *Nature Medicine*, 5, 359 (1999).
- [3] N.F. deRoos, S. Gautsch, *et al.*, “MEMS for Space”, *Proc. Transducers 2009, IEEE: New York* (2009); pp. 17-24.
- [4] J.J. Cefai, D.A. Barrow, P. Woias, and E. Muller, “Integrated Chemical Analysis Microsystems in Space Life Sciences Research,” *J. Micromech. Microeng.*, 4, 172 (1994).
- [5] A.J. Ricco, J.W. Hines, *et al.*, “Autonomous Genetic Analysis System to Study Space Effects on Microorganisms: Results,” *Proc. Transducers 2007, IEEE: New York* (2007); pp. 33-37.
- [6] A.J. Ricco, E. Agasid, *et al.*, “Integrated System to Analyze the Genetic Effects of the Space Environment on Living Cells in Culture: GeneSat,” *Proceedings µTAS 2005, Transducers Research Foundation: Cleveland* (2005), pp. 527–529.
- [7] J. O’Brien, I. Wilson, *et al.*, “Investigation of the Alamar Blue (Resazurin) Fluorescent Dye for the Assessment of Mammalian Cell Cytotoxicity,” *Eur. J. Biochem.*, 267, 5421 (2000).
- [8] “Reference Method for Broth Dilution Antifungal Susceptibility Testing of Yeasts. Approved Standard M27-A2”, 2nd ed. National Committee for Clinical Laboratory Standards, Villanova, PA (2002); Appendix A and Table 6.

## CONTACT

\*A.J. Ricco, tel: +1-650-604-4276; antonio.j.ricco@nasa.gov

# AUTOMATED PROTEIN IMMUNOBLOTTING BY PHOTOPATTERNING OF POLYACRYLAMIDE GEL IN TWO-DIMENSIONAL MICRODEVICE

Mei He and Amy E. Herr\*

Department of Bioengineering, University of California, Berkeley, CA 94720, USA

## ABSTRACT

Here we report on automated protein immunoblotting using microfluidic technology. This technology utilizes a novel two-dimensional microfluidic architecture photopatterned with polyacrylamide gel to yield polyacrylamide gel electrophoresis (PAGE), transfer, and in-situ antibody-based immuno-detection. The high-resolution polyacrylamide (PA) gel photopatterning provides the ability to mimic both a miniature slab gel and a protein-binding membrane, albeit with enhanced performance. In this paper, native prostate specific antigen (PSA) extracted from a human seminal fluid sample was used to demonstrate the direct mapping of analyte mobility to antibody-affinity based protein identification in a fully programmable manner. Our design paradigm has adaptable performance for relevance to all categories of immunoblotting, including the western, southern, northern and eastern blotting. The approach reported here forms the basis for a new approach to protein assays.

## INTRODUCTION

Immunoblotting is exquisitely specific – allowing detection of a single protein species amidst a sea of confounding species [1]. The unrivaled specificity of immunoblotting arises from direct mapping of analyte mobility to the presence/absence of an antibody-binding interaction [2]. Immunoblotting comprises a suite of powerful protein measurement techniques used in virtually every life sciences laboratory in the world – paradoxically, the methodologies are fraught with errors, require trained operators, and demand up to two days (48 hrs) to complete [3]. Recently, automated immunoblotting has been reported using a capillary format [4, 5]. Capillary isoelectric focusing (IEF) was used to separate proteins, including protein isoforms [6]. However, in capillary systems, integration of multiple assays is difficult without external fixturing to multiple reservoirs and interfaces. In contrast, microsystems provide a format amenable to integration of multiple functions in a single microfluidic system, which substantially benefits automation of multi-stage assays by obviating cumbersome interfacing at each channel junction [7]. The ability to fabricate interconnecting channels with zero dead volume further contributes to high performance and low sample loss. We build on additional compelling advantages of microfluidic systems that include: reduced manual intervention, nominal sample consumption, rapid results, improved assay precision, and digital

data collection essential for archiving and comparison [8, 9], which are exceptionally well-suited formats for multi-step analyses [10, 11].

To surmount the noted limitations of macroscale slab-gel immunoblotting our group reports here on the first known attempt to automate immunoblotting using microfluidic technology. In a significant improvement on our published work [12], the technology introduced utilizes a well-suited two-dimensional microfluidic architecture to yield protein separations in < 30 s followed by quantitative antibody-based protein detection, in one monolithic sub-millimeter polyacrylamide gel structure. In this report, we discussed design, fabrication, and validation of the approach that harnesses two-dimensional high-resolution polyacrylamide (PA) gel photopatterning in microfluidic device to provide both a miniature slab gel and a protein-binding membrane. To our knowledge, limited effort has been made to streamline the multiple steps needed to obtain mobility and binding-based identity information in one continuous assay [13]. Our design paradigm may have sweeping performance ramifications for all categories of immunoblotting, as well as for proteomic assays more broadly. The work detailed here forms the basis for a new approach to protein assays relevant to questions spanning basic science to clinical assays.

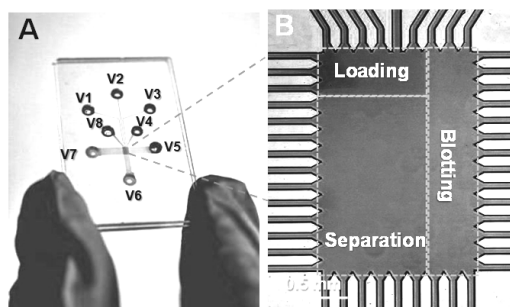


Figure 1. Polyacrylamide gel photopatterning in 2D microfluidic geometry enables fully-integrated protein immunoblotting. Bright-field images of: (A) glass device housing patterned PA gels and liquid reservoirs (indicated by V1, V2, V3, V4, V5, V6, V7 and V8) for fluid access & electrical control. (B) magnified chamber with photopatterned gels for sample loading, PAGE separation and transfer to antibody functionalized blotting region (right side).

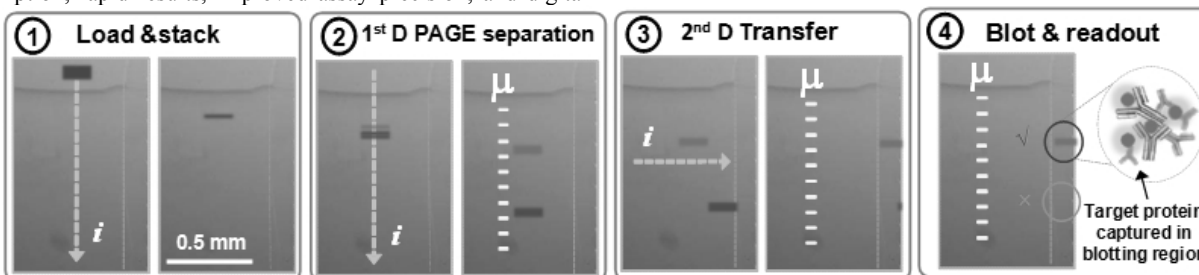


Figure 2. The automated multi-stage assay protocol ①-④ consists of sample loading and stacking, vertical dimension separation, horizontal dimension transfer, and immuno-detection. “ $\mu$ ” indicates mobility; “ $i$ ” indicates direction of electrical current flow.

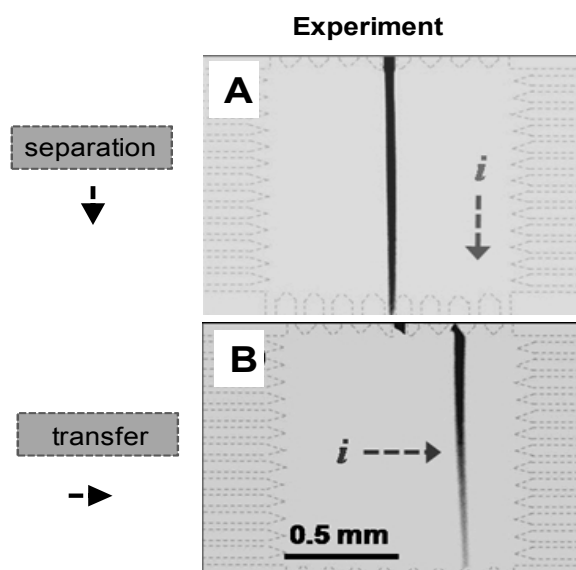


Figure 3. Dispersionless protein injection and transfer in chamber. (A) Vertical electric field for separation; (B) horizontal electric field for sample transfer to blotting region. Electrophoretic transfer visualized by loading and manipulating 0.1 M free dye.

## EXPERIMENTAL

### Gel Photopatterning

High resolution regional photopatterning of PA gel precursor solutions allows fabrication of spatially-varying pore-size and chemical functionality in microfluidic devices with minimal integration dead volume. In this paper, the gel regions were sequentially photopatterned using a three-step process. Patterning was conducted in glass microfluidic chambers. The photopatterning approach provides a crucial tool for integrating the immunoblotting functionality (Figure 1A). The lithography was accomplished via a UV objective (UPLANS-APO 4 $\times$ , Olympus) in combination with a transparency film mask and epi-fluorescence microscope system (IX-70, Olympus, Melville, NY). Using this photolithography approach, the blotting gel was fabricated by exposing a region filled with a 6%T precursor solution (including streptavidin-acrylamide) to UV light for 8 min. Here, the neutral density filter was used to achieve a UV intensity at  $\sim 13$  mW/cm $^2$ . The notation %T and %C indicate the percentage of total acrylamide and cross-linker, respectively. Here covalently bonded streptavidin in the gel matrix was used to immobilize biotinylated antibodies for immunoblotting and detailed in reference [14]. This functional immunoblotting region is indicated in Figure 1B. The unpolymerized region was replaced by introducing the second gel precursor solution through vacuum. In the second step, mask alignment to the chip was performed using a manual adjust x-y translation stage on the microscope (Olympus, Melville, NY) to subsequently photopattern the 6%T separation gel (5 min). The PAGE separation gel had a composition and structure similar to the blotting matrix albeit with no immobilized antibodies present. Finally, in the third step, a larger pore-size loading gel was formed using 3%T acrylamide solution and an 8-min flood exposure of the chip to a filtered mercury lamp (300-380 nm, 10 mW/cm $^2$ , UVP B100-AP, Upland, CA) with cooling fan. Here the photopolymerization times were determined empirically based on the UV intensity, composition of acrylamide precursor solution,

and desired pore-size to achieve optimal gel performance for the desired functions.

### Electric Field Simulation and Control

To control sample dispersion common in chamber-like geometries, an array of field-control channels was included in the chip chamber design. Simulation of the load and transfer electric fields was performed using COMSOL Multiphysics (Version 3.5a, COMSOL AB). The simulation was conducted under two-dimensional conductive media DC conditions. Modeling of the electrostatics within a buffer filled microfluidic channel network under variable voltages provided guidance on the optimized voltage program for experimental operation.

After sample addition to the chip, assay operation was programmable and controlled via a power supply equipped with platinum electrodes (Caliper Life Sciences). The sample (V1), sample waste (V3), buffer (V2, V4, V7, V8), and buffer waste (V5, V6) reservoirs are indicated in Figure 1A. To assure minimal cross-contamination between samples and reproducible runs, all channels were electrophoretically flushed with buffer every other run.

## RESULTS

We utilize our multi-stage photopatterning approach to locate several PA gel regions (sample loading, PAGE separation and immunoblotting) in one microfluidic chamber. The chip (geometry and gel) design yields both a miniature slab gel and a protein-binding membrane, as shown in Figure 2. After vertical PAGE separation, the resolved protein species are transferred laterally across the 2D chamber and target proteins are in-situ identified by antibodies immobilized in blotting region. Importantly, after sample loading and PAGE separation, our chip design enables blotting of all protein bands against the blotting region in a single electrophoretic transfer step that is fully programmable, as illustrated in Figure 2 ①-④.

The lateral transfer step links the vertical separation position to horizontal affinity-based binding information, thus providing a 1:1 mapping of mobility to antibody interaction. Retaining information about protein mobility, as well as binding interaction (or lack thereof) for each resolved species in a sample is critical to developing and completing a successful immunoblot. Therefore, we investigated means to achieve a uniform and efficient transfer of resolved species from the separation dimension to the blotting region of the chamber. As described in the experimental section, we employed numerical simulations to determine the applied electrical potentials to achieve minimal dispersion in sample loading, separation, transfer and blotting stages. The experimental data showed a well-controlled transfer process in both the vertical and horizontal dimensions (Figure 3). In contrast to the injection with no electric field shaping, appropriate voltage control ensured that the injected sample plug preserved its original shape with little distortion after entering into the wider separation chamber. A uniform electric field distribution within the chamber for each step provided the basis for precisely manipulating the sample during separation and transfer.

To optimize the first step (PAGE), we use a discontinuous gel (large-to-small pore-size) near the sample injector to minimize injection dispersion for improved separation resolution (SR, where  $SR > 1$  is desired). Here the discontinuity was created by 3%T loading gel adjacent to 6%T separation gel, and used to differentially retard the migration of proteins based on their size. Further, the separation performance benefits from the “stacking”

effect and decreased the protein band dispersion. As compared in Figure 4, with the gel discontinuity, PAGE separation achieves an  $SR = 1.5$  for the two highest mobility peaks in Figure 4A. The separation was completed in 30 seconds in just a fraction of the separation axis length. While without the stacking gel discontinuity (i.e., a uniform 6%T gel), a low separation resolution of  $SR = 0.4$  was achieved for the same two species (Figure 4B).

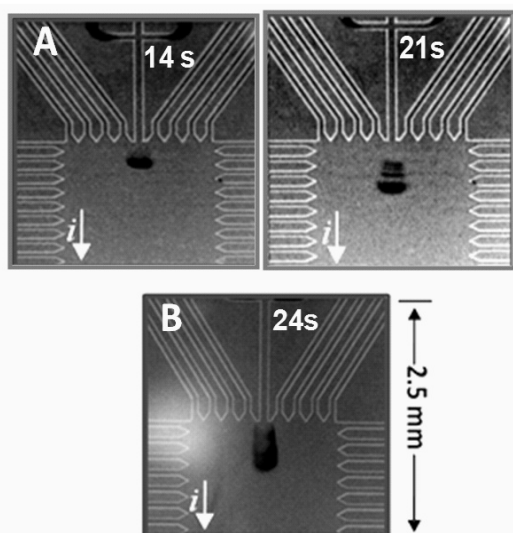


Figure 4. Discontinuous stacking gel improves separation resolution. (A) Large-to-small pore-size gel discontinuity at PAGE start yields ultra-efficient size-based PSA sample stacking and separation, compared with (B) no stacking gel. (inverted grayscale)

To demonstrate this automated immunoblotting format, we assay native free prostate specific antigen (fPSA) extracted from human seminal fluid (Figure 5). Free PSA is a tumour marker currently used for serum diagnosis of prostate cancer [15]. Much recent interest centers on improving prognostic performance through analysis other forms of PSA, including the glycosylation, and alternate diagnostic fluids (non-serum) [16].

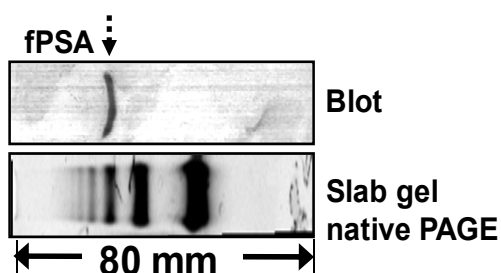


Figure 5. Gold-standard native immunoblotting analysis of the human seminal fluid extract shows multiple proteins resolved in the native PAGE step, with a single band (marked fPSA) binding to the fPSA antibody in the blotting step.

Using our microfluidic immunoblot, the PSA sample was analyzed using full automation of the protocol (i.e., no manual intervention), as shown in Figure 6. The sample was separated by

native PAGE within 36 s with an  $SR$  of 1.59. After PAGE, the on-chip transfer step required 30-60 s. The on-chip approach is significantly faster compared with 2 h in slab-gel systems. In the blotting stage, species exhibiting an affinity for the blotting membrane were retained in the blotting region, while species with low-to-no affinity freely migrated through the blotting region, as desired for the three non-fPSA proteins (Figure 6). The fPSA immunoblot was completed in 65 s, a time reduction of 10,000-fold compared with conventional slab-gel. We also note the importance of conserving the separation resolution of the PAGE in transfer and subsequent blotting (Figure 7). Large dispersion associated with the transfer or blotting essentially “smears” the separation information and results in loss of information regarding the sample. For conventional slab gel immunoblotting, the transfer efficiency indicates the amount of transferred sample during the transfer step from gel to membrane, which is calculated by comparing the amount of protein in the gel before transfer and the amount of protein on the membrane after transfer [17]. Here, the calculated average on-chip transfer efficiency for the PSA sample is 89.5%, which is comparable to conventional slab gel transfer. The conventional native slab mini-gel blot of the same PSA sample showed consistency with on-chip data.

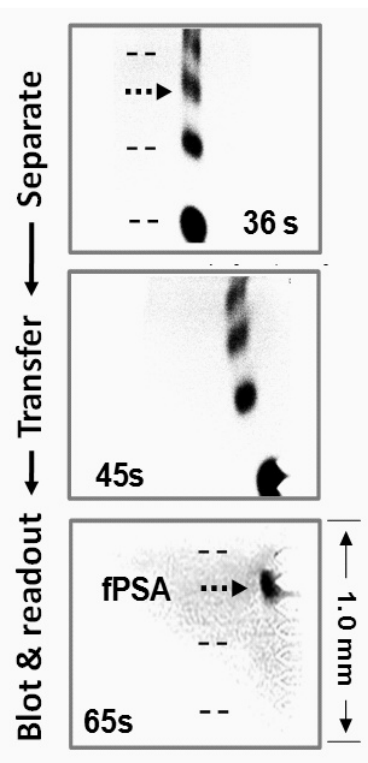


Figure 6. On-chip immunoblotting of native fPSA extracted from human seminal fluid is automated and completes in 36-seconds (compared to 1-2 days for slab-gels). CCD images show the PA gel-patterned chamber during: separation, transfer and blot. As indicated in the figure, the blotting chamber is patterned with multiple functional regions of PA gel for optimized performance.

Previously, we developed two general strategies for antibody immobilization, which afford application flexibility for the native PAGE *in-situ* immunoblot [12]. While not demonstrated in the work presented here, the approaches are applicable to this two



dimensional microdevice. In strategy one, streptavidin PA precursor is copolymerized with biotinylated antibodies during photopatterning step. Strategy two provides the more flexibility, which allows end-user to select the antibodies by decoration of the blotting gel containing streptavidin only through post-introducing. Additionally, it required less biotinylated blotting reagents (e.g., antibodies, aptamers, Fab fragments) in the patterning well, typically 10  $\mu$ L of  $\sim$ 1  $\mu$ M. [12]

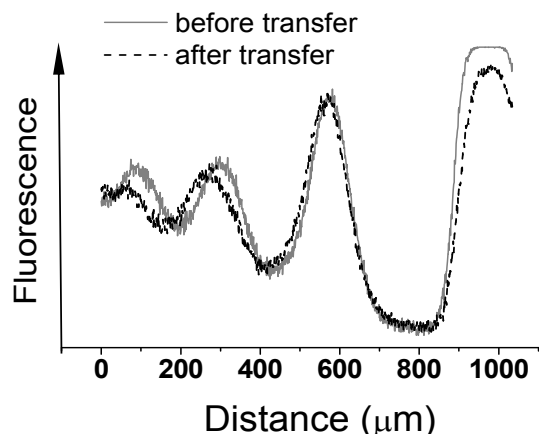


Figure 7. Dispersion associated with transfer or blotting steps can reduce the information content of the complete assay. Further, shifts in the position of protein peaks (also arising from transfer or blotting) reduce the total informational content of the assay. Through using an optimized electrophoretic transfer of species from the separation axis to the blotting gel, the approach presented here results in little transfer-associated dispersion and little peak shifting.

## CONCLUSION

We introduce an effective, rapid immunoblotting assay that utilizes a single microfluidic chamber photopatterned with heterogeneous gel elements to unify PAGE protein separation, electrophoretic transfer, and antibody-based in-gel blotting. Mapping of the separation axis to the blotting region yields both electrophoretic mobility and binding information for each resolved protein. The transfer of resolved protein peaks to a blotting gel region yields no discernable sample loss and high transfer efficiency.

Initial demonstration of native PSA on-chip immunoblotting indicates that the scheme is an effective, high specific approach, suggesting a well-suited format for automated, quantitative microfluidic immunoblotting. Multiple protein peaks were detected in sample extracted from human seminal fluid, both by our new method and in comparative gold-standard PAGE slab gels. While the PAGE slab gel comparisons required up to two days to complete, the automated approach completed in  $\sim$  1 minute.

Currently, optimization of the blotting gel function, enhanced applicability through integration of the immunoblot with protein sizing (sodium dodecyl sulfate PAGE), and analysis of complex protein samples relevant to both basic science and clinical questions are underway, as well as further improvements in detection sensitivity through on-chip protein enrichment. Additional design goals include reproducible quantitation (blot-to-

blot reproducibility) with minimal sample consumption are also underway and can be achieved using the fine control of protein transfer demonstrated here.

We see great potential to extend the basic assay developed and presented here to panels of unique blotted proteins. The approach demonstrated here holds substantial promise as the basis for a suite of automated immunoblotting technologies, and it is applicable to a broad range of multi-stage assays, including DNA/RNA immunoblotting assays and multi-dimensional separation strategies relevant to both basic science and clinical questions.

## ACKNOWLEDGEMENT

We thank Prof. D. Peehl (Stanford) for providing the PSA sample, as well as Dr. Yong Zeng and Mr. Samuel Tia for their assistance. We thank the University of California, Berkeley, the QB3/Rogers Family Foundation Award, and UC Berkeley NSF COINS for financial support.

## REFERENCE:

- [1] J. M. Gershoni, G. E. Palade, *Anal. Biochem.*, **131**, 1 (1983).
- [2] H. Towbin, T. Staehelin, J. Gordon, *Proc. Natl. Acad. Sci. USA*, **76**, 4350 (1979).
- [3] Y. Wu, Q. Li, X. Z. Chen, *Nat. Protoc.*, **2**, 3278 (2007).
- [4] N. A. Guzman, S. S. Park, D. Schaufelberger, L. Hernandez, X. Paez, P. Rada, A. J. Tomlinson, S. Naylor, *J Chromatogr B*, **697**, 37 (1997).
- [5] M. C. Peoples, T. M. Phillips, H. T. Karnes, *J Pharmaceut Biomed*, **48**, 376 (2008).
- [6] R. A. ÓNeill, A. Bhamidipati, X. Bi, A. Deb-Basu, L. Cahill, J. Ferrante, E. Gentalen, M. Glazer, J. Gossett, K. Hacker, C. Kirby, J. Knittle, R. Loder, C. Mastroieni, M. MacLaren, X. Mills, U. Nguyen, N. Parker, A. Rice, D. Roach, D. Suich, D. Voehringer, K. Voss, J. Yang, T. Yang, P.B. V. Horn, *Proc. Natl. Acad. Sci. USA*, **103**, 16153 (2006).
- [7] C. Hou, A. E. Herr, *Electrophoresis*, **29**, 3306, (2008).
- [8] M. G. Mauk, B. L. Ziober, Z. Chen, J. A. Thompson, H. H. Bau, *Ann. N. Y. Acad. Sci.* **1098**, 467, (2007).
- [9] J. West, M. Becker, S. Tombrink, A. Manz, *Anal. Chem.*, **80**, 4403, (2008).
- [10] S. H. Yeung, P. Liu, N. D. Bueno, S. A. Greenspoon, R. A. Mathies, *Anal. Chem.*, **81**, 210, (2009).
- [11] R. J. Meagher, A. V. Hatch, R. F. Renzi, A. K. Singh, *Lab Chip*, **8**, 2046, (2008).
- [12] M. He, A. E. Herr, *Anal. Chem.*, **81**, 8177 (2009).
- [13] A. C. Fan, D. Deb-Basu, M. W. Orban, J. R. Gotlib, Y. Natkunam, R. ÓNeill, R. A. Padua, L. Xu, D. Taketa, A. E. Shirer, S. Beer, A. X. Yee, D. W. Voehringer, D. W. Felsher, *Nat. Med.*, **15**, 566 (2009).
- [14] M. He, A. E. Herr, *J. Am. Chem. Soc.*, **132**, 2512 (2010).
- [15] M. H. Black, C. L. Grass, J. Leinonen, U. H. Stenman, E. P. Diamandis, *Clin. Chem.*, **45**, 347 (1999).
- [16] S. Prakash, P. W. Robbins, *Glycobiology*, **10**, 173 (2000).
- [17] P. Jungblut, C. Eckerskorn, F. Lottspeich, J. Klose, *Electrophoresis*, **11**, 581, (1990).

## CONTACT

\*A. E. Herr, tel: +1-510-666-3396; aeh@berkeley.edu

# RADIAL THERMOELECTRIC GENERATOR MODULES FOR IN-LINE POWER GENERATION FROM HOT GAS STREAMS

Israel Boniche\* and David P. Arnold

Interdisciplinary Microsystems Group, University of Florida, Gainesville, FL, USA

## ABSTRACT

This paper reports the fabrication and characterization of stackable silicon-micromachined thermoelectric generator (TEG) modules for power generation from hot gas streams. Each module employs radially oriented thermoelements on a thermally insulating polyimide layer extending between inner and outer finned silicon structures. Power is generated by flowing hot gas through the center orifice, which creates a radial thermal gradient across the thermopile. Metal thermoelements are used to demonstrate the concept, resulting in 60 mV open-circuit voltage and delivery of 0.45  $\mu$ W of power (0.01 mW/cm<sup>3</sup> power density) from a single TEG module to a 1.5 k $\Omega$  resistive load using a 200 °C hot gas stream. Analytic models indicate that replacing the metal thermoelements with higher-performing semiconductor alloys can increase the output power, e.g.  $\sim$ 0.5 mW (10 mW/cm<sup>3</sup>) using Bi<sub>2</sub>Te<sub>3</sub> at 200 °C, or  $\sim$ 1.3 mW (27 mW/cm<sup>3</sup>) using PbTe alloys at 400 °C.

## MOTIVATION

The need for long-lasting wireless electronic devices with increasing functionality has stimulated research of alternative power sources to traditional batteries. Additionally, there is great interest for energy harvesters that can locally generate power for wireless sensor networks from ambient environmental energy. Some popular scavenging methods include solar cells, vibrational devices, and thermoelectric generators (TEGs) [1, 2]. If a persistent heat source is available, TEGs are attractive solid-state devices that can directly convert heat energy into electrical energy. The lack of moving parts and the ability to create electrical power from any heat source facilitates a reliable and versatile power generation mechanism.

The goal of the proposed TEG device is to convert waste thermal energy into electrical energy from hot gas exhaust streams. For instance, the device could be coupled to the hot exhaust of a microcombustor or micro heat engine to directly generate useful load power, or perhaps for supplementary power to run auxiliary components such as switches, valves, pumps, or sensors [2, 3]. Alternatively, a TEG module could be used for self-powered sensors/systems wherever hot gas or liquid lines are present, e.g. automobiles, aircraft, or industrial environments.

At PowerMEMS 2007, we demonstrated the feasibility of micromachining silicon substrates with polymer membranes as thermally insulating platforms for radially oriented in-plane thin-film TEGs [4]. This work expands on those efforts by evaluating the overall device performance with the inclusion of functional thermoelements (the prior proof-of-concept demonstrators did not include thermoelements). The focus of this paper is the fabrication and characterization of the individual TEG modules using thin-film metal thermoelements. Stacked modules are not reported here. These results validate the concept and provide baseline experimental data for thermoelectric models. This in turn paves the way for second-generation devices using semiconductor thermoelements with substantially improved power output.

## DEVICE DESCRIPTION

The overall structure consists of silicon-micromachined thermoelectric modules that can be stacked to form a cylindrical

heat exchanger with finned surfaces on both the hot and cold sides. As shown in Fig. 1, each module consists of two concentric silicon rings connected by a thermally insulating 5- $\mu$ m-thick polyimide membrane that supports radially patterned thin films thermoelements. Hot gas flows through the finned central channel heating the inner surface, while outer annular fins keep the outer surfaces cool via natural or forced convection. A large, uniform temperature gradient ( $\Delta T$ ) is thus established across the radially oriented thermoelements (1 mm long, 0.5  $\mu$ m in thickness) within each module.

This design provides good thermal isolation and easy in-line insertion into hot gas streams, which overcomes a key inadequacy of the standard parallel-plate thermoelectric module for the intended application. Moreover, the ability to stack modules enables scalability, so that multiple modules can be connected for more power.

The work here presents modules using Ni and Au thermoelements. It is well known that semiconductors such as Bi<sub>2</sub>Te<sub>3</sub> and PbTe alloys yield superior thermoelectric performance [2], but these films are more difficult to fabricate as compared to simple sputtering of metal thin-films. Also, the Ni and Au films exhibit desirable properties such as good adhesion to the polyimide layer and good solderability for electrical connections.

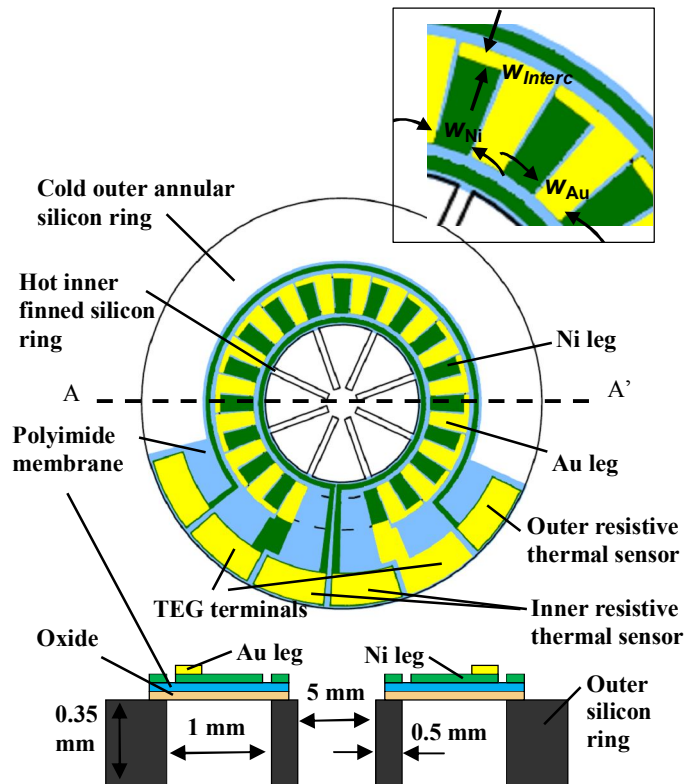


Figure 1: Top view and cross-section of thermoelectric generator module with hot center ring and cold outer silicon ring connected by a polyimide membrane.

## FABRICATION

Three different module designs with different number of Ni/Au thermocouple pairs ( $n$ ) were fabricated. The geometries for the selected designs are shown in Table 1. The TEG modules also included circular Ni resistive structures for temperature sensing of the inner and outer silicon rings, as shown in Fig. 1. On-wafer electrical test structures were also fabricated for characterization of the thin-film resistivities and contact resistance.

Table 1. Selected TEG designs using thin-film Ni and Au thermoelements.

Leg Pairs, $n$	18	65	90
Ni leg width, $w_{Ni}$ ( $\mu\text{m}$ )	377	40	10
Au leg width, $w_{Au}$ ( $\mu\text{m}$ )	377	50	10
Spacing between legs ( $\mu\text{m}$ )	90	90	90
Inner and outer interconnect width, $w_{Interc}$ ( $\mu\text{m}$ )	100	100	100
Ni thickness, $t_{Ni}$ ( $\mu\text{m}$ )	0.5	0.5	0.5
Au thickness, $t_{Au}$ ( $\mu\text{m}$ )	0.5	0.5	0.5

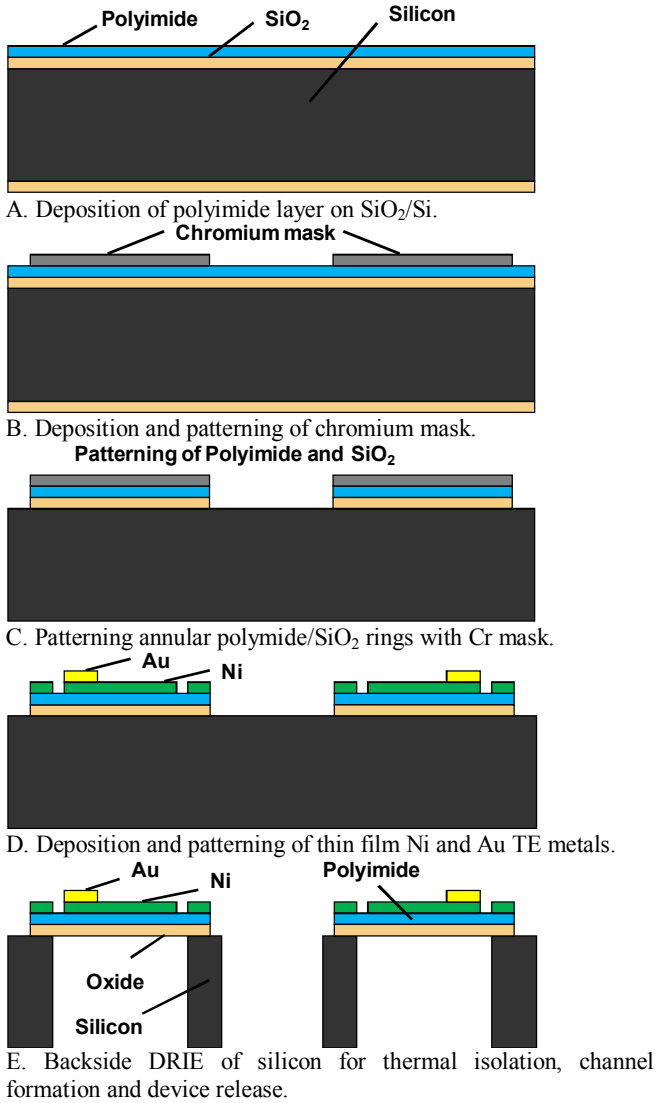


Figure 2: Fabrication process of a radial TE generator module.

The fabrication process starts with a  $\sim 345\text{-}\mu\text{m}$ -thick, double-side polished, and thermally oxidized silicon wafer. First, a non-photodefinable polyimide film (PI 2611 from Microsystems Inc.) is spin-deposited on the top surface (Fig. 2a). Then, by using a thin-film chromium mask (Fig. 2b), annular polyimide ( $\sim 5\ \mu\text{m}$ ) and oxide rings are patterned with an  $\text{O}_2$  plasma etch and buffered-oxide etch, respectively (Fig. 2c). Next, dc-sputter deposition and lift-off is used to form the Ni ( $\sim 0.5\ \mu\text{m}$ ) thermoelement legs and the Ni resistive sensors. This is followed by sputtering and lift-off of Au ( $\sim 0.5\ \mu\text{m}$ ) (Fig. 2d).

After completing the topside processing, the wafer is mounted face down with photoresist to a handle wafer for backside processing. A deep reactive ion etch (DRIE) is performed to form the fin arrays and hot gas channel (Fig. 2e). Simultaneously, silicon is selectively etched away from underneath the thermopile, stopping on the oxide. After completion, the individual chip modules, shown in Fig. 3, are carefully removed from the handle wafer by immersion in acetone and rinsing with methanol and de-ionized water.



Figure 3: TEG modules fabricated on silicon substrates using thin-film Ni-Au thermoelements. Resistive thin film Ni also included for temperature sensing of the inner and outer silicon rings. Inner and outer diameters are 5 mm and 13 mm, respectively.

## RESULTS

Using the on-wafer test structures (van der Pauw and transfer length method), the thin-film metal electrical resistivities ( $\rho$ ) were characterized [5]. The Au thin film exhibited a resistivity ( $2.6 \pm 0.7\ \mu\Omega\text{-cm}$ ) similar to the bulk value ( $2.3\ \mu\Omega\text{-cm}$ ), while the Ni showed a high resistivity of up to  $108.2 \pm 7.8\ \mu\Omega\text{-cm}$ ,  $>10\text{X}$  than the bulk value [6]. While the variance from bulk was not entirely unexpected, the results for the sputtered Ni films here also differed from other reported Ni thin films [7]. The large resistivity differences may be attributed to differences in film thickness, deposition conditions, substrate, and film defects. From the electrical resistivity measurements, the thermal conductivities ( $\kappa$ ) of the thin metal films were estimated by using the Wiedemann-Franz law [2]. The Au thin film was estimated with a thermal conductivity of  $285.2 \pm 73.4\ \text{W/m}\cdot\text{K}$ , while the Ni was estimated with a relatively low thermal conductivity of  $6.8 \pm 0.5\ \text{W/m}\cdot\text{K}$ . From the transfer length method test structures, the Au-Ni specific contact resistivity ( $\rho_c$ ) was estimated at  $\sim 15 \pm 15\ \mu\Omega\text{-cm}^2$ .

For the module characterization, thin copper wires were soldered to the gold bond pads for external electrical connections. First, the thermal resistive sensors integrated on the TEG were

characterized by measuring the temperature-resistance behavior to determine the linear temperature coefficient of resistance (TCR),  $\alpha_{\text{TCR}}$ . Each TEG module was placed inside an oven (Lindberg Blue M) with the resistive sensor wire leads leading out to Keithley 2400 source meters for 2-pt resistance measurement. The temperature sensors were calibrated from ambient temperature up to  $\sim 200$  °C. The extracted TCR values for various Ni rings were fairly consistent with each other, with the mean of the 8 different rings estimated at  $2.67 \times 10^{-3}$  °C<sup>-1</sup>, and the lower and upper (95%) confidence intervals ranging from  $2.55 \times 10^{-3}$  °C<sup>-1</sup> to  $2.79 \times 10^{-3}$  °C<sup>-1</sup>.

Next, the module thermopile resistances were measured and compared against calculated values. The estimated resistances were determined from thin-film properties, and for all cases, the total contact resistance (despite the large uncertainty) was negligible ( $< 0.1$  % of the total resistance) and thus ignored. A breakdown of the resistance is shown in Table 2 for the three different modules. For the  $n=65$  design, the legs and interconnects contributed 95% and 5%, respectively, of the total resistance. Interconnects contributed only 1% for the  $n=90$  design (having the largest resistance at 11.3 k $\Omega$ ), but 39% for the  $n=18$  design.

Table 2. Two-point dc current measurements and model estimates of electrical resistance at 25°C for TEGs using Au-Ni leg pairs. In parenthesis are the percentages of the total TEG resistance attributed to the legs and interconnects [8].

Leg Pairs ( $n$ )	18	65	90
Measured total resistance, $R_{\text{Total}}$ (k $\Omega$ )	$0.123 \pm 0.003$	$1.63 \pm 0.003$	$11.3 \pm 0.003$
Estimated total resistance, $R_{\text{Total}}$ (k $\Omega$ )	$0.108 \pm 0.036$	$2.24 \pm 0.74$	$12.4 \pm 4.1$
Estimated legs resistance, $R_{\text{Legs}}$ (k $\Omega$ )	$0.065$ (61%)	$2.13$ (95%)	$12.3$ (99%)
Estimated interconnect resistance, $R_{\text{Interc}}$ (k $\Omega$ )	$0.042$ (39%)	$0.101$ (5%)	$0.137$ (1%)

For thermoelectric characterization, individual TEG modules were evaluated using a heat gun as the source of a hot gas stream as shown in Fig. 4. Output voltage measurements were made using a high-precision digital voltage meter (SIM 970 module from SRS). A segment of a high-temperature-resistant tubing (0.25-inch diameter) and a custom-made aluminum fixture were coupled to the heat gun outlet to channel the hot gas to the 5 mm inner diameter of the TEG module. The module was positioned within 2 mm of the fixture, and aligned to the hot gas stream. The upstream and downstream hot gas temperatures were simultaneously measured using two bare-wire type K thermocouples. The inner and outer Ni resistances were measured with two source meters and temperatures extracted using the TCR values.

The open-circuit voltage ( $V_{oc}$ ) as a function of the downstream gas temperature ( $T_{\text{GAS}}$ ) is shown in Fig. 5. For a given gas temperature, the design with largest number of legs ( $n=90$ ) exhibited the largest generated voltage (e.g. 45 mV at  $\sim 120$  °C). However, at a test temperature of  $\sim 200$  °C, the design with  $n=65$  leg pairs generated up to 60 mV. Fig. 6 shows  $V_{oc}$  as a function of  $\Delta T = T_{\text{Hot}} - T_{\text{Cold}}$ , which should follow the relationship given by [2]

$$V_{OC} = n \cdot (\alpha_{\text{Au}} - \alpha_{\text{Ni}}) \cdot \Delta T = n \cdot (\alpha_{\text{Au-Ni}}) \cdot \Delta T \quad (1)$$

For each module, the Seebeck coefficient,  $\alpha_{\text{Au-Ni}}$  is thus given by the slope of the least-square fit line divided by  $n$ . The extracted Seebeck values were close to one another with 95% certainty bounds of  $14.3 \pm 0.9$   $\mu\text{V}/\text{K}$ . The values here were higher than the Seebeck coefficient ( $\sim 10$   $\mu\text{V}/\text{K}$ ) reported for evaporated thin-film Au/Ni (0.2/0.1  $\mu\text{m}$  in thickness) thermoelements on SiO<sub>2</sub>/Si [9].

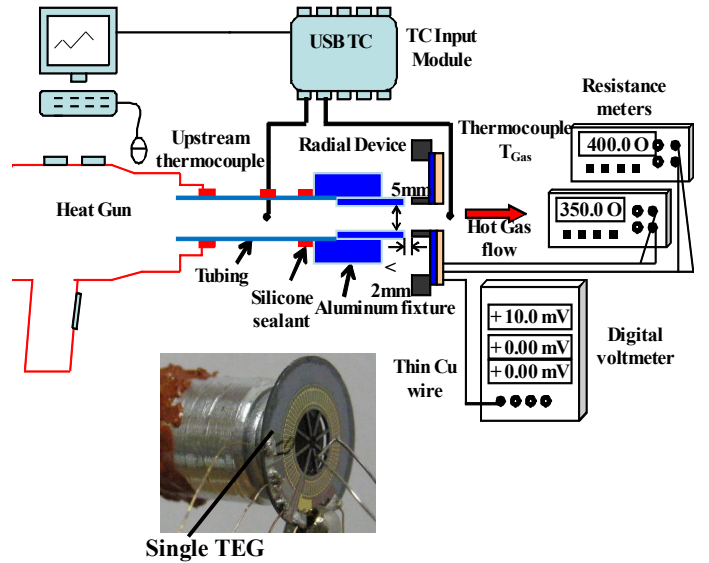


Figure 4: Setup for thermal and electrical characterization of single radial TEGs using a heat gun as source for a hot gas stream.

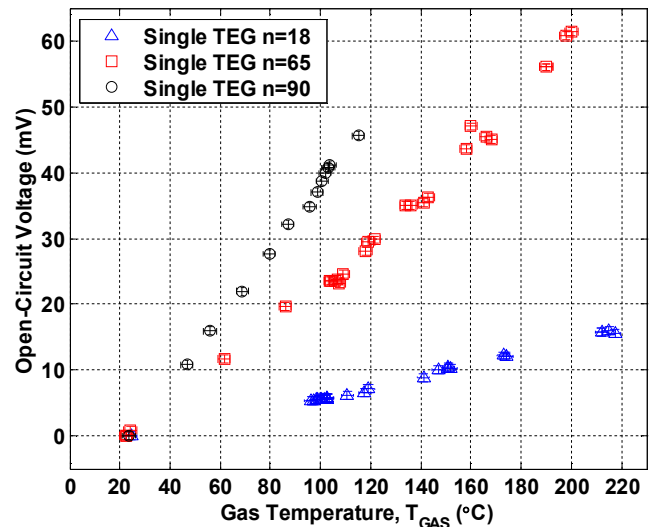


Figure 5: Open-circuit voltage as a function of gas temperature for various TEG modules having small uncertainties in the voltage ( $\pm 0.6$  mV) and  $T_{\text{GAS}}$  ( $\pm 2.5$  °C).

In addition to the open-circuit voltages, the TEG modules were tested with resistive loads, and the power output was measured for the different TEG designs. Initially, “matched” resistive loads were used where the load resistance roughly equals the module resistance, for maximum power transfer. Specifically, load resistances of 0.120 k $\Omega$ , 1.55 k $\Omega$ , and 11.5 k $\Omega$  were used to approximate the resistance for the  $n=18$ , 65, and 90 designs, respectively. The power output was calculated by measuring the voltage across the resistive load according to the equation

$$P_L = \frac{V_L^2}{R_L} \quad (2)$$

where  $V_L$  is the load voltage, and  $R_L$  is the load resistance.

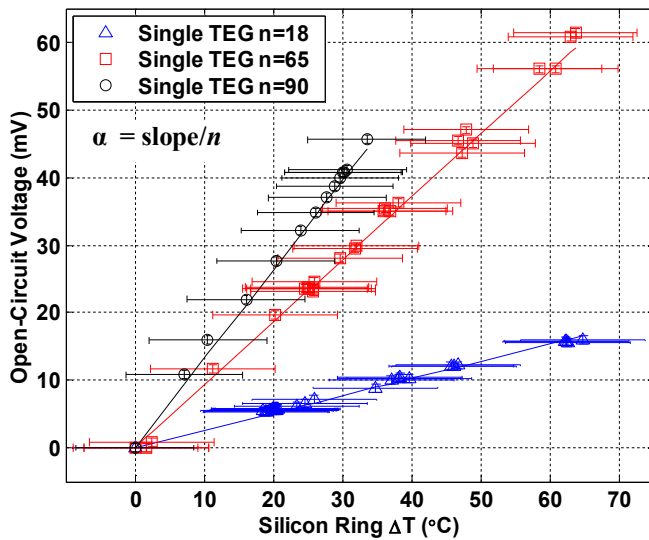


Figure 6: Open-circuit voltage as a function of silicon ring temperature difference for various TEG modules.

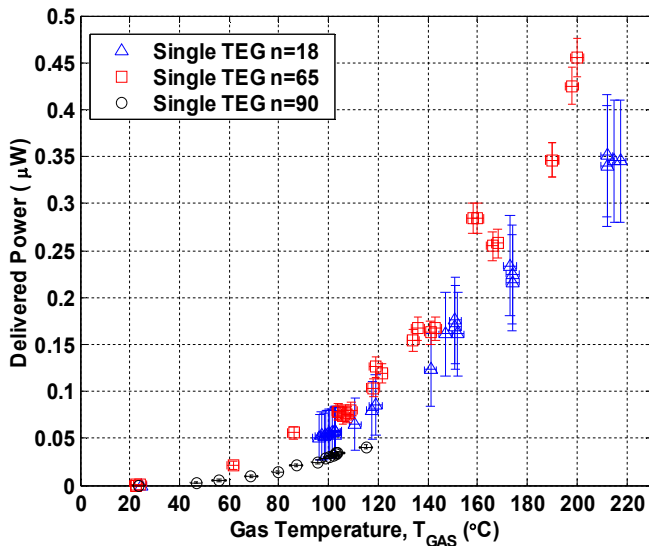


Figure 7: Power output for single TEG modules as a function of gas temperature by using resistive loads ‘matching’ the TEG device resistance.

As shown in Fig. 7, the output power increased quadratically with gas temperature, as expected from Eq. 2 (since the voltage increased linearly with gas temperature). The intermediate design ( $n=65$ ) showed higher output power compared to the other two designs ( $n=18$  and  $n=90$ ). Overall, at a gas temperature of 200 °C, a maximum power output of  $\sim 0.45 \mu\text{W}$  was measured for the  $n=65$  design by using a 1.55 k $\Omega$  load, which approximated the TEG module resistance of  $\sim 1.63 \text{ k}\Omega$ .

Fig. 8 shows the power output for the  $n=65$  design for various loads and temperatures. An unexpected cooling of the outer silicon ring (at a gas temp. of 171 °C) resulted in a larger than expected  $\Delta T$  resulting in an increase in load voltage and power. Ignoring the anomalous behavior at 171 °C, a maximum power of 0.36  $\mu\text{W}$  was measured for 191 °C gas flow using a 2 k $\Omega$  load which was slightly higher than the room-temperature TEG module resistance ( $\sim 1.63 \text{ k}\Omega$ ).

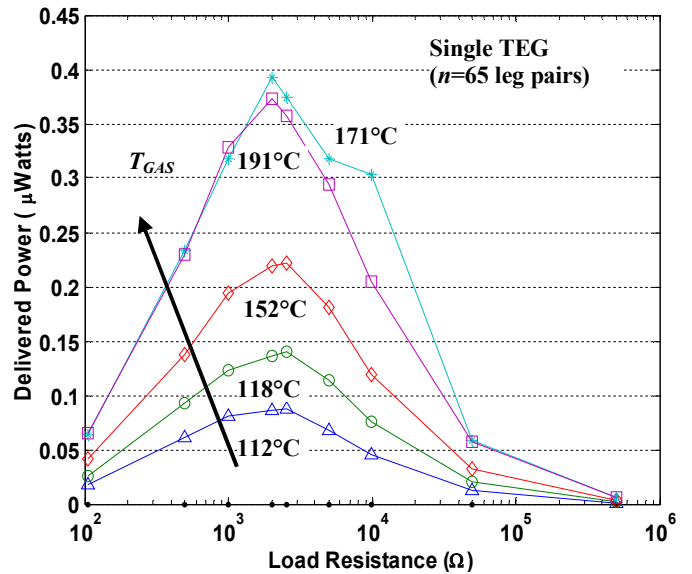


Figure 8: Power output for various resistive loads over different gas temperatures for a single TEG module ( $n=65$ ).

## CONCLUSIONS

Coin-sized, radial thermoelectric modules using thin-film Au-Ni thermoelements were micromachined on silicon substrates and characterized using hot gas streams. For an inlet gas temperature of 200 °C, a single TEG module ( $n=65$  leg pairs) sustained a  $\Delta T$  of  $\sim 65$  °C. Moreover, the thermocouple pair Seebeck coefficient ( $\alpha_{Au-Ni}$ ) was determined to be  $\sim 14 \mu\text{V/K}$ , in line with expectations for the thin-film metals used. Additionally, the TEG module with  $n=65$  leg pairs ( $\sim 1.6 \text{ k}\Omega$ ), generated open-circuit voltages,  $V_{OC}$ , of up to 60 mV per module, corresponding to a delivered power of 0.45  $\mu\text{W}$ , for a gas temperature of 200 °C. Analytic models [8] indicate that replacing the metal thermoelements with higher-performing semiconductor alloys can increase the output power, e.g.  $\sim 0.5 \text{ mW}$  ( $10 \text{ mW/cm}^3$ ) using  $\text{Bi}_2\text{Te}_3$  at 200 °C, or  $\sim 1.3 \text{ mW}$  ( $27 \text{ mW/cm}^3$ ) using PbTe alloys at 400 °C. Future work includes investigating semiconductor TE films on the radial TEG module as well as developing interconnect methods for stacking of multiple modules for higher power output.

## REFERENCES

- [1] J.P. Thomas, et al. *J. Power Sources*, Vol. 159, (2006), p. 1494-1509.
- [2] D.M. Rowe (editor), *Thermoelectrics Handbook: Macro to Nano*, Boca Raton, FL (2006).
- [3] A.H. Epstein, *J. Eng. for Gas Turbines and Power, Trans. of the ASME*, Vol. 126, (2004), p. 205-226.
- [4] S. Masilamani, et al. *PowerMEMS 2007*, Germany, (2007), p. 249-252.
- [5] D.K. Schroder, *Semi. Mat. and Device Charact.*, 2<sup>nd</sup> Ed., N.Y.: Wiley, (1998).
- [6] D.R. Lide (editor), *CRC Handbook Chem. and Phys.*, Boca Raton, FL, London: CRC (2008).
- [7] M.A. Angadi, et al., *Thin Solid Films*, Vol. 79, (1981), p.149-153.
- [8] I. Boniche, *Elect. Comp. Eng.*, Doctorate, Gainesville, FL, Univ. of FL, (2010).
- [9] D. Chu, et al., *Transd. 2003, 12<sup>th</sup> Int. Conf. Solid-State, Sens., Act., and Microsyst.*, Boston, Mass. (2003), p. 1112-1115.

## CONTACT

\*Israel Boniche, tel: +1-505-794-8593; [iboniche@gmail.com](mailto:iboniche@gmail.com)

# ELECTROLYSIS-BASED INCHWORM ACTUATORS

L.Giacchino\*, Y.C. Tai

California Institute of Technology, Pasadena, California, USA

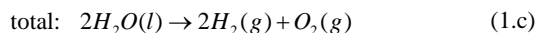
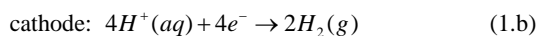
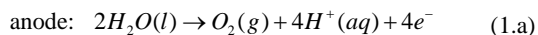
## ABSTRACT

We have designed, fabricated and tested an inchworm actuator using water electrolysis as the mechanical power source. To facilitate the inchworm mechanism, each actuator is made of two sealed silicone balloons. When electrolysis is run inside a balloon, the balloon expands due to gas generation. When electrolysis is stopped, the balloon shrinks due to gas recombination and permeation through the silicone. Bidirectional movement of a rotor, e.g., a metal probe, is obtained by applying specific expansion/shrinkage sequences to the balloons. The device works at low voltage and current, with peak power consumption around 100  $\mu$ W. Displacement of silicon and metal probes from 20  $\mu$ m to 75  $\mu$ m per cycle was demonstrated. Also reported here is a new hydrogel-enabled balloon fabrication process.

## INTRODUCTION

### Electrolysis Actuation

Electrolysis of water has been successfully employed in a number of MEMS devices, even though it is not as common as more traditional actuation principles (such as electrostatic or piezoelectric). The actuation mechanism is based on the volume expansion of hydrogen and oxygen gases generated by the electrolysis of water on the surface of two electrodes. The well known electrochemical reaction is (if protons are assumed to transport the charge)



The conversion of water from liquid to gas can produce a significant displacement if volume expansion is allowed at low pressure, or it can produce a high pressure (hence a large force) in case of constrained volume. Electrolysis can also operate at a relatively low voltage and power. Electrolysis actuation has been previously employed in microdevices such as micropumps [3] and microfluidic valves [4]. Our group has already demonstrated the basic electrolysis balloon based on water electrolysis [1,2]. This work is to demonstrate an inchworm actuator to move a metal neural probe using two electrolysis balloons.

### Movable Neural Probes

Over decades of cortical neural prosthesis, it is found that a "movable" neural probe [5] that can track or follow a neuron is highly desirable for long-term, reliable prosthesis. This is challenging, however, because the ideal movable probes should have the merits of low voltage, small power, bidirectional and latchable movement, large force (to penetrate the brain tissue), and large total traveling distance (i.e., ~mm). On the other hand, speed is not an important requirement because neuron movement is sporadic and slow. Therefore, electrolysis actuation embedded in an inchworm mechanism is an interesting candidate for this application.

## DESIGN

Each inchworm stator is made of two balloon actuators. Detailed analysis and experimental results for balloon actuators were already reported in [1]. Each balloon is made of silicone with

two platinum electrodes and electrolyte inside. In our previous devices, however, balloons were fabricated with parylene. In the current design, parylene is replaced by silicone. There are two major improvements from using silicone over parylene. Silicone is more flexible (because of smaller elastic modulus) and much more permeable to gases and water. The higher permeability allows faster relaxation, which reduces the inchworm cycle time. Even though permeation causes a net loss of water from the balloon interior, osmosis is used to replenish water back into the balloon when immersed in aqueous environment. In the body, the device is in a saline solution; therefore, osmosis is available as a mechanism to replenish the balloons.

In our inchworm design, one balloon is used to clamp the probe horizontally; the other balloon is to provide vertical displacement. The metal probe rotor is placed between two discs, which clamp the probe from both sides when the clamping balloon expands. The inchworm movement is obtained by expanding and relaxing the balloons in a specific order, as illustrated in Fig. 1. The vertical displacement (i.e., up or down direction) can be reversed by modifying this order.

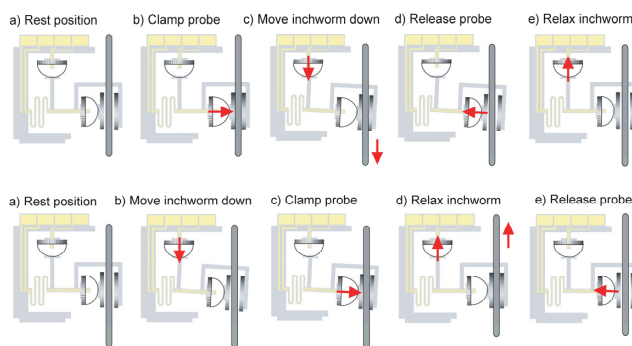


Figure 1: Inchworm principle. The first row illustrates forward displacement (downward in the figure), while the second row illustrates backward displacement (upward in the figure). For forward displacement, the probe is first clamped, and then the inchworm is moved down. For backward displacement, the inchworm is first moved down, and then the probe is clamped. The probe is moved backwards during the relaxation of the inchworm.

The inchworm mechanism can provide variable displacement per cycle, depending on the expansion of the displacing balloon. The system does not impose a minimum step, which is determined by the accuracy of actuation of the displacing balloon. Large traveling distance can be obtained in multiple cycles, and the constraints are the probe length and the amount of water in the balloons.

The inchworm design has three advantages. First, the inchworm is able to provide large displacement in multiple cycles. Second, the inchworm is inherently latchable. Third, the inchworm decouples the fabrication of the actuator from that of the probe, and it is, therefore, able to be adapted to various probes.

The position of the spring on the frame was chosen to create a lever effect. As shown in Fig. 1, the displacing balloon is connected to a point close to the spring. Due to the distance between this point and the probe, the displacement applied by the balloon is amplified at the probe. This is confirmed by a finite-element simulation. The lever design, however, causes the

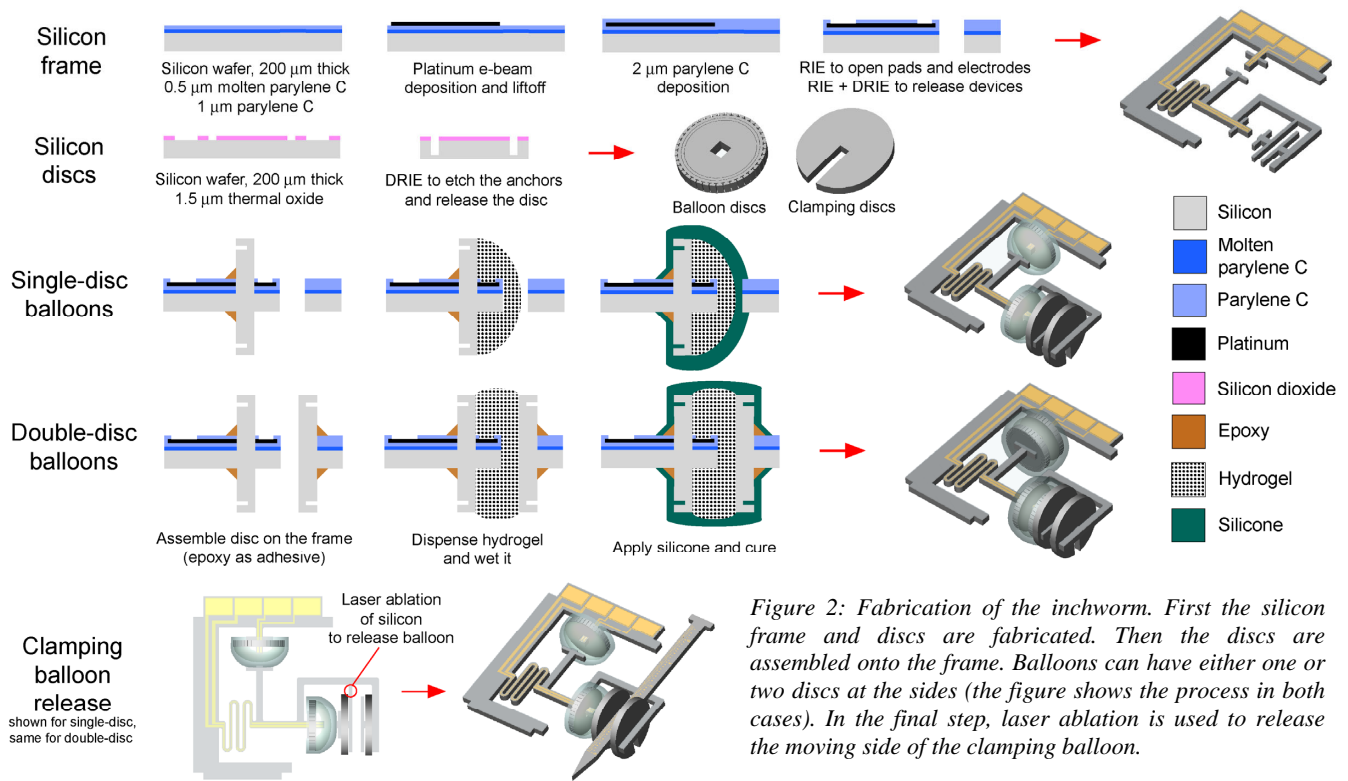


Figure 2: Fabrication of the inchworm. First the silicon frame and discs are fabricated. Then the discs are assembled onto the frame. Balloons can have either one or two discs in the sides (the figure shows the process in both cases). In the final step, laser ablation is used to release the moving side of the clamping balloon.

inchworm arm and the probe to move along a curved path during actuation. This is particularly noticeable for large displacement in a single cycle. Placing the spring in-line with the displacing balloon would allow the probe to move along a straight line, but it would not provide any displacement amplification.

## FABRICATION

### Silicon Frame and Ruler Probe

The main component of the inchworm is a silicon frame. The frame provides a spring mechanism, and it supports the platinum electrodes needed for electrolysis. The fabrication steps are illustrated in the first row of Fig. 2. A picture of a fabricated frame is shown in Fig. 3a. The fabrication starts with a 200  $\mu\text{m}$  thick silicon wafer. The wafer is coated with 0.5  $\mu\text{m}$  of Parylene C (Specialty Coating Systems), which is then melted at 350  $^{\circ}\text{C}$  in  $\text{N}_2$  atmosphere. This molten layer is used as an adhesion layer for a subsequent 2  $\mu\text{m}$  Parylene C deposition. Platinum is then deposited by e-beam evaporation and patterned with a lift-off process. Another layer of Parylene C is deposited, thus completing the insulation of the metal traces. Pads and electrodes are opened in the top parylene layer by reactive ion etching (RIE) using  $\text{O}_2$  plasma. To release the devices, parylene is completely removed by  $\text{O}_2$  RIE around the outline of the frames. The exposed silicon is then etched by deep reactive ion etching (DRIE) to define and release the frames.

Silicon probes with a ruler pattern on the top surface are fabricated on the same wafer as the silicon frames (see Fig. 3d). The ruler pattern is obtained on the platinum layer. The pattern is convenient to measure the displacement of the probe. In some experiments, a commercial metal neural probe is mounted on top of the ruler probe, which then acts as a shuttle for the metal probe (see Fig. 7). Mounting a commercial probe on the silicon probe makes it possible to use different kinds of neural probes (with different width) without redesigning the inchworm clamp.

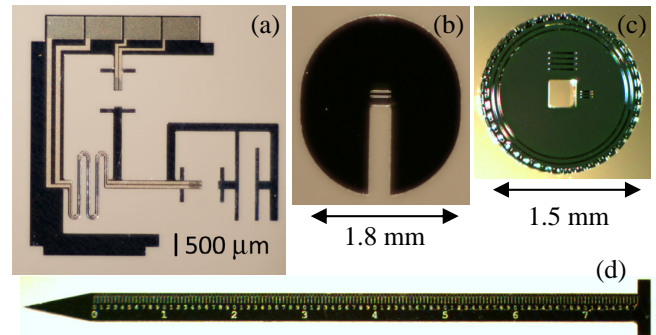


Figure 3: Fabricated components. a) Silicon frame. b) Clamping disc. c) Balloon disc. Discs of different sizes are fabricated. The marks on the discs indicate the diameter and the size of the central opening. d) Ruler probe. The spacing between the large numbers is 1 mm, for a total length of 9 mm.

### Silicon Discs

Special silicon discs are used to better define the balloon shape (balloon discs) and to create the probe-clamping mechanism (clamping discs). The two types of disc are fabricated with the same process. The balloon discs provide anchor trenches for silicone to improve the balloon sealing. There are two circular anchor trenches on the front side of the disc and trenches all around the disc sidewall.

The fabrication process of the discs is illustrated in the second row of Fig. 2. A 1.5  $\mu\text{m}$  thick layer of silicon dioxide is grown on thin wafers (200  $\mu\text{m}$  thick) by wet oxidation at 1050  $^{\circ}\text{C}$ . The oxide is then patterned and used as a mask for DRIE. Two kinds of trenches are needed: anchor trenches (5  $\mu\text{m}$  wide) and release trenches (100  $\mu\text{m}$  wide). The DRIE etching rate is lower in narrower trenches (DRIE lag), making it possible to obtain both types of trench with a single-mask process. When the release trenches are etched all the way through the wafer (thus releasing

the discs from the wafer), the anchor trenches are only about 80-90% through. Pictures of the fabricated discs are shown in Fig. 3b and Fig. 3c.

### Balloons

For support during assembly and balloon fabrication, the silicon frame is glued to the edge of a glass slide. The silicon discs (balloon and clamping discs) are then assembled onto the frame using an xyz micrometer stage equipped with tweezers. The discs are secured to the frame using biocompatible epoxy (Epoxy Technology, EPO-TEK 301-2), which also seals the frame-disc interface. Balloons can be fabricated with either one or two discs, as shown in the third and fourth row of Fig. 2. A silicon frame with assembled balloon discs is shown in Fig. 4a.

Hydrogel (i.e., sodium polyacrylate) is then dispensed on the balloon discs. Alternatively, hydrogel can be dispensed on the discs before assembly. Water is dispensed on the hydrogel using a commercial fluid dispenser (EFD 2000XL) with a 33-gauge tip. When the hydrogel is made wet, it expands. Biocompatible silicone (Dow Corning MDX4-4210) is painted around the hydrogel and the discs using a thin wire. It is important to keep the hydrogel wet and expanded while silicone is cured because the hydrogel determines the balloon internal volume. For this purpose, the curing is done at 60 °C in a humid environment, so there is no net permeation of water from the hydrogel to the outside through the silicone. Raising the temperature over 60 °C causes some condensation on the silicone during the cure process, causing its surface to be hazy. When the silicone is cured, the device is immersed in water, and more water is driven into the balloon by osmosis.

This process is very convenient because no hole in the balloons is required to release any sacrificial material or to fill the balloon with electrolyte. The hydrogel provides the mechanical support for the silicone, and it stays inside the balloon in the finished device. Filling of the balloon is obtained by osmosis through the silicone membrane. This is very advantageous compared to our previous process [1]. The balloons were previously fabricated with sacrificial photoresist, which had to be released in acetone through a hole in the silicone membrane. The device was then filled through the same hole by immersing the device into an electrolyte solution in vacuum. The hole then had to be sealed by epoxy or silicone. The hole, even after sealing, represented a weak point and the most common cause of seal failure. The hydrogel process avoids the hole completely, thus improving the reliability of the device.

The last step in the inchworm fabrication is the release of the clamping balloon, as shown in the last row of Fig. 2. In order to provide the support necessary for fabrication, the front side of the clamping balloon is part of the silicon frame. The connection to the frame is removed by laser ablation of silicon. In this way, the clamping balloon is free to expand and clamp the probe.

### Cable Connection

When the inchworm is operated in water (or saline in the body), the electrical connection to the pads must be isolated from the surrounding environment. A commercial flat cable with 0.5 mm pitch (Parlex Corp.) is electrically connected to the pads by conductive epoxy. This is done before the balloons are fabricated. The connections are then encapsulated into biocompatible epoxy and biocompatible silicone for insulation (see Fig. 5).

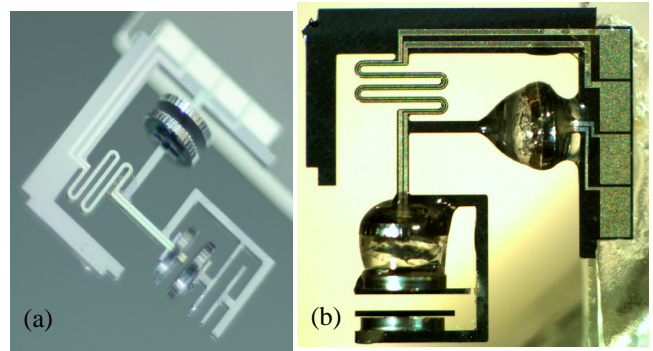


Figure 4: a) Silicon frame with assembled balloon discs (double-disc balloons case). b) Finished inchworm after release of the clamping balloon by laser ablation.

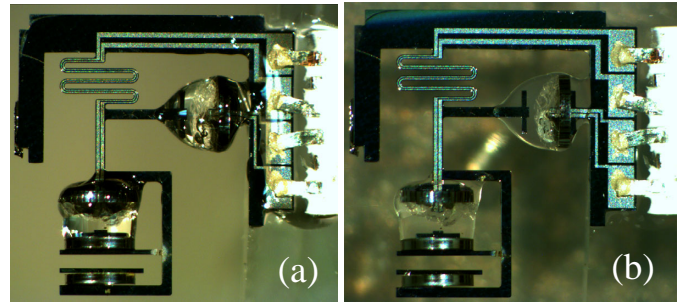


Figure 5: Finished inchworm with cable: a) in air, b) in water.

## RESULTS

### Standalone Balloons

Balloon actuators are the building blocks of the inchworm. For this reason standalone silicone balloons were first tested. Fig. 6 shows experimental results for the actuation and relaxation of a silicone balloon. The relaxation time is largely improved compared to parylene balloons due to the faster permeation of gases through silicone (from 20-30 minutes for a 10  $\mu\text{m}$  thick parylene balloon to about one minute for a 100  $\mu\text{m}$  thick silicone balloon). The displacement is measured by a linear variable differential transformer (LVDT). The LVDT is spring-loaded, with a spring constant of 2.5  $\text{mN}/\mu\text{m}$ . The actuator has to overcome the spring force, which limits the achievable displacement. However, this shows that the balloon is able to generate force in the tens of mN. Without the LVDT, a single-cycle displacement in excess of 100  $\mu\text{m}$  was demonstrated.

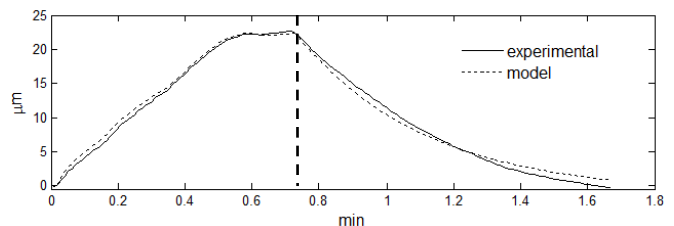


Figure 6: Expansion and relaxation of a standalone balloon. The displacement was measured with an LVDT (spring constant 2.5  $\text{mN}/\mu\text{m}$ ). Electrolysis was stopped at the dashed line. Silicone is about 100  $\mu\text{m}$  thick. The model fits the experimental data closely.

### Balloon Model

In [1] we illustrated a model for the balloon actuation. The model is able to keep track of the amount of  $\text{H}_2\text{O}$ ,  $\text{O}_2$ ,  $\text{H}_2$  and  $\text{N}_2$  (from air) inside the balloon as a function of time. It is based on



mass balance equations for each component ( $n_x$  represents the moles of species  $x$  inside the balloon):

$$dn_{O_2}(t)/dt = g(t) - r(t) - c_{O_2}w\Delta p_{O_2}(t) \quad (2.a)$$

$$dn_{H_2}(t)/dt = 2g(t) - 2r(t) - c_{H_2}w\Delta p_{H_2}(t) \quad (2.b)$$

$$dn_{H_2O}(t)/dt = -2g(t) + 2r(t) - c_{H_2O}w\Delta\mu_{H_2O}(t) \quad (2.c)$$

$$dn_{N_2}(t)/dt = -c_{N_2}w\Delta p_{N_2}(t) \quad (2.d)$$

The model includes the effects of gas generation by electrolysis,  $g(t)$ , gas recombination,  $r(t)$ , and permeation through the balloon walls. The permeation flux for gas  $x$  is assumed proportional to the gas partial pressure gradient  $\Delta p_x$  across the membrane, where  $c_x$  is the permeation coefficient and  $w$  is the ratio of surface area and membrane thickness. Several improvements are introduced to the model in [1]. First, the treatment of water permeation is extended to also model osmosis. The amount and direction of water permeation is determined by the chemical potential gradient across the membrane  $\Delta\mu$ . Second, the balloon volume is not assumed to be constant, and balloon expansion as a function of internal pressure is included. This dependence is approximated by a linear relationship. Third, solubility of gases into water is included. The balloon internal volume is divided between a liquid and a gas phase. Due to solubility,  $O_2$ ,  $H_2$  and  $N_2$  are present both in the gas and in the liquid phase. The amount of each component in solution is assumed proportional to its partial pressure. Fig. 6 shows that the model fits the experimental data very closely.

### Inchworm Actuators

The fabricated ruler probe is used to calibrate the inchworm. The displacement is read by observing the ruler pattern under a stereoscope. The experiments are video-recorded using an eyepiece camera. In some experiments, a commercial metal neural probe is also mounted onto the ruler probe (Fig. 7a). The inchworm is able to displace the probe in both directions, with a displacement per cycle between 20  $\mu\text{m}$  and 75  $\mu\text{m}$  (Fig. 7b). The applied voltage is typically 3.5 V, with a resulting current of 20-30  $\mu\text{A}$ . Each cycle is completed in about 10 minutes. Experiments were run both in air and in water. The maximum number of cycles before a break for osmosis-refilling is needed is around 10. The refilling time ranges from a few hours to several days, depending on the amount of water consumed and the number of additional cycles desired.

When actuated in water, gas bubbles form on the balloon surface during actuation. This is due to gas permeating out of the balloon through the silicone. This gives a visual confirmation of the role of permeation for balloon relaxation.

The principal failure mode is the formation of a leak in the balloons. In some cases, the leak forms at the disc-frame interface, and it is probably due to the epoxy not completely filling the gap between the disc and the frame. This kind of leak is usually visible only when the balloon reaches a certain pressure, and it is typically small enough that the balloon can still be operated. In other cases, the leak forms at the edge of the disc due to stress concentration in the silicone. This can be prevented by making sure the silicone is thick enough around the edge of the disc. A leak of this kind is easily repaired by another application of silicone.

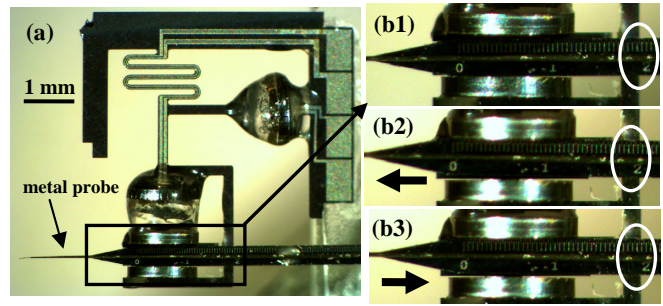


Figure 7: a) Complete inchworm system. A commercial metal probe is mounted on top of a silicon ruler probe. b1-b3) Close-ups of the probe, with frames showing the probe displacement (experiment run in air). b1) Initial position of the probe. b2) Probe after 4 cycles of forward displacement (cumulative displacement: about 100  $\mu\text{m}$ ). b3) Probe after 1 cycle of backward displacement from b2 position (displacement: about 75  $\mu\text{m}$ ).

### CONCLUSIONS

Inchworm actuators based on two electrolysis-actuated silicone balloons were designed, fabricated and tested. Standalone silicone balloons were tested, and a model for their behavior was also developed. The inchworm was demonstrated to provide variable displacement per cycle (up to 75  $\mu\text{m}$  per cycle), with the balloons generating forces in the mN range. The inchworm operates at low voltage (typically around 3.5 V) and low current (typically between 20 and 30  $\mu\text{A}$ ), and it completes one cycle in about 10 minutes. The inchworm was tested both in air and in water. Displacement of a silicon probe and a commercial metal neural probe was demonstrated and video-recorded.

### ACKNOWLEDGEMENTS

The funding of the work is provided by NIH, under Award Number R01 EY015545.

### REFERENCES

- [1] L. Giacchino, Y-C Tai, "Electrolysis-based Parylene-balloon Actuators", The 15th IEEE International Conference on Solid-State Sensors, Actuators and Microsystems (Transducers '09), Denver, USA, Jun. 21-25, 2009, pp. 2397-2400.
- [2] C. Pang, Y.C. Tai, J.W. Burdick, R.A. Andersen, "Electrolysis-based Parylene Balloon Actuators for Movable Neural Probes", The 2<sup>nd</sup> IEEE International Conference on Nano/Micro Engineered and Molecular Systems (NEMS '07), Jan 16-19, 2007, pp. 913-916.
- [3] Xie, Q. Hie. Y.C. Tai, J. Liu, T. Lee, "Electrolysis-based On-chip Dispensing System for ESI-MS", The 16th IEEE International Conference on Micro Electro Mechanical Systems (MEMS '03), Jan 19-23, 2003, pp. 443-446.
- [4] A. P. Papavasiliou, D. Liepmann, A. Pisano, "Electrolysis-bubble Actuated Gate Valve", The 2000 Solid-State Sensor and Actuator Workshop, Hilton Head Isl., SC, pp. 48-51.
- [5] J.G. Cham, E.A. Branchaud, Z. Nenadic, B. Greger, R.A. Andersen, J.W. Burdick, "Semi-Chronic Motorized Microdrive and Control Algorithm for Autonomously Isolating and Maintaining Optimal Extracellular Action Potentials", J Neurophysiol 93 (2005), pp. 570-579.

### CONTACT

\* L. Giacchino, tel: +1-626-395-5899; lucagiag@caltech.edu

# NANOENERGETIC SILICON AS A THRUST ACTUATOR FOR JUMPING MICROROBOTS

L. J. Currano<sup>1\*</sup>, W. Churaman<sup>1,2</sup>, J. Rajkowski<sup>2</sup>, C. J. Morris<sup>1</sup>, and S. Bergbreiter<sup>2</sup>

<sup>1</sup>U.S. Army Research Laboratory, Adelphi, MD, USA

<sup>2</sup>University of Maryland, College Park, MD, USA

## ABSTRACT

The first reported jumps of an untethered, sub-cm scale microrobot are reported. The microrobot weighs 300 mg, is 8 mm long, and uses nanoporous energetic silicon to create thrust for jumping. A polymer hexapod skeleton was used, with the energetic silicon chip placed on the underside of the skeleton facing down to provide upward thrust. Experiments were first conducted with off-board circuitry and power, and then the circuitry and power were integrated onto the robot to obtain fully autonomous untethered jumps. Tethered jump heights (with offboard power and control) are estimated at 40 cm, while a 6 cm maximum height was measured for untethered jumps (fully autonomous robot with on-board power and control).

## INTRODUCTION

While microrobots have long been of interest, they are only recently becoming a reality. The majority of the work to date on small scale robotics consists of centimeter-scale systems assembled from conventional components. Crawling, flying, and jumping robots have been demonstrated on the centimeter scale [1-3]. Microfabricated crawling robots on the sub-cm scale have been demonstrated [4,5], but mobility remains a major challenge. Microfabricated actuators generally have very limited force or range of motion. While jumping is a common type of mobility in insects at these size scales, is a particularly difficult type of motion to achieve in MEMS because of the high power required for takeoff. The primary challenge is a high density energy storage mechanism which can release its energy on a millisecond timescale. Bergbreiter et al. proposed an elastomer to store energy as elastic strain in [6]. We propose energy storage in an energetic material which provides thrust when the energy is released through rapid combustion. The system can be designed with several discrete pockets of energetic material so multiple jumps can be taken over the course of a mission. We also provide an on-board sensor that provides intelligence, instructing the robot to jump when a specific change in the environment is sensed. This is the first time a sub-cm robot has been demonstrated with the intelligence to decide when to move based on a change in its environment.

## MICROROBOT DESIGN AND CONSTRUCTION

### Overall Design

While there are many definitions for microrobots, we stipulate that a microrobot requires these features at a minimum: a form/skeleton of some sort, a means for mobility, some level of intelligence or decision-making, and a power supply for the mobility and decision making. Our microrobot provides each of these aspects, and while its intelligence and mobility are certainly rudimentary, these can be improved with future iterations.

The overall design of the microrobot is pictured in Figure 1. The skeleton used in our design is a hexapod made from a polymer. While four legs would be sufficient for stability in a jumping-only platform, we elected to use 6 legs to allow for future integration of crawling-type actuation in an alternate-tripod gait. The polymer provides durability, flexibility, and low mass. In addition, electronic elements may be enclosed inside the polymer

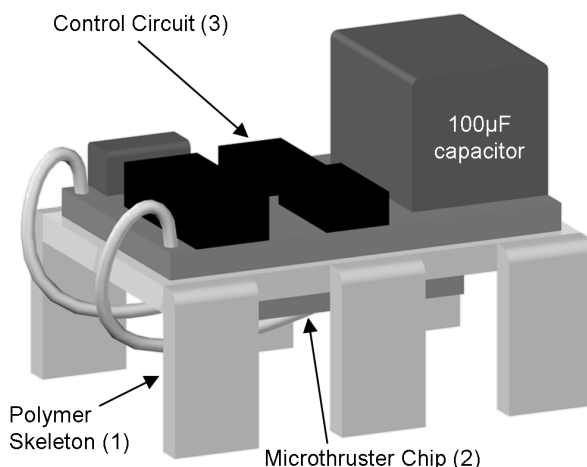


Figure 1. Computer modeled rendering of jumping microrobot, with 1) photodefined polymer skeleton, 2) nanoporous energetic silicon thruster, and 3) control circuit including light sensor and power supply.

for protection in lieu of traditional packaging approaches that may add unnecessary mass.

The mobility is provided by a nanoporous energetic silicon microthruster. This material is attractive because it can be initiated at low voltage and energy levels (as low as 3 V, 0.25 mJ [7,8]) compatible with the limited power supply available on a small robotic platform. It can also be batch-fabricated in very precise, controllable quantities as small as 100 µg using MEMS fabrication processes. Upon initiation, the material burns and gas is produced, which is ejected from the chip to produce thrust.

Because of power, size and weight considerations, we took the approach of providing the most basic level of intelligence in this first iteration of the jumping microrobot. This consists of a sensor that, upon detecting a specific environmental change, outputs a signal to tell the energetic thruster to initiate and cause the robot to jump.

### Skeleton

A UV-cure polymer process for rapid prototyping [9] was used to create the microrobot platform shown in Figure 2. The process uses photolithography and Loctite® photopatternable adhesives. For this platform, Loctite® 3525, an acrylic, was deposited on a transparency substrate between microscope slides to achieve the desired thickness. The polymer was then patterned in plane using an ink-jet printed mask and a hand held UV lamp (Spectroline®, EN-180, 365nm).

After curing, the mask was removed and excess polymer was washed away with acetone. At this point, the robot was released from the substrate and an additional thin layer of polymer was coated on the underside of the robot. The legs were then manually folded out of plane and constrained in this position before the robot was again exposed to the UV light for additional curing. After

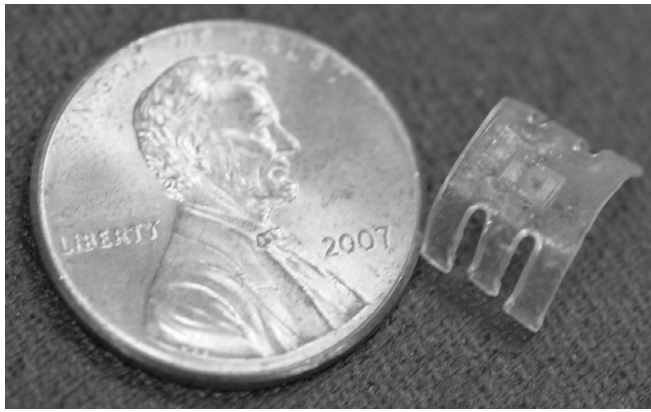


Figure 2. Polymer hexapod microrobot skeleton, with dummy embedded microcontroller.

removing the constraints, the robot had assumed this new form. This resulted in the three dimensional robot skeleton used in this work.

### Nanoporous Energetic Silicon Microthruster

The nanoporous silicon energetic chip is created in a  $\langle 100 \rangle$  p-type silicon wafer via an electrochemical etching process in hydrofluoric acid and ethanol described in detail in [7]. The desired porous silicon regions are defined using an LPCVD silicon nitride as a masking layer, and an integrated thin-film Cr/Pt/Au resistor is deposited on top of the porous silicon to provide a low-power initiator. The pores are filled with oxidizer by dissolving sodium perchlorate ( $\text{NaClO}_4$ ) in methanol and applying a drop to the porous silicon surface with a syringe [10]. Capillary forces pull the solution into the pores, and the sodium perchlorate precipitates onto the surface of the pores as the methanol evaporates away. This leaves a very densely packed mixture of silicon (which acts as the fuel) and an oxidizer. The energetic reaction can be initiated by rapidly heating to  $225^\circ\text{C}$ , achieved via joule heating of the integrated resistive initiator. The reaction produces water vapor due to hydrogen surface termination of the nanoporous silicon [11]. While nanoporous energetic silicon is not an ideal propellant, the volume of gas produced per gram of energetic is larger than that for black powder. This evolved gas is the mechanism for thrust generation.

The porous silicon chip was attached to the underside of the microrobot skeleton with double-sided tape, with the active side facing away from the hexapod body, as shown in Figure 3. No confinement cavity or expansion nozzle was used for this initial version of the microrobot. Electrical connections between the initiator and the off-board DC power supply or the on-board control circuit were made by wirebonding with 5 mil or 12 mil diameter aluminum wire.

### Control Circuit and Power Supply

The control circuit was designed using discrete, surface-mount parts. Integration of the electronic controls for sensing and actuation is limited to a  $8\text{ mm} \times 5\text{ mm}$  area, since this is the overall footprint of the microrobot. The control circuit is shown schematically in Figure 4. To minimize size and weight, we kept the number of parts to a bare minimum of only 5 parts. Together the  $100\ \mu\text{F}$  and  $10\ \mu\text{F}$  capacitors comprise the power supply for the microrobot, the SFH3710 phototransistor provides sensing, and the 2N7002 n-channel enhancement mode field effect transistor (FET) provides the logic. The  $10\ \text{k}\Omega$  resistor ensures the bias applied from the phototransistor is high enough to open the FET gate. The

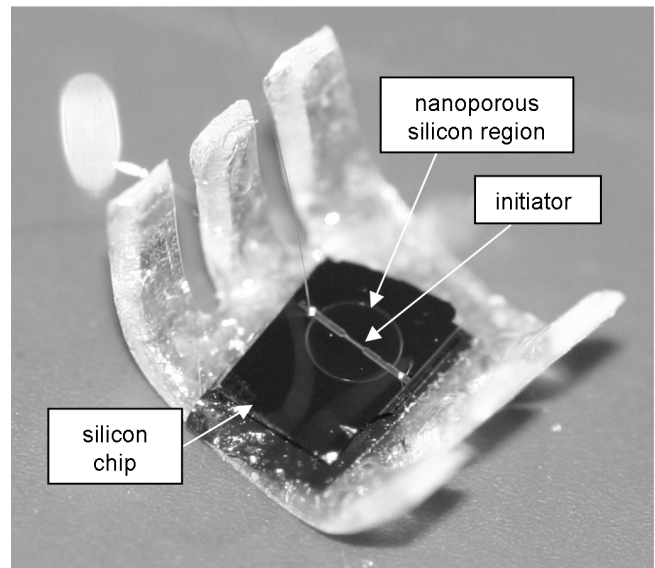


Figure 3. Nanoporous silicon microthruster positioned on underside of microrobot.

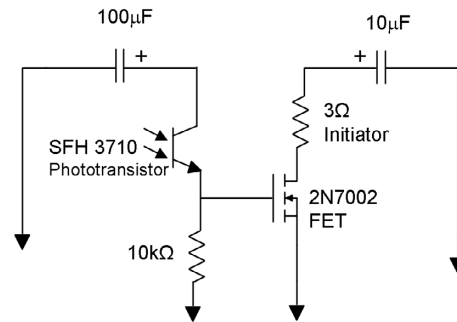


Figure 4. Schematic of control circuit, which supplies power, sensing, and logic to microrobot.

circuit is assembled by attaching the parts with solder onto pre-patterned gold traces on a silicon chip. A picture of the assembled circuit connected with wirebonds to the porous silicon chip and attached to the top of the microrobot is shown in Figure 5.

When charged to 5 V, the  $100\ \mu\text{F}$  capacitor provides the operating voltage to power the phototransistor. The spectral sensitivity of the phototransistor is 350-950 nm, with a maximum sensitivity wavelength of 570 nm. When the phototransistor senses light in this range, the 5 V from the  $100\ \mu\text{F}$  capacitor is also applied to the gate of the FET. At this 5 V gate-source voltage, the source-drain resistance of the FET is on the order of  $15\ \Omega$ . This causes the  $10\ \mu\text{F}$  capacitor (also charged to 5 V) to discharge through the initiator (pictured in Figure 4 as a  $3\ \Omega$  resistor).

## RESULTS

### Tethered Jumps

The nanoporous silicon energetic was patterned in a 2mm diameter active area for these experiments. For the tethered jumps, the control circuit was not included on the back of the robot. The wirebonding wires were bonded to the initiator on the silicon chip, then clipped about 6 inches long and the ends left hanging. These wires were connected to a DC power supply. Initiation was achieved by turning on the power supply to 3 V. The total weight

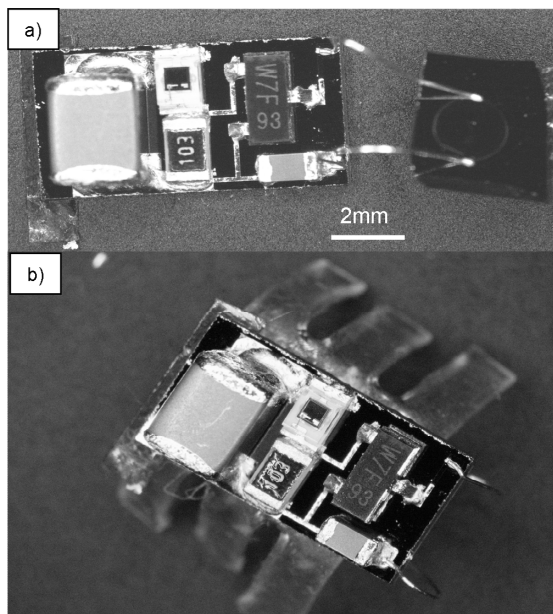


Figure 5. Picture of assembled control circuit, a) attached to porous silicon chip with wirebonds, and b) assembled onto top of microrobot.

of the robot with energetic silicon chip and the electrical leads in this configuration was 100 mg.

Two tethered jumps were made, one with a 40 $\mu$ m deep porous layer and 12-mil wires to supply power, the second with a 60 $\mu$ m deep porous layer and 5-mil wires. The depth of the porous silicon corresponds roughly to the volume of the energetic material. The resulting jumps were captured using a high speed camera recording at 1000 frames per second (Figure 6). A scale with 1-cm gradations was positioned behind the launch platform to allow measurement of the vertical position. A simple MATLAB routine was used to analyze each frame and record the position of the microrobot with the user pointing and clicking at the approximate location of the microrobot. The routine stores the pixel locations selected for each

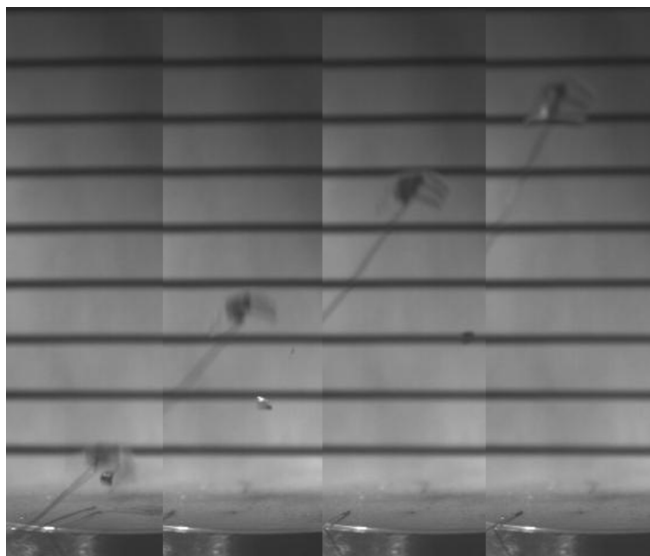


Figure 6. Images from high speed video for jump with 12-mil wire tethers. Images are spaced 10 frames (10ms) apart. A piece of the nanoporous silicon chip that detached from the robot can be seen in frames 1-3.

frame. The same procedure was used to determine the conversion factor from pixels to centimeters. There were 46 pixels/cm in one video and 38 pixels/cm in the other. Therefore, the precision of the measurement is much better than 1 cm. The error in position is estimated at 5 pixels, around 0.1 cm.

The trajectory for both jumps is plotted in Figure 7. The first jump used 12-mil wire to supply DC power to the initiator to ignite the porous silicon, but the wire was too stiff and constrained the motion to a maximum height of 10cm. The experiment was repeated with 5-mil wire and the starting trajectory was similar, but the robot continued upwards out of the ~11cm field of view. If drag effects are neglected and the initial velocity of approximately 2.8m/s is used, the projectile motion equation predicts a maximum height of 40cm, which is 50 times larger than the maximum dimension of the robot (8mm long x 4.7mm high x 5mm wide). If a drag coefficient of 1 is used, the maximum projected height is 36.6cm. The robot did land on its feet in both experiments, although it is unclear if this was due to the location of the center of mass, the stiffness of the wires, or pure chance.

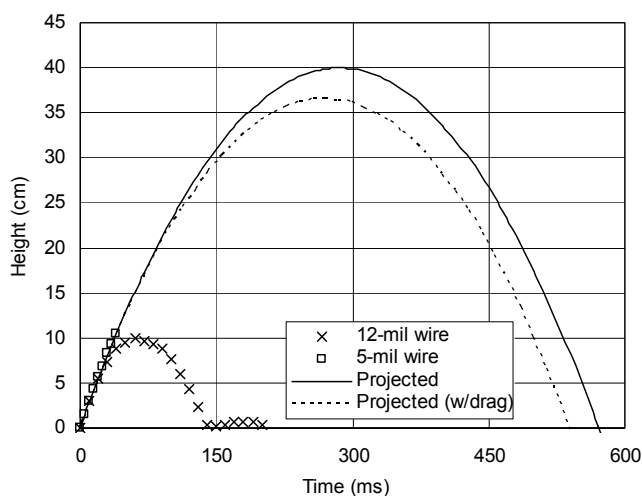


Figure 7. Trajectory for each of two jumps, along with the projected unconstrained trajectory for the 5-mil wire jump with and without drag.

As noted above, we did not include a confinement chamber or expansion nozzle for this initial demonstration. Therefore the efficiency of the chemical to kinetic energy conversion is expected to be very low. Based on bomb calorimetry measurements, the energy density of our nanoporous silicon energetic material has been reported as 5.74 kJ/g [7]. The estimated mass of the energetic material in our jumping experiments is 150-200  $\mu$ g, for a net chemical energy content of 0.86-1.1 J. For the test with 5-mil tether wires, the total mass of the microrobot was 99.5mg and the takeoff velocity approximately 2.8 m/s. The kinetic energy is therefore 0.39 mJ, for a chemical to mechanical conversion efficiency of less than 0.01%. Microthrusters made by Rossi et al [12] with and without chambers and expansion nozzles showed up to a 100x increase in force generated when the chamber and nozzle were added, so there is room for vastly improved performance.

### Untethered Jump

The full circuit was attached to the top of the microrobot with double-sided tape for untethered experiments. The nanoporous energetic silicon was attached to the underside of the microrobot in the same manner, with 5-mil aluminum wirebonding wire connecting the circuit to the energetic silicon chip (see Figure 1

and Figure 5). The mass including the circuit was 300 mg, with the 100  $\mu$ F capacitor accounting for almost half of the total mass (see Table 1).

Table 1. Mass breakdown of microrobot by component. Note the 100  $\mu$ F capacitor is by far the largest piece of the overall mass.

Component	Mass (mg)
Si substrate	74
10 $\mu$ F capacitor	8.7
100 $\mu$ F capacitor	131.3
2N7002 FET	8.4
SFH3710	3.3
10k $\Omega$ resistor	4.5
Hexapod	69.8
<b>Total Mass</b>	<b>300</b>

The untethered experiments were set up and the capacitors charged in a darkened room to prevent the phototransistor from triggering. Once charged, the jumps were triggered by turning on a set of 3 high-intensity LEDs, which also provided the light source for the high speed video capture of the jump.

The first successful untethered jump is shown in Figure 8, with a maximum height of 6 cm achieved. The expected jump height based on the estimated 40 cm from the tethered experiments is approximately 13 cm given the 3x increase in mass. One possible reason for the lower than expected jump height is that the microrobot flipped end-over-end at about 29 revolutions per second during the jump. This is primarily due to the massive 100  $\mu$ F capacitor positioned at the extreme end of the microrobot (see Figure 1), so the thrust was not directed through the overall center of mass. Using rough estimates for rotation axis and moment of inertia, the rotational energy calculated from the video only accounts for about 15% of the total energy, however. Variations in the nanoporous silicon properties or oxidizer deposition may account for the additional 30% discrepancy.

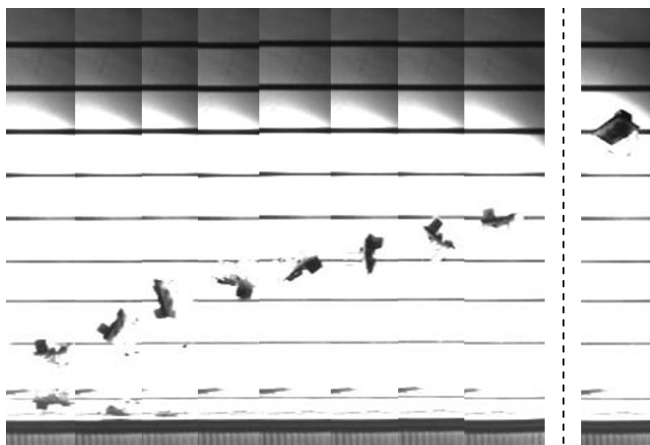


Figure 8. Sequence of frames from high speed video of second untethered jump. Interval between depicted frames is 5 ms, with dashed line indicating an omitted interval of 60 ms. The final pictured frame shows the maximum height achieved (~6 cm).

## CONCLUSION

We have presented the first sub-cm scale jumping microrobot, using nanoporous energetic silicon as a thrust actuator. The maximum untethered jump height was 6 cm, over 7 times the body

length. Tethered experiments suggest that even larger jumps should be possible. Jumping is a promising new mode of mobility for microrobots, and nanoporous energetic materials provide a convenient mechanism for achieving large jumps with minimal input energy. The jump performance may be improved in future iterations through integration of confinement and expansion nozzles into the microthruster, and the circuit and actuators can be expanded to allow for multiple jumps.

## REFERENCES

- [1] A. M. Hoover, E. Steltz, and R. S. Fearing, "RoACH: An autonomous 2.4 g crawling hexapod robot," in Proc. of IEEE/RSJ International Conference on Intelligent Robots and Systems (IROS), 9/22-26/2008, Nice, France (2008), pp. 26-33.
- [2] R. J. Wood, "The first takeoff of a biologically inspired at-scale robotic insect," IEEE Transactions on Robotics 24, pp. 341-347 (2008).
- [3] M. Kovac, M. Schlegel, J. C. Zufferey, and D. Floreano, "A Miniature Jumping Robot with Self-Recovery Capabilities," in Proc. of IEEE International Conference on Robotics and Automation (ICRA), 5/12-17/09, Kobe, Japan (2009), pp. 583-588.
- [4] S. Hollar, A. Flynn, C. Bellew, and K. S. J. Pister, "Solar powered 10 mg silicon robot," in Proc. of IEEE International Conference on Micro Electro Mechanical Systems, 1/19-23/03, Kyoto, Japan (2003), pp. 706-711.
- [5] B. R. Donald, C. G. Levey, C. D. McGray, I. Paprotny, and D. Rus, "An untethered, electrostatic, globally controllable MEMS micro-robot," Journal of Microelectromechanical Systems 15, pp. 1-15 (2006).
- [6] S. Bergbreiter and K. S. J. Pister, "Design of an autonomous jumping microrobot," in Proc. of IEEE International Conference on Robotics and Automation (ICRA), 4/10-14/07, Rome, Italy (2007), pp. 10-14.
- [7] L. J. Currano and W. A. Churaman, "Energetic Nanoporous Silicon Devices," Journal of Microelectromechanical Systems 18, 799-807 (2009).
- [8] W. Churaman, L. Currano, and C. Becker, "Initiation and reaction tuning of nanoporous energetic silicon," Journal of Physics and Chemistry of Solids 71, pp. 69-74 (2010).
- [9] J. E. Rajkowski, A. P. Gerratt, E. W. Schaler, and S. Bergbreiter, "A Multi-material milli-robot prototyping process," in Proc. of IEEE/RSJ International Conference on Intelligent Robots and Systems (IROS), 10/11-15/09, St. Louis, MO (2009), pp. 2777-2782.
- [10] D. Clément, J. Diener, E. Gross, N. Künzner, V. Y. Timoshenko, and D. Kovalev, "Highly explosive nanosilicon-based composite materials," physica status solidi (a) 202, pp. 1357-1364 (2005).
- [11] L. Currano, W. Churaman, and C. Becker, "Nanoporous silicon as a bulk energetic material," in Proc. of the International Conference on Solid-State Sensors, Actuators and Microsystems (Transducers), 6/21-25/09, Denver, CO (2009), pp. 2172-2175.
- [12] C. Rossi, B. Larangot, P. Q. Pham, D. Briand, N. F. de Rooij, M. Puig-Vidal, J. Samitier, and T. LAAS-CNRS, "Solid Propellant Microthrusters on Silicon: Design, Modeling, Fabrication, and Testing," Journal of Microelectromechanical Systems, pp. 1805-1815 (2006).

## CONTACT

\*L.J. Currano, tel: +1-301-394-0566; luke.currano@us.army.mil.

# PARAMETER SWEEP STRATEGIES FOR SENSING USING BIFURCATIONS IN MEMS

C.B. Burgner<sup>1\*</sup>, K.L. Turner<sup>1</sup>, N.J. Miller<sup>2</sup>, and S.W. Shaw<sup>2</sup>

<sup>1</sup>University of California-Santa Barbara, Santa Barbara, California, USA

<sup>2</sup>Michigan State University, East Lansing, Michigan, USA

## ABSTRACT

In this work we consider a sensing strategy using dynamic bifurcations in MEMS resonators. We examine the statistics of jump events that occur as a result of a linear parameter sweep through a subcritical pitchfork bifurcation in a parametrically driven MEMS resonator in the presence of noise. The statistics of jump events are compared to those derived from a simple one-dimensional model and are found to have good agreement. Issues related to how system and input parameters affect these statistics are described, and sweeping strategies that lead to precise, fast estimates of the bifurcation point, as essential for these sensors, are derived. It is shown that for a typical MEMS resonator an optimal sweep rate exists, and noise may need to be added to achieve optimal sensitivity.

## INTRODUCTION

Nonlinear systems often exhibit jump events near bifurcation points. Common examples include the jump events encountered in the frequency response of nonlinear MEMS resonators; see, for example, Figure 1 (top). These jump events result in sudden and significant changes in response and thus may be exploited for highly sensitive measurements. Examples include threshold and linear amplification modes of the Josephson bifurcation amplifier [1], parametric measurements of a NEMS Duffing resonator [2], and frequency estimation of a parametrically forced MEMS resonator [3]. It has been proposed that such measurement methods be employed for mass sensing [4]. Noise in MEMS result in a smearing of the observed bifurcation point. Accordingly, we examine the statistics of jump events as a result of linear parameter sweeps.

In this paper we concern ourselves with the jump events that occur during a sweep through the subcritical pitchfork bifurcation in a parametrically resonant MEMS device. The frequencies at which the jumps occur are not fixed. Indeed they depend on the parameter sweep rate, and even for a fixed sweep rate they are randomly distributed as a result of thermal noise. As an example, distributions of jump events for a particular device for sweep rates spanning 0.004-0.4Hz/sec at ambient noise are shown in Figure 2. The device is the parametrically driven gyroscope described in [5]. For this resonator, which has linear natural frequency 8.4888kHz, the jump events vary by up to 3Hz, depending on sweep rate. In addition, jumps generally occur after the bifurcation point, which is estimated to be at 8.4851kHz according to the measured parameters of our model. The width of the distributions ranges from approximately 0.1Hz to 0.5Hz for individual sweep rates, see Figure 2. The aim of this work is to examine the distributions of these jump events and compare them to the predictions from a one-dimensional, single parameter model, and to use the results to derive optimal sweeping strategies. Results such as these are required for one to effectively exploit dynamic bifurcations for sensing in MEMS.

## THEORY

Near simple bifurcation points, such as the pitchfork considered here, there is a slowing down of the system dynamics in the phase space along the direction of the critical eigenvalue, and a

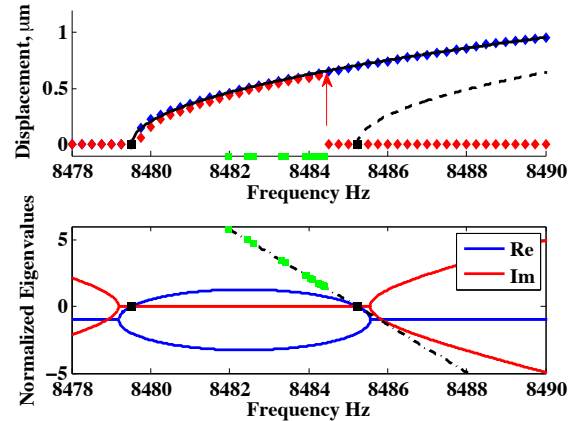


Figure 1: Nonlinear frequency response (top) showing sweeps up (blue) and down (red), compared to predicted frequency response (black), for the device shown in Figure 4. The jump events of interest are indicated. Eigenvalues of the fixed point at zero (bottom), real (blue) and imaginary (red) parts. Black dashed line illustrates the linear sweep approximation. Dots (green) show mean values of measured escape events from Figure 5.

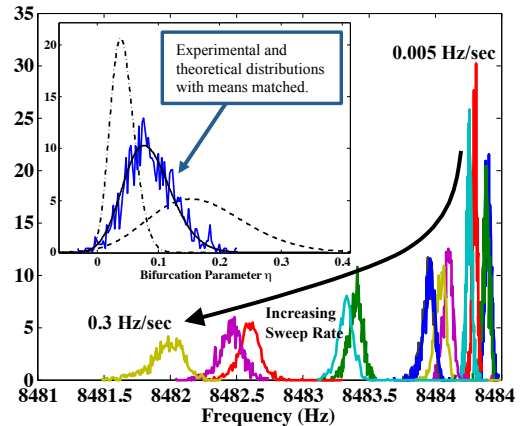


Figure 2: Distributions of jump events for a variety of sweep rates at ambient noise. Jump events result from thermal and electrical noise with effective temperature  $T=388.7^{\circ}\text{K}$ . Inset shows three distributions for  $\alpha=0.041$  along with mean-value-shifted measured distribution, as described in the text.

collapse onto an attendant one-dimensional manifold. When noise is present, the reduction onto the slow manifold must simultaneously treat the deterministic and stochastic aspects of the system [6]. We assume the noise to be additive, Gaussian, and white. For the subcritical pitchfork bifurcation the nondimensional stochastic normal form is given by

$$\dot{x} = 2\eta x + 4x^3 + \sqrt{D}\xi(t), \quad (1)$$

where  $x$  is the dynamic state on the slow manifold,  $\eta$  is the

bifurcation parameter (proportional to the slow eigenvalue) taken to be zero at the bifurcation point,  $D$  is the effective noise strength, and  $\xi$  is a Gaussian white noise process with zero mean and covariance equal to 2. The system can be thought of as a particle in a time-varying potential, as illustrated in Figure 3, subject to a random force. As the system is swept through the bifurcation point,  $\eta$  changes from negative to positive, resulting in the change of the effective potential as shown in Figure 3, and a loss of local stability at  $x=0$ . To create a simple linear sweep model, we approximate this change with a first order expansion of  $\eta$  in time. Thus, we assume

$$\eta = \eta_0 + rt, \quad \eta_0 < 0, \quad \text{and} \quad r > 0, \quad (2)$$

where  $r$  is the effective sweep rate and is proportional to the lab frame sweep rate (e.g., the time rate of change of the forcing frequency). The linear approximation of the bifurcation parameter corresponds to a linear approximation of the slow eigenvalue, shown in Figure 1 (bottom). This approximation is valid as long as escape occurs close to the bifurcation. Since  $\eta$  is linearly related to time, we replace time in equation (1) with bifurcation parameter and scale according to

$$\eta = r^{1/2}\tau, \quad x = r^{1/4}y. \quad (3)$$

This yields the one-parameter normal form,

$$\frac{\partial y}{\partial \tau} = 2\tau y + 4y^3 + \sqrt{\alpha}\xi(\tau), \quad (4)$$

$$\alpha = D/r. \quad (5)$$

Equation (4) universally captures the dynamics near a subcritical pitchfork bifurcation during a parameter sweep, and thus the model is not device dependent, but is broadly applicable in the manner of a normal form. Equation (4) allows one to solve for a one-parameter family of normalized escape distributions. These normalized distributions describe the probability density of a jump event occurring at a specific  $\tau$ . The single parameter,  $\alpha$ , is the ratio of noise strength to sweep rate.

As stated above, the model employed in this work is local to the vicinity of the bifurcation point. Accordingly, we define a jump event to have occurred when  $y$  escapes to  $\pm\infty$ . Closed form approximate solutions for the distribution of jump events may be found when  $\alpha$  is either very small or very large compared to unity [6]. In the interim region the problem must be solved numerically [7]. These solutions are identical for a large class of initial conditions because the system is diffusive and settles into a quasi-steady-state early in the sweep process [7,8].

The escape distributions found by solving equation (4) are functions of  $\tau$  and depend on the single parameter,  $\alpha$ . Equation (3) is used to transform these solutions into functions of the bifurcation parameter  $\eta$ , which now depend on two parameters,  $r$  and  $D$ . Thus for two sets of  $r$  and  $D$  that have identical ratio, the escape distributions, as a function of the bifurcation parameter, are related by a simple scaling. To illustrate this, the inset in Figure 2 shows three escape distributions with identical  $\alpha$  but different  $r$  and  $D$ . A corresponding experimentally measured distribution is also shown. The mean of this experimentally measured distribution is artificially shifted, for reasons discussed, to compare its shape with the theoretical curve.

Despite the discrepancy in the mean escape times predicted

by the model, it is clear that this system exhibits a distribution of escape events after the bifurcation point. Escape may, in principle, also occur before the bifurcation point. Whether it is likely to occur before or after depends on the value of  $\alpha$ . For large  $\alpha$  the sweep rate to noise is small and jump events tend to occur before the bifurcation point is reached; this is known as noise-activated escape [9-11]. For small  $\alpha$ , the sweep rate to noise is large, and jumps generally occur beyond the bifurcation; this is known as delayed bifurcation [12-14], which occurs, for example in laser turn-on dynamics. See [7] for further discussion and references.

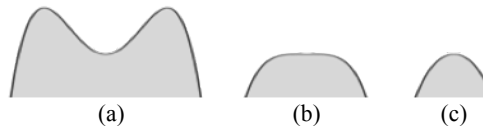


Figure 3: Illustration of the effective one-dimensional potential at three times; before (a), at (b), and after (c) the bifurcation point.

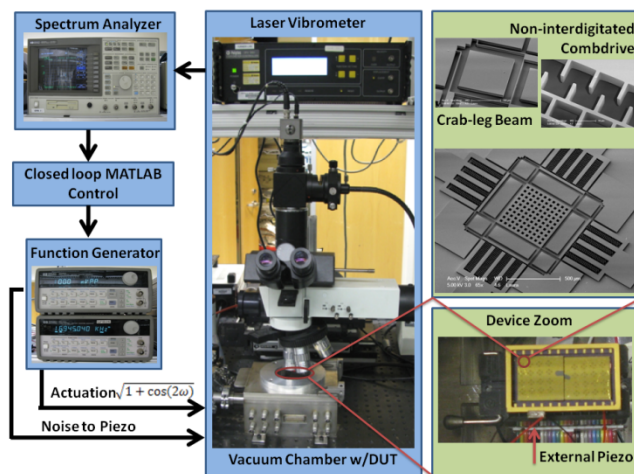


Figure 4: Experimental setup schematic with SEM of the device and close ups of the noninterdigitated combdrives and suspension.

## EXPERIMENT

The aforementioned MEMS gyroscope is fully characterized to quantitatively compare experimentally measured jump distributions with the predictions. The experimental setup is shown in Figure 4 and consists of a function generator to sweep the parametric drive frequency, a laser vibrometer to measure the device response, and a spectrum analyzer to detect bifurcation events, all controlled in MATLAB. Frequency is swept downward; if a jump event is detected, the frequency at which it occurred is noted, the input voltage is cut to allow the device time to settle back to the noise floor, and the frequency is returned to a value well above the bifurcation point before the procedure is repeated. The actuation voltage was determined to be 15Volts to allow for a wide frequency window in which escape might occur. The widest range of frequency sweep rates allowable by the lab equipment was conducted. The range of sweep rates, 0.004-0.4Hz/sec, is limited by the interplay of the characteristic response time of the device, delay in communication between hardware components, and the resolution of the frequency generator. The device is placed in vacuum and maintained at 1mTorr, resulting in a quality factor of near 3000.

In order to explore a wide range of sweep rate to noise ratios ( $\alpha$  values), a piezo-element is mounted next to the device and white noise is injected into the system, inducing random base

excitation. Both the ambient and piezo-enhanced noise are characterized by fitting a Lorentzian to the resonant peak, which rises above the laser vibrometer noise floor. The ambient noise is found to have an effective temperature of 388.7°K.

While the device used in this work exhibits two resonant modes [5], the drive and sense modes are mismatched by over 7%. This mismatch permits us to ignore the sense mode and model the drive mode as a 1DOF mass spring damper system with position dependent forcing from the non-interdigitated combdrives and cubic stiffness from the crab-leg suspension. The reduced 1DOF system dynamics is governed a nonlinear Mathieu equation and has been studied extensively [15,16],

$$\ddot{z} + Q^{-1}\dot{z} + z + \lambda(1 + \cos \Omega t)z + \gamma z^3 = \sqrt{\frac{k_B T}{mQ\omega_0^2}} \xi(t) \quad (6)$$

where  $z$  is the position,  $\omega_0$  is the natural frequency,  $\Omega$  is the normalized forcing frequency,  $Q$  is the quality factor,  $\lambda$  is the parametric forcing parameter,  $\gamma$  is the nonlinear stiffness coefficient,  $k_B$  is Boltzmann's constant,  $T$  is temperature,  $m$  is the resonator mass, and  $\xi$  is a white noise force. The device parameters were determined by fitting the experimental measured power spectral densities, measured for  $\lambda=0$  (not shown), and parametric resonance response (Figure 1).

In order to have good statistical confidence, thousands of jump events were recorded for several sweep rates and noise levels. The resonant frequency is recorded at the beginning of each test to correlate the mean of each distribution, thus accounting for the effects of drift. The drift observed was noted to be periodic, and correlated to the HVAC cycles of the lab environment.

## DISCUSSION

The frequency distributions are shown to be in good qualitative agreement with theory; see Figures. 5 and 6. As expected from theory, faster sweep rates result in wider jump distributions and a shift in the mean value further past the bifurcation frequency. Figures. 5 and 6 show data and theoretical curves (from equation (4)) for the normalized values of escape mean and variance respectively. The data points appearing inside the box with heading ‘gyro’ correspond to experiments done under ambient noise. The remaining data points correspond to experiments in which artificial noise was added. The boxes with headings ‘Manalis’ and ‘Roukes’ illustrate the estimated ranges of the sweep to noise ratio we expect from devices studied by Manalis [17] and Roukes [18], were they to be operated under thermal noise in a manner similar to the gyro. This illustrates how the effect of thermal noise depends on device size, as the Manalis device is 140, and the Roukes device is 242, times smaller (by mass) than the gyro. The strength of thermal noise was estimated according to the fluctuation-dissipation theorem. Thus the quality factors of these devices come into play as well. They are 15000 and 1200 for the Manalis and Roukes devices, respectively. It is interesting to note that even with the smallest device, thermal noise is still hardly sufficient to result in noise-activated escape before the bifurcation.

Both the mean and variance are underestimated by the theory, as seen in Figures 5 and 6. We suspect that this is because the escape events are occurring sufficiently far past the bifurcation point that the first order series expansion approximation of  $\eta$  breaks down. In Figure 1 green dots illustrate the mean values of escape frequencies (under ambient noise) and in Figure 1 (bottom) the black line illustrates the linear approximation. It is clear that the unstable eigenvalue is not linear in frequency over the range of

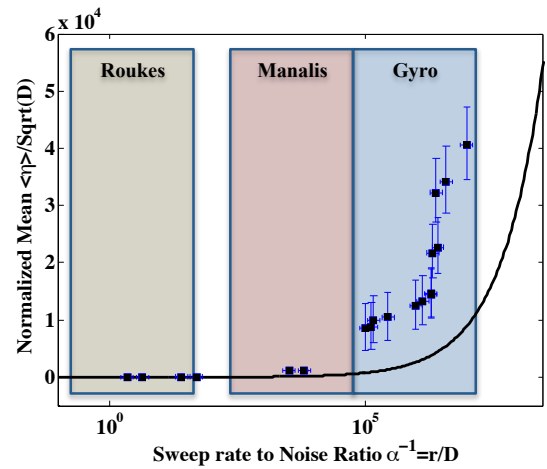


Figure 5: Normalized mean of jump frequency distributions plotted against the theoretical curve.

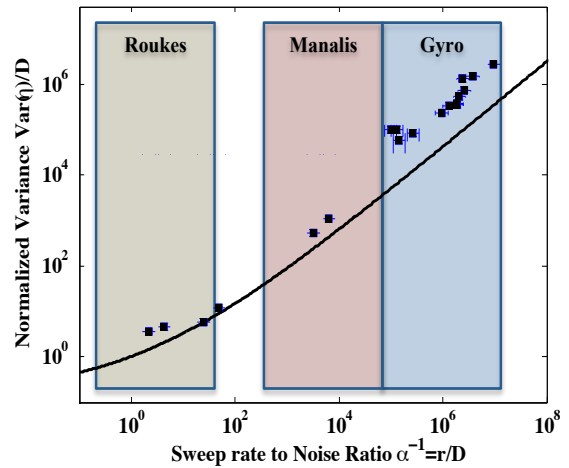


Figure 6: Normalized variance of frequency jump events plotted against theoretical curve. Slope of theoretical curve is about 1.

escape events. Accordingly, the hill shaped potential after the bifurcation point, Figure 3c, is not as sharp as our model predicts. This means that it takes more time for the system ‘particle’ to roll down the hill, and thus escape occurs later than predicted. It is because of this underestimation in the mean that we shifted the measured distribution displayed in the inset of Figure 2 in order to compare it with theory. The variance, and even the skewness (not shown), of this data matches the prediction very well. A modified theory that more accurately describes the variation of the eigenvalue may yield improved results.

One interesting application of these results is the determination of the sweep rate for a given noise level that provides the best estimate the bifurcation point within some confidence interval. Such a result is applicable when considering bifurcation point tracking as a means of mass sensing [4]. We choose a confidence interval about an estimated bifurcation point in which the real bifurcation point should exist with 90% probability. This calculation was done using the linear sweep 1D model and assuming a finite number of measurements is the only source of uncertainty. The estimated bifurcation point is found from the measured mean and variance of escape events, and using the theoretical result curves shown in Figures 5 and 6. The normalized confidence interval is shown in Figure 7. Here reset



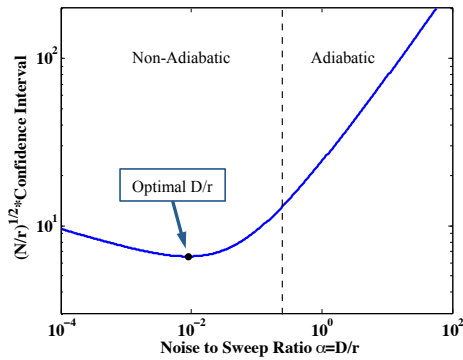


Figure 7: For a given noise level, sweep rate parameter  $r$  can be chosen to minimize the confidence interval or maximize sensitivity.

time was ignored and it was assumed that the number of escape events is  $N=crT$ , where  $c$  is some constant,  $r$  is the sweep rate, and  $T$  is the measurement time. Thus, we can use this result to determine the optimal sweep rate, given a fixed measurement time. The optimal normalized sweep rate turns out to be in the non-adiabatic region (small  $\alpha$ ), resulting in delayed bifurcations. However, since thermal noise is relatively small in MEMS devices, this rate may correspond to a relatively slow sweep in the lab frame. In order to increase measurement speed the optimal value of  $\alpha$  could be achieved by increasing noise, rather than decreasing sweep rate. This suggests that adding noise might aid in rapidly locating bifurcation points, an interesting and counterintuitive result since noise typically broadens distributions and decreases sensitivity. In this case, however, it is seen from Figure 6 that the variance of escape distributions is not increased by adding noise, at least not until a great deal of noise has been added.

## CONCLUSION

A 1D model for escape as a result of a linear parameter sweep through a pitchfork bifurcation was used to model escape events encountered in a noisy MEMS parametric resonator. The MEMS device was tested over a wide range of sweep rates and noise levels. Qualitative trends from measured data were found to be in good agreement with those predicted by theory, and variances matched quantitatively. These results illustrate the processes involved in a stochastic-dynamic bifurcations and point out the key noise to sweep rate relationship that must be understood to use this phenomenon for sensing. The model is generic and can be applied to a wide range of systems. By using the developed theory and investigating the role between noise and sweep rate, it is shown that an optimal sweep rate exists for reducing the confidence interval on the location of a bifurcation point, which can then be directly applied to determining sensitivity values in bifurcation detection schemes. Moreover, it is shown that for MEMS devices with small effective thermal noise, adding additional noise may decrease measurement time, or conversely, increase sensitivity.

## ACKNOWLEDGEMENTS

This work was supported by NSF Sensors and Sensor Systems Program Grants [0758419](#) and [0800753](#). The authors would like to thank Prof. Mark Dykman for his invaluable assistance and Dr. Laura Oropeza for device fabrication.

## REFERENCES

[1] R. Vijay, M.H. Devoret, and I. Siddiqi, "Invited Review Article: The Josephson bifurcation amplifier," *Rev. of Sci. Inst.*, Vol. 80, 111101, 2009.

[2] J.S. Aldridge and A.N. Cleland, "Noise-Enabled Precision Measurements of a Duffing Nanomechanical Resonator," *Phys. Rev. Lett.*, Vol. 94, 156403, 2005.

[3] M.V. Requa and K.L. Turner, "Precise frequency estimation in a microelectromechanical parametric resonator," *App. Phys. Lett.*, Vol. 90, 173508, 2007.

[4] W. Zhang and K.L. Turner, "Applications of parametric resonance amplification in a single-crystal silicon micro-oscillator based mass sensor," *Sensors and Actuators A*, Vol. 122(1), 23-30, 2005.

[5] L.A. Oropeza-Ramos, C.B. Burgner, and K.L. Turner, "Robust micro-rate sensor actuated by parametric resonance," *Sensors and Actuators A: Physical*, Vol. 152(1), 80-87, 2009.

[6] E. Knobloch and K.A. Wiesenfeld, "Bifurcations in Fluctuating Systems: The Center-Manifold Approach," *J. of Stat. Phys.*, Vol. 33(3), 1983.

[7] S. Shaw, N. Miller, M. Dykman, K. Turner, and C. Burgner, "Fast estimation of bifurcation conditions using noisy response data," *Proceedings of the SPIE smart structures conference*, San Diego, CA, March 2010.

[8] M.I. Dykman, B. Golding, and D. Ryvkine, "Critical Exponent Crossovers in Escape near a Bifurcation Point," *Phys. Rev. Lett.*, Vol. 92(8), 080602, 2004.

[9] M.H. Devoret, D. Esteve, J.M. Martinis, A. Cleland, and J. Clarke, "Resonant activation of a Brownian particle out of a potential well: Microwave-enhanced escape from the zero-voltage state of a Josephson Junction," *Phys. Rev. B*, Vol. 36(1), 1987.

[10] W. Wersndorfer, E. Bonet Orozco, K. Hasselbach, A. Benoit, B. Barbara, N. Demoncey, A. Loiseau, H. Pascard, and D. Maily, "Experimental Evidence of the Neel-Brown Model of Magnetization Reversal," *Phys. Rev. Lett.*, Vol. 78(9), 1997.

[11] M. Evstigneev, "Statistics of Forced Thermally Activated Escape Events out of a Metastable State: Most Probable Escape Force and Escape-Force Moments," *Phys. Rev. E*, Vol. 78(1), 011118, 2008.

[12] P. Mandel and T. Erneux, "The Slow Passage through a Steady Bifurcation: Delay and Memory Effects," *J. of Stat. Phys.*, Vol. 48(5/6), 1987.

[13] N.G. Stocks, R. Mannella, and P.V.E. McClintock, "Influence of random fluctuations on delayed bifurcations: The case of additive white noise," *Phys. Rev. A*, Vol. 40(9), pg. 5361-5369, 1989.

[14] K.M. Jansons and G.D. Lythe, "Stochastic Calculus: Application to Dynamic Bifurcations and Threshold Crossings," *J. of Stat. Phys.*, Vol. 90(1/2), 1998.

[15] J. F. Rhoads, S. W. Shaw, K.L. Turner, J. Moehlis, B. E. DeMartini and W. Zhang, "Generalized parametric resonance in electrostatically actuated microelectromechanical oscillators," *Sound and Vibration*, 296, 797, 2006.

[16] M.I. Dykman, C.M. Maloney, V.N. Smelyanskiy, and M. Silverstein, "Fluctuational phase-flip transitions in parametrically driven oscillators," *Phys. Rev. E*, Vol. 57(5), 1998.

[17] T.P. Burg, M. Godin, S.M. Knudsen, W. Shen, G. Carlson, J.S. Foster, K. Babcock, and S.R. Manalis, "Weighing of Biomolecules, Single Cells, and Single Nanoparticles in Fluid," *Nature*, Vol. 446, pg.1066, 2007.

[18] He, R.R., Feng, X.L., Roukes, M.L., & Yang, P.D, "Self-transducing silicon nanowire electromechanical systems at room temperature," *Nano Letters* 8, 1756-1761 (2008)..

## CONTACT

\*C.B. Burgner, tel: +1-714-313-1867; [cburgner@engr.ucsb.com](mailto:cburgner@engr.ucsb.com)

# 3D NEURAL PROBES WITH COMBINED ELECTRICAL AND CHEMICAL INTERFACES

Y. Li<sup>1</sup>, J. John<sup>1,2</sup>, X. Zhang<sup>3</sup>, J. Zhang<sup>3,4</sup>, J. A. Loeb<sup>2</sup> and Y. Xu<sup>1\*</sup>

<sup>1</sup>Electrical & Computer Engineering, Wayne State University, Detroit, MI

<sup>2</sup>Neurology and the Center for Molecular Medicine and Genetics, Wayne State University, Detroit, MI

<sup>3</sup>Department of Otolaryngology, Wayne State University, Detroit, MI

<sup>4</sup>Department of Communication Sciences & Disorders, Wayne State University, Detroit, MI

## ABSTRACT

This paper reports a novel neural probe technology that enables the manufacture of 3D arrays of electrodes and the integration of microchannels simultaneously. This new technology is based on a silicon island structure and a simple folding procedure. This method simplifies the assembly or packaging process of 3D neural probes, leading to higher yield and lower cost. Prototypes with 3D arrays of electrodes have been successfully developed. Preliminary animal tests have been carried out to verify the recording capability of the developed neural probes. Microchannels have been successfully integrated into 3D neural probes as well and the flow characteristic has been preliminarily measured.

## INTRODUCTION

Neural probes have played critical roles in developing an understanding of the function of neural networks within the brain, and have been implanted in different regions of the brain to study and treat many neural diseases and disorders. A variety of MEMS neural probes have been developed, including the well known Michigan probes and Utah electrodes [1-3].

There is an increasing need for 3D arrays of high-density electrodes because of the 3D nature of the nervous system. The 3D versions of Michigan probes were realized by microassembling multiple planar chips on a silicon platform with the help of vertical and horizontal spacers [4]. 3D neural probes were also constructed by stacking discrete 2D devices [5-6]. Polymer 3D electrode arrays were developed by bending the polymer shanks out of the plane [7-8]. The NeuroProbes consortium of the European Union reported a 3D technology by slotting planar 2D devices into cavities on a silicon backbone [9]. The electrical contact was made using gold clips hanging over the edge of the cavities.

Currently, electrical stimulation is the most common way of activating neurons. However, neural action potentials are more naturally triggered by the neurotransmitters released from presynaptic neurons. Neurotransmitters may be excitatory or inhibitory in postsynaptic neurons. On the contrary, electrical stimulation only excites the neurons it directly stimulates. There are also other problems associated with pure electrical stimulation. For example, electrical stimulation usually has wide spatial spread, leading to poor spatial resolution. The currents required to depolarize neurons are fairly large, which may cause degradation of metal electrodes and dissociation of water. These electrochemical reactions pose a serious risk of device failure and neuron damage. Many of these limitations could be overcome or circumvented by using more naturalistic chemical stimulation based on neurotransmitters.

Furthermore, it is widely recognized that tissue inflammation, biofouling, encapsulation, or death of neuron cells caused by the implanted neural probes are major obstacles for successful chronic implantation. One potential approach to address this problem is to deliver drugs to implantation sites using integrated microchannels [10-11]. Therefore, it is highly desirable to integrate microfluidic

channels with neural probes to deliver substances that reduce and even prevent the inflammation and biofouling associated with probe implantation.

There have been many efforts to integrate microchannels with electrodes. Solid state channels have been integrated with neural probes using anisotropic silicon etching, boron etch stop, and thermal oxidation/Low pressure chemical vapor deposition (LPCVD) sealing [12]. The integration of microfluidic channels with electrodes using wafer-bonding method has been reported [9]. K.I. Koo *et al.* presented single-unit neural probe containing in-plane shanks with buried microchannels [13]. A method of fabricating multielectrode arrays with integrated fluidic channels using silicon-on-insulator (SOI) wafers has also been developed [14]. However, it is very challenging to integrate channels into 3D arrays of electrodes.

In this paper, we demonstrated a novel technology of developing 3D neural probes based on a silicon island structure and a simple folding procedure. This technology brings several highly desirable features. First, it provides a simple and reliable method to fabricate and assemble high-density 3D arrays of electrodes. Second, this technology enables the integration of microchannels for chemical stimulation or local drug delivery to reduce tissue response. In addition, this technology allows the easy incorporation of a flexible cable between probe shanks and the interfacing die, which leads to very low-profile implants and helps to reduce the movement between brain tissue and probes [15]. These important features will make the developed devices a valuable tool for various neural prostheses and neural disorder studies/treatments.

## DESIGN

The new neural probe technology is schematically illustrated in Fig.1. First, planar devices consisting of multiple silicon islands are fabricated on a Si wafer using conventional MEMS technology and a flexible skin process [16]. In Fig. 1, the top two silicon islands are actually 2D neural probe devices, each of which carries a 2D electrode array and drug delivery ports. The electrodes and microchannels on different islands can be accessed by the bonding pads and inlet ports on the bottom silicon island. These silicon islands are connected by a parylene C layer, in which metal interconnects and microchannels are embedded. Parylene C is widely used for implantable devices due to its good biocompatibility. The planar devices are assembled into 3D probes by folding the two islands on top of each other. A spacer is inserted between these two silicon islands to adjust the distance between two rows of probes, as shown in Fig.1 (b). Compared with the stacking method utilizing discrete electrode arrays, the major difference here is the built-in interconnects between the 2D devices. Here we just show the folding of two silicon islands (which results in a 2×3×2 3D array of electrodes) for simplicity. More islands or denser electrodes can be integrated to make 3D arrays with larger dimensions. It is also worth noting that drug

reservoirs and micropumps can be integrated for on-chip drug delivery or chemical stimulation.

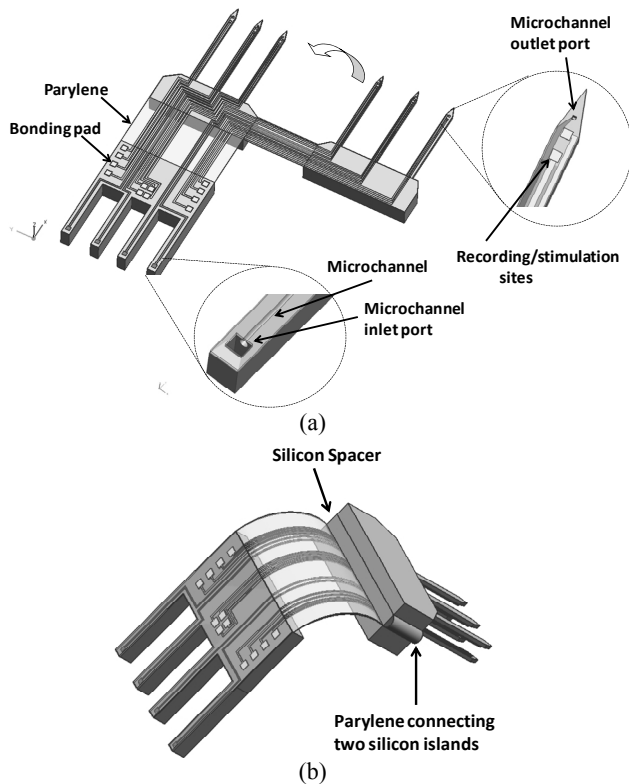


Figure 1: (a) Schematic of the planar device consisting of multiple silicon islands before folding. (b) the assembled 3D neural probe with a  $2 \times 3 \times 2$  array of electrodes (2 silicon islands, 3 shanks per island and 2 electrodes per shank) and integrated microchannels.

## FABRICATION PROCESS

The fabrication of the neural probe started with one double-side polished silicon wafer. First, a 200 nm  $\text{SiO}_2$  layer was grown using thermal oxidation, and then a 20 nm Cr thin film and a 200 nm Au thin films were sequentially deposited using E-beam evaporation. These two metal layers were then patterned to form electrical recording/stimulating sites, interconnects and bonding pads. The exposed  $\text{SiO}_2$  was subsequently removed by buffered HF (BHF). A 2  $\mu\text{m}$  thick parylene layer was deposited and patterned to open the access areas for the microchannels (including inlet ports and outlet ports).  $\text{XeF}_2$ , an isotropic gas phase silicon etchant, was then used to form trenches with semi-sphere cross sections in the silicon substrate. The parylene microchannels were formed and sealed in the next step by depositing another layer of parylene with a thickness greater than the half width of the opening. The parylene deposition is a very conformal process. Therefore, this parylene layer was able to deposit on the inside surfaces of the trench, forming the bottom and side walls of the parylene channels (Fig.2(c)). This parylene layer, together with the first one, was then patterned with a thick photoresist (AZ4620) mask. Next, DRIE was carried out from the front side of the Si wafer without stripping the photoresist mask. This etching was carried out to shape the outline of the probes and stops after the etching depth was about 150  $\mu\text{m}$  (Fig.2(d)). Next, DRIE etching was carried out on the backside of the wafer to release the silicon

islands and probe shanks. Due to the different etching depths of silicon islands and probe shanks, this DRIE etching was carried out using two masks. Note that the probes with only electrodes were fabricated by simply eliminating the microchannel processes, i.e.,  $\text{XeF}_2$  etching and parylene refilling.

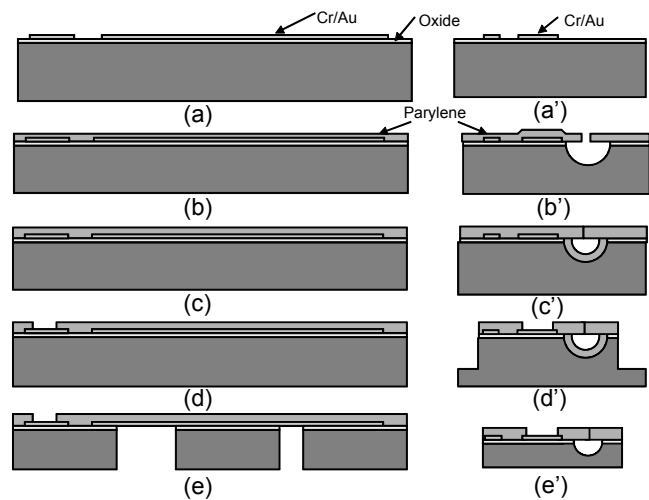


Figure 2: Simplified fabrication process of neural probes with integrated microchannels: (a) grow a thermal oxide layer; evaporate/pattern Au/Cr; (b) deposit and pattern a 2  $\mu\text{m}$  thick parylene C layer; etch with  $\text{XeF}_2$ ; (c) deposit the 2nd parylene C layer to seal the channel; (d) pattern parylene and continue with DRIE; (e) DRIE from back side to release the silicon islands and shanks. Left column: cross sectional view of silicon islands. Right column: cross sectional view of one probe shank.

## RESULTS AND TEST

Neural probes with different parameters have been designed and fabricated. Fig. 3(a) shows a photograph of one fabricated planar device with two shank islands and one interfacing island (with bonding pads). The fabricated probe shanks are 2800  $\mu\text{m}$  long, 100  $\mu\text{m}$  wide and 150  $\mu\text{m}$  thick. The open electrode area is  $40 \times 40 \mu\text{m}^2$ . The interfacing die is connected to the shank island with a flexible parylene cable, which leads to low-profile implants and reduction of micro-motion between probes and brain tissues. The assembled 3D neural probe with  $2 \times 3 \times 2$  array of electrodes is shown in Fig. 3(b). The folded parylene C layer connecting the Si islands can be clearly observed.

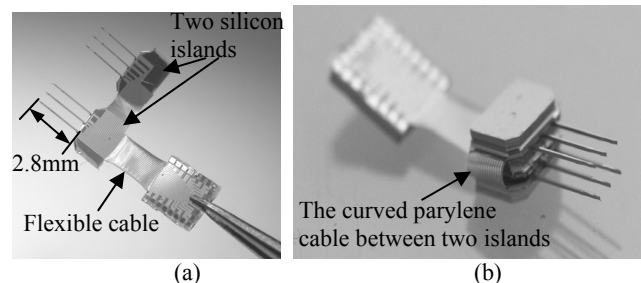


Figure 3: (a) Planar silicon islands structure before folding; (b) One assembled neural probe with  $2 \times 3 \times 2$  electrode array (2 silicon islands, 3 shanks per island, and 2 electrodes per shank).

3D neural probes with integrated microchannels have been demonstrated as well. A prototype with a  $2 \times 3 \times 2$  3D array of electrodes and four microchannels is shown in Fig. 4(a). The four

beams on the interfacing die are used to couple external tubing to on-chip microchannels. Figure 4(b) shows an SEM picture of a shank with two electrodes and two microchannel outlet ports. Note that both metal traces and microchannels are embedded in the flexible parylene cables. The SEM image of the backside of a bent parylene cable is shown in Fig. 4(c). The embedded microchannels and metal traces can be observed. No breaks or cracks were observed on the folded microchannels. The cross section of a microchannel is shown in Fig. 4(d). It is clearly seen that the microchannels are sealed completely by the thick parylene.

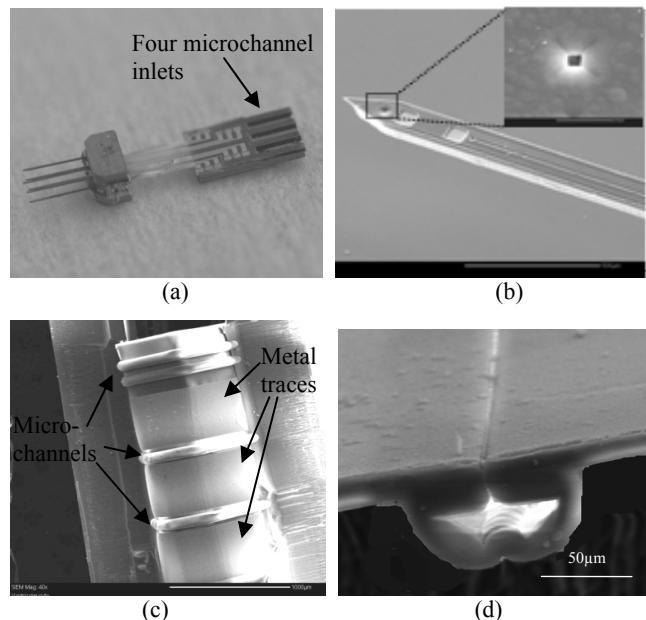


Figure 4: (a) Photograph of a neural probe device with a  $2 \times 3 \times 2$  3D array of electrodes (2 silicon islands, 3 shanks per island and 2 electrode per shank) and 4 integrated microchannels; (b) SEM image of a probe shank with 2 electrodes and 2 microchannels outlet ports (the inset shows a  $5 \mu\text{m} \times 5 \mu\text{m}$  outlet port); (c) SEM image of the backside of a bent parylene cable between two islands; (d) SEM image of the cross section of a parylene microchannel.

The electrode impedance was measured in diluted Phosphate Buffered Saline solution (PBS) with an HP 4284A Precision LCR meter. Pt wire was used as the counter electrode. The results for one electrode with a recording area of  $40 \times 40 \mu\text{m}^2$  are plotted in Fig. 5.

The microchannel flow rate was also measured using DI water. A flexible Microbore tubing (with an inner diameter of 620 microns) was coupled to the microchannel and then sealed using epoxy. A programmable syringe pump and digital pressure gauge were used for dispensing liquid and measuring pressure. No leaks were observed on the surface of the microchannels when DI water was pumped into the channel. The flow rate as a function of pressure applied was measured preliminarily and plotted in Fig. 6.

To preliminarily test the functionality of the developed arrays, one prototype has been acutely implanted in the primary auditory cortex of the rat. Figure 7 (a) shows clearly differentiated spikes from two neurons. Using unit sorter software, we were able to separate the spike activity from both neurons (Fig. 7 (b)).

The device was also acutely implanted into the somatosensory cortex of an adult rat. The rat was placed under general anesthesia using pentobarbital after which a craniotomy

was performed to expose the somatosensory cortex. The packaged neural probe device was then placed into the cortex of the animal via a stereotactic frame and the package was fixed in place with methyl methacrylate (dental cement). With the rat still under general anesthesia, the connector of the device package was joined with the connector of our Stellate EEG/ECOG recording system. As shown in Fig. 8, burst suppression-like neural signals associated with pentobarbital anesthesia were identified across all of the working channels, thereby verifying proper placement of the electrodes.

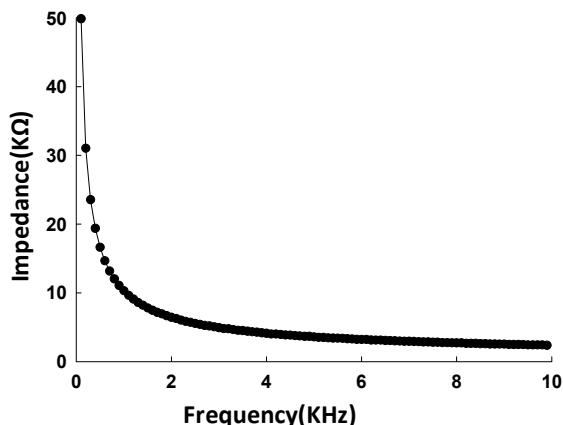


Figure 5: Impedance of one electrode ( $40 \times 40 \mu\text{m}^2$ ) on an assembled 3D neural probe

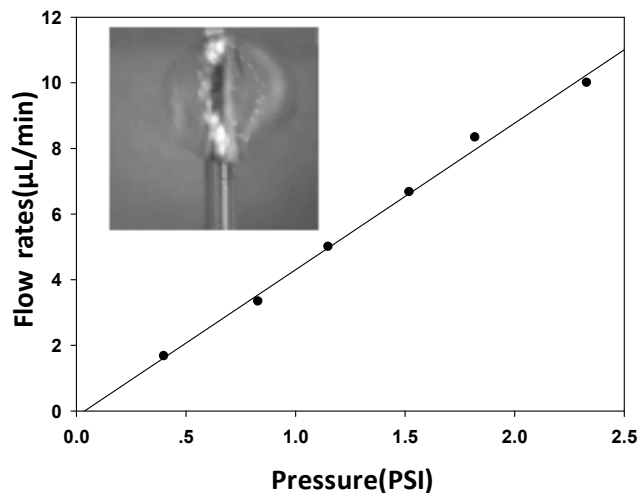
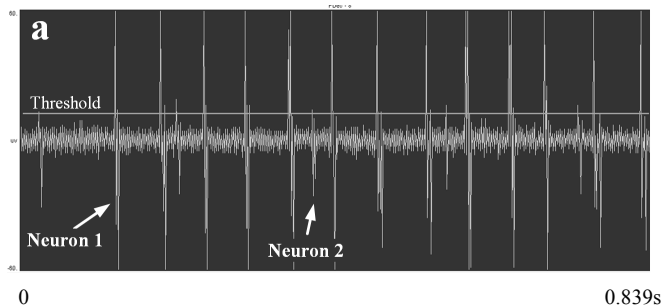


Figure 6: The measured relationship between flow rate and pressure. The inset picture shows a liquid droplet emerged from the outlet port of the microchannel at the probe tip.



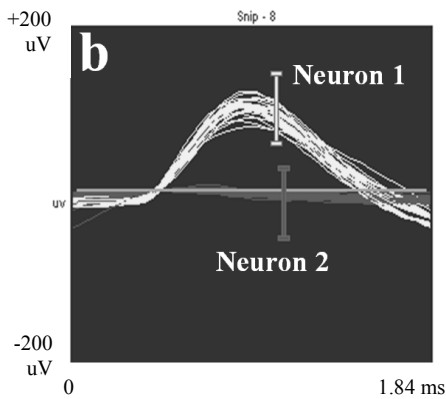


Figure 7: (a) Spikes from two neurons recorded from the primary auditory cortex of a rat. Note the difference in amplitude and spike rate between the two neurons. (b) The spikes from the two neurons were well differentiated using a unit sorter program.

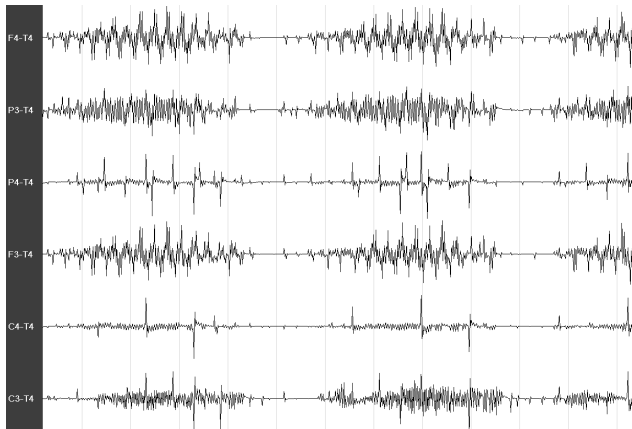


Figure 8: Acute field potential recordings of somatosensory cortex demonstrating burst suppression response associated with pentobarbital anesthesia.

## CONCLUSION

A novel neural probe technology based on a silicon island structure and a simple folding process is proposed and successfully demonstrated. This technology simplifies the fabrication and assembly process, leading to high density 3D arrays of electrodes with integrated micro-channels. These microchannels, together with electrodes, enable combined electrical and chemical stimulation, or local drug delivery, opening the door to many new applications. In addition, a flexible cable structure can be readily integrated to make low-profile implants and reduce micro-motion between the implant and tissues, improving the reliability. 3D neural probes with  $2 \times 3 \times 2$  electrode arrays and integrated microchannels have been fabricated and characterized. The electrical recording capability of the 3D neural probes has been preliminarily demonstrated by acute animal tests. The flow rate of the microchannel as a function of the pressure has been preliminarily characterized. The proposed neural probes are expected to make significant impacts in various neuroscience research and clinical applications.

## REFERENCES

[1] P. K. Campbell, K. E. Jones, R. J. Huber, K. W. Horch, and R. A. Normann, "A silicon-based, 3-dimensional neural

interface - manufacturing processes for an intracortical electrode array," *IEEE Transactions on Biomedical Engineering*. 38, 8 (1991).

- [2] K. D. Wise, "Micromachined interfaces to the cellular world," *Sensors and Materials*. 10, 6 (1998).
- [3] K. D. Wise, D. J. Anderson, J. F. Hetke, D. R. Kipke, and K. Najafi, "Wireless implantable microsystems: High-density electronic interfaces to the nervous system," *Proceedings of the IEEE*. 92, 1 (2004).
- [4] Y. Yao, M. N. Gulari, J. A. Wiler, and K. D. Wise, "A microassembled low-profile three-dimensional microelectrode array for neural prosthesis applications," *Journal of Microelectromechanical Systems*. 16, 4 (2007).
- [5] C. Pang, "Parylene technology for neural probes applications," Ph.D thesis, Electrical Engineering, California Institute of Technology, Pasadena, 2007.
- [6] D. R. Kipke, W. Shain, G. Buzsaki, E. Fetz, J. M. Henderson, J. F. Hetke, and G. Schalk, "Advanced Neurotechnologies for Chronic Neural Interfaces: New Horizons and Clinical Opportunities," *Journal of Neuroscience*. 28, 46 (2008).
- [7] P. J. Rousche, D. S. Pellinen, D. P. Pivin, J. C. Williams, R. J. Vetter, and D. R. Kipke, "Flexible polyimide-based intracortical electrode arrays with bioactive capability," *IEEE Transactions on Biomedical Engineering*. 48, 3 (2001).
- [8] S. Takeuchi, T. Suzuki, K. Mabuchi, and H. Fujita, "3D flexible multichannel neural probe array," *Journal of Micromechanics and Microengineering*. 14, 1 (2004).
- [9] P. Ruther, A. Aarts, O. Frey, S. Herwik, S. Kisban, K. Seidl, S. Spieth, A. Schumacher, M. Koudelka-Hep, O. Paul, T. Stieglitz, R. Zengerle, and H. Neves, "The NeuroProbes Project - Multifunctional Probe Arrays for Neural Recording and Stimulation," the 13th Annual Conf. of the IFESS, Freiburg, Germany, 2008.
- [10] J. L. Hendricks, J. A. Chikar, M. A. Crumling, Y. Raphael, and D. C. Martin, "Localized cell and drug delivery for auditory prostheses," *Hearing Research*. 242, 1-2 (2008).
- [11] S. T. Retterer, K. L. Smith, C. S. Bjornsson, K. B. Neeves, A. J. H. Spence, J. N. Turner, W. Shain, and M. S. Isaacson, "Model neural prostheses with integrated microfluidics: A potential intervention strategy for controlling reactive cell and tissue responses," *IEEE Transactions on Biomedical Engineering*. 51, 11 (2004).
- [12] J. K. Chen, K. D. Wise, J. F. Hetke, and S. C. Bledsoe, "A multichannel neural probe for selective chemical delivery at the cellular level," *IEEE Transactions on Biomedical Engineering*. 44, 8 (1997).
- [13] K. I. Koo, J. M. Lim, S. J. Paik, J. Park, S. Byun, A. Lee, S. Park, T. Song, H. M. Choi, M. J. Jeong, and D. I. D. Cho, "Multifunctional probe for chemical stimulation and neural signal recording," *Sensors and Materials*. 17, 2 (2005).
- [14] K. C. Cheung, K. Djupsund, Y. Dan, and L. P. Lee, "Implantable multichannel electrode array based on SOI technology," *Journal of Microelectromechanical Systems*. 12, 2 (2003).
- [15] J. F. Hetke, J. L. Lund, K. Najafi, K. D. Wise, and D. J. Anderson, "Silicon ribbon cables for chronically implantable microelectrode arrays," *IEEE Transactions on Biomedical Engineering*. 41, 4 (1994).
- [16] Y. Xu, Y.-C. Tai, A. Huang, and C.-M. Ho, "IC-integrated flexible shear-stress sensor skin," *Journal of Microelectromechanical Systems*. 12, 5 (2003).

## CONTACT

\*Y. Xu, tel: +1-313-577-3850; [yxu@ece.eng.wayne.edu](mailto:yxu@ece.eng.wayne.edu)

# LARGE AREA SPRAYING OF TERAHERTZ MATERIALS ON FREE-STANDING BIOCOMPATIBLE SILK FILMS

H. Tao<sup>1</sup>, J.J. Amsden<sup>1</sup>, A.C. Strikwerda<sup>1</sup>, K. Fan<sup>1</sup>, D.L. Kaplan<sup>2</sup>, F.G. Omenetto<sup>2</sup>, R.D. Averitt<sup>1</sup>, and X. Zhang<sup>1,\*</sup>

<sup>1</sup>Boston University, Boston, Massachusetts, USA

<sup>2</sup>Tufts University, Medford, Massachusetts, USA

## ABSTRACT

We report the first large area metamaterials patterned on free-standing biocompatible silk substrates using shadow mask evaporation techniques. The as-fabricated silk metamaterial composites show strong electromagnetic resonant responses at terahertz frequencies, providing a promising path to developing a new class of bioelectric and biophotonic devices.

## INTRODUCTION

The strongest natural fiber known, silk is favored by tissue engineers because it is mechanically tough but degrades harmlessly inside the body, offering new opportunities as a robust, bio-compatible and implantable material substrate [1]. To date, most of work has been focused on 2D or 3D patterning of the silk films to create biocompatible optical elements such as silk lenses and diffractive gratings [2]. It is desirable to incorporate resonant electromagnetic structures, such as metamaterials, with the silk films. Furthermore, silk fibroin has been proven to be a biologically favorable carrier that enables bio-dopants such as enzymes and proteins to maintain their functionality. This opens the door to a new class of biophotonic devices that could potentially be implanted into the human body to monitor interactions between specific targets and embedded dopants.

Metamaterials are resonant sub-wavelength electromagnetic composites typically consisting of highly conducting metals. Importantly, metamaterials provide the means to design and control both the effective electric permittivity ( $\epsilon$ ) and magnetic permeability ( $\mu$ ) [3]. The power of metamaterials lies in the fact that it is possible to construct materials with a user designed electromagnetic response (often not available with naturally occurring materials) at a precisely controlled target frequency [4], leading to novel electromagnetic responses which include, but are certainly not limited to, negative refractive index [5], perfect lensing [6], perfect absorbers [7, 8], and invisibility cloaks [9, 10].

This would enable hybrid silk-based sensors that couple bio-functionality with an easily measured electromagnetic response that changes in response to the local environment.

## FABRICATION

The microfabrication on silk films presents unique challenges in comparison to patterning on other widely used substrates such as silicon and PDMS. The main obstacle lies in that potential contamination caused by the conventional photolithography process would dramatically degrade the biocompatibility of the silk films.

### Biocompatible Silk Film Preparation

The typical preparation process of the silk films is shown in Fig. 1. It starts from the processing of silk cocoons, which are cut and cleaned (a), then boiled with sodium carbonate to extract the water soluble sericin (b), dissolved in lithium bromide (c), dialyzed against water to remove the lithium bromide (d) and filtered into a clear water-based silk solution. The silk solution (either undoped or doped with desired biodopants such as enzymes or proteins) is cast on a PDMS mold (e), then cured overnight (f) and detached after transition to the solid phase (g), yielding an optical transparent

bio-compatible silk film (h). The thickness could be controlled for various applications by controlling the coating & curing parameters. In this work, 80  $\mu\text{m}$  thick silk films are fabricated.

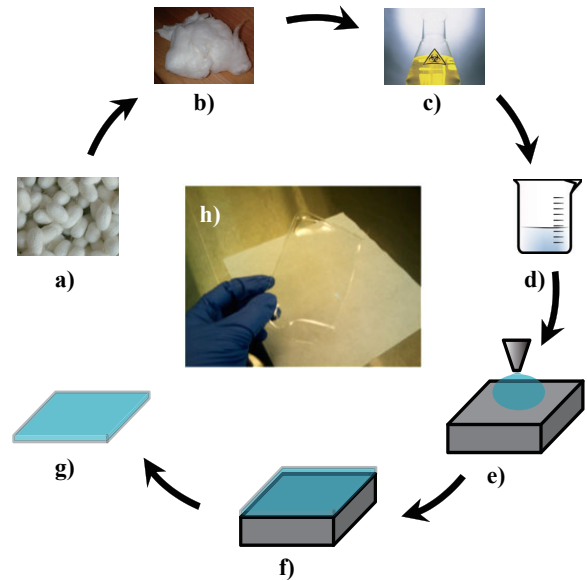


Figure 1: Silk film fabrication process.

### Directly Spraying of Metamaterials on Biocompatible Silk Substrates Using Shadow Mask Evaporation Technique

To prevent the contamination of the silk substrate while maintain its bio-compatibility, the silk films are prevented from exposing to any photoresist (PR) and chemical solutions such as acetone and PR developers, which are normally used for typical lift-off metal patterning process.

A shadow mask metal patterning fabrication process was therefore used in this work, as shown in Fig. 2. The shadow mask patterning is based on selective deposition of target material, i.e. gold in our case, through shadow mask, namely micro stencils. The micro stencils with desired metamaterial patterns were fabricated using a 4" silicon wafer with 400nm thick LPCVD pre-deposited silicon nitride film on both sides. The split ring resonators (SRRs), widely used as the canonical metamaterial elements, were patterned using lithography and RIE on the top side. Open windows were patterned on the backside and then etched through in KOH solution to release the structure. Then the micro stencils were attached to the silk films in contact mode, followed by E-beam evaporation of 100nm thick gold. The whole evaporation process was controlled under 40°C, a safe temperature for maintaining the silk quality.

The as-fabricated free-standing samples show good uniformity and mechanical robustness and flexibility, which allow being wrapped into a capsule-like cylinder with a diameter of  $\sim 3$  mm with no distortion or cracking observed, as shown in Fig. 3 & 4.

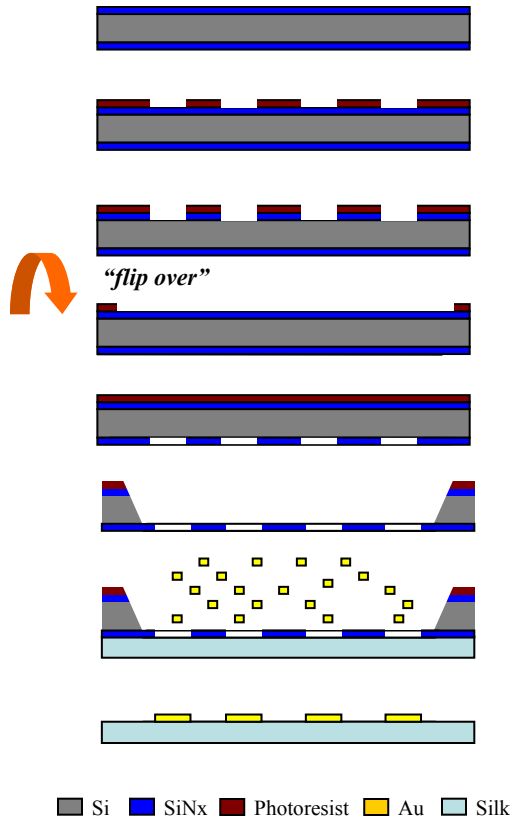


Figure 2: Fabrication process of directly spraying metamaterial structures on silk substrates.

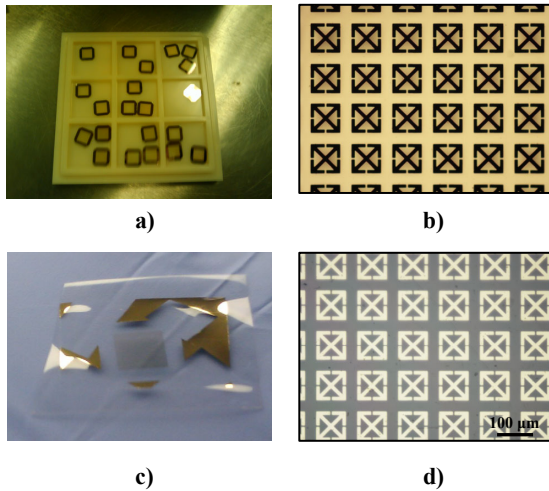


Figure 3: a) Photo of micro metamaterial stencils; b) microscopy photo of one portion of as-fabricated stencil; c) photo of as-fabricated THz silk metamaterials; d) microscopy photo of one portion of as-fabricated metamaterial array.

The entire fabrication process is conducted in a dry, chemical-free environment preventing any possible contamination that might be involved in other photolithography based metal patterning methods such as lift-off processes and wet etching. Our approach thereby helps to maintain the integrity and

biocompatibility of the silk films.



Figure 4: A wrapped "capsule" made of the THz metamaterials patterned on silk films.

## CHARACTERIZATION

Terahertz time-domain spectroscopy (THz-TDS) was used to characterize the electromagnetic response of the metamaterial silk composites. The measurements were performed at room temperature in a dry (< 0.1% humidity) air atmosphere. The transmission of the THz electric field was measured for the sample and a reference, which in the present case is simply air. The electric field spectral amplitude and phase were then calculated through Fourier transformation of the time-domain pulses. The spectral transmission was obtained by dividing the sample by the reference, as shown in Fig. 5.

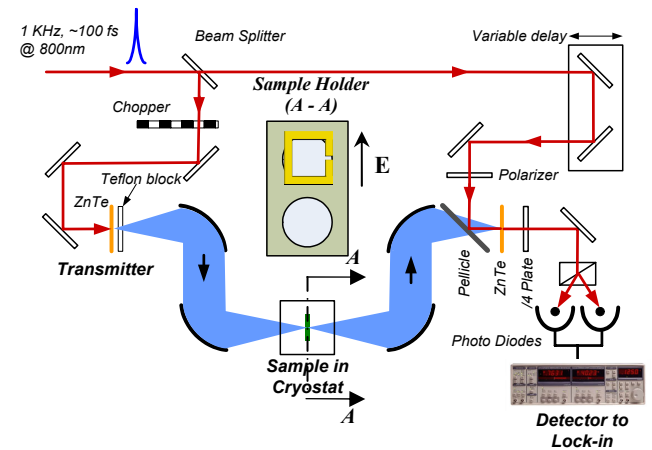


Figure 5: THz Time Domain Spectroscopy (THz-TDS) setup for the metamaterial sample performance characterization. (Top hole: sample; bottom hole: reference/air.)

THz-TDS measurement was first carried out on a series of 80  $\mu\text{m}$  thick pure silk films, which show high field transmission of  $\sim 60\%$  of terahertz radiation from 0.15 THz to 1.5 THz, as shown in Figure 2a. The refractive index of the silk films ( $n=1.91+i0.12$ , from 0.15 THz to 1.5 THz) was then experimentally determined using standard approach described in previous publications, as shown in Fig. 6.

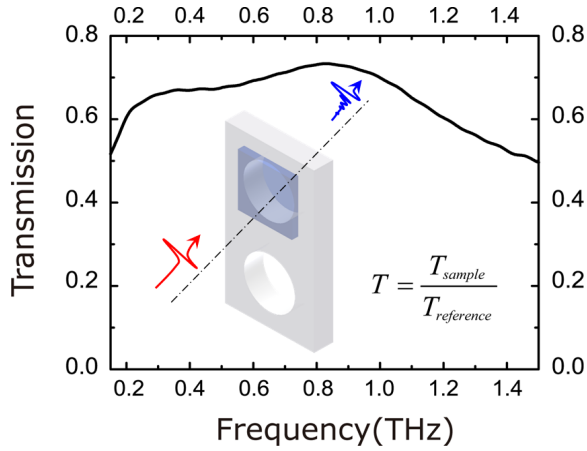


Figure 6: THz-TDS measured transmission spectrum of an 80 micron thick pure silk film without metamaterials.

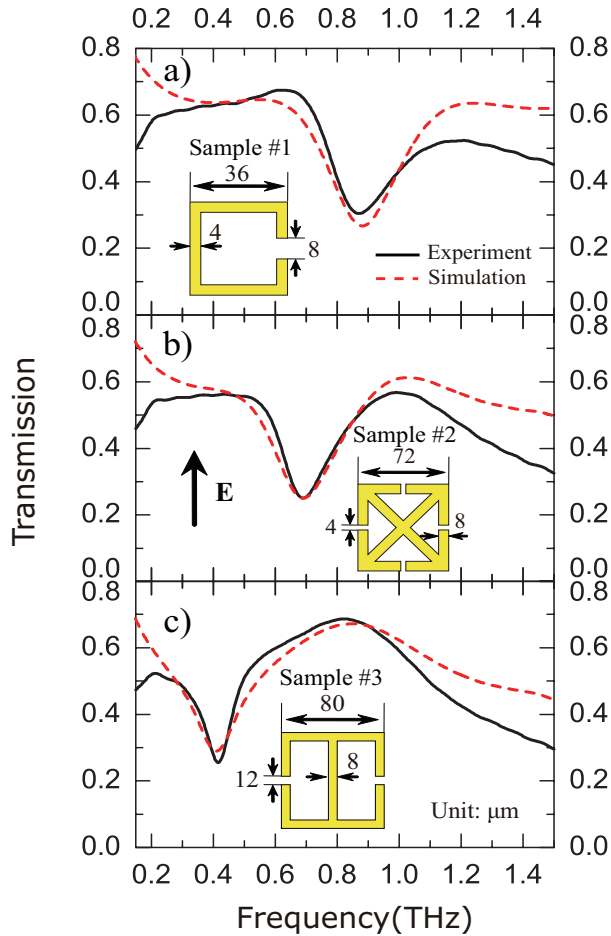


Figure 7: Experiment and simulation results of THz silk metamaterials, showing strong resonance "fingerprints" in transmission spectrum.

While numerous samples were fabricated and characterized with THz-TDS, we focus on three of samples that include the canonical split ring resonators (#1, single SRR) and purely electric resonators (#2, polarization non-sensitive electric resonator and #3, polarization sensitive electric resonator). Sample #1 has a unit cell

size of  $50 \mu\text{m} \times 50 \mu\text{m}$ , and samples #2 & #3 have a unit cell of  $100 \mu\text{m} \times 100 \mu\text{m}$ . The samples were diced into  $1 \text{ cm} \times 1 \text{ cm}$  squares and mounted at normal incidence to the THz beam with the electric field perpendicular to the SRR gap.

As shown in Fig. 7, sample #1 has a resonance at 0.85 THz, which is, as expected from simulations, higher than the resonance frequencies of sample #2 at 0.7 THz and sample #3 at 0.4 THz which have larger unit cells. The experimental results are in reasonable agreement with the simulation data, though noticeable off-resonance disagreement occurs consistently in all three samples, which may arise partly from fabrication imperfections and surface roughness of the samples. All of the samples display strong resonances comparable to those measured on semiconducting and polymer substrates. We note that these resonances are associated with the LC resonant response that arises from circulating currents driven by the electric field that is aligned perpendicular to the SRR gap. That is, the resonant changes in transmission correspond to an effective permittivity.

## DISCUSSION

The SRR, which was used for constituting metamaterials in this work, can be thought of as an LC resonator in a simple representation with a resonance frequency of  $\omega \sim (1/LC)^{1/2}$ , where the inductance (L) results from the current path of the SRR and capacitance (C) is mainly determined by the split gap. Any change in the capacitance or the inductance will result in a change in the resonant response making metamaterials sensitive to the local environment. Therefore, metamaterials would offer an interesting option for integration with silk films for novel sensing and detection applications by providing a natural and potentially biologically active material matrix as the support for the SRR.

The shadow mask evaporation technique as used in this work has stringent requirements on the flatness of the substrates upon which materials are to be deposited. This approach is quite suitable for silk films because the silk substrates exhibit sufficient flatness over large areas resulting from the all-aqueous processing of the protein. This facilitates direct spraying of large area metallic and/or non-metallic patterns with good uniformity onto the silk films. The fabrication process could be readily adopted to fabricate silk metamaterials at other frequencies from the microwave to visible. For example, the technique for making the micro stencils could be easily modified for making nano stencils by switching from standard UV photolithography to electron-beam writing for much smaller features down to tens of nanometers. For isolated patterns with no connecting paths to the stencil supporting frame such as features inside other closed patterns that are difficult to directly deposit in contact mode, it will be possible to use appropriate compensation strategies. The flexibility offered using large area stencil-based deposition in conjunction with available soft fabrication techniques for processing silk films provides a promising path to developing novel flexible electronics on silk substrates.

## SUMMARY

In conclusion, we provide a methodology to fabricate metamaterial structures on silk substrates showing strong resonances at desired frequencies, which opens opportunities for new bio-photonics applications including in vivo bio-tracking, bio-mimicking, implantable biosensor and biodetectors. Furthermore, our results are not limited only to THz frequencies but may be used over much of the electromagnetic spectrum. Basic technologies are already in place, it's simply a matter of designing the right moulds.



## ACKNOWLEDGEMENTS

We acknowledge partial support from NSF under Contract No. ECCS 0802036, AFOSR under Contract No. FA9550-09-1-0708, DARPA under Contract No. HR0011-08-1-0044, and DOD/Army Research Laboratory under Contract No. W911NF-06-2-0040. This material is based upon work supported in part by the U.S. Army Research Laboratory and the U.S. Army Research Office under Contract No. W911 NF-07-1-0618 and by the DARPA-DSO. The authors would also like to thank the Photonics Center at Boston University.

## REFERENCES

- [1] F.G. Omenetto and D.L. Kaplan, "A New Route for Silk", *Nature Photonics*, 2, 2008.
- [2] J.J. Amsden, P. Domachuk, A. Gopinath, R. White, D.L. Kaplan, L. Dal Negro, and F.G. Omenetto, "Rapid Nanoimprinting of Silk Fibroin Films for Biophotonics Applications," *Advanced Material*, 22, 2010.
- [3] D.R. Smith, W.J. Padilla, D.C. Vier, S.C. Nemat-Nasser, and S. Schultz, "Composite Medium with Simultaneously Negative Permeability and Permittivity", *Physical Review Letters*, 84, 2000.
- [4] C.M. Bingham, H. Tao, X. Liu, R.D. Averitt, X. Zhang, and W.J. Padilla, "Planar Wallpaper Group Metamaterials for

- Novel Terahertz Applications", *Optics Express*, 16, 2008.
- [5] R.A. Shelby, D.R. Smith, S. Schultz, "Experimental Verification of a Negative Index of Refraction", *Science*, 292, 2001.
- [6] J.B. Pendry, "Negative Refraction Makes a Perfect Lens", *Physical Review Letters*, 85, 2000.
- [7] N.I. Landy, S. Sajuyigbe, J.J. Mock, D.R. Smith, and W.J. Padilla, "Perfect Metamaterial Absorber", *Physical Review Letters*, 100, 2008.
- [8] H. Tao N.I. Landy, C.M. Bingham, X. Zhang, R.D. Averitt, and W.J. Padilla, "A Metamaterial Absorber for the Terahertz Regime: Design, Fabrication and Characterization", *Optics Express*, 16, 2008.
- [9] R. Liu, C. Ji, J.J. Mock, J.Y. Chin, T.J. Cui, and D.R. Smith, "Broadband Ground-Plane Cloak", *Science*, 323, 2009.
- [10] D. Schurig, J.J. Mock, B.J. Justice, S.A. Cummer, J.B. Pendry, A.F. Starr, D.R. Smith, "Metamaterial Electromagnetic Cloak at Microwave Frequencies", *Science*, 314, 2006.

## CONTACT

\*X. Zhang, tel: +1-617-358-2702; xinz@bu.edu

# POLYCRYSTALLINE DIAMOND-ON-POLYMER MICROELECTRODE ARRAYS FOR MECHANICALLY-FLEXIBLE NEURAL INTERFACING

A. Hess<sup>1</sup>, D.M. Sabens<sup>2</sup>, H.B. Martin<sup>2</sup>, and C.A. Zorman<sup>1</sup>

<sup>1</sup>Department of Electrical Engineering and Computer Science, Case Western Reserve University

<sup>2</sup>Department of Chemical Engineering, Case Western Reserve University, Cleveland, Ohio, USA

## ABSTRACT

This paper reports the development of mechanically-flexible, polycrystalline diamond-on-polymer electrodes for use as neural interfaces. Boron-doped diamond has a number of properties that are attractive for use as electrodes in neural recording, stimulation, and electrochemical sensing. However, because the growth of polycrystalline diamond by chemical vapor deposition requires high temperatures (>800°C), diamond thin films cannot be directly deposited on polymer substrates. To address this limitation, a transfer process was developed to incorporate diamond electrodes onto a polymer substrate. It was demonstrated that the diamond-on-polymer devices made using this transfer process retain the mechanical properties of the polymer. Electrical characterization showed that the diamond electrodes have an impedance of ~2-3 MΩ at 1 kHz. This and other tests indicate that the diamond-on-polymer electrodes have suitable characteristics for neural recording and stimulation.

## INTRODUCTION

Microelectrode arrays for neural stimulation and recording at single and multiple contact points have been successfully fabricated on both silicon and polymer substrates. Flexible polymer substrates offer the advantages of conformability to peripheral neural structures and reduced strain on cortical tissue due to movement [1]. Common electrode materials include gold, platinum, tungsten, titanium nitride, and iridium oxide [2]. These conductive materials are typically deposited by sputtering or evaporation, allowing for straightforward monolithic processing with most substrates, especially temperature-sensitive polymers.

Polycrystalline, boron-doped diamond is an alternative electrode material that has been successfully used for both neural recording [3,4] and stimulation of single neurons [3]. Diamond is also an exceptional electrochemical sensing material, capable of detecting neurotransmitters, such as dopamine and serotonin. The release of these molecules is one way in which neurons communicate. As such, *in-situ* monitoring of these chemicals is highly desirable.

The distinctive set of properties that make diamond a particularly good electrode are due to its structure and unique surface chemistry. Diamond is a mechanically robust, hard and stiff material with a Young's modulus of ~1000 GPa arising from its sp<sup>3</sup> C-C bonding structure [7]. Diamond is also chemically stable, as evidenced by its resistance to corrosion, which ensures that it will not degrade in the biological environment and that its surface will not become contaminated by fouling [8]. Diamond's wide potential water window (-1.25/+2.3 V) [9] is advantageous for stimulation applications because it permits larger electrode potential excursions without hydrolyzing water and potentially damaging both neural tissue and the electrode itself. Further, the wide water window enables a larger number of analytes to be detected and studied using electrochemical techniques [9]. A high analyte sensitivity for electrochemical sensing is provided by diamond due to its low background current [3,9].

Chemical vapor deposition (CVD) is the typical method used to grow polycrystalline diamond. CVD generally requires the substrate to be exposed to temperatures >800°C. Diamond

electrodes have previously been grown on high temperature substrates like tungsten wires [3] and silicon wafers [4]. Unfortunately, polymers are incompatible with the high temperatures required for microcrystalline diamond growth, preventing direct monolithic processing of boron-doped, polycrystalline diamond electrodes on a polymer substrate. To address this issue, we have developed a novel "diamond-first" fabrication process to create diamond-on-polymer structures suitable for mechanically-flexible, polycrystalline diamond-based, neural microelectrode arrays capable of recording and stimulation, as well as electrochemical recording.

## DEVICE FABRICATION

To enable the integration of diamond electrodes onto a polymer substrate, the transfer process shown in Figure 1, in which the diamond components are grown on a Si handle substrate prior to incorporating thermally-sensitive polymers in the fabrication sequence, was used. This allows the diamond growth process to be performed at preferred temperatures, enabling high quality diamond growth without damaging the polymer layers.

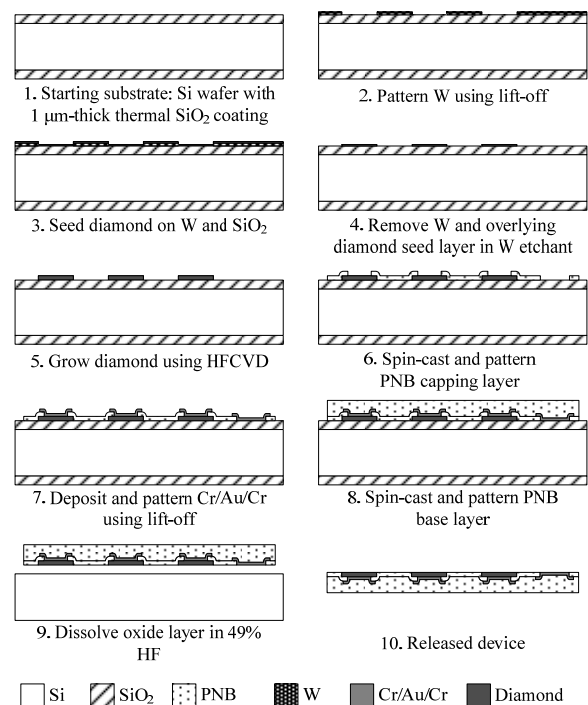


Figure 1: Cross-sectional views of the diamond on polymer electrode array fabrication process

The process begins with the selective growth of diamond thin films. In specific, a 1 to 2 μm-thick boron-doped diamond layer was selectively grown on a 3" Si wafer coated with a 1 μm-thick thermal SiO<sub>2</sub> film. A metal template defining the diamond electrodes was patterned on the SiO<sub>2</sub> by first spin-casting and patterning a 1.3 μm-thick Shipley 1813 photoresist film. Next, a

100 nm-thick tungsten layer was sputter-deposited and patterned using a lift-off process in acetone with ultrasonic agitation. The wafer was then seeded by sonication in 50mL of deionized water containing 20 mg of 1 to 2  $\mu\text{m}$  diamond powder, followed by sonication-aided cleaning in pure ethanol. The wafer was then loaded into a hot filament chemical vapor deposition (HFCVD) reactor for a two hour growth process. The filament temperature was 2000°C, as measured by dual emission optical pyrometry. Pressure was held at 20 Torr with flow rates of 196 sccm, 1.8 sccm and 4 sccm for hydrogen, methane and 0.01% trimethylboron in hydrogen, respectively. After the initial growth phase, samples were removed and exposed to a tungsten etch (10% sulfuric acid, 10% hydrogen peroxide in water). After etching, samples were cleaned using a two step sonication process, first in ethanol followed by acetone. The wafer was loaded into the reactor for an additional 4 hours of HFCVD under the conditions described above to selectively grow diamond to a thickness of 1 to 2  $\mu\text{m}$ . In this final CVD step, diamond growth was limited to the areas with an established diamond seed layer. Diamond does not grow in the field region that had been coated with tungsten.

Next, the first of two polymer layers was processed on the wafer. A 1  $\mu\text{m}$ -thick polynorborene (PNB) “capping” layer was spin-cast at 1000 rpm for 30 seconds and soft-baked for 5 minutes at 120°C on a hotplate. The capping layer was then patterned with UV radiation (365 nm) at a dose of 288 mJ, followed by a post-exposure bake for 4 minutes at 90°C on a hotplate. The capping layer was spray-developed at 2000 rpm using methyl n-amyl ketone (MAK) for 5 seconds and rinsed using PGMEA for 5 seconds. The layer was then cured in a furnace at 160°C for 1 hour.

Following the capping layer formation, metal interconnects and connector contact pads were patterned using a lift-off process. A 3.5  $\mu\text{m}$ -thick layer of AZ nLOF 2035 negative-tone photoresist was spin-cast, soft-baked at 110°C for 60 seconds, and defined by 365 nm UV radiation at a dose 80 mJ. The resist was then baked at 110°C for 60 seconds and immersion-developed for 2 minutes in AZ 300 MIF. A three-layer metal combination consisting of 20 nm-thick Cr/250 nm-thick Au/20 nm-thick Cr was then sputter-deposited and patterned with lift-off. The lift-off step was performed in AZ EBR 70/30 with ultrasonic agitation to dissolve the photoresist and remove all excess metal. The two Cr layers serve to promote adhesion between the Au layer and the polymer films. Prior to metal deposition, the PNB capping layer was exposed to a 90 second RF pre-clean step to improve metal-polymer adhesion.

Deposition of the “base” polymer layer comprises the final structural layer of the fabrication process. A 50  $\mu\text{m}$ -thick PNB layer was spin-coated at 800 RPM for 10 seconds, then 1000 RPM for 30 seconds. The base layer was then soft-baked on a hotplate for five minutes at 120°C, then defined using i-line UV light at a dose of 2000 mJ. The film was then baked on a hotplate at 90°C for 4 minutes, then spray-developed for 90 seconds with MAK rinsed with PGMEA. Finally, the base layer was cured in a furnace at 160°C for 1 hour.

The devices were released from the wafer by dissolving the SiO<sub>2</sub> sacrificial layer in 49% HF, exposing the diamond electrode pads from below the polymer and metal layers. The release was performed by applying HF droplets first to the diamond electrode end of the device, then to the device shank, and finally to the connector end of the device. This droplet technique allowed for controlled device removal from the wafer, avoiding damage due to incomplete release at the electrode end of the devices.

In the transfer of the diamond electrodes from the Si substrate to the polymer substrate, the nucleation surface of the diamond becomes the exposed top surface of the electrode, while the growth surface becomes the interface to the metal interconnects. To the

best of our knowledge, this is the first time that the nucleation surface has been used as a diamond electrode.

## DEVICE DESIGN

A commercially-available, PNB-based polymer (Avatrel™ 2585P) was chosen as the substrate and capping layers of the diamond-on-polymer devices. Avatrel™ is attractive because it is spin-castable, photodefinable, and is resistant to moisture absorption and the wet chemical etchants typically used in microfabrication processes. Spin casting allows the solution-based polymer to conform to the diamond sidewalls and faceted growth surface prior to curing, and the chemical resistance ensures device survival during the HF-based release step. The fabrication process is not limited to PNB for the base and capping layers, but does require a material that can conform to the diamond to ensure good adhesion between diamond electrodes and transfer substrate, and survive the release step.

Devices designed for two distinct neural interface applications were fabricated using the diamond transfer technique. A cortical-probe style structure is shown in Figure 2. These devices are designed to be inserted directly into the cortex. These devices have two diamond contacts: an oval electrode with an area of 224  $\mu\text{m}^2$ , and a triangular electrode 1644  $\mu\text{m}^2$  in area. The electrodes are near the tip of a 2 mm-long, 50  $\mu\text{m}$ -wide shank. Windows through the capping layer expose two large metal contact pads on the 1 x 1 mm<sup>2</sup> tab at the back-end of the device. Connection to external electronics can be made through a wired connection to these pads via conductive epoxy or wirebond. Metal traces 10  $\mu\text{m}$  in width connect the diamond electrodes to the contact pads. A via in the capping layer under the diamond electrode enables contact between the diamond electrode and underlying metal trace.

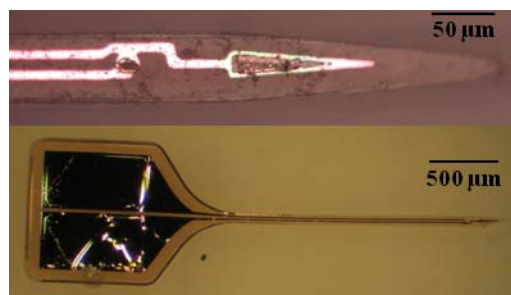


Figure 2: Plan view images of a diamond-on-polymer penetrating cortical probe: (top) close-up of diamond electrodes; (bottom) global view.

The second design, shown in Figure 3, represents a much larger device, better suited for surface contact interfacing with peripheral nerves. Each array is comprised of ten 64 x 64  $\mu\text{m}^2$  diamond electrodes at one end, ten corresponding metal contact pads on the other end, with a flexible shaft approximately 2.7 cm in length and 1.3 mm in width to support ten 30  $\mu\text{m}$ -wide metal traces connecting the two ends. Vias in the capping layer underneath the diamond electrodes define the metal-diamond contact area. The connector end is designed to interface with a commercial flexible circuit connector (Hirose™ FH-19).

A variation of the second design (not shown) has been developed for applications requiring an electrode with a large surface area. Due to the rigidity of the diamond films, flexing would induce cracking in large diamond electrodes. Therefore, the larger electrodes were divided into ten electrically connected diamond segments, with each segment consisting of one 64 x 64  $\mu\text{m}^2$  diamond pad and 64  $\mu\text{m}$  separating the diamond segments.

The effective area of the electrode is thus increased by a factor of ten, while retaining the flexibility of the device.

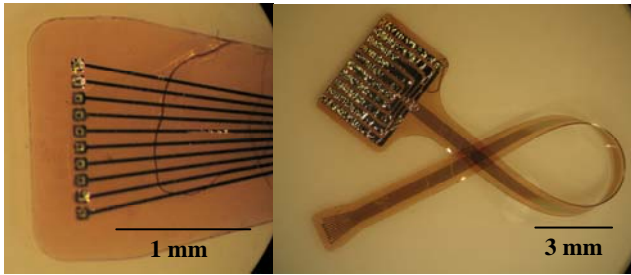


Figure 3: Completed diamond electrode array: (left) close-up of the diamond electrode array with associated metal interconnects; (right) global view showing the flexibility of the device

### MECHANICAL CHARACTERIZATION

The mechanical durability of the diamond-on-polymer structures was investigated using the devices shown in Figure 4. Flexibility was demonstrated through the use of the dog-bone-shaped structures, which included eight  $100\ \mu\text{m}$ -diameter diamond electrodes equally distributed along the length of the beam. The devices were wrapped around a cylinder with a radius of  $\sim 650\ \mu\text{m}$  and observed for delamination or cracking as a result of the flexing. No deformation of the diamond or polymer was detected, indicating that the flexibility of the polymer substrate was preserved.



Figure 4: (left) Dog-bone structure with embedded diamond electrodes, and (right) flexed structure.

Further mechanical characterization was performed using a custom-built microtensile tester described in detail in [9]. One pad of the dog-bone structure was placed in a grip that was mounted to a linear piezomotor drive rod, while the other pad was held in a fixed position. As the beam was stretched by movement of the piezomotor, the strain induced in the sample was measured using a digital indicator, and the force on the beam was measured with a load cell. The motor, indicator, and load cell were all computer-controlled using data acquisition software.

Devices with eight  $100 \times 100\ \mu\text{m}$  square diamond pads along the length of the beam were tested using the microtensile tester by pulling to fracture, and results were compared to the stress-strain plots from PNB-only samples. It was found that the Young's modulus, as determined by the slope in the linear region of the stress-strain plot, of the samples with diamond closely matched that of the PNB-only sample, which was  $\sim 800\ \text{MPa}$ . This value is consistent with the reported value of Young's modulus for Avatrel™ 2585P. The stress-strain curve for the device with diamond pads is shown in Figure 5. It can be seen that the device remains in the elastic region until approximately 2.4% strain, at

which point the elastic limit is reached. The device broke under a stress of  $39.5\ \text{MPa}$  at a strain of 17.4%, which is consistent with the tensile results from the PNB-only samples.

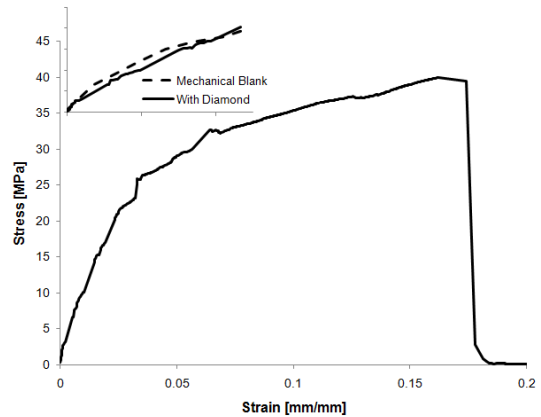


Figure 5: Stress-strain tensile plot for PNB tensile device with eight  $100 \times 100\ \mu\text{m}^2$  diamond contacts down the length; (inset) comparison of slope of sample with diamonds to PNB-only sample.

The inset in Fig. 5 shows that in the linear regime, the diamond-based device behaves very similarly to a polymer-only device in terms of stiffness. Although the Young's modulus of diamond is very high ( $\sim 1000\ \text{GPa}$ ), and the Young's modulus of the polymer is several orders of magnitude lower, the small diamond segments spaced relatively far apart allow the overall device to retain its flexibility and behave as a low-modulus structure. Further, upon breaking, the devices were inspected under an optical microscope. No evidence of diamond cracking or delamination was observed, suggesting that even at a strain of 17.4%, the adhesion between the diamond and polymer was strong.

### ADHESION

Adhesion of the diamond to the polymer substrates was evaluated using a qualitative adhesive-tape test. A piece of pressure-sensitive tape was pressed onto a tensile device with eight diamond electrodes, similar to the devices in Figure 4. The tape was then pulled up from the device, and both the tensile structure and tape were inspected. No delamination of the diamond pad from the polymer substrate was seen. The tape test was also performed on metalized diamond-based structures. It was observed that some of the metal was transferred to the tape, indicating that the adhesion between the metal and polymer is not as strong as between the polymer and diamond, indicating that a method to improve adhesion between the metal and base polymer is required.

### ELECTRICAL CHARACTERIZATION

Electrical testing was performed in solution to evaluate the quality of the diamond electrodes as well as the integrity of the metal/diamond interfaces. Impedance spectra for a cortical electrode and a single square electrode from one of the 10 electrode arrays are shown in Figure 6. The electrode impedance at 1 kHz is an important indicator of the ability of the electrode to record neural signals. The cortical electrode had an impedance of  $2.8\ \text{M}\Omega$ , and the array electrode had an impedance of  $2.3\ \text{M}\Omega$  at 1 kHz. These data are comparable to Au electrodes used in neural recording [10], suggesting that the inverted diamond electrodes would be able to record neural action potentials. Compared to Au electrodes, the impedance is relatively independent of frequency, resulting from the dominant resistive component of the impedance at low frequencies. A high-resistance metal-diamond contact or the

diamond nucleation surface contributing to a low capacitance at the electrode-electrolyte interface may lead to the large resistive component of the electrode impedance.

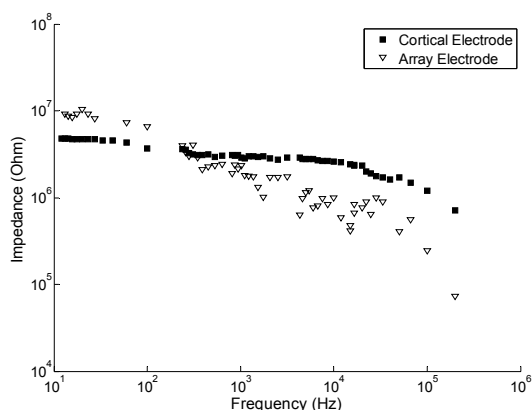


Figure 6: Impedance spectrum of a diamond-on-polymer electrode structure.

The electrodes were characterized for neurostimulation by applying charge-balanced, biphasic 1 mA, 100  $\mu$ s current pulses generated by a multichannel stimulator at 5 Hz, similar to those used in clinical prosthetic applications. A typical measured response for a single, 64 x 64  $\mu$ m<sup>2</sup> electrode is shown in Figure 7. The electrode voltage is superimposed onto the input signal as measured across a 1 k $\Omega$  resistor. The voltage drop was approximately 7 V, which corresponds to an electrode resistance of  $\sim$ 7 k $\Omega$  for a 1 mA signal. The access voltage was measured to be approximately 4.2 V and the electrode-electrolyte polarization is 2.8 V at a current density of 24 A cm<sup>-2</sup>. The ability to charge, and then discharge, the electrode-electrolyte interface and remain within the compliance voltage of the stimulator suggests that these electrodes can be used for neurostimulation applications.

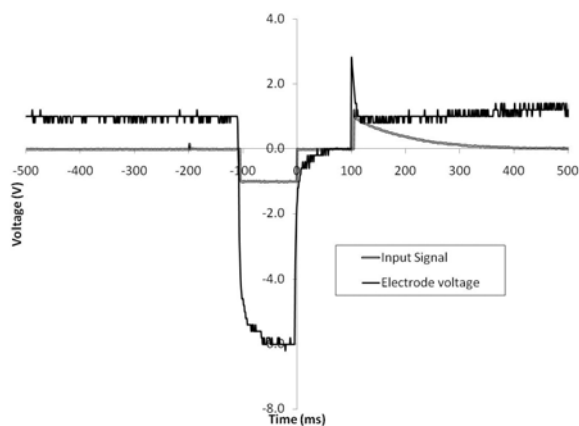


Figure 7: Voltage waveform recorded from diamond electrode during biphasic current pulse testing.

## ELECTROCHEMICAL CHARACTERIZATION

Cyclic voltammetry was used to evaluate the use of the diamond-on-polymer electrodes for electrochemical sensing. It was found that there is a significant resistance inherent in the system, greatly reducing the sensitivity of the diamond as a sensor. There are a number of possible causes of the high resistance. The highly disordered nucleation surface of the diamond may be inappropriate for electrochemical sensing, or may be inadequately doped for good signal transduction. Alternatively, the contact resistance

between the metal and diamond may be too high. Because the first polymer layer enters the fabrication process prior to metal deposition, an anneal step cannot be performed without modifying the fabrication process.

## CONCLUSION

Mechanically-flexible, microfabricated, polycrystalline diamond-on-polymer electrode arrays have been fabricated using a novel transfer technique that avoids the problems associated with high-temperature diamond growth. Cortical probe electrodes and larger electrode arrays were fabricated to demonstrate the application of the fabrication process to a range of sizes and geometries. Mechanical testing has shown that the diamond-on-polymer structures are flexible despite the integration of the highly rigid diamond electrodes. Electrical characterization suggests that these electrodes may be useful in neural recording and stimulation applications. Further investigation is required to determine whether the inverted diamond electrodes can be used for chemical sensing.

## ACKNOWLEDGEMENTS

This work was funded by grants from NIH (EB004018) and NSF (CTS 0449098) and (ECS 0621984). The authors thank Promerus, Inc. of Brecksville OH for providing Avatrel<sup>TM</sup>.

## REFERENCES

- [1] S.F. Cogan, "Neural Stimulation and Recording Electrodes", Annual Review of Biomed. Engineering, 10 (2008) 275-309.
- [2] H-Y Chan, D.M. Aslam, J.A. Wiler, B. Casey, "A Novel Diamond Microprobe for Neuro-chemical and -Electrical Recording in Neural Prosthesis", JMEMS, 18 (2009) 511-522.
- [3] H.B. Martin, A. Argoitia, U. Landau, A.B. Anderson, J.C. Angus, "Hydrogen and Oxygen Evolution on Boron-Doped Diamond Electrodes", J. Electrochem. Soc., 143 (1996) L133-L136.
- [4] J.M. Halpern, S. Xie, G.P. Sutton, B.T. Higashikubu, C.A. Chestek, H. Lu, H.J. Chiel, H.B. Martin, "Diamond electrodes for neurodynamic studies in *Aplysia californica*", Diamond and Related Materials, 15, 183 (2006).
- [5] T. Rao, A. Fujishima, "Recent advances in electrochemistry of diamond", Diamond and Rel. Mat., 9 (2000) 384-389.
- [6] E. Popa, H.Notsu, T. Miwa, D.A. Tryk, A. Fujishima, "Selective Electrochemical Detection of Dopamine in the Presence of Ascorbic Acid at Anodized Diamond Thin Film Electrodes", Electrochem. Solid-State Lett, 2 (1999) 49-51.
- [7] B.V. Sarada, T.N. Rao, D.A. Tryk, A. Fujishima, "Electrochemical oxidation of Histamine and Serotonin at Highly Boron-Doped Diamond Electrodes", Anal. Chem., 72 (2000), 1632-1638.
- [8] P. Ariano, A.L. Gludice, A. Marcantoni, E. Vittone, E. Carbone, D. Lovisolo, "A diamond-based biosensor for the recording of neuronal activity", Biosensors and Bioelectronics, 24 (2009) 2046-2050.
- [9] A. Hess, J. Dunning, J. Harris, J.R. Capadona, K. Shanmuganathan, S.J. Rowan, C. Weder, D.J. Tyler, C.A. Zorman, "A Bio-inspired, Chemo-Responsive Polymer Nanocomposite for Mechanically Dynamic Microsystems", Transducers Conference, Denver, CO, June 21-25, 2009.
- [10] N.A. Blum, B.G. Carkhuff, H.J. Charles Jr., R.L. Edwards, R.A. Meyer, "Multisite microprobes for neural recordings", IEEE Trans. Biomed. Eng., 38, 68 (1991).

## CONTACT

\*C.A. Zorman, tel: +1-216-368-6117; [caz@case.edu](mailto:caz@case.edu)

# MICROCANTILEVER ARRAY SENSORS USING NANOPOROUS METAL-ORGANIC FRAMEWORKS (MOFs) FOR GAS DETECTION

Jin-Hwan Lee<sup>1</sup>, Ronald J. T. Houk<sup>2</sup>, Jeff A. Greathouse<sup>2</sup>, Mark D. Allendorf<sup>2</sup>, and Peter. J. Hesketh<sup>1</sup>

<sup>1</sup>G. W. Woodruff School of Mechanical Engineering, Georgia Institute of Technology, Atlanta, GA, USA

<sup>2</sup>Sandia National Laboratories, Livermore, CA, USA

## ABSTRACT

This paper describes stress induced sensing mechanism with two different MOFs, specifically HKUST-1 and Cu(NDC)DABCO, on n-type piezoresistive microcantilever array. Thermomechanical responses of microcantilever sensors were characterized using water and methanol vapor in a designed gas test cell. The sensors exhibited substantially high sensitivity, 25.1 ohms/Mole % for H<sub>2</sub>O with HKUST-1, at room temperature and 5 times faster response time with Cu(NDC)DABCO at elevated temperature. The key advantages of this new sensor are: 1) higher strain sensitivity due to n-type piezoresistors; 2) high selectivity with a nanoporous MOFs; 3) reversible response; and 4) possibility of multi-analyte detection due to array structure.

## INTRODUCTION

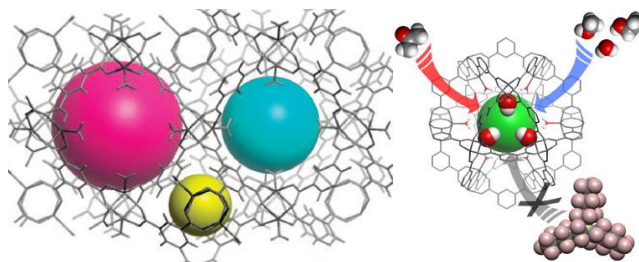
There is a critical need for highly sensitive and selective low power chemical sensors for environmental monitoring, food safety, health diagnostics, security and defense. Detection is particularly critical when it is desired to know chemical weapons of mass destruction (CWMD), explosives, toxic industrial chemicals (TICs), and volatile organic compounds (VOCs). Although many sensitive transducer platforms have been developed, but the long-standing fundamental problem of sufficient sensitivity (sub-ppm) and selectivity of analytes has not yet been solved. The key component for accomplishing ultra-high sensitive sensors is an innovative improvement of sensor technology.

Metal-Organic Frameworks (MOFs) are flexible nanoporous materials with ultra high surface area and are attracting a great deal of attention for gas storage, gas purification and separation applications [1-9]. Metal organic frameworks (MOFs) are a diverse class of crystalline nanoporous materials with the potential to serve as highly tailorable recognition chemistries. Selective binding of CO<sub>2</sub> vs. Ar, N<sub>2</sub>, or CH<sub>4</sub> and O<sub>2</sub> vs. CO by MOFs has been observed [1-3, 8-10]. There are many other MOFs involving a range of metals, linker groups, and pore sizes whose environments can be tailored to achieve specific molecular sorption properties. The permanent nanoporosity in MOFs results in exceptionally high surface areas in some cases (>6,000 m<sup>2</sup>/g, the highest for any crystalline material) and thus the potential adsorb large quantities of gases. In fact, in addition to materials designed as storage materials for H<sub>2</sub>, CO<sub>2</sub>, and CH<sub>4</sub>, MOFs adsorbing benzene, alcohols, volatile organic compounds (e.g. toluene and other substituted benzenes), polyaromatic hydrocarbons, ammonia, and organophosphates are known. Fig. 1 shows a schematic diagram of possible cavities and sensing concept in MOF HKUST-1 [3].

Although this attractive potential is often well-known, little focus has been given to sensor applications. One of bottlenecks is that growing thin films of MOFs is a difficult process because they are neither soluble nor volatile. Typical solutions based deposition methods including spin coating, drop casting, liquid-phase epitaxial growth, CVD, ALD, sputtering, vapor phase epitaxial growth are not viable. Each MOF requires a specialized film growth procedure. Recently, there are several different reported methods for producing thin films of specific MOFs [4,5].

Our past work has demonstrated that the thin MOF HKUST-1 could be grown on a microcantilever surface and detect gases at room temperature, which was the first report of a MOF-integrated functional device as we know [9]. The step-by-step method using a series of immersion steps [4,5] was used to deposit thin HKUST-1 film on gold surface, yielding an average film thickness of ~100 nm/20 cycles [9]. Recently, interdigital electrodes (IDE) were coated with several MOFs and tested in a range of 120–240 °C. The printable thick-film pastes which are mixed MOF powers with an organic vehicle were used to form 10 μm thick films [10].

This paper focuses on stress induced sensing mechanism with two different MOFs, specifically HKUST-1 and Cu(NDC)DABCO. Our interest in MOFs was to explore the chemically induced stress produced by analyte adsorption on a microcantilever array sensor and to tailor the pore dimensions and chemical environment for improved selectivity. Microcantilever sensors were characterized using water vapor and methanol vapor in a custom designed gas test cell. The sensors exhibited substantially high sensitivity at room and elevated temperature. The long term goal of this work is to develop Stress induced microcantilever sensor system to provide selectivity and sensitivity for a broad range of analytes including explosives, nerve agents, and volatile organic compounds (VOCs).



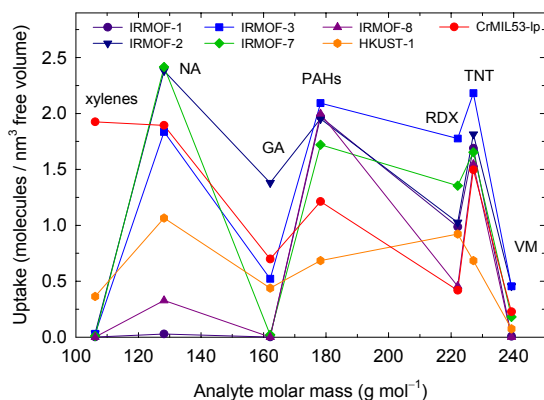
**Figure 1.** Schematic diagram of possible cavities and sensing concept in HKUST-1, a Cu-containing MOF, with ~11.2 Å diameter (left), ~8.4 Å diameter (right), and ~5.4 Å diameter (center). The pore size can be tailored for the adsorption of specific analytes [3].

## DESIGN AND FABRICATION

### Monte Carlo Modeling

The more than 1000 new MOFs are reported annually. To screen MOFs for the potential use in chemical detection schemes, a comparison of analyte uptakes at trace concentrations is needed. To accomplish this we performed grand canonical Monte Carlo simulations, using the universal force field to simulate MOF-analyte interactions. The predicted volumetric uptake of each MOF at 10<sup>-6</sup> kPa is shown in Figure 2. At this low pressure, short-range interactions between analyte and MOF should dominate over pore size or pore volume considerations. Several features characteristic of individual MOFs are noteworthy. First, CrMIL-53lp is the only MOF we considered that shows a significant uptake of xylenes, even at this low pressure. The small pores in CrMIL-53lp are lined

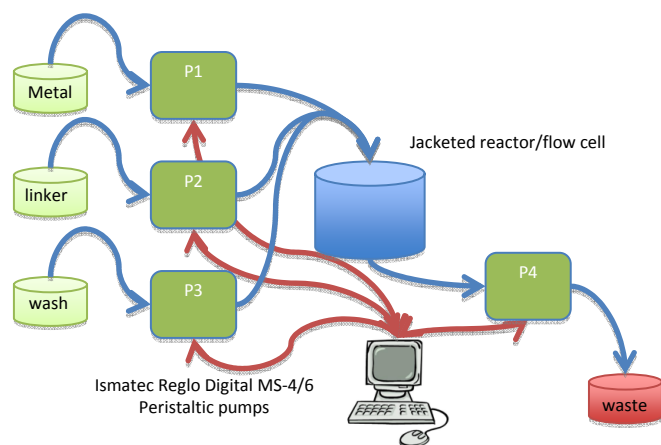
with phenyl groups, creating an ideal environment for the adsorption of small aromatic molecules. Second, IRMOF-2, which contains the Br functional group, shows relatively high analyte uptake across the entire pressure range, with an exceptional uptake of GA compared to the other MOFs. Finally, the amine functional group in IRMOF-3 results in high uptake of heavier analytes, particularly the explosives class (RDX and TNT).



**Figure 2.** Uptake as a function of molar mass at a loading pressure of  $10^{-6}$  kPa. Labels indicate each analyte type.

### MOF Coatings

Figure 2 is schematically illustrated MOF coating setup. Thin films of the MOF HKUST-1 and Cu(NDC)DABCO were grown on 300 Å Cr/2000 Å Au layers deposited microcantilever surfaces using thiol-based self-assembled monolayers (SAMs). SAMs layer was functionalized for ~20 hrs. For HKUST-1, there are a couple of key advantages. First, it is one of the known permanently porous MOFs with extensive studies into its properties and adsorption characteristics. Therefore, the behavior of HKUST-1 coated microcantilever can be expected. Second, there are well established methods for growing thin HKUST-1 films [4,5]. With respect to Cu(NDC)Dabco, there are known methods for growing thin film formed. It is reported to have enhanced flexibility over HKUST-1 to grow much closer to actual epitaxial growth, but there is not much literature on its properties. The layer-by-layer method was used for MOF film growth using a sequential repeating immersion paradigm [4,5]. Microcantilevers are immersed in a heated solution of 1 mM Cu(OAc)<sub>2</sub> in for HKUST-1 followed by immersion in a dilute solution of the MOF linker, 0.1 mM benzene tricarboxylic acid (BTC) in ethanol. Ethanol was used as a washer followed each process. The cycle is repeated over multiple iterations to generate a uniform polycrystalline film. The process is automated through the use of peristaltic pumps programmed to alternately pump the desired solutions in and out of a reactor flow cell. The flow rate was 9  $\mu$ L/s with 90 sec/fill and 95 sec/drain. The flow cell includes a heating jacket to allow the growth temperature (50°C) to be controlled. The growth period for a 40 cycle was less than 26 hrs. The same method used for Cu(NDC)DABCO with 0.2 mM (naphthalenedicarboxylate (NDC) and diazabicyclo[2.2.2]octane (DABCO). X-ray diffraction (XRD) and micro-surface-enhanced Raman spectroscopy ( $\mu$ SERS) were used to verify the presence of the MOF film on the substrate surface.



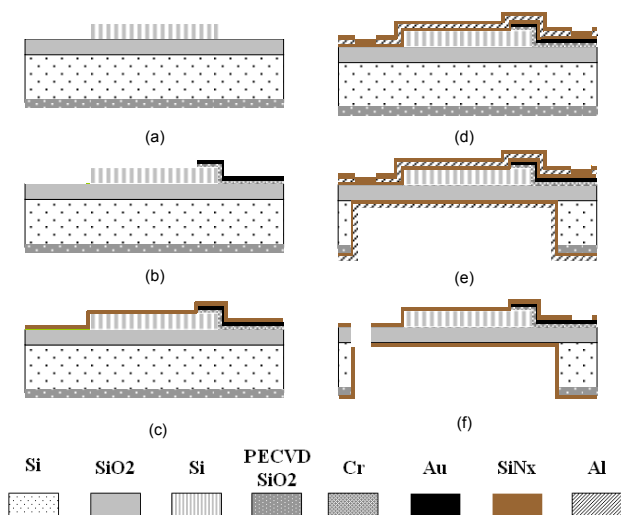
**Figure 3.** Schematic diagram of MOF coating setup.

### Fabrication

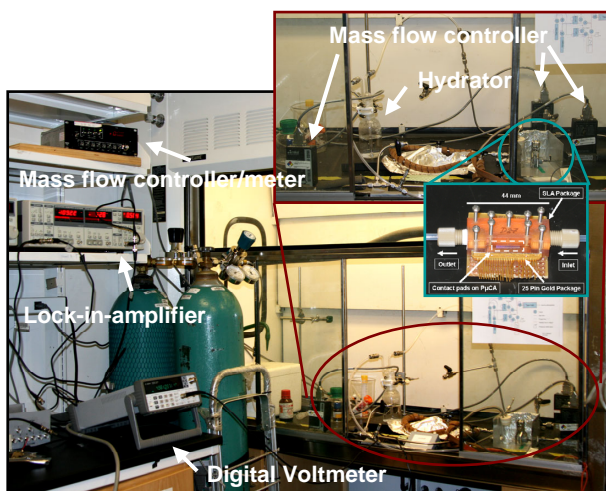
N-type piezoresistive microcantilever arrays with 230  $\mu$ m in length and 100  $\mu$ m in width were successfully fabricated using batch microfabrication processes in Figure 4. While the advantages and fabrication process of this device (without MOFs) was described in [11], this paper includes an improved fabrication process and optimized sensor dimensions for gas detection with MOFs. Piezoresistive microcantilever arrays were initially formed from a silicon-on-insulator (SOI) wafer with (100) single crystal silicon (SCS) layer for the piezoresistive resistors. The SOI wafers were doped by ion implantation with phosphorus to create n-doped piezoresistors and then activated by annealing process. The silicon piezoresistors were defined by reactive ion etch (RIE) in Fig. 4a. A Ti/Au was deposited as metal contacts to the resistors (Fig. 4b), and a thin layer of silicon nitride was carefully chosen to have a compressive stress and was deposited on top of these contacts as an insulating layer for the electrical components of the device and the piezoresistors (Fig. 4c). An aluminum layer was sputter-deposited and patterned to create a mask for the definition of the cantilevers and the chip. Then a low-stress silicon nitride was deposited on top of the aluminum mask to effectively strengthen the microcantilever area upon release (Fig. 4d). After the backside oxide as a mask was patterned, deep RIE through the wafer was used as a first release step (Fig. 4e). Finally, microcantilever arrays were released followed by RIE etching for the silicon nitride layer and the aluminum layer (Fig. 4f).

### Gas Testing

The response of the sensor for H<sub>2</sub>O, and CH<sub>3</sub>OH was measured in a custom designed gas test cell in Figure 5. Dry nitrogen was used as a carrier gas. Water and methanol were regulated using a hydrator with a mass flow controller 2 (MFC 2). The total gas volume was 100 sccm with MFC 1 and 2 to keep the same flow rate. The stress response was obtained by the subtraction of the uncoated reference microcantilever response from the MOF-coated cantilever response using an AC Wheatstone bridge in order to remove the effect of temperature. The signal frequency was 10 kHz and the time constant on the SR830 lock-in amplifier (SRS Instruments, Sunnyvale, CA) was 300 ms. A PC computer with LabVIEW for data acquisition was connected to a lock-in-amplifier and digital voltmeter for measurements. The microcantilever array chip was mounted in a designed stereolithography package for gas tests.



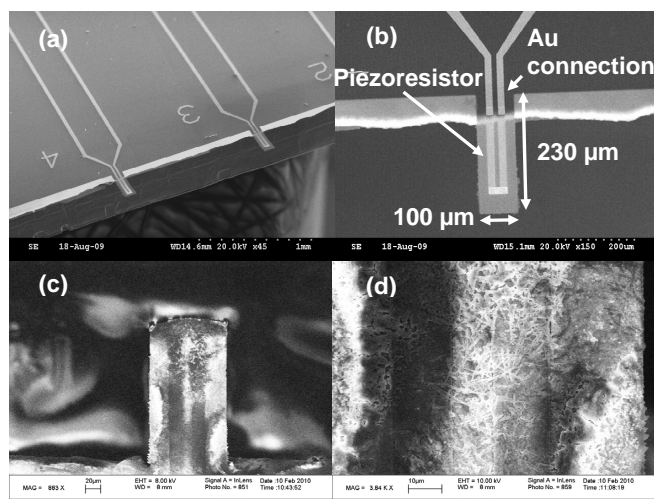
**Figure 4.** Batch piezoresistive microcantilever array sensor fabrication sequence. (a) Patterning piezoresistors on SOI wafer; (b) patterning conductive connections; (c) deposition of silicon nitride; (d) deposition of Al and silicon nitride as a mask; (e) backside etch through wafer by RIE followed by deposition of bottom silicon nitride and Al; (f) release of the piezoresistive microcantilever arrays by RIE etch.



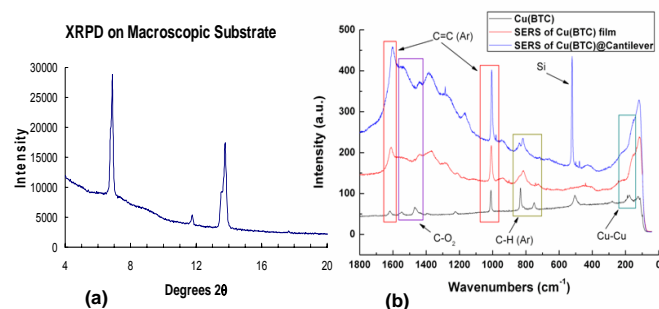
**Figure 5.** Schematic diagram of gas test setup.

## RESULTS AND DISCUSSION

Microcantilevers with 230  $\mu\text{m}$  in length and 100  $\mu\text{m}$  in width were successfully fabricated in arrays of ten per chip, with 38 devices per a wafer using batch microfabrication technologies. The width and length of resistors are 20  $\mu\text{m}$  and 195  $\mu\text{m}$  in Fig. 6a and 6b. Thin MOF layer (Fig. 6c and 6d) is clearly visible on a microcantilever compared with uncoated cantilever (Fig. 6b). XRD and  $\mu\text{SERS}$  were used to verify that MOFs are present on the surface (Fig. 7). Even though XRD can verify MOF film (>1  $\mu\text{m}$  thick), the microcantilever is too small to be characterized. We found that micro-surface-enhanced Raman spectroscopy ( $\mu\text{SERS}$ ) is a viable characterization method for MOF films on microcantilevers with small spatial resolution (<~2.0  $\mu\text{m}^2$ ) [9]. Figure 7b shows the same SERS spectrums of HKUST-1 on a microcantilever (top), on a



**Figure 6.** SEM of piezoresistive microcantilever. (a) each microcantilever array consisted of ten cantilevers; (b) reference microcantilever without HKUST-1 MOF coating; (c) and (d) HKUST-1 coated microcantilever sensor.

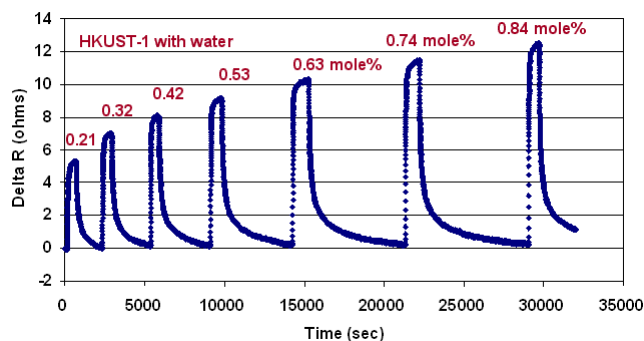


**Figure 7.** (a) Powder X-ray pattern of an oriented thick HKUST-1 film on a silicon substrate and (b) micro-surface-enhanced Raman spectroscopy ( $\mu\text{SERS}$ ) pattern of an HKUST-1 film on a microcantilever [9].

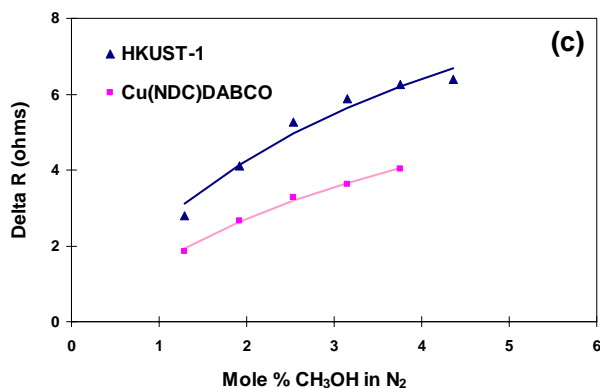
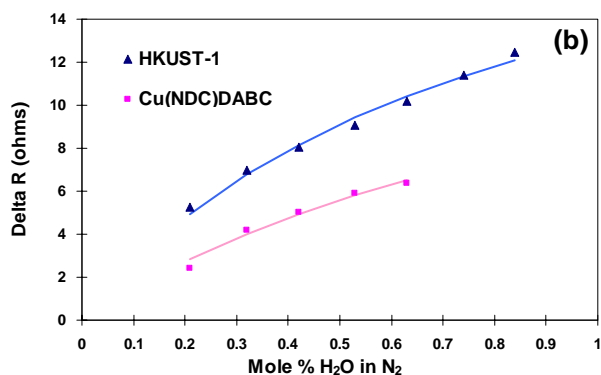
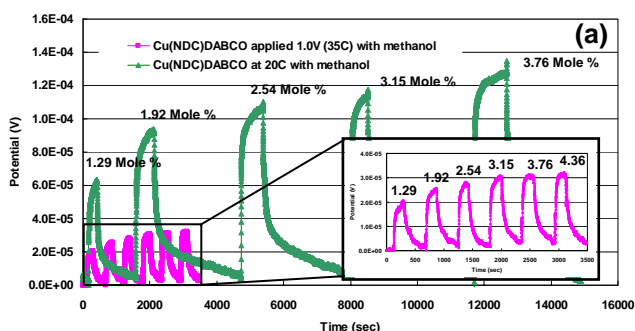
macroscopic substrate (middle) and unenhanced Raman (without Ag layer) of a thick HKUST-1 layer as a reference (bottom).

MOF-coated microcantilevers exhibit substantial resistance changes and fast response times, with completely reversible response for adsorption and desorption of water and methanol, as seen in Fig. 8 and 9. HKUST-1 displays a higher resistance change for a given analyte concentration than Cu(NDC)DABCO. Both the response and recovery times can be increased substantially by heating the sensor. For example, the response of the Cu(NDC)DABCO-coated sensor was 5 times faster at 35  $^{\circ}\text{C}$  than at 20  $^{\circ}\text{C}$  when a direct voltage of 1V was applied to the heat cantilever (Fig. 9a). The measured response depends on concentration and conforms to Langmuir type saturation, as seen in Fig. 9b and 9c. The sensors exhibited a high sensitivity; for HKUST-1 coatings, a resistance change of 25.1 ohms/Mole % (at 1 atm) was observed for  $\text{H}_2\text{O}$  adsorption at room temperature. These results show that stress-induced piezoresistive microcantilever array sensors with nanoporous MOFs can provide a highly sensitive and reversible sensing mechanism for multiple analytes. This research is now being extended to test various gases such as CO,  $\text{CO}_2$ , NO,  $\text{C}_2\text{H}_4$ , and  $\text{C}_2\text{H}_6$  with various MOF compounds.





**Figure 8.** Response curves of HKUST-1 coated microcantilever sensors with water vapor at room temperature.



**Figure 9.** Characterization curves of microcantilever sensors. (a) Response time with Cu(NDC)DABCO at room and 35°C temperature; Langmuir curves for (b) water vapor and (c) methanol vapor at room temperature.

## CONCLUSIONS

Stress induced piezoresistive microcantilever array sensors with nanoporous MOFs, HKUST-1 and Cu(NDC)DABCO, have been successfully demonstrated to provide a highly sensitive and reversible sensing mechanism. Thin films of MOFs were successfully grown with SAMs layer on microcantilever surface using the layer-by-layer method, which repeated a sequential immersion paradigm. MOF-coated microcantilevers exhibit substantial resistance changes and fast response times, with completely reversible response for adsorption and desorption of water and methanol. The response and recovery times on elevated temperature can be faster substantially than on room temperature. This successful development of MOFs coated microcantilever array sensor will enable a highly sensitive and reversible sensing mechanism for multiple analytes.

## ACKNOWLEDGEMENTS

This work was supported by the Sandia Laboratory Directed Research and Development (LDRD) program. The authors would like to gratefully acknowledge Dr. Xiaohui Lin for his valuable technical assistance in device characterization.

## REFERENCES

- [1] S. S. -Y. Chui, S. M.-F. Lo, J. P. H. Charmant, A. G. Orpen, I. D. Williams, "A Chemically Functionalizable Nanoporous Material [Cu<sub>3</sub>(TMA)<sub>2</sub>(H<sub>2</sub>O)<sub>3</sub>]<sub>n</sub>", *Science*, 283, 1148 (1999).
- [2] K. Uemura, Y. Komagawa, Y. Yamasaki, H. Kita, "Characterization of organic solvents adsorption desorption on hydrophobic porous coordination polymers and their micro-crystals aggregation on mullite support", *Desalination*, 234, 1 (2008).
- [3] K. W. Chapman, G. J. Halder, P. J. Chupas, "Guest-Dependent High Pressure Phenomena in a Nanoporous Metal-Organic Framework Material", *J. Am. Chem. Soc.*, 130, 10524 (2008).
- [4] O. Shekhah, H. Wang, S. Kowarik, F. Schreiber, M. Paulus, M. Tolan, C. Sternemann, F. Evers, D. Zacher, R. A. Fischer, C. Wöll "Step-by-Step Route for the Synthesis of Metal-Organic Frameworks", *J. Amer. Chem. Soc.*, 129, 15118 (2007).
- [5] D. Zacher, O. Shekhah, C. Woll et al., "Thin films of metal-organic frameworks", *Chemical Society Reviews*, 38, 1418 (2009).
- [6] E. Biemmi, C. Scherb, and T. Bein, "Oriented growth of the metal organic framework Cu<sub>3</sub>(BTC)2(H<sub>2</sub>O)3·xH<sub>2</sub>O tunable with functionalized self-assembled monolayers", *J. Am. Chem. Soc.*, 129, 8054 (2007).
- [7] Q. M. Wang, D. M. Shen, M. Bulow et al., "Metallo-organic molecular sieve for gas separation and purification", *Microporous Mesoporous Mater.*, 55, 217 (2002).
- [8] S. Bordiga, L. Regli, F. Bonino et al., "Adsorption properties of HKUST-1 toward hydrogen and other small molecules monitored by IR", *Phys. Chem. Chem. Phys.*, 9, 2676 (2007).
- [9] M. D. Allendorf, R. J. T. Houk, L. Andruszkiewicz, A. A. Talin, J. Pikarsky, A. Choudhury, K. A. Gall, P. J. Hesketh, "Stress-Induced Chemical Detection Using Flexible Metal-Organic Frameworks", *J. Am. Chem. Soc.*, 130, 14404 (2008).
- [10] S. Achmann, G. Hagen, J. Kita, I. M. Malkowsky, C. Kiener, R. Moos, "Metal-Organic Frameworks for Sensing Applications in the Gas Phase", *Sensors*, 9, 1574 (2009)
- [11] A. Choudhury, P. J. Hesketh, Z. Hu, T. Thundat, "A piezoresistive microcantilevers array for surface stress measurement: Curvature model and fabrication", *J. Micromech. Microeng.*, 17, 2065 (2007).

# POROUS SILICON RESONATORS FOR SENSITIVE VAPOR DETECTION

Yongha Hwang<sup>1</sup>, Feng Gao<sup>2</sup>, and Rob N. Candler<sup>1</sup>

<sup>1</sup>Department of Electrical Engineering, University of California, Los Angeles, USA

<sup>2</sup>Department of Mechanical Engineering, University of California, Los Angeles, USA

## ABSTRACT

Common top-down processing techniques were used to fabricate porous silicon resonant mass sensors, allowing for microscale devices with nanoscale features. Porous resonators have an increased surface area for molecular binding and therefore offer improved sensitivity to chemical vapor when compared to non-porous resonators. The porous resonators showed up to 99% improvement in sensitivity to isopropyl alcohol over non-porous resonators fabricated in the same process.

## INTRODUCTION

Micro- and nanometer scale resonators have been explored as highly sensitive mass sensors. Binding events on the surface of a resonator alter the mechanical stress and total mass of the resonator. This allows for measurement of the adsorbed mass via a shift in resonant frequency. Scaling the devices to smaller size increases the relative mass change of adsorbed species, thus improving the sensitivity of the devices as mass sensors [1]. A variety of methods have been developed to improve the sensitivity of these resonant sensors, including treatments of sensor surfaces to improve the quality factor [2,3], modifications of readout schemes to measure the sensors more efficiently [4], and materials for decreased energy dissipation and improved robustness [5,6]. To date, porous silicon has been investigated for applications including enhanced sensitivity of pressure sensors via a reduced Young's modulus [7] and detection of chemicals via changes of electronic [8] and optical characteristics [9]. This work focuses on using the large internal surface area of porous silicon for sensitivity enhancement in resonant mass sensors.

Porous materials have previously been coated on the surface of resonators to increase the surface area of adsorption. As previously mentioned, nanomechanical resonant sensors with dimensions in the submicron regime have also been employed as tools to offer impressive mass sensitivity by increased surface area-to-volume ratios. Both scaling and the addition of surface coatings can add complexity to fabrication and readout, whereas nanoscale sensitivity from widely available microscale fabrication techniques can be achieved in the approach described here, where the entire resonant structure is fabricated of porous silicon.

## FABRICATION PROCESS

We have designed and fabricated torsional beam resonant gas sensors using surface micromachining process as shown in Figure 1. We simultaneously fabricated porous and non-porous silicon resonators on the same silicon wafer to quantify the sensitivity enhancement. Fabrication started with 4 in. (100) silicon wafers, followed by depositions of 470-nm-thick silicon dioxide serving as a sacrificial layer and 470-nm-thick polysilicon by LPCVD (Tystar Titan II furnace). The structures of the resonators were then defined by photolithography (KarlSuss MA-6 aligner) and deep reactive ion etcher (SLR 770 ICP). Electroless metal-assisted etching of the silicon surface was used to porosify the silicon structures [10]. A 5-nm-thick Au layer was deposited by e-beam evaporation (CHA Mark 40) in order to form thin Au clusters, which served as catalysts for silicon etching. Silicon molecules underneath Au clusters were etched away in an etching solution (49% HF, 30% H<sub>2</sub>O<sub>2</sub>, and H<sub>2</sub>O with a volume ratio of 1:5:10) for 20 seconds. The remaining Au

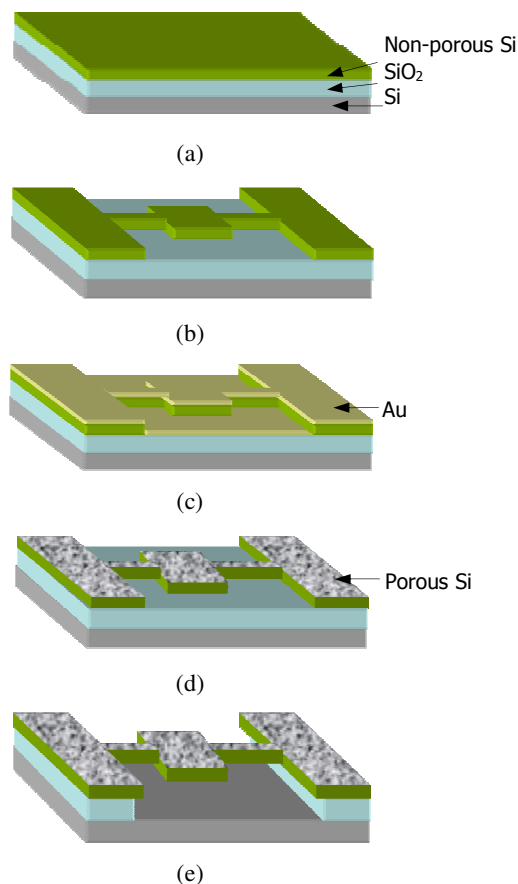
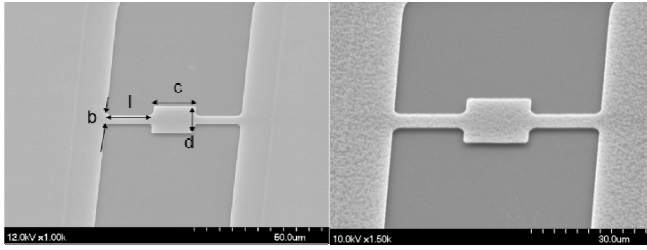


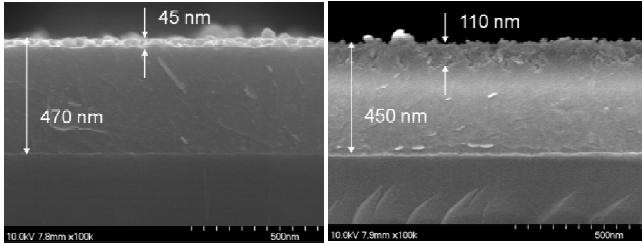
Figure 1. Fabrication process for a porous silicon resonator. (a) deposition of SiO<sub>2</sub> and polysilicon by LPCVD. (b) photolithography and polysilicon etching by DRIE. (c) Au catalyst layer deposition by E-beam evaporator. (d) porous silicon etching and Au layer removal. (e) sacrificial layer etching and drying with CPD.. Steps (c) and (d) are omitted for non-porous silicon resonators.

clusters were subsequently removed by immersing the samples in Au etchant (651818, Sigma Aldrich) for 20 seconds. The electroless metal-assisted porous etching steps were omitted for non-porous silicon resonators. Finally, silicon dioxide layers of both non-porous silicon and porous silicon resonators were removed by 49% HF solution for 2 minutes and rinsed by deionized water, followed by drying using a critical point dryer (CPD, Automegasamdri-915B) to prevent stiction.

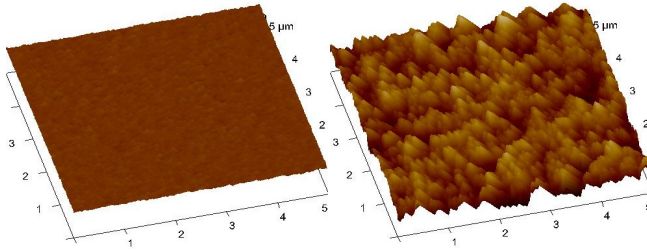
Figure 2 shows the change of roughness from the porous etching process, which allows the porous silicon resonator to have a larger surface area than the non-porous silicon resonator of the same dimensions. It is observed that the non-porous silicon film initially has a 45 nm-deep hemispherical grain region, while the porous silicon film has nanoscale pores 110 nm into the surface.



(a)



(b)



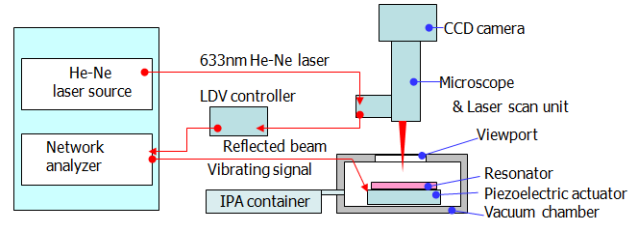
(c)

Figure 2. A non-porous silicon resonator (left) and a porous silicon resonator (right). (a) SEM images showing  $l = 15 \mu\text{m}$ ,  $b = 5 \mu\text{m}$ , and  $c = d = 15 \mu\text{m}$  resonators. (b) zoomed-in SEM images of resonators in cross section. (c) AFM images. The RMS roughness of the non-porous silicon and the porous silicon are  $3.8 \text{ nm}$  and  $32.9 \text{ nm}$ , respectively.

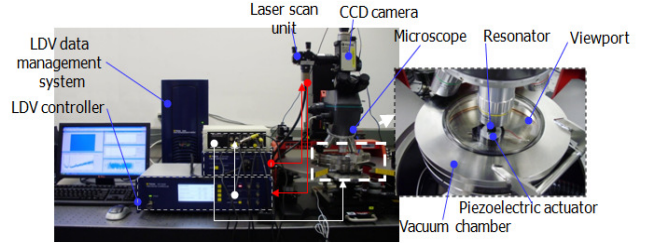
## RESULTS

### Experimental setup

The frequency spectra of the resonant mass sensors were measured with a test setup that consists of a Laser Doppler Vibrometer (LDV, Polytec OFV-5000), a custom-built vacuum chamber, a microscope unit (Mitutoyo FS70) and a network analyzer (HP 8753D), as shown in Figure 3. To induce mechanical resonance, the device is mounted on a piezoelectric actuator (Thorlabs AE0203D08F) controlled by stimulus signal of the network analyzer. Measurements are performed in a vacuum chamber in order to avoid energy losses by air damping. Since the vacuum chamber has a glass viewport, observation and measurement are possible. A stainless-steel container that is connected with the vacuum chamber via a metering valve is used to control IPA (Isopropyl alcohol) vapor flow. A 633 nm He-Ne laser is used as the light source of the LDV system. Actuation of the resonator is detected by reflected light. The reflected beam is converted to an electrical signal by the LDV controller, and the network analyzer records the resonant frequency of the resonator mass sensor with a frequency resolution of 2.5 Hz.



(a)



(b)

Figure 3. (a) Schematic diagram and (b) photos of the experimental setup for mechanical actuation and readout by using a Laser Doppler Vibrometer.

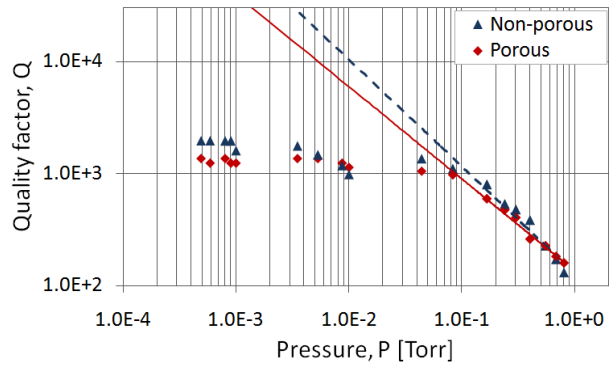


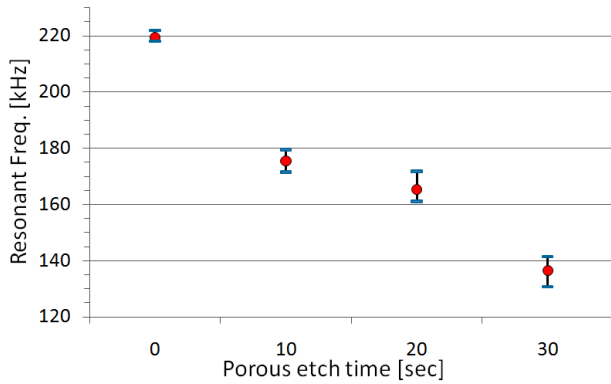
Figure 4. Measured quality factor of resonators. Above 0.1 Torr, data of the non-porous silicon resonator and the porous silicon resonator are described by  $Q=129/P^{0.953}$  (dashed line) and  $Q=135/P^{0.823}$  (solid line), respectively. Below that pressure, intrinsic energy loss mechanism limits the quality factor.

### Changes in characteristics by porosification

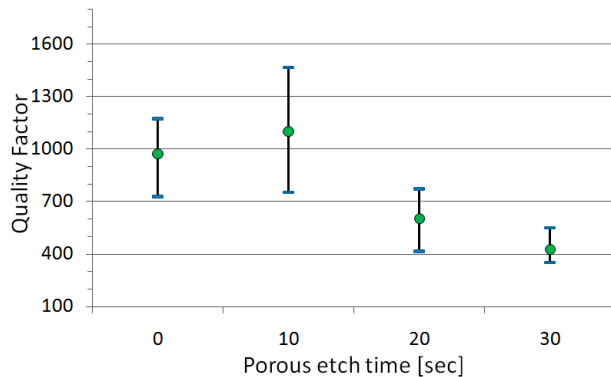
Air damping is frequently a dominant energy loss mechanism in sub-GHz devices that are not operated under high vacuum [11]. Since operating pressure affects air damping and is dependent on vapor concentration, it is necessary to understand the dependence of resonator quality factor on pressure. Figure 4 shows quality factor as a function of pressure for a porous silicon resonator and a non-porous silicon resonator. The quality factors of both types of resonators are strong functions of pressure down to 0.1 Torr. The quality factor dependence on pressure for the non-porous and porous silicon resonators are of the form  $Q=129/P^{0.953}$  and  $Q=135/P^{0.823}$ , respectively. The relationship between quality factor and pressure for the simplest case has a relationship of the form  $Q \propto 1/P$  [12]. Below 0.1 Torr, the quality factors are determined by damping mechanisms other than air damping. We find that the pressure range where quality factor is limited by air damping is

roughly independent of the resonators' porosity.

Resonators with a 460 nm-thick, 45  $\mu\text{m}$ -long square paddle and 45  $\mu\text{m}$  long, 10  $\mu\text{m}$ -wide support beams have been utilized to investigate how resonant frequency and quality factor are affected when the resonators are porosified. Resonant frequency decreases as porous etch time increases due to decreased mechanical stiffness of the porous material, which is only partially offset by the reduced mass of the porous material (Figure 5 (a)). In addition, variations of the quality factor depending on porous etch condition seem to be decreased as porous etch time increases (Figure 5 (b)), although further investigation is necessary to provide any conclusions regarding the impact of porosification on quality factor.



(a)



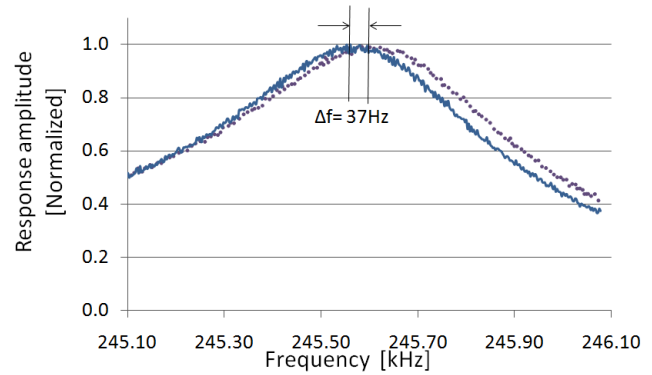
(b)

Figure 5. Measured (a) resonant frequencies and (b) quality factors depending on etch times for porous silicon resonators. The error bars indicate the standard deviation in the data, which comprised five measurements.

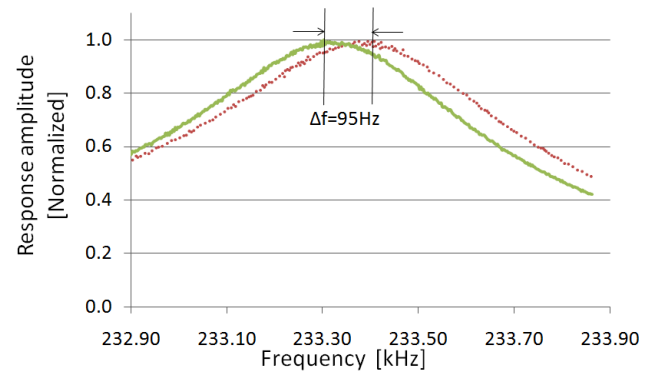
### Vapor detection

Figure 6 contains characteristic frequency spectra showing shifts in the torsional mode resonant frequency under 5000 ppm of IPA vapor. The resonant frequency shift is measured with respect to the partial pressure of IPA, which is normalized to one atmosphere to provide units of ppm. The porous silicon resonator displays a frequency shift significantly greater than that of the non-porous silicon resonator.

Figure 7 illustrates the different responses of the non-porous and porous silicon resonators by the change of the resonant frequency shift versus the IPA concentration during a 30 minute



(a)



(b)

Figure 6. Measured frequency spectra of (a) non-porous and (b) porous silicon resonators with no IPA (dashed line) and 5000 ppm of IPA (solid line).

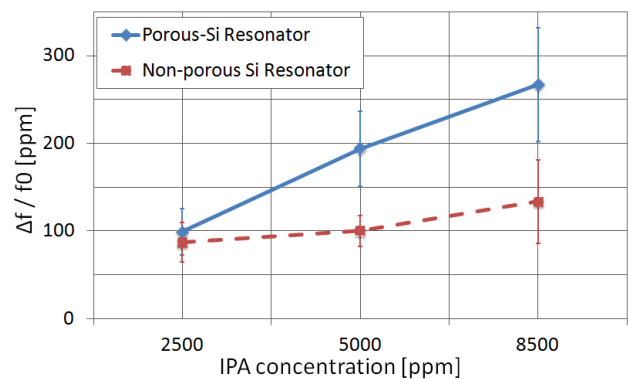


Figure 7. A comparison of resonant frequency shift to gas concentration. The error bars indicate the standard deviation in the data, which consist of five measurements at five minute intervals for each concentration.

period. The porous silicon resonators show higher frequency shift ranging between 99% and 22% for different gas concentrations compared to the non-porous silicon resonators. The results demonstrate that the porous silicon-based resonators have an enhanced sensitivity to IPA vapor as compared to the non-porous silicon-based resonators.

## CONCLUSION

We have demonstrated a 99% sensitivity improvement in chemical vapor sensing using porous silicon resonators. By using a microscale device with nanoscale features, we were able to leverage the best of both size scales (*i.e.*, microscale ease of fabrication with nanoscale sensitivity). Future work will focus on investigating the limits of porosity on quality factor and mechanical stability. Specifically, we will explore selectively porosifying parts of the resonators to obtain enhanced sensitivity while maintaining mechanical robustness.

## ACKNOWLEDGEMENTS

The authors gratefully thank Prof. C.-J. Kim and C.Y. Lee for helping us to process the porous silicon etching. We would also like to thank Tom Lee of the Nanoelectronics Research Facility at UCLA for assistance in fabrication of the test chamber. This work was supported by the BRIGE program of the National Science Foundation under award # 0926228.

## REFERENCES

- [1] B. Ilic, Y. Yang, and H.G. Craighead, "Virus detection using nanoelectromechanical devices", *Applied Physics Letters*, 85, 13 (2004).
- [2] Y. Wang, J.A. Henry, A.T. Zehnder, and M.A. Hines, "Surface Chemical Control of Mechanical Energy Losses in Micromachined Silicon Structures", *J. Phys. Chem. B*, 107 (2003).
- [3] Xinxin Li, "Cantilever sensors equipped with nano sensing effects for ultra-sensitive detection of bio/chemical molecules", *Proc. Transducers* (2009), pp.1620 - 1625.
- [4] P.A. Truitt, J.B. Hertzberg, C.C. Huang, K.L. Ekinci, and K.C. Schwab, "Efficient and sensitive capacitive readout of nanomechanical resonator arrays", *Nano Letters*, 7, 1 (2007).
- [5] L. Sekaric, D.W. Carr, S. Evoy, J.M. Parpia, H.G. Craighead, "Nanomechanical resonant structures in silicon nitride: fabrication, operation and dissipation issue", *J. Sensors and Actuators A*, 101 (2002).
- [6] N. Sepulveda, D. Aslam, and J.P. Sullivan, "Polycrystalline diamond MEMS resonator technology for sensor applications", *Proc. Diamond and Related Materials* (2006), pp. 398 – 403.
- [7] L. Sujatha and E. Bhattacharya, "Enhancement of the sensitivity of pressure sensors with a composite Si/porous silicon membrane", *J. Micromechanics and Microengineering*, 17, 8 (2007).
- [8] P. Han, H. Wong, and M. Poon, "Sensitivity and stability of porous polycrystalline silicon gas sensor", *Proc. Colloids and Surfaces* (2001), pp. 171 - 175.
- [9] H. Ouyang, C.C. Striemer, and P.M. Fauchet "Quantitative analysis of the sensitivity of porous silicon optical biosensors", *Applied Physics Letters*, 88, 163108 (2006).
- [10] C. Lee and C.-J. Kim, "Maximizing the giant liquid slip on super hydrophobic microstructures by nanostructuring their sidewalls", *Langmuir*, 25, 12812 (2009).
- [11] Y.J. Yang, M.A. Gretillat, and S.D. Senturia, "Effect of air damping on the dynamics of nonuniform deformations of microstructures," *Proc. Transducers* (1997), pp. 1093 - 1096.
- [12] W.E. Newell, "Miniaturization of tuning forks," *Science*, 161, 3848 (1968).

## CONTACT

\*Yongha Hwang, Engr IV 64-144, 420 Westwood Plaza, Los Angeles, CA 90095, Phone: +1-213-925-8243, Email: hwangyongha@ucla.edu

# A MICROFLUIDIC PLATFORM FOR THE FLUIDIC ISOLATION AND OBSERVATION OF CELLS CHALLENGED WITH PATHOGENS

C. D. James<sup>1</sup>, M.W. Moorman<sup>1</sup>, B.D. Carson<sup>1</sup>, J. Joo<sup>2</sup>, C.S. Branda<sup>3</sup>,  
R.P. Manginell<sup>1</sup>, J. Lantz<sup>4</sup>, R. Renzi<sup>3</sup>, A. Martino<sup>1</sup>, A.K. Sing<sup>3</sup>

<sup>1</sup>Sandia National Laboratories, Albuquerque, NM, USA

<sup>2</sup>University of Tennessee, Knoxville, TN, USA

<sup>3</sup>Sandia National Laboratories, Livermore, CA, USA

<sup>4</sup>GAITS, Albuquerque, NM, USA

## ABSTRACT

Single-cell analysis offers a promising method of studying cellular functions including investigation of mechanisms of host-pathogen interaction. We are developing a microfluidic platform that integrates single-cell capture along with an optimized interface for high-resolution fluorescence microscopy. The goal is to monitor, using fluorescent reporter constructs and labeled antibodies, the early events in signal transduction in innate immunity pathways of macrophages and other immune cells. The work presented discusses the development of the single-cell capture device, the iCellator chip, that isolates, captures, and exposes cells to pathogenic insults. We have successfully monitored the translocation of NF- $\kappa$ B, a transcription factor, from the cytoplasm to the nucleus after lipopolysaccharide (LPS) stimulation of RAW264.7 macrophages.

## INTRODUCTION

Our team at Sandia National Laboratories has developed a microfluidic system to facilitate single cell imaging and analysis. This system is currently being utilized for real-time monitoring of fluorescent reporter constructs and labeled antibodies to examine the early events of signal transduction in the innate immune response. Traditional methods to study this pathway provide population averaged measurements, and thus it is difficult to interpret individual cell responses because not all cells in a population reside in the same initial physiological state or undergo the same degree of infection. Further, cell-intrinsic and extrinsic events cannot be separated when groups of cells are exposed in bulk culture (cytokines, cell-cell interaction). By isolating individual cells, we are able to perform real-time, quantitative analysis of cell signaling cascades involved in host-pathogen interactions, with a special emphasis on the early events that occur during immune response.

The system consists of two components: a microfluidic platform, called the iCellator chip, that enables single cell capture, isolation, challenge, and high-resolution microscopy, and an instrument for fluid handling and platform temperature control that uses a simple computer interface. Figure 1 shows a schematic of the iCellator chip design. Other work has demonstrated single cell capturing techniques optimized for optical interrogation such as DiCarlo [1] and Tourovskaia [2], but neither approach has achieved complete cell isolation as this effort has.

## iCELLATOR DEVICES

The chip design described here is an improvement over earlier prototype designs that we have reported in [3]. Compared to these earlier designs, the more recent designs feature more efficient cell trapping structures, better cell isolation, an improved imaging interface, and dual imaging chambers. The dual imaging chambers allow us to run simultaneous control and challenge experiments on the same chip. Each chamber contains 150 fluidically isolated traps where the cells are captured by micron-scale constrictions.

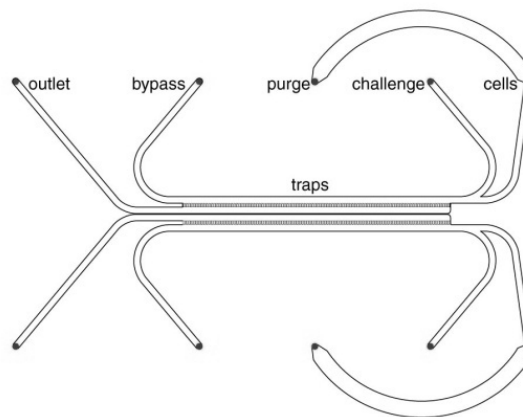


Figure 1: Schematic of the iCellator chip showing challenge and cell loading inlets, trap location, and outlets with separated imaging chambers to allow challenge and control experiments.

These cell constrictions are semi-circular to allow the cell to easily conform to its shape. The constrictions place cells approximately 3  $\mu$ m immediately beneath the coverslip lid for low background fluorescence imaging, unlike the prior design which had a tendency to trap cells in the middle of the flow channels, approximately 15  $\mu$ m below the surface of the coverslip. Figure 2 shows a schematic and optical image of our most recent trapping structures.

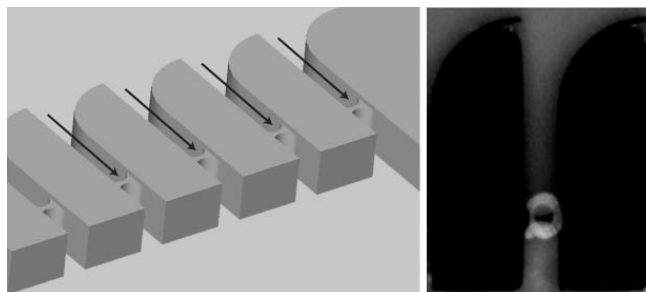


Figure 2: A schematic view of the 3D nature of the trapping features, with arrows showing the direction of fluid flow into the traps. The adjacent fluorescence image shows a RAW264.7 cell on a trapping feature.

Computational modeling was used to inform the design of the new cell trap structures. Placement of the constrictions at the end of long channels was done to better control the fluidic isolation of each cell trap. Once trapped, the combination of continuous fluid flow and architecture isolates each trapped cell from the secreted cytokines of other cells. This enables study of the effects of paracrine signaling on long-term host cell response to pathogenic

challenges. Figure 3 shows the results of fluidic modeling on the previous cell trap structures. These results show that the prior design had a critical trap depth, measured by the value  $D_i$ , which indicated how deep into the trap a cell must lie in order to be isolated. Above the  $D_i$  height the cell could be exposed to cytokine secretions from other cells. The  $D_i$  height for the majority of the traps was less than half of the overall trap height  $D$ , indicating a large area of each trap was not fluidically isolated.

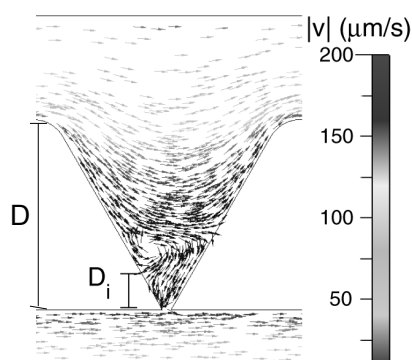


Figure 3: Flow streamlines in the device at the middle trap. The trap depth ( $D$ ) and the depth of isolation ( $D_i$ ) are noted.

Similar fluidic modeling was performed on the new trapping structures. This modeling showed that the  $D_i$  value was essentially equal to the length of the channels leading to the cell constrictions. Figure 4 shows results of this modeling. This meant that not only were captured cells much more likely to be fluidically isolated, but also that there was a greater overall uniformity of  $D_i$  values across all the cell trap locations, which made for better experimental conditions overall.

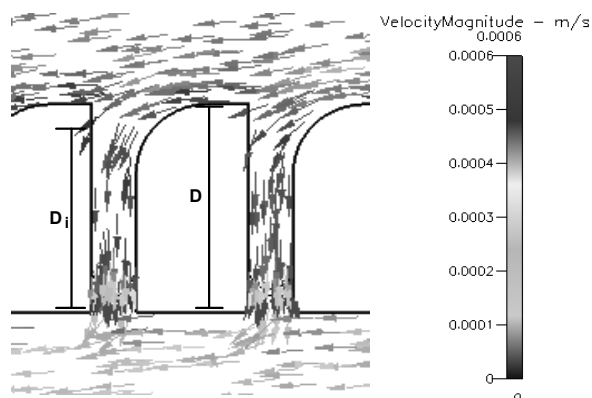


Figure 4: Flow streamlines in the middle trap devices showing a nearly equivalent trap depth ( $D$ ) and depth of isolation ( $D_i$ ).

### iCellator Fabrication

The devices followed a fairly simple microfabrication process. All chips were fabricated using 6-in. 450  $\mu\text{m}$  thick double polished silicon wafers. A series of deep reactive ion etch (DRIE) steps on the front-side of the wafer defined the device channels and trap structures, while a through-wafer backside DRIE defined the 200  $\mu\text{m}$  diameter inlet and outlet ports. After an  $\text{O}_2$  plasma (150 W

for 30 s) and acetone sonication to remove resist, wafers were then diced into individual die. No. 1.5 Pyrex coverslips were then bonded to the silicon chips using a custom-made anodic bonder system. Excess glass was trimmed from the die before being placed into the chip's testing manifold.

### TESTING SETUP

Figure 5 shows an iCellator chip installed in a manifold that provides heating, fluid exchange, and a low-profile optical interface enabling high-resolution oil-immersion imaging with upright or inverted microscopes. The instrumentation for fluid

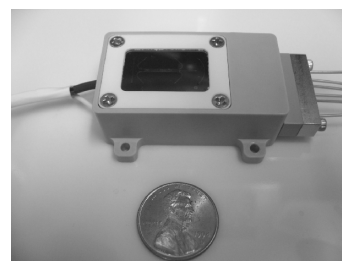


Figure 5: PEEK fixturing featuring fluidic interconnects, integrated heating, and a compression frame to seal the chip against the manifold.

handling and temperature control consists of a pneumatic and electrical control module joined by an umbilical cord to heated fluid reservoirs and valving. The larger control module can be placed near the workspace, while necessary fluid reservoirs can be mounted directly on the microscope stage to minimize swept fluid volumes. Fluid control is provided by six pneumatic modules, two high-flow and four low-flow, that provide a flow rate through the chip of 0.5-110  $\mu\text{l}/\text{min}$ . The temperature control system can maintain a range of cell environmental temperatures, from room temperature to boiling, to within  $\pm 0.3$   $^\circ\text{C}$ . The stage-mounted fluid reservoirs are built to accept commercially available microcentrifuge tubes for ease of solution preparation and transport, while the valving is based on a novel design that minimizes fluid pressure pulses during valve actuation. Using these innovative features, the system pictured in Figure 6 provides precise control of the on-chip cellular environment.

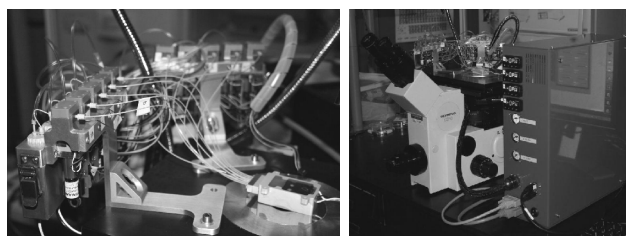


Figure 6: Fluid control reservoirs and valves mounted on microscope stage. The adjacent image shows the flow control box with pressure umbilical connection.

### EXPERIMENTATION

Experiments with the chip have thus far utilized the RAW 264.7 mouse macrophage line. Testing begins by flushing the chip and manifold with endotoxin-free water then medium. The total volume of a single imaging chamber is  $\sim 60$  nL, thus enabling rapid

medium exchange within the device. After this cleaning/passivation step, the cells are flowed into the device and captured at the cell constrictions. Prior to their use on the iCellator chip the cells, which have a fluorescent reporter construct (GFP-RelA), are stained with Hoechst 33258 (nuclear) and propidium iodide (live/dead). Figure 7 demonstrates a typical cell capture.

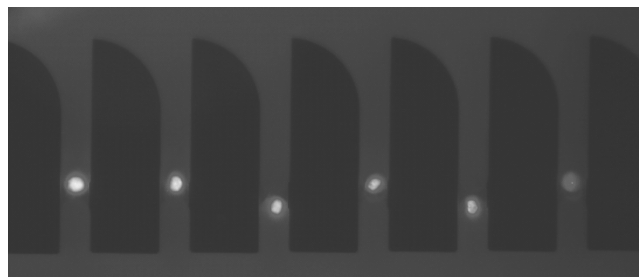


Figure 7: Hoechst stained single cells after trapping in the iCellator chip. Fluid flow is coming from the top of the image.

Once captured, the cells can be maintained in the chip for extended periods of time, requiring only temperature maintenance of the fluid manifold and steady perfusion of medium. The longest incubation period of the cells thus far has been approximately a 3 day long experiment. During longer duration experiments it is not uncommon to record cell division, as shown in Figure 8.

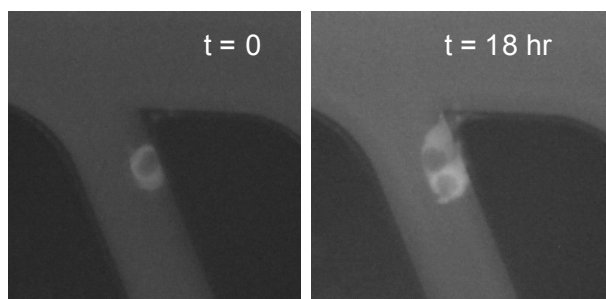


Figure 8: Division of cell adhering to entrance channel of a trap during an extended duration test.

After capture, a short incubation of  $\sim 0.5$  hr is performed to assure the cells are healthy and uncontaminated. This is verified by monitoring the propidium iodide live/dead stain and looking for premature translocation events. Once this is verified, the challenge channel can be exposed while the control channel is left unexposed. Challenges we have used include live *E. coli* bacteria and LPS purified from *E. coli* and other bacteria.

## RESULTS

After challenge, we monitor the translocation of RelA, a subunit of the transcription factor NF- $\kappa$ B, from the cytoplasm to the nucleus. Figure 9 shows a trapped macrophage with GFP labeled RelA. Figures 9a-c show GFP:RelA translocation progress after cell exposure to purified *E. coli* LPS. In figure 9d are image analysis results showing GFP fluorescence as a function of position and time. The dashed line in Figure 9a shows the location where the intensity measurements were taken. On-chip studies of these responses have lasted for  $\sim 3$  days with greater than 95% cell viability at conclusion.

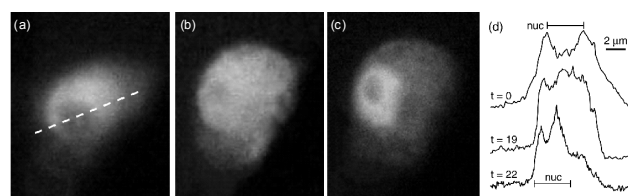


Figure 9: GFP:RelA translocation in a trapped RAW cell at  $t = -12$  (a), 7 (b), and 10 min (c). The cell was challenged with  $1 \mu\text{M}$  *E. coli* LPS at  $t = 0$ . (d) The intensity of GFP:RelA fluorescence in the cell as a function of position and time.

In our prior work, we demonstrated that a high concentration LPS challenge led to an early and rapidly completed GFP:RelA translocation in host cells, while a lower concentration challenge led to a delayed and slowly completed translocation. While simple translocation events, such as the one described in the figure above were recorded, our work also revealed the possibility of more complex kinetic events involving the oscillation of NF $\kappa$ B within the cell. Figure 10 shows the analysis of a cell that has undergone oscillation behavior in response to an *E. coli* LPS challenge.

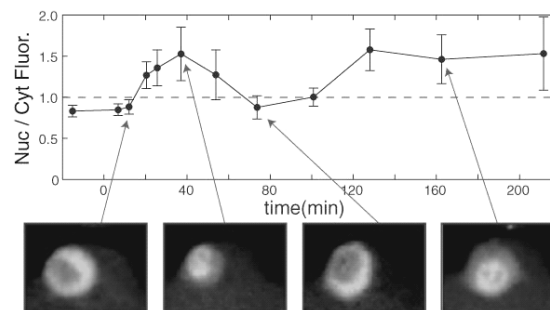


Figure 10: Oscillation of RelA in an iCellator-captured single cell challenged with *E. coli* LPS as a function of time. The Nuc/Cyt axis represents the ratio of GFP:RelA imaged in the nucleus to the cytoplasm.

Analysis of the GFP:RelA in the nucleus and the cytoplasm shows that not only is the oscillation phenomenon widespread, but that individual cells translocate and oscillate in unique manners. The oscillation magnitude and rate of response has also been found to depend not only on LPS dose but its chemotype (i.e. source species). These laboratory observations of oscillation agree with our computational modeling efforts of simulated immune response which predicted NF- $\kappa$ B oscillations after LPS exposure. Figure 11 shows the four general types of oscillation behavior predicted. Specifics on the computational modeling effort will be detailed in another forum.

Figure 12 shows a chart comparing the oscillation behavior of nine single cells to the same *E. coli* LPS exposure. Analysis of the oscillation patterns reveals heterogeneity in the oscillation behavior of each of the cells. This is demonstrated by asynchrony in timing of the first translocation event compared to subsequent translocations. In this specific experiment, it was observed that the percentage of single cells undergoing an initial translocation event in response to LPS is high ( $\sim 90\%$ ), however the percentage of cells that undergo a secondary translocation event is somewhat lower



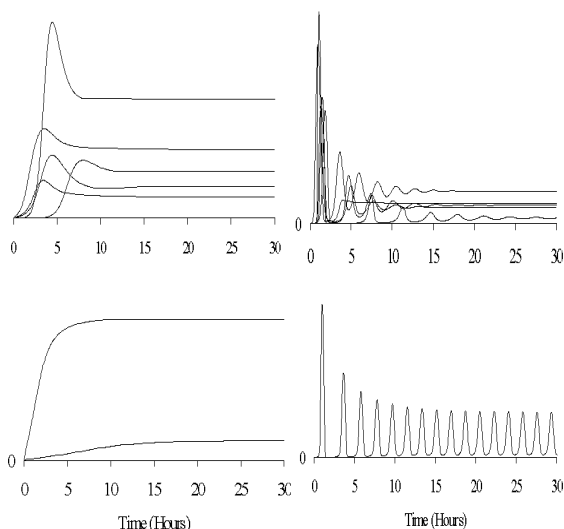


Figure 11: Four general classes of  $NF\kappa B$  oscillation behavior as predicted by computational modeling.

(~53%). Additionally, cells are shown to exhibit the different oscillation patterns predicted by our computational modeling efforts. The oscillation patterns shown in Figure 12 reveal the manifestation of the top two generalized patterns predicted by our modeling, though evidence of all four of the patterns have been observed in other experiments.

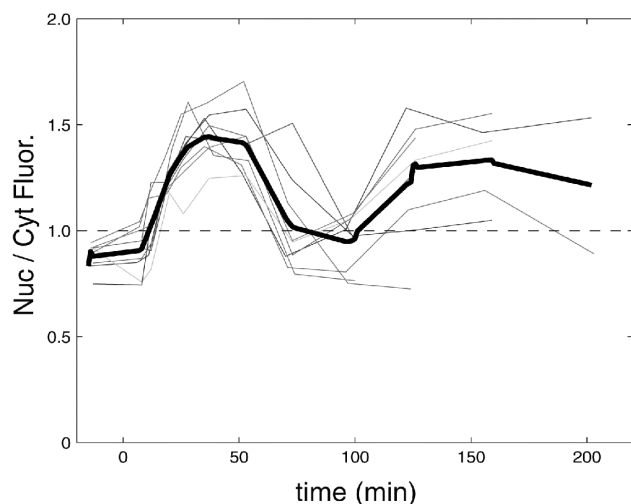


Figure 12: Compiled oscillation behavior of nine single cells responding to the same *E. coli* LPS challenge. The thick line indicates a population averaged measurement.

## CONCLUSIONS

We have developed an integrated microfluidic platform for imaging and analysis of host-pathogen interactions with single cell resolution - validated by performing LPS and bacterial challenge experiments on macrophages. Using reporter constructs and labeled antibodies, we observed  $NF\kappa B$  translocation events and oscillations in localization (nucleus vs cytoplasm) for the first time. TLR-4 signaling kinetics in macrophages were quantified as a function of LPS dosage, and it has been found that high concentrations lead to an early, rapid, and synchronous translocation response, while low concentrations produce a delayed and less synchronous response. Our work with computational models of the immune response predicated oscillation patterns of the  $NF\kappa B$  in response to LPS challenge, which has been clearly observed at the single cell level. Single cell measurement at this level provides unique insight into the operation of the global signaling network, and will be a valuable tool in studying the role of cell-intrinsic and extrinsic events in innate immunity.

## FUNDING STATEMENT

Sandia National Laboratories is a multi-program laboratory operated by Sandia Corporation, a wholly owned subsidiary of Lockheed Martin company, for the U.S. Department of Energy's National Nuclear Security Administration under contract DE-AC04-94AL85000.

## COPYRIGHT NOTICE

This material has been authored by Sandia National Laboratories under Contract No. DE-AC04-94AL85000 with the U.S. Department of Energy. The United States Government retains and the publisher, by accepting the material for publication, acknowledges that the United States Government retains a non-exclusive, paid-up, irrevocable, world-wide license to publish or reproduce the published form of this manuscript, or allow others to do so, for United States Government purposes.

## REFERENCES

- [1] D. Di Carlo et al, "Single-cell enzyme concentrations, kinetics, and inhibition analysis using high-density hydrodynamic cell isolation arrays", *Analytical Chemistry*, Vol. 78, 2006.
- [2] A. Tourovskaia, et al, "Differentiation-on-a-chip: A microfluidic platform for long-term cell culture studies", *Lab on a Chip*, Vol 5, 2005.
- [3] James, C.D. et al, "Nuclear translocation kinetics of  $NF\kappa B$  in macrophages challenged with pathogens in a microfluidic platform", *Biomedical Microdevices*, 11, 2009.

## CONTACT

Conrad James, cdjame@sandia.gov  
 Sandia National Laboratories  
 Biosensors and Nanomaterials  
 PO Box 5800, MS 0892  
 Albuquerque, NM 87185-0892

# A MONOLITHIC EWOD CHIP BY SURFACE MICROMACHINING

Wyatt C. Nelson\* and Chang-Jin "CJ" Kim

Mechanical and Aerospace Engineering Department, University of California, Los Angeles, (UCLA)

## ABSTRACT

We present a surface micromachining process to build monolithic two-plate electrowetting-on-dielectric (EWOD) droplet microfluidic chips. Our fabrication method removes the need for device alignment and assembly, and provides excellent control of cavity heights, which can be as small as a few microns. The monolithic EWOD chip is evaluated by performing creation, transport, splitting, and merging of 100 pL water droplets immersed in silicone oil.

## INTRODUCTION

Evolved from device ideas implementing conventional electrowetting [1], almost all electrowetting devices of today use a thin dielectric layer on surface electrodes, thus called electrowetting-on-dielectric (EWOD) [2; 3]. The two-plate configuration (Figure 1) is most often used in lieu of a single planar chip in order to facilitate droplet creation and splitting even in air (vs. in oil) [4]. While it is possible to draw random liquid branches from a sessile droplet using the electrowetting force [5] or to transport sessile droplets on one-plate EWOD devices on coplanar electrodes with the droplet electrically floating [6] or grounded-from-below [7], facile creation and splitting has not been demonstrated on a one-plate device without the use of additional forces such as dielectrophoresis [8]. Squeezing the droplet between hydrophobic parallel plates into a disk-like shape increases its internal pressure. In this state the dominant radius of curvature is related to the cavity height rather than the droplet radius. Under this condition, the contact angle change due to electrowetting can generate pressures sufficient for splitting. [4; 9]

A common way to produce a two-plate EWOD chip involves separate fabrication of the bottom substrate and top plate, followed by alignment, assembly, and bonding. The typical EWOD substrate is a glass or silicon wafer with photolithographically patterned surface electrodes covered by a thin dielectric, e.g. silicon dioxide or parylene. The typical top plate is ITO-coated glass to allow for visual inspection and electrical grounding. Both plates are coated with a spin-on hydrophobic fluoropolymer such as Teflon® or Cytop® prior to assembly. A variety of materials are used for spacing and/or bonding, including double-sided adhesive tape, SU-8, and rubber gaskets. With the exception of SU-8, spacers are manually aligned before the top plate is aligned and bonded. These post-processing steps make it challenging for the user to create a two-plate chip with precise cavity dimensions, especially at the micron scale. Additionally, top plate alignment and bonding complicates batch fabrication and integration of other fluidic and electrical components.

Several innovative alternatives to traditional cleanroom microfabrication have been reported for building EWOD substrates, including post-processed printed circuit boards [10], and a rapid prototyping technique in which electrodes are patterned by inkjet printing onto flexible copper-coated polyimide substrates [11]. Currently, though, no fabrication process has been reported to yield monolithic two-plate EWOD chips.

The monolithic chip presented here alleviates many of the limitations associated with assembled devices. For example, in the two-plate scenario the minimum droplet size that can be split by the electrowetting force is directly related to the cavity height, e.g. the cavity height should be less than about 1/5 the droplet radius [4,9], and therefore manipulation of picoliter droplets requires

micron cavity heights, which are easy to achieve using our proposed surface micromachining process. Reports of creating and splitting picoliter droplets in two-plate EWOD chips [12; 13] have demonstrated downscaling of the typical nanoliter devices by simply using more precise spacers and more careful assembly techniques in order to achieve ~10 micron cavity heights. The next-generation monolithic device, however, will accurately create pico- and femtoliter droplets without any assembly necessary, opening the door to more complex systems, such as pressurized processing, chip stacking, and integration with other electronic or fluidic devices.

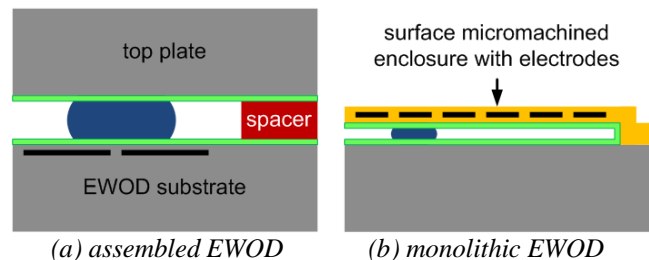


Figure 1: (a) The typical two-plate device consists of a top plate bonded by a spacer to an EWOD substrate, which has patterned electrodes and a dielectric layer. (b) The monolithic device has a thin-film enclosure embedded with EWOD electrodes. In both (a) and (b), working inner surfaces are coated hydrophobic.

## CHIP FABRICATION

### Materials selection

The characteristics of the inner cavity surfaces are important to EWOD performance for several reasons, which guided our choice to use the silicon device layer of a SOI wafer to serve as a sacrificial mold for the cavity. First, the device layer is extremely smooth, minimizing the number of defects that will exist in the membrane layer upon release. In most cases, surface roughness and pinhole defects are hindrances to EWOD droplet actuation and may prevent movement of the contact line altogether. Second, the device layer enables excellent control of cavity height because it can be ordered to have a uniform thickness ranging from less than a micron to over one hundred microns. Such precise control of cavity height enables precious control of droplet volumes. Finally, silicon is an excellent sacrificial material for this application because it can be removed by  $\text{XeF}_2$ , which is clean and highly selective to the dielectrics silicon dioxide and silicon nitride.

The four micron thick surface micromachined membrane, which serves as the top plate, is about 100 times thinner than plates used for assembled chips. By using a special low-stress silicon nitride grown by plasma-enhanced chemical vapor deposition (PECVD), it was possible to span over three hundred microns without warping or buckling. In fact, the nitride membranes reported here, which are suspended 10 microns above the substrate, were subject to wet photoresist stripping and repeating rinsing steps upon release, with no stiction.

A key requirement for EWOD actuation of aqueous liquids is that the dielectric surface must be sufficiently hydrophobic; otherwise the droplet will not slide. For the typical case of coating a flat, open surface hydrophobic, spin-coating a fluoropolymer

solution is straightforward, and the deposited thickness is easy to measure, *e.g.* by profilometry. Coating the inner surfaces of a 10  $\mu\text{m}$  cavity, however, is somewhat more complicated. Our current method is to fill the cavity with fluoropolymer solution and spin the chip at a very high speed (7000 rpm) so that the liquid flows out of the cavity via release openings. While we observed through electrowetting experiments that this technique can yield hydrophobic inner surfaces, we have not characterized the resultant film thickness or uniformity. In some cases, we observed thick polymer residues where membrane anchors had obstructed the coating flow. We are currently developing a more controlled coating technique that will be far less sensitive to the chip layout and cavity height.

### Fabrication process flow

A SOI wafer was used as the substrate for the monolithic chip. Figure 2 shows the process flow, which begins with deep reactive ion etching (DRIE) of the 10  $\mu\text{m}$  silicon device layer using photoresist (AZ5214) as a mask. The device layer serves as a mold for the eventual thin-film membrane and thus determines the cavity height. Next, a 100 nm thermal oxide is grown on the etched device layer. This layer was found to be necessary as an etch stop defining the inner top surface of the cavity during the  $\text{XeF}_2$  release etch, which showed poor selectivity to the low-stress silicon nitride that was subsequently grown by PECVD. This nitride and the underlying oxide form a composite insulating layer which sustains the electric field necessary to generate EWOD force.

Metal electrodes, composed of 200 nm thick gold upon a 5 nm titanium or chromium adhesion layer, are deposited by e-beam evaporation and wet etched. When it was desirable to have transparent electrodes, the gold was completely etched away from the device area, leaving only the highly transparent titanium layer, through which droplets can be seen. The membrane is completed by another PECVD low-stress nitride, which is then etched by RIE to form release openings. Importantly, the photoresist mask used to pattern the release openings is also used to protect the top surface of the membrane during the  $\text{XeF}_2$  release etch, which exhibited selectivities of less than 1:20 to our low-stress nitride.

As shown in Figure 2, the  $\text{XeF}_2$  first removes the exposed silicon, and then continues to etch the sacrificial silicon under the enclosure and between the anchors to completely evacuate the cavity. Upon release, the chips are stripped of photoresist using ALEG 355 at 100  $^\circ\text{C}$  and thoroughly rinsed in DI water. A drop of 6 wt% solution of Cytosol<sup>®</sup> is then placed onto chip, which it spontaneously wets, filling up the cavity. The chip is then affixed to a carrier wafer, which is spun at 7000 rpm for 2 minutes to ensure that most of the fluoropolymer solution flows out of the cavity via the release openings. Finally, the chip is baked on a hot plate at 200  $^\circ\text{C}$  for ten minutes to ensure that the solvent is completely evaporated.

### Chip layout

The monolithic chip layout is composed of three basic elements: anchors, electrodes, and release openings. Figure 2 illustrates a very basic layout, and Figure 3a shows the layout of an actual chip that was fabricated using the process of Figure 2 used to demonstrate EWOD. In our experiments, liquids were pumped into the cavity manually by a syringe. To establish a fluid connection, a NanoPort<sup>®</sup> was placed over the inlet, located several millimeters away from the EWOD electrodes.

Regions of the membrane in which there are embedded EWOD actuation electrodes span several hundred microns. To measure membrane flatness, a profilometer scan was performed

along the dashed line path shown in Figure 3a. The profile, plotted in Figure 3b, indicate a maximum deflection of about 200 nm, resulting in an approximate slope of 0.0013 from the edge to the center of the cavity, or a 1.3 % error associated with the height of a 100 pL droplet in this region.

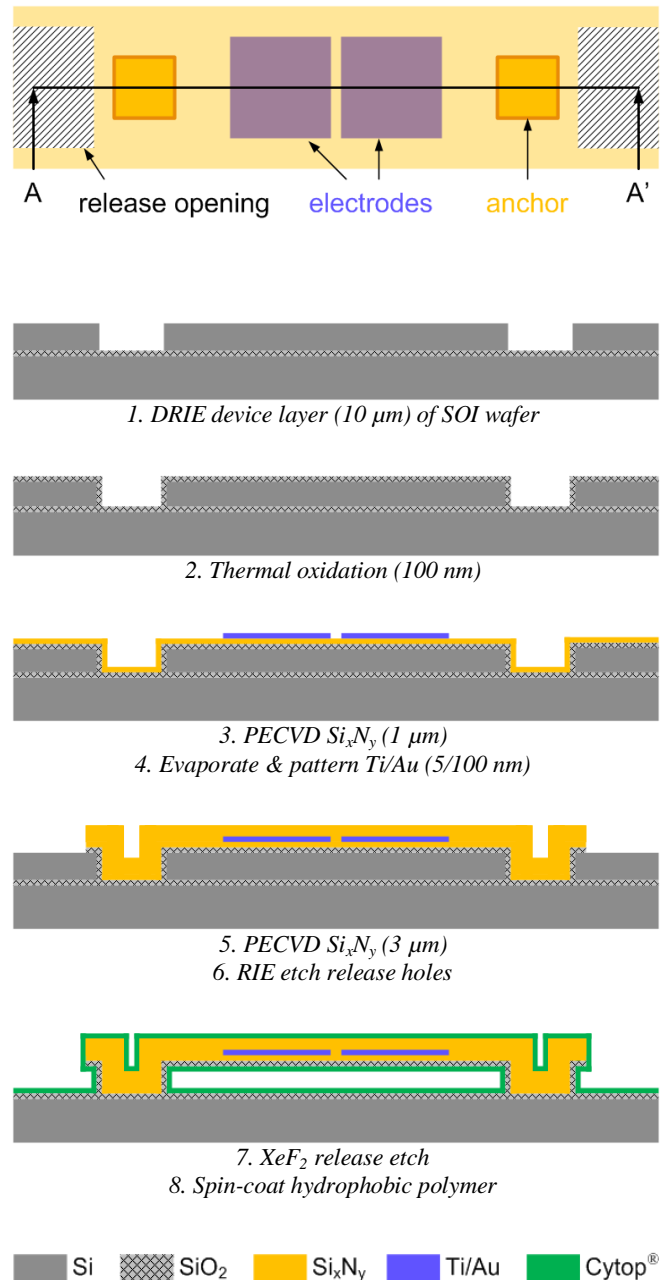
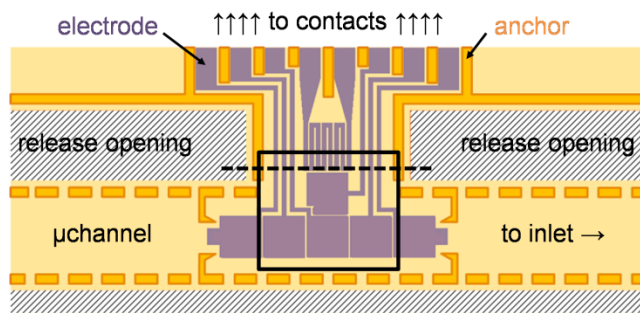
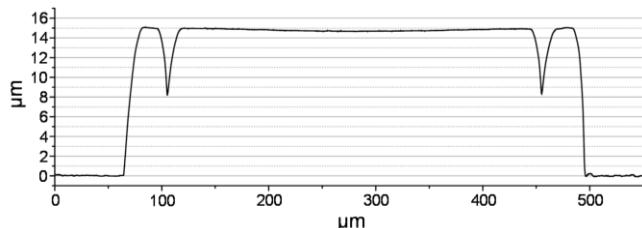


Figure 2: Top view of basic layout for enclosed EWOD devices, and the process flow at cross section A-A'. The process begins with DRIE through the device layer of an SOI wafer having 200 nm buried oxide.



(a) device layout



(b) Profilometer scan along dashed line

Figure 3: (a) device layout (black box indicates field of view in Figure 4) and (b) a profilometer scan along the path indicated by the dashed line in (a). Note that the profilometer stylus is too large to capture the shape of the 20  $\mu\text{m}$  wide anchors.

## RESULTS AND DISCUSSION

Droplet creation, transport, splitting, and merging were performed in order to evaluate the chip. Figure 4, for which the field of view corresponds to the black box in Figure 3, shows video frames of creation and transport (a.1 to a.6) and splitting and merging (b.1 to b.4). Actuations of DI water in silicone oil (0.6 cSt) were achieved by applying driving voltages  $36 V_{\text{rms}}$  at 100 Hz.

Figure 4a.1 provides the initial conditions prior to EWOD actuation and indicates the water-oil interface which separates the water reservoir from the oil medium. The water reservoir is in contact with anchors above the field of view. The faint grey  $100 \times 100 \mu\text{m}$  electrodes are made of a very thin (5 nm thick) titanium to ensure that the water-oil interface can be clearly seen. During actuations, biased electrodes are labeled “ON” and all other electrodes as well as the silicon substrate were grounded. Frames a.2 to a.4 depict the liquid extension process in which a small volume of water is pulled away from the reservoir, but still connected by a fluid neck. After the droplet is about three electrode lengths away, the neck breaks and a droplet is created (a.5) and transported (a.6).

Splitting and merging is shown by the series of video frames in Figure 4b. A parent droplet is pulled in opposite directions by EWOD (b.2), producing two daughter droplets having similar volumes (b.3), which are merged by biasing the central electrode (b.4).

Water droplets were actuated in an oil medium in order to avoid evaporation. Evaporation plays a much greater effect in this scale, which is  $\sim 10$  times smaller than the usual EWOD devices of today having  $\sim 1 \text{ mm}$  pad size. Another consequence of using oil instead of air as the filler medium in any EWOD chip is that the

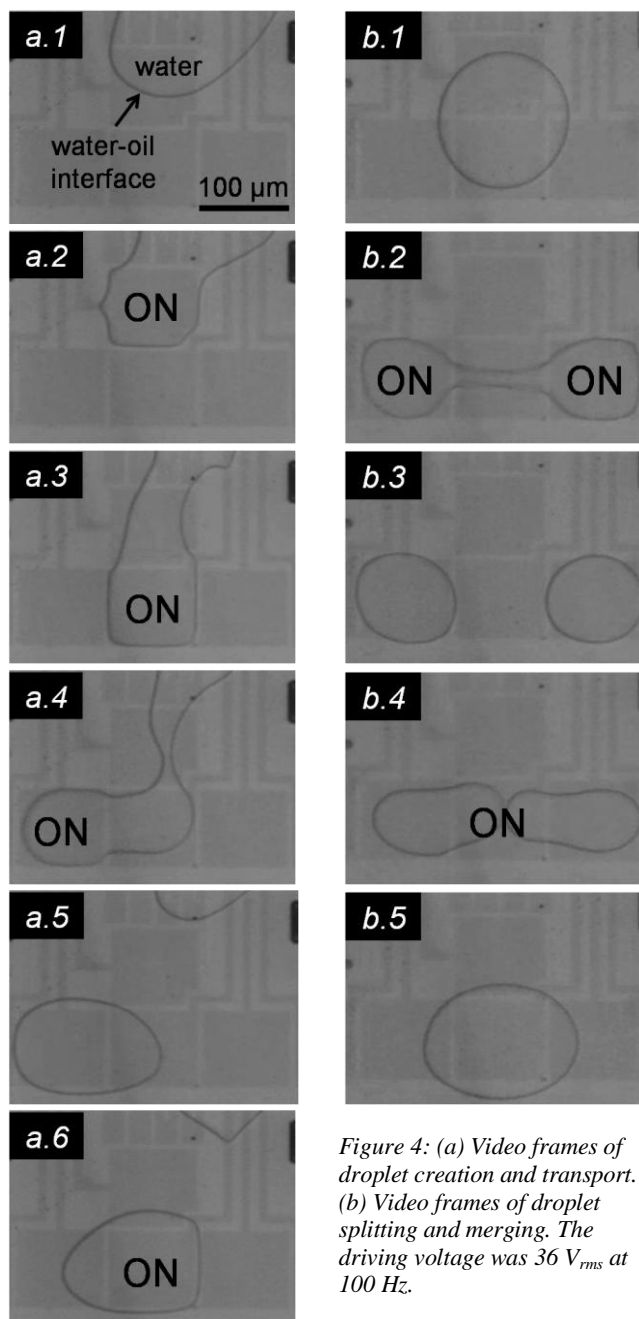


Figure 4: (a) Video frames of droplet creation and transport. (b) Video frames of droplet splitting and merging. The driving voltage was  $36 V_{\text{rms}}$  at 100 Hz.

actuation voltage is relatively low as a result of reduced hysteresis drag [14]. In many applications, though, oil-free operation is preferred and can be achieved via humidity control.

## CONCLUSIONS

We have developed a surface micromachined monolithic two-plate EWOD chip and used it to demonstrate creation, transport, splitting, and merging of 100 pL water droplets in a  $10 \mu\text{m}$  high oil-filled cavity. Many of the limitations associated with alignment and bonding of conventional two-plate EWOD chips are bypassed through this new fabrication process, which holds great potential for producing highly integrated, picoliter digital microfluidic systems.

## ACKNOWLEDGEMENTS

The authors would like to thank Dr. Prosenjit Sen and all members of the UCLA Micro and Nano Manufacturing Laboratory for participating in helpful discussions. For this work WN was supported by the NIH (R01 RR020070) and the NSF Graduate Research Fellowship Program (GRFP) and an NSF Integrative Graduate Education and Research Traineeship (DGE-0654431) through the UCLA Materials Creation Training Program (MCTP).

## REFERENCES

- [1] E. Colgate, H. Matsumoto, "An investigation of electrowetting-based actuation," *J. Vac. Sci. Technol. A*, **8**, 4, pp 3625-3633 (1990).
- [2] J. Lee, H. Moon, J. Fowler, T. Schoellhammer, and C.-J. Kim, "Electrowetting and electrowetting-on-dielectric for microscale liquid handling," *Sens. Actuators, A*, **95**, pp 259-268 (2002).
- [3] H. Moon, S. K. Cho, R. L. Garrell, and C.-J. Kim, "Low voltage electrowetting-on-dielectric," *J. Appl. Phys.*, **92**, 7, pp 4080-4087 (2002).
- [4] S. K. Cho, H. Moon, and C.-J. Kim, "Creating, Transporting, Cutting, and Merging Liquid Droplets by Electrowetting-Based Actuation for Digital Microfluidic Circuits," *J. Microelectromech. Syst.*, **12**, 70 (2003).
- [5] F. Mugele, S. Herminghaus, "Electrostatic stabilization of fluid microstructures," *App. Phys. Lett.*, **81**, 12, pp 2303-2305 (2002).
- [6] U.-C. Yi and C.-J. Kim, "Characterization of electrowetting actuation on addressable single-side coplanar electrodes," *J. Microelectromech. Syst.*, **16**, pp 2053-2059 (2006).
- [7] C.G. Cooney, C.-Y. Chen, M.R. Emerling, A Nadim, and J.D. Sterling, "Electrowetting droplet microfluidics on a single planar surface," *Microfluid. Nanofluid.*, **2**, pp 435-446 (2006).
- [8] T.B. Jones, M. Gunji, M. Washizu, and M.J. Feldman, "Dielectrophoretic liquid actuation and nanodroplet formation," *J. Appl. Phys.*, **89**, pp 1441-1448 (2001).
- [9] H. Ren, "Electrowetting-based sample preparation: an initial study for droplet transportation, creation and on-chip digital dilution," Ph.D. Thesis, Duke University (2004).
- [10] J. Gong and C.-J. Kim, "Direct-Referencing Two-Dimensional-Array Digital Microfluidics Using Multi-Layer Printed Circuit Board," *J. Microelectromech. Syst.*, Vol. 17, 2008, pp. 257-264.
- [11] M. Abdelgawad and A. R. Wheeler, "Rapid Prototyping in Copper Substrates for Digital Microfluidics," *Adv. Mater.*, **19**, pp 133-137 (2007)
- [12] S. U. Son, D. Chatterjee, and R. L. Garrell, "Electrically-induced splitting and generation of sub-nanoliter droplets in air on a digital microfluidic device," *Proc. Int. Conf.  $\mu$ TAS 2006*, pp 128-130.
- [13] J. H. Song, R. Evans, Y.-Y. Lin, B.-N. Hsu, and R. B. Fair, "A scaling model for electrowetting-on-dielectric microfluidic actuators," *Microfluid. Nanofluid.*, **7**, 75 (2009).
- [14] M. G. Pollack, A. Shenderov, and R. B. Fair, "Electrowetting-based actuation of liquid droplets for microfluidic applications," *Appl. Phys. Lett.*, **77**, pp 1725-1727 (2000).

## CONTACT

\*W.C.Nelson, tel: +1-310-883-8971; wyattnelson@UCLA.edu

# AN ESCHERICHIA COLI CONCENTRATOR USING MAGNETIC PARTICLES IN A MICROFLUIDIC CHANNEL FOR THE URINARY TRACT INFECTION (UTI) APPLICATION

Yongmo Yang, Sangpyeong Kim, and Junseok Chae

School of Electrical, Computer and Energy Engineering (ECEE), Arizona State University  
Tempe, Arizona 85287-5706, United States of America

## ABSTRACT

This paper reports a miniaturized lab-on-a-chip device to detect *Escherichia coli* (*E. coli*) from simulated urine using magnetic particles (MPs) in a microfluidic channel. The lab-on-a-chip device consists of two chambers connected in series, *E. coli* concentration and sensing chamber, integrated with a label free impedance sensor to detect the concentration of *E. coli* for urinary tract infection (UTI) application. The two chamber configuration is designed to reduce potential false-positive response caused by proteins in urine. The integrated impedance sensor in the concentration chamber shows little impedance change in different *E. coli* concentrations due to masking effect by proteins while the one in the sensing chamber shows a significant (30 kΩ) change between control (no *E. coli*) and a concentration of  $6.4 \times 10^4$  CFU/mL, close to the threshold of UTI infection, which is above  $10^5$  CFU/mL. This demonstrates the effectiveness of the dual-chamber design to detect *E. coli* for the UTI application.

## INTRODUCTION

Urinary Tract Infection (UTI) is one of the common infections in human, resulting in 8 million hospital visits in US annually [1]. The urine of UTI patients may contain a microbial strain, which can cause UTI, such as *Escherichia coli*, *Proteus mirabilis*, *Klebsiella*, *Enterobacter*, *Enterococcus*, *Staphylococcus saprophyticus* and others [2]. Among them, *E. coli* is responsible for up to 80% of UTI [2]. Current standard methods of *E. coli* detection include multiple-tube fermentation, membrane filter and plate count [3]. Among them, the plate count method is the most widely used, which cultures *E. coli* on an agar plate and counts cultured colony forming units (CFU). If CFU exceeds  $10^5$  CFU/mL, the patient has a high chance of having symptomatic UTI [4]. Typically, people do not have symptoms below  $10^5$  CFU/mL [5]. The plate count method offers accurate diagnose, however it is not a feasible method when patients need an immediate medical treatment because it requires lengthy, from 24 to 48hrs, cultivation of urine samples and laborious procedure. In order to avoid such lengthy processes, alternative methods have been developed. Goodridge *et al.* used a fluorescent bacteriophage assay (FBA), Subramanian *et al.* developed immunosensor techniques to utilize antibody-derivatized surface plasmon resonance devices, and Wang *et al.* used piezoelectric crystals and enzyme-linked immunosorbent assays (ELISA) techniques [6-8]. Other researchers developed electrochemical impedance spectroscopy (EIS) to detect *E. coli* by monitoring the binding of antibody-antigen reaction [9-13]. All those methods offer a quick diagnose of *E. coli*; however capturing efficiency of *E. coli* is low.

In this paper, we take advantage of microfluidics in immunomagnetic separation (IMS) to overcome the limitation, low capturing efficiency. IMS uses magnetic particles (MPs) that are covered by anti-*E. coli* antibody to capture *E. coli*. The captured *E. coli* is transported via microfluidic channels and the impedance of *E. coli*-immobilized magnetic beads is measured to estimate the concentration of *E. coli*. The impedance results are verified by counting cultured colonies of *E. coli*, the current standard practice.

## DESIGN

The schematic of the lab-on-a-chip device is illustrated in Figure 1. The *E. coli* concentrator/detector device consists of two mechanical valves [14] and two chambers, concentration and sensing, to reduce non-specific absorption by proteins potentially co-existing with *E. coli* in urine.

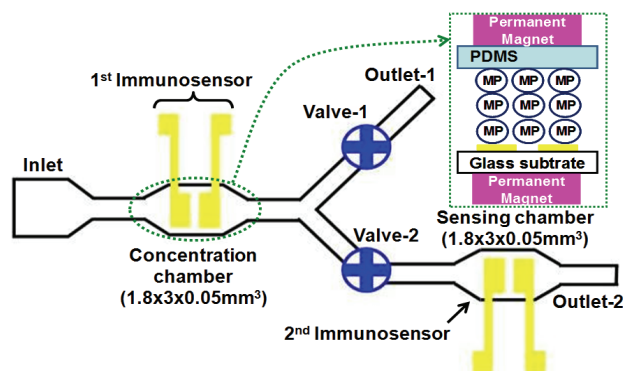


Figure 1: A schematic of the lab-on-a-chip *E. coli* concentrator/detector. Two separate (concentration and sensing) chambers capture and sense *E. coli*, respectively. Magnetic particles (MPs) inside the chambers are manipulated by external magnets.

Two mechanical valves control the fluidic stream to Outlet 1 and the sensing chamber. Two immunosensors to measure impedance are integrated in the concentration and sensing chambers and made of two gold (Au) electrodes. MPs were retained in the chamber by placing, two permanent magnets above and beneath of the chambers. Figure 2 shows the length of the chambers as a function of *E. coli* capturing rate.

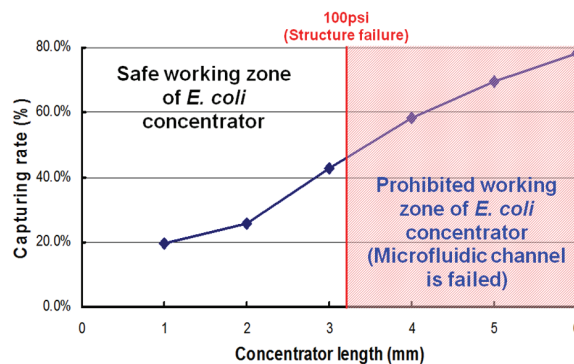


Figure 2: Design criteria for concentration and sensing chamber: the length of the concentrator chamber is determined by the structural failure limit, 100 psi.

As the length of the chamber increases the capturing rate enhances. Practical limitation exists; as the length increases the fluidic pressure increases as well. The current structure of the lab-on-a-chip device allows up to 100 psi where the structural failure starts. Thus, we chose the length of the chambers as 3 mm.

### Fabrication

Similar to our previous approaches, we used a replica molding technique using a silicon mold [15]. This two-masks process is shown in Figure 3.

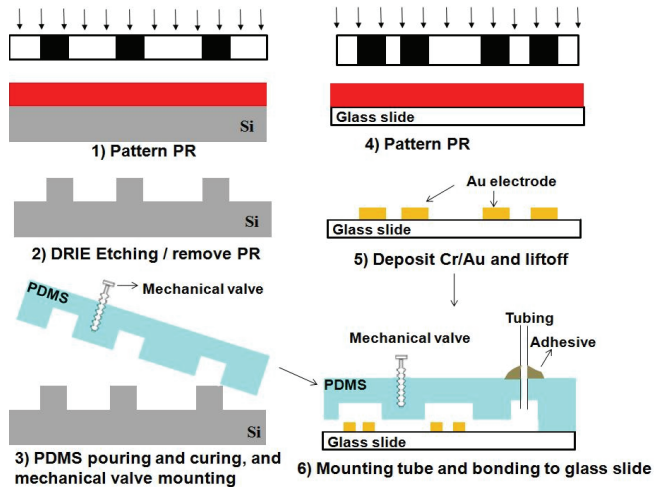


Figure 3: Fabrication flow: forming the top using the replica molding technique (1-3) and the bottom substrate that has electrodes for impedance measurements (4-6).

The silicon mold fabrication starts from photoresist (PR) coating and patterning for the concentrator, followed by Deep RIE etching,  $\sim 10 \mu\text{m}$ . PDMS (Polydimethylsiloxane) was mixed (10:1) with base and curing agents and then poured on the silicon mold. After 20 min curing in an oven at  $80^\circ\text{C}$ , the PDMS replicas were peeled off, and two mechanical valves were assembled on the PDMS replica [14]. Then, PR was coated on the glass slide substrate and lithographically patterned. Cr/Au films for electrodes were evaporated (Edward II). The surfaces of the glass slide and PDMS replica were treated by oxygen plasma (Harrick Plasma) for 1 min at 100 W. Finally the PDMS top was bonded to the glass slide, and they were cured in the oven at  $80^\circ\text{C}$  for 40 min. Figure 4 shows the fabricated lab-on-a-chip device.

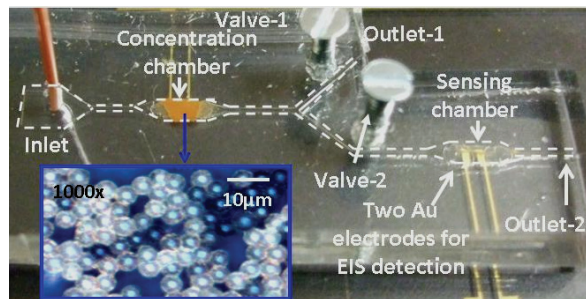


Figure 4: Fabricated lab-on-a-chip *E. coli* concentrator/sensor (permanent magnets are not shown).

## EXPERIMENTAL

### Reagent

PDMS (Sylgard 184 elastomer kit) was obtained from Dow Corning. MPs from Spherotech, Inc were  $4.5 \mu\text{m}$  in diameter and coated with COOH-terminated self-assembled monolayers (SAM) on the surface. Sodium acetate (NaAc), 1-ethyl-3-(3-dimethylaminopropyl) carbodiimide (EDC) and N-hydroxysuccinimide (NHS) were obtained from Pierce and GE health. Phosphate buffered saline solution (PBS) from Fisher scientific was used as a washing solution. Simulated urine was a cocktail of  $\text{CaCl}_2 \cdot \text{H}_2\text{O}$ ,  $\text{Na}_2\text{SO}_4$ ,  $\text{MgSO}_4 \cdot 7\text{H}_2\text{O}$ ,  $\text{NH}_4\text{Cl}$ , KCl, Urea, Creatinine and tryptic soy. *E. coli* K-12 (ATCC 10798) was obtained from American Type Culture Collection. The pure culture of *E. coli* K-12 was prepared in a tryptic soy broth at  $37^\circ\text{C}$ .

### Test setup

MPs were immobilized with anti-*E. coli* antibody. MPs coated with COOH-SAM were mixed with EDC and NHS in order to activate the functional group of SAM, followed by PBS wash. The anti-*E. coli* antibody was blended with 10 mM NaAc, and the mixture of them was mixed with MPs to conjugate the anti-*E. coli* antibody with activated COOH-terminated SAM on the surface of MPs. In order to avoid non-specific absorption, Bovine serum albumin (BSA) was added with MPs. We prepared different concentrations of *E. coli* solution (100%, 10%, 1%, 0.1%, and 0.01%) with BSA in simulated urine.

Figure 5 shows the characterization setup. A syringe pump delivered MPs, mannitol solution and a mixture of *E. coli*, albumin and simulated urine to the concentration chamber. Permanent magnets were used for manipulating MPs. MPs, mannitol solution, and the sample were flowed by  $5 \mu\text{L}/\text{min}$ ,  $2 \mu\text{L}/\text{min}$  and  $2 \mu\text{L}/\text{min}$ , relatively. A LCR meter measured impedance at concentration and sensing chambers and the data were recorded via LabVIEW.

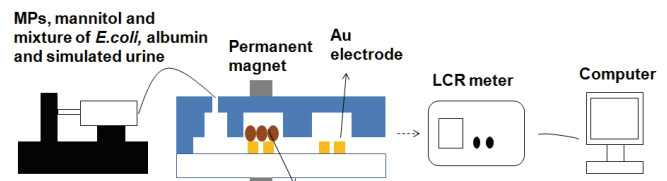


Figure 5: Characterization setup of *E. coli* lab-on-a-chip device.

### Test Procedure

MPs conjugated with anti-*E. coli* antibody were injected inside the concentration chamber. Two permanent magnets were placed above and beneath of the chambers to control MPs release and retention. When valve-1/2 were open/close, we retained MPs in the concentration chamber and flew  $10 \mu\text{L}$  of *K-12 E. coli* and albumin ( $1 \text{mg}/\text{mL}$ ) in simulated urine as shown in Figure 6(a). After *E. coli* was captured by anti-*E. coli* antibody on the MPs, we flew  $90 \mu\text{L}$  of 0.1 M mannitol solution and the impedance sensor in the concentration chamber measured the impedance. When valve-1/2 were close/open and the two permanent magnets guided the MPs conjugated with *E. coli* to the sensing chamber, the impedance of the MPs was measured again as shown in Figure 6(b). The mannitol solution was used to allow *E. coli* alive at high solution impedance.

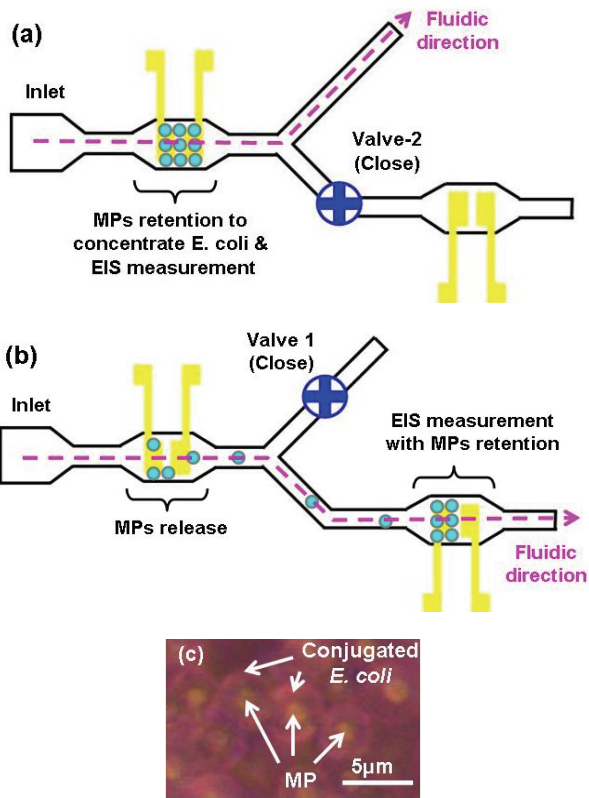


Figure 6: *E. coli* concentration and impedance measurements procedure: a) MPs retention, *E. coli* insertion, and measurement in the concentration chamber, b) MPs release, retention, and measurement in the sensing chamber, and c) *E. coli* conjugated by MPs (after gram stain).

## RESULT

Figure 7 shows the immunosensor measurement in the concentration chamber. In the range of  $6.4 \times 10^4$  to  $6.4 \times 10^6$  CFU/mL, covering the threshold of UTI ( $10^5$  CFU/mL), the measured impedance changes were almost negligible. This suggests that albumin in the simulated urine was absorbed on the surface of Au electrodes by the hydrophobic interaction to mask the impedance changes [16-21]. Due to the masking, the impedance measurements did not reflect the change of the *E. coli* concentrations.

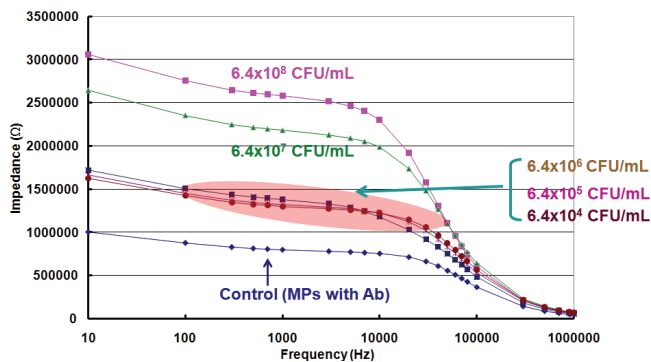


Figure 7: Measured impedance data in the concentration chamber.

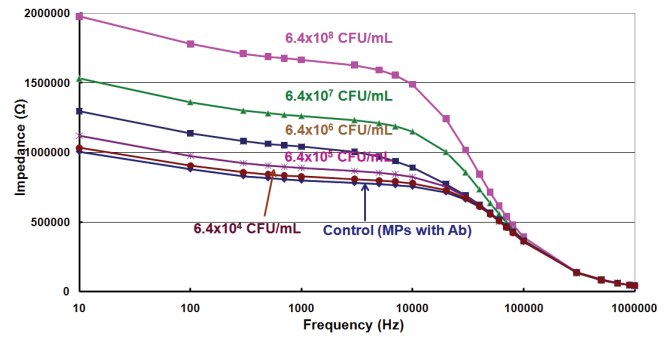


Figure 8: Measured impedance data in the sensing chamber.

Figure 8 shows the impedance measurement in the sensing chamber. As *E. coli* concentration increases, the impedance increases because the membrane of *E. coli* behaves as an insulator [3]. Comparing with the results in the concentration chamber, the impedance changes were bigger in the range from  $6.4 \times 10^4$  to  $6.4 \times 10^6$  CFU/mL. This is because albumin in the sample was removed effectively in the concentration chamber by hydrophobic interaction of albumin with Au electrodes. This result demonstrates the need of the two chamber configuration to detect *E. coli*. Figure 9 compares the impedance changes and traditional cultured colony forming unit method, the current standard practice, as a function of the concentration of *E. coli*. The impedance change at 1 kHz was 30 kΩ between control (no *E. coli*) and  $6.4 \times 10^4$  CFU/mL, which is large enough to distinguish using a commercially-available portable impedance meter [22]. As the concentration of *E. coli* increases the impedance consistently increases. The threshold of UTI,  $10^5$  CFU/mL, was shown as a reference in the figure. The impedance data was further verified by counting cultured colonies of *E. coli* in Figure 9(b). We believe that the dual-chamber configuration allows reducing false positive UTI detection in the urine.

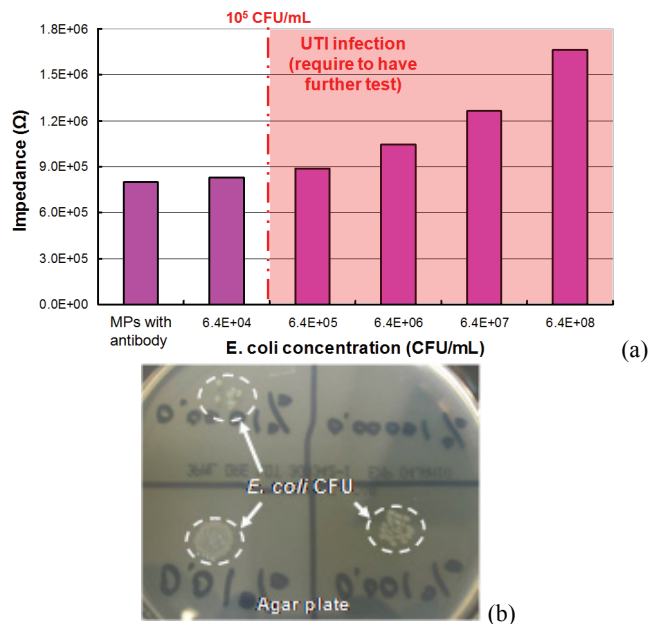


Figure 9: a) Impedance data at 1 kHz, b) *E. coli* CFU on a culturing agar plate at the different *E. coli* concentrations.



## CONCLUSION

We demonstrated a dual-chamber lab-on-a-chip device to detect *E. coli* in simulated urine for UTI applications. The dual chamber configuration allows detecting the concentration of *E. coli* at the presence of protein in the sample. Impedance data at the concentration chamber results show that impedance changes were very little between  $6.4 \times 10^4$  and  $6.4 \times 10^6$  CFU/mL due to hydrophobic interaction of albumin on Au electrodes. Albumin masks the electrodes surfaces so that the measured impedance cannot be responsive to the concentration of *E. coli* in the sample. On the other hand, the impedance data in the sensing chamber did not show such masking effect because albumin was removed effectively in the concentration chamber. The impedance change between the control (no *E. coli*) and  $6.4 \times 10^4$  CFU/mL was approximately 30 k $\Omega$ . Our successful detection result suggests that the dual chamber lab-on-a-chip device may be useful for diagnosis of symptomatic UTI.

Future work includes a reproducibility testing of the *E. coli* lab-on-a-chip device and improving sensitivity of impedance measurement by changing the design of the electrodes for distinguishing asymptomatic and symptomatic UTI.

## ACKNOWLEDGEMENT

The authors thank to Mr. Seokheun Choi for numerous and valuable discussions, and staff in CSSER (Center for Solid-State Electronics Research) at Arizona State University. This work is partially supported by NSF (ECCS-0901440).

## REFERENCES

- [1] J. W. Warren and H. L. Mobley, "Urinary Tract Infections", Washington, DC, ASM Press, 1996.
- [2] C. M. Kunin, "Detection, prevention and management of urinary tract infections," 4<sup>th</sup> ed. PA: Lea&Febiger, 1987.
- [3] P. Geng, X. Zhang, W. Meng, Q. Wang, W. Zhang, L. Jin, Z. Feng and Z. Wu, "Self-assembled monolayers-based immunosensor for detection of *Escherichia coli* using electrochemical impedance spectroscopy", *Electrochimica Acta*, 53, 14, (2008).
- [4] M. T. N. Campanha, S.Hoshino-Shimizu, and M. B. Martinez, "Urinary tract infection: detection of *Escherichia coli* antigens in human urine with an ELIEDA immunoenzymatic assay", *Journal of Public Health*, 6, 2 (1999)
- [5] C. M. Kunin, L. V. White and T. H. Hua, "A Reassessment of the Importance of "Low-Count" Bacteriuria in Young Women with Acute Urinary Symptoms", *Annals of Internal Medicine*, 119, 6 (1993)
- [6] L. Goodridge, J. Chen and M. Griffiths, "Development and characterization of a fluorescent-bacteriophage assay for detection of *Escherichia coli* O157:H7", *Applied and Environmental Microbiology*, 65, 4 (1999).
- [7] A. Subramanian, J. Irudayaraj, and T. Ryan, "A mixed self-assembled monolayer-based surface plasmon immunosensor for detection of *E. Coli* O157:H7", *Biosensors and Bioelectronics*, 21, 7 (2006).
- [8] N. Wang, M. He and H. C. Shi, "Novel indirect enzyme-linked immunosorbent assay (ELISA) method to detect Total *E. Coli* in water environment", *Analytica Chimica Acta*, 590, 2 (2007).
- [9] C. Ruan, L. Yang and Y. Li, "Immunobiosensor Chips for Detection of *Escherichia coli* O157:H7 Using Electrochemical Impedance Spectroscopy", *Analytical Chemistry*, 74, 18 (2002).
- [10] V. E. Gomez, S. Campuzano, M. Pedrero and J. M. Pingarron, "Gold screen-printed-based impedimetric immunobiosensors for direct and sensitive *Escherichia coli* quantisation", *Biosensors and Bioelectronics*, 24, 11 (2009).
- [11] L. Wang, Q. Liu, Z. Hu, Y. Zhang, C. Wu, M. Yang, and P. Wang, "A novel electrochemical biosensor based on dynamic polymerase-extending hybridization for *E. Coli* O157:H7 DNA detection", *Talanta*, 78, 3 (2009).
- [12] R. Maalouf, C. F. Wirth, J. Coste, H. Chebib, Y. Saikali, O. Vittori, A. Errachid, J. P. Cloarec, C. Martelet and N. J. Renault, "Label-Free Detection of Bacteria by Electrochemical Impedance Spectroscopy: Comparison to Surface Plasmon Resonance", *Analytical Chemistry*, 79, 13 (2007).
- [13] L. Yang and R. Bashir, "Electrical/electrochemical impedance for rapid detection of foodborne pathogenic bacteria", *Biotechnology Advances*, 26, 2 (2008).
- [14] D. B. Weibel, *et al.*, "Torque-Actuated Valves for Microfluidics," *Analytical Chemistry*, 77 (2005).
- [15] Y. Yang and J. Chae, "A miniaturized protein separation using a liquid chromatography column on a flexible substrate," *Journal of Micromechanics and Microengineering*, 18, 12 (2008).
- [16] T. Ederth, P. Claesson and B. Liedberg, "Self-Assembled Monolayers of Alkanethiolates on Thin Gold Films as Substrates for Surface Force Measurements. Long-Range Hydrophobic Interactions and Electrostatic Double-Layer Interactions", *Langmuir*, 14 (1998)
- [17] B. Catimel, A. M. Scott, F. T. Lee, N. Hanai, G. Ritter, S. Welt, L. J. Old, A. W. Burgess, and E. C. Nice, "Direct immobilization of gangliosides onto gold-carboxymethyl-dextran sensor surfaces by hydrophobic interaction: applications to antibody characterization", *Glycobiology*, 8 (1998)
- [18] E. Ostuni, L. Yan and G. M. Whitesides, "The interaction of proteins and cells self-assembled monolayers of alkanethiolates on gold and silver", *Colloids and Surfaces B: Biointerfaces*, 15, 1 (1999)
- [19] W. Melander and C. Horvath, "Salt effects on hydrophobic interactions in precipitation and chromatography of proteins: An interpretation of the lyotropic series", *Archives of Biochemistry and Biophysics*, 183, 1 (1977)
- [20] S. Zhang and Y. Sun, "Further studies on the contribution of electrostatic and hydrophobic interactions to protein adsorption on dye-ligand adsorbents", *Biotechnology and Bioengineering*, 75, 6 (2001)
- [21] P. Roach, D. Farrar and C. C. Perry, "Interpretation of Protein Adsorption: Surface-Induced Conformational Changes", *Journal of American Chemical Society*, 127 (2005)
- [22] TOA Electronics, Inc, [http://www.toaelectronics.com/spec\\_sheets/zm-104.pdf](http://www.toaelectronics.com/spec_sheets/zm-104.pdf)

## CONTACT

Y. Yang, tel: +1-602-741-0193; [yongmo.yang@asu.edu](mailto:yongmo.yang@asu.edu)

# LOW PRESSURE DROP MICRO PRECONCENTRATORS WITH A COBWEB TENAX-TA FILM

B. Alfeeli<sup>1,2\*</sup> and M. Agah<sup>1</sup>

<sup>1</sup>Virginia Polytechnic Institute and State University, Blacksburg, Virginia, USA

<sup>2</sup>Kuwait Institute for Scientific Research, KUWAIT

## ABSTRACT

This paper reports the design, simulation, and experimental evaluation of high performance low pressure drop (<100Pa/cm) micropreconcentrator ( $\mu$ PC) chips (7mm $\times$ 7mm $\times$ 0.38mm) for micro total analytical systems. The  $\mu$ PC's high performance is attributed to the multiple inlets/outlets, novel high-aspect-ratio (380 $\mu$ m) parabolic reflectors, and cobweb configuration of adsorbent films all in which promote the adsorption of chemical species. Flow pattern simulations were used to verify the underlying concept of the design. The adsorption capacity of hydrocarbons was used to evaluate the  $\mu$ PCs experimentally. The performance of the new design was found to be more than 2 orders of magnitude higher than the first generation reported previously.

## INTRODUCTION

Generally speaking, preconcentrators (PCs) are concentration amplifiers used to improve the detection limit of analytical systems such as spectroscopy [1], mass-spectrometry [2], and chromatography [3]. They are also an integral part of handheld chemical detection systems. However, to meet the size and power constraints, handheld systems rely on microfabricated components (fluidic ports/channels, pumps, valves, etc.) which operate at low pressures. For example, a state-of-the-art micromachined pump designed for micro gas chromatographers can only provide a maximum back pressure of 7 kPa [4] whereas a typical MEMS-based  $\mu$ PC can introduce large pressure drop as high as 14 kPa [5]. Therefore, reducing the pressure drop in  $\mu$ PCs is a key development in handheld systems.

Conventional PCs are troubled by large pressure drop, dead volume, and high power consumption. Microfabrication technology has enabled high efficiency preconcentration in terms of sample capacity, device size, and the energy consumed. Recently, our group and others have utilized 3D microstructures embedded within a microcavity and coated with adsorbent films to realize low pressure drop  $\mu$ PC [6-8]. The microstructures provide large surface-to-volume ratio and low flow resistance compared to conventional microporous granular packing arrangement. This paper reports the design, simulation, and experimental evaluation of high performance low pressure drop  $\mu$ PC chips for micro analytical instruments including a micro gas chromatography system ( $\mu$ GC) [9]. In addition to our unique design enabling very low pressure drops, less than 100 Pa/cm, we present a new deposition method which results in a cobweb structure of the adsorbent material, thereby significantly increasing the concentration efficiency without obstructing the gas flow.

The new design consists of an array of parabolic reflectors embedded within a 7 mm  $\times$  7 mm  $\times$  0.38 mm cavity. The unit cell of the array consists of three reflectors as shown in Fig. 1. The reflectors are arranged to split the flow in the forward direction and combine them back in the reverse direction. The spacing between the reflectors (side and middle spacing) was varied to investigate its effect on the device performance. Table 1 list the different spacing values for both side and middle spacing along with the symmetry ratios (SR) of different designs. The SR was defined as the ratio of side to middle spacing. High SR represents narrow passage of flow which increases the probability of molecules

scattering and interacting with the adsorption surface. Full scale (actual chip size) computational fluid dynamics (CFD) simulation was consummated to investigate the flow behavior in such geometries. To establish confidence in the CFD model, calculated flow rates were compared with experimental results as shown in Fig. 2. The CFD results of the flow velocity profile showed high velocity in the middle spacing region of PC100 design as presented in Fig. 3. The data suggested that high SR value is desirable. The CFD results confirmed the anticipated flow behaviors. The simulated pressure drops in the different designs are listed in Table 1. The pressure drop profile is shown in Fig. 4 indicates uniform pressure drop which is also desirable.

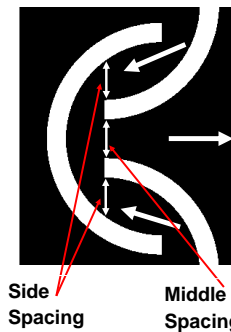


Figure 1: The  $\mu$ PC unit cell. Arrows indicate the flow direction.

Table 1: Different spacing arrangements and their corresponding symmetry ratio along with the simulated pressure drops at 1.5mL/min flow rate.

Design Label	Middle spacing ( $\mu$ m)	Side Spacing ( $\mu$ m)	SR	Pressure drop (Pa)
PC100	100	250	2.5	145
PC200	200	200	1	97
PC300	300	150	0.5	94

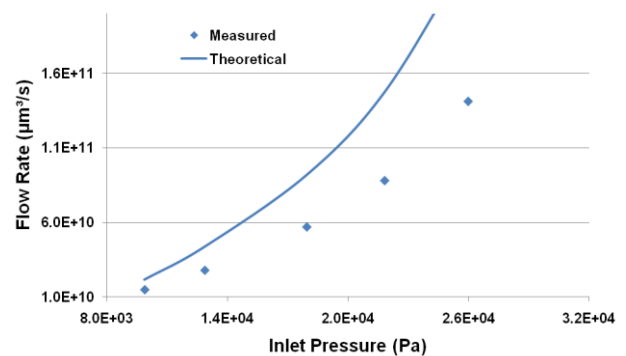


Figure 2: Comparison of calculated and experimental flow rates to establish confidence in the CFD model

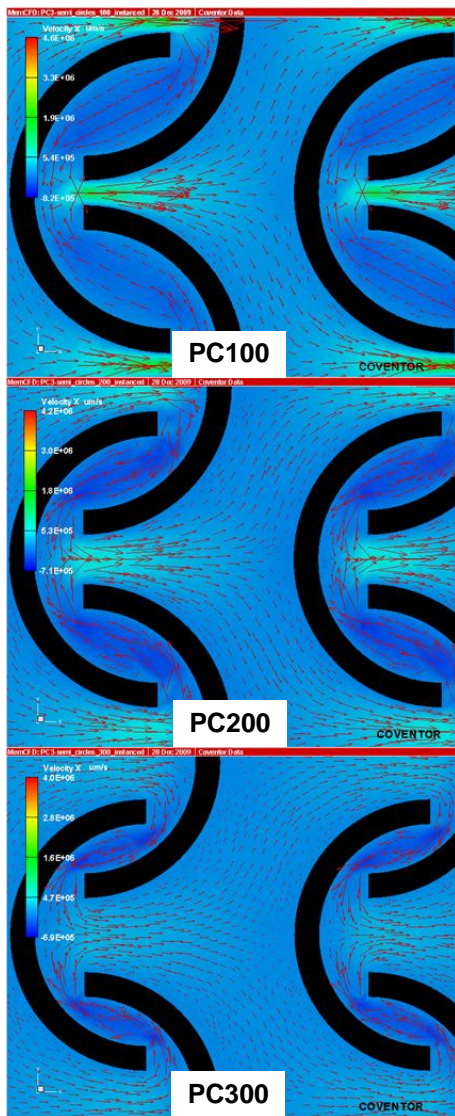


Figure 3: Simulation of the flow profile through different design spacing arrangements

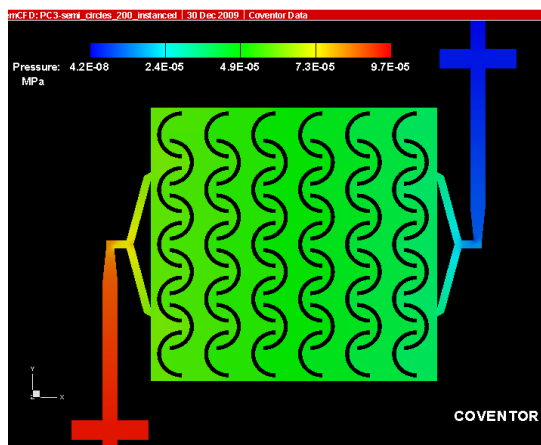


Figure 4: Pressure-drop profile in the  $\mu$ PC

The microstructures were realized according to the process flow in Fig. 5. The process starts with (a) photolithography of microstructures and fluidic ports on 4 inches test grade silicon wafer using high resolution, superior aspect ratio thick film photoresist (PR9260). This step was followed by (b) etching the patterned wafer using deep reactive ion etching (DRIE) to form 380  $\mu\text{m}$  deep 3D structures. Tenax-TA particles were dissolved in dichloromethane at 50 mg/mL concentration to create a solution to fill the etched cavity with. Adsorbent deposition (c) was achieved by adding drops of 2-propanol into solution before it evaporates from the cavity. Cobweb Tenax-TA evolves when 2-propanol contacts Tenax-TA solution. The cobweb structure anchors to the sidewalls once the solvent evaporates as shown in Fig. 6. The cavity was then sealed (d) by anodic bonding the silicon substrate to a Pyrex wafer at 1250 V and 300°C instead of conventional 350-400°C bonding temperature to avoid damaging the polymer. The expansion reservoirs shown in Fig. 7 were incorporated into the inlet/outlet design to prevent the sealing adhesive from overflowing into the inner cavity. This was a new addition to the first generation design reported previously [7]. The silicon-Pyrex stack was then diced into individual devices like the one shown in Fig. 7. Each device was connected on both sides with 300  $\mu\text{m}$ -OD, 170  $\mu\text{m}$ -ID deactivated fused silica tubing using high temperature ceramic based adhesive. The addition of Tenax-TA did not create a measurable difference in the flow rate. Fig. 8 presents a scanning electron microscopy (SEM) image of cobweb Tenax-TA

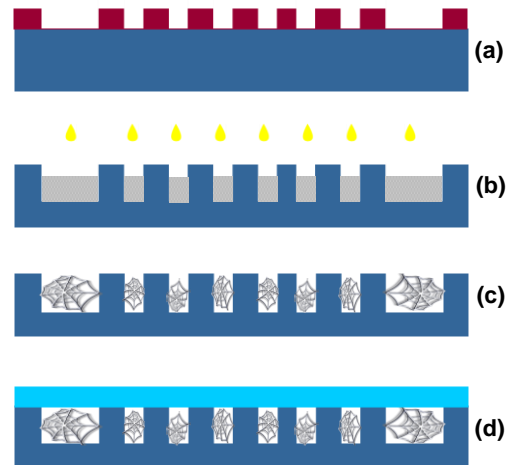


Figure 5:  $\mu$ PC fabrication process flow

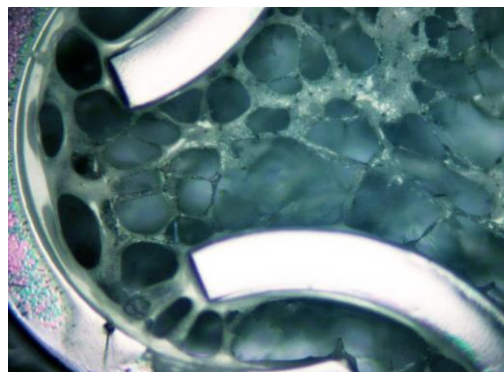


Figure 6: Optical image of the cobweb Tenax-TA.

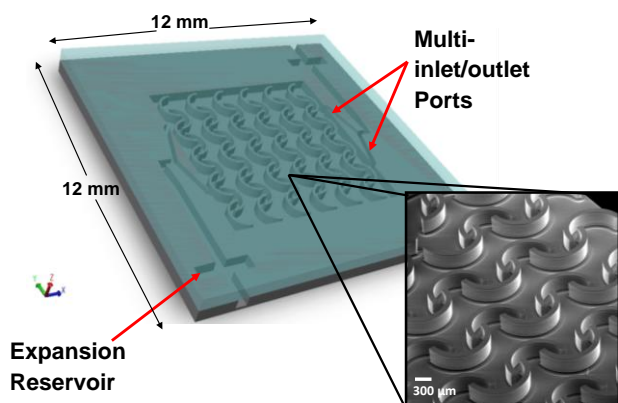


Figure 7: 3D rendering of the  $\mu$ PC, insets are SEM micrographs of the fabricated microstructures

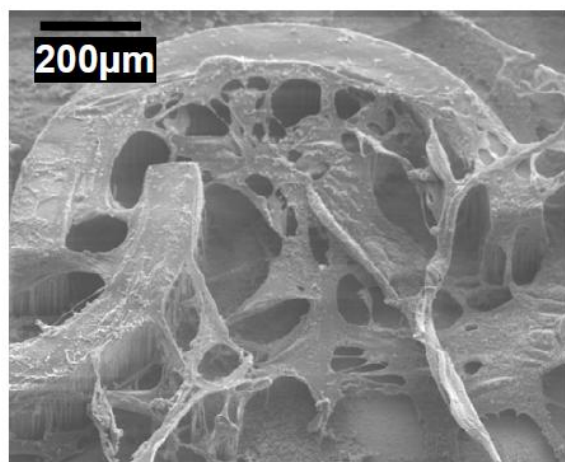


Figure 8: SEM image of cobweb Tenax-TA on the micro parabolic reflectors

The  $\mu$ PCs were evaluated experimentally by using the adsorption capacity as a figure of merit. The testing was performed inside a temperature controlled chamber to accurately maintain the testing temperature at 35°C. An electronic gas flow controller was used to supply and control the carrier gas which was selected to be nitrogen to resemble actual field operation conditions. The flow rate through the  $\mu$ PC was set to constant 1 mL/min. A flame ionization detector (FID) was utilized to detect the hydrocarbon samples used in the experiments. An off-board high-performance ceramic heater (ultra-fast ramp rate) was used for thermal desorption along with K-type thermocouple for manual temperature monitoring and control. In future work, on-chip thermal desorption capability will be added to the  $\mu$ PCs. The chips were saturated with benzene at 35°C and then desorbed at 100°C/sec to 250°C. The FID peak area is proportional to the analyte concentration. The benzene concentration in the desorption peak reflects the sample amount collected by the device. It is evident from Fig. 9 that the SR parameter has a significant effect on the performance of the parabolic reflectors design. Moreover, Fig. 9 shows that the performance of PC100 design is more than 2 orders of magnitude higher than the micro pillar design presented in HiltonHead'08 [10]. In the first generation design inkjet printing of Tenax-TA was used to provide uniform film deposition. Cobweb Tenax-TA offers better utilization of the space between the microstructures with the  $\mu$ PC

cavity. Reproducibility of the results in terms of peak area was 10% relative standard deviation (RSD) with more than 10 manual injections is shown in Fig. 10.

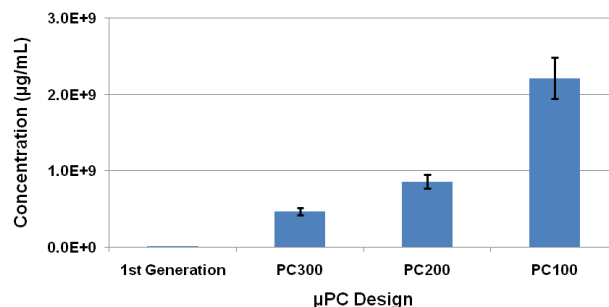


Figure 9: Benzene desorption concentration for the three designs as well as the first generation design

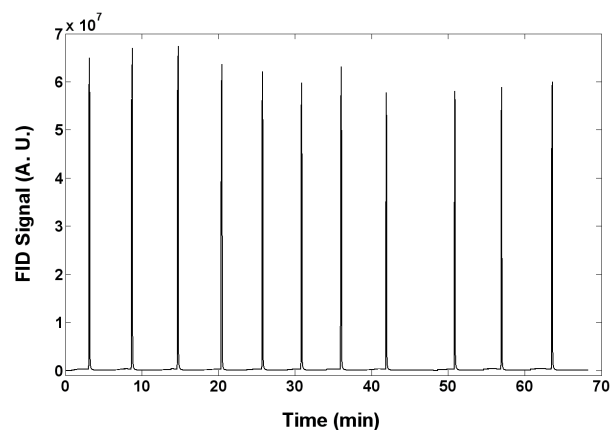


Figure 10: Reproducibility of  $\mu$ PC desorption pulses

For proof of concept, the  $\mu$ PC was put in series with a 1m 100% methylpolysiloxane microfabricated column [11] to demonstrate the possibility of  $\mu$ PC- $\mu$ GC integration. Under the same loading/desorbing conditions as the benzene test, the  $\mu$ PC was loaded with a mixture of toluene, nonane, decane, undecane, dodecane, tridecane, tetradecane, and pentadecane diluted in pentane at 1ppm concentrations. The sample concentration was below the FID detection limit; thus, preconcentration was needed to make the sample detectable. Fig. 11 illustrates a chromatogram of the preconcentrated sample injected into the micro column via thermal desorption. The initial and final temperatures of the column were 35 °C and 150 °C at 30 °C/min. The carrier flow rate was 1mL/min.

## CONCLUSIONS

The performance of analytical instruments especially handheld systems can be improved with sample pretreatment techniques such as preconcentration. This paper has demonstrated the possibility of developing lower pressure drops, small sizes, and high performance MEMS-based  $\mu$ PCs. This was realized by utilizing findings from previous designs, novel parabolic reflectors configuration, and cobweb Tenax-TA. The simulation analyses verified by experimental results have shown the effect of the SR parameter in the parabolic reflectors design. Future work will aim to better understand and model the behavior of the  $\mu$ PCs under different conditions. The reproducible desorption peaks needed for fast on-field analytical analysis has been demonstrated by the  $\mu$ PC.

The presented device was successful in concentrating a diluted multi-compound hydrocarbon mixture.

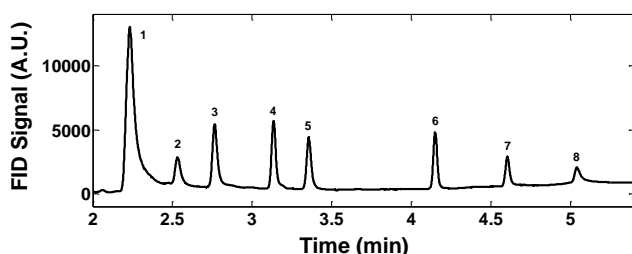


Figure 11: Preconcentration and separation of a mixture of (1) toluene, (2) nonane, (3) decane, (4) undecane, (5) dodecane, (6) tridecane, (7) tetradecane, and (8) pentadecane diluted in pentane below the FID detection limit.

## ACKNOWLEDGMENT

The authors thank Mr. Richard Wilson for his assistance in creating the mask layout. This research has been primarily supported by the National Science Foundation under Award No CBET-0854242. The authors also express their appreciation to Virginia Tech Center for Microelectronics, Optoelectronics, and Nanotechnology (MicRON) and Nanoscale Characterization and Fabrication Laboratory (NCFL) of Virginia Tech Institute for Critical Technology and Applied Science (ICTAS) for assisting with the fabrication and characterization presented in this work.

## REFERENCES

- [1] W. A. Groves, E. T. Zellers, and G. C. Frye, "Analyzing organic vapors in exhaled breath using a surface acoustic wave sensor array with preconcentration: Selection and characterization of the preconcentrator adsorbent," *Analytica Chimica Acta*, 371 (2-3) pp. 131-143, 1998.
- [2] C. Hornuss, S. Praun, J. Villinger, A. Dornauer, P. Moehnle, M. Dolch, E. Weninger, A. Chouker, C. Feil, J. Briegel, M. Thiel, and G. Schelling, "Real-time Monitoring of Propofol in Expired Air in Humans Undergoing Total Intravenous Anesthesia," *Anesthesiology*, 106 (4) pp. 665-674, 2007.
- [3] K. Dettmer and W. Engewald, "Adsorbent materials commonly used in air analysis for adsorptive enrichment and thermal desorption of volatile organic compounds," *Analytical and Bioanalytical Chemistry*, 373 (6) pp. 490-500, 2002.
- [4] A. A. Astle, H. S. Kim, L. P. Bernal, K. Najafi, and P. D. Washabaugh, "Theoretical and experimental performance of a high frequency gas micropump," *Sensors and Actuators A: Physical*, 134 (1) pp. 245-256, 2007.
- [5] W.-C. Tian, S. W. Pang, L. Chia-Jung, and E. T. Zellers, "Microfabricated preconcentrator-focuser for a microscale gas chromatograph," *Microelectromechanical Systems, Journal of*, 12 (3) pp. 264-272, 2003.
- [6] J. Yeom, D. D. Agonafer, J.-H. Han, and M. A. Shannon, "Low Reynolds number flow across an array of cylindrical microposts in a microchannel and figure-of-merit analysis of micropost-filled microreactors," *J. Micromech. Microeng.*, 19 (6) p. 065025, 2009.
- [7] B. Alfeeli, D. Cho, M. Ashraf-Khorassani, L. T. Taylor, and M. Agah, "MEMS-Based Multi-Inlet/Outlet Preconcentrator Coated by Inkjet Printing of Polymer Adsorbents," *Sens. Actuators, B*, 133 (1) pp. 24-32, 2008.
- [8] E. H. M. Camara, P. Breuil, D. Briand, L. Guillot, C. Pijolat, and N. F. de Rooij, "A micro gas preconcentrator with improved performances for environmental monitoring," in *Solid-State Sensors, Actuators and Microsystems Conference, 2009. TRANSDUCERS 2009. International, 2009*, pp. 983-986.
- [9] M. Agah, G. R. Lambertus, R. Sacks, and K. Wise, "High-speed MEMS-based gas chromatography," *Journal of Microelectromechanical Systems*, 15 (5) pp. 1371-8, 2006.
- [10] B. Alfeeli, M. Ashraf-Khorassani, L. T. Taylor, and M. Agah, "Multi-inlet/outlet Preconcentrator with 3-D m-structures Coated by Inkjet Printing of Tenax TA," in *Solid-State Sensors, Actuators, and Microsystems Workshop, Hilton Head Island, South Carolina, 2008*, pp. 118-121.
- [11] M. Agah, J. A. Potkay, G. Lambertus, R. Sacks, and K. D. Wise, "High-Performance Temperature-Programmed Microfabricated Gas Chromatography Columns," *Journal of Microelectromechanical Systems*, 14 (5) pp. 1039-1050, 2005.

## CONTACT

\*B. Alfeeli, tel: +1-540-231-4180; alfeeli@vt.edu

# LUMPED-ELEMENT ANALYSIS OF AN ELECTROSTATIC SQUEEZE-FILM MEMS DROPLET EJECTOR

*E.P. Furlani<sup>1</sup>, H.V. Panchawagh<sup>1\*</sup>, and T.L.Sounart<sup>2</sup>*

<sup>1</sup>Eastman Kodak Company, Research Laboratories, Rochester, NY, USA

<sup>2</sup>Sandia National Laboratories, Albuquerque, NM 87185, USA

## ABSTRACT

We present a theoretical model of an electrostatically driven, squeeze-film dominated, MEMS droplet ejector. The ejector consists of a microfluidic chamber filled with fluid to be ejected, an orifice plate, and a piston positioned a few microns beneath the orifice. Drop ejection occurs when a high-frequency drive voltage is applied between the orifice plate and the piston. The lumped-element model of the ejector takes into account the coupled electrical-structural-fluidic interactions that occur during drop ejection. The model is used to study effect of fluid properties and drive waveform on key performance parameters such as piston displacement and ejected fluid volume.

## INTRODUCTION

MEMS are finding increasing use for applications that require the controlled generation and delivery of picoliter-sized droplets. Common applications include biomedical and biochemical microdispensing and most notably, inkjet printing. The most common MEMS drop ejectors operate in a drop-on-demand (DOD) mode. In DOD devices, micro-droplets are produced as needed by generating a sharp, short-lived pressure pulse within a microfluidic chamber beneath an orifice plate. The pressure profile is tuned to eject a droplet with a desired volume and velocity. The most common methods for producing the drop ejection pressure involve piezoelectric actuation or the generation of a thermally induced vapor bubble (bubble-jet).

In this paper, we discuss an alternative method of drop generation that is based on electrostatic actuation [1-4]. Specifically, we study a MEMS drop ejector that consists of a microfluidic chamber with a piston that is suspended a few micrometers beneath and orifice plate (Fig. 1). The piston is supported by cantilevered polysilicon flexure members that act as restoring springs when the piston is displaced from its equilibrium position (Fig. 1a). To eject a drop, a potential difference is applied between the orifice plate and the piston, and this produces an electrostatic force that moves the piston toward the orifice. The moving piston generates a squeeze-film pressure distribution in the gap region above it that acts to eject the drop (Fig. 2). Specifically, a peak pressure (stagnation pressure) obtains at a specific radius (stagnation radius), which is greater than the orifice radius. Thus, the fluid within the stagnation radius is confined, and forced through the nozzle as the piston moves toward it. A portion of this fluid ultimately detaches from the ejector and forms into a droplet; the remainder retracts back into the ejector as the piston returns to its equilibrium position. A drop ejector based on this principle has been fabricated and characterized at Sandia National Laboratories (Fig. 1) [2-3].

In this paper, we discuss the basic operating physics of the ejector, and we present an analytical lumped-element model for predicting its performance. We use the model to study device performance. We compare the analytical predictions with CFD analysis that takes into account the coupled piston-fluid interactions as well as to the experimental data.

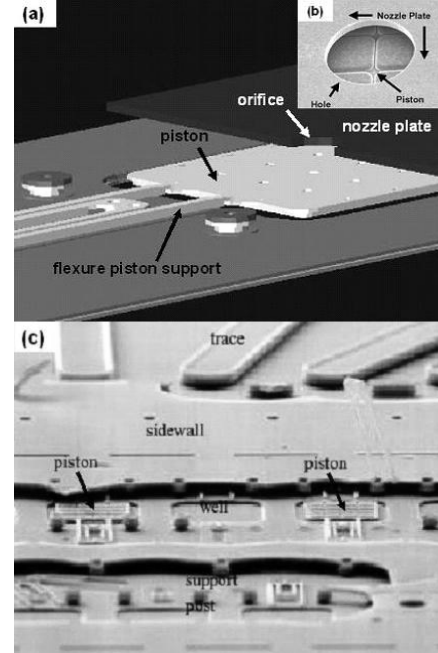


Figure 1: MEMS drop ejector (adapted from [2-3]): (a) schematic showing cantilevered piston and cut away view of nozzle plate; (b) close-up view of orifice and piston, and (c) SEM image of ejectors (cover removed).

## THEORY

### Equation of Motion

We model the drop ejector using a lumped-element axisymmetric analysis (Fig. 2). The motion of the piston is obtained from the equation for the force balance on the piston

$$\left(m_p + m_{eff}(t)\right) \frac{dv_p}{dt} = F_a(t) - kx_p(t) - 2\pi \int_0^{r_p} p(r, v_p, t) r dr + \sum F_f \quad (1)$$

where  $m_p$ ,  $x_p(t)$ , and  $v_p(t)$  are the mass, position, and velocity of the piston,  $m_{eff}(t)$  is the effective mass of the fluid that it accelerates,  $F_a(t)$  is the applied electrostatic force,  $k$  is a spring constant for the polysilicon support members, and  $p(r, v_p, t)$  is the squeeze-film pressure distribution that develops between the piston and the nozzle, which acts to resist the piston motion. The term  $\sum F_f$  represents other forces due to the fluid motion.

## Pressure Distribution

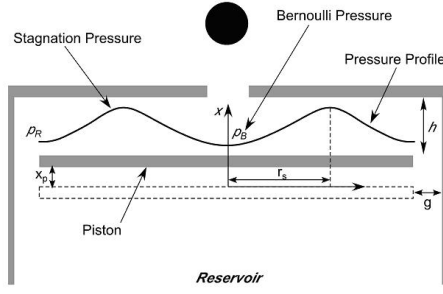


Figure 2: Axisymmetric model of MEMS drop ejector.

The pressure distribution  $p(r, v_p, t)$  developed by the moving piston is obtained by applying Reynolds lubrication theory to the axisymmetric geometry shown in Fig. 2. The pressure above the piston satisfies the following equation

$$\frac{1}{r} \frac{\partial}{\partial r} \left( r \frac{\partial p(r, t)}{\partial r} \right) = -\frac{12\mu}{h^3(t)} v_p(t) \quad (r_o \leq r \leq r_p) \quad (2)$$

where  $\mu$  is the fluid viscosity,  $v_p$  is the piston velocity,  $r_o$  and  $r_p$  are the radius of the orifice and the piston, respectively, and  $h(t)$  is the distance from the piston to the nozzle plate. The general solution to this equation is of the form

$$p(r, t) = -\frac{3\mu v_p(t)}{h^3} r^2 + c_1 \ln(r) + c_2, \quad (3)$$

where  $C_1$  and  $C_2$  are constants determined from boundary conditions [2-3]. The pressure distribution (3) peaks at a value  $p_s$  called as stagnation pressure at the stagnation radius  $r_s(t)$ ,

$$r_s(t) = \sqrt{\frac{h^3 C_1}{6\mu v_p(t)}}, \quad (4)$$

as shown in Fig. 2. We assume that fluid above the piston and within the stagnation radius ( $r \leq r_s(t)$ ) flows toward the orifice, while fluid beyond this point ( $r > r_s(t)$ ) flows into the reservoir. The boundary conditions for this problem are

$$\begin{aligned} p(r, t) &= p_B(t) & (r = r_o) \\ p(r, t) &= p_R(t) & (r = r_p) \end{aligned} \quad (5)$$

where  $p_B(t)$  and  $p_R(t)$  are the pressures beneath the orifice ( $r \leq r_o$ ), and at the edge of the piston, respectively, which are related to the flow rates at those points. Analytical expression for  $p(r, t)$ ,  $r_s(t)$ ,  $p_B(t)$ , and  $p_R(t)$  can be found in the literature [4].

## Effective Mass

We take into account inertial effects by estimating the mass of fluid accelerated by the piston as it moves. As above, we assume that the fluid within the stagnation radius flows toward the orifice, while the fluid beyond this point flows through the gap into the reservoir. From our analysis we find that the total effective mass of the fluid is [4]

$$\begin{aligned} m_{eff}(t) &= \rho\pi \left[ \frac{r_p^3 + r_o^3 + 4r_s^3}{3} - r_s^2 (r_p + r_o) \right] \\ &+ \rho\pi l_o r_s^2(t) + \rho\pi l_o r_s^2(t) + \rho\pi l_p (r_p^2 - r_s^2(t)) \end{aligned} \quad (6)$$

## Electrostatic Force

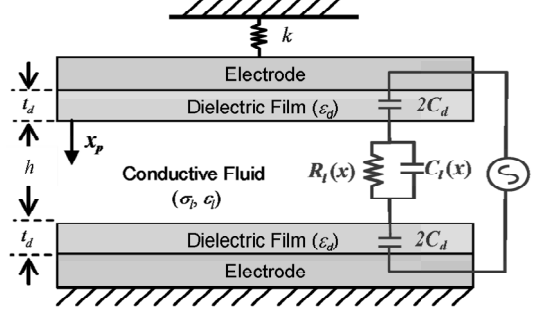


Figure 3: Electrical equivalent circuit of the electrostatic actuator in conducting liquids [5].

An expression for frequency-dependent electrostatic force between two parallel passivated electrodes separated by a conductive medium is given by Panchawagh [5]. This force is computed from an electrical equivalent circuit of the device shown in Fig. 3. The average electrostatic force  $F_d(t)$  is given by

$$F_d(t) = \frac{V_l^2(t)}{2} \frac{dC_l(x)}{dx_p} = \frac{1}{2} \frac{\epsilon_o \epsilon_l A V_l^2}{(h - x_p)^2}, \quad (7)$$

where  $C_l = \epsilon_o \epsilon_l A / (h - x_p)$  and  $V_l$  are the capacitance and the effective actuation voltage across the liquid gap between the piston and the orifice plate.  $C_d = \epsilon_o \epsilon_d A / (2t_d)$  is the total capacitance of the native oxide passivation on the piston and orifice plate. Here,  $A$  is the electrode area,  $t_d$  is the passivation film thickness on each electrode, and  $\epsilon_l$  and  $\epsilon_d$  are the relative permittivities of the fluid and passivation film.  $V_l$  is calculated from

$$\left( 1 + \frac{C_l}{C_d} \right) \frac{dV_l}{dt} + \left( \frac{1}{C_d} \frac{dC_l}{dx_p} \frac{dx_p}{dt} + \frac{1}{C_d R_l} \right) V_l = \frac{dV}{dt}, \quad (8)$$

where  $R_l = (h - x_p) / (\sigma_l A)$  is the bulk resistance of the liquid between electrodes and  $\sigma_l$  is the electrical conductivity of the fluid. The electrostatic force given by Eq. (7) depends on piston position, device geometry, fluid electrical properties, and actuation waveform.

## Other Forces

The equation of motion, Eq. (1) contains an expression  $\sum F_f$  that accounts for additional forces due to fluid flow. Two such forces arise from the flow across the top surface of the orifice, and boundary of the gap at the reservoir. These additional forces have the form,

$$F_o(t) = \rho\pi r_o^2 v_o^2(t), \quad (9)$$

$$\text{and} \quad F_g(t) = \rho 2\pi r_p g v_g^2(t), \quad (10)$$

where  $v_g(t)$  is the average velocity across the gap/reservoir interface. Time-dependent piston displacement can be thus

calculated from Eq. (1) by collecting all of the relevant terms and solving it simultaneously with Eqs. (3) and (8). To perform device simulation, we integrate this nonlinear ODE using a fourth-order Runge-Kutta method.

### Fluid Ejection

We use Eq. (1) to study the behavior of the drop ejector. We solve for the piston velocity, and use this to obtain the average velocity  $v_o(t)$  and volume flow rate  $Q_o(t)$  of the fluid ejected through the nozzle,

$$v_o(t) = \frac{r_s^2(t)v_p(t)}{r_o^2}, \quad (11)$$

$$\text{and} \quad Q_o(t) = \pi r_s^2(t)v_p(t). \quad (12)$$

It is important to note that this analysis does not take into account the complex free-surface dynamics that govern the fluid-nozzle interaction and the ultimate formation of the drop, i.e. pinch-off, satellites etc. To compensate for this, we estimate the actual observed flow rate  $Q_{exp} = \beta Q_o$  using a fitting parameter  $\beta$ , which we determine using CFD analysis. Once determined, this parameter is fixed for all of the analysis. We also track the total volume of fluid  $V_{eject}$  ejected during actuation by integrating the flow rate through the orifice during the applied force,

$$V_{eject} = \int_0^{\tau} Q_{exp}(t) dt, \quad (13)$$

where  $\tau$  is the duration of the applied voltage or electric field.

## RESULTS

Important parameters used in analysis are listed in Table 1. The device geometry, fluid properties are based on experimentally tested devices from [2-3]. In experiments, high-frequency carrier frequencies of greater than 2.5 MHz were used to prevent electrode screening and electrolysis in conductive ink. In the analytical model results presented here, we used a 1 MHz sinusoidal carrier waveform. During the experimental studies, it was observed that if the carrier frequency (internal signal frequency) was amplitude modulated over a short time pulses, on the order of 4 to 5  $\mu$ s, the sudden piston motion created sufficient pressure to eject a drop. The drop ejection rate was on the order of 1-10 kHz. Here, we limit the analysis time to 4.4  $\mu$ s as per reference [3]. Additionally, in the experiments, a custom shape of drive waveform was developed that kept the total electric field across the liquid gap between the piston and orifice plate to a constant value that was below the breakdown limit [2] in order to create a constant electrostatic force. The predicted piston displacement for a constant actuation force is plotted in Figure 4. The analytical model predicted a maximum piston displacement just over 2  $\mu$ m when the initial gap between the piston and the nozzle is 3.5  $\mu$ m. This calculation was verified using a CFD model of the drop ejector that assumed an equivalent constant actuation force over the pulse time and accounted for the fluid-structural interactions.

From Figure 4, it is clear that the piston dynamic response is sufficiently fast to follow the drive waveform at the time scale of electrical pulse. The CFD analysis predicted the volume of ejected fluid during the pulse to be 5.6 pL. Note that only the primary drop volumes were recorded in CFD analysis, i.e. satellite drops were not included. This was used to calibrate the fitting parameter  $\beta=0.75$  to determine ejected fluid volume using analytical model. These

predicted ejected fluid volumes are comparable to experimental data published in [2-3].

Table 1: Typical values of parameters used in analysis.

Piston radius	70 $\mu$ m
Piston thickness	2 $\mu$ m
Orifice diameter	20 $\mu$ m
Orifice-Piston Gap	3.5 $\mu$ m
Fluid density	1000 kg/m <sup>3</sup>
Fluid viscosity	1 cp
Fluid conductivity	0.001 S/m
Fluid relative permittivity	70
Passivation film	2 nm thick native oxide
Native oxide relative permittivity	4.5
Spring stiffness	100 N/m
Carrier frequency	1 MHz
Electrical pulse time	4.4 $\mu$ s

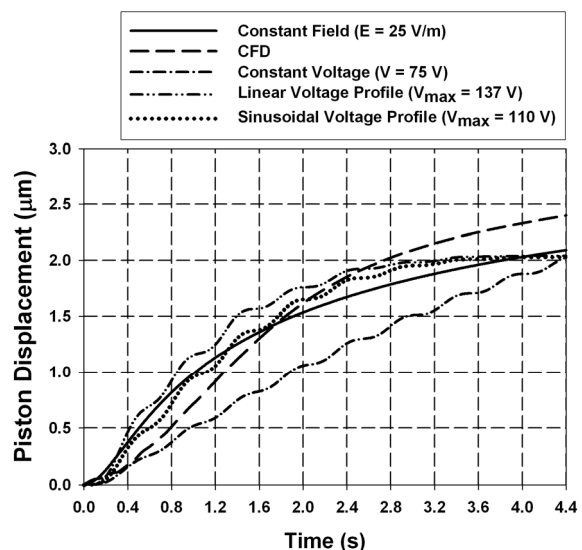


Figure 4: Comparison of piston displacement during the actuation pulse for different drive waveforms with parameters as specified in Table 1. The constant field waveform analytical model assumes a constant field of 25 V/ $\mu$ m for the duration of the pulse. Other waveforms analyzed include constant amplitude waveform (75 V), a linear reduction in applied voltage from 137V at the start to zero, and a sinusoidal amplitude modulation of 110 V at the start of the pulse to zero at the end. The results are compared to a CFD model that includes fluid-structural interactions but assumes a constant electric field or actuation force during the actuation pulse.

Next, we illustrate effect of drive waveform on drop ejector performance. Generally, the carrier frequency, actuation pulse duration, and the modulation of the peak voltage amplitude during the pulse are important parameters that affect the piston displacement and ejected fluid volume. Results for three additional waveforms are plotted in Figure 4. Here, the magnitudes of peak



voltages in each of the waveforms were adjusted to get a maximum final piston displacement close to that for the constant field case. Required peak actuation potential, the piston trajectory, and therefore the ejected fluid volume depended on the waveform shape. A lower peak potential was required for the constant voltage waveform while piston displacement reached a plateau with amplitude modulated waveforms. The ejected fluid volumes are listed in Table 2 for these cases.

Table 2: Predicted ejected fluid volumes for different drive waveforms.  $\beta = 0.75$ .

Waveform	Model	Volume (pL)
Constant Field	CFD	5.60
Constant Field	Analytical	5.52
Constant peak potential	Analytical	5.95
Linearly modulation of potential	Analytical	7.16
Sinusoidal modulation of potential	Analytical	6.26

The predicted values of electric field in fluid for different waveforms are plotted Figure 5. The peak electric field determines the breakdown of the fluid and should be maintained below a threshold that is on the order of 30-100 V/ $\mu$ m and depends on the pulse width [3]. Other considerations in selection of the drive waveform include the maximum field across the passivation film (native oxide) and joule heating caused by the power dissipation due to conductivity of liquid between the electrodes. The model presented here can be used to determine these limits on the actuation waveforms.

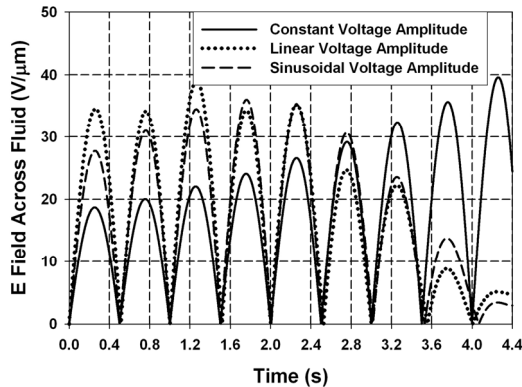


Figure 5: Instantaneous electric field across the liquid gap between the orifice plate and piston for different actuation waveforms.

In addition to the waveform optimization, the model is also useful in studying effect of device geometry, passivation film and fluid properties. For example effect of fluid electrical conductivity and fluid viscosity are plotted in Figure 6. As expected the piston displacement was lower for higher electrical conductivity of the fluid because of the electrode screening [5] while the higher fluid viscosity resulted in increased squeeze film force on the piston and therefore lower displacements.

## CONCLUSIONS

An analytical model for electrostatic drop ejector is presented that accounts for the coupled interaction between the electrostatic

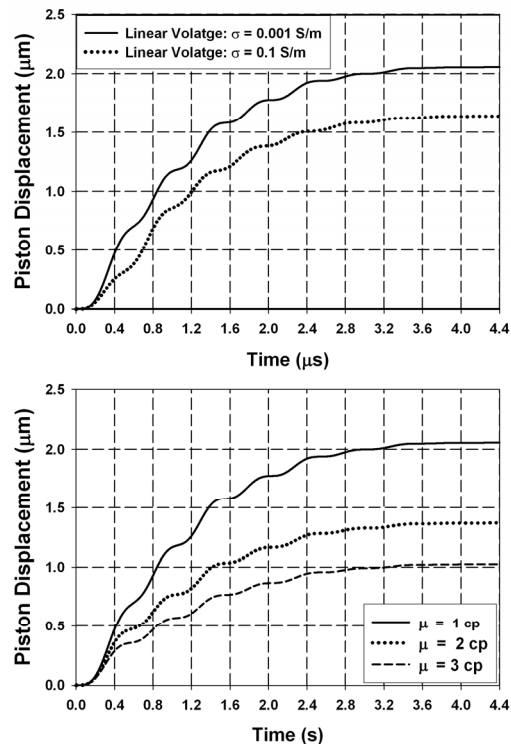


Figure 6: Piston displacement for different values of fluid conductivity and viscosity for linearly modulation of drive potential. Other parameters same as in Table 1.

actuation in electrically conductive viscous fluids. The model is useful to optimize device geometry and waveform as well as to study effect of important parameters on its performance. The modeling approach is applicable to a wide range of other MEMS devices including resonating structures for bio-sensing applications, integrated MEMS pumps and valves in microfluidic devices and other applications where electrostatic actuators are operated in viscous conductive fluids.

## REFERENCES

- [1] S. Kamisuki, T. Hagata, C. Tezuka, Y. Nose, M. Fujii, and M. Atobe, "A low power, small, electrostatically driven commercial inkjet head," Proc. IEEE MEMS Workshop, Heidelberg, Germany, (1998).
- [2] Paul Galambos, Kevin Zavadil, Rick Givler, Frank Peter, Art Gooray, George Roller, Joe Crowley, "A Surface Micromachined Electrostatic Drop Ejector," Transducers '01 Conference, Munich, Germany, (2001).
- [3] A. Gooray, G. Roller, P. Galambos, K. Zavadil, R. Givler, F. Peter, and J. Crowley, "Design of a MEMS ejector for printing applications," J. of Imaging Science and Technology, 46, 5, (2002) pp. 415-432.
- [4] E. P. Furlani, "Theory of microfluidic squeeze-film dominated fluid ejection," J. Phys. D: Appl. Phys., 37, (2004) pp. 2483-2488.
- [5] H. V. Panchawagh, T.L. Sounart, and R.L. Mahajan, "A model for electrostatic actuation in conducting liquids", J. Microlithography, 18, 5, (2009), pp. 1105-1117.

## CONTACT

\*H.V. Panchawagh, Tel: +1-585-722-2501;  
hrishikesh.panchawagh@kodak.com

# SURFACE MEDIATED FLOWS IN GLASS NANOFUIDIC DEVICES

Shaurya Prakash\* and M.B. Karacor

Department of Mechanical Engineering, The Ohio State University, Columbus, Ohio, USA

## ABSTRACT

In this paper, use of chemical modification to selectively direct flow in glass devices is discussed. Glass devices with a slit-like nanochannel and a depth of 100 nm were fabricated by conventional methods. Velocity profile analysis was performed by manipulating the existing theoretical models to explicitly show influence of surface charge density and changing the electric double layer thickness. Theoretical models predict velocity profiles for a wide range of surface charge densities as function of surface functionalization, electrolyte concentration, and electrolyte pH. In addition, experimental data shows selective flow directing in devices is possible by engineering the surface charge density through chemical modification. Use of fluorescent dyes by using both a positive marker dye and a negative marker dye demonstrate selective flow control as pathway to ‘valve-less’ flow control. The positive dye shows a preference for the aminated channels, which is the more negative surface in the tested devices.

## INTRODUCTION

Nanofluidics finds an important place in Lab-on-Chip applications due to the dominance of interfacial forces [1]. Applications for Lab-on-Chip systems in electrophoretic separations, DNA and protein analyses, and PCR, etc. require exquisite control over analyte and sample manipulation and technologies such as molecular gates [2] and entropic traps have been developed [3] for this purpose. High surface-area-to-volume ratios ( $\sim 10^9 \text{ m}^{-1}$  are possible) in nanochannels provide a unique opportunity to exploit surface-species interactions for sample manipulation [4].

Chemically modified surfaces within nanofluidic channels with critical dimensions on the order of 100 nm for surface mediated flow control were fabricated and tested. Chemical modifications were carried out by using methods of ‘click’ chemistry [5]. The modified surfaces can be used to selectively drive flows in these devices. Therefore, the ability to systematically modify surface properties to directly influence confined flows can be a powerful technology for sample manipulation in nanofluidics. In this paper, pre-designed surface properties (e.g., surface charge and surface energy) were used to demonstrate control over electrokinetically driven nanoscale flow phenomena.

## Theoretical Background

It has previously been shown [6] that for a slit-like channel driven by electrokinetic flow, the velocity profile for a steady, no-slip, 1-D flow in the axial direction is governed by

$$\mu \frac{d^2 V_z}{dy^2} + E_z \rho(y) = 0 \quad (1)$$

where,  $\mu$  is the viscosity of the fluid,  $V_z$  denotes the velocity in the  $z$ -direction or axial direction along length of channel,  $E_z$  is the applied electric field in the axial flow or in the  $z$ -direction, and  $\rho$  denotes the charge density governed by the Poisson equation

$$\frac{d^2 \psi}{dy^2} + \frac{\rho}{\epsilon_r \epsilon_0} = 0 \quad (2)$$

where,  $\psi$  denotes the potential,  $\epsilon_r$  is the dielectric constant of the medium, and  $\epsilon_0$  is the permittivity of free space. If we assume the

Boltzmann distribution for the ions in the channels and apply the low-zeta potential assumption, then the velocity profile is given by

$$V_z(y) = -\frac{E_z \epsilon_0 \epsilon_r \zeta}{\mu} \left( 1 - \frac{\cosh(\kappa y)}{\cosh(\kappa a)} \right) \quad (3)$$

where,  $\zeta$  denotes the zeta potential of the surface,  $y$  is the vertical coordinate,  $a$  is the channel half-depth, and  $\kappa$  is the electrokinetic radius or the reciprocal of the Debye length, often approximated as the thickness of the electric double layer. On integrating equation (3) along the  $y$ -direction for the entire channel depth and dividing through by the channel height,  $2a$  the average velocity,  $V_{avg}$  is obtained and can be expressed as

$$V_{avg} = -\frac{E_z \epsilon_0 \epsilon_r \zeta}{\mu a} \left( \frac{\kappa a \sinh(\kappa a) - \cosh(\kappa a) + 1}{\kappa \sinh(\kappa a)} \right) \quad (4)$$

It is now established that surface charge is critical to ionic control in nanofluidics [7] as the slip plane may not always be well defined [4], and it is known from Grahame’s equation that the  $\zeta$  potential and surface charge density,  $\sigma_s$  are related,

$$\frac{\sigma_s \lambda_D e}{2 \epsilon_0 \epsilon_r k_B T} = \sinh \left( -\frac{e \zeta}{2 k_B T} \right) \quad (5)$$

where,  $e$  is the elementary charge,  $T$  is the absolute temperature,  $k_B$  is Boltzmann constant, and  $\lambda_D$  is the Debye length. Therefore, the velocities in equations (3) and (4) can be expressed in terms of the surface charge density to yield equations (6).

$$V_z(y) = \frac{2 k_B E_z \epsilon_0 \epsilon_r T}{\mu e} \sinh^{-1} \left( \frac{\sigma_s e}{2 \kappa \epsilon_0 \epsilon_r k_B T} \right) \left[ 1 - \frac{\cosh(\kappa y)}{\cosh(\kappa a)} \right] \quad (6)$$

$$V_{avg} = \frac{2 k_B E_z \epsilon_0 \epsilon_r T}{\mu e} \sinh^{-1} \left( \frac{\sigma_s e}{2 \kappa \epsilon_0 \epsilon_r k_B T} \right) \left[ \frac{\kappa a \sinh(\kappa a) - \cosh(\kappa a) + 1}{\kappa \sinh(\kappa a)} \right]$$

Therefore, it can be seen from equations (6) that systematically varying the surface charge density will cause a change in the observed velocities. Systematic manipulation of surface charge density was carried out by changing the solution pH and surface functionalization. Results reported in the next few sections show the effects of each of the parameters on observed velocity trends in electrokinetic flows.

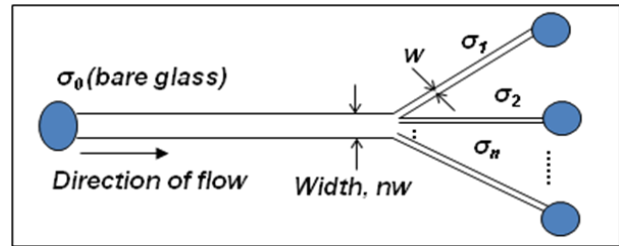


Figure 1: A schematic representation for the channel network used. Each exit channel is  $50 \mu\text{m}$  wide and  $1 \text{ cm}$  long. The depth of the channel is  $100 \text{ nm}$ . Inlet channel is base glass and the exit channels are modified with different functionalization to alter the surface charge density,  $\sigma_i$ .

## Experimental Methodology

Glass substrates (No. 2 cover glass, Corning) were patterned

with conventional UV lithography to generate the channel network shown in Figure 1. The channels were wet-etched using buffered oxide etch to yield channels with 100 nm depth. A Cr/Au layer was used as an etch mask for the glass etch step. As shown in Figure 1, each channel is 1 cm long and the exit channels are 50  $\mu\text{m}$  wide. The inlet channel width is scaled to the number of exit channels to allow even flow rates in each channel under the case of no surface modification. Through holes were drilled in a top cover of the same type of glass and the two glass slides were then fusion bonded thermally at 110°C after a thorough clean. An SEM image of the channel cross-section is shown in Figure 2.



Figure 2: SEM image showing the cross-section of a bonded channel. Part of the slit-like channel with a channel depth of 100 nm is seen.

The channels were flushed with DI water and observed under a microscope to verify bonding and absence of leakage. After bonding, the surfaces were modified by a previously developed methodology [5]. Figure 3 shows the process for modifying the surfaces schematically. Briefly, first a self-assembled monolayer with a nucleophilic end-group (-Br) was deposited followed by a  $S_N2$  nucleophilic substitution to generate an azido terminated surface followed by ‘click’ chemistry to create functionalized surfaces with pre-designed properties. The ‘click’ solutions of the aminated terminal alkyne (with propyl backbone) and the methylated alkyne (octyne) were prepared as 10 mM solutions in ethanol. Three surface terminations (-Br, -NH<sub>2</sub>, and -CH<sub>3</sub>) were tested in contrast to bare glass or unmodified surfaces. All experiments were conducted with a NaCl solution prepared in DI water at  $\text{pH } 7 \pm 0.2$  and obtained by titrating NaOH against HCl. The total electrolyte concentration for NaCl was 10 mM.

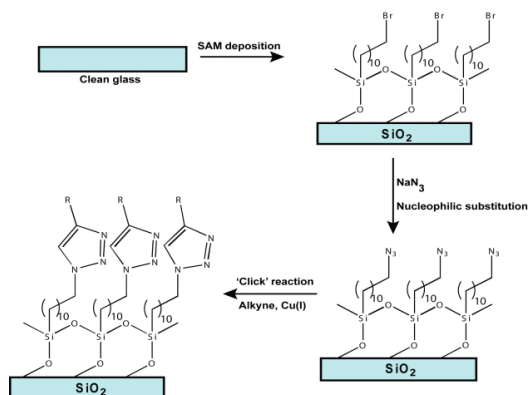


Figure 3: The schematic shows formation of surface layers through the ‘click’ process. The functionalizations discussed in this work include bare glass (-OH), brominated surfaces (-Br), aminated surfaces (-NH<sub>2</sub>), and methylated surfaces (-CH<sub>3</sub>)

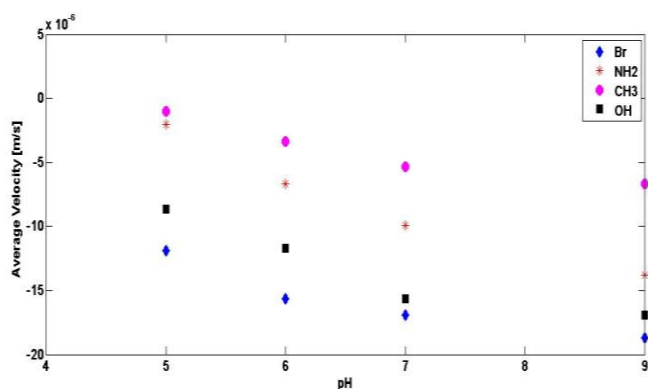


Figure 4: Average velocity as predicted by conventional 1-D electrokinetic model for slit-like channel. The velocity is plotted as function of pH, which regulates surface charge density.

## RESULTS AND DISCUSSION

The model above describes electrokinetic flow in a slit-like channel. Figure 4 shows the average velocity in the nanochannel along the channel length ( $z$ -direction) as function of solution pH as predicted by the model.

Typically, in most cases surface charge density has also been reported to be increasing with pH. It can be seen from Figure 4 that the velocity increases in magnitude with increasing pH. Using the model, the pH dependence was further explored and  $V_z(y)$  i.e. the axial velocity profile as function of channel depth is shown in Figures 5 and 6 for pH 3 and pH 9. It can be seen from Figure 5 that the velocity profile for the aminated and methylated surfaces are positive. This can be expected since at acidic pH the aminated surfaces are likely protonated and have a positive surface charge. The methylated surfaces have also been reported to acquire partial positive surface charge and thus the velocity profiles reflect the charge distribution. At 10 mM NaCl, the electric double layer is close to the walls and the 100 nm nanochannels behave like microchannels and the velocity profile is a plug-like flow, as shown by the plot. The velocity profiles for the bare-glass and brominated surfaces also show trends similar to those as expected. One point to note from Figure 6 is the relative magnitude of the velocities. For example, comparing an aminated surface to the bare-glass surface it can be seen that at the center-point of the channel (location where velocity is maximum), the velocity for the aminated surface is lower in magnitude by approximately 22%; however, the surface charge density for an aminated surface

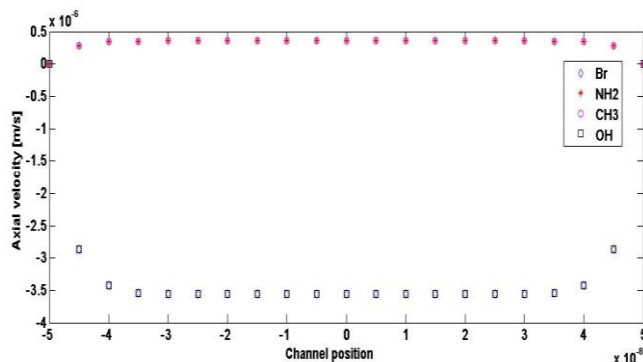


Figure 5: Velocity profile in a 100 nm channel at pH 3 for a 10 mM NaCl electrolyte as function of different surface functionalizations.

functionalized by the ‘click’ method is approximately 61% higher than that of a bare glass surface [8].

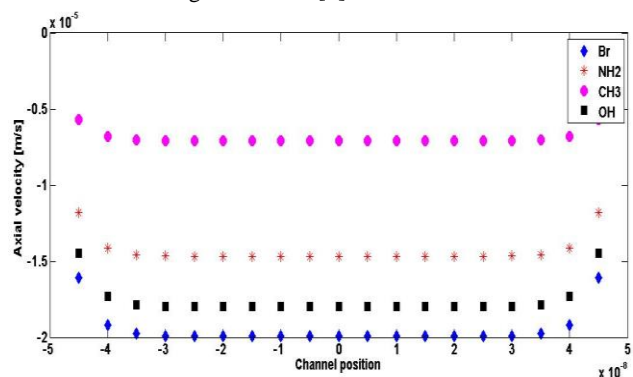


Figure 6: Velocity profiles in a 100 nm channel at pH 9 for a 10 mM NaCl electrolyte as function of different surface functionalizations.

The model described in the theoretical background permits an analysis that allows changing the channel critical dimensions and also the ionic concentration. Figure 7 shows the velocity profile for a channel with depth 20 nm at pH 9. It can also be seen from

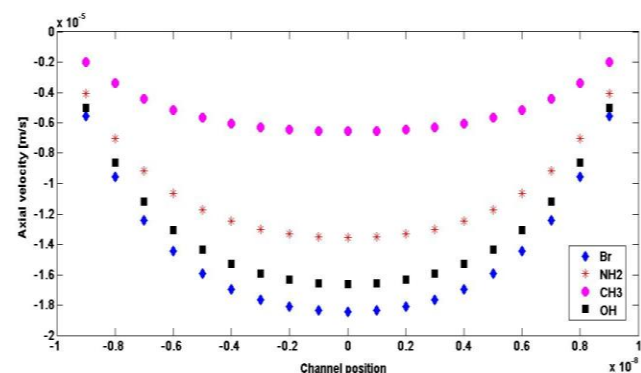


Figure 7: Velocity profiles in a 20 nm channel at pH 9 for a 10 mM NaCl electrolyte as function of different surface functionalizations.

Figure 7 that with the EDL occupying a larger fraction of the nanochannel the flow profile becomes more parabolic and the maximum velocity decreases in contrast to the values for the 100 nm channel.

Figure 8 presents another aspect of the theoretical analysis, which shows the effect at pH 9 by changing the concentration of the NaCl electrolyte. Since the EDL thickness scales inversely with the square root of concentration, Figure 8 shows the plot for the case of a 100 nm channel with a concentration of 0.4 mM. Figure 8 shows that by reducing the concentration by 25 times i.e. increasing the EDL by approximately 5 times in contrast to the case presented in Figure 6, the velocity profile becomes markedly more parabolic. In addition, the absolute magnitude of velocity is also observed to increase.

One of the main goals of the theoretical analysis was to determine conditions that can enable choice of conditions that will allow flow directing in the devices. Initial experiments with a 2-channel exit configuration show that with a surface charge difference of approximately 2.6 times between the exit channels (*cf.* Figure 1,  $\sigma_2 = 2.6\sigma_1$ ). Figure 9 shows fluorescence data for two dyes, one positively charged (Rhodamine B) and one negatively charged (Fluorescein). It should be noted here that the fluorescein

data is for a microchannel with depth at 10  $\mu\text{m}$  as the negatively charged walls during experiments exclude the fluorescein, even for the 100 nm case with 10 mM NaCl i.e. conceptually similar to a microchannel. This suggests that the theoretical models are unable to predict the charge exclusion, even though they predict the correct plug-like flow profile for the small EDL case. Furthermore, the use of aqueous solutions also prevented any experiments with the hydrophobic methylated surfaces. Further experiments to contrast the influence of other polar solvents (e.g., alcohols) are currently underway to examine the role of surface modified devices for applications in flow control at the nanoscale.

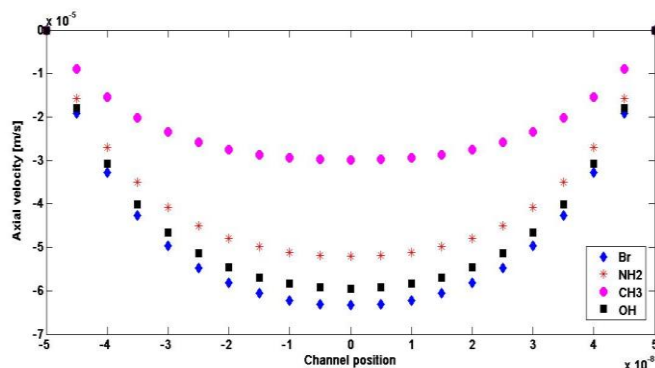


Figure 8: Velocity profiles in a 100 nm channel at pH 9 for 0.4 mM NaCl electrolyte as function of different surface functionalizations.

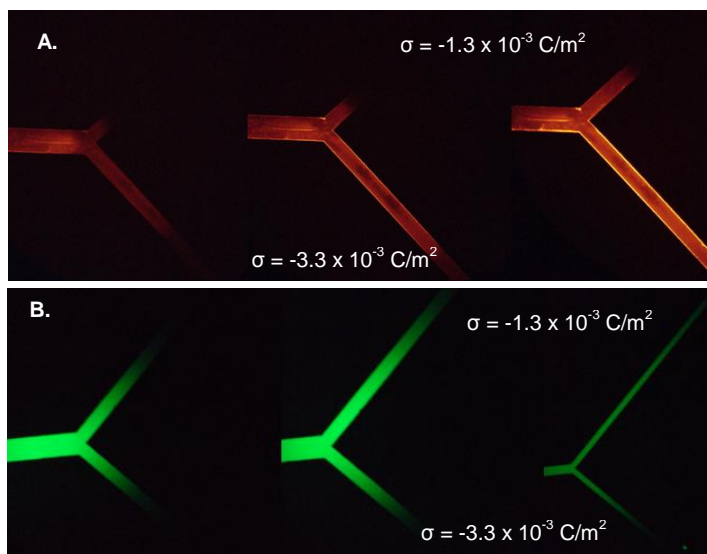


Figure 9: **A.**  $-\text{NH}_2$  (amine) functionalized microchannel shows a higher affinity for the positively charged dye (Rhodamine B) at pH 7. Glass surfaces by contrast show less dye transport in time elapsed images. **B.** Same configuration as A but by contrast the channels with lower negative surface charge density in absolute magnitude show more affinity for Fluorescein (negatively charged dye). Total time elapse is approximately 400 s in images going from left to right.

## CONCLUSIONS

Results reported show that by systematically manipulating surface charge density surface mediated flow control can be achieved in nanochannels. Velocities in the channels change non-linearly with changes in surface charge as a consequence of chemical

modification. Even without interacting or overlapping EDLs, co-ions were excluded from the nanochannels as evidenced by fluorescein being excluded from the negatively charged channels while Rhodamine B did not show exclusion at the neutral pH during experiments. Theoretical models predict velocity profiles in agreement with previous reports; however, they fail to predict several subtleties as observed experimentally, including co-ion exclusion. The selective flow control demonstrated in this paper by use of chemically modified surfaces presents one avenue for development of 'valve-less' electrokinetic nanofluidic flow manipulation strategies.

## REFERENCES

- [1] M. Napoli, J.C.T. Eijkel, S. Pennathur, "Nanofluidic Technology for Biomolecule Applications: a Critical Review", *Lab on a Chip*, 10, 957, (2010).
- [2] M. Gong, B.Y. Kim, B.R. Flachsbar, M.A. Shannon, P.W. Bohn, J.V. Sweedler, "An On-Chip Fluorogenic Enzyme Assay using a Multilayer Microchip Interconnected with Nanocapillary Array Membranes", *IEEE Sensors Journal*, 8, 601 (2008).
- [3] J. Han, H.G. Craighead, "Separation of Long DNA Molecules in a Microfabricated Entropic Trap Array", *Science*, 288, 1026 (2000).
- [4] S. Prakash, M.B. Karacor, S. Banerjee, "Surface Modification in Microsystems and Nanosystems", *Surface Science Reports*, 64, 233 (2009).
- [5] S. Prakash, T.M. Long, J.C. Selby, J.S. Moore, M.A. Shannon, "'Click' Modification of Silica Surfaces and Glass Microfluidic Channels", *Analytical Chemistry*, 79, 1661 (2007).
- [6] R. Karnik, R. Fan, M. Yue, D. Li, P. Yang, A. Majumdar, "Electrostatic Control of Ions and Molecules in Nanofluidic Transistors," *Nano Letters*, 5, 1633 (2005).
- [7] D. Li, *Electrokinetics in Microfluidics*, Elsevier, Inc., Amsterdam, 2004.
- [8] Y. Wu, M.B. Karacor, S. Prakash, M.A. Shannon, "Solid/Water Interface of Functionalized Silica Surface Studied by Dynamic Force Measurement", *Proceedings of ASME 2010 3rd Joint US-European Fluids Engineering Summer Meeting and 8th International Conference on Nanochannels, Microchannels, and Minichannels*, 2010, Paper number: FEDSM-ICNMM2010-30851.

## CONTACT

\*Shaurya Prakash, tel: +1-614-688-4045; [prakash.31@osu.edu](mailto:prakash.31@osu.edu)

# THREE-DIMENSIONAL TIME RESOLVED MEASUREMENTS OF CHARGED QUANTUM DOTS IN NANOCONFINED CHANNELS USING TOTAL INTERNAL REFLECTION FLUORESCENCE MICROSCOPY (TIRFM)

T. Wynne and S. Pennathur

University of California, Santa Barbara, CA, USA

## ABSTRACT

In this work, we use total internal reflection fluorescence microscopy (TIRFM) to excite CdSe/ZnS core-shell quantum dots (QD) in 100nm deep fused silica fluidic channels. Since the channels are shallower than the evanescent wave depth we can continuously probe the QD dynamics within the electrostatic environment of our system. We systematically perform experiments at varying salt concentrations to gain insight about the electrostatic behavior of finite sized charged particles in confined nanochannel environments. First, we describe the governing equation of electrostatics in confined environments. Next, we show successful TIRF measurements in both nanofluidic channels as well as unconfined coverslips. Finally, we compare transverse distributions of quantum dots in both environments for various background salt concentrations. Our data shows that as the electric double layer thickness increases, the particle is repelled from the wall by repulsive electrostatic interactions between the particle and the wall, and confinement shows increasingly different behavior than the traditional Poisson Boltzmann theoretical approach may suggest.

## INTRODUCTION

In the last few years, nanofluidics has emerged as its own field for the lab-on-chip community due to the unique coupling physics that occur at the nanometer length scale. For example, nanofluidic channels have been shown to have better separation efficacy, concentration ability, and new modalities for biomolecule manipulation and interrogation [1]. Nanofluidics can also be used to study biomolecules in confined environments that are on the length scale of in-vivo biological environments. Here, both the surfaces of the system as well as the surfaces of the biomolecules are important in governing the behavior of the system. Such studies will not only give us insight towards the effects of confinement in biomolecular systems, but will also serve as a design tool for the nanofluidic biomolecular analytical devices.

To date, there have been many theoretical and experimental studies of small ions in confined nanofluidic systems, with excellent agreement between theory and experiment [2, 3]. However, only few experimental and theoretical address finite size particles within nanofluidic channels, where the size of the particle can significantly change the background potential distribution. Although many molecular dynamics and density functional theory (DFT) models simulations have been performed in ion channels, nanofluidics for lab on chip systems generally relies on fluidic channels that are between 50-100nm [1]. In terms of larger sized channels, Gillespie [4], recently presented analytic theory for dilute colloids in charged slits, and Boy et al. [5] are developing a computational model that describes the electrostatics and Brownian motion of large (finite-sized) particles of arbitrary geometry confined in nanochannels using non-graded adaptive grids and level set methods to represent interfaces.

In this work, we propose to use a novel imaging technique, Total Internal Reflectance Fluorescence Microscopy (TIRF) to experimentally interrogate 17 nm quantum dots in 100 nm

confined nanofluidic channels. Total internal reflection fluorescence microscopy (TIRF) is a powerful analysis tool that exploits the evanescent wave produced by total internal reflection to excite fluorescent particles within a few hundred nanometers of a surface. Generally, TIRF has been used for imaging biological samples at the surface, since it gives superior signal to noise ratios as it does not excite background fluorescence [6], but since the advent of microfluidics [7], TIRF has been used to study fundamental properties of microfluidic systems near the surface. For example, Guasto and Breuer [8] used TIRF to probe near-wall velocimetry in microfluidic channels (~40 microns) to measure fluidic slip in Poiseuille flows with a variety of tracer particles, high-speed near wall measurements of QDs with TIRF in Poiseuille flows [9], and Sadr et al. studied near wall measurements of electro-osmotic flow in rectangular driven flow [10]. All microchannel TIRF studies have tracking times limited to a few milliseconds because the fluorescent tracers diffuse transversely out of the evanescent wave illumination region.

Therefore, although microchannel TIRF has allowed for great insight into the composition of surfaces in terms of the slip length, this technique has not been used to probe the electrostatic environment of the surface. Here we confine QDs in nanoscale fluidic channels that do not allow the evanescent wave to fully decay before reaching the far wall, as seen in Figure 1a. This enables us to study QDs for long periods of time (on the order of 20s) and use intensity distributions to characterize how finite sized charged particles behave in buffers of different ionic strengths.

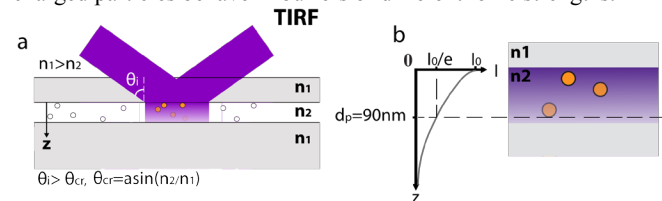


Figure 1: Total internal reflection (TIR) schematic (a) and evanescent wave exponential decay intensity profile (b). (a) TIR occurs when light reaches a sharp dielectric interface of decreasing index of refraction with an angle greater than the critical angle  $\theta_c$  as defined in Snell's law. (b) An exponentially decaying wave is transmitted into the less dense medium. TIRF uses this light to excite fluorescence within a few hundred nanometers of the surface. In this study, we use channels that do not allow the evanescent wave to fully decay which enables us to continuously excite QDs with a non-uniform excitation field in  $z$ .

## GOVERNING EQUATIONS

To solve for the electrostatic distribution of ions in a nanofluidic channels, we assume that the distribution of species  $i$  will follow the Boltzmann distribution

$$c_i = c_{\infty,i} \exp\left(-\frac{z_i e \psi(z)}{k_B T}\right) \quad (1)$$

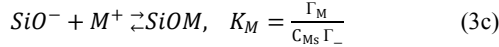
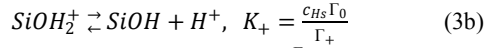
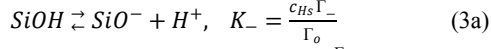
where  $c_{\infty}$  is the concentration (mol/L) in the bulk,  $\psi$  is the potential,  $e$  is the elementary charge,  $k_B$  is the Boltzmann constant,

$T$  is the temperature,  $Z$  is the valence number,  $n_{\infty}$  is the number density ( $\text{m}^{-3}$ ) in the bulk, and  $z$  is the distance from the wall. This distributions allows us to write the governing equation for electrostatics as follows [11]:

$$\frac{d^2\psi}{dz^2} = -\frac{e}{\epsilon} \sum_{i=1}^N Z_i n_{\infty,i} \exp\left(-\frac{Z_i e \psi(z)}{k_B T}\right) \quad (2)$$

This nonlinear Poisson Boltzmann equation is then solved subject to the boundary conditions at the solid-liquid interface.

To solve for Dirichlet boundary condition of zeta potential, we use a self-consistent charge and triple layer model following that of Wang [3]. First, the chemistry at the silica wall is governed by 3 reaction equations:



where  $K_i$  is the known reaction constant for each reaction equation,  $\Gamma$  is the number of available sites and  $M$  is a metal cation species that can adsorb to the silica surface. Next, the total number of available sites is conserved, and surface charge is defined by the difference between the number of positive and negatively charged sites at the silica surface. Finally, one can relate the potential drop across each layer with  $C_i$  being the Stern capacitance between triple layer planes:

$$\psi_0 - \psi_\beta = \frac{\sigma_0}{C_1} \quad (4)$$

Furthermore, we can eliminate the surface charge and solve directly for zeta potential as a function of concentration by using Grahame's equation as follows:

$$\sigma_0 = \sqrt{2\epsilon k_B T} \left( \sum_{i=1}^N n_{\infty,i} \left[ \exp\left(-\frac{Z_i e \zeta}{k_B T}\right) - 1 \right] \right)^{\frac{1}{2}} \quad (5)$$

where  $\sigma$  is the surface charge and  $\zeta$  is the potential at the slip plane. Similar relations must be applied to the QD, which has a carboxyl coating with a specified charge distribution. Note that a significant parameter used to define our systems is the Debye length,  $\lambda_D$ , which is the characteristic length scale for the thickness of the electric double layer (EDL). The Debye length decreases for higher ionic strengths and scales as  $n_{\infty}^{-1/2}$

$$\lambda_D = \left( \frac{\epsilon k_B T}{e^2 \sum_{i=1}^N z_i^2 n_{\infty,i}} \right)^{\frac{1}{2}} \quad (6)$$

Non-zero zeta potentials on the wall result in a non-uniform hydronium ion distribution and hence a spatial  $p\text{H}$  gradient across the channel for large Debye lengths. The zeta potential can therefore be used as a boundary condition for finding the correct  $p\text{H}$  at various transverse positions in the channel and the average  $p\text{H}$  in the channel can be defined by:

$$\langle p\text{H} \rangle_i = -\log_{10} \left( \frac{\int_0^h dz c_i c_H}{\int_0^h dz c_i} \right) \quad (7)$$

## MATERIALS AND METHODS

### Buffer and Sample Preparation

Boric acid crystals (EMD, BX0865-1) were dissolved in filtered ultra-pure deionized water (Millipore, Milli-Q) to create 200mM ionic strength stock solution. We monitor  $p\text{H}$  (Oakton,  $p\text{H}$  11) and titrate all buffer solutions with sodium hydroxide solution (Fisher Scientific, S318-500) to  $p\text{H}$  9.15 then dilute to 5, 10, 20 and 50mM ionic strengths. Due to confinement in the nanochannel, it has been shown that the  $p\text{H}$  in a nanochannel will be lower than the bulk  $p\text{H}$  [12], the effect is significant at lower ionic strengths. Since the intensity of QD emission is very sensitive to  $p\text{H}$  [13], we further titrate the solutions to corrected  $p\text{H}$  values according to Eqs. 1-7. This is an iterative process due the coupling between total ionic strength (which increases during

titration) and the corrected  $p\text{H}$ , resulting in set of buffer concentrations corresponding to that shown in Table 1.

We use water-soluble CdSe/ZnS core-shell quantum dots with carboxyl polymer coating (Invitrogen; model# A10200) with core diameter of  $\sim 7\text{nm}$  and overall hydrodynamic diameter of  $\sim 17\text{nm}$ . The peak wavelength for emission is centered at 625nm with FWHM of 30nm. We dilute the stock 8  $\mu\text{M}$  QD solution down to 10pM in sodium-borate buffer at  $p\text{H}$  9.15 for coverslip experiments and 50pM in  $p\text{H}$  corrected sodium-borate solutions for channel experiments. We chose these dilutions of QDs to be able to resolve individual quantum dots for coverslip measurements (10 pM) and isolate single QDs in the channel for confined experiments (50 pM).

Table 1: Corrected  $p\text{H}$  values for nanofluidic confined TIRF

$\lambda_D$	Borate [C]	NaOH[C]	Corrected $p\text{H}$
4.29 nm	5mM	3.05 mM	9.35
3.04 nm	10mM	5.67 mM	9.27
2.15 nm	20mM	10.9 mM	9.20
1.35 nm	50mM	23.3 mM	9.15

studies. Column 1 - Debye length, defined by Eq. 6, Column 2 - Borate buffer concentration, Column 3 - sodium-hydroxide ionic strength, Column 4 - corrected  $p\text{H}$  based on Eqs. 1-7

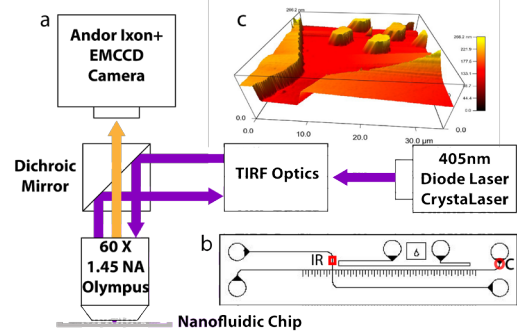


Figure 2: (a) Schematic of the home built TIRF system. (b) Layout of the nanofluidic chip. The interrogation region (IR) is in the top-left channel 2mm before the intersection. (c) AFM of the 100nm etched fused silica features.

### Nanochannel Fabrication and substrates

Nanofluidic channels are fabricated on 525 $\mu\text{m}$  thick, 100mm diameter fused silica wafers (Hoya Corp.; model# 4W55-325-15C-STD) using contact lithography (EVGroup, EValign 620) with positive tone photoresist (Shipley, 3217M) and NF3 plasma dry etch (Applied Materials, AMT 8100) to create 100nm deep rectangular trenches, AFM viewgraph in Figure 2c (Asylum Research, MFP-3D). 1.8mm access holes are CNC-drilled into a 170 $\mu\text{m}$  thick, 100mm diameter quartz wafer (Montco Silicon; Lot# 4QUARTZ/B). Both wafers are RCA cleaned before fusion bonding at 1050C. The wafer is diced into 12x50mm nanofluidic chips with pattern in Figure 2b.

### Experimental Setup

TIRF illumination is created from home built system (Figure 2a) that includes a 405nm 50mW continuous wave diode laser (CrystaLaser TL405-050), the beam is directed with free space optics (ThorLabs, Newport) that feed into the laser port of an upright microscope (Olympus BX41) with QD optimized fluorescence filters (Chroma; Z405RDC, HQ620/25m) and an oil immersion objective lens (Olympus; 60x TIRF, 1.45 NA). The laser beam is expanded and focused off axis at the back focal plane of a 1.45 NA objective lens to produce a collimated beam incident at  $\sim 70$  degrees from the normal for total internal reflection. The

emitted fluorescence from the QDs is captured on a back-illuminated EMCCD (Andor, Ixon+).

## EXPERIMENTAL PROCEDURE

### Coverslip TIRF

Approximately 5-10mm wide, 170  $\mu\text{m}$  thick quartz coverslips are sonicated in acetone then isopropyl alcohol for 5 minutes then rinsed with ultra-pure deionized water and dried with nitrogen before each experiment. For each buffer concentration, we pipette 5  $\mu\text{L}$  of 10pM QD solution onto a 1mm thick glass slide (Corning, 2974-3x1) and cover with a second 170  $\mu\text{m}$  thick coverslip. Each experiment measures the intensity of 1 to 15 different QDs at a time that diffuse in and out of the evanescent wave, due to the  $\sim 3\text{ms}$  residence time of each particle.

### Confined FTIRF

For these frustrated TIRF (FTIRF) experiments, our experimental procedure is as follows. First, we fill the nanochannel with DI water by capillary action. All subsequent flushing steps are performed using a 7.1kV/m electric field applied to the top-left channel (see Figure 2). First, we flush with DI water to remove any bubbles in the channel. Next, the channel is electrokinetically flushed with 100mM NaOH for 15 minutes, which removes surface contaminants by etching the surface slightly. The channel is then flushed with DI water for 30 minutes. After cleaning, pH corrected sodium-borate buffer solution is electrokinetically driven into the channel and allowed to equilibrate in the channel for at least 30 minutes to ensure chemical equilibrium of the EDL structure. Finally, we replace the buffer in the top-left well with pH corrected 50pM QD of the same buffer ionic strength and drive them into the channel until we can isolate one in the region of interest (Figure 2) with the camera. We then focus the objective and acquire 1500 frames at a 3 ms exposure time, at 82 Hz and with 300EM gain. Note that in these experiments, only one QD is imaged at a time.

### Data Reduction

The images are converted to 16 bit TIFF files and processed with Blair and Dufresne [14] PIV functions using commercial software (MATLAB, inc) to locate the particle. We sum a 3x3 array around a peak corresponding to a QD to count all of the light emitted from the QD, then subtract noise (based on the average noise for 9 pixels), and normalize with the flat field based on the x-y coordinates of the peak. We perform this operation for every frame and find the corresponding distribution of measured intensities. Figure 3 shows an example of a distribution for 10mM buffer concentration in a confined 100 nm channel, which also shows the phenomena of quantum dot coagulation and blinking. Figure 3 (a) shows a “normal” single QD distribution whereas (b) shows a QD cluster distribution. Some histograms appeared to be heavily influenced by QD blinking or clusterings, and therefore were omitted from the averaged distributions over all experiments.

## RESULTS

### Coverslips

For a baseline, we first measure unconfined intensity distributions of 10 pM QD solutions between a fused silica coverslip and glass slide which are separated by a distance much larger than the evanescent wave penetration depth. The normalized intensity distributions are shown in Figure 4a for 5, 10 and 20mM sodium-borate buffer at pH 9.15 along with a fitted curve. The data shows that QD concentration near a charged surface increases with increased buffer concentration, Figures 4c,d,e show example images at 5, 10 and 20mM respectively. The negatively charged

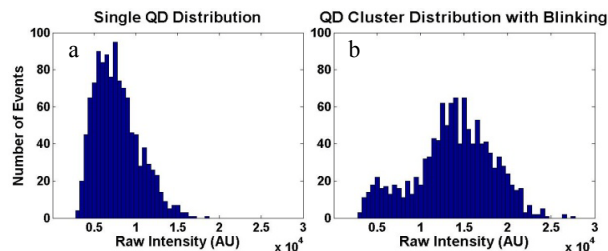


Figure 3: (a) Sample intensity distribution with 500 intensity unit bins, for a single confined QD in 10mM sodium-borate buffer. (b) Sample intensity distribution of a QD cluster, seen by the high mean intensity. There is also with significant blinking characterized by the secondary peak.

particles have repulsive interactions with the negatively charged walls, thus for longer  $\lambda_D$ , the QDs distribution will be closer to the wall. Figure 4b shows the corresponding theoretical small ion potential distribution for a flat wall [11] for the same concentrations/conditions, which qualitatively agrees to the coverslip data. Note that the experimental data has a peak in concentration (as opposed to the theoretical distributions and exponential fits) because of the low probability that particles will have trajectories that are barely above the detection limits.

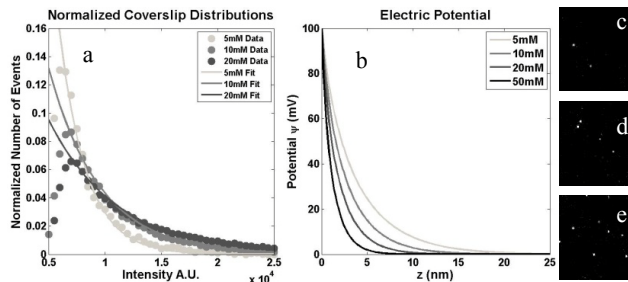


Figure 4: Normalized intensity distributions of 10pM QD in 5, 10 and 20mM sodium-borate buffer. The curves show that the QD density distribution is lowest near the surface for 5mM and increases with increased buffer concentrations. Sample images are shown in (c) 5mM (d) 10mM and (e) 20mM. These show that the near surface QD density is higher for higher buffer concentrations, indicating the length scale of the repulsive force is shorter.

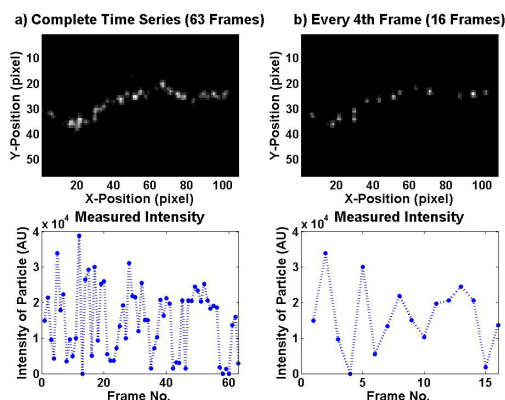


Figure 5: Demonstration of confined TIRF showing superposed frames of a single QD electrokinetically driven with 1.56kV/m applied electric field in a 100nm channel. (a) Top: Compilation of 63 frames superposed, Bottom: measured intensity (A.U.) of the QD in each corresponding frame. (b) Top, Bottom: same data as (a) but analyzing every 4<sup>th</sup> frame for visual clarity. Images acquired at 64.5 Hz with 3ms exposure time and 300 EM gain.



## Nanofluidic Confined Experiments

First, we demonstrate confined TIRF by showing a time series of a single quantum dot kinetically driven with 1.56kV/m electric field in a 100nm deep channel in Figure 5. In this figure we show 64 consecutive frames of a single electrokinetically driven QD in a nanofluidic channel for 1 second, traveling (from left to right) a total distance of 108  $\mu\text{m}$ . Although the particle is completely confined within the illumination depth, the quantum dot is not detected in all frames due to blinking, which is a property exhibited by QDs where they enter a "dark state" do not emit fluorescence for a random period of time [13]. In any case, this figure shows that we can study quantum single quantum dots with TIRF over much longer time scales than previously capable [11].

To compare QD intensity distributions in confinement for different electrostatic environments we analyze 900-1100 (out of 1500 frames) intensity values for a single QD diffusing by pure hindered Brownian motion over  $\sim 18$  seconds. Note that the time for 17nm QDs to diffuse across the 100 nm depth of the channel is on the order of 1ms, and therefore the 3ms exposure intensity measurements quantify detected photons from the QD over multiple oscillations through the channel in the z dimension. Figure 6 shows the normalized intensity distributions of confined single quantum dots for different ionic strengths. Note that since we accounted for the change in pH within the channels, we can assume the quantum dots have the same emission response for all ionic strengths. Therefore, our data shows that the intensity peak of the distribution is greater for lower ionic strengths. This suggests that for higher ionic strengths, the quantum dot samples a larger range of the channel (and therefore an average intensity that is smaller) than the QDs in lower ionic strengths. We suggest that this result is due to the effect of thicker double layers, and results in a broader distribution.

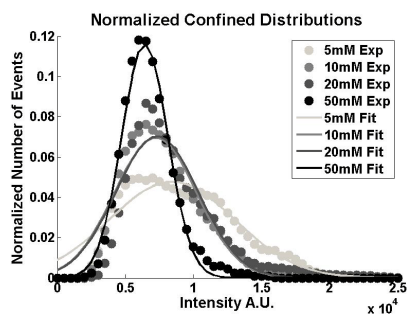


Figure 6: Normalized intensity distributions of single quantum dots confined in a  $20\mu\text{m} \times 100\text{nm}$  fused silica channel. The distributions show that the peak intensity is higher for lower ionic strengths. This suggests that for higher ionic strengths the QD samples a larger range of channel resulting in a lower average intensity than at low ionic strength where the QD samples a smaller range due to repulsion at the walls.

The differences of the confined distributions and the coverslips distributions can also give us insight to the effect of confinement on finite sized particles. For example, the 5mM experiment is significantly broader in confined nanochannels, suggesting that confinement repels the quantum dot further than in the coverslip case. This makes sense because the channel walls each contribute electrostatic repulsion due to the double layer, effectively confining the quantum dots to a smaller region of the channel, whereas in coverslips quantum dots are free to diffuse to infinity in the transverse dimension. These measurements are the first such fundamental measurements to quantify confinement effects of finite size particles in nanoconfined channels.

## DISCUSSION

We demonstrate the confined TIRF with quantum dots using 100nm fused silica channels with a model for necessary pH corrections due to confinement. We present unconfined distributions that qualitatively agree with PB theory, and compare these with confined distributions which show some deviation at lower ionic strengths. We attribute this to the fact that the confined environment must force particles to be near the center of the channel, whereas unconfined particles are free to diffuse large lengths scale away from the wall. These studies are the first fundamental studies of finite sized charged particles within confined channels, and may lead to breakthroughs in nanofluidic separation studies and understanding of fundamental biomolecule behavior in confined channels.

## ACKNOWLEDGEMENTS

The authors thank Jesper Toft Kristensen and Kristian Lund Jensen for their numerical calculations for nanochannel pH corrections. This work is supported by grant from the Institute for Collaborative Biotechnologies (ICB) and UCSB startup fund. The fabrication was completed at UCSB, a National Nanotechnology Infrastructure Network (NNIN) member.

- [1] M. Napoli, J.C.T. Eijkel, and S. Pennathur, "Nanofluidic technology for biomolecule applications: a critical review". *Lab on a Chip*, 10, 8 (2010).
- [2] S. Pennathur and J.G. Santiago, "Electrokinetic transport in nanochannels. 2. Experiments". *Anal. Chem.*, 77, 21 (2005).
- [3] M. Wang and A. Revil, "Electrochemical charge of silica surfaces at high ionic strength in narrow channels". *Journal of Colloid and Interface Science*, 343, 1 (2010)
- [4] D. Gillespie, "Analytic Theory for Dilute Colloids in a Charged Slit". *The J. of Phys. Chem. B*, 114, 12 (2010)
- [5] D. Boy, et al., "Particle Separation by Capillary Electrophoresis in Nanochannels", *IMA Microfluidics: Electrokinetic and Interfacial Phenomena*. 2009.
- [6] D. Axelrod, T. Burghardt, and N. Thompson, "Total Internal Reflection Fluorescence". *Ann. Rev. Biophys. Bioengr.*, 93, 13 (1984).
- [7] T. Squires and S. Quake, "Microfluidics: Fluid physics at the nanoliter scale". *Rev. Mod. Phys.*, 77, 3 (2005).
- [8] P. Huang, J. Guasto, and K. Breuer, "Direct measurement of slip velocities using three-dimensional total internal reflection velocimetry". *J. Fluid Mech.*, 566 (2006)
- [9] J. Guasto and K. Breuer. "Micro-Velocimetry using time-resolved measurements of quantum dots in a microchannel". *ECI International Conference on Heat Transfer and Fluid Flow in Microscale*. Whistler (2008).
- [10] R. Sadr, et al., "An experimental study of electro-osmotic flow in rectangular microchannels". *J. Fluid Mech.*, 506 (2004)
- [11] R. Hunter, *Foundations of Colloid Science*. Oxford: Oxford Science Publication. 1993
- [12] D. Bottenus et al., "Experimentally and theoretically observed native pH shifts in a nanochannel array". *Lab on a Chip*, 8, 9 (2008).
- [13] N. Durisic, et al., "A Common Mechanism Underlies the Dark Fraction Formation and Fluorescence Blinking of Quantum Dots". *ACS Nano*, 3, 5(2009).
- [14] D. Blair and E. Dufresne. "The Matlab Particle Tracking Code Repository". <http://physics.georgetown.edu/matlab/>.

# A HYBRID TECHNOLOGY FOR Pt-Rh AND SS316L HIGH POWER MICRO-RELAYS

F.M. Ozkeskin<sup>1\*</sup> and Y.B. Gianchandani<sup>1,2</sup>

<sup>1</sup>Department of Mechanical Engineering, University of Michigan, Ann Arbor, USA

<sup>2</sup>Department of Electrical Engineering and Computer Sciences, University of Michigan, Ann Arbor, USA

## ABSTRACT

This paper reports a hybrid technique to microfabricate relays from platinum-rhodium and stainless steel 316L bulk foil and to directly assemble them on printed circuit boards with gold coated copper interconnect for high power handling capability. Devices of 6mm<sup>2</sup> size serve as relays for DC current levels >1 A, and are suitable for circuits dissipating >250 W power.

## BACKGROUND AND ADVANCES

The most commonly used processes for microsystem device manufacturing and assembly rely upon semiconductor technology and silicon based substrates. Although these processes are mature, the properties of silicon are seldom adequate for high power applications; additionally environmental limitations impose significant burden upon hermetic packaging of silicon based devices. Recent research reports have described device microfabrication on non-silicon substrates such as printed circuit boards (PCBs) and liquid crystal polymer to ease packaging and system integration [1-3]. Semiconductor based fabrication techniques typically provide very limited access to metal alloys, relying more on thin film sputtering [4-5], which limits the power-handling capability of the components. A hybrid technology by which hard metal alloy devices can be fabricated from bulk robust metal foils is of interest.

Micro-electrodischarge machining ( $\mu$ EDM) provides a lithography compatible manufacturing method for bulk metal foil based micro devices with feature sizes down to 5  $\mu$ m. Both serial and batch mode machining have been developed and characterized in our group [6]. A  $\mu$ EDM'ed oscillating micro-relay on a glass substrate was also reported earlier [7]. This paper presents a hybrid technique whereby hard metal bulk foils such as platinum-rhodium (Pt-Rh) and stainless steel 316L (SS316L) are first  $\mu$ EDM'ed, then assembled on PCBs to demonstrate high power DC switching capability without compromising device footprint.

## DESIGN

The central element of the device is an electrostatically actuated cantilever beam that is assembled on a power-rated PCB. The bulk metal foil cantilever (2400  $\mu$ m x 950  $\mu$ m x 40  $\mu$ m) provides mechanical robustness and chemical resistance to corrosion. In particular, Pt-Rh prevents adhesion problems, and can withstand high temperatures without softening, alloying or microwelding to the contact surface. A lower cost alternative, SS316L, is used for benchmarking.

The cantilever beam is orthogonally placed with respect to the signal line, being suspended above a break in a PCB metal trace (Figure 1), and anchored by alignment posts that perforate it; these posts are positioned in blind vias on the PCB. A paddle at the distal end of the cantilever serves as an actuation (pull-down) electrode. Below it is a ground electrode, patterned on the PCB. The cantilever has two recessed zones: one over the ground electrode that is designed to prevent contact, and a shallower one over the signal line to ensure contact when it is actuated. This design also provides a protrusion that rests against stand-off bumps on the PCB, preventing contact between the pull-down electrode and the ground electrode.

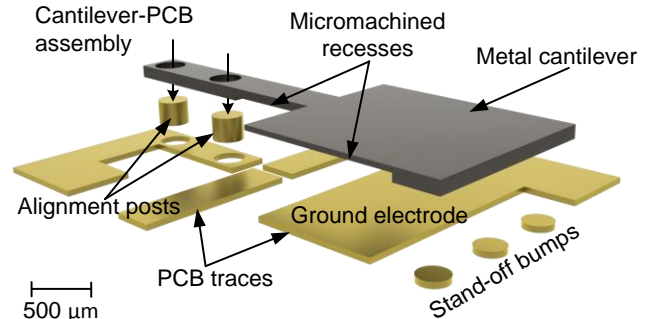


Figure 1: Exploded view of structure showing cantilever relay. Recesses are machined (2  $\mu$ m across contact, 8  $\mu$ m across electrodes) for DC-contact switching. Gold posts align and hold the cantilever over gold-coated copper traces on the PCB.

## FABRICATION/ASSEMBLY

### Micro-Relays

Micro-relays were fabricated in both Pt-Rh (80:20) and SS316L using 50  $\mu$ m thick stock metal foils. The patterns were serially  $\mu$ EDM'ed. The lowest available discharge energy was used to ensure smooth surface finish. (Batch mode fabrication is also possible by using lithographically fabricated tool electrodes.) Perforations of 310  $\mu$ m diameter were located in the anchor regions for subsequent alignment and attachment to the PCB. Machined hole diameters were slightly larger than the tool electrode diameter due to EDM discharge gaps of 5  $\mu$ m in all directions.

### PCB

A standard FR-4 with 1.6 mm thickness constituted the PCB substrate. Cu traces of 90  $\mu$ m thickness were chosen for high current ratings (up to 4.5 A for 300  $\mu$ m wide signal lines). In such PCBs, a 4  $\mu$ m Ni layer is sandwiched between a Cu base layer and a 0.15  $\mu$ m thick outer gold layer. Through holes formed by vias were positioned for subsequent assembly and electrical contact to the micro-relays.

### Assembly

Alignment posts (1750  $\mu$ m height; 300  $\mu$ m diameter), were  $\mu$ EDM'ed as slices from gold wire. These were inserted as tight fits into the same diameter PCB vias by tweezers (Figure 2a). The length of the posts was designed to extend above the PCB trace by approximately 50  $\mu$ m, to precisely accommodate the cantilever beam. The micro-relays were assembled into the posts by aligning over the posts (Figure 2b). A gold particle-filled conductive epoxy (Creative Materials, volume resistivity: 300  $\mu\Omega$ -cm) was manually applied through a syringe around the alignment posts (Figure 2c). Other techniques such as the use of solder balls are optional. The flatness of the cantilever beam was maintained during the assembly process by monitoring the height of the beam tip from a laser displacement sensor (Keyence LK-G) and adjusting to ensure

that the cantilever tip is in contact with stand-off bumps during the epoxy curing. An assembled device is shown in Figure 3.

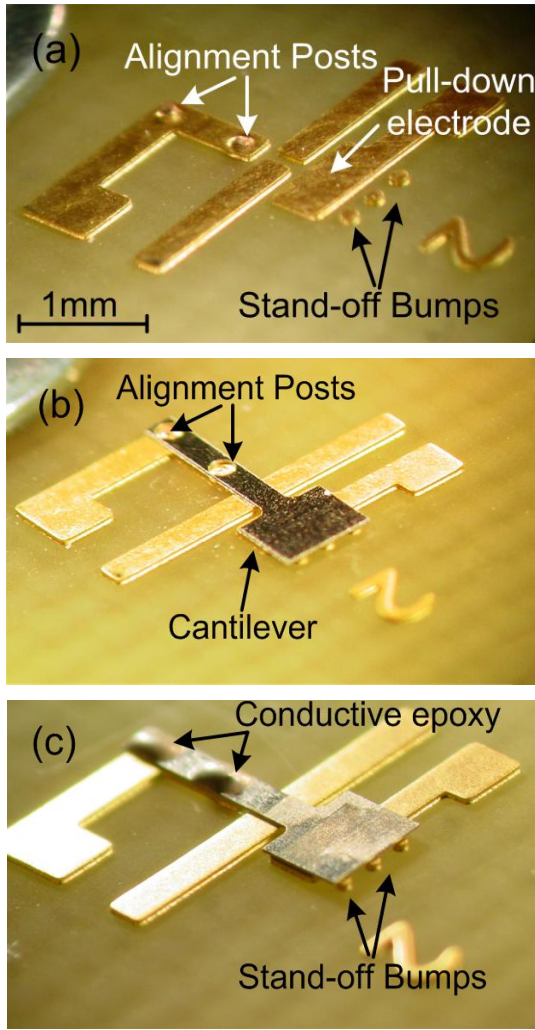


Figure 2: Assembly sequence for Pt-Rh and SS316L devices showing: (a) electrodes with alignment posts inserted. (b) The cantilever placed so that posts fit in vias in the thick foil. (c) Conductive epoxy applied for fixing.

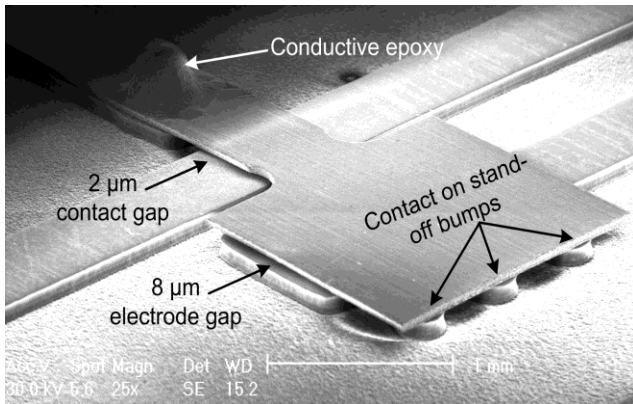


Figure 3: SEM image of the assembled device showing machined gaps, conductive epoxy and the stand-off bumps.

## TESTING

The test circuit is shown in Figure 4a. It consists of a control voltage ( $V_{SS}$ ) and two sets of power-rated load resistors:  $R_{L1}$  and  $R_{L2}$  along with a standard high value resistor to ensure that current pathway is on the signal line. Voltage values in boxes:  $V_S$ ,  $V_D$  and  $V_G$  indicate measurements taken.  $V_G$  was always lower than 300  $\mu$ V, indicating good switch isolation due to stand-off bumps. For testing, two different circuit configurations with different load resistors were used, as described in Table 1. These configurations tested different voltage and current limits. In addition, tests were conducted both in air and nitrogen ambient. Nitrogen tests were conducted in a 0.2 Torr vacuum chamber. All the tests were repeated for both Pt-Rh and SS316L devices.

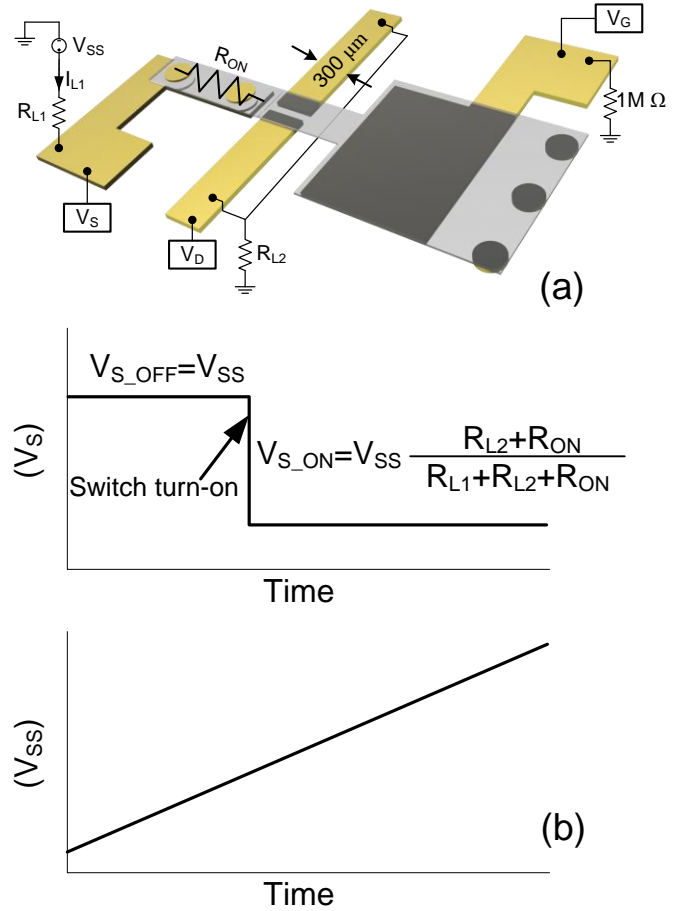


Figure 4: (a) Circuitry for testing; voltages in boxes are for measurements.  $V_D$  and  $V_S$  are used to determine ON-state resistance ( $R_{ON}$ ). (b) The transient behavior of  $V_S$  as  $V_{SS}$  is progressively increased, showing  $V_{S\_OFF}$  and  $V_{S\_ON}$  conditions.

Table 1: Device test configuration details. Config1 provides higher voltage testing (>300 V) whereas Config2 is suited for high current (>1 A).

Configuration	Description
Config1	$R_{L1}=400\Omega, R_{L2}=125\Omega, 0.6A$ max. allowed current
Config2	$R_{L1}=100\Omega, R_{L2}=83\Omega, 1.34A$ max. allowed current

$R_{ON}$  in Figure 4a is ON-state resistance and is a sum of the cantilever resistance and contact resistances at the epoxy transfer

points.  $R_{ON}$  can be reduced with improved contact materials.

Figure 4b shows the transient response of  $V_S$  to a progressive increase of  $V_{SS}$ . When the switch is in OFF-state,  $V_S$  is the same as  $V_{SS}$  (denoted as  $V_{S,OFF}$ ). When the switch is turned on and goes to ON-state,  $V_S$  is reduced sharply and is defined as a combination load resistors and  $R_{ON}$  during ON-state (denoted as  $V_{S,ON}$ ).

## RESULTS

Figure 5 shows  $R_{ON}$  as a function of series current in the circuit ( $I_{L1}$ ) for 6 different test conditions that include the two types of relay materials, air and nitrogen environments, and the two different circuit load configurations presented in Table 1. In general, the Pt-Rh micro-relay offers the best overall performance, and in a nitrogen ambient, it can support  $>1$  A DC current. The lowest recorded ON-state resistance was  $2.8 \Omega$ . The current handling capability of Pt-Rh devices was tested to the point of failure in Config2 and nitrogen environment. Device failure for this configuration occurred at approximately 1.2 A due to excessive heating of the contacts causing microwelding. The switch was operated around 600 cycles before failure took place.

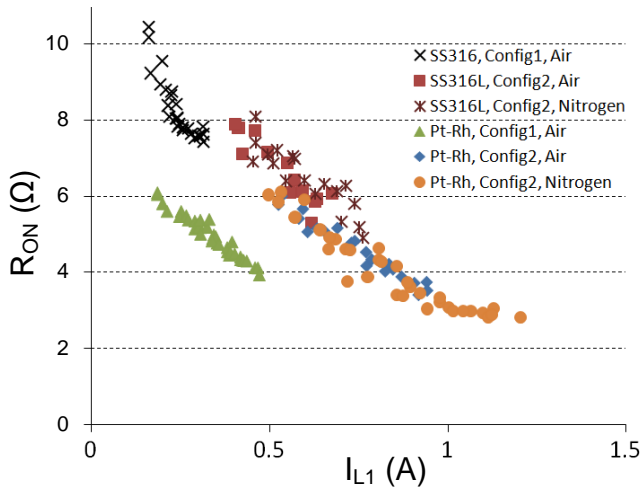


Figure 5: Switch ON resistance vs. series current. Highest current handling is for Pt-Rh in Nitrogen environment where  $R_{ON}$  is  $2.8 \Omega$ .

Figure 6 shows  $R_{ON}$  as a function of supply power ( $P_{SS}$ ), which is the circuit dissipated power, for the same 6 conditions aforementioned, indicating that these micro-relays can be used in circuits that dissipate  $>250W$  power. The switch failure occurring at 1.2 A current translates to 332 W of DC power for Pt-Rh, Config2 and nitrogen ambient.  $P_{SS}$  is provided by  $V_{SS}I_{L1}$ , i.e. the total power dissipated in the circuit.

Figure 7 shows the voltage  $V_S$  at the anchor of the micro-relay when it is turned on (denoted as  $V_{S,ON}$ ). This value is used to calculate the  $R_{ON}$ :  $(V_{S,ON} - V_D)/I_{L1}$ .

Switch actuation voltage  $V_{SS}$  was designed to be 100 V. Test results, however indicate an actuation voltage of 107-110 V. Relatively small deviation (10% maximum) of experimental value from theoretical value can be correlated to structural imperfections or circuit parasitics. Note that the supply voltage can be increased past 300V for Pt-Rh switches.

Figure 8 shows the typical transient response of a Pt-Rh micro-relay. Typical turn-on/turn-off times are 30-40 ms. The device can actuate faster with perforations on the actuation

electrode paddle which would decrease air damping, however a compromise could be made with increased actuation voltage due to decreasing electrode overlap area.

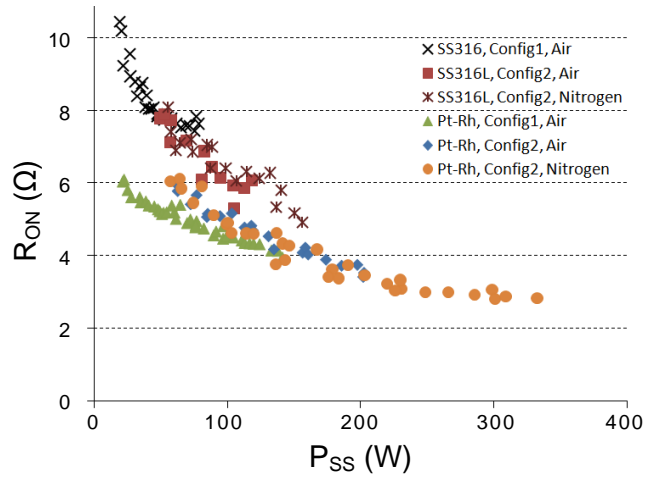


Figure 6: Switch ON ( $R_{ON}$ ) resistance vs. supply power  $P_{SS}$  which goes up to 332 W for Pt-Rh switch.  $P_{SS}$  denotes circuit dissipated power.

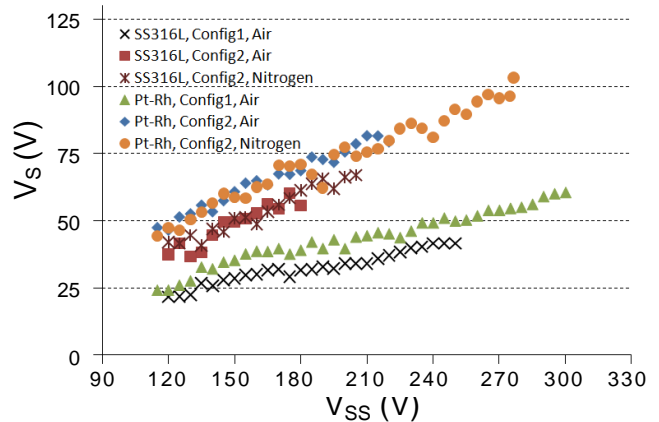


Figure 7:  $V_S$  measurement for control values of  $V_{SS}$ . This  $V_S$  is denoted by  $V_{S,ON}$  in Figure 4b.

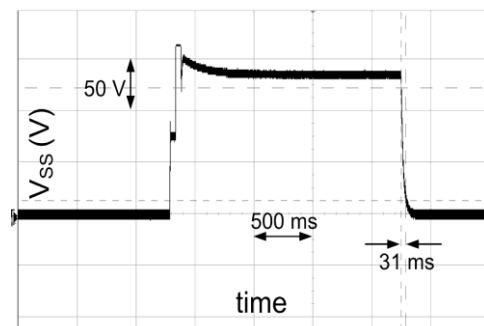


Figure 8: Switch response is shown for a  $V_{SS}$  of 135 V. The fall time measured is 31 ms and rise time is similar.

Table 2: Switch performance and size comparison to solid state and MEMS relays. Pt-Rh metal cantilevers provide high current carrying capability and small footprint.

Property	Devices					
	SKKD 57/08 Thyristor	ISL9V 2040S3S IGBT	SiC Schottky Diode	Omron MEMS Switch	Cronos MEMS Switch	This Study (Pt-Rh and Config2)
Footprint (mm <sup>2</sup> )	1302	112	303	15.6	36	6
Max current (A)	45	10	10	0.1	0.35	1.2
Current per mm <sup>2</sup> (A/mm <sup>2</sup> )	0.035	0.089	0.033	0.006	0.01	0.2
On resistance ( $\Omega$ )	0.005	0.6	0.1-0.15	2	0.7	2.8
Actuation time (ms)	0.002	0.002	0.0001	0.02	10	30

Table 2 benchmarks this work to cross-technology (solid-state) options as well as in-technology (MEMS) relays. Commercial solid state alternatives include a high power thyristor [8], an insulated-gate bipolar transistor (IGBT) [9], and a high power SiC Schottky diode [10]. MEMS counterparts include a commercially available switch [11] and a research device [12]. It can be seen that solid state devices often have very fast actuation times and higher current ratings; however, these devices require compromises on footprint. Available MEMS devices have smaller footprint, but also low current ratings. While  $R_{ON}$  is larger for this work, the compactness is very competitive and the power handling is adequate for several applications.

## CONCLUSIONS

A hybrid technology for fabrication and assembly of bulk foil hard metal high power micro-relays has been developed. Micro-electrodischarge machined cantilevers were directly assembled on PCBs with gold coated power rated traces, to facilitate system integration. Fabricated Pt-Rh devices demonstrated up to 1.2 A of current rating, for operation in circuits dissipating >250 W of DC power. The micro-relays have a footprint of 6mm<sup>2</sup> and provide high current rating per area compared to solid-state and MEMS counterparts.

## ACKNOWLEDGEMENT

This study is supported in part by Defense Advanced Research Projects Agency, Microsystems Technology Office (DARPA MTO) contract # W31P4Q-09-1-0009.

## REFERENCES

- [1] B.S. Weber and L.C. Kretly, "PCB-MEMS RF Switch: Parametric analysis and design guide lines," *IEEE MTT-S International Microwave Theory and Techniques Symposium Proc.* (2007), pp. 141-144.
- [2] M. Maddela and R. Ramadoss, "A MEMS-based tunable coplanar patch antenna fabricated using PCB processing techniques," *Journal of Micromechanics and Microengineering*, 17 (2007), pp. 812-819.
- [3] R. Dean, J. Weller, M. Bozack, B. Farrell, L. Jauniskis, J. Ting, D. Edell and J. Hetke, "Micromachined LCP connectors for packaging MEMS devices in biological environments," *Journal of Microelectronics and Electronic Packaging*, 4, 1 (2007), pp. 17-22.
- [4] H. Lee, R.A. Coutu, S. Mall and K.D. Leedy, "Characterization of metal and metal alloy films as contact materials in MEMS switches," *Journal of Micromechanics and Microengineering*, 16 (2006), pp. 557-563.

- [5] R.A. Coutu, P.E. Kladitis, K.D. Leedy, and R.L. Crane, "Selecting metal alloy electric contact materials for MEMS switches," *Journal of Micromechanics and Microengineering*, 14 (2004), pp. 1157-1164.
- [6] K. Takahata and Y.B. Gianchandani, "Batch Mode Micro-Electro-Discharge Machining," *Journal of Microelectromechanical Systems*, 11, 2 (2002), pp. 102-110.
- [7] K. Udeshi, and Y. B. Gianchandani, "A DC-powered high-voltage generator using a bulk Pt-Rh oscillating micro-relay," *IEEE International Conference on Solid-State Sensors and Actuators (Transducers '07)* (2007), pp. 1151-1154.
- [8] [http://www.semikron.com/internet/webcms/online/asim/07894300\\_DS.pdf](http://www.semikron.com/internet/webcms/online/asim/07894300_DS.pdf), referenced November 2009.
- [9] <http://www.fairchildsemi.com/ds/IS/ISL9V2040D3S.pdf>, referenced November 2009.
- [10] [http://www.cree.com/products/power\\_docs2.asp](http://www.cree.com/products/power_docs2.asp), referenced October 2009.
- [11] [http://www.components.omron.com/components/web/PDFLIB.nsf/0/9AAA9A30064393CA862574F80078809C/\\$file/SB\\_RFMEMS-02+SalesBrochure.pdf](http://www.components.omron.com/components/web/PDFLIB.nsf/0/9AAA9A30064393CA862574F80078809C/$file/SB_RFMEMS-02+SalesBrochure.pdf), referenced February 2010.
- [12] R. D. Streeter, C. A. Hall, R. Wood and R. Madadevan, "VHF high-power tunable RF bandpass filter using microelectromechanical (MEM) microrelays," *International Journal of RF & Microwave CAE*, 11, 5 (2001), pp. 261-275.

## CONTACT

\*F.M. Ozkeskin, tel: +1-979-218-1087; ozkeskin@umich.edu

# A STUDY OF NONLINEAR DYNAMICS OF MEMS INERTIAL SENSOR UNDER OVERLOAD CONDITIONS

David Lin, Todd Miller, and Krithivasan Suryanarayanan  
 Freescale Semiconductor, Inc., Tempe, Arizona, USA

## ABSTRACT

This paper reports the study results on the nonlinear dynamics of a z-axis MEMS capacitive acceleration sensor in the context of overload conditions. Two dominant sources of nonlinearity are discussed - nonlinear squeeze-film damping and higher order eigenmodes of the mechanical structure. The nonlinear damping results were obtained by solving large displacement Reynolds equation and FEA simulation. Reduced order model is employed to incorporate the higher order modes into microsystem model for crash analysis. It is shown that the microsystem model can accurately simulate the crash overload event when properly taking into accounts these two sources of nonlinearity.

## INTRODUCTION

The dynamic performance of microelectromechanical system (MEMS) inertial sensors is a critical criterion for success in automotive safety application [1]. Typically the device is designed to operate within a specified range. Acceleration beyond the range of the device (overload) can generate a DC shift at the output of the device that is dependent upon the overload frequency and amplitude. In particular, the high frequency, high amplitude stimulus during crash event often causes nonlinear dynamic behavior of MEMS sensors, which manifests itself as DC shift at the output, resulting in erroneous airbag deployment.

In this work, two dominant sources of nonlinearity in MEMS dynamics are studied in the context of overload conditions - nonlinear squeeze-film damping and higher order eigenmodes of the mechanical structure.

As an example to illustrate our methodology and computational results, a teeter totter style Z-axis MEMS capacitive acceleration sensor (Fig. 1) was designed and fabricated. This transducer was designed to operate at a full-scale acceleration range of 250g but was tested at overload condition of more than 4000g acceleration stimulus. The MEMS sensor was fabricated by a two-layer polysilicon surface micromachining process and sealed in a hermetic cavity with a controlled pressure. Under large Z-axis acceleration, the proof mass will have significant rotation about the pivot point. Such a large displacement can cause unexpected nonlinear response which is the focus of this study.

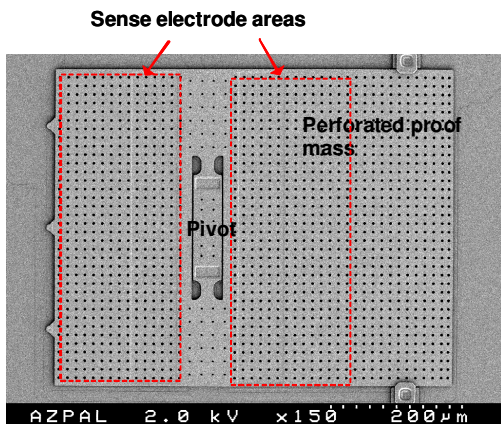


Figure 1: SEM picture of the teeter totter MEMS acceleration transducer for crash sensing application.

## NONLINEAR SQUEEZE-FILM DAMPING Analytical Solutions

Reynolds equation known from lubrication theory is often used to model the squeeze film damping for plate-like microstructure moving towards a fixed wall [2] [3]. Reynolds squeeze film equation assumes a continuous fluid flow regime, but can be conveniently adjusted to expand into the results of transition or molecular regime by introducing the effective dynamic viscosity proposed in [4]. This holds true for MEMS acceleration sensors which are typically encapsulated in a non-vacuum environment in order to have over-damping characteristics. However, due to the large displacement of MEMS structure under the overload conditions (Fig. 2), the microstructure will demonstrate nonlinear damping behavior. When the proof mass moves from the nominal position towards the substrate, damping will increase with the reduction of film gap. When the proof mass is moving away from substrate, damping will decrease.

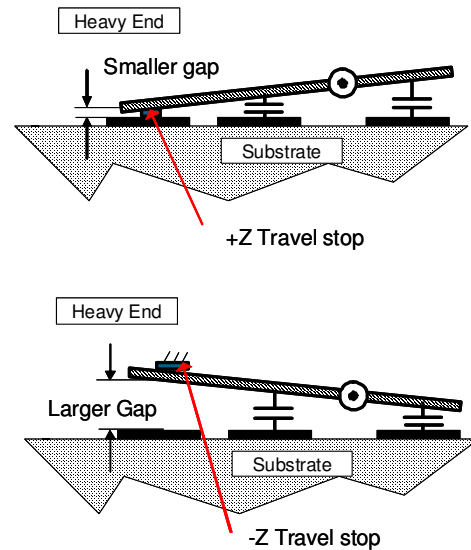


Figure 2: Non-linear squeeze film damping caused by the large displacement of the proof mass.

In the large displacement case, the actual gap change is in the same order of magnitude of the initial film gap. The linearized Reynolds equation is no longer valid for squeeze-film damping. Instead, the nonlinear Reynolds equation (Eq. 1) has to be used:

$$\frac{\partial}{\partial x} \left( \frac{PH^3}{\mu} \frac{\partial P}{\partial x} \right) + \frac{\partial}{\partial y} \left( \frac{PH^3}{\mu} \frac{\partial P}{\partial y} \right) = 12 \frac{\partial(PH)}{\partial t}$$

$$H = h_0 + h(t, x, y),$$

$$P = p_0 + p(t, x, y),$$

$\mu$  - viscosity       $p_0$  - cavity pressure  
 $h_0$  - film gap       $p(t, x, y)$  - pressure change  
 $h(t, x, y)$  - gap change

(1)

In the simplest cases where no damping from the perforated holes is assumed, modal transformation technique was applied to separate the spatial variables ( $x, y$ ) and time variable ( $t$ ). The squeeze film gap variation and the pressure variation can be written as:

$$h(t, x, y) = q(t)f(x, y) \quad (2)$$

$$p(t, x, y) = \sum_{n,m=1}^{\infty} p_{mn}(t) \sin \frac{m\pi x}{L} \sin \frac{n\pi y}{W} \quad (3)$$

where  $f(x,y)$  is the eigenvector of the first mode of the teeter totter transducer and  $q(t)$  is the modal time function. A lower-order equation written in the Fourier coefficients of the pressure distributions ( $P_{mn}$ ) can be obtained by substituting Eq. 2 and 3 into Eq. 1 and applying a harmonic excitation:

$$q(t) = \sin(\omega t) \quad (4)$$

The resulted equation has nonlinear terms and is therefore solved by Runge-Kutta Method. Fig. 3 shows the solution results for a simplified model of the MEMS structure under 20KHz 7500g sinusoidal acceleration. The result is presented in the frequency domain. Compared with the constant damping case, the higher order harmonics caused by the nonlinear squeeze film damping can clearly be seen.

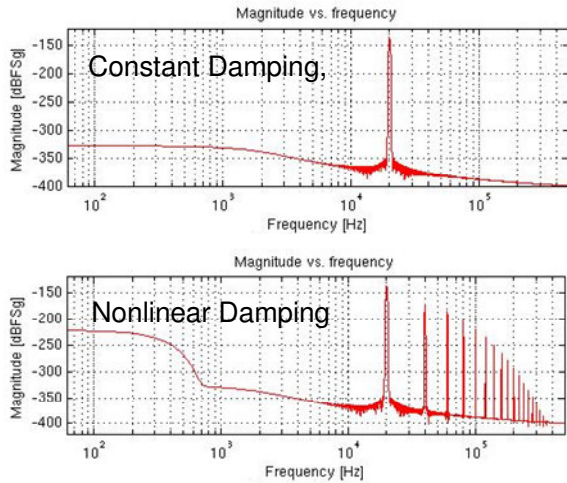


Figure 3: Frequency domain modeling results of MEMS structure subject to 20KHz 7500g sinusoidal acceleration.

### Finite Element Analysis (FEA)

For complicated structures with inhomogeneously distributed perforations, analytical solution has limits. FEA modeling was instead utilized to study the non-linear squeeze film damping behavior. The squeeze film damping was simulated based on the fluid-structure interaction by using a commercial FEA tool. Both structural and thin-film fluid models were built. Additional flow rate elements were introduced to model the flow resistance through the perforations [5]. Modal analysis on the structural domain was performed to determine the resonant frequencies and extract the eigenvectors for each desired mode. Harmonic analysis was performed on the thin-film elements to reveal the pressure distribution for each considered mode. Modal pressures are projected onto the particular vibrations modes to obtain generalized modal squeeze film damping forces.. This procedure was repeated for various film gaps to extract the damping ratio as a function of gap change. Figure 4 shows the FEA model and the

simulated pressure distribution within the proof mass region for the first eigenmode of the teeter totter z-axis transducer.

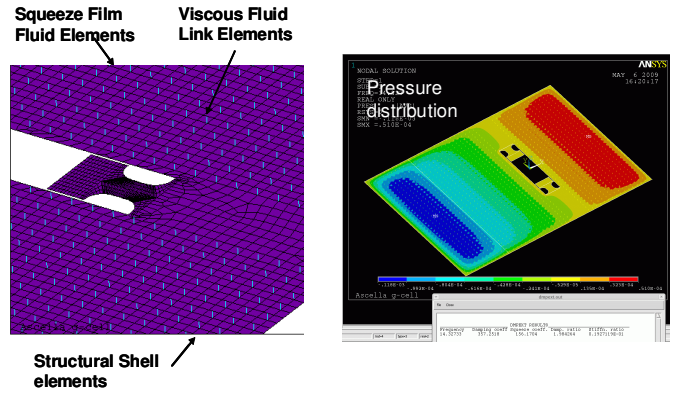


Figure 4: FEA simulation of the nonlinear squeeze film damping of the teeter totter MEMS sensor.

Characterization by using a white light interferometer was also performed to verify the FEA simulation results. The MEMS sensor was mounted inside a chamber where the pressure can be regulated to match the actual micro-cavity pressure from wafer bonding. A high DC voltage bias and a small AC signal were applied between the movable plate and the stationary electrodes. The DC voltage is used to create electrostatic force to move the proof mass around the pivot point, thus to change the film gap between the proof mass and substrate. The AC signal is to actuate the proof mass dynamically so that the resonant frequencies and damping factor can be extracted. An exemplary white-light interferometer image of the deformed microstructure and the test setup are shown in Fig. 5. By varying the DC control voltage, the damping ratio change with respect to gap change can be obtained experimentally.

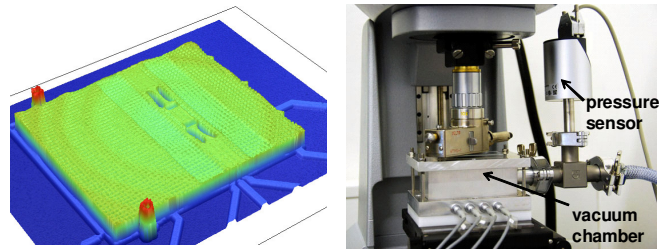


Figure 5: Characterization of the squeeze film damping by white light interferometer.

Both simulation and characterization results of the squeeze-film damping are presented in Fig. 6. The increase of squeeze-film due to gap closing can clearly be seen on both the simulation and experiment. A reasonable good agreement is also found between them. Note the characterization can only be performed in a smaller range of gap change because of the pull-in phenomenon of moving plate. The simulation results in general deviate more from test data at larger film gap. This is due to the additional impact of fluidic transition regions at plate boundaries and hole apertures, which is considered in simulation as an additional correction factor but with limited accuracy.

Fig. 7 further shows the time domain simulation results of the MEMS accelerometer when being subject to 10KHz 7500g

acceleration. Simulation reveals that the transducer output can deviate by more than 20% if the nonlinear squeeze film damping is not properly considered. This shows the significance of including the nonlinear squeeze film effect in overload investigation.

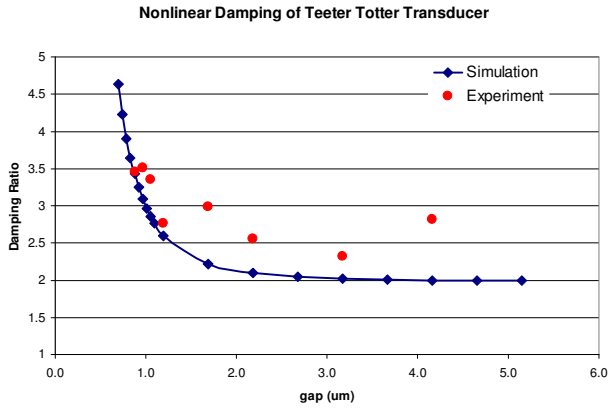


Figure 6: Comparison of the FEA results and characterization results.

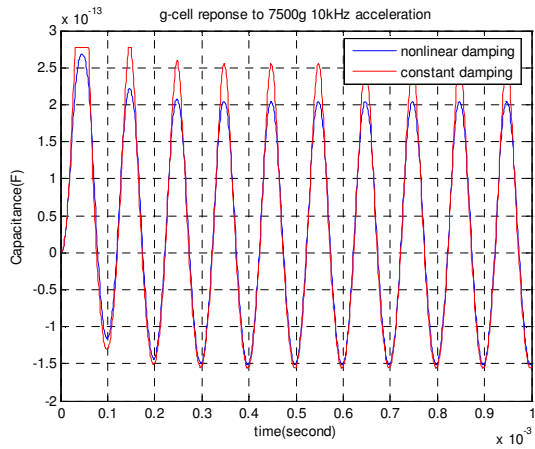


Figure 7: Time domain modeling results of the MEMS structure subject to 10KHz 7500g acceleration.

## HIGHER ORDER EIGENMODES

### Electrical Nonlinearity

Mode projection technique has been discussed in the previous section for solving the modal squeeze film damping. This section deals with the other nonlinear effect contributed by the higher order eigenmodes. As shown in Fig. 8, the teeter totter acceleration transducer has other higher frequency eigenmodes in addition to the desired eigenmode (primary mode) for sensing Z-axis acceleration stimulus. Because of the high frequency contents of crash signal and lower damping at higher order modes, these high order eigenmodes can be excited and cause undesirable DC shift.

In mechanical domain, the high order modes do not necessarily create nonlinearity problem because the amount of the proof mass displacement is still small compared with the overall dimension of the structure and stress-stiffening effect is usually very small. This is important in that modal superposition technique can still be applied. However, the capacitance transfer function is a nonlinear transfer function of the proof mass displacement. Often the sensor is designed to have differential

architecture such that the nonlinear capacitance output from the primary mode is kept at minimum. However, this generally does not work for higher order modes. The electrical nonlinearity from the higher order modes becomes a significant contributor of nonlinear device output under the large acceleration amplitude and high frequency stimulus, i.e. overload conditions. In other words, the high order eigenmodes of the mechanical structure, when coupled with electrostatics, can produce nonlinear capacitance output.

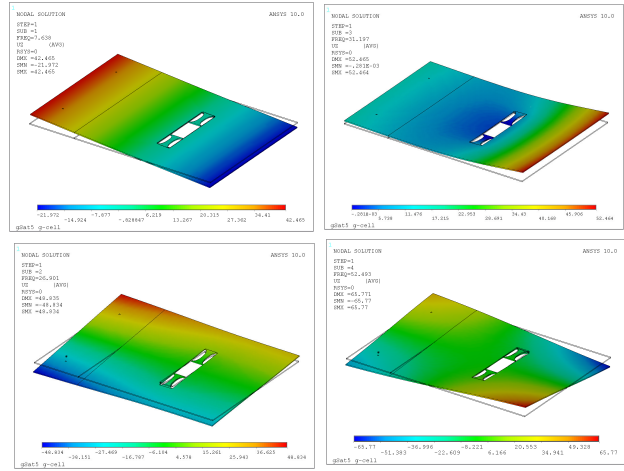


Figure 8: Different eigenmodes of the teeter totter acceleration sensor.

### Reduced Order Modeling

In order to study the contribution of higher order eigenmodes under overload conditions, one must have a high fidelity model which can not only capture the full dynamic behavior of the MEMS device, but also enable fast simulation. Our approach to simulate this behavior was to represent the deformation state of mechanical components by a superposition of finite numbers of eigenmodes. This created a reduced order model (ROM) which enables fast dynamic simulations of linear systems ([6]). Hence, the number of parameters can be reduced from several thousands to a few ten state variables with reasonable accuracy.

ROM has been extended to account for electrostatic-structural interactions in MEMS by introducing multivariable capacitance-stroke-functions ( $C_{rk}$ ) where stroke is represented by modal amplitudes [7]. The capacitance-stroke relationships are automatically derived from finite element data sampling procedures and subsequent functions fit algorithms. The governing equations for modal amplitudes  $q_i$  in the mechanical domain become

$$m_i \ddot{q}_i + 2 \xi_i \omega_i m_i \dot{q}_i + m_i \omega_i^2 q_i = f_i + \sum_r \frac{\partial C_{rk}}{2 \partial q_i} (V_r - V_k)^2 \quad (5)$$

where  $\xi_i$  are modal damping ratios,  $\omega_i$  are eigen-frequencies,  $f_i$  are load contribution factors,  $V_k$  and  $V_r$  electrode voltages.

Figure 9 shows the schematic view of the ROM for the teeter totter MEMS sensor. The natural frequencies and eigenvectors, capacitance functions used in ROM were obtained from FEA while the modal damping factors were obtained from the interferometer measurement. The ROM was implemented in behavioral models and incorporated into microsystem model (next section) so that the nonlinearity of device output caused by the higher order modes can be correctly assessed.



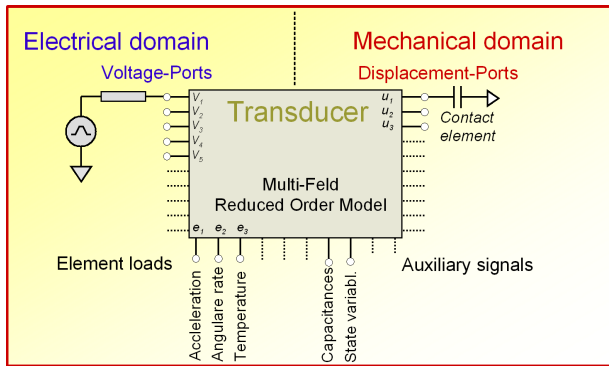


Figure 9: Schematic view of the reduced order sensor model.

## MICROSYSTEM INTEGRATION

Finally, the nonlinear transducer model was incorporated into a microsystem model (Fig. 10). The microsystem model consists of a package model, the MEMS transducer model (with nonlinear damping and higher order modes) and the ASIC signal chain block. System level simulation was performed which took the input from the reference accelerometer and predicted the device output. Experimental verification was also performed using a commercial mechanical shock tester (Fig 11). Fig. 12 shows the good agreement between the modeling and the testing results for the MEMS device subject to 3000g, 2ms shock pulse.

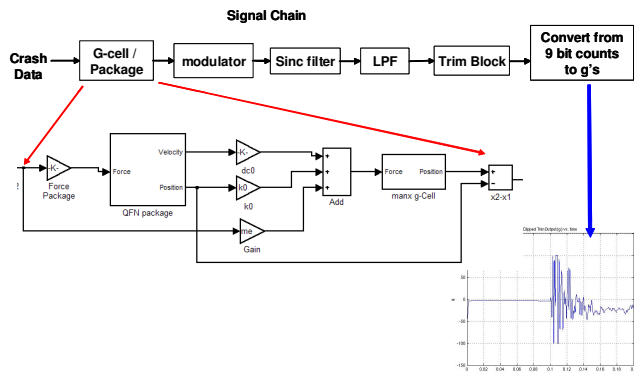


Figure 10: Microsystem model for crash simulation.

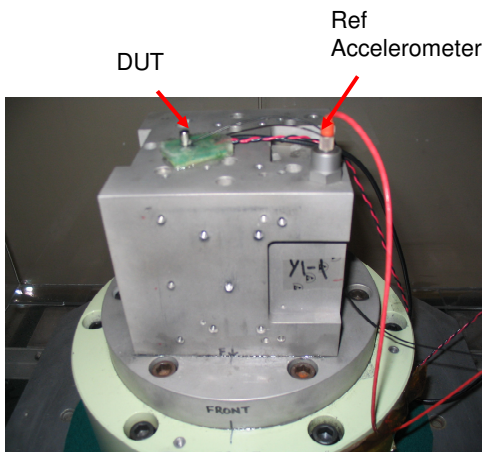


Figure 11: Experimental setup to characterize sensor overload performance.

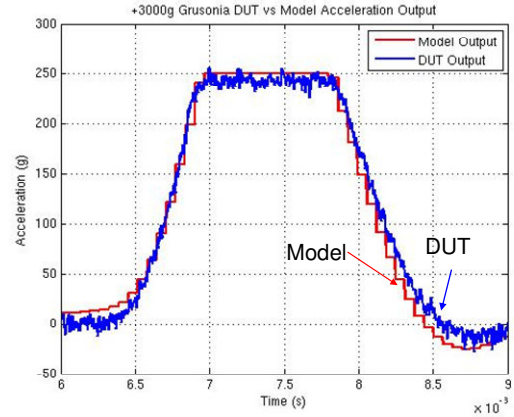


Figure 12: Comparison between overload microsystem simulation results and shock test data.

## CONCLUSIONS

Nonlinear damping and higher order eigenmodes make significant contribution to the overload performance of MEMS inertial sensors. The nonlinear squeeze film damping is caused by the large gap change due to the large displacement of the proof mass under overload conditions. Higher order modes, when coupled with capacitance transfer function can cause nonlinear device output. It is shown that the microsystem model can accurately simulate the crash overload event when properly taking into accounts of these two sources of nonlinearity in MEMS dynamics.

## ACKNOWLEDGEMENTS

The authors would like to thank Jan Menher, Torsten Hauck, Ilko Schmadlak, Patricia Ong and Lisa Zhang for insightful discussion and providing some of the experimental and simulation data.

## REFERENCES

- [1] M. Furmann and T. Miller, "Overload Performance of Inertial Sensors", Freescale Technical Enrichment Matrix Workshop, 06/26, Tempe, AZ (2007)
- [2] J. J. Blech, "On Isothermal Squeeze Films", Journal of Lubrication technology, Vol. 105, pp 615-620 (1983).
- [3] W. S. Griffin, et al., "A Study of Squeeze-film Damping", J. of Basic Engineering, pp. 451-456 (1966)
- [4] T. Veijola, "Equivalent Circuit Models for Micromechanical Inertial Sensors", Circuit Theory Laboratory Report Series CT-39, Helsinki Univ of Tech (1999)
- [5] G. Schrag and G. Wachutka, "Accurate System-Level Damping Model for Highly Perforated Micromechanical devices", Sensors and Actuators A, 111, pp. 222-228 (2004)
- [6] J. Mehner, L. Gabbay, S. Senturia, "Computer-Aided Generation of Nonlinear Reduced-Order Dynamic Macromodels", J. Microelectromech. Syst., vol. 9, pp. 269-278 (2000).
- [7] J. Mehner, et al., "The Influence of Packaging Technologies on the Performance of Inertial MEMS Sensors", the 15th International Conference on Solid-State Sensors, Actuators, and Microsystems, 06/21-25, pp. 1885-1888, Denver, CO (2009).

# AN SPM-BASED CONTACT TESTER FOR STUDY OF MICROCONTACTS

L. Chen<sup>1</sup>, Z.J. Guo<sup>2</sup>, N. Joshi<sup>1</sup>, H. Eid<sup>1</sup>, G.G. Adams<sup>1</sup> and N.E. McGruer<sup>1\*</sup>

<sup>1</sup>Northeastern University, Boston, Massachusetts, USA

<sup>2</sup>University of Pennsylvania, Philadelphia, Pennsylvania, USA

## ABSTRACT

In this paper, we report on an SPM (Scanning Probe Microscope)-based contact tester. The tester is designed for contact material selection and micro-contact studies, with a special focus on metal-contact MEMS switch applications. It uses a silicon force sensor with an integrated contact bump and a mating silicon pillar to simulate switch operation. After coating the sensor and the pillar with contact materials, a wide range of contact metals and metal pairs can be evaluated. The tester provides accurate force measurement with a resolution of 1 $\mu$ N. Both force and resistance can be measured simultaneously during the contact tests. A custom-built test chamber is used to introduce both the plasma and the UV-ozone to the contact area for contact cleaning and surface modification. After having tested Au, Ru, Ir contact pairs, it is found that the Au-Ru dissimilar contact pair with O<sub>2</sub> plasma cleaning can provide low contact adhesion and low resistance.

## INTRODUCTION

Contact material selection is critical for the performance and reliability of metal-contact RF MEMS switches. The selection of contact materials requires the study of contact force, resistance, adhesion, power handling, reliability, as well as thin film preparation, contact surface treatment, and operational ambient. It can be extremely time-consuming to evaluate a wide range of materials if such tests are performed in MEMS switches.

To improve the efficiency in material selections, and also to directly measure contact adhesion, contact force, and contact resistance, our group previously used an SPM-based contact tester for contact studies. The setup used a custom built cantilever with an integrated contact bump and a planar mating surface to simulate contact operation in microswitches. The cantilever served as a force sensor, i.e. the contact force between the bump and the surface is equal to the cantilever deflection multiplied by the cantilever stiffness. After coating various contact materials on both the cantilever and the mating surface for contact studies, the contact tests were performed in an SPM system. The tester was successfully used to study several contact metals and metal alloys [1], contact failure mechanisms [2] and the rate-dependent pull-off force of micro-contacts [3].

Despite its versatility, our previous setup has some limitations. By using a cantilever structure as a force sensor, we encounter sliding effects during the contact tests. The higher the loading force, the larger deflection at the end of the cantilever and, therefore, the larger the sliding. Also, the measured resistance in our previous setup always included the sheet resistance components of the metal films on the cantilever and testing pads. For instance, using the previous setup, the measured resistance for a Au-Au contact at 250 $\mu$ N was 0.85 $\Omega$ , which is about one order of magnitude higher than the constriction resistance of pure Au-Au contacts. The third limitation is that our previous setup lacked surface cleaning capabilities. Most samples had been exposed to room-air before contact tests were started, allowing surface films or contamination to form on the contacts. Contamination failures were commonly observed during our previous contact tests. On

the other hand, clean contact tests are reported within hermetic-packaged MEMS switches [4]. In order to mimic metal contact operation within a packaged switch, it is highly desirable to create a clean environment for contact tests.

In this paper, we report on a new SPM-based contact tester. The new system has been improved in three ways: 1) more accurate force measurement; 2) better resistance measurement; and 3) the capability for both plasma and UV-ozone treatments. The improvements in the new tester help us to obtain high quality resistance and force data.

## CONTACT TESTER SYSTEM

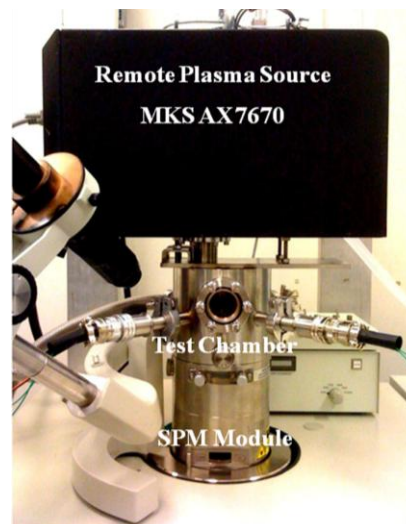


Figure 1: A photograph of the SPM-based contact tester with the vacuum chamber and plasma source.

Figure 1 shows the chamber setup of our SPM-based contact tester. There are three parts in this system: 1) the SPM module which is used for both test control and force measurement; 2) The test chamber which is a custom-built vacuum chamber providing a controlled environment for the contact test and allowing us to introduce plasma and/or UV-ozone cleaning to the contact area; and 3) The MKS-AX7670 remote plasma source used to clean the contacts with plasmas containing Ar, O<sub>2</sub>, N<sub>2</sub> and NF<sub>3</sub>.

We changed the force sensor structure from a cantilever to a fixed-fixed beam. For the fixed-fixed beam structure, the contact bump is located in the middle of the beam (Figure 2 a). The deflection of the bump, and hence the force, is determined by shining the laser beam on one of the two optical paddles located on either side of the contact tip (Figure 2 b). By using a fixed-fixed beam structure, the sliding effect during contact tests can be significantly reduced. Also, compared with a cantilever structure with the same length, the fixed-fixed beam can provide more rotation at the optical lever paddle for a given deflection at the bump, which helps to improve the force measurement dynamic range.

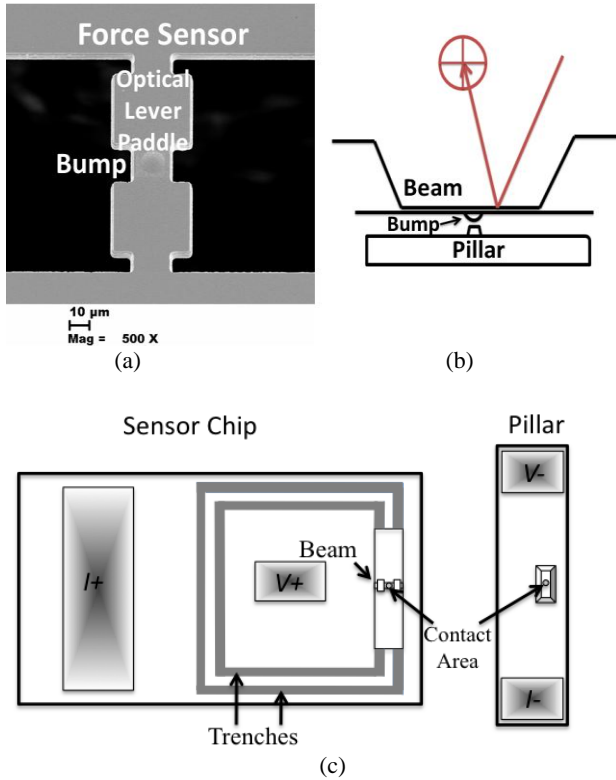


Figure 2: (a) An SEM image of a force sensor with the fixed-fixed beam structure. The optical lever paddles are necessary to deflect the laser beam in the SPM; (b) the deflection of the laser beam is monitored by an optical level system; (c) Test layout for contact resistance measurement.

In addition, we included two trenches on the force sensor for better contact resistance measurements. The trenches are located between a current sourcing pad (I+) and a voltage sensing pad (V+), as shown in Figure 2(c). These trenches are micro-fabricated with intentional undercuts. Because of the undercuts, electrical isolation is created between the current sourcing pad and the voltage sensing pad, even after a blanket coating of a contact metal, allowing us to perform 4-wire contact resistance measurements.

Table 1: Comparison between old and new force sensors.

Force Sensor	New	Old
Structure	Fixed-Fixed	Cantilever
Dimension ( $\mu\text{m}$ )	120x20x4.5	180x50x30
Stiffness (N/m)	2500	15000
Force Resolution ( $\mu\text{N}$ )	1	12.5
Contact Sliding	Minimum	Yes
Measured Resistance ( $\Omega$ ) (Au-Au at $250\mu\text{N}$ )	0.15	0.85

Table 1 shows a comparison of old and new force sensors. The new sensor provides better resistance and force measurements along with minimal sliding.

## CONTACT TESTS/EXPERIMENTS

Here we demonstrate the capabilities of the contact tester in contact surface cleaning; contact resistance vs. force

characterization; and contact cycling testing.

All contact materials reported in this paper, Gold (Au), Ruthenium (Ru) and Iridium (Ir), are thin films prepared by sputtering. The thin films have been deposited on both the force sensors and pillars with a nominal thickness of 300nm. To reduce the sheet resistance components from the pillar side, a layer of 500nm of plated gold was electroplated on the pillars prior to deposition of contact materials. Au contact materials were prepared with 20nm Cr as an adhesion layer; no adhesion layers were added for Ir or Ru thin films. The resistivity for sputtered Au, Ru and Ir thin films are  $3.46\mu\Omega\cdot\text{cm}$ ,  $13.8\mu\Omega\cdot\text{cm}$  and  $18.9\mu\Omega\cdot\text{cm}$ , respectively. All materials were tested within 72 hours of deposition.

### Contact Cleaning Experiments:

With capabilities for plasma and UV-Ozone treatments, the tester provides a platform for contact cleaning and surface modification studies. In this paper we show the results of three treatments –  $\text{O}_2$  plasma, Ar plasma and UV/Ozone – on contact resistance of Ru-Ru contacts.

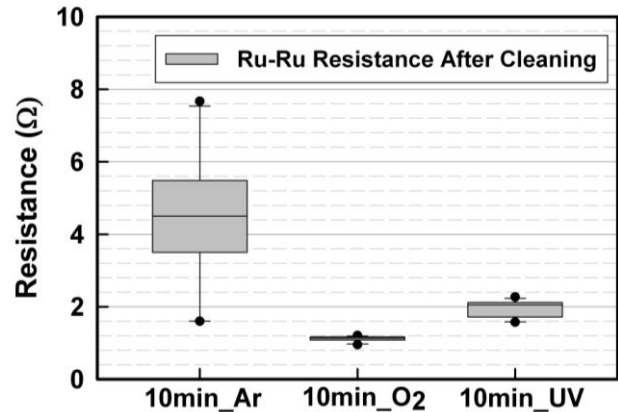


Figure 3: Measured contact resistance of Ru-Ru contacts, at a loading force of  $100\mu\text{N}$ , after three different cleaning procedures: 10-minute Ar plasma, 10-minute  $\text{O}_2$  plasma, and 10-minute UV-Ozone.

The MKS AX7670 is used to generate Ar and  $\text{O}_2$  plasmas. The Ar plasma is generated at 1.7Torr. The  $\text{O}_2$  plasma is generated at 4Torr with a mixture of Ar and  $\text{O}_2$  at a ratio of Ar: $\text{O}_2$ =3:5. In order to introduce UV-Ozone to the contact area, we use a deuterium lamp HAMAMTSU L7292. The cut-off wavelength of the HAMAMTSU L7292 is 115nm. The lamp is mounted on the vacuum chamber through a vacuum side flange, and radiates UV light to the contact area. While doing UV-ozone cleaning, the chamber is filled with  $\text{O}_2$  at a pressure of 50Torr when the lamp is on. The UV light can directly break the contaminant molecule bonds. At the same time, the UV light can be absorbed by  $\text{O}_2$  which creates atomic oxygen and ozone [5]. Oxygen radicals and ozone can accelerate the removal of organic layers on the metal surfaces.

Figure 3 shows the contact resistances of Ru-Ru contacts (seven samples for each condition), after a 10-minute  $\text{O}_2$  plasma treatment, a 10-minute Ar plasma treatment and a 10-minute UV-ozone treatment. At a loading of  $100\mu\text{N}$ , the lowest resistance was observed after 10 minutes of  $\text{O}_2$  plasma treatment, and the UV-Ozone treatment was also effective, in contrast to the Ar plasma treatment, which was not. The results indicate that O radicals are essential for Ru contacts cleaning.

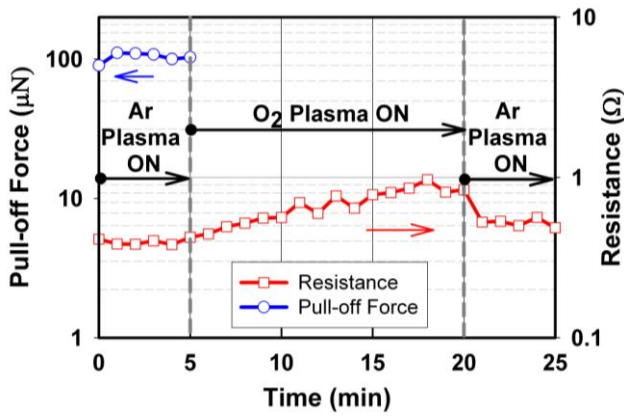


Figure 4: Contact resistance and pull off force of a Au-Au contact during an in-situ plasma treatment test. The contact was cycled at 1Hz, with a loading force of 100  $\mu\text{N}$ . The Ar plasma was on for five minutes (0-5min), and then the  $\text{O}_2$  plasma fifteen minutes (5-20min), followed by another five minutes Ar plasma (20-25min).

However, the  $\text{O}_2$  plasma treatment can increase the resistance of Au-Au contacts. Figure 4 shows an *in-situ* plasma test result of a Au-Au contact. The contact was cycled within the chamber, at 1Hz, with a loading force of 100 $\mu\text{N}$ . The plasma was turned on during the cycling test and the resistance and force were measured simultaneously. It shows that the Ar plasma had little effect on the pull-off force or the contact resistance. However, the  $\text{O}_2$  plasma rapidly caused the pull-off force to decrease below the detectable level, and the contact resistance increased gradually during the period when the  $\text{O}_2$  plasma was on. When after 15 minutes, the  $\text{O}_2$  plasma was turned off and the Ar plasma was turned on, the resistance started to drop, while the pull-off force did not recover within 5 minutes. The drop of adhesion for the Au-Au contact, as well as the increase of the resistance during the  $\text{O}_2$  plasma treatment, could be due to the formation of layers of  $\text{Au}_2\text{O}_3$  layer on the contact surfaces [6].

#### Resistance vs. Force Curves:

With good measurements of both resistance and force, we can compare resistance vs. contact force data for different contact materials with a special focus on the low force region (< 500 $\mu\text{N}$ ). This is the force region of greatest interest for most MEMS switch applications.

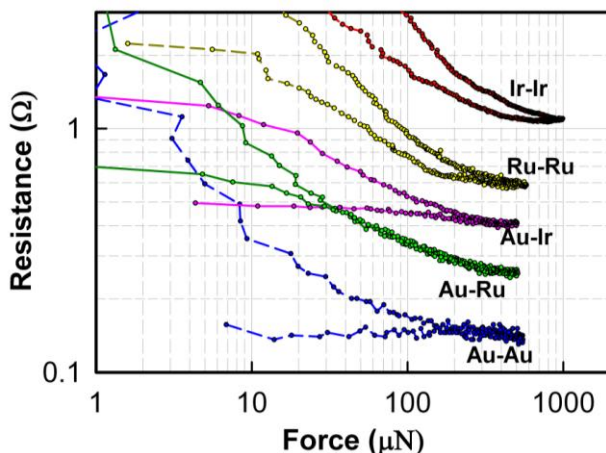


Figure 5: Resistance vs. contact force for five different metal contact pairs.

Before the tests, both the Ru and Ir surfaces were cleaned using an  $\text{O}_2$  plasma for 10 minutes. To collect the resistance vs. force data, the contacts were cycled at 1Hz in a low-voltage, low-current hot-switching mode. The resistance was measured using a 0.2V voltage source in series with a 22 $\Omega$  current-limiting resistor and with the contact. All contacts were cycled to a maximum load of 500 $\mu\text{N}$  for at least 50 cycles before the data was collected.

As shown in Figure 5, the Au-Au contact yielded the lowest contact resistance. It is due to the low resistivity and low hardness (creating a larger contact area) of Au thin films. Hard metal contact pairs, such as Ru-Ru and Ir-Ir, have higher resistance compared to Au-Au. Dissimilar metal contact pairs, i.e. Au-Ru and Au-Ir, have intermediate contact resistance.

#### Contact Cycling Tests:

Contact cycling tests are important for contact material evaluation. They show evolution features of contact resistance and contact adhesion for each material pair, which can help to reveal potential reliability issues of these metal combinations during real switch applications. This tester can perform cycling tests at a rate of 800Hz, and measure contact resistance and force at 1Hz after a certain number of cycles.

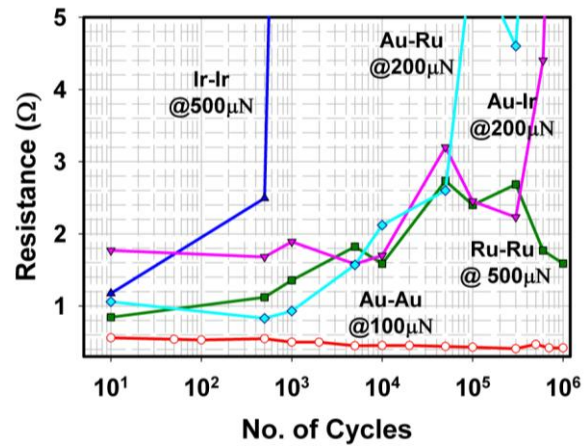


Figure 6: Resistance vs. number of cycles for different metal contact pairs; the maximum loading force for each cycling test is labeled in the graph.

Figure 6 shows resistance vs. number of cycles of different metal contact pairs. Current was only applied during the contact cycles resistance data was obtained. The resistances plotted here are the average values of three samples tested under the same conditions. Without strict ambient control, the resistance usually increased after cycling test, expect for the Au-Au contacts. Upon inspection, contaminates were observed, in particular in the presence of Ru and Ir surfaces. Susceptibility to the contaminates is related to the surface reactivity of the metals. The Au surfaces are known to be relatively inert to contamination, but Ru and Ir are not. Compared to the Ru-Ru contacts, the Ir-Ir contacts show a much higher contamination rate. The resistance of the Ir-Ir contacts doubled within 500 cycles of testing, which makes Ir less promising for use as a contact material.

To create a clean test ambient, we added a nitrogen tube with flowing nitrogen from a liquid source introduced immediately adjacent to the contact area. It was found that such an arrangement is an efficient way to reduce the contamination.

Figure 7 shows the results of cycling tests of three Au-Au contacts and three Au-Ru contacts in a clean nitrogen ambient. The loading forces for all tests were controlled to be 100 $\mu\text{N}$ .

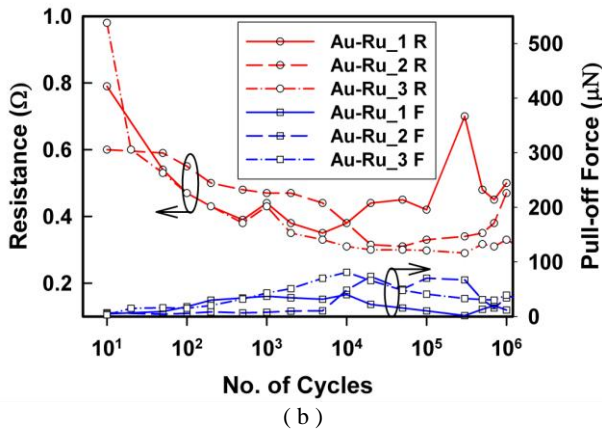
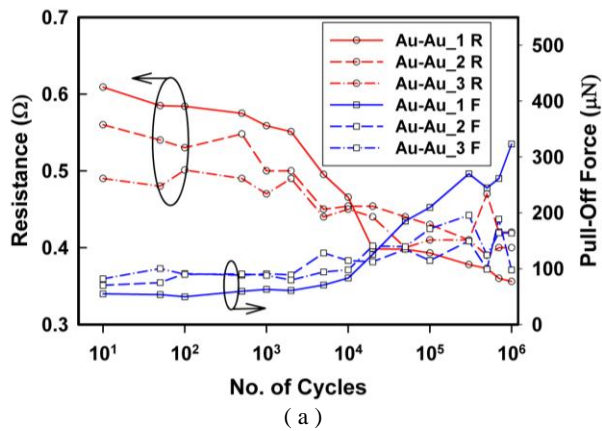


Figure 7: Resistance and pull-off force vs. number of cycles for pure sputtered Au-Au (a) and Au-Ru (b), with a maximum loading of 100 $\mu$ N and zero current.

For Au-Au contacts, a clear drop of contact resistance and a simultaneous increase of contact adhesion (pull-off force) are observed during the cycling tests. The maximum adhesion force is seen to be three times the contact force, clearly demonstrating the very large amount of contact separation force necessary for reliable operation of a MEMS switch using unhardened gold for contacts.

For Au-Ru contacts, the drop of resistance and the increase of adhesion are also observed. However, the pull-off forces for Au-Ru contacts are below 100 $\mu$ N, much lower than those for Au-Au contacts. Also noted is that, after 10<sup>6</sup> cycles of testing the Au-Ru contacts, the Au bumps were plastically deformed and there was no severe contact wear (Figure 8). These preliminary results suggest that a Au-Ru contact may be a good candidate for switch applications, especially when the available loading force is low (<150 $\mu$ N).

## CONCLUSIONS

A new SPM-based tester with accurate force and resistance measurements and plasma treatment capabilities has been built for contact studies. In this paper, we demonstrate its capabilities in contact surface cleaning; contact resistance vs. force characterization; and contact cycling testing. It is found that: O<sub>2</sub> plasma and UV-Ozone treatments are effective methods for cleaning Ru contact surfaces; The O<sub>2</sub> plasma treatment can modify gold surfaces by significantly reducing the contact adhesion between Au-Au contacts, and slightly increasing the contact resistance. Without strict ambient control, most cycling tests experienced contamination issues, especially with the presence of

Ru and Ir surfaces. The Ir-Ir contacts show higher contamination rates than Ru-Ru contacts during the cycling tests. By introducing flowing nitrogen close to the contact area, the contamination problem has been greatly reduced. In a clean ambient, Au-Ru contacts show the decrease of resistance and increase of adhesion after the cycling tests. With less contact adhesion and minimum contact wear, Au-Ru contacts show better potentials than Au-Au contacts for use as contact materials, especially in low force applications.

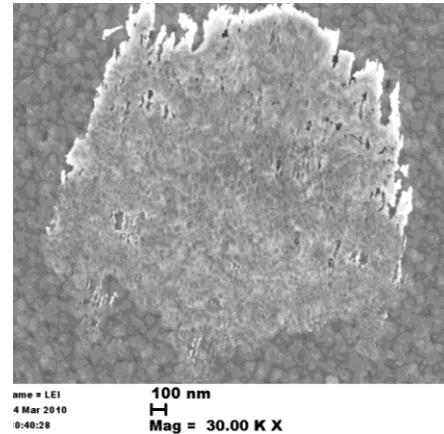


Figure 8: An SEM micrograph of a Au contact bump after 10<sup>6</sup> cycles Au-Ru contact test, with a maximum loading of 100 $\mu$ N.

## ACKNOWLEDGEMENT

This work is supported by the DARPA Center for RF MEMS Reliability and Design Fundamentals, Dr. Dennis Polla, Program Manager.

## REFERENCES

- [1] L. Chen, H. Lee, Z.J.Guo, K. Gilbert, S. Mall, K. Leedy, G. Adams, and N.E. McGruer, "Contact Resistance Study of Noble Metals and Alloys Films Using a Scanning Probe Microscope Test Station", *Journal of Applied Physics*, 102, 074910, (2007).
- [2] N.E. McGruer, G.G. Adams, L.Chen, Z.J.Guo, and Y.Du, "Mechanical, Thermal, and Material Influences on Ohmic-Contact-Type MEMS Switch Operation", *Proceedings of IEEE Microelectromechanical Systems*, Turkey, (2006), pp. 230-233.
- [3] L. Chen, N.E. McGruer, G.G. Adams, and Y. Du, "Separation Modes in Microcontacts Identified by The Rate Dependence of the Pull-Off Force", *Applied Physics Letters*, 93, 0535003 (2008).
- [4] H.S. Newman, J.L. Ebel, D. Judy, and J. Maciel, "Lifetime Measurements on a High-Reliability RF-MEMS Contact Switch", *IEEE Microwave and Wireless Components Letters*, 18, 100 (2008)
- [5] W. Kern, *Handbook of Semiconductor Wafer Cleaning Technology, Chapter 6*, Noyes Publications, New Jersey, 1993.
- [6] T. Sakata, Y. Okabe, K. Kuwabara, N. Sato, K. Ono, N.Shimovama, K. Machida, and H. Ishii, "Surface Cleaning of Gold Structure by Annealing during Fabrication of Microelectromechanical System Devices", *Japanese Journal of Applied Physics*, 48, 026501 (2009)

## CONTACT

\*N.E. McGruer, tel: +1-617-373-2066; [mcgruer@ece.neu.edu](mailto:mcgruer@ece.neu.edu)

# ATOMIC LAYER DEPOSITED ALUMINA FOR USE AS AN ETCH BARRIER AGAINST XENON DIFLUORIDE ETCHING

Gabriel L. Smith<sup>1\*</sup>, Ronald G. Polcawich<sup>1\*\*</sup>, Jeffrey S. Pulskamp<sup>1</sup>,  
Todd Waggoner<sup>2</sup>, and John F. Conley, Jr.<sup>2</sup>

<sup>1</sup> US Army Research Laboratory, Adelphi, MD, USA

<sup>2</sup> Oregon State University, Electrical Engineering and Computer Science, Corvallis, OR, USA

## ABSTRACT

Xenon difluoride ( $\text{XeF}_2$ ) isotropic etching is widely used to release silicon MEMS parts. To realize more complex devices using silicon-on-insulator (SOI) wafers requires the use of a conformal coating of patterned photoresist to selectively protect the device layer Si during the isotropic etch release of the handle wafer. As an alternative to the photoresist protective layer, an ion-mill patterned atomic layer deposited (ALD) alumina ( $\text{Al}_2\text{O}_3$ ) layer was investigated to dramatically improve device yields, particularly in avoiding edge defects and corner pinholes resulting in unintended etching of the silicon. Promising results have been obtained using 25 nm – 200 nm layers of alumina on deeply etched silicon features. This will enable the fabrication of new MEMS silicon devices with reduced feature size for improved performance.

## INTRODUCTION

Isotropic silicon etching with sulfur hexafluoride ( $\text{SF}_6$ ) and xenon difluoride ( $\text{XeF}_2$ ) has been used for more than a decade to release MEMS parts [1, 2, 3]. The process requires the use of a conformal coating to selectively protect critical silicon features from etch gases. One limitation with using  $\text{XeF}_2$  has been the difficulty in fabricating parts on relatively thick SOI wafers, especially as the Si device layer thickness increases into the 10's of microns. Previous work on using a photoresist encapsulation layer to protect the device layer has proven successful for both piezoelectric MEMS (PiezoMEMS) resonators [4] and PiezoMEMS lateral actuators [5] (see Figure 1). However, the process has been limited to device layers less than 20  $\mu\text{m}$  thick for a resist thickness of 10  $\mu\text{m}$ . Even at these thicknesses, slight imperfections in resist coating lead to unintended etching of the Si device layer and compromised device yield (see Figures 2 & 3).

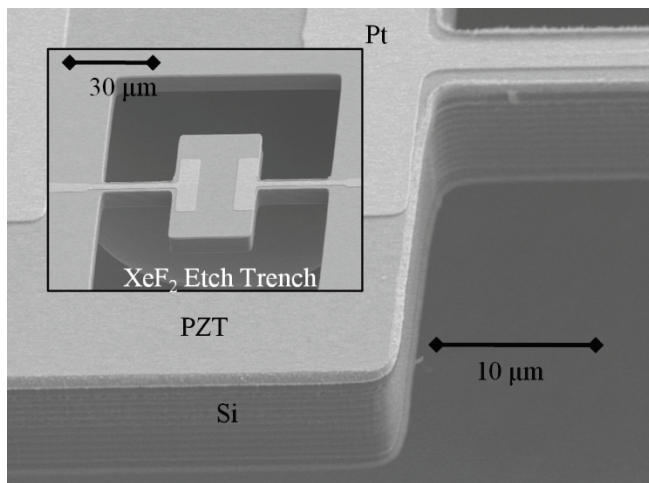


Figure 1: SEM micrographs of piezoelectric MEMS on SOI resonators, a) full device and b) resonator sidewall utilizing a successful photoresist encasement layer to protect the device silicon layer during a  $\text{XeF}_2$  etch release of the handle wafer silicon.

In order to provide improvements to the existing PiezoMEMS on SOI device release process, an alternative approach has been investigated using atomic layer deposition (ALD) films to provide etch protection. ALD films are appealing because they provide highly conformal protective coatings [6], are thin enough so as to

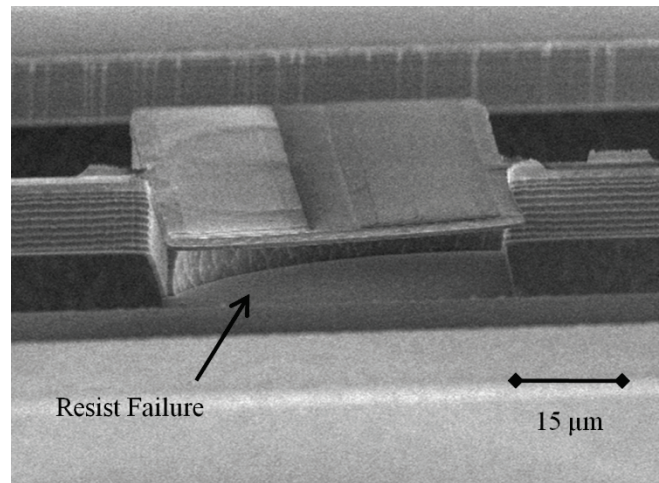


Figure 2: SEM highlighting unintended  $\text{XeF}_2$  etching of the Si device layer due to a resist encapsulation layer failure in a piezoelectric MEMS resonator.

not drastically alter mechanical properties such as stiffness (actuators) or loss (resonators), and could improve device performance by relaxing fabrication design rules. Additionally, photolithographically patterned ion milling of the ALD materials was investigated to demonstrate compatibility of the ALD coatings with photolithography and etch processes.

## RESULTS

Four sets of experiments were conducted. The first experiment assessed the  $\text{XeF}_2$  etch selectivity of silicon to both ALD  $\text{Al}_2\text{O}_3$  and ALD  $\text{TiO}_2$ . The second experiment determined the required ALD thickness for adequate protection using the superior of the two materials. The third experiment was done to determine if the results of ALD films deposited at Oregon State (Picosun Sunale tool) could be repeated on a Cambridge Nanotech ALD tool located at US Army Research Laboratory (ARL). The final experiment was to demonstrate released silicon features in a SOI process utilizing photolithographically defined conformal ALD films as device passivation followed by  $\text{XeF}_2$  etching of the unpassivated handle wafer silicon.

The following experiments were performed to identify suitable ALD materials and thicknesses that would adequately protect areas of exposed silicon. First, a 15  $\mu\text{m}$  deep reactive ion

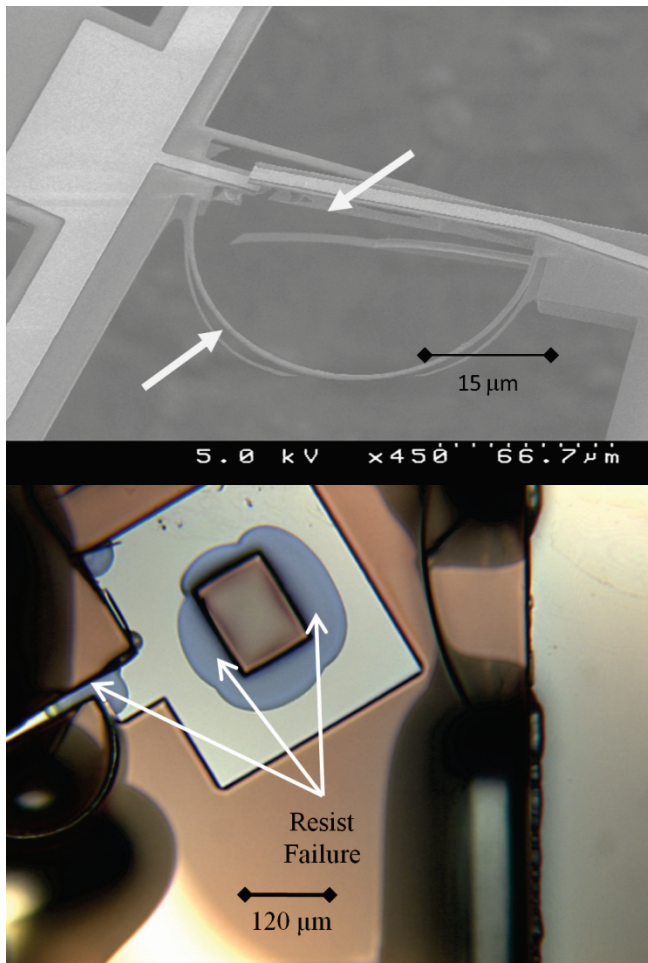


Figure 3: a) SEM and b) Optical micrograph highlighting resist encapsulation layer failures resulting in unintended  $\text{XeF}_2$  etching of the Si device layer in a PZT lateral actuator. Arrows are used to highlight cracks in the photoresist, failed flexures, and etched corners.

etched (DRIE) pattern was formed into a silicon substrate. Subsequently, the wafer was cut into sections with each section receiving a different ALD coating. ALD coatings of  $\text{Al}_2\text{O}_3$  and  $\text{TiO}_2$  were deposited in a continuous flow Picosun Sunale R-150 reactor.  $\text{Al}_2\text{O}_3$  films were deposited at  $300^\circ\text{C}$  using alternating pulses of trimethyl aluminum (TMA) and deionized water separated by  $\text{N}_2$  purges. The  $\text{Al}_2\text{O}_3$  deposition rate was 0.089 nm/cycle or  $\sim 1.3$  nm / min.  $\text{TiO}_2$  films were deposited at  $250^\circ\text{C}$  using alternating pulses of titanium tetraisopropoxide (TTIP) and deionized water separated by  $\text{N}_2$  purges. The  $\text{TiO}_2$  deposition rate was 0.03 nm / cycle or 0.14 nm / min. Following the deposition (see Figure 4 for SEM cross-section), the wafer sections were exposed to 50 etch cycles in a Xactix Xetch system using an etch configuration of 20 s per cycle, 2 T  $\text{XeF}_2$ , and 20 T  $\text{N}_2$ .

The initial experiments focused on thicker coatings of 200 nm for each material. As shown in Figure 5 and 6, only the alumina coating successfully protected the underlying Si from the  $\text{XeF}_2$  etch. The  $\text{TiO}_2$  layer etched and became porous enough to allow the free fluorine radicals to attack the underlying Si. In order to determine the minimum required thickness, alumina coatings of 10, 25, 50 and 100 nm were coated and subjected to the same 50 cycles of  $\text{XeF}_2$ . Plan view optical micrographs taken after the etch highlight small areas of etched Si in both the 10 nm and 25 nm

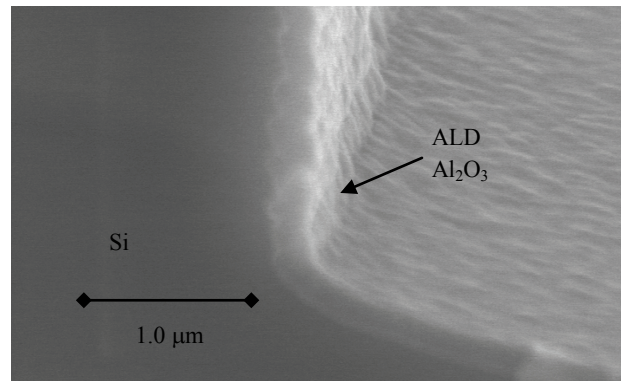


Figure 4: SEM micrograph highlighting the conformal coating of a 200nm ALD  $\text{Al}_2\text{O}_3$  near the base of a cleaved cross-section of a 15  $\mu\text{m}$  DRIE trench.

samples (see Figure 7-8). These etch areas appear to be indicative of small defects in the coating either related to inadequate coverage or pinholes from contaminants. In contrast, both the 50 nm and 100 nm samples exhibited no evidence of silicon etching (see Figure 9-10). The results from this initial experiment indicate the minimum thickness for adequate protection of device Si features using ALD alumina may be in the range of 25 – 50 nm using the non-optimized coating process mentioned early.

Subsequent testing was performed to verify the results of the tests on the Oregon State Picosun Sunale ALD films using a Cambridge Nanotech Fiji F200 ALD reactor installed at ARL. Another process difference is the reaction temperature was reduced from  $300^\circ\text{C}$  to  $200^\circ\text{C}$  improving the thermal process compatibility with ARL's PiezoMEMS fabrication process. The Fiji alternates 60 ms TMA and deionized water separated with 16 second purge cycles. Deposition times were on the order of 0.1 nm/cycle or 0.2 nm/min. ALD films with thicknesses of 10, 25 and 50 nm were deposited. Similar excellent results were obtained with these films as with those deposited by the Oregon State reactor. Additional  $\text{XeF}_2$  etch cycles were performed (up to 500 cycles) to further examine of the survivability of the  $\text{Al}_2\text{O}_3$  films. After 500 etch cycles, the films continued to show no signs of decreased etch protection.

The final test for this study involved a mask set that created patterned features in the conformal ALD film using a process flow compatible with the back end of the PiezoMEMS resonator fabrication process (see Table 1). The wafers were first deposited with a  $\text{SiO}_2$  coating followed by a Ti/Au coating for bond pads. Next, the 10 micron device silicon, buried oxide, and a small portion of the handle wafer were etched by a series of DRIE, RIE, and DRIE etches.

Next, a 50 nm ALD alumina coating was deposited on the wafer. The ALD features were patterned with AZ 9245 photo resist and argon ion-milled to expose regions of the silicon handle wafer to the  $\text{XeF}_2$  gas. After ion milling the devices were stripped and subsequently etched in  $\text{XeF}_2$ . Figures 11 and 12 show the results of a partially undercut device. The silicon disk is protected from the  $\text{XeF}_2$  gas by the ALD film on the top and sides and the buried  $\text{SiO}_2$  layer on the bottom. Examination of a majority of devices from this wafer has failed to identify any significant failures in the ALD protective coating on the sidewalls of the device layer silicon. This process should reliably eliminate the undesired etch problems illustrated in Figures 2 and 3 where broken structures and random etch holes in the device silicon caused failure.

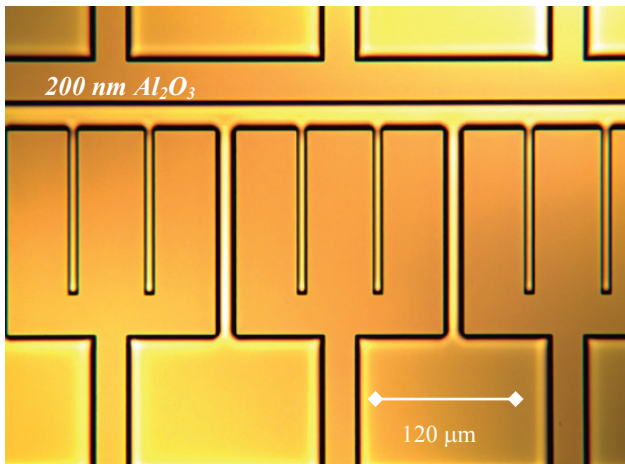


Figure 5: Optical micrograph showing excellent protection of silicon from  $XeF_2$  with a 200nm ALD  $Al_2O_3$  layer.

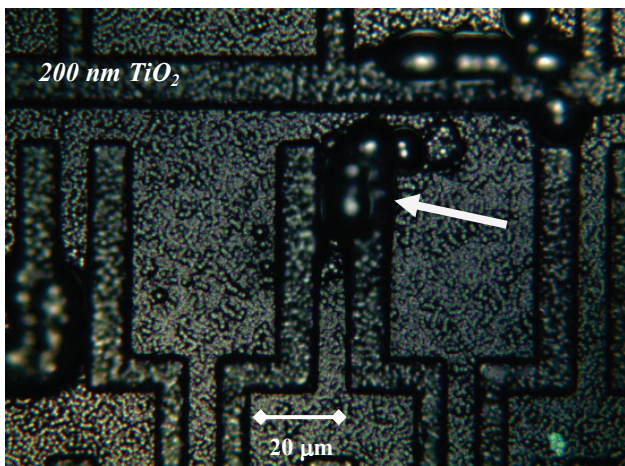


Figure 6: Optical micrograph showing failed  $XeF_2$  protection of silicon structures with 200nm of  $TiO_2$ .

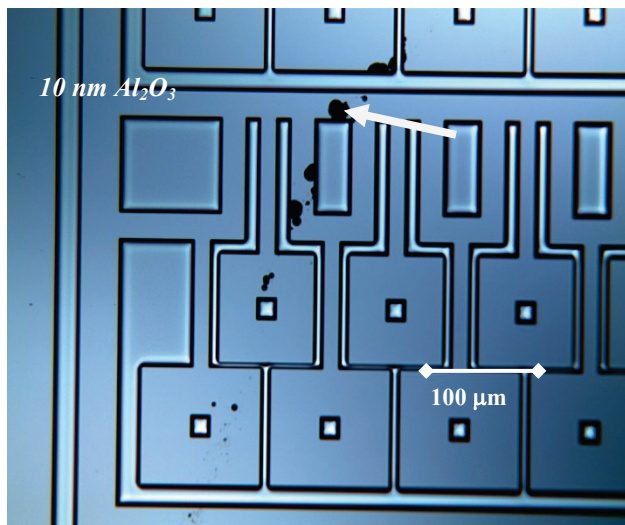


Figure 7: Optical micrograph of 10 nm of ALD  $Al_2O_3$  on Si features after 50  $XeF_2$  etch cycles showing unintended etching. The pattern indicates a contaminate on the wafer caused the failure.

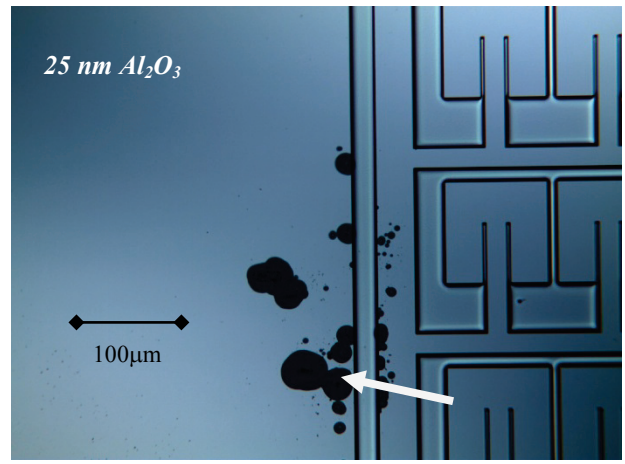


Figure 8: Optical micrograph of 25 nm of ALD  $Al_2O_3$  on Si after 50  $XeF_2$  etch cycles showing unintended etching.

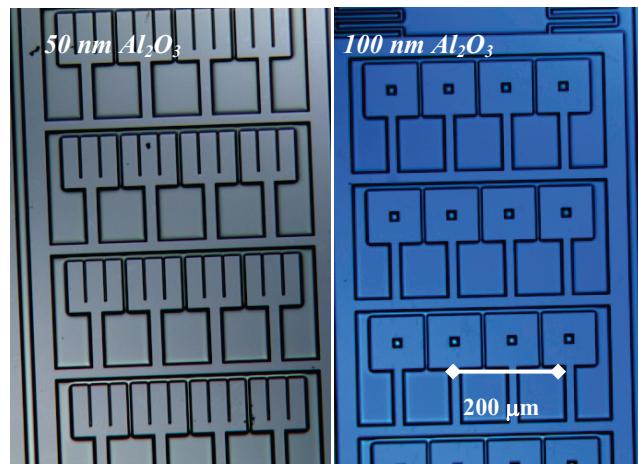
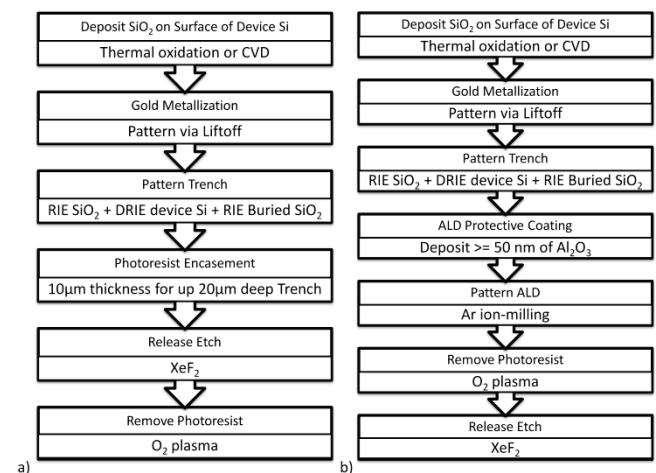


Figure 9: Optical micrographs of 50 nm (left) and 100nm (right), of ALD  $Al_2O_3$  on Si after 50  $XeF_2$  etch cycles showing no unintended etching.

Table 1: SOI fabrication process flows using either a) photoresist encasement or b) ALD protective coating to provide etch protection of the Si device layer.





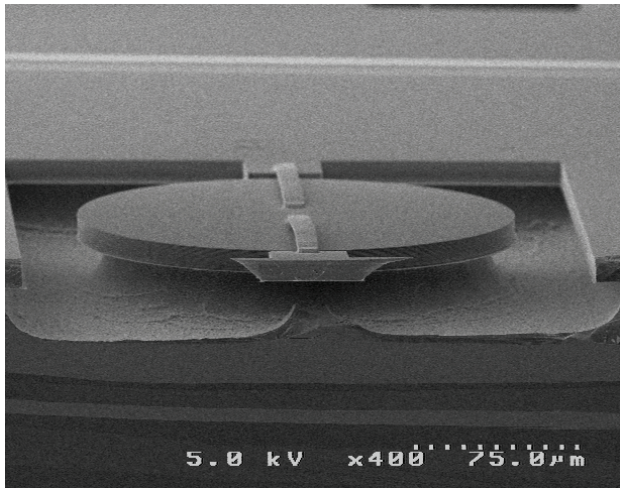


Figure 10: SEM micrograph showing excellent selective protection of Si structure with of 50 nm of ion milled patterned  $Al_2O_3$  film etched in 50 cycles of  $XeF_2$ . Images were taken prior to full release of devices and after cleaving to illustrate  $XeF_2$  etch front. The arrow indicates the isotropic etch.

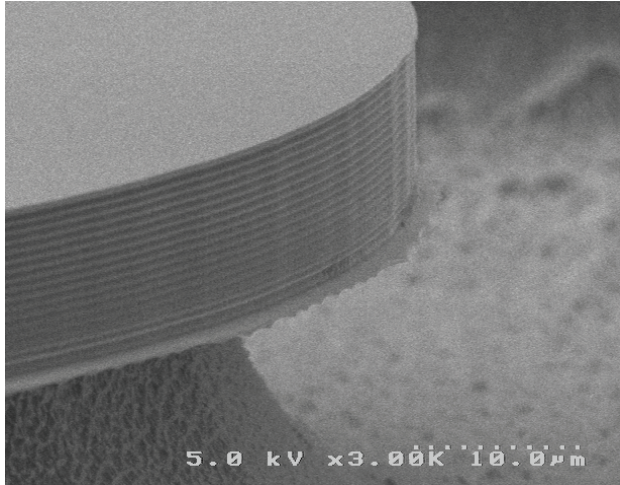


Figure 11: Magnified view of Figure 11. The disk is protected with ALD on the top and sides and  $SiO_2$  on the bottom.

## CONCLUSIONS

ALD alumina is a MEMS process compatible, patternable, and etch-resistant mask material to  $XeF_2$  etching. Furthermore, it can enable higher performance SOI devices providing improvements in fabrication yield and ease of fabrication integration. Layer thicknesses on the order of 10-50 nm showed good conformal coverage in 15  $\mu m$  deep trench features. Experiments showed that  $Al_2O_3$  films greater than or equal to 50 nm exhibit excellent etch resistance and virtually no pinholing to the  $XeF_2$  etch gases for etch cycles ranging from 50 to 500 cycles. Etch failures in films less than 50 nm thick were clustered, streaked, or at corner features and may be attributed to small contaminants on the wafer or thin areas at sharp convex corner features. It is anticipated that thinner coatings may be successfully utilized but additional research is required to examine the effect of feature size, coating uniformity, and surface contamination.

## ACKNOWLEDGEMENTS

The authors would like to acknowledge Joel Martin, Brian Power and Manrico Mirabelli for their fabrication assistance.

## REFERENCES

- [1] N. MacDonald, SCREAM MicroElectroMechanical Systems, Microelectronic Engineering, 32, 1996, 47-73
- [2] J. D. Brazzle, M. R. Dokmeci, and C. H. Mastrangelo, "Modeling and characterization of sacrificial polysilicon etching using vapor-phase xenon difluoride," in Proc. 17th IEEE Int. Conf. MEMS, 2004, pp. 737-740.
- [3] T. Zhu, P. Argyrakis, E. Mastropaolo, K. Lee and R. Cheung, J. Vac. Sci. Technol. B, 2007, pp. 2553-2557 .
- [4] H. Chandralim, S.A. Bhave, R. Polcawich, J. Pulskamp, D. Judy, R. Kaul, M. Dubey, Proceedings of 2008 Solid State Sensor—Actuator and Microsystems Workshop, Hilton Head Island, SC, 2008, pp. 360-363.
- [5] K. Oldham, J.S. Pulskamp, R.G. Polcawich, M. Dubey, J. MEMS 17, 2008, 890 - 898.
- [6] I.W.T. Chan, K.B. Brown, R.P.W. Lawson, A.M. Robinson, Y. Ma and D. Strembicke D, Proc. IEEE Canadian Conf. on Electrical & Computer Engineering (Edmonton, May 1999), 1999, pp 1637-42.

## CONTACT

\*Gabriel Smith, tel: 1-301-394-3722;  
gabe.smith@us.army.mil

\*\*Ronald G. Polcawich, tel: 1-301-394-1275;  
ronald.g.polcawich@us.army.mil

# CONTACT GEOMETRY EFFECTS ON FRICTON IN MEMS PROBE ARRAYS

W.S. Smith<sup>1\*</sup>, P.G. Hartwell<sup>2</sup>, R.G. Walmsley<sup>2</sup>, and T.W. Kenny<sup>1</sup>

<sup>1</sup>Stanford University, Stanford, California, USA

<sup>2</sup>HP Labs, Palo Alto, California, USA

## ABSTRACT

This paper examines the friction and wear properties between a laterally unconstrained slider and an array of AFM-like probe tips. Specifically, it focuses on how variations in the actual number of contacts and contact geometry (varied by tip wear) influence the friction forces. Results show that the steady state friction coefficient increases dramatically as the number of contact points increases. Additionally, initial variations in the friction forces due to rapid tip wear become steady after sliding distances greater than 1 mm. These results combined with SEM images of the tip wear imply that the wear rate becomes minimal as the contact pressure is reduced to approximately 20 MPa.

## INTRODUCTION

Friction and wear are important aspects of the performance and reliability of many MEMS devices such as atomic force microscopes (AFMs), probe data storage devices, and tip based nano-fabrication [1-3]. The magnitude of the friction force affects the ability to control and position an actuator, which is critical when atomic resolution and rapid movement are needed. In addition to creating debris, tip wear can dull a sharp tip, reducing the density of bits stored in a data storage device or increasing the minimum feature size in a tip-based fabrication device [1,3]. Thus, understanding the contributing parameters to friction forces and wear is critical to the design and reliable operation of MEMS structures that include contacting and sliding surfaces.

Friction involves a complex combination of material properties, environmental conditions, sliding conditions, and contact properties. Although relatively simple relationships for friction have been established at the macro-scale, surface forces such as van der Waals forces, electrostatic forces, and capillary forces must be accounted for when considering friction at the micro- and nano-scale [4-7].

One of the most common methods for examining friction at the nano-scale is the single point scanning probe microscope [6,7]. This method correlates the reaction of an AFM cantilever as it is slid across a surface to the friction forces. This method has been instrumental in understanding many of the atomistic origins of friction forces. Typical results for a silicon tip sliding on a silicon surface produce a friction coefficient of 0.05 [7]. Commercial tribology testers are another common method to measure friction and adhesion forces at micro-scale contacts. These experiments

typically yield friction coefficients that are an order of magnitude larger than the nano-scale scanning probe results [7]. Other commonly used methods to measure friction forces include *in situ* methods where friction forces are a part of the device operation [8]. Although these methods mimic how actual MEMS devices will respond to friction forces, very few careful studies have been performed on statistically significant sample sets.

The experimental method used in these experiments represents a unique approach to examine the friction forces between an array of nano- to micro-scale contact points and a flat surface. Friction forces are calculated from the relative motion of a slider as it moves over the array of tips. First presented in [9], this method has been refined and automated to produce statistically significant results. The contacting and sliding surfaces mimic MEMS probe arrays such as those used for probe data storage and tip based nano-fabrication. Figure 1 shows an example of the AFM-like tips that are used to contact the flat surface of a slider. The sharp tips represent the asperities in contact between two surfaces where the total number of contact points can be controlled. Depending on the material properties and loading conditions, these probe arrays can have many more actual contact points than two nominally flat surfaces contacting each other [5].

## EXPERIMENTAL SETUP

Based on the previously published method [9], friction forces are measured between a laterally unconstrained slider and an array of upward pointing tips as shown in Figure 2. A horizontal shaker laterally actuates the array allowing only friction forces at the contact points to move the slider. The array is mounted to the shaker's stage using a stainless steel "fence." This fence constrains the total motion of the slider to remain over the array, but its opening is large enough to allow 95 $\mu$ m of free motion in the lateral directions (see Figure 3). This entire setup is placed in a vacuum chamber capable of achieving pressures of 2e-5 torr (2.7e-3 Pa).

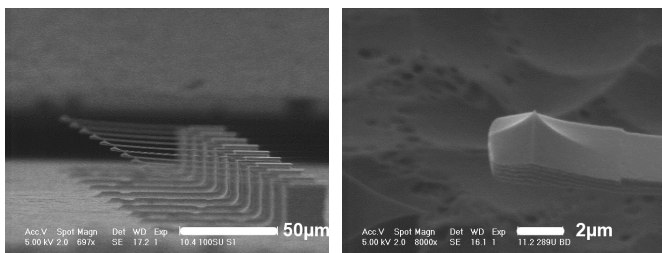


Figure 1. SEM images of a row of cantilevered probe tips that serves as the contact points for the friction experiments and a close up image of a single tip.

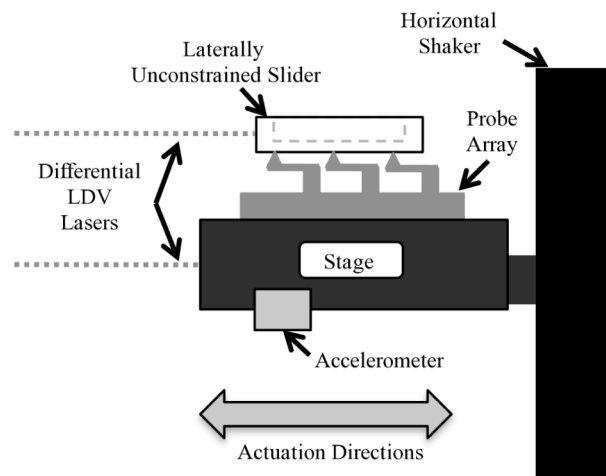


Figure 2. Schematic of friction test setup with the slider sitting on top of the probe array.

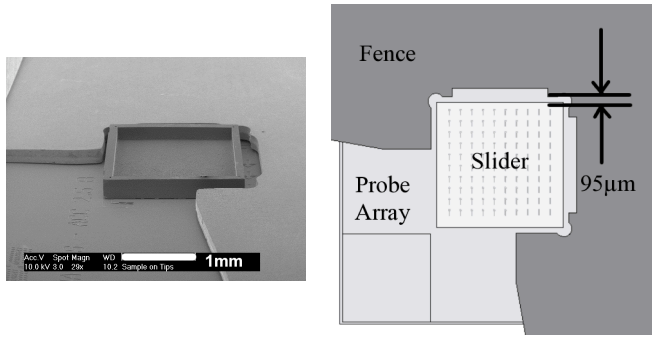


Figure 3. SEM image and schematic of the slider sitting on top of an array surrounded by the stainless steel fence.

An accelerometer attached to the shaker's stage measures the lateral motion applied to the array by the shaker. Additionally, a differential laser Doppler vibrometer (LDV) provides a non-contact method for measuring the relative motion of the slider on top of the array. As shown in Figure 2, the reference laser of the LDV is focused on the shaker's stage and the other laser is focused on the edge of the slider.

The tip arrays used in these experiments consist of pyramidal single crystal silicon tips (20 nm initial radius of curvature) made by a combination of isotropic etching and oxidation sharpening. Each tip is located at the end of a rectangular cantilever. To compensate for variations in tip height and increase the probability that all the tips contact the slider, the compliance of the cantilever is tuned to deflect 300-400 nm under the normal load of the slider. SEM images showing that each tip in the array is worn confirm the assumption that the slider contacts all the tips in the array. Arrays with 3, 100, 196, and 289 tips are analyzed in this paper.

The slider that sits on top of the arrays provides the normal force between the two surfaces and a controlled, nominally flat surface for the tips to slide across. The slider is a 2 mm x 2 mm x 0.3 mm polished single crystal silicon chip with a RMS surface roughness of 0.3 nm. The slider's dimensions allow it to slide freely on top of the array of probe tips spanning a 1.6x1.6 mm<sup>2</sup> area (see Figure 3) and sufficiently reflect the LDV laser back to the emitter. To minimize the total mass and the distance between the center of mass and the sliding surface, a 1.8x1.8 mm<sup>2</sup> square is etched to approximately 210 μm from the top surface.

## RESULTS AND DISCUSSION

The forces that act on the slider include the slider's weight (mass times gravity) and the normal forces at the contact points in the vertical direction and friction forces in the horizontal direction. Thus, the nominal normal force at each contact is approximately equal to the total weight divided by the number of tips. A moment created by the friction forces acting a distance from the center of mass can vary the normal forces across the array up to ±5% from the nominal normal force per tip. In addition, non-uniform tip height can lead to variations in the normal force at each tip. Table 1 lists the nominal normal force per tip for the arrays used in these experiments and the corresponding dynamic friction coefficients.

Figure 4 shows a sample of the accelerometer and LDV measurements and the corresponding friction analysis for a single release and slide event. The slider acceleration is obtained by numerically differentiating the relative velocity and adding it to the shaker acceleration. Automation of the actuation, measurement, and analysis has allowed for investigation of over 20 different arrays in varying environments and over 4000 individual release events producing statistically significant results.

Table 1. Average loading and friction parameters for the arrays of various number of contact points.

Number of Tips	Slider Mass	Nominal Force per Tip	Dynamic Friction Coefficient
3	.99 mg	3.7 μN	0.61
100	1.34 mg	120 nN	1.27
196	1.22 mg	67 nN	1.77
289	1.12 mg	34 nN	2.75

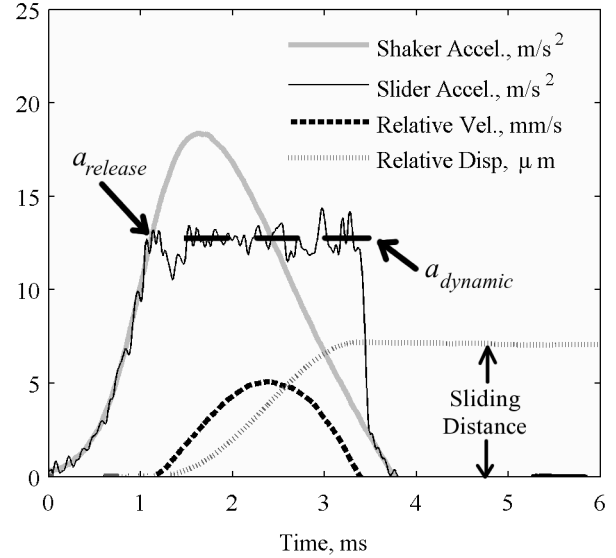


Figure 4. Analysis of an individual release and slide event for a slider on a 100-tip structure at 1.9e-5 torr. The release and dynamic acceleration correspond to the static and dynamic friction coefficients when the acceleration is divided by gravity.

The labels in Figure 4 show the key events that correspond to the friction forces. The release event is where the slider overcomes the static friction force and begins to move relative to the array (Equation 1). After a brief transition period, the dynamic friction governs the subsequent motion of the slider (Equation 2). As shown in the figure, the dynamic friction is averaged to a constant value. Since only friction forces are acting in the lateral direction, the sum of the friction forces at each contact is equal to the inertial force of the slider.

$$\sum F_{f,static} \leq m_s a_{release} \quad (1)$$

$$\sum F_{f,dynamic} = m_s a_{dynamic} \quad (2)$$

The dimensionless friction coefficient is used to compare the friction values obtained from the various arrays and sliders used in these experiments. The friction coefficient is the friction force normalized by the total normal force, which simplifies to the measured acceleration of the slider divided by gravity as shown below:

$$\mu = \frac{F_f}{F_n} = \frac{m_s a_{meas}}{m_s g} = \frac{a_{meas}}{g} \quad (3)$$

## FRICITION VARIATION WITH CONTACT NUMBER

Friction measurements between a MEMS probe array and a flat surface present a unique situation where the total number of contact points can be controlled. The number of contact points affects the total contact area between the two surfaces and the capillary forces. The attractive capillary forces originate from the pressure created by the curvature of the liquid meniscus acting over the area of the meniscus. The contact geometry of the probe tips leads to a liquid meniscus forming around every contact point. Thus, the attractive capillary forces will increase linearly with the total number of contact points [4].

Although the experiment is run in a vacuum chamber at low pressures, thin adsorbed films of water continue to exist on the surfaces [4,5,10]. To normalize the effects of the capillary forces, all of the probe arrays and sliders were subjected to the same conditions leading up to the friction experiments. To maintain a clean sliding surface, the sliders are stored in deionized water and dried with nitrogen before mounting on top of the probe array. The probe array is stored at room temperature in a nitrogen dry box until the slider is mounted to it. Once mounted, the array and slider are installed in the vacuum chamber and pumped down to a base pressure less than  $2 \times 10^{-5}$  torr.

The relationship between the total number of contact points and the dynamic friction force is shown in Figure 5. Despite the fact that parameters such as actual contact area do not necessarily vary linearly with the number of contact points, the linearity of Figure 5 indicates that the capillary forces play a significant role in the friction forces even at low pressures.

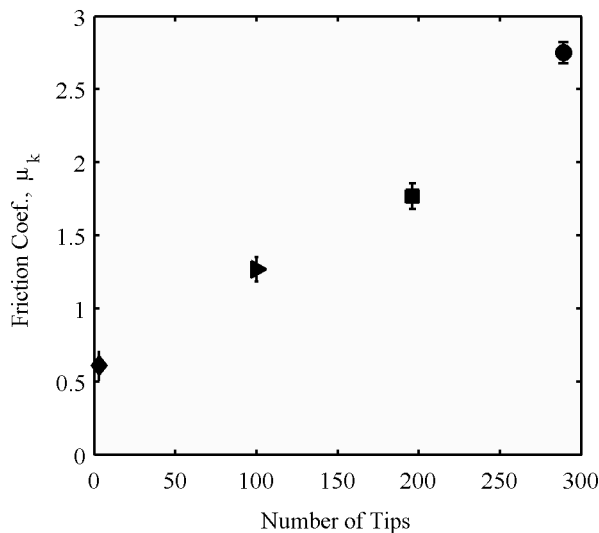


Figure 5. Increasing friction with the number of contact points. Each point on this plot is the average of 200 individual sliding events after steady friction behavior is reached.

## FRICITION VARIATION WITH CONTACT GEOMETRY

In addition to the role that the number of contact points plays in friction, small geometric changes of the tips also significantly affect the friction and adhesion forces. As the tips wear, the total contact area increases. The results shown in Figure 6 indicate that there is a large initial variation in the friction force as the slider moves for the first 20-200  $\mu\text{m}$ . High contact pressures combined with tangential friction forces at the sharp tips result in large shear stresses and rapid wear. This rapid wear continues until the contact area is sufficient to sustain the contact stresses of the slider moving on top of the tips.

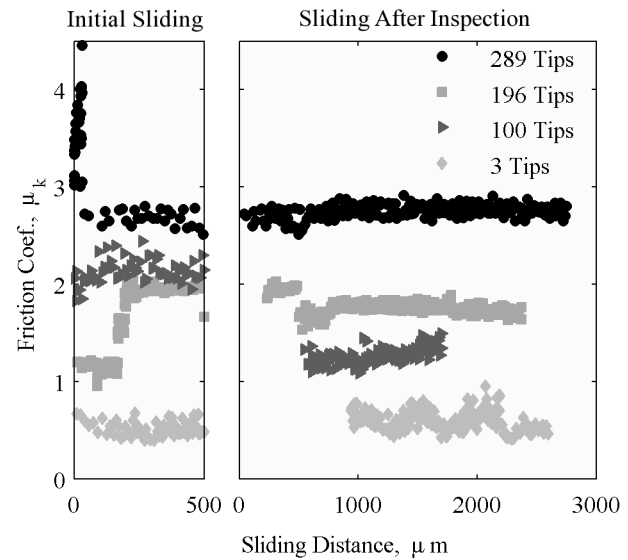


Figure 6. Friction coefficients as a function of the total sliding distance. Each data point represents the average dynamic friction coefficient of an individual sliding event. The large initial variation of the friction coefficient levels off to a constant value after sufficient sliding distance indicating that tip wear no longer significantly changes the friction force.

After the rapid initial change in friction force, a steady friction coefficient is reached as the slider moves longer distances. Figure 6 shows that after the inspection of the initial wear of the tips, the friction coefficient stabilizes to constant friction values with a standard deviation of less than 0.09 (100 tips and up). The standard deviation for the 3-tip array is larger since the slider positioning plays a significant role in the distribution of the normal force per tip. The stability of the friction force as the slider moves longer distances indicates that the effects from tip wear have become minimal.

Tip wear causes the tip to flatten, which increases the surface area and changes the friction coefficient. Figure 7 shows SEM images highlighting the geometric changes of the tips at various distance intervals. An increase in the total contact area due to wear serves to lower the total contact pressure on the tips. Although the slider placement on the tips can cause damage, the sharpness of tips after the slider is placed and removed without sliding is shown in column (a) of Figure 7 and the minimal geometry change from column (b) to column (c) shows that the initial sliding is responsible for the majority of the tip wear.

## WEAR AND CONTACT PRESSURE

The wear rate of the tips is related to the total shear stress at the tip. This shear stress is a combination of the contact stresses acting in the normal direction and the lateral stresses from the friction forces. As the number of contact points increases, the combination of the decreased normal load per tip and the increased total contact area reduces the contact pressure at each tip. Thus, as shown in Figure 7, larger contact pressures (fewer number of tips) result in greater amounts of wear per tip. Figure 8 compares the resulting wear lengths, defined as the diagonal of the flat area created as the pyramidal tip is worn, after the friction forces have reached steady values versus the total number of contact points. The average contact pressure, the slider weight divided by the average total contact area, when the tip wear rate becomes minimal is  $20 \pm 10$  MPa for all of the arrays.

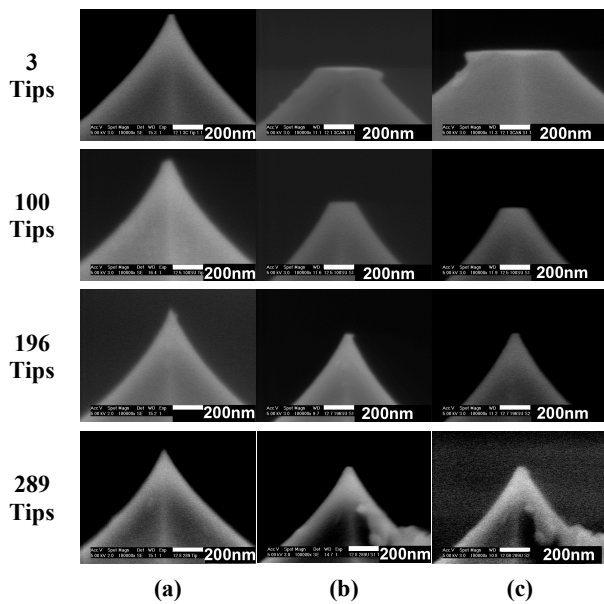


Figure 7. SEM profiles of tips indicating amount of wear after initial placement with no sliding (a), after initial sliding of less than 1 mm (b), and after extensive sliding > 2 mm (c).

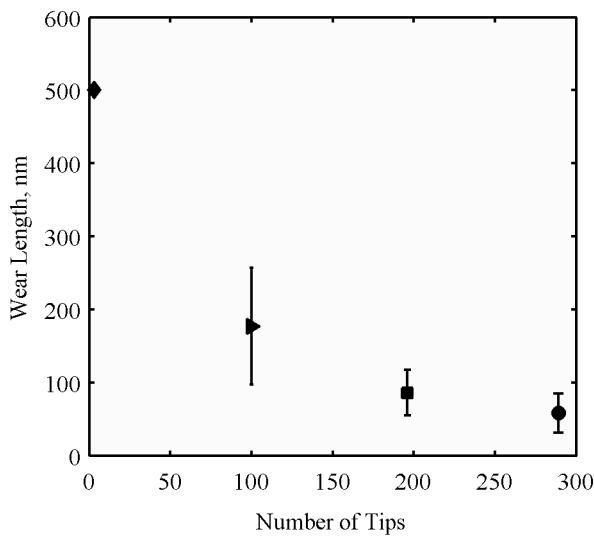


Figure 8. Averaged individual tip wear versus the number of contact points. The wear length in this case is the diagonal measured across the flat of the worn tip.

## CONCLUSIONS

This work takes a careful look at the friction and wear properties between a MEMS probe array with varying number of contact points and flat surfaces. The results from this work show that the unique nature of multiple probe tip contacts causes large variations in the friction force with the number of contacts. Since the probe tips are located at the end of compliant cantilevers, the actual number of contact points for probe arrays can be much larger than typical flat surfaces in contact. Thus, the total friction

forces for applications such as probe-based data storage and tip based nano-fabrication can be significantly larger than flat contacting surfaces.

The findings of this work show that tip wear rate reaches a minimum value for a given contact pressure. In addition to the contact numbers, contact properties, and contact pressures discussed here, friction forces and wear depend on many other parameters including the material properties and additional environmental conditions. Generally, lower contact pressures result in less detrimental effects of wear, but other methods of improving the reliability of sliding surfaces exist including the use of different materials or controlled environments. Further investigations into these areas are needed to enhance the understanding of friction and wear at the micro- and nano-scale and improve the reliability of MEMS applications with contacting and sliding surfaces.

## ACKNOWLEDGEMENTS

This work is supported by the DARPA CIEMS program, Hewlett-Packard, Bosch, Epson, Agilent, Boeing, and Qualcomm, the Stanford Nanofabrication Facility (a member of the National Nanotechnology Infrastructure Network), which is supported by the National Science Foundation under Grant ECS-9731293. We also thank HP Labs, Palo Alto for its support of this work.

## REFERENCES

- [1] P. Vettiger, G. Cross, M. Despont, U. Drechsler, U. Durig, B.Gotsmann, W. Haberle, M.A. Lantz, H.E. Rothuizen, R. Stutz, G.K. Binnig, "The 'Millipede'-Nanotechnology Entering Data Storage", IEEE Trans. On Nanotech., 91, 1 (2002).
- [2] S.C. Minne, G. Yaralioglu, S.R. Manalis, J.D. Adams, J. Zesch, A. Atalar, C.F. Quate, "Automated parallel high-speed atomic force microscopy", App. Phys. Ltrrs. 72, 18 (1998).
- [3] A.A. Tseng, A. Notargiacomo, T.P. Chen, "Nanofabrication by scanning probe microscope lithography: A review", J. Vac. Sci. Technol. B 23(3), (2005), pp. 877-893.
- [4] J. Israelachvili. *Intermolecular and Surface Forces. 2<sup>nd</sup> Ed.*, Academic Press, London, 1992.
- [5] C.M. Mate, *Tribology on the Small Scale*, Oxford University Press, New York, 2008.
- [6] B. Bhushan, J. Israelachvili, U. Landman, "Nanotribology: friction, wear, and lubrication at the atomic scale." Nature. 374 (1995).
- [7] N. Tambe, and B. Bhushan, "Scale dependence of micro/nano- friction and adhesion of MEMS/NEMS materials, coatings and lubricants". Nanotech., 15 (2004).
- [8] E.E. Flater, A.D. Corwin, M.P. de Boer, R.W. Carpick, "In situ wear studies of surface micromachined interfaces subject to controlled loading," Wear, 206, 6, (2006).
- [9] W.S. Smith, P.G. Hartwell, and R.G. Walmsley, "Adhesion and friction measurement method for a MEMS probe array", Tech. Dig. 2006 Sld-St Sensors, Actuators, and Transducers Workshop, Hilton Head Isl., SC, 6/4-8/06, Transducer Research Foundation, Cleveland (2006), pp. 264-267.
- [10] M. Scherge, X. Li, J. A. Schaefer, "The effect of water on friction of MEMS," Tribology Ltrrs., 6 (1999).

## CONTACT

\*W.S. Smith, tel: +1-650-646-5937; wessmith@stanford.edu

# FABRICATION OF MULTIPLE HEIGHT MICROPROBES USING UV LITHOGRAPHY ON TIMED-DEVELOPMENT-AND-THERMAL-REFLOWED PHOTORESIST

*Jungkwun 'JK' Kim\**, *Hyochun Ahn*, *Xiaoyu Cheng*, *Kyoung-Tae Kim*, *Gwan-Ha Kim*, and *Yong-Kyu 'YK' Yoon\*\**  
Electrical Engineering, University at Buffalo, the State University of New York, Buffalo, NY 14260, USA

## ABSTRACT

A three dimensional (3-D) microprobe array with multiple heights has been fabricated using the timed-development-and-thermal-reflow (TDTR) process and an additional UV lithography process. After the TDTR process, the reflowed polymer profiles between the substrate and a micro wall are differing as a function of the development time and the surface properties of the side wall such as hydrophobicity and the contact angle between the wall and the reflowed polymer, resulting in a convex, linear, and concave shape. A polymeric micro slab array with continuously varying heights and a micropillar array with multiple heights, where the overall surface profile follows the reflowed surface after the TDTR step are successfully demonstrated. As an application, a 2 x 5 microprobe array with linearly changing multiple heights and metallic signal traces has been fabricated for 3-D neural probing and stimulation. Three different microprobe sets with a pillar diameter of 40 $\mu\text{m}$  and a different probe height range of 381 $\mu\text{m}$  to 482 $\mu\text{m}$ , 97 $\mu\text{m}$  to 164 $\mu\text{m}$ , and 21 $\mu\text{m}$  to 60 $\mu\text{m}$ , have been also demonstrated. DC resistance property of a probe has been tested.

## INTRODUCTION

3-D microprobes with multiple heights are highly demanded in many advanced biomedical applications such as neural mapping or signaling [1] in multilayered cells or tissues. Many conventional methods for cell or tissue investigation use a printed type flat electrode array or an extruded micro electrode array with a uniform height. While many diagnoses on the cells or the tissues are conducted by measuring voltages, currents, and therefore their impedance using such micro electrodes, the measurements with the conventional probes with a uniform height would provide very limited information available only from a single layer, which does not fully reveal cell and tissue activities and communications occurring between cells and tissues from different layers and functional groups. For example, retina tissues are composed of several layers such as a ganglionic layer, a plexiform layer, and a nuclear layer. These layers are connected and reacted as one functional tissue [2]. To understand and study such inter/intra layer activities, appropriately spaced 3-D probes with multiple heights are highly desired.

Recently, a multiple height micro needle array using advanced micro/nano fabrication processes has been reported including the doped silicon array made by the vapor-liquid-solid growth method [1] and an inclined UV lithography and micromolding process [3]. However, the Si process requires several alignments, the needle growth process is complicated, and the fabrication time is relatively long. The inclined UV lithography approach requires a different foot print for a micro needle with a different height, therefore requiring a relatively large area for a multiple height probe array. Very recently, a timed-development-and-thermal-reflow (TDTR) process has been reported as a simple fabrication method for 3-D microstructures with various shape and heights such as a micro lens, rounded microfluidic channels, and pillar arrays with multiple heights by the authors [4, 5].

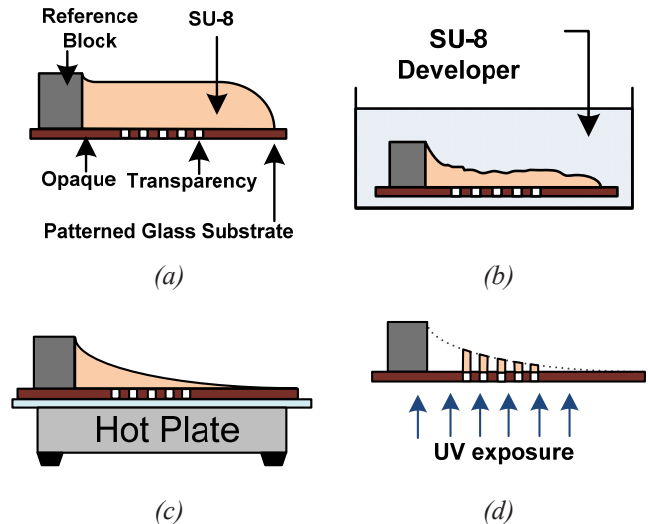


Figure 1. Fabrication process: (a) Softbake and primary exposure, (b) Timed development, (c) Thermal reflow, (d) Backside exposure for multiple height pillars

In this work, a 3-D microprobe array with multiple heights using the TDTR process has been fabricated in a controllable manner by applying an additional or multiple UV lithography step(s) on the profile controlled photoresist, and a metallization step. The TDTR process can produce a convex, linear and concave profile by controlling the amount of the remaining polymer after timed development and using the surface phobicity of the substrate surface and a wall during the thermal reflow step. To show the process feasibility and utility, a 3-D microprobe array with discrete multiple heights integrated with the electrode trace is demonstrated.

## MULTIPLE HEIGHT MICROPROBES

### Multiple height micro pillar array

To fabricate the multiple height pillar array, the timed-development-and-thermal-reflow (TDTR) fabrication process is utilized. The TDTR process is divided into two steps: the timed development step which controls the amount of remaining uncrosslinked polymer and the thermal reflow step which forms a smooth surface profile in a convex, linear, or concave shape. Figure 1 describes a general TDTR fabrication process for a multiple height pillar array. With a prepatterned glass photomask which is also served as a substrate, both topside exposure and backside exposure have been applied for polymer block and pillar definition, respectively. First, SU-8 (2025, Microchem, Inc.), negative tone photopatternable epoxy, is coated on a chromium patterned glass substrate, followed by softbake at 95 $^{\circ}\text{C}$ , UV exposure from topside, and post exposure bake steps (1a). The topside UV exposure defines a reference position where the curve of the 3-D microstructure starts. Uncrosslinked polymer on the sample is partially developed using propylene glycol monomethyl ether acetate (PGMEA) in a time controlled manner (1b). The partial developing process is conducted without stirring in room temperature. The sample is baked at 95 $^{\circ}\text{C}$  for an hour.

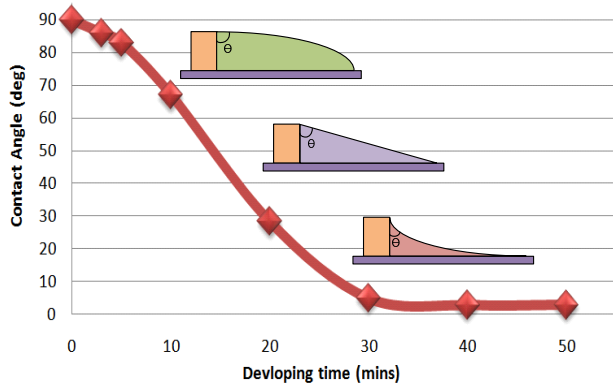


Figure 2. Contact angle as a function of developing time

The solid state uncrosslinked polymer is turned into a liquid state when it is heated above its glass transition temperature forming smooth surface curvature, which is called as the thermal reflow process, to form a concave curvature on the surface (1c) and cooled down to room temperature. The remaining amount of the uncrosslinked SU-8 is varied by the SU-8 developing time. The curvature profile is controllable by adjusting the developing time and surface property. Additional backside UV exposure is applied on the concave structure to form a multiple height pillar array (1d) after the complete developing process in the PGMEA solution. The lateral distance from the reference block determines the pillar height. The farther distance from the reference, the shorter pillar height will be.

To examine the variation of the curvature profile, 1 mm thick SU-8 photoresist is coated on a glass substrate. The sample is baked at 95°C for 40 hours and cooled down to room temperature. The reference block is patterned by topside UV exposure. After one hour post exposure bake at 95°C on a hot plate, the sample is timed-developed and observed in different developing time. As development proceeds in the uncrosslinked area, the resultant contact angle also varies as shown in Figure 2, transitioning from the semi convex shape at the earlier stage of development to the semi concave shape at the later stage of development. The contact

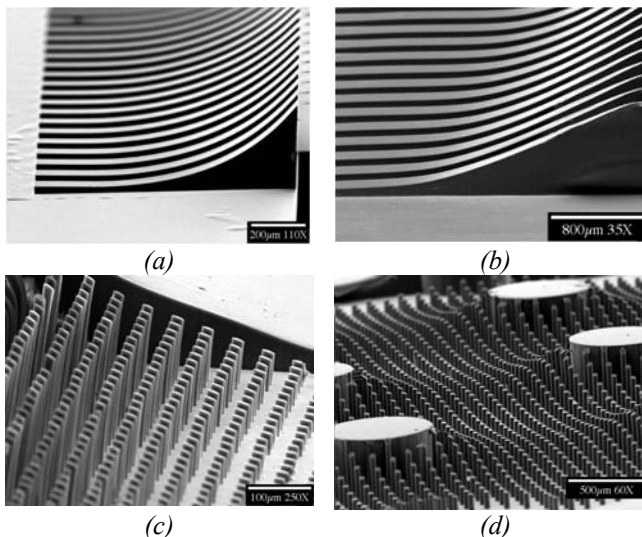


Figure 3. 3-D structures with tapered profiles: (a) Semi concave slab, (b) Linearly tapered slab, (c) Linearly decreased pillar array, (d) Pillar array with a wavy profile

angle is defined as the angle between the reference side wall and the surface of the uncrosslinked polymer. A linear tapered shape is formed when the half amount of the uncrosslinked polymer is developed. Finally further development forms a concave shape after thermal reflow. The contact angle decreases for the sample with longer development time. It reaches to a critical angle of 2.8° for the sample with 30 minute or longer development. An additional UV lithography step after the TDTR process forms a pillar array with various heights or other 3-D microstructures. The profile of the top portion of each pillar follows that of the surface profile formed by the TDTR process. Figure 3 shows various microstructures with continuously or discretely varying heights. The semi concave slab (3a) and the linearly tapered slab (3b) result from the different developing time. By applying additional UV exposure through the prepatterned hole array on the Cr coated glass substrate, a linearly decreasing pillar array (3c) is formed. The micro pillar array with more arbitrarily varying multiple heights (3d) shows that the position and the shape of the reference block can be utilized to form a complex surface profile and an ultimate pillar array with the profile.

The heights of the multiple pillars are calculated from an equation for a curvature profile derived from the Young-Laplace equation [6].

$$\eta(\chi) = \ell_c \cot(\theta) e^{(-\chi/\ell_c)} \quad (1)$$

where  $\eta(\chi)$ ,  $\ell_c$ ,  $\theta$ , and  $\chi$  are the curvature profile, the capillary length, the contact angle and the distance from the reference block. The function  $\eta(\chi)$  shows the height of the pillar located in the distance  $\chi$  in millimeter (mm), between the reference block and the pillar. The capillary length,  $\ell_c$ , is experimentally measured between the glass substrate and the SU-8 interface as 1.3mm.

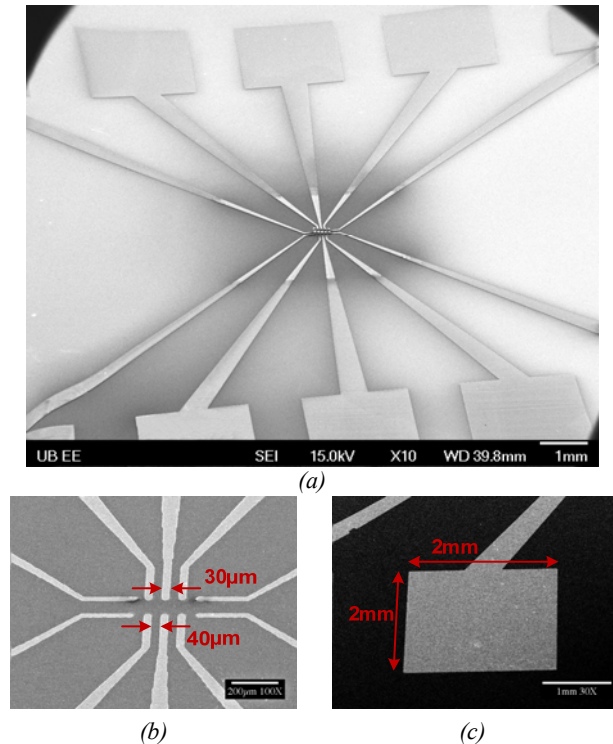


Figure 4. SEM images of the electrode trace design: (a) Overview of the addressing electrodes, (b) The center electrodes, (c) The pad dimension

## TRACE ELECTRODE DESIGN

For a multiple height microprobe array, each microprobe is electrically connected to the external circuit through an electrode trace. The electrode traces for a 2 x 5 pillar array with different heights are designed as shown in Figure 4, where an overall view (4a), a trace electrode view (4b), and a pad (4c) are highlighted. The electrode trace is designed in a glass substrate with an area of 1 inch by 1 inch. The width and the gap of the center electrode are 30  $\mu\text{m}$  and 40  $\mu\text{m}$ , respectively. The size of the electrode pad is designed to be 2 mm by 2 mm for easy connection. Each electrode line is evenly spread out and symmetrically aligned to reduce the signal noise and the crosstalk between probes and traces. The electrode is made of 10  $\mu\text{m}$  thick copper.

## FABRICATION PROCESS OF A MICROPROBE ARRAY

The multiple height pillar array is integrated to the electrode traces. Figure 5 shows the fabrication process of the multiple height microprobe array. After cleaning a glass substrate (5a), a titanium adhesion layer and a copper seed layer of 30nm and 300nm, respectively, are deposited. A 2 x 5 hole array for pillar definition is patterned using UV lithography and metal etching (5b). The electrode traces are defined on the metal layer by UV lithography with a photoresist, NR9-8000 (FUTUREX, Inc.) (5c) followed by electroplating with 10  $\mu\text{m}$  copper (5d). After removing the photoresist (5e), the negative photoresist, SU-8, is applied for the TDTR process (5f) as described earlier. Additional UV lithography with the backside exposure scheme produces a multiple height pillar

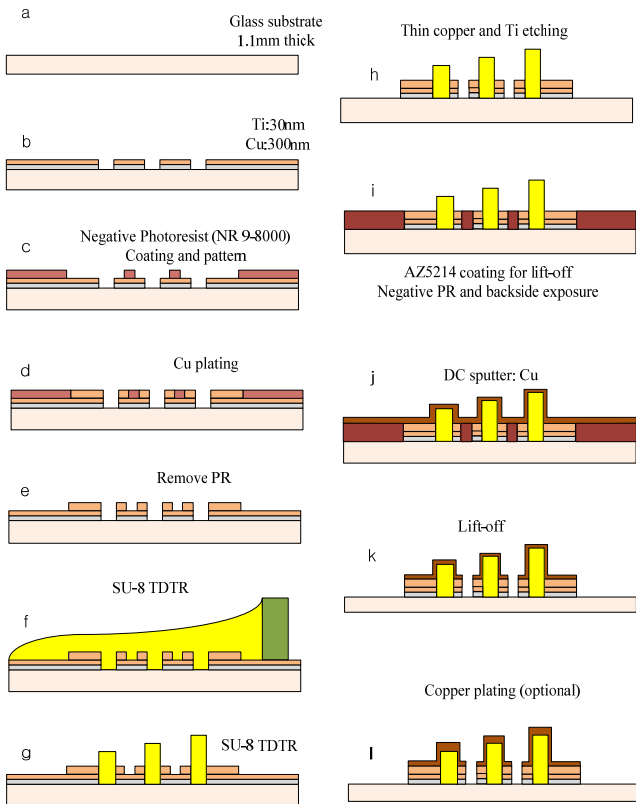


Figure 5. Fabrication process of the multiple height microprobe array

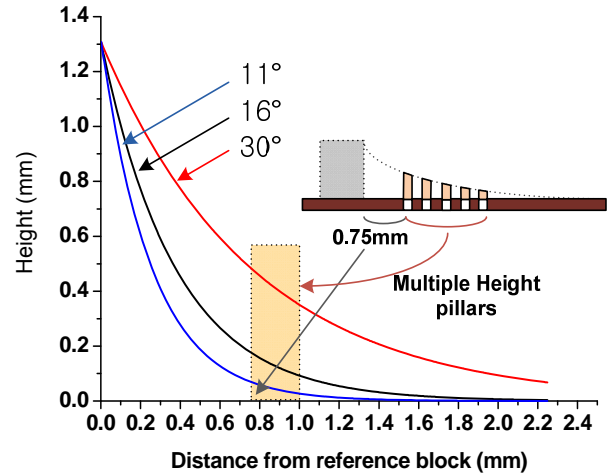


Figure 6. Curvature profile with contact angles of 11°, 16°, 30°

array (5g). The titanium and copper seed layer are timed-etched in a diluted hydrofluoric acid (HF) and sulfuric acid with hydrogen peroxide, respectively. (5h). Negative tone photoresist, AZ5214, is coated and exposed from the back side of the sample, using the pre-patterned metal layer as a self aligned photomask (5i). An additional copper layer with a thickness of 100nm is coated on the sample using sputtering (5j). In this step, titanium instead of copper can be coated on the sample requiring biocompatible metallization. The standard lift-off process isolates each electrode (5k) and additional electroplating is optionally conducted for thicker metallization on the multiple height pillars (5l).

## RESULT

The heights of the multiple pillar array are controllable by the TDTR process. The developing time and the lateral distance from the reference block are two parameters to determine the height of the pillar. Three samples for the multiple height microprobes are prepared with a different period of development such as 20, 25, and 27 minutes. The distance between the reference block and the first pillar is set as 0.75mm. The different developing time results in a different contact angle such as 30°, 16°, and 11°, respectively. The multiple height pillar profiles are calculated using Eq. (1) and plotted in Figure 6. The heights vary from 380  $\mu\text{m}$  to 480  $\mu\text{m}$  with a contact angle of 30° in the red line, from 95  $\mu\text{m}$  to 165  $\mu\text{m}$  with 16° in the black line, and from 20  $\mu\text{m}$  to 60  $\mu\text{m}$  with 11° in the blue line. Figure 7 shows the fabricated three different microprobe sets with multiple heights showing good agreement with the calculated pillar profile as summarized in Table 1. The photomask of the 2 x 5 micro hole array has each hole diameter of 40  $\mu\text{m}$ . And the tip of each pillar is not flat but slanted and the measured heights are the average values. Each electrode trace has a line width of 30  $\mu\text{m}$  at the end, on which a micro pillar is located. The other end of the electrode trace is connected to outside circuitry.

The fabricated microprobe has been tested for the DC I-V curve as shown in Figure 8. A 480  $\mu\text{m}$  tall probe has been chosen for the characterization. One test probe is connected to the top of the pillar and the other is at the end of the electrode pad. The voltage from -1.5V to 1.5V has been measured while the current from -0.8A to + 0.8A has been applied.



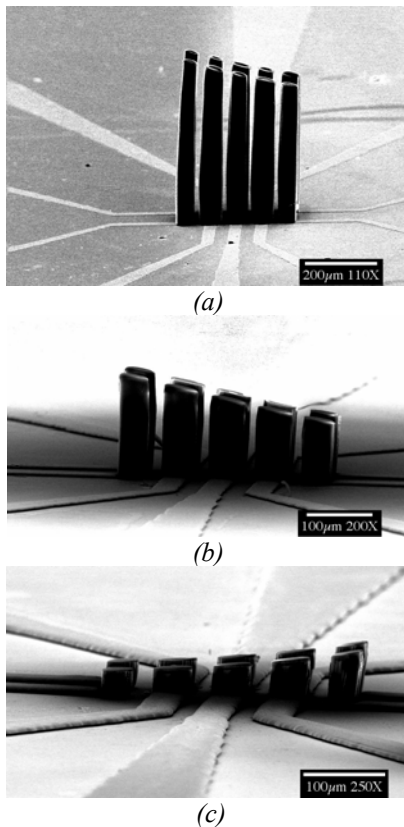


Figure 7. Multiple height microprobe array: (a) 380.51 $\mu\text{m}$ , 407.18 $\mu\text{m}$ , 433.86 $\mu\text{m}$ , 458.86 $\mu\text{m}$ , and 482.05 $\mu\text{m}$  in the increasing order, (b) 96.86 $\mu\text{m}$ , 110.40 $\mu\text{m}$ , 128.40 $\mu\text{m}$ , 145.86 $\mu\text{m}$ , and 164.44 $\mu\text{m}$  in the increasing order, (c) 20.92 $\mu\text{m}$ , 30.83 $\mu\text{m}$ , 39.08 $\mu\text{m}$ , 49.76 $\mu\text{m}$ , and 59.61 $\mu\text{m}$  in the increasing order

Table 1: Summary of the dimension of the fabricated probes

	Contact angle	Pillar height [ $\mu\text{m}$ ]*				
		1	2	3	4	5
Device 1 (Fig 7a)	30°	<u>380.5</u> (380)	<u>407.1</u> (405)	<u>433.9</u> (430)	<u>458.5</u> (455)	<u>482.0</u> (480)
Device 2 (Fig 7b)	16°	<u>96.86</u> (95)	<u>110.40</u> (112.5)	<u>128.40</u> (130)	<u>145.86</u> (147.5)	<u>164.44</u> (165)
Device 3 (Fig 7c)	11°	<u>20.92</u> (20)	<u>30.83</u> (30)	<u>39.08</u> (40)	<u>49.76</u> (50)	<u>59.61</u> (60)

\*Pillar height in a center point of each pillar: measured, and (calculated)

## CONCLUSION

Multiple height microprobes have been implemented using the TDTR method, additional UV lithography, and metallization. The TDTR process has been extended to the fabrication of convex, linear, and concave microstructures without an additional micromolding step, and the fabrication of pillar arrays with multiple heights using an additional UV lithography process. By controlling the development time and therefore changing the amount of the remaining uncrosslinked polymer, or adopting a different geometry of the reference blocks, various surface profiles could be produced. Using an additional backside exposure scheme, discrete micro pillar arrays with multiple heights have been successfully demonstrated.

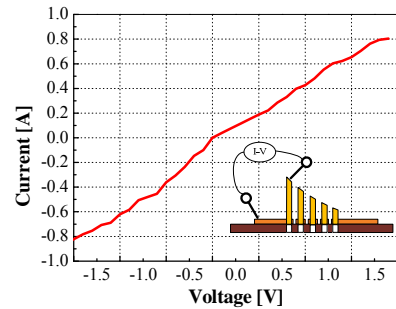


Figure 8. I-V curve measurement of a single microprobe

The TDTR process has shown many advantages such as its simplicity in microfabrication for complex 3-D structures with continuous or discrete height change, and process compatibility with conventional micromachining processes. The development time in the TDTR process and the lateral distance from the reference block determine the profile curvature ultimately affecting the height of the pillars. The Young-Laplace equation is utilized to design the multiple height pillars array. The surface profiles of the fabricated three different sets of a 2 by 5 micro probe array with different heights shows good agreement with those of the calculated ones. A fabricated multiple height microprobe has been tested for a DC I-V curve. Potentially, the multiple height microprobe can be used for stimulating or sensing neurosignals of the different layers of tissues in retina or brain.

## ACKNOWLEDGMENT

This work is funded by National Science Foundation CAREER-ECCS 0748153 and CMMI 0826434.

## REFERENCES

- [1] T. Kawano, A. Ikedo, T. Kawashima, K. Sawada and M. Ishida, "Vertically aligned various lengths doped-silicon microwire arrays by repeated selective vapor-liquid-solid growth," *IEEE MEMS Conference 2009*, Sorrento, Italy, Jan 2009.
- [2] X. X. Luo, A. Baba, T. Matsuda, C. Romano, "Susceptibilities to and Mechanisms of Excitotoxic Cell Death of Adult Mouse Inner Retinal Neurons in Dissociated Culture," *Invest Ophthalmol Vis Sci.*, 45 (2004), pp. 4576–4582.
- [3] S.-O. Choi, J.-H. Park, Y. Choi, Y. Kim, H.G. Gill, Y.-K. Yoon, M.R. Prausnitz, and M.G. Allen, "An Electrically Active Microneedle Array for Electroporation of Skin for Gene Delivery," *Transducers '05*, Seoul, Korea, June 5-9, 2005, pp. 1513-1516.
- [4] J.K. Kim, K. Lee, K.W. Oh and Y.-K. Yoon, "Microfabrication of rounded channel and waveguide integrated microres using timed development and thermal reflow process," *13<sup>th</sup>  $\mu\text{TAS}$  Conference*, Jeju, Korea, Nov 2009.
- [5] J.K. Kim, K. Lee, H. Jee, K.W. Oh, and Y.-K. Yoon, "Fabrication of multiple height microstructures using UV lithography on timed-development-and-thermal-reflowed photoresist," *IEEE MEMS Conference 2010*, Hong Kong China, pp. 376-379, Jan. 2010.
- [6] J.W.M. Bush (May 2004). "MIT Lecture Notes on Surface Tension, lecture 3" (PDF). Massachusetts Institute of Technology. <http://web.mit.edu/1.63/www/Lec-notes/Surfactension/Lecture3.pdf>.

## CONTACT

\* JK Kim, [jkkim5@buffalo.edu](mailto:jkkim5@buffalo.edu)

\*\*YK Yoon, [ykyoon@buffalo.edu](mailto:ykyoon@buffalo.edu)

# HIGH CURRENT PROPERTIES OF A MICROSPRING CONTACT FOR FLIP CHIP PACKAGING

*Bowen Cheng*<sup>1,2</sup>, *Eugene M. Chow*<sup>1</sup>, *Dirk DeBruyker*<sup>1</sup>, *Ivan Shubin*<sup>3</sup>,  
*John Cunningham*<sup>3</sup>, *Alex Chow*<sup>3</sup>, *Jing Shi*<sup>3</sup>, *Matt Giere*<sup>3</sup>, *Karl F. Böhringer*<sup>2</sup>  
<sup>1</sup>Palo Alto Research Center, Inc., Palo Alto, CA, USA  
<sup>2</sup>University of Washington, Seattle, WA, USA  
<sup>3</sup>Oracle, San Diego, CA, USA

## ABSTRACT

The high current properties of a micro spring pressure contact are characterized. The spring has large compliance ( $>30\ \mu\text{m}$ ) compared to other packaging technologies and fits in a  $180\ \mu\text{m}$  pitch 2d array. At 250 mA and  $65\ ^\circ\text{C}$ , daisy chains of 134 spring contacts in a silicon package show stable resistances and hotspot temperature rises of less than a degree. At 1 amp, failure near the spring tip or body is observed. Finite element modeling is performed to study the current distribution and provide failure mode insight. Simultaneous force and resistance measurements suggest there is no spring force softening. The results suggest a 10 mg ( $100\ \mu\text{N}$ ) micro spring with large compliance can be reliable for high current applications.

## INTRODUCTION

We are developing pressure contacts based on stress-engineered thin film springs for next generation microelectronics flip-chip packaging. The springs are fabricated with wafer-scale processing, lithographically defined and self-assembled as they are released. Their advantages for flip chip packaging include: solder-free, low stress (helps low K dielectric problem), compliant (helps substrate thermal expansion mismatch) and scalable to fine pitch and low heights. They enable integrated test and packaging to address the known-good-die problem hindering high performance multi-chip modules. In addition to packaging, the technology has been used for a variety of MEMS devices, including coils, actuators, and AFM tips [1-5].

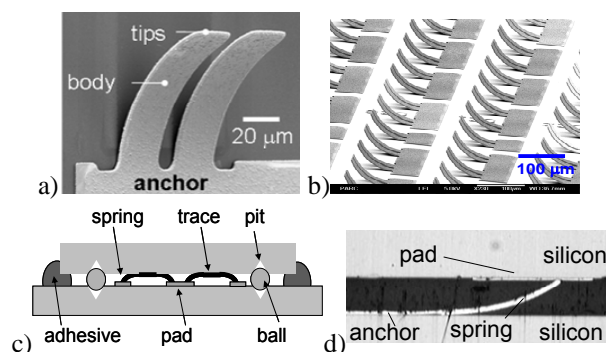


Figure 1. a) Fabricated contact consisting of a spring pair. b) array of contacts before assembly ( $>3000$  per die on  $14\ \text{mm} \times 16\ \text{mm}$  die). c) Si package schematic and d) cross section ( $18\ \mu\text{m}$  airgap). [6-7]

We previously reported on a spring designed to fit a standard flip-chip 2d grid ( $180\ \mu\text{m} \times 180\ \mu\text{m}$ ) and achieve a unique combination of high compliance ( $>30\ \mu\text{m}$ ) and low resistance ( $<100\ \text{m}\Omega$ ). Thousands of springs on silicon substrates with integrated alignment pits were assembled into flip chip packages and shown to pass basic thermocycle and humidity reliability tests [6-7]. Each contact consisted of 2 springs, where each spring was  $100\ \mu\text{m}$  long,  $30\ \mu\text{m}$  wide, and  $3.5\ \mu\text{m}$  thick. The middle  $1\ \mu\text{m}$

core of the spring was composed of MoCr and the outer shell was  $1.25\ \mu\text{m}$  of electroplated gold. Springs were isolated from the silicon substrate with  $0.2\ \mu\text{m}$  nitride.

Current densities continue to increase with the steady downscaling of technologies. Current density has a square effect on joule heating, which may lead to failure mechanisms such as melting or chemical dislocation [8]. Electromigration induced failures, due to mass transport with electric fields, scales with current density [9]. Solder bump current densities can be  $10^3$ - $10^4\ \text{A}/\text{cm}^2$  [10]. Copper is low resistance and enables on-chip wiring to handle densities as high as  $10^2$ - $10^6\ \text{A}/\text{cm}^2$  [11]. Gold also has low resistivity and can form stud bumps for flip chip packaging. Stud bumps at  $5 \times 10^4\ \text{A}/\text{cm}^2$  have been shown to be reliable [12]. Comparing current densities is challenging though, because there are many factors related to current carrying ability. The power dissipation and thermal design is critical, as temperature strongly affects failure. Mechanical stress levels also effect how the interconnect performs. For metallurgical bonds like solder and stud bumps, stresses can be very high, which reduces reliability.

Micro pressure contacts for packaging have not been studied at high current densities to our knowledge. In the future, we will package a custom prototype high power processor with these springs [13], which at maximum performance will consume 355 W and have an average of 90 mA per contact, corresponding to  $7 \times 10^4\ \text{A}/\text{cm}^2$  average current density. This is less than what has been shown to be stable in previously reported MEMS switches ( $4 \times 10^5\ \text{A}/\text{cm}^2$ , 2 watts), which also depends on gold, spring-based pressure contacts [14]. A spring for flip chip packaging, though, has different requirements than switches. The required compliance of our springs is much higher, typically tens of microns, as they need to accommodate large thermal expansion mismatches and nonplanarities between substrates. This means thinner metals need to be used, accacerbating cooling challenges. The spring interconnect should be reworkable with zero current, but does not have to survive billions of hot on/off cycles like some switches. Lateral scrubbing can induce wear in flip chip packages. Stiction is fatal for switches, but might not be an issue for a packaging application. Adsorbed film contamination is a risk for any gold surface. Both devices need to maintain force ( $\sim 100\ \mu\text{N}$ ) to maintain electrical contact.

The aim of this work is to study the high current properties of the springs for high power flip chip packaging applications such as IC processors. In this paper, the contacts in silicon packages are experimentally tested with high current until failure is observed. Thermal imaging is performed to study the temperature distribution in the package. Modeling is then performed to give more insight into possible failure mechanisms. Finally force softening, a possible failure mechanism particularly important for springs, is studied.

## PACKAGE CURRENT TESTS

The silicon-silicon package of springs (Figure 1) is heated and simultaneously subject to high current, to simulate a high

power IC. Four-wire resistance structures of 134 contacts in series form a long daisy chain which is electrically monitored while the package is placed on a 65 °C thermoelectric heater (Figure 2). The daisy chain consists of gold metal traces on each silicon substrate connected with spring contacts. At 250 mA, stable, but slightly decreasing resistances are observed (Figure 3). A slight decrease in the resistance with time is typical of gold contacts [15]. After 1700 h a failure is observed (resistance went open), and non-destructive confocal infrared inspection into the chip shows that a chip trace had failed. No spring failures are found, even in the regions predicted to be high current density. The trace has an average current density 3× higher than the spring average, and appears to fail first. All 134 spring contacts conduct 250 mA for 1700 h without failure, corresponding to an average current density of  $2 \times 10^5$  A/cm<sup>2</sup> in each pair of springs. This suggests that the springs should perform well in the future when we package a 355 W processor with an average of 90 mA per contact [13].

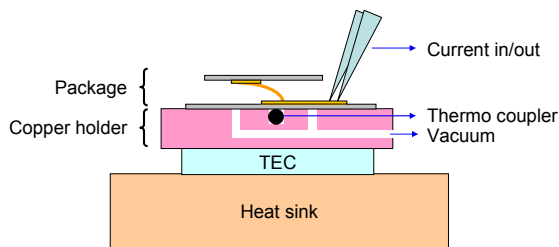


Figure 2. High current test setup. Silicon-silicon flip chip package with micro-springs on a temperature controlled stage is subject to DC current. No backside cooling structures are used on the package.

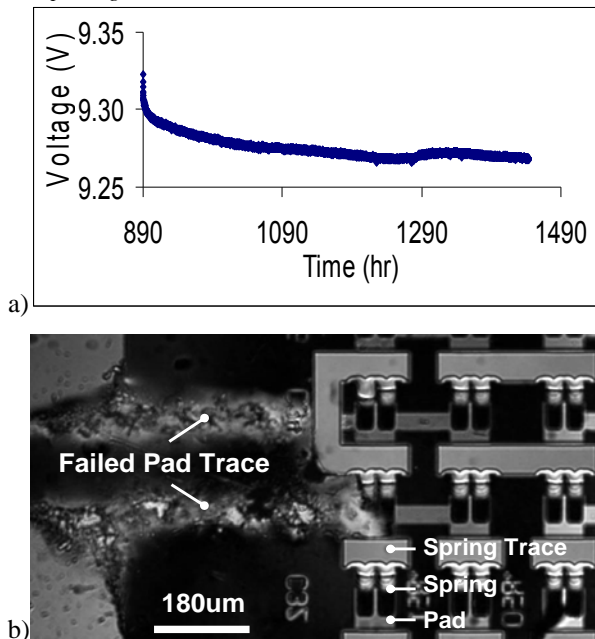


Figure 3. a) Four-wire measured voltage of a daisy chain (134 contacts in series) at 250 mA and 65 °C, showing stable resistance values. b) IR image into the package, showing failure of the trace metal and clean spring contacts.

To try and fail the spring contact, higher current is used. One ampere current is forced from  $I_{in}$  to  $I_{out}$ . The resistance is observed to be stable at  $\sim 9.5 \Omega$  and then failed after 181 hours

(Figure 4). The spring tip and body regions are severely damaged. The spring anchor region is intact.

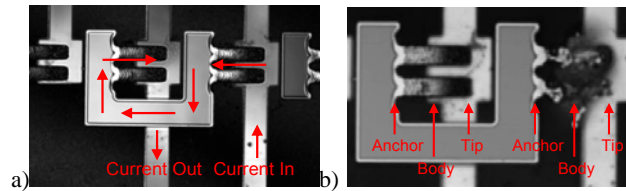


Figure 4. a) Initial image of 2-contact daisy chain. b) final image after 1 amp and 181 hrs at 65 °C, showing a failed spring on the right.

## TEMPERATURE MAPPING

Temperature maps were measured while different DC currents were applied. The temperatures were stable after less than a second and the images were recorded within a few minutes of changing the current. The stage was maintained at 65 °C. A hot spot at the corner of the bottom spring (near the current source) was observed (Figure 5). The trace connecting the spring was observed to heat as well as the anchor region of the springs. Less than a degree of increase in temperature was observed anywhere in the contact structure, including the hotspot on the tip, for currents up to 250 mA. The spatial resolution of the imager is 2.8 μm. At 500 mA the tip corner temperature increased a few degrees and by 800 mA was over 100 °C. The peak temperature increase of the anchor was also a few degrees at 500 mA and approximately 10 °C at 800 mA (Table 1). Large temperature rises can lead to asperity heating, material melting and transfer, increased constriction resistance, more heating, and eventually failure, while low temperature increases are associated with stable contacts [16].

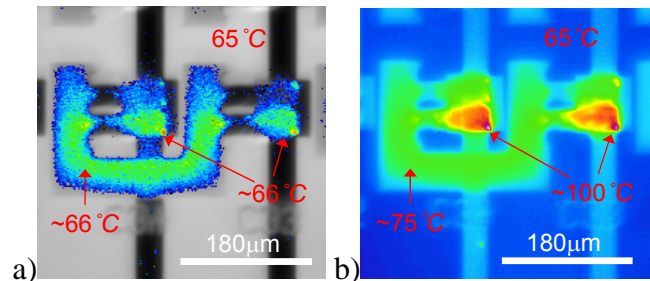


Figure 5. IR thermal image of two-wire test structure at 250 mA (a) and 800 mA (b). The figures have different temperature scales.

current [mA]	temperatuer increase [°C]	
	tip corner	anchor corner
10	<1	<1
150	<1	<1
250	<1	<1
500	8	5
800	35	10

Table 1. Observed temperature increase of tip corner and anchor corner.

The qualitative current distribution was observed through a laser excitation imaging technique (LSIM, Laser Signal Injection Microscope) synchronized with a current measurement, also

showing high current densities at the bottom tip corner and the traces (Figure 6).

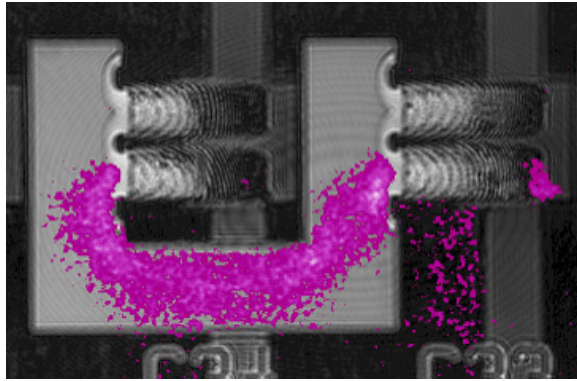


Figure 6. Observed current distribution.

## MODELING

Previously we modeled a single contact 4-wire test structure and fitted to measurements to determine the effective resistance components of the spring [7]. In one contact (two springs), the interface resistance between the spring tips and the pad chip metal was estimated at 11-41 mΩ. This information was combined with known dimensions to build a multilayer 3D finite element model (COMSOL) of the 2-contact daisy chain inside of the package used for high current tests. At 800 mA, the model predicts a peak current density of  $\sim 1.1 \times 10^7$  A/cm<sup>2</sup> at the corner of the bottom tip (Figure 7). About 63% of the current is passing through the bottom spring and 27% through the top spring, due to asymmetry of the geometry (Figure 8). This suggests that rotating the spring contacts 90° with respect to the pad trace so both tips see the same current distribution could lower the peak current density. This 90° rotation design was simulated and the current crowding spots were located in the anchor corner (Figure 9). The spring tip is not highest current density region anymore, suggesting that spring softening due to anchor weakening could be a relevant failure mechanism. Note that the anchor hot spots are not symmetrical, due to the spring chip trace connecting the two neighboring contacts. In a symmetric geometry, such as the spring anchor sitting on a large metal via connecting to a lower level of metal routing, lower peak current is expected.

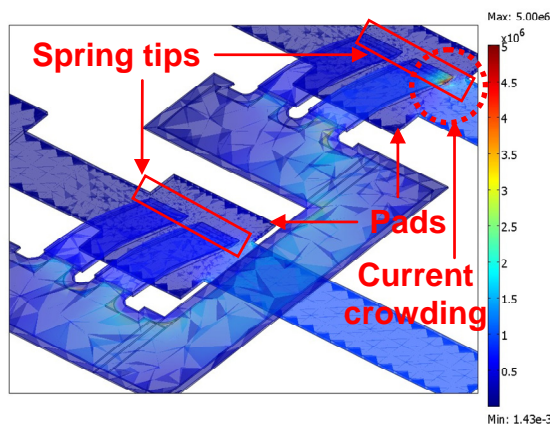


Figure 7. a) FEM model of current density distribution of 2-contact daisy chain at 800 mA.

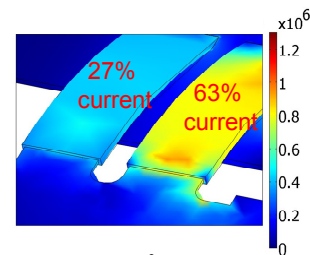


Figure 8. Current density (A/cm<sup>2</sup>) of the spring anchors and body at 800 mA. The right spring takes 63% of the current.

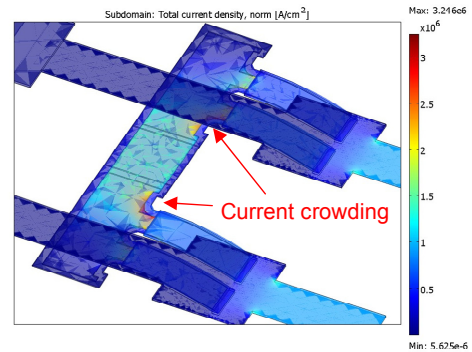


Figure 9. 90° rotation (compared to Figure 7) of spring contacts at 800 mA. The spring tips have lower current density than the anchor corners.

## FORCE MEASUREMENTS

The electrical integrity of the spring contact depends strongly on maintaining adequate force, unlike metallurgical bonded contacts like solder or stud bumps. The force is generated from the bending moment of the entire spring, but peak stress is at the anchor. The mechanical integrity of the springs was previously indirectly measured by observing stable 4-wire resistances in 0 °C – 100 °C thermocycling and 85 RH/ 85 °C humidity tests [6-7]. However these studies were performed at low (1 mA) or zero current. Modeling also shows current crowding in the anchor (Figure 8). Temperature imaging shows increases in the anchor temperature at 500 mA. In a die to substrate package, such as silicon to organic, the temperature increases could be more severe because of reduced substrate thermal conductivity. If the force of the spring weakens, the tip interface contact resistance could increase and more quickly fail, such as thermal runaway.

Possible force softening under high current heating was studied with a three contact 4-wire resistance measurement previously used for electrical measurements only [7]. This resistance measurement setup was integrated with a force scale to enable simultaneous force vs resistance measurements with ~1 mg resolution (more sensitive setups are possible). Current steps of 100 mA were applied but no force or resistance change was observed, suggesting the absence of any immediate heat induced force softening (Figure 10). Higher current tests were not compatible with the existing setup.

Measurements of the spring height as a function of temperature show the spring to be very stable, as the height does not change until heated by 300°C (Figure 11). The symmetry of the spring structural layers is believed to facilitate this. In contrast, stress induced self assembly springs made with bimorphs are inherently temperature sensitive. Future work includes investigating liftheights after being under load for extended times, to discern when creep effects are relevant.

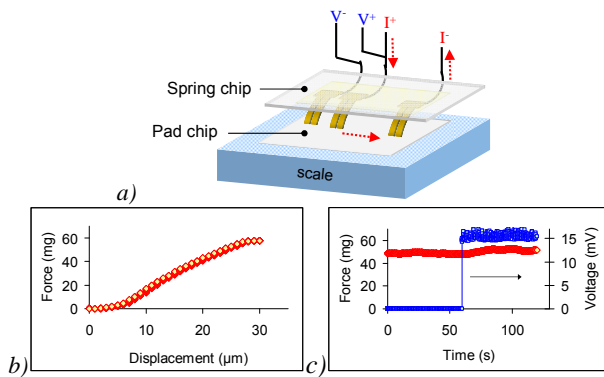


Figure 10. a) Single contact test structure schematic. The device under test is the center pair of springs and the pad sits on a force scale to simultaneously measure spring force. b) Force curve for the 6 spring test structure and c) A 100 mA current step (at 25  $\mu\text{m}$  compression), showing no force change.

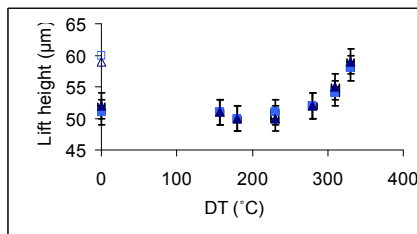


Figure 11. Measured lift height vs. temperature, showing stable heights until 300°C.

## CONCLUSIONS

Gold to gold microspring pressure contacts in silicon-silicon packages are capable of carrying 250 mA ( $2 \times 10^5 \text{ A/cm}^2$  average current density) for more than 1700 hours and 1A ( $1 \times 10^6 \text{ A/cm}^2$  average current density) for 181 hours at 65 °C. Finite element simulation of the current density distribution matches well with observed hot spot locations and failure locations. An improved design is proposed to reduce density by 40 times at the spring tip. No mechanical softening of the spring is observed for 100 mA current stressing. Recently we have flip-chip-assembled active silicon IC die onto an organic substrate with 2d array spring contacts [17], and plan to next study the high current properties of this package.

## ACKNOWLEDGEMENTS

We thank Lai Wong for fabrication support, and Quantum Force Instruments and Olympus for use of measurement tools.

## REFERENCES

- [1] E. M. Chow, C. Chua, T. Hantschel, K. Van Schuylenbergh, and D. K. Fork, "Pressure contact micro-springs in small pitch flip-chip packages," *IEEE Transactions on Components and Packaging Technologies*, vol. 29, pp. 796-803, (2006).
- [2] E. M. Chow, D. K. Fork, C. L. Chua, K. V. Schuylenbergh, and T. Hantschel, "Wafer-level packaging with soldered stress-engineered microsprings," *IEEE Transactions on Advanced Packaging*, vol. 32, pp. 372-378, (2009).
- [3] C. L. Chua, D. K. Fork, K. V. Schuylenbergh, and J.-P. Lu, "Out-of-plane high-Q inductors on low-resistance silicon,"

- Journal of Microelectromechanical Systems*, vol. 12, pp. 989-995, (2003).
- [4] M. A. Rosa, D. De Bruyker, A. R. Volkel, E. Peeters, and J. Dunec, "A novel external electrode configuration for the electrostatic actuation of MEMS based devices," *IOP Journal of Micromechanics and Microengineering*, vol. 14, pp. 446-451, (2004).
- [5] T. Hantschel, E. M. Chow, D. Rudolph, and D.K. Fork, "Stressed metal probes for atomic force microscopy," *Applied Physics Letters*, vol. 81, pp. 3070-3072, (2002).
- [6] I. Shubin, E. M. Chow, J. Cunningham, D. DeBruyker, C. Chua, B. Cheng, J. C. Knights, K. Sahasrabudde, Y. Luo, A. Chow, J. Simons, A. V. Krishnamoorthy, R. Hopkins, R. Drost, R. Ho, D. Douglas, J. Mitchell, "Novel packaging with rematable spring interconnect chips for MCM," 59th Electronic Components and Technology Conference (ECTC), May 26-29, (2009), pp.1053 – 1058.
- [7] B. Cheng, E. M. Chow, D. DeBruyker, C. Chua, K. Sahasrabudde, I. Shubin, J. Cunningham, Y. Luo and A. V. Krishnamoorthy, "Microspring Characterization and Flip Chip Assembly Reliability," 42th International Microelectronics and Packaging Society (IMAPS), November 1-5, (2009).
- [8] D. Yang, Y. C. Chan and K. N. Tu, "The time-dependent melting failure in flip chip lead-free solder interconnects under current stressing," *Applied Physics Letters*, vol. 93, 041907, (2008).
- [9] K. N. Tu, "Recent advances on electromigration in very-large-scale-integration of interconnects," *J. of Applied Physics*, vol. 94, pp. 5451-5473, (2003).
- [10] Chih Chen and S. W. Liang, "Electromigration issues in lead-free solder joints", *J Mater Sci: Mater Electron*, vol. 18, pp. 259–268, (2007).
- [11] "Interconnect," *The International Technology Roadmap for Semiconductors*, (2007) Edition.
- [12] W.-S. Kwon and K.-W. Paik, "High Current Induced Failure of ACAs Flip Chip Joint," 52th Electronic Components and Technology Conference (ECTC), May 28-31, (2002), pp. 1130-1134.
- [13] J. Schauer, N. Pinckney, N. Nettleton, and D. Popovic, "A test platform for the thermal electrical and mechanical characterization of packages," 42nd International Symposium on Microelectronics (IMAPS), November 1-5, (2009).
- [14] J. Maciel, S. Majumder, R. Morrison, J. Lampen, "Lifetime characteristics of ohmic MEMS switches," *Proceedings of the SPIE - The International Society for Optical Engineering*, vol. 5343, pp. 9-14, (2003).
- [15] O. Rezvanian, C. Brown, M. A. Zikry, A. I. Kingon, J. Krim, D. L. Irving, and D. W. Brenner, "The role of creep in the time-dependent resistance of ohmic gold contacts in radio frequency microelectromechanical system devices", *J. Applied Physics*, vol. 104, 024513, (2008).
- [16] Christopher John Brown, "Impact of environmental conditions on the contact physics of gold contact RF Microelectromechanical Systems (MEMS) switches," Doctor of Philosophy thesis, (2008).
- [17] I. Shubin, E. M. Chow, J. Cunningham, D. Debruyker, M. Grier, B. Cheng, N. Nettleton, G. Anderson, J. Simons, D. Douglas, "A Package Demonstration with Solder Free Compliant Flexible Interconnects," 60th Electronics Components and Technology Conference (ECTC), accepted for publication, (2010).

# LITHOGRAPHICAL PATTERNING AND CARBONIZATION OF ELECTROSPUN SU-8 NANOFIBERS FOR A HIGH CAPACITY ELECTRODE

Gwan-Ha Kim<sup>1</sup>, Gloria J. Kim<sup>2</sup> and Yong-Kyu "YK" Yoon<sup>1\*</sup>

<sup>1</sup> Electrical Engineering, University at Buffalo, The State University of New York, Buffalo, NY 14260, USA

<sup>2</sup> Biomedical Engineering, University at Buffalo, The State University of New York, Buffalo, NY 14260, USA

## ABSTRACT

To fabricate large surface area conductive nanofibers for a high capacity electrode application in energy storage devices, we have successfully developed a three-step fabrication process: (1) generation of electrospun nanofibers with a photopatternable negative tone epoxy, SU-8, (2) lithographical patterning of the SU-8 nanofibers in a desired microscopic shape, and (3) subsequent thermal treatment for carbonization in an inert environment. Also, a multiple intermittent electrospinning scheme has been successfully established to stack the nanofibers as thick as 80  $\mu\text{m}$ , demonstrating the possibility of three dimensional (3-D) nanofiber electrodes. This thickness can be further increased by repeating the scheme. We show the fiber diameter as a function of bias voltage and distance between the nozzle and the collector electrodes, the thickness of nanofiber stacks, lithographical patterning capability, and the electrical resistivity of the carbonized SU-8. This process will greatly impact research on high-density and fast-response battery and super capacitor development.

## INTRODUCTION

Electrospinning provides a simple and a cost effective method for generating thin fibers from various materials that include polymers, composites, and ceramics [1]. The thin diameter of fibers provides a large surface area to volume ratio and superior mechanical performance that makes their extensive applications such as filtration for submicron or nanomaterials, separator, tissue scaffolding, drug delivery system, artificial organ and so on [2-5]. However, electrospun nanofibers are generally collected as two-dimensional membranes with randomly arranged structures and small bulk thickness, and also there are not much efficient ways available for micro scale patterning of such randomly grown electrospun nanofibers, which greatly limits their applicability for many future usages in biomedical, chemical, and nanotechnology. A few literatures have reported on the patterning of electrospun nanofibers requiring a dexterous fabrication technique [6-8]. Zhang and Chang have demonstrated that ultrafine electrospun nanofibers can be fabricated in three dimensional (3-D) fibrous tubes by a novel static method [9]. Li and colleagues have demonstrated that the nanofibers can be uniaxially aligned by introducing an insulating gap into the conductive collector [10]. However, these studies have limited their compatibility with other processes such as an accurate definition of 3-D microstructures using UV lithography patterning.

Meantime, the electrical characteristics of conductive polymers, such as polyaniline, polypyrrole, and polyethylene oxide, have attracted much interest recently [11-13]. However, the electrically conductive fiber shows relatively high resistivity. On the other hand, the carbonization of SU-8 microstructures is known to provide outstanding electrical, mechanical and chemical performance [14]. Very recently, research on electrospun SU-8 nanofibers and its carbonization have been reported by the authors [15]. We have further developed a simple method to prepare a bulk electrospun nanofibers and their patterning by using multiple times continuous growing and the UV lithography process, respectively. The advantages of this approach are twofold. It allows microscopic patterning and the process would be compatibility with the

semiconductor process.

In this study, we demonstrate a thick stack of electrospun nanofibers using an intermittent approach, electrospun nanofiber patterning by using ultraviolet (UV) lithography, and the carbonization of electrospun nanofibers. Also, we report on the low resistivity carbon nanofibers. We investigate the controllability of the average nanofiber diameter, the thickness of patterned nanofiber structures, and an adequate resistivity of electrospun nanofibers.

## EXPERIMENTS DETAILS

Random SU-8 nanofibers are fabricated using the electrospinning process under various conditions. SU-8 2025 (Microchem Inc.) is used as the working fluid. SU-8 2025 is diluted using cyclopentanone in a range of a concentration of 60.87% to 68.55% (by weight). All solutions are stored in room temperature and all experiments are conducted in room temperature in air.

The experimental setup used for the electrospinning process consists of an adjustable DC power supply (DEL HVPS MOD 603 30KV POS, Spellman High Voltage Electronic Corp., USA) capable of generating DC voltage in a range of 0–30 kV, a syringe pump (NE-1000, New Era Pump Systems, Inc., USA) on which a 5 ml syringe is connected with a stainless steel needle having an inner diameter of 0.2 mm. The working distance between the needle and the collector is in a range of 7.5–25 cm. Positive voltages applied to SU-8 solutions are in a range of 12.5–17.5 kV. The solution flow rates are controlled by a syringe pump and the pumping rate is 0.02 ml/min. The electrospun nanofibers have diameters ranging between 340 nm and 3.3 $\mu\text{m}$ , depending upon different electrospinning conditions. The diameter of SU-8 electrospun nanofibers is measured by a field emission scanning electron microscopy (FE-SEM) system (SU-70, Hitachi, Japan). A UV exposure system (LS30, OAI, Inc) has been used for the patterning of electrospun nanofibers.

A thick stack of electrospun SU-8 nanofibers are deposited on a Si substrate (Figure 1a). Ultraviolet (UV) exposure (i-line,  $\lambda=365\text{nm}$ ) is applied for patterning the nanofibers, followed by post exposure bake (Figure 1b). After the electrospun nanofibers are

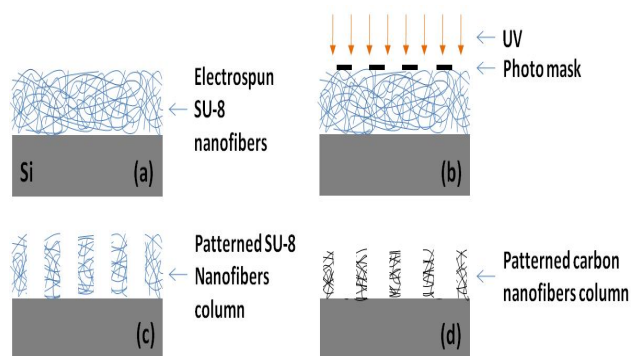


Figure 1. Schematic of the fabrication process: (a) preparation of electrospun SU-8 nanofibers, (b) lithographic patterning of fibers, (c) development of UV exposed fibers, and (d) formation of patterned carbon nanofiber columns by pyrolysis.

developed (Figure 1c), the substrate undergoes pyrolysis (Figure 1d). Electrospun SU-8 nanofibers are converted into the carbon nanofiber by pyrolysis [14, 15].

The resistivities of carbonized SU-8 thin films are measured by using a four-point probe head (C4S, Cascade Microtech, Inc., USA), a current source (HP 6177C, HP, USA), a current meter (194A, Keithley Instruments Inc., USA), and a voltage meter (195A, Keithley Instruments Inc., USA), at room temperature. And the Auger electron microscopy (AES) (Microlab 310-D, Thermo VG Scientific, USA) analysis is conducted to verify change in the composition of electrospun nanofibers after pyrolysis.

## RESULTS AND DISCUSSION

SU-8 Electrospun nanofibers are fabricated by the electrospinning process under various conditions. One of the most important parameters among the controlled variables is the effect of the applied voltage and working distance between the needle and the collector. Figure 2 shows the variation of an average electrospun fiber diameter as a function of distance between the needle and the collector at various applied voltages. The average diameter of electrospun nanofibers becomes smaller as the travel distance increases due to: (i) more solvent evaporation, and (ii) continuous stretching due to electrostatic force [16, 17]. As the working distance increases, the average diameter of electrospun fibers decreases. It has been found that a minimum distance is required to allow the fibers to have sufficient time to remove solvent before reaching the collector [18].

Meanwhile, the average diameter of the electrospun fibers increases when a higher voltage is applied. In case of SU-8, the higher voltages yield the larger fiber diameters. In electrospinning, the charge transport under the applied electric field is a main mechanism for electrospun fiber deposition, which is attributed to the mass flow of SU-8 from the needle tip. Deitzel and colleagues have reported that an increase in applied voltage causes a change in the shape of the jet initiating point, and hence the structure and morphology of fibers [19]. In case of SU-8, the diameter of electrospun fibers largely varies depending on the applied voltage.

The relationship between the SU-8 concentrations and the diameter of electrospun fibers has been studied. Solution

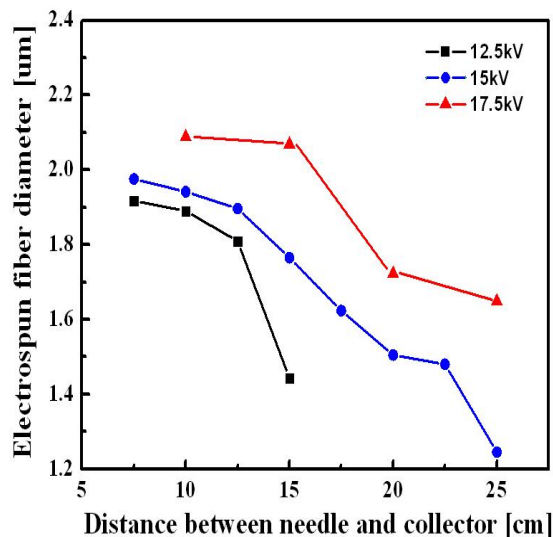


Figure 2. Variation in the diameter of electrospun fibers as a function of distance between the needle and the collector at various applied voltages.

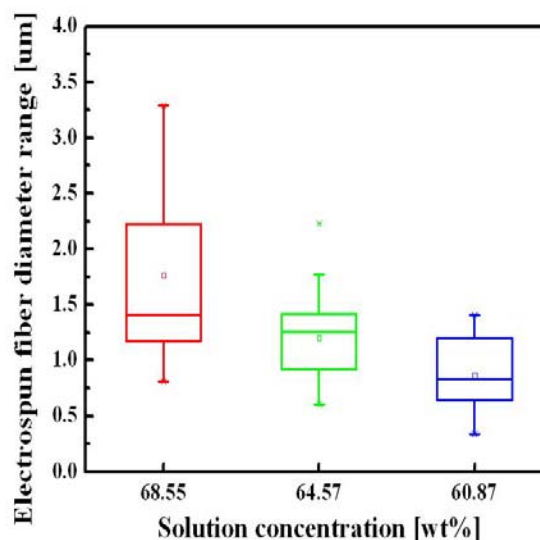


Figure 3. Variation in electrospun fiber diameter as a function of SU-8 solution concentration.

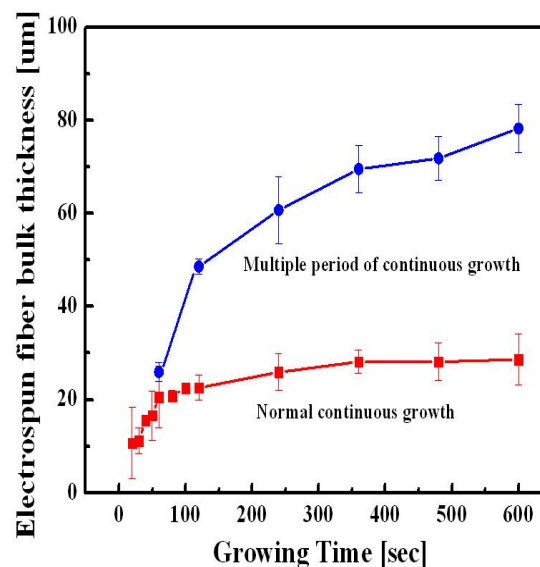


Figure 4. Effect of multiple periods of continuous growth and normal continuous growth on nano fiber stacking.

concentration along with viscosity and surface tension affects the condition of the electrospun fiber formation [20]. Figure 3 shows a distribution of fiber diameters obtained from SU-8 electrospinning with three different concentrations of 68.55, 64.57, and 60.87 wt% and all other variables maintained constant. A decrease in solution concentration results in fibers with smaller diameters. In this case, decreasing the concentration of a SU-8 solution can also affect its surface tension. The effects of solution properties on fiber diameter have previously been discussed for other polymeric systems [17, 19]. As seen with other polymers, SU-8 has a linear relationship between solution concentration and resulting fiber diameter. The increase in viscosity that comes with concentration increase causes this effect. These relationships indicate that solution concentration plays an important role in determining the fiber diameter.

Although we can obtain a uniform and appropriate thickness of the electrospun fiber, we need a thicker bulk electrospun fiber stack

for some applications like an energy storage device, electronic device, and bio chemical applications. For such applications, high fiber packing density and high porosity may be desirable. We demonstrate an easier approach. Figure 4 shows two electrospinning conditions: multiple periods of continuous deposition (growth) and normal continuous deposition (growth) of electrospun fibers. These plots can be divided into two sections. When SU-8 fiber growing time is less than 60sec, the growth rate of SU-8 electrospun fibers increases linearly. But, growth rate is saturated after 60sec as shown in the normal continuous growth plot. It is attributed to that deposited electrospun fibers on the collector are positively charged due to the slow discharge time of the positive ions through the none conducting nanofibers. Accumulated positive ions in the electrospun fibers are repelling the subsequent nanofibers and preventing further growing. This charge repelling phenomenon has been much relieved by using a multiple periods of continuous growth approach where the electrospinning process has been performed for 30 sec followed by a rest period of 30 sec before the next electrospinning step begins. Charge in the electrospun fibers is slowly discharged during the rest time. And the repelling force has been significantly reduced and we have achieved a thick stack of electrospun fiber upto 80  $\mu\text{m}$  after twelve 30 sec cycles.

For micro/nanometer scale integrated devices, accurate definition of electrospun fibers using ultraviolet (UV) lithography will be very useful. Although patterned electrodes or micro-contact printing can allow nanofiber patterning to some extent [19], it is quite limited from the viewpoint of the patternable thickness and the patternability in arbitrary shape. A new approach applying UV lithography directly on electrospun nanofibers is proposed and detailed. This approach does not require an additional process like a reactive ion etching process after lithography or micro molding. Figure 5 show SEM images of (a) a line with a width of 120  $\mu\text{m}$  and (b) a circle with a diameter of 100  $\mu\text{m}$ . While some edges look rough because of the edge of some nanofibers, the overall shape is well defined by the original photo mask geometry with a good fidelity.

In addition, these patterned nanofibers have been further processed using pyrolysis, converting the patterned electrospun fibers into carbon nanofibers, resulting in chemically and

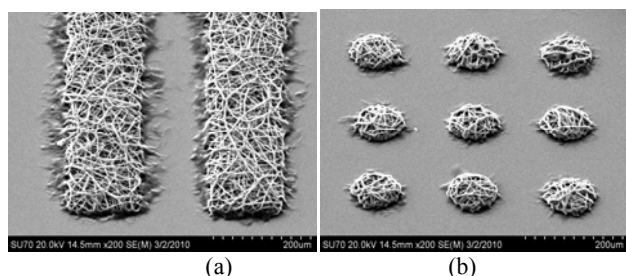


Figure 5. SEM images of patterned SU-8 electrospun fibers: (a) 120  $\mu\text{m}$  wide lines and (b) 100  $\mu\text{m}$  diameter circles.

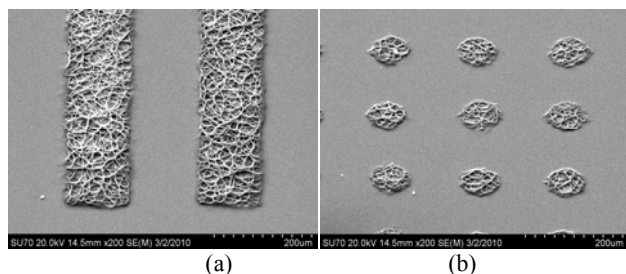


Figure 6. SEM images of pyrolyzed SU-8 electrospun fiber patterns: (a) 120  $\mu\text{m}$  wide lines and (b) 100  $\mu\text{m}$  diameter circles.

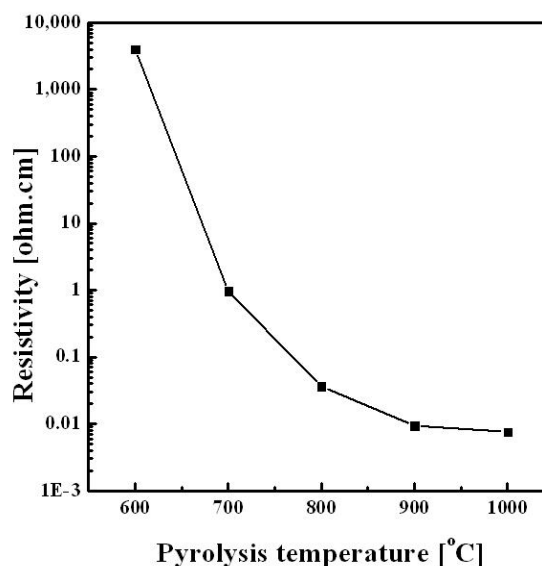


Figure 7. Resistivity of pyrolyzed SU-8 as a function of pyrolysis temperature.

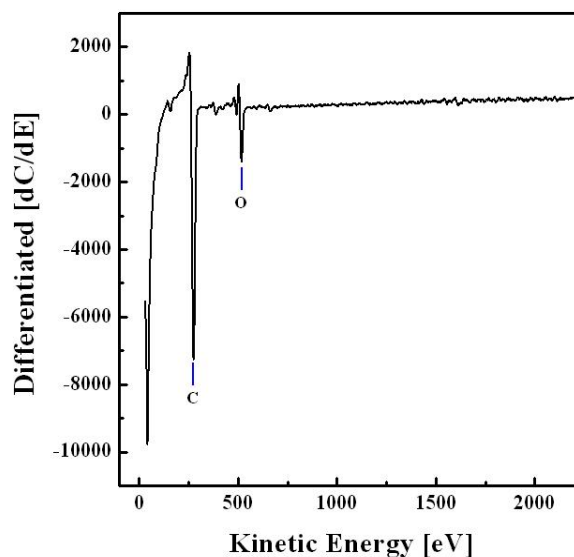


Figure 8. AES analysis of pyrolyzed SU-8 electrospun fiber.

mechanically stable, low cost, high surface area electrodes. Carbon nanofibers are finding enormous applications in unconventional energy sources and storage cells due to their enhanced conductivity and high aspect ratio. Carbon nanofiber reinforced composites offer increased stiffness, high strength and low electrical resistivity [21]. Figure 6 shows SEM images of patterned electrospun fibers of (a) a line with a line width of 120  $\mu\text{m}$  and (b) a circle with a diameter of 100  $\mu\text{m}$ , obtained after pyrolysis in a nitrogen purged quartz tube furnace.

A thin SU-8 film is prepared for resistivity measurement after the pyrolysis by using four-point probe system. Figure 7 shows the resistivity of the pyrolyzed carbon film at different pyrolysis temperatures. The resistivity decreases as the pyrolysis temperature increases. The decrease in resistivity with an increase in temperature is attributed to the degree of graphitization [22]. The higher



temperature of pyrolysis, the higher the extent of graphitization, and thus the lower resistivity.

The AES analysis has been conducted to verify change in composition of electrospun fibers after the pyrolysis. The direct analysis of the surface composition of carbon film can give us certain information about it. Figure 8 shows an AES surface scan result on the carbon film after the pyrolysis of a thin SU-8 film. From the AES surface scan result, it is expected that all polymer components in SU-8 has been changed into carbon. The existence of the oxygen element may be due to the exposure of the sample in air before and during AES analysis.

## CONCLUSION

We have highlighted studies that examine the effect of each parameter in the SU-8 (a photopatternable negative tone epoxy) electrospinning process. Electrospun SU-8 nanofibers have been successfully obtained. The diameter of the fiber is affected by the solution concentration, electric field and the distance between the needle tip and the collector. A multiple periods of continuous growth method enables thick bulk electrospun fiber deposition. After twelve 30 second cycles in alternating electrospinning and pose steps, a stack as thick as 80  $\mu\text{m}$  has been successfully obtained. The achievable thickness is not limited to the thickness though. Furthermore, a conventional UV lithography process has been used to pattern the electrospun fibers. This method greatly facilitates the micropatterning of nanofibers and must be very versatile and useful for micro/nano fiber integrated devices requiring accurate pattern size and shape. The patterned electrospun SU-8 nanofibers have been further pyrolyzed, turning into the patterned carbon nanofibers, which are considered as a good candidate of a high capacity electrode for high density energy storage devices such microbatteries and capacitors.

## ACKNOWLEDGEMENT

This work is supported by the National Science Foundation (CAREER:ECCS 0748153 and CMMI 0826434) and the Korea Research Foundation Grant funded by the Korean Government (KRF-2008-357-D00104). Also, the authors would like to thank Dr. Seong-Hyok Kim and Dr. Mark G. Allen in the Georgia Institute of Technology for valuable discussion and some dielectric material deposition.

## REFERENCES

- [1] D. Li and Y. Xia, "Electrospinning of nanofibers: Reinventing the Wheel", *Adv. Mater.*, 16, 1151 (2004).
- [2] J.R. Kim, S.W. Choi, S.M. Jo, W.S. Lee, and B.C. Kim, "Characterization and Properties of PVdF-HFP-Based Fibrous Polymer Electrolyte Membrane Prepared by Electrospinning", *J. Electrochem. Soc.*, 152, A295 (2005).
- [3] W.-J. Li, C.T. Laurencin, E.J. Caterson, R.S. Tuan, and F.K. Ko, "Electrospun nanofibrous structure: A novel scaffold for tissue engineering", *Journal of Biomedical Materials Research Part A*, 60, 613 (2002).
- [4] J.R. Venugopal, S. Low, A.T. Choon, A.B. Kumar, and S. Ramakrishna, "Nanobioengineered Electrospun Composite Nanofibers and Osteoblasts for Bone Regeneration", *Artificial Organs*, 32, 388 (2008).
- [5] N.M. Neves, R. Campos, A. Pedro, J. Cunha, F. Macedo, and R.L. Reis, "Patterning of polymer nanofiber meshes by electrospinning for biomedical applications", *International Journal of Nanomedicine*, 2, 433 (2007).
- [6] E.P.S. Tan, S.Y. Ng, and C.T. Lim, "Nano tensile testing of a single ultrafine polymeric nanofiber", *Biomaterials*, 26, 1453

- (2005).
- [7] R. Inai, M. Kotaki, and S. Ramakrishna, "Structure and Properties of Electrospun PLLA Single Nanofibres", *Nanotechnology*, 16, 208 (2005).
- [8] Y. Ishii, H. Sakai, and H. Murata, "Fabrication of a submicron patterned electrode using an electrospun single fiber as a shadow-mask", *Thin Solid Films*, 518, 647 (2009).
- [9] D. Zhang and J. Chang, "Electrospinning of Three-Dimensional Nanofibrous Tubes with Controllable Architectures", *Nano Letters*, 8, 3283 (2008).
- [10] D. Li, G. Ouyang, J.T. McCann, and Y. Xia, "Collecting Electrospun Nanofibers with Patterned Electrodes", *Nano Letters*, 5, 913 (2005).
- [11] I.D. Norris, M.M. Shaker, F.K. Ko, and A.G. MacDiarmid, "Electrostatic Fabrication of Ultrafine Conducting Fibers: Polyaniline/Polyethylene Oxide Blends," *Synth. Met.*, 114, 109 (2000).
- [12] I.S. Chronakis, S. Grapenson, and A. Jakob, "Conductive polypyrrole nanofibers via electrospinning: Electrical and morphological properties", *Polymer*, 47, 1597 (2006).
- [13] J.W. Lu, Y.L. Zhu, Z.X. Guo, P. Hu and J. Yu, "Electrospinning of sodium alginate with poly(ethylene oxide)", *Polymer*, 47, 8026 (2006).
- [14] C. Wang, G. Jia, L.H. Taherabadi, and M.J. Madou, "A Novel Method for the Fabrication of High-Aspect Ratio C-MEMS Structures", *Journal of Microelectromechanical Systems*, 14, 348 (2005).
- [15] G.H. Kim, E. Kozarsky, H.S. Jee, K.T. Kim, J. Kim, E. Takeuchi, and Y.K. Yoon, "Carbon Nanotube Embedded Three Dimensional (3-D) Carbon Microelectrodes for Rechargeable Microbatteries", AVS 56th International Symposium & Exhibition, 11/8-13/09, San Jose, CA (2009).
- [16] J. Doshi and D.H. Reneker, "Electrospinning Process and Applications of Electrospun Fibers", *J. Electrostatics*, 35, 151 (1995).
- [17] M.M. Demir, I. Yilgor, E. Yilgor, and B. Erman, "Electrospinning of polyurethane fibers", *Polymers*, 43, 3303 (2002).
- [18] X.Y. Geng, O.H. Kwon, and J.H. Jang, "Electrospinning of chitosan dissolved in concentrated acetic acid solution", *Biomaterials*, 26, 5427 (2005).
- [19] J. Shi, L. Wang, and Y. Chen, "Microcontact Printing and Lithographic Patterning of Electrospun Nanofibers", *Langmuir*, 25, 6015 (2009).
- [20] J.M. Deitzel, J. Kleinmeyer, D. Harris, N.C. Beck Tan, "The Effect of Processing Variables on the Morphology of Electrospun Nanofibers and Textiles", *Polymer*, 42, 261 (2001).
- [21] T. Subbiah, G.S. Bhat, R.W. Tock, S. Parameswaran, S.S. Ramkumar, "Electrospinning of Nanofibers", *Journal of Applied Polymer Science*, 96, 557 (2005).
- [22] A. Singh, J. Jayaram, M.J. Madou, and S. Akbar, "Pyrolysis of negative photoresists to fabricate carbon structures for microelectromechanical systems and electrochemical applications", *Journal of the electrochemical Society*, 149, E78 (2002).

## CONTACT

Gwan-Ha Kim [gwanhaki@buffalo.edu](mailto:gwanhaki@buffalo.edu),

\*Yong-Kyu Yoon, tel: +1-716-645-1029; [ykyoon@buffalo.edu](mailto:ykyoon@buffalo.edu)

# OHMIC CONTACT WITH ENHANCED STABILITY TO POLYCRYSTALLINE SILICON CARBIDE VIA CARBON INTERFACIAL LAYER

F. Liu<sup>1,2\*</sup>, B. Hsia<sup>2</sup>, D. G. Senesky<sup>1,3</sup>, C. Carraro<sup>1,2</sup>, A. P. Pisano<sup>1,3</sup>, and R. Maboudian<sup>1,2</sup>

<sup>1</sup>Berkeley Sensor & Actuator Center, Berkeley, California, USA

<sup>2</sup>Department of Chemical Engineering, University of California at Berkeley, Berkeley, California, USA

<sup>3</sup>Department of Mechanical Engineering, University of California at Berkeley, Berkeley, California, USA

## ABSTRACT

The development of electrical contacts to silicon carbide with low specific resistivity and stability is a critical requirement for harsh environment MEMS applications. In this paper, we present a novel method to lower the ohmic contact resistivity and enhance the stability of Pt contacts to polycrystalline 3C-SiC (poly-SiC) operated at elevated temperatures. In particular, nanocrystalline graphite is grown at the interface between poly-SiC and Pt. The contact resistance of Pt/C/SiC is found to be half the value of Pt/SiC at room temperature. In addition, the temperature dependence of the contact resistivity results show that with a carbon interfacial layer, stable ohmic contacts to poly-SiC are achieved at 540°C temperature in air.

## INTRODUCTION

Recently, for industries such as automobile, petroleum and aerospace, there has been growing interest in harsh environment electronic and sensor technologies. Harsh environment, involving high temperature, high radiation, corrosion and erosion, requires thermally stable and robust materials for device applications. Silicon carbide is well known for its high mechanical strength, chemical stability, high thermal conductivity and electrical stability at elevated temperatures [1]. As a consequence, SiC electronics and microelectromechanical system (MEMS) devices have attracted much attention [2, 3]. For these SiC semiconductor devices, one of the most critical processes is the formation of low resistivity and thermally stable ohmic contacts for electrical contacts and interconnects.

Generally, an ohmic contacts to single crystalline 4H, 6H and 3C-SiC are formed by deposition of metals or metal alloys on highly doped SiC films, followed by high temperature annealing. Various metal-to-SiC ohmic contacts have been reported for n-type SiC metallization [4]. For example, it has been reported that Ni can form low ohmic contact to n-type SiC [4]. However, the oxidation of Ni is found to occur at temperatures as low as 300 °C in air, with subsequent increase in the contact resistivity (by several orders of magnitude within a few hours) [5]. Compared to other metals, Pt, with its high thermal stability and high phase change temperature, is an outstanding candidate for SiC metallization. It is known polycrystalline SiC can be deposited at lower temperature compared to single crystalline SiC, thus is compatible for MEMS process. Although Pt to poly-SiC contact has been reported previously [4, 5], the effect of interfacial chemistry on the Pt to poly-SiC contact has not been studied.

It was reported that the presence of a C-rich layer at the SiC-nickel interface could be responsible for the low resistivity ohmic contact formation [6]. Among the various carbon forms, graphite holds the distinction of being the most stable form of carbon under standard conditions. The presence of a graphitic carbon layer at the interface between the metal and SiC not only could lower the contact resistivity, but also could build a barrier to diffusion and reactions between the metal and SiC at high temperature. Therefore, the graphitization of the SiC film before metallization could improve its metallization performance

afterwards. Recently, graphene, a single layer of graphite, has been synthesized on single crystalline SiC by Si sublimation from a SiC substrate in an ultrahigh vacuum (UHV) or inert-ambient annealing chamber [7]. This process is compatible with planar semiconductor processing. In contrast to the post metal deposition annealing, SiC film pre-annealing could play a critical role in its metallization behavior.

The objective of this paper is to demonstrate thermally stable, low resistivity ohmic contacts to poly-SiC films for harsh environment MEMS applications. Graphitized poly-SiC film metallization is studied in comparison with the as-deposited poly-SiC film. In particular, the poly-SiC film is annealed at 1300 °C in an UHV environment, resulting in the growth of a nanocrystalline graphite layer. The contact resistivity measurements show that Pt/C/SiC contact resistivity is reduced to half the value of Pt/SiC at room temperature. Furthermore, the Pt/C/SiC contact resistivity changes minimally from room temperature to 540 °C in the air, while the Pt/SiC increases from  $1.3 \times 10^{-5} \Omega \cdot \text{cm}^2$  to  $2.5 \times 10^{-5} \Omega \cdot \text{cm}^2$ . The results yield valuable information on SiC metallization stability and approaches to enhancing it, and may open the door to investigations of various metals to graphitized SiC contact studies.

## EXPERIMENTAL

### Fabrication process

In this work, the circular transmission line model (CTLM) [8] method is used to characterize the contact behavior and contact resistivity (Fig.1). The advantage of this structure is that only one lithography step is needed. The fabrication process of the as-deposited and annealed poly-SiC CTLM structures are shown in Fig.2. Nitrogen-doped (in-situ) poly-SiC films are grown by low pressure chemical vapor deposition (LPCVD) at 800 °C, using methylsilane and dichlorosilane precursors. The details of the film deposition process can be found in Ref. [9]. Poly-SiC film thickness is 2.5 μm, with the resistivity of 0.01 Ω-cm. The poly-SiC film is electrically isolated from Si (100) substrate by 1 μm LPCVD low temperature grown silicon oxide. After poly-SiC film deposition, samples are annealed in a UHV chamber (~10<sup>-9</sup> Torr) at 1300 °C for 5 min. Raman (HORIBA Jobin Yvon) spectra are used to characterize the carbon structure on top of the annealed poly-SiC surface. Further analysis of raman spectra will be discussed in later sections. The annealed and the as-deposited samples are dipped in HF to remove oxide, and then are patterned by photolithography of 1 μm g-line and 1 μm i-line to yield an undercut profile, which disallows sidewall coverage in the metal deposition step, yielding smooth edges. Then, 200 nm-Pt is sputtered in an Edwards RF sputter coater, followed by lift-off in acetone. Finally, the annealed samples are exposed to O<sub>2</sub> plasma to remove the nanocrystalline graphite layer in the unexposed SiC region. Raman spectroscopy is used to confirm the removal of the carbon layer after etching.

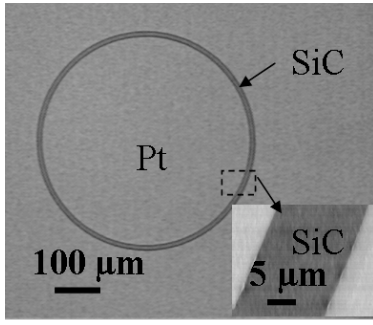


Figure 1: Optical and SEM image of CTLM structure. The radius of the ring is 250  $\mu\text{m}$ , and the width of the gap is varied at 5 $\mu\text{m}$ , 10 $\mu\text{m}$ , 15 $\mu\text{m}$  and 20 $\mu\text{m}$ .

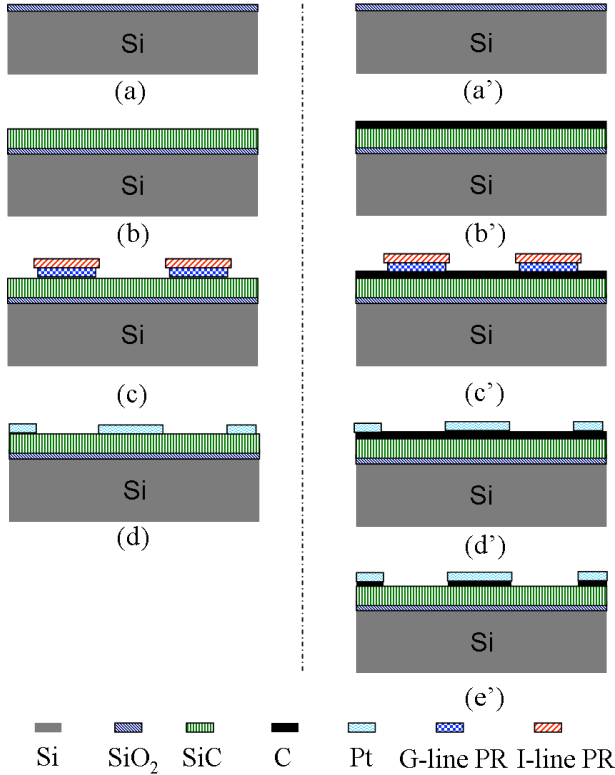


Figure 2: CTLM test structure fabrication process. (a)-(d), as-deposited poly-SiC fabrication process; (a')-(e') annealed poly-SiC fabrication process.

### Testing setup

After microfabrication, the samples are fixed in a 24-pin ceramic package, using Resbond 940LE ceramic adhesive, which can withstand up to 1370  $^{\circ}\text{C}$ . The test structure is wirebonded to the package by Al wire, and the package pins are connected to the testing circuit by Durabond 952 Ni adhesive, which can withstand up to 1100  $^{\circ}\text{C}$ . Four-point I-V measurement is realized by a Keithley model 2400 system to avoid parasitic resistance from the probe to metal contact and the testing circuits.

According to CTLM, the measured resistance ( $R$ ) is:

$$R = \frac{R_s}{2\pi} \ln\left(1 + \frac{d}{r_0}\right) + \frac{R_s}{2\pi} \sqrt{\frac{\rho_c}{R_s}} \left(\frac{1}{r_0} + \frac{1}{r_0 + d}\right) \quad (1)$$

where  $R_s$  is the sheet resistance of the SiC film,  $d$  and  $r_0$  are the

CTLM gap width and radius, and  $\rho_c$  is the contact resistivity. By measuring  $R$ , contact resistivity is calculated from Eq. 1.

The samples are heated up by an Isotemp hotplate in air. After high temperature I-V measurement, the samples are characterized by a Siemens D5000 x-ray diffraction (XRD) to probe possible interfacial reactions.

## RESULTS AND DISCUSSION

As shown in Fig. 3, the SiC transverse-optical (TO) and longitudinal-optical (LO) peak of the as-deposited and annealed samples indicate the cubic structure of the SiC film. The Raman TO peak of the as-deposited poly-SiC is located at around 790  $\text{cm}^{-1}$ , while that of the annealed poly-SiC is located at around 792  $\text{cm}^{-1}$ . The shift of the TO peak position ( $\nu_{\text{TO}}$ ) away from the standard TO peak position 796  $\text{cm}^{-1}$  has been used to characterize the in-plane bi-axial residual strain ( $\epsilon_{\text{bi}}$ ) of the single crystalline 3C-SiC films grown [10]. The proposed strain induced Raman TO shift by deflecting suspended single crystalline 3C-SiC membrane is given by the empirical equation [9]:

$$\epsilon_{\text{TO}} = \frac{796 - \nu_{\text{TO}}}{1125} \quad (2)$$

As calculated from Eq. 2, the bi-axial strain of the as-deposited poly-SiC and the annealed poly-SiC are 0.51% and 0.33%, respectively. The annealing leads to less tensile strain of the film.

For carbon structure, raman spectra for disordered and ideal graphite is dominated by two modes - the D and G modes, around 1350  $\text{cm}^{-1}$  and 1580-1600  $\text{cm}^{-1}$ , respectively. The D mode is associated with disordered or defective hexagonal graphitic plane structures, while the G mode corresponds to stretching vibrations in the basal-plane of ideal graphite. From the carbon D and G peaks intensity, width and position, one can differentiate the carbon structure from nanocrystalline to amorphous carbons [11]. In Fig. 2, the G peak for the annealed sample lies at 1595.8  $\text{cm}^{-1}$ , and the D peak is at 1345.5  $\text{cm}^{-1}$ . The intensity ratio of the two peaks,  $I(\text{D})/I(\text{G})=1.8$ , is indicative of a highly defective, nanocrystalline nanocrystalline graphitic film. In order to study the effect of pre-annealing on the poly-SiC metallization performance, Pt to the as-deposited and annealed poly-SiC contacts are investigated next.

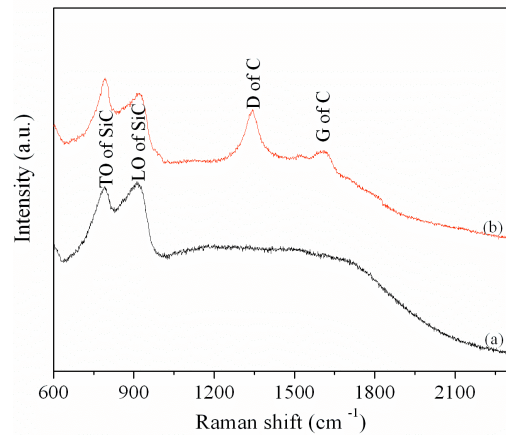


Figure 3: Raman spectra of (a) as-deposited poly-SiC, (b) after annealing at 1300  $^{\circ}\text{C}$  under ultrahigh vacuum.

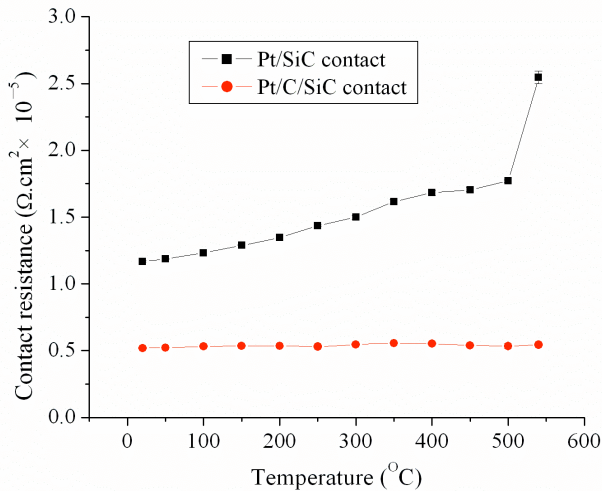


Figure 4: Pt to SiC contact resistivity vs. temperature for 3 min duration at each temperature.

The Pt to the as-deposited poly-SiC and the annealed poly-SiC contacts are both ohmic, and the contact resistivity from room temperature to 540 °C are calculated from Eq.1 and are shown in Fig.4, where Pt/SiC refers to the Pt to the as-deposited poly-SiC contact, while Pt/C/SiC refers to the Pt to the annealed poly-SiC contact. The room temperature contact resistivity of the Pt/C/SiC contact is  $5.2 \times 10^{-6} \Omega \cdot \text{cm}^2$ , which is about half of the Pt/SiC contact resistivity. Pt/SiC contact increases progressively with temperature and reaches  $2.5 \times 10^{-5} \Omega \cdot \text{cm}^2$  at 540 °C. This is to be contrasted to the contact resistivity of the Pt/C/SiC contact, which exhibits little change with temperature.

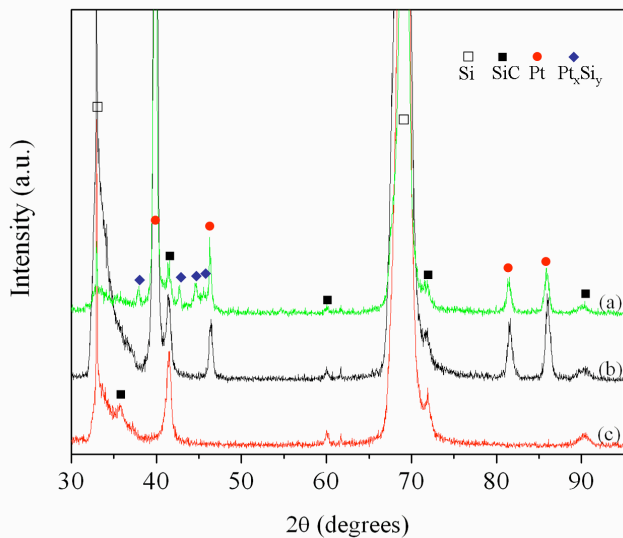


Figure 5: X-ray diffraction spectra of (a) Pt/SiC contact, (b) Pt/C/SiC contact (both after 540 °C testing in the air), (c) SiC film with surface C layer.

The metal to semiconductor contact resistivity value is affected by the interfacial states. After annealing, the change in poly-SiC film stress and surface chemistry could both be responsible for the lower value of contact resistivity. It is known

that tensile stress can be generated from voids and missing atoms in the grain boundaries of polycrystalline films. The larger the tensile stress, the higher the density of defects in the grain boundaries, which leads to increased electron scattering and larger contact resistivity. According to the strain analysis, the UHV annealing at 1300 °C leading to lower tensile strain of the poly-SiC film may be responsible for the decrease of the contact resistivity to Pt. On the other hand, the presence of nanocrystalline graphite could further lower the contact resistivity to Pt. Lu et al., have demonstrated that the contact resistivity of Ni and Co to graphitic SiC surface is lower than that of the non-graphitic SiC surface contacts [12]. Our annealed poly-SiC results in a graphitic surface that can lead to further reduction of contact resistance.

In addition, the Pt/C/SiC contact shows enhanced stability at high temperature in air, as shown in Fig.2. In order to study the phase change after high temperature testing, XRD spectra of the Pt/SiC and Pt/C/SiC contacts after exposure in air at 540 °C are shown in Fig. 5. In comparison to the as-deposited poly-SiC, the Pt/SiC and Pt/C/SiC both show Pt(111), Pt(220), Pt(311) and Pt(222) peaks. In addition, the Pt/SiC show Pt<sub>12</sub>Si<sub>5</sub>(440), PtSi(112), PtSi(202) and Pt<sub>6</sub>Si<sub>3</sub>(611) phases, while no Pt silicide phase is observed in Pt/C/SiC contact after high temperature testing. The reaction between Pt and SiC may be responsible for the increase in contact resistivity of the Pt/SiC contact structure. The presence of graphitic carbon builds a thermal barrier to the reaction between Pt and SiC leading to thermally stable contacts. It should be noted that oxidation of Pt or SiC may also change the contact resistivity. As future work, we will investigate the role of oxidation in Pt/SiC and Pt/C/SiC contact structures.

## CONCLUSION

In conclusion, the reduced tensile strain and formation of nanocrystalline interfacial graphite could both be responsible for the reduced ohmic contact resistivity of Pt to SiC. The controlled growth of interfacial nanocrystalline graphite, as presented here, could serve as a thermal barrier to the chemical reactions between SiC and metals, which opens the door to investigations of various metals to SiC contact studies and stable contact performance at elevated temperatures.

## REFERENCES

- [1] D. Gao, M. B. J. Wijesundara, C. Carraro, R. T. Howe, and R. Maboudian, "Recent Progress Toward A Manufacturable SiC Surface Micromachining Technology", IEEE Sens. J. 4, 441 (2004).
- [2] S. Roy, R. G. DeAnna, C. A. Zorman and M. Mehregany, "Fabrication and Characterization of Polycrystalline SiC Resonators", IEEE Transactions on Electron Devices, 49, 2323 (2002).
- [3] D.R. Myers, K.B. Cheng, B. Jamshidi, R.G. Azevedo, D.G. Senesky, L. Chen, M. Mehregany, M.B.J. Wijesundara, and A.P. Pisano, "Silicon carbide resonant tuning fork for microsensing applications in high-temperature and high G-shock environments," Journal of Micro/Nanolithography, MEMS, and MOEMS, 8,021116 (2009).
- [4] L. M. Porter and R. F. Davis, "A Critical Review of Ohmic and Rectifying Contacts for Silicon Carbide", Materials Science and Engineering, B34, 83 (1995).
- [5] J. Zhang, C. Carraro, R. T. Howe, and R. Maboudian, "Electrical, mechanical and metal contact properties of polycrystalline 3C-SiC films for MEMS in harsh environments," Surface & Coatings Technology, 201, 8893 (2007).

- [6] J. H. Park and P. H. Holloway, "Effects of nickel and titanium thickness on nickel/titanium ohmic contacts to n-type silicon carbide", *J. Vac. Sci. Technol. B*, 23,486 (2005).
- [7] A. K. Geim, "Graphene: Status and Prospects", *Science* 324, 1530 (2009).
- [8] G. S. Marlow and M. B. Das, "The effects of contact size and non-zero metal resistance on the determination of specific contact resistance," *Solid-State Electronics*, 25, 91 (1982).
- [9] F. Liu, C. Carraro, A. P. Pisano and R. Maboudian, "Growth and characterization of nitrogen-doped polycrystalline 3C-SiC thin films for harsh environment MEMS applications", *Journal of Micromechanics and Microengineering*, 20, 03501 (2010).
- [10] S. Rohmfeld, M. Hundhausen, L. Ley, C. A. Zorman and M. Mehregany, "Quantitative evaluation of biaxial strain in epitaxial 3C-SiC layers on Si(100) substrates by Raman spectroscopy", *Journal of Applied Physics*, 91, 1113 (2002).
- [11] A. C. Ferrari and J. Robertson, "Interpretation of Raman spectra of disordered and amorphous carbon", *Physical Review B*, 61, 14094 (2000).
- [12] W. Lu, W. C. Mitchel, G. R. Landis, T. R. Crenshaw, and W. Eugene Collins, "Catalytic graphitization and Ohmic contact formation on 4H-SiC", *J. Appl. Phys.* 93, 5397 (2003).

#### **ACKNOWLEDGEMENT**

The authors thank Siemens Corporate Research, Inc. (Award Number 20100118), NSF (Grant Number CMMI-0825531) for financial support. The authors also thank Sarah Wodin-Schwartz in Mechanical Engineering, University of California at Berkeley for supplying the high temperature adhesive.

#### **CONTACT**

\*F. Liu, tel: +1-510-643-3489; fangliu@berkeley.edu

# ONE MASK ONE EXPOSURE IN-SITU MAGNETIC ACTUATOR FABRICATION METHOD

S. E. Chung, J. Kim, S. Min, L. N. Kim, and S. Kwon  
Seoul National University, Seoul, South Korea

## ABSTRACT

We demonstrate *in-situ* magnetic actuator fabrication technique via one-mask one-exposure method. A single magnetic microstructure or magnetic actuator is photopatterned from magnetic nanoparticles (MN) containing ultraviolet (UV) light curable resin in PDMS microfluidic channels. Oxygen inhibition layer generated from the PDMS surface allows magnetic microstructure to move and float without a sacrificial layer concurrently with the fabrication process. Thus, we only need one-time UV patterning with one-mask to fabricate a single complex magnetic actuator. We generated various magnetic structures such as both anchored and floating actuators with the above simple one-mask one-exposure system. These magnetic structures are actuated by external permanent magnet controlled outside of the channel. Overall magnetic actuator fabrication and control are take place in the same area without extra step to transfer the position from the fabrication site to the actuation site. Therefore, the entire process is very simple and fast enabling *in-situ* fabrication and real-time actuation.

## INTRODUCTION

Electroplating and micromachining is a fundamental process to manufacture general magnetic actuators in conventional microelectromechanical systems (MEMS) technology. Electrodeposition of magnetic materials and micromachining such as etching after lithographical patterning form metal layers for various magnetic actuators [1-2] and these are very popular methods due to higher microscale accuracy. However, this conventional MEMS technique to fabricate actuators is very complex and time-consuming method. It is necessary to deposit sacrificial layer and remove it after the patterning [3] to fabricate a simple movable magnetic actuator, such as electrostatic clamping structure [4], or anchored cantilever beams [5-6].

Instead of using top-down approach by micromachining the bulky metal solids, fabrication of magnetic actuators from magnetic nanoparticles would be easier, simpler and more flexible. Recently, magnetic nanoparticles are encapsulated in a polymer matrix by photopolymerizing magnetic beads within UV curable resin [7-8]. By embedding these magnetic nanoparticles in hydrogels via photopolymerization, various elastic magnetic actuators are fabricated due to its flexibility of solidified polymers.

In this paper, we have developed very simple and fast fabrication method of magnetic actuators via one-mask one-exposure lithography. With optofluidic maskless lithography (OFML) technique [9], a magnetic microactuator, or a magnetic microstructure, is directly photopatterned from the mixture of magnetic nanoparticles (MN) and ultraviolet (UV) light curable resin within a second. The PDMS channel used as fabrication and actuation sites provides good environment for magnetic microstructures to move and float, because oxygen inhibition layer is generated during the photopolymerization process [10]. The inhibition layer allows magnetic actuators to be fabricated without sacrificial layer. Different from magnetic actuator fabrication technology in MEMS field, our technique only execute one-step lithography to fabricate various actuators even a three-dimensional anchored cantilever beam using PDMS patterned glass substrate by taking advantage of inhibition layer. Therefore, we only need

one-time UV patterning with one-mask to fabricate a single complex magnetic actuator.

Both floating actuators in microfluidic channels and anchored actuator outside of the channel such as magnetic microcantilever are easily fabricated using our simple one-mask one-exposure *in-situ* fabrication technique. Each photopatterned microstructure contains MN embedded inside, and those nanoparticles react to the external magnetic force and cause the polymeric microstructure to actuate. These magnetic structures are easily actuated by controlling external permanent magnet outside around the channel. The actuators move through the magnetic field directions formed by the applied magnet. Free-floating actuators, bounded actuators using anchors of the microfluidic channel and railed actuators in railed microfluidic channels [11] are presented as actuation demonstration of *in-situ* fabricated magnetic structures. Furthermore, selective magnetic actuation is also demonstrated from heterogeneous assembly of magnetic structures and non-magnetic structures.

## EXPERIMENTALS

### Fabrication and control of magnetic microactuators

A magnetic actuator, which is MN, magnetite ( $\text{Fe}_3\text{O}_4$ ) embedded microstructure, is fabricated by optofluidic maskless lithography (OFML) within microfluidic channels. As shown in Fig. 1, two types of magnetic actuators are fabricated; floating actuators (Fig.1(a)) and anchored actuators (Fig.1(b)). First, MN are mixed with photocurable resin and introduced into the prepared microfluidic device. Then, we polymerize the liquid-phase MN resin using one-mask one-exposure process via OFML system. The thickness of the actuators is determined by the height of the channel and the lubricating inhibition layer[10]. During the photopolymerization, MN are embedded in the polymeric microstructures, thus it enables that the magnet pulls the fabricated microstructures due to embedded MN. Note that solidified microstructures containing MN are *in-situ* fabricated magnetic actuators.

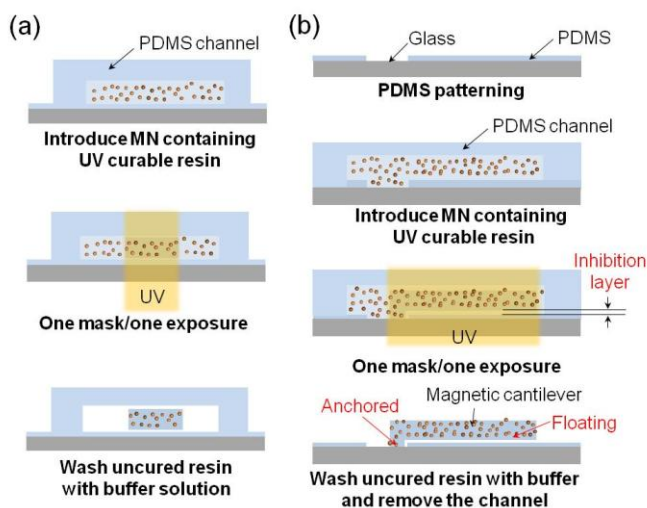


Figure 1. *In-situ* fabrication process of magnetic nanoparticles (MN) embedded microstructures, which are magnetic microactuators, using one-mask and one-exposure process

General fabrication process of floating actuators and anchored actuators is similar except the substrate types. The substrate of floating actuators is PDMS coated slide glass to generate free-floating photopolymerized structures due to oxygen inhibition layers [10]. Oxygen inhibition layer enables that cured polymeric structure on the PDMS layer does not adhere to the substrate allowing free actuation using external permanent magnet. However, the substrate of the anchored actuator is patterned PDMS coated slide glass, meaning that some portion of the substrate is not coated with PDMS. Without PDMS layer, synthesized part sticks to the glass, functioning as an anchor.

After the fabrication, we finally wash uncured MN containing UV curable resin with buffer solution, usually ethyl alcohol. For the anchored magnetic cantilever beam, we remove the channel for further actuation process.

Conventional cantilever beam fabrication technology requires complex fabrication process to make anchors and beams because sacrificial layer is necessary to get bendable cantilever beam. However, our magnetic actuator fabrication technique enables one-step fabrication of anchored cantilever beam via one-mask one-exposure process without a sacrificial layer by taking advantage of oxygen inhibition layer in PDMS device. During the fabrication process, an anchor of the cantilever is adhered to a glass and a beam is generated on the PDMS region enabling free-deflection.

Figure 2(a) shows the anchored magnetic cantilever fabricated on the patterned PDMS glass substrate and its actuation by applying magnetic field. Due to the magnetic force applied perpendicular to the substrate, the cantilever beam bends toward the field as the end of the beam is anchored to the substrate.

The actual experimental results are demonstrated in Fig. 2(b) as sequential images. At the initial state, the cantilever beam free-floats on the PDMS coated substrate due to lubricating inhibition layer and the end of the beam is anchored at the glass substrate (Fig. 2(b) (Top)). When the low vertical magnetic field is applied, the cantilever is lifted up overcoming the mechanical torque to straighten the beam. In this process, only unanchored part of cantilever beam, which is floating part on the PDMS layer, moves up. Under the high magnetic field, it is lifted up to almost 90° degrees as shown in Fig.2(b)(Bottom).

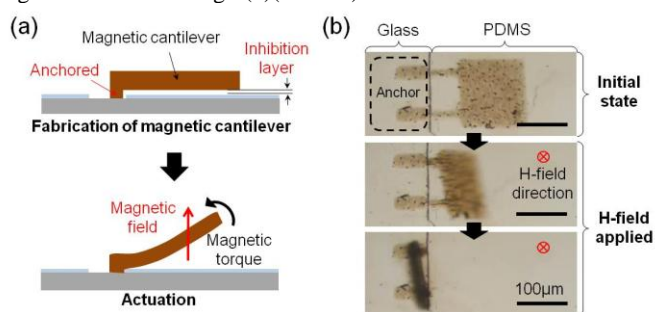


Figure 2. Actuation of anchored magnetic cantilever (a) Schematic diagram of a magnetic cantilever actuation. (b) Magnetic cantilever actuation.

Figure 3 shows the experimental setup of *in-situ* floating magnetic actuators fabrication and actuation. The setup is composed of photopatterning part utilized by OFML system and magnetic controlling part using permanent magnet. OFML *in-situ* synthesizes magnetic microactuators by a patterned UV light projected from the DMD as shown in Fig.3(a). Each photopatterned microstructure contains MN embedded inside, and those nanoparticles react to the external magnetic force and cause the polymeric microstructure to actuate. Fabricated MN embedded microstructures are actuated by

controlling external permanent magnet from the outside of the channel. The magnet induces a magnetic field to control actuators. The fabricated structures move along the magnetic field directions generated by the magnet.

Three types of floating magnetic actuators are demonstrated in the experiments (Fig.3(a)-(b)). Free-floating structure actuation uses free-floating MN embedded microstructures. Fig.3(c) shows Scanning Electron Microscope (SEM) images of free-floating magnetic structure. 100~120nm sized magnetic nanoparticles are fixed in a polymeric structure during photopatterning process. Bounded actuator is fabricated at the PDMS anchor enabling bounded actuation such as rotation. Since one of basic movements is rotation, anchored actuators are applied to mixer or particle sorter at branches using rotational movement. Similarly, rail-guided actuator is fabricated on the rail and guided along the rail. Since railed microfluidics is an agile method to guide and assemble microstructures inside fluidic channels, it enables efficient magnetic structure sorting at the rail branches or various heterogeneous assemblies for selective actuation.

Free-floating magnetic actuators are affected from both applied magnetic field and flow stream through the fluidic channel. The magnetic field outside from the channel controls the transition direction of the free-floating actuators and initiates their movement. Then, the flow stream accelerates the transition of the actuators.

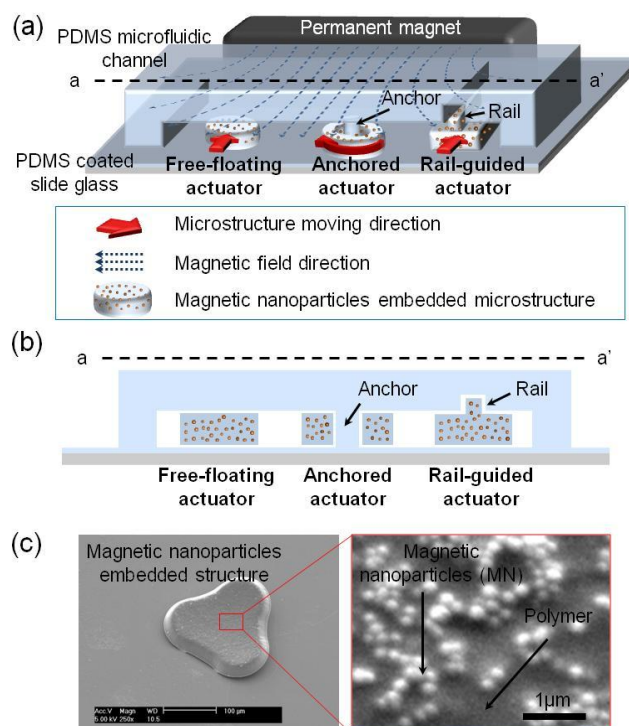


Figure 3. Experimental setup and fabricated magnetic actuators

## RESULTS AND DISCUSSION

Figure 4 shows the free-floating actuation of MN embedded microstructure. As an initial state, the actuator keeps its position within the channel as in Fig.4(a)(i). When the magnetic field is applied to the structure from the outside of the channel, the actuator transits to the field direction (Fig.4(a)(ii) and (iii)). In addition to the transition, the fluidic force is also applied from the inlet of the channel to complete the blocking of the branch. After the blocking, free-flowing polymeric microparticle is fabricated to demonstrate

selective flowing due to blocked channel branch using free-floating magnetic actuator. The microparticle freely moves to the unblocked branch with the flow stream as shown in Fig. 4(b) or (c).

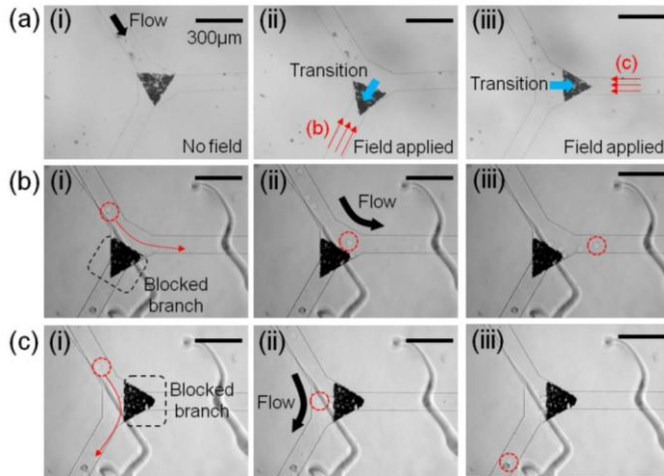


Figure 4. Free-floating actuation.

Bounded actuators are fabricated centering on the PDMS anchor, thus holes at the center of the structures are generated due to the oxygen inhibition layer of the PDMS anchor. These structures rotate in response to the induced magnetic field which rotates externally using permanent magnet around the channel.

Rotating mechanism enables various micromotor-type applications as demonstrated in Fig. 5. Figure 5(a)-(b) show free-floating particle sorter and transporter. Basically, the magnetic structure rotates bounded at the PDMS anchor while external magnetic field is rotating. If the rotating direction changes to the opposite way, the structure would also rotate in the opposite direction. This fact is applied to a magnetic sorter. In a two-phase microfluidic channel with a center PDMS anchor at the branch, the magnetic sorter receives a free-floating particle and sends it to upper branch of the channel by rotating in counterclockwise direction as shown in Fig. 5(a).

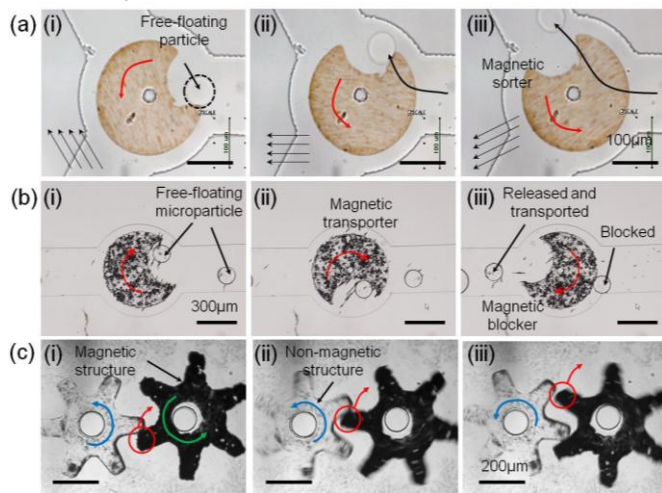


Figure 5. Full-bounded actuations of in-situ fabricated magnetic structures. The magnetic structures are fabricated centering at PDMS anchors and rotate in response to the rotating magnetic field.

Free-floating particle transporter works in a similar way with the

magnetic sorter. In one-way fluidic path, the magnetic transporter selectively releases free-floating microparticle and blocks others. Therefore, the actuator works as both transporter and blocker.

In addition to single magnetic micromotor actuation, heterogeneous actuation is also demonstrated in Fig. 5(c). Two toothed wheels, composed of magnetic structure and non-magnetic structure, go in gear with each other due to rotating magnetic field. In the system, magnetic wheel only responds to the applied magnetic field, thus non-magnetic wheel rotates engaging with the rotating magnetic wheel.

Figure 6(a) shows a basic magnetic control of MP embedded microstructures on the rails. Since the finned microstructures only go along the rail, moving direction of magnetic structures is controlled using magnetic field and the path of movement exactly same with the rails. By taking advantage of railed microfluidics, many interesting applications are proposed.

A sliding valve in two-phase microfluidics alternatively blocks a selective fluid as shown in Fig. 6(b)-(c). The position of magnetic structure on the rail depends on the field direction of external magnet. By effectively controlling the direction of external magnet, we selectively block unwanted flow streams using sliding valve moving along the rail and change the mainstream of the channel.

In addition to valve-type application, we effectively sort out lots of microstructures to designated branches by utilizing rails. Figure 6(d)-(f) show sorting mechanisms of the magnetic microstructures on the rails. At a branch point, the moving direction of each approaching magnetic structure is controlled by the direction of magnetic field. In Fig. 6(d), all microstructures move to the left branch due to the magnetic field applied from the bottom side of the channel, and in Fig. 6(e), all of them move to the right branch due to the field from left bottom side of the channel. However, magnetic field control also enables that each magnetic microstructure move to all different directions as shown in Fig. 6(f). Railed microfluidic based particle sorter system is a simple way of selecting the targeted rail for magnetic microstructures to ride in the second place. By only flowing fabricated magnetic structures and controlling magnetic field direction, numerous particles can selectively choose the desired path within microfluidic channels.

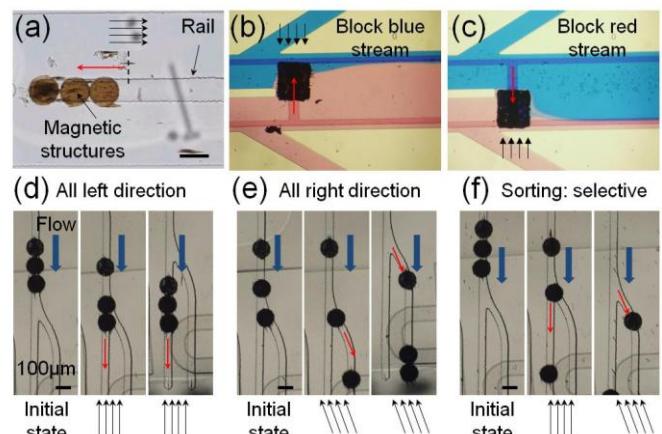


Figure 6. Rail-guided actuations of in-situ fabricated magnetic structures



By alternatively flowing MN containing resin and non-magnetic resin into the microfluidic channels, and then fabricating the microstructures, heterogeneous assembly of magnetic and non-magnetic structures is illustrated (Fig. 7(a)). Furthermore, selective magnetic actuation of heterogeneously assembled structures in multiple rails is shown in Fig. 7 (b).

The railed microfluidic process is an innovative technique to guide the movement of *in situ* photopolymerized microstructures and self-assemble the structures. All guided microstructures are finally blocked and unable to move forward owing to the rail's structural geometry at the end of the rail as in Fig. 7(a). Therefore, the end of the rail works as a barrier to block the movement of the microstructures and to initiate the assembly process.

Heterogeneous assembly is achieved on the basis of multiple rails with the ends. Introduced UV curable resin is alternatively exchanged between MN containing polymers and non-magnetic resin to allow heterogeneous microstructures fabrication. Thus, magnetic structures and non-magnetic structures are assembled simultaneously at the end of the rails. After the assembly, only magnetic parts are selectively moved due to the applied magnetic fields as demonstrated in Fig. 7(b). A skeleton assembly is composed of non-magnetic parts and magnetic parts. Arms only react to the magnetic force without any control of the flow field after the assembly.

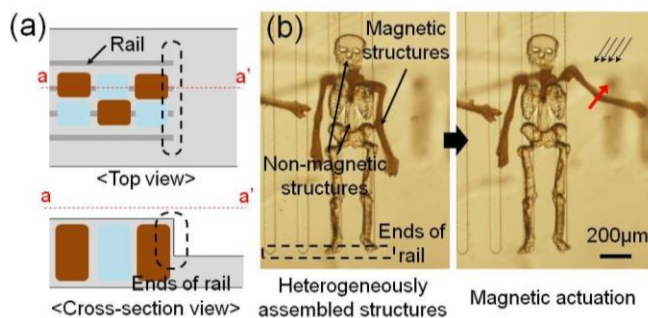


Figure 7. Heterogeneous assembly of magnetic structures and non-magnetic structures, and selective actuation

## CONCLUSION

In this article, we demonstrate *in situ* fabrication of magnetic actuators via one-mask one-exposure method using optofluidic maskless lithography (OFML) system and their real-time actuation technique. Various magnetic actuators are fabricated using magnetic nanoparticles containing photocurable resin. Both anchored actuator such as microcantilever and unanchored actuator are easily generated with one-step fabrication process. Different from conventional MEMS technology to fabricate anchored microcantilever beam requiring complex steps including sacrificial layer, our technique using UV patterning method only requires one-mask one-exposure which extremely reduces fabrication process time. Both photopatterning and actuation of magnetic structures take place in the same spot using our system. With this system, transportation of fabricated actuator from the fabrication site to actuation site is not necessary. All the actuation is executed by controlling external permanent magnet from the outside of the microfluidic channel. Many types of actuation such as free-floating, bounded, railed actuation and selective actuation are demonstrated within microfluidic channels. Owing to its simplicity and flexibility,

we believe one-mask one-exposure magnetic actuator fabrication and actuation method will not only impact current MEMS technology but also encourage innovation in a wide range of application areas in the future.

## REFERENCES

- [1] H. Rothuizen, et al., "Fabrication of a micromachined magnetic X/Y/Z scanner for parallel scanning probe applications," *Microelectronic Engineering*, 53, 509-512 (2000)
- [2] H. Guckel, et al., "Fabrication and testing of the planar magnetic micromotor," *Journal of Micromechanical Microengineering*, 1, 135 (1991)
- [3] J. W. Judy, "Microelectromechanical systems (MEMS): fabrication, design and applications," *Smart Materials and Structures*, 10, 1115 (2001)
- [4] J. W. Judy and R. S. Muller, "Magnetically actuated, addressable microstructures," *Journal of Microelectromechanical Systems*, 6, 249, (1997)
- [5] C. Liu and Y. W. Yi, "Micromachined magnetic actuators using electroplated permalloy," *IEEE Transactions on Magnetics*, 35, 1976 (1999)
- [6] J. W. Judy, et al., "Magnetic microactuation of polysilicon flexure structures," *Journal of Microelectromechanical Systems*, 4, 162 (1995)
- [7] D. C. Pregibon, et al., "Magnetically and biologically active bead-patterned hydrogels," *Langmuir*, 22, 5122 (2006)
- [8] D. K. Hwang, et al., "Microfluidic-based synthesis of non-spherical magnetic hydrogel microparticles," *Lab on a Chip*, 8, 1640 (2008)
- [9] S. E. Chung, et al., "Optofluidic maskless lithography system for real-time synthesis of photopolymerized microstructures in microfluidic channels," *Applied Physics Letters*, 91, 041106 (2007)
- [10] D. Dendukuri, et al., "Modeling of oxygen-inhibited free radical photopolymerization in a PDMS microfluidic device," *Macromolecules*, 41, 8547 (2009)
- [11] S. E. Chung, et al., "Guided and fluidic self-assembly of microstructures using railed microfluidic channels," *Nature Materials*, 7, 581 (2008)

## ACKNOWLEDGEMENTS

This work was partly supported by the Korea Research Foundation Grant and the Korea Science and Engineering Foundation (KOSEF) grant funded by the Korean Government (MEST) (KRF-2009-220-C00010 and No. 0414-20090036).

## CONTACT

\*S. Kwon, tel: +82-2-880-1736; [skwon@snu.ac.kr](mailto:skwon@snu.ac.kr)

# SELF-POWERED ION GAUGE AND SELF-POWERED ION PUMP

Yuerui Lu, and Amit Lal

SonicMEMS Laboratory

School of Electrical and Computer Engineering

Cornell University, Ithaca, NY

## ABSTRACT

We used a radioisotope  $^{63}\text{Ni}$  thin-film source as a cold cathode to realize a Self-Powered Ion Gauge (SPIG), demonstrating the largest sensitivity range among all reported pressure sensors, from high vacuum ( $10^{-6}$  Torr) to high pressure ( $10^3$  Torr). We also show that SPIG can be transformed into a Self-Powered Ion Pump (SPIP) due to self-charge generated voltage induced ion-implantation of ionized gas atoms. The combination of SPIG and SPIP provides a near-zero-power solution to measuring and maintaining high vacuum in micro-system packages. The amount of radioactivity is in the micro-Ci to milli-Ci range, which is a commercially viable from both the point of view of safety and cost in a sealed package.

## INTRODUCTION

Obtaining high-vacuum in cm-cubic chambers has been an active field of research in MEMS packaging. Several solutions of hermetic packages have been developed [1-3] for inertial sensors and resonators. Recently a number of solutions have used thin-film sealing to achieve partial vacuum [4]. A few efforts, mainly stemming from U-Michigan have demonstrated sustained pressure of a few milli-Torr. Using UHV packaging techniques and use of getters, some solutions have demonstrated micro-Torr pressures, but the lifetime of good vacuum is limited by getter life. As the size of the vacuum package become small, the surface to volume ratio increases. If a pumping mechanism is found based on radioisotope films, then the pumping rate will be proportional to the film area, resulting in more efficient pumping as package become smaller.

Moreover, in order to measure the pressure in a high vacuum package, ionization gauges are widely used, which can be classified into hot and cold cathode gauges, depending on the generation methods of electrons. Conventional hot cathode ionization gauges use thermally generated electrons, causing power for heating. Cold cathode ionization gauges, using a glow discharge to generate free electrons, suffer from the requirement of a few kilovolts to function and the instability of the glow discharge at low pressures. In the case of miniature vacuum systems (1-10cc), power and volume dedicated to an ion-gauge is highly limited, specially for battery powered portable applications.

Radioactive isotopes  $^{63}\text{Ni}$  thin film emitter has been used as fuel for low power batteries [5-7], nano-lithography sources [8], because of its 100 years long half-life, suitable beta electron energy range ( $E_{av}=14.9\text{keV}$ ,  $E_{max}=67\text{keV}$ ) and safe radiation applications. The low-energy beta electrons from  $^{63}\text{Ni}$  source can be shielded by thin layers ( $\sim 25\mu\text{m}$ ) of most materials, and can not penetrate the dead-cell layer of skin [9]. The beta emitter has high stability, since the beta emission is independent of pressure or temperature. This stable beta emitter with long life is an attractive candidate for cold cathode ionization gauges application.

Here, we used a radioisotope  $^{63}\text{Ni}$  thin-film source as a cold cathode to realize a Self-Powered Ion Gauge (SPIG) (Fig.1), demonstrating the largest sensitivity dynamic range among all reported pressure sensors, from high vacuum ( $10^{-6}$  Torr) to high pressure ( $10^3$  Torr). Since  $^{63}\text{Ni}$  emits electrons with average energy 14.9 keV, this eliminates the high voltage and temperature for field emissions and thermal emission typically required in high vacuum

gauges.  $^{63}\text{Ni}$  has 100 years' half-life ensuring SPIG long time operation. The  $^{63}\text{Ni}$  source is also highly stable as the radioisotope electron emission is independent of pressure or temperature [10]. We also show that SPIG can be transformed into a Self-Powered Ion Pump (SPIP) due to self-charge generated voltage induced ion-implantation of ionized gas atoms. The combination of SPIG and SPIP provides a near-zero-power solution to measuring and maintaining high vacuum in microsystem packages. The amount of radioactivity is in the microCi to milliCi range, which is a commercially viable from both the point of view of both safety and cost in a sealed package.

## SELF-POWERED ION GAUGE (SPIG)

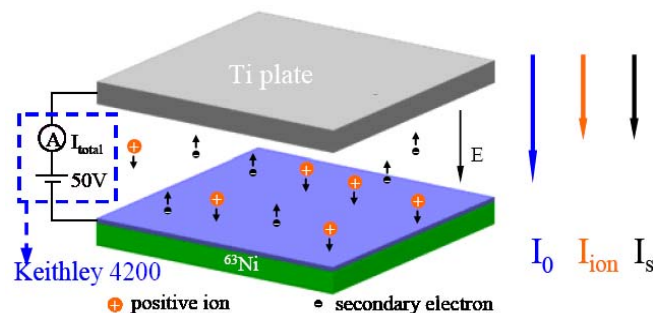


Figure 1: Schematic of Self-Powered Ion Gauge (SPIG). The gap between the  $^{63}\text{Ni}$  and the Ti plate is 1mm. The size of the  $^{63}\text{Ni}$  thin film source is 1cm X 2cm. We define  $I_{total} = I_0 + I_{ion} + I_s$ .

In the case of miniature, potentially battery-powered vacuum systems (1-10cc), power and volume dedicated to an ion-gauge is highly limited, and is often the performance limiting component of MEMS portable vacuum instruments. Attempts at realizing miniature ion gauges have utilized nanostructures to amplify emitted electron flux, such as carbon nanotubes (CNTs) ion gauges [11]. But the degradation of the field-emission current leading to short life time remains a serious problem for CNT-based ion-gauges. This damage is possibly due to local heating and nano-tip reaction with oxygen. Hence, the problem of realizing a stable electron source operable over wide operating dynamic range of pressure and temperature is unsolved. Here, we use the stable radioisotope  $^{63}\text{Ni}$  thin film source as the cold cathode to realize a SPIG (Fig. 1&2). A capacitor formed of a titanium plate and  $^{63}\text{Ni}$  thin film were placed in a package that was placed in a 10cc vacuum chamber, being pumped by a turbo pump and pressure was controlled by a leak-valve. The current across the capacitor consists of the emitted current and ion current due to electron ionization. Figure 3 shows the ability to measure pressure down to  $10^{-6}$  Torr by calibrating the ionization current versus pressure. Pressure measured over several days shows no drift in the current measurement.

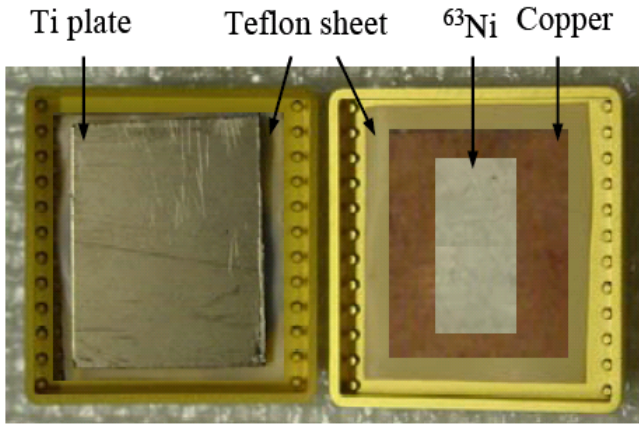


Figure 2: Photo of the device set up; the Teflon was chosen as outgassing is minimal.

Based on Monte Carlo calculation, the high-energy beta electrons with average energy of 14.9 keV, emitted from the  $^{63}\text{Ni}$  thin film source, can travel 4 cm in air under atmosphere pressure at room temperature. Some of these primary high energy electrons will penetrate deeply into the titanium metal plate, while the rest will be back-scattered. These back-scattered electrons might still have high energy and they are possible to be scattered back and forth between the  $^{63}\text{Ni}$  thin film and titanium plate capacitive structure, for hundreds of times, before they are absorbed. These back-scattered electrons and the primary beta electrons from  $^{63}\text{Ni}$  thin film, will lead to many gas ionization events, producing flux of positively charged ions, and related amount of secondary electrons. The density of these positive ions and secondary electrons is proportional to the gas molecule number volume density, which is proportional to pressure.

The  $^{63}\text{Ni}$  thin film was grounded and 50V constant DC bias was applied on the stainless steel plate. The positive ions and the gas secondary electrons will be collected by the  $^{63}\text{Ni}$  thin film and stainless steel plate, respectively (Fig.1). Keithley 4200, which has a high current resolution down to 1fA, was used for the DC voltage supply, and the total current measurement. The total current  $I_{\text{total}}$  includes both the basic current, defined as  $I_0$  due to primary electrons and back-scattered electrons, and the ionization current, defined as  $I_{\text{ionization}}$  due to the positive ions and the secondary electrons.

$$I_{\text{ionization}} = I_{\text{total}} - I_0 \quad (1)$$

The measured Total current  $I_{\text{total}}$  vs Pressure curve is shown in a log plot in Figure 3(a), with pressure ranging from  $10^{-6}$  Torr up to  $10^3$  Torr ( $\sim 1.4$  atm). The high pressure was measured using commercially available Pfeiffer compact full range gauge with useful sensitivity range from  $10^{-3}$  Torr down to  $10^{-8}$  Torr as the standard. For high pressure measurement, we used Pirani gauge and membrane-type pressure manometer. In high vacuum region with pressure ranging from  $10^{-6}$  Torr to  $10^{-4}$  Torr, we could see that  $I_{\text{total}}$  is linearly proportional to the pressure, in the double linear plots  $I_{\text{ionization}}$  is much smaller than current  $I_0$ , since there is a small amount of ionizations due to very small number density of gas molecules. The  $I_0$  current could be considered to be a constant value shown in figure 3(a) inset, since the ionization is small and will give an insignificant effect on the back-scattered electrons. Therefore, an extrapolated  $I_0$  value of 20.5pA can be obtained by extrapolating the linear experimental data to the ideal real vacuum with zero Pa pressure (Fig.3(a) inset). The ionization current  $I_{\text{ionization}}$  can be

obtained by reducing  $I_0$  from the total current  $I_{\text{total}}$ , as shown in

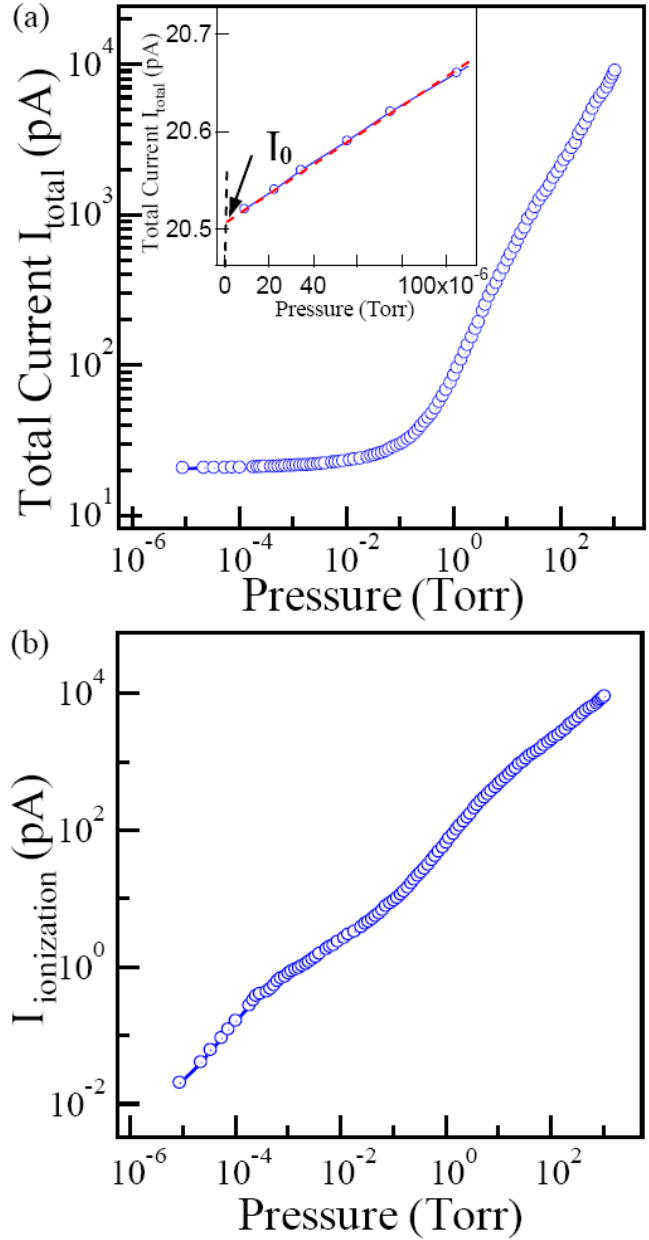


Figure 3: (a) Log plot of the measured Total current  $I_{\text{total}}$  vs Pressure curve of the device, with pressure ranging from  $8.9 \times 10^{-6}$  Torr up to  $1.6 \times 10^3$  Torr ( $\sim 1.4$  atm), at room temperature. Inset shows the linear plot curve of Total current vs Pressure for high vacuum region. The total current is almost linear to the pressure. We extrapolate the curve to the ideal absolute vacuum case (zero Pa pressure) and get a constant current value  $I_0$ . (b) Log plot of the measured ionization current  $I_{\text{ionization}}$  vs Pressure. Here, we define ionization current by  $I_{\text{ionization}} = I_{\text{total}} - I_0 = I_{\text{ion}} + I_s$

Eq.1. The double log plot of  $I_{\text{ionization}}$  vs Pressure curve (Fig.3(b)) shows good linearity, from high vacuum down to  $10^{-6}$  Torr to high pressure  $10^3$  Torr.

## SELF-POWERED ION PUMP (SPIP)

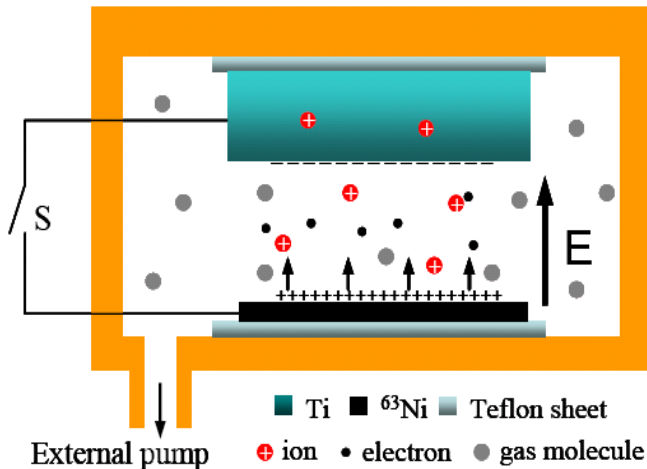


Figure 4: Schematic drawing for Self-Powered Ion Pump (SPIP) set up. When the switch *S* is open, there will be an electrical field *E* between the Ti and <sup>63</sup>Ni plates, due to the built up voltage (up to 10kV) by the Ti self-charging from <sup>63</sup>Ni beta emission. The positive ions, from air gas ionization, will be accelerated and implanted into the Ti plate permanently. This will cause pumping effect. The SPIP is on when *S* is open, while it is off when *S* is closed.

To solve the vacuum problem, we develop ion-pumps that use the electron emission from <sup>63</sup>Ni directly. If no bias is applied across the SPIG capacitor at low initial vacuum (< 0.01 Torr), voltage as high as 7-10kV can be generated across the capacitor [5]. This high voltage is able to accelerate the ions, created from gas ionization by emitted electrons, to high energy, and implant these ions into the top metal plate permanently. Energies as low as 1kV are needed to implant a few nm into the top plate (Fig.6). This pumping effect makes the capacitor a Self-Powered Ion Pump (SPIP) (Fig. 4).

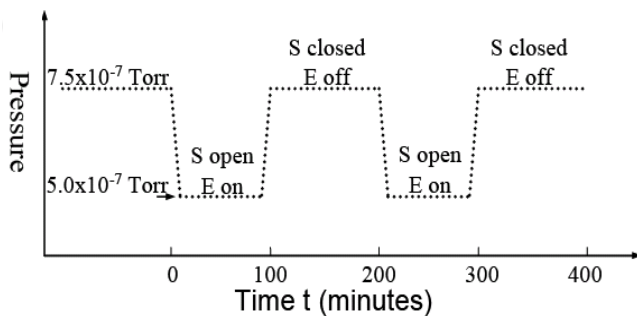


Figure 5: Experimental demonstration for SPIP. When SPIP is off (*S* closed), the highest vacuum we could reach is  $7.5 \times 10^{-7}$  Torr, due to the balance of the external pumping with the vacuum system leaking. When SPIP is on (*S* open), the highest vacuum turns to be  $5.0 \times 10^{-7}$  Torr, due to the new balance of the vacuum system leaking with the external pumping and the pumping from SPIP. As shown in figure 3b, if we turn on and off the SPIP back and fourth, by controlling the switch open and closed, the minimum vacuum point will be switched up and down according. This experimentally demonstrated the SPIP pumping.

SPIP is experimentally demonstrated in Figures 4 and 5. When SPIP is off (*S* closed), the highest vacuum we could reach is  $7.5 \times 10^{-7}$  Torr, due to the balance of the external pumping with the vacuum system leaking. When SPIP is on (*S* open), the highest

vacuum turns to be  $5.0 \times 10^{-7}$  Torr, due to the new balance of the vacuum system leaking with the external pumping and the pumping from SPIP. As shown in Figure 5, if we turn SPIP on and off, by controlling the switch to open and closed position, the minimum vacuum level change accordingly. This experimentally demonstrates the SPIP pumping.

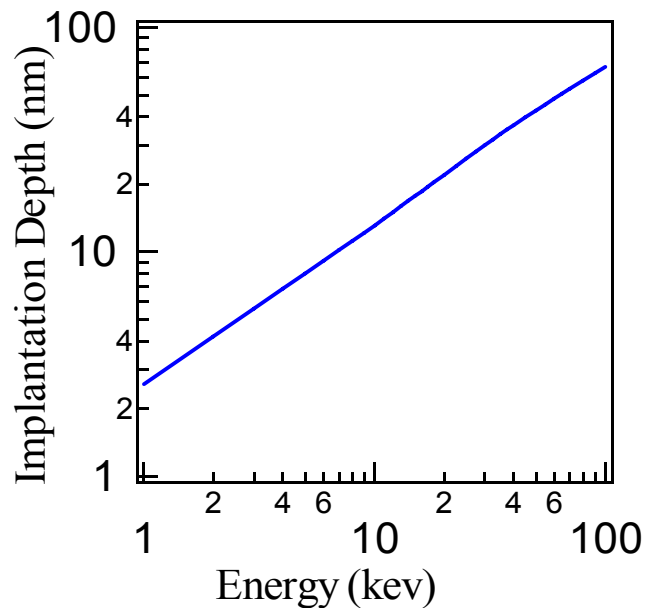


Figure 6. Ion implantation depth vs ion energy curve. The ion is oxygen and the target is Ti metal.

## SPIP PUMPING SPEED MODEL ANALYSIS

The emitted electrons can undergo many energy transfer interactions with the gas atoms. As the electrons travel across a gap, they undergo ionization reactions with the gas atoms resulting in ion creation. As the initial electron energy is quite high (average  $E_{av}=14.9\text{keV}$ ), the cross-section of ionization is very small. The electrons eventually hit the opposing electrode and the impact can result in secondary electron emission. The secondary electron energy is on the order of a few to hundreds of eV. We believe it is the secondary electrons that lead to a larger amount of ionization of the gas molecules, as the cross-section is higher at lower electron energies. The original emitted electrons build up charge on the collector and also result in positive charge on the emitting plate. This leads to a voltage and electric field buildup in the gap that accelerates away the secondary electrons toward the emitter, if the initial pressure is low enough for voltage to build up. The number of electrons emitted for high-energy electrons is very low, causing the back current due to secondary electrons being less than the emitted current. Our current measurements in vacuum indicate that 20 secondary electrons are emitted from the cathode for every 100 emitted from the anode to the cathode. In addition to the secondary electrons, the ionization due to the emitted and secondary electrons lead to an ionic current that also reduces the current due to the emitted electrons.

The ions are generated by secondary electrons with kinetic energies of approximately 10-300 eV, which can collide with other gas atoms or can impact the cathode sputtering the atoms off the cathode. Atoms that have energy higher than the ionization potential of 100-200 V govern the sputtering process. The ions that collide with the cathode can undergo two actions. First, most of ions will be accelerated by the high build up voltage and be implanted into the

top metal plate permanently. Second, the ions can also sputter the Ti metal plate the sputtered Ti atoms can also remove atoms from the gas due their specific reactivity. The rate at which ions are generated can be approximated by:

$$n_{ion} = \frac{\sigma}{A} N n_{gas} \quad (2)$$

where  $n_{ion}$  is the rate of ion generated per  $cm^3$  per second,  $\sigma$  is the cross-section of the incident electron and gas particle impact,  $A$  is the total area of the emission,  $N$  is the rate of electrons emitted per second from the radioactive thin film, and  $n_{gas}$  is the density of gas. The cross-section  $\sigma$  is a strong function of the energy of the electron and is low at high energies beyond a few hundred eV. The secondary electrons produced during the electron impact also contribute to the gas ionization with a similar rate given by Eq.2.

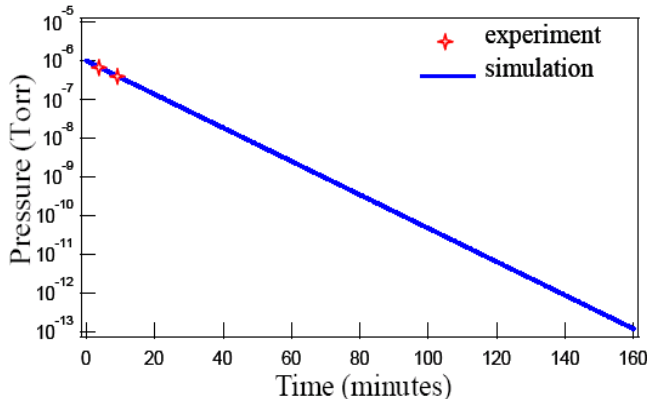


Figure 7: Pumping speed Simulation for SPIP. We assume to use  $1cm^3$  small volume chamber, which is pre-pumped to initial pressure  $P_0 = 1 \times 10^{-6}$  Torr.

$$n_{ion-se}(E) = \frac{\sigma_{se}(E)}{A} N_{se} n_{gas} = \frac{\sigma_{se}}{A} n_{seg}(E) N n_{gas} \quad (3)$$

Here,  $\sigma_{se}(E)$  is the cross-section of ionization for electrons with energy  $E$ ,  $N_{se}$  is the total number of secondary electrons generated per second,  $n_{seg}(E)$  is the number of secondary electrons generated with incident electrons of energy  $E$ , and  $N$  is the rate of incident electron generation. We need to integrate over the  $^{63}Ni$  energies and particle densities to get the total ion generation.

The generated ions can also undergo secondary reactions with the gas creating further electrons and ions. Since the secondary ion generation rate is proportional to the initial ion generation, the total generation rate for the ions is proportional to the gas concentration and the incident electron rate. The rate of sputtering of atoms from the Ti plate and the corresponding rate of pumping will also be proportional to this product. The total rate of gas atom removal assuming removal of all ions (assuming no recombination) will therefore be

$$\frac{dn_{gas}(E)}{dt} = -(n_{ion} + G n_{ion}) = -(1 + G)(\sigma + \sigma_{se} n_{seg}(E)) \frac{N}{A} n_{gas} \quad (4)$$

Here  $G$  is the number of secondary ion generated.

Once the solution for the gas density is obtained, the expression for the gas pressure can be written as:

$$p = n_{gas} kT \quad (5)$$

where  $P$  is the pressure;  $k$  is Boltzmann constant and  $T$  is temperature,

In the case of externally pump system, outgassing is balanced by the pump. The pressure modulation due to SPIP can be

calculated by Eq. 4, as showed in Figure 7.

## CONCLUSION

We have realized a Self-Powered Ion Gauge (SPIG), using radioisotope  $^{63}Ni$  thin-film source as the cold cathode, which has the largest sensitivity range among all reported pressure sensors, from high vacuum ( $10^{-6}$  Torr) to high pressure ( $10^3$  Torr). SPIG can also be transformed into a Self-Powered Ion Pump (SPIP) due to self-charge generated voltage induced ion-implantation of ionized gas atoms. The pumping model for our SPIP is analyzed, which matches well with our current available experimental data. Here, the combination of SPIG and SPIP provides a near-zero-power solution to measuring and maintaining high vacuum in micro-system packages.

## REFERENCE

- [1]. J. S. Mitchell, and K. Najafi, "A detailed study of yield and reliability for vacuum packages fabricated in a wafer-level Au-Si eutectic bonding process", 6/21-25/2009, TRANSDUCERS, (2009), pp. 841 – 844.
- [2]. S. H. Lee, J. Cho, S.W. Lee, M.F. Zaman, F. Ayazi, and K. Najafi, "A Low-Power Oven-Controlled Vacuum Package Technology for High-Performance MEMS", 01/25-29/2009, MEMS, (2009) pp.753 – 756.
- [3]. C. Junseok, J. M. Giachino, and K. Najafi, "Fabrication and Characterization of a Wafer-Level MEMS Vacuum Package With Vertical Feed throughs", JMEMS, Vol. 17(1), (2008), pp.193-200.
- [4]. R. N. Candler, M. A. Hopcroft, B. Kim; W. T. Park, R. Melamud, M. Agarwal, G. Yama, A. Partridge, M. Lutz, and T.W. Kenny, "Long-Term and Accelerated Life Testing of a Novel Single-Wafer Vacuum Encapsulation for MEMS Resonators", JMEMS, Vol. 15(6), (2006), pp.1446-1456.
- [5]. R. Duggirala, H. Li, and A. Lal, "High efficiency  $\beta$  radioisotope energy conversion using reciprocating electromechanical converters with integrated betavoltaics", Appl. Phys. Lett. 92, (2008), pp.153105.
- [6]. M. V. S. Chandrashekhar, R. Duggirala, M. G. Spencer, and A. Lal, "4H SiC betavoltaic powered temperature transducer" Appl. Phys. Lett. 91, (2007), pp.053511.
- [7]. M. V. S. Chandrashekhar, C. I. Thomas, H. Li, M. G. Spencer, and A. Lal, "Demonstration of a 4H SiC betavoltaic cell", Appl. Phys. Lett., 88, (2006), pp. 033506.
- [8]. Y. R. Lu, N. Yoshimizu, and A. Lal, "Self-powered near field electron lithography", J. Vac. Sci. Technol. B. 27, (2009), pp.2537.
- [9]. H. Cember, "Introduction to Health Physics", Pergamon, New York, (1983).
- [10]. Klapdor, J. Metzinger, and T. Oda, "Beta decay half lives of nuclei far from stability", H. V. Zeitschrift für Physik A Hadrons and Nuclei, (1982), 309, pp.91.
- [11]. Y. C. Yang, L. Qian, J. Tang, L. Liu, and S. S. Fan, "A low-vacuum ionization gauge with HfC-modified carbon nanotube field emitters", Appl. Phys. Lett., (2008), 92, pp.153105.

# VERTICAL PILLAR ARRAYS AS PLASMON NANOCAVITIES

Mihail Bora\*, Benjamin J. Fasnfest, Elaine M. Behymer, Allan S-P Chang, Hoang T. Nguyen, Jerry A. Britten, Cindy C. Larson, Tiziana C. Bond\*

Lawrence Livermore National Laboratory, Livermore CA, USA

## ABSTRACT

We investigate tunable plasmon resonant cavity arrays in paired parallel nanowire waveguides. Resonances are observed when the waveguide length is an odd multiple of quarter plasmon wavelengths, consistent with boundary conditions of node and antinode at the ends. Two nanowire waveguides satisfy the dispersion relation of a planar metal-dielectric-metal waveguide of equivalent width equal to the square field average weighted gap. Confinement factors over  $10^3$  are possible due to plasmon focusing in the inter-wire space.

Surface plasmons, charge density waves propagating along metal-dielectric interfaces are applied in bio-molecular detection,[1-3] sub-wavelength optics[4-6] and photovoltaic technology.[7-9] Different geometries have been employed to study plasmonic structures. Horizontal layer approach provides excellent thickness control, but results in fewer plasmonic nanostructures per unit area.[10] The vertical structures provide good coverage, but require complex fabrication and are less amenable to large area substrates.[11] Here we propose fabrication of tunable plasmon resonant cavities in vertical wire arrays that combines the benefits of both approaches providing high density and good control over the cavity size over a large area (4 inch wafer) uniform plasmonic substrate. Tuning of the plasmon resonance in the 500-800 nm range is demonstrated by controlling the geometrical dimensions of the cavity. Future applications for the nano-cavities are envisioned in high sensitivity Raman spectroscopy[12,13] that requires high local electromagnetic fields and alignment between the plasmon resonance and excited and scattered light. The tunable nanocavity is of particular relevance for fabrication of plasmonic lasers which use surface plasmons instead of light to pump the lasing medium. [14,15] Since the device structure relies on vertical free standing nano-wires the plasmonic cavity region can be filled with any material of choice. In addition to the high confinement factors shown, the cavity plasmon resonance can be adjusted for maximum overlap with the absorbance of the active material.

The resonant cavity relies on paired nanowire waveguides that supports propagation of gap plasmon modes[16,17] (Figure 1a) when the separation is less than 50 nm. The cavity is delimited by a reflective metallic mirror at one side and an open end on the other for a more effective incident light-plasmon coupling. [18] Resonances occur when the cavity length is an odd multiple of quarter plasmon wavelengths due to boundary conditions of node at the mirror and anti-node at the open end. A two dimensional rectangular array of vertical resonant cavities is fabricated on a planar substrate (Figure 1b-e). Each nanowire is surrounded by four closest neighbors corresponding to two resonant cavities per nanowire, for a density of  $3.85 \cdot 10^8$  cavities/cm<sup>2</sup>. The vertical wire geometry enables large area fabrication (Figure 1c) and far field optical characterization. No inter-coupling between cavities is expected in these structures, since the size of the nanowires is an order of magnitude larger than the penetration depth of the electric field in the metal.

Photoresist wire arrays are patterned on a fused silica substrate using laser interference lithography under conditions described previously. [19] The pattern was transferred on the silica substrate by reactive ion etching. The silica nanowires are

coated with alumina by atomic layer deposition so that inter-wires gap is approximately 75 nm. Since the alumina deposition is self limiting, the thickness can be increased in conformal single molecule layer steps. Finally, a 20-40 nm thick gold coating was deposited by sputtering until the edge to edge distance between adjacent wires approaches 20-40 nm.

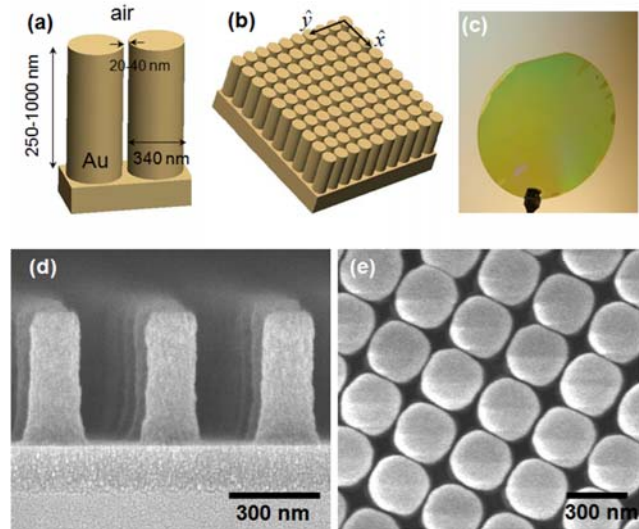


Figure 1. Vertical nanowire array substrate. (a) Single plasmon resonant cavity based on a two-nanowire waveguide. The separation medium is air of dielectric permittivity 1. Nanowire thickness is approximately 340 nm, and the height ranges from 250 to 1000 nm. The wavevector of the incident light is oriented along the waveguide in the transverse magnetic mode (b) Rectangular array of cavities on a planar substrate. Arrows indicate the lattice vectors of the array. (c) Large area fabrication of the plasmon nanocavities on a four-inch diameter substrate. (d) Side view of photoresist nanowires fabricated by laser interference lithography. (e) Top view of metallic nanowire cavity array coated with gold. The wire center-to-center distance is 360 nm and the edge to edge gap is 35 nm.

The two nanowire plasmon waveguide properties can be explained using an underlying planar metal-dielectric-metal (MDM) waveguide that is composed of two semi-infinite metal volumes separated by a dielectric of finite thickness (Figure 2, inset). The MDM waveguide is sufficiently simple to allow an analytical calculation of the dispersion curve based on the geometry and materials dielectric properties.

The two nanowire waveguide is approximated as an MDM waveguide of effective width  $w_{\text{eff}}$  that is calculated using the appropriate gap weighting metric. For example, for the optical extinction coefficient, the effective width is equal to the gap weighted with the square average of the field strength. The technique of decomposing the two nanowire waveguide into a continuum of elementary planar waveguides can be extended to other geometries providing a straightforward way to calculate the dispersion of arbitrary shape waveguides (e.g. wedges, grooves).

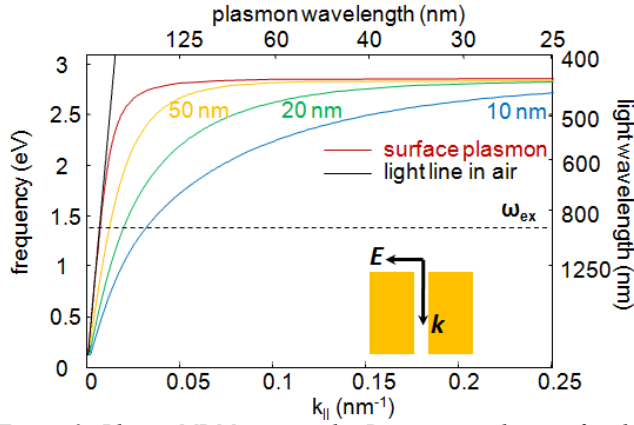


Figure 2. Planar MDM waveguide. Dispersion relations for the gold-air-gold (MDM) symmetric plasmon for different air thicknesses. The numbers near the curves indicate the width of the dielectric (air). For incident light along the waveguide of frequency  $\omega_{ex}$ , plasmon modes of the same frequency and wavevector given by dispersion curve are excited. Inset: schematic representing the MDM waveguide. The plasmon modes are excited by light propagating with wavevector  $k$ , along the planar waveguide with the electric field vector  $E$ , perpendicular to the metal sidewall.

Dispersion relations for MDM plasmons are determined by solving for propagating modes along the waveguide under continuity conditions at metal dielectric boundaries while satisfying Maxwell's equations. [20,21] The MDM solutions degenerate into symmetric and anti-symmetric modes, defined by the parity of the electric field in the direction perpendicular to the dielectric sheet, with respect to the mid-plane. Single interface surface plasmon modes are recovered when the separation is increased beyond the evanescent decay length.

The plasmon degeneracy can be understood in the plasmon hybridization model [22] in which the MDM plasmon is decomposed into two interacting single metal interface plasmons. The low energy or "bonding" state corresponds to the symmetric mode and the high energy or "anti-bonding" state to the anti-symmetric mode.

The coupling efficiency between light and MDM plasmons is proportional with the spatial and temporal overlap of the modes [23]:

$$\eta = \frac{\langle H_{plasmon} | H_{photon} \rangle^2}{|H_{plasmon}|^2 \cdot |H_{photon}|^2} \quad (1)$$

where  $\eta$  is the coupling efficiency and  $H_{plasmon}$  and  $H_{photon}$  are the field profiles for the plasmon and electromagnetic plane wave excitation modes. The electric field of the incident light is constant across the gap (symmetric) if the dielectric width is much smaller than the light wavelength; hence, the coupling efficiency is non-zero only for the symmetric mode.

The dispersion relation for the symmetric mode is given by the equation:[20]

$$\tanh\left(ik_{\perp}^d \frac{w}{2}\right) = -\frac{\epsilon_d k_{\perp}^m}{\epsilon_m k_{\perp}^d} \quad (2)$$

where  $k_{\perp}^d$  and  $k_{\perp}^m$  are the perpendicular components of the

plasmon wavevector in the dielectric and metal,  $\epsilon_d$  and  $\epsilon_m$  are the relative permittivities for the dielectric and metal, respectively, and  $w$  is the width of the dielectric sheet. In Figure 2, the dispersion relations for gold-air-gold waveguides of different air thicknesses are plotted. The dielectric function of gold is based on a Drude model fit for the published optical constants of gold.[24]

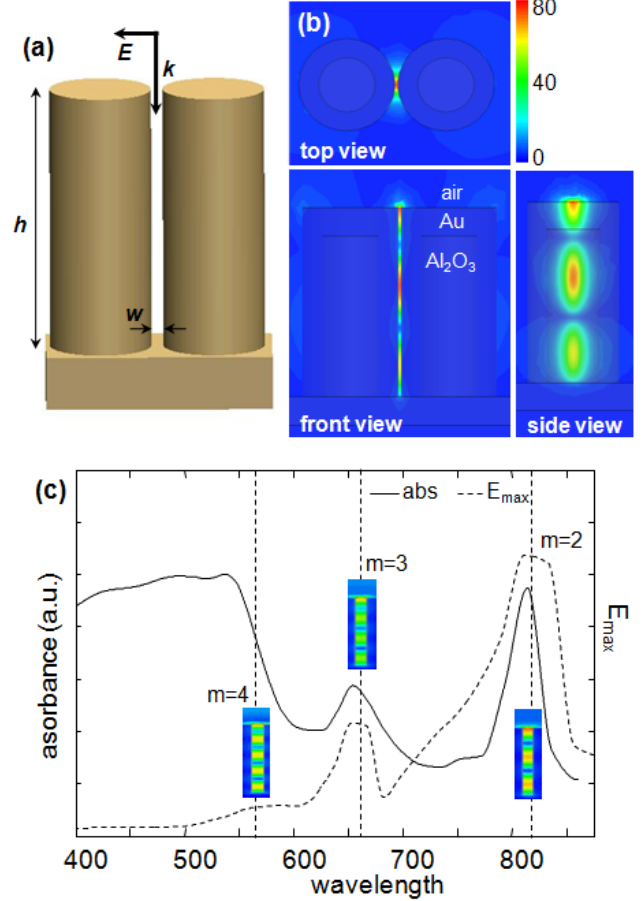


Figure 3. (a) Two-nanowire plasmon resonant cavity. The incident light field is oriented normal to the side surface of the wires (transverse magnetic mode). (b) Numerical simulations of the electric field as viewed from the front, top and side directions. (c) Resonances of order 2 and 3 and 4 are observed at 800, 650 and 565 nm.

Two different cavity types are analyzed. The first, the MDM slot waveguide, is a rectangular groove of height  $h$  and width  $w$  and infinite length indented in a semi-infinite metallic volume. This ideal structure allows direct comparison with the exact analytical dispersion relation calculated above for the MDM waveguide. The second case considered is a vertical wire nanocavity, composed of two metallic cylinders separated by a small distance (Figure 3a). The plasmonic features of vertical wire nanocavity are similar to those of the MDM slot waveguide, both showing resonances when the length of the cavity is an odd multiple on quarter plasmon wavelengths. Furthermore, the two nanowire waveguide satisfies the dispersion relation a modified planar MDM waveguide.

The two cavities are modeled as a waveguide of finite length, delimited by a metallic interface at the bottom and dielectric on top. Plasmon MDM type modes are excited by light normally incident on the open end side of the cavity. The photon field

overlaps with the plasmon cavity over a thin region with a thickness comparable to the skin depth of gold. The free electrons in the metal oscillate with the excitation light frequency  $\omega_{\text{ex}}$  and plasmon waves with wavevector given by the dispersion relation calculated in Equation 2 propagate along the waveguide. On the closed metallic end, a reflection with a  $\pi$  phase shift occurs and a plasmonic standing wave forms along the waveguide.

The structure resonant features are derived from the boundary conditions at the metal mirror (anti-node) and open dielectric side (node):

$$kh = \pi \left( m + \frac{1}{2} \right) \quad (3)$$

where  $k$  is the plasmon wavevector along the inter-wire region,  $h$  is the wire height, and  $m = 0, 1, 2, \dots$  is the resonance order. The plasmon states for which the wavevector satisfies the resonance condition in Equation 3 couple more strongly with the incident light and have a higher extinction coefficient, resulting in minima in the reflection spectrum.

A three-dimensional simulation of the two nanowire cavity is compared with the MDM slot model (Figure 3). Similar characteristics are observed for the electric field profile, and absorbance spectrum. As in the previous simulations the plasmon modes are excited by transverse magnetic normal incident light. Resonances are observed when the height of the wire is an odd multiple of quarter plasmon wavelengths. The plasmon modes are strongly confined to the inter-wire space where the amplitude of the electric field is two orders of magnitude larger than in the rest of the structure.

The MDM slot model predicts the optical properties of the two nanowire cavity when the equivalent spacing is taken into account. The effective distance between the wires can be calculated using coupling mode theory (Equation 1). Assuming that both photon and plasmon magnetic fields are normalized to unity and that the photon field is nearly constant across the gap, the coupling efficiency at each point along the  $y$  axis, is proportional to:

$$\eta_{(y_0)} \propto \left( \int_{y=y_0} H_{plasmon}^y dx dz \right)^2 \quad (4)$$

where  $H_{plasmon}^y$  is the  $y$  component of the plasmon magnetic field ( $x$  and  $z$  components are null). The coupling efficiency between photons and plasmons is therefore proportional to the square of the field average. Based on coupling mode theory argument presented above, we can calculate the effective separation of two adjacent cylinders as the average width weighted by the metric described earlier. This key finding allows derivation of the dispersion relation of complex plasmonic waveguides using a much simpler planar waveguide. Although outside the inter-wire region the cylindrical geometry deviates from the parallel interface model, 90% of the total electromagnetic field is concentrated in a circular sector with a  $\pm 12$  degrees opening. For the dimensions fabricated array (wire center-to-center distance of 360 nm), the effective width is approximately two times the edge to edge wire distance (15-35 nm).

The two-nanowire plasmons are confined in both lateral dimensions; along the direction normal to the wire surface the confinement is determined by the charge screening of the electric field in the metal layer. The confinement in the second orthogonal lateral direction results from the formation of a plasmon energy trap. Opposite polarity surface charges of the symmetric mode

minimize the dipole interaction energy when the distance is shortest. Since the effective MDM waveguide separation is increasing rapidly away from the inter-wire region, a strong energy gradient will focus the plasmons in the inter-wire space. This self-confinement feature makes the two wire plasmonic waveguides ideal candidates for high density plasmonic interconnects since the packaging density is increased significantly. Three dimensional sub-wavelength confinement becomes possible if the cavity length is smaller than the wavelength of the excitation light. For the 250 nm tall cavities we estimate the confinement factor to be approximately 1800.

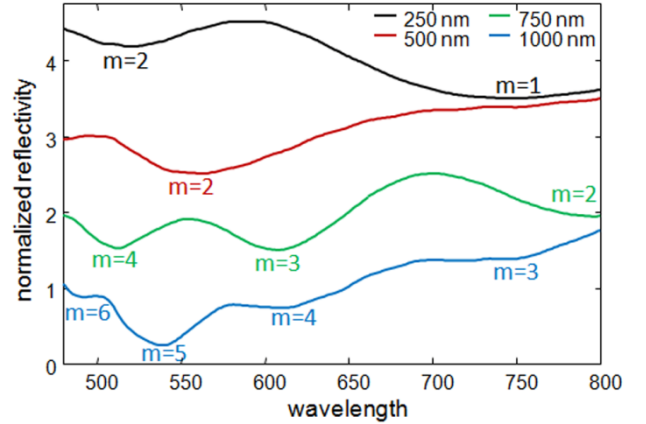


Figure 4. Normalized reflectivity plots for wire array of height 250, 500, 750 and 1000 nm. Incident light is non-polarized and perpendicular to the substrate. The reflectivity minima correspond to nanocavity excitation of plasmon resonances labeled by their order  $m$ .

The nanowire cavity array substrates were optically characterized by measuring the wavelength dependent normal incidence reflectivity. The plots were normalized to a 100 nm thick gold film to account for material specific absorbance (Figure 4). Excitation of plasmons within the cavity increases the extinction coefficient of the substrate and resonances are observed as minima in the reflectivity data. The cavity order was identified using numerical simulations and the analytical expression of the dispersion curve.

The plasmon wavelength can be calculated from Equation 3, knowing the cavity length and cavity order. The resonances measured in the experimental reflectivity are compared with numerical simulations to determine the resonance order and to calculate the plasmon wavevector. Further, the wavevector and frequency points are plotted along the dispersion curve for the MDM waveguide (Figure 5) from the analytical expression in Equation 2, using a separation value that best fitted the data. The good agreement between the analytical calculation of dispersion relation, numerical simulation of electric field and absorbance, and experimental data reflectivity show that the two-nanowire plasmon nanocavity can be approximated using a variable width MDM waveguide. The nanowire geometry allows for a stronger confinement resulting in higher fields and quality factors.

In conclusion, we demonstrate plasmonic resonant cavities that are supported along a two nanowire waveguide. Three dimensional subwavelength confinement is realized by adjusting the longitudinal length of the cavity for lower order resonance, and by focusing the plasmon modes between two adjacent wires in an energy gradient. Confinement factors over of  $10^3$  are realized for the 1<sup>st</sup> order resonance of the 250 nm tall cavity considered,



however this factor can be increased to considerably larger values using smaller height and diameter wires and shorter wavelength excitation light.

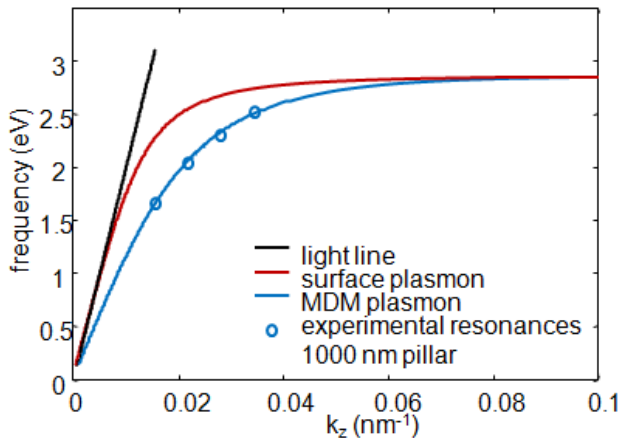


Figure 5. Analytical and experimental dispersion relations. Solid blue curve: analytical calculation based on MDM infinite waveguide using an effective gap separation. Blue circles: experimental points calculated from the 1000 nm tall wire reflectivity measurements.

We have also shown that the optical properties of complex plasmonic structures (e.g. two-nanowire waveguides) can be derived from elementary structures (MDM planar waveguide) by using a squared field average weight for the effective geometrical dimensions. The high electric field in the cavity and the tunability of the plasmon resonance with height and separation make cavity based substrates promising candidates for surface enhanced Raman spectroscopy and plasmonic lasers.

## ACKNOWLEDGEMENTS

This work performed under the auspices of the U.S. Department of Energy by Lawrence Livermore National Laboratory under Contract DE-AC52-07NA27344. LLNL-PROC-427303.

## REFERENCES

- [1] L.R. Hirsch, J.B. Jackson, A. Lee, N.J. Halas, J. West, "A whole blood immunoassay using gold nanoshells", *Analytical Chemistry*, 75, 2377, (2003).
- [2] R.L. Rich, D.G. Myszka, "Advances in surface plasmon resonance biosensor analysis", *Current Opinion in Biotechnology*, 11, 54, (2000)
- [3] M. Bora, K. Celebi, J. Zuniga, C. Watson, K.M. Milaninia, M.A. Baldo, "Near field detector for integrated surface plasmon resonance biosensor applications", *Optics Express*, 17, 329, (2009).
- [4] W.L. Barnes, A. Dereux, T.W. Ebbesen, "Surface plasmon subwavelength optics", *Nature*, 424, 824, (2003).
- [5] H.F. Ghaemi, T. Thio, D.E. Grupp, T.W. Ebbesen, H.J. Lezec, "Surface plasmons enhance optical transmission through subwavelength holes", *Physical Review B*, 58, 6779, (1998).
- [6] H. J. Lezec, A. Degiron, E. Devaux, R.A. Linke, L. Martin-Moreno, F.J. Garcia-Vidal, T.W. Ebbesen, "Beaming light from a subwavelength aperture", *Science*, 297, 820, (2002).
- [7] A.J. Morfa, K.L. Rowlen, T.H. Reilly, M.J. Romero, J. van de Lagemaat, "Plasmon-enhanced solar energy conversion in organic bulk heterojunction photovoltaics", *Applied Physics*

- Letters, 92, (2008).
- [8] K. Tvingstedt, N.K. Persson, O. Inganas, A. Rahachou, I.V. Zozoulenko, "Surface plasmon increase absorption in polymer photovoltaic cells", *Applied Physics Letters*, 91 (2007).
- [9] M. Westphalen, U. Kreibig, J Rostalski, H. Luth, D. Meissner, "Metal cluster enhanced organic solar cells", *Solar Energy Materials and Solar Cells*, 61, 97, (2000).
- [10] H.T. Miyazaki, Y. Kurokawa, "Controlled plasmon resonance in closed metal/insulator/metal nanocavities", *Applied Physics Letters*, 89, (2006).
- [11] C.L. Haynes, R.P. Van Duyne, "Nanosphere lithography: A versatile nanofabrication tool for studies of size-dependent nanoparticle optics", *Journal of Physical Chemistry B*, 105, 5599, (2001).
- [12] C.L. Haynes, R.P. Van Duyne, "Plasmon-sampled surface-enhanced Raman excitation spectroscopy", *Journal of Physical Chemistry B*, 107, 7426, (2003).
- [13] A.M. Michaels, M. Nirmal, L.E. Brus, "Surface enhanced Raman spectroscopy of individual rhodamine 6G molecules on large Ag nanocrystals", *Journal of the American Chemical Society*, 121, 9932, (1999).
- [14] M. Noginov, G. Zhu, A. Belgrave, R Bakker, V. Shalaev, E. Narimanov, S. Stout, E. Herz, T. Suteewong, U. Wiesner, "Demonstration of a spaser-based nanolaser", *Nature*, 460, 1110, (2009).
- [15] R.F. Oulton, V.J. Sorger, T. Zentgraf, R.M. Ma, C. Gladden, L. Dai, G. Bartal, X. Zhang, "Plasmon lasers at deep subwavelength scale", *Nature*, 461, 629, (2009)
- [16] A. Manjavacas, F.J.G. de Abajo, "Robust Plasmon Waveguides in Strongly Interacting Nanowire Arrays", *Nano Letters*, 9, 1285, (2009).
- [17] A. Manjavacas, F.J.G. de Abajo, "Coupling of gap plasmons in multi-wire waveguides", *Optics Express*, 17, 19401 (2009).
- [18] G.I. Stegeman, R.F. Wallis, A.A. Maradudin, "Excitation of surface polaritons by end-fire coupling", *Optics Letters*, 8, 386, (1983).
- [19] A. Fernandez, H.T. Nguyen, J.A. Britten, R.D. Boyd, M.D. Perry, D.R. Kania, A.M. Hawryluk, "Use of interference lithography to pattern arrays of submicron resist structures for field emission flat panel displays", *Journal of Vacuum Science & Technology B*, 15, 729, (1997).
- [20] J.A. Dionne, L.A. Sweatlock, H.A. Atwater, A. Polman, "Plasmon slot waveguides: Towards chip-scale propagation with subwavelength-scale localization", *Physical Review B*, 73, (2006).
- [21] H.J. Lezec, J.A. Dionne, H.A. Atwater, "Negative refraction at visible frequencies", *Science*, 316, 430, (2007).
- [22] E. Prodan, C. Radloff, N.J. Halas, P. Nordlander, "A hybridization model for the plasmon response of complex nanostructures", *Science*, 302, 419, (2003).
- [23] Z.J. Sun, D.Y. Zeng, "Coupling of surface plasmon waves in metal/dielectric gap waveguides and single interface waveguides", *Journal of the Optical Society of America B-Optical Physics*, 24, 2883, (2007).
- [24] P.B. Johnson, R.W. Christy, "Optical constants of noble metals", *Physical Review B*, 6, 4370, (1972).

## CONTACT

\*M. Bora, tel +1-925-423-2042; bora1@llnl.gov  
 \*T. Bond, tel +1-925-423-2205; bond7@llnl.gov

# A BIAxIAL MICROMIRROR FOR ANGULAR AND DEPTH SCANNING IN OPTICAL COHERENCE TOMOGRAPHY (OCT)

U. Izhar<sup>1\*</sup>, B.S. Ooi<sup>2</sup>, and S.Tatic-Lucic<sup>1</sup>

<sup>1</sup>Sherman Fairchild Center, Electrical & Computer Engineering Department, Lehigh University, Bethlehem, PA 18015, USA

<sup>2</sup>Division of Physical Sciences and Engineering, King Abdullah University of Science and Technology (KAUST), Thuwal, KSA

## ABSTRACT

A novel gimbal-less, thermally actuated micromirror is developed which can be used as both a reference and scanning mirror in optical coherence tomography (OCT) applications. Maximum deflection angle of up to 28° has been achieved at 12mW in scanning mode. A vertical displacement of 116µm at 12mW (78±4°C) was observed in piston mode. Our design goal for this mirror is to undergo 5° angle. This deflection was accomplished at a temperature increase of 17±5°C with respect to ambient. Our device can be integrated with GaAs optics due to this moderate temperature increase during its operation.

## INTRODUCTION

Multi-axis micromirrors have been widely reported in different design topologies with different actuation methods, such as electrostatic, electromagnetic, piezoelectric and electrothermal. These micromirrors are used in various applications including biomedical imaging, optical switching, beam positioning, and displays.

Zara and Smith [1] demonstrated an electrostatic design where a single axis micromirror was described. Angular displacement close to 30° at a voltage of 90V was reported in this work. An electromagnetic design was proposed in [2] with a reported angular displacement of 45° at an input current of 450mA in [2]. Similarly, a piezoelectric actuation scheme was used by Kim et. al. in [3] resulting in angular displacement of up to 6.1° at 16V. Finally, many electrothermal micromirrors have been reported for scanning applications. A typical example is shown by Buhler et. al. [4] and this micromirror used bimorph actuation To achieve a rotation angle of 5° for an applied power of 5mW. Later, Lammel et. al. [5] reported rotation angles of up to 30-40° for applied power of 15mW. Recently, electrothermal designs that were used in OCT application were reported by Xie et. al. [6] and Singh et al. [7]. In latter work, an angle of 17° was achieved with the temperature of 90°C in the actuator with applied power of approximately 37mW [7].

In this paper, we propose a multi-axial design that can achieve large angular deflection of up to 28° at low power of 12mW. The proposed design results in modest temperature increase of 78±4°C with respect to ambient during the operation at maximum angular deflection.

## MICROMIRROR DEVICE LAYOUT AND OPERATION

The micromirror device consists of a 3µm thick single crystal silicon mirror with a 1µm thick aluminum reflective coating on it. The mirror is connected to four electrothermal actuators (ETAs) through four 1.5µm thick undoped polysilicon flexural connectors, see Figure 1. The electrothermal actuators consist of 1.5µm thick undoped polysilicon as their lower structural layer and 1µm thick aluminum as their upper layer. When a voltage is applied to the heater contact pads, the actuator undergoes vertical displacement due to Joule heating. This motion is then transferred to the mirror through a corresponding flexural connector.

Our envisioned system-on-chip OCT system setup is also shown in Figure 1. The chip includes integrated waveguides

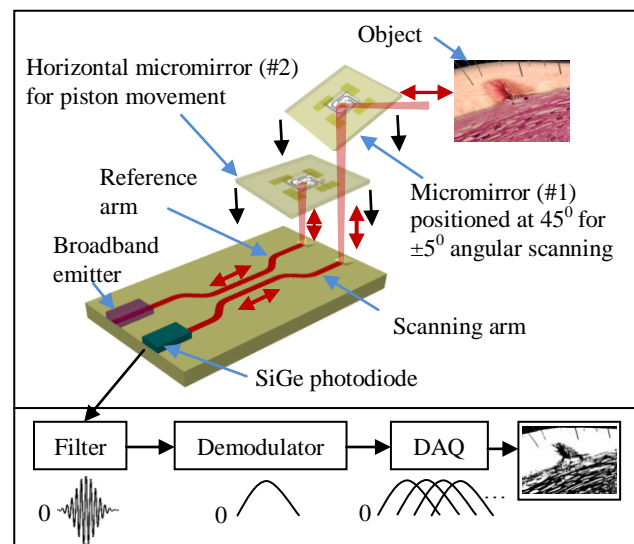
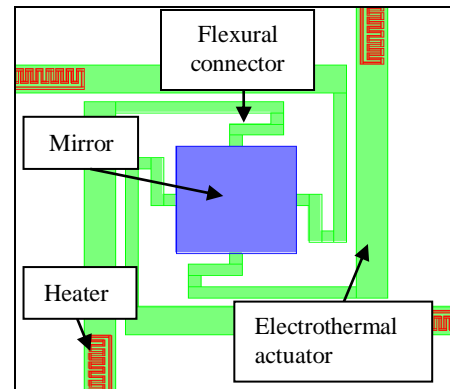


Figure 1: (Top) Schematic of the proposed micromirror design, (Bottom) 3D representation of envisaged integrated (miniature) OCT system

for the reference and sample arms of the interferometer, a broadband light source and photo diode. The proposed micromirror would be integrated horizontally for depth scanning (piston motion) at the end of reference arm, whereas the micromirror would be positioned at an angle of 45° (to direct light to and from the target sample) at the end of sample arm. The broadband light source will be monolithically integrated with the device. A silicon germanium photo diode would be used in the return path to detect the intensity of the incoming interference signal in time-domain. This time varying signal usually has a DC offset which can be removed by the bandpass filter. The signal will be demodulated for the envelope retrieval of the interference pattern. The signal can then be sampled by a data acquisition (DAQ) card and after processing the corresponding image can be displayed.

For feasible integration, temperature increase and power dissipation must be limited. Several design parameters were developed as goals for our micromirror device and are listed in Table 1.

Table 1: Design goals for MEMS micromirror

Design Property	Specification
Mirror Scanning Axis	2 Axes
Mirror Scanning Angle	+ / - 5 degrees
Temperature Increase	< 20 degrees C
Mirror Actuation Voltage	< 15 V
Mirror Actuation Frequency	≥ 4Hz

According to Table 1, minimum out-of-plane displacement of  $\pm 5$  degrees and maximum temperature increase of 20 deg. C are desired. These initial goals do not require the mirror to undergo vertical displacement. However, for a complete OCT setup a piston motion in the reference arm is required for depth perception of the target. For this reason, the device was designed such that it has dual functionality.

The thermo-physical behavior of the bimorph device (i.e. the change in curvature with the increase in temperature), when width of the actuator is constant can be given as [8]:

$$\frac{1}{r} = \frac{6(t_1 + t_2)(\Delta\alpha)(\Delta T)}{t_1 t_2 \left[ \epsilon \tau^2 + \frac{1}{\epsilon \tau^2} + 4\tau + \frac{4}{\tau} + 6 \right]} \quad (1)$$

where  $r$  is the curvature,  $t_1$  and  $t_2$  are the thicknesses of upper and lower layers respectively. Parameter  $\Delta\alpha$  is the difference in coefficients of thermal expansion between the two layers and  $\Delta T$  is the temperature increase from ambient. In the equation above,  $\tau = \frac{t_1}{t_2}$ ,  $\epsilon = \frac{E_1}{E_2}$  and  $E_1$  and  $E_2$  represents the Young's modulus of upper and lower layers respectively.

Moreover, if the convection and radiation are neglected, the temperature increase in the heater with applied power can be given as:

$$\Delta T = P_e R_t = \left( \frac{V^2}{R_e} \right) R_t \quad (2)$$

where  $R_t = \frac{l}{\kappa wt}$  is the thermal resistance,  $\kappa$  is thermal conductivity, and  $l$ ,  $w$ , and  $t$  are length, width and thickness of the heater respectively.

Optimal thickness ratio of the actuator layers was found out to be 0.707 [9] which gives  $1\mu\text{m}$  thick upper aluminium layer for a  $1.5\mu\text{m}$  thick lower polysilicon structural layer.

## FINITE ELEMENT ANALYSIS

Finite element analysis of the device was carried out using MEMS specific software, CoventorWare™ (Coventor, Inc.). Static analysis was performed using the software's electro-thermo-mechanical solver.

In the simulation model, the silicon substrate was covered with an insulating layer of oxide above it. Actuators were anchored on the oxide layer of the substrate. The bottom face of the substrate was assigned a fixed mechanical boundary condition and a thermal boundary condition of 300K (ambient temperature). Effects from convection and radiation were also considered from exposed aluminium surfaces. Though convection and radiation boundary conditions were later found to have less than 1% effect on the results, they were included in the analysis presented here. A bias was applied to one of the actuators to simulate the static deflection of the mirror.

The flexibility of design options in the software was used to observe the response of the mirror device for different actuator lengths (500 $\mu\text{m}$  and 550 $\mu\text{m}$ ), heater positions, and flexural connector shapes. For the heater, it was found that its position

affects the amount of power required to displace the actuator. If the heater is positioned solely on the anchor (over the substrate), it requires 333% more power to introduce the same temperature increase than the heater positioned on the substrate and extended into the actuator. This can be due to the fact that most of the heat flux is used to increase the temperature of the substrate which acts as temperature sink. However, when the heater is extended into the actuator, the heat flux encounters a much smaller mass compared to the substrate and thus the temperature along its length increases.

The flexural connector width and length was also studied as it relates to the flexibility and the amount of force that can be exerted on a mirror edge. Angular displacement and temperature increase observed from the analysis are presented in Figure 2. It can be seen from the figure that according to simulations, angular displacement of 5 degrees can be achieved at 2mW for actuator length of 550 $\mu\text{m}$  and at 4.5mW for actuator length of 500 $\mu\text{m}$ .

The temperatures at these angular displacements are 18°C for 550 $\mu\text{m}$  and 32°C for 500 $\mu\text{m}$ . Though the temperature is slightly higher in the latter design than was expected, it is worth noticing

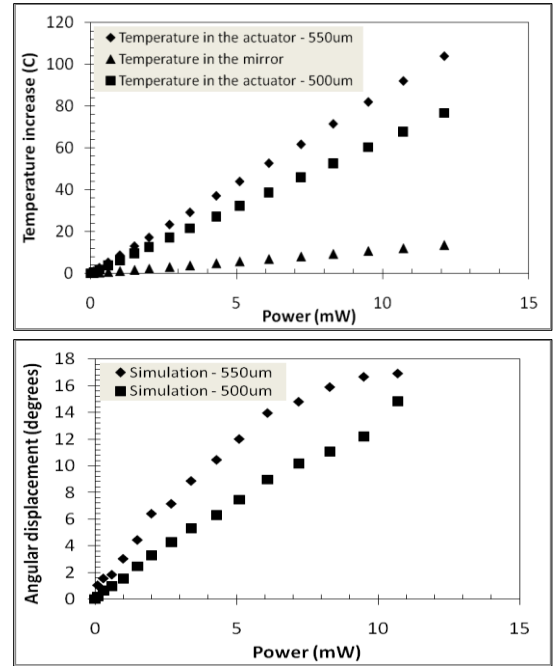


Figure 2: (Top) Simulated temperature increase from the ambient with applied power, (Bottom) Simulated angular displacement of 500 $\mu\text{m}$  and 550 $\mu\text{m}$  long actuators with the applied power

here that the simulations depicted the substrate temperature increase much lower ( $< 5^\circ\text{C}$ ) than in the actuator. As the substrate (not the actuator) would be in contact with optics this temperature increase would not affect the integration. Moreover, according to this simulation the temperature of the mirror was much lower than the temperature of the actuator during operation. This low temperature on the mirror ensured that there was no significant curvature change in the mirror due to temperature increase. After the preliminary feasibility of the device was studied through this analysis, actual fabrication was carried out.

## DEVICE FABRICATION

The fabrication process was carried out in Cornell's Nanofabrication Facility (CNF). The six mask fabrication process started with a four inch (100mm) diameter, silicon on insulator

(SOI) wafer with 3 $\mu$ m thick p-type device layer (boron-doped, 100 $\Omega$ cm), 2 $\mu$ m oxide layer and 500 $\mu$ m handle wafer (Ultrasil Corp. CA). The first step in the process was to define 3 $\mu$ m thick mirror base in the wafer device layer for support of aluminum mirror. Deep reactive ion etching (DRIE) using UNAXIS 770 ICP etcher was used for this purpose. Second, an undoped polysilicon layer was deposited using low pressure chemical vapor deposition (LPCVD) in two steps to embed the platinum heater. In the first step, 1 $\mu$ m thick layer (@ 590 $^{\circ}$ C, 150 sccm SiH $_4$ ) was deposited. Before the second step, a 0.1 $\mu$ m thick platinum was evaporated using e-beam evaporator, SC4500 (CVC Inc.) and patterned by lift off in Microposit 1165 stripper (Shipley). A 50nm thick titanium layer was used under the platinum for better adhesion. The second step was deposition of 0.5  $\mu$ m thick polysilicon (@ 590 $^{\circ}$ C, 150 sccm SiH $_4$ ) that followed after defining the heater.

To fabricate the upper layer of actuator and mirror, 1 $\mu$ m thick layer of aluminum was evaporated using e-beam and patterned using lift-off in Microposit 1165. Next, polysilicon was etched using reactive ion etching (RIE) in an Oxford 80 etcher (Plasma Lab) to define actuators, and flexural connectors with aluminum as a mask. Following this, aluminum was removed from the flexural connectors and contact pads using wet etching. The whole front side fabrication was completed by removing the 0.5 $\mu$ m thick polysilicon layer from the platinum contact pads using SF $_6$ /O $_2$  (30 sec.) and CF $_4$  (150 sec.) to expose the electrical contacts.

To release the device, dry etch (instead of wet KOH etch) was selected, as it needs less space for opening windows. One micron thick plasma enhanced chemical vapor deposition (PECVD) oxide and 7 $\mu$ m of photoresist (SPR 220-7) were used as masks for backside etching of the 500 $\mu$ m handle wafer. DRIE etch was carried out to remove all 500 $\mu$ m of the handle wafer with 30 minute cool-down cycles between 50 $\mu$ m intervals to get better sidewall profiles. The last step in the release process was oxide etch. Dry etching was used again with CHF $_3$ /O $_2$  (50sccm/2sccm, 240W) for this purpose as it is less violent than the wet etch, in which the fluid pressure can break the released structures. The process flow diagram is given in Figure 3 and an optical micrograph of the released device is shown in Figure 4.

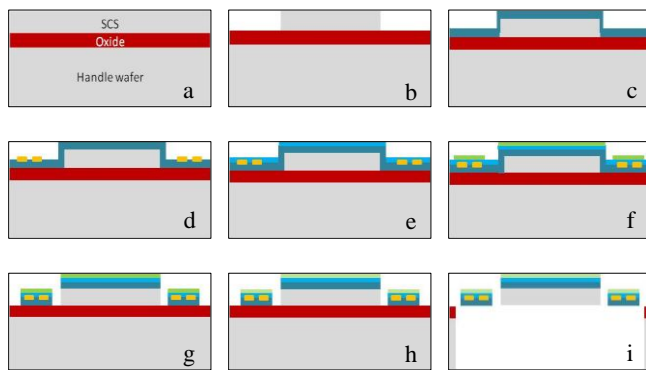


Figure 3: a) 100mm diameter SOI wafer (3 $\mu$ m device layer, 2 $\mu$ m oxide layer), b) photolithography and deep reactive ion etching (DRIE) to define the mirror base, c) LPCVD of first portion of polysilicon (1 $\mu$ m), d) E-beam evaporation of titanium(Ti) and platinum(Pt) and patterning by lift-off (100nm), e) LPCVD of second portion of polysilicon to embed the platinum resistor (500nm), f) E-beam evaporation of aluminum (Al) and patterning by lift-off (1 $\mu$ m), g) RIE of polysilicon using aluminum as a mask, h) etching of aluminum and second portion of polysilicon to expose the platinum contact pads, i) DRIE of silicon and RIE of oxide from backside to release the device

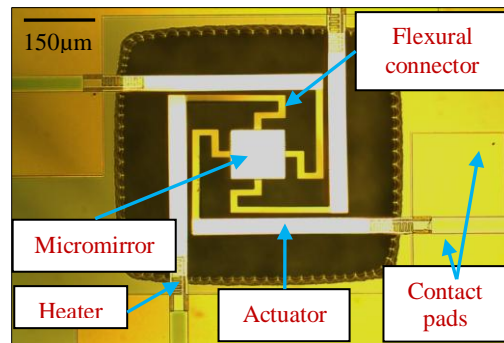


Figure 4: Optical micrograph of a released micromirror device

## CHARACTERIZATION AND DISCUSSION

### Angular displacement for scanning arm application

First, we performed measurements for the angular displacement of the mirror. A 633nm HeNe red laser was placed perpendicular to the mirror plane with light incident vertically down on the mirror. A millimeter scaled screen was placed 55mm above the mirror. To pass the light from the screen, a pinhole in the screen was created. The angular displacement of the mirror was then calculated by observing the displacement of laser spot on the screen, see Figure 5 (Top). The standard deviation of each mean value measured for five device samples is also shown. The maximum angles of 23 $^{\circ}$ , and 28 $^{\circ}$  were measured at 12mW for 500 $\mu$ m and 550 $\mu$ m long actuator designs respectively.

These results were better than what we predicted through simulations (Figure 2) and yielded higher angular displacements than anticipated. This is believed to be due to rotation or vertical displacement of the mirror introduced by the stiffness of adjacent actuators and flexural connectors. Simulations were repeated with taking the vertical displacement into account. The results are shown in Figure 5 (bottom).

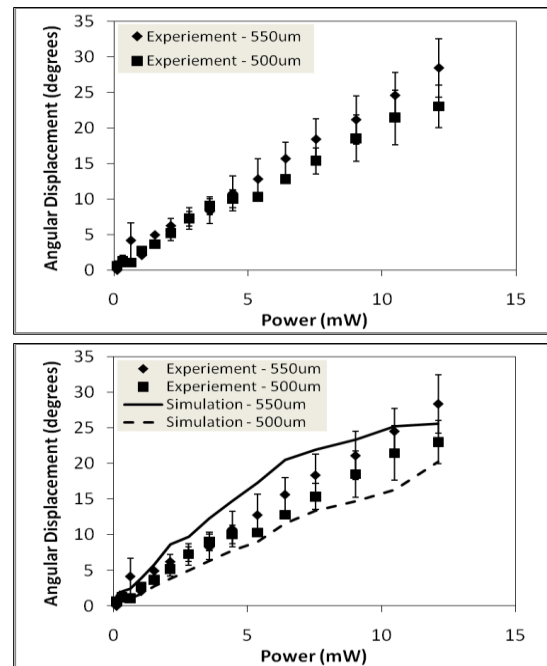


Figure 5: (Top) Angular displacement as a function of applied power, (Bottom) Comparison between angular displacements acquired with experiment and simulations taking into account the undesirable vertical displacement of the mirror in scanning mode

It can be seen that the angular displacement from simulation and experiment shows better agreement with an average difference of 23% between the values.

### Electrothermal response

As stated earlier, for the integration of the mirror in future with the miniaturized OCT system it is critical that the temperature increase in the device should remain low. For this purpose, we experimentally determined the temperature increase by measuring the change in resistance of the heater as a function of input power and is shown in Figure 6. The average error of the mean value from simulation is 19%.

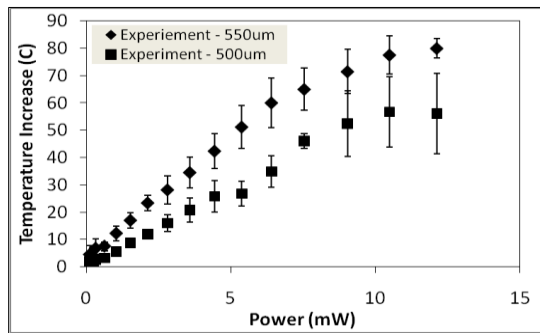


Figure 6: Temperature increase from ambient as a function of the applied power

### Vertical displacement for reference arm application

As our device has dual functionality, it was also characterized for vertical displacement using optical profilometer. The results are presented in Figure 7 and show that a vertical displacement of up to 64 $\mu$ m for 500 $\mu$ m and 116 $\mu$ m for 550 $\mu$ m long actuators can be achieved for a power input of 12mW with a temperature increase of 57 $\pm$ 14 deg. C and 78 $\pm$ 4 deg. C respectively (Figure 6). The results are compared with analytical calculations (using Equation 1). It can be seen that the difference between the two results lies between the standard deviation of the mean experimental values.

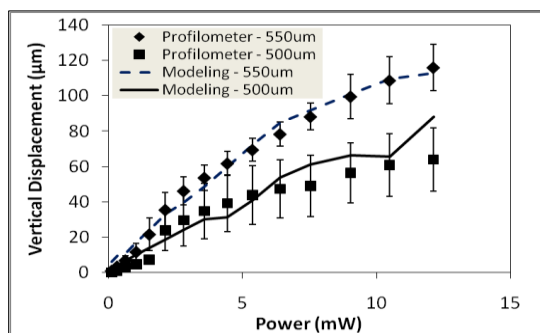


Figure 7: Comparison between vertical displacement (of different mirror designs) measured using profilometer with values calculated using Equation 1

### Transient response

The frequency response of the mirror was characterized to measure the minimum and maximum time it would take for one scan and it is shown in Figure 8. It was found out that the output value falls to 70% of its value at 10Hz.

Curvature and roughness were measured as they affect the focus depth in OCT imaging. For the current mirror, the curvature was found out to be 2.4mm $\pm$ 0.26mm. This curvature is significant. It is believed to be due to the insufficient thickness of the silicon

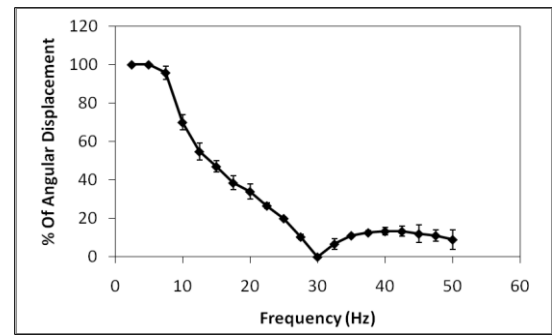


Figure 8: Transient response of the mirror device

supporting layer (3 $\mu$ m) beneath the 1 $\mu$ m reflective aluminum layer. Moreover, there can be mismatch at the interface of polysilicon layer which is deposited in two steps. The curvature can be improved by increasing the thickness of supporting single crystal silicon, decreasing the aluminum thickness and removing any sandwich layer between the two. The roughness of the mirror was found to be 100nm $\pm$ 20nm.

### CONCLUSION

We have presented, for the first time, an electrothermally-actuated, gimbal-less, multi-axis mirror which has the capability to operate in both scanning and piston mode and to achieve high angular (up to 28 $^\circ$ ) and vertical displacements (116 $\mu$ m) at low powers of 12mW and voltages of up to 6V. The temperature increase at this maximum angular and vertical displacement is 78 $\pm$ 4 deg. C. Our original specification of  $\pm$ 5 $^\circ$  scanning angle can be achieved at a low power of 2mW and at a maximum temperature increase of 17 $^\circ$ C  $\pm$  5 $^\circ$ C from ambient. The temperature increase of the substrate is less than 5 $^\circ$ C for this input. These properties make it compatible with other integrated optics to realize miniature OCT imaging. Currently, we are testing the mirror in a benchtop OCT system and experiments to get one dimensional intensity profiles are underway.

### ACKNOWLEDGEMENTS

This work was supported by PITA (Pennsylvania Infrastructure Technology Alliance), PITA-743-07 and the fabrication was carried out in CNF (Cornell Nanoscale Science and Technology Facility) at Cornell University.

### REFERENCES

- [1]. J. Zara, S. Smith, Sens. and Act. A 102 (2002), p. 167-174.
- [2]. J. W. Judy, R. S. Muller, JMM 63 (1997), p 249-256.
- [3]. S. J. Kim, Y. H. Cho, H. J. Nam and J. U. Bu, JMM 18 (2008), p 1-7.
- [4]. J. Bühler, J. Funk, O. Paul, F.-P. Steiner, H. Baltes, Sens. and Act. A 46-47 (1995), p 572-575.
- [5]. G. Lammel, S. Schweizer, P. Renaud, Kluwer Academic, Boston, 2002.
- [6]. A. Jain, S. T. Todd, G. K. Fedder, H. Xie, 2003 OSA Annual Meeting, Tucson, AZ, October 2003.
- [7]. J. Singh, J.H.S. Teo, Y. Xu, C.S. Premchandran, N. Chen, JMM, 18 (2008) p. 1-9.
- [8]. C. Liu, "Foundations of MEMS", Pearson Prentice Hall (2006).
- [9]. W. Peng, Z. Xiao, and K. R. Farmer, Proceedings of the 2003 Nanotechnology Conference, CA, 1 (2003), p. 376-379.

### CONTACT

\*U. Izhar, tel: +1-610-758-2003; umi205@lehigh.edu

# ACOUSTIC TRANSDUCERS BUILT ON EDGE-RELEASED MEMS STRUCTURES

Shih-Jui Chen\*, Youngki Choe, and Eun Sok Kim

University of Southern California, Los Angeles, California, USA

## ABSTRACT

This paper presents acoustic transducers built on edge-released MEMS structures, i.e., cantilever diaphragm and spiral-beam-supported diaphragm that are designed to release residual stress and also to avoid in-plane tension when bent. Sputter-deposited ZnO on the diaphragms is used as the piezoelectric thin film to sense and generate acoustic pressure. Typical diameter and thickness of the edge-released diaphragm are 1 mm and 1.6  $\mu\text{m}$ , respectively. The maximum strain on the spiral-beam-supported diaphragm is about an order of magnitude larger than that of a cantilever diaphragm transducer for a given pressure level and diaphragm size. The spiral offers a higher sensitivity at the cost of a lower usable bandwidth and less tolerance on the fabrication process variation.

## INTRODUCTION

Piezoelectric MEMS acoustic transducers offer advantages of simple fabrication process, no need for a polarization voltage, bi-directional actuation and wide dynamic range. A piezoelectric MEMS transducer is built on a thin micromachined diaphragm with a piezoelectric thin film. The bending of the diaphragm due to an applied sound pressure causes a stress change in the piezoelectric film, which generates an electric polarization in the film. To detect acoustic sound pressure level (e.g., for a microphone application), the diaphragm must be compliant. In this paper, we present a piezoelectric bimorph acoustic transducer built on a cantilever and a spiral-beam-supported diaphragm, both single-transducer and arrayed transducer.

## TRANSDUCER DESIGN

In case of the spiral-beam-supported transducer (Fig. 1), we used bimorph (with two ZnO layers) on a spiral beam to minimize the beam curling. A straight bimorph beam (500  $\mu\text{m}$  long, 50  $\mu\text{m}$  wide) acts as a strain detector, while one-turn spiral is used to relieve the boundary constraint on the free end of the strain-detecting beam and to support a large center circular diaphragm (500  $\mu\text{m}$  in diameter). The spiral-beam-supported diaphragm is mechanically compliant, and generates large electrical polarization on the piezoelectric bimorph when an acoustic pressure is applied to the diaphragm. A number of such transducers can be connected into an appropriate array to increase the sensitivity as a microphone and/or the sound output as a speaker.

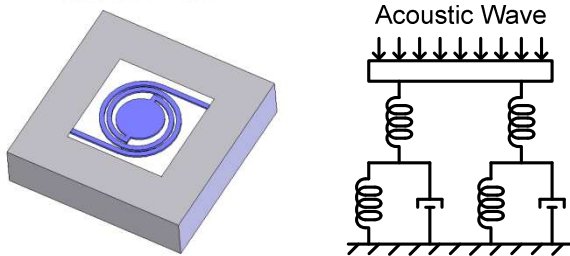


Figure 1: Schematic diagram of the spiral-beam-supported diaphragm (Left) and mechanical model (Right).

The voltage induced on a piezoelectric transducer (built on a diaphragm) when an acoustic pressure impinge up the diaphragm can be obtained by

$$V = \frac{P (\text{Pa}) \times M \times A_{\text{active}} (\text{m}^2) \times d_{31} (\text{pC/N})}{C_{\text{load}} (\text{pF}) + C_{\text{active}} (\text{pF})} \quad (1)$$

where  $P$  is the applied acoustic pressure;  $M$  is the average stress-magnification factor over  $A_{\text{active}}$ , the active area (i.e., the piezoelectric area covered by top and bottom electrodes);  $d_{31}$  is the piezoelectric coefficient;  $C_{\text{load}}$  is the load capacitance of the pre-amplifier; and  $C_{\text{active}}$  is the capacitance of the piezoelectric film over  $A_{\text{active}}$  ( $=\epsilon A_{\text{active}}/t$  with  $\epsilon$  and  $t$  being the dielectric constant and thickness of the piezoelectric film, respectively). Piezoelectric ZnO is a sensible choice for sensing applications with its proven and reliable sputter deposition. Though PZT has a higher piezoelectric coefficient (Table 1), its dielectric constant is also higher, consequently canceling the beneficial effect of the larger  $d_{31}$ , as you can see in Eq. 1, when  $C_{\text{active}}$  dominates over  $C_{\text{load}}$ .

Table 1: Piezoelectric thin film properties [11]

Material	Density (kg/m <sup>3</sup> )	Relative Dielectric Constant	Piezoelectric Coefficient $d_{31}$ (pC/N)
ZnO	5,680	8.8	-3.4
AlN	3,300	8.5	-2
Sol-Gel PZT	7,500	1,300	-70

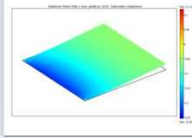

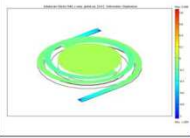
## Mechanical Simulation

Finite element modeling (FEM) with COMSOL software was used to explore the stress distribution and dynamic response of the cantilever and spiral-beam-supported diaphragms. All diaphragms were chosen to have the same area (1 mm by 1 mm) and thickness (0.7  $\mu\text{m}$ ) in the simulations (Table 2).

The FEM static analyses gave us the distributions of stress developed in the edge-released transducers under a uniform acoustic pressure of 1  $\mu\text{Pa}$ . The induced stress is integrated over the piezoelectric areas covered by top and bottom electrodes to obtain the average stress-magnification factor  $M$  in Eq. 1. The largest stress is distributed along the anchor of the diaphragm edges for all the diaphragm cases investigated. Thus, the electrodes are located near the diaphragm edges. If the induced stress level were the only parameter that affects the sensitivity, it would be desirable to make the electrode area as small as possible and place it as close to the edge as possible. But in that case, the capacitive loading effect that is described in the next section would have killed the sensitivity.

Among the cantilever square diaphragm, cantilever-supported circular diaphragm and spiral-beam-supported diaphragm (Table 2), the spiral-beam-supported diaphragm is most compliant, and produces the largest strain (and stress on the piezoelectric bimorph beam) in response to an applied pressure. Thus, the transducer built on a spiral-beam-supported diaphragm is expected to give a better sensitivity than that built on a cantilever diaphragm.

Table 2: FEM simulations of cantilever square diaphragm, cantilever-supported circular diaphragm, and spiral-beam-supported diaphragm (1 mm<sup>2</sup> large and 0.7μm thick)

Cantilever square diaphragm	Cantilever-supported circular diaphragm	Spiral-beam-supported circular diaphragm
		
pressure:1μPa maximum value E=-0.254 V/m strain=-3.46e-11	pressure:1μPa maximum value E=-0.255V/m strain=-4.18e-11	pressure:1μPa maximum value E=-1.054 V/m strain=-2.07e-10

### Modeling and Analysis of Equivalent Circuit with Voltage Amplifier

A piezoelectric microphone (based on a unimorph structure) and a voltage amplifier are equivalently modeled with a circuit in Fig. 2. A diode D (shown in Fig. 2a) is present only to provide a very high resistance ( $>10^{10}\Omega$ ) so that a tiny leakage path will be present to drain off stray charges that might otherwise accumulate on the exposed electrode. Without the diode, the input node will have a resistance in the range of  $10^{12}$  ohm for an op-amp that uses a pair of field effect transistors at its input, and the amplifier will be out of a proper bias. The capacitor  $C_e$  is comprised of parasitic capacitances due to the amplifier, the diode, and the conductor line connecting the microphone to the amplifier.

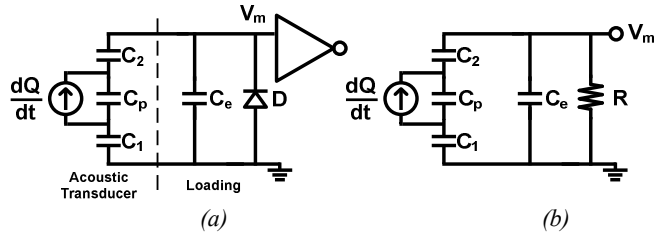


Figure 2: (a) Equivalent circuit for the piezoelectric microphone with a voltage amplifier. (b) Simplified circuit for analysis.

The capacitances on the equivalent circuit for the microphone are due to the ZnO layer ( $C_p$ ), and to the two insulating layers on the top and bottom of the ZnO layer ( $C_1$  and  $C_2$ ). The current source represents the piezoelectric activity of the ZnO that becomes strained when pressure deflects the silicon-nitride diaphragm. Strain in the piezoelectric material produces a polarization and surface charges that are mirrored on the top and bottom aluminum electrodes. For a sinusoidal pressure variation at a radial frequency  $\omega$ , there is a piezoelectrically induced sinusoidal charge of  $Q_0 e^{j\omega t}$  where  $Q_0$  is proportional to the applied pressure. The current delivered by the current source is  $dQ/dt (=j\omega Q_0 e^{j\omega t})$ .

The simplified circuit shown in Fig. 2b simplifies further to a parallel-connected RC with an equivalent current source and capacitance as follows:

$$\frac{dQ_a}{dt} = \frac{dQ/dt}{1 + C_p \left( \frac{1}{C_1} + \frac{1}{C_2} \right)} \quad C_T = C_e + \frac{C_p}{1 + C_p \left( \frac{1}{C_1} + \frac{1}{C_2} \right)}$$

Solving for  $v_m$ , the unamplified output of the microphone, we find

$$v_m = \frac{j\omega R}{1 + j\omega RC_T} \cdot \frac{Q_0 e^{j\omega t}}{1 + C_p (1/C_1 + 1/C_2)}$$

For  $\omega RC_T \gg 1$ , the condition for a good low frequency response,

$$\text{we have } v_m \approx \frac{1}{C_T} \cdot \frac{Q_0 e^{j\omega t}}{1 + C_p (1/C_1 + 1/C_2)} = \frac{Q_a}{C_T}$$

Parallel combination of many piezoelectric transducers usually increases the sound output when those are used as a transmitter, but does not necessarily improve the receiving sensitivity when those are used as a receiver. Thus, we simulated the equivalent circuit model (Fig. 3) with Agilent's ADS to determine an optimal number for serial connection of certain parallel-connected transducers. For example, for a total of 256 cantilever-like-diaphragm transducers, we calculated the sensitivity as a function of number of parallel connection, and found that 64 transducers in parallel followed by serial connection of 4 such sets (64x4) would give the highest sensitivity (Fig. 4).

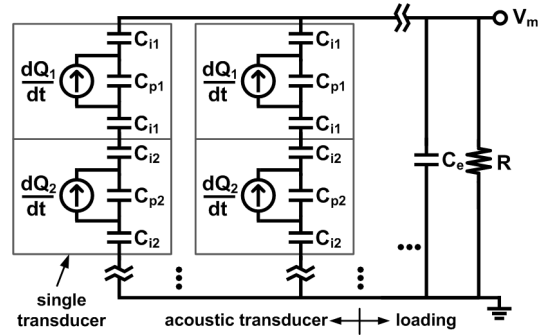


Figure 3: Equivalent circuit model of the arrayed ultrasound transducer and the loading capacitance and resistance.

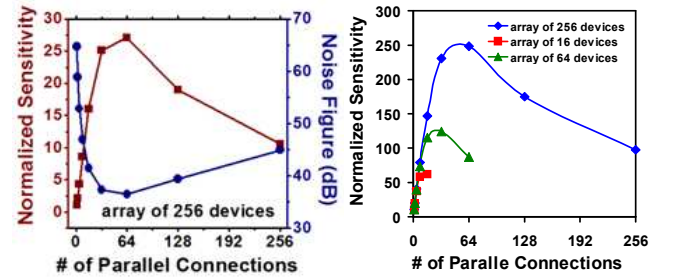


Figure 4: (Left) Normalized sensitivity and noise floor for an array of 256 transducers as a function of number of parallel connection for a given loading capacitance. Since the total number of transducers is 256, the number of parallel connection automatically determines the number of serial connection (Right) Normalized sensitivity vs. number of parallel connections as a function of total number of devices.

### FABRICATION

Cantilever diaphragms were bulk-micromachined with KOH on a (110) silicon wafer, while the spiral diaphragms are bulk-micromachined with KOH on a (100) wafer, with LPCVD low-stress silicon nitride as a supporting layer for ZnO film and electrodes.

To balance out the residual stresses in the films and also to increase the sensitivity, a bimorph structure with two 0.3-μm-thick ZnO films is used. Each of the ZnO films is encapsulated with two

0.1- $\mu\text{m}$ -thick plasma-enhanced chemical-vapor-deposited (PECVD)  $\text{Si}_x\text{N}_y$  insulating layer to improve the transducer's low-frequency response. A 0.2- $\mu\text{m}$ -thick aluminum is used for the top, middle, and bottom electrodes. The top and bottom aluminum electrodes are electrically grounded (Fig. 5).

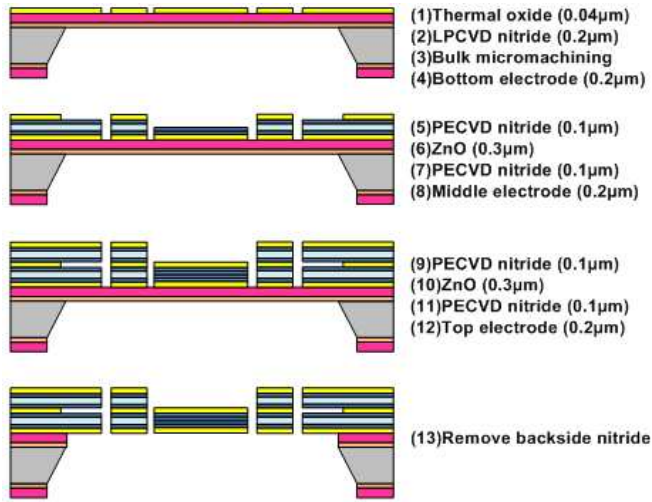


Figure 5: Brief fabrication process flow for a piezoelectric bimorph transducer built on a spiral-beam-supported diaphragm

For forming an array of cantilever-diaphragm transducers, a (110) silicon wafer is used to exploit the vertical sidewalls in densely packing the diaphragms over a relatively small area. Consequently, we were able to put a 64 element array of  $250 \times 250 \mu\text{m}^2$  transducers over a mere  $2 \times 2.5 \text{ mm}^2$ . The individual diaphragm having  $250 \times 250 \mu\text{m}^2$  area was chosen for a fundamental resonant frequency of 20 kHz (Fig. 6).

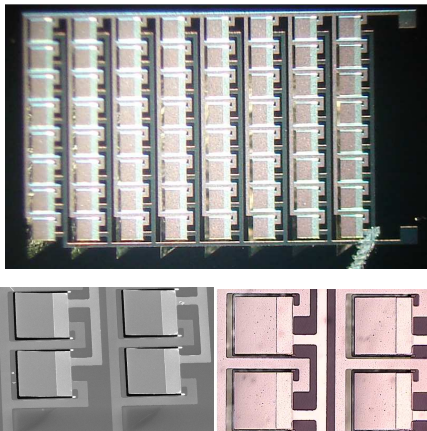


Figure 6: (Top) 64 transducers connected in parallel on a (110) Si wafer. (Bottom) SEM and CCD photos of the transducers

In case of the spiral-beam-supported-diaphragm transducers, we fabricated an array of 16 transducers as show in figure 7. There is some warping on the center circular diaphragm, which stiffens the diaphragm, and affects the sensitivity and frequency response of the transducer. The warping is due to residual stress gradient in the multiple-layer diaphragm, and can be reduced by increase the thicknesses and/or stiffness of the diaphragm.

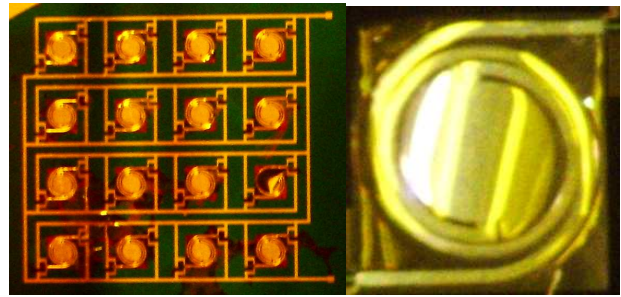


Figure 7: Photo of 16 spiral transducers connected in parallel.

## MEASUREMENT RESULTS

The fabricated microphones were tested in an anechoic box with a set-up shown in Fig. 8, with sound wave generated by a commercial speaker. The sound signal detected by the fabricated microphone was then amplified before being input to the oscilloscope, collected and analyzed with Labview software. A similar setup was used to measure sound output from the fabricated transducers.

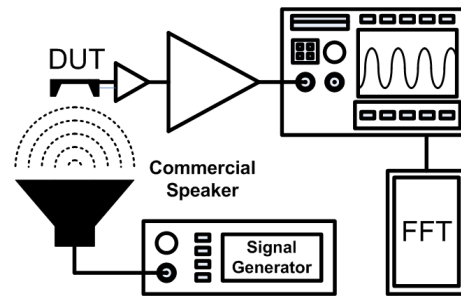


Figure 8: Testing setup

### Cantilever Diaphragm Transducer

In case of the fabricated microspeaker, the sound pressure output was measured about 3 mm away from the microspeaker in an open field with a calibrated microphone. A single microspeaker built on a cantilever diaphragm was measured to produce 0.8 Pa at 22 kHz when it was driven with  $75V_{\text{peak-to-peak}}$ . The same device was measured in a setup shown in Fig. 8 to have a receiving sensitivity of  $100 \mu\text{V}/\text{Pa}$  at the resonant frequency of 22 kHz. When 16 such transducers were connected in parallel, both the sound output and the sensitivity were improved to 4 Pa and 1.05 mV/Pa, respectively. When 64 such transducers were connected in parallel, followed by 4 such sets in series, the sound output and the sensitivity were improved to 10Pa and 2.9 mV/Pa, respectively (Fig. 9).

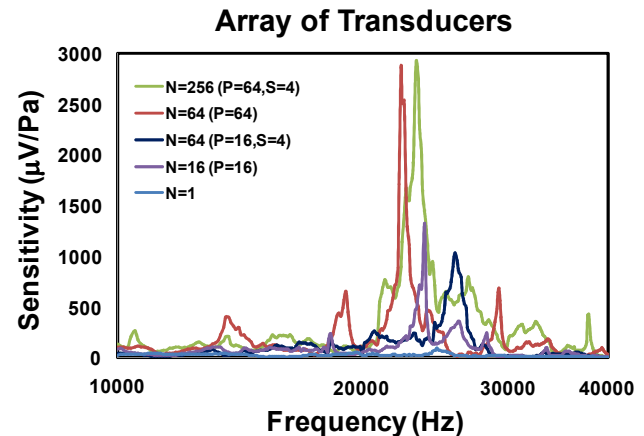


Figure 9: Acoustic sensitivity for array of cantilever-like transducers connected in parallel and/or series.



### Spiral-beam-supported Diaphragm Transducer

The bending displacement of a single spiral-diaphragm transducer was measured to be 300 and 50 nm/V at its fundamental frequency of 1.5 kHz and at 0.1 – 1 kHz range, respectively. It was also measured to have a receiving sensitivity of 1 mV/Pa at the resonant frequency and 150  $\mu\text{V}/\text{Pa}$  in 0.1 – 1 kHz range (Fig. 10). When 16 such transducers were connected in parallel, the sensitivity was improved to 5.5 mV/Pa at the first resonant frequency and 420  $\mu\text{V}/\text{Pa}$  in 0.1 – 1 kHz range.

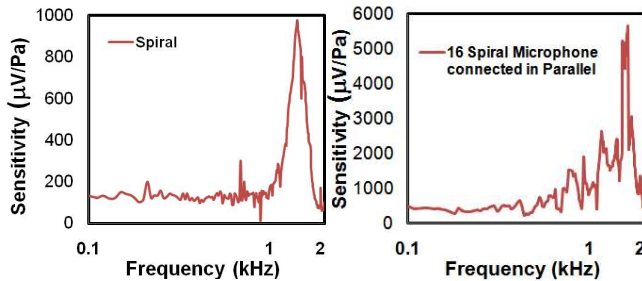


Figure 10: (Left) Measured sound sensitivities of a single spiral transducer. (Right) 16 spiral transducers connected in parallel.

### CONCLUSION

Acoustic transducers built on edge-released MEMS structures transducers have been designed and fabricated on silicon wafers. The transducers were tested both as a sound receiver and a sound transmitter, and were appropriately connected in a form of array for higher sensitivity and broader bandwidth. When 64 cantilever diaphragm transducers were connected in parallel, followed by 4 such sets in series, the sound output and sensitivity at the fundamental resonant frequency of 22 kHz were 10Pa and 2.9mV/Pa, respectively. By parallel connections of 16 spiral-beam-supported diaphragm transducers, the receiving sensitivity at the fundamental resonant frequency was improved to 5.5mV/Pa, more than 5 times that of a single device.

### ACKNOWLEDGMENT

This manuscript is based on work supported by Defense Advanced Research Projects Agency under grant W31P4Q-08-1-0010.

### REFERENCES

- [1] E. S. Kim and R. S. Muller, "IC-Processed Piezoelectric Microphone," IEEE Electron Device Letters, Vol. EDL-8, No. 10, pp. 467-468, Oct. 1987.
- [2] E.S. Kim, J.R. Kim and R.S. Muller, "Improved IC-Compatible Piezoelectric Microphone and CMOS Process," Transducers '91, IEEE International Conference on Solid-State Sensors and Actuators (San Francisco, CA), June 23-27, 1991, pp. 270-273.
- [3] S.S. Lee, R.P. Ried and R.M. White, "Piezoelectric Cantilever Microphone and Microspeaker," IEEE Solid-State Sensors and Actuators Workshop, pp. 33-37, Hilton Head, South Carolina, June 13-16, 1994.
- [4] G. M. Sessler, "Silicon Microphones" J. Audio Eng. Soc., Vol. 44, No. 1/2, pp. 16-21, Jan. 1996.
- [5] C. H. Han and E. S. Kim, "Fabrication of Piezoelectric Acoustic Transducers Built on Cantilever-like Diaphragm," Proceedings of the 14th IEEE International Conference on Micro Electro Mechanical Systems (MEMS'2001), Interlaken, Switzerland, Jan. 21 - 25, 2001.
- [6] A.S. Ergun, G.G. Yaralioglu, and B.T. Khuri-Yakub, "Capacitive micromachined ultrasonic transducers: Theory and technology," Journal of Aerospace Engineering, vol. 16, no. 2, pp. 76 - 84, Apr. 2003.
- [7] R.G. Polcawich, M. Scanlon, J. Pulskamp, J. Clarkson, J. Conred, D. Washington,
- [8] R. Piekarz, S. Trolrier-Mckinstry, M. Dubey, Design and fabrication of a lead zirconate titanate (PZT) thin film acoustic sensor, Integr. Ferroelectr. 54 (2003) 595-606.
- [9] P.V. Loeppert and S.B. Lee, "SiSonic - The First Commercialized MEMS Microphone," Solid-State Sensors, Actuators, and Microsystems Workshop, pp. 27-30, Hilton Head, South Carolina, June 4-8, 2006.
- [10] J.F. Lo, S.J. Chen, H. Yu, E.S. Kim, L. Marcu, and M. Gundersen, "Multi-Cantilever-Driven Rotational Translation for Actuated Micro Optical Grating," Transducers '07, IEEE International Conference on Solid-State Sensors and Actuators, Lyon, France, June 10-14, 2007, pp. 2421-2424.
- [11] S. Prasanna and S. S. Mark, "Optimal Materials Selection for Bimaterial Piezoelectric Microactuators," Journal of Microelectromechanical Systems, 2008, 17 (2) 462-472.

### CONTACT

\*Shih-Jui Chen, Tel: 1-213-821-1611; shihjuic@usc.edu

# FABRICATION AND ELECTRICAL CHARACTERIZATION OF MICROSCALE DIELECTRIC BARRIER DISCHARGE DEVICES

Justin C. Zito\*, and David P. Arnold

Interdisciplinary Microsystems Group, University of Florida, Gainesville, Florida, USA

## ABSTRACT

In this paper we report the microfabrication and electrical characterization of microscale dielectric barrier discharge (DBD) plasma devices on glass substrates. The devices employ Au electrodes (5 mm long,  $\leq 40 \mu\text{m}$  wide) separated by a polyimide dielectric (10  $\mu\text{m}$  or 50  $\mu\text{m}$  thick). Under ac sinusoidal excitation at 14 kHz, the plasma discharges ignite around 1  $\text{kV}_{\text{pk}}$  input amplitude. The power consumption of a single device is on the order of 3 – 6  $\text{mW}/\text{mm}$  and power delivery is found to increase linearly when multiple devices are connected in parallel. The effective plasma load impedance is extracted from the measured voltage/current waveforms, and the parameters for a parallel R-C load model are computed. Since most of the tested devices sustained plasma for only a few minutes before failure, reliability of the devices is also briefly discussed.

## INTRODUCTION

### Background & Motivation

Atmospheric plasma discharge devices are finding growing application in aerodynamic flow control, biological sterilization, water purification (ozone generation), surface treatment (e.g. corona charging), and more recently microfluidic propulsion [1]. For flow control and propulsion applications, advantages of plasma actuators include a lack of moving parts, construction simplicity, and near instantaneous response.

As shown in Figure 1, a standard DBD device consists of two parallel electrodes offset from one another on either side of a dielectric material. The top electrode is exposed to air while the bottom electrode is encapsulated by another dielectric to prevent discharge on the bottom side of the device. A high-voltage dc or ac source is applied to the exposed (top) electrode, while the lower electrode is grounded. When a sufficiently high voltage is applied to the electrodes, the air weakly ionizes near the surface of the dielectric. This imparts an electrohydrodynamic (EHD) body force to the fluid, providing momentum to the flow.

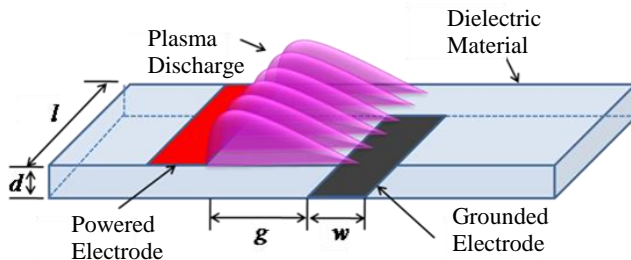


Figure 1: Schematic of a single dielectric barrier discharge (DBD) plasma device.

One motivation for exploring microscale DBD devices stems from numerical simulations of parallel plate *volume discharges* that suggest a significant increase in the electric force density ( $\text{N}/\text{m}^3$ ) may be achievable using micron-sized electrode gaps [2]. The numerical predictions of [2] showed close agreement with electric field measurements from micron-scale gapped devices [3], thus building confidence in the numerical models. While difficult to experimentally measure, the charge density and electric force

were computed using the numerical models. For electrode gaps below  $\sim 30 \mu\text{m}$ , the electric force density is estimated to increase by over two orders of magnitude. While these simulations and experiments were for parallel-plate *volume discharges*, if higher force densities can similarly be achieved for *surface-discharge* DBD configurations, this could have significant impact on flow control or propulsion devices.

A brief explanation for the increased force density is as follows. With decreasing gap, the sheath region of the plasma discharge occupies a greater portion of the discharge, reducing the quasi-neutral region (where electron density  $\approx$  ion density) [2]. The momentum transfer to the fluid is due to the Lorentz force,  $qE$ , where  $q$  is the net charge separation, and  $E$  is the electric field. Since the sheath region has the largest charge separation  $q$ , (the ion density is much higher than the electron density in the sheath region), using a smaller gap should provide a larger electric force density, and thus increasing the local body force to the fluid.

Further motivation for microscale discharge is that the voltage required to achieve the electric field necessary for plasma ignition is reduced. This lowers the power requirements for device operation, thus translating to smaller and lighter power supplies for flight vehicles. Moreover, batch microfabrication enables high-throughput manufacturing of complex electrode shapes with good alignment and dimensional control. The ability to fabricate electrodes on flexible substrates is also of great interest.

### Prior Work

In addition to the work of Longwitz [3], other researchers have begun to investigate microscale discharge devices. Ono et al. [4] investigated the breakdown threshold voltages for parallel-plate micro-gaps on the order from 2 – 50  $\mu\text{m}$ . They showed that breakdown voltages for Si-Si electrodes closely follows Paschen's curve, though Si-metal breakdown voltages deviated significantly from Paschen's curve at gap widths below 5  $\mu\text{m}$ . Ono et al. [5] also showed that both metal and Si electrodes are subject to sputtering/erosion during the discharge process. The evaporated material increases the local pressure in the gap region, resulting in a decrease in the breakdown threshold voltage. This erosion is an important consideration in the reliability of micro discharge devices, since this may limit the time before failure. Bass et al. [6] developed a capacitive-coupled helium microplasma that was formed in a narrow channel by electrodes on either side of a quartz plate. This design was intended as an atomic emission detector having a minimum channel cross-section of 0.2 x 0.2 mm, and can be thought of as a DBD volume discharge device. Mitra and Gianchandani [7] developed pulsed micro-discharge devices using two- and three-electrode geometries with a 200  $\mu\text{m}$  electrode gap for use in species detection and optical emission spectroscopy. Okochi et al. [8] have developed and tested mm-size DBD plasma devices using MEMS fabrication processes.

### This Work

In this paper, we focus our efforts on generating DBD surface plasma using electrodes and gaps with microscale dimensions. As shown in Figure 2, the electrode widths are 20  $\mu\text{m}$  (top) and 40  $\mu\text{m}$  (bottom), and each electrode is 5 mm long (spanwise). The lateral gap between the electrodes ranges from 50 – 120  $\mu\text{m}$ . The

electrodes are 300 nm thick (50 nm Ti, 250 nm Au), separated by a polyimide dielectric, of either 10  $\mu\text{m}$  or 50  $\mu\text{m}$ . The structures are fabricated on soda lime glass substrates. Polyimide was chosen for its good metal adhesion and its common use as a dielectric in macroscale DBD plasma devices. Rounded edges are used to avoid field-concentration points and resulting plasma “streamers.”

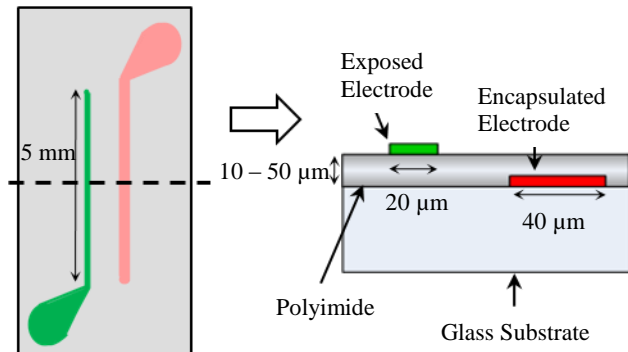


Figure 2. Top view and cross-section schematics of DBD devices.

### DEVICE FABRICATION

The process flow for these devices is shown in Figure 3. The first steps involve sputtering and lift-off to define the lower Ti/Au electrodes. The Ti layer is used to improve the adhesion of the Au. A low-stress polyimide (HD Microsystems PI2611) is used as the ‘barrier’ or insulation layer. The polyimide was spun and soft-baked multiple times to reach the desired dielectric thickness. The substrate is then placed on a hotplate to cure the polyimide layer. Before patterning the top electrodes, the polyimide is etched with an O<sub>2</sub>-based reactive ion etch (RIE) to open contacts to the lower electrode bond pads (not shown in the cross-sections). A sputtered chrome layer was used as the etch mask for the RIE process. Following the polyimide etch, the chrome mask is removed using a wet chrome etchant. The top electrodes are then sputtered and patterned using lift-off.

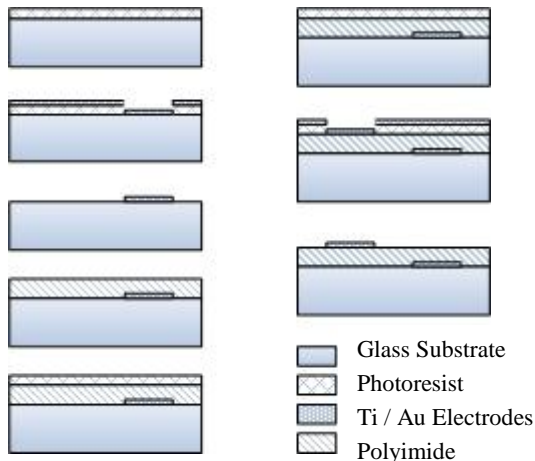


Figure 3. Fabrication process for DBD plasma devices.

### EXPERIMENT

Optical images of various completed devices are shown in Figure 4. Directed plasma discharge is shown (left-to-right) for the linear designs, top-to-bottom for the curved design) across the micro-gap in three of the four images. While various electrode configurations were fabricated, the remainder of this paper focuses on test results from the simple straight-electrode configuration,

both single devices and parallel connected devices. The parallel connected designs comprised 4 to 6 devices connected together, which all have the same gap.

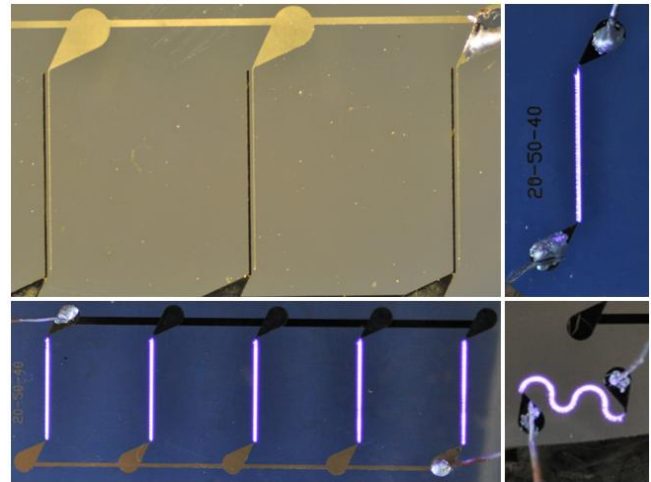


Figure 4. Various DBD plasma devices; clockwise from top right: single actuator with 50  $\mu\text{m}$  gap; serpentine geometry,  $g = 80 \mu\text{m}$ ; five actuators in parallel,  $g = 50 \mu\text{m}$ ; fabricated parallel devices (no discharge present) showing electrode detail.

### Test Set-Up

The schematic for the experiment set-up is shown in Figure 5. The devices were tested using ac sinusoidal excitation at 14 kHz, with input amplitude on the order of 1 kV<sub>pk</sub>. The power supply consisted of a standard function generator (Tektronix AFG 3022B), an audio amplifier (QSC Audio RMX 2450) to increase the signal to the 10’s of volts range, and a custom transformer (Corona Magnetics, Inc.) to further increase the voltage into the kV range. A digital oscilloscope (Tektronix DPO 3014) was used to capture the voltage and current waveforms. A Tektronix P6015A high-voltage probe was used, along a Pearson 2100 current probe. The current probe has a 20 MHz bandwidth, and the oscilloscope was set with a 20 MHz bandwidth limit for the current channel.

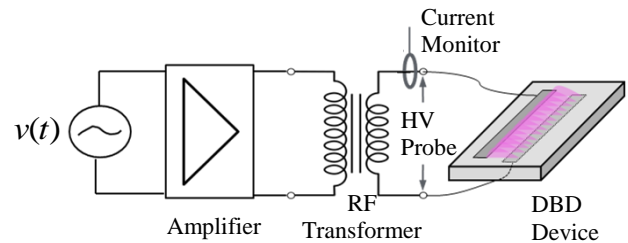


Figure 5. Schematic of the experiment set-up.

For each device tested, 10 data records were captured. Each data record consisted of one million data points, sampled at 250 MS/s, corresponding to 56 periods of data within each record. The 10 data records yielded a total of 560 periods of data for analysis. The data was analyzed to determine average power consumption and equivalent impedance characteristics.

Ideally, several different devices were tested for each gap width and dielectric thickness. Due to burn-out and reliability issues (discussed in a later section), the number of devices that produced stable discharge that allowed for data collection was not consistent for each geometry. Hence, the number of devices tested for each geometry varied from 2 to 10.

### Parameter Extraction

The average power is calculated by integration of the product of the voltage and current waveforms. Discretely, this was done by the point-by-point multiplication of the voltage and current waveforms, which is then summed and divided by the number of data points. From the voltage and current waveforms, load impedance parameters can be extracted, assuming a simple R-C circuit model to represent the impedance behavior of the plasma. The extraction process follows a previously developed plasma impedance extraction methodology, described in [9]. The resistance is used to model the real power consumed by the device, while the capacitance is used to represent the reactive behavior.

### RESULTS

Plasma was typically ignited around 1 kV<sub>pk</sub> input amplitude, much lower than the 5+ kV<sub>pk</sub> range required for macroscale DBD devices. The average power consumed by a single device is plotted against varying gap widths in Figure 6. The voltage necessary to create discharge for the devices with a 50 μm dielectric is, on average, 140 V higher in amplitude than that for the 10 μm dielectric devices, although the average power consumed is greater for the thinner dielectric. This may be attributed to a better conduction path established with the 10 μm barrier, causing more current flow and increased power consumption. The data shows a small increase in the average power consumed with increasing gap size, most likely due to an increase in the input voltage required to generate discharge with larger gap sizes. (The device with 110 μm gap did not create a discharge that remained stable for data collection. It would fail during the data capture process and did not provide reliable data.) The uncertainties (error bars) shown in the figure were computed using a t-distribution with a 95 % confidence interval. For some of the gap sizes, only a few devices were successfully tested and hence the corresponding uncertainty is significant.

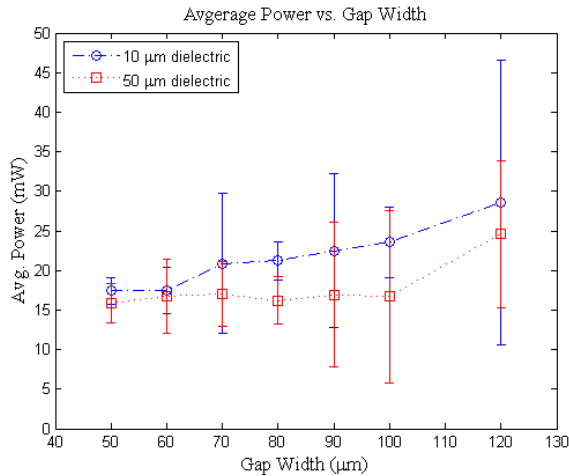


Figure 6. Average power consumed by a single device plotted against varying gap width.

Figure 7 compares the average power consumption with the number of devices connected in parallel for devices with a 10 μm thick dielectric. The data implies that an increased amount of power is necessary to actuate several plasma devices with an apparently linear trend, though more data is required to better quantify the relationship between the power requirement and number of devices.

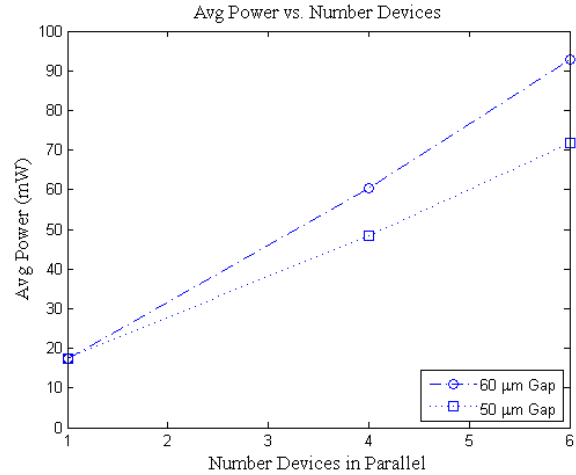


Figure 7. Average power consumed plotted against number of devices connected in parallel. Data shown for linear electrodes with  $g = 50 \mu\text{m}$  and  $60 \mu\text{m}$ , and a  $10 \mu\text{m}$  thick dielectric.

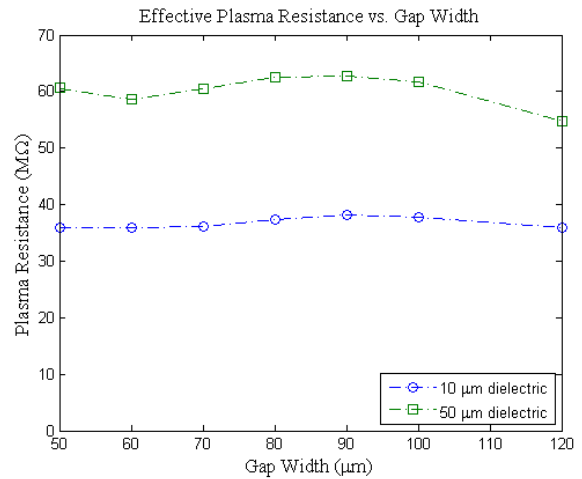


Figure 8. Effective plasma load resistance plotted against varying gap width.

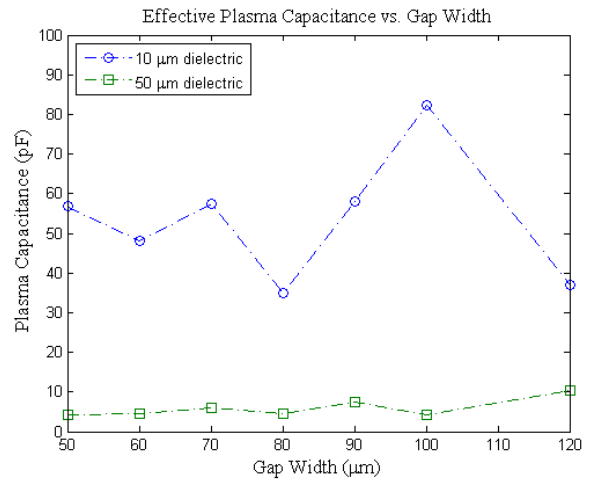


Figure 9. Effective plasma load capacitance plotted against varying gap width.

The effective plasma load resistance and capacitance were calculated and are plotted in Figures 8 and 9, respectively. Both the resistance and capacitance values remain fairly constant as a function of gap ( $g$ ). The resistance values fluctuate by up to 5 % of their mean value. The capacitance values vary significantly more, by about 35 % of its mean value. There is a clear difference between the two dielectric thicknesses, however. The thinner dielectric barrier has less resistance and higher capacitance. The larger capacitance values are consistent with a smaller dielectric thickness. Compared to macroscale DBD devices [9], these microscale devices exhibit smaller resistance and larger capacitance, also consistent with the smaller physical dimensions.

### Reliability Concerns

While prior work by the researchers have shown quite reliable and stable DBD plasma devices at the macroscale, these microscale DBD devices seem more prone to failure. Electric field concentration points often result in an intense “streamer” of plasma which erodes the dielectric barrier (as opposed to a uniform glow discharge). The length of time for which discharge was sustained varied among the devices tested. A device was considered “successful” if it sustained discharge for over one minute. A few devices sustained discharge for upwards of five minutes without failure. At the other extreme, some devices would fail before generating a stable discharge.

The source of failure may come from a combination of variables, such as non-uniformities in the dielectric material, jagged electrode edges, and/or electrode erosion eventually leading to failure. The quality, or smoothness, of the electrodes is thought to be a significant factor in the device reliability. Fabrication details such as photomask quality, metal deposition and metal patterning process may all have an impact on device performance and reliability. The three images in the left half of Figure 10 show examples of several failed devices, showing that points of failure most often occur near one of the ends of the powered electrode. Areas of charred/burned dielectric can be identified near the ends of the electrodes in the three images on the left. The three images in the right half of Figure 10 show example devices just after/at the onset of failure.

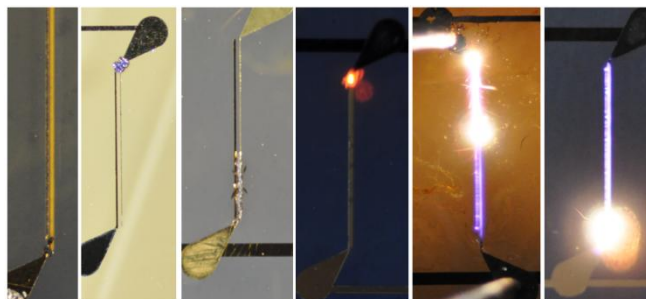


Figure 10. Images of device failure; the left three images show devices after failure; the right three images show devices at the onset of failure.

### CONCLUSION

Microscale DBD plasma devices were successfully fabricated and demonstrated sustainable plasma discharge. The power requirement for these devices depends upon the number and length of the devices used, although for a limited number of devices the power requirement was between 3 – 6 mW/mm for a single device. The power requirement appears to scale linearly with increasing number of devices, although more data are necessary to make a definite conclusion. The impedance data are similar, qualitatively,

to the trends reported for macroscale DBD devices [9]: the effective plasma resistance is lower for the thinner (10  $\mu$ m) dielectric, while the effective capacitance and the average power consumed are greater for the thinner (10  $\mu$ m) dielectric.

The reliability of DBD devices remains an open topic for exploration. As discussed previously, local points of concentrated electric field often lead to device failure and are difficult to mitigate. The source of failure may come from a combination of variables, from the material properties/defects to the fabrication processes used. Electrode erosion is an inevitable process that is a byproduct of micro-discharge devices and must be further studied.

Ongoing efforts aim to characterize the flow actuation of these devices. The ultimate goal is to improve the performance of these devices by imparting the maximum momentum to the flow. To characterize their flow effects, micro particle imaging velocimetry (micro-PIV) can be used to collect velocity measurements. Other polymer materials, such as SU-8, PMMA, PDMS, and KMPR, as well as thinner inorganic dielectrics are also being investigated for use as the dielectric barrier layer. Furthermore, reductions of the gap width and dielectric thickness are to be fabricated and tested as well.

### ACKNOWLEDGEMENTS

This work was supported in part by the US Air Force Office of Scientific Research (AFOSR) grant #FA9550-09-1-0416.

### REFERENCES

- [1] E. Moreau, “Airflow Control by Non-Thermal Plasma Actuators,” *J. Phys. D: Appl. Phys.*, 40 (2007), pp. 605-636.
- [2] C.-C. Wang, and S. Roy, “Microscale Plasma Actuators for Improved Thrust Density,” *J. Appl. Phys.*, 106, (2009).
- [3] R.G. Longwitz, “Study of Gas Ionization in a Glow Discharge and Development of a Micro Gas Ionizer for Gas Detection and Analysis”, Ph.D. Thesis, Swiss Federal Institute of Technology, Lausanne, Switzerland, 2004.
- [4] T. Ono, D.Y. Sim, and M. Esashi, “Micro-Discharge and Electric Breakdown in a Micro-Gap”, *J. Micromech. Microeng.*, 10 (2000), pp. 445 - 451.
- [5] T. Ono, D.Y. Sim, and M. Esashi, “Imaging of Micro-Discharge in a Micro-Gap of Electrostatic Actuator”, *MEMS 2000, 13<sup>th</sup> Annual Int’l Conf. on, Miyazaki, Japan (2000)*, pp. 651 - 656.
- [6] A. Bass, C. Chevalier, and M.W. Blades, “A Capacitively Coupled Microplasma (CC $\mu$ P) Formed in a Channel in a Quartz Wafer”, *J. Anal. At. Spectrometry*, 16 (2001), pp. 919 - 921.
- [7] B. Mitra, and Y.B. Gianchandani, “The Detection of Chemical Vapors in Air Using Optical Emission Spectroscopy of Pulsed Microdischarges From Two- and Three- Electrode Microstructures,” *J. IEEE Sensors*, 8, 8 (2008), pp. 1445-1454.
- [8] S. Okochi, N. Kasagi, Y. Suzuki et al., “Development of Micro Plasma Actuator for Active Flow Control”, *Exp. Heat Transfer, Fluid Mechanics and Thermodynamics, 7<sup>th</sup> World Conf. on, Krakow, Poland (2009)*.
- [9] J. Zito, R. Durscher, D.P. Arnold et al., “Investigation of Impedance Characteristics and Power Delivery for Dielectric Barrier Discharge Plasma Actuators”, *Proceedings, 48<sup>th</sup> AIAA Aerospace Sciences Meeting, Orlando, FL (2010)*.

### CONTACT

\*J.C. Zito, tel: +1-352-392-1484; jcz@ufl.edu

# INTEGRATED VERTICAL PARALLEL PLATE CAPACITIVE HUMIDITY SENSOR

N. Lazarus\* and G. K. Fedder

Department of Electrical and Computer Engineering and the Institute for Complex Engineered Systems  
Carnegie Mellon University, Pittsburgh, Pennsylvania, USA

## ABSTRACT

An integrated capacitive humidity sensor on-chip with CMOS interface electronics is demonstrated to have a sensitivity of 0.31% change in capacitance per percent relative humidity, 72% higher than the highest previously demonstrated in an integrated sensor. The vertical parallel-plate sensor made in CMOS is a high sensitivity topology that had not been previously integrated. The sensitized dielectric between two metal electrodes is formed by first forming a cavity by etching an intermediate layer of metal in the CMOS stack and then filling the cavity with polymer through inkjet deposition. This topology is demonstrated with polyimide to make a humidity sensor, but with appropriate polymer selection can also be used to sense other chemicals.

## INTRODUCTION

### Background

A capacitive chemical sensor consists of a pair of electrodes across a dielectric layer that changes its dimensions or dielectric constant when it absorbs analyte, resulting in a change in capacitance. Water has a dielectric constant of approximately 78 at room temperature while most polymers have dielectric constants below 10, resulting in a large change in capacitance when water vapor is absorbed. Capacitive sensing is also a good candidate for an integrated humidity sensor because the metal layers available in CMOS can be used as electrodes to minimize fabrication cost.

One possible technique for integrating a capacitive sensor would be to deposit polymer on the exposed top metal layer of a CMOS chip, forming the structure shown in Fig. 1(a). However, oxide is in the most direct path for electric field between the electrodes, resulting in a large oxide capacitance in parallel to the capacitance through the polymer. Since only the polymer capacitance changes upon humidity exposure, the fractional sensitivity of the capacitor will be very small. In a non-planarized CMOS process, the electrodes can be structured by having one electrode consist of a two-metal stack (Fig. 1(b)) to obtain a larger polymer capacitance ([1], [2]). A large oxide capacitance remains, however; in [2] the polymer capacitance is only 18% of the total capacitance, resulting in a large degradation in sensitivity. The oxide directly between the electrodes and the substrate underneath can also be etched away, allowing polymer to fill the space directly between the electrodes (Fig. 1(c)) [3]. This design gives the highest sensitivity previously demonstrated in an integrated capacitive humidity sensor (0.18% change in capacitance per percent relative humidity), but a significant parallel capacitance through the air above and below the electrodes remains, reducing the sensitivity.

In non-integrated capacitive sensors, a vertical parallel-plate structure (Fig. 1(d)) [4] is commonly used. The sensor consists of a layer of polymer sandwiched between two electrode layers; the top electrode is patterned to allow water vapor to absorb into the polymer layer. Since all of the electric field lines must pass through the polymer layer, the vertical parallel-plate sensor gives the highest possible sensitivity for a given polymer layer. The sensitivity for polyimide was measured to be 0.31%/RH [4]. This paper presents the successful monolithic integration of a high sensitivity vertical parallel-plate structure with CMOS interface electronics.

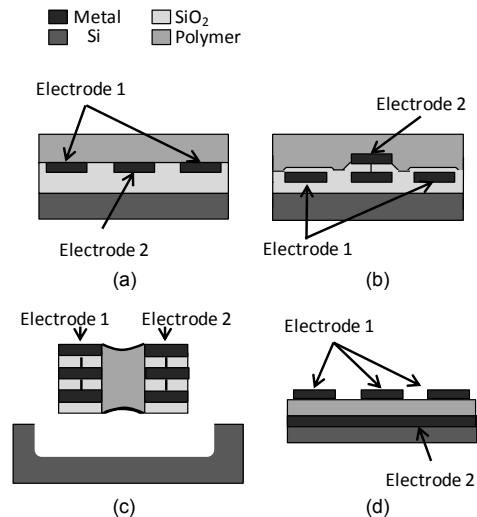


Figure 1: Capacitive chemical sensor designs

### Fabrication

In order to obtain a vertical parallel-plate capacitor in a CMOS stack, a conductive layer must be obtained on either side of a cavity. One possibility, shown in Fig. 2(a), is to use two metal layers as electrodes, while etching the metal layer in between to form the cavity. This technique results in an oxide capacitance above and below the polymer layer due to the inter-metal dielectrics, reducing the sensitivity. However, in many CMOS processes, the metal layers consist of TiW adhesion layers above and below aluminum. By using a selective aluminum etch, these TiW layers can be left intact, and can be used as the top and bottom electrodes of a vertical parallel-plate sensor, as illustrated in Fig. 2(b). Vias connect the adhesion layers to other metal layers that wire the sensor to interface circuitry.

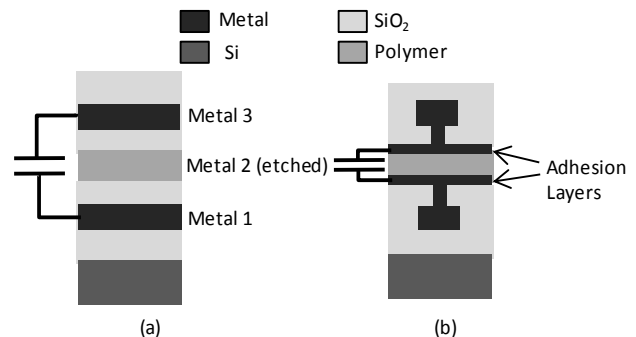


Figure 2: Options for integrating vertical parallel-plate sensor

The fabrication steps necessary to create the sensor are shown in Fig. 3. The process begins with a CMOS chip fabricated using the Jazz Semiconductor 0.35  $\mu\text{m}$  process (Fig. 3(a)). An anisotropic oxide etch is performed down to the second lowest metal layer (Fig. 2(b)). The aluminum part of this layer is then wet etched (Transense Aluminum Etchant Type A), leaving the TiW

layers intact (Fig. 2(c)). Photoresist is patterned to protect the aluminum bondpads and the topmost metal layer is used as a mask to protect the first and third metal layers from the aluminum etch. The chip is rinsed in DI water, followed a rinse in acetone and a final rinse in methanol. This is necessary to avoid surface tension pulling the cavity closed. Polymer is then added in solution using inkjet deposition into an access hole in the center of the structure, with capillary forces pulling the polymer solution into the structure (Fig. 3(d)). The polymer used was a formulation of polyimide in solution (HD Microsystems PI 2556) that was further diluted by a factor of 24:1 with a 50:50 solvent mixture of n-methyl-2-pyrrolidone and methoxy propanol (HD Microsystems T-9039) to obtain a low enough viscosity to deposit with the inkjet. A similar fill structure in a non-integrated sensor was made previously using the MUMPS process [5].

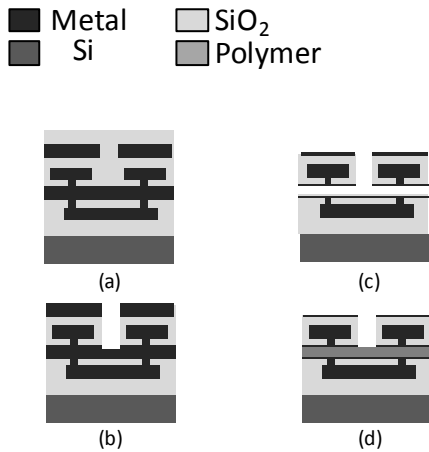


Figure 3: Fabrication process flow

### Design

A cross section of the sensor design is shown in Fig. 4 a. A 300  $\mu\text{m}$  diameter circular capacitive sensor was fabricated using the above process. An 80  $\mu\text{m}$  diameter circular access hole in the center of the device is the inkjet target. Multiple square holes (2.6  $\mu\text{m}$  on a side) act both as release holes and to allow water vapor to absorb more easily into the polymer layer. Oxide pillars are placed around the center hole to hold the plates apart (Fig. 4b).

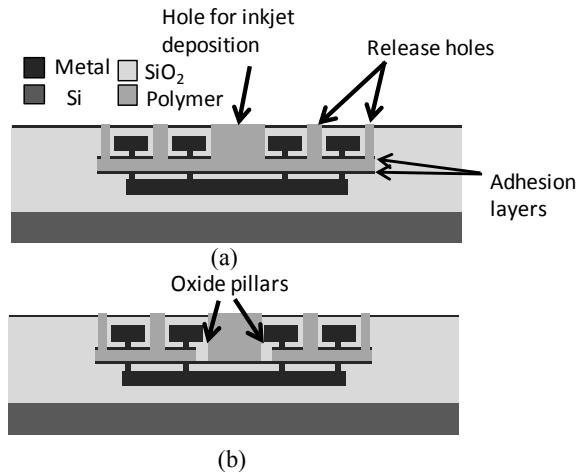


Figure 4: (a) Cross section of integrated sensor and (b) cross section that passes through oxide pillars

SEM images of the sensor before and after polymer jetting are shown in Fig. 5. Since it is difficult to judge optically whether the sensor is full of polymer, the structure was deliberately overloaded, resulting in a polymer residue on the top surface of the chip (Fig. 5(b)). This residue layer will reduce the speed of the device slightly, since water vapor will need to diffuse a longer distance into the device to reach the dielectric in the cavity. However, the process could be optimized to minimize the excess polymer and improve the response time.

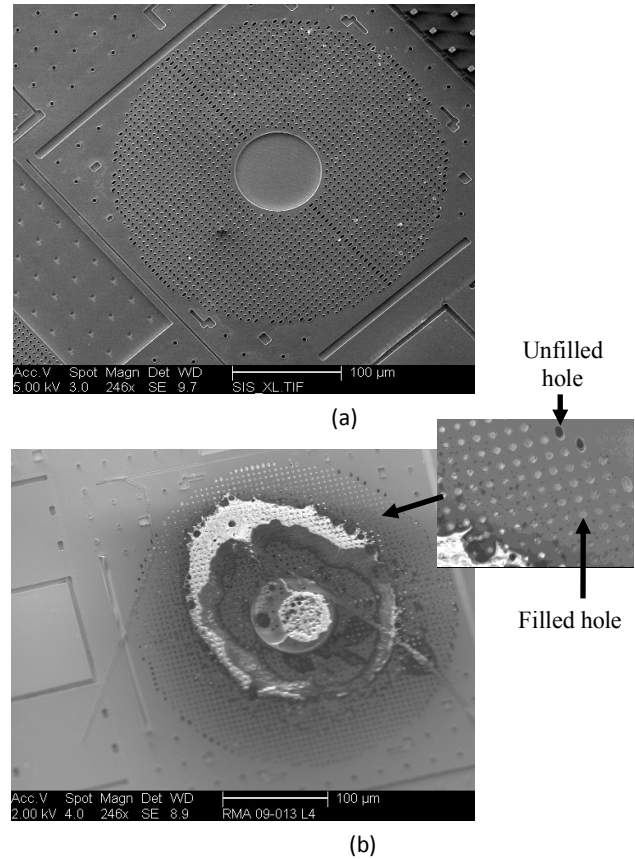


Figure 5: SEM image of sensor (a) before and (b) after inkjetting of polymer with inset picture of filled release holes

### Theoretical Model

The humidity sensor is modeled using a parallel-plate capacitor approximation, since the gap between the electrodes (nominally 450 nm) is very small relative to the area of the structure. The dielectric constant for polymer with absorbed water vapor is [6]

$$\varepsilon = [\gamma(\varepsilon_{H_2O}^{1/3} - \varepsilon_P^{1/3}) + \varepsilon^{1/3}]^3 \quad (1)$$

where  $\gamma$  is the volume fraction of water in the film, and  $\varepsilon_P$  and  $\varepsilon_{H_2O}$  are the dielectric constants of polymer and water, respectively. For humidity sensing, the most common polymer used is polyimide due to its linear response to relative humidity. Polyimide has a volume fraction of water approximately given by [6]

$$\gamma = c_1(\%RH)^{c_2} \quad (2)$$

The terms  $c_1$  and  $c_2$  are temperature-dependent constants.

## TESTING

### Testing Circuit

The sensor was integrated with the charge-based capacitance measurement (CBCM) circuit shown in Fig. 6 [7]. This circuit uses two separate measurements to isolate the parasitic capacitance of the wiring and circuit from the sensor capacitance. In the first measurement, the Clk input is grounded while the center node is first discharged to ground and then brought up to  $V_{dd}$ . The charge during this measurement is

$$Q_1 = V_{dd}(C_p + C) \quad (3)$$

In the second measurement, the Clk input is held at ground while the center node is discharged, then brought to  $V_{dd}$  when the node is charged. This results in no voltage drop across the sensing capacitance during the charging phase, giving a charge equal to:

$$Q_2 = V_{dd}C_p \quad (4)$$

The charge necessary to charge the center node in each measurement is measured by repeating the charging at a set frequency  $f$  and measuring the current with a DC picoammeter. The sensor capacitance is found by the expression:

$$C = \frac{I_1 - I_2}{fV_{dd}} \quad (5)$$

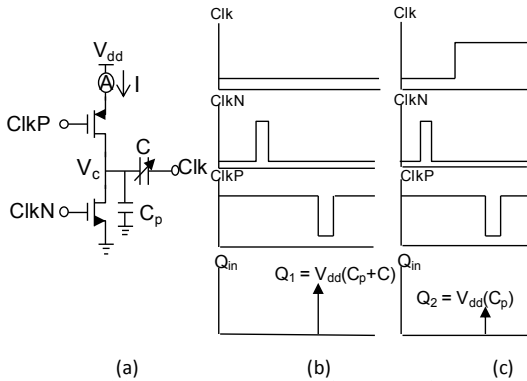


Figure 6: (a) CBCM circuit and timing diagrams for (b) first measurement and (c) second measurement

### Flow System

The sensor was tested using the flow system shown in Fig. 7. A Milligat M6 solvent pump pumps liquid water into a 1 L/min nitrogen flow; a brass block heated to 48°C is used to encourage the water to vaporize. The airflow passes into a 250 mL mixing volume, and then into the test box containing the sensor. A Honeywell HIH 4000 humidity sensor in the test box is used to obtain actual reference humidity value.

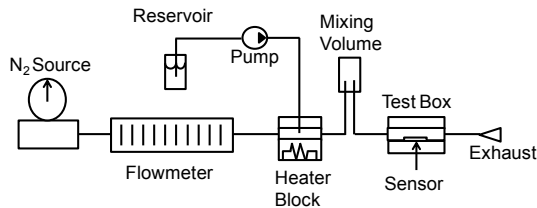


Figure 7: Humidity sensor test setup

## RESULTS

### Humidity Testing

The sensor was measured for a range of relative humidity from 0% to 40%, resulting in the response curve in Fig. 8. The sensor response was fitted to the theoretical model for polyimide, giving an adjusted  $R^2$  value of 0.9964. The sensitivity in the linear region of the sensor was fitted to be 0.31% change in capacitance per percent relative humidity.

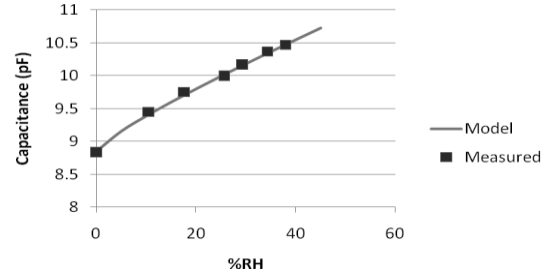


Figure 8: Humidity sensor response curve

### Response Time

In the integrated vertical parallel-plate structure, polymer wicks to the top of the release holes, as shown schematically in Fig. 4. As a result, water vapor must diffuse through several microns of polymer before reaching the area between the two plates that forms the actual capacitor, potentially resulting in a slow response time. Fig. 9 shows result from a finite-element simulation of the response time to a humidity step of 3% change in relative humidity using the diffusion model in [8] and a diffusion coefficient for water vapor in polyimide of  $15 \times 10^{-14} \text{ m}^2/\text{s}$  [9]. The simulated time constant of the sensor is 68 s.

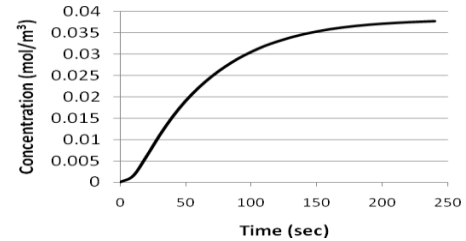


Figure 9: Simulation of humidity concentration between plates in response to stepped humidity pulse

In order to verify the response time, the sensor was compared to the reference Honeywell humidity sensor, which has a response time constant to changes in relative humidity of 15 s [10]. Fig. 10 shows the response to both sensors to two pulses of humidity with different amplitudes. As expected, the sensor was noticeably slower than the reference sensor; this effect was particularly pronounced in the falling portion of the humidity pulse.

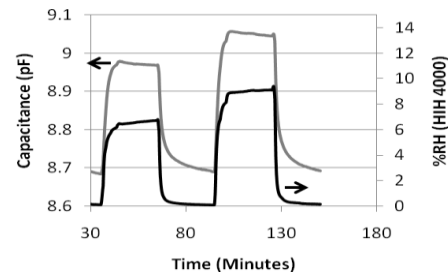


Figure 10: Sensor response to humidity pulses



## Noise

Another important specification of a chemical sensor is the noise performance. One method for characterizing the noise response and limit of detection of a sensor is the Allan variance:

$$\sigma_C^2 = \frac{1}{M} \sum_{k=1}^{M-1} \frac{1}{2} (C_k - C_{k-1})^2 \quad (6)$$

where  $M$  is the number of samples.  $C_i$  is the  $i^{\text{th}}$  measured capacitance value, normalized by the initial capacitance  $C_0$ . Since the Allan variance measures the sample to sample variation, it can be used to calculate an approximate minimum detectable capacitance change,

$$\Delta C = C_0 \sqrt{\sigma_C^2} \quad (7)$$

The Allan variance is dependent on the sampling period, since averaging samples together reduces the variation from higher frequency noise. At longer averaging times, however, low frequency drift causes the Allan variance to rise. A plot of the Allan variance versus averaging time of the sensor is shown in Fig. 11.

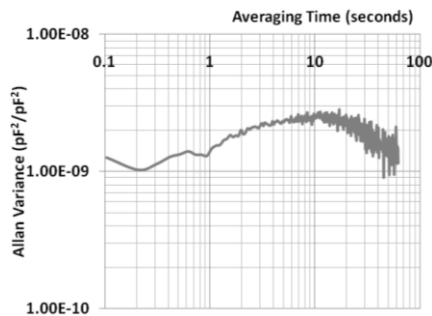


Figure 11: Allan variance of sensor

As shown, the Allan variance is flat over the averaging times tested. The lowest Allan variance was  $1.023 \times 10^{-9} \text{ pF}^2/\text{pF}^2$  for an averaging time of 0.2 s. The minimum detectable signal is 0.26 fF, corresponding to a limit of detection of 0.01% relative humidity.

## Temperature Response

The response of the sensor to changes in temperature was also measured (Figure 12), giving a sensitivity of 0.19% change in capacitance per °C. The measured sensitivity to temperature is 2.7 times higher than the sensitivity of the released interdigitated sensor measured in [3]. The high sensitivity to temperature may be because the low density of the oxide pillars in the current structure allows the top capacitor plate to move slightly as temperature changes. A design using a larger number of pillars to hold the plate distance constant is currently being fabricated.

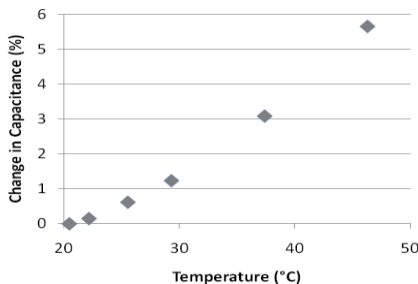


Figure 12: Temperature response

## CONCLUSION

The measured results demonstrate a vertical parallel-plate capacitive humidity sensor successfully integrated with CMOS

testing electronics. The sensitivity of the sensor is 0.31%/RH, an increase of 72% over the highest sensitivity previously demonstrated for an integrated capacitive humidity sensor [3]. The sensitivity matches the sensitivity for polyimide previously measured in a non-integrated vertical parallel-plate sensor [4]. The sensor was found to be relatively slow, with a time constant on the order of a minute, since water vapor must diffuse several microns to reach the active part of the sensor. The limit of detection of the sensor was found to be 0.01% relative humidity.

## ACKNOWLEDGEMENT

The authors thank Lawrence Schultz and Lee Weiss for advice and assistance with inkjetting and Suresh Santhanam for performing the oxide etch. This work is funded in part by NIOSH/CDC (contract 200-2002-00528), in part by AFOSR FA9550-07-1-0245, and in part by the U.S. Department of Homeland Security under an Interagency Agreement with the Centers for Disease Control. The findings and conclusions in this publication have not been formally disseminated by the National Institute of Occupational Safety and Health, the U.S. Department of Homeland Security, or the U.S. Office of Scientific Research and should not be construed to represent any agency determination or policy.

## REFERENCES

- [1] C. Hagleitner, D. Lange, A. Hierlemann, O. Brand, and H. Baltes, "CMOS single-chip gas detection system comprising capacitive, calorimetric and mass-sensitive microsensors," *IEEE J. Solid-State Circuits*, vol. 37, no. 12, pp. 1867-1878, Dec. 2002.
- [2] A. Hierlemann, *Integrated Chemical Microsensor Systems in CMOS Technology*, Berlin, Germany: Springer-Verlag, 2005.
- [3] N. Lazarus, S. S. Bedair, C.-C. Lo, G. K. Fedder, "CMOS-MEMS capacitive humidity sensor," *J. Microelectromech. Syst.*, vol. 19, no. 1, pp. 183-191, Feb. 2010.
- [4] M. Dokmeci and K. Najafi, "A high sensitivity polyimide capacitive relative humidity sensor for monitoring anodically bonded hermetic micropackages," *J. Microelectromech. Syst.*, vol. 10, no. 2, pp. 197-204, June 2001.
- [5] S. V. Patel, T. E. Mlsna, B. Fruhberger, E. Klaassen, S. Cemalovic and D. R. Baselt, "Chemical capacitive microsensors for volatile organic compound detection," *Sensors and Actuators B*, vol. 96 no. 1 pp. 541-553, Dec. 2003.
- [6] H. Shibata, M. Ito, M. Asakura, and K. Watanabe, "A digital hygrometer using a capacitance to frequency converter," in *Proc. of IEEE IMTC 1995*, Waltham, MA, April 1995, pp. 100-106.
- [7] Y. Chang, H. Chang, T. Lu, Y. King, W. Ting, Y. Ku and C. Lu, "Charge-based capacitance measurement for bias-dependent capacitance," *IEEE Electron Device Letters*, Vol. 27, No. 5, pp. 390-392, 2006.
- [8] A. Tetelin and C. Pellet, "Accurate model of the dynamic response of a capacitive humidity sensor," in *Proc. IEEE Sensors*, Toronto, ON, Canada, 2003, pp. 378-383.
- [9] J. Seo and H. Han, "Water Diffusion studies in polyimide thin films," *J. Appl. Polym. Sci.*, vol. 82, no. 3, pp. 731-737, Oct. 2001.
- [10] Honeywell, "HIH-4000-01", HIH-4000 datasheet, July 2006.

## CONTACT

\*N. Lazarus, tel: +1-412-268-4403; nlazarus@cmu.edu

# MICROMACHINED MULTIFUNCTIONAL PIEZOELECTRIC T-BEAM TRANSDUCERS

Z. Zhang<sup>1</sup>, K. Mateti<sup>2</sup>, C.D. Rahn<sup>1</sup> and S. Tadigadapa<sup>2\*</sup>

<sup>1</sup>The Pennsylvania State University, Department of Mechanical Engineering, Pennsylvania, USA

<sup>2</sup>The Pennsylvania State University, Department of Electrical Engineering, Pennsylvania, USA

## ABSTRACT

This paper presents a novel MEMS piezoelectric cantilever beam with a T-shaped cross-section that can be used as both an actuator and a sensor. The micro T-beams are directly micromachined from bulk lead zirconate titanate (PZT) via deep reactive ion etching. The micromachined PZT T-beams are capable of in-plane and out-of-plane motion sensing and actuation via selective activation and measurements at different electrodes. The T-beam structures are tested as flexural actuators and also configured as accelerometers for sensing applications. Nine micromachined T-beams are fabricated and achieve up to 129  $\mu\text{m}$  of out-of-plane displacement, 11.6  $\mu\text{m}$  of in-plane displacement, 694  $\mu\text{N}$  of out-of-plane blocking force, and an average acceleration sensitivity of 30.5 mV/g in 1 - 4.6 g's range at a frequency of 1.3 kHz.

## INTRODUCTION

Piezoelectric MEMS sensors and actuators have many applications, including micropositioning systems, RF switches, micropumps, and accelerometers [1, 2]. Lead zirconate titanate (PZT) is attractive for MEMS sensors and actuators because it provides large piezoelectric coefficient and electromechanical coupling coefficients [3, 4]. Additionally, bulk PZT has superior properties than thin films and new fabrication processes allow bulk micromachining of PZT [1]. An inherent challenge of PZT actuators is amplifying the low strain (0.1%) to produce large displacement. Multilayer actuators increase displacement by summing the displacement of multiple electroded PZT layers using the  $d_{33}$  coefficient [5]. Unimorph, bimorph, and multilayer beam bending actuators amplify displacement using the  $d_{31}$  piezoelectric coefficient, and are capable of much larger deflections [6, 7]. Both of these types of actuators require bonding of one or more layers of passive material. De-lamination, adhesive wear and resistance associated with these layers reduce performance and lifetime. Recently, piezoelectric T-beam actuators have been micromachined from bulk PZT using a deep reactive ion etching process [8]. The T-beam transducer structure has top of flange, top of web and bottom electrodes deposited. Selective application of electric field to the web region or flange regions of the beam can produce in-plane and out-of-plane displacement. Also, by using the direct piezoelectric effect, T-beams can sense accelerations by measuring the charge generated in the web and flange regions. This work presents the piezoelectric T-beam as a multifunctional transducer structure capable of both in-plane and out-of-plane actuation and sensing.

## FABRICATION PROCESS

Figure 1 shows the fabrication process of the T-beam transducers. Previous modeling [9] determines the optimal cross section design for maximum mechanical energy output with T-beams parameters,  $L$ , length,  $b$ , web width,  $s$ , total width,  $t$ , flange thickness, and  $h$ , total thickness as shown in Figure 2. 12.5 mm  $\times$  12.5 mm  $\times$  100  $\mu\text{m}$ , finely polished, bulk PZT-4 with 100 nm of Cr and 350 nm of Au electrodes from Boston Piezo-Optics are used as the substrates to micromachine the T-beam structures as in Figure 1(a).

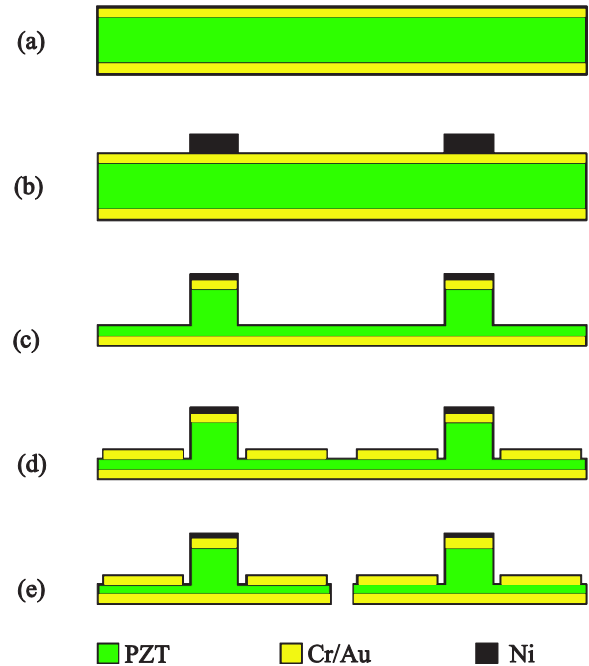


Figure 1: Fabrication process for piezoelectric T-beams: (a) bulk 100  $\mu\text{m}$  PZT, (b) 12-14  $\mu\text{m}$  Ni electroplated, (c) 65  $\mu\text{m}$  DRIE etch, (d) flange electrode deposition and (e) released by 100  $\mu\text{m}$  dicing saw.

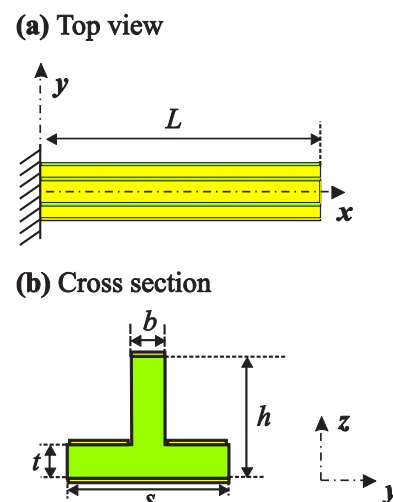


Figure 2: (a) Top view and (b) cross section of T-beam structure.

To reach an etch depth of 65  $\mu\text{m}$  at an etch rate of 15  $\mu\text{m}/\text{hr}$ , the PZT must be deep reactive ion etched for over four hours. This requires a hard mask with high etch selectivity over PZT that protects the web regions to define a T-shaped cross section. Nickel is chosen as the hard mask because of its high resistivity against ion

bombardment and ease of electroplating. In preparation, the substrates are cleaned and mounted onto a carrier glass slide using a drop of SU-8-10 photoresist. 13  $\mu\text{m}$  thick SPR-220 7.0 photoresist features are then patterned on the PZT wafer to define the web-regions of the T-beams. The substrate is then put into the oxide etcher for surface cleaning and functioning under 75 W for 3 minutes. Using a Techni Nickel S electroplating solution, 12~14  $\mu\text{m}$  Ni is deposited over 80 minutes at room temperature, using constant agitation and a current density of approximately 16  $\text{mA}/\text{cm}^2$  (Figure 1(b)).

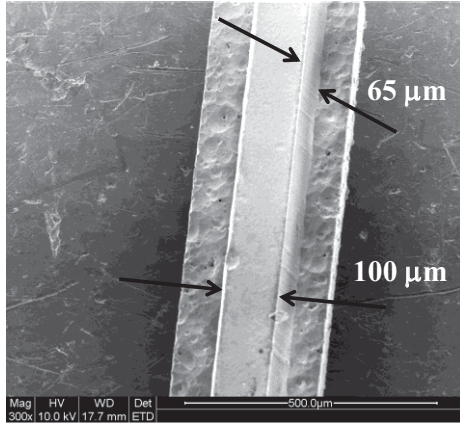


Figure 3: SEM image of the micromachined T-beam transducer.

The PZT is etched (see Figure 1 (c)) using an Inductively Coupled Plasma-Reactive Ion Etching (ICP-RIE) system that can achieve an etch rate of 15  $\mu\text{m}/\text{hr}$  using 2000 W of ICP power, 475 W of substrate power, 5 sccm of sulphur-hexafluoride ( $\text{SF}_6$ ), and 50 sccm of argon (Ar) [10]. During the etch process, surface temperatures can reach very high levels causing damage and burning. The bulk PZT is mounted onto a 4" silicon wafer using an indium-tin alloy to allow thermal conductivity to the sample holder, which is maintained at 20° C by helium gas. Figure 3 shows an SEM photograph of a T-beam etched 65  $\mu\text{m}$  in 5 hours. The selectivity of nickel over PZT-4 is calculated to be around 1:5.

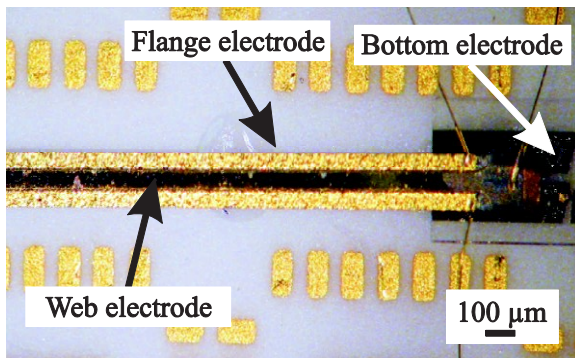


Figure 4: Top view of the micromachined T-beam transducer and package.

Flange electrodes are deposited using an evaporation and liftoff process shown in Figure 1(d). Shipley 1805 photoresist is spray coated and patterned to prevent metal vapor deposition on the side walls of the web and flanges. 100 nm of Cr and 200 nm are deposited forming a conformal coating over the T-beams using an electron-beam (E-beam) evaporator with planetary sample holder. An ultrasonic bath with Remover PG® completes the liftoff process. Individual T-beams are released using a K&S 980 Series high precision dicing saw with a 100  $\mu\text{m}$  wide diamond coated blade spinning at 30 krpm as in Figure 1(e). The dimensions of the micromachined T-beams are given in Table 1. T-beams are mounted onto a flat alumina package using silver epoxy, and wire bonded using a K&S Model 4524 wire bonder, as shown in Figure 4.

Table 1: Dimensions of and tests performed on fabricated T-beam transducers.

Device	$L$ (mm)	$b$ ( $\mu\text{m}$ )	$s$ ( $\mu\text{m}$ )	$t$ ( $\mu\text{m}$ )	$h$ ( $\mu\text{m}$ )	Test*
1	7.7	61	139	39	100	$w, a$
2	3.8	52	208	36	100	$w$
3	10.4	49	149	35	100	$w$
4	5.8	62	144	42	100	$w$
5	7.8	195	601	35	100	$f$
6	11.7	203	599	36	100	$f$
7	3.6	53	143	35	100	$bf$
8	4.4	49	153	35	100	$bf$
9	5.8	30	72	38	100	$bf$

\*  $w$  for web actuated out-of-plane displacement,  $f$  for single flange in-plane displacement,  $bf$  for out-of-plane blocking force, and  $a$  for accelerometer testing.

## EXPERIMENTAL RESULTS

### T-beam Actuator

A photograph of the experimental setup for the T-beam actuator is shown in Figure 5. A Trek Model 609E-6 high voltage amplifier amplifies the output voltage signal from a LabView system. A Polytec laser vibrometer with a 10 $\times$  objective focuses a 20  $\mu\text{m}$  laser onto the T-beams with 20 nm resolution. An Aurora Scientific, Inc. force transducer measures blocking force with 10  $\mu\text{N}$  resolution. Newport and Misumi linear stages allow precise positioning of the T-beams, vibrometer and force transducer.

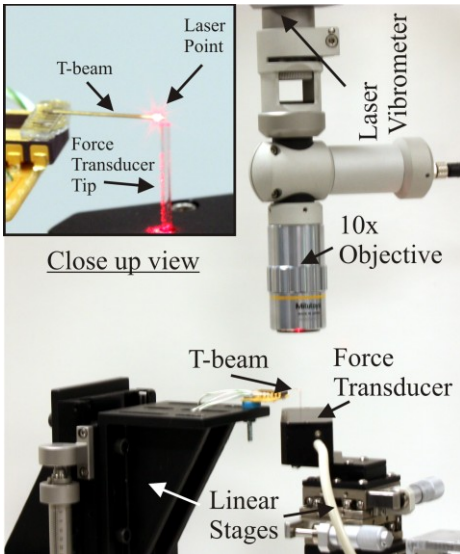


Figure 5: Experimental setup for T-beam actuator measurements.

Applying a positive field in the direction of poling from the web electrode to the bottom electrode produces out-of-plane displacement. The out-of-plane results in Figure 6 show a linear and predictable response with displacement proportional to applied voltage. Different devices yield different slopes of displacement versus field, showing that displacement depends on the square of the actuator length. Device 3 produces the largest response while Device 2 produces the smallest. These two devices also have the longest and shortest beam length, respectively. The experimental results are compared with a model developed previously in [9]. The model and theory match quite well and show that displacement is proportional to the length squared (see inset in Figure 6).

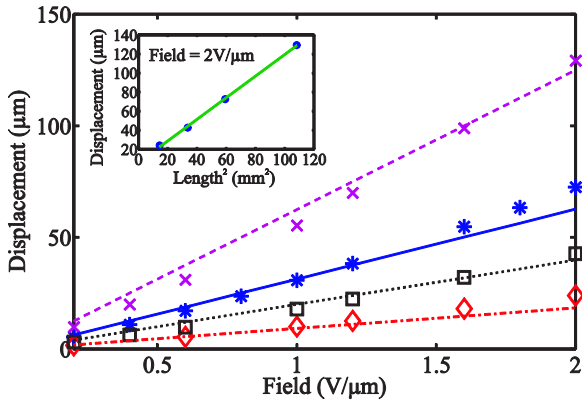


Figure 6: Experimental data and theoretical prediction of out-of-plane displacement ( $\mu\text{m}$ ) versus electric field ( $\text{V}/\mu\text{m}$ ): Device 1: predicted (solid), measured (star); Device 2: predicted (dash-dot), measured (diamond); Device 3: predicted (dashed), measured (x); Device 4: predicted (dotted), measured (square).

Applying a positive field in the direction of poling from a single flange electrode to the bottom electrode produces in-plane displacement. It should be noted that lower voltages produce equivalent fields compared to web actuation. Figure 7 shows left and right in-plane displacement of fabricated Devices 5 and 6.

These devices show a linear response at lower fields, but an increase in displacement over the model at higher fields. The right (square) and left (circle) flange actuated results for Device 5 should be identical but opposite in sign. The in-plane magnitude plotted in Figure 7 for Device 5 showed slightly different response, indicating asymmetries in the fabricated device. Device 6, however showed symmetric left (diamond) and right (x) in-plane response. The model in [9] matched well with the measured response.

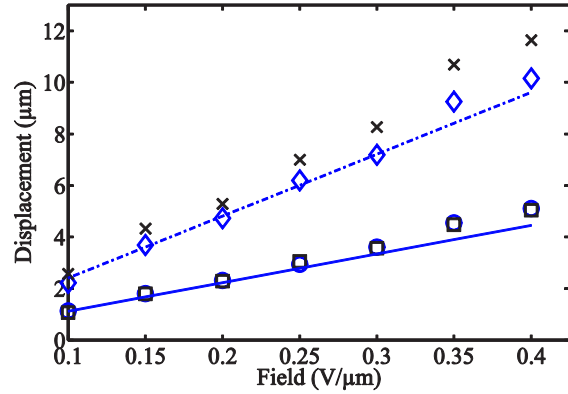


Figure 7: Experimental data and theoretical prediction of in-plane displacement ( $\mu\text{m}$ ) versus electric field ( $\text{V}/\mu\text{m}$ ): Device 5: predicted (solid), measured left(circle), measured right (square); Device 6: predicted (dash-dot), measured left (diamond), measured right (x).

To measure the blocking force, the device is packaged such that it extends out of the package. The web electrode is actuated and the glass tube of the force transducer is positioned just in contact with the end (tip) of the beam. Figure 8 shows the blocking force measurement result of Devices 7 to 9. Experimental data shows much greater blocking force than the model predicts. The cause of the observed over performance and the saturation behavior is currently being investigated.

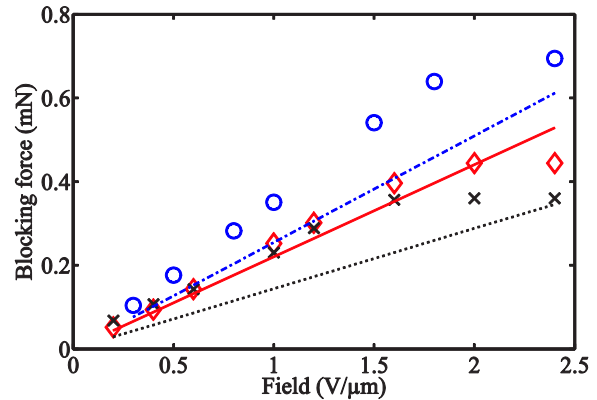


Figure 8: Experimental data and theoretical prediction of blocking force ( $\mu\text{N}$ ) versus electric field ( $\text{V}/\mu\text{m}$ ): Device 7: predicted (dash-dot), measured (circle); Device 8: predicted (solid), measured(diamond); Device 9: predicted (dotted) , measured (x).

## T-beam Accelerometer

Figure 9 shows a schematic of the experimental setup in which the T-beam transducer is tested as an accelerometer. Device 1 is rigidly mounted onto a Wilocxon Research Model F3 electromagnetic shaker system powered by a AE Techron LVC5050 linear amplifier. The laser vibrometer measures velocity data from the rigid base which is differentiated to obtain input acceleration. A charge amplifier with 10× gain amplifies the T-beam signal. A

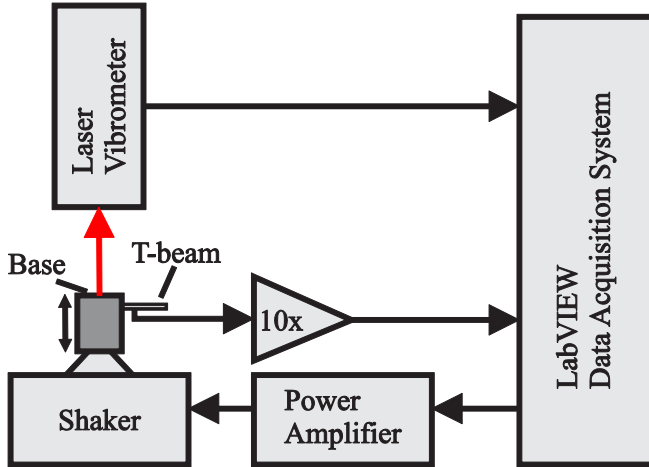


Figure 9: Schematic of experimental setup of T-beam accelerometer measurement.

Test results in the 1-4 g's ( $g = 9.81 \text{ m/s}^2$ ) range at 1.3 kHz are shown in Figure 10 and demonstrate the sensitivity and linearity of the T-beam as an accelerometer. The output voltage amplitude scales linearly with applied acceleration. The sensitivity is constant over the range of accelerations tested. Since the T-beam structure or the proof mass design is not particularly optimized for acceleration measurements, these results show the initial unoptimized performance of the transducer structure as an accelerometer.

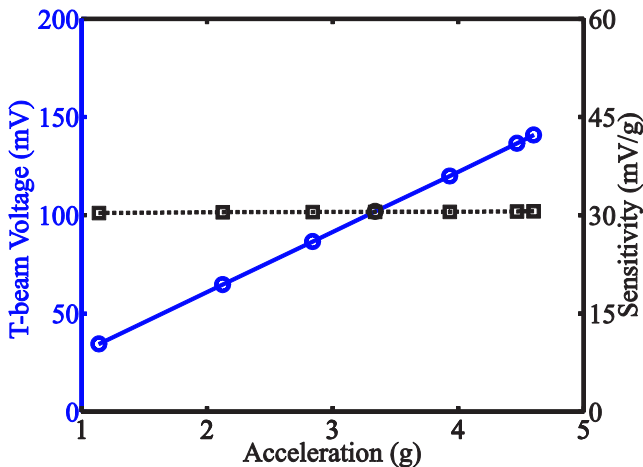


Figure 10: T-beam voltage (solid circle) and sensitivity (dashed square) versus acceleration at 1.3 kHz.

## CONCLUSIONS AND FUTURE WORK

Piezoelectric T-beam transducers can be reliably micromachined from bulk PZT using an ICP-RIE process. The fabricated T-beams are capable of producing in-plane and out-of-plane displacement, and out-of-plane blocking force. They can also be used to sense out-of-plane acceleration. Nine prototype micromachined T-beams are fabricated and tested, showing up to 129  $\mu\text{m}$  of out-of-plane displacement, 11.6  $\mu\text{m}$  of in-plane displacement, 694  $\mu\text{N}$  of out-of-plane blocking force, and an average acceleration sensitivity of 30.5 mV/g in the 1- 4.6g's range at 1.3kHz. Future work includes dynamic modeling of out-of-plane and in-plane displacement and force. Flange sensing of in-plane acceleration would allow two-axis sensing with one transducer.

## ACKNOWLEDGEMENTS

The authors would like to thank the Air Force Office of Scientific Research for their support of this work under grant #FA9550-07-1-0367.

## REFERENCES

- [1] S. J. Gross, S. Tadigadapa, T. N. Jackson, S. Trolier-McKinstry, and Q. Q. Zhang, "Lead-zirconate-titanate-based piezoelectric micromachined switch," *Applied Physics Letters*, vol. 83, pp. 174-176, 2003.
- [2] H. G. Yu, L. Zou, K. Deng, R. Wolf, S. Tadigadapa, and S. Trolier-McKinstry, "Lead zirconate titanate MEMS accelerometer using interdigitated electrodes," *Sensors and Actuators A: Physical*, vol. 107, pp. 26-35, 2003.
- [3] P. Murali, "Ferroelectric thin films for micro-sensors and actuators: a review," UK, 2000, pp. 136-46.
- [4] S. Trolier-McKinstry and P. Murali, "Thin film piezoelectrics for MEMS," *Journal of Electroceramics*, vol. 12, pp. 7-17, 2004.
- [5] V. Giurgiutiu, C. A. Rogers, and Z. Chaudhry, "Energy-based comparison of solid-state induced-strain actuators," *Journal of Intelligent Material Systems and Structures*, vol. 7, pp. 4-14, 1996.
- [6] V. Giurgiutiu, C. A. Rogers, and Z. Chaudhry, "Design of displacement-amplified induced-strain actuators for maximum energy output," *Journal of Mechanical Design, Transactions of the ASME*, vol. 119, pp. 511-517, 1997.
- [7] G. Percin and B. T. Khuri-Yakub, "Micromachined piezoelectrically actuated flexensional transducers for high resolution printing and imaging," in *Ultrasonics Symposium, 2001 IEEE*, 2001, pp. 921-924 vol.2.
- [8] H. K. R. Kommepalli, C. D. Rahn, A. D. Hirsh, and S. A. Tadigadapa, "Piezoelectric T-beam microactuators," New York City, NY, United states, 2009, pp. 909-914.
- [9] H. K. R. Kommepalli, "Design, modeling and optimization of piezoelectric actuators," in *Mechanical Engineering*. vol. Doctoral University Park: the Pennsylvania State University, 2010.
- [10] S. S. Subasinghe, A. Goyal, and S. Tadigadapa, "High aspect ratio plasma etching of bulk lead zirconate titanate," USA, 2006, pp. 61090-1.

## CONTACT

\*S. Tadigadapa, tel: +1-814-865-2730; [SAT10@PSU.EDU](mailto:SAT10@PSU.EDU)

# PIEZORESISTIVE MICROCANTILEVERS FROM ULTRANANOCRYSTALLINE DIAMOND

Natalya L. Privorotskaya<sup>1</sup>, Hongjun Zeng<sup>2</sup>, John A. Carlisle<sup>2</sup>, Rashid Bashir<sup>3,4</sup>, and William P. King<sup>1,4,\*</sup>

<sup>1</sup>Department of Mechanical Science and Engineering, University of Illinois, Urbana-Champaign, Urbana IL

<sup>2</sup>Advanced Diamond Technologies, Romeoville, IL

<sup>3</sup>Department of Electrical and Computer Engineering and Bioengineering, University of Illinois, Urbana-Champaign, Urbana IL

<sup>4</sup>Micro and Nanotechnology Laboratory, University of Illinois, Urbana-Champaign, Urbana IL

## ABSTRACT

This paper reports the temperature-dependant electrical resistivity and piezoresistive characteristics of boron-doped ultrananocrystalline diamond (UNCD), and the fabrication of piezoresistive microcantilevers using boron-doped and undoped UNCD. The devices consist of 1  $\mu\text{m}$  thick doped UNCD on either 1 or 2  $\mu\text{m}$  thick undoped UNCD. Over the temperature range 25-200  $^{\circ}\text{C}$ , the doped UNCD has a temperature coefficient of electrical resistance of  $-1.4 \times 10^{-3} \text{ }^{\circ}\text{C}^{-1}$ . The doped UNCD exhibits a significant piezoresistive effect with gauge factor of 7.5 and a piezoresistive coefficient of  $8.12 \times 10^{-12} \text{ Pa}^{-1}$  at 25  $^{\circ}\text{C}$ . The piezoresistive properties of UNCD are constant over the temperature range 25-200  $^{\circ}\text{C}$ . Microcantilevers of length 300  $\mu\text{m}$  have deflection sensitivity of 0.186  $\text{m}\Omega/\Omega$  per  $\mu\text{m}$  of cantilever end deflection. These measurements of electrical and piezoresistive properties of doped UNCD could aid the design of future diamond microsystems.

## INTRODUCTION

Chemical vapor deposited diamond films are an attractive material for microsystems due to their mechanical properties, chemical stability, and biocompatibility [[1], [1]]. In particular, ultrananocrystalline diamond (UNCD) is a 95% or more  $sp^3$ -bonded polycrystalline diamond material with a high structural uniformity that results from small grain size, which gives it chemical, mechanical, and electrical properties that are close to those of bulk diamond [3-5]. The electrical properties of UNCD can range from insulating to conductor-like by varying doping concentration [6], with electrical resistivity that can be controlled over five orders of magnitude. UNCD films can be synthesized at temperatures as low as 400 $^{\circ}\text{C}$ , while film thickness can vary from several nanometers to tens of microns [7-9].

The design of UNCD-based microelectromechanical devices is however impaired by a lack of understanding of the electrical, thermal, and mechanical properties of electrically conducting doped UNCD films. This paper presents electrical resistivity test structures and microcantilevers fabricated from doped and undoped UNCD heterostructures. This paper also presents characterization of the temperature-dependant electromechanical properties of these microcantilevers over the range 25-200  $^{\circ}\text{C}$ .

## DESIGN AND FABRICATION

Figure 1 shows a microcantilever consisting of a UNCD multilayer. The top layer is electrically conducting doped UNCD of thickness 1  $\mu\text{m}$ , and the bottom layer is electrically insulating undoped UNCD of thickness either 1  $\mu\text{m}$  or 2  $\mu\text{m}$ . Detailed electrical resistivity measurements are reported later in the paper, however at this point we note that electrical resistivity of doped UNCD is 0.1  $\Omega\text{-cm}$  at room temperature, which is five orders of magnitude smaller than the electrical resistivity of undoped UNCD. The relatively high electrical resistivity of undoped UNCD is due to the very high  $sp^3$  content in the UNCD. The large

difference in electrical resistivity of the doped vs. undoped UNCD layers, along with the doped UNCD offset from the cantilever neutral axis, enables the piezoresistive cantilever behavior.

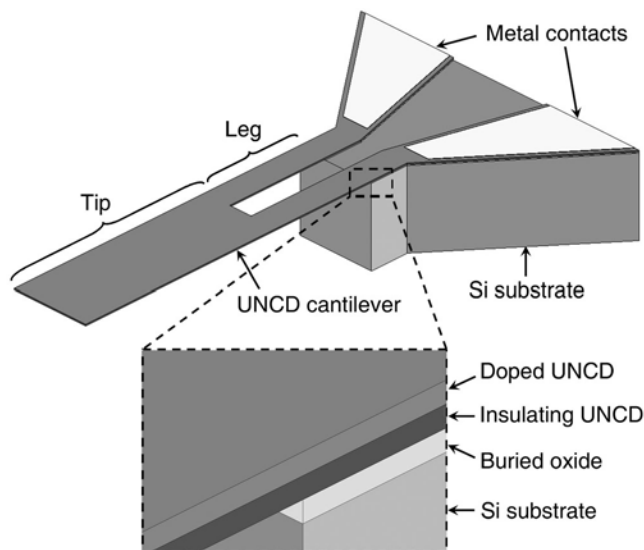


Figure 1. Schematic view of an all-diamond microcantilever having doped and insulating UNCD layers.

In the present design, the UNCD layers are electrically isolated from a silicon handle wafer with a 1  $\mu\text{m}$  thick silicon dioxide layer. We consider four different cantilever designs, shown in Figure 2, having overall cantilever thickness of either 2  $\mu\text{m}$  or 3  $\mu\text{m}$  for a total of eight device types. The cantilevers vary in length from 300  $\mu\text{m}$  to 400  $\mu\text{m}$  and have a notch that extends 1/3 or 2/3 of the length starting from the cantilever substrate. The notched region is referred to as the “leg”, while the rest of the cantilever is the “tip”.

The cantilever fabrication starts with silicon dioxide-coated silicon wafers. The diamond layers are deposited to the desired thickness using hot-filament chemical vapor deposition (HFCVD) with methane/hydrogen chemistry and a 5%  $\text{CH}_4/\text{H}_2$  gas mixture. Boron-doped UNCD is synthesized by adding trimethylboron [ $\text{B}(\text{CH}_3)_3$ ] as a source gas with a boron-to-carbon ratio of 1/330 inclusive of both carbon-containing source gases. Both UNCD layers are then etched in oxygen plasma. Metal contacts allow for electrical access to the electrically conducting doped UNCD layer. The cantilevers are released with a through-wafer backside etch.

Figure 2 shows scanning electron micrographs of fabricated cantilevers named A, B, C, or D, followed by a number that is the cantilever total thickness. The cantilevers exhibit some curvature due to the intrinsic differential stress introduced during the growth process. For cantilevers of total length 400  $\mu\text{m}$ , the cantilever deflection was about 23  $\mu\text{m}$  for the 2  $\mu\text{m}$  thick cantilevers and 16

$\mu\text{m}$  for the  $3\ \mu\text{m}$  thick cantilevers. We also fabricated van der Pauw structures [10] on the same wafers for precise measurements of the UNCD sheet resistance and its temperature-dependence.

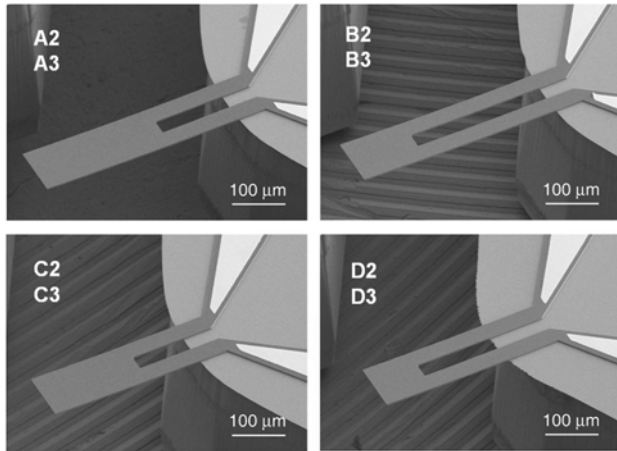


Figure 2. Scanning electron micrographs of fabricated UNCD microcantilevers.

### EXPERIMENTAL SETUP

Figure 3 shows the experimental setup to measure device temperature-dependant electrical resistance and piezoresistive coefficient.

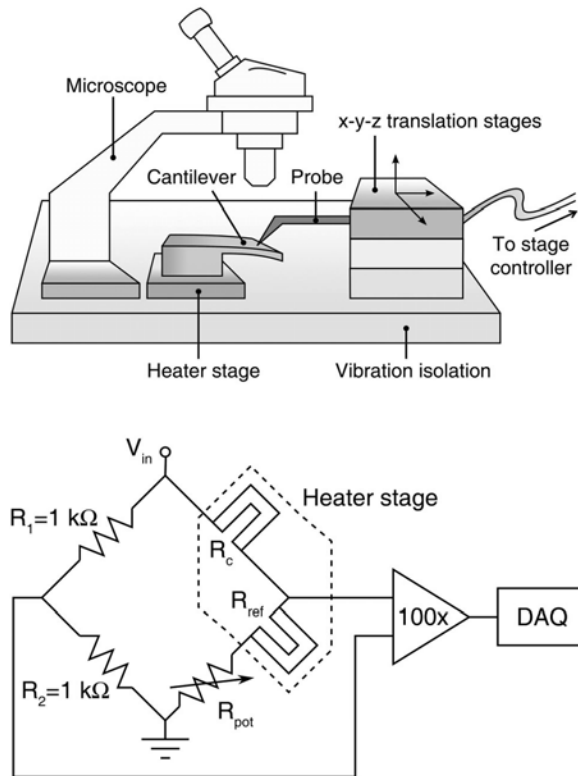


Figure 3. Schematic of the experimental setup for piezoresistivity measurements showing cantilever deflection setup and cantilever wiring diagram. The cantilever is deflected using a tungsten needle probe mounted on three-axis motorized nanopositioning stages having  $7\ \text{nm}$  resolution. The probe was moved in  $13.7\ \mu\text{m}$  increments with the output signal amplified 100 times before collection in a data acquisition system.

Two cantilevers were configured in Wheatstone bridge for a differential measurement and mounted on a temperature-controlled stage capable of maintaining temperature to within  $0.2\ ^\circ\text{C}$  in the range of  $25\text{--}200\ ^\circ\text{C}$ . The cantilever electrical resistance was measured while the tip was deflected using a tungsten needle probe attached to a closed-loop nanopositioner. The location of the probe on the cantilever surface was measured under the microscope with  $150\times$  total magnification.

The cantilever electrical resistance change was measured from the Wheatstone bridge voltage output when the applied bridge bias was  $1\ \text{V}$ . Probe deflection varied from  $6.87\ \mu\text{m}$  to  $68.66\ \mu\text{m}$  in  $13.73\ \mu\text{m}$  increments, except for the first step of  $6.87\ \mu\text{m}$ . Sixty differential voltage measurements were made at each deflection point in 1 second intervals and were repeated three times for averaging purposes and to correct for signal drift. This procedure was repeated three times with the probe lifted off the cantilever surface and brought back into contact between subsequent trials to establish uncertainty due to the probe location.

## RESULTS AND DISCUSSION

### Deflection sensitivity

Figure 4 shows cantilever deflection sensitivity,  $S$ , defined by equation (1) as resistance change,  $\Delta R$ , due to applied tip deflection,  $\delta$ .

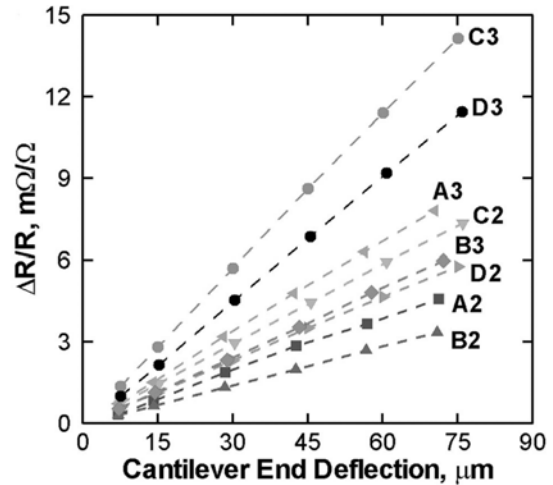


Figure 4. Measured cantilever electrical resistance change as a function of cantilever deflection. Deflection sensitivity, which is the slope of each curve, varies from  $0.047$  up to  $0.186$  depending on cantilever geometry.

For small deflections, the deflection sensitivity is directly proportional to the stiffness of the cantilever and depends on the location of piezoresistor with respect to the cantilever neutral axis. Thus deflection sensitivity is a strong function of geometry.

$$S = \frac{\Delta R}{R} \frac{1}{\delta} \quad (1)$$

The deflection of the cantilever free end was determined from the measured probe displacement and the measured probe-cantilever contact point combined with ANSYS structural finite element model. The measured electrical resistance change was linear over the entire range of deflections with the slope corresponding to the deflection sensitivity in the range of  $0.047\text{--}0.186\ \text{m}\Omega/\Omega$  per  $\mu\text{m}$  of deflection. The observed difference in

deflection sensitivity values between cantilevers is attributed to the stiffness variations and the distance of doped UNCD layer to the neutral bending axis of the respective cantilever. In general, short and thick cantilevers with a small notch have the highest deflection sensitivity of the cantilevers tested.

### Resistivity Measurements

The electrical resistivity of UNCD was measured over the temperature range of 25-200 °C using the van der Pauw structures fabricated on the same wafers as the cantilevers. At 25 °C, the resistivity of UNCD was  $(94.1 \pm 0.4) \times 10^{-3} \Omega\text{-cm}$  for the 2  $\mu\text{m}$  devices and  $(99.7 \pm 0.2) \times 10^{-3} \Omega\text{-cm}$  for the 3  $\mu\text{m}$  devices. These values are comparable to those reported in the literature on polycrystalline and nanocrystalline diamond [11, 12]. A decrease in resistivity was observed with increasing temperature as shown in Figure 5. The negative temperature coefficient of resistance may be due to the increase in carrier concentration resulting from thermal activation.

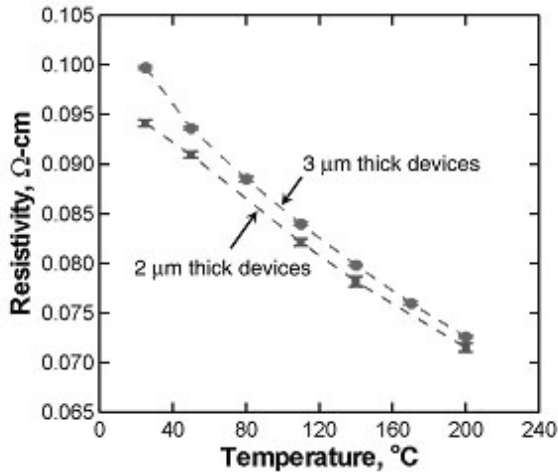


Figure 5. Van der Pauw resistivity measurement results for 2  $\mu\text{m}$  (squares) and 3  $\mu\text{m}$  (circles) UNCD stacks at different temperatures.

### Gauge Factor

While deflection sensitivity depends on cantilever geometry, longitudinal gauge factor,  $K_L$ , is a material property. Assuming transverse gauge factor is negligible,  $K_L$  is related to the deflection sensitivity of the cantilever through the longitudinal strain in the leg region,  $\epsilon_{leg,l}$  and transverse strain in the cantilever free end  $\epsilon_{tip,t}$  as

$$K_L = \frac{\Delta R}{R} \frac{1}{\epsilon} = \frac{\Delta R}{R_{leg} \epsilon_{leg,l} + R_{tip} \epsilon_{tip,t}} = \frac{S\delta}{\epsilon} \quad (2)$$

Figure 6(a) shows gauge factor for each cantilever type. Electrical resistance change was measured using the setup described above. ANSYS structural and electrical finite element simulations of cantilever structure under experimentally applied load calculated mechanical strain and three-dimensional electrical potential in the cantilever during bending, allowing precise correlation between measured electrical and mechanical behaviors. The average gauge factor value is  $7.53 \pm 0.32$ , which is close to the measured value for microcrystalline diamond [13]. The consistency of gauge factors across all cantilever types supports the assumption that transverse gauge factor is negligible in these

cantilevers. The UNCD cantilever gauge factor is approximately 5 times smaller than polycrystalline silicon [14]. Error bars in Figure 6(a) show the variation within three measurements on the same cantilever with 10  $\mu\text{m}$  uncertainty in the probe location resulting in  $\pm 0.39$  variation in  $K_L$ .

Figure 6(b) shows gauge factor over the temperature range 25-200 °C for cantilever C3. The gauge factor was constant over the measured temperature range, although a slight deviation is seen at 200°C due to substantial increase in cantilever noise. The temperature insensitivity of UNCD piezoresistivity compares very well to highly doped silicon, in which piezoresistive coefficient decreases by 28% over the same temperature range [14].

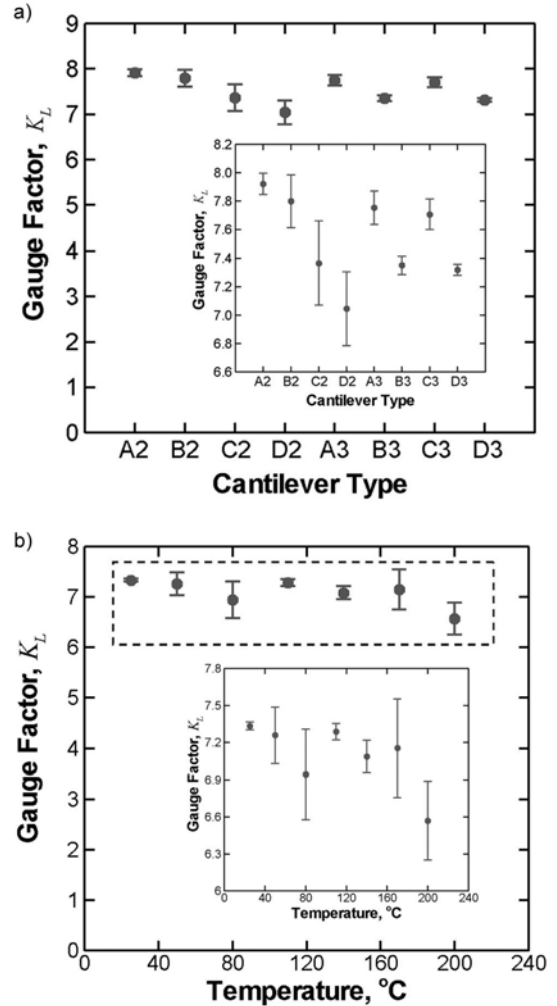


Figure 6. a) Measured gauge factor for eight cantilever types at room temperature with inset showing zoomed in data. The average gauge factor of UNCD is  $7.53 \pm 0.32$ . Error bars represent standard deviation of three measurements. Similarity in gauge factor values over all cantilever types indicates negligible transverse gauge factor. b) UNCD gauge factor dependence on temperature with inset showing zoomed in data. Gauge factor remains constant up to 200 °C. Data is shown for C3 type cantilever. The gauge factor in similarly doped silicon decreases by 28% over the same temperature range.



## CONCLUSION

In summary, we have shown design, fabrication, and characterization of all-UNCD piezoresistive microcantilevers. The electrical and piezoresistive properties of the UNCD are determined and the cantilever characteristics are reported. This work could inform the design of future microelectromechanical devices fabricated from doped UNC.

## REFERENCES

- [1] A.R. Krauss, O. Auciello, D.M. Gruen, A. Jayatissa, A. Sumant, J. Tucek, D.C. Macini, N. Moldovan, A. Erdemir, D. Ersoy, M.N. Gardos, H.G. Busmann, E.M. Meyer, and M.Q. Ding, "Ultrananocrystalline diamond thin films for mems and moving mechanical assembly devices," *Diamond Related Mater.*, 10 (2001).
- [2] E. Kohn, M. Adamschik, P. Schmid, A. Denisenko, A. Aleksov, and W. Ebert, "Prospects of diamond devices," *J. Phys. D*, 34 (2001).
- [3] S. Jiao, A. Sumant, M.A. Kirk, D.M. Gruen, A.R. Krauss, and O. Auciello, "Microstructure of ultrananocrystalline diamond films grown by microwave Ar-CH<sub>4</sub> plasma chemical vapor deposition with or without added H<sub>2</sub>," *J. Appl. Phys.*, 90 (2001).
- [4] V.P. Adiga, A.V. Sumant, S. Suresh, C. Gudeman, O. Auciello, J.A. Carlisle, and R.W. Carpick, "Mechanical stiffness and dissipation in ultrananocrystalline diamond microresonators," *Phys. Rev. B*, 79 (2009).
- [5] A. V. Sumant, D. S. Grierson, J. E. Gerbi, J. A. Carlisle, O. Auciello, and R. W. Carpick, "Surface chemistry and bonding configuration of ultrananocrystalline diamond surfaces and their effects on nanotribological properties," *Phys. Rev. B*, 76 (2007).
- [6] S. Bhattacharyya, O. Auciello, J. Birrell, J.A. Carlisle, L.A. Crutiss, A.N. Goyette, D.M. Gruen, A.R. Krauss, J. Schlueter, A. Sumant, and P. Zapol, "Synthesis and characterization of highly-conducting nitrogen-doped ultrananocrystalline diamond films," *Appl. Phys. Lett.*, 79 (2001).
- [7] X. Xiao, J. Birrell, J.E. Gerbi, O. Auciello, and J.A. Carlisle, "Low temperature growth of ultrananocrystalline diamond," *J. Appl. Phys.*, 96 (2004).
- [8] A.R. Krauss, O. Auciello, D.M. Gruen, A. Jayatissa, A. Sumant, J. Tucek, D.C. Mancini, N. Moldovan, A. Erdemir, D. Ersoy, M.N. Gardos, H.G. Busmann, E.M. Meyer, M.Q. Ding, "Ultrananocrystalline diamond thin films for MEMS and moving mechanical assembly devices," *Diamond Related Mater.*, 10 (2001).
- [9] W.S. Huang, D.T. Tran, J. Asmussen, T.A. Grotjohn, and D. Reinhard, "Synthesis of thick, uniform, smooth ultrananocrystalline diamond films by microwave plasma-assisted chemical vapor deposition," *Diamond Related Mater.*, 15 (2006).
- [10] L.J. van der Pauw, "A method of measuring the resistivity and Hall coefficient on lamellae of arbitrary shape," *Philips Technical Rev.*, 20 (1958).
- [11] M. Werner and R. Locher, "Growth and application of undoped and doped diamond films," *Rep. Prog. Phys.*, 61 (1998).
- [12] W. Gajewski, P. Achatz, O.A. Williams, K. Haenen, E. Bustarret, M. Stutzmann, and J. A. Garrido, "Electronic and optical properties of boron-doped nanocrystalline diamond films," *Phys. Rev. B*, 79 (2009).
- [13] P. Gluche, M. Adamschik, A. Vescan, W. Ebert, F. Szücs, H.J. Fecht, A. Flöter, R. Zachai, and E. Kohn, "Application of highly oriented, planar diamond (HOD) films of high mechanical strength in sensor technologies," *Diamond Related Mater.*, 7 (1998).
- [14] P. French and A. Evans, "Properties of silicon," in *EMIS datareviews series no. 4. INSPEC*, chapter 3.4, New York, (1988).

## CONTACT

\* W.P. King, tel: 217-244-3864; wpk@illinois.edu

# THIN SILICON MEMS CONTACT-STRESS SENSOR

J. Kotovsky<sup>1\*</sup>, A.C. Tooker<sup>1</sup>, and D.A. Horsley<sup>2</sup>

<sup>1</sup>Lawrence Livermore National Laboratory, Livermore, California, USA

<sup>2</sup>University of California, Davis, California, USA

## ABSTRACT

This thin, MEMS contact-stress (CS) sensor continuously and accurately measures time-varying, solid interface loads in embedded systems over tens of thousands of load cycles. Unlike all other interface load sensors, the CS sensor is extremely thin ( $< 150 \mu\text{m}$ ), provides accurate, high-speed measurements, and exhibits good stability over time with no loss of calibration with load cycling. The silicon CS sensor,  $5 \text{ mm}^2$  and  $65 \mu\text{m}$  thick, has piezoresistive traces doped within a load-sensitive diaphragm. The novel package utilizes several layers of flexible polyimide to mechanically and electrically isolate the sensor from the environment, transmit normal applied loads to the diaphragm, and maintain uniform thickness. The CS sensors have a highly linear output in the load range tested ( $0 - 2.4 \text{ MPa}$ ) with an average accuracy of  $\pm 1.5 \%$ .

## INTRODUCTION

This work offers the first, thin, MEMS contact-stress (CS) sensor capable of accurate *in situ* measurements of time-varying, contact-stresses between two solid interfaces (e.g. *in vivo* cartilage contact-stress and body armor dynamic loading) across thousands of load cycles. This CS sensor measures loads only over its surface area, which is typically small compared to the contact area under study, unlike a force sensor in which the entire load is transmitted through the sensor. The CS sensor described here responds only to solid, normal loads, not to hydrostatic and/or shear loads.

Although similar in design to MEMS pressure sensors, the primary characteristic differentiating this CS sensor (other than the lack of a reference volume) is its thickness and package. CS sensors must be thin so that placement between two solid contacting surfaces will not induce changes in the load distribution to be measured. Attempts have been made to measure interface loads [1 – 5], however, these sensors are typically incapable of extended measurements and are  $> 500 \mu\text{m}$  thick. The CS sensor described here is extremely thin ( $< 150 \mu\text{m}$  fully packaged) so that it can be unobtrusively placed between contacting structures to provide accurate, long-term measurements.

All existing commercial technologies use polymer-based sensors. Although these commercially available sensors can be thin ( $\sim 200 \mu\text{m}$ ), since the sensing mechanism is the polymer material, the accuracy, speed, and longevity is limited by the time-varying, viscoelastic behavior of those materials. The CS sensor, in contrast, relies upon the phenomenal material properties of silicon, which shows no wear, is perfectly elastic, and has an exceptional gauge factor.

The two most commonly used commercial sensors for measuring interface loads are: the Fuji Prescale film (Fuji Photo Film Company, Tokyo, Japan) and the Tekscan FlexiForce sensor (Tekscan Corporation, Boston, MA). The Fuji Prescale film is comprised of dye-filled capsules that rupture when load is applied. The film produces a stain with an intensity proportional to the maximum applied load during the entire loading period. Analogous to photographic film, the material is only useful for a single exposure to load and is not relevant for embedded or dynamic applications.

The Tekscan FlexiForce sensor is comprised of two polyester sheets patterned with piezoresistive ink electrodes. Due to inelastic changes in the sensing ink, however, the Tekscan sensor is renowned for its loss of calibration over multiple load cycles, severely limiting its accuracy. This minimizes its utility for repeated, long-term load measurements.

The thin, MEMS CS sensor presented here provides a continuous, accurate contact-stress measurement. It is specifically designed to be extremely stable over the long-term, exhibiting no loss of calibration with load cycling. The CS sensor is built from elastic, well-characterized materials, providing accurate and high-speed ( $50+ \text{ kHz}$ ) measurements over a potential embedded lifetime of decades. This work explored sensor designs for an interface load range of  $0 - 2.4 \text{ MPa}$ ; however, the CS sensor has a flexible design architecture to measure a wide variety of interface load ranges.

## CS SENSOR DESIGN AND FABRICATION

### Silicon MEMS CS Sensor Design

This first-generation CS sensor is  $2 \text{ mm} \times 2.5 \text{ mm}$  and is  $65 \mu\text{m}$  thick (Fig. 1). It is a MEMS-fabricated, silicon device with a load sensitive diaphragm. The sensor is similar in performance to established silicon pressure sensors; however, it is reliably produced down to a thickness of  $50 \mu\text{m}$ .

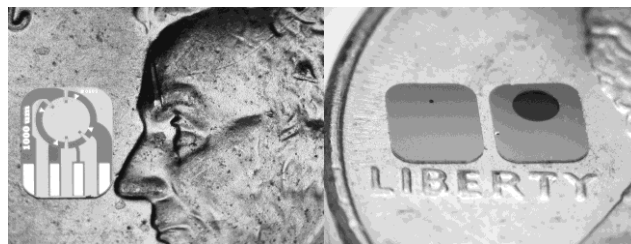


Figure 1: These images show the silicon MEMS CS sensor with a penny (for scale). The left image shows the front-side of a silicon MEMS CS sensor with a  $500 \mu\text{m}$  radius diaphragm. The right image shows the backside of two silicon MEMS CS sensors ( $50 \mu\text{m}$  and  $500 \mu\text{m}$  radius diaphragm, left and right, respectively) showing the etched diaphragms.

Four radially oriented piezoresistors are arranged in a full Wheatstone bridge at the edges of the diaphragm, where the tensile bending stresses are greatest, optimizing the signal-to-noise ratio (Fig. 2). Utilizing a full Wheatstone bridge, as well as the direction-dependent piezoresistive properties of silicon, the CS sensor is designed to be thermally compensating and self-balancing, eliminating the need for a completion bridge. The piezoresistors lead to large metal-covered contact pads at the edge of the device for direct electrical connection to the package. The silicon CS sensors are designed to show no temperature or humidity dependence and to be drift-free with long-term use.

The load-sensitive, circular diaphragms are designed to be free of stress concentrations, making them mechanically strong and tolerant of  $10\times$  overloading. Diaphragm thicknesses of  $0.5 - 25 \mu\text{m}$  and radii of  $50 - 500 \mu\text{m}$  have been produced to accommodate load ranges for various applications.

### Silicon MEMS CS Sensor Fabrication

The silicon CS sensor is fabricated using a silicon-on-insulator (SOI) wafer with a device layer that defines the final diaphragm thickness. The SOI wafer enables reproducible control of the diaphragm thickness, regardless of the etch process or wafer thickness variation. Use of a thin buried-oxide layer minimizes the residual stresses on the finished diaphragms resulting in excellent sensor performance.

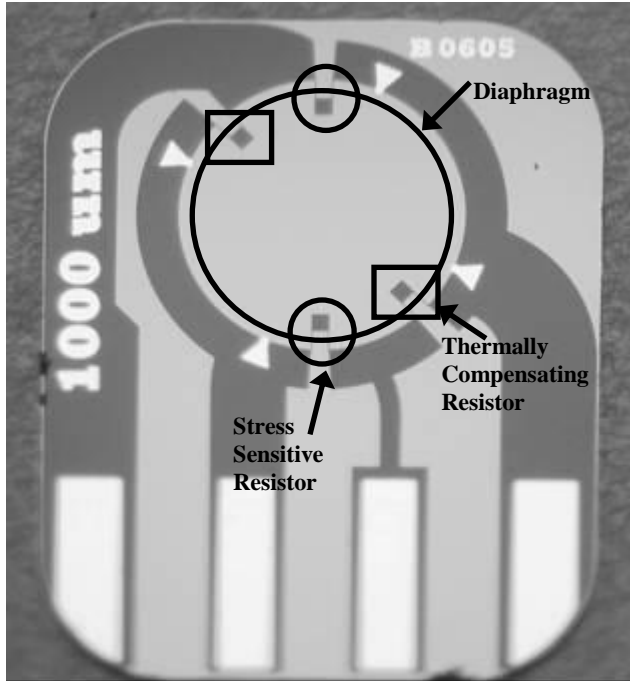


Figure 2: This image shows the implanted piezoresistors (dark gray) placement relative to the diaphragm location (large circle). The thermally compensating resistors (small boxes) and the stress-sensitive resistors (small circles) are marked. At the bottom of the silicon sensor are four large, metal contact pads for connection to external electronics. This silicon CS sensor has a 500  $\mu\text{m}$  radius diaphragm. (The CS sensor has text “1000  $\mu\text{m}$ ” denoting the diaphragm diameter and “B0605” denoting the sensor ID.)

An insulating layer is added to the device layer to electrically isolate the doped traces. Ion implantation into the device layer defines the piezoresistive Wheatstone bridge. The implant is annealed and windows are opened at the metal contact locations. Metal is patterned over the contact windows to form ohmic contacts with the implant.

The SOI wafer is then lapped to its final thickness of 65  $\mu\text{m}$  and mounted on a handle wafer for the final processing steps. The diaphragms are etched from the backside into the SOI wafer using a Deep Reactive Ion Etch (DRIE) process until the BOX layer is exposed, leaving only the device and insulating layers. The sensors are released after a second DRIE process etches through the entire wafer thickness to define the sensor outlines. Individual sensors are electrically tested to verify their piezoresistive response and then soldered to the package.

### CS Sensor Package

In addition to the challenge of reliably producing a thin silicon MEMS sensor, the CS sensor demands a novel package

utilizing several layers of flexible polyimide (DuPont, USA) to fully encapsulate the silicon sensor. The package provides a direct electrical connection between the silicon sensor and the external electronics while maintaining mechanical and electrical isolation from the environment (Figs. 3 and 4). The packaging is designed to maintain a uniform thickness ( $< 150 \mu\text{m}$ ), including the region where the silicon sensor is mounted. The use of flexible, narrow polyimide strips ensures the packaged CS sensor can accommodate curved surfaces. The packaged CS sensor can withstand extreme loads without failure (no solder-joint failure) over tens of thousands of load cycles and survives repeated cycling between  $-40 \text{ }^\circ\text{C}$  and  $+70 \text{ }^\circ\text{C}$  while maintaining accuracy.

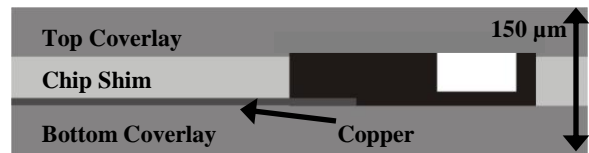


Figure 3: A cross-section of the packaged CS sensor (not drawn to scale). The silicon CS sensor (in black) is soldered to the package and is completely encapsulated by the polyimide (Top and Bottom Coverlays and Chip Shim). The Bottom Coverlay has an electro-deposited copper layer with solder for making electrical connections to the sensor and the external electronics. The package maintains a uniform thickness of  $< 150 \mu\text{m}$  and can be arbitrarily shaped to accommodate a variety of applications.

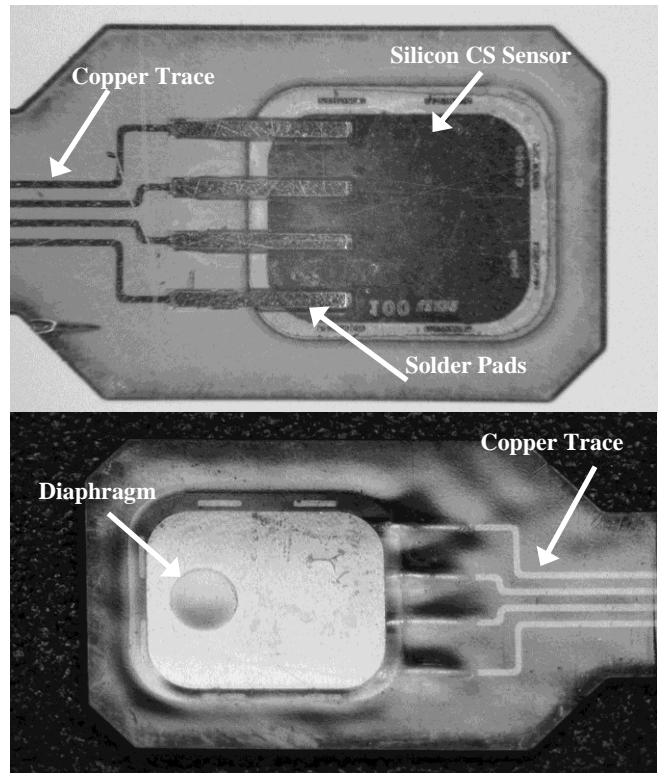


Figure 4: The top image shows the front-side of a packaged CS sensor. The silicon CS sensor is soldered to the package and the copper traces ensure electrical communication with the external electronics. The silicon CS sensor is completely encapsulated by the polyimide. The bottom image shows the back-side of a packaged CS sensor, including the etched diaphragm.

The package is designed to transmit normal contact loads to the diaphragm, while isolating the silicon sensor from shear loads. In addition, the package is mechanically decoupled from the silicon sensor so that material property changes in the packaging materials do not adversely affect sensor performance. Finally, the package is patternable in arbitrary shapes for a wide array of applications.

## TESTING AND RESULTS

### Testing Assembly

Basic mechanical testing of the CS sensor is conducted using an Instron 5565 (Instron, Norwood, MA) fitted with 2 inch diameter flat, rigid plates. A compliant silicone rubber material is added between the two plates to mimic the contact environment (modulus and stiffness) of the sensor's application, although this layer is not required for sensor function. The Instron 5565 can be programmed to apply a variety of different load profiles. This particular testing assembly, including the load cell, limits the maximum load that can be applied to the CS sensor to approximately 2.4 MPa. Prior to testing, the CS sensors were conditioned by applying a minimum of 100 load cycles.

The standard input voltage to the Wheatstone bridge on the CS sensor is 12 V DC. Depending upon the application, though, any DC or AC voltage from 1 – 20 V can be used for the bridge input.

### Results

Basic characterization data is presented here for a diaphragm thickness of 15  $\mu\text{m}$  and radius of 50  $\mu\text{m}$ . Other diaphragm geometries were tested and exhibit similar results.

CS sensor drift was measured by applying and holding constant loads at 0 MPa, 0.4 MPa, 0.7 MPa, and 1.4 MPa. Drift is a measure of change of the output over time. With these constant loads, the maximum drift after 2 hours is  $< \pm 0.7\%$  of full-scale output (FSO). For no load (0 MPa), the maximum drift after 18 hours is  $< \pm 0.8\%$  of FSO.

Figure 5 shows the CS sensor output for 5 load cycles (2429 data points) over a load range of 0.04 – 2.41 MPa. The typical CS sensor has an excellent linear calibration curve, shown in Fig. 6, with a coefficient of determination ( $R^2$ )  $> 0.99$ . (The coefficient of determination is calculated from the ratio of the regression sum of squares to the residual sum of squares in the least squares fit calculation.) Calibration curves with  $R^2 > 0.99$  can be found for the diaphragm geometries tested, however, for larger diaphragms the curves are typically non-linear. The linearity of the smaller-diaphragm CS sensors is advantageous for the simplicity in both use and calibration.

The calibrated sensor is then subjected to known load cycles and the measured response is compared to the applied load (Fig. 6). This second load cycling test, consisting of 15 load cycles (7297 data points) over a load range of 0.04 – 2.41 MPa, determines the accuracy of the CS sensor after the calibration curve is established.

The absolute error is the maximum difference between the measured and predicted pressure; this represents the maximum measurement uncertainty. For this typical CS sensor, the absolute error is measured to be 0.17 MPa. The absolute accuracy of the device can then be described as the maximum absolute error divided by the full-scale range of the device. Thus, the absolute accuracy is  $\pm 7.0\%$  of FSO.

This absolute accuracy of  $\pm 7.0\%$  of FSO is based on the absolute error and, therefore, represents the greatest uncertainty of the CS sensor measurement. The CS sensor error can also be expressed as the average error; this provides a typical measure of

the CS sensor performance, although it hides the extremes of the uncertainty. The average error is the difference between the average measured and predicted pressure. The average accuracy of the device can then be described as the average error divided by the FSO of the device. The average error is 0.04 MPa, corresponding to an average accuracy of  $\pm 1.5\%$  of FSO.

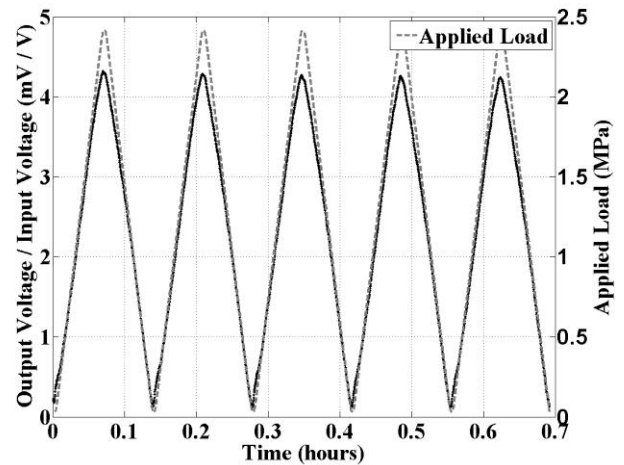


Figure 5: Graph of the CS sensor output (solid black line) for 5 load cycles (dashed gray line) over a load range of 0.04 – 2.41 MPa. The data shown is for a diaphragm thickness of 15  $\mu\text{m}$  and a radius of 50  $\mu\text{m}$ .

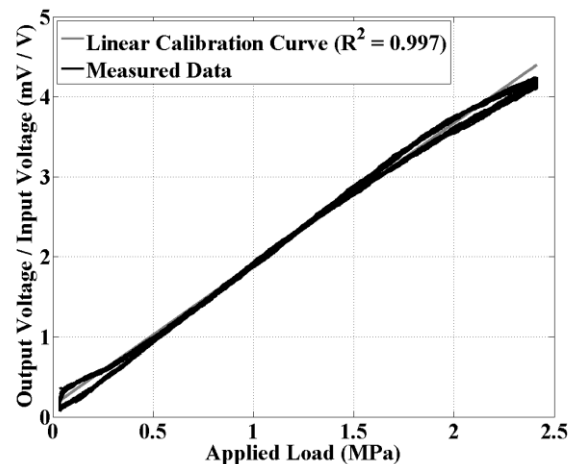


Figure 6: Graph of the linear calibration curve (thin gray line) for the 5 load cycles shown in Fig. 5. The measured data (thick black line) from a second load cycling test (15 load cycles) is also shown for comparison with the established calibration data. The average accuracy for this data, compared with the calibration data, is  $\pm 1.5\%$  of FSO, demonstrating the excellent performance of the CS sensor. The data shown is for a diaphragm thickness of 15  $\mu\text{m}$  and a radius of 50  $\mu\text{m}$ ; other diaphragm geometries exhibit similar performance.

The precision of the devices is calculated by looking at the standard deviation of the error. The standard deviation of the errors is 1.3%, indicating the devices show excellent precision.

Hysteresis of the CS sensor is assessed by repeated loading and unloading of the sensor. The hysteresis is the largest difference in CS sensor output for increasing and decreasing loads

(for the same applied load). As shown in Fig. 6, the CS sensors do exhibit small hysteresis, especially for smaller loads. For the typical CS sensor shown in Figs. 5 and 6, the hysteresis is  $\pm 6.5\%$  of FSO. The primary source of the hysteresis is in the testing assembly, as discussed below.

## DISCUSSION

The CS sensors presented here have good accuracy and precision in the load range tested (0.04 – 2.41 MPa). The load range tested was limited by the mechanical testing apparatus, not the CS sensors, themselves. Preliminary high-load tests, up to 4 MPa, and low-load tests, from 6.9 kPa, have been conducted and the CS sensors also demonstrate excellent performance for alternate load ranges.

### Calibration, Hysteresis, and the Testing Assembly

Due to limitations of the testing system, the accuracy and hysteresis of the sensor are overstated. The mechanical testing assembly, unfortunately, contributes to the error and hysteresis calculations. The calibration of the CS sensors is affected by placement of the sensor in the testing assembly. During testing, it must be assumed that a uniform load distribution exists within the testing assembly. It is known, however, that variations in the load distribution exist. The compliant layer used in these experiments has a Poisson ratio of nearly 0.5 and is incompressible. As a result, the material shears and tends to extrude out of the testing platform. These effects limit the assumption of a uniform load distribution. Testing is performed at the center of the testing assembly to help minimize these effects. To control against this effect, a custom, fluid-diaphragm loading system is being created to produce a well-defined normal load to the device.

The compliant layer in the mechanical testing assembly is a viscoelastic material and its ability to mechanically “restore” itself on unloading is limited. As the load is increased and decreased, the viscoelastic behavior of the compliant layer affects the pressure distribution within the testing assembly, resulting in the observed hysteresis. Preliminary tests have shown that replacement of this compliant layer with a thinner or more elastic material minimizes this effect, thereby minimizing the hysteresis. In addition, maintaining a higher load during testing (i.e. testing from 0.40 – 2.41 MPa instead of 0.04 – 2.41 MPa) further minimizes the hysteresis. Based on known material properties of the sensor and the testing assembly, as well as measurements that have shown no hysteresis, it is believed the hysteresis of the sensor itself is overstated.

### DC Bias

The CS sensors have a full Wheatstone bridge. Ideally, the diaphragm would be in a zero stress-state with no applied load. With no stress, the four resistors comprising the bridge would be perfectly matched and, thus, the CS sensor output would be zero. Residual stresses in the diaphragm, however, produce a non-zero bridge output, even in a no-load state. This combined with minor variations in the resistors generated during fabrication can generate a non-zero output with no applied load (i.e. a DC bias). This DC bias has been subtracted from the CS sensor outputs shown in Figs. 5 and 6.

The DC bias values are typically between 5 mV / V and 30 mV / V and do not show a correlation to diaphragm geometry. Indeed, two CS sensors with the same diaphragm geometry often exhibit different DC bias values. This effect may be explained by stress variations across a wafer due to varied insulation film

thicknesses. Although this DC bias does not affect the CS sensor performance or sensitivity, it necessitates individual calibration of the CS sensors. Further refinements in the film deposition and resistor design should minimize the film stress and resistor variations.

## SUMMARY AND FUTURE WORK

The CS sensor presented here is a silicon-based MEMS sensor with piezoresistive traces strategically doped within a load-sensitive diaphragm. It is designed to repeatedly measure time-varying loads, with a high long-term accuracy. The silicon MEMS CS sensor can be reliably produced with thicknesses down to 50  $\mu\text{m}$  and the packaged CS sensor is  $< 150\ \mu\text{m}$  thick, ensuring the sensor minimally perturbs the interface loads of the system under study. The load sensitive diaphragms have been produced with radii between 50  $\mu\text{m}$  and 500  $\mu\text{m}$  and thicknesses between 0.5  $\mu\text{m}$  and 25  $\mu\text{m}$  to accommodate a variety of load ranges. The smaller diaphragm CS sensors have a highly linear response in the load range tested (0 – 2.4 MPa). The sensors have an absolute accuracy between  $\pm 7\%$  of FSO, with an average accuracy between  $\pm 1.5\%$  of FSO.

The primary cause of the error and hysteresis for these CS sensors is in the mechanical testing assembly. A custom fluid-driven pressure testing assembly is being built to minimize the shearing effects, non-uniform loading, and hysteresis of the system described here. This will also enable testing of the next generation sensors at higher and dynamic loads, as well as varied temperatures. Currently, smaller, next-generation sensors, for both flat and curved environments, are in testing and very large (1000-element), flexible, stretchable stress-sensing arrays of similar design have been prototyped.

## ACKNOWLEDGEMENTS

This work performed under the auspices of the U.S. Department of Energy by Lawrence Livermore National Laboratory under Contract DE-AC52-07NA27344. The technology is protected by Patent #2060107752 and patents pending and is available for commercial license. LLNL Release Number: LLNL-PROC-427227.

## REFERENCES

- [1] M.L. Harrison, P. Morberg, W.J.M. Bruce, and W.R. Walsh, “An improved method for measuring tibiofemoral contact areas in total knee arthroplasty: a comparison of K-scan sensor and Fuji film”, *Journal of Biomechanics*, 32, 951 (1999).
- [2] M. Ferguson-Pell, S. Hagiwara, and D. Bain, “Evaluation of a sensor for low interface pressure applications”, *Medical Engineering and Physics*, 22, 657 (2000).
- [3] M. Manouel, H.S. Pearlman, A. Belakhlef, and T.D. Brown, “A miniature piezoelectric polymer transducer for in vitro measurement of the dynamic contact stress distribution”, *Journal of Biomechanics*, 25 (6), 627 (1992).
- [4] P.H. Chappell and J.A. Elliot, “Contact force sensor for artificial hands with a digital interface for a controller”, *Measurement Science Technology*, 14, 1275 (2003).
- [5] T.N. Tun, T.S. Lok, T.C. Jui, R. Akkipeddi, and M. Rahman, “Contact pressure measurement using silicon-based  $\text{Al}_x\text{Ga}_{1-x}\text{As}$  semiconductor pressure sensors”, *Sensors and Actuators A*, 118, 190 (2005).

## CONTACT

\*J. Kotovsky, tel: +1-925-424-2398; kotovsky1@llnl.gov

# A FULLY-PASSIVE WIRELESS MICROFABRICATED NEURO-RECORDER

Helen N. Schwerdt<sup>1</sup>, Wencheng Xu<sup>1</sup>, Sameer Shekhar<sup>1</sup>,

Abbas Abbaspour-Tamijani<sup>1</sup>, Bruce C. Towe<sup>2</sup>, and Junseok Chae<sup>1</sup>

<sup>1</sup>School of Electrical, Computer, and Energy Engineering, Arizona State University, Tempe, USA

<sup>2</sup>School of Biological and Health Systems Engineering, Arizona State University, Tempe, USA

## ABSTRACT

This paper reports a completely passive and wireless MEMS device for potential use in recording neuro-potentials *in-vivo*. Its operating principle utilizes an implantable circuit or “tag” to backscatter data to an external interrogator that supplies the fundamental carrier. The backscattering circuit relies solely on its nonlinear components, varactor diodes, which mix and backscatter neuro-potentials with the supplied carrier. Performance of the MEMS neuro-recorder was demonstrated using emulated and *in-vivo* neuro-potentials as low as 500  $\mu\text{V}_{\text{P-P}}$  and up to 3 kHz.

## INTRODUCTION

Current wireless neuro-recording microsystems employ multi-component packages comprised of sophisticated circuitry located between the scalp and skull, which is then wired to micromachined electrode arrays implanted into the cortex of the brain [1-2]. In order to remove these interconnects and improve signal acquisition quality some have monolithically integrated the circuits onto the electrodes and/or fabricated die-level post-CMOS electrodes on-chip [3]. These advancements make it possible to monitor *in-vivo* potentials with extremely high spatial and temporal resolution. Nevertheless, challenges remain due to the complexity of wireless telemetry. To bypass some of this complexity, fully-passive techniques have been previously implemented in meso-scale systems [4-5]. In this paper, we present an alternative, significantly less complex microsystem for passive and wireless neuro-recording consisting of only two varactors, three MIM capacitors, and an on-chip planar antenna.

## DEVICE OPERATION AND FABRICATION

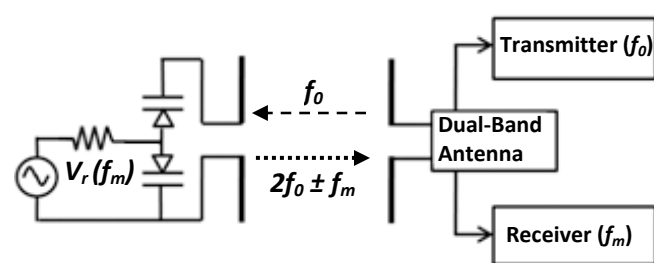


Figure 1: A simplified schematic of the fully-passive and wireless neuro-recorder.  $V_r(f_m)$  is the low frequency neuro-potential signal,  $f_0$  is the carrier, and  $2f_0 \pm f_m$  is the backscattered modulated signal.

The basic passive and wireless operation is illustrated in Fig. 1. An RF excitation carrier ( $f_0$ ) generated by an external interrogator mixes neuro-potentials ( $f_m$ ) through nonlinear varactors, backscattering third-order intermodulation products  $2f_0 \pm f_m$ . An illustration of the neuro-recorder is shown in Fig. 2a. The fabrication process uses seven masks (Fig. 2b). KOH-etched trenches on the front and back form the sockets for the varactors and probe feedthroughs, respectively. The frontside consists of a planar antenna, MIM capacitors, and varactors, and the backside is patterned with through-wafer interconnects to interface with neuro-potentials (Fig. 3).

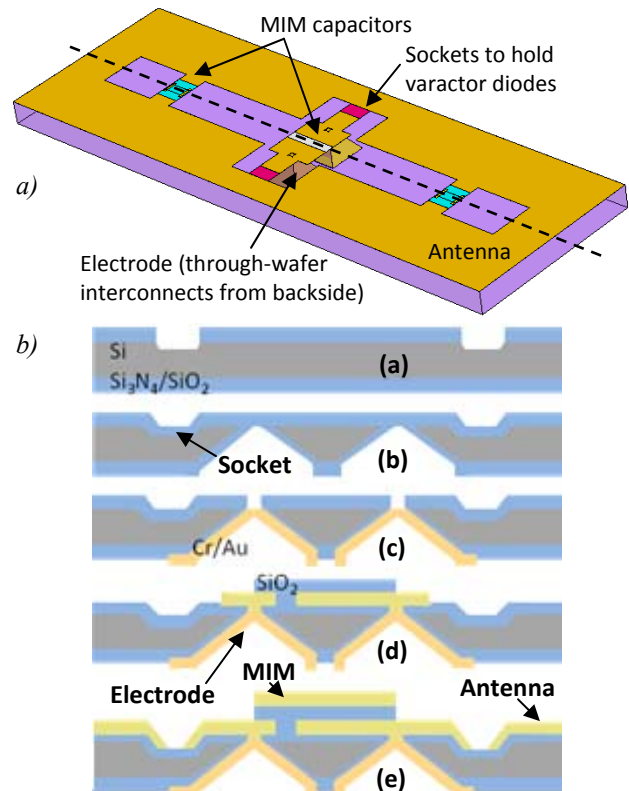


Figure 2: a) An oblique view of the MEMS neuro-recorder with on-chip components and cross-sectional axis labeled (dashed line). b) Cross-sectional fabrication process flow: (a) patterning of  $\text{Si}/\text{Si}_3\text{N}_4/\text{SiO}_2$  on front, (b) backside KOH etching for through-wafer interconnects and PECVD of  $\text{SiO}_2$  for insulation, (c) depositing Cr/Au, and defining vias to electrodes on front, (d) depositing Cr/Au for bottom MIM plate and via interconnect, and PECVD of  $\text{SiO}_2$  for MIM oxide layer, (e) depositing Cr/Au for antenna, MIM, and pads for diodes.

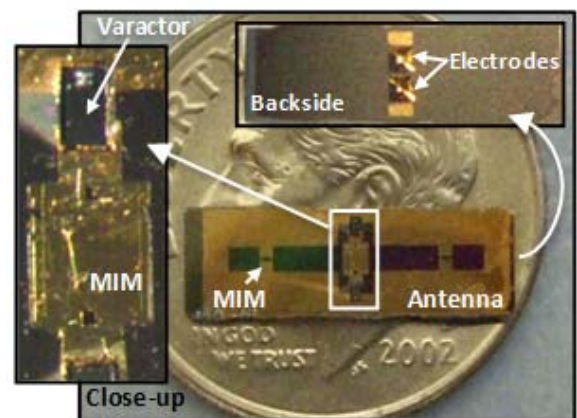


Figure 3: Photograph of a fabricated MEMS neuro-recorder placed above a dime (topside) with backside and close-up views.

## TESTING

The MEMS neuro-recorder was characterized using i) emulated neuro-potentials and ii) *in-vivo* compound action potentials (CAPs) from a frog's sciatic nerve. A phase-synchronous demodulator was built to retrieve the wirelessly transmitted signals. The frog's nerve was stimulated by pulsing current into the lower end of the spinal column generating CAPs in the range of 10–1000  $\mu\text{V}$  down the nerve bundle. The CAPs acquired with the MEMS recorder ranged from 2–140 Hz and 500–1000  $\mu\text{V}$ .

## RESULTS

The passive wireless telemetry operates at 2.2–2.45/4.4–4.9 GHz ( $f_0/2f_0$ ) for emulated neuro-potentials up to 3 kHz ( $f_m$ ) and as low as 500  $\mu\text{V}$ . Fig. 4 shows the measured frequency spectrum where a sinusoidal input signal generated by a function generator, of 3.4 mV at 400 Hz ( $f_m$ ) is mixed with the backscattered carrier ( $2f_0$ , 4.41 GHz) resulting in the observed sidebands at 15 dB above the noise floor. Table 1 summarizes the measured specifications of the MEMS neuro-recording device. Fig. 5 shows CAPs from the frog as detected from the MEMS device and from measurements using the reference electrode.

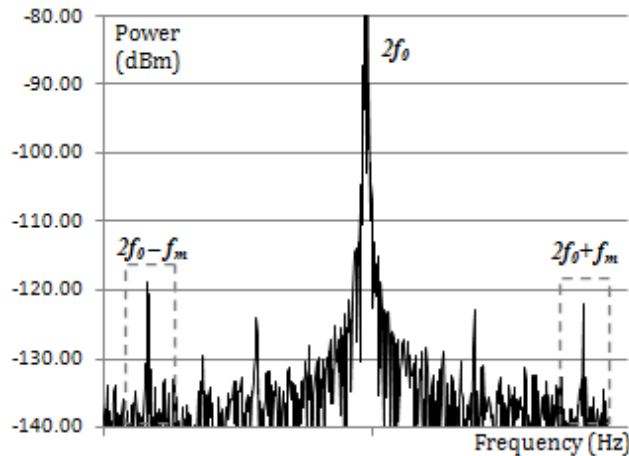


Figure 4: Measured spectrum for 3.4 mV ( $f_m = 400$  Hz) sinusoidal input and 14.8 dBm radiated from the source. Center backscattered frequency ( $2f_0$ ) shown at 4.409999220 GHz with 400 Hz offset sidebands approximately 15 dB above the noise floor (boxed in).

Table 1: Summary of specifications for MEMS device.

Size		$12 \times 4 \times 0.5 \text{ mm}^3$
Detected Input Signals	Bandwidth	5 – 3000 Hz
	Amplitude	$\geq 500 \text{ } \mu\text{V}$
	Distance	$\leq 2.5 \text{ cm}$
RF Transmission	Radiated Power	0 – 18 dBm
	Frequency	2.2 – 2.45 GHz
RF Reception	Sideband Level	$\leq -105 \text{ dBm}$
	Noise Floor	$\approx -134 \text{ dBm}$
	Frequency	4.4 – 4.9 GHz

## DISCUSSION

At this stage, the MEMS neuro-recorder may be suitable for detecting signals in the peripheral nervous system (PNS), especially in motor nerve bundles where CAPs reach up to hundreds of microvolts to several millivolts. The CAP measurements (Fig. 5) suggest the neuro-recorder may be capable of detecting neurological

signals as low as 500  $\mu\text{V}$ . Below 500  $\mu\text{V}$ , the current system becomes dominated by noise, including 60 Hz noise. The frequency of the noise may coincide with the frequency of the neuro-potentials and can completely screen out the targeted CAPs. However, because the current limitations in minimum detectable signal may result from external noise sources, future work to diminish noise may improve the device's sensitivity and enable signal detection on the same order as cortical potentials.

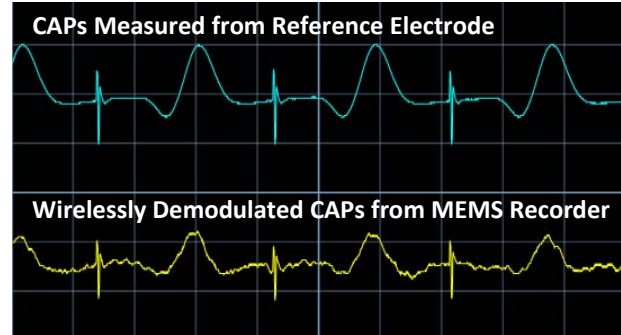


Figure 5: CAPs generated from a frog measured by a reference electrode (top, 0.1 V/div, 0.0025 s/div) at 500  $\mu\text{V}_{p-p}$  and wirelessly acquired from the MEMS neuro-recorder (bottom, 0.5 V/div, 0.0025 s/div). The sharp spikes represent artifacts of the pulsed current stimulation, which also travel down the nerve. The oscilloscope used 128 point averaging to remove some of the background noise.

## ACKNOWLEDGEMENT

The authors thank Mr. Jaeyoung Cho for depositing PECVD films, and Patrick Larson for his assistance with frog testing. This work is partially supported by NSF (ECCS-0702227), NIH (5R21NS059815-02), and NASA-GRC fellowship (NNX09AK93H).

## REFERENCES

- [1] A.M. Sodagar, G.E. Perlin, Y. Yao, K. Najafi, K. D. Wise, "An Implantable 64-Channel Wireless Microsystem for Single-Unit Neural Recording," IEEE J. Solid-State Circuits, 44 (9), 2591-2604, 2009.
- [2] Y.K. Song, D.A. Borton, S. Park, W.R. Patterson, et. al., "Active Microelectronic Neurosensor Arrays for Implantable Brain Communication Interfaces," IEEE Trans. Neural Sys. Rehab. Eng., 17 (4), 339-345, 2009.
- [3] M. Ho, H. Chen, F. Tseng, S. Yeh, M. S. Lu, "CMOS Micromachined Probes by Die-Level Fabrication for Extracellular Neural Recording," J. Micromech. Microeng., 17, 283-290, 2007.
- [4] B.C. Towe, "Passive Backscatter Biotelemetry for Neural Interfacing," Proc. IEEE Int. EMBS Conf. Neural Engineering, 144-147, 2007.
- [5] A. Abbaspour-Tamijani, M. Farooqui, B. Towe, and J. Chae, "A Miniature Fully-passive Microwave Back-scattering Device for Short-range Telemetry of Neural Potentials," IEEE EMBS, Vancouver, Canada, 2008.

## CONTACT

H.N. Schwerdt, hschwerd@asu.edu

# NOVEL METHOD OF PROTECTING AND CONNECTING CMOS CHIPS ENABLES NETWORKED PACING LEADS

R. Azevedo, B. Costello, J. Frank, M. Jensen, T. Thompson, M. Zdeblick<sup>1</sup>

<sup>1</sup>Proteus Biomedical, Inc., Redwood City, California, USA

## BACKGROUND

Implantable Pulse Generators (IPGs) are implantable, programmable devices intended to deliver electrical energy to body tissues over a period of five to ten years. This energy is typically delivered to the targeted tissue via an elongate lead. Cardiac leads, for example, are ~ 80 cm long and are comprised of two or more insulated wires, each connected to a connector on the proximal end and an electrode ring on the distal end. In such systems, all of the electronics are in the IPG and the leads simply deliver energy. This architecture limits the number of electrodes and sensors available in a small form factor, and, thus has limited the clinical utility, cost-effectiveness and acceptance of implanted therapies.

A networked lead has enhanced functionality that is enabled by having active electronics embedded in the lead. In order to have commercial and clinical relevance, these electronics need to be protected from attack by body fluids and electrochemical reactions that result from delivering electrical energy to nearby tissue. Connections between the wires in the lead and the chip, and between the chip and the electrodes, must be made in a way that is robust and protected from corrosion and fatigue.

MEMS discipline offers unique planar methods of both protecting the CMOS chip that is embedded in the lead and providing means to connect to it in a robust fashion. This work describes this Chipskin™ technology applied to a Networked Lead for application in cardiac rhythm management.

## EXPERIMENTAL SETUP

An adaptive pacing system is comprised of a Networked Lead and an IPG capable of communicating with devices on the lead. The Networked Lead, in turn, is comprised of a standard IS-1 connector on one end and a number of “satellites” on the other. Inside each satellite is a Chipskin protected CMOS chip connected to two wires and four electrodes (Figures 1 & 2).

### Networked Lead

A Networked Lead is capable of receiving communication signals from a central controller using a duplex communication system. As shown in Figure 1, two wires are used to communicate with four “satellites” near the distal end of the lead, each satellite supporting four addressable electrodes.

The primary commands associated with this device include: Clear, Switch (or configure), Talkback, and Sleep. The latter puts the satellite in a state where it is directing energy while consuming less than 10 pA. These commands are communicated by impressing a high-frequency pattern on a pace pulse: the satellite scavenges the energy from the pace pulse, interprets the command, and executes the instruction if its address matches. Talkback is a command used to confirm the configuration by a given satellite.

Shown in Figure 2 is a Finite Element Analysis with the voltage distribution surrounding these electrodes during a pacing pulse, and the radially-specific distribution that is enabled by this networked lead design. In one application for cardiac resynchronization therapy, radially-selective pacing is used to mitigate the “capture” of the nearby phrenic nerve at the most preferred pacing site. Phrenic nerve capture is a common side-effect of pacing from a cardiac vein, reported by patients as a “hiccup” occurring once per second. Current leads with two or four

hard-wired electrodes allow electronic repositioning, but at the expense of pacing site location, which is a critical factor in optimizing clinical outcome.

The use of smaller electrodes also reduces the amount of energy required to capture cardiac tissue, and thus increases battery life. In addition to radially-selective pacing, the same networked lead can increase both the volume and fidelity of electrical field sensing. For example, by switching from a dipole on one satellite to a dipole on another satellite, it is possible to measure the time it takes for a depolarization wave to travel from one satellite to another. This multi-dimensional information may be helpful in titrating dosage of certain anti-arrhythmia drugs, such as Amiodarone.

### Chipskin Technology & Satellite Construction

Each Chipskin satellite is welded to four electrodes. The satellite is comprised of a CMOS silicon chip protected with Chipskin technology that is attached to a Pt/Ir chip carrier and potted in epoxy.

The Chipskin technology provides two important and innovative functions: first, it provides a corrosion-resistant, hermetic package that protects the silicon chip *and its interconnects* from corrosion in very harsh environments. Second, it provides a method for integrated and weldable interconnects, assuring robust mechanical and electrical connections from the IC to the conductors and the electrodes. The cross section shown in Figure 3 depicts a cantilever of a thick, corrosion-resistant Pt/Ir alloy. Figure 4 shows a micrograph of an early-model chip illustrating the cantilevered connectors.

The Chipskin process starts with a complete CMOS wafer. In this work, ON Semiconductor’s C5 process was used. In the first step the wafer is coated with a series of corrosion-resistant dielectric coatings and metals, including SiC, Ir, PtIr, etc. These coatings have been characterized for corrosion inside the body by implanting them in animals for extended periods and measuring the change in thickness, with and without pacing occurring nearby. From this, one can determine the amount of dissolution that may be expected over ten years, which is a small fraction of the thickness of the films. Next, a thin layer of Pt is deposited and patterned. This is followed by a second layer of the dielectric, which is deposited and patterned. Next, a thick layer of Pt/Ir is deposited using a custom, vacuum-based physical deposition system. This produces a low stress layer of Pt/Ir that is between 50 and 75 um thick. Then, the back surface of the silicon wafer is patterned and etched using Reactive Ion Etching. This leaves the bulk of the chip suspended from the wafer by the thick Pt/Ir beams. The backside of the chip is then coated with one or more of a number of different protection materials, including, for example, TaO, TiO, and SiC, which completely surround the chip and cantilever beams. This effectively puts a protective IPG “can” on the chip using planar-processed feedthroughs to connect the electronics to its package. The cantilevers are thick enough to support the stress of welding during connection to surrounding Pt/Ir structures and are designed and tested to withstand over 400M cycles of bending typically seen by a lead in the heart over a ten year period.



## RESULTS

The described leads made with the construction techniques described above have been subjected to the equivalent of over 50 years of pacing *in vitro* and over one year *in vivo*. These and other testing results confirm that this technique is robust against the corrosion expected during a ten year period of cardiac pacing.

In addition, as shown in Figure 5, the networked lead has been shown to eliminate phrenic nerve capture at the ideal pacing site location. This pre-clinical study compared conventional lead pacing in the “band-to-band” and “band-to-coil” configurations versus the radially-selective networked lead pacing, using “intra-band” configurations, i.e., from one electrode on a satellite to the pair of electrodes on either side of that electrode on the same satellite. While conventional leads, which feature axially symmetric pacing electrodes capture the phrenic nerve at clinically unacceptable low voltages (between 4 and 5 volts), identical electrodes in identical positions using the networked lead programmed for intraband pacing do not capture the phrenic nerve even at 18 V pacing.

## CONCLUSIONS AND RECOMMENDATIONS

Protecting a silicon chip from corrosion within a Networked Lead has been shown to be possible using *in vitro* and *in vivo* studies. In addition, this packaging and connection technology expands and enables new applications for distributed electronics and sensors, particularly in environments where harsh conditions, size, cost and durability of tags or sensors is critical. Examples include marine chemistry, petroleum exploration, and portable electronics that need to be robust against exposure or immersion in water or other corrosive environments.

The use of Networked Leads is likely to expand from cardiac applications to neural pacing for pain, epilepsy, Parkinson’s, hearing loss, and other ailments. While this generation is focused on the multiplex function, future devices are likely to add sophisticated analog sensing circuitry applied at the point of interest and technology to improve the procedure reliability of pulse-delivering leads. For example, it is likely that circuitry that protects the body from currents in lead wires exposed to MRI fields will be perfected, allowing cardiac pacemaker patients to benefit from MRI imaging anywhere in their body.

Distributing electronics away from a central computer created internet computing; networking electronics *in vivo* may lead to a similar generation of innovation of sensing, computing and communicating from the skin ... in

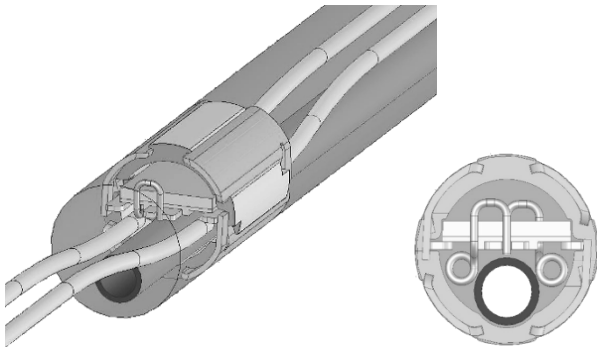


Figure 1: CAD views of silicon chip between lead wires and electrodes

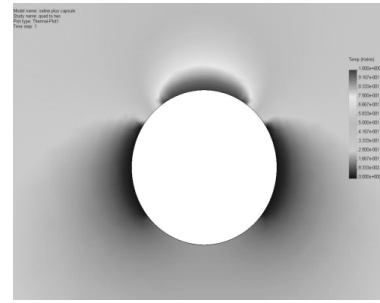


Figure 2: Finite element result of radially-selective (intra-band) pacing

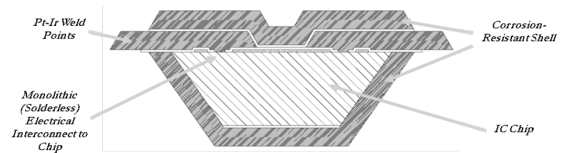


Figure 3: Cross section of a Chipskin™ protected silicon chip

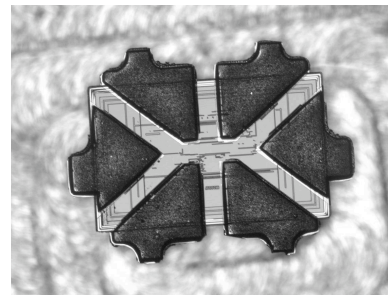


Figure 4: Microphotograph of a Chipskin™ protected silicon chip

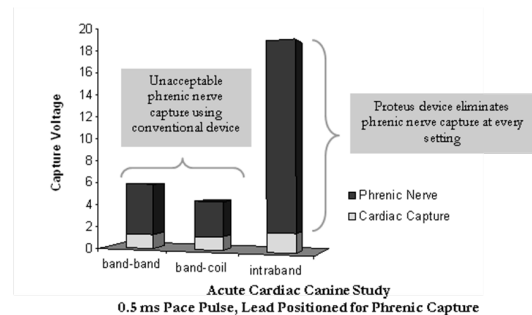


Figure 5: In-vivo cardiac model demonstration of radially-selective (intra-band) pacing using a Networked Lead to eliminate phrenic nerve capture vs. conventional leads

# NUMERICAL MODELING AND EXPERIMENTAL VERIFICATIONS OF SINGLE-STEP, DEPOSITION-FREE, HERMETIC SEALING USING SILICON MIGRATION

Rishi Kant\* and Hyuck Choo<sup>1</sup>

<sup>1</sup>Molecular Foundry, Lawrence Berkeley National Lab, 1 Cyclotron Road, Berkeley CA USA

## ABSTRACT

We present, for the first time, a silicon-migration-based process for sealing release thru-holes in single crystal silicon (SCS), its detailed numerical modeling and evaluation of the hermetic seal. Utilizing silicon migration at 1100-°C in a 10-Torr hydrogen ambient, we successfully formed 2.6- $\mu\text{m}$ - and 1.85- $\mu\text{m}$ -thick, continuous, hermetically sealing membranes from 3- $\mu\text{m}$ -thick SCS layers with two different perforation patterns. To understand and model the process, we developed a 3-D simulator and investigated over 300 release-hole designs. Our simulator predicted the final membrane geometries within 10% of experimental measurements. The quality of the hermetic seals was also robust: 90% of the sealed cavities maintained their initial pressure of 10-Torr over 210 days.

## INTRODUCTION

Single-step, wafer-scale vacuum packaging can greatly simplify packaging processes for MEMS/NEMS, improve device reliability, and reduce production costs. Previously reported deposition-based approaches leave reactive gases and unintended material deposition within the encapsulated cavities [1], limiting their application. Silicon migration presents an alternative possibility for sealing release holes that avoids these problems.

Silicon migration is a phenomenon that minimizes the surface energy of SCS through physical migration of surface atoms and occurs in various reducing/inert environments at high temperatures (>850°C) [2-4]. This phenomenon can lead to significant 3-D shape transformations, including the splitting or joining of surfaces. Additionally, the phenomenon has been shown to work with high uniformity [2]. So far, sealing of trenches, but not thru-holes, has been considered possible and demonstrated [2,4]. Inspired by our detailed simulation work, we successfully transformed release thru-holes in SCS into stable, continuous membranes. Potential application to hermetic packaging is depicted in Figure 1.

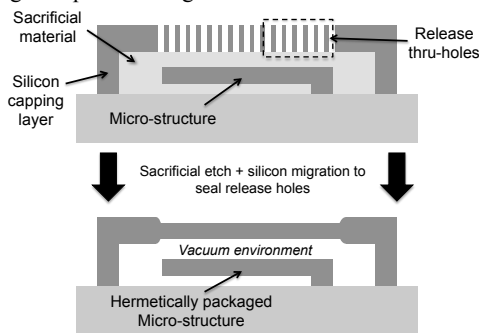


Figure 1: Conceptual sketch of hermetic packaging application.

## SIMULATION, DESIGN AND FABRICATION

Using our 3-D silicon-migration simulator [4], we studied the outcomes for 341 release-hole designs. We observed three salient features of the final structures: (1) thickness reduction in the sealed region relative to the un-patterned region; (2) step height at the region boundaries; and (3) trapped voids within the sealed membrane for certain designs (Figure 2).

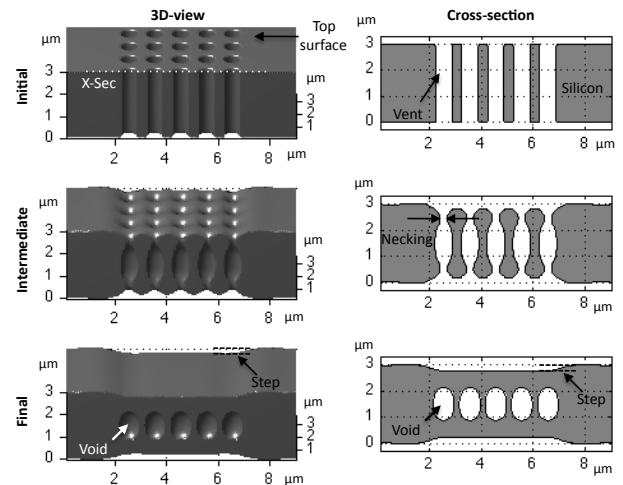


Figure 2: Transient simulation of release-hole-array ( $0.62\mu\text{m}$  diameter,  $1\mu\text{m}$  pitch,  $3\mu\text{m}$  thick layer) evolution.

Varying the hole's diameter-to-pitch ratio from 0.2 to 0.8 and the thickness-to-pitch ratio from 1 to 3 in simulation showed: (1) the number of trapped voids increased with the thickness-to-diameter ratio (Figure 3a dashed line); (2) very large trapped voids coalesced with their neighbors to form continuous cavities within the membrane (Figure 3a top right); and (3) as the diameter-to-pitch ratio increased, the functional dependence of final step height on thickness-to-pitch ratio became stronger (Figure 3b).

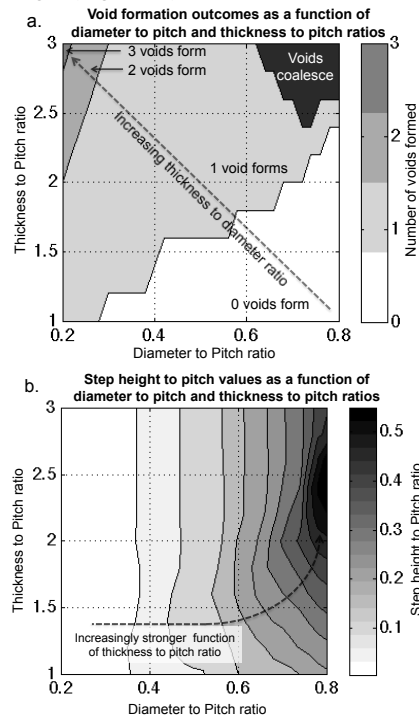


Figure 3: Summary of simulation results for 341 designs.

For experiments, we selected two starting patterns: an array of circular (0.62- $\mu\text{m}$  diameter, 1- $\mu\text{m}$  pitch) and an array of square (0.99- $\mu\text{m}$  width, 1.5- $\mu\text{m}$  pitch) holes in a 3- $\mu\text{m}$ -thick. Figure 4 describes our process flow.

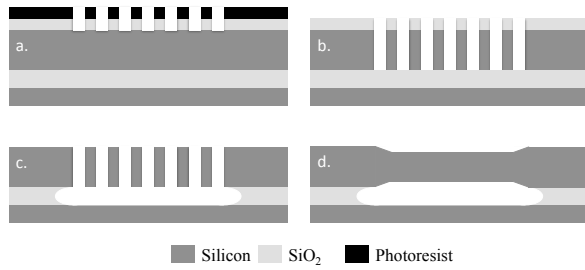


Figure 4: Fabrication process: (a) Oxidize SOI wafer and pattern array of release holes, (b) Etch pattern through 3 $\mu\text{m}$  device layer, (c) Release structure in HF, (d) Induce silicon migration at 1100 $^{\circ}\text{C}$  for 40mins in 10-Torr  $\text{H}_2$  to seal release holes. Various temperature-time products will work because the final outcome of shape transformation depends on total thermal budget.

## RESULTS AND DISCUSSION

SEM images before and after migration confirmed the formation of continuous membranes from the perforated structures (Figure 5). A tilt-angle-compensated side view taken at 80 $^{\circ}$  closely resembled the cross-sectional profile predicted by our simulator (Figure 6).

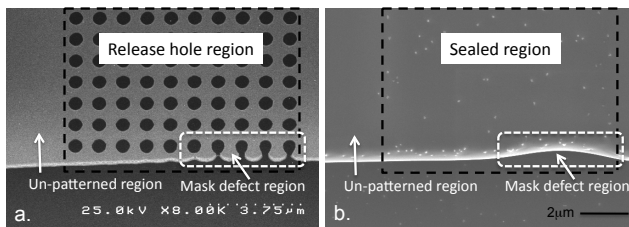


Figure 5: SEM images: Top views of circular release holes (a) before silicon migration, (b) after migration. The latter SEM clearly shows the formation of a continuous top surface.

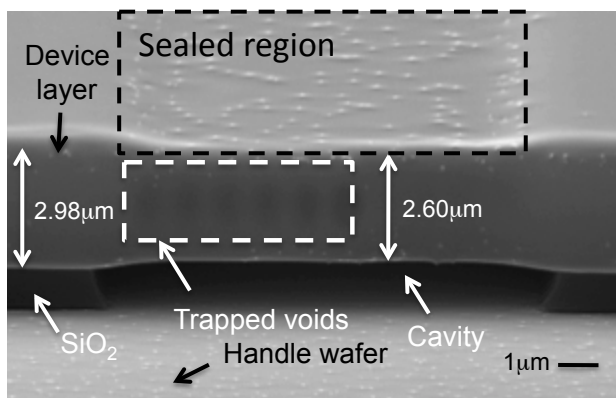


Figure 6: SEM at 80 $^{\circ}$ -tilt view confirms the thickness difference between initial device layer (2.98 $\mu\text{m}$ ) and sealed region (2.60 $\mu\text{m}$ ). It also shows a faint projection of the trapped voids.

The release holes were sealed in a 10-Torr environment, resulting in  $\sim 750$ -Torr difference across the sealed membrane in atmosphere ambient. We used a white-light interferometer to characterize the pressure differential induced membrane

deflection (Figure 7) and calculated the membrane thickness [5]. Membrane thicknesses and step heights (AFM measurement) were within 10% of the simulation values (Table 1).

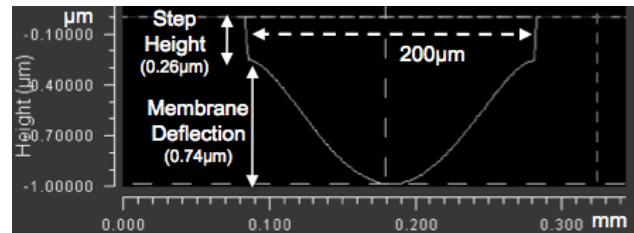


Figure 7: Deflection measurement (white light interferometer).

Design	Circular	Square
# of devices	5	5
Step height (sim)	0.23 $\pm$ 0.02 $\mu\text{m}$	0.63 $\pm$ 0.05 $\mu\text{m}$
Step height (exp)	0.26 $\pm$ 0.02 $\mu\text{m}$	0.65 $\pm$ 0.06 $\mu\text{m}$
Thickness (sim)	2.50 $\pm$ 0.10 $\mu\text{m}$	1.70 $\pm$ 0.16 $\mu\text{m}$
Thickness (exp)	2.6 $\mu\text{m}$	1.85 $\mu\text{m}$

Table 1: Comparison of simulation (sim) and experimental (exp) results. Results were within 10%.

To study the hermetic seal quality, we stored the membranes at an atmospheric pressure and monitored for deflection change: over 210 days, 9 out of 10 structures maintained their initial cavity pressure.

## CONCLUSIONS

Using silicon migration, we have sealed release holes to form stable, hermetically sealed cavities. Using our 3-D simulator, we have accurately modeled experimental results and also investigated a broad range of design parameters to establish design/process guidelines. In the future, our technique can be combined with wafer bonding to create commercial-quality, hermetic seals for micro-/nano-structures at the wafer-scale.

## REFERENCES

- [1] R. N. Candler, et. al., "Single Wafer Encapsulation of MEMS Devices", IEEE Transactions on Advanced Packaging, 26 (2003), pp. 227-232.
- [2] T. Sato, et. al., "Micro-structure Transformation of Silicon: A Newly Developed Transformation Technology for Patterning Silicon Surfaces using the Surface Migration of Silicon Atoms by Hydrogen Annealing", Japanese J. of Applied Physics, 39 (2000), pp. 5033-5038.
- [3] R. Kant, et. al., "Silicon surface migration in low-pressure non-reducing gas ambient", Electrochemical Solid-State Letters, 12 (2009), pp. H437-H440.
- [4] R. Kant, et. al., "Suspended Microstructures Made Using Silicon Migration", Technical Digest Transducers'09, Denver (2009), pp. 1091-94.
- [5] O. Tabata, et. al., "Mechanical property measurements of thin films using load-deflection of composite rectangular membranes," Sensors and Actuators, 20 (1999), pp. 135-141.

## CONTACT AUTHOR:

\*Rishi Kant, 121 Laurie Meadows Dr #362, San Mateo, CA, USA 94403. +1-510-847-6676. [rishi.kant.81@gmail.com](mailto:rishi.kant.81@gmail.com)

# SILICON MICROMACHINING TECHNIQUES FOR SUBMILLIMETER WAVE APPLICATIONS

Choonsup Lee\*, B. Thomas, G. Chattopadhyay, A. Peralta, R. Lin, C. Jung, and I. Mehdi  
Jet Propulsion Laboratory, California, USA

## ABSTRACT

Silicon micromachined terahertz passive components such as silicon washers, waveguide blocks for W-band (75-110 GHz) power amplifiers, and waveguides for 325-500 GHz band have been designed, microfabricated, and characterized. Based on these results, an integrated 600 GHz silicon micromachined Radiometer-On-a-Chip (ROC) has been demonstrated for the first time. It reduced in mass by an order of magnitude compared to the conventional metal machining.

## INTRODUCTION

There is an increasing interest in the millimeter and submillimeter wave frequency range for various applications such as compact range radar, terahertz imaging, and the space [1-2]. The frequency bands for these applications are in the range of 300 GHz to 3 THz corresponding to a wavelength of 1 mm to 100  $\mu\text{m}$  which silicon micromachining can contribute significantly. At submillimeter wave frequency range, the hollow waveguide has been used due to the low loss, and manufactured by conventional milling and drilling machines. However, at frequencies above 500 GHz, waveguides become so small (less than 0.3 by 0.15 mm) that conventional machining technique becomes extremely difficult, expensive, and/or impossible to manufacture. Thus, silicon micromachining technique have been attempted to make passive components below 100 GHz. [3]. Silicon micromachining technique is capable of achieving micron feature size with excellent process control such as high aspect-ratio, uniformity, and surface quality. While there have been several demonstrations of waveguide circuits fabricated with silicon micromachining and other techniques, few if any of these circuits have been subjected to any significant electrical testing [3-4]. In this paper, we have demonstrated THz passive components such as silicon washer, waveguide blocks for W-band amplifiers, and waveguides for the 325-500 GHz band, and applied it to 600 GHz ROC for the first time ever.

## IMPLEMENTATION AND RESULTS

A common hurdle to date to test these components has been the eventual interface of the Si pieces with the metallic waveguide. We have developed a silicon washer where the surface of the Si wafer is used to make the Si-metal interface. It showed the same behavior as metal washer (Figure 1).

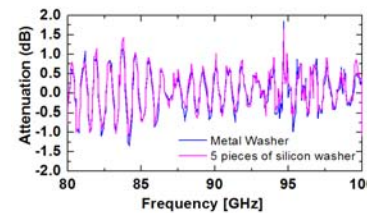
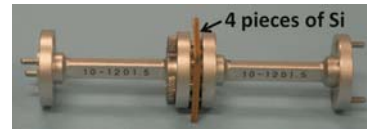


Figure 1. Measured attenuation data plot of both 2.5 mm-thick metal and 2.5 mm-thick silicon washers. Si washer is composed of 4 pieces of wafers. It shows almost identical behavior.

Subsequently, we have designed and microfabricated a silicon based W-band (75-110 GHz) power amplifier module (Figure 2). This circuit is based on a stack of four Si wafers and provides the standard UG-387 flange for interface to metallic waveguides. The performance of the silicon block is similar to a block fabricated using conventional metal machining (Figure 3).

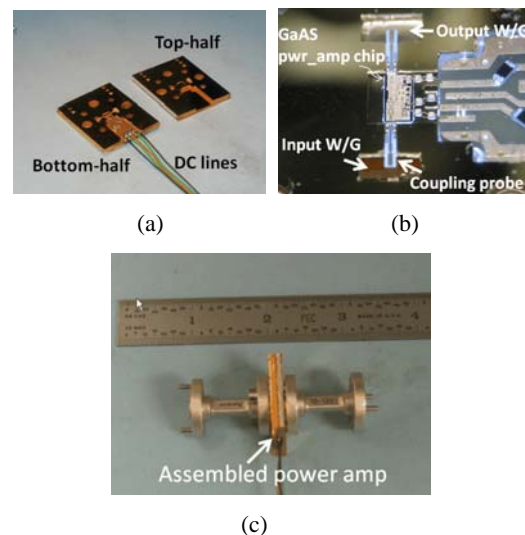


Figure 2. (a) View of top and bottom half of the silicon blocks. (b) It shows the GaAs power amplifier sitting on the channel in silicon micromachined waveguide. (c) Photograph of assembled GaAs power amplifier using silicon micromachined waveguide block.

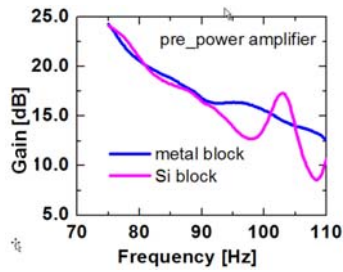


Figure 3. Measured data plot of GaAs pre-power amplifiers assembled in both metal and silicon blocks. It shows similar behavior.

The pre-power amplifier assembled in metal module and the power amplifier assembled in silicon module are connected in a cascade (Figure 4). We have demonstrated over 140 mW at 94 GHz from the cascaded power amplifiers (Figure 4).

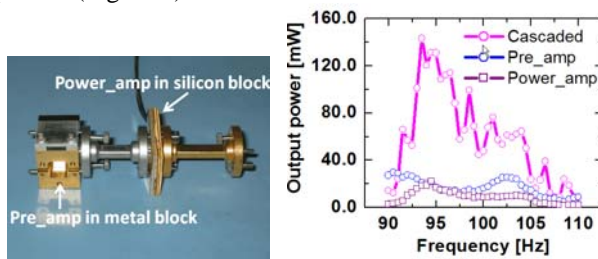


Figure 4. (left) Photograph of cascaded pre-amplifier and power amplifier (right) Measured output power of cascaded power amplifiers. Over 140 mW has been achieved.

Furthermore, we have developed silicon micromachined waveguide components in WR-2.2 (325-500 GHz) band (Figure 5). We used a 40mm straight section of waveguide with two two-step H-plane bends bringing the waveguide flanges on top surface of the silicon. We measured approximately 5-6 dB of loss at 350 GHz for the testing fixture (Figure 5). These results are consistent with theoretical simulations and demonstrate that this approach can be used for building passive THz components.

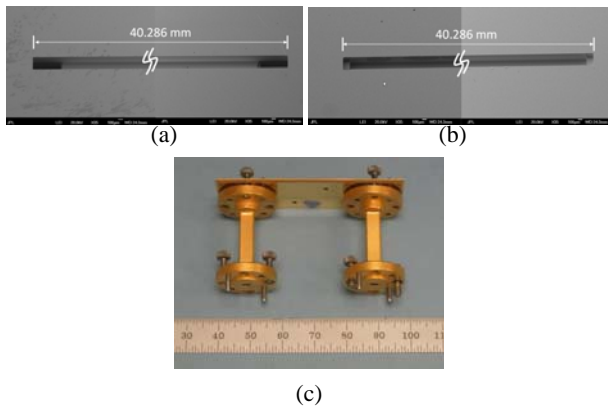


Figure 5. SEM images of 325-500 GHz waveguide. (a) bottom half of Si waveguide (b) top half of Si waveguide. (c) assembled waveguide

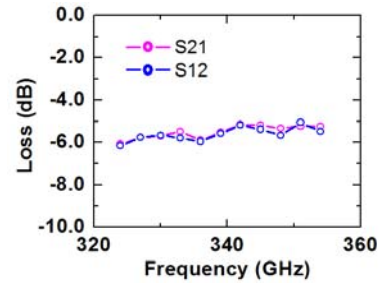


Figure 6. Measured data plot of 325-500 GHz waveguide block. The loss is about 5-6 dB according to HFSS simulation. It matches the measurement results.

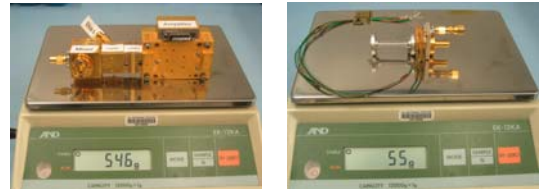


Figure 7. (a) conventional machined 600 GHz receiver (b) silicon micromachined 600 GHz receiver. It reduces an order of magnitude in weight.

Finally, we have applied silicon micromachining techniques to build a 600 GHz integrated heterodyne receiver. Double Side Band (BDS) receiver noise temperature of 4200 K and 13 dB conversion losses have been measured at 540 GHz. It dramatically reduced both mass and size (Figure 7).

## CONCLUSIONS

This is the very first demonstration of a novel receiver using silicon micromachining techniques. This architecture will open the new door for the development of large arrays of receivers in the sub-millimeter wave range.

## ACKNOWLEDGEMENT

The research described in this paper was carried out by the Jet propulsion Laboratory, California Institute of Technology under a contract with the National Aeronautics and Space Administration.

## REFERENCES

- [1] P. H. Siegel "THz technology," IEEE Trans. Microw. Theory Tech., 50, 3 (2002)
- [2] Peter de Maagt, Janet Charlton, "Terahertz Space Applications and Technology," J. IEEE MTT-S (2005)
- [3] J. P. Becker, J. R. East, and L. P. B. Katehi, "Performance of Silicon Micromachined Waveguide at W-band," Electron. Lett., vol. 38, p. 638 (2002)
- [4] G. Chattopadhyay, J. Ward, H. Manohara, R. Toda, and R. Lin, "Silicon Micromachined Components at Terahertz Frequencies for Astrophysics and Planetary Applications," ISSIT (2008)

## CONTACT

\*Choonsup Lee,  
tel: +1-818-392-7140; [Choonsup.Lee@JPL.NASA.GOV](mailto:Choonsup.Lee@JPL.NASA.GOV)

# A MONOLITHIC MICRO DEVICE FOR GLUCOSE-RESPONSIVE INSULIN DELIVERY

Jian Chen<sup>1\*</sup>, Claudia R. Gordijo<sup>2\*</sup>, Michael Chu<sup>2</sup>, Xiao Yu Wu<sup>2\*\*</sup> and Yu Sun<sup>1\*\*</sup>

<sup>1</sup>Institute of Biomaterials and Biomedical Engineering, University of Toronto, Toronto, Canada

<sup>2</sup>Department of Pharmaceutical Sciences, University of Toronto, Toronto, Canada

## ABSTRACT

This paper presents a glucose-responsive device capable of modulating insulin diffusion rates according to changes in environmental glucose levels. A new glucose-responsive composite membrane was developed by crosslinking an albumin-based membrane with a micropatterned PDMS backbone. The membrane was made glucose responsive by the chemical immobilization of glucose oxidase (GOx) and catalase (CAT) along with embedded pH-responsive hydrogel nanoparticles. The nanoparticles act as intelligent 'nano-valves' in response to the enzymatic oxidation of glucose. The membrane responsiveness to glucose concentration was determined by testing the diffusion rates of bovine insulin at alternating glucose levels relevant to diabetic patients. Insulin diffusion across the membrane increases with increasing glucose concentration in the medium, and decreases when glucose is returned to lower levels. The glucose regulated profile of insulin

release was also measured on proof-of-concept devices made with PDMS drug reservoirs and integrated glucose-responsive membrane.

## INTRODUCTION

Diabetes is a chronic disease that occurs either when the pancreas does not produce enough insulin or when the body cannot effectively use the insulin it produces. The most effective approach for diabetes management would be a closed-loop insulin delivery system [1]. In this system, a sensing component detects changes of glucose level and produces feedback signals for a releasing component. One limiting factor such a delivery system is the unavailability of a continuous glucose sensor capable of performing fast, accurate measurements with relatively long-term stability for *in vivo* conditions [2], despite the tremendous efforts in glucose

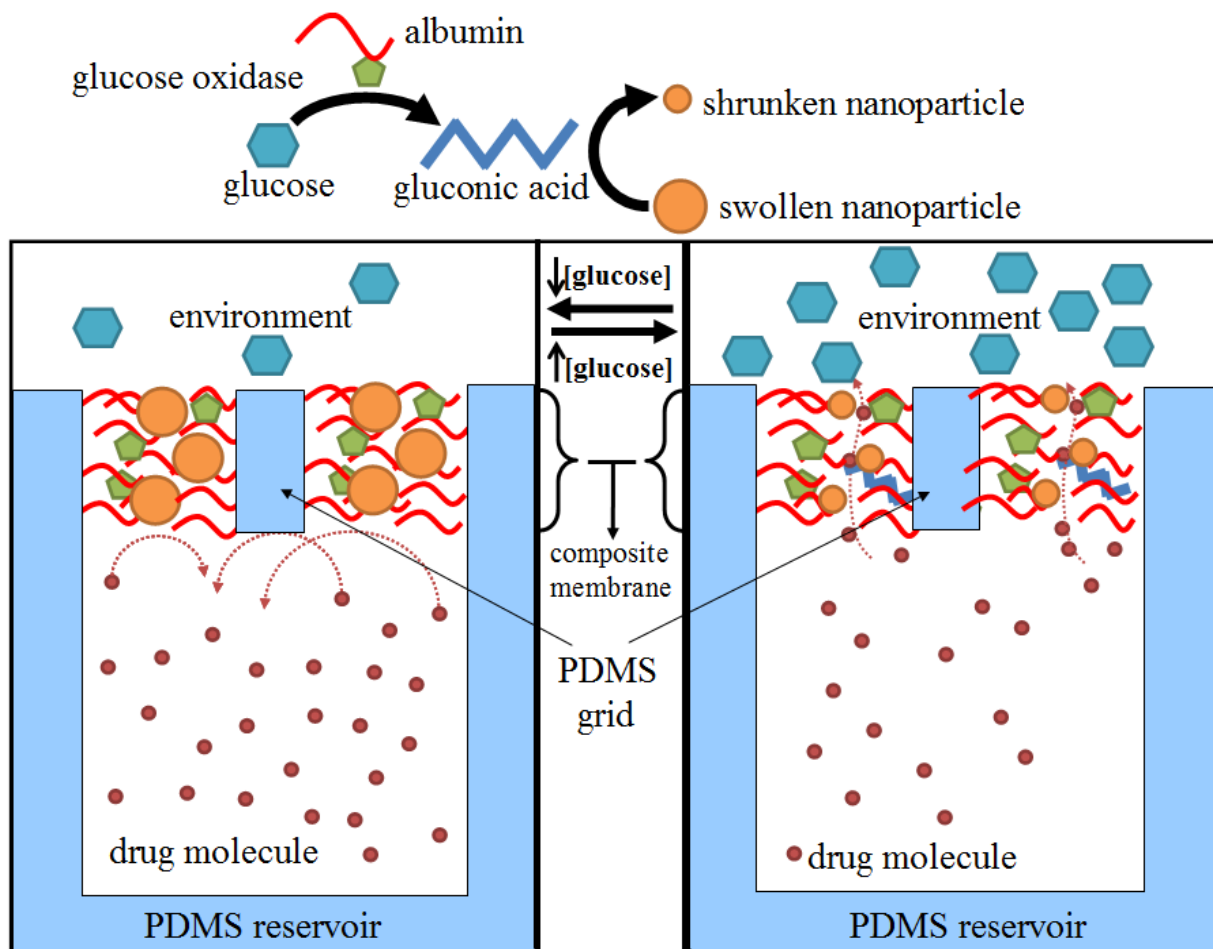


Figure 1: A PDMS drug reservoir holds drug molecules. A layer of PDMS grids on device top provides physical support for the albumin-based composite membrane. Within membrane, enzymes (e.g., glucose oxidase) are chemically crosslinked with the base membrane composed of albumin macromolecules. The embedded hydrogel nanoparticles detect local pH changes caused by gluconic acid resulting from the oxidation of glucose, acting as intelligent nanovalves. Corresponding volumetric swelling and shrinking of the hydrogel nanoparticles in response to environmental glucose values control drug-release rates.

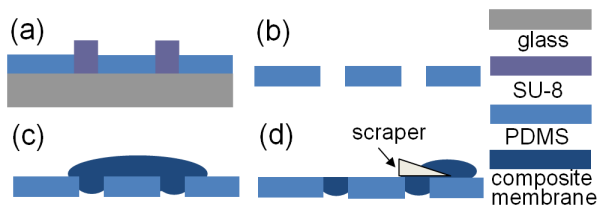


Figure 2: (a) and (b) Standard soft lithography to form PDMS grids. (c) Membrane solution is poured onto the PDMS grids. (d) After removing excess membrane solution using a scraper, the glucose-responsive membrane with PDMS grids as backbone is formed.

sensor development from industrial and academic communities.

Glucose-responsive hydrogels (e.g., combination of enzyme GOx with pH-responsive hydrogels) have been widely applied in the development of self-regulated closed-loop insulin delivery systems [3]. Since transient behavior of the hydrogel is limited by the diffusion of glucose into the hydrogel matrix and by the absorption and expulsion of solvent, glucose-responsive hydrogels at smaller scales have been developed for controlled drug delivery with shorter response times [4,5].

Previously, controlled release of drugs was achieved by microfabricated devices via electrochemical dissolution, electrothermal activation or chemical degradation approaches [6-8]. Despite the on-demand drug release capability, these implantable drug-delivery micro devices are not able to self-regulate the drug delivery rates in response to local micro-environmental signals, such as pH and glucose changes.

We previously demonstrated proof-of-principle glucose-responsive insulin release through a composite membrane consisting of a hydrophobic base membrane containing embedded pH-responsive hydrogel nanoparticles, GOx, and CAT [5]. We recently developed a new glucose-responsive membrane by introducing bio-inorganic nanohybrid composite and chemical crosslinking of albumin with the enzymes [9]. This new nanohybrid material has been successfully applied as a glucose-responsive plug in a small prototype implantable device for a controlled insulin delivery system [10]. However, owing to the soft nature of this membrane, the material would not be suitable for use as a free membrane in relatively large areas.

In the present work, we propose (1) the application of micro patterned PDMS grids to support the albumin-based composite membrane to enhance its mechanical strength; and (2) the design of a monolithic glucose-responsive drug-delivery micro device by integrating the composite membrane and a micro drug reservoir.

## DESIGN AND FABRICATION

### General considerations about the device's mechanism

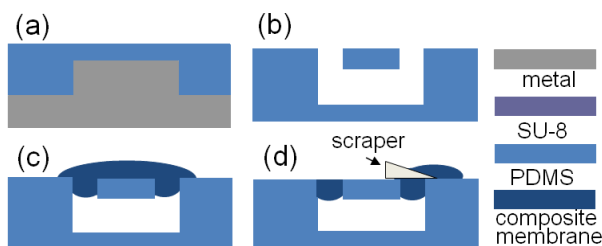


Figure 3: Microfabrication steps for forming glucose-responsive micro devices with enhanced mechanical strength

As shown schematically in Fig. 1, a PDMS drug reservoir and a layer of PDMS grid provided physical support for the composite membrane. In this composite membrane, the enzymes GOx and CAT are directly crosslinked with the albumin macromolecules, forming the base membrane. The embedded hydrogel nanoparticles detect and respond to local pH changes caused by gluconic acid resulted from the oxidation of glucose by GOx, acting as intelligent nanovalves. Corresponding volumetric swelling and shrinking behaviors of the hydrogel nanoparticles controls the porosity of the membrane, leading to lower or higher drug release rates according to the glucose concentration in the medium.

### Preparation of glucose-responsive composite membranes with PDMS grid backbone

To fabricate glucose-responsive membranes with a PDMS backbone, SU-8 pillars of  $500 \times 500 \times 250 \mu\text{m}^3$  were formed via photolithography (Fig. 2(a)), as a mold master by spinning SU-8 2100 at 1000 RPM. PDMS was spin coated on the SU-8 mold master at 1000 RPM, and fully cured PDMS membrane with a thickness of  $150 \mu\text{m}$  was peeled off from the substrate, producing a PDMS grid (Fig. 2(b)).

The surface of the PDMS grid was activated with oxygen plasma, prior to the application of the glucose-responsive membrane solution on grids' surface. The glucose-responsive albumin-based membrane was prepared as previously described [10] by the crosslink of BSA and  $\text{MnO}_2$  nanoparticles (10 wt%) with glutaraldehyde in the presence of the pH-responsive hydrogel nanoparticles (30 wt%) and the enzymes GOx (5 wt%) and CAT (1.6 wt%).

In contrast to our previous work where the membrane was allowed to crosslink on a glass surface, we apply a homogenous mixture of nanoparticles, enzymes, crosslinker and albumin in aqueous solution onto the PDMS grid after surface activation (Fig. 2 (c)). After removing the excess of membrane solution from the top of the grids, the remaining solution between the grids continues to crosslink, forming a glucose-responsive membrane strengthened by the PDMS backbone (Fig. 2(d)).

### Fabrication of glucose-responsive micro devices

To fabricate glucose-responsive micro devices, firstly a PDMS reservoir was made via standard soft lithography using a metal mold master with a thickness of 2 mm (Fig. 3(a)). After the PDMS drug reservoir was peeled off from the mold master, the PDMS grid described earlier was bonded with the drug reservoir via a thin layer of pre-cured PDMS as an adhesive layer (Fig. 3 (b)). The mixture of the composite membrane solution was then cast on the PDMS grid as described in the previous section (Fig. 3 (c) and (d)).

Fig. 4(a) shows a 3-D model of the device. Pictures of the prototype devices are shown in Fig.4 (b). The drug reservoirs were constructed with PDMS due to its mechanical stability, the feasibility of precise patterning using microfabrication, and its

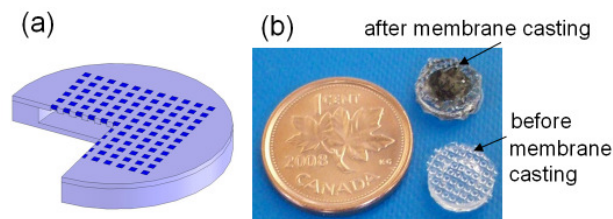


Figure 4: (a) 3D model of the device. (b) Prototypes of fabricated glucose-responsive micro devices.

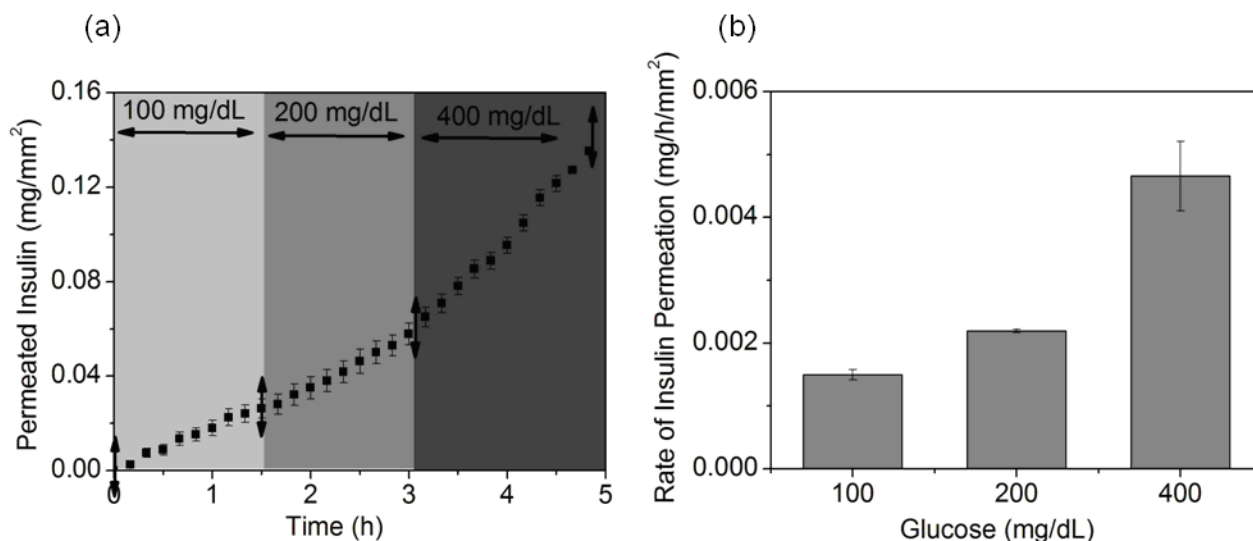


Figure 5: Glucose-responsive permeation of insulin through microstructured membranes ( $n=3$ ) with integrated PDMS backbone. (a) Profile of insulin permeated across the membrane in response to changes of step-wise glucose concentration (100, 200, and 400 mg/dL, respectively). (b) Permeability of insulin as a function of glucose concentration calculated from the slopes of the curves. Errors bars represent standard deviation.

short-term biocompatibility. Other biocompatible materials such as PEVA, poly(ethylene-co-vinyl acetate) are also viable options. Bovine insulin solution (10 mg/mL in HEPES buffer,  $M_w$  5808) was used to fill the devices. Insulin filling and refilling was conducted through the backside of the PDMS reservoir with a small-gauge syringe needle, utilizing the self-sealing property of PDMS.

## EXPERIMENTAL RESULTS

### Insulin permeation testing of glucose-responsive membranes

The permeation of insulin ( $P_i$ ) through the membrane was determined as a function of time and glucose concentration using a horizontal side-by-side diffusion cell system at controlled temperature (37°C) as we previously described [10]. Briefly, the membrane was placed between two cells: a donor cell containing insulin in pH 7.4 PBS buffer (insulin 2 mg/mL, phosphate 10 mM, NaCl 0.15M, Pluronic F-68 0.02 mM and glucose 100 mg/dL) and a receptor cell filled with the same solution but without insulin (release medium). After 1.5 h and 3h the glucose concentration in the cells was increased to 200 mg/dL and 400 mg/dL, respectively, by adding aliquots of highly concentrated glucose solution (20 g/dL). During the course of the experiment the release medium was continually pumped through a UV-flow cell, and the insulin permeation was determined by measuring insulin absorbance at 10 min intervals at  $\lambda = 276$  nm using an UV spectrophotometer. The rate of insulin permeation was determined by calculating the slope of the curves. Fig. 5 shows a representative set of permeability testing data, which demonstrates the glucose responsiveness of the composite membrane. As shown in the figure, when the glucose concentration in the medium was increased from normal (100 mg/dL) to hyperglycemic levels (200 - 400 mg/dL) the insulin permeation rate increased from 0.0015 mg/h/mm<sup>2</sup> to 0.0022 mg/h/mm<sup>2</sup> and 0.0046 mg/h/mm<sup>2</sup>, respectively (1.5-fold and 3.1-fold increase in insulin permeation, respectively, as determined by the relative insulin permeation rates  $P_{1-200}/P_{1-100}$  and  $P_{1-400}/P_{1-100}$ ).

### Insulin release testing of glucose-responsive devices

Insulin release from the microdevices was measured as a function of time and glucose concentration in pH 7.4 PBS buffer

containing Pluronic F-68 (0.02 mM), at 37°C. Microdevices filled with bovine insulin (solution 10 mg/mL) were individually placed in vials containing 5 mL of 100 mg/dL glucose in the PBS medium. Vials were sealed and kept under constant mixing in a mini blot mixer. No leakage of insulin via the interface between composite membranes and PDMS drug reservoirs was observed in the *in vitro* insulin release tests of the devices. After two hours, glucose concentration was increased from 100 mg/dL (normal glucose level) to 300 mg/dL (hyperglycemic glucose level). The same procedure was repeated for testing each device. The released insulin was determined by measuring insulin absorbance manually every 30 min at  $\lambda = 276$  nm using what using the UV spectrophotometer. The rate of insulin release was determined by calculating the slope of the curves.

Fig. 6 shows insulin release profiles of two-cycle tests for four microdevices. A 2.4-fold increase in the insulin release rate was observed when the glucose concentration was increased to hyperglycemic levels (from 100 mg/dL to 300 mg/dL). Additionally, the insulin release rate decreased to the initial rate ( $\sim 0.0030$  mg/h/mm<sup>2</sup>) when the glucose concentration was decreased to the normal level 100 mg/dL in the second cycle. This behavior demonstrated the device's capability for regulated release.

## CONCLUSION

This paper demonstrated a new type of monolithic glucose-responsive drug-delivery device. The microdevices integrated glucose-responsive composite membranes with PDMS backbones in which pH-responsive nanoparticles were embedded and glucose oxidase was chemically crosslinked. Diffusion testing demonstrated the capability of these devices for glucose-responsive insulin release, with an increase in release rates in response to increasing glucose levels. This device concept may serve as a platform technology for intelligent drug delivery in response to environmental glucose variations. Further work will continue to optimize and fine tune the composite membrane parameters as well as the quantification of insulin stability and delivery kinetics *in vitro* and *in vivo*.



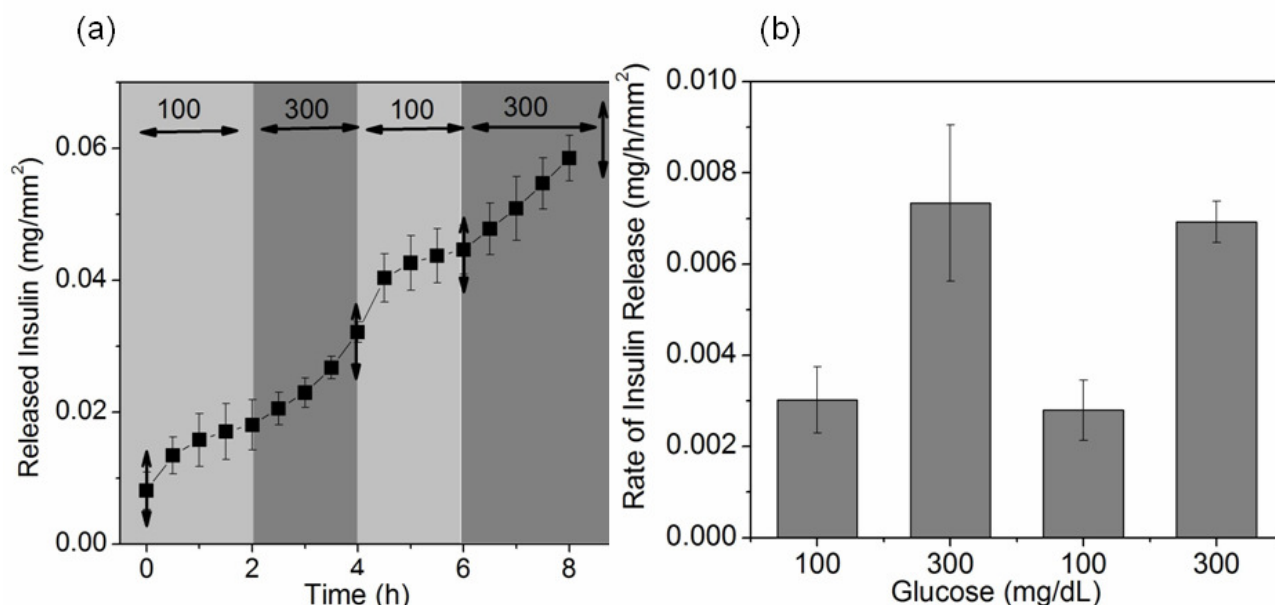


Figure 6: (a) Profile of insulin released from micro devices in response to changes in glucose concentration in two alternated cycles ( $n=4$ ). Glucose concentration was alternated between 100 mg/dL and 300 mg/dL to simulate changes in blood glucose levels of diabetic patients (normal and hyperglycemic levels, respectively). (b) Insulin release rates of the micro devices as a function of glucose concentration. Error bars represent standard deviation.

## REFERENCES

- [1] M.Shichiri et al., "Enhanced Simplified Glucose Sensors Long-term Clinical Application of Wearable Artificial Endocrine Pancreas", *Artificial Organs*, 22, 32 (1998).
- [2] R. Hovorka, "Continuous Glucose Monitoring and Closed-loop Systems", *Diabetic Medicine*, 23, 1 (2006).
- [3] E.Renard et al., "Closed Loop Insulin Delivery Using Implanted Insulin Pumps and Sensors in Type 1 Diabetic Patients", *Diabetes Research and Clinical Practice*, 74, 173 (2006).
- [4] R. Siegel, B. Ziaie et al., "A Hydrogel-Actuated Environmentally Sensitive Microvalve for Active Flow Control", *J. Microelectromechanical System*, 12, 613 (2003).
- [5] K. Zhang, X.Y.Wu, "Modulated Insulin Permeation Across a Glucose-sensitive Polymeric Composite Membrane", *J. Control Release*, 80, 169 (2002).
- [6] R. Langer et al., *Nature*, "A Controlled-release Microchip", *Nature*, 397, 335 (1999).
- [7] J. Prescott et al., "Chronic, Programmed Polypeptide Delivery from an Implanted, Multi-reservoir Microchip Device", *Nature Biotechnology*, 24, 437 (2006).
- [8] R. Langer et al., "Multi-pulse Drug Delivery from a Resorbable Polymeric Microchip Device", *Nature Material*, 2, 767 (2003).
- [9] C.R. Gordijo, A.J. Shuhendler, X.Y. Wu, "Glucose-responsive Bio-inorganic Nanohybrid Membrane for Self-regulated Insulin Release", *Advanced Functional Materials*, In press (2010).
- [10] C.R.Gordijo, K.Koulaijan, A.Giacca, X. Y. Wu, "Closed-Loop Insulin Delivery Device: Fabrication, In Vitro and In Vivo Evaluation of Self-Regulated Insulin Release", *Diabetes Technology Meeting, San Francisco, USA (2009)*, pp A188.

## ACKNOWLEDGEMENTS

This work was supported by a NSERC-CIHR Collaborative Health Research Grant (CHRP#482996).

### \* THOSE AUTHORS CONTRIBUTED EQUALLY \*\*CO-CORRESPONDING AUTHORS:

Xiao Yu Wu, Leslie Dan Faculty of Pharmacy, University of Toronto, 144 College Street, Toronto, Canada M5S 3M2. Tel: 1-416-978-5272; Email:sxy.wu@utoronto.ca

Yu Sun, Institute of Biomaterials and Biomedical Engineering, University of Toronto, 5 King's College Road, Toronto, Canada M5S 3G8. Tel: 1-416-946-0549; E-mail: sun@mie.utoronto.ca

# MANDUCA SEXTA OLFACTORY NEURAL INTERFACE

C.J. Shen<sup>1,2\*</sup>, A. Ramkumar<sup>1,2</sup>, A. Lal<sup>1,2</sup>, and R.F. Gilmour, Jr.<sup>2,3</sup>

<sup>1</sup>SonicMEMS Laboratory, School of Electrical and Computer Engineering

<sup>2</sup>Department of Biomedical Engineering

<sup>3</sup>Department of Biomedical Sciences

Cornell University, Ithaca, NY, USA

## ABSTRACT

We present wireless transmission of neural signals from an insect based hybrid bio-electromechanical sensor. Previous work demonstrated the feasibility of creating an insect-based olfactory sensor with integration of a microfabricated silicon microprobe. By expanding this system to include wireless transmission, we can move towards taking full advantage of tapping into an insect's olfactory system to serve as a gas sensor. Moth species have one of the most sensitive gas sensors available with parts-per-quadrillion sensitivity to pheromones. A 0.35- $\mu\text{m}$  technology application specific integrated circuit is integrated with a silicon microprobe neural interface. The chip provides a 40-dB amplification over a 10 kHz bandwidth and wirelessly transmits the input signals with a voltage controlled oscillator. The microprobe sensor, with a weight of  $\sim 80$  mg can be integrated with the hawk moth *Manduca sexta*, using Early Metamorphosis Insertion Technology (EMIT). The moth is able to emerge successfully with the microprobe intact, demonstrating a pathway towards a tetherless hybrid flying insect gas sensor.

## INTRODUCTION

Typical olfactory sensors function by monitoring a change in a given sensor device property (mass, strain, resistance, etc.) as odorant molecules adhere to the sensor. Strain based microcantilever detectors are able to detect odorants down to parts per trillion, while chemiresistive sensors are able to detect with very low powers of 0.1-1 mW [1, 2]. In this work, we draw upon a natural insect olfactory system which is capable of detecting odorants down to parts per quadrillion sensitivities [3]. By interfacing to this system and detecting neural responses to given

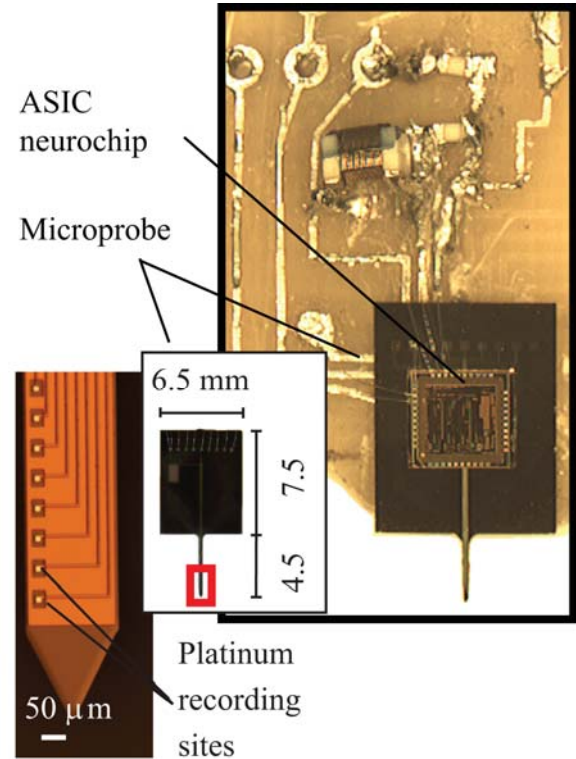


Figure 2: Prototype integrated ASIC neurochip and microprobe. The probe and ASIC were integrated with a custom printed circuit board, and surface mount inductors, capacitors, and resistors were used for the Colpitts oscillator.



Airborne System Component	Weight
6-mil thick polyimide PCB	32 mg
ASIC neurochip	13 mg
Microprobe	42 mg
<b>TOTAL</b>	<b>87 mg</b>

Figure 1: Photograph of silicon microprobe, without metal lines, inserted into *Manduca sexta* pupae, and insect emergence to adult stage with probe intact. The table shows the estimated weight for an airborne interface system without batteries.

odorants, this opens up the possibility of a low power, high system sensitivity environmental gas detector. Previous work presented at MEMS 2009 demonstrated the feasibility of an insect sensor with a silicon microprobe inserted in the pupal brain of the moth *Manduca sexta* [4]. By inserting the probe early during the pupal stage with Early Metamorphosis Insertion Technology (EMIT), we can achieve better mechanical coupling with the tissue than if the probe were inserted later in the adult stage [5]. The inserted silicon microprobe, with outputs fed to an external amplifier, captured extracellular neural signals in the antennal lobe stimulated in response to specific odors incident upon the insect's antenna. In this work, we demonstrate an extension of the previous work by incorporating a specially designed application specific integrated circuit (ASIC) consisting of an amplifier and a radio that can be integrated on an airborne moth. Previous work from our group has demonstrated using muscle embedded microfabricated electrodes for flight control [6]. By incorporating neural sensing of insect responses to various gases at very high sensitivity with the technology for flight control in the future, we demonstrate a pathway to a low-cost wireless airborne neural interface to serve as a gas sensor node.

## TETHERLESS NEURAL INTERFACE SYSTEM

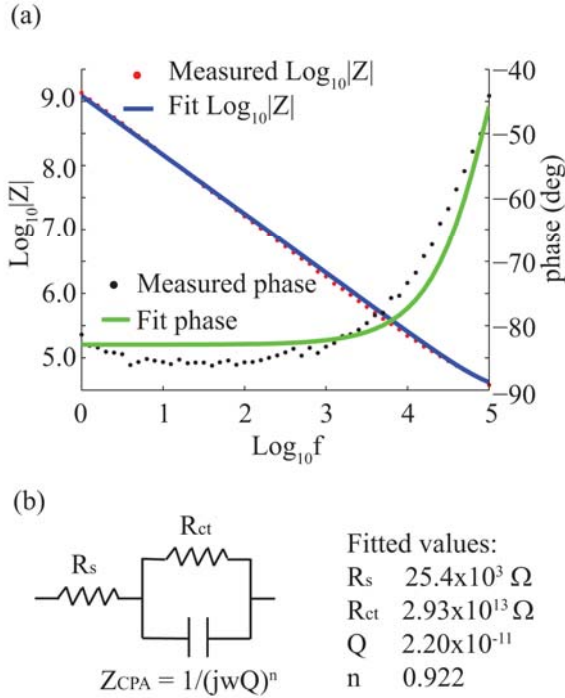


Figure 3: Equivalent circuit parameters of silicon microfabricated probe electrode-electrolyte interface. The interface consists of an interfacial capacitance  $Z_{CPA}$  from the double layer, a charge transfer resistance  $R_{CT}$  that serves as a DC path, and the spreading resistance  $R_s$ . The electrode impedance was also measured with electrochemical impedance spectroscopy in (a) and the fit values to the equivalent circuit are shown in (b).

### Integration: Survivability, Weight, and Power Considerations

Using Early Metamorphosis Insertion Technology (EMIT), polyimide-reinforced silicon microprobes were first inserted into pupal stage *Manduca sexta* to confirm the survivability of insects. The weight of the silicon microprobe and polyimide reinforcement was approximately 80 mg. As shown in Fig. 1, the insects were able to successfully emerge to adulthood and the probes remained intact. For a functional airborne system, the components would compose of the silicon microprobe, the newly developed ASIC neurochip, and a thin flexible polyimide printed circuit board to form electrical connections. The estimated weight of such an airborne wireless system without batteries would be 87 mg. Studies on *Manduca sexta* indicate their payload capacity is  $\sim 1$  g indicating the need for integration with light battery power and/or power harvesting from the insect. A recent paper has shown the ability to scavenge power of 1 mW from moth flight vibrations using a magnet in a wire coil [7]. Additionally, higher payloads may be possible with larger moths. Based on these considerations, it is possible to realize an insect behaving in its natural environment while providing wireless transmission of gathered sensor data. This could potentially include visual cues as well as olfactory cues, as there are specific neurons which relay signals for looming or receding objects, and for lateral and vertical motion [8, 9]. In comparison, micro-aerial vehicles (MAVs) with corresponding capabilities would require much higher power consumption with feedback control systems for avoiding obstacles and guiding flight, as well as on board sensors to capture visual and olfactory information from the environment.

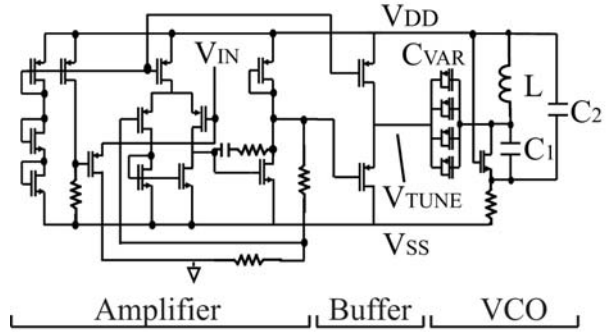


Figure 4: Schematic of ASIC neurochip. The circuit includes a 40 dB amplifying stage, a buffer stage, and a voltage controlled oscillator (VCO). The VCO components  $L$ ,  $C_1$ , and  $C_2$  are surface mount components.

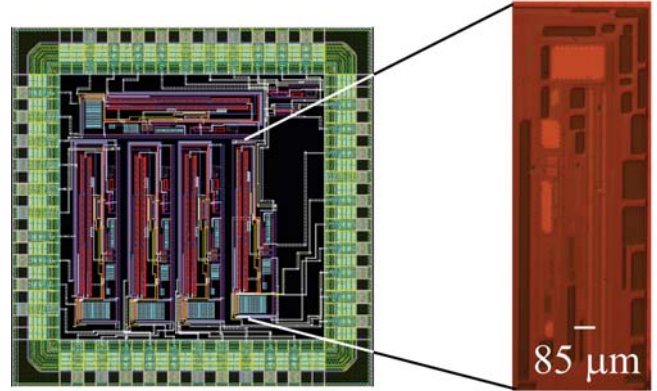


Figure 5: CADENCE layout and microphotograph of designed ASIC. The chip has four complete amplifier, buffer, and VCO channels and one set of individual channel components for testing.

### Silicon Microprobe Neural Interface

The neural interface is composed of a microfabricated neural probe, as shown in Fig. 2. This probe has platinum lines to ensure biocompatibility, and an insulating material of silicon nitride. The equivalent circuit parameters of the electrode-electrolyte interface including the interfacial capacitance  $Z_{CPA}$ , the charge transfer resistance,  $R_{CT}$ , and the spreading resistance,  $R_s$ , are shown in Fig. 3, as well as the measured electrochemical impedance spectroscopy data for the interface.

### ASIC Neurochip Design and Measured Performance

An integrated circuit was designed in AMS 0.35- $\mu\text{m}$  technology with an amplifier and voltage controlled oscillator (VCO). This circuit is designed to interface with the microfabricated neural probe for wireless transmission of the captured signals. The schematic of the chip is shown in Fig. 4. The neurochip consists of an amplifier and radio and occupies a 9 mm<sup>2</sup> design area for four fully assembled channels, plus one channel of individual test components. The CADENCE layout and a microphotograph of a single channel are shown in Fig. 5.

The amplifier is composed of a differential first stage followed by a common source stage to allow large output swings. The amplifier is maintained in resistive feedback to give a 40 dB gain over 10 kHz. The simulated phase margin is 104° and the simulated input referred noise is 7.47  $\mu\text{V}$ . The measured and simulated gain-frequency curves of the amplifier are shown in Fig. 6. Additionally, the chip incorporates a DC offset filtering component to remove DC potentials from metal-electrolyte half

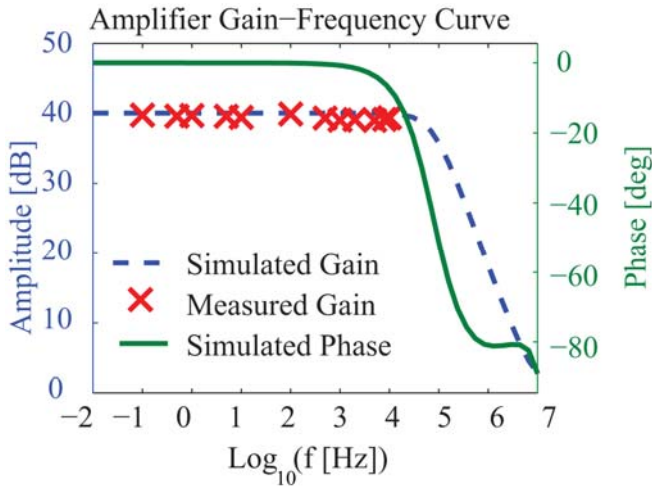


Figure 6: Simulated and measured amplifier performance. The amplifier has a 40 dB gain over a 10 kHz bandwidth, which is the expected bandwidth of interest for biological signals.

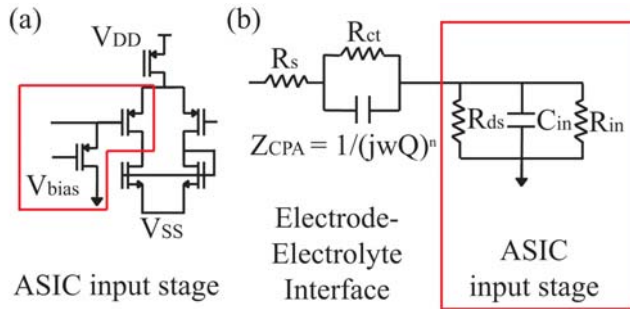


Figure 7: (a) Amplifier input stage used in combination with electrode-electrolyte interface to high pass filter incoming signals and remove DC offset (highlighted in box). (b) Equivalent circuit of electrode-electrolyte interface and amplifier input.

cell potentials that form spontaneously when metals are immersed in electrolytes. These potentials can be several hundred millivolts and would otherwise saturate the amplifier. The high pass filter incorporates a subthreshold transistor which serves as a megaohm resistance at the amplifier input [10]. In combination with the interfacial capacitance of the microfabricated probe, as shown in Fig. 7, this forms a high pass filter to remove DC offsets. It is designed for  $f_{3dB} = 12$  Hz. The buffer stage serves to isolate the amplifier and voltage controlled oscillator (VCO).

The VCO is designed using a Colpitts topology with an oscillation frequency as shown in Fig. 7. Since  $L$ ,  $C_1$ , and  $C_2$  are surface mount components, these can be used to easily adjust the carrier frequency of the VCO in the FM range 88-108 MHz. The variable capacitance  $C_{VAR}$  is adjusted by the input signal  $V_{TUNE}$  which modulates the capacitance over the MOSCAPs. The VCO stage simulated and measured tuning curves are shown in Fig. 8. The measured data is fit to a model which takes into account parasitic inductances and capacitances arising from the antenna and metal lines. Using a best-fit regression curve, the parasitic inductance is estimated to be  $10^{-13}$  H and the parasitic capacitance is 5.42 pF. These values are added as parasitic components and used to re-simulate the expected oscillation frequencies, as shown in Fig. 8. It is seen that the simulated and measured curves match well, within the +/- 5% error tolerance limits of the surface mount devices.

The ~100-MHz FM wave is fed to a 2-cm wire antenna, and

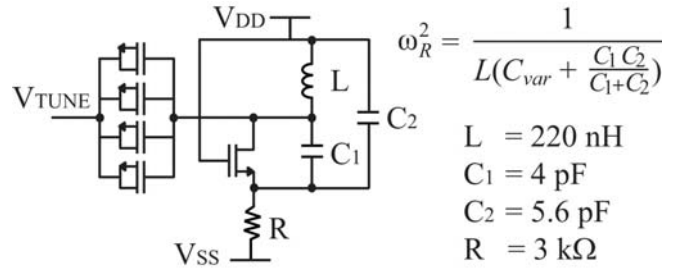


Figure 8: Schematic of voltage controlled oscillator with Colpitts topology. The ideal oscillation frequency, as well as surface mount components values used are listed above.

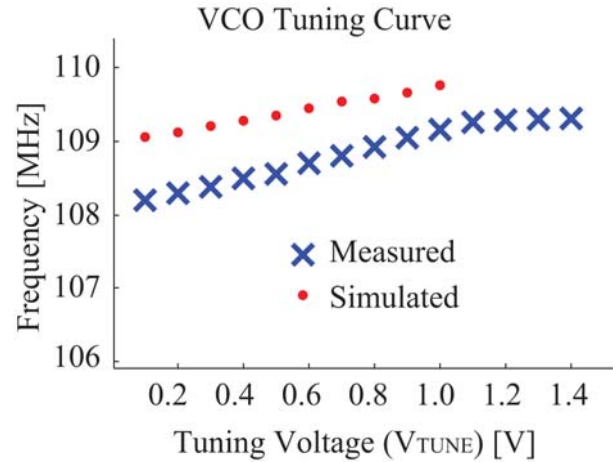


Figure 9: Simulated and measured voltage controlled oscillator (VCO) change in frequency for given tuning voltages.

signals can be detected at a range of 3-m, although a range of 100-m is possible with increased power consumption. For example, by increasing the gate-source voltage over the voltage controlled oscillator transistor, we can increase the  $g_m$  and improve oscillator gain, at the cost of consuming more current. The system uses +/- 1.5 V and is compatible with power harvester and flexible battery voltages [7, 11].

The ASIC was interfaced with the microfabricated silicon probe with a custom printed circuit board, as shown in Fig. 2. To characterize the VCO tunability when integrated with the microprobe, the probe was immersed in saline. An Ag/AgCl wire was used to feed a generated square wave from an Agilent 33250A function generator to the system. The VCO tunability was measured to be 150 kHz/mV input to the probe neurochip system.

## WIRELESS TRANSMISSION OF SIGNALS

### Transmission of Simulated ECG Pulses

To demonstrate wireless transmission of signals with the radio, an Agilent 33250A arbitrary function generator was first used to generate a 1.2 mVpp, 1-Hz electrocardiogram (ECG) signal. The signal was fed into insect saline with an Ag/AgCl electrode. A microfabricated probe interfaced with a radio chip was immersed in the saline, and a FM radio was used to receive and demodulate the signal. The audio output was fed into a National Instruments data acquisition card, and a custom LabVIEW program was used to record the data. The received waveform is shown in Fig. 10.

### Transmission of Potentials from Insect Brain

A late pupal stage male *Manduca sexta* insect was first chilled on ice to anesthetize it. A Pt wire was inserted in the insect's

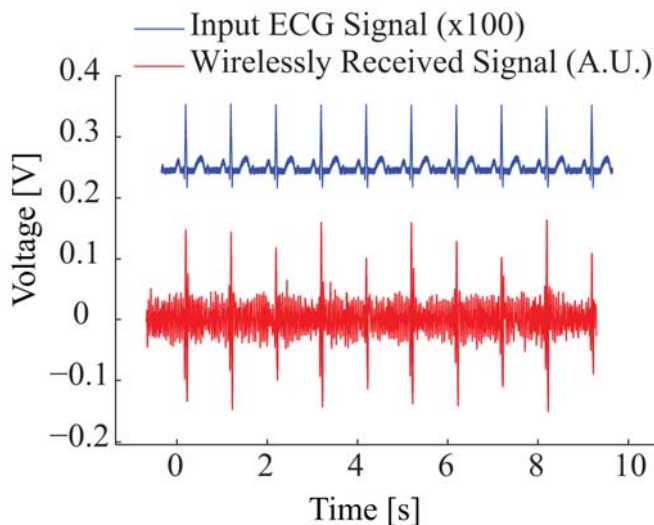


Figure 10: An 1-Hz ECG signal (top) was fed through an Ag/AgCl wire into saline. The microprobe was immersed in saline and outputs were wirelessly transmitted with the newly design neurochip. The signals were picked up with an FM receiver and demodulated, as shown in the bottom trace.

abdomen to serve as a ground. The microfabricated probe interfaced to the radio chip was inserted into the head of the insect, and first interfaced with an external Dagan Corp. amplifier. Insect neuronal responses to external stimuli of tobacco and air were recorded. The system was then switched to wirelessly transmit recorded pulses from the insect. The recorded signals are shown in Fig. 11.

## CONCLUSION

In this paper, we have demonstrated the incorporation of a newly designed radio chip with a microfabricated neural probe to serve as a neural interface sensor of insect responses to olfactory cues in the environment. This allows us to potentially tap into the parts-per-quadrillion olfactory sensitivity of insects. Future work and challenges include fully miniaturizing the system and integrating the system with sufficient power at a low enough weight to be carried by the moth during flight.

## ACKNOWLEDGEMENTS

The authors would like to thank members of the Boyce Thomson Institute for hawk-moth facilities and assistance. We would also like to thank DARPA-MTO for funding and the Cornell Nanofabrication Facility (CNF) at Cornell University for fabrication and microscopy facilities.

## REFERENCES

- [1] L.A. Pinnaduwege, et al. "A sensitive, handheld vapor sensor based on microcantilevers," *Review of Sci. Instruments*, 75(11): 4554-4557, 2004.
- [2] S. Maldonado, et al. "Detection of organic vapors and NH<sub>3</sub>(g) using thin-film carbon black-metallophthalocyanine composite chemiresistors," *Sensors and Act. B*, 134: 521-531, 2008.
- [3] R.L. Metcalf, "Ultramicrochemistry of Insect Semiochemicals," *Mikrochim. Acta*, 129: 167-180, 1998.

## Wirelessly Transmitted Extracellular Signals from Insect Brain

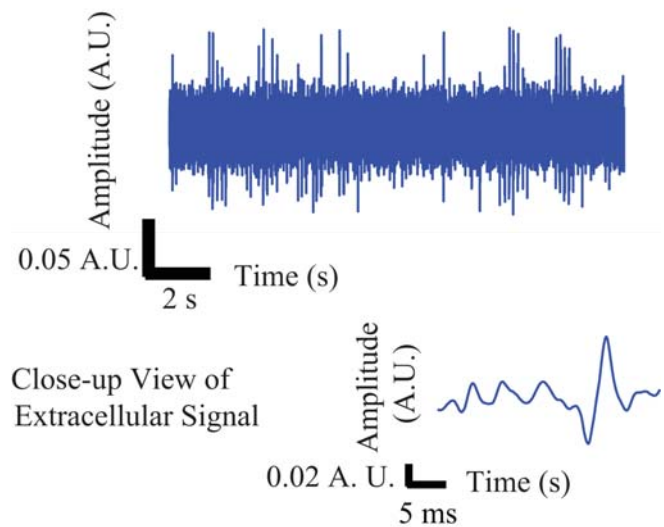


Figure 11: Wirelessly transmitted signals from coupled microprobe radio system inserted in *Manduca sexta* brain.

- [4] C.J. Shen, R. Gilmour, A. Lal, "Pupal-Stage Inserted Silicon Microprobe Neural Interface In Insects for Gas Sensing," *Proc. of IEEE 22<sup>nd</sup> Internat. Conference on MEMS*, Sorrento, Italy, Jan. 2009, pp. 336-339.
- [5] A. Paul, A. Bozkurt, J. Ewer, B. Blosssey, A. Lal, "Surgically implanted micro-platforms in *Manduca sexta* moths", in *2006 Solid State Sensor and Actuator Workshop*, Hilton Head Island, June 2006, pp. 209-211.
- [6] A. Bozkurt, R.F. Gilmour, Jr., and A. Lal, "Balloon-assisted flight of radio-controlled insect biobots," *IEEE Trans. Biomed. Eng.*, 56(9): 2304-7, 2009.
- [7] S. C. Chang, F.M. Yaul, et al. "Harvesting Energy from Moth Vibrations During Flight", *PowerMEMS*, Washington D.C., Dec. 2009.
- [8] M. Wicklein and N.J. Strausfield, "Organization and significance of neurons that detect change of visual depth in the hawk moth *Manduca sexta*", *J. Comp. Neuro.*, 424(2): 356-376, 2000.
- [9] J.J. Milde, "Tangential medulla neurons in the moth *Manduca sexta*: Structure and responses to optomotor stimuli," *J. of Comparative Physiology A*, 173: 783-799, 1993.
- [10] P. Mohseni, et al., "Wireless Multichannel Biopotential Recording Using an Integrated FM Telemetry Circuit," *IEEE Trans. on Neural Systems and Rehabilitation Engineering*, 13(3), pp. 263-271, 2005.
- [11] T. Reissman and E. Garcia, "Surgically Implanted Energy Harvesting Devices for Renewable Power Sources in Insect Cyborgs," *ASME Internat. Mechanical Engineering Congress and Exposition*, October 31 - November 6, 2008, Boston, MA.

## CONTACT

\*C.J. Shen, tel: +1-607-255-1815; cjs77@cornell.edu

# SENSING SINGLE CELL CONTRACTILITY UTILIZING MOIRE FRINGES

X. Zheng<sup>1</sup>, H. Surks<sup>2</sup>, and X. Zhang<sup>\*1</sup>

<sup>1</sup>Boston University, Boston, Massachusetts, USA

<sup>2</sup>Tufts Medical Center, Boston, Massachusetts, USA

## ABSTRACT

Abnormal vascular cell contractile performance is a hallmark of cardiovascular diseases. Conventional cell force measurement technique requires individually tracking the sensing units and complex computation efforts for further studying cell contractility. We developed instead a robust and simple compact optical moiré system that measures phase changes encoded in carrier moiré patterns generated from two layers of gratings. Cell mechanics study including cell contractile forces, stress and strain distributions during normal and abnormal cell contractions can thus be conveniently analyzed. The distinct signals from moiré patterns in longitudinal and transverse directions revealed abnormal cell mechanical contractility linked to cardiovascular disease.

## INTRODUCTION

The mechanical interaction of cells with their extracellular matrix (ECM) is fundamentally important for cell division, growth, phagocytosis, apoptosis and migration [1], [2]. Bidirectional chemical and mechanical signals between cells and their ECM result in the regulation of cellular processes and the remodeling of the extracellular environment. The mechanical interaction, presented as cell traction forces, is therefore a crucial factor in physiological processes such as development and wound healing. For example, the physiological regulation of vascular cell contraction is critical to the maintenance of normal vascular function. The regulation of cell function occurs as a result of the tension in the cytoskeleton and the distortion of the cells. Abnormal contraction forces distribution in vascular cells is an early indication of vascular diseases including hypertension, atherosclerosis and myocardial infarction. Any study of single vascular cells function requires a way to quantify mechanical forces in a precise, dynamic and reproducible manner with high fidelity and accuracy.

Many of the previous approaches for cell force mapping are not satisfactory since they require fixation, dehydration and induce undesirable external stimulation to the cells. As a result such approaches cannot make the cell force determination capable of revealing the contractile state of cells. Recently, micro and nano patterned polymeric substrates have been introduced for measuring cell traction forces [3]. These new methods introduce a local determination of the traction forces upon discretized adhesion areas between the cells and their underlying polymeric substrates. In these techniques the discrete displacement vectors are derived by tracking and monitoring deflections of each individual microstructure. Despite this, these methods require intensive computation and expertise to locate individual sensing units, track and derive their displacement fields. Moreover, with fixed numerical aperture of the objective lens, the deflection or motion of individual sensing unit is often in the range of sub-micrometers. As a result tracking such deflection or motion of each individual high-density micro structure is time-consuming and thus cannot meet the demands for real-time monitoring of cellular and subcellular behaviors.

We have previously demonstrated a method for cell traction force measurement based on optical moiré effect [4]. Moiré methods have been used extensively in engineering as diagnostic

tools to measure microscopic strain and stress because of their high sensitivity to spatial displacements and distortions within small structures. They have also been used in conventional lithography and soft lithography fabrications to determine the alignment state between periodic substrates. Inspired by this phenomena and its ability to measure in-plane displacement and distortion, we have reported that the magnification effects of 1-dimensional (1D) and 2-dimensional (2D) moiré patterns are capable of magnifying cells contraction forces. The employed interferometric moiré offers precise and high resolution moiré mapping. This technique takes the advantage of moiré magnification effect by calculating the moiré fringe distortions and map into the distortions of polymeric periodic substrate. The distortion of moiré fringes provides a magnified map of cell force distributions in whole field. The magnification factor of the optical moiré typically ranges from 2-20× by adjusting the relative angle between two coherent beams. The periodicity of the moiré pattern is determined by the intersecting angle of the two beams and the orientation of the periodic substrate. However, the reported system was limited for practical use due to the requirement for interference facilities. Optical alignment added difficulty for achieving on-chip compact moiré system for real time observation of cell contractility. In addition, the method used for retrieving force distribution was based on geometric fringe centering approach which prevents further automation of the system into laboratory use.

## THEORY

Interferometric moiré offers precise and high resolution moiré mapping. We have demonstrated that by illuminating the periodic substrate with two symmetric light beams [Figure. 1(a)], the moiré pattern can be generated by two symmetrical beams diffracted by periodic substrate. The periodicity of the moiré pattern is determined by intersecting angle of the two beams and the orientation of the periodic substrate, i.e.,

$$\frac{1}{d_m} \exp(-j\varphi) = \frac{2 \sin \alpha}{\lambda} \exp(-j\psi) - \frac{1}{d} \quad (1)$$

Incident angle  $\alpha$  and  $\psi$  which is the orientation of the polymeric periodic substrate, are two adjustable parameters that determine the orientation and spatial periodicity of the moiré patterns. The symmetrical arrangement of the two incident beams ensured that the moiré pattern is only sensitive to in-plane deformation on gratings whereas out-of-plane distortions carried by two beams are canceled out by being diffracted through the substrate. If replacing one plane wave with a thin periodic substrate with the same period, by adjusting the relative orientation of the two substrates, moiré patterns can be generated by the diffraction of the coherent wave through two separated layers of the periodic substrates. Description of such compact moiré pattern generation system is elaborated as follows.

The two grating patterns  $T_1(x)$ ,  $T_2(x)$  (with grating lines perpendicular to the x-axis), with spatial period  $d_1$  and  $d_2$  can be expressed in Fourier series [5]:

$$T_1(x) = \sum_{n=-\infty}^{+\infty} T_n \left( \exp \left( j \frac{2\pi}{d_1} (x \cos \theta_1 + y \sin \theta_1) \right) \right) \quad (2)$$

$$T_2(x) = \sum_{n=-\infty}^{+\infty} T_n \left( i n \frac{2\pi}{d_2} (x \cos \theta_2 + y \sin \theta_2) \right) \quad (3)$$

$\theta_1$ ,  $\theta_2$  are the absolute orientation of the two substrates with respect to the X axis and their relative orientation is denoted in the insert of Figure [1(b) and (c)], as  $\theta$ , namely:  $\theta = \theta_1 - \theta_2$ . For simplicity, let the two periodic substrates have the same spatial periodicity and their relative orientation is  $\theta$ . This assumes collimated illumination, i.e., a plane incoming wavefront. From far-field Fresnel Diffraction theory, the two grating patterns intercept [Figure 1(b)] to have a diffraction field which can be expressed as:

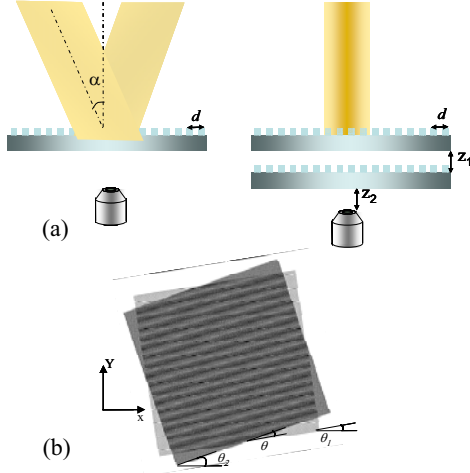


Figure 1: Representative unwrapped phase map in cardiac myocyte (a) and converted wrapped 3-D phase map in cardiac myocyte (b). The phase is linearly correlated with the force.

Where  $z_1$  is the distance between the two substrates,  $z_2$  is the distance between the second substrate to the observation plane, shown in Figure. 1(b).  $n$  and  $m$  are integer numbers. Part of the expression which has the lowest frequencies is the one that describes the moiré pattern. When the two periodic substrates have a small misalignment angle  $\theta$  ( $\theta < 30^\circ$ ), the spatial distribution of the moiré pattern in space can be described as [5]

$$U(x_3, y_3) \approx \sum_{n=-\infty}^{\infty} T\left(\frac{n}{d}\right) T\left(-\frac{n}{d}\right) \quad (4)$$

$$= \exp\left\{-i\pi \frac{n^2 \lambda}{d^2} (z_1 + 4z_2 \sin^2 \theta)\right\} \exp\left\{i2\pi n / \frac{y_3 d}{2 \sin \theta}\right\}$$

The above equation shows that the moiré fringes can be treated as a grating pattern with spatial period  $d/2\sin\theta$ , with contrast changing along the  $z$  axis with an interval of  $d_T = 2(d/\sin\theta)^2/\lambda$ . At distances that are integer multiples of  $d_T$ , the blur owing to the grating's diffraction is minimized, meaning the contrast of the fringe pattern attains a local maximum. By adjusting the gap between the two gratings to integer multiples of  $d_T$ , we can avoid diffraction by the gratings and justify our approach.

The periodicity of the moiré pattern is invariant with the distance between the two periodic substrates, i.e.,

$$d_m = d/2\sin\left(\frac{\theta}{2}\right) \quad (5)$$

With small angle approximation, the last equation is simplified as  $d_m = d/\theta$ . Eq. (5) is the same as Eq. (1), except that the reference layer in interferometric configuration is the

interference pattern. The orientation and spatial period of the moiré pattern corresponding to the relative angle  $\theta$  between two periodic substrates of equal spatial period is numerically plotted in Figure 2. In Figure 2 the periodicity of moiré pattern versus the angle  $\theta$  is shown for five grating periods ( $3\mu\text{m}, 4\mu\text{m}, 5\mu\text{m}, 6\mu\text{m}, 7\mu\text{m}$  from bottom to top respectively). The orientation of the moiré fringes ranges from  $80^\circ$ - $90^\circ$  as the relative orientation of the periodic substrates increases from  $0$ - $30^\circ$ . It can be observed that the spatial period of moiré pattern decreases when the angle  $\theta$  increases. However, this decreasing is not linear, but three distinct regions can be observed. The first region is between  $0$  to  $10$  degrees: the magnification factor is relatively large and they diminish quickly as  $\psi$  increases. This is, therefore, a very sensitive region. In the second region, with  $\theta$  ranging from  $10$  to  $20$  degrees, the variations in  $d_m$  are moderate (smaller than a dozen  $\mu\text{m}$ ). For example, when the period of the arrays is  $d = 4 \mu\text{m}$ , the period of the moiré fringes goes from  $40 \mu\text{m}$  (at  $\theta = 5^\circ$ ) to  $11 \mu\text{m}$  (at  $\theta = 20^\circ$ ). In the third region, from  $20$  to  $30$  degrees, the variations of  $d_m$  are small, approaching to a constant asymptotic value, noted as the least sensitive region.

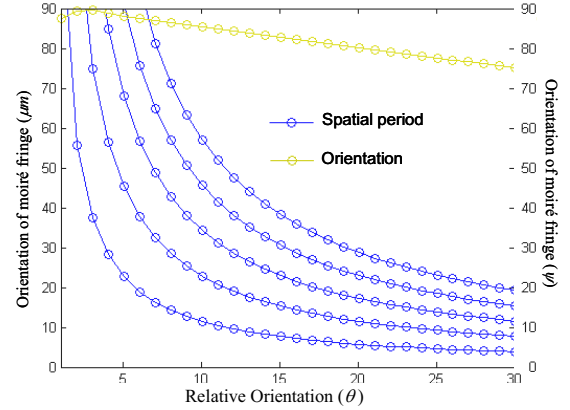


Figure 2: Magnification factor and orientation of moiré fringes versus the relative angle of two superimposing gratings of periods. The red curve represents orientation of the moiré pattern; the blue curve represents magnification factor.

## EXPERIMENT AND RESULTS

The experimental setup shown in Figure 3 for our compact 2D moiré mapping system includes an illumination source of 1.5-mW 633-nm He-Ne laser (Research Electro-Optics Inc, a beam expander, a CCD video camera (Pixelink 623), an inverted microscope (Nikon), a digital computer with MATLAB programs for automated moiré fringes analysis, and two identical PDMS periodic substrate substrates mounted on the translational stage. The grating lines and grids patterns are separated by sidewalls. The reference layer can be shifted by a translational stage so that 1D and 2D moiré patterns can be conveniently switched. The sidewalls also serve as guidance to separate periodic pillar arrays so that the cardiac myocytes will be aligned in the direction of the wall. The cell culturing substrate was sealed into a polycarbonate flow perfusion chamber with an internal volume of 30mL. Cell culture media with Rat aortic smooth muscle cells were injected through the inlet of the perfusion chamber with the culturing substrate. The plane of the reference substrate is kept parallel to that of the cell culture substrate and the orientation is controlled by a rotation stage. Testing marks on the sidewalls were designed to help locate the periodic features and relative orientation between the two substrates. The glass environmental chamber is maintained at  $37.2^\circ\text{C}$  with 5%  $\text{CO}_2$  concentration.

The cell culture chip and reference layer were fabricated by following a pressure-assisted replica molding process. AZ 9260 (AZ Electronics, Inc) was spin-coated on glass slides (2cmx2cm) at 3000 rpm for 60 s and soft-baked for 2.5 min at 100 °C. After being exposed under a UV light at 1550 mJ, the samples were developed in AZ 400K diluted as 1:4 (AZ Electronics) for about 20 s. PDMS prepolymer (Sylgard 184, Dow Corning, 10:1 base solution to curing agent) was then spin-coated on patterned photoresist on glass slide at 1000 rpm for 5 s, put into vacuum oven for 10min for bubble removal and soft baked at 65 °C for 2 h.

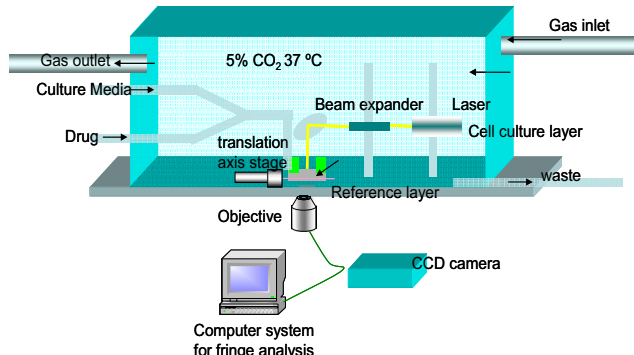


Figure 3: Optical moiré biomechanical sensing system integrated with cell culture facilities.

The resulting thickness of the PDMS was approximately 200  $\mu\text{m}$  upon removal from the glass substrate. And the resulting diameter of the PDMS posts is 2 $\mu\text{m}$  with height of 4 $\mu\text{m}$ .

The cell culture chip needs to be activated by extracellular matrix (ECM) protein (Laminin for cardiac myocyte and fibronectin for smooth muscle cell) to render cell adhesion to the substrate. This process was performed by inverted micro contact printing ECM proteins on top of the cell culture substrate [6]. After releasing the PDMS from the mold, the cell culture layer was treated in oxygen plasma in a Plasma Asher (TePla M4L PVA Plasma Asher) at 150w for 2 mins. This oxygen plasma treatment made the PDMS surface change from being hydrophobic to being hydrophilic which facilitates the absorption of fibronectin in the PBS buffer solution. The PDMS stamps were cut from thick layered PDMS chunk, immersed in 50  $\mu\text{g}/\text{mL}$  fibronectin PBS buffer solution, and then washed and blow dried under a nitrogen gun. These protein coated PDMS stamps were finally put in conformal contact with the surface oxidized cell culture samples for 5 min and then carefully deconstructed. For cardiac myocytes culture, the polymer substrate was sterilized and 15mmol  $\text{l}^{-1}$  of laminin.

To demonstrate the operation of our moiré contouring system based on Fourier carrier fringe analysis, we propose to map the anisotropy of cardiac myocyte contraction driven by electric current. Rat cardiac myocytes were isolated from Wistar rat hearts according to a previously described protocol [7]. The laminin solution was removed and the cells were plated on the PDMS substrate for 2 h to allow for cell attachment. After that, the polymeric substrate was gently rinsed with fresh culture media to remove the unattached cells. The cells were incubated in 5%  $\text{CO}_2$  at 37°C, and the culture media was changed every 72 h. Cardiac myocytes contraction induced distortion on testing grids patterns consisting of short cantilever like pillar arrays, and thus the measurement of contractility of single cardiac myocytes was performed by plating isolated living cells on our chip with short-cantilever like grids pattern confined within sidewalls. The cells formed focal adhesions on the tops of the deflectable grids patterns

consisting of the posts and were thus free to contract unhindered by their attachments causing movement of the posts. The perfusion chamber was perfused with 1.2 mM  $\text{Ca}^{2+}$  Tyrode buffer solution and maintained at 37 °C for 24 h on the substrate. The cells were electrically stimulated to contract at a frequency of 5 Hz from IonOptix. During the experiment, the orientation of interference patterns was adjusted to contain a small angle (8°) with respect to one (X) direction of the spatial periodicity of the substrate. The grating line was translated to be directly on top of the cell culturing layer to serve as reference grating. Figure 4(a) shows a typical 1D initial undistorted moiré pattern. Figures 4 (b) and (c) show typical moiré pattern at the peak of cardiac myocyte contraction in two perpendicular directions respectively.

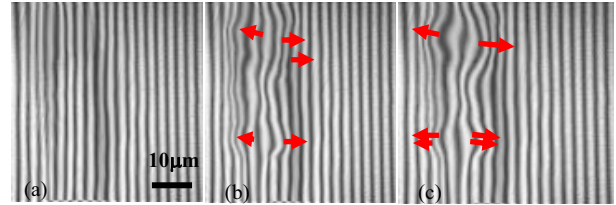


Figure 4: Moiré fringe evolution in cardiac myocytes contraction. (a) Initial fringe pattern. (b) 0.5 period of cell contraction. (c) 1 period of cell contraction.

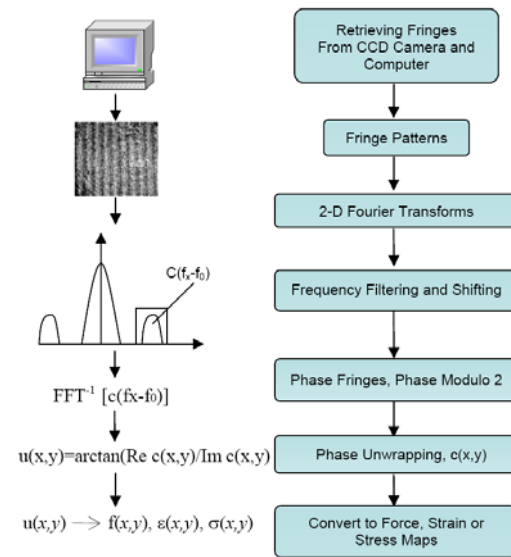


Figure 5: Scheme for automated fringe analysis procedure based on carrier fringe Fourier transform method for cell force mapping.

With the stimulation at 5 Hz at 2.5 volts, the contraction period of cardiac myocytes is 0.2s. The distortion of 1D moiré pattern clearly reveals distortion induced by cardiac myocyte contraction. To compute the contraction force distribution from the moiré maps, Fourier transform was applied to the image (Figure 5). A reverse transform on the masked data after frequency filtering then carries noise-free phase information. Each pixel contains a complex number of which the phase can be calculated. The phase records the position of a pixel under the distortion pattern, since a  $\pi$  change in phase is equivalent to shifting from a null to a peak in the distortion fringes. Phase unwrapping was then carried out by subtracting any  $2\pi$  phase jumps. Figure 6 (a) shows the unwrapped phase change pattern from the moiré pattern when



cell contraction was at its peak upon stimulation. Unwrapped phase patterns directly revealed cell contraction distribution in the whole cell. Utilizing the load-displacement relationship characterized from nanoindentation, of which the Young's Modulus was determined to be 3 MPa, the traction force distribution was converted from the phase distortion map [Figure. 6(b)]. 1D moiré pattern in two directions can be achieved by rotating the grating pattern by 90° clockwise.

We studied the moiré pattern evolution during smooth muscle cell spreading and cell contraction in response to agonist [8]. The amount of cell contraction in response to agonist is closely related to level of cell traction forces already established in cells. Therefore, it is important to study the cell contractile forces evolution prior to stimulating the cells with contractile agonists. We examined the cell force evolution through moiré pattern evolution and investigated the contractile forces in response to agonist.

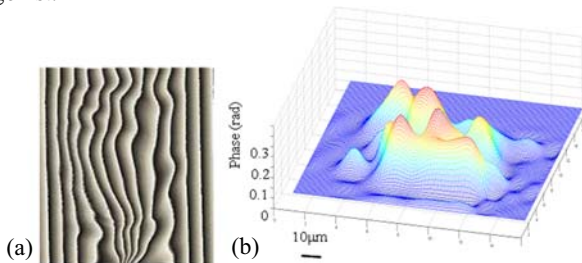


Figure 6: Representative unwrapped phase map in cardiac myocyte (a) and converted wrapped 3-D phase map in cardiac myocyte (b). The phase is linearly correlated with the force.

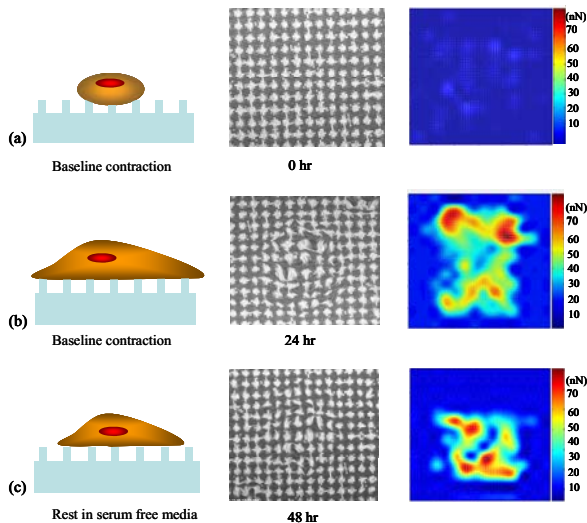


Figure 7: Cell patterning and moiré pattern evolution: (a) VSMC cell just seeded on the substrate. (b) Cell spread out and traction forces were developed. (c) Cell relaxed in serum free media.

The force exerted by cell traction can then be conveniently studied through moiré pattern evolution. The substrate was slightly rotated with respect to the first substrate to form an angular moiré pattern and the resulting spatial period of moiré pattern was found to be to be 8  $\mu\text{m}$ . The reference layer consisted of periodic pillar patterns with aspect ratio of 2. After being plated on the cell culture layer, the cells started to establish focal adhesions and further spread out on the fibronectin coated periodic patterns.

The corresponding moiré image reveals undistorted moiré

grids patterns, as shown in Figure 7 (a)-(c). As the cells started to spread out, the moiré patterns started to deform for approximately 12 h until its fully distorted pattern. The evolution of moiré fringes confirmed that the smooth muscle cells fully spread out and that the traction force accumulates due to the increase in cytoskeleton tension dependent on serum. To map cell traction forces during cell spreading, a 2D Fourier transform was applied and the phase change was retrieved from the carrier fringes with a spatial period of 8  $\mu\text{m}$ . The moiré image magnified and recorded the original deformation map into deformed carrier fringe patterns. The distortion of the fringes was then converted to a phase distortion map  $u(x,y)$ , followed by being converted into a force map  $f(x,y)$ .

## CONCLUSIONS

We have demonstrated a real time optical moiré mapping system using coherent light. The premise of this work is that the optical moiré interface will provide automatic whole-field mapping of cell mechanical interactions with its living environment in real time. Optical moiré techniques have unique properties such as its automatic displacement and strain contouring and its magnification effect for small strains and displacements. Given these unique properties, this new approach would be an improvement over existing techniques since it can be integrated with the existing engineered cell culture substrates and provide a direct contour mapping of the displacements and strain distribution without tracking individual sensing units.

## ACKNOWLEDGEMENTS

We would like to acknowledge National Science Foundation (CBET 0933653, CMMI 0826191, and CMMI 0239163) for the support of this research.

## REFERENCES

- [1] K. A. Beningo and Y. L. Wang "Flexible substrata for the detection of cellular traction forces", Trends in Cell Biology, **12**, 79 (2002).
- [2] N. Q. Balaban, U. S. Schwarz, D. Riveline, P. Goichberg, G. Tzur, I. Sabanay, D. Mahalu, S. Safran, A. Bershadsky, L. Addadi, and B. Geiger, "Force and focal adhesion assembly: a close relationship studied using elastic micropatterned substrates," Nature Cell Biology, **3**, 466 (2001).
- [3] J.L. Tan, et al., "Cells lying on a bed of microneedles: An approach to isolate mechanical force", Proceedings of the National Academy of Sciences of the United States of America, **100**, 1484 (2003).
- [4] X. Zheng and X. Zhang, "An optical Moiré technique for cell traction force mapping", Journal of Micromechanics and Microengineering, **18**, 125006 (2008).
- [5] O. K. a. I. Glatt, The Physics of Moiré Metrology. New York: John Wiley and Sons, 1990.
- [6] C. D. James, R. C. Davis, L. Kam, H. G. Craighead, M. Isaacson, J. N. Turner, and W. Shain, "Patterned protein layers on solid substrates by thin stamp microcontact printing," Langmuir, **14** (1998).
- [7] J. Tytgat, "How to Isolate Cardiac Myocytes," Cardiovascular Research, vol. 28, pp. 280-283, Feb 1994.
- [8] A. P. Somlyo and A. V. Somlyo, "Signal-transduction and regulation in smooth-muscle," Nature, **372**, 231 (1994).

## CONTACT

\*Xin Zhang; 617-358-2702, xinz@bu.edu

# A MICROFABRICATED GAS CHROMATOGRAPH FOR SUB-PPB DETERMINATIONS OF TCE IN VAPOR INTRUSION INVESTIGATIONS

Hungwei Chang,<sup>1</sup> Sun Kyu Kim,<sup>1</sup> Thitiporn Sukaew,<sup>1</sup> Forest Bohrer,<sup>2</sup> Edward T. Zellers<sup>1,2</sup>

Center for Wireless Integrated Microsystems (WIMS), University of Michigan, Ann Arbor, MI, USA

Departments of <sup>1</sup>Environmental Health Sciences and <sup>2</sup>Chemistry, University of Michigan, Ann Arbor, MI, USA

## ABSTRACT

A microfabricated gas chromatograph ( $\mu$ GC) is described and its application to the determination of low-parts-per-billion (ppb) concentrations of trichloroethylene (TCE) in mixtures is demonstrated, relevant to investigations of vapor intrusion (VI) into homes and offices. The system employs a MEMS focuser, dual MEMS separation columns, and MEMS interconnects along with a microsensor array. These are interfaced to a (non-MEMS) pre-trap and high-volume sampler module in order to reduce overall analysis time. The response patterns generated from the sensor array for each vapor are combined with the chromatographic retention time to identify and differentiate the components of VOC mixtures. All functions are controlled by a Labview routine written in house. A chemometric method based on multivariate curve resolution has also been developed for analyzing partially resolved mixture components. First results are presented of the capture, separation, recognition, and quantification of TCE in a mixture at 4 ppb, with a projected detection limit of 50 parts-per-trillion.

## INTRODUCTION

The measurement of volatile organic compounds (VOC) in complex mixtures is critical to numerous public health efforts. Current VOC monitoring instrumentation is too large and expensive for routine implementation in many such applications. While stand-alone microsensor arrays (so-called electronic noses) can be used for the determination of individual VOCs in simple mixtures [1,2], reliable quantitative analysis of complex gas/vapor mixtures with microsensor arrays demands chromatographic separation prior to measurement. Several reports have appeared over the past decade on microfabricated gas chromatographic ( $\mu$ GC) separation columns coupled with one or more sampling, pretreatment and/or detection devices. However, reports on fully integrated  $\mu$ GC systems that incorporate microfabricated sampling/preconcentration, separation, and detection devices are relatively rare [3-6].

Vapor intrusion (VI) refers to VOC infiltration into buildings overlying contaminated soil or groundwater. VI is an emerging problem in the U. S., affecting thousands of civilian and military locations [7]. TCE is the most common contaminant of concern at VI-impacted sites, where concentrations in homes and buildings have been documented in the low-parts-per-billion to mid-parts-per-trillion (ppt) range. In response to the need for inexpensive on-site monitoring instrumentation, we are developing a fieldable prototype  $\mu$ GC whose design and operating parameters are tailored for the determination of TCE from VI in near-real-time in the presence of common interfering VOCs. Performance specifications include a limit of detection (LOD) of < 100 ppt of TCE, discrimination of TCE from typical indoor contaminants, and a total analytical cycle period of < 30 minutes.

The schematic diagram of the  $\mu$ GC, which has been named SPIRON, is shown in Figure 1 along with images of the core microfabricated components. This microsystem builds on previous work in our group on partially-integrated or single-column prototypes [3,4] and on component-level testing of critical

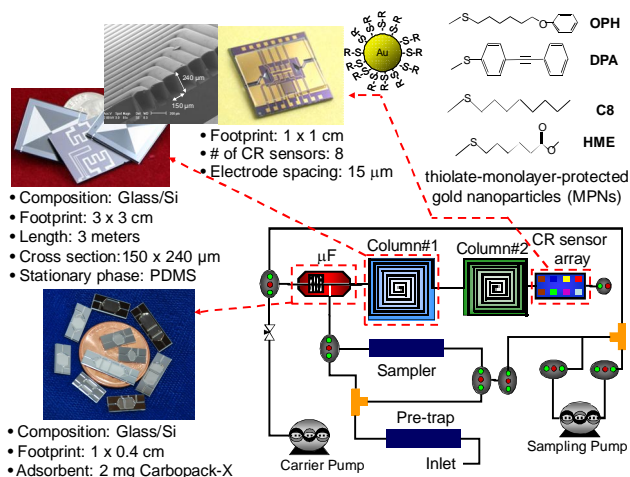


Figure 1: The SPIRON  $\mu$ GC layout diagram and images of major components, microfocusers, dual 3-m microcolumns, and nanoparticle-coated chemiresistor-array detector

microsystem elements [8-11]. The key components are an adsorbent-packed DRIE-Si/glass single-stage focuser ( $\mu$ F), dual 3-meter DRIE-Si/glass microcolumns and a chemiresistor (CR) sensor array incorporating thiolate-monolayer-protected gold nanoparticle (MPNs) films as sensing materials on interdigital electrodes [3]. To measure TCE in the desired concentration and analytical time ranges, a front-end high-volume sampler (non-MEMS) was added. In addition, a pre-trap (non-MEMS) was added to filter out low volatility interferences that might degrade system performance after prolonged use.

An analytical cycle comprises four steps. First, air samples are passed through the pre-trap and collected on the high-volume sampler at a flow rate of  $\sim$ 1 L/min. Second, the VOCs captured on the sampler are thermally desorbed onto the  $\mu$ F at a low flow rate. Third, the  $\mu$ F is rapidly heated to inject the VOC mixture onto the first of two microcolumns for separation and detection of eluting peaks by the sensors in the CR array. Finally, the identification and quantification of each VOC is performed by combining retention time with array response patterns in chemometric analyses.

The work described herein focuses on various aspects of microsystem integration and performance. This includes the integration of the core MEMS components on a PCB with fluidic and electrical interconnections to supporting devices; the design, optimization, and integration of the front-end pre-trap, high-volume sampler, and  $\mu$ F; demonstration of the analysis of TCE in a test mixture at low concentrations with the integrated microsystem, and methodology for chemometric discrimination of TCE from co-contaminants with similar elution times.

## RESULTS AND DISCUSSION

### System Components and Integration

The key components of the SPIRON  $\mu$ GC are presented in the prototype (mock-up) shown in Figure 2. The single-stage  $\mu$ F has

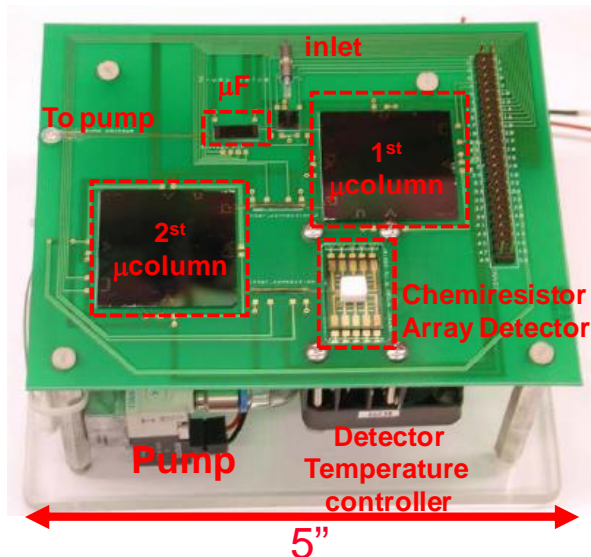


Figure 2: The SPIRON  $\mu$ GC prototype (mock-up).

overall dimensions of 9.76 mm x 4.18 mm x 0.6 mm and was fabricated from double-polished Si wafers (0.5 mm thick). Deep-reactive-ion-etching (DRIE) was used to form a 3.2 mm x 3.45 mm cavity in the lower section of the device as well as to define inlet and outlet ports and an additional port for adsorbent filling (0.40 mm). The device was capped with an anodically bonded Pyrex plate. A Ti/Pt RTD was evaporated onto the backside along with Cr/Au contact pads for bulk heating of the device. A 2.3 mg quantity of a graphitized carbon adsorbent (Carbopack X, specific surface area of 250 m<sup>2</sup>/g) was sieved and then drawn into the  $\mu$ F by gentle suction and retained with DRIE pillars within the cavity blocking the exit port. Deactivated fused silica capillaries are used for fluidic interconnections.

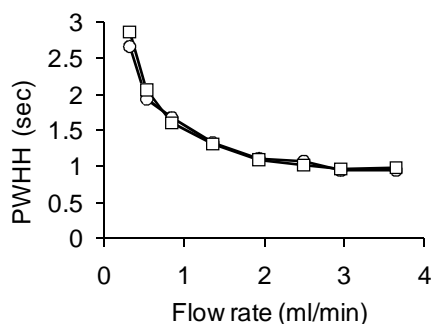


Figure 3: Desorption bandwidth (peak width and half height, PWHH) of TCE from the  $\mu$ F as a function of desorption flow rate from 0.3 to 3.6 mL/min for TCE alone (squares) and TCE in a mixture with 9 co-contaminants (circles). A higher flow rate leads to narrower injection bands, and there is no influence on PWHH by other VOCs.

Microcolumn fabrication and stationary-phase deposition methods used in this study have been described previously [8]. Rectangular channels, 150  $\mu$ m wide by 240  $\mu$ m deep, were formed in Si by DRIE. A Pyrex cover was anodically bonded to the lower Si wafer to seal the channels. The 3-m microcolumns have a 3-cm x 3-cm footprint. Each of the 3-m-long columns was coated with

PDMS using a static coating method and crosslinked *in situ*. The calculated PDMS film thickness is 0.15  $\mu$ m. Hexamethyldisilazane (HMDS) is used to passivate the channel walls. The microcolumns can be independently temperature-programmed from room temperature to  $\sim$ 200  $^{\circ}$ C by integrated heaters using a pulse-width-modulation (PWM) method with a proportional-integral-derivative (PID) algorithm.

The chemiresistor (CR) array consists of 8 Au/Cr interdigital electrodes (IDEs) a 4x2 layout on thermally grown SiO<sub>2</sub> over silicon. Each IDE had 24 finger pairs with 5  $\mu$ m width and spacing and finger lengths of 0.5 mm. The array was capped with Macor lid with ports that accepted inlet and outlet capillaries to create a detector cell with an internal volume of  $\sim$ 3  $\mu$ L. The device is mounted on a carrier PCB with a cut-out beneath the sensor to permit contact with a thermo-electric cooler beneath the PCB used to thermostat the array at 20  $^{\circ}$ C. Chemical alteration of the MPN thiolate monolayer gives rise to differential responses for the different sensors; thiols used include n-octanethiol (C8), 1-mercapto-6-phenoxyhexane (OPH), methyl 6-mercaptohexanoate (HME), and 4-mercaptodiphenylacetylene (DPA). Two sensors are coated with each MPN for redundancy.

The individual microfabricated components were mounted on discrete carrier PCBs with high temperature epoxy and then mounted in patterned openings cut in the main PCB. Electrical contacts were made to the PCBs via aluminum wire bonding. Two miniature diaphragm pumps (KNF Neuberger, Trenton, NJ) and six micro-solenoid valves (Lee Co., Westbrook, CT) are mounted beneath the PCB and used to direct air flow. All valves were integrated on a stainless steel manifold (not shown). Short sections of deactivated fused silica capillary tubing (250  $\mu$ m i.d.) were used to fluidically interconnect the components, and MEMS heater sleeves were used at the inlets and outlets of both microcolumns to avoid cold spots.

The system functions are run automatically with user-defined timing and temperature profiles by routines written and compiled in Labview run on a laptop computer equipped with a USB-interfaced multifunction data acquisition card, (USB-6229 National Instruments, Austin, TX).

### Sampler, Pre-trap, and $\mu$ F Performance

The pre-trap is designed to capture less volatile interfering background vapors with minimal pressure drop, while allowing TCE to pass through unretained. We found that a 50-mg bed of the graphitized carbon Carbopack B (100 m<sup>2</sup>/g, 212-250  $\mu$ m o.d.) packed in a thin-walled stainless-steel tube (6-mm i.d.) achieves this goal. Using a 20-L sample volume as the maximum sample volume, all compounds with a vapor pressure below 3 torr are completely retained, and TCE is only partially retained from the first 1.5 L of sample (minimal retention). The sampler is designed to capture TCE along with other VOCs with similar volatility quantitatively for sample volumes up to 20 L. This has been confirmed using a thin-walled stainless-steel tube (6 mm i.d.) packed with 100 mg of Carbopack X in tests of TCE at concentrations ranging from 1-500 ppb, with up to 25 other relevant interferences in the sample, both in dry air and in air at 100% relative humidity. Note that highly volatile interferences are allowed to pass through the system unretained.

Transfer of TCE from the sampler to the  $\mu$ F must be quantitative. Testing has shown that at a flow rate of 30 mL/min heating the sampler to 220  $^{\circ}$ C results in complete transfer of TCE to the  $\mu$ F in < 3 min. It was also shown that breakthrough of TCE through the  $\mu$ F under these conditions is < 1%.

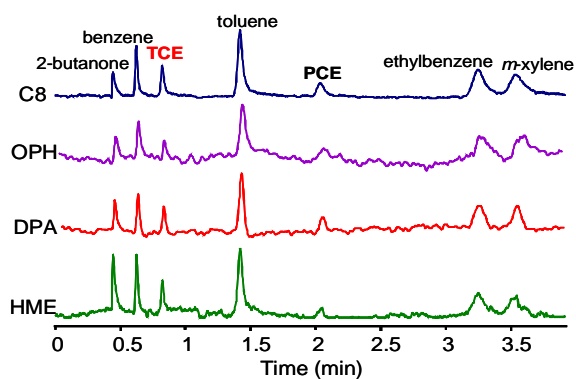


Figure 4. Chromatographic traces from the CR array detector for a preconcentrated test atmosphere of TCE and relevant interferences.

The final step in the preconcentration process is injection of the TCE from the  $\mu$ F to the first microcolumn. For desorption bandwidth determinations, a mass equivalent to 1 ppb-L was loaded in the  $\mu$ F and the desorption bandwidth was measured as a function of flow rate from 0.3 to 3.6 mL/min with the  $\mu$ F heated to 225 °C within 0.6 sec. Tests were performed with TCE alone and also as a mixture with benzene, ethylacetate, heptane, toluene, octane, ethyl benzene, o-xylene,  $\alpha$ -pinene, and cumene (1 ppb-L each). As shown in Figure 3, the minimum bandwidth of 1 sec is achieved at flow rates > 2 mL/min and there is no effect from the presence of VOCs. Since separation efficiency is maximized at flow rates of 0.8-1 mL/min, this indicates that only a slight tradeoff in separation efficiency is made to operate at a flow rate that gives the sharpest injection band from the  $\mu$ F.

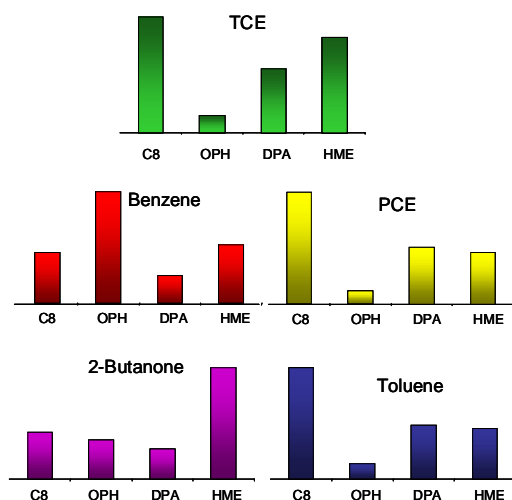


Figure 5: CR sensor array unique responses patterns for TCE, benzene, PCE, 2-butanone and toluene. Response patterns are combined with retention times to recognize and differentiate the VOCs

#### SPIRON $\mu$ GC TCE determination and calibration

A 4-L sample of a test-atmosphere containing 4 ppb each of TCE and 6 representative co-contaminants found in homes suffering from VI at our planned field-testing site (2-butanone,

benzene, toluene, perchloroethylene (PCE), ethylbenzene, and m-xylene, in air) was drawn through the high-volume sampler (pre-trap excluded for this test) with an on-board mini-pump. Captured VOCs were thermally desorbed and transferred to the  $\mu$ F and then thermally injected from the  $\mu$ F (200 °C in 0.4 sec) onto the micro-column ensemble. As shown in Figure 4, TCE was easily separated from the other 6 VOCs and had a retention time of 50 sec with the microcolumns held at room temperature initially and then ramped up to 120 °C to accelerate elution of the later-eluting interferences.

As shown in Figure 5, unique response patterns are obtained for TCE, benzene, PCE, 2-butanone and toluene from the MPN-coated CR array. Like GC/MS, TCE can be identified by combination chromatographic retention time and unique pattern response.

Figure 6 shows calibration curves for all 4 sensors in the array for TCE with 4-L sample volume. All curves are linear from 2.1 ppb up to 21 ppb and intersect the origin. As shown in Table 1, for C8 sensor, the calculated LOD for TCE is 0.23 ppt. When the sample volume is increased to 20 L, 3 of the 4 sensors have projected TCE LODs  $\leq$  70 ppt.

Table 1. TCE Limits of Detection (LOD, ppb)

	C8	OPH	HME	DPA
LOD (ppb in 4-L)	0.23	2.9	0.32	0.35
LOD (ppb in 20-L)	0.047	0.58	0.064	0.07

#### Multivariate curve resolution analysis

Rapid analysis by  $\mu$ GC often results in partial co-elution (overlap) of peaks, which can reduce the ability to identify and quantify the components. An advantage of using a sensor-array detector is that it permits the use of multivariate curve resolution (MCR) to detect hidden peaks in a chromatogram and to resolve overlapped peaks at any degree of chromatographic resolution.

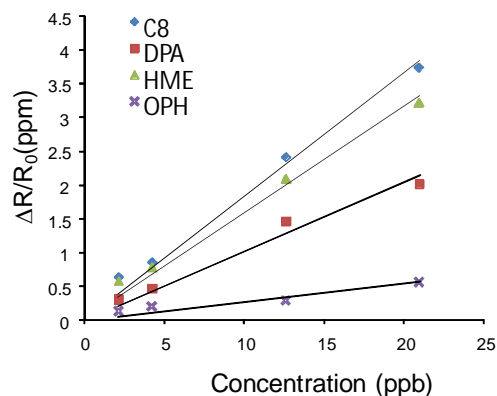


Figure 6. TCE Calibration curves for each of the 4 MPN-coated CR sensors in the SPIRON  $\mu$ GC.

In the previous study [12], we developed an MCR algorithm that combines evolving factor analysis with adaptive least-squares. It was applied successfully to simulated data to illustrate the performance of the technique with a CR array used as a GC detector. We are now applying this technique to experimental data. To illustrate, we chose TCE and heptane as possibly co-eluting compounds, since heptane is often found as a co-contaminant in VI-impacted homes and these two VOCs will overlap in analyses performed with the SPIRON  $\mu$ GC. Response patterns for heptane and TCE were generated experimentally, and the degree of overlap (chromatographic resolution, R) was varied

by simulation (Matlab) from a value of 0.25 (nearly complete overlap) to 1.0 (nearly completely resolved).

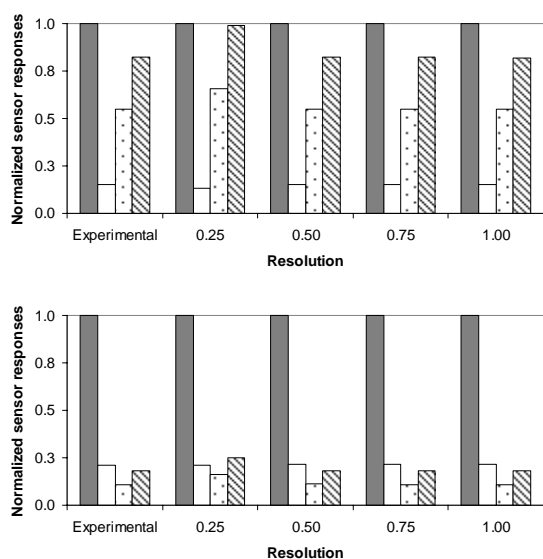


Figure 7. Comparison of response patterns obtained from fully resolved peaks (experimental) of TCE (top) and heptane (bottom) and those recovered from MCR analysis of overlapping peaks of TCE and heptane for different simulated degrees of overlap (resolution). Bars: from left to right: C8, OPH, DPA, and HME.

Figure 7 shows the response pattern for each individual compound along with the recovered response pattern for different degrees of chromatographic resolution (R ranges from 0.25-1.0). As shown, the patterns for these co-eluting compounds were recovered with high fidelity (correlation coefficients  $\geq 0.98$ ), for all R values. This methodology is being applied to all possible overlapping compounds to guide the separation strategies.

## CONCLUSIONS

First results from a prototype MEMs micro gas chromatograph ( $\mu$ GC) adapted for the determination of TCE at low-/sub-ppb concentrations in homes and offices suffering from vapor intrusion have been presented. A front-end pre-trap and high-volume sampler (non-MEMS) have been incorporated to reduced analysis time and facilitate achieving desired LODs. Efficient capture and transfer of TCE samples at low concentrations have been confirmed experimentally, along with sharp injection bands from the microfocuser. TCE was separated a subset of anticipated interferences in  $\sim 50$  sec and response patterns from the CR array, when combined with retention time, permit facile discrimination of TCE from resolved interferences. An MCR technique has been developed to address possible co-eluting interferences in samples with more complex mixtures of interferences. Calibrations are linear from 2-20 ppb. Projected detection limits for a 20-L sample, which can be analyzed in  $< 30$  minutes, are as low as 50 ppt.

## ACKNOWLEDGEMENTS

The authors want to thank Katharine Beach for MEMs device fabrication, Brendan Casey for wire bonding, Robert Gordenker for PCB carrier board design, and David Burriss and Jim Reisinger for critical technical guidance. This work was supported by DoD ESTCP ER 200702 through a subcontract with Integrated Science

& Technology, Inc. and by the National Science Foundation Engineering Research Centers Program (WIMS Center) ERC-9986866.

## REFERENCES

- [1] M. D. Hsieh, E.T. Zellers, "Limits of recognition for simple vapor mixtures determined with a microsensor array," *Anal. Chem.*, 76, 1885 (2004).
- [2] J. C. Jin, P. Kurzwaski, A. Hierlemann, E.T. Zellers, "Evaluation of multitransducer arrays for the determination of organic vapor mixtures," *Anal. Chem.*, 80, 227 (2008).
- [3] C. J. Lu, W. Steinecker, W. C. Tian, M. Oborny, J. Nichols, M. Agah, J. Potkay, H. Chan, J. Driscoll, R. D. Sacks, K. Wise, S. Pang, E. T. Zellers, "First-generation hybrid MEMS GC," *Lab-on-Chip*, 5, 1123-31 (2005).
- [4] E. T. Zellers, S. Reidy, R. A. Veeneman, R. Gordenker, W. H. Steinecker, G. R. Lambertus, H. Kim, J. A. Potkay, M. P. Rowe, Q. Zhong, C. Avery, H. K. L. Chan, R. D. Sacks, K. Najafi, K. D. Wise "An integrated micro-analytical system for complex vapor mixtures," *Proc. Transducers '07*, Lyon, FR, June 10-14, 2007, pp. 1491-1496.
- [5] P.R. Lewis, R.P. Manginell, D.R. Adkins, R.J. Kottenstette, D.R. Wheeler, S.S. Sokolowski, D.E. Trudell, J.E. Bymes, M. Okandan, J.M. Bauer, R.G. Manley, G.C. Frye-Mason, "Recent advancements in the gas-phase  $\mu$ ChemLab", *IEEE Sensors J.*, 6, 784 (2006).
- [6] S. Zampolli, I. Elmi, F. Mancarella, P. Betti, E. Dalcanale, G. C. Cardinali, M. Severi, "Real-time monitoring of sub-ppb concentrations of aromatic volatiles with a MEMS-enabled miniaturized gas-chromatograph,". *Sens. Actuator B-Chem.* 141, 322 (2009).
- [7] D. N. Cox, W. B. Howard, M. A. Smith, "Heuristic model for predicting the intrusion rate of contaminant vapors into buildings" *Environmental science & technology* 25, 1445 (1991).
- [8] G. Serrano, S. M. Reidy, E. T. Zellers, "Assessing the reliability of wall-coated microfabricated gas chromatographic separation columns," *Sens. Actuator B-Chem.*, 141, 217-226 (2009).
- [9] S. K. Kim, H. Chang, E. T. Zellers, "Prototype microGC for breath biomarkers of respiratory disease" *Proc. Transducers '09*, Denver, Colorado, USA, June 21-25, 2009, pp. 128-131.
- [10] G. Serrano, H. Chang, E. T. Zellers, A micro gas chromatograph for high-speed determinations of explosive vapors, *Proc. Transducers '09*, Denver, CO, June 21-25, 2009, pp. 1654-1657.
- [11] F. Bohrer, E. Covington, Ç. Kurdak, E. Zellers, "Nanoscale chemiresistor arrays with patterned nanoparticle interface layers for microGC," *Proc. Transduc. '09*, Denver, CO, June 21-25, 2009, 148-151.
- [12] C. Jin and E. T. Zellers, "Chemometric analysis of gas chromatographic peaks measured with a microsensor array: methodology and performance assessment," *Sensors and Actuators B - Chemical*, 139, 548-556 (2009).

## CONTACT

\*Edward T. Zellers, tel: +1-734-936-0766; ezellers@umich.edu

# A MICROMACHINED CLOG-FREE EJECTOR FOR LONG-TERM RELIABLE HYDROGEL PRINTING

Riberet Almeida\* and Jae Wan Kwon

Department of Electrical and Computer Engineering, University of Missouri, Columbia, MO, U.S.A.

## ABSTRACT

This paper presents a novel technique for long-term reliable hydrogel printing by employing a thin liquid-film based microfluidic valve mechanism. Common and major clogging problems of microfluidic ejectors by various bio-fluids such as hydrogels and oligonucleotides are very well known. By employing electrowetting technique to drive a thin liquid film of oil, which is immiscible to the hydrogels to be printed, an effective microfluidic valve mechanism has been implemented. Based on the new microfluidic valve technique, we have successfully demonstrated very reliable printing of hydrogels (carrying media of tissue cells) without any clogging problem. While the nozzle was clogged completely in an hour under ambient condition without any protection from the microfluidic valve, it shows clean and fresh printing even after 72 hours of standby time due to the discontinued evaporation by closing of the thin liquid-film based microfluidic valve.

## INTRODUCTION

In recent years, contactless and controlled microfluid delivery techniques by ejection have been widely used in many applications in chemistry and life sciences. Many of continuous or drop-on-demand ejections of the bio-fluids have been achieved by utilizing various piezoelectric-based microfluidic ejectors due to no-heat requirements [1][2]. Especially, printings of cells and biomaterials have been broadly used to generate three-dimensional tissue constructs. Former attempts in tissue printing offer the ability to deposit cells and other biomaterials in a rapid layer-by-layer fashion for creating tissue structures with the aid of gels [3]. Hydrogels are widely being used in tissue printing because they provide an aqueous and porous environment for cells' health and help retain cells' shape after printing. Protein and carbohydrate based polymers are used in the design and fabrication of organic scaffolds in skeletal tissue engineering [4][5].

Despite lots of the impressive results of organ printing, nozzle failure due to clogging is one of the biggest problems that need to be circumvented before such a process can gain widespread acceptance [6-8]. Most of the nozzle-based ejectors are prone to clogging due to fast evaporation and accumulation of the biofluid and biomaterials at the nozzle tip. In general, clogging problem is caused when the ink fluid (the solution to be ejected) is exposed to the air and dried very quickly. Similarly, the polymers in the aqueous solutions begin to crosslink and transform into hydrogel networks when the solution's evaporation occurs. To avoid the known problems above, we have invented a microfluidic ejector equipped with a microfluidic valve having a similar protective mechanism for evaporation control as seen in the human eye. An oily lipid layer protects tear evaporation avoiding dryness of the eye balls very effectively. As seen in nature, a liquid is a good substance to control another liquid. For example, when oil (non-volatile and immiscible liquid with water) covers a water surface, a thin layer of oil is formed on the top and isolates water completely from direct air exposure. Thus, we have employed the thin oil layer as a microfluidic valve to control the evaporation speed of

the ink fluid (hydrogel) as illustrated in Figure 1. The thin oil layer provides a complete separation and protection layer at the bio-fluid/air interface in the nozzle.

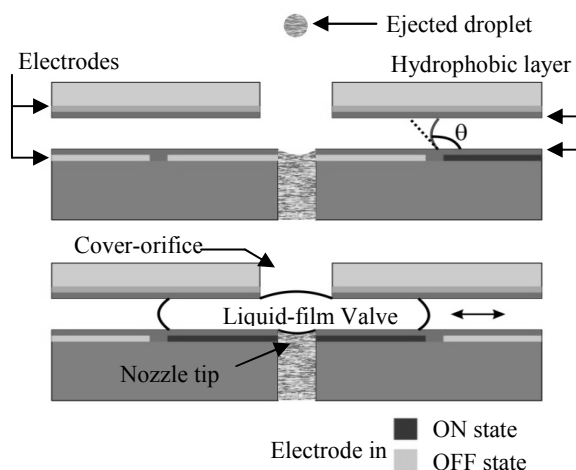


Figure 1. Cross-section view of liquid-film based microfluidic valve. It can open and close the ejector nozzle by using electrowetting technique.

## THEORY

In this device, an immiscible liquid droplet which acts as a protective sheath is actuated over the ejector nozzle by using the electro-wetting mechanism. The actuation force is caused by the change in contact angle or wettability of the surface which in turn is caused by the change in the solid liquid surface tension  $\gamma_{SL}$  that results in the droplet motion. The change in  $\gamma_{SL}$  occurs on the hydrophobic Cytop layer. The relationship between the applied voltage across the electrode and the liquid and the change in surface tension is given by the Lippmann equation:-

$$\gamma = \gamma_0 - \frac{1}{2} CV^2 \quad (1)$$

where  $\gamma_0$  is the surface tension when there is no voltage applied across the liquid-electrode interface and 'C' is the capacitance per unit area of the dielectric layer. In electrowetting-on-dielectric (EWOD) devices,  $\gamma$  needs to be interpreted as  $\gamma_{SL}$ , the surface tension in the solid-liquid interface.

The total electrostatic energy  $E(x)$  of the system can be estimated as

$$E(x) = \frac{1}{2} C_{eqv}(x) V^2 \quad (2)$$

where  $C_{eqv}$  is the equivalent capacitance arising from the different energy storage elements in a typical electrowetting system employing a sandwiched droplet between electrodes. The actuation force acting on the sandwiched droplet during transition can be estimated by the positive derivative of this energy function as follows;

$$F_{act}(x) = \left( \frac{dE(x)}{dx} \right)_V \quad (3)$$

## FABRICATION AND EXPERIMENT

The device consists of three main components (microfluidic valve, reservoir and ejector), which are prepared separately and then integrated into a single system. The microfluidic valve can be built on the top surface of the microfluidic ejector with an indium tin oxide (ITO) coated glass as a cover substrate. Thus, a thin and immiscible liquid droplet can move and slide over the nozzle of the ejector to provide the function of microfluidic valve as illustrated in Figure 1. An orifice in the cover substrate was vertically aligned very well with the ejector's nozzle so that the cover will not disturb the clean ejection path. The ITO served as a transparent ground electrode for the valve. The orifice in the cover substrate was fabricated by using laser micromachining.

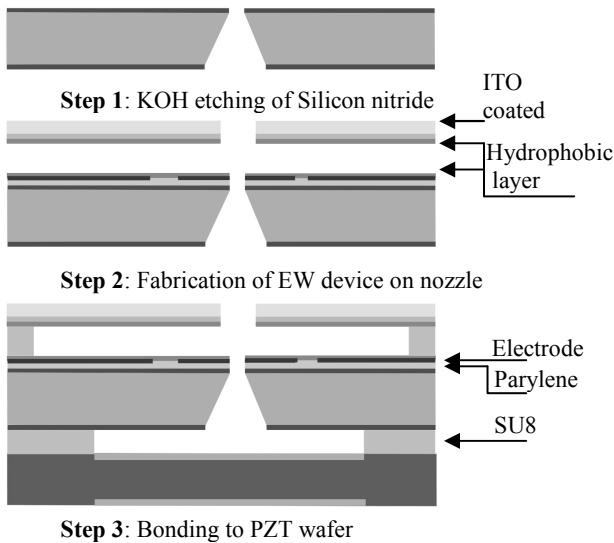


Figure 2. Fabrication Steps outlined

As briefly shown in Figure 2, fabrication of the microfluidic ejector starts by RIE patterning the backside of a 3 inch silicon nitride coated wafer for silicon etching in a solution of potassium hydroxide (KOH). The KOH etching was done in a 45% solution at 80°C. It forms thin diaphragms on the other side of the wafer. The wafer is then gently sonicated in deionised (DI) water for a minute to break away the thin silicon nitride diaphragms to make open-tip nozzles for the ejectors. A 1mm-thick lead zirconate titanate (PZT) substrate has been used as a

driving piezoelectric crystal. Then, the microfluidic valve was built on the front side of the ejector. A 5µm thick parylene deposition was followed by a 0.5µm thick aluminum deposition and patterning for the electrodes of the microfluidic valve. The underlying parylene layer was used as an insulating layer to prevent electrical breakdown through the silicon nitride since the thin oil film needs relatively high voltage to drive. Cytop was then spin-coated on the cover substrate and cured on a hot plate at 150°C for 10min to render the surfaces hydrophobic. The cover substrate was placed over the ejector with a 150µm gap formed by SU8 spacer. For the last step, a 250µm thick SU-8 spacer layer was added between the bottom of the silicon substrate and PZT crystal to create a large reservoir and to accommodate an inlet tube (Zeus PTFE 190µm OD).

To begin the ejection experiment, the microfluidic ejectors were first primed with DI water and tested for finding successful ejection conditions by varying many different ejection parameters such as the driving pulse width and amplitude. Once we confirmed good ejections, the ejector was filled with a freshly prepared aqueous solution, which is one of naturally occurring hydrogels such as gelatin, agarose and collagen. All these solutions were tested with the ejectors employing the liquid-film based microfluidic valve. Fluorescent dyes such as rhodamine 6G (R6G), acridine and alcian blue were added to the hydrogel solutions to aid visualization of the ejected droplets onto coverslips in using fluorescence microscopy. Once the ejectors were filled with the hydrogel solutions, a 700mV<sub>pp</sub> sinusoidal signal (2.1MHz) was fed into an RF switch (Mini-circuits, ZX80-DR230-S+) which was modulated with a 29.97Hz signal having a pulse width of 40µs and amplified. The microscope was positioned properly for capturing side view of the vertical ejection of hydrogels and the horizontal movement of the liquid-film valve (oil droplet) simultaneously. In the microfluidic valve, silicone oil was chosen as valve-core material since it is one of the most inert and immiscible liquids with many water-based bio-fluids. Silicone oil has a dielectric constant of 2.71 and a dielectric strength of 390KV/100mil. In addition, the silicone oil has superior properties over various liquid metals such as mercury and galinstan, which have serious toxicity and oxidation problems, respectively. However, the silicone oil requires relatively high electrowetting actuation voltage for droplet movement as shown in the result section.

## RESULTS

We have operated the ejector containing DI water under various operating conditions (e.g. frequency and amplitude of the driving ac signal), and found three distinct modes of ejection; (1) no ejection (idling mode) (2) ejection of individual droplets (also known as drop on demand (DOD) mode) and (3) ejection of a continuous jet (jet mode). The microfluidic ejector runs at its resonance frequency of 1.9-2.2MHz to generate acoustic pressure gradients to eject small droplets or continuous streams. The formation of capillary waves at the liquid-air interface located at the nozzle tip plays a critical role in determining which modes dominate resulting in either DOD or continuous jetting modes [9].

As shown in Figure 3, the movement of the thin silicone oil droplet for the microfluidic valve operation was precisely controlled by using the electrowetting technique. The nozzle was completely closed when the thin liquid-film was actuated

with a voltage of 400VDC and moved over the nozzle area. In addition, the microfluidic valve was kept open while the microfluidic ejector was running as shown in Figure 4.

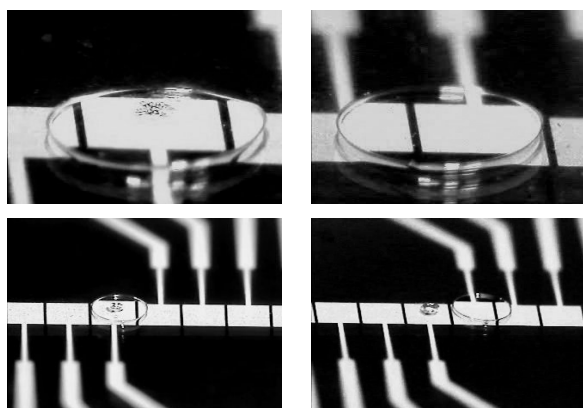


Figure 3. Images show that a thin liquid (silicone oil) film valve opens and closes the ejector nozzle by using eletrowetting technique.

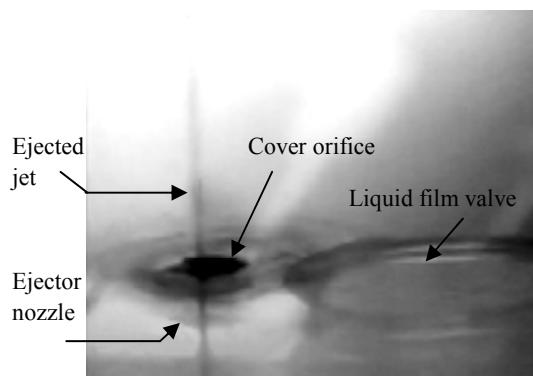


Figure 4. Photo taken by using strobing white LED shows an ejected jet (about  $50\mu\text{m}$  in diameter) passing through the top cover orifice

Since the silicone oil droplet and the hydrogel solution are immiscible with each other, no material exchange has been observed across the liquid-liquid interface. It was observed that for any given ejector, the nozzle ejecting the hydrogel solution completely clogged within a few hours when the valve was left open under ambient conditions and failed in any further ejection. On the other hands, a good quality of ejection was continuously achievable even after a standby period of 72 hours, when the nozzle was closed and protected by the liquid-film based microfluidic valve. The evaporation speed of ink fluids (water and hydrogels) and nozzle condition was summarized in Table 1. We believe that this technique can be extended to a wide range of micro-engineered hydrogels that are currently used in tissue printing.

As can be seen in Figure 5, fluorescence microscopy of the glass coverslips onto which the hydrogels were ejected revealed droplets of different sizes including larger agglomerates

of greater than  $500\mu\text{m}$ . Size of single ejected droplets ranged between  $10\text{-}30\mu\text{m}$ .

All ejection tests were repeated after every few hours to check the durability of the hydrogel ejectors by closing the microfluidic valve between tests thereby preventing evaporation.

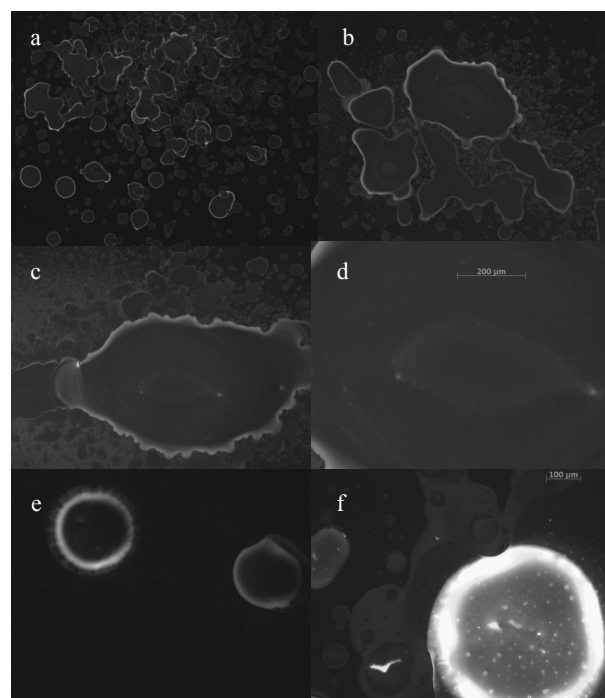


Figure 5. Ejected hydrogel(a-d:gelatin, e,f:collagen) with Rhodamine 6G & Acridin orange on glass slides using Fluorescence microscope.

Larger sized features as seen in every sub image of Figure 5 were due to the overlap of single ejected hydrogel droplets. Once ejected from the nozzle and upon reaching the target coverslip, the ejected hydrogel droplets began to crosslink at a faster rate due to the loss of liquid content through evaporation which is similar to the drying mechanism as seen in commercial inkjet printers. Also since no crosslinking agents that could otherwise lead to instantaneous hydrogel crosslinking were used on the substrate, overlapped ejected droplets simply coalesce into larger diameter features.

Further imaging and surface characterizations of the substrates onto which the hydrogel droplets are ejected would be required to determine the vertical growth of overlapped droplets. Since during these tests neither the substrates nor the piezo ejectors were connected to X-Y manipulation stages, ordered placement of ejected hydrogel droplets in defined paths as seen in the printing of 3D hydrogel scaffolds could not be achieved. Future testing using this technology would involve the use of manipulative stages for printing pre-defined hydrogel patterns as used in tissue printing setups elsewhere. At this point, further improvements in the microfluidic valve in terms of fabrication and material selection for immiscible liquids is being looked into which could possibly lead to a higher ejection quality.



Table 1. Evaporation speed data when the liquid-film based microfluidic valve is opened or closed.

Liquid-film valve (silicone oil)	Evaporation time of ink fluids stored in the ejector	
	D.I. water	Hydrogels
Close	N/A (> 30 days)	N/A (>72 hrs)
Open	25 min	Dried and Clogged in 1hr

## CONCLUSIONS

We have successfully demonstrated very reliable printing of hydrogels for a long time without any clogging problem in the microfluidic ejector. Electrowetting technique was used for the actuation mechanism to open and close the fluidic valve. The liquid-film based microfluidic valve built on the ejector using an environmentally friendly immiscible fluid was proven to be a very effective way to prevent evaporation of various volatile fluids from the air-liquid interface at the nozzle of the microfluidic ejectors. This mechanism could have high impacts on many applications requiring evaporation controlled ejection processes such as various inkjet-based printers including bio-ink printers for tissue printing.

## ACKNOWLEDGEMENTS

Authors would like to thank Dr. Luis Polo-Parada in the Department of Biological Engineering for his help in fluorescent imaging. This material is based upon work supported by the National Science Foundation under Grant No. ECS0901618.

## REFERENCES

[1] H.B Hsieh et al; "Ultra-High-Throughput Microarray Generation and Liquid Dispensing Using Multiple Disposable Piezoelectric Ejectors" J Biomol Screen 2004; 9; 85

[2] J.W. Kwon, H. Yu, Q. Zou and E.S. Kim "Directional droplet ejection by nozzleless acoustic ejectors built on ZnO and PZT" J. Micromech. Microeng. 16 (2006) 2697–2704

[3] S. Moon, S.K. Hasan, Y.S. Song, F. Xu, H.O. Keles, F. Manzur, S. Mikkilineni, J.W. Hong, J. Nagatomi, E. Haeggstrom, A. Khademhosseini, U. Demirci "Layer by Layer Three-dimensional Tissue Epitaxy by Cell-Laden Hydrogel Droplets" Tissue Engineering Part C: Methods

[4] N. Fedorovich, J. Alblas, J.R. de Wijn, W.E. Hennink, A.J. Verbout, and W.J Dhert, "Hydrogels as Extracellular Matrices for Skeletal Tissue Engineering: State-of-the-Art and Novel application in Organ Printing" Tissue Engineering Volume 13, Number 8, 2007

[5] D. Ben-David, T. Kizhner, E. Livne, S. Srouji "A tissue-like construct of human bone marrow MSCs composite scaffold support in vivo ectopic bone formation" J Tissue Eng Regen Med 2010; 4: 30–37

[6] A.Khademhosseini, R.Langer; "Microengineered hydrogels for tissue engineering." Biomaterials 28: 5087–5092.

[7] A. Khademhosseini, Y. Du, B. Rajalingam, P.Joseph "Microscale Technologies for Tissue Engineering;"

[8] V. Mironov, T. Boland, T. Trusk, G. Forgacs and R.R. Markwald, "Organ printing: computer-aided jet-based 3D tissue engineering." Trends Biotechnol.21, 157–161 (2003)

[9] Eric R. Lee Microdrop generation

## CONTACT

Riberet Almeida; Ph: +1 573-673-7735;  
rab5b@mail.missouri.edu

# CHARACTERIZATION OF COLLOIDAL SYSTEMS IN A STANDALONE PZT-GLASS CAPILLARY MICROFLUIDIC ULTRASONIC TWEEZER

M.K. Araz\* and A. Lal

SonicMEMS Laboratory, School of Electrical and Computer Engineering,  
Cornell University, Ithaca, New York, USA

## ABSTRACT

This paper presents an acoustic PZT-glass capillary actuator mechanism for the characterization of colloidal systems. This actuator enables monitoring of the cumulative effect of the nanoscale force interactions between many individual nanoparticles at the millimeter scale which can be tracked by conventional optics. Since the actuation is through acoustical radiation and streaming forces, optical, dielectric or magnetic properties of the materials do not interfere with the actuation method, enabling accuracy in the measurements with applicability to a wide range of samples with different ionic concentrations. In this paper we show that the effect of the ionic charges on silica beads can be measured by collective squeezing and expansion of bead collections.

## INTRODUCTION

Colloid characterization is used in many industrial applications such as pharmaceutical products, paints, inks, printing, ceramic casting, paper coating, solvent recovery, water purification, food industry, waste water treatment and disposal of radioactive waste [1]. Surface Plasmon Resonance of colloidal systems also plays a crucial role in biosensors at microscale. While in some applications long term stability of the colloidal system is the aim, in some cases destruction of the colloidal system is desired. Colloidal systems are stable due to counterbalancing of attractive and repulsive interactions present in the system such as; electrostatic, long range and retarded van der Waals, hydrodynamic and steric interactions. In most cases, electrostatic repulsion is the dominant interaction mechanism determining colloidal stability. Due to the many parameters affecting the surface charge and the surrounding ionic diffuse layer, and the shortcomings of the current theoretical models, characterization of the stability of the colloidal systems is mostly done experimentally in manufacturing.

In this paper a PZT(Lead Zirconate Titanate) driven glass capillary microfluidic actuator is used for the characterization of the colloidal systems. A picture of the device is shown in Figure 1. As a novel advantage, actuator mechanism enables monitoring of the cumulative effect of the nanoscale force interactions between many individual nanoparticles at the millimeters scale which can be tracked by simple optics. Acoustic radiation forces generated inside the microfluidic capillary enable collection of the colloidal structures at desired locations [2-3]. With the release of the acoustic forces particles collectively diffuse back to the medium. Through the monitoring of the collective diffusion behavior, the stability characteristic of the colloidal system is obtained. Since the actuation is done through acoustical forces, optical, dielectric or magnetic properties of the materials do not interfere with the actuation method, enabling accuracy in the measurements with applicability to a wide range of samples. There is no need of electrical contacts within the fluid inner-core, eliminating the need of calibration of electrode-fluid contacts for various samples (ionic, polar, non-polar, acidic, etc.), prevents bubble formation and makes the actuator mechanism usable for delicate biological samples and plasmonic biodetection.

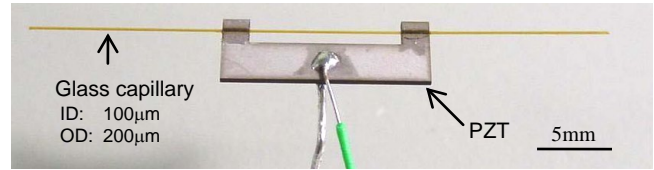


Figure 1. Picture of the PZT-glass capillary actuator. Capillary inner diameter is 100µm and outer diameter is 200 µm. Outside of the capillary is coated with polyimide enabling the flexibility of the glass capillary.

## COLLOIDAL BEHAVIOR AND THE SURFACE CHARGE

The term colloid can be defined as a system of two substances, in which one substance is distributed evenly in a discrete phase throughout the second substance of continuous phase. The dispersed materials and the continuous medium may be in gaseous liquid or solid phases. In this study, point of interest is given to the colloidal particles suspended in liquids, which is the most common type of colloidal system, and is relevant for micro and nanofluidic systems.

### Diffusion

Microscopic particles suspended in liquids exhibit Brownian motion due to the random momentum transfer of the colliding molecules of the medium they are suspended in. This random motion enables single particles to move, and in case of many particles leads to diffusion. Laws of diffusion were first formulated by Fick [4] and for  $N_0$  number of non interacting colloidal particles introduced to a medium at zero time and location,  $t=0$ ,  $z=0$ , the particle distribution,  $n(z,t)$ , is given by

$$n(z, t) = \frac{N_0}{\sqrt{4\pi Dt}} e^{-(z-z_0)^2/4Dt} \quad (1)$$

where  $D$  is the diffusion constant. Theoretically derived by Einstein [5],  $D$  is given by

$$D = \frac{kT}{6\pi\eta a} \quad (2)$$

where  $k$  is the Boltzmann constant,  $T$  is the temperature in Kelvin,  $\eta$  is the viscosity of the medium and  $a$  is the particle radius. This expression is valid for low-concentration of solute colloids. For a particle having size of 500 nm, suspended in water, at room temperature, the diffusion constant is expected to be around 0.85 µm<sup>2</sup>/s which is in the order of experimentally obtained values given in the literature [6].

Equations 1 and 2 explain diffusion phenomena for non-interacting particles. However, this is not a very common scenario as usually particles undergo hydrodynamic, Van der Waals and electrostatic interactions.

### Surface Charge and the Zeta potential

Many particles bear surface charges when they are suspended inside a fluidic medium. Usually this phenomenon stems from capturing of ions present inside the fluid, or losing some surface ions present on the particle or both. Due to this ionic exchange, as shown in Figure 2, an electrical double layer forms in the fluid particle boundary region. Inner ions in the double layer are attached to the particle surface and move with it, and they form the

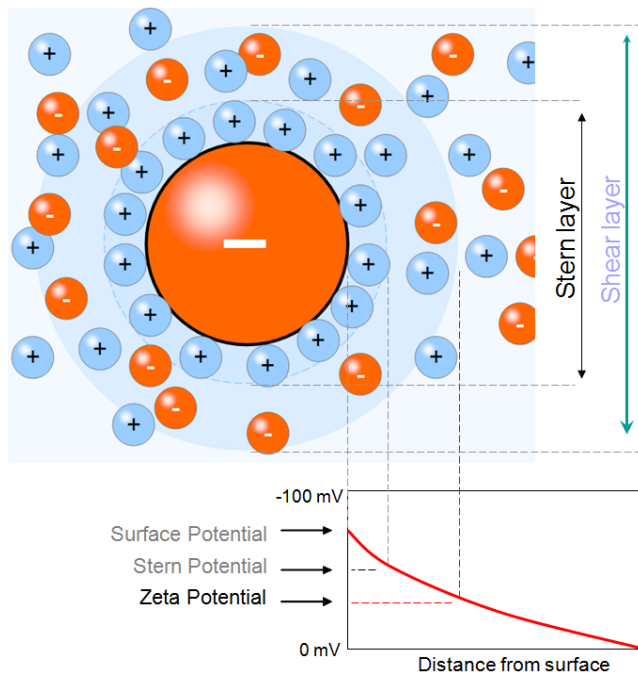


Figure 2. Electrostatic behavior of a nanoparticle in an ionic fluid is determined by the ionic double layer and the surrounding shear layer. Zeta potential value at the end of the shear layer is the only measurable potential defining the characteristics.[8]

Stern layer [7]. Outside the Stern layer, remaining counter ions form a diffuse region which defines the shear layer in which particle moves with respect to the stationary fluid molecules. The electric potential at this shear layer is called the zeta potential ( $\zeta$ ) which defines the electrokinetic properties of the particle. Being the only measurable quantity related to the charge information of the particle inside the fluid, zeta potential is used in place of surface potential in analytical calculations. Zeta potential can be obtained from the electrophoretic mobility of the particles by formula

$$\zeta = \frac{3\eta v}{2\varepsilon E f(\kappa a)} \quad (3)$$

where  $\eta$  is the viscosity,  $v$  is the particle velocity,  $\varepsilon$  is the dielectric constant of the medium,  $E$  is the electric field, and  $f(\kappa a)$  is a constant number, and  $a$  the radius of the particle; in this case  $f(\kappa a)$  is around 1.5 [7].  $\kappa^{-1}$  is the Debye (diffuse) layer thickness and is related to the ionic strength of the solution. In our experiments Zetasizer Nano Z series by Malvern Instruments is used to characterize zeta potential of the particle samples.

The interaction potential between two colloidal particles is modeled by DLVO (Derjaguin, Landau, Verwey and Overbeek) theory, which is an approximation obtained by taking attractive van der Waals interactions and double layer electrostatic repulsion into consideration and given by

$$U = -\frac{A_{12}a}{12h} + \pi\varepsilon\zeta^2 a e^{-\kappa h} \quad (4)$$

where the first term represents the attractive van der Waals interaction and the second term electrostatic repulsion. In the formula,  $A_{12}$  is the Hamaker constant and  $h$  is the separation between two particles [7].

While this formula has been tested for two particle systems in well defined media extensively, practical applicability to experiments is mostly limited. This is first due to existence of many particles in a colloidal system and secondly many parameters such as zeta potential and the Debye length depend strongly in the

pH and the ionic concentration of the media as well as the media type. In this regard, zeta potential becomes one of the key parameters defining colloidal stability in experimental studies. By changing the pH of the medium, colloidal stability can be altered drastically due to the change in the zeta potential. Colloidal particles which have zeta potential value of between  $\pm 30$  mV tend to aggregate as the electrostatic repulsion cannot balance the attractive forces.

Because of the challenges mentioned above, experimental characterization of colloidal systems is an inevitable step in the product development or research. Characterization can be costly due to the long time span of experiments and the requirement of bulky and expensive equipment. For example, from early development to FDA approval timeline of a pharmaceutical product can take up to 10-20 years and cost hundreds of millions of dollars. While the significant portion of this effort goes into clinical trials, manufacturing of the drugs with proper delivery methods add also considerably to the cost and time spent.

## EXPERIMENTAL RESULTS

### Fast collective diffusion behavior

As shown in Figure 1, microfluidic actuator consists of a polyimide coated fused silica capillary (ID: 100 $\mu$ m, OD: 100 $\mu$ m, PolyMicro Technologies) which is adhesively bonded to a laser cut PZT-4 plate. PZT plate is driven at one of the resonance frequencies of the flexural modes of the cylindrical capillary in the 30kHz-2MHz regime. Flexural modes of the capillary generate sub-wavelength stationary acoustic waves inside the capillary at vibration maxima. As shown in Figure 3, these stationary acoustic waves lead to acoustic radiation forces at the center of vibration maxima [3]. These acoustic forces act as periodic planar centrifugal fields collecting colloidal particles at preferred locations. Collection of 3  $\mu$ m size particles shown in Figure 3 is in agreement with the theoretically predicted force field. Details of the fluid-structure coupling and the analytical model will be presented in a future reference (also given in [3]).

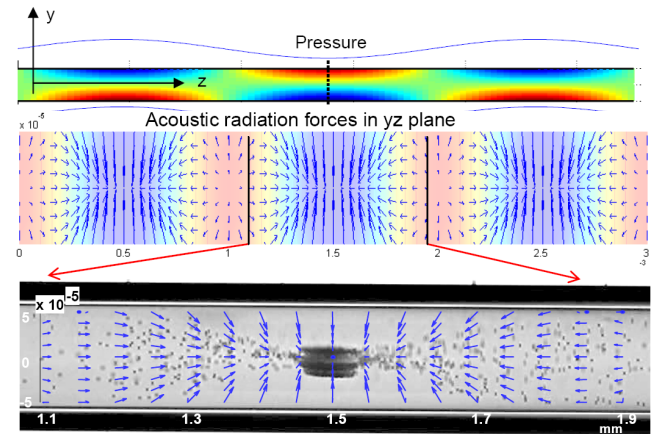


Figure 3. Flexural vibrations generate sub-wavelength stationary acoustic fields (top) which lead to acoustic radiation forces at the vibration maxima (middle). Microscope image shows theoretical forces and the collection of 3 $\mu$ m beads suspended in the fluid enclosed in the capillary at a vibration maxima (bottom).

Size of the colloidal nanoparticles (Kisker Scientific, Bangs Laboratories) used in the experiments presented here are 500 nm silica nanoparticles dispersed in de-ionized water. Since the glass capillary is transparent, collection and the dispersion of the regular nanoparticles can be monitored through light scattering. Experimental setup sketched in Figure 4 eliminates the necessity of

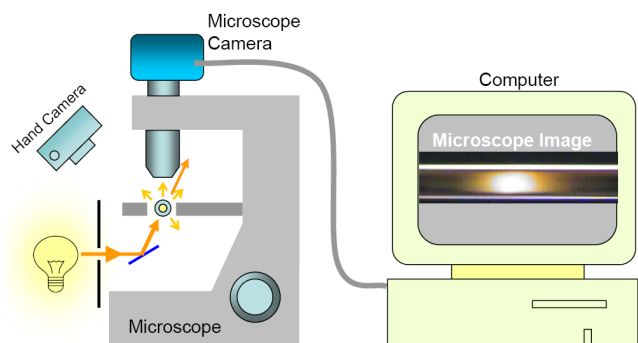


Figure 4. Schematics showing the experimental setup related to the imaging. Part of the light scattered from the colloidal particles inside the capillary is collected at the microscope objective and transferred to the computer through the microscope digital camera.



Figure 5. Hand held camera images of the actuator with 500nm silica beads suspended in DI water. Locations where there are silica nanobeads shine due to the scattering of the light coming from the bottom. Top: before the actuation, beads are dispersed. Middle: Nanoparticles are collected. Bottom: Actuation is off and the collective diffusion of the nanoparticles is observed (650 times faster than expected diffusion rate for individual beads).

fluorescent labels for the monitoring of the colloidal particles. Hand held camera images displayed in Figure 5 show that, results are visible to eye without any magnification. Before the actuation, a continuous scattering through the capillary is observed. After actuation is turned on, light is scattered only at certain locations where silica particles are focused.

After the collection of particles, with the turning off the actuation, particles tend to diffuse back to their original dispersed state over time. This expansion can be seen in hand held camera images in Figure 5 and timed microscope images shown in Figure 6. From the series of images shown in Figure 6, it is possible to correlate the scattered light intensity with the particle number density. Since the capillary inner diameter is small, particle concentration assumed to depend linearly on the light intensity.

The graph displayed on top in Figure 7 shows the normalized particle volume fraction obtained from intensity distributions. As the particles disperse with time, spatial particle volume fraction decreases.

Here, the observed collective diffusion constant of the collected 500 nm silica particles ( $550\mu\text{m}^2/\text{s}$ ) is found to be about 650 times

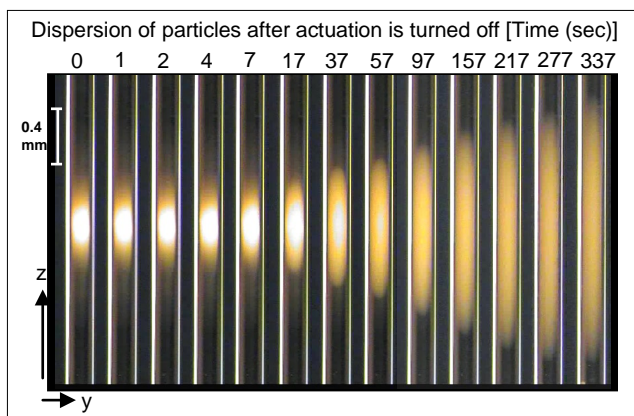


Figure 6. Following the collection of particles when the actuation is turned off, particles spread back inside the capillary. Particle size density or volume fraction is correlated to the intensity of the light scattered by the colloidal silica nanobeads.

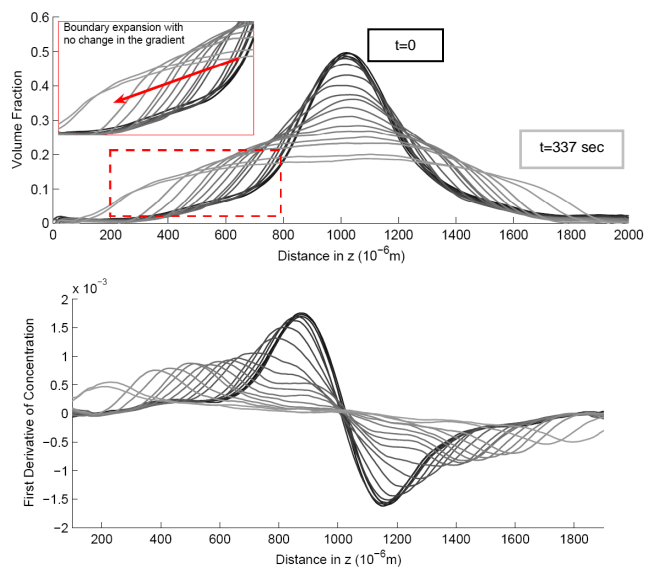


Figure 7. Top: Change in the volume fraction over time after the release of the acoustic force. Boundary moves 650 times faster than the expected diffusion constant of the 500nm nanoparticles. Bottom: Derivative of the concentration profile; peaks indicate the location of the boundary at a specific time.

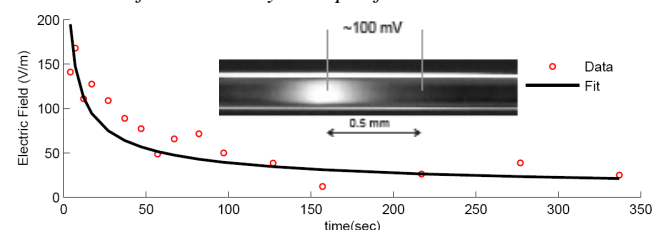


Figure 8. Fast expansion of the concentrated colloid system is associated with the self generated macroscopic electric field. From the velocity of the moving boundary, magnitude of the electric field, which gives the charged particles their momentum, can be obtained.

higher than the expected diffusion constant of individual particles ( $0.85\mu\text{m}^2/\text{s}$ ), which gives a measure of the collective diffusion behavior of the colloidal system. This fast collective diffusion behavior cannot be explained by regular diffusion or built up of

osmotic pressure due to the particle collection, and can only be attributed to electrostatic effects generated due to the collection particles in a small volume. Through the monitoring of the moving boundary in the volume fraction plots in Figure 7, which are obtained from scattered light intensity, built in electric field values causing this fast collective diffusion behavior are calculated. Velocity of the expansion at the beginning of radiation force removal is in the order of tens of  $\mu\text{m/s}$  which correspond to macroscopic electric field values around  $200\text{V/m}$ . Electric field values calculated from experimental data over the course of expansion is given in Figure 8. This high electric field values are reached because of the fact that all particles, initially dispersed inside the capillary over a region of few millimeters, are confined to a range of  $400\ \mu\text{m}$ . This collection raises the particle volume fraction from 0.11 to about 0.6 which is very close to the close packed crystal structure in which all particles are packed being in touch with their closest neighboring particles. In this regard the electrical potential built up can be attributed with the sedimentation potential obtained during the gravitational or centrifugal sedimentation experiments. Here since the particles are confined to a smaller microscopic region results are amplified.

### Acoustic focusing at various pH values

As mentioned above, zeta potential depends on the pH of the solution. Figure 9 shows the actual zeta potential measurements of 300 nm and 500 nm silica nanoparticles in solutions having various pH values. Measurements are performed in a Zetasizer Nano by Malvern Instruments. It is observed that as the acidity of the solution increases (decreasing pH), zeta potential around the particle starts to decrease. This is due to the collection of  $\text{H}^+$  ions around the negatively charged particles. At pH levels below 4, concentration of  $\text{H}^+$  ions are high enough to even reverse the polarity of the zeta potential at the diffuse layer. When zeta potential is between 30 mV and -30 mV, it has been known that electrostatic repulsion cannot balance the attractive forces and flocculation is expected. In this case, some nanoparticles start to stick to each other and the effective particle size gets higher. Particle size characterization experiments reveal that, for instance at low pH values, rather than a single peak at 500 nm, a broader spectrum with peaks at higher values such as 700 nm or 1200 nm are observed. This change can also be observed in PZT-glass capillary actuator without any need of particle size or zeta potential measurement. As shown in Figure 10, collection of 500 nm silica particles at different pH values give different particle distributions due to charge effects. In the top image, at pH 7, 500 nm silica particles collect in a cloudy pattern where as at pH 3, there are narrower and denser collections at the center. This is due to the fact that as particles aggregate, they feel a bigger radiation force which leads to a higher collection efficiency. Hence, this device enables the monitoring of the diminished colloidal stability.

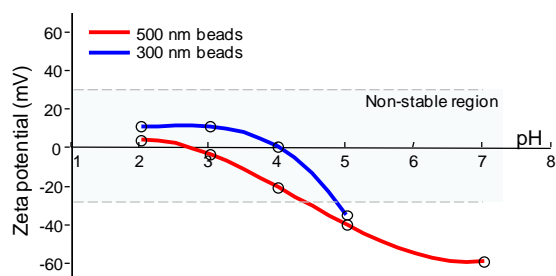


Figure 9. Zeta potential measurements of 300 nm and 500 nm silica beads suspended in aqueous solution of different pH levels.

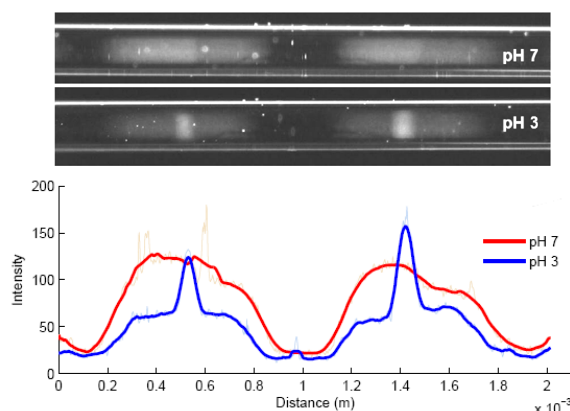


Figure 10. Collection of 500 nm nanoparticles. The top image shows the particles suspended in a pH 7 solution. The middle image shows particles suspended in a pH 3 solution. Plotted at the bottom is the intensity of the scattered light measured at the central axis along the capillary.

### CONCLUSIONS

A possible use of PZT-glass capillary actuator for the characterization of the colloidal systems is introduced. The actuator presented here may replace bulky centrifugal systems or eliminate time consuming sedimentation experiments. In addition results can be obtained very fast with low sample volume requirement (0.6 microliters). Since the amount of power consumed by the actuator is very low, portable battery operated hand held devices are also possible. Even the internal diameter of the capillary is 100 micrometers; results are observable to the naked eye and can be monitored in detail with a regular hand held digital camera or a document scanner. The capillary used is the standard fused silica capillary and can be integrated with wide range of other larger or same size bio analytical tools such as HPLC or other microfluidic systems. Device can be used to monitor behavior of the colloids at various pH values. In the analysis of the colloidal systems, since the theory can deviate from experimental results especially in high salt concentrations or acidity, direct experimental observation is always performed in product development. In this regard, PZT-glass capillary actuator may be a fast, reliable and cost efficient solution for the characterization of colloidal stability problem.

### REFERENCES

- [1] D.H. Everett, *Basic Principles of Colloid Science*, Royal Society of Chemistry, 1988
- [2] C.H. Lee, A. Lal, *Low-Voltage High-Speed Ultrasonic Chromatography for Microfluidic Assays*, Hilton Head, 2002
- [3] M.K. Araz, *Generation of Sub-wavelength Acoustic Stationary Waves in Microfluidic Platforms: Theory and Applications to...*, Ph.D. Thesis, Cornell University, 2010.
- [4] A. Fick. On liquid diffusion. *Phil. Mag.*, 10:30, 1855.
- [5] A. Einstein. *Investigations on the Theory of the Brownian Movement*. Dover Publications, 1956.
- [6] B. Rieger, H.R.C. Dietrich, L.R. van den Doel, and L.J. van Vliet. Diffusion of Microspheres in Sealed and Open Microarrays. *Microscopy Res and Tech*, 65:218–225, 2004.
- [7] I.D. Morrison and S. Ross. *Colloidal Dispersions: Suspensions, Emulsions and Foams*. Wiley, 2002.
- [8] <http://www.malvern.com/>

### CONTACT

\*M.K. Araz, tel: +1-607-255-1815; mka22@cornell.edu

# ELASTOMERIC RESERVOIR FOR MEMS-BASED TRANSDERMAL DRUG DELIVERY SYSTEMS

Cara T. Smith<sup>1,2</sup>, Pinghung Wei<sup>2,3</sup>, Mehran Mojarad<sup>4</sup>, Michael Chiappetta<sup>4</sup>, Babak Ziaie<sup>2,3</sup>, and Masaru P. Rao<sup>5\*</sup>

<sup>1</sup>School of Mechanical Engineering, Purdue University, West Lafayette, Indiana, USA

<sup>2</sup>Birck Nanotechnology Center, Purdue University, West Lafayette, Indiana, USA

<sup>3</sup>School of Electrical and Computer Engineering, Purdue University, West Lafayette, Indiana, USA

<sup>4</sup>Eli Lilly & Company, Pharmaceutical Delivery Systems, Indianapolis, Indiana, USA

<sup>5</sup>Department of Mechanical Engineering, University of California, Riverside, California, USA

## ABSTRACT

While MEMS-based drug delivery research often strives towards development of tightly-integrated device solutions, the authors present an alternate conception based upon a novel, decoupled drug reservoir approach. The salient features of this modular reservoir approach, which is the focus of this report, include an expandable PDMS enclosure within which the drug formulation is stored, an integrated rigid frame to provide mechanical integrity, and a vapour barrier to minimize diffusion-based losses. The design and fabrication of the reservoir is presented herein, as are favorable results from preliminary characterization of its fluid filling, retention, and extraction performance.

## INTRODUCTION

The proposed reservoir is intended to serve as a key component in a MEMS-based transdermal drug delivery system that seeks to enhance patient acceptance and compliance with parenteral drug therapies. While such therapies are intended to improve both quality and duration of life for those with chronic disease, it is often found that patients do not follow their prescribed regimens, especially when frequent dosing is required [1]. For example, noncompliance is often observed in insulin therapy for the treatment of diabetes, which affects an estimated 170 million people worldwide [2]. While poor management of diabetes can lead to a variety of complications including vision impairment, heart disease, and neuropathy, upwards of 1/3 of patients with type 2 diabetes nonetheless report aversion to insulin injections, due to fear of pain from needles, and 44% express lack of confidence in adhering to insulin therapy requirements [3]. Consequently, need exists for development of new delivery systems and strategies that address these issues, thus providing potential for increased patient compliance and overall health.

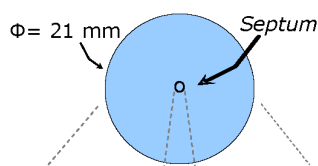
There currently exists a limited number of ways to treat diabetes with insulin, including administration via syringe and vial, pre-filled pen injectors, and insulin pumps [4]. Insulin pumps offer automated delivery, thus providing greater sense of freedom relative to manual injection, as well reduced demand upon the patient for self-management of their disease. However, insulin pumps are often found to be bulky, inconvenient to use, and hard to conceal. Miniaturized MEMS-based insulin pumps may provide a means for addressing these issues by offering greater convenience and discretion, due to decreased size. Moreover, when coupled with minimally invasive, microneedle-based, transdermal delivery, opportunity exists for mitigating needle anxiety and apprehension, as well as increasing ease of use.

These perceived benefits have driven significant interest in development of integrated MEMS-based components and systems for transdermal drug delivery. For example, of direct relevance to the current report, a number of compact, highly-integrated devices that rely on microneedle-based delivery have been recently reported [5-7]. However, only limited consideration has been given thus far to issues associated with filling and storage of drug formulations within such devices, particularly with regard to compatibility with conventional pharmaceutical practices. To this end, the authors propose that decoupling of the reservoir from the delivery system may, in fact, provide greater flexibility with respect to sterilization, plant-filling, delivery, mass production and manufacturing cost. Herein, we describe the design, fabrication, and preliminary characterization of a reservoir device based on this modular approach.

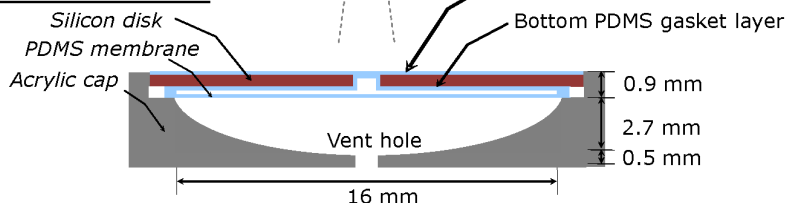
## RESERVOIR DESIGN

The reservoir design, shown schematically in Figure 1, is comprised of a polydimethylsiloxane (PDMS) membrane and gasket enclosure with a centralized septum. An integrated rigid frame comprising of a silicon disk and vented acrylic cap provides

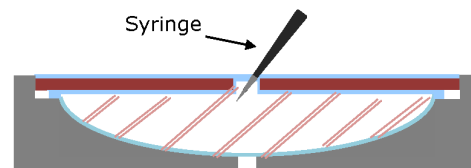
### Top view



### Cross section view



### Cross section with fluid filled membrane



### Cross section with polyimide seal

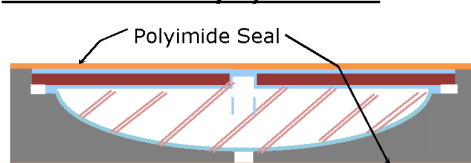


Figure 1: Reservoir schematic and filling process.

mechanical support and protection for the enclosure and its contents, as well as reliable interfacing with the aforementioned transdermal drug delivery system. The specific details of this system are not presented here, but include a hollow microneedle for septum penetration, a micropump for metered extraction of reservoir contents, and hollow microneedles for minimally invasive transdermal drug delivery.

The reservoir is intended to serve as a single-use cartridge that can be sterilized, filled, and stored long-term prior to assembly into the delivery system. Although the reservoir is currently filled manually via septum penetration with a syringe, its design is intended to provide future compatibility with conventional automated pharmaceutical vial filling operations. Final fill volume is fixed by the expansion of the elastic membrane to the inner dimensions of the cap. While the reservoir has been initially designed to contain 400  $\mu\text{l}$ , other fill volumes can be easily accommodated with slight design modifications. After filling, the syringe is removed and the septum seals upon itself, thereby retaining the reservoir contents. Polyimide sealing layers are then applied to minimize diffusion-based fluid loss and ensure hermeticity.

The elastomeric and vapor-permeable nature of the PDMS membrane provides many advantageous features, including: a) membrane conformance to content volume; b) bubble-free dead-filling and drug storage; and c) mild internal pressurization to aid drug extraction ( $\sim 10$  kPa), due to strained membrane restoring force. Collectively, these features maximize reservoir content extraction, facilitate priming of the delivery system, and minimize overall reservoir size, complexity, and cost. Furthermore, the widespread use of silicone in pharmaceutical processing suggests potential for drug formulation stability during long-term storage, while membrane and cap transparency enables inspection for quality control and patient verification. Finally, reservoir decoupling allows sterilization without concerns for affecting other drug delivery system components, and also facilitates independent optimization of design, materials, and fabrication for each system component.

## MATERIALS AND METHODS

### Fabrication

The reservoir device is comprised of three primary components that are fabricated separately and then assembled into the final device. The first of these is the interface plate, which is fabricated by double-side molding of PDMS around a silicon disk. This interface plate serves as the fixed wall of the drug enclosure, as well as a rigid member that protects the contents and facilitates interfacing with the drug delivery system. The second component is the membrane, which is fabricated by PDMS molding and is then attached to the interface plate using uncured PDMS as a bonding adhesive. The membrane serves as the expandable wall of the drug enclosure, providing direct conformance of the enclosure to the content volume and thus minimizes dead volume and maximizes extraction efficiency. Finally, the third component is a vented acrylic cap, which is fabricated via conventional machining techniques. This cap serves to define the final fill volume of the enclosure and acts as a vapor barrier to prevent diffusion-based loss. It also provides protection for the membrane and enclosure contents and ensures that the device possesses sufficient rigidity to withstand handling during filling, packaging, and assembly into the drug delivery system by the patient.

Details of the reservoir fabrication process are schematically illustrated in Figure 2. The process begins with photolithographic patterning and deep etching of 100 mm diameter silicon wafers (Step 1) to create 500  $\mu\text{m}$  thick, 21 mm diameter disks that serve as backbone of the interface plate. Similar processes are then used to define silicon mold masters (Step 2a), which are then coated in a vacuum chamber with trichloro(3,3,3-trifluoro-propyl)silane to form a release layer. PDMS-based molds for the upper and lower faces of the interface plate are then made by pouring uncured elastomer (Sylgard 184, Dow Corning) into the silicon mold masters (Step 2b). The uncured molds are placed in a vacuum desiccator for 1 hr to remove bubbles, followed by oven-curing for 30 min at 120  $^{\circ}\text{C}$ . Upon removal from the mold masters, the PDMS-based molds are coated with Parylene C (thickness  $\sim 2\mu\text{m}$ ), followed by silane coating. The former enhances the mechanical integrity of the molds, while the latter facilitates demolding.

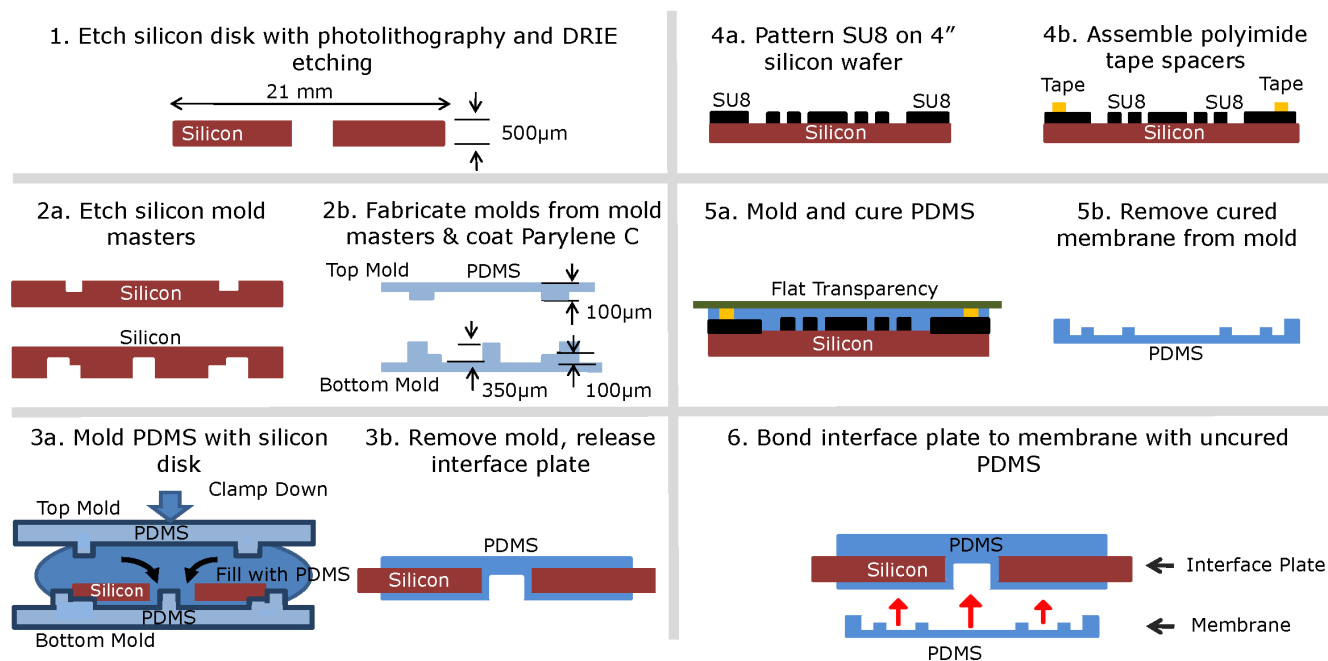


Figure 2: Reservoir fabrication process.

Next, the interface plate is double-side molded by filling the bottom PDMS mold with uncured PDMS, followed by placement of the silicon disk, further filling with uncured PDMS, and placement of the upper PDMS mold (Step 3a). The stack is then mechanically clamped and oven cured for 30 min at 120 °C. After curing is completed, the upper and lower molds are peeled away from the interface plate, and excess PDMS is trimmed from the boundaries (Step 3b).

Molding for the PDMS membrane is fabricated by photolithographic patterning of 100 μm thick SU8 negative photoresist (SU8 2100, MicroChem Corp.) on a 100 mm diameter silicon wafer (Step 4a). This mold defines the membrane perimeter walls, as well as an array of cylindrical standoff posts (50 μm diameter, 100 μm height, 100 μm pitch) on the inner face of the membrane, which serve to prevent irreversible adhesion of the membrane to the opposing enclosure surface. Small strips of polyimide tape (KPT2-4, 2 mil Kapton HN with 1.5 mil adhesive, Bertech-Kelex) are then placed at the perimeter of the mold (Step 4b) to serve as spacers that define the membrane thickness. The mold is then coated with a silane release layer.

The PDMS membrane is fabricated by filling the SU-8 membrane mold with uncured PDMS (Step 5a), followed by degassing in a vacuum desiccator for up to 1 hr. A standard transparency film is then placed on the uncured PDMS, followed by a blank silicon wafer, which serves as the upper part of the mold to ensure membrane planarity and thickness uniformity. The stack is then clamped and cured on a hot plate for four (4) hours at 60 °C, followed by demolding (Step 5b). Once the membrane has been demolded, uncured PDMS is applied to the contacting surfaces at the perimeter to serve as an adhesive, and the membrane is manually aligned and brought into contact with the interface plate (Step 6). The reservoirs are then oven cured to complete the bonding process. Once cured, the acrylic cap is attached and the assembled reservoir device is filled by penetrating the septum of the interface plate with a fine gauge needle (32 g) attached to a syringe. Finally, the upper and lower faces of the device are sealed by applying polyimide tape.

### Fluid Retention

The fluid retention performance of the filled reservoir devices was evaluated to provide preliminary indication of their potential for use in long-term storage applications. Retention performance was evaluated over a 3 week period using deionized water as a drug formulation analogue. Devices with and without the acrylic cap were tested, to determine the extent to which the caps mitigated vapor-based fluid loss through the membrane. Each device type was tested at three different storage temperatures to simulate a range of conditions that might be reasonably encountered in service, including refrigerated storage (4 °C), room temperature storage (21 °C), and extended exposure to body temperature (37 °C). Five (5) devices of each type were tested and were weighed daily to determine the amount of fluid loss.

### Fluid Extraction

The fluid extraction performance of the filled reservoir devices was evaluated to provide preliminary indication of their potential to efficiently deliver the majority of their contents. Extraction performance was evaluated by penetrating the septum of filled, uncapped devices with a 30 gage needle connected to a syringe. The contents of the reservoirs were then manually withdrawn by retracting the syringe plunger. Six (6) devices were

tested and the extracted fluid volumes were compared to the initial filled volumes to determine extraction efficiency.

## RESULTS AND DISCUSSION

Photographic images of completed and filled reservoir devices are shown in Figure 3. The integrity of the bonded interface between the membrane and the interface plate is apparent, as is the significant strain capability of the PDMS-based membrane. Although not shown here, additional experiments seeking to identify failure mechanisms associated with overfilling demonstrated that fill volume (in absence of the cap) was most often limited by delamination of the bonded interface between the membrane and the interface plate, typically at volumes well in excess of the design specification. There were no failures of devices filled to design specification, aside from those with clear manufacturing defects, e.g. incompletely bonded membrane or bubbles present in the membrane. This is as expected, since the design strain (~0.08) is well below the failure strain of PDMS ( $\gg 0.5$ ) [8], thus demonstrating the utility of this material for the current application with regard to mechanical performance.

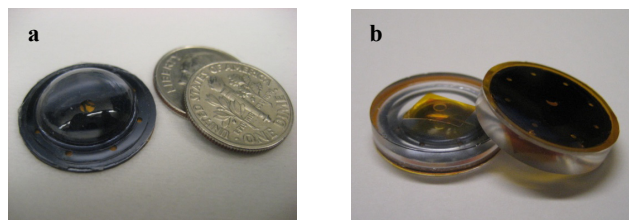


Figure 3: Devices filled with de-ionized water (a) without cap and (b) with cap and polyimide seals.

### Fluid Retention

Fluid retention performance over a period of three (3) weeks under varying storage conditions for both capped and uncapped devices is shown in Figure 4. For each storage condition, devices without caps were observed to have higher fluid loss rates, as would be expected, given the high vapor permeability of PDMS. Moreover, in both device types, fluid loss rates were observed to increase with increasing temperature, as would be expected due to increased kinetics and thus increased atomic mobility. Finally, fluid loss rates were observed to be linear in all cases, regardless of internal fluid volume. The observation of negligible fluid loss in capped devices under refrigerated storage conditions is encouraging, since such storage conditions are required for many drug formulations. However, the increased losses observed at elevated storage temperatures indicate a need for further device refinement to ensure storage reliability under adverse conditions.

### Fluid Extraction

Fluid extraction performance via manual withdrawal from six devices is shown in Table 1. High extraction efficiency is observed for all devices tested, ranging from 92.6% to 99.0% with average value of 96.1% (SD= 2.3). This can be primarily attributed to the minimal initial dead volume of the reservoir design, as well as the elasticity of the PDMS membrane, which precludes vacuum-induced inhibition of extraction by contraction during reservoir draining. Moreover, internal pressurization produced by the restoring force of the strained membrane further aids extraction. Although not shown here, additional experiments have demonstrated that measured internal pressures are in reasonable agreement with those predicted by theory. The demonstration of high extraction efficiency in these devices is encouraging, since



this is a key factor in minimizing overall device size and waste of drug formulation.

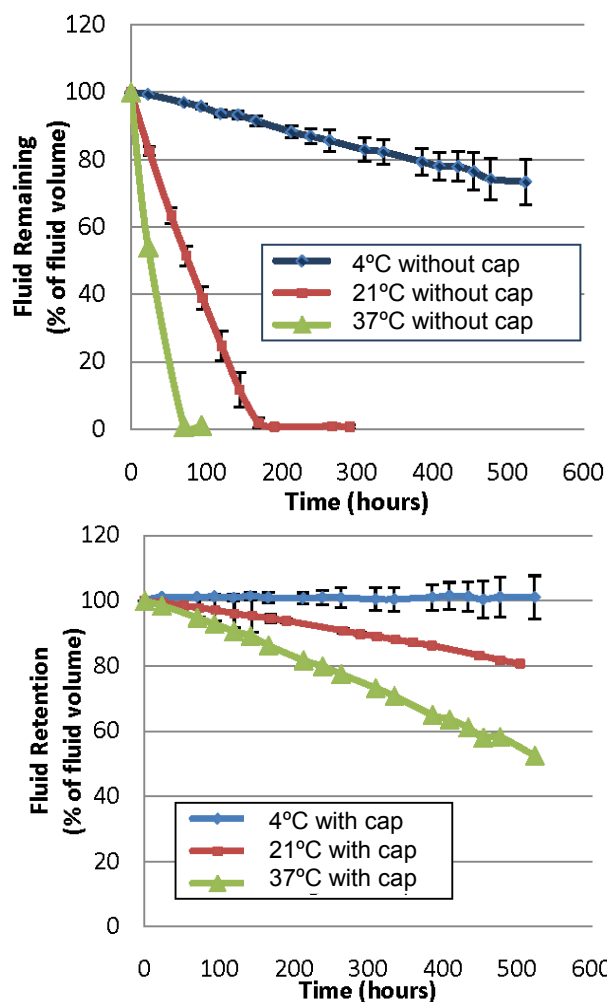


Figure 4: Fluid retention performance of reservoir devices stored at 4 °C, 21 °C, and 37 °C, without caps (top), and with caps (bottom) over a period of 3 weeks.

Table 1: Fluid extraction results.

Reservoir Number	Initial Liquid Volume ( $\mu\text{L}$ )	Extracted Liquid Volume ( $\mu\text{L}$ )	Liquid Extraction (%)
1	365	338	92.6
2	374	364	97.3
3	394	372	94.4
4	372	357	96.0
5	339	329	97.1
6	386	382	99.0
Average Fluid Extraction (%)		96.1	
Standard Deviation (%)		2.3	

## CONCLUSIONS

The modular reservoirs described herein offer a unique approach for drug storage within MEMS-based drug delivery systems. They have demonstrated good delivery characteristics and long-term fluid storage potential, as evidenced by capability for reproducible delivery of over 95% of their contents, as well as negligible fluid loss under refrigerated storage conditions, which is

required for many drug formulations. However, validation of sterility and stability of actual drug formulations within the reservoirs under pharmaceutically-relevant storage durations is needed. Moreover, device functionality has yet to be evaluated within the context of the transdermal drug delivery system within which the reservoir will operate. Finally, although the materials and fabrication process used for the reservoirs have proven sufficient for current needs, consideration of alternate materials and fabrication processes may be ultimately required to assure scalability to low-cost/high-volume manufacturing.

## ACKNOWLEDGEMENTS

The authors acknowledge Eli Lilly & Company, Pharmaceutical Delivery Systems, for the funding of this research. The authors also acknowledge the staff of the Birk Nanotechnology Center at Purdue University for their help with equipment, supplies, and processes, in particular John Coy, Hassan Sharif, Geoff Gardner, Jeff Grau, and Ira Young.

## REFERENCES

- [1] J. Cramer, R. Rosenheck, G. Kirk, W. Krol, J. Krystal, "Medication Compliance Feedback and Monitoring in a Clinical Trial: Predictors and Outcomes", *Value in Health*, 6 (2003), pp. 566-573.
- [2] S. Wild, G. Roglic, A. Green, R. Sicree, H. King, "Global Prevalence of Diabetes: Estimates for the Year 2000 and Projections for 2030", *Diabetes Care*, 27 (2004), pp. 1047-1053.
- [3] W.H. Polonsky, S. Guzman, L. Villa-Caballero, S. Edelman, "Psychological Insulin Resistance in Patients With Type 2 Diabetes: The Scope of the Problem", *Diabetes Care*, 28 (2005), pp. 2543-2545.
- [4] A.W. Brown, "Clinicians' Guide to Diabetes Gadgets and Gizmos", *Clinical Diabetes*, 26 (2008), pp. 66-71.
- [5] B. Stoeber, D. Liepmann, A. Mokhtari, U.O. Häfeli, "In vivo evaluation of a microneedle-based miniature syringe for intradermal drug delivery", *Biomedical Microdevices* (2009).
- [6] N. Roxhed, B. Samel, L. Nordquist, P. Griss, G. Stemme, "Compact, Seamless Integration of Active Dosing and Actuation with Microneedles for Transdermal Drug Delivery", the IEEE 19th International conference on Micro Electro Mechanical Systems (MEMS 2006).
- [7] S. Park, Y. Jang, H.C. Kim, K. Chun, "Fabrication of Drug Delivery System with Piezoelectric Micropump for Neural Probe", the 23rd International Technical Conference on Circuits/Systems, Computers and Communications (ITC-CSCC 2008), pp. 1149 - 1152.
- [8] F. Schneider, J. Draheim, R. Kamberger, U. Wallrabe, "Process and material properties of polydimethylsiloxane (PDMS) for Optical MEMS", *Sensors and Actuators A*, 151 (2009), pp. 95-99.

## CONTACT

\*M. P. Rao, tel: +1- 951-827-5870; [mp rao@engr.ucr.edu](mailto:mp rao@engr.ucr.edu)

# FLOW RATE INSENSITIVE THERMAL CONDUCTIVITY DETECTOR

B.C. Kaanta<sup>1</sup>, H. Chen<sup>2</sup>, and X. Zhang<sup>1\*</sup>

<sup>1</sup>Boston University, Boston, MA, USA

<sup>2</sup>Schlumberger Doll Research, Cambridge, MA, USA

## ABSTRACT

We present a novel thermal conductivity detector design in which output is minimally affected by changing flow rates in a microchannel. In gas chromatography systems, pressure fluctuations can result in false peaks and an unstable baseline, reducing the systems limit of detection. Furthermore, ramping the temperature of a separation column, a method used in many chemical separations, changes the viscosity and therefore the flow rate of the carrier gas, resulting in an unstable baseline. Therefore, the development of a flow rate invariant detector is extremely important in reducing the complexity and increasing the portability of gas chromatography systems.

## INTRODUCTION

### $\mu$ Gas Chromatography

Rapid detection of gas phase chemicals is critical in a number of wide-ranging applications, such as environmental monitoring, industrial process control, public safety and point of care health services. The miniaturization of gas chromatography (GC) devices has greatly increased the portability and the number of applications for this powerful analytical tool. However, further advancements can be made to increase the simplicity and portability of these systems.

Gas chromatography systems make it possible to identify and quantify compounds of interest by using a column to separate individual components in space and time. The sample is transported along the length of the separation column in a carrier gas, commonly helium. Interaction between the sample and a stationary phase in the column physically delays the elution of the components to different degrees based on their chemical properties. Temperature ramping is often used to increase the speed of elution of heavier chemical components [1, 2]. These separated gas components are subsequently passed through a detector and quantified.

Traditionally, carrier gas flow perturbations in a thermal conductivity detector's (TCD) signal has been accounted for by using a second TCD as a reference cell. However, this can double the consumable requirements (such as carrier gas) and the number of fluidic connections, as well as introducing numerous additional potential sources of error. Ideally, a TCD should not be affected by changing flow velocity.

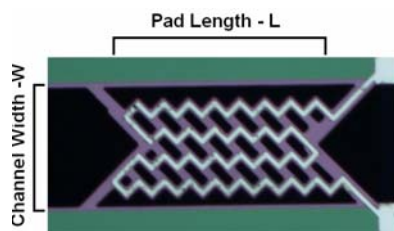


Figure 1: Single element  $\mu$ TCD. Power is applied to device and only the average temperature over the whole length of the pad can be detected.

### $\mu$ Thermal Conductivity Detector Models

As the gas sample passes over a  $\mu$ TCD, power dissipation in the filament causes joule heating, increasing the electrical

resistance of the filament. Filament resistance is directly related to the detector temperature. Heat is carried away from a suspended heater element in 4 ways; conduction along the supports, conduction through the gas, mass transport by moving gas, and radiation [2, 3].

A TCD signal comes from the magnitude of the conductive heat flux between the heated detector element and the channel walls, via the gas surrounding the element. The three other heat loss pathways are not affected by the makeup of the sample gas.

To date, all  $\mu$ TCDs have been composed of a single resistive heating element. (Figure 1) When a single element is exposed to a moving gas stream, the leading edge cools down, changing the detector output. However, the thermodynamic models of planar TCDs hypothesize that if an element is held at a constant temperature, the central region will be flow invariant [5, 6]. The technical challenge has been to design a TCD which can maintain a fixed temperature along the entire structure.

## MODELING AND SIMULATION

To achieve a flow rate independent detector, our new device is composed of several electrically and mechanically independent active regions, each maintained at a constant temperature (Figure 2). This represents a significant enhancement on our previously reported high sensitivity thermal conductivity detectors [7].

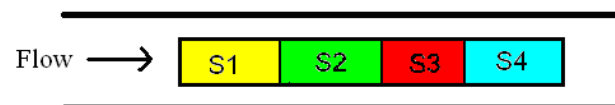


Figure 2: TCD with multiple independent active regions S1-S4. S1 preheats the flow. S2-4 is in a fully developed thermal region and responds only to the changing thermal conductivity of the gas surrounding it.

The central region of the flat filament is flow independent because it is past the thermal entry region of the pad and the thermal gradient is fully developed. (Figure 3) Once the isothermal lines are parallel to the hot filament, the heat is transported through the surrounding gas as if it were stationary, effectively decoupling mass transport from the heat flux equation. The upstream heating element is used to generate this stable thermal gradient for the following detector elements.

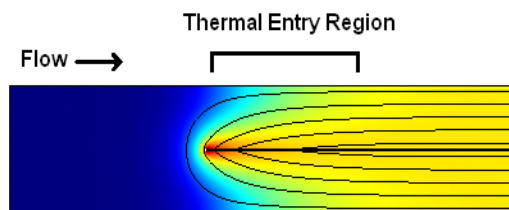


Figure 3: Simulation of heat flux showing temperature isotherm development after the flow contacts the heater pad. 'Thermal Entry Region' is where the isotherms are not parallel to flow and convection cannot be discounted as a heat flow pathway.

Work has been done in modeling the thermal performance of a  $\mu$ TCD. Finite element modeling tests confirm some of the

theoretical work of Huang & Bau [5], and Chen & Wu [6], which concluded that heat loss from forced convection, is proportional to thermal entry length. However, their calculations were based on the assumption that the heater pad completely isothermal, which is invalid for most situations, especially for physical single element TCDs.

Modeling and finite element simulations have been performed to calculate the effects of changing flow rate on a series of closely spaced constant temperature  $\mu$ TCDs as opposed to a single constant temperature element. Figure 4 shows the results from a model of four 500 $\mu$ m heater pads with 20 $\mu$ m spacing between pads placed in a 100 $\mu$ m tall channel. The model was created using a symmetry plain through the center of the heater pads. As the flow rate increases, more and more power is required to maintain TCD1 at a fixed temperature. As the flow is increased from 0.5m/s to 3m/s, all of these gas velocities are in the laminar flow regime. However, TCD2 and TCD3 are almost completely isolated from the effects of the changing flow rate up to 2m/s. At 3m/s, TCD2 is affected as the thermal boundary layer is no longer completely generated by the end of TCD1. TCD4 experiences some tailing effects at lower flow rates, as it is required to heat the area downstream of the structure.

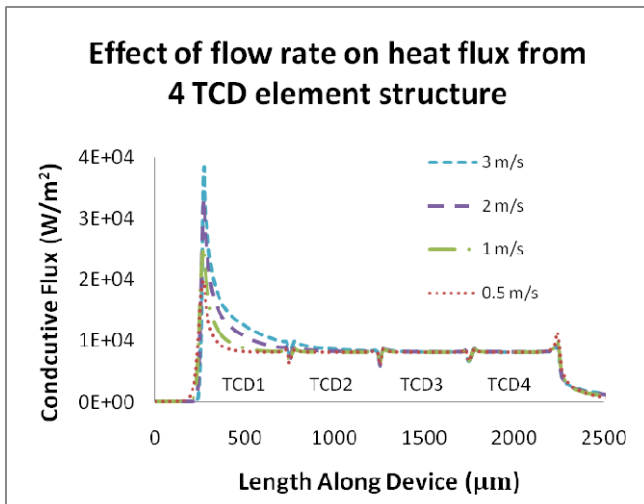


Figure 4: FEM model of heat flux from TCDs in a micro channel at 4 different flow rates, flow moving from left to right. All TCDs are set to an equal constant temperature. TCD1 is much more affected by changing flow rate than other elements.

## FABRICATION

The presented multiple element  $\mu$ TCD was fabricated by depositing nickel over a chromium adhesion layer. This metal

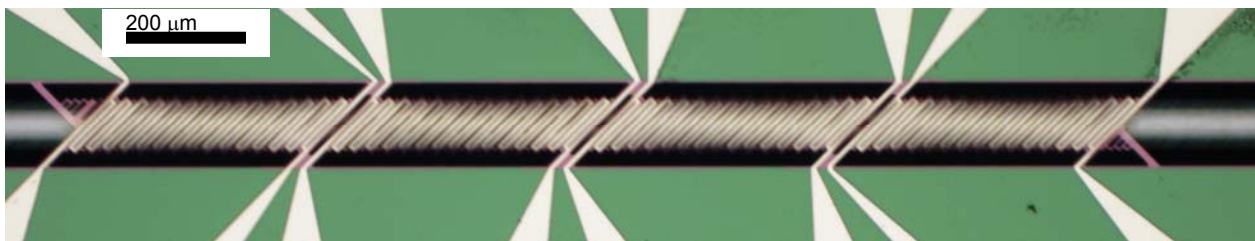


Figure 6: The optical image of 4 electrically independent high sensitivity thermal conductivity detectors. The power input and temperature of each detector can be controlled and monitored independently.

layer was supported on a 0.5 $\mu$ m silicon nitride film (SiN). Before the metal layer was deposited, the SiN layer was pre-etched 150nm in the pattern of the mask for the metal layer. The metal was then deposited, filling these pre-etched grooves (Figure 5a). This process creates a flush surface, which is critical for bonding a sealing cover over the flow channel. The nickel layer connects contact pads with wide traces to 5 $\mu$ m-wide resistive heaters.

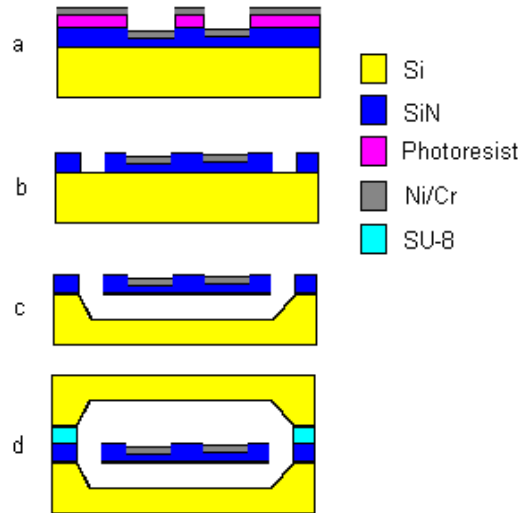


Figure 5: Device fabrication sequence for suspended  $\mu$ TCD. a) Pre-Etch of SiN and lift-off of metal layer. b) Etch of SiN film to define heater pad and channels. c) Release of heater pad with KOH etch. d) Device is sealed with silicon covers using a polymer intermediate layer.

After lift-off, the flow channels and support pad forming the resistive heating element were defined by patterning and etching through the SiN layer (Figure 5b). The structure was released using an anisotropic potassium hydroxide (KOH) etch. The channel was sealed by bonding a cover, which also had a channel etched using the same KOH process. A SU-8 intermediate layer was used bond the two chips together. Alignment and bonding between the device and cover chip was performed using an FC150 Flip Chip Bonder. Two versions of the multiple element  $\mu$ TCD were fabricated, with pad length as the only variable parameter. Completed device before bonding with 4 electrically independent TCD's is shown in figure 6.

After the channels were sealed, fused silica capillary tubing was inserted into the channels and sealed in place using an epoxy. Leak testing was performed by pressurizing the device and placing it in a water bath to check for bubbles.

## TESTING SETUP & CALIBRATION

After fabrication, each 4 element device was tested for continuity and thermally calibrated by placing it in a temperature-controlled oven and measuring the resistance of each element as the oven temperature was increased. This thermal calibration was used to calculate the resistance the  $\mu$ TCDs must be set to for any given operating temperature.

Each of the four sections used a constant temperature control circuit to maintain its  $\mu$ TCD element at a set resistance (Figure 7). The resistance (and therefore the temperature) of each independent section was maintained by a current source with a feedback loop. This circuit used a reference resistance and adjusted the current by resistive heating until the resistance of the  $\mu$ TCD matched the reference resistance. The analog output of each control circuit was digitized using a National Instruments analog to digital converter and recorded on a computer.

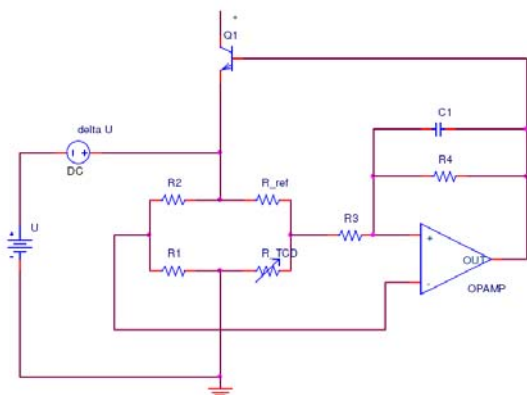


Figure 7: Simple constant temperature feedback circuit. By adjusting  $R_{ref}$ , each TCD can be set at an operating temperature. Top of the Wheatstone bridge,  $\Delta U$ , is the output signal from the detector.

Flow rate testing was performed using the pressure controller from an Agilent Technologies 7890A Gas Chromatography System. This pressure controller made it possible to ramp the inlet pressure between 1 and 90psi at a 60psi per minute. Original trials used a 5 meter capillary column between the pressure controller and the  $\mu$ TCDs. However, this setup failed to achieve a sufficiently high flow rate to ever effect the second or third TCD in the flow path. The column was removed, drastically decreasing the fluidic restriction and increasing the flow rates through the detector. The flow rates achieved in this setup are more than 10 times greater than those used in normal GC systems.

## TESTING AND RESULTS

### Flow Rate Independence

Two different 4 element  $\mu$ TCDs were tested. The difference between the devices was the length of the  $\mu$ TCD elements in the channel, one contained four  $\sim 500\mu\text{m}$   $\mu$ TCDs and the other contained four  $\sim 1000\mu\text{m}$   $\mu$ TCDs in series. The testing was performed in a temperature-controlled convection oven maintained at  $30^\circ\text{C}$ . The thermal calibration data was used to select the set point resistance so that the temperature of all four  $\mu$ TCDs would be  $60^\circ\text{C}$  which was  $30^\circ\text{C}$  over the ambient environment.

Both devices showed a significant reduction in the response of the downstream  $\mu$ TCDs to changing flow rates (Table 1). Furthermore, the device with the shorter  $\mu$ TCD pads showed a larger effect and earlier breakdown of flow insensitivity for the

trailing pads. This fit with the modeled expectations. Both devices matched our modeling and showed that the third TCD was least effected by changing flow rates. This is because the last TCD in the flow path is expected to experience tailing effects.

Table 1: Maximum response of  $\mu$ TCD sections as a percentage of the change in the leading TCD section (TCD1) at 90psi. TCD 1 is the leading upstream section follow in order by TCD2, TCD3, and TCD4.

Device	TCD2	TCD3	TCD4
500 $\mu\text{m}$ TCDs	14.61%	3.22%	4.25%
1000 $\mu\text{m}$ TCDs	5.75%	0.27%	1.40%

Figures 8 and 9 show the TCD response plotted against the system head pressure. The downstream elements in the device with the shorter  $\mu$ TCDs began have a significant response at around 50psi.

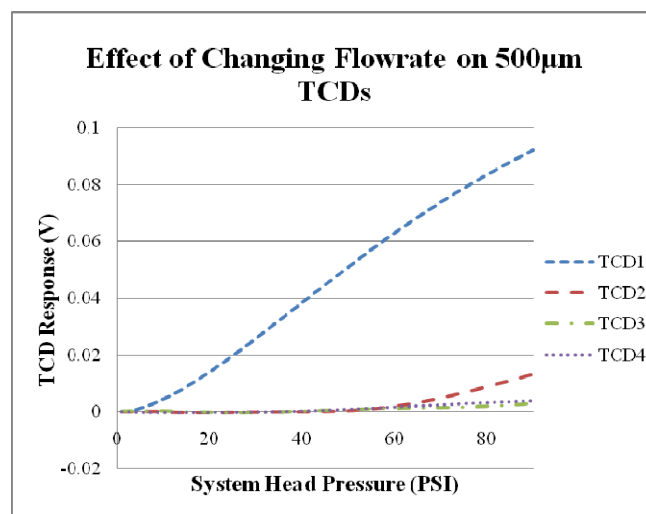


Figure 8: Effect of ramped input pressure on the four 500 $\mu\text{m}$  elements. TCD1 is clearly the most affected with TCD2 beginning to be affected at 50psi.

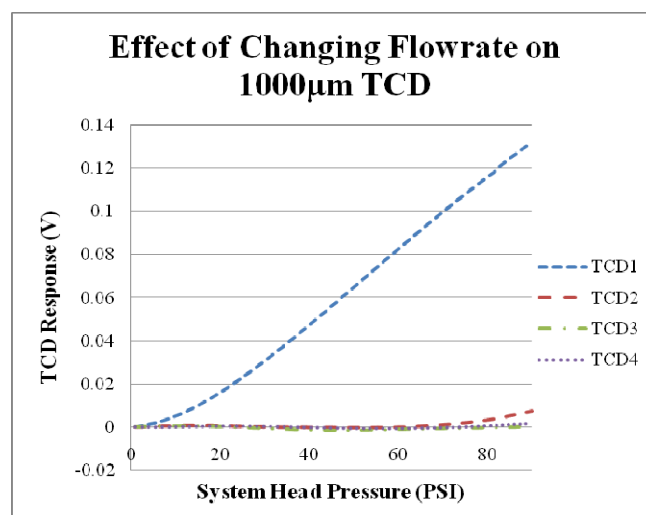


Figure 9: Effect of ramped input pressure on the four 1000 $\mu\text{m}$  elements. TCD1 is clearly the most affected with TCD2 beginning to be affected at around 70psi.

In the device with the longer  $\mu$ TCD elements, power dissipation from the second  $\mu$ TCD only began to increase with a head pressure of 70psi.

These tests show that the thermal entry region causes flow rate variation in the output of the detector. Longer preheating regions result in a broader range of flow independence for the detector.

In both devices, the  $\mu$ TCDs 2-4 had a small negative response (required less power to maintain the set point temperature). This is most likely because of errors in the set point resistance of the individual  $\mu$ TCD elements. All TCDs were suppose to be set to 60°C, however, if an upstream TCD was set hotter than 60°C, then the isotherms would be distorted and as the flow rate increases the power required for the following TCD to maintain its set temperature will decrease. Work is being continued to improve the calibration of the  $\mu$ TCDs and the control and stability of the set point to try and minimize these problems.

### TCD Interdependence

To show that the close spacing of the  $\mu$ TCD elements was key to the flow rate insensitivity, a test was performed only powering the first and third  $\mu$ TCDs. In this test, the two active TCDs were separated by  $\sim 500\mu\text{m}$ . The two devices showed nearly identical responses up to 20psi head pressure. This implies that no heat from the first element was reaching the second element  $500\mu\text{m}$  downstream. After 20psi, the third  $\mu$ TCD element was affected by the first  $\mu$ TCD; however, at the maximum tested system head pressure, the third  $\mu$ TCD only required 55% of the power used by the first  $\mu$ TCD to maintain its set point temperature (Figure 10).

The first element has the same response as with all four  $\mu$ TCDs powered which shows there is little or no thermal crosstalk up stream in the carrier gas flow.

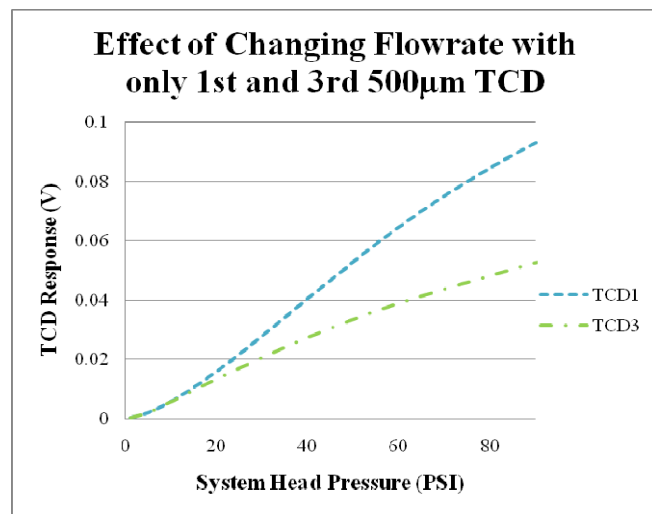


Figure 10: Effect of ramped input pressure on the 1<sup>st</sup> and 3<sup>rd</sup> 500 $\mu\text{m}$  elements in device. TCD1 and TCD3 have similar responses up to 20psi. After 20psi heat from TCD1 affect TCD3.

## CONCLUSION

The design, fabrication and testing of several  $\mu$ TCDs with a high degree of independence to carrier gas flow have been shown. The heat flux in the system has been modeled and tested experimentally to increase understanding of microchannel thermodynamics and improving the device performance. Initial testing has shown no noticeable loss of sensitivity in the detection of analytes for these multiple element  $\mu$ TCDs as compared to a traditional single element  $\mu$ TCD. Combining this detector with a micro-fabricated separation column and injector would create a complete  $\mu$ GC system with a simpler design, fewer interconnections and lower gas consumption requirements.

## ACKNOWLEDGEMENTS

We would like to acknowledge National Science Foundation (ECCS 0901702), Schlumberger-Doll Research and the Boston University Photonics Center for their support of this research.

## REFERENCES

- [1] M. Agah et al., "High-Performance Temperature-Programmed Microfabricated Gas Chromatography Columns," J. Microelectromech. Syst. Vol. 14, pp. 1039-1050, 2005
- [2] J. Potkay, et al., "A Low-Power Pressure- and Temperature-Programmable Micro Gas Chromatography Column," J. Microelectromech. Syst. Vol. 16, pp. 1071-1079, 2007
- [3] Y.E. Wu, K. Chen, C.W. Chen, K.H. Hsu, "Fabrication and Characterization of Thermal Conductivity Detectors (TCDs) of Different Flow Channel and Heater Designs", Sensors and Actuators A, 100, 37, (2002).
- [4] Chen, K., and Wu, Y. E., "Thermal Analysis and Simulation of the Microchannel Flow in Miniature Thermal Conductivity Detectors," Sensors and Actuators A, vol. 79, pp. 211–218, 2000.
- [5] Y. Huang, H. H. Bau, "The Effects of Forced Convection on the Power Dissipation of Constant-Temperature Thermal Conductivity Sensors," Transactions of the ASME, Vol. 119, 1997.
- [6] Y. M. Kim, W. S Kim, W. G. Chun, "A Numerical Study of the Thermal Entrance Effect in Miniature Thermal Conductivity Detectors", Heat Transfer Engineering, 26, 65 (2005).
- [7] B.C. Kaanta et al, "High sensitivity micro-thermal conductivity detector for gas chromatography," Proc. IEEE MEMS 2009, (2009), pp. 264.

## CONTACT

\*X. Zhang, tel: +1-617-358-2702; xinz@bu.edu

# NANOPARTICLE SEPARATION AND METROLOGY BY THREE-DIMENSIONAL NANOFLUIDIC SIZE EXCLUSION

S.M. Stavis\*, J. Geist, and M. Gaitan

Semiconductor Electronics Division, National Institute of Standards and Technology, USA

## ABSTRACT

A nanofluidic approach to the size separation and metrology of nanoparticles by three-dimensional (3D) nanofluidic size exclusion is presented. This approach is fundamentally different from serial methods of nanoparticle purification (*i.e.* filtration) and characterization (*i.e.* electron microscopy); 3D nanofluidic devices enable the parallel actuation and sensing of a mixture of nanoparticles of different sizes by three-dimensional nanofluidic size exclusion. In this manuscript, the design, fabrication and characterization of a 3D nanofluidic device is described in detail. The preliminary application of this 3D nanofluidic device to the size separation and metrology of nanoparticles is introduced.

## INTRODUCTION

Nanoparticles are of immense scientific and technological interest, and nanoparticle size often determines the beneficial or detrimental characteristics of nanoparticles. However, current technology for nanoparticle size processing and characterization is a bottleneck to the study and application of many types of nanoparticles [1]. Conventional methods of nanoparticle size separation and purification (*i.e.* filtration) can be slow and inefficient. These limitations are compounded by the subsequent use of conventional methods of nanoparticle characterization (*i.e.* electron microscopy) which can be slow and specialized.

Engineered nanofluidic devices provide microsystem scaling benefits while simultaneously facilitating control and visualization of nanoscale interactions with nanoparticles. These interactions are typically controlled through the confinement of nanoparticles within an engineered nanometer scale fluidic structure and visualized with fluorescence microscopy. However, the vast majority of nanofluidic structures have been characterized by simple geometries defined by at most several structure depths. This has limited the range and resolution of nanofluidic approaches to the manipulation and metrology of nanoparticles. As nanofluidic device functionality is determined by nanofluidic structure dimensionality and complexity, the development of more complex three dimensional nanofluidic structures would confer improved control over interactions with nanoparticles. This could result in new nanofluidic technologies for the manipulation and metrology of nanoparticles [2]. Progress in this regard has been restricted by conventional nanofabrication processes, which become limiting if many layers of lithography are performed in a research nanofabrication facility.

In this manuscript, a nanofluidic technology is presented to address these limitations. A nanofabrication process is described to construct nanofluidic devices with numerous nanometer-scale critical dimensions. In aggregate, these numerous critical device dimensions form a complex three-dimensional surface enabling the simultaneous on-chip actuation and sensing of nanoparticles of different sizes. The preliminary application of a 3D nanofluidic device to the size separation and metrology of a mixture of nanoparticles of different sizes is introduced.

## THEORY

To fabricate nanofluidic devices with numerous nanometer-scale critical dimensions, grayscale photolithography is used in conjunction with a nanometer-scale pattern transfer process. As

shown in Figure 1, a chromium-on-quartz photomask is used with a projection photolithography system (*i.e.* a wafer stepper) as a diffraction filter [3, 4]. The photomask is patterned with arrays of

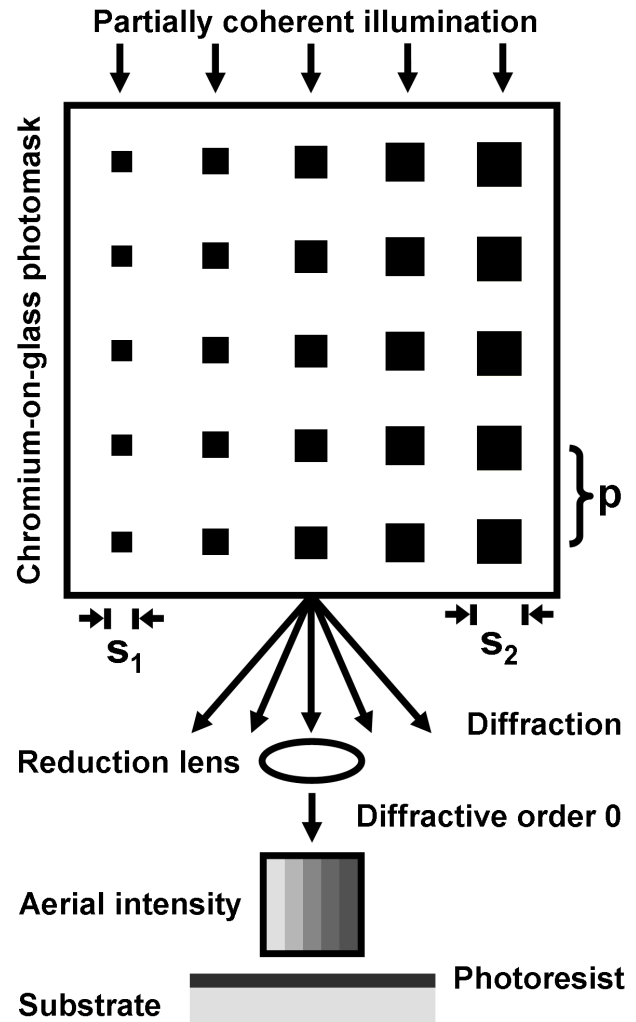


Figure 1: Schematic of a chromium-on-quartz photomask used in conjunction with a reduction photolithography system as a diffraction filter to pattern grayscale patterns of varied intensity.

diffraction gratings of size  $s$  and pitch  $p$ , with amplitude transmittance  $T(x,y)$  of 0 and 1 for chromium and quartz regions. The photomask is illuminated with light of wavelength  $\lambda$  and coherence parameter  $\sigma$ , and the lithographic system projects and reduces the device pattern through the lithographic lens and onto a fused silica substrate wafer. For a diffraction-limited optical system,  $T(x,y)$  and its Fourier spectrum in the image plane  $T'(k_x,k_y)$  are related as conjugates:

$$T(x,y) = \frac{1}{(2\pi)^2} \int T'(k_x,k_y) e^{-i(k_x x + k_y y)} dk_x dk_y \quad (1)$$

$$T'(k_x, k_y) = \int T(x, y) e^{i(k_x x + k_y y)} dx dy \quad (2)$$

with lateral components of the angular wave number  $k_x = (2\pi/\lambda) \sin \alpha$  and  $k_y = (2\pi/\lambda) \sin \beta$ , and projected angles  $\alpha$  and  $\beta$  between the wave vector  $k$  and the optical axis. With appropriate selection of  $s$  and  $p$ , diffractive orders other than  $k_x = k_y = 0$  are rejected by the lens aperture. As the zeroth diffractive order determines only the amplitude of the image intensity, individual elements within the diffractive arrays are not resolved, and a grayscale of uniform intensity results. The critical angle  $\theta_c$  for entry into the lens is determined by its numerical aperture  $NA_s = \sin \theta_c$ , giving a critical wave vector number  $k_c = (2\pi/\lambda) NA$ . The complex amplitude of the aerial image is then

$$A(x', y') = \int_{-k_c}^{k_c} \int_{-k_c}^{k_c} T'(k_x, k_y) \cdot e^{i(k_x x' + k_y y')} dk_x dk_y \quad (3)$$

and the aerial image intensity is  $I(x', y') = |A(x', y')|^2$ . Taking into account the partial coherence of the illuminator, the stepper resolution determines the critical aerial pitch

$$p'_c = \frac{1}{1 + \sigma_s} \cdot \frac{\lambda_s}{NA_s} \quad (4)$$

while the diagonal spacing between adjacent elements in the diffractive array determines the critical square size [5]

$$s_c = p \cdot \sqrt{\frac{p_c^2}{2}} \quad (5)$$

Pitches larger than  $p_c$  or squares smaller than  $s_c$  will result in fluctuations in aerial intensity as diffractive elements begin to resolve. When equations (4) and (5) are satisfied,  $k_x = k_y = 0$  and  $T'(k_x, k_y)$  is given in equation (2) as the integral of  $T(x, y)$ , which is the fractional opaque area of each grayscale on the photomask. The aerial image intensity of a grayscale is then

$$I_{GS}(x', y') = I_0 \left( 1 - \left( \frac{s^2}{p^2} \right) \right)^2 \quad (6)$$

where  $I_0$  is the incident illumination intensity.

## RESULTS

An aerial intensity profile approximated by a staircase function with thirty steps was patterned using arrays of diffractive chromium squares varied in size from  $s = 1.37 \mu\text{m}$  to  $s = 2.24 \mu\text{m}$  on a pitch  $p = 4.00 \mu\text{m}$ . The square sizes had a tolerance of 15 nm (absolute error) and a uniformity of 15 nm (maximum range), as specified by the manufacturer. Each grayscale had an aerial width  $w_{GS} = 4.00 \mu\text{m}$ , defined by a sub-array on the photomask of five diffractive chromium squares. The intensity of each grayscale  $I_{GS}$  in the aerial plane (normalized by the incident illumination intensity  $I_0$ ), as calculated using Equation 6, is shown as a function of diffractive square size  $s$  in Figure 2. This range of chromium square sizes were selected to produce an approximately response variation in grayscale intensity, as shown by the corresponding fit. This linear relationship simplified the subsequent design of the nanofabrication process.

A fused silica substrate wafer with thickness  $t_s = 0.50 \text{ mm}$  and surface roughness  $r_s < 5 \text{ \AA}$  was vapor primed and spin-coated with  $1.07 \mu\text{m}$  of broadband positive tone photoresist. The photomask was used with a reduction photolithography tool of magnification  $M_s = 0.2$ , wavelength  $\lambda_s = 436 \text{ nm}$ , coherence parameter  $\sigma = 0.43$ , and numerical aperture  $NA_s = 0.3$  to render grayscales for the partial top-down exposure of the photoresist thin film. The photoresist was then fully developed using a positive tone developer. Prior to

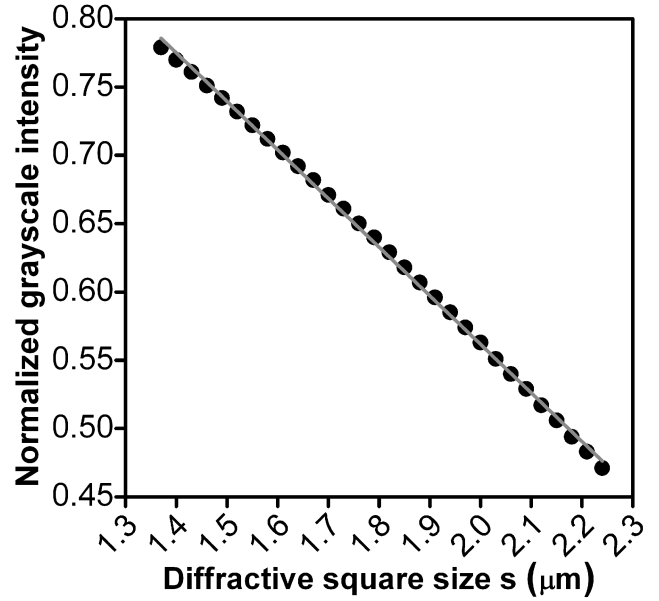


Figure 2: Normalized grayscale intensity ( $I_{GS}/I_0$ ) as a function of diffractive chromium square  $s$ . Square sizes were selected to produce an approximately linear variation in grayscale intensity.

fabrication of the device presented here, a calibration photomask was used to characterize the response of the photoresist film to grayscale exposure, the results of which are shown in Figure 3. The incident illumination intensity  $I_0$  was the illumination intensity required to produce an exposure dose that completely cleared the photoresist etch mask during the subsequent development process.

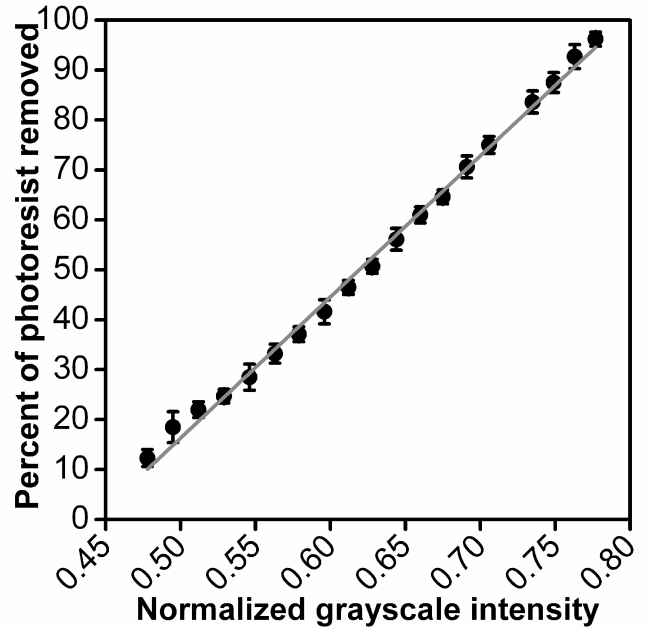


Figure 3: Response of photoresist to grayscale exposure following development. The photoresist responds in an approximately linear manner across the selected range of grayscale intensities.

Following photolithography, the 3D device pattern in the photoresist etch mask was transferred into the fused silica substrate

at the nanometer length scale by an isotropic  $\text{CHF}_3/\text{O}_2$  reactive ion etch process. The selectivity of the etch process was tuned by varying the two gas flow rates to achieve the desired etch depth profile. Following the pattern transfer process, the resulting 3D topography of the etched surface of the nanofluidic channel was spatially mapped with a scanning probe surface profilometer. The results of this measurement are shown in Figure 4. The radius of curvature of the surface profilometer probe tip was  $\approx 1 \mu\text{m}$ , as determined by measurement artifacts (*i.e.* rounded corners) that resulted from the probe tip scanning over sharp nanofluidic step edges. Surface profilometry provided the minimum etch depth of the nanofluidic channel, since the micrometer-scale profilometer tip was not able to probe surface roughness at the nanometer-scale. Etch depth variation was controlled to within 10 nm (standard deviation) over the entire 1.2 cm channel length, as measured by 13 scanned probe measurements repeated along the length of the structure. This variation encompassed all of the non-uniformity in the nanofabrication process as implemented, including variation in initial patterning of the photomask, grayscale exposure, photoresist development, and reactive ion etching. The channel had an average minimum depth of  $\approx 70$  nm, an average maximum depth of  $\approx 620$  nm, and an average step size of  $\approx 18$  nm. A fabrication

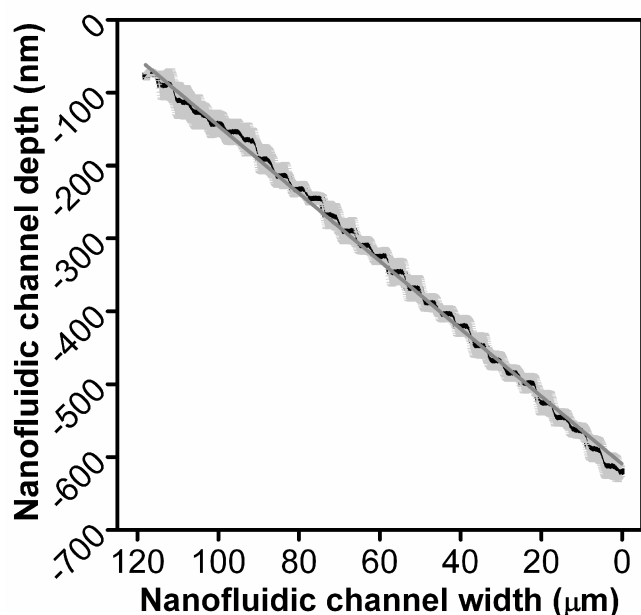


Figure 4: Numerous (30) nanometer-scale etch depths as measured by scanning probe surface profilometry. Error bars denote the standard deviation of 13 scans down the length of the etched channel structure. The etch depth profile of the device is approximated by a staircase function which demonstrates the linearity of the nanofabrication process from grayscale exposure to photoresist response to pattern transfer.

process defect resulted in periodic distortions of the nominal staircase function depth profile, as shown in Figure 4. These distortions produced regions of the structure with increased variation in etch depth. The root-mean-square roughness of the etched channel surface was measured with atomic force microscopy to be  $\approx 2$  nm. The radius of the curvature of the etched single crystal silicon probe tip was  $\leq 10$  nm, as specified by the manufacturer, and the tip was operated in tapping mode.

Inlet and outlet holes were micro-abrasive blasted through the

back of the substrate wafer, which was then cleaned and bonded to a fused silica cover wafer with thickness  $t_c=0.17$  mm and surface roughness  $r_s < 5 \text{ \AA}$ . The wafer stack was fused at  $1100^\circ\text{C}$ . No nanoglassblowing occurred [6], as determined by scanned probe measurements of the cover wafer surface after this annealing process. This measurement (not shown) confirms that the etch depths measured to prior wafer bonding accurately represent the resulting nanofluidic channel depths after wafer bonding.

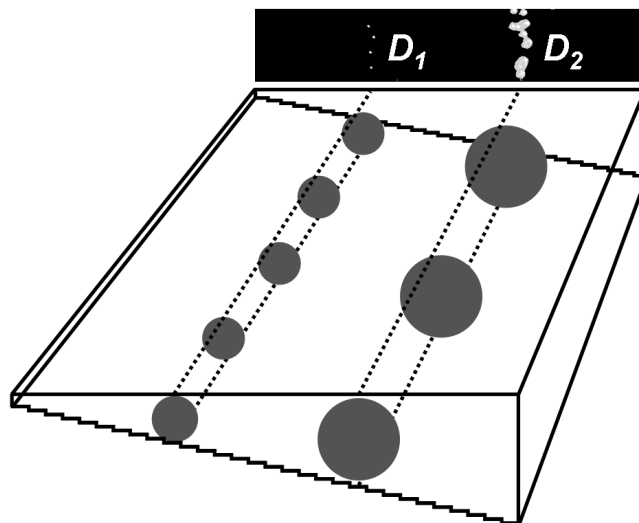


Figure 5: Fluorescence micrograph and schematic showing the size separation of nanoparticles with sizes  $D_1$  and  $D_2$  by three-dimensional nanofluidic size exclusion. Nanoparticles were electrokinetically driven down the length of the nanofluidic channel and across its width from the deep side towards the shallow side. The stepped reductions in nanofluidic channel depth excluded nanoparticles from spatially separate regions of the channel.

Following device fabrication, reservoirs were attached to the substrate to introduce nanoparticle samples into the 3D structure. An aqueous solution of fluorescent nanoparticles of sizes  $D_1$  and  $D_2$  was injected into the deep end of the nanofluidic channel and electrokinetically driven down the length and across the width of the 3D nanofluidic channel from the deep side towards the shallow side, as shown in Figure 5. Stepped reductions in the depth of the nanofluidic channel excluded nanoparticles by size from regions of the nanofluidic channel with depths that were less than the particle sizes, as shown by a fluorescence micrograph at the top of Figure 5. Future work will use epifluorescence microscopy to map the size exclusion positions of numerous individual nanoparticles to corresponding nanofluidic channel depths. This statistical analysis will be used to directly measure the nanoparticle size distributions in order to validate the size separation mechanism of three-dimensional nanofluidic size exclusion.

#### DISCLAIMER

Official contribution of the National Institute of Standards and Technology; not subject to copyright in the United States.

#### NOTE

Certain commercial materials and equipment are identified in order to adequately specify experimental procedures. In no case does such identification imply recommendation or endorsement by the National Institute of Standards and Technology, nor does it imply



that the items identified are necessarily the best available for the purpose.

## **ACKNOWLEDGEMENTS**

This research was performed while S.M. Stavis held a National Research Council Research Associateship Award at the National Institute of Standards and Technology (NIST). Device fabrication was performed at the Cornell Nanoscale Science and Technology Facility (CNF), a member of the National Nanotechnology Infrastructure Network, and the Cornell Center for Materials Research, both supported by the NSF. Device characterization was performed in part at the NIST Center for Nanoscale Science and Technology. The authors thank the CNF staff for assistance with device fabrication.

## **REFERENCES**

- [1] E.K. Richman and J.E. Hutchison, "The Nanomaterial Characterization Bottleneck", *ACS Nano*, 3, 9, (2009).
- [2] S.M. Stavis, E. A. Strychalski, and M. Gaitan, "Nanofluidic structures with complex three-dimensional surfaces", *Nanotechnology*, 20, 7 (2009).
- [3] W. Henke, W. Hoppe, H. J. Quenzer, P. Staudtfischbach, and B. Wagner, "Simulation and process design of gray-tone lithography for the fabrication of arbitrarily-shaped surfaces", *Japanese Journal Of Applied Physics Part 1 – Regular Papers Short Notes & Review Papers*, 33, 12B (1994).
- [4] J. W. Goodman, *Introduction To Fourier Optics*, Third Ed., McGraw-Hill, 2004.
- [5] C. M. Waits, A. Modafe, and R. Ghodssi, "Investigation of gray-scale technology for large area 3D silicon MEMS structures", *Journal Of Micromechanics And Microengineering*, 13, 170 (2003).
- [6] E. A. Strychalski, S. M. Stavis, and H. G. Craighead, "Non-planar nanofluidic devices for single molecule analysis fabricated using nanoglassblowing", *Nanotechnology*, 19, 8 (2008).

## **CONTACT**

\*S.M. Stavis, tel: +1-301-975-3246; sstavis@nist.gov

# PLANAR PHOSPHOLIPID MEMBRANES IN MICROFLUIDICS ENABLING KINETICS STUDIES OF CERAMIDE CHANNELS

Chenren Shao<sup>1\*</sup>, Marco Colombini<sup>2</sup>, and Don. L. DeVoe<sup>2</sup>

<sup>1</sup>Department of Mechanical Engineering, University of Maryland, College Park, Maryland, USA

<sup>2</sup>Department of Biology, University of Maryland, College Park, Maryland, USA

## ABSTRACT

Here we present recent developments on the integration of planar phospholipids membrane (PPM) into microfluidic platform. With robust PPM formed in our polycarbonated based microchip, we can further incorporate one of the most interesting naturally occurring lipids channel ceramide (*N*-acylated spingosine), and then integrate perfusion pathway to change the reagent condition of aqueous solution in one of the chambers. It demonstrates the ability to study the dynamic responses of ion channel to different perfusion conditions and to capture the kinetic activities which would provide mechanistic insight for ion channels study.

## INTRODUCTION

Ceramide (*N*-acylated spingosine), a sphingolipid found in mitochondrion membranes, is involved in several important cellular activities, including differentiation, growth suppression, cell senescence and apoptosis. Recent research shows that it may regulate apoptosis by forming stable channels to release mitochondrial proapoptotic intermembrane proteins to the cytoplasm [1-3]. Further understanding of the structure and function of lipid ion channels will require kinetic interaction studies with different ligands such as trehalose and Bcl-2 family proteins [3]. However, traditional in vitro electrophysiology platforms employ large fluid volumes which make it impossible to rapidly and dynamically modulate the local (bio)chemical environment at the channel site. Miniaturization is an obvious solution but simple, cost effective and user friendly microsystems for dynamic ion channel studies remain elusive due to innate fragility of lipid membranes and also from complications associated with fluid controls and electrical access. Previously we reported a convenient fabrication process for a robust microfluidic planar phospholipid membrane (PPM) platform enabling stable membrane formation and ion channel introduction [4]. Here we present recent developments on the integration of perfusion pathways, and demonstrate the ability to capture the kinetic activities of ceramide channels under different dynamic reagent perfusion conditions.

## FABRICATION AND MATERIALS

As shown in Fig. 1, the polycarbonate (PC) microfluidic PPM chip consists of two microchannels, each in a different PC substrate, separated by a 13  $\mu\text{m}$  thick polyvinylidene chloride (PVDC) film. The chip-to-world fluidic connection is realized by micro unions and the electrodes are held by nanoports, both from Upchurch, MA. An aperture of 80~150  $\mu\text{m}$  in diameter is fabricated by a precisely controlled hot needle (Fig. 2) as a membrane hosting site. The inset in Fig.1 shows a top view from open well of a PPM site in PVDC film.

The reagents of interest are delivered by syringe pumps through the perfusion channels to bottom chamber, and to waste reservoir located at the end of bottom chamber. In this study,  $\text{LaCl}_3$ , ethylenediaminetetraacetic acid (EDTA) and trehalose are investigated.

Unlike protein ion channels, the highly hydrophobic nature of the lipid ceramide molecule imposes unique challenges for ion channel integration due to their poor solubility. Here we describe a new approach based on pre-mixing ceramide and membrane lipid

and using a diffusion “painting” method to encourage efficient and repeatable channel formation. Briefly, a mixture of 1,2-dipalmitoyl-sn-glycero-3-phosphocholine (DPPC), asolectin, and cholesterol (Avanti Polar Lipids, AL) is dissolved in hexane as a pre-coating solution. The solution is pipetted directly onto the PPM site through the open reservoir, and residual hexane is evaporated by a gentle stream of nitrogen. After filling the open reservoir and microchannels with buffer, a glass tip is rolled in a painting solution and gently wiped across the hole. The painting solution has same lipid concentration as pre-coating except has *N*-hexadecyl-*D*-erythro-sphingosine ( $\text{C}_{16}$ -ceramide) at 1:50 molar fraction with respect to phospholipids in hexanol/hexadecane (10:1, v/v). By diffusing hexanol to surrounding buffer, the lipid plug can thin into bilayer and ceramide can eventually assemble into a channel.

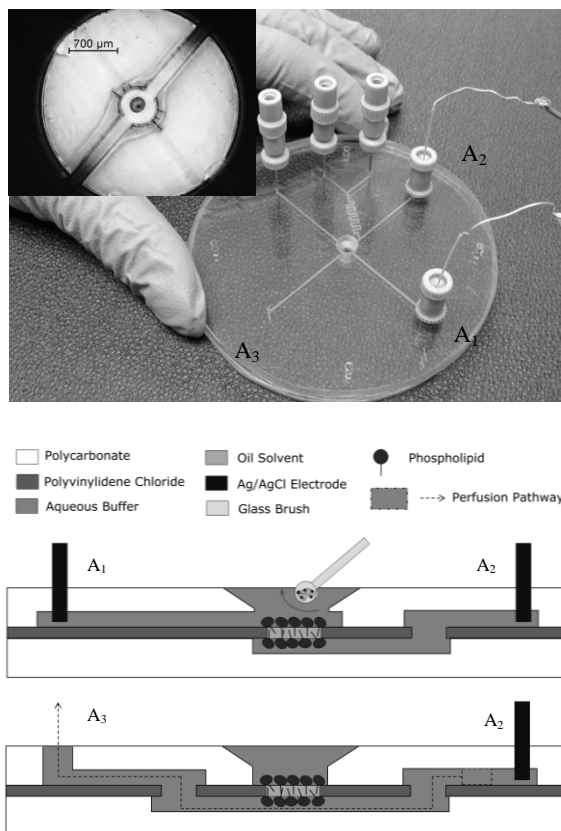


Figure 1: Schematic view of microfluidic PPM chip. Cross section view of  $A_1$ - $A_2$  and  $A_3$ - $A_2$  show the electrical pathway and perfusion pathway respectively.

## EXPERIMENTS AND DISCUSSION

Unlike previous efforts to develop automated ion channel analysis systems using microfluidics, our goal here is to develop a simple and practical benchtop platform suitable for biophysical investigation of ion channels, including both protein and lipid channels, requiring the application of time-varying chemical concentrations on either side of the channel membrane. This is especially useful to study the physiological functions of relevant ion channels such as ceramide.

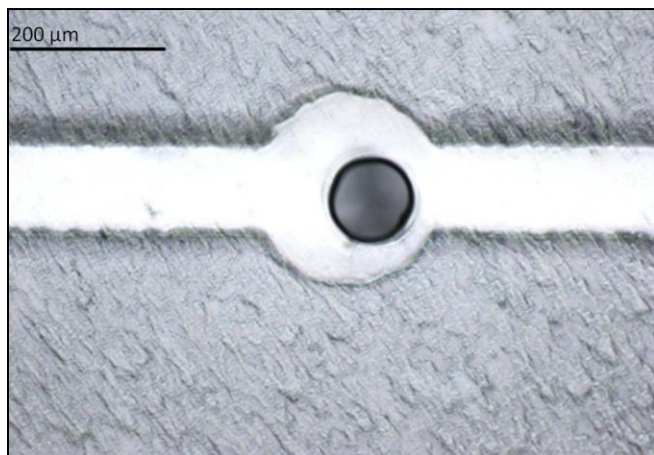


Figure 2: A 100X view of an aperture burnt by a hot needle on PVDC film right above bottom channel. The diameter of the aperture ranges from 80 μm to 150 μm in different chips.

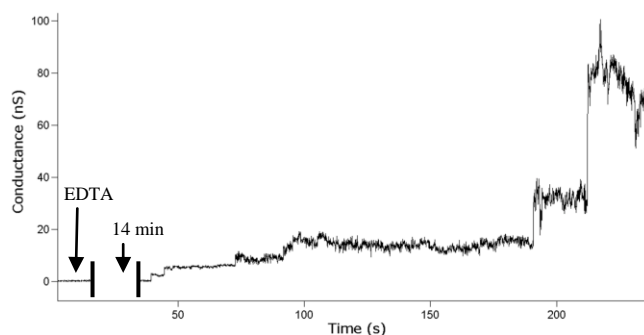


Figure 3: A membrane pretreated with 50 μM  $\text{LaCl}_3$  showed ceramide formation activities when 50 μM EDTA is injected through bottom channel. Buffer contains 1M KCl, 1mM  $\text{MgCl}_2$ , 20mM PIPES, pH 6.98.

An example of this capability using  $\text{LaCl}_3$  and EDTA is revealed in Fig. 3.  $\text{LaCl}_3$  is known to disassemble ceramide channels, while EDTA works as chelator, deactivating the inhibiting function of  $\text{La}^{3+}$  ions. Upon the introduction of 50 μM  $\text{La}^{3+}$  through the lower microchannel, ceramide channel formation is inhibited. Next, 50 μM EDTA is controllably delivered to the membrane site with flow rate 0.2 μL/min. Progressive chelation of  $\text{La}^{3+}$  by EDTA ultimately leads to formation of a ceramide channel, with a maximum conductance up to 80 nS. The total waiting time for the formation is 14 minutes, matching with the time needed by EDTA frontier to be pumped to the bottom chamber.

In another example, trehalose, a sugar with a specific arrangement of hydroxyls, is predicted to interact with hydroxyl groups in the inner wall of a ceramide channel and alter the pore size. In a preliminary test shown in Fig.4, we successfully see timely response of ceramide channel upon addition and removal of trehalose.

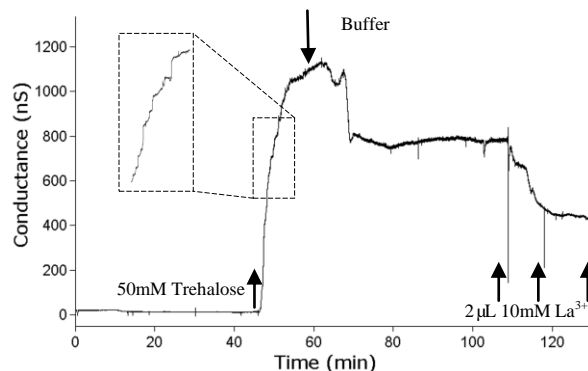


Figure 4: A two-hour current recording of ceramide interacting with trehalose. The perfusion of trehalose enhanced the conductance from ~20nS to ~1150nS. Removal of trehalose by buffer decreased it to ~800nS. Following addition of  $\text{La}^{3+}$  reduce the conductance further. Buffer contains 0.25M KCl, 0.25mM  $\text{MgCl}_2$ , 20mM PIPES, pH 6.98.

## REFERENCES

- [1] L.J. Siskind and M. Colombini, "The Lipids C<sub>2</sub>- and C16-ceramide Form Large Stable Channels: Implications for Apoptosis", *Journal of Biological Chemistry*, 275, 38640 (2000).
- [2] L.J. Siskind, A. Davoody, N. Lewin, S. Marshall and M. Colombini, "Enlargement and Contracture of C2-Ceramide Channels." *Biophysical Journal*, 85, 1560 (2003).
- [3] L. J. Siskind, "Mitochondrial Ceramide and the Induction of Apoptosis." *Journal of Bioenergetics and Biomembranes*. 37, 143 (2002).
- [4] C. Shao, M. Colombini, D. L. DeVoe, "Planar Phospholipid Membrane Formation in Open Well Thermoplastic Chips". 2009 ASME International Mechanical Engineering Congress and Exposition, Lake Buena Vista, FL, 11/13-19/09.

## CONTACT

\*Chenren Shao, tel: +1-301-405-1023; chenren@umd.edu

# A LARGE-SCALE FLEXIBLE MOLDING TECHNOLOGY FOR PRODUCING BIOMIMETIC DRY ADHESIVES IN MULTIPLE MATERIALS USING A COMMERCIAL ACRYLIC MASTER

D. Sameoto<sup>1,2\*</sup> and C. Menon<sup>2</sup>

<sup>1</sup>Mechanical Engineering Department, University of Alberta, Edmonton, Alberta, Canada

<sup>2</sup>MENRVA Research Group, Simon Fraser University, Burnaby, British Columbia, Canada

## ABSTRACT

We present a novel fabrication method that uses 254 nm light from germicidal lamps to convert commercial acrylic substrates into master molds for biomimetic dry adhesives. These gecko-inspired adhesives use appropriately shaped fibers to make intimate contact with surfaces and adhere using van der Waals interactions. While previous molding technologies for synthetic dry adhesives were limited by the size of the substrates used, our technology makes use of bulk acrylic, and is technically possible to scale up to dozens of square feet per master mold. Nearly any castable polymer may be converted to a dry adhesive using this technology.

## INTRODUCTION

Biomimetic dry adhesives are inspired by the fibrillar structures found on the feet of geckos and certain spiders which allow the animals to adhere through van der Waals interactions. Synthetic versions of these materials are typically manufactured using polymers cast on nano and microscale molds. These molds have usually been based on silicon [1-2] or photoresists on silicon wafers [3-4] which severely limits the maximum size of adhesive sheets. Mushroom shaped fibers are desirable to produce significant normal adhesion forces, requiring either direct molding from undercut holes [5], or dipping methods [6-7] to produce overhanging caps on pre-formed fibers. While we have previously reported a photoresist based manufacturing technology that allows direct casting of mushroom shaped silicone dry adhesives [3-4], both the lifetime and size of the mold were limited. In the manufacturing technology that we are reporting in this paper, a master mold made of acrylic and SU-8 is used for casting negative silicone molds which are flexible and easily release other cured polymers. It is difficult to make other materials bond to silicones, making them an ideal choice for casting the final dry adhesives out of polyurethanes, epoxies and other curable polymers. Additionally, the bulk acrylic used as a substrate may be purchased in sizes up to 4'x8' providing an upper limit on the mold size far in excess to that of the largest silicon wafers. The qualities of the particular silicone chosen for making negative molds also permit the assembly of large molds from multiple individual sheets.

## FABRICATION PROCESS

The direct photopatterning of polymethylmethacrylate (PMMA) using 254 nm light was originally conceived as a low-cost alternative to LIGA or e-beam lithography and later on was used for self-sacrificial polymer MEMS processing [8-9]. The sensitivity of PMMA to 254 nm light is extremely low, leading to lengthy exposure times (>5 hours), but the relative low cost of this light source (used industrially as germicidal lamps) is attractive for exposing large areas. Germicidal lamps have previously been used to expose commercial acrylic (OPTIX® from Plaskolite) to directly form microfluidics channels [10]. Acrylic is primarily PMMA with some additives and can be an inexpensive alternative to silicon or SU-8 micromachining when directly photopatterned. The aspect ratio and feature sizes produced in OPTIX® were severely limited by the uncollimated 254 nm light source that was

used (Stratalinker 2400 [10]). Our modified process is capable of producing higher aspect ratio structures, and more importantly, is capable of producing the overhanging structures that are critical for strongly adhering polymer dry adhesives. The basic process is outlined in Figure 1 and described below.

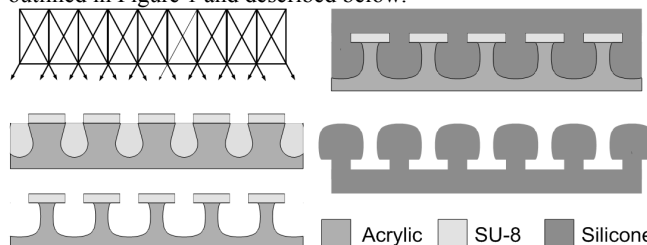


Figure 1. Schematic of the basic process steps used to convert commercial acrylic to dry adhesive molds. Partially collimated 254 nm light exposes commercial acrylic using a thin SU-8 layer as a mask. The acrylic is developed to produce fibers with thin overhanging SU-8 caps. The mold is replicated in silicone, and the negative silicone mold is ready to replicate the acrylic/SU-8 fibers in softer materials.

## Fabrication Steps

- SU-8 2002 is spun on a commercial acrylic substrate (OPTIX® from Plaskolite) then prebaked in an oven to form a thin layer (~1.6 μm) on the acrylic surface.
- The SU-8 is exposed to i-line light from a standard UV aligner to define the fiber cap size and shapes.
- The SU-8 is post exposure baked for longer than 1 hour at 80°C to maximize the crosslinking, while keeping the acrylic well below the temperature at which it may warp or sag.
- The SU-8 is developed to form a hard mask on the acrylic
- The acrylic is exposed to 254 nm light with the presence of either a single level or dual level anti-scatter grid made from a plastic grating. The SU-8 is mostly opaque to 254 nm light and acts as a mask in perfect contact with the acrylic. Exposure to 254 nm light lowers the molecular weight of the acrylic through main chain scission, and increases its dissolution rate in developers.
- After exposure, the acrylic is developed using SU-8 developer at room temperature (18 °C). A slightly lower selectivity of this solvent than the IPA:H<sub>2</sub>O developer used earlier [8-10] allows for better undercutting of SU-8 features. The final fiber shape depends on the exposure dose, anti-scatter grid design and development time.
- A high-strength, high temperature tolerant silicone (TC-5045 from BJB-Enterprises) is used to cast a negative mold from the acrylic/SU-8 master. This silicone has much higher tear strength than Sylgard® 184 silicone, making it a more attractive option for large size, high durability molds.
- Casting of polyurethanes is completed using TC-5045 molds and the adhesion performance of different fibers is compared.

A custom 254 nm source is used to provide higher power exposures and consists of a stainless steel box containing 12 25W bulbs. A sample is placed on a battery powered turntable (AUTOArt 8" Rotary Display Turntable Stand) immediately under

an anti-scatter grid and exposed through the anti-scatter grid while rotating. This rotation during exposure evens out the exposure dose and avoids shadowing specific areas. The anti-scatter grid is a plastic grating 12.5 mm thick with square holes 12.5x12.5mm in size arranged in a single or dual level configuration to make 1:1 or 2:1 aspect ratio grids. Although anti-scatter grids are quite common for reducing noise in X-ray imaging, they are not commonly used for UV light because a lot of light intensity is lost. However, a semi-collimated exposure can be completed over large areas at one time using this method. The effect of the anti-scatter grid is also assisted by the natural effect of Snell's Law as the UV passes from the air to the higher index of refraction acrylic. This angle enhancement is most apparent for the low aspect ratio grids, but still assists for 2:1 aspect ratio grid features (Figure 2).

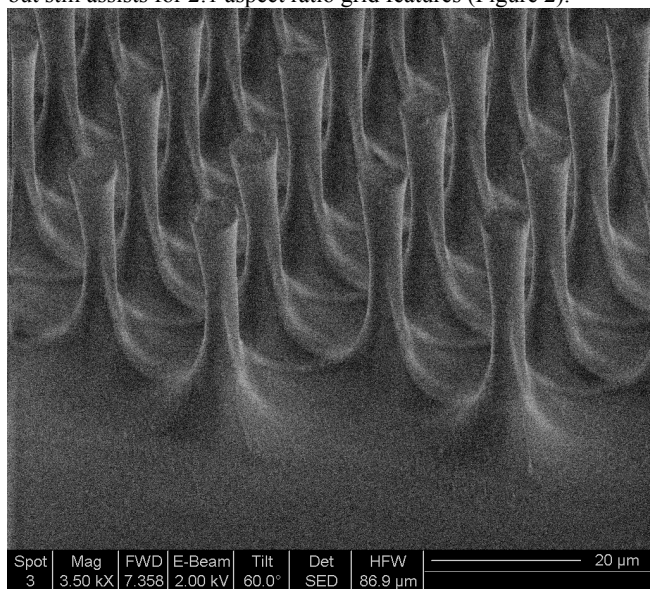


Figure 2. 4:1 aspect ratio acrylic fibers defined with a 2:1 aspect ratio anti-scatter grid. A metal mask rather than SU-8 defined fibers without caps.

## EXPERIMENTS

A series of experiments were completed on two 5"x5" acrylic squares where the aspect ratio of the anti-scatter grid, the exposure time to 254 nm light and development time were varied. Circular SU-8 caps on a square array were defined with thickness of 1.6 μm. Two different diameters of caps were defined, but the variations with best yield and adhesion behavior at this cap thickness were 12 μm in diameter with a center to center spacing of 20 μm. The substrates were exposed to 254 nm light with different anti-scatter grid aspect ratios to four different doses. After exposure, development in SU-8 proceeded in 10 minute increments, after which the molds were rinsed and dried. The developed depth in wide open areas was measured and a negative mold was cast from TC-5045 to later make dry adhesives with the resulting geometry at each stage of development. Visual inspection was done at each stage as well to determine failure modes and estimate the yield of fibers for each process condition.

The TC-5045 silicone molds were cast with low-modulus polyurethane (ST-1060 from BJB Enterprises) that has been characterized by other researchers for use as a dry adhesive [1, 6-7]. This particular polyurethane has extremely high tear strength, reducing the likelihood of damage during demolding, but its modulus is relatively low (~3MPa) making fibers vulnerable to collapse if they are too tall or narrow. For higher aspect ratio fibers, stiffer polyurethane (WC-755 from BJB Enterprises) was

also used to make dry adhesive structures. Its tensile modulus is approximately 100 MPa and it has a listed Shore D hardness of 55.

To test the relative adhesion performance of fibers produced using this process, a custom measurement system was used. This system consisted of a sensitive force probe (GSO-25 from Transducer Techniques) combined with a 6mm diameter hemispherical sapphire tip (Edmund Optics, NT49-556), attached to a linear stage controlled by custom software. Adhesion vs. preload was recorded for multiple trials at a pull speed of 5 μm/s.

## RESULTS

We have found that the degree of crosslinking in the SU-8 appears to be a critical factor in its adhesion to acrylic and is best controlled by the use of exposure dose because the baking temperature is limited by the thermal tolerance of the acrylic. Initial experiments indicated that i-line exposure doses in excess of 600 mJ/cm<sup>2</sup> (approximately 10X the recommended dose), were required in combination with baking times of greater than 1 hour at 80°C to achieve best adhesion results. Baking temperatures were limited to 80°C to prevent plastic deformation of the acrylic. SU-8 features must remain on acrylic after silicone demolding from overhanging features, requiring very large interfacial adhesion strengths if the fibers are to survive multiple demold cycles.

To calibrate the dose provided by the custom UV source, the developed depth of acrylic was measured for different exposures doses from a commercial 254 nm source. The doses correspond to a 0, 5, 10 and 15 hour exposure at a nominal intensity of 4 mW/cm<sup>2</sup> in a Stratalinker 2400. The resulting depths vs. development time are shown in Figure 3 and the unexposed acrylic dissolved at approximately 60 nm per minute. Because this development rate is highly dependent on the average molecular weight of the acrylic these calibration curves are not valid for all commercial acrylics but high consistency is usually obtained for substrates cut from any individual sheet of OPTIX®.

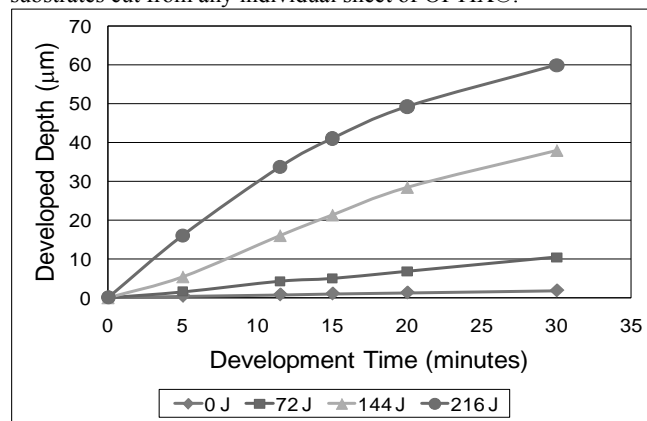


Figure 3. Developed depth of OPTIX® in SU-8 developer at 18 °C with different exposure doses of uncollimated 254 nm light. Depth measurements are on wide open areas – uncollimated light will produce smaller depths between tightly spaced features.

The developed depth vs. time can be used to calibrate the approximate dose received by samples exposed in the custom source using different anti-scatter grid designs. Direct comparison between the two grid designs revealed that the 2:1 aspect ratio grid transmitted approximately 35% of the power compared with a 1:1 aspect ratio grid – requiring 3X the exposure time to achieve similar development rates. Fibers defined with a 1:1 aspect ratio grid had lower true fiber heights than those defined by a 2:1 grid with the same measured depth because a plateau would form under

closely spaced fibers, as shown in Figure 4. Depending on the dose, the individual fiber heights could be 1/2 – 2/3 the total depth in wide open areas for 1:1 aspect ratio grid exposures.

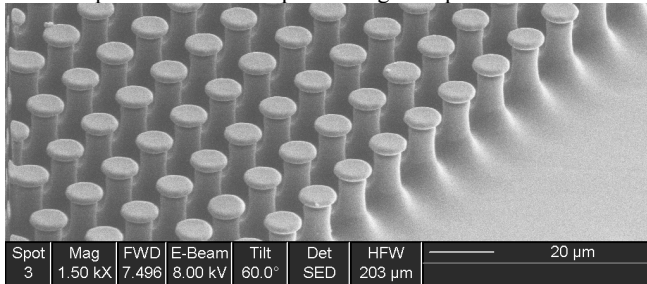


Figure 4. Fibers cast from a mold defined with a 1:1 aspect ratio grid. The fiber base is higher than the base of the open areas.

All fibers defined using a 200 J exposure dose through the 1:1 grid failed at development times longer than 10 minutes. These fibers were cut off before sufficient undercutting of the cap occurred, making this choice of exposure time impractical for producing an effective adhesive structure. For all other conditions, yield was primarily reduced by caps falling off of the fiber tips during silicone demolding. This was noticeably worse around the perimeter of the 5”x5” acrylic mold. The reduced light intensity at those locations was found to be responsible for the lower SU-8 adhesion to acrylic (Figure 5). This issue was resolved for other molds by increasing i-line exposure dose to 900 mJ/cm<sup>2</sup>.

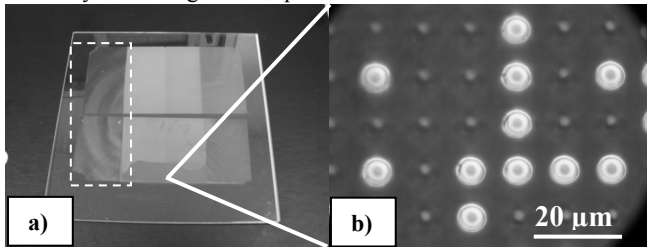


Figure 5. a) 5”x5” acrylic substrate used for tests after a 20 minute development. Cap failure of 6 μm diameter features is greatest at the perimeter (b), but fibers are reduced to less than 2 μm in diameter under these conditions. Dashed line indicates where fibers were completely undercut from overexposure.

The geometries that were successfully produced in acrylic and subsequently manufactured in ST-1060 polyurethane were measured using optical methods and scanning electron images of the fibers. The primary dimensions of importance were the cap overhang and fiber height. The adhesion strength increased with increasing cap overhang, while increased fiber height made the dry adhesive designs more effective at conforming to the rounded surface of the hemispherical probe. Because some 254 nm light does pass through the SU-8 caps, small differences in overhang occur between fibers exposed for different doses at the same development time. The average fiber dimensions are found from profilometer data, SEM and optical images.

Each sample of ST-1060 polyurethane fibers tested for adhesion was 1.5 mm thick and the pull speed of the hemispherical tip was set to be 5 μm/second for each trial. To save space not every data trial is listed, but a dramatic difference in adhesion strength is observed once the cap overhang becomes slightly larger than its thickness (Figure 6). For ST-1060 fibers with an overhang to thickness ratio greater than 1:1, the fiber height has a larger influence, as the adhesive surface can conform better to the hemispherical probe and results in a higher maximum adhesion at larger preloads (Figure 7). All reported data are for the 12 μm

diameter fiber tip designs defined with a 1:1 aspect ratio grid, which had the highest fabrication yields. Fiber height (including SU-8 cap) and cap overhang in micrometers are listed for each data set.

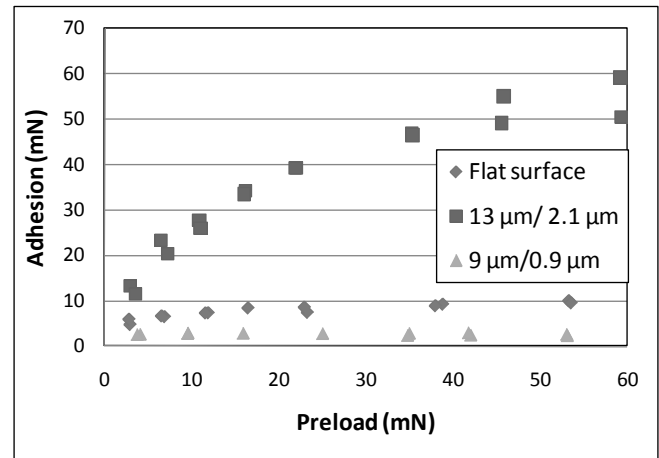


Figure 6. Comparison of adhesion vs. preload for an unstructured ST-1060 surface and fiber height/overhang defined with a 10 and 20 minute development. Exposure dose was approximately 120 J through a 1:1 aspect ratio grid.

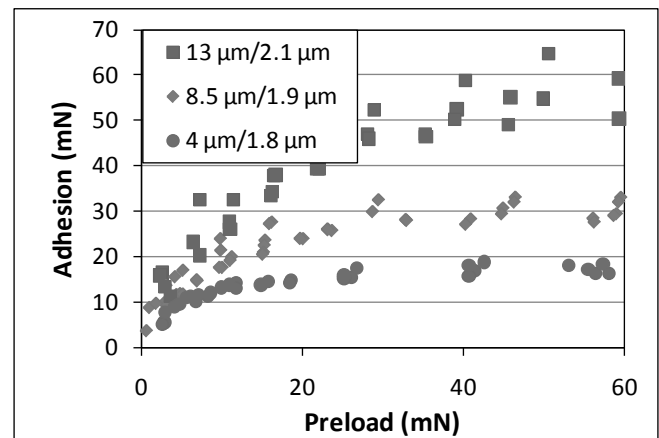


Figure 7. Typical adhesion data for ST-1060 polyurethane fibers defined with different geometries tested at different locations. 254 nm dose of 120, 80 and 40 J though a 1:1 grid was used with a development time of 20 minutes

Although the fill factor of each design was identical at approximately 28%, very large differences in adhesion performance are observed for different fiber geometries. As seen in Figure 6, as the cap overhang increased from 0.9 to 1.9 μm the adhesion performance changed from worse to much better than an unstructured surface processed in the same manner. Figure 7 shows that there is much more variability in adhesion, but also a higher maximum adhesion value reached for taller fibers with similar cap dimensions. There is an upper limit to this effect however, as still taller fibers will have greatly reduced adhesion as they collapse immediately after demolding or during testing. This was seen primarily with over developed fibers and those defined with equal doses through 2:1 aspect ratio grids.

In comparison to the more flexible ST-1060, both higher aspect ratio fibers and larger cap overhangs can be successfully demolded using WC-755. A sample of WC-755 cast from a mold defined using a 100J, 1:1 exposure and 40 minute development is

shown in Figure 8. This geometry was not appropriate for ST-1060, but good adhesion and yield was achieved for WC-755 fibers. Qualitative tests indicated that while the structured WC-755 would show much greater normal and peel strength on flat surfaces than its unstructured state, adhesion to rounded surfaces like those on our test system was less effective. Plotting preload vs. adhesion strength for this material does not provide an accurate assessment of the performance because the viscoelasticity of the WC-755 was much greater than that of the ST-1060. While the maximum adhesion force of WC-755 did not always increase as dramatically as ST-1060 compared to its unstructured state, the energy dissipated (from the area under the force/displacement curve) was far higher for the structured WC-755 (Figure 9). The uneven adhesion force with displacement is suspected to be due to individual fibers losing contact intermittently. If higher preloads were used, WC-755 fibers would remain deformed for at least a few minutes, and occasionally would not recover.

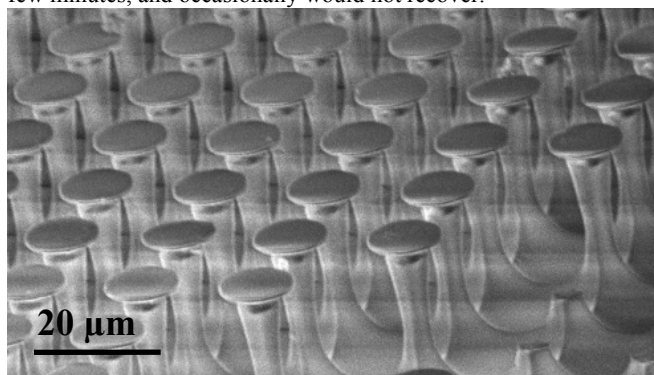


Figure 8. SEM images of WC-755 polyurethane fibers tested for adhesion. Height is approximately 30  $\mu\text{m}$  and minimum fiber diameter is approximately 5  $\mu\text{m}$ .

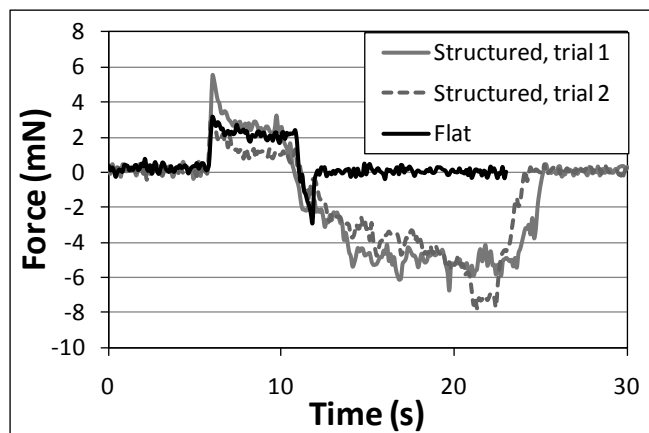


Figure 9. Two individual adhesion trials of the structured WC-755 fibers shown in figure 8 and a flat control. A large reduction in preload force is seen after first contact, demonstrating viscoelasticity.

## CONCLUSIONS

We have developed a novel and unique method of producing biomimetic dry adhesives in a variety of materials and geometries. Using a bulk acrylic substrate can dramatically lower the cost per area of producing dry adhesive structures, and direct photopatterning of acrylic allows a very large variety of fiber geometries to be produced using different process parameters. For low modulus polyurethanes like ST-1060, an anti-scatter grid with a 1:1 aspect ratio is sufficient to make effective dry adhesives.

While a 2:1 aspect ratio grid can produce higher aspect ratio fibers, there is a diminishing return past this point due to the severe reduction in light intensity. These higher aspect ratio fibers are required for stiff materials, but switching to a lower exposure dose and longer development time can also produce the narrow fiber, large cap overhang structures necessary to make stiffer polyurethanes behave as effective dry adhesives. Our primary focus now is on reducing the minimum feature size while maintaining high yield, and finding the best structural materials for long lifetime dry adhesives. The fabrication process developed in this work is very promising for large scale commercial structuring of dry adhesives and other biomimetic materials. Our long term goals will be to determine optimal fiber geometries for synthetic dry adhesives produced in a variety of materials and develop practical design rules for manufacturing these structures.

## ACKNOWLEDGEMENTS

We would like to thank Marius Haiducu and Dr. Ian G. Foulds for the construction of the custom UV source. Thanks are also extended to Dr. M. Parameswaran and the IMMR group at Simon Fraser University for use of their fabrication facilities and equipment. This work was financially supported by NSERC.

## REFERENCES

- [1] S. Kim and M. Sitti, "Biologically inspired polymer microfibers with spatulate tips as repeatable fibrillar adhesives," *Applied Physics Letters*, vol. 89, pp. 261911 1-3, 2006.
- [2] H. E. Jeong, *et al.*, "A non transferring dry adhesive with hierarchical polymer nanohairs," *Proc. Nat. Acad. Sciences*, vol. 106, pp. 5639-5644, 2009.
- [3] D. Sameoto and C. Menon, "A low-cost, high yield fabrication method for producing optimized biomimetic dry adhesives," *J. Micromech. Microeng.*, vol. 19, p. 115002, 2009.
- [4] D. Sameoto and C. Menon, "Direct molding of dry adhesives with anisotropic peel strength," *J. Micromech. Microeng.*, vol. 19, p. 115026, 2009.
- [5] A. del Campo, *et al.*, "Contact shape controls adhesion of bioinspired fibrillar surfaces," *Langmuir*, vol. 23, pp. 10235-10243, 2007.
- [6] M. Murphy, *et al.*, "Adhesion and Anisotropic Friction Enhancements of Angled Heterogeneous Micro-Fiber Arrays with Spherical and Spatula Tips," *Journal of Adhesion Science and Technology*, vol. 21, pp. 1281-1296, 2007.
- [7] B. Aksak, *et al.*, "Gecko inspired micro-fibrillar adhesives for wall climbing robots on micro/nanoscale rough surfaces," *IEEE International Conference on Robotics and Automation*, pp. 3058-3063, 2008.
- [8] R. W. Johnstone, *et al.*, "Deep-UV exposure of poly(methyl methacrylate) at 254 nm using low-pressure mercury vapor lamps," *Journal of Vacuum Science and Technology B: Microelectronics and Nanometer Structures*, vol. 26, pp. 682-285, 2008.
- [9] R. W. Johnstone, *et al.*, "Self-sacrificial surface micromachining using poly(methyl methacrylate)," *J. Micromech. Microeng.*, vol. 18, p. 115012, 2008.
- [10] M. Haiducu, *et al.*, "Deep UV patterning of commercial grade PMMA for low cost, large scale microfluidics," *J. Micromech. Microeng.*, vol. 18, p. 115029, 2008.

## CONTACT

\*D. Sameoto, tel: +1-780-248-2052; sameoto@ualberta.ca

# APPLICATION OF MILLISECOND PULSED LASER WELDING IN MEMS PACKAGING

*P. Bozorgi\**, *C.B. Burgner*, *Z. Yie*, *C. Ding*, *K.L. Turner* and *N.C. MacDonald*

Department of Mechanical Engineering, University of California Santa Barbara, California, USA

## ABSTRACT

This paper reports a new packaging method for a wide range of MEMS applications on both the wafer and device scale. Titanium is used as the packaging material in this work and both Si-MEMS and Ti-MEMS devices are integrated into a 350  $\mu\text{m}$  titanium substrate. A Nd:YAG pulsed laser is used as a localized heating source to micro-weld a 350  $\mu\text{m}$  titanium cap to the substrate. Simulation of the heat conduction of a two-dimensional time-dependent pulse laser between the substrate and cap was carried out using COMSOL to investigate pulsed laser melting properties. To avoid thermal distortion of the welding, several geometries at the cap and substrate interface were investigated to minimize laser intensity in order to achieve the required melting depth.

## INTRODUCTION

Packaging provides structural and environmental protection for MEMS devices to enhance their reliability but poses a critical challenge for the commercialization of MEMS products. Techniques that are compatible with wafer level fabrication, low temperature processing, vacuum and hermetic encapsulation, and standard MEMS post-fabrication approaches are needed in many applications.

Although Au-Au and Si-Au eutectic bonding [1] and anodic bonding [2] have been widely used in MEMS packaging, these global heating packaging approaches still have several drawbacks. They are not reproducible, have surface and intermediate film dependency, and require various high temperature steps for bonding. As such, no temperature sensitive material survives through the bonding process.

In this work, we use titanium as the packaging material with a pulsed laser to locally heat and weld a titanium cap to the substrate. The proposed method addresses the drawbacks of eutectic and anodic bonding approaches. Titanium has been studied as a new material to produce MEMS [3]. This paper introduces titanium as an advantageous MEMS packaging material due to its high fracture toughness, weldability and potential *in vivo* applications in biotechnology [4].

## APPROACH AND MODELING

When a laser beam is irradiated onto the surface of a material, the absorbed energy causes heating, melting and evaporation of the material depending on the absorbed laser power intensity [5]. Laser welding is performed by moving the focused beam over the surface of the work piece along the desired contour that separates the two pieces to be joined. If the laser beam intensity is sufficiently high and the scanning speed is not too large, evaporation throughout the full depth of the workpiece can be obtained and the so called keyhole is formed, see Figure 1. This keyhole absorbs a considerable amount of the laser beam power. Thus, the keyhole plays an important role in transferring and distributing the laser energy deep into the material and provokes melt depth, Figure 1 [6]. The thickness  $h$  of a laser-induced melting layer is an important parameter in pulsed laser interaction with the material surface. It is a key factor for quantifying the hydrodynamic aspect of laser ablation and hermiticity of laser welding.

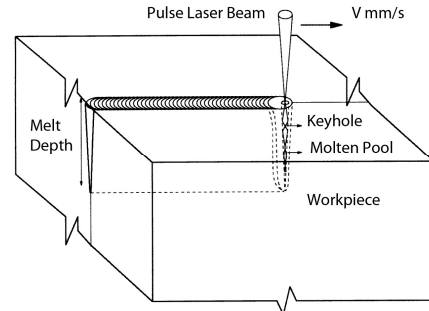


Figure 1: Schematic of keyhole, melt depth and molten pool in pulse laser welding.

Previous studies on the melt depth of pulsed laser [7] showed that the thickness  $h$  is a function of many parameters

$$h \propto (I, \tau, \alpha, A, \chi, C, \varphi, q, T_m, T_b, T_i, D), \quad (1)$$

where  $I$  is the laser intensity,  $\tau$  is the pulse duration,  $\alpha$  is the absorption coefficient,  $A$  is the surface absorptivity,  $\chi$  is the thermal diffusivity,  $C$  is the specific heat,  $\varphi$  is the angle of incidence,  $q$  is the latent heat of melting,  $T_m$  and  $T_b$  are the melting and boiling points,  $T_i$  is the initial temperature, and  $D$  is the laser focal spot size.

Hermiticity of the proposed packaging method is directly related to the melt depth of the titanium cap to the substrate in welding. The melted titanium at the interface of the cap and substrate is merged and solidified afterwards. Increasing the melt depth will generate a bigger molten pool at the interface and consequently stronger bonding between the cap and substrate. We assumed in our simulation the material properties during the welding stay constant, therefore the laser intensity plays a main role in increasing the melt depth. However, increasing the laser intensity generates more heat during the welding and this raises heat distortion issues.

Optimization of melt depth requires knowledge of the behavior of  $h$  over a wide range of the parameters. As a first step, vaporization effects are not considered in our simulation. We present a 2D time and spatial heat conduction model, Equation (2), in COMSOL to determine the melt depth and generated heat for various laser parameters such as intensity, pulse duration, pulse frequency, laser focal spot size, and welding speed. The correlation between the melt depth and generated heat was investigated to optimize  $h$  based on minimizing the heat

$$\frac{\partial}{\partial x} \left( k_x \frac{\partial T}{\partial x} \right) + \frac{\partial}{\partial y} \left( k_y \frac{\partial T}{\partial y} \right) + I = \rho c \left( \frac{\partial T}{\partial t} - v \frac{\partial T}{\partial x} \right), \quad (2)$$

where  $k_x$  and  $k_y$  are thermal conductivity in  $x$  and  $y$  directions,  $I$  is laser power per unit volume,  $\rho$  is density,  $t$  is time and  $v$  is velocity of the laser welder.

As shown in Figure 2, the Nd:YAG pulse laser was modeled as a Gaussian heat source. The laser has a rectangle pulse shape and the heat source is turned on and off with frequency of pulse laser. The focal size of the laser was determined in accordance



with the cap thickness as prescribed in [8]. The titanium cap and substrate are  $350\ \mu\text{m}$  thick and the laser focal spot size is  $300\ \mu\text{m}$ , and the pulse duration is  $1\ \text{ms}$  with a frequency of  $14\ \text{Hz}$ . Initial simulation results show a linear relationship between the laser intensity and temperature along the cross-section of the cap and substrate, Figure 2. Simulation result shows a pulse energy of  $6\ \text{J}$  is required to melt the substrate at the interface. The pulse generates  $6\ \text{kW}$  of heat which can be harmful to any MEMS device.

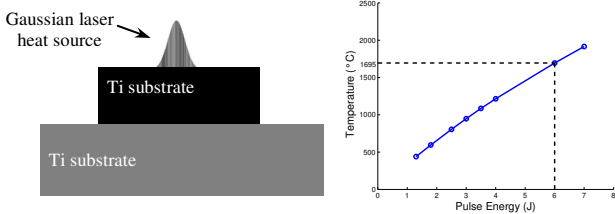


Figure 2: The required pulse energy to weld  $300\ \mu\text{m}$  Ti cap to the substrate was determined by modeling laser as a Gaussian heat source.

Simulations seen in Figure 3 show the thickness and geometry of the cap and substrate at the interface play a significant role in determining laser parameters. In order to balance the melt depth and generated heat, three different bridge geometries were investigated for the substrate at the interface and the cap thickness was decreased to  $100\ \mu\text{m}$ . The simulation results in Figure 3(c) reveal that decreasing the bridge width and adding a trench reduces the power required for welding, thus reducing the unwanted heat transferred to the enclosed MEMS device. From these results, it is expected we achieve deeper melt depth on the narrow bridge with a trench for a given pulse laser compared to bridge configurations without a trench. Specifically, Figure 4(c) shows that changing the trench depth,  $d$ , from  $20$  to  $10\ \mu\text{m}$  does not impact the temperature of the substrate at the interface. But changing the trench width from  $100$  to  $250\ \mu\text{m}$  causes an increase in the temperature of the substrate from  $3860$  to  $4600\ ^\circ\text{C}$ .

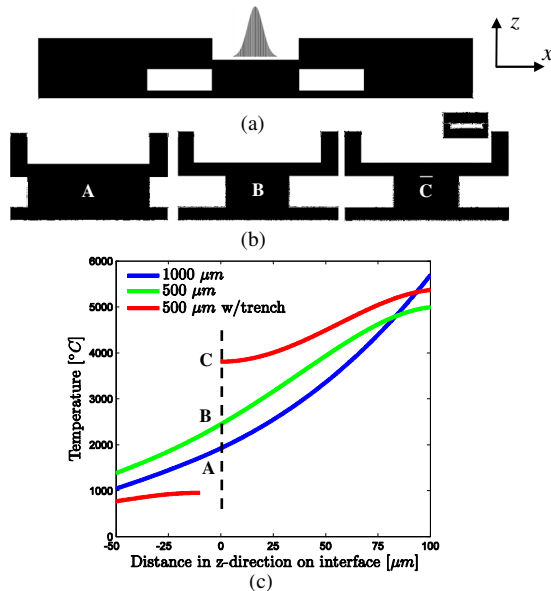


Figure 3: (a) Applied pulse laser with energy of  $1.3\ \text{J}$  and  $1\ \text{ms}$  pulse duration, (b) bridge A and B have a widths of  $1000$ ,  $500\ \mu\text{m}$  respectively and bridge C has width of  $500\ \mu\text{m}$  with a trench (c) temperature gradient on the cap and the interface for each bridges.

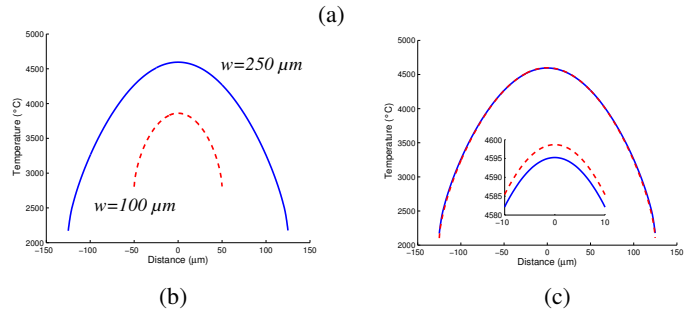
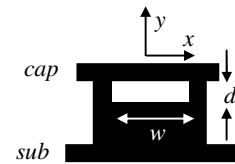


Figure 4: (a) The trench dimension on the substrate (b) Temperature gradient on the cap at the interface when the trench depth is  $20\ \mu\text{m}$  and width is changed from  $100$  to  $250\ \mu\text{m}$ . (c) temperature gradient on the substrate does not change notably when the depth is increased from  $10$  to  $20\ \mu\text{m}$  ( $d=250\ \mu\text{m}$ ).

As shown in Figure 5, welding the cap to the substrate causes a bending down of the cap at the interface to meet the substrate. This residual bending stress can generate micro cracks at the interface. To avoid this problem, the trench width should be increased from  $100$  to  $250\ \mu\text{m}$ . By increasing the width of the trench, a deeper melt depth occurs, Figure 4(b), and prevents cracks at the interface.

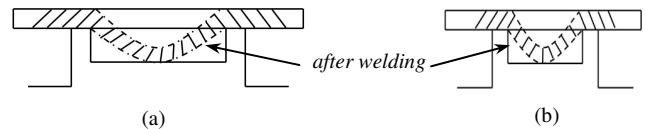


Figure 5: Schematic of the cap curvature after bending in welding for a trench with (a)  $250\ \mu\text{m}$  width (b)  $100\ \mu\text{m}$  width.

Simulation results in Figure 6 reveal that the temperature gradient in the substrate determines what distance from the heat source the MEMS device can be mounted. It can be seen that at a distance of  $400\ \mu\text{m}$  from the laser heat source, the temperature on the substrate drops to  $100\ ^\circ\text{C}$  and the MEMS device can be safely mounted beyond this point.

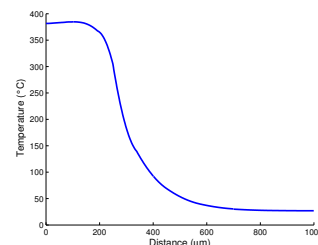


Figure 6: Temperature of substrate in welding process drops to  $100\ ^\circ\text{C}$  at a distance of  $400\ \mu\text{m}$  from the laser spot.

## FABRICATION AND EXPERIMENT

In order to verify the simulation results on a bridge with a trench and show that creating a trench increases the melt depth, several experiments were carried out. The designed bridges on the substrate were fabricated via macro-machining and various laser parameters were applied to weld the cap to the substrate. Both the cap and substrate were taken from 350  $\mu\text{m}$  thick titanium wafers. Figure 7 presents a schematic of the fabrication process. The cap was macro-machined down to a thickness of 100  $\mu\text{m}$ , Figure 7(a). Figure 7(b) shows the macro machining fabrication process of three bridges. The first two bridges have a width of 1000 and 500  $\mu\text{m}$ , respectively. The third bridge has a width of 500  $\mu\text{m}$  with a trench that is 250  $\mu\text{m}$  wide and 20  $\mu\text{m}$  deep. The cap and substrate were mated firmly, as presented in Figure 7(c). A millisecond YAG pulsed laser with a focal spot size of 300  $\mu\text{m}$ , a pulse energy of 0.8 J and a pulse duration of 1 ms was used to weld the titanium cap to the substrate.

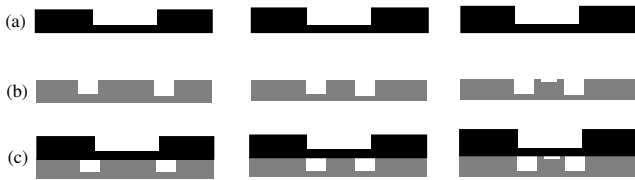


Figure 7: (a) Macro-machining of the titanium cap (b) Macro-machining of the titanium substrate to fabricate the bridges (c) bringing the cap and substrate together using vacuum chuck.

The experimental results in Figure 8 show that for the bridges without a trench, the cap and substrate were not solidified at their interface and no melt residue was seen on the substrate. But as shown in Figure 10(d) in the bridge with a trench, the cap and substrate were welded at their interface and melt residue was clearly seen on the substrate.

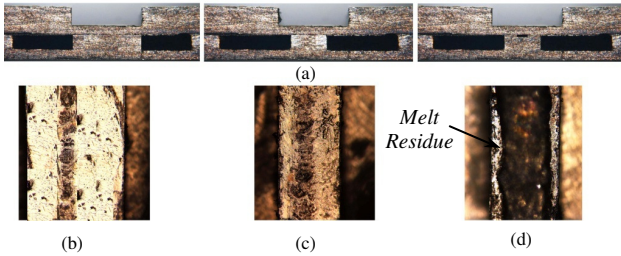


Figure 8: (a) Fabricated bridges before welding (b) and (c) The bridge with width of 1000 and 500 $\mu\text{m}$ , respectively. A burnt line of welding can be seen on substrate (d) Showing the bridge with width of 500  $\mu\text{m}$  and a trench. The melt residue of welding between the cap and the substrate can be clearly seen.

The three different bridges for the substrate were characterized and shown the bridge with a trench is the optimized geometry to balance heat and melt depth in laser welding. The bridge with a trench was implemented on a titanium wafer for large scale packaging. A 100 mm titanium wafer with thickness of 300  $\mu\text{m}$  was used as the substrate and cap in this work. Figure 9 presents the packaging process for both Si-MEMS and Ti-MEMS devices. The titanium cap and substrate were macro-machined as

shown in Figure 9(a) and (b) respectively. Gold-ceramic-titanium or GCT feedthroughs were fabricated on the substrate and the MEMS devices were mounted and wire bonded to GCTs, Figure 9(c). Figure 9(d) shows the cap and substrate were brought together firmly by using a vacuum chuck. The laser parameters used to weld the cap to substrate shown in Table 1. Figure 11(d) shows a schematic of the packed device.

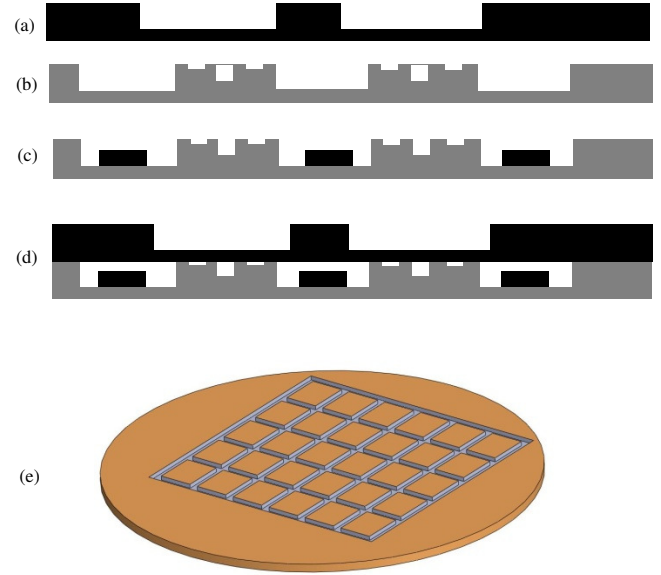


Figure 9: (a) and (b) Macro-machining a titanium wafer to fabricate the cap and substrate (c) Mounting the MEMS device on the substrate and wire bonding to GCTs (d) The cap and substrate are brought together by using a vacuum chuck (e) Schematic of the packaged wafer.

The hermeticity of the packaged device was measured by helium leaking rate test base on MIL-STD-883E standard. The helium leak detector was used in this work is Alcatel ASM 142 and the leaking rate of  $3.45 \times 10^{-10}$  atm.cc/s for volume of 0.18  $\text{cm}^3$  was measured.

Table 1: Laser parameters were used to weld the titanium cap to the substrate in wafer scale packaging.

Laser Spot		Seam Welding	
Pulse shape	Rectangular	Welding speed	0.85 mm/s
Peak power	1.3 KW	Focal spot size	300 $\mu\text{m}$
Pulse duration	1 ms	Pulse frequency	14 Hz
Energy per pulse	1.3 J	Spot overlap	80%

To verify the proposed packaging method and its functionality on device scale, it was applied to package an AFM tips on titanium substrate. The device tested is a self-actuating self-sensing AFM cantilever tip (MPA-41100-S, Veeco Instruments) and is shown wire bonded to the GCTs, Figure 10 (a) and (c). By measuring the resonant frequency and quality factor before and after packaging as shown in Figure 10 (d) it is determined that the applied technique has no effect on the packaged device or GCT feedthroughs.

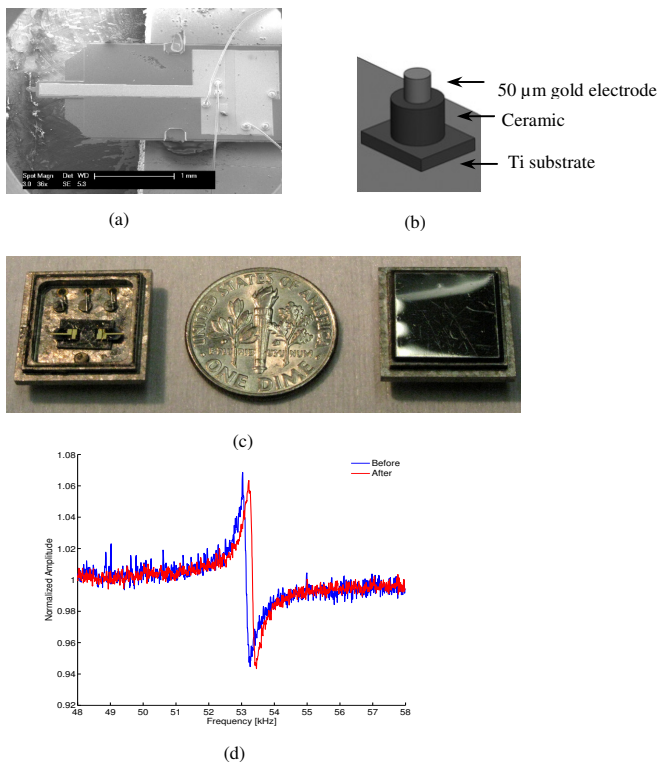


Figure 10: (a) AFM cantilever was used to measure resonance frequency and quality factor before and after packaging (b) GCT feedthroughs (c) the packaged device (d) resonance frequency of the AFM tips was consistency after and before packaging.

## CONCLUSION

The new packaging method was modeled, simulated, fabricated and experimentally characterized. We combined titanium as a new material for packaging and YAG millisecond pulse laser as a localized heat source to introduce a new packaging technique for MEMS on both the wafer and device scale. The pulsed laser serves as a localized heat source and overcomes other packaging technique issues such as heat distortion and MEMS device damage from global heating packaging processes. The demonstrated packaging method applies directly to the titanium cap and substrate with no need of any interface material or films between them. This is considered a main advantage over the current methods. Our packaging method provides low cost, fast operation, high precision with low thermal distortion, reliable and biocompatible packaging for MEMS devices. This technique can be applied to both titanium and silicon MEMS making it a potential bridge between silicon Bio-MEMS and biotechnology applications.

## ACKNOWLEDGEMENT

The authors would like to thank Veeco Instruments for providing the AFM tips.

## REFERENCES

- [1] H. Tachibana, K. Kawano, H. Ueda and H. Noge, "Vacuum wafer level packaged two-dimensional optic scanner by anodic bonding ", IEEE MEMS 2009, Sorrento, Italy.
- [2] J.S. Mitchell and K. Najafi, "A detailed study and reliability for vacuum packages fabricated in a wafer-level Au-Si eutectic bonding process ", Transducer 2009, Denver, USA.
- [3] M.F. Aimi, M.P. Rao, N.C. Macdonald, A. Zuruzi and D.P. Bothman, "High-aspect-ratio bulk micromachining of titanium", Nature Materials, 3, 103 (2004).
- [4] D. Brunette, Titanium in Medicine, Springer, 2001.
- [5] N.B. Dahotre, Laser Fabrication and Machining of Materials Springer Science, 2008, pp. 4-9.
- [6] N. A.F.H Kaplan, "A model of deep penetration laser welding base on calculation of the keyhole profile", Journal of Physics D: Applied Physics 27:1805-1814
- [7] V.N. Tokarev and A.F.H. Kaplan, "An analytical modeling of time dependent pulsed laser melting", Journal of applied physics, volume 86, number 5, September 1999.
- [8] W.W. Duley, Laser Welding, Wiley, New York, 1999.
- [9] Department of Defense, MIL-STD-883, "Test Method Standard, Micro-Circuits", method 1014.9, March 14, 1995

## CONTACT

\*P. Bozorgi, tel: +1-323-206-1506; payam@engineering.ucsb.edu

# CHARACTERIZATION OF THE COMPLETE STRESS STATE IN THIN-FILM CMOS LAYERED MATERIALS

F. Fachin<sup>1\*</sup>, M. Varghese<sup>2</sup>, S.A. Nikles<sup>2</sup>, B.L. Wardle<sup>1\*\*</sup>

<sup>1</sup>Massachusetts Institute of Technology, Cambridge, MA, USA

<sup>2</sup>MEMSIC Inc., Andover, MA, USA

## ABSTRACT

We present a new methodology for characterizing the complete stress state (effective mean compressive and gradient stresses) in CMOS layered materials that also assesses non-ideality of clamped boundaries. The approach uses a closed-form solution for the nonlinear post-buckling of micromachined beams also including non-ideal boundaries, and experimental measurements of deflected beams. For the CMOS materials examined here, the accuracy was  $\pm 2$ MPa for mean compressive stress and  $\pm 3$ MPa/ $\mu\text{m}$  for gradients, limited by measurement errors and uncertainty on material properties. Boundary non-ideality is found to be  $\sim 90\%$  of perfectly clamped for the CMOS-released structures and has a significant effect on the extracted stresses such that it must be modeled appropriately. The method is transferrable from test structures to device level, and can be used to measure packaging stress as well.

## INTRODUCTION

Characterization of thin-film layered materials is critical to the development of many MEMS devices. Residual stresses from production determine both the final shape and the performance of microdevices, and should therefore be accurately assessed if possible. Mean residual stress determination is especially relevant for many microbridge-type devices, as large compressive stresses may cause the device to buckle (Figure 1a) and, in some instances, to fail. On the other hand, stress gradients become particularly acute as the films become thinner [1], which may lead to (undesired) large out-of-plane deformation (Figure 1b). To date, a variety of approaches to characterize the stress state of thin materials have been developed, most of which are based on the information obtainable by studying the post-release deformation (e.g., bending, buckling, twisting) of simple micromechanical components. As an example, mean compressive stress is typically determined using arrays of clamped-clamped beams of different lengths [2], whereas tensile stress is extracted using more complicated geometries such as crossbar rings and "T"- or "H"-like structures or from wafer/cantilever beam measurements utilizing the well-known Stoney's relation [1, 3]. Curvature of released microcantilevers is instead measured to estimate the gradient stress in thin-films, as first demonstrated by Chu and Mehregany [4]. Although well-established, these approaches to material characterization have two major limitations. First, their accuracy is directly proportional to their cost. This is especially true for mean compressive stress, where more accurate estimates require a larger number of different test structures. Second, they oversimplify the test-structure boundary conditions by assuming them to be ideal (e.g., perfectly clamped in the case of buckled beams for mean compressive stress determination [1]). A first attempt to resolve these issues was performed by Fang and Wickert in 1995. In their paper [6], the authors discuss the effect of boundary condition on the deformation of single material micromachined cantilevers, and propose a new way of estimating residual stresses by measuring cantilever curvature and boundary rotation. Based on a numerically-derived description of the deformation of micromachined structures, this approach requires the field to be made of the same material combination as the

cantilevers, and therefore cannot be generalized to the analysis of general test structures (or, more broadly, of actual devices). Furthermore, the extant techniques cannot provide information regarding the effect of packaging on the final stress state of the device, as packaging does not affect fully released cantilevered structures.

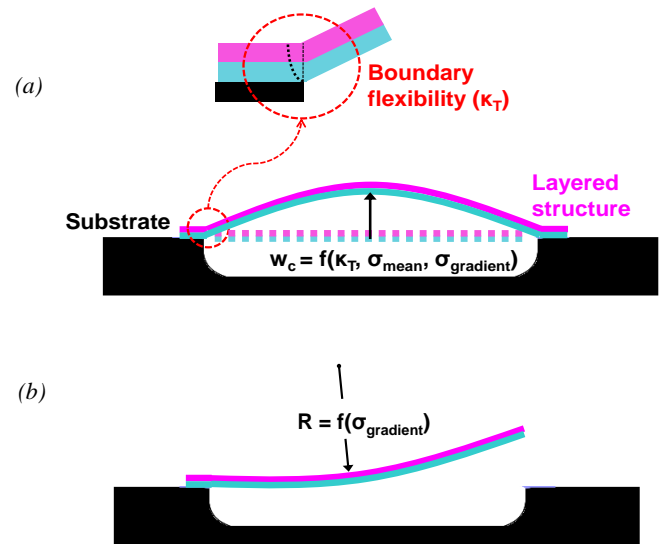


Figure 1: Post-release out-of-plane deformation of (a) doubly-clamped microbridge and (b) microcantilever

Here we introduce a new approach to the characterization of the complete stress state in multi-layered thin-film materials which addresses the issues above, and demonstrate it for CMOS layered films. The technique is based on a closed-form solution of the buckling problem of micromachined beams including non-ideal boundaries (see detail in Figure 1a), and allows for extraction of the effective mean and gradient stresses using as few as two different sets of test structures (namely, one set of cantilevers, and one set of doubly-clamped beams per layered material combination). Non-ideality of the boundary is considered by introducing a flexible boundary with spring constant  $\kappa_T$ , determined experimentally concomitant with the residual stresses. In the CMOS examples herein, the method provides stress estimates accurate up to  $\pm 2$ MPa for mean stresses and  $\pm 3$ MPa for gradients, significantly better than what standard critical-length buckling approaches can provide. The accuracy is largely due to proper quantification of the boundary-condition, a main determinant of extracted stress values. For the structures analyzed here, the results point to non-ideal boundaries having approximately 10% less fixity than the perfectly-clamped boundary. The accuracy in the results is limited by displacement profile error (non-contact profilometry) and uncertainty in material properties of the films comprising the layers. The approach is

applicable to both micromachining and CMOS processing, and can be extended to packaging and processing stress characterization at a device level.

## THEORY

In our analytical method we model a microfabricated layered beam as a homogenized structure characterized by effective weighted-properties in bending and extension [7], and constrained at both ends by torsional springs allowing a range of boundary conditions from simply-supported to clamped (Figure 2). The layered beam has length  $L$ , width  $b$ , and thickness  $h$ . The torsional spring constant ( $\kappa_T$ ) represents the boundary bending stiffness, and is determined experimentally along with the mean and gradient stresses. The in-plane boundary condition is assumed to be completely fixed (no in-plane sliding). The released layered beam structure is subjected to residual stresses ( $\sigma_{\text{intrinsic}} = \sigma_{\text{mean}} + \sigma_{\text{gradient}}$ ) which may cause bending and buckling.

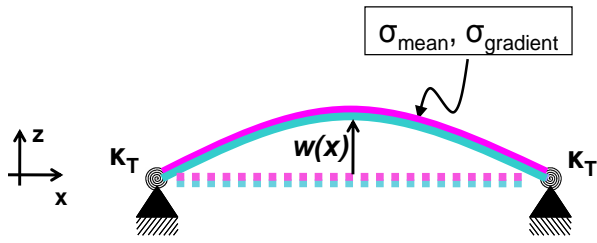


Figure 2: Schematic representation of a micromachined beam subjected to residual stresses ( $\sigma_{\text{mean}}$ ,  $\sigma_{\text{gradient}}$ ), with non-ideally clamped boundary modeled by torsional springs ( $\kappa_T$ ). Deflections  $w$  do not require buckling.

Using a linear through-thickness variation to approximate the distribution of stresses gives rise to an effective  $\sigma_{\text{gradient}}$  [1]. Linear-elastic Euler-Bernoulli beam-column theory is utilized to obtain the governing equations for the system of Figure 2:

$$\frac{\bar{E}I}{EI} \frac{d^4 w}{dx^4} + \frac{\bar{E}A}{2L} \int_0^L \left( \frac{dw}{dx} \right)^2 dx \frac{d^2 w}{dx^2} = -P_0 \quad (1)$$

$$M = M_0 + \bar{E}I \frac{d^2 w}{dx^2} \quad (2)$$

where  $w$  is the vertical (z-axis) displacement along the beam,  $A$  is the cross-sectional area,  $\bar{E}I$  is the layered beam effective bending modulus,  $\bar{E}A$  is the layered beam effective axial modulus,  $P$  is the thrust developed inside the structure, and  $P_0$  ( $=\sigma_{\text{mean}}A$ ) and  $M_0$  ( $=\sigma_{\text{gradient}}Ah^2/6$ ) are the thrust and the moment due to residual stresses, where  $A$  is the total cross-sectional area of the layered beam, and  $h$  is the total beam thickness. The boundary conditions are:

$$w(0) = 0 \quad , \quad M(0) = +\kappa_T w' \quad (3)$$

$$w(L) = 0 \quad , \quad M(L) = -\kappa_T w' \quad (4)$$

where the effect of boundary flexibility becomes apparent. Using a sinusoidal post-buckling deformation mode for the structure:

$$w(x) = C_1 \sin(\lambda x) + C_2 \cos(\lambda x) + C_3 \frac{x}{L} + C_4 \quad (5)$$

with  $C_1$ ,  $C_2$ ,  $C_3$ , and  $C_4$  being constants, the following formula for the critical buckling load ( $P_{\text{cr}}$ ) of doubly-hinged columns can be obtained [8]:

$$P_{\text{cr}} = \frac{\pi^2 EI}{L^2} \left( \frac{0.4 + \varphi}{0.2 + \varphi} \right)^2 = P_{\text{Euler}} \left( \frac{0.4 + \varphi}{0.2 + \varphi} \right)^2 \quad , \quad \varphi = \frac{EI}{\kappa_T L} \quad (6)$$

Equation 6 is plotted in Figure 3 for a typical CMOS polysilicon beam ( $400\mu\text{m} \times 40\mu\text{m} \times 3.3\mu\text{m}$ ), where we show the dependence of the non-dimensional critical load ( $\bar{P}_{\text{cr}} = P_{\text{cr}}/P_{\text{Euler}}$ ) on the boundary stiffness ( $\kappa_T$ ). The non-dimensional critical load ranges from 1 for simply-supported beams, to 4 for clamped structures. Importantly, the results show the presence of two different boundary flexibility values ( $\kappa_{T,ss}$  and  $\kappa_{T,clamped}$ ) below/above which the microbridge can be effectively considered simply-supported/clamped (no variation in buckling load). Whereas most structural models assume  $\kappa_{T,ss}=0$  and  $\kappa_{T,clamped}=\infty$ , the results of Figure 3 show the existence of large ranges of finite  $\kappa_T$  where, from a buckling load perspective, the beam response behaves like one of the ideal boundary conditions, with an intermediate range that is between these behaviors.  $\kappa_{T,ss}$  and  $\kappa_{T,clamped}$  depend on the beam's material and geometrical properties, and their quantification is fundamental for proper characterization of microfabricated structures.

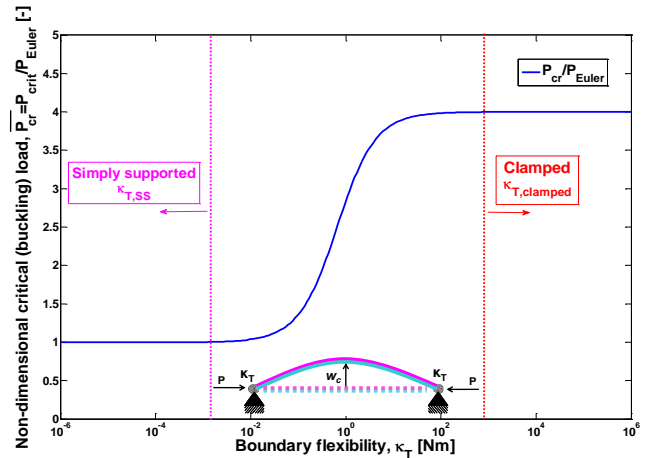


Figure 3: Effect of boundary flexibility on the critical buckling load of a doubly-hinged polysilicon beam ( $400\mu\text{m} \times 40\mu\text{m} \times 3.3\mu\text{m}$ ,  $E=129 \text{ GPa}$ )

Defining the non-dimensional boundary flexibility ( $K$ )

$$\begin{cases} K = 0 & , \quad \kappa_T < \kappa_{T,ss} \\ K = \kappa_T / \kappa_{T,clamped} & , \quad \kappa_{T,ss} \leq \kappa_T \leq \kappa_{T,clamped} \\ K = 1 & , \quad \kappa_T > \kappa_{T,clamped} \end{cases} \quad (7)$$

where  $K=0$  and  $K=1$  respectively indicate simply-supported and clamped boundaries, and noticing that:

$$\frac{P}{P_{\text{Euler}}} = \left( \frac{\lambda L}{\pi} \right)^2 \quad (8)$$

Eqs. 3-4 can be re-written into a non-dimensional form that, given

the intrinsic stresses ( $\sigma_{\text{mean}}$ ,  $\sigma_{\text{grad}}$ ) and the boundary condition ( $\kappa_T$ ), depend on the deformation wavelength ( $\lambda$ ) only. The resulting system of non-dimensional equations can be solved using any numerical method (e.g., Newton-Raphson), providing a full description of the post-buckling of micromachined beams. For a layered beam with known geometry and effective axial (EA) and bending ( $\bar{EI}$ ) stiffnesss, the solution can be expressed as:

$$w(x) = f(x, \sigma_{\text{mean}}, \sigma_{\text{gradient}}, K) \quad (9)$$

where we note that the post-buckling deflection along the beam's axis ( $x$ ) is a function of  $\sigma_{\text{mean}}$ ,  $\sigma_{\text{grad}}$  and  $K$  only. Eq. 9 is plotted in Figure 4, where we show the effect of boundary flexibility and mean stress on the stress-center displacement ( $w_c = w(L/2)$ ) relation of a CMOS polysilicon beam subjected to a +37 MPa/ $\mu\text{m}$  gradient stress. Here, the effect of boundary condition ( $K$ ) on the beam's structural response is apparent: microbridges with flexible boundaries buckle at lower loads (lower  $\sigma_{\text{mean}}$ ) and deform more (larger center deflection for the same mean stress) than more effectively clamped structures. Also, the effect of gradient stresses ( $\sigma_{\text{gradient}}$ ) on center deflection vanishes as  $K$  reaches unity, which can be noticed from the reduction in "0-load" displacement (i.e., the center deflection associated with  $\sigma_{\text{mean}}=0$ ) as  $K$  increases.

## METHOD FOR EXTRACTING STRESSES AND BOUNDARY FLEXIBILITY

When combined with experimental data, the analytical model presented in the previous section can be used to characterize the intrinsic stress state and the effective boundary condition of microbridges. Taking the inverse of Eq. 9, we can now express intrinsic stresses and boundary flexibility as a function of experimental measurements of  $w_c$ :

$$(\sigma_{\text{mean}}, \sigma_{\text{gradient}}, K) = f^{-1}(w_{c,\text{experimental}}) \quad (10)$$

Equation 10 is key in the analytical-experimental method, as it allows one to characterize microstructures by using experimental data on center deflection of buckled beams. If three or more  $w_c$  measurements are available, a least squares approach can be applied using Eq. 10 to find the intrinsic stresses and boundary condition that correspond to the experimentally measured deflections. The minimum number of measurements required is three (one per unknown:  $\sigma_{\text{mean}}$ ,  $\sigma_{\text{grad}}$  and  $K$ ), with higher accuracies associated with larger sample populations. Distinct from critical buckling-length approaches, our technique does not require the beams to be of different lengths, thus significantly reducing costs and characterization complexity. The method's accuracy depends on the total number of  $w_c$  measurements, independent of whether they are associated with beams of different/same length. The only requirement on test structures is that they should allow for some deformation to occur at release, thus making slender designs (i.e.,  $L \gg b, h$ ) preferable. The method relies on knowledge of material and geometrical properties for the structures, and on accurately measuring the post-buckled deformation of microstructures.

Given the fast decay of gradient effects as boundary stiffness increases (see Figure 4), and the relative ease of characterizing gradient stresses using cantilevered test structures [4], an alternative characterization approach exists in which cantilever curvature measurements are used to extract gradient stresses ( $\sigma_{\text{gradient,experimental}}$ , Figure 1b), while mean stresses and boundary condition are characterized using a reduced version of the analytical model:

$$(\sigma_{\text{mean}}, K) = f^{-1}(w_{c,\text{experimental}}, \sigma_{\text{gradient,experimental}}) \quad (11)$$

This alternative approach requires two sets of test structures (one set of clamped microbridges and one set of cantilevers), but it does overcome the possible numerical difficulties associated with characterizing structures with very stiff boundaries. Expecting our structures to be characterized by a 'close-to-clamped' boundary condition, both approaches were utilized in this work. An application example of Eq. 11 is presented in Figure 4 for a CMOS polysilicon beam. Here analytical results, deflection measurements ( $w_{c,\text{experimental}}$ ), and gradient stress measurements ( $\sigma_{\text{gradient,experimental}}$ ) are combined to obtain the  $\sigma_{\text{mean}}$ - $K$  relation that, using a least-squares approach, provides the mean stress and boundary condition for the structure (Table 1).

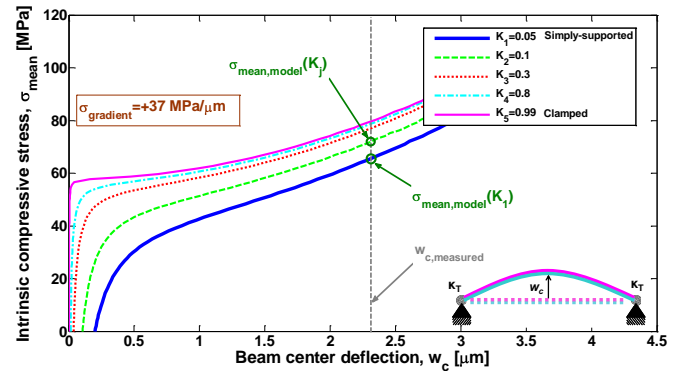


Figure 4: Effect of boundary condition on the stress-displacement relation of CMOS polysilicon beams

## RESULTS

Four sets of CMOS layered structures were designed and fabricated using standard CMOS techniques, each set having a different material composition (Table 1). All sets consisted of three groups (200-, 400-, and 600  $\mu\text{m}$ -long) of twenty clamped beams, and one group of twenty 300  $\mu\text{m}$ -long cantilevers. The material properties for each of four layered films (A, B, C, D in Table 1) comprising the structures were provided by the foundry, and resulted in the effective moduli of Table 1. Effective bending stiffness ( $\bar{EI}$ ) for the layered structure was computed from the layer thickness (Table 1). All structures were packaged in house, and successively measured using non-contact profilometry (Zygo white-light interferometer, Figure 5). The center deflection of each clamped beam and the curvature of each cantilever were recorded.

Cantilever curvature measurements were used for gradient stress extraction [4], showing that three out of four material combinations were characterized by positive gradients (Table 1). The extracted gradients were then utilized as input in a numerical implementation of Eq. 11, whose solution was computed using a least-squares approach. The results for the CMOS materials tested show mean stresses ranging between 15 and 105MPa, thus demonstrating the method's capability to characterize structures subjected to both large and small compressive stresses. This is in contrast with traditional critical length methods that encounter difficulties in quantifying small compressive stresses due to their inability to distinguish between mean stress and gradient stress effects.

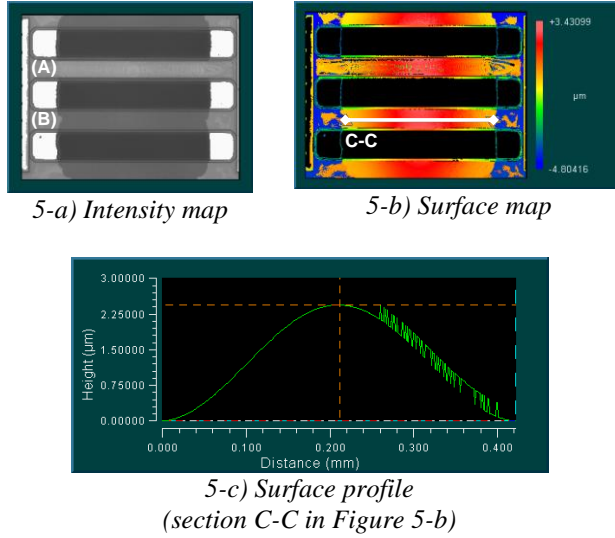


Figure 5: Profilometric images of an array of 400  $\mu\text{m}$  long buckled CMOS beams (beam A: PolySi/dielectric composite; beam B: dielectric composite)

The extracted values show a standard deviation of  $\pm 3\text{MPa}$  for gradients and  $\pm 2\text{MPa}$  for mean stresses (Table 1), significantly lower than critical length approaches can provide using the same number of test structures. Critical length and analytical approaches are compared in Table 2 for CMOS polysilicon beams, showing a 41MPa reduction in standard deviation when analytical approaches are utilized. The higher accuracy is largely due to proper quantification of the boundary condition, a main determinant of extracted stress values. Given the non-linear dependence of buckling load on edge flexibility (Figure 3), boundary estimation is paramount to ensure accurate stress extraction. For the CMOS layered structures analyzed here, the results point to a non-perfectly clamped boundary with  $K=0.9$ , i.e. 90% as stiff in bending as a perfectly-clamped boundary.

Finally, Table 2 contains a comparison between the fully-analytical (Eq. 10) and the semi-analytical (Eq. 11) methods for the same CMOS polysilicon beams. The results show that for the structures analyzed here, which are characterized by relatively stiff boundaries ( $K \sim 0.9$ ), the semi-analytical model provides more accurate estimates. This finding agrees with what we discussed in the previous section, which pointed to the numerical complexity associated with solving Eq. 10 when characterizing structures with very stiff boundaries.

Table 1: Characterization of thin-film CMOS layered materials

Beam composition	Effective Young's modulus <sup>1</sup> [GPa]	Effective thickness <sup>1</sup> [ $\mu\text{m}$ ]	Effective mean (compressive) stress [MPa]	Effective gradient stress [MPa/ $\mu\text{m}$ ]	Effective boundary condition [-]
A: PolySi/Dielectric Composite	129	2.9	$105 \pm 2.1$	$37 \pm 2.9$	$0.89 \pm 0.01$
B: Dielectric Composite/ILD/Oxide	111	2.86	$90.35 \pm 2.3$	$42 \pm 3.1$	$0.9 \pm 0.01$
C: Al/Poly/Dielectric Composite	132	2.92	$37.1 \pm 1.5$	$25.9 \pm 2.8$	$0.91 \pm 0.01$
D: Al/Dielectric Composite	113	2.91	$15 \pm 1.8$	$-2.7 \pm 2.1$	$0.9 \pm 0.01$

<sup>1</sup> With these effective Young's modulus and thickness,  $\overline{EA}$  and  $\overline{EI}$  may be calculated.  $\overline{EA}$  and  $\overline{EI}$  are derived from actual layer moduli and thicknesses via equivalent weighted properties [7].

Table 2: Characterization of thin-film CMOS polysilicon beams ( $L=200, 400, 600\mu\text{m}$  x  $w=40\mu\text{m}$  x  $h=3.3\mu\text{m}$ ,  $E=129\text{GPa}$ ) using critical length and analytical approaches

Extraction method	Effective mean (compressive) stress [MPa]	Effective gradient stress [MPa/ $\mu\text{m}$ ]	Effective boundary condition [-]
Critical length ( $P_{cr}=4EI\pi^2/L_{crit}^2$ )	$71.5 \pm 43.5$	$37 \pm 2.9$	1
Semi-analytical (Eq. 11)	$105 \pm 2.1$	$37 \pm 2.9$	$0.89 \pm 0.01$
Fully-analytical (Eq. 10)	$101 \pm 11.2$	$45 \pm 14$	$0.91 \pm 0.04$

## CONCLUSIONS AND RECOMMENDATIONS

We present a new versatile approach to the characterization of stresses (compressive mean and gradient) in thin-film CMOS layered materials using analytical solutions. The method takes into account boundary non-ideality, and it provides significantly higher accuracy compared to critical length approaches. The technique is applicable to the estimation of both very large and very small mean compressive stresses, and it can be extended to packaging stress estimation as well. The method also ensures significant savings in characterization costs and complexity by requiring fewer structures than other traditional approaches. Future work includes packaging characterization, device design and performance prediction using the developed analytical methods.

## ACKNOWLEDGEMENTS

We thank Leyue Jiang, Junde Zhang, Hanqin Zhou, and Mathieu Lagoue at MEMSIC Inc. for their contributions throughout the project.

## REFERENCES

- [1] M. Madou, *Fundamentals of Microfabrication*, CRC Press, USA, 2002
- [2] H. Guckel, T. Randazzo, D.W. Burns, "A simple technique for the determination of mechanical strain in thin films with applications to polysilicon", *J. Appl. Phys.* 57, 1671 (1985)
- [3] M. Mehregany, R.T. Howe, S.D. Senturia. "Novel microstructures for the in situ measurement of mechanical properties of thin films", *J. Appl. Phys.*, 62, 3579-84 (1987)
- [4] W.H. Chu, M. Mehregany, "A study of the residual stress distribution through the thickness of  $p^+$  silicon films", *IEEE Trans. on Electron Devices*, 40, 1245-1250 (1993)
- [5] H. Guckel, D. Burns, C. Rutigliano, E. Lowell, B. Choi, "Diagnostic microstructures for the measurement of intrinsic strain in thin films", *J. Micromech. Microeng.*, 2, 86-95 (1992)
- [6] W. Fang, J.A. Wickert, "Determining mean and gradient residual stressed in thin films using micromachined cantilevers", *J. Micromech. Microeng.*, 8, 301-309 (1995)
- [7] R.M. Jones, *Mechanics of Composite Materials - Second Edition*, Taylor & Francis Inc., New York (1999).
- [8] N.M. Newmark, "A Simple Approximate Formula for Effective End-Fixity of Columns", *J. Aero. Sci.*, 16:116 (Sec 1.4)

## CONTACT

\*F. Fachin; +1-617-253-0096, ffachin@mit.edu

\*\*B.L. Wardle; +1- 617-252-1539, wardle@mit.edu

# DERIVING A SIMULATION MODEL OF A 40-KHZ CMUT CELL FROM IMPEDANCE AND INTERFEROMETER MEASUREMENTS

I.O. Wygant<sup>1,2\*</sup>, M. Kupnik<sup>1</sup>, and B.T. Khuri-Yakub<sup>1</sup>

<sup>1</sup>Stanford University, Stanford, California, USA

<sup>2</sup>National Semiconductor, Santa Clara, CA, USA

## ABSTRACT

A spring-mass-damper system and corresponding equivalent circuit help design and analyze capacitive micromachined ultrasonic transducers (CMUTs). The ability to extract similar models from measured devices helps design verification and development of simulation models that match fabricated devices. Impedance measurements yield the CMUT's clamped capacitance and motional impedance, which fits a 4-element equivalent circuit. Additional measurements help extract a more complete equivalent circuit that includes the electromechanical transformer ratio and effective mechanical elements. In this work, we combine impedance measurements, the tightly specified mass of the CMUT plate, and interferometer displacement measurements to compute a more complete equivalent circuit. The circuit obtained for two 40-kHz CMUT cells exhibits a good fit to the model derived from the device geometry alone. The experimentally-obtained model exhibits larger damping which is likely due to energy loss in addition to radiated ultrasound.

## INTRODUCTION

Capacitive micromachined ultrasonic transducers (CMUTs) are ultrasonic transducers fabricated using microfabrication techniques. CMUTs find use in a variety of applications including airborne ultrasound, medical imaging, medical therapy, and chemical sensing.

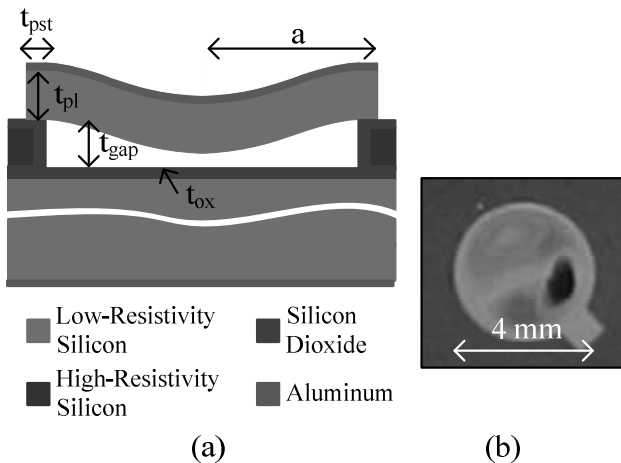


Figure 1: A single 40-kHz CMUT cell. (a) Diagram of cell cross section. (b) Photograph of a single cell that was mounted on a printed circuit board for testing.

Development of CMUTs for a particular application benefits from careful characterization of fabricated devices. This characterization helps evaluate the accuracy of models used to design the devices, and, furthermore, helps develop models for interface circuit design and signal processing that match measured performance.

Impedance measurements are particularly useful for characterizing fabricated CMUTs. Impedance is conveniently measured at wafer level without support circuitry and provides

device information over a wide frequency range.

Early work on capacitive ultrasonic transducers made extensive use of impedance measurements and equivalent circuits. Simple inspection of impedance graphs yields information about resonance frequency, quality factor, and efficiency [1]. Linking the measured impedance with equivalent circuits of mechanical structures aids design and analysis [2]. Continuing advances in CMUT analysis [3], equivalent circuit modeling, and simulation [4] enables extraction of even more utility from impedance measurements.

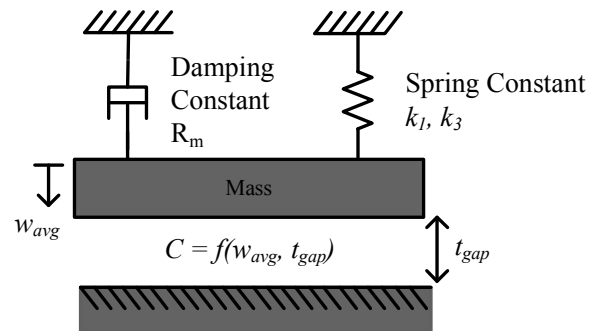


Figure 2: A spring-mass-damper model of the CMUT.

A single impedance measurement gives the impedance of the clamped capacitance in parallel with the motional impedance. From this data we can extract a basic 4-element model of the device. For example, [5] describes extracting the effective spring-constant, equivalent mass, and damping components of the motional impedance. In [6], impedance data measured as a function of bias voltage helps separate the effects of spring softening from the mechanical spring. The components of the 4-element model gives information about resonance frequency, quality factor, and energy dissipation, but do not give acoustic parameters such as radiated power or source pressure. To model these, we need to extract additional circuit parameters.

Additional measurements can provide these parameters. In [5], variation in static pressure helps isolate sources of damping. Impedance measurements made in gases with different acoustic impedances gives information about the radiation impedance [1]. These techniques, however, don't give the electromechanical transformer ratio  $n$ , which couples the acoustic and mechanical parts of the equivalent circuit. In [1], Hunt suggests making an additional impedance measurement with a known mass on the device to extract the transformer ratio; however, this technique is not practical for many MEMS devices. In this work, we leverage interferometer measurements and the tight specification of certain device dimensions and material properties to extract an electromechanical model of a 40-kHz CMUT air transducer.

## DEVICE GEOMETRY AND CLAMPED PLATE ANALYSIS

In this work, we analyze single CMUT cells designed for generating high-intensity ultrasound for a directional audio application. We fabricated the devices using the wafer-bonding



process described in [7]. Fig. 1 shows the basic device geometry and a picture of a typical cell. Table 1 gives the critical dimensions of the two characterized devices.

Device	1	2
Cell radius, $a$ (mm)	2.22	2.08
Post width, $t_{pst}$ ( $\mu\text{m}$ )	75	75
Plate thickness, $t_{pl}$ ( $\mu\text{m}$ )	40	40
Oxide thickness, $t_{ox}$ ( $\mu\text{m}$ )	5	5
Gap thickness, $t_{gap}$ ( $\mu\text{m}$ )	60	60

Table 1: Device cell dimensions.

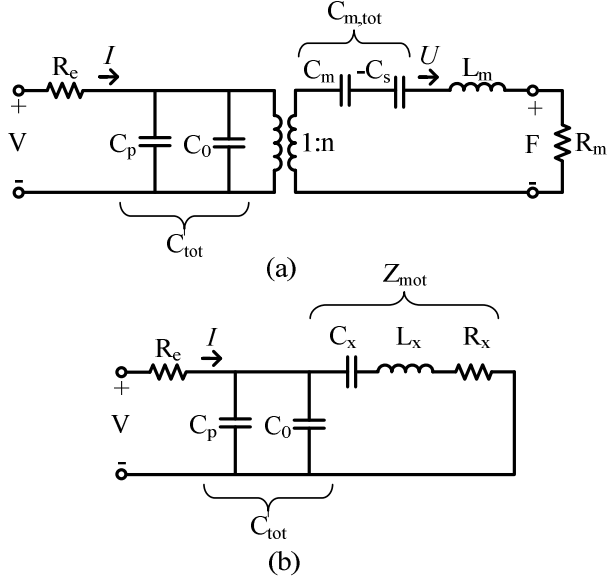


Figure 3: Small-signal CMUT equivalent circuit models. (a) Full electromechanical model. (b) Model with all components referred to the electrical side. Fitting to the measured impedance data yields values for the electrically-referred components.  $R_e$  is an optional series resistance representing contact resistance.

Assuming a perfectly clamped plate, we can derive a spring-mass-damper model of the cells (Fig. 2) [3]. The effective spring constant equals (1), where  $D$  is the flexural rigidity given by (2). In these expressions,  $a$  is the plate radius,  $t$  is the plate thickness,  $E$  is the Young's modulus of silicon (148 GPa), and  $\nu$  is the Poisson ratio for silicon (0.177).

$$k_1 = \frac{192\pi D}{a^2} \quad (1)$$

$$D = \frac{Et^3}{12(1-\nu^2)} \quad (2)$$

Because the static plate deflection of the cells is significant relative to their thickness, tensile membrane forces described by  $k_3$  affect the deflection.

$$k_3 = 4.1 \frac{k_1}{t^2} \quad (3)$$

Finally, the effective mass of the plate equals (4), where  $\rho$  equals the density of silicon (2330 kg/m<sup>3</sup>).

$$m = 1.84\pi a^2 \rho t \quad (4)$$

Damping is the most complex parameter to predict. Although

we expect multiple sources of damping such as energy lost to the substrate and posts, we assume damping is due solely to radiated ultrasound. The radiation impedance of a clamped circular cell is given in [8] and approximately equals (5), where  $k$  is  $2\pi$  divided by the wavelength in air and  $Z_0$  equals the acoustic impedance of air (409 Rayls).

$$Z_{rad} \approx Z_0 \frac{(ka)^2 + jka}{1 + (ka)^2} \quad (5)$$

With these equations we compute the spring-mass-damper parameters given in the last three rows of Table 2.

The capacitance as a function of gap is given by (6). In this expression,  $w_{avg}$  equals the average plate deflection, which is 1/3 the peak deflection, and  $g_0$  is the effective gap, which equals the gap height plus the oxide thickness divided by its dielectric constant (3.78 for SiO<sub>2</sub>). With (6) and the spring-mass-damper parameters, we can calculate the equivalent circuit of the CMUT cell shown. Fig. 3 shows the CMUT equivalent circuit which includes parasitic capacitance  $C_p$ , which we calculate from the device geometry.

$$C = \frac{\pi a^2 \epsilon_0 \operatorname{atanh}\left(\sqrt{\frac{3w_{avg}}{g_0}}\right)}{\sqrt{3g_0 w_{avg}}} \quad (6)$$

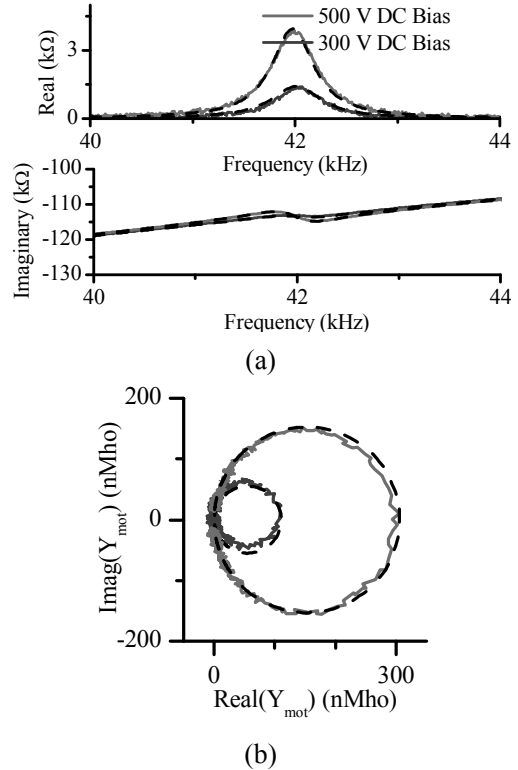


Figure 4: Electrical input impedance. (a) Real and imaginary parts of measured (solid) and fitted (dashed) input impedance. (b) Subtracting the parallel-capacitance from the impedance leaves the motional impedance [1]. A fit to the motional impedance demonstrates a simple spring-mass-damper system.

## MEASUREMENTS AND ANALYSIS

Using an impedance analyzer (Agilent 4294A, Agilent Technologies, Palo Alto, CA), we measured the input impedance of two CMUT cells mounted on printed circuit boards (PCBs). Fig. 3 shows the real and imaginary parts of the measured impedance at different bias voltages.

	Geometry	Meas.	Geometry	Meas.
Device	1		2	
$C_p$ (pF)	30.0	-	29.0	-
$C_o$ (pF)	2.97	-	2.58	-
$C_{o,tot}$	33.0	33.4	31.6	32.5
$n$ ( $\mu\text{N}/\text{V}$ )	50.1	51.2	43.5	39.8
$C_{m,tot}$ ( $\mu\text{m}/\text{N}$ )	4.89	5.28	4.25	5.28
$L_m$ ( $\mu\text{g}$ )	2.67	2.72	2.32	2.37
$R_m$ ( $\text{mN}\cdot\text{s}/\text{m}$ )	6.63	8.57	5.77	10.4

Table 2: Comparison of equivalent circuit parameters derived from the device geometry and from measured data for a 500-V dc bias.

From a single impedance measurement, we can extract the 4-element model shown in Fig. 3(b). Key features of the impedance plot help fit a circuit to the measured data. At frequencies far from resonance, the clamped capacitance,  $C_{tot}$ , dominates the imaginary part of the impedance. Thus, a least squares fit to the imaginary impedance at these frequencies yields  $C_{tot}$ . Similarly, a frequency-independent real part of the impedance indicates a series contact resistance, which for these devices was negligible.

Subtracting the contribution of  $C_{tot}$  and  $R_s$  from the measured impedance yields the motional impedance. Plotted in Cartesian coordinates, the motional admittance should resemble a circle with additional resonances appearing as additional loops. The real part of the motional impedance equals  $R_x$ ; we fit  $C_x$  and  $L_x$  to the imaginary part. Fig. 3 shows a visibly good fit with the equivalent circuit indicating the circuit captures the key features of the device.

To isolate the mechanical components of the equivalent circuit, we need the transformer ratio  $n$ , or equivalently, some mechanical value on the mechanical side of the circuit. In air, because of the high quality factor, the mass loading from the medium is negligible. Thus, we expect  $L_x$  to equal  $L_m/n^2$ , where  $L_m$  is the effective mass of the plate.

Relative to the other device parameters, the mass of the plate is well-known. Single-crystal silicon has a known density. The thickness of the plate is specified within several percent by the silicon-on-insulator (SOI) wafer manufacturer. Standard optical lithography precisely defines the plate diameter although some lateral etching of the cavities adds uncertainty about the plate diameter.

The effective mass of the plate,  $L_m$ , is a function of its mass and the mode shape. Fig. 5 shows the mode shape at the resonance frequency, which gives the effective mass according to (7).

$$L_m = 2\pi\rho h \int_0^a w^2(r) r dr \quad (7)$$

The measured mode shape corresponds to an effective mass equal to 1.88 times the plate mass, which is close to the theoretical value for a clamped plate of 1.84.

Using the known effective mass yields a value for the transformer ratio equal to (8).

$$n = \sqrt{\frac{L_m}{L_x}} \quad (8)$$

Table 2 compares the fit values with the computed values. The extracted parameters are consistent with the design. The biggest discrepancy is that the measured damping is significantly larger than predicted. However, numerous modes of energy loss exist beyond radiation impedance. Examples include energy radiated into the substrate, posts, and along the surface.

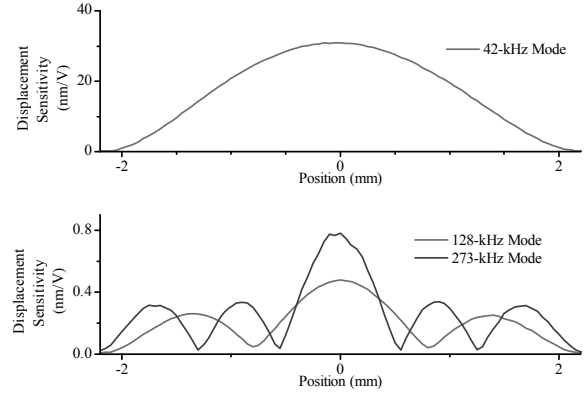


Figure 5: Cell displacement profiles and mode shapes measured with a laser vibrometer. The effective mass for the fundamental mode equals 1.88 times the mass of the cell plate, which compares to 1.84 for an ideal clamped radiator. Fig. 6 shows the impulse response and harmonics of the device, which we used to identify the mode frequencies.

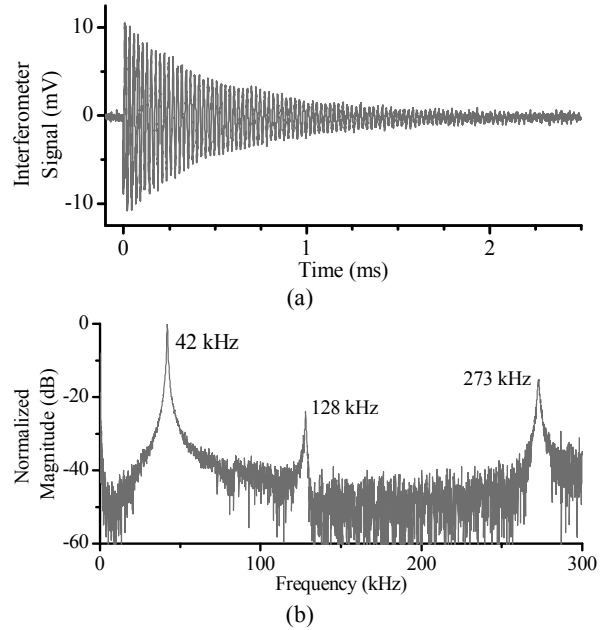


Figure 6: Impulse response measured at the device center with a laser vibrometer for a 500-V dc bias and a 20-V excitation pulse. (a) Impulse response. (b) The Fourier transform shows the fundamental and two higher-order modes. The single degree-of-freedom model assumes frequencies centered about the fundamental mode.

Although the extracted model compares well with the analytically derived model, the devices show less average displacement sensitivity than expected. Based on the measured model for device 1 given in Table 2, we expect an average displacement sensitivity of about 22 nm/V compared to our measured average sensitivity of about 10 nm/V. Similarly, device 2 exhibits less sensitivity than the model predicts. This discrepancy in sensitivity may be due to loss mechanisms not modeled by a simple resistor and is an area for further investigation.

## CONCLUSION

The characterization process described in this work yields a useful electromechanical model of the CMUT and aids comparison of design models with fabricated devices. This method leverages routine impedance measurements, the tight tolerances on certain parameters provided by microfabrication, and interferometer measurements. Pressure measured in the far field using a calibrated microphone could supplement or replace the information obtained with the interferometer.

Additional measurements could help refine the model further. Because of the significant tensile forces in the device, the effective spring constant is influenced by linear and nonlinear spring forces. Static displacement measurements would help separate the spring constants  $k_1$  and  $k_3$ , which would be particularly useful for large-signal models.

The methodology could be extended to devices designed for operation in water, particularly since impedance testing is routinely made in air first. Additional impedance measurements and pressure measurements made with a hydrophone would help resolve the radiation impedance in water.

The process of extracting a model from measured data is important to CMUT development, and MEMS devices in general, as it closes the loop between design, test, and fabrication.

## REFERENCES

- [1] F. V. Hunt, *Electroacoustics: The Analysis of Transduction, and Its Historical Background*. Cambridge: Harvard University Press, 1982.
- [2] W. P. Mason, *Electromechanical Transducers and Wave Filters*, 2nd ed. New York: D. Van Nostrand, 1948.
- [5] I. O. Wygant, M. Kupnik, and B. T. Khuri-Yakub, "Analytically calculating membrane displacement and the equivalent circuit model of a circular CMUT cell," in *IEEE Ultrasonics Symposium*, 2008, pp. 2111-2114.
- [6] H. K. Oguz, S. Olcum, M. N. Senlik, V. Tas, A. Atalar, and H. Koymen, "Nonlinear modeling of an immersed transmitting capacitive micromachined ultrasonic transducer for harmonic balance analysis," *IEEE Transactions on Ultrasonics, Ferroelectrics and Frequency Control*, vol. 57, pp. 438-447.
- [3] I. J. Oppenheim, A. Jain, and D. W. Greve, "Electrical characterization of coupled and uncoupled MEMS ultrasonic transducers," *IEEE Transactions on Ultrasonics, Ferroelectrics and Frequency Control*, vol. 50, pp. 297-304, 2003.
- [4] S. Kalicinski, H. A. C. Tilmans, M. Wevers, and I. De Wolf, "A new characterization method for electrostatically actuated resonant MEMS: Determination of the mechanical resonance frequency, quality factor and dielectric charging," *Sensors and Actuators A: Physical*, vol. 154, pp. 304-315, 2009.
- [7] I. O. Wygant, M. Kupnik, B. T. Khuri-Yakub, M. S. Wochner, W. M. Wright, and M. F. Hamilton, "The design and characterization of capacitive micromachined ultrasonic

transducers (CMUTs) for generating high-intensity ultrasound for transmission of directional audio," in *IEEE Ultrasonics Symposium*, 2008, pp. 2100-2102.

- [8] M. Greenspan, "Piston radiator: Some extensions of the theory," *The Journal of the Acoustical Society of America*, vol. 65, pp. 608-621, 1979.

## CONTACT

\*I.O. Wygant, tel: +1-650-566-8980; ira.wygant@nsc.com

# ELECTRICAL CHARACTERIZATION OF PECVD SILICON CARBIDE FOR APPLICATION IN MEMS VAPOR HF SACRIFICIAL RELEASE

L.Chen<sup>1\*</sup>, T. Lee<sup>2</sup>, C.Regan<sup>1</sup>, F.Sammoura<sup>1</sup>, C.Tsau<sup>1</sup>, M. Mehregany<sup>2</sup>, K.Nunan<sup>1</sup>, and K.Yang<sup>1</sup>

<sup>1</sup> Analog Devices Inc., Wilmington, Massachusetts, USA

<sup>2</sup> Case Western Reserve University, Cleveland, Ohio, USA

## ABSTRACT

This paper reports results from the characterization of dielectric properties and the electrical conduction mechanism in PECVD amorphous silicon carbide (a-SiC) films. We demonstrate that a-SiC is a good dielectric and passivation film for MEMS devices: (i) leakage current density is well acceptable under typical operating voltages (i.e., fields up to 3 MV/cm); and (ii) the films have super chemical inertness and corrosion resistance, can act as excellent etch stop/passivation layer for vapor HF sacrificial release in various type of transducer fabrication, compared to silicon nitride which has poorer selectivity and requires post-cleaning to remove generated particles. This has large significance to the MEMS community.

## INTRODUCTION

Silicon dioxide is the most commonly used sacrificial material in MEMS micromachining. Various wet etch release methods had been developed but all require extra steps to prevent re-stiction which complicated the whole process, like supercritical or sublimation drying, or the use of self-assembled monolayer to modify surface energy. Recently, HF vapor phase release has had broad attention [1]. One key material directly related to the success of integrating vapor release into the whole MEMS process is the suitable dielectric material as etch stop layer and passivation layer. Silicon nitride and some other thin films had been studied and reported in [2].

The ideal dielectric in this target application needs to be resistant both chemically and electrically. Popular dielectric thin films, like SiO<sub>2</sub> and Si<sub>3</sub>N<sub>4</sub>, are well understood and extensively used. It is known that primary charge transport mechanisms in these films are Fowler-Nordheim tunneling and Poole-Frenkel emission effects [3-4]. However, these films have limitations for MEMS, where harsh environment-resistant is needed because of exposure to release chemicals during fabrication and corrosive media during field use. SiC has high chemical inertness and corrosion resistance, and is stable at higher temperatures. Hence, it has gained increasing attention in the MEMS community. a-SiC by low-temperature deposition methods like PECVD and Ion Beam Sputtering has been demonstrated in applications such as Cu-Damascene interconnect process, SiOC and SiCN/SiC composite as Cu diffusion barrier and low-k dielectric layer [5], encapsulation layer for MEMS structures [6], or even as MEMS structure layer through doping (n- or p-aSiC) [7]. Although the dielectric breakdowns of SiOC and SiCN/SiC have been investigated [5], little is known about the temperature and field bias stability of and charge transport mechanism in a-SiC.

In this paper, a-SiC is selected as a potential candidate and brought into detailed investigation. Initial HF vapor etch test is demonstrated and the focus is the electrical characterization. The goal is to evaluate the capability of a-SiC in meeting the requirements from integrated process and proper device function.

## EXPERIMENTAL

### Vapor HF etch test sample

First, the a-SiC films were deposited onto both bare Si and

thermally-grown oxide coated Si wafers at 350°C by PECVD using tri-methyl-silane ((CH<sub>3</sub>)<sub>3</sub>SiH) as precursor [8]. Sample film thicknesses were designed to range from 50 to 120 nm, to determine minimum thickness required for achieving pin-hole free high integrity film. The oxide under the a-SiC can help to reveal the presence of pin holes and bare Si monitor wafer was used for more accurate film thickness and stress measurement. The vapor HF etch system used is commercially available PRIMAXX-CET25. Some simple polysilicon test structures were patterned on top of the a-SiC layer for vapor HF exposure to test the etch stop layer concept.

### Electrical test sample preparation

Metal-insulator-semiconductor (MIS) capacitor test structures with various sizes on the same wafer were designed for I-V and C-V testing. Thin film intrinsic properties were evaluated using small features sized 10x10μm<sup>2</sup> and 50x50μm<sup>2</sup>, while larger ones up to 1000x1000μm<sup>2</sup> were used to capture defects and estimate defect density from the wafer yield point of view. The fabrication started with 6-inch N(100) silicon wafers coated with 1.3μm thermally-grown silicon dioxide, followed by 250nm thick LPCVD phosphorous -doped poly-Si (Rs of 25Ω/□), which was patterned to form the bottom electrode. Then, the a-SiC capacitive dielectric of 120nm was deposited with ≤5% cross wafer non-uniformity. Temperature annealing was performed on select wafers. The residual stress of these films changed from as-deposited low compressive (~ -150MPa) to low tensile (~ 24MPa) after 450°C anneal and about 315MPa after 1150°C anneal. Contact windows were patterned using SF<sub>6</sub>/CHF<sub>3</sub> based plasma etch through the a-SiC thin layer to connect the metal probe pad to the bottom poly-Si electrode. AlCu(1%Cu) of 1μm by sputtering was coated on top of dielectric and patterned to form top electrode as well as the final probe pads. LPCVD standard stoichiometric Si<sub>3</sub>N<sub>4</sub> (stdNitride) and Si-rich silicon nitride (LSN) films were included in this investigation for comparison.

CASCADE probe station with temperature controlled chuck was used to run wafer level probe, Agilent B1500A semiconductor device analyzer was used to perform C-V and I-V.

## RESULTS AND DISCUSSIONS

### Vapor HF etching

It is found that the a-SiC film with thickness less than 80nm does have some pin holes, while 120nm thick film is pin-hole free. Thickness measurement after continues 24 hr vapor HF exposure confirms no detectable film loss, indicating extremely low etch rate. The simple test structure wafer with patterned poly-silicon on top of the a-SiC and silicon dioxide beneath it was etched in vapor HF for 30mins. The resulting SEM image (Figure 1) shows a-SiC functioning well in protecting underneath films. As a comparison, Figure 2 presents a silicon nitride blank film after exposed to vapor HF for the similar amount of time. Besides significant thickness loss, lots of etch by-products (residuals) remain on the surface and post treatment clean step is required.

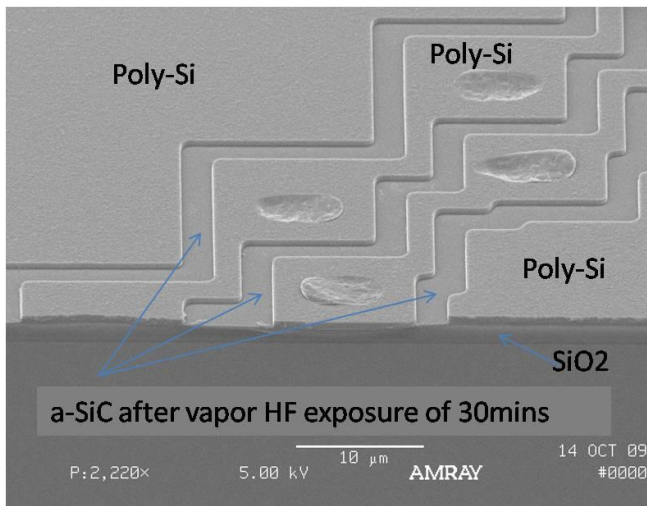


Figure 1: Tilted view of a cross-sectional scanning electron micrograph: a-SiC film of about 120nm is used in this simple test structure wafer, under vapor HF exposure for 30mins, the SiO<sub>2</sub> film underneath the a-SiC is well protected.

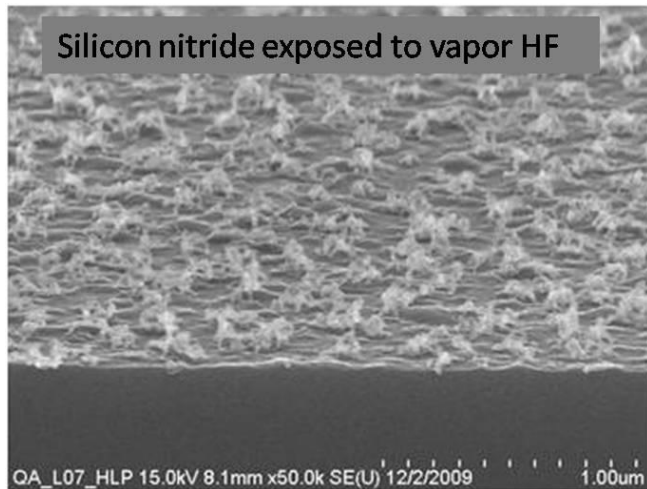


Figure 2: Scanning electron micrograph of a blanket coated silicon nitride film after vapor HF etch and lots of etch residuals remain on the film surface which requires post-treatment to clean.

### Capacitance drift

For both temperature and voltage bias drift tests, five different films including PECVD as deposited a-SiC, 450°C and 1150°C annealed a-SiCs, and LPCVD standard silicon nitride (stdNitride) and silicon-rich low stress nitride (LSN) were probed. The tests evaluate the dielectric film stability with the common bias conditions. Figure 3 is a bar chart illustrating capacitance drifts from small signal C-V measurement with DC voltage bias sweeping from -25V to +25V. Both as-deposited and 450°C annealed a-SiC have a much lower drift (~30ppm/V) compared to the others; LSN exhibits the largest drift of ~230ppm/V. The 1150°C annealed SiC shows higher drift than as-deposited and 450°C annealed a-SiC, but close to stdNitride (~100ppm/V); film shrinkage and dielectric permittivity change induced by very high temperature annealing are thought responsible. Figure 4 shows temperature bias (0°C to 150°C) dielectric stability results, again, it

is observed that as-deposited and 450°C annealed a-SiC samples had lowest drift of about 16 ppm/°C, while other 3 films exhibit 3-4 times higher drifting.

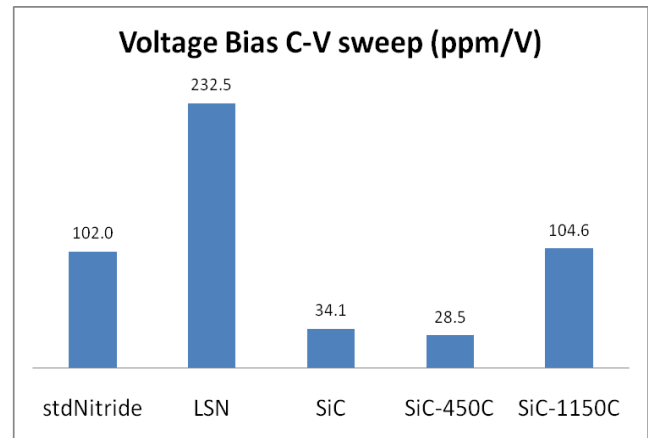


Figure 3: Capacitance drift determined from C-V measurement under a voltage bias sweeping from -25V to +25V. a-SiC annealed at 450°C is noted as SiC-450C. a-SiC annealed at 1150°C is notes as SiC-1150C.

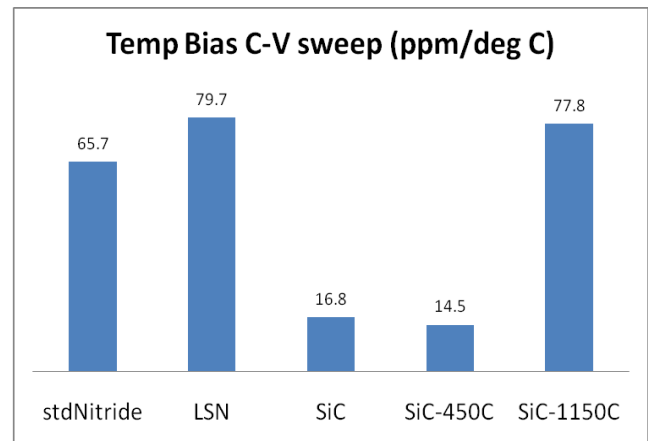


Figure 4: Capacitance drift determined from C-V measurement under a temperature bias from 0°C to 150°C.

### Leakage current density

I-V measurement was conducted with voltage stepping from 0 to 79V (instrument limit). The leakage current from films with different thicknesses under voltage bias was converted to the current at bias electric field for comparison. Figure 5 presents field dependence of leakage current density; stdNitride exhibits the best breakdown performance (>6MV/cm), followed by the 450°C annealed a-SiC, which has the 2<sup>nd</sup> highest breakdown field among all (>3MV/cm); LSN has the highest leakage (breakdown <1MV/cm), while as-deposited and 1150°C annealed a-SiC are in the middle (~2MV/cm). From both dielectric capacitance drift and leakage performance, it is shown that 450°C anneal process help a-SiC (deposited at 350°C by PECVD) to enhance dielectric property by annihilating defects, but the very high 1150°C anneal is thought to distort the film to some extent and some new defects might be generated so that the dielectric stability and leakage performance became poorer.

### Leakage current density vs. Bias Field

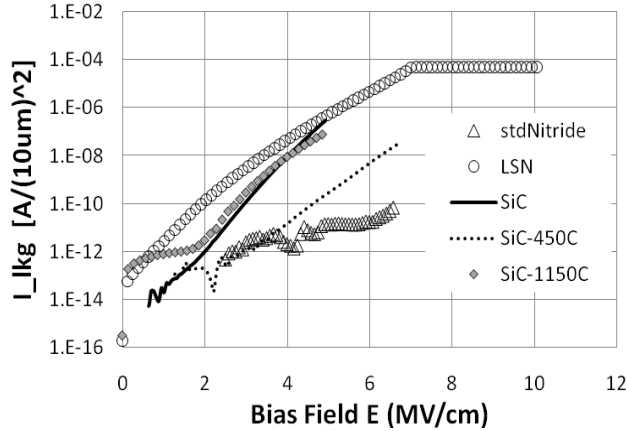
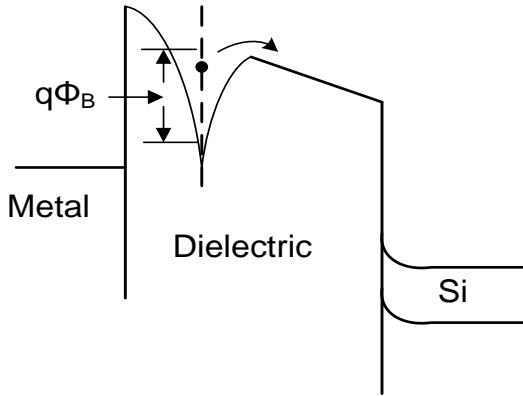


Figure 5: Field dependence of leakage current density.

### Conduction mechanism study

The Poole-Frenkel charge transport model [4] can be used to describe a bulk limiting field enhanced thermal ionization of the trapped electrons (illustrated in Figure 6). In the model,  $J$  is the current density,  $E$  is the electric field,  $\Phi_B$  is the barrier height,  $\epsilon$  is dynamic permittivity which equals to  $\epsilon_0\epsilon_D$ ,  $\epsilon_D$  is dynamic dielectric constant,  $C_1$  is a constant to be fitted.



$$J = C_1 E \exp \left[ \frac{-q \left( \Phi_B - \sqrt{qE/\pi\epsilon} \right)}{kT} \right]$$

Figure 6: Illustration of Poole-Frenkel charge transport model: bulk limiting field enhanced thermal ionization of trapped electrons.

Figures 7 & 8 show the samples' temperature and field dependence on leakage current density. To check the suitability of the Poole-Frenkel emission model to the sample films under investigation, the raw data from I-V measurements at various temperatures were reformatted to be plotted as  $\ln J$  vs.  $1/T$  and  $\ln(J/E)$  vs.  $\sqrt{E}$ , respectively. This way, the rearranged linear equations (1) and (2):

$$\ln J = \ln C_1 E + \left[ -\frac{q}{k} \left( \Phi_B - \sqrt{\frac{qE}{\pi\epsilon}} \right) \right] * \frac{1}{T} \quad (1)$$

&

$$\ln \left( \frac{J}{E} \right) = \left[ \ln C_1 + \left( -\frac{q\Phi_B}{kT} \right) \right] + \left( \frac{q}{kT} \sqrt{\frac{q}{\pi\epsilon}} \right) * \sqrt{E} \quad (2)$$

from Poole-Frenkel model can be used for parameter fitting. The linear regions of the plots identify conditions in which charge transport in a-SiC is also governed by Poole-Frenkel emission. At higher fields, an expected competing mechanism (i.e., phonon assist tunneling) is not strong because no linear region was present by plotting leakage current density as a function of the square of the electric field as suggested in [9]. Through least-square fitting, trap barrier height ( $\Phi_B$ ), dynamic dielectric permittivity ( $\epsilon_D$ ), and trap density and mobility related factor ( $C_1$ ) are determined and summarized in Table 1. Data from stdNitride and LSN show good agreement with those reported in [10]. The barrier height data from three a-SiC samples correlates to our previous explanation on as-deposited and annealed film relative dielectric stability and bias drifting.

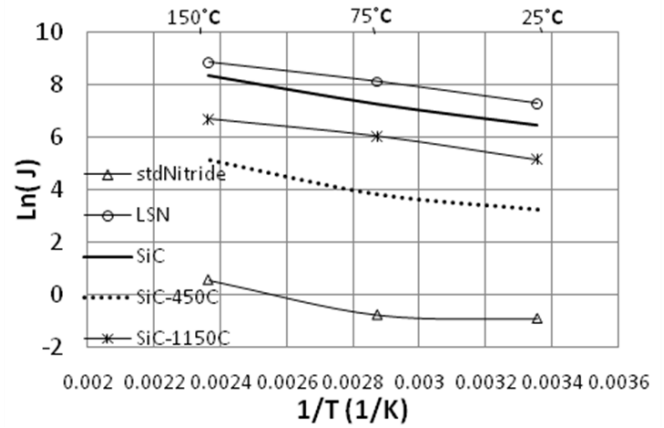


Figure 7: Constant field (~6.4 MV/cm for stdNitride and SiC-450C, and 4.5 MV/cm for LSN, SiC, and SiC-1150C) leakage at various temperatures. Linear least squares fits to the data in the 75–150°C range. The electric field for each film was chosen to correspond to conditions in which Poole-Frenkel effect is active.

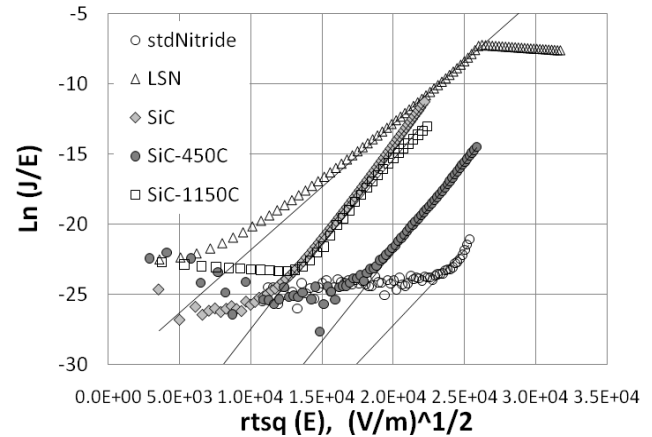


Figure 8: Poole-Frenkel characteristic at 75°C (348 K). Film thicknesses are 70-120 nm. The high field tail on the LSN sample is due to current constraint. The straight lines represent least squares fits to the linear regions of the data.

Table 1: Extracted constants for various films from P-F model fitting. Data in “( )” is from [10].

	StdNitride	LSN	SiC	SiC-450	SiC-1150
$C_1$	1.26e-06 (1.44e-05)	6.70e-04 (2.75e-04)	9.60e-04	1.14e-04	6.70e-05
$\Phi_B$	1.05 (1.08)	0.71 (0.69)	1.01	1.15	0.85
$\epsilon_D$	5.60 (5.51)	7.92	3.79	3.79	4.17

A scorecard is summarized (Table 2) for all the five films under investigation in this work to reflect figure of merit in both dielectric and vapor HF etch stop functions.

Table 2: Scorecard of electrical/chemical characteristics of the films under investigation.

films	Leakage /Breakdown	Capacitance drift at bias	Vapor etch stop	HF
stdNitride	+++ Best	-	---	
LSN	--	--	++ Good	
SiC	+	++	+++	
SiC-450	++ Good	+++ Best	+++ Best	
SiC-1150	-	--	++	

## CONCLUSION

Amorphous silicon carbide by PECVD is evaluated as a potential etch stop material for application in MEMS vapor phase sacrificial release. The initial etch test does show inertness of a-SiC film to the aggressive etchant. In order to verify if it can be integrated into real device for proper function, dielectric characterization including leakage current and capacitance drift under thermal and electrical field bias are conducted. Furthermore, the study on electron conduction mechanism improves the understanding of this new dielectric material intrinsically. It is found the a-SiC film after 450°C annealing performed best with very low bias drift and good breakdown performance and is suggested to be used in MEMS or MEMS/CMOS co-fabrication process.

## ACKNOWLEDGEMENTS

The authors would like to acknowledge Dr. Paul D. Mumbauer from Primaxx Inc. and process engineers from TSMC for various vapor HF etch tests and Analog Devices Cambridge Fab process engineers for electrical test chip wafer fabrication.

## REFERENCES

- [1] A. Witvrouw, B. Du Bois, P. De Moor, A. Verbist, C. Van Hoof, H. Bender and K. Baert, “A comparison between wet HF etching and vapor HF etching for sacrificial oxide removal”, proceedings of SPIE-Micromachining and Microfabrication, vol 4174, Santa Clara, CA, September 18, 2000, pp.130-141
- [2] T. Bakke, J. Schmidt, M. Friedrichs, and B. Volker, “Etch Stop materials for release by vapor HF etching”, proceedings of 16<sup>th</sup> MicroMechanics Europe Workshop, MME 2005, Goteborg, pp.103-106
- [3] M.Lenzlinger, and E.H. Snow, “Fowler-Nordheim Tunneling into Thermally Grown SiO<sub>2</sub>”, IEEE Transaction of Electronic Devices, 1968, pp.686
- [4] D. Mangalaraj, M. Radhakrishnan, and C. Balasubramanian, “Electrical Conduction and Breakdown Propoerties of Silicon Nitride Films”, Journal of Materials Science, 17 (1982), pp. 1474-1478
- [5] C.C. Chiang, M.C. Chen, Z.C. Wu, L.J. Li, S.M. Jang, C.H. Yu, and M.S. Liang, “TDDB Reliability Improvement of Cu Damascene with a Bilayer-Structured  $\alpha$ -SiC:H Dielectric Barrier”, Journal of The Electrochemical Society, 151 (2) G89-G92 (2004)
- [6] S. Wodin-Schwartz, D.R. Myers, R.K.Kramer, S. Choi, A. Jordan, M.B.J. Wijesundara, M.A. Hopcroft, and A.P. Pisano, “Silicon and Silicon Carbide Survivability in an In-Cylinder Combustion Environment”, Proceedings of PowerMEMS 2008 + microEMS2008, Sendai, Japan, 11/9-12/2008, pp.477-480
- [7] H.T.M. Pham, T. Akkaya, C. de Boer, C.C.G. Visser, and P.M. Sarro, “Electrical and Optical Propoerties of PECVD SiC Thin Films for Surface Micromachined Devices”, Proceedings of workshop on Semiconductor Sensor and Actuator Technology (SeSens. 2002), Veldhoven, the Netherlands, 11/29/2002, pp.662-666
- [8] J. Du, N. Singh, and C.A. Zorman, “Development of PECVD SiC for MEMS Using 3MS as the Precursor”, Proceedings of Materials Research Society symposium, San Francisco, CA, 4/17-21/2006, Vol.911, B05-28
- [9] S.D. Ganichev, E. Ziemann, and W. Prettl, “Distinction between the Poole-Frenkel and Tunneling Models of Electric-field-stimulated Carrier Emission from deep levels in Semiconductors”, Physical Review B, Vol.61, No.15, (2002) pp. 361-365
- [10] S. Habermehl, and C. Carmignani, “Correlation of Charge Transport to Local Atomic Strain in Si-rich Silicon Nitride Thin Films”, Applied Physics Letters, 80 (2002) pp. 261-263

## CONTACT

\*L. Chen, tel: +1-781-937-2377; li-m.chen@analog.com

# GROWTH OF HIGHLY C-AXIS ORIENTED ALN FILMS ON 3C-SiC/Si SUBSTRATE

Chih-Ming Lin<sup>1</sup>, Wei-Cheng Lien<sup>1</sup>, Ting-Ta Yen<sup>1</sup>, Valery V. Felmetzger<sup>2</sup>, Debbie G. Senesky<sup>1</sup>,  
Matthew A. Hopcroft<sup>3</sup>, and Albert P. Pisano<sup>1</sup>

<sup>1</sup>Berkeley Sensor and Actuator Center, University of California, Berkeley, California, USA

<sup>2</sup>Tegal Corporation, Petaluma, California, USA

<sup>3</sup>Hewlett-Packard Laboratories, Palo Alto, California, USA

## ABSTRACT

For the first time, highly *c*-axis oriented heteroepitaxial AlN thin films have been successfully grown on epitaxial 3C-SiC films on Si (100) substrates. The AlN films deposited by the AC reactive magnetron sputtering at temperatures of approximately 300–450 °C were characterized using the scanning electron microscope (SEM), atomic force microscopy (AFM), X-ray diffraction (XRD), and transmission electron microscopy (TEM). X-ray diffraction rocking curve of 1- $\mu$ m-thick AlN film exhibits a full width at half maximum (FWHM) value of 1.73° on the 3C-SiC/Si substrate which correlates to the excellent crystal alignment of the AlN film. Finally, two-port surface acoustic wave (SAW) devices were fabricated on the AlN/3C-SiC/Si composite structure, and the expected Rayleigh mode of the SAW device exhibits a high acoustic velocity of 5,200 m/s, demonstrating the potential for high frequency applications. The AlN/3C-SiC/Si composite structure developed in this work has potential for realizing radio frequency (RF) MEMS resonators and filters as well as piezoelectric MEMS sensors and actuators for operation in harsh environments.

## INTRODUCTION

Recently, silicon carbide (SiC) has been investigated as a platform material to create electronics, sensors, and actuators for harsh environments (high temperature, high shock, and chemically corrosive conditions) due to the thermal, mechanical, and electrical stability of this material [1]. Although SiC has over 200 different crystal symmetries, the cubic (3C-SiC) and the hexagonal (4H-SiC and 6H-SiC) polytypes are most commonly synthesized. Among these polytypes, chemical vapor deposition (CVD) of in-situ doped polycrystalline 3C-SiC deposited on Si substrates has been achieved by many academic research groups [1, 2]. An industrial group also has commercialized epitaxial 3C-SiC thin films deposited on Si substrates [3]. The advancement of SiC manufacturing technology enabled the fabrication of electrostatic SiC comb-drive actuators and sensors [4] using low-pressure chemical vapor deposition (LPCVD) polycrystalline 3C-SiC films. Electrostatic resonators made from polycrystalline 3C-SiC have been developed for RF MEMS applications [5, 6] and show promise for these applications due to the high acoustic velocity of 13,000 m/s and low losses [7].

Piezoelectric actuation method is a viable alternative to the electrostatic actuation method frequently used for MEMS devices. Although SiC exhibits piezoelectric properties, its low piezoelectric coefficient makes it unsuitable for device designs [8]. To overcome this limitation, the deposition of piezoelectric thin films onto 3C-SiC could be an alternative method to drive SiC-based MEMS devices utilizing the piezoelectric effect. Aluminum nitride (AlN) has been widely applied to RF MEMS devices because of its relatively high piezoelectric coefficient, CMOS compatibility, and high acoustic velocity of 12,000 m/s [8]. In general, AlN and SiC exhibit the well-matched thermal expansion coefficient and low lattice mismatch [9]. AlN can maintain its piezoelectric properties at high temperatures as well [10, 11]. Therefore, coupling AlN and 3C-SiC to create a composite structure could be advantageous for RF MEMS and harsh environment applications.

Several research groups have investigated and successfully deposited ZnO or AlN films on hexagonal SiC substrates [7, 12, 13]. However, the hexagonal SiC polytypes are unsuitable for MEMS devices because it is difficult to grow hexagonal SiC films on silicon wafers. In addition, there are a few reports detailing the deposition of AlN thin films on 3C-SiC substrates. For example, Tanaka *et al.* deposited AlN (100) thin films on 3C-SiC (001) using low-pressure metal-organic chemical vapor deposition (LP-MOCVD) method [14]. Chung *et al.* used a layer of polycrystalline 3C-SiC film as the buffer layer for AlN (002) deposition on Si (100) substrates using the AC magnetron reactive sputtering because the polycrystalline 3C-SiC buffer layer and AlN film have only 1% lattice mismatch and 7% difference in the thermal expansion coefficient [15].

In this study, the deposition of highly oriented AlN (002) films on 3C-SiC(100)/Si(100) substrates using AC reactive magnetron sputtering is developed and experimentally investigated. Although the heteroepitaxial AlN film (002) and the epitaxial 3C-SiC (100) film have a larger lattice mismatch of 28.6%, this issue could be overcome by a two-step deposition process. After AlN deposition on the SiC/Si substrate, two-port SAW devices were fabricated on the AlN/3C-SiC/Si composite structure to confirm that the AlN thin film has strong piezoelectric response. These results create a basis for the development of piezoelectric AlN/3C-SiC-based MEMS devices for frequency control and sensing applications in harsh environments.

## EXPERIMENTS

For this research, wafers with 2.3- $\mu$ m-thick epitaxial 3C-SiC (100) films grown on Si (100) substrates were purchased from the NOVASiC Inc. [3]. AlN thin films with different thicknesses in the range of 1  $\mu$ m to 3  $\mu$ m were deposited on 3C-SiC/Si substrates by AC (40 kHz) powered S-Gun magnetron. A unique feature of the S-Gun is its coaxial dual target arrangement that enables arc-less operation in poison mode with capability for independent control of the film crystal orientation, stress, and uniformity [16].

Prior to AlN thin film deposition, the surface of the 3C-SiC/Si substrate was treated in a separate etching module by low energy (150–200 eV) Ar ions from capacitively coupled RF (13.56 MHz) plasma. In order to diminish the lattice mismatch between the AlN film and the 3C-SiC substrate, a two-step sputter deposition process was employed in this study to create better conditions for nucleation of AlN grains at the beginning of the film condensation. For this purpose, a first 50-nm-thick AlN film was deposited with high nitrogen concentration in argon and nitrogen gas mixture. The initial grains served as the seeds for the growth of higher quality columnar grains with the increase of AlN film thickness. This seed layer also enabled reducing the negative effect of lattice mismatch between the AlN thin film and the 3C-SiC substrate.

The seed layer deposition processes were performed at the ambient temperature (around 300 °C) and the elevated temperature (around 450 °C) using an external infrared heater. S-Gun magnetron was powered with an AC power of 3 kW during the seed layer deposition and 5.5 kW during the deposition of the remaining AlN film, providing a deposition rate of approximately 66 nm/min.



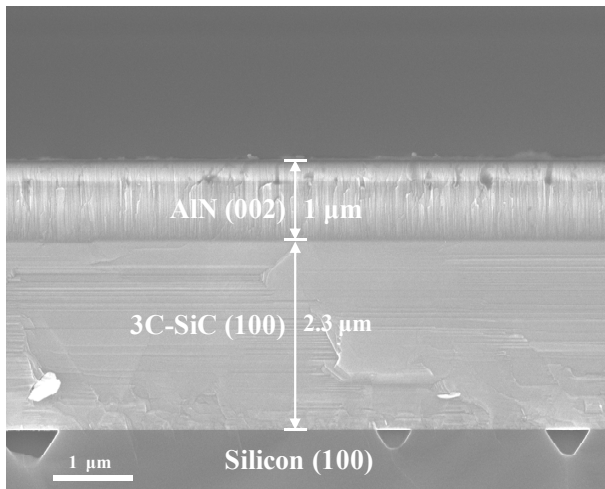


Figure 1: Cross-sectional SEM image of 1- $\mu\text{m}$ -thick AlN (002) film on the 3C-SiC(100)/Si(100) layered structure.

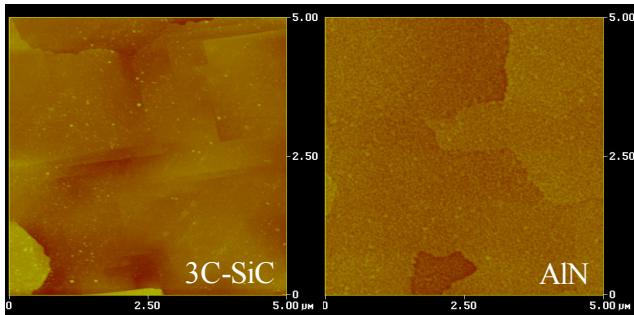


Figure 2: AFM images of 3C-SiC (100) and AlN (002) films.

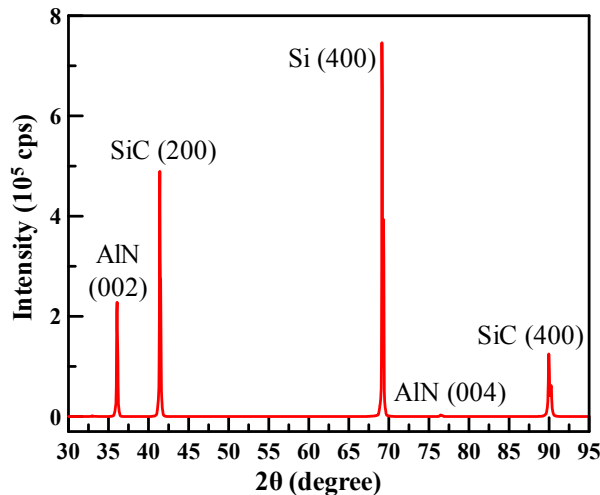


Figure 3: XRD spectrum of the AlN(002)/3C-SiC(100)/Si(100) layered structure where AlN is 1  $\mu\text{m}$  and 3C-SiC is 2.3  $\mu\text{m}$ .

## RESULTS AND DISCUSSIONS

### A. Heteroepitaxial AlN (002) films on 3C-SiC(100)/Si(100)

Figure 1 shows the cross-sectional SEM image of the AlN(002)/3C-SiC(100)/Si(100) composite structure where the AlN and 3C-SiC film thicknesses are 1  $\mu\text{m}$  and 2.3  $\mu\text{m}$ , respectively. The void defects with pyramidal shape at the 3C-SiC/Si interface are due

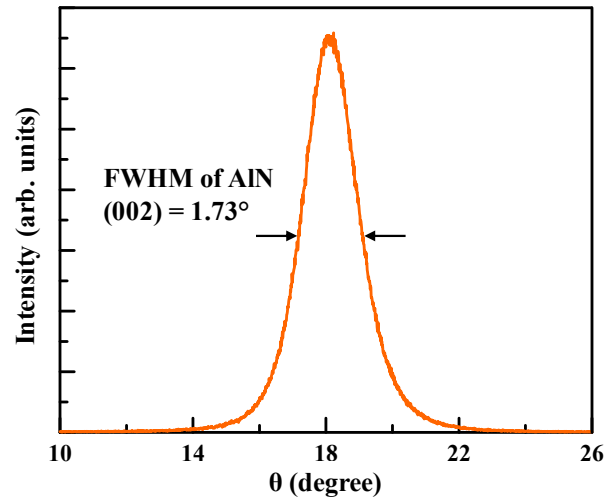


Figure 4: Rocking curve of 1- $\mu\text{m}$ -thick AlN (002) film.

to silicon outdiffusion. The interface between AlN and 3C-SiC is smooth and no delamination is observed. The AlN thin film exhibits numerous columnar grains which are perpendicular to the surface of the 3C-SiC/Si substrate. The surface morphology of the 3C-SiC and AlN films is shown in Figure 2. According to the AFM data, the root mean square (RMS) roughness of the 3C-SiC and AlN films are 5.9 nm and 2.9 nm, respectively. The preservation of the 3C-SiC grain boundary and the RMS roughness on the AlN surface implies that the nucleation is two-dimensional growth.

The crystalline structure was determined by XRD as shown in Figure 3 where the diffraction peaks correspond to a hexagonal wurtzite-type AlN (002) film, a cubic zinc-blende-type SiC (100) film, and a Si (100) substrate, respectively. The presence of (002) and (004) AlN reflections gives the indication of a highly  $c$ -axis oriented AlN film that has been grown on the 3C-SiC(100)/Si(100) substrate. As shown in Figure 4, the rocking curve FWHM of the 1- $\mu\text{m}$ -thick AlN film is 1.73° which implies the highly oriented AlN film and good piezoelectric property.

Besides directly depositing AlN thin films onto the 3C-SiC/Si substrate, several different surface pretreatments of the substrate and deposition at the ambient or elevated temperatures were employed to investigate their effects on AlN film crystallinity as shown in Figure 5 and Table 1. The rocking curve FWHM of the AlN film can be improved from 2.61° to 2.29° when the deposition temperature in the first step deposition (i.e. seed layer deposition) was increased from ambient temperature to elevated temperature.

In addition to the sputter conditions, the degree of  $c$ -axis texturing of the reactively sputtered AlN film is closely related to the substrate texture and the surface roughness. Therefore, the pretreatment of the 3C-SiC/Si substrate can significantly influence the AlN film orientation. It is well-known that pre-deposition RF plasma etching can improve the film nucleation and coalescence processes due to removal of impurities. Furthermore, the RF plasma etching can decrease the surface roughness of the substrate and hence improve the AlN crystal alignment. As depicted in Figure 5, a relatively longer RF plasma etching duration of 600 s is required to achieve the better crystallinity of AlN thin films on 3C-SiC substrates. For comparison, the RF plasma etching duration of 180 s is enough to get highly  $c$ -axis oriented AlN thin films on silicon wafers under the same sputter conditions. This phenomenon might be due to the higher atomic binding energy and the lower sputtering yield of SiC. The sputtering yield ratio for silicon carbide to silicon is approximately 0.5 [8].

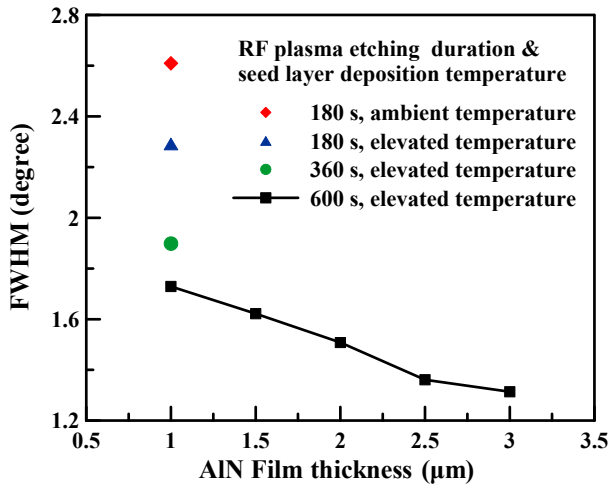


Figure 5: The plot of measured FWHM of AlN under different pre-deposition conditions versus AlN film thicknesses.

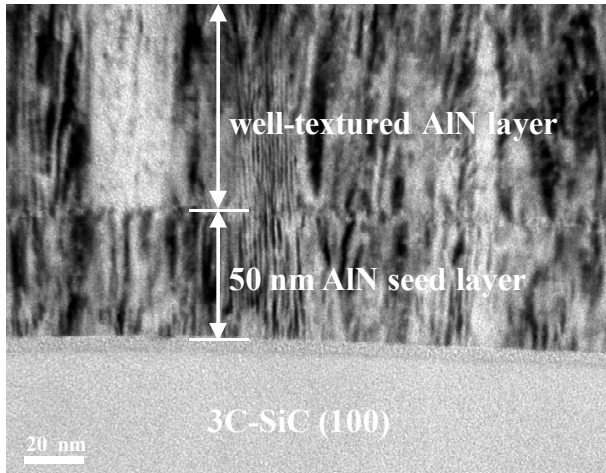


Figure 6: The cross-sectional bright field TEM image of the interface between AlN (002) and 3C-SiC (100).

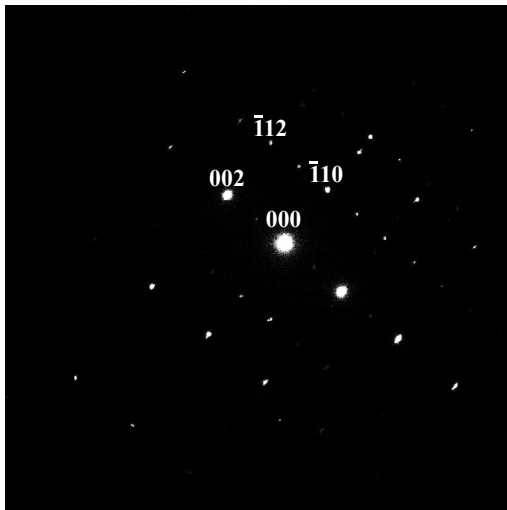


Figure 7: Electron diffraction patterns of 1-μm-thick AlN film grown on the 3C-SiC(100)/Si(100) substrate along the [110] zone axis of the AlN film.

Table 1: Pre-deposition treatment conditions for different AlN film thicknesses and their related FWHM values.

Duration of RF plasma etching	Seed layer deposition temp.	AlN thickness	AlN FWHM
180 s	ambient	1 μm	2.61°
180 s	elevated	1 μm	2.29°
360 s	elevated	1 μm	1.89°
600 s	elevated	1 μm	1.73°
600 s	elevated	1.5 μm	1.62°
600 s	elevated	2 μm	1.51°
600 s	elevated	2.5 μm	1.36°
600 s	elevated	3 μm	1.31°

The X-ray rocking curve measurements have shown that the crystal orientation of AlN films on 3C-SiC/Si substrates can be improved with increasing the film thickness due to development of more thorough columnar grains. The best texture with a FWHM value of 1.31° was achieved in the 3-μm-thick AlN film, which was deposited using two-step process: the first seed layer of 50-nm-thick AlN film was deposited at elevated temperature and the following well-textured AlN film was deposited at ambient conditions during the second step deposition process. Actually, a permanent heating at elevated temperature during the entire deposition process did not remarkably improve the crystal orientation, indicating that higher adatom mobility is required mostly at the nucleation stage which ensures the grain formation with less structural defects and releases the relatively large lattice mismatch of AlN and 3C-SiC as well. For comparison, 1-μm-thick AlN films deposited at ambient conditions and using the two-step deposition process exhibit the FWHM values of 2.61° and 1.73°, respectively.

As shown in Figure 6, two different layers of AlN thin films can be identified using the bright field (BF) TEM image. It is clear that the AlN thin film exhibits numerous columnar grains which are perpendicular to the surface of 3C-SiC. The electron diffraction (ED) patterns of 1-μm-thick AlN film grown on the 3C-SiC/Si substrate along the AlN [110] zone axis are shown in Figure 7. The electron beam size is approximately 300 nm which is large enough to cover many AlN columnar grains shown in Figure 6. This result supports that the AlN grains on the surface of 3C-SiC are well-textured and approximately along the same direction.

## B. SAW device on AlN/3C-SiC/Si composite structure

To demonstrate the practical operation of the AlN/3C-SiC/Si composite structure, two different designs of two-port SAW device were fabricated utilizing the lift-off technique. In the composite structure, surface acoustic waves propagate in the plane normal to the *c*-axis of AlN films and along the [001] axis of the 3C-SiC/Si (100) substrates.

Figure 8 is a microscope image of a two-port SAW device consisting of two sets of interdigital transducer (IDT) which was fabricated on the AlN/3C-SiC/Si composite structure. SAW devices with two different designs summarized in Table 2 are used to examine the piezoelectricity of the AlN thin film. The transmission characteristics of the SAW devices were measured using an Agilent E5071B network analyzer. Figure 9 details the measured frequency responses of SAW devices on the AlN/3C-SiC/Si layered structure after time-gating which was employed to remove the feedthrough effect. An expected Rayleigh mode shows a center frequency of 260 MHz while the wavelength is 20 μm. In other words, the Rayleigh mode exhibits a high phase velocity up to 5,200 m/s for 1-μm-thick AlN film and 2.3-μm-thick 3C-SiC film on the Si (100) substrate. This result confirms that the AlN/3C-SiC/Si structure possesses a high acoustic velocity, beneficial for high frequency applications.

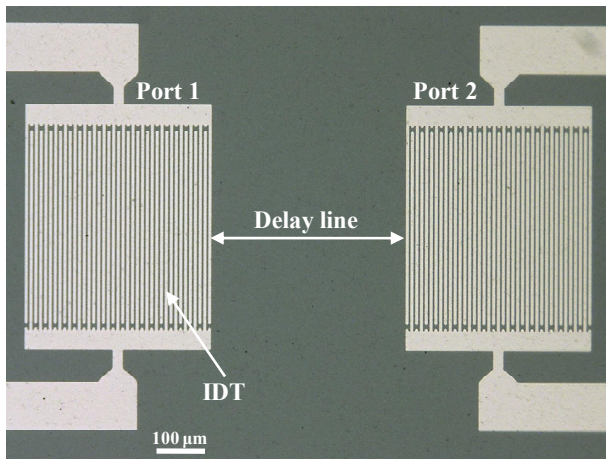


Figure 8: The microscope image of the fabricated SAW device (Design 1) on the AlN/3C-SiC/Si composite structure.

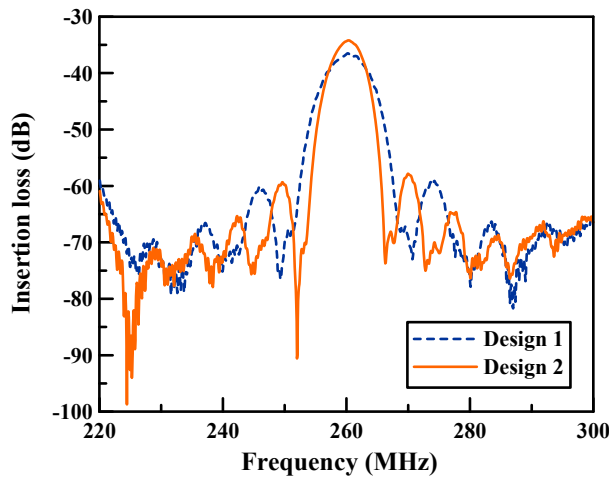


Figure 9: Measured frequency responses of SAW devices on the AlN/3C-SiC/Si layered structure after time-gating.

Table 2: Dimensions of SAW Devices.

	Design 1	Design 2
IDT pairs	30	40
Aperture	400 μm	400 μm
Electrode width	5 μm	5 μm
Delay line	400 μm	400 μm
Al electrode thickness	150 nm	150 nm

## CONCLUSION

For the first time, the heteroepitaxial AlN (002) thin films were successfully deposited on 3C-SiC(100)/Si(100) substrates using AC reactive magnetron sputtering at temperatures around 300-450 °C. A two-step deposition process is used to overcome the large lattice mismatch of 28.6% between AlN and 3C-SiC. The lowest FWHM value of 1.31° was achieved with a 3-μm-thick heteroepitaxial AlN film, indicating that highly *c*-axis oriented AlN films have been grown on the 3C-SiC/Si substrate. Two-port SAW devices were fabricated on the AlN/3C-SiC/Si composite structure and exhibited the expected Rayleigh mode with an acoustic velocity of 5200 m/s. The results confirm that the AlN/3C-SiC/Si composite structure can be utilized to create RF MEMS devices as well as piezoelectric MEMS sensors and actuators for operation in harsh environments.

## ACKNOWLEDGEMENTS

The authors offer special thanks to Professor Yung-Yu Chen at the Tatung University in Taiwan for the helpful discussion and the Microfabrication Lab staff at UC Berkeley for their assistance.

## REFERENCES

- [1] M. Mehregany, C.A. Zorman, S. Roy, A.J. Fleischman, C.-H. Wu, and N. Rajan, "Silicon carbide for micro-electro-mechanical systems," *Int. Mater. Rev.*, **45**, 286 (2000).
- [2] M.B.J. Wijesundara, D. Gao, C. Carraro, R.T. Howe, and R. Maboudian, "Nitrogen doping of polycrystalline 3C-SiC films grown using 1,3-disilabutane in a conventional LPCVD reactor," *J. Cryst. Growth*, **259**, 18 (2003).
- [3] <http://www.novasic.com/>, Apr. 5th (2010).
- [4] R.G. Azevedo, D.G. Senesky, A.V. Jog, B. Jamshidi, D.R. Myers, L. Chen, X.-A. Fu, M. Mehregany, M.B.J. Wijesundara, and A.P. Pisano, "A SiC MEMS resonant strain sensor for harsh environment applications", *IEEE Sensors J.*, **7**, 568 (2007).
- [5] S.A. Bhawe, D. Gao, R. Maboudian, and R.T. Howe, "Fully-differential poly-SiC Lamé mode resonator and checkerboard filter", *Tech. Dig. IEEE Int. Conf. MEMS*, Miami Beach, FL, 223 (2005).
- [6] W.-T. Chang and C.A. Zorman, "Electrical characterization of microelectromechanical silicon carbide resonators", *Sensors*, **8**, 5759 (2008).
- [7] F.S. Hickernell, "Characterization of the SAW propagation properties for zinc oxide films on silicon carbide", *Proc. IEEE Intl. Ultrason. Symp.*, Sendai, Japan, 273 (1998).
- [8] V. Cimalla, J. Pezoldt, and O. Ambacher, "Group III nitride and SiC based MEMS and NEMS: materials properties, technology and applications", *J. Phys. D: Appl. Phys.*, **40**, 6386 (2007).
- [9] V.V. Luchinin, A.V. Korlyakov, and A.A. Vasilev, "Silicon carbide-aluminium nitride: a new high stability composition for MEMS", *Proc. SPIE*, **3680**, 783 (1999).
- [10] R.C. Turner, P.A. Fuierer, R.E. Newnham, and T.R. Shrout, "Materials for high temperature acoustic and vibration sensors: a review", *Appl. Acoustics*, **41**, 299 (1994).
- [11] T.-T. Yen, C.-M. Lin, X. Zhao, V.V. Felmetsger, D.G. Senesky, M.A. Hopcroft, and A.P. Pisano, "Characterization of aluminum nitride Lamb wave resonators operating at 600°C for harsh environment RF applications", *Tech. Dig. IEEE Int. Conf. MEMS*, Hong Kong, China, 731 (2010).
- [12] Y. Takagaki, P.V. Santos, E. Wiebicke, O. Brandt, H.-P. Schonherr, and K.H. Ploog, "Superhigh-frequency surface-acoustic-wave transducers using AlN layers grown on SiC substrates", *Appl. Phys. Lett.*, **81**, 2538 (2002).
- [13] D. Doppalapudi, R. Mlcak, J. Chan, H. Tuller, A. Bhattacharya, and T. Moustakas, "MBE grown AlN films on SiC for piezoelectric MEMS sensors", *Proc. Mat. Res. Soc. Symp.*, **798**, Y10.61 (2004).
- [14] Y. Tanaka, Y. Hasebe, T. Inushima, A. Sandhu, and S. Ohoya, "Comparison of AlN thin films grown on sapphire and cubic-SiC substrates by LP-MOCVD", *J. Cryst. Growth*, **209**, 410 (2000).
- [15] G.S. Chung, J.M. Chung, and T.W. Lee, "Deposition of AlN thin films on Si substrates using 3C-SiC as buffer layer by reactive magnetron sputtering", *Electron. Lett.*, **44**, 1034 (2008).
- [16] V.V. Felmetsger, P.N. Laptev, and S.M. Tanner, "Innovative technique for tailoring intrinsic stress in reactively sputtered piezoelectric aluminum nitride films", *J. Vac. Sci. Technol. A* **27**, 417 (2009).

# HIGH PERMEABILITY PERMALLOY FOR MEMS

Michael Glickman<sup>1\*</sup>, Trevor Niblock<sup>2</sup>, Jere Harrison<sup>1</sup>, Ira B. Goldberg<sup>1</sup>, Peter Tseng<sup>1</sup>, and Jack W. Judy<sup>1</sup>

<sup>1</sup>Electrical Engineering Department, University of California, Los Angeles, CA, USA

<sup>2</sup>Magzor, Inc. Thousand Oaks, CA,

## ABSTRACT

We have demonstrated a thick electrodeposition process for NiFe 80/20 (Permalloy80) that can achieve a permeability of 8500 as measured by VSM and *in situ* measurements. The key features of our electroplating process that have enabled us to obtain this permeability are: electroplating in an inert N<sub>2</sub> atmosphere, separating the anode from the cathode by means of a porous plastic frit, and agitating the wafer with an array of parallel fins less than 500 μm from the wafer surface. This electrodeposition method could be used to produce a wide variety of magnetic MEMS sensors and actuators that consume far less power.

## INTRODUCTION

Magnetic MEMS have the promise to produce very powerful actuators and sensitive sensors, but have been limited by the difficulty of depositing thick high-quality magnetic material on the microscale [1, 2]. There are a wide variety of ferromagnetic alloys that can be plated for magnetic MEMS, but many materials have very high internal stress, making them difficult to use in released structures or for thick layers. These materials curl up or buckle when released, thereby deforming the engineered structures. Therefore, most magnetic MEMS processes are done with either NiFe 80/20 (80% Ni and 20% Fe) or nickel. Nickel is the simplest to plate, and can have very low stress. However, the permeability is significantly lower than that of permalloy, and it has a lower saturation magnetization.

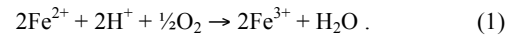
NiFe 80/20, is popular because of its ability to be plated very thickly (> 100 μm), fairly low stress, low magnetostriction, good mechanical properties, excellent corrosion resistance, reasonably high saturation (1 to 1.1 T), and relatively high permeability (200 to 5000) as shown in (Fig.1) [3–9]. Permalloy has been widely used in magnetic recording heads, and demonstrated for use in micropumps [10], magnetic micromotors [11], microrelays and switches [12], delta-wing control [7], magnetic separators [13], and microfluxgate magnetometers [14].

Other alloys, such as NiFeMo have demonstrated maximum relative permeabilities of up to 20,000 (corrected for demagnetization), but with 300% higher stress than NiFe 80/20, and has only successfully been electroplated to 5 μm. This work demonstrates electroplated NiFe 80/20 with a permeability of 8500 that is significantly higher than the highest previously reported NiFe 80/20 permeability of 5000. The improvement in permeability is achieved without using new additives, high temperature annealing or a magnetic field during plating (Fig. 1) [3–9]. In addition, the high permeability electrodeposit also maintains the other favorable properties of NiFe 80/20.

Plating nickel-iron alloys effectively is difficult for several reasons. The first reason is that nickel and iron must be deposited at the same time (codeposition) and at a precise ratio. In theory, this deposition rate is determined by the galvanic potential at the electrode surface and the concentration of the individual ions in the bath, but in practice, iron (the less noble metal), is deposited preferentially to nickel, which makes the codeposition anomalous [15]. To compensate for the faster iron deposition, the Ni<sup>2+</sup> / Fe<sup>2+</sup> ratio in the electroplating solution is made to be much higher than the desired stoichiometry of the electroplated material, so that the iron becomes mass-transfer limited. As a consequence, the

concentration of iron in the deposited material is determined by the diffusion of iron ions to the working electrode. Therefore, it is important for all electroplated surfaces to be adequately and uniformly agitated, so the percent of Fe in the deposit can be controlled more easily. Variations in the composition can lead to higher coercivity and lower permeability [6].

An important concern is that during plating, Fe<sup>2+</sup> is oxidized to Fe<sup>3+</sup> at the surface of the anode or when exposed to oxygen and a sufficiently low pH through the reaction,



The Fe<sup>3+</sup> can then form an insoluble iron-oxide compound called hematite FeO(OH)<sub>(s)</sub>, which can then contaminate the electroplated material. In addition Fe<sup>2+</sup> reduces more readily at the working electrode (the wafer), than Fe<sup>3+</sup>, which reduces the quantity of iron deposited in the film. Because the plating efficiency is not 100%, hydrogen bubbles that form at the wafer surface during plating can be incorporated into the film if the agitation is inadequate [16]. The hydrogen bubbles create voids in the film that lead to lower saturation magnetization and permeability. By addressing the aforementioned concerns, our electroplating system is able to substantially improve permeability using a typical NiFe 80/20 electroplating bath (Table 1). First we will discuss our electroplating setup, then our measurement methods.

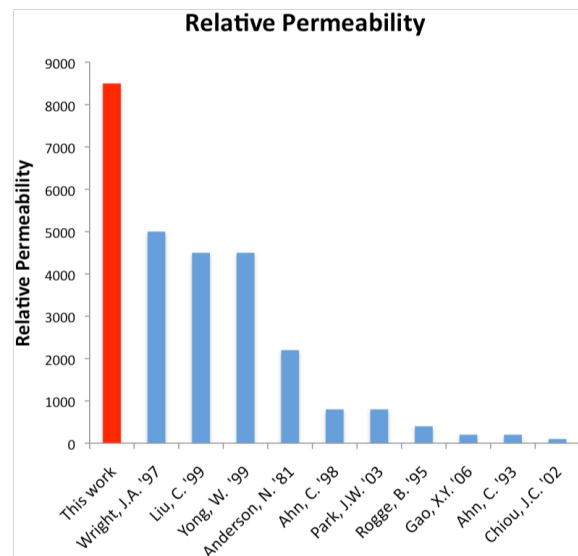


Figure 1: Comparison of maximum permeability of various published work.

Ingredient	Concentration
Nickel Sulfate Hexahydrate	250 g/l
Ferrous Sulfate Heptahydrate	5 g/l
Boric Acid	25 g/l
Sodium Saccharin	1 g/l
Sodium Lauryl Sulfate	0.1 g/l

Table 1: The plating recipe.

## EXPERIMENTAL SETUP

During electroplating, the low levels of iron in the bath become depleted near the counter-electrode surface (the wafer). In order to help ensure uniform stoichiometry, the electroplating surface should be replenished with fresh solution by vigorous agitation. In addition, the uniform distribution of additives, such as saccharin and sodium lauryl sulfate, help to create more uniform material deposition and morphology. To achieve vigorous agitation, we built an agitator with multiple fin-like structures that move perpendicular to the plane of the wafer, as shown in Fig 2. The fins are less than 0.5 mm from the wafer in order to force the movement of solution across the wafer. This method of agitation uniformly agitates the solution and reduces the thickness of the diffusion boundary layer [17]. The agitator fins are moved by an external motor and rod to convert the rotational movement to linear movement. The agitator travels 11.7 cm for each rotational cycle of the motor, and is operated at 30 RPM, for a fin speed of 5.8 cm/s. The plating is current controlled at 5 mA/cm<sup>2</sup>, and at room temperature (22°C).

As the fins of the agitator repeatedly move across the wafer, they physically remove any accumulated hydrogen bubbles, which results in a smoother and denser film with higher permeability. In addition to removing hydrogen bubbles and ensuring a uniform mixture, the thinning of the boundary layer allows for more uniform height distribution of different sized openings, as shown in Fig. 3 [17].

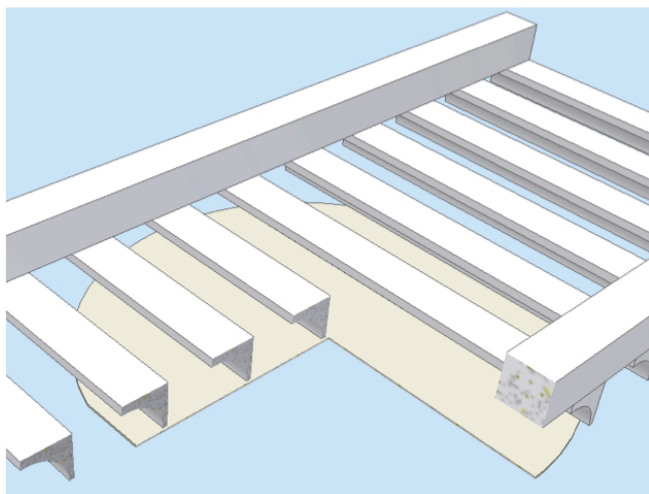


Figure 2: A 3/4 view of multi-fin agitation scheme over a wafer.

To ensure that Fe<sup>2+</sup> is not oxidized to Fe<sup>3+</sup> at the anode surface, one must keep the anode surface in a solution that is free of iron ions, yet maintains conductivity with the rest of the solution. The separation is accomplished by keeping the pure Ni mesh anode in a container filled with plating solution that does not contain Fe ions. The anode and its neighboring solution are separated from the cathode and its neighboring solution by a porous plastic sheet with a 10 μm pore size as shown in Fig 4. Over the relatively short timescales of electrodeposition (~ 3 hrs), Ni ions are driven by an electric-field gradient across the membrane to allow for plating, but little iron diffuses back across

the membrane. In addition, the porous barrier contains most of the contaminating Ni particles that are shed during the electrochemical etching of the anode.

Because Fe<sup>2+</sup> can be oxidized to Fe<sup>3+</sup> by dissolved oxygen, the plating solution should not be exposed to air for extended periods of time, as this would cause particulates to form in the solution and then plate onto the wafer. To prevent particulate formation, the plating solution is always kept under nitrogen atmosphere. Additionally, the solution must be filtered using a 100-nm-pore-diameter filter, since hematite particles have nanoscale dimensions, in the event of oxygen intrusion.

Since the filter has such diameter small pores, we use a large-surface-area (Polycap\* TF Disposable Filter Capsule Whatman, Maidstone, Kent UK), which has an effective surface area of 1000 cm<sup>2</sup>, and thus impose a minimal fluidic resistance. A low fluidic resistance is important because the plating bath is pumped by a peristaltic pump to minimize contamination of the bath. The filter is placed between the reservoir and the plating tank to prevent hematite particles that form in the reservoir from passing into the plating tank. The storage reservoir allows nitrogen to be bubbled through the solution continuously in a stoppered flask. The anode compartment is stored in a nickel-containing solution when not in use.

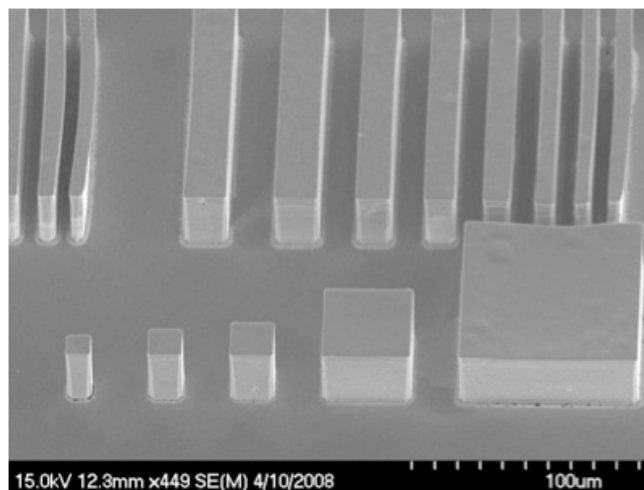


Figure 3: Permalloy deposited to 30 μm.

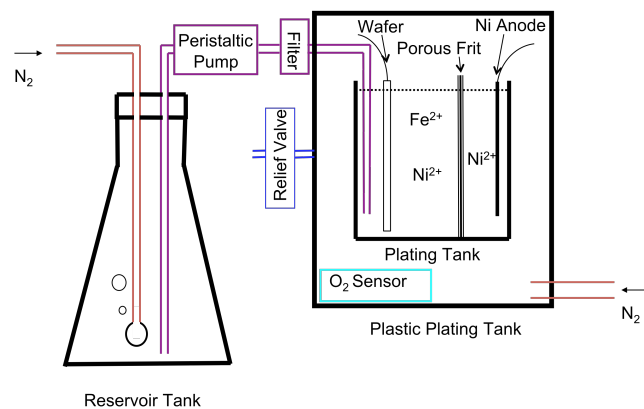


Figure 4: A schematic diagram of the NiFe 80/20 electroplating setup. The agitator and wafer chuck are not shown.

## MAGNETIC PROPERTIES

The magnetic properties of the electroplated NiFe 80/20 were measured by two methods. The first method was by vibrating sample magnetometer (VSM) using 6-mm-diameter samples of 400 nm and 7  $\mu\text{m}$  thickness, as measured by a surface profilometer (Veeco Dektak 6, Edina, MN, USA). When electroplating samples, it is important not to cut or break the film, as this can create large coercivities on the edge of the sample, so we electroplated through a 10- $\mu\text{m}$ -thick KMPR mold (a negative photoresist with vertical sidewalls). The samples were cleaved from the wafer (exterior to the electroplated region) and placed in the 7300-series VSM (Lake Shore Cryotronics, Inc., Westerville, OH, USA) to obtain an  $M$ - $H$  plot (Fig. 5), from which we could calculate the apparent permeability,

$$\mu_a = (M/H) + 1 . \quad (2)$$

The apparent permeability  $\mu_a$  is a very strong function of the material geometry as shown in Fig. 6. The demagnetization factor  $D$  of a thin disk has been solved analytically by Chen *et al.* [18], so there is no need to use an ellipsoidal approximation. Using the calculated demagnetization factor, we must convert the apparent permeability to an actual relative material permeability  $\mu_r$  using the formula

$$\mu_r = (\mu_a - \mu_a D) / (1 - \mu_a D) , \quad (3)$$

which can result in substantial errors if the true permeability is of the order of  $1/D$ , as shown in Fig. 7. If a sample dimension with too large of a demagnetization factor is chosen, tiny errors due to VSM drift or inaccuracies in sample thickness measurement can lead to an order-of-magnitude error when the true material permeability is estimated from the apparent permeability.

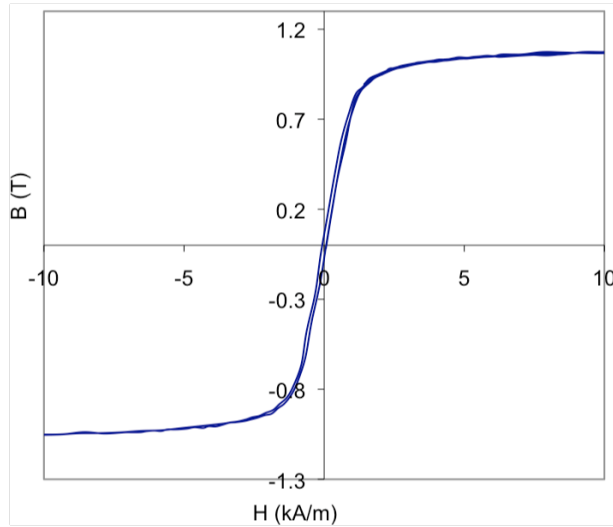


Figure 5: NiFe 80/20, not corrected for demagnetization factor.

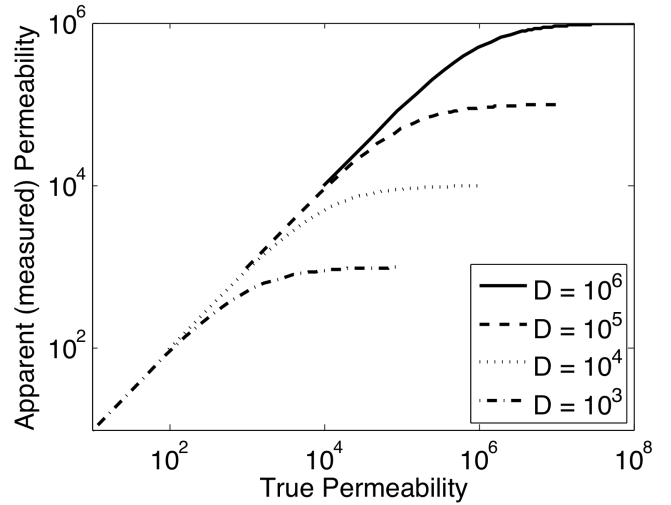


Figure 6: The apparent permeability for various demagnetization factors. The apparent permeability asymptotes to  $(1/D) + 1$  for infinite permeability.

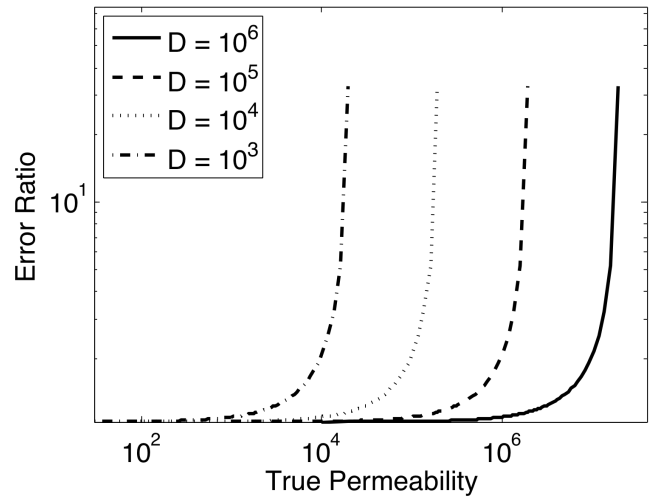


Figure 7: Ratio of calculated relative permeability to actual permeability, for a 5 % measurement error for various demagnetization factors,  $D$ . As the apparent permeability approaches  $1/D + 1$ , the measurement becomes highly inaccurate.

In addition to VSM measurements, we have also confirmed the permeability by *in situ* inductance measurements using a microfabricated inductor with 3D solenoidal coils (Fig. 8). We determined the maximum relative permeability by finding the maximum inductance as measured by an Agilent 4294A Impedance Analyzer at 620 Hz with an input of 5.3 mA. The inductor had 87 turns, a coil resistance of 37  $\Omega$ , a thickness of 7  $\mu\text{m}$ , core width of 300  $\mu\text{m}$ , and an inductance of 55  $\mu\text{H}$ .

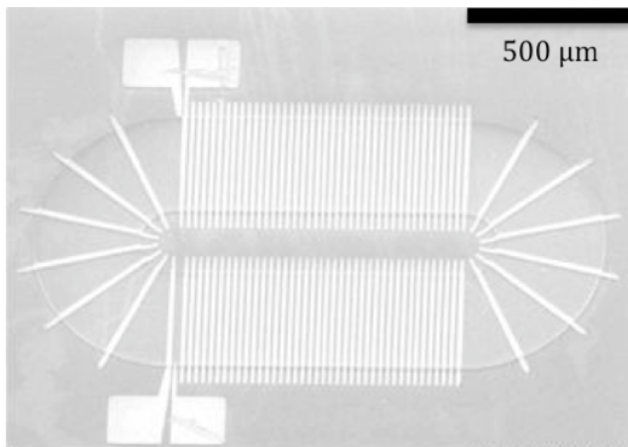


Figure 8: Inductor test structure for measuring inductance.

## CONCLUSION

By using multiple knife-edge agitators to agitate the electroplating solution, we have reduced the incorporation of hydrogen bubbles into the plating bath, as well as created a more uniform composition. We have also greatly reduced hematite contamination of the electroplating solution and the conversion of  $\text{Fe}^{2+}$  to  $\text{Fe}^{3+}$ , which can affect the amount of iron deposited in the film. By combining these methods we have been able to create a film that has an order of magnitude higher permeability than a typical electrodeposited NiFe 80/20 film, and substantially higher permeability than the highest reported permeability (which gave no details on their methods).

## ACKNOWLEDGEMENTS

The authors would like to thank the UCLA Nanoelectronics Research Facility for their help in the fabrication of the MEMS inductor.

## REFERENCES

- [1] J. Judy and N. Myung, "Magnetic materials for MEMS," in *MRS Workshop on MEMS Materials, San Francisco, California, (April 5-6, 2002)*, pp. 23-26.
- [2] N. Myung, D. Park, B. Yoo, and P. Sumodjo, "Development of electroplated magnetic materials for MEMS," *Journal of Magnetism and Magnetic Materials*, vol. 265, no. 2, pp. 189-198, 2003.
- [3] C. Ahn and M. Allen, "Micromachined planar inductors on silicon wafers for MEMS applications," *IEEE Transactions on Industrial Electronics*, vol. 45, no. 6, pp. 866-876, 1998.
- [4] X. Gao, Y. Cao, Y. Zhou, W. Ding, C. Lei, and J. Chen, "Fabrication of solenoid-type inductor with electroplated NiFe magnetic core," *Journal of Magnetism and Magnetic Materials*, vol. 305, no. 1, pp. 207-211, 2006.
- [5] J. Park and M. Allen, "Ultralow-profile micromachined power inductors with highly laminated Ni/Fe cores: application to low-megahertz DC-DC converters," *IEEE Transactions on Magnetics*, vol. 39, no. 5, pp. 3184-3186, 2003.

- [6] N. Anderson and C. Grover Jr, "Electroplating of nickel-iron alloys for uniformity of nickel/iron ratio using a low density plating current," Jul. 21 1981, uS Patent 4,279,707.
- [7] C. Liu, T. Tsao, Y. Tai, T. Leu, C. Ho, W. Tang, and D. Miu, "Out-of-plane permalloy magnetic actuators for delta-wing control," in *Proceedings of IEEE Micro Electro Mechanical Systems (MEMS 95)*, 1995, pp. 7-12.
- [8] C. Ko, J. Yang, and J. Chiou, "Efficient magnetic microactuator with an enclosed magnetic core," *Journal of Microlithography, Microfabrication, and Microsystems*, vol. 1, p. 144, 2002.
- [9] C. Liu and Y. Yi, "Micromachined magnetic actuators using electroplated permalloy," *IEEE transactions on magnetics*, vol. 35, no. 3, pp. 1976-1985, 1999.
- [10] W. Zhang and C. Ahn, "A bi-directional magnetic micropump on a silicon wafer," in *Solid-State Sensor and Actuator Workshop, Hilton Head Island, South Carolina, June 3-6, 1996: technical digest*. The Foundation, 1996, p. 94.
- [11] B. Wagner, M. Kreutzer, and W. Benecke, "Linear and rotational magnetic micromotors fabricated using silicon technology," *IEEE Micro Electro Mechanical Systems, 1992, MEMS'92, Proceedings. An Investigation of Micro Structures, Sensors, Actuators, Machines and Robot*, pp. 183-189, 1992.
- [12] M. Ruan, J. Shen, and C. Wheeler, "Latching micro magnetic relays with multistrip permalloy cantilevers," *Micro Electro Mechanical Systems, 2001. MEMS 2001. The 14th IEEE International Conference on*, pp. 224-227, 2001.
- [13] T. Liakopoulos, J. Choi, and C. Ahn, "A bio-magnetic bead separator on glass chips using semi-encapsulated spiral electromagnets," in *Solid State Sensors and Actuators, 1997. TRANSDUCERS' 97 Chicago., 1997 International Conference on*, vol. 1, 1997.
- [14] T. Liakopoulos and C. Ahn, "A micro-fluxgate magnetic sensor using micromachined planar solenoid coils," *Sensors & Actuators: A. Physical*, vol. 77, no. 1, pp. 66-72, 1999.
- [15] D. Gangasingh and J. Talbot, "Anomalous Electrodeposition of Nickel-Iron," *Journal of the Electrochemical Society*, vol. 138, p. 3605, 1991.
- [16] R. Orinakova, A. Turonova, D. Kladekova, M. Galova, and R. Smith, "Recent developments in the electrodeposition of nickel and some nickel-based alloys," *Journal of Applied Electrochemistry*, vol. 36, no. 9, pp. 957-972, 2006.
- [17] B. Wu, Z. Liu, A. Keigler, and J. Harrell, "Diffusion boundary layer studies in an industrial wafer plating cell," *Journal of the Electrochemical Society*, vol. 152, p. C272, 2005.
- [18] D. Chen, E. Pardo, and A. Sanchez, "Radial magnetometric demagnetizing factor of thin disks," *IEEE Transactions on Magnetics*, vol. 37, no. 6 Part 1, pp. 3877-3880, 2001.

## CONTACT

\* Michael Glickman: michael.glickman@ucla.edu

# MICROFABRICATED QUASIPERIODIC OPTICAL DIFFRACTION APERTURE ARRAYS FOR THE NANOMETROLOGY OPTICAL RULER IMAGING SYSTEM

N. Yoshimizu\*, A. Lal, and C. R. Pollock

School of Electrical and Computer Engineering, Cornell University, Ithaca NY, 14853

## ABSTRACT

This work demonstrates wafer-scale, path-independent, atomically long term-stable position nanometrology. The system can position multiple objects simultaneously, and could also measure their rotation. This nanometrology optical ruler imaging system uses the diffraction pattern of an atomically stabilized laser from a microfabricated quasiperiodic aperture array as a two dimensional optical ruler. Nanometrology is accomplished by cross correlations of image samples of this optical ruler. This work demonstrates new results showing positioning errors down to 17.2 nm over wafer scales and long term stability below 20 nm over six hours. This work also numerically demonstrates the robustness of the optical ruler to variations in the microfabricated aperture array, and discretization noise in imagers.

## INTRODUCTION

Tip-based nanofabrication, such as dip-pen writing or thermal surface modification, is a promising technology that will enable future computational and sensor/actuator technologies. In addition, scanning probe microscopy is critical to semiconductor device process characterization and development as future device milestones of sizes down to tens of nanometers. However, their success will rely critically on fast, precise nanometrology of nanoscale features at length scales varying up to seven orders of magnitude. State-of-the-art capacitive sensors and strain sensors lack long travel range and high precision optical encoders require a large reflective block which limits the frequency of movement. The resulting technological roadblock is the inability for a scanning probe microscope to quickly return to the same location after moving distances as small as tens of microns, much less an entire wafer. Consequently, time is laboriously spent searching for nanoscale features, limiting the throughput of nano-science and technology.

The nanometrology optical ruler imaging system (NORIS) uses an atomically stabilized laser as a stable base for metrology. The laser can be stabilized down to parts per billion. Just as atomic clocks use alkali atoms to stabilize a frequency source over long times, here the atoms stabilize the optical source for a long-term stabilized wavelength-determined optical ruler. The wavelength-stabilized laser beam is diffracted by a micropatterned metal thin film, which projects an optical ruler over the wafer-scale workspace and acts as a precise optical ruler. A quasiperiodic pattern is used, which generates sharper features than periodic or randomly generated patterns. Using such a pattern yields much greater precision than using a periodic structure. The system is described elsewhere, but we show a schematic for recall in Figure 1.

A basic idea for NORIS was presented earlier [1]. However, the earlier implementation used a periodic grating aperture array, resulting in a hexagonal lattice diffraction optical ruler. Using a quadrature photodiode, an analogue proportional-integral-differential control loop was used to position the photodiode on the center of peak in the optical ruler. Marks were made in poly(methyl methacrylate) at points corresponding to the optical ruler. The work resulted in a precision of  $\pm 3 \times 10^{-4}$  precision over a 75 mm wafer.

In this paper, the system has evolved to using a quasiperiodic

aperture array which results in a diffraction pattern that has very dense features. This results in great improvement in the precision of NORIS. Preliminary results and the principles of the system are described elsewhere. Here, we numerically demonstrate the robustness of the precision against defects or variations in the microfabricated quasiperiodic aperture array. Finally, this work demonstrates stability of 20 nm over six hours and precision down to 17 nm.

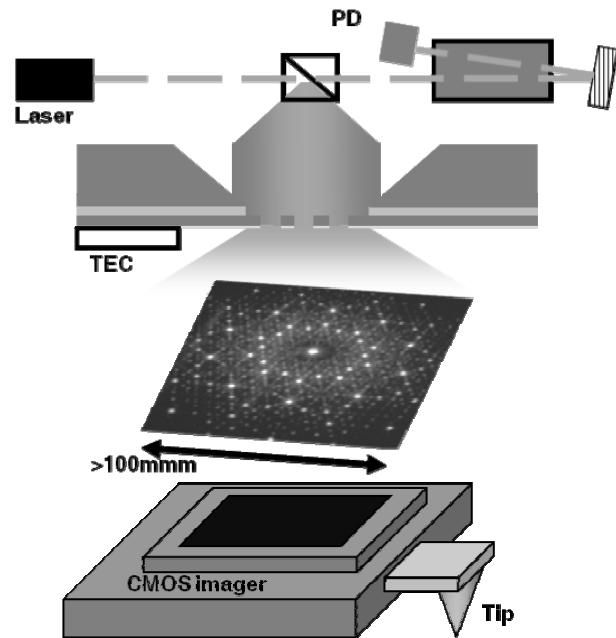


Figure 1: Nanometrology Optical Ruler Imaging System schematic: An external cavity laser is frequency stabilized within 6 MHz, or a relative accuracy of  $1.5 \times 10^{-8}$ , to a saturated resonance ( $F=2$  to 1) of the D2-line of  $^{85}\text{Rb}$ . A  $22.77 \pm 0.03$  °C temperature stabilized microfabricated Penrose vertices grating diffracts the laser beam (fabricated using ebeam lithography on SOI device layer; device layer Si etch; thru carrier wafer backside KOH etch; buffered HF release; Ti/Au evaporation). Wafer-scale optical ruler is shown, and CMOS camera acquired image of a small section of the optical ruler. Tip/CMOS imager is mounted on a commercial stage. Upsampled Fourier transform cross correlation calculates the CMOS imager position within the optical ruler.

## QUASIPERIODIC DIFFRACTION

The optical ruler is generated by the diffraction of an atomically stabilized laser beam by a microfabricated metal thin film. In the far field, or Fraunhofer diffraction region, the amplitude of the diffracted optical field is given by,

$$U(x, y) = e^{ikz} e^{ik(x^2+y^2)/2z} / (i\lambda z) \times \iint_{\pm\infty} U(\xi, \eta) \exp[-i2\pi(x\xi + y\eta)/(\lambda z)] d\xi d\eta, \quad (1)$$



where the amplitude  $U$  is calculated at position  $(x,y,z)$  due to the diffraction of amplitude  $U$  at  $(\xi,\eta)$  by an optical field of wave vector  $k$  and wavelength  $\lambda$  [2]. The first factor decreases the optical power density as the optical field diffracts away from its origin. The second factor corresponds to a decrease in the optical field away from its center. The diffraction pattern will have more optical power towards the center of the image, and the optical power will generally decay towards the outer parts of the diffraction pattern. The double integral contains the information for the features in the diffraction pattern, a critical component in achieving high precision in NORIS.

The double integral in Equation (1) is a Fourier transform of the amplitude  $U(\xi,\eta)$  at the diffraction plane. If the amplitude is constant across the aperture array, the double integral is a Fourier transform of the geometric shape of the aperture array where the openings are a constant intensity (normalized to one), and the nontransmitting regions are zero. In order to maximize the precision of the NORIS system, an optical ruler is needed whereby the cross correlation techniques yield the highest precision in the estimates of displacement. As pointed out in [3], the precision can be estimated based on the mean square error of the image registration at some offset  $\mathbf{r}$ . The lower bound of the mean square error is given by the Cramér-Rao bound,

$$MSE(\mathbf{r}) \geq J^{-1}(\mathbf{r}), \quad (2)$$

assuming an unbiased estimator, where the Fisher information matrix  $J$  is,

$$[J(\mathbf{r})]_{ij} = -E[\partial^2(\log f)/(\partial \mathbf{r}_i \partial \mathbf{r}_j)], \quad (3)$$

which is the negative expectation value of the partial derivatives of the log of the likelihood function. Here, the likelihood function refers to the image registration, or the calculation of the translational offset of two images.

As might be expected, Equations (2) and (3) show that high precision in image registration will be achieved by using images with image gradients. Most image registration techniques are normalized by intensity to account for lighting or sampling effects, for example. NORIS, which also normalizes its images before the image registration cross correlations, will therefore need image gradients that are different across the whole image so that image registration will see high gradient features of different directions. This will result in high contrast in the cross correlation, resulting in higher image registration precision. Therefore, we are looking for a diffraction array that generates very dense, very sharp features across the optical ruler area. In addition, we would like a diffraction pattern that is translationally asymmetric resulting in unambiguous positioning across a large area.

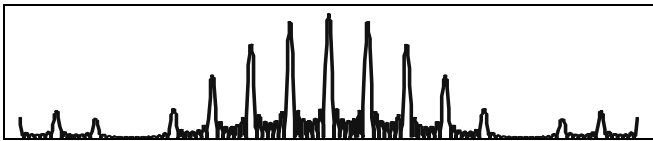


Figure 2: One dimensional diffraction pattern from a seven element, periodic aperture array, estimated by a Fourier transform. The resulting pattern, a sum of sinc functions, results in evenly spaced peaks with an intensity envelope.

An interesting solution can be found by considering different types of periodicity for the diffraction aperture arrays. To simplify the analysis, we consider one-dimensional diffraction, such as in Young's slit experiments. First, consider a very simple one dimensional periodic structure. The screen is opened periodically

by some opening of constant width. Therefore, the diffraction plane amplitude  $U(\xi,\eta)$  is a periodic array of *rect*, or *unit step*, functions. As expected from the readily available analytical solution, the diffraction pattern or Fourier transform of the screen aperture is a shifted sum of *sinc* functions. The diffraction pattern is a number of peaks with a decaying, periodic envelope of the intensity which decays away from the center of the diffraction pattern. In Figure 2, we show the one dimensional diffraction pattern from a periodic, seven aperture screen. A Fourier transform is used to estimate the resulting diffraction pattern.

Figure 2 shows a number of peaks that are periodic, limited by the bandwidth of the aperture array. However, despite the bandwidth available there are gaps where there is an apparent lack of features. We would like to decrease the mean square error of image registration shown in Equation (1) by increasing the optical gradients across the one dimensional image. As a first attempt, randomness is introduced to the aperture array. Rather than periodically placing the apertures, their locations are randomly shifted. The resulting diffraction pattern is shown in Figure 3. While some smaller intensity structure has appeared, there are number of large peaks that were clearly visible in the periodic case that have completely disappeared. The incoherent shifts in the aperture positions, i.e. white back ground noise, also slightly raises the noise floor of the diffraction pattern resulting in a less signal to noise of the peaks overall.

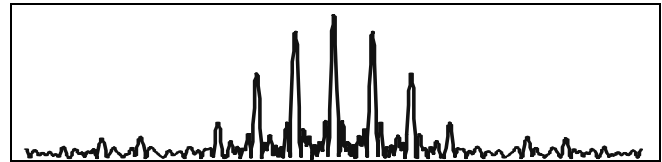


Figure 3: One dimensional diffraction pattern from a seven element, aperiodic aperture array in an attempt to increase features in the diffraction pattern. The aperture positions are nearly periodic, located at slight displacements from their periodic locations in Figure 2; the total bandwidth has even been increase slightly. Some low intensity structure appears to emerge, but some of the larger structures seen in the periodic case have disappeared.

Finally, we consider a quasiperiodic structure. Rather than displacing the periodic structure by random shifts, they are positioned at multiples of an irrational factor. Here, we use the golden ratio  $\phi = (1 + \sqrt{5})/2 \approx 1.61803$ , and we again give the same amount of bandwidth as the periodic case. The quasiperiodic structure, using an irrational factor, generates a denser diffraction pattern.

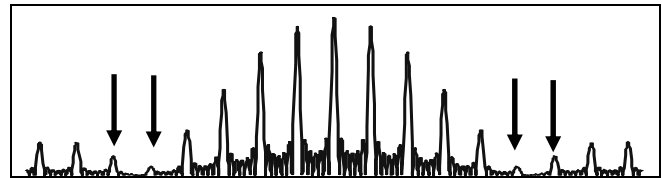


Figure 4: One dimensional diffraction pattern from a seven element, quasiperiodic structure using the irrational Golden Ratio  $\phi = (1 + \sqrt{5})/2 \approx 1.61803\dots$ . Comparing this diffraction pattern that in Figure 2, we see that already several new peaks are introduced, marked by arrows. The increase in sharp features increases the precision of NORIS.

Intuitively, the quasiperiodicity increases the features in the optical diffraction because the irrationality requires more modes in the Fourier transform. Suppose, for example, that the apertures were displaced by a rational shift  $m=b/a$ . In the Fourier analysis and calculation of the diffraction pattern, each shifted aperture would introduce new components to the diffraction pattern. However, after  $a$  number of shifts, the new aperture is shifted by an integer factor  $b$  and the new aperture is again in phase with the first aperture. These two apertures belong to the same modes of the Fourier analysis, and no new additional peaks are introduced into the diffraction than would otherwise exist. Quasiperiodicity induced by using irrational numbers, such as the Golden Ratio, results in new components from all the apertures and greatly increases the features in the diffraction pattern. Some of the interesting literature on quasiperiodicity is given in [4-10].

Figure 4 shows the resulting one dimensional diffraction pattern from a quasiperiodic aperture array with equal bandwidth as the periodic case in Figure 2. Although only seven apertures are used, the quasiperiodicity already introduces two new peaks per side in the diffraction pattern, as seen in Figure 4. The introduction of new peaks in the diffraction pattern decreases the mean square error of image registration, as described in Equation (1).

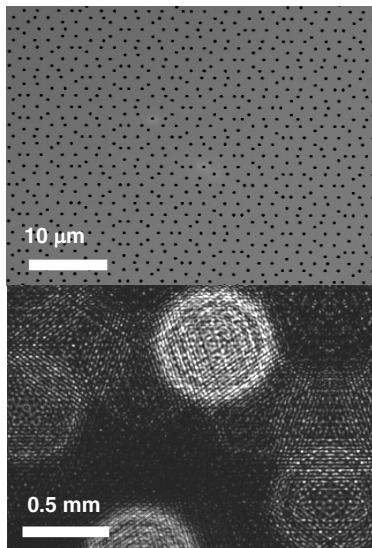


Figure 5: Top: Electron micrograph of a metal thin film quasiperiodic aperture array generated by using the vertices of a Penrose tiling. Bottom: CMOS imager sample of the resulting diffraction pattern. Note the high density of sharp peaks, due to the diffraction from a quasiperiodic structure.

In NORIS, a two-dimensional quasiperiodic structure is required to generate the diffraction optical ruler. We use the quasiperiodic Penrose tiling of the plane using thin and thick rhombuses whereby aperture circles are placed at the vertices of the tiling [11]. The aperture array and the resulting diffraction pattern are shown in Figure 5. Note the high density of peaks in the diffraction pattern, a result of the quasiperiodicity of the location of the apertures.

### APERTURE ARRAY PRECISION

The basis for the stability for NORIS comes from the atomically stable frequency of the laser beam that is diffracted. By using saturation spectroscopy, for example, the laser frequency can be stabilized down to parts per billion which corresponds to

nanometers over a six or twelve inch wafer. However, the accuracy of the positioning depends on the accuracy of the optical ruler. The image sampling clearly cannot directly calculate an image registration spanning wafer scale distance, unless the imager itself were that large. Instead, the imagers can be locally positioned accurately to the optical ruler at some position in space and rely on the precise location of that optical feature within that optical ruler. Since the optical ruler diffracts a parts per billion stabilized laser, the stability of the optical wavelength should not be a problem.

The diffractive aperture array, however, can induce errors in the diffraction optical ruler. This is caused by mechanical distortions of the geometry of the aperture array. Mechanical stability data, previously and currently shown in this manuscript, have demonstrated that vibrational and temperature fluctuation effects are insignificant. For example, the aperture array is a thermally conductive thin film metal spanning only a millimeter. A large thermoelectric cooler can easily stabilize the temperature of such a small thermal load to within 0.03 °C. With thermal coefficients of expansion of parts per million and rigid support around structure, dynamic thermal changes are expected to remain in the parts or many parts per billion as required by NORIS.

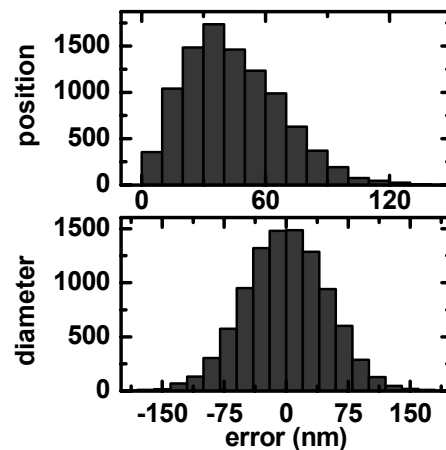


Figure 6: Histogram of aperture diameter and positioning errors, for simulated errors of 50 nm in microfabrication.

There is, however, a dependency on the resulting diffraction optical ruler due to errors in the actual microfabrication of the aperture array. There are possible sources for microfabrication errors in the aperture array. The size of the holes are nonuniform for slight variations in etching rates and aspect ratios, mask exposure and development, etc. However, the diffraction pattern is a result of the sum of the amplitudes from all apertures which is expected to dilute the effect of small variations in the microfabrication of the aperture array. In addition, as discussed in the section above, the Fourier transform of incoherent changes in the aperture array will tend to add white noise to the diffraction pattern, i.e. raise the noise floor, rather than change the peak structures within the optical ruler.

To characterize the dependence of NORIS precision on variations in the aperture array, numerical simulations were carried out. A 780 nm optical plane wave was simulated to illuminate an aperture array of 9662, 3 μm holes spanning a millimeter in size placed at the vertices of a Penrose tiling, with a 10 μm length constant. This is the configuration shown in the electron micrograph in Figure 5. The Fraunhofer diffraction at a distance of 25.4mm is calculated, and the resulting optical ruler used to

calculate NORIS positioning. The aperture array is varied by both the position of the apertures and the diameter of the apertures, using a randomly generated normalized distribution.

The aperture arrays were varied by their diameter and position offset of 20, 50, 100 and 500 nm; a sample histogram for 50 nm offset is shown in Figure 6.

The resulting position errors are shown in Figure 7, using a  $500 \times 500$ ,  $1 \mu\text{m}$  pixel imager and displaced in  $x$  from 0 to  $200 \mu\text{m}$ . Error is added to the aperture array, then the optical ruler is image registered to the image from a zero error aperture array. Microfabrication errors up to  $200 \text{ nm}$  appear to have little effect on the positioning, but microfabrication errors of  $500 \text{ nm}$  have a noticeable effect on NORIS precision. The quasiperiodic diffraction optical ruler appears to be robust to tolerance in microfabrication.

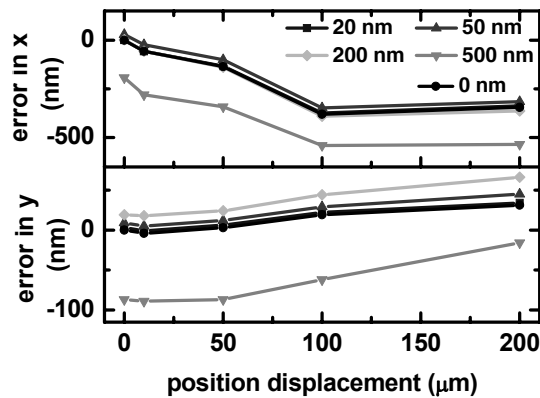


Figure 7: NORIS positioning errors due to microfabrication errors. Positions are calculated by positioning NORIS based on image registration to error aperture array to zero error aperture array. Errors of up to  $200 \text{ nm}$  appear to have no impact on positioning error; a  $500 \text{ nm}$  fabrication error shows an effect on NORIS positioning error.

## EXPERIMENTAL RESULTS

Finally, we show empirical results of NORIS. Figure 8 shows NORIS positioning compared to a short range, high precision capacitive sensor on a piezoelectric flexural stage (nPoint NPYZ100B), with  $17.2 \text{ nm}$  mean absolute deviation. The inset shows the residual. Figure 9 shows the stability of NORIS over 6 hours, at less than  $20 \text{ nm}$ .

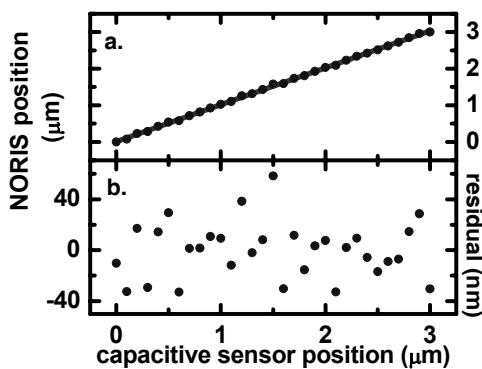


Figure 8: NORIS positioning errors across  $3 \mu\text{m}$  displacement, compared to short range, high precision capacitive sensors in a piezoelectric flexural stage.

## CONCLUSION

We have demonstrated the high precision and stability of NORIS, a system for parallel, path-independent, wafer-scale high precision nanometrology for scanning probe microscopes and nanoresolution stages. We have also demonstrated the robustness of the system against microfabrication variations in its quasiperiodic aperture array.

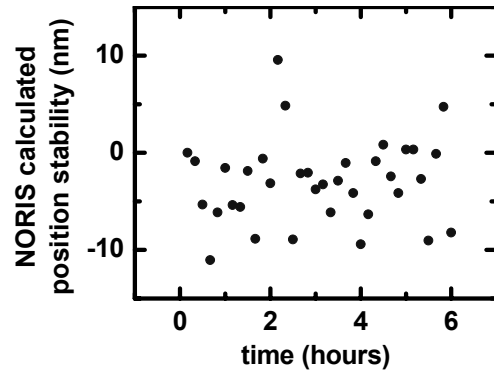


Figure 9: NORIS positioning errors across  $3 \mu\text{m}$  displacement.

## ACKNOWLEDGEMENTS

This work was generously funded by the DARPA/TBN program and performed, in part, at the Cornell NanoScale Facility.

## REFERENCES

- [1] N. Yoshimizu, A. Lal, C. R. Pollock, "MEMS Diffractive Optical Nanoruler Technology for Tip-Based Nanofabrication and Metrology," Proceedings of the IEEE MEMS 2009, pp. 547-550.
- [2] J. W. Goodman, "Introduction to Fourier Optics," Roberts & Company Publishers Colorado, 2005.
- [3] D. Robinson, P. Milanfar, "Fundamental Performance Limits in Image Registration," IEEE Trans. Image. Process 13, pp 1185-1199 2004.
- [4] R. K. P. Zia, W. J. Dallas, "A Simple Derivation of Quasi-Crystalline Spectra," J. Phys. A: Math. Gen. 18, pp. L341-L345 1985.
- [5] V. Elser, "The Diffraction of Projected Structures," Acta. Cryst. A42, pp. 36-43 1986.
- [6] F. Gähler, J. Rhyner, "Equivalence of the Generalized Grid and Projection Methods for the Construction of Quasiperiodic Tilings," J. Pys. A.: Math. Gen. 19, pp. 267-277 1986.
- [7] D. Levine, P. J. Steinhardt, "Quasicrystals I. Definition and Structure," Phys. Rev. B 34, pp 596 - 616 1986.
- [8] J. E. S. Socolar, P. J. Steinhardt, "Quasicrystals II. Unit-cell Configurations," Phys. Rev. B 617 - 647 1986.
- [9] C. Janot, "Quasicrystals: A Primer," Oxford University Press, 1997.
- [10] M. Senechal, "Quasicrystals and Geometry," Cambridge University Press, 1995.
- [11] N. G. de Bruijn, "Algebraic theory of Penrose's non-periodic tilings of the plane I & II," Ned. Akad. Wetensch. Proc. Ser. A 43, pp 39-66, 1981.
- [12] N. Yoshimizu, A. Lal, C. R. Pollock, "Nanometrology Using a Quasiperiodic Pattern Diffraction Optical Ruler," to be published in IEEE JMEMS.

## CONTACT

\*N. Yoshimizu, tel: +1-925-998-3299; ny22@cornell.edu

# PACKAGING OF LARGE LATERAL DEFLECTION MEMS USING A COMBINATION OF FUSION BONDING AND EPITAXIAL REACTOR SEALING

M. W. Messana\*, A. B. Graham, S. Yoneoka, R. T. Howe, and T. W. Kenny  
Stanford University, Stanford, California, USA

## ABSTRACT

The fabrication process described in this paper combines fusion bonding with a thin film sealing technique to package various MEMS devices. This combination allows large variations in trench widths (1.5 $\mu\text{m}$  up to 100 $\mu\text{m}$ ), which is necessary for encapsulating structures that include combdrives or large parallel plate capacitor arrays. The design rules are flexible enough to allow many different capacitively actuated, lateral displacement MEMS devices. Structures with resonant frequencies ranging from 5kHz up to 1.4MHz have been successfully encapsulated using this process with yields greater than 80%. In contrast to many other wafer bonding methods, fusion bonding allows the footprint of these fully encapsulated structures to be only slightly larger than the structure itself.

## INTRODUCTION

Packaging is often one of the most important design considerations in microelectromechanical systems (MEMS). It must provide a clean and stable environment for the device to reside in as well as allow electrical connection to the outside world. Ideally, the packaging would be low-cost and robust enough to withstand harsh post-processing (such as wafer dicing and wire bonding) while being fully integrated into a final system.

Traditional packaging techniques involve assembling each device into its final wafer package after singulation. This is expensive because each complex package is created individually. Additionally, if the MEMS structures are released prior to singulation, there will likely be a significant reduction in yield. Wafer level packaging techniques attempt to address these issues by integrating the device packaging into the overall fabrication process. Najafi provides a good overview of the various wafer level packaging methods commonly utilized in MEMS [1].

Anodic and eutectic bonding are commonly used to encapsulate MEMS devices at the wafer level. Typically, a wafer with aligned pockets is bonded to a wafer with released devices. While sometimes able to produce a very hermetic package, these bonding techniques typically require large bond areas which increases cost due to a reduction in the number of devices that can be made on a single wafer. Additionally, making electrical contact to the encapsulated devices often requires lateral traces which further increase the package footprint.

For thin film encapsulation, a sacrificial material is usually deposited over the MEMS structures, followed by the deposition of the encapsulation layer material. Upon removal of the sacrificial material, the released devices are re-sealed in their cavity. Depending on the materials used, this can result in a very hermetic package with a much smaller overall footprint than the wafer bonding techniques described above. However, if thicker device layers are desired, which provide improved performance in capacitively actuated and sensed devices, the design rules for thin film encapsulation techniques are typically very limiting. The sacrificial material must either bridge over the trenches defining the structures or be thick enough to fill them entirely. Both methods have been accomplished, however the design rules were either very restricting or the fabrication process impractical.

Candler *et al.* encapsulated piezoresistive and capacitive structures by releasing devices using hydrofluoric acid vapor and

then sealing the etch access holes using low pressure chemical vapor deposition (LPCVD) silicon dioxide [2]. Later iterations of this process improved the stability performance by sealing the etch access holes in an epitaxial silicon reactor, demonstrating excellent long term stability [3]. Both of these methods relied on the sacrificial material bridging over trenches approximately 2 $\mu\text{m}$  wide, thus limiting designs to these narrow gaps. This precludes the incorporation of such traditional structures as combdrives. Ayanoor-Vitikkate *et al.* attempted to address this problem by thermally oxidizing sacrificial beams in the device layer to create a thick sacrificial material, but working devices were never demonstrated [4]. Recently, Graham *et al.* presented a method for successfully encapsulating MEMS devices capable of 20 $\mu\text{m}$  of lateral deflection [5]. While both narrow and wide trench width devices were fabricated, the process relied on the deposition and partial planarization of a thick sacrificial oxide exceeding 20 $\mu\text{m}$  in thickness.

The process described in this work is intended to expand the design rules of the process outlined by Kim *et al.* to allow various trench widths while maintaining its long term stability [3]. To bridge the large trenches, a sacrificial wafer is fusion bonded to the device wafer. Fusion bonding is preferable to other types of bonding because it requires less bond area and all of the materials and processes involved with fusion bonding are CMOS compatible. This bonded wafer is subsequently thinned and small vent holes are etched for releasing the buried devices. The resulting cavity is then resealed with epitaxially grown silicon to fully encapsulate the released devices. Figure 1 depicts a released and sealed device using this process.

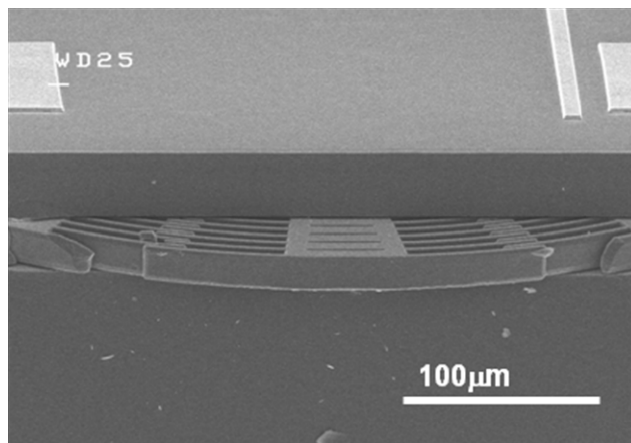


Figure 1: SEM image showing a resonating fan structure that is driven by combdrives. The metal electrical contacts can be seen on top of the encapsulation wafer.

## FABRICATION PROCESS

The process, shown in Figure 2, begins with a fusion bonded SOI wafer having a 20 $\mu\text{m}$  thick device layer and a 2 $\mu\text{m}$  thick buried oxide layer. Devices are patterned in photoresist and etched into the device layer using deep reactive ion etching (DRIE), as shown in Figure 2(a). The etch recipe used in this step was tuned to minimize feature blowout, eliminate grass formation, and

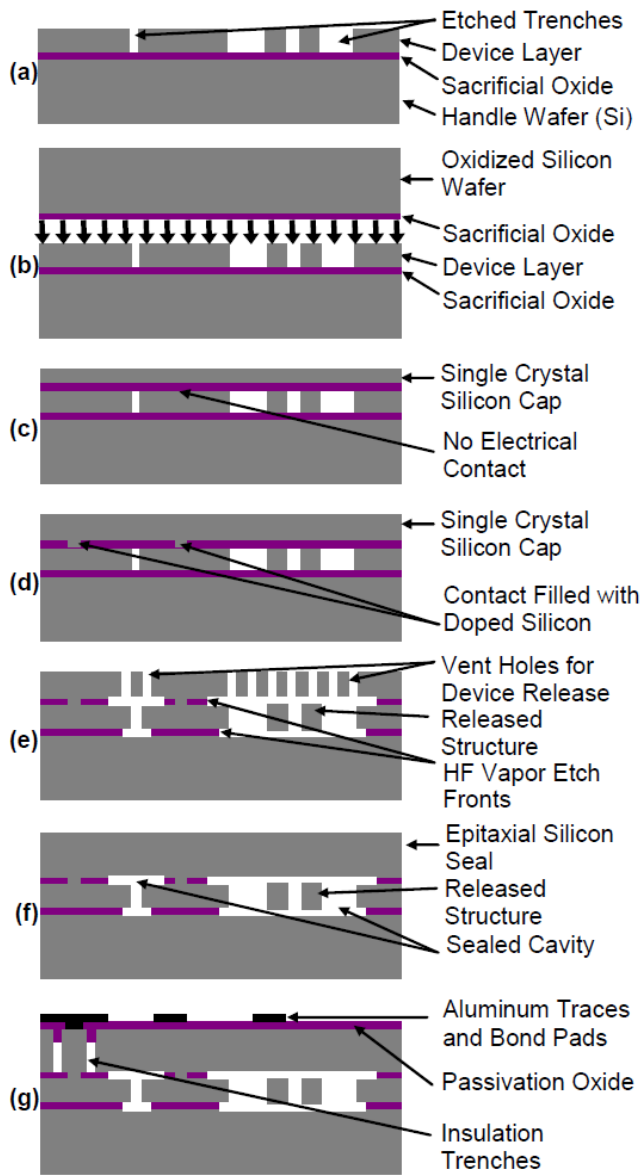


Figure 2: Schematic cross section of the encapsulation process. (a) Devices are defined in SOI wafer with a DRIE etch. (b) An oxidized silicon wafer is fusion bonded to the patterned SOI wafer. (c) The cap wafer is ground and polished to a specified thickness. (d) Electrical contact is made by etching holes and refilling with silicon. (e) Vents are etched in the cap layer and HF vapor removes SiO<sub>2</sub> in the cavity. (f) The cavity is sealed with silicon in an epitaxial reactor. (g) Electrical isolation trenches are etched, insulation oxide is deposited and etched, and metal is sputtered and etched.

minimize footing at the buried oxide interface. The sidewall polymer is removed using a short O<sub>2</sub> plasma etch and the resist is stripped in a sulfuric acid solution.

In preparation for wafer bonding, both this patterned SOI and a blank silicon wafer with 2μm of thermally grown oxide receive a standard RCA-2 clean. In addition to this clean, a final clean of the wafers in a 5:1:1 mixture of H<sub>2</sub>O:NH<sub>4</sub>OH:H<sub>2</sub>O<sub>2</sub> at 70°C for 20 minutes is performed in an effort to increase the bond strength [6].

The two wafers are then bonded together using a Karl Suss fusion bonding tool at a pressure less than 1mTorr. Since the encapsulation wafer is unpatterned, a flat alignment between the two wafers is sufficient for this process. To increase the bond strength as described by Plöbl *et al.* [7], the bonded wafer stack is annealed at 1100°C for 4 hours. Vacuum bonding is used because the etched features create various sized cavities that may degrade the bond local to the devices as a result of the pressure increase during the subsequent high temperature steps. As shown in Figure 2(c), the bonded wafer is then thinned to approximately 15μm via a combination of grinding and polishing. After thinning, the wafer stack is annealed for an additional 20 hours at 1100°C to further improve bond strength. This overall process of bonding followed by grinding and polishing is very similar to the process used to make fusion bonded SOI wafers [8].

Contact vias are then patterned on the thinned wafer and etched to the oxide on top of the electrodes using DRIE. The oxide is cleared from the bottom of the vias using HF vapor. The vias are then filled with highly doped silicon using a process similar to filling trench capacitors in DRAM [9]. For this process, the filling of these trenches was performed in an epitaxial silicon reactor to maintain single crystal silicon across the bulk of the encapsulation wafer.

Thin vents (0.7μm wide) are then patterned and etched in the encapsulation layer using a DRIE recipe optimized for high aspect ratio trenches. The SiO<sub>2</sub> on the top and bottom of the device is removed using a timed HF vapor etch. An IR microscope is used to confirm that the devices are fully released as shown in Figure 3.

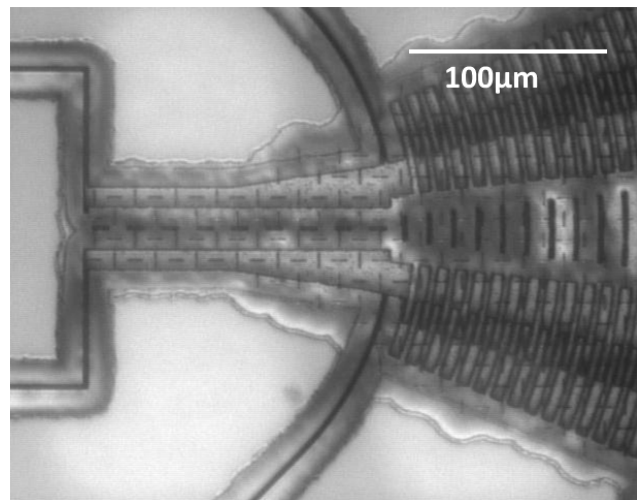


Figure 3: IR image of a MEMS device encapsulated in this process. The cross hatches over the structure are the vents that allow HF vapor to remove the SiO<sub>2</sub> off the top and bottom of the device. Vapor etch fronts can be seen in the image and, with the exception of where the vents are located, the top and bottom vapor etch fronts are nearly on top of each other.

Immediately following the release, the wafers are placed in an epitaxial silicon reactor. The wafers are first baked at 1130°C for 5 minutes to remove any native oxide that might have formed on the wafer surface after vapor etching [10]. This step also serves to smooth out the scallop features left by the DRIE. The vents are then sealed with silicon at high temperature (925°C) and low pressure (20Torr) using a recipe that selectively deposits on silicon over silicon dioxide. This selectivity prevents electrical shorting between the encapsulation layer and the device layer across the

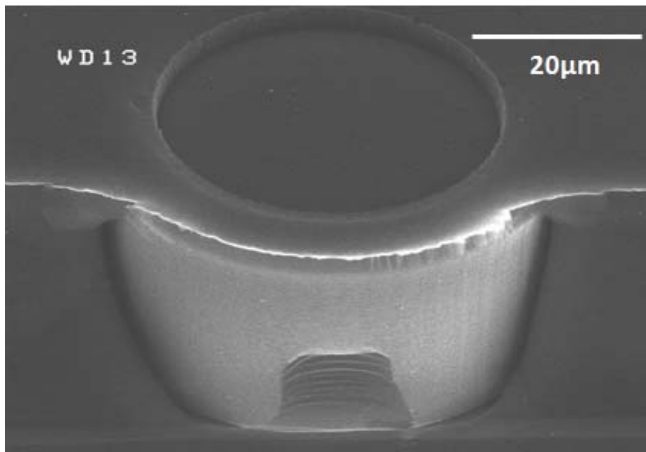


Figure 4: SEM image showing a vertical electrical connection. The circle on top is a via etched through the passivation oxide which has been covered with metal to contact the silicon plug below. The cylindrical plug is the electrical contact through the cap to the device layer below.

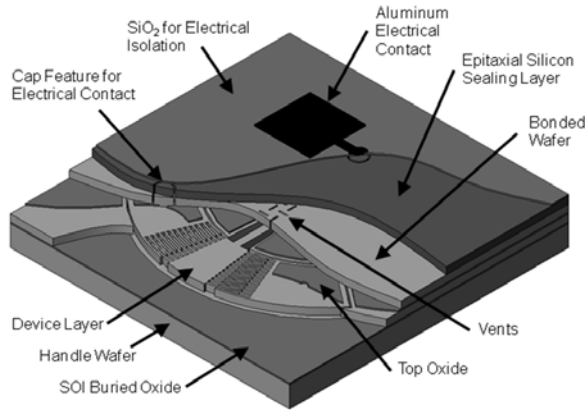


Figure 5: Isometric view of all the layers of the final packaged device.

sacrificial oxide. With hydrogen as a carrier gas, the reaction gases,  $H_2SiCl_2$ ,  $PH_3$ , and  $HCl$ , represent less than 4% of the composition of gases in the chamber. This sealing process results in a cavity free of native oxide that contains primarily hydrogen as a residual gas. To increase the strength of the cap layer, approximately  $6\mu m$  of additional silicon is added to the silicon needed to seal the vents. To improve subsequent lithography steps, the wafers are polished using a CMP, removing approximately  $1\mu m$  of silicon in the process. A schematic cross section of the wafer stack at this step can be seen in Figure 2(f).

The remaining steps are needed to make isolated electrical contact to the devices and the various electrodes needed to actuate the device. Isolation trenches are patterned around the contact vias and etched to the top oxide using DRIE. Approximately  $3\mu m$  of LPCVD  $SiO_2$  is deposited on the wafer to cover over the isolation trenches. Contact vias are patterned and plasma etched into this oxide to allow metal contact to the cap layer.

To create the wire traces and bond pads, aluminum is sputtered on the top surface of the wafer. This metal layer is plasma etched to complete the process, as shown in Figure 2(g). An SEM showing the complete vertical interconnect is shown in Figure 4. An isometric view of the final wafer stack can be seen in Figure 5.

## RESULTS AND DISCUSSION

Using the process described in this paper, numerous working devices were fabricated and successfully encapsulated. These devices include double ended tuning fork (DETF) resonators with resonant frequencies ranging from 190kHz to 1.4MHz and comb-driven, fan shaped resonators with resonant frequencies ranging from 50kHz to 150kHz. In addition to these, many other resonant structures, inertial sensors, and structures for fundamental studies of such things as fatigue and friction were included, but have yet to be tested.

As was demonstrated by Candler *et al.*, the pressure inside the cavity can be reduced by elevated temperature ( $400^\circ C$ ) annealing in a nitrogen environment [11]. While this is not necessary or even desirable for all MEMS devices, a decrease in pressure leads to an increase in the quality factor of many types of resonators. This trend is shown in Figure 6 for two different designs of tuning fork resonators. Figure 7 shows the change in the frequency response plot for one such resonator for three different times throughout the

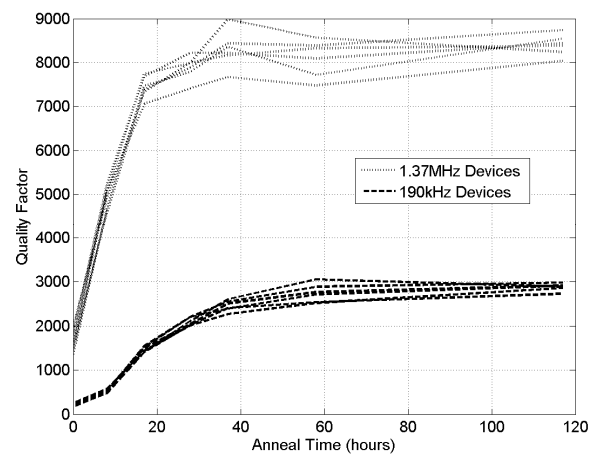


Figure 6: This plot shows resonator quality factor,  $Q$ , increasing during a  $400^\circ C$  anneal in a nitrogen ambient. Increasing quality factor corresponds to a decrease in the cavity pressure. Data is shown for multiple DETF resonators at 1.37MHz and 190kHz.

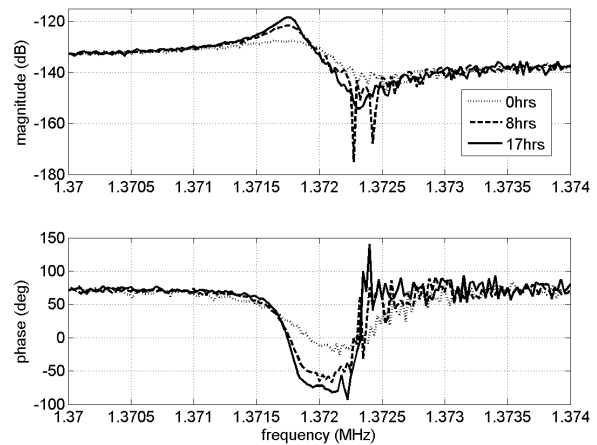


Figure 7: This plot shows example frequency response plots for a 1.37MHz double ended tuning fork resonator. The multiple lines correspond to different times during a  $400^\circ C$  anneal. Signal quality is improving with increased anneal time.

anneal. The amount of time required for the resonators' quality factor to reach a maximum is comparable with that previously reported for packages shown to be quite hermetic [3, 5].

Table 1 gives a summary of the yield for several different resonating structures tested on a single wafer for 20 instances of each design. The yield being lower than 100% can be attributed to slight process variations such as particles on the wafers during bonding, various etch or lithography problems, and possible shorting resulting from an epitaxial reactor seal recipe that was not perfectly selective in its deposition on silicon over silicon dioxide.

Table 1: Summary of yield for various devices on a single wafer.

Device	Yield
Single anchored 1.38MHz DETF	75%
Double anchored 1.4MHz DETF	65%
Single anchored 190kHz DETF	100%
100kHz Comb Drive Resonator	90%

## CONCLUSION

This new fabrication process for the wafer level packaging of MEMS devices combines two existing encapsulation techniques: fusion wafer bonding and epitaxial reactor sealing. The use of fusion bonding allows smaller bond areas than most other bonding techniques while maintaining a single crystal silicon cap and CMOS compatible materials. Because of the single crystal silicon cap layer, optical transparency is improved over the use of polysilicon, making this packaging method especially suitable for encapsulating optical devices working in the infrared range. The use of epitaxial reactor sealing provides a sealed environment free of native oxide and maintains the single crystal silicon cap layer. The combination of these two techniques has allowed the encapsulation of devices capable of large lateral deflections while not sacrificing the ability to include the smaller gaps desired for many electrostatic devices. Additionally the overall package footprint needs only to be slightly larger than the device itself.

A variety of structures were included in this process, with resonant devices having frequencies ranging from 5kHz to 1.4MHz. In addition, yield was quite high for a process developed and carried out in a research-oriented academic fabrication facility. Future work will focus on evaluating the hermeticity of the package by monitoring long term frequency stability and on characterizing the numerous other devices fabricated in this process.

## ACKNOWLEDGEMENTS

This work was performed under the Center on Interfacial Engineering for Microelectromechanical Systems, funded by DARPA grant HRO011-06-0049 and managed by Dr. D. L. Polla. Additional support was provided by the National Nanofabrication Users Network facilities funded by the National Science Foundation under award ECS-9731294. The authors would also like to thank Gary Yama, Mario Kupnik, and J Provine for helpful discussions. Travel support was provided by the Transducers Research Foundation for M. W. Messana.

## REFERENCES

- [1] K. Najafi, "Micropackaging technologies for integrated microsystems: Applications to MEMS and MOEMS," *Proc. SPIE - Micromachining and Microfabrication Process Technology VIII*, pp. 1-19, 2003.
- [2] R.N. Candler, W.-T. Park, H. Li, G. Yama, A. Partridge, M. Lutz, and T.W. Kenny, "Single wafer encapsulation of MEMS devices," *IEEE Trans. Adv. Packag.*, vol. 26, no. 3, pp. 227-232, 2003.
- [3] B. Kim, R.N. Candler, R. Melamud, M.W. Hopcroft, S. Yoneoka, H.K. Lee, M. Agarwal, S. Chandorkar, G. Yama, and T.W. Kenny, "Hermeticity and diffusion investigation in polysilicon film encapsulation for microelectromechanical systems," *Journal of Applied Physics*, vol. 105, 013514 2009.
- [4] V. Ayanoor-Vitikkate, K.-L. Chen, W.-T. Park, and T. W. Kenny, "Development of wafer scale encapsulation process for large displacement piezoresistive MEMS devices," *Sens. Actuators A, Phys.*, vol. 156, pp. 275-283, 2009.
- [5] A.B. Graham, M.W. Messana, P.G. Hartwell, J. Provine, S. Yoneoka, R. Melamud, B. Kim, R.T. Howe, and T.W. Kenny, "A Method for wafer scale encapsulation of large lateral deflection MEMS devices," *Journal of Microelectromechanical Systems*, vol.19, no.1, pp.28-37, Feb. 2010.
- [6] Y.-L. Chao, Q.-Y. Tong, T.-H. Lee, M. Reiche, R. Scholz, J.C.S. Woo, and U. Gösele, "Ammonium hydroxide effect on low-temperature wafer bonding energy enhancement," *Electrochemical and Solid-State Letters*, vol. 8, pp. G74-G77 2005.
- [7] A. Plöbl, and G. Kräuter, "Wafer direct bonding: tailoring adhesion between brittle materials," *Materials Science and Engineering*, vol. R25, pp. 1-88, 1999.
- [8] C. Harendt, W. Appel, H.-G. Graf, B. Höfflinger, and E. Penteker, "Wafer fusion bonding and its application to silicon-on-insulator fabrication," *Journal of Micromechanics and Microengineering*, vol. 1, pp. 145-151, 1991.
- [9] M. Taguchi, S. Ando, N. Higaki, G. Goto, T. Ema, K. Hashimoto, and T. Yabu, "Dielectrically encapsulated trench capacitor cell," *Electron Devices Meeting, 1986 International*, vol.32, pp. 136-139, 1986
- [10] S.T. Liu, L. Chan, and J.O. Borland, "Reaction kinetics of SiO<sub>2</sub>/Si (100) interface in H<sub>2</sub> ambient in a reduced pressure epitaxial reactor," *Proc. 10th Int. Conf. Chemical Vapor Deposition. Electrochem. Soc.*, pp. 428-434, 1987.
- [11] R.N. Candler, W.-T. Park, M. Hopcroft, B. Kim, and T.W. Kenny, "Hydrogen diffusion and pressure control of encapsulated MEMS resonators," *Proc. 13th Int. Conf. Solid-State Sens. and Actuators (TRANSDUCERS '05)*, pp. 920-923, 2005.

## CONTACT

\*M. Messana, tel: +1-650-723-0277; mmessana@stanford.edu

# PDMS AND SILICON MICROMECHANISMS IN A MONOLITHIC PROCESS

A. P. Gerratt<sup>1\*</sup>, I. Penskiy<sup>1</sup>, and S. Bergbreiter<sup>1,2</sup>

<sup>1</sup>Department of Mechanical Engineering, University of Maryland, College Park, USA

<sup>2</sup>Institute for Systems Research, University of Maryland, College Park, USA

## ABSTRACT

A new PDMS and silicon fabrication process that integrates a soft elastomer in-plane with silicon features has been developed, characterized and demonstrated. The simple three-mask process uses deep reactive ion etching of silicon trenches on a silicon-on-insulator wafer to pattern high aspect ratio silicon and elastomer features from 2  $\mu\text{m}$  to hundreds of micrometers in size. The process has been characterized with Sylgard 184 and is demonstrated in compliant hinges that can be operated both in- and out-of-plane and in a micromechanical thruster. These components demonstrate a new versatility in MEMS processing that allows for simple fabrication of robust features that can undergo large deformations.

## INTRODUCTION

The most universal materials used in microfabrication include semiconductors, metals, and dielectrics, all materials with Young's moduli on the order of GPa's [1]. Softer materials are common in microfluidic applications and are typically fabricated with soft lithography [2-3]. The material most commonly used for soft lithography is poly(dimethylsiloxane) (PDMS). The advantages of PDMS over typical microfabrication materials are robustness, ability to withstand strains in excess of 100% without plastic deformation, and a low Young's modulus. While there are a few examples of systems that have integrated typical silicon bulk and surface micromachining process with PDMS processing [4-5], these devices requires complex fabrication that would be difficult to adapt for other applications.

The purpose of this research was to develop a process that enables integration of PDMS into a standard silicon-on-insulator (SOI) fabrication process for manufacturing monolithic micromechanisms. This process has to be repeatable, have a high yield, and use batch fabrication techniques (require no manual assembly).

Two devices that exemplify the value of integrating PDMS and silicon in a monolithic process are compliant hinges and a micromechanical elastomer-based thruster. A hinge with a

compliant joint would allow for more robust manipulation both in- and out-of-plane using smaller forces compared to a similar device fabricated with traditional MEMS materials. A micromechanical thruster with an embedded elastomer would allow for repeatedly storing and quickly releasing energy with an elastomer spring in a monolithic device. Smaller forces are required to store the energy in elastomer compared to similar silicon devices [6].

## FABRICATION PROCESS

The fabrication process for PDMS and silicon micromechanisms is shown in Figure 1. The process is very similar to the commercially available SOI-MUMPS process with the addition of an extra mask step to define the PDMS features [7]. Devices were all fabricated on a silicon-on-insulator (SOI) wafer (430  $\mu\text{m}$  handle layer thickness, 2  $\mu\text{m}$  buried oxide (BOX) layer thickness, and 20  $\mu\text{m}$  device layer thickness). In step 1, photoresist was patterned on the device layer and a deep reactive ion etch (DRIE) was performed down to the buried oxide layer.

Sylgard 184 PDMS from Dow Corning was mixed in a 10:1 ratio of base to curing agent and degassed in vacuum at 1 Torr for 15 minutes. In step 2, the PDMS was spread across the surface, degassed again, and cured.

The PDMS was planarized to the surface of the wafer in step 3. This was accomplished by using a razor blade as a squeegee to scrape the wafer surface. The remaining after step 1 photoresist was used to liftoff any residual PDMS. The liftoff leaves small particles of PDMS on the surface of the wafer, so a brief soak in *n*-methylpyrrolidone (NMP) and tetrabutylammonium fluoride (TBAF) in a 3:1 ratio was performed [2].

In step 4, photoresist was again patterned on the device layer of the wafer and another DRIE was performed down to the buried oxide. Photoresist was then spun on the top of the wafer to protect it during later processing steps.

In step 5, photoresist was patterned on the backside of the wafer, after which the device layer of the wafer was bonded with a thin layer of photoresist to another handle wafer. A DRIE was performed on the backside of the SOI wafer down to the buried

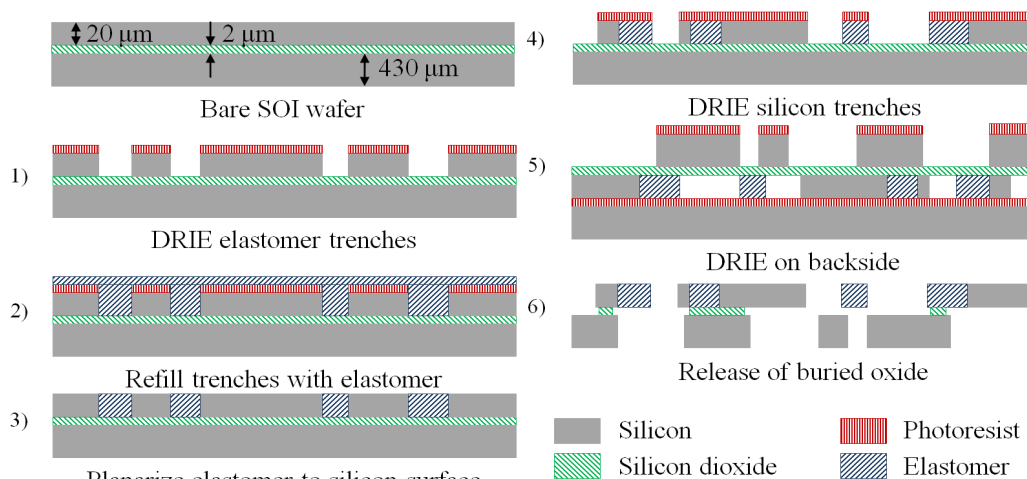


Figure 1: Microfabrication Process



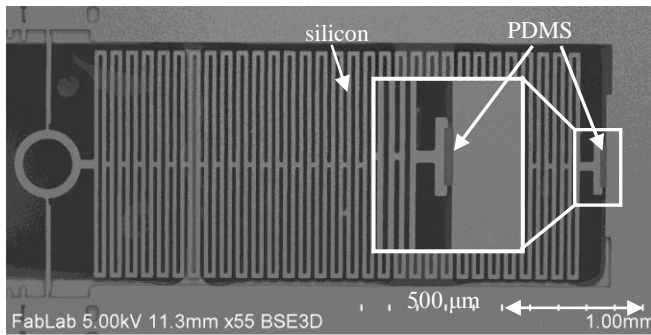


Figure 2: SEM of the test structure used to measure normal adhesion

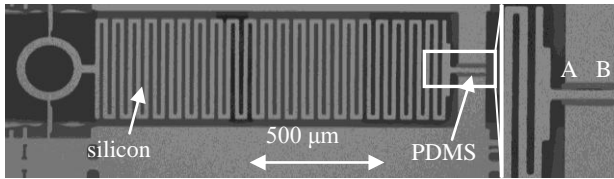


Figure 3: SEM of the test structure used to measure shear adhesion

oxide layer. A solvent release was used to separate the SOI wafer from the handle wafer. Finally in step 6, an 18:1 buffered hydrofluoric acid (BHF) etch of the buried oxide layer was used to release some of the silicon and PDMS features.

## PROCESS CHARACTERIZATION

The microfabrication process described above was developed to enable the manufacture of PDMS and silicon features in an SOI wafer. The unique challenges for this process are refilling high aspect ratio trenches with viscous elastomers, survival of PDMS features during release etch, sufficient adhesion between the silicon and PDMS so that the two materials do not delaminate, and comparable mechanical properties between unprocessed and processed PDMS, particularly the ultimate strain and Young's modulus.

### Feature size and Aspect ratio

High aspect ratio trenches in excess of 20:1 have been successfully refilled with several different elastomers. The viscosities of the implemented pre-cure elastomers range from 4,575 centipoise to 66,700 centipoise [8]. Features widths from 2  $\mu\text{m}$  to hundreds of micrometers have been fabricated at lengths up to several millimeters. The yield for features less than about 30  $\mu\text{m}$  in width was near 100%. As the width of the features increases above 30  $\mu\text{m}$ , the yield decreases. Any variations in the surface topology around the elastomer features will result in a local thinning of the photoresist, especially at wider features. This is problematic for SOI wafers with thick device layers as the photoresist masking layer is not always sufficient around the elastomer features to withstand the entire DRIE in step 4. This issue can be mitigated by using a thicker masking layer or a masking material with a superior selectivity with silicon, such as silicon dioxide.

### Silicon-Elastomer Adhesion

Adhesion of the silicon and elastomer features is crucial for proper operation of the fabricated devices. Ideal adhesion would allow the elastomer to reach its ultimate strain before the silicon and elastomer delaminate. Test structures to examine the shear

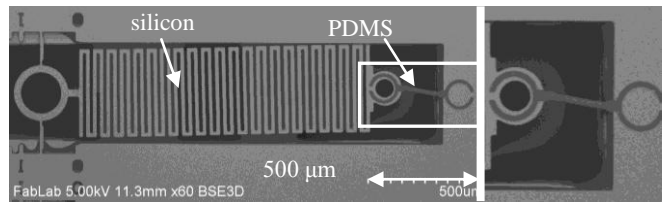


Figure 4: SEM images of the test structure used to measure stress-strain and the Young's modulus

and normal adhesion have been designed and fabricated. These structures consist of the elastomer that is under investigation in series with a silicon spring. The silicon spring was designed using ANSYS to have a spring constant of 4.35 N/m. The spring constant was recalculated after fabrication to account for any lateral etch during the DRIE. A probe was used to manually apply a force to the end of the silicon spring and the same force was transferred to the elastomer. For analysis, micrographs are taken at several stages as the applied force was increased.

The test structure used to measure the normal adhesion is shown in Figure 2. The ultimate pressure at which the elastomer delaminated from the silicon due to a normal force occurred over the range of 0.8 MPa to 1.6 MPa in eight tests. The test structure used to measure the shear adhesion is shown in Figure 3. The ultimate pressure at which the elastomer delaminated from the silicon due to a shear force occurred over the range of 40 to 70 kPa in five tests, which is significantly lower than the normal condition.

In the normal force condition, the force is well distributed across the width of the elastomer, resulting in a constant pressure across the elastomer. In the shear force condition, the force is not well distributed along the length of the elastomer and the section closest to the silicon spring (point A in Figure 3) experiences a larger stress than the elastomer section farthest from the silicon spring (point B in Figure 3). This stress concentration leads to a premature delamination of the elastomer from the silicon that progresses along the length of the elastomer from point A to point B. For future designs, adhesion can be maximized by increasing the surface area of the silicon and elastomer interface and eliminating any stress concentrations.

### Stress-Strain Behavior

The ultimate strain and stress-strain behavior of the elastomer is important for understanding the mechanics of any device, especially one which may use the elastomer for mechanical energy storage or for hinges that will undergo large strains. The test structure used to determine these behaviors is shown in Figure 4. The structure has a silicon spring in series with a long elastomer spring. The tests brought the structures to failure, which was typically due to delamination of the elastomer at an average elongation of 116% over eight tests, but was twice due to failure of the elastomer spring. Elongation of both the elastomer spring and the silicon spring are used to calculate the response of the elastomer. The measured stress-strain curves of Sylgard 184 for seven separate test structures are shown in Figure 5. The initial linear region of the curve was used to calculate an average Young's modulus of 1.4 MPa for the Sylgard 184. This is in close agreement with the reported modulus for unprocessed Sylgard 184 at the macro-scale [9]. It is important to note that at strains above about 75%, the response becomes non-linear, so the measured 1.4 MPa Young's modulus is only valid below that threshold.

While the failure mechanism for most structures was delamination from the silicon surface, strains as high as about

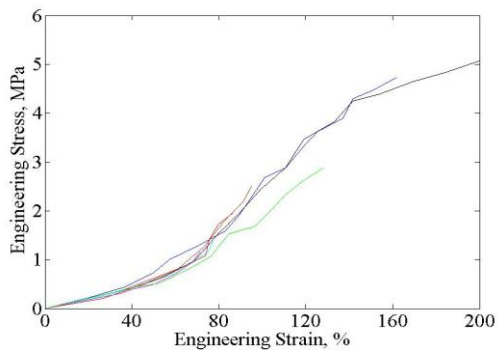


Figure 5: Eight stress-strain curves for Sylgard 184

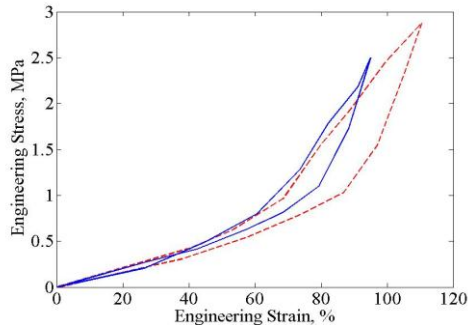


Figure 6: Two hysteresis curves for Sylgard 184

200% have been achieved, which is slightly greater than the 180% maximum strain that has been reported in literature for unprocessed Sylgard 184 [9].

### Hysteresis

Stretching and relaxing an elastomer incurs losses due to heating and friction from the rubbing of the crosslinked polymer chains as they reorganize during elongation or contraction of the bulk [10]. Two tests of the hysteresis for fabricated Sylgard 184 are shown in Figure 6. The solid blue curve had 15% energy losses in the relaxation of the Sylgard 184 and the dashed red curve had 27% energy losses in the relaxation at a higher maximum strain. These tests were performed by slowly straining and relaxing the elastomer spring, as opposed to the rapid release that will be demonstrated later. Prior work showed negligible hysteresis in unprocessed Sylgard 184 [11], so it is possible that additional process development can mitigate the energy loss.

## RESULTS

The PDMS and silicon process presented here has been used to fabricate both micromechanical thrusters and hinges. Both of these micromechanisms have enhanced performance over prior works, which are discussed.

### Micromechanical Thrusters

One application of this process is in the storage and quick release of mechanical energy in a microthruster. In prior work, Rodgers demonstrated storage and release of 19 nJ of energy in a surface micromachined device that used electrostatic comb drive actuators to store energy in bending of polysilicon flexures [6]. This device, however, could only be operated once as it used a fuse-like mechanism that had to be blown in order to release the stored energy. Bergbreiter demonstrated the storage and release of 1.2  $\mu$ J of energy in an elastomer spring with a process that used separately fabricated and manually assembled silicon and

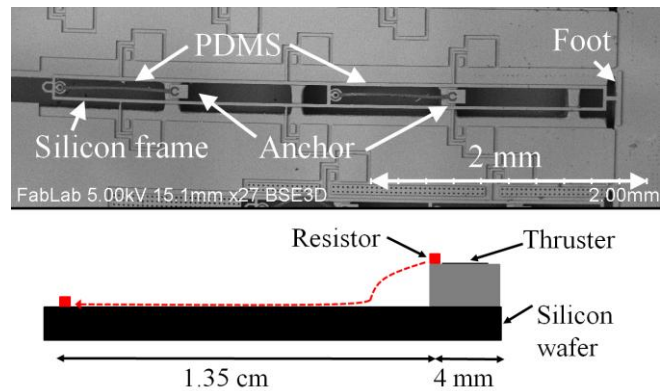


Figure 7: Micromechanical silicon and elastomer thruster and a schematic showing the thruster setup

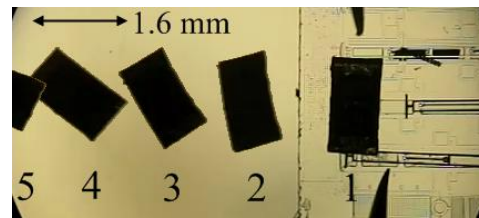


Figure 8: Superimposed screenshots of a thruster kicking a 2 mg resistor

elastomer components, resulting in a serial process [12].

In this work, a reusable monolithic thruster capable of storing and releasing 1.3  $\mu$ J to propel a 2 mg projectile 1.35 cm has been demonstrated. A full description of this device was presented in [13] and is summarized here. The thruster, shown in Figure 7, has two elastomer springs that are anchored at one end and attached to a silicon frame at the other end. The silicon frame surrounds the springs and has a foot at the front end that can be used to kick projectiles.

The fabricated thruster in Figure 7 was used to propel a 2 mg 1.6 mm by 0.8 mm by 0.45 mm surface mount resistor in order to demonstrate the quick energy release capabilities of the elastomer. A probe was used to pull the frame of the thruster back, straining the two Sylgard 184 springs. The springs were stretched about 1 mm, or to 130% strain. The energy stored in the springs was estimated at 1.3  $\mu$ J. If the hysteretic losses are conservatively estimated to be 30%, this corresponds to the release of 0.9  $\mu$ J.

The probe was then removed, releasing the frame which then kicked the resistor. Five frames from a video of the resistor moving from right to left are shown in Figure 8; 1 is at 0 ms, 2 is at 8 ms, 3 is at 12 ms, 4 is at 17 ms, and 5 is at 23 ms. The remaining trajectory of the resistor is unknown since it was outside the view of the microscope, but the resistor travelled a measured distance of 1.35 cm. The release took 5 ms, and assuming 0.9  $\mu$ J was released, the elastomer has a power output of 233 mW/mm<sup>3</sup>. The same thruster was used to propel the resistor several times, demonstrating repeatable actuation.

### Micromechanical Hinges

Microfabricated hinges and joints typically use thin polysilicon staples to hold silicon or polysilicon pins in place [14]. In this section, compliant, high yield, and robust hinges are demonstrated that integrate a silicon beam with a compliant PDMS joint, as shown in Figure 9. The hinges shown here allow for rotation both in- and out-of-plane. Silicon cantilevers are connected to the wafer substrate with small sections of elastomer.

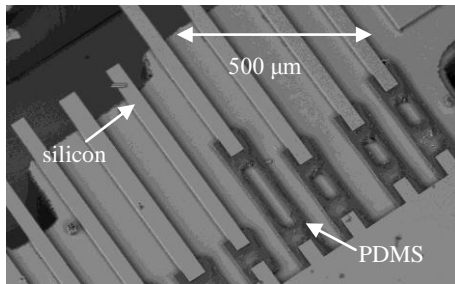


Figure 9: SEM image of silicon and PDMS hinges

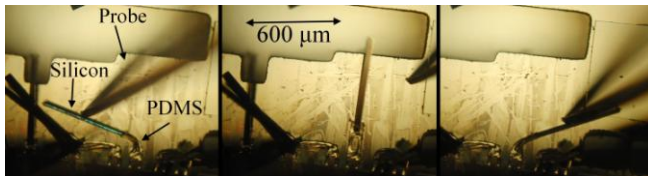


Figure 10: Manipulation of a silicon cantilever with a probe in-plane

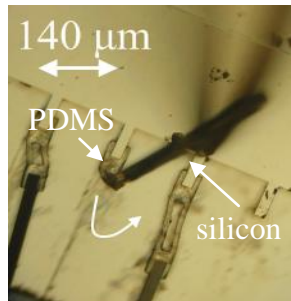


Figure 11: Manipulation of a silicon cantilever with a probe out-of-plane

A close-up SEM of several hinges is shown in Figure 9. These cantilevers can be easily rotated both in- and out-of-plane, after release, with a probe tip. Testing of manipulation in-plane is demonstrated in Figure 10 and testing out-of-plane is demonstrated in Figure 11. The cantilever is shown in three positions, pushed 90° to the left with a probe, as fabricated, and pushed 90° to the right with a probe. This cantilever was rotated in-plane 180° over 200 times and up out-of-plane 90° over 500 times with no visual signs of wear. When it was rotated side-to-side, the cantilever would also occasionally twist about 90° along its length. While these are initial demonstrations of hinges, optimized hinges can provide robust and compact replacements of polysilicon hinges.

## CONCLUSIONS AND FUTURE WORK

This paper describes the fabrication, characterization, and demonstration of monolithic PDMS and silicon micromechanisms. The mechanical properties of the post-processed elastomer were studied and a modulus of 1.4 MPa was measured. The process was demonstrated in fabrication of a micromechanical thruster that was used to store and release about 1 μJ of energy to propel a 2 mg resistor 1.35 cm, with an energy density of 233 mW/mm<sup>3</sup>. The process was also used to demonstrate compliant hinges. These hinges are an improvement over previous attempts at MEMS-fabricated hinges [14] because of their compliance and their ability to be manipulated both in- and out-of-plane.

Future work will expand this process to new materials, such as the MRTV-1 (another soft elastomer), which can withstand many hundreds of percent strain with no plastic deformation, and more rigid materials such as SU-8 or parylene. Lifetime tests need

to be performed and new elastomers still need to be characterized for further application of the process. The energy release system will also be integrated with electrostatic inchworm motors in order to demonstrate an autonomous jumping silicon chip with embedded elastomer.

## ACKNOWLEDGEMENTS

The authors gratefully acknowledge the support of the Maryland NanoCenter and its FabLab. This work was supported under DARPA YFA Grant No. HR0011-08-1-0043.

## REFERENCES

- [1] K.E. Peterson, "Silicon as a Mechanical Material," *Proceedings of the IEEE*, 70, 1982, 420-457.
- [2] J.N. Lee, C. Park, and G.M. Whitesides, "Solvent compatibility of poly(dimethylsiloxane)-based microfluidic devices," *Analytical Chemistry*, 75, 2003, 6544-6554.
- [3] D.C. Duffy, J.C. McDonald, O.J.A. Schueller, and G.M. Whitesides, "Rapid Prototyping of Microfluidic Systems in Poly(dimethylsiloxane)," *Analytical Chemistry*, 70, 1998, 4974-4984.
- [4] Y. Tung and K. Kurabayashi, "A single-layer PDMS-on-silicon hybrid microactuator with multi-axis out-of-plane motion capabilities-Part II: Fabrication and Characterization," *Journal of Microelectromechanical Systems*, 14, 2005, 558-566.
- [5] J.C. Lotters, W. Olthuis, P.H. Veltink, and P. Bergveld, "Design, realization and characterization of a symmetrical triaxial capacitive accelerometer for medical applications," *Sensors and Actuators A: Physical*, 61, 1997, 303-308.
- [6] M.S. Rodgers, J.J. Allen, K.D. Meeks, B.D. Jensen, and S.L. Miller, "A micromechanical high-density energy storage / rapid release system," *SPIE Conference on Micromachined Devices and Components V*, Santa Clara, CA: 1999, 212-222.
- [7] "SOIMUMPS," <http://www.memscap.com/>, 2008.
- [8] "Information about Dow Corning Brand Silicone Encapsulants," <http://www2.dowcorning.com/DataFiles/090007c88020bcc a.pdf>, 2010.
- [9] F. Schneider, T. Fellner, J. Wilde, and U. Wallrabe, "Mechanical properties of silicones for MEMS," *Journal of Micromechanics and Microengineering*, 18, 2008, 065008.
- [10] Y.P. Khanna, E.A. Turi, T.J. Taylor, V.V. Vickroy, and R.F. Abbott, "Dynamic mechanical relaxations in polyethylene," *Macromolecules*, 18, 1985, 1302-1309.
- [11] K.L. Mills, X. Zhu, S. Takayama, and M.D. Thouless, "The mechanical properties of a surface-modified layer on poly (dimethylsiloxane)," *Journal of materials research*, 23, 2008, 37.
- [12] S. Bergbreiter, D. Mahajan, and K.S.J. Pister, "A reusable micromechanical energy storage/quick release system with assembled elastomers," *Journal of Micromechanics and Microengineering*, 19, 2009, 055009.
- [13] A.P. Gerratt, I. Penskiy, and S. Bergbreiter, "High Power Micromechanical Thrusters with Embedded Elastomer," *Proceedings of PowerMEMS 2009*, Washington, DC, Dec. 1-4 2009.
- [14] K.S.J. Pister, M.W. Judy, and others, "Microfabricated hinges," *Sensors and Actuators A*, 33, 1992, 249-256.

## CONTACT

\*A. P. Gerratt; gerratt@umd.edu

# TIME EVOLUTION OF RELEASED HOLE ARRAYS INTO MEMBRANES VIA VACUUM SILICON MIGRATION

J Provine<sup>1\*</sup>, N. Ferralis<sup>2</sup>, A.B. Graham<sup>1</sup>, M.W. Messana<sup>1</sup>, R. Kant<sup>3</sup>, R. Maboudian<sup>2</sup>, T.W. Kenny<sup>1</sup>, R.T. Howe<sup>1</sup>  
<sup>1</sup>Stanford University, Stanford, California, USA <sup>2</sup>University of California, Berkeley, California, USA  
<sup>3</sup>University of California, San Francisco, California, USA

## ABSTRACT

This work reports on experimental evaluation of the evolution of suspended silicon hole arrays into membranes through silicon migration in an ultrahigh vacuum (UHV) environment. Multiple identical hole arrays were imaged and measured through scanning electron microscopy after different migration conditions. Many designs of hole arrays eventually progress to continuous membranes, however, despite imperceptible differences in initial geometry the intermediate steps indicate significant non-uniformity of migration. Small deviations from complete volume conservation were observed and evidence of silicon evaporation from the surface supported this volumetric change.

## INTRODUCTION

As microfabrication continues to push toward smaller and smaller dimensions, surface effects become more dominant. Cost of equipment is a limiting factor for true nanostructuring based on top-down fabrication alone. To this end, silicon migration is an attractive technique to add to the micromachining tool box because of its capability to produce three dimensional, smooth structures resulting from a surface curvature minimization method.

Silicon migration has been utilized to smooth rough surfaces [1], modify optical components [2], and create nanofluidic devices [3]. More recently, efforts on analyzing migrated silicon for controlled time steps indicate different gaseous environments affect the migration process [4]. Previous studies of silicon migration have not reported intermediate monitoring of the process, instead allowing migration to approach an asymptotic equilibrium structure. For instance, the migration of silicon trenches to form continuous membranes was reported [5].

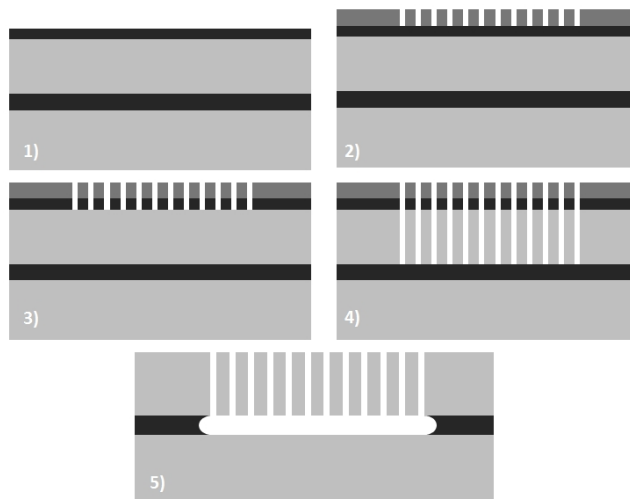
Much of the literature on silicon migration has focused on migrating a given top-down, lithographically defined feature into its final, fully curvature minimized structure. However, to fully realize the potential of silicon migration as a tunable fabrication technique, it is important to understand the progression of a structure toward the lowest curvature state via silicon migration so we can utilize the intermediate structures as well. In an attempt to study this regime, we created a large sample set of similar structures to perform a range of comparative migration experiments. We chose released uniform hole arrays as our test structure because of the ability to study migration phenomena at both large (100s of microns) and small scales (less than 1 micron) while simultaneously observing millions of identical “unit cells” undergoing identical migration treatments.

## EXPERIMENTAL SETUP

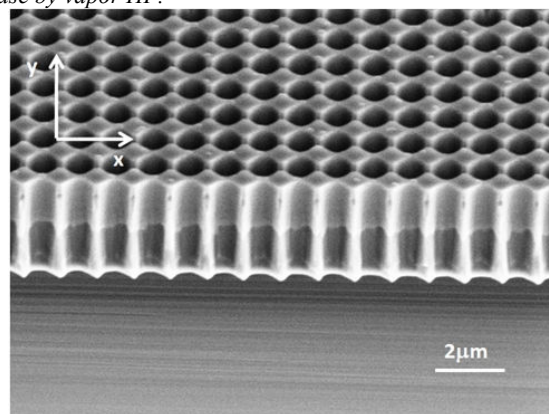
### Test Structure Preparation

Starting with an SOI with a 4 $\mu$ m thick, <100> oriented device layer, hole arrays of various dimensions were fabricated through optical lithography and RIE. A thermally grown SiO<sub>2</sub> hard mask was grown, and patterned using an ASML wafer stepper to expose the single mask layer. The oxide layer was reactively ion etched in Cl<sub>2</sub> chemistry, then the same masking layer was used to reactively ion etch the device layer silicon with a combination of HBr and Cl<sub>2</sub>. The device layer of the SOI was released by vapor HF etch of the buried oxide layer, which also served to remove the remaining

oxide hard mask. Figure 2 shows an SEM of a representative as-fabricated device.



**Figure 1:** Schematic of the process flow sample preparation. 1) Growth of thermal oxide hard mask. 2) Photolithographic patterning of hole array. 3) Pattern transfer into oxide hard mask by RIE. 4) Pattern transfer into device layer Si by RIE. 5) Device release by vapor HF.



**Figure 2:** Scanning electron micrograph of a fabricated perforated membrane with no Si migration that has been cleaved through the membrane. The sample is tilted 45° with respect to the imaging beam. For this sample the pitch is 1100nm and the diameter of the holes is 900nm. Note the slight asymmetry in x and y directions.

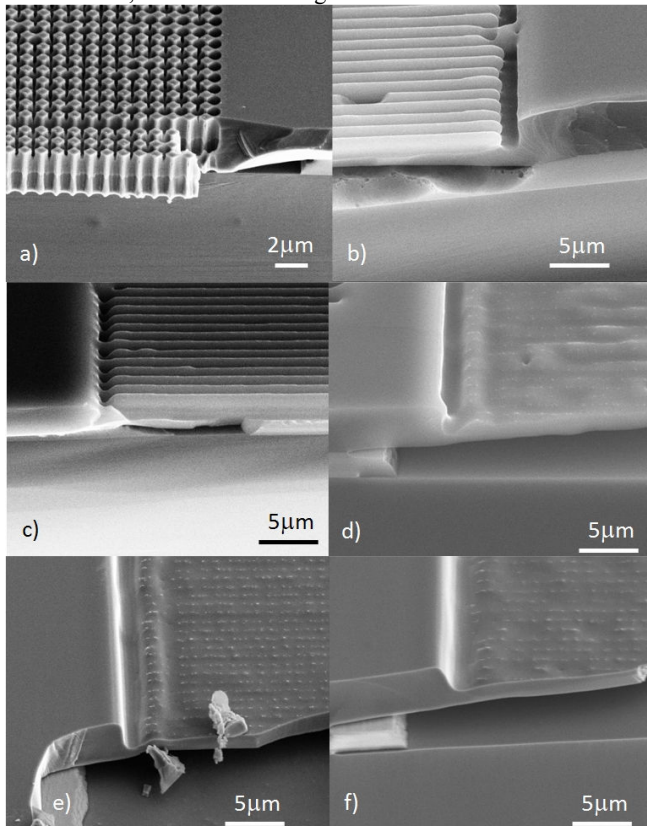
Silicon migration was performed at various temperatures and times in UHV (10<sup>-9</sup> Torr). Samples are heated by electron bombardment on the back of the sample, using a tungsten filament. Temperature is monitored using a K-type thermocouple that is placed in close proximity to the sample holder. The thermocouple is calibrated using comparative measurements performed with an optical pyrometer on a molybdenum sample. The statistical error in temperature measurements is 5°C. We report 20°C as the overall uncertainty to account for potential heater drift after several

heating cycles. The samples were cleaved through the hole arrays and imaged using a SEM to track the progress of silicon migration.

## RESULTS & DISCUSSION

### Time Evolution at a Constant Temperature

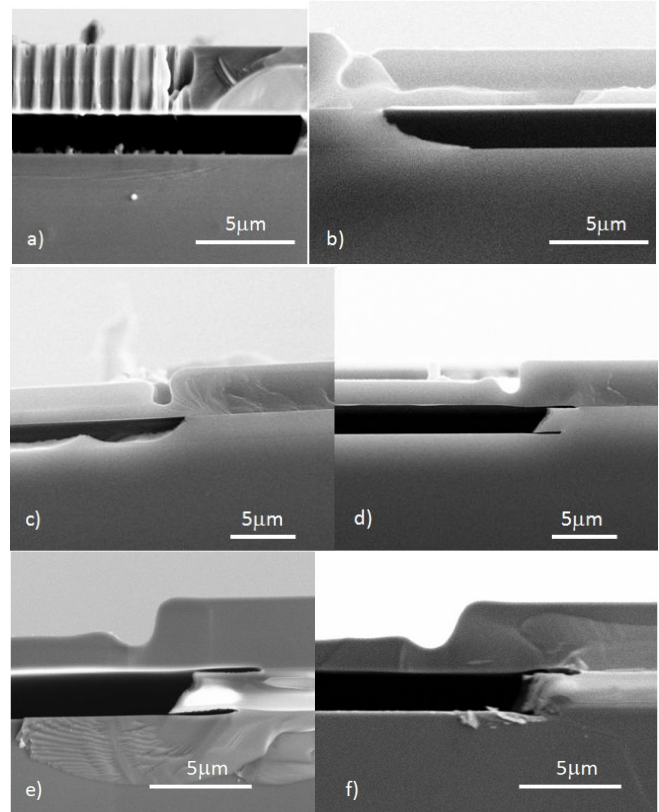
Figures 3 & 4 show the time evolution under vacuum migration of a particular hole array at an imaging angle of 45° and 90°, respectively. Because of a lithography, issue the hole array is initially non-symmetric in the x & y directions with many sharp features. This non-uniformity manifests within a few minutes of migration as the formation of ridges in the x-direction as the hole array begins to seal across the surface where the buried oxide has been removed. Initially these sharp lithographically defined features and the sharp edges from the etch hard mask are removed to produce the overall smaller curvature of the ridge system. After 16 minutes the membrane is continuous and the ridges continue to migrate into a smooth membrane. By 64 minutes the membrane has some noticeable features left from the original hole array but is otherwise an uninterrupted silicon membrane over the entire array area. The system asymptotically approaches a smooth flat membrane and the difference between 32 and 64 minutes of anneal time is small, as fine features begin to be removed.



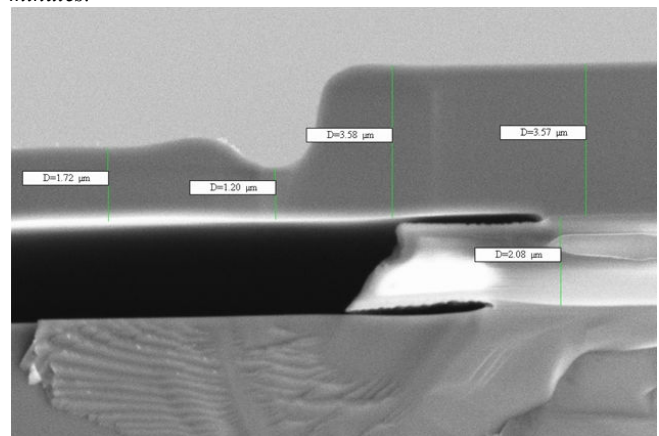
**Figure 3:** SEMs of a hole array with pitch of 1000nm and hole diameter of 800nm. The sample is a 45° angle to the imaging beam. Migration performed at 1100°C for: a) No migration; b) 4 minutes; c) 8 minutes; d) 16 minutes; e) 32 minutes; and f) 64 minutes.

A close examination of the sample without any anneal performed indicates that the sidewalls from the Si etch are not perfectly straight and thus the holes are slightly wider at the top than at the bottom. This asymmetry is a contributing factor to the membranes sealing from the bottom up. In Figure 4 the changing thickness of the membrane can be clearly observed. As the

perforated membrane migrates to a continuous membrane, we can monitor the relative thickness in comparison to the relatively unchanging thickness of the unpatterned region of the device layer.



**Figure 4:** SEMs of a hole array with pitch of 1000nm and hole diameter of 800nm. The sample is a 90° angle to the imaging beam. Migration performed at 1100°C for: a) No migration; b) 4 minutes; c) 8 minutes; d) 16 minutes; e) 32 minutes; and f) 64 minutes.



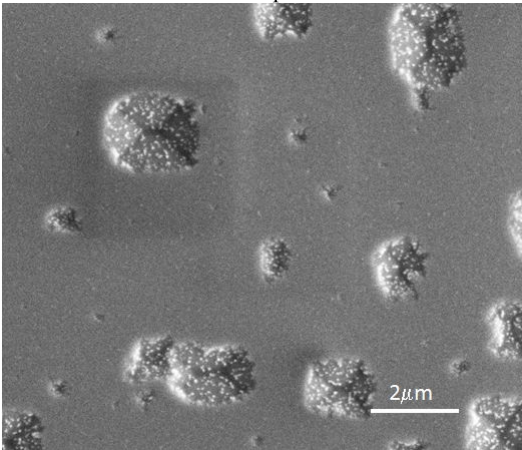
**Figure 5:** SEM with measurements of various dimensions for a sample after 64 minutes of vacuum anneal.

In Figure 5, measurements of various dimensions of continuous membrane formed after 64 minutes of vacuum anneal at 1100C are given. For a hole array with 1000nm pitch and 800nm diameter, the etched volume is  $400^2\pi/1000^2 \approx 0.50$ . The thickness of the membrane is measured as 1.72 $\mu\text{m}$ , which can be compared to the original device layer thickness (after oxide hard

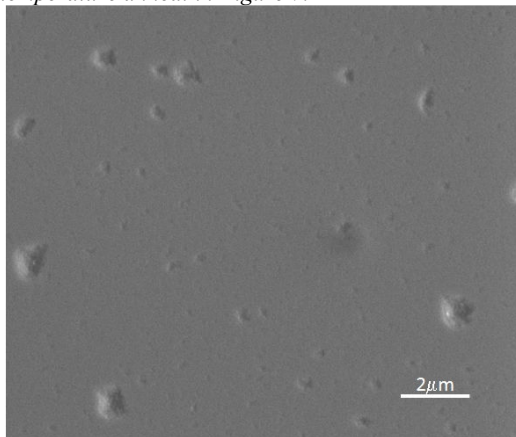
mask growth) of  $3.57\mu\text{m}$  for a final thickness that is  $\sim 0.48$  of the original thickness. This is similar but slightly smaller than the amount expected if volume is conserved in the migration.

### Silicon Evaporation

The concern about volume conservation during this process stems from previous work [6] and the authors experience with silicon evaporation at these temperatures and pressures. The evidence of evaporation is confirmed by SEM of regions separate from the hole array where pits of removed silicon are observed (Figure 6). These pits are not present in the initial wafers and present themselves as an overall “hazy” appearance after annealing at higher temperatures, in this case  $1100^\circ\text{C}$ . At these elevated temperatures and reduced pressures there are two competing surface modification processes: 1) volume conserving silicon migration and 2) volume non-conserving silicon evaporation. Some of the evaporated silicon will be redeposited on the sample substrate, but the majority will be deposited on the annealing chamber. The balance of these two competing processes must be understood for manipulation of surfaces at the nanoscale. The rate of migration is lower for a lower temperature, but the effect of evaporation is also reduced as can be seen in Figure 7 where an anneal of 64 minutes in  $1000^\circ\text{C}$  is performed.



**Figure 6:** SEM of a region of a sample distant from a hole array showing pits formed by silicon evaporation sites. This anneal was performed at  $1100^\circ\text{C}$  for 64 minutes and can be compared to the lower temperature anneal in Figure 7.

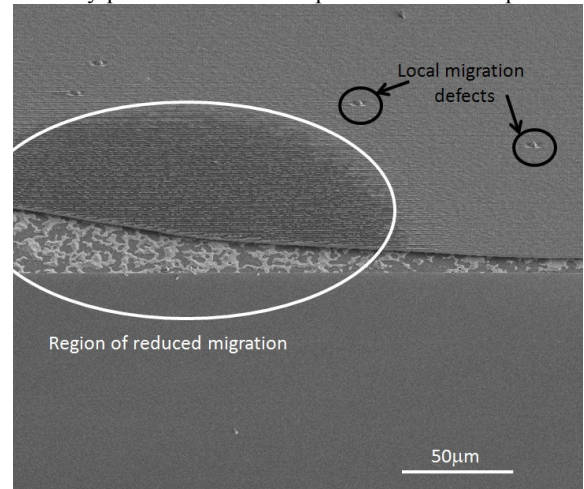


**Figure 7:** SEM of a region of a sample distant from a hole array showing pits formed by silicon evaporation sites. This anneal was performed at  $1000^\circ\text{C}$  for 64 minutes and can be compared to the higher temperature anneal in Figure 6.

### Non-uniform Migration

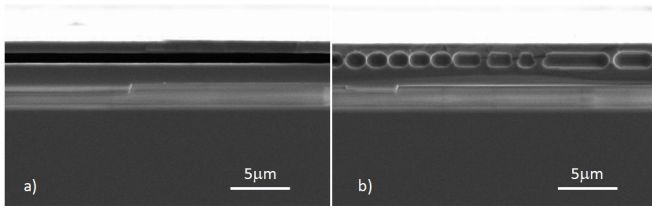
Silicon migration is thought of as an energy minimization process, and as such it has been considered as a method for nanostructuring on the large lateral scale of a chip or even wafer. When pushing structures to their asymptotic final state, this is a good supposition to employ. However, during the process of evolution through intermediate steps toward the final structure, migration between nearly identical original shapes can lead to drastically different structures. Examples of this phenomenon can be seen in Figures 8, 9, and 10.

In Figure 8, a large area where the migration rate has been slower than in the surrounding structure is shown. This is for an anneal of 96 minutes at  $1100^\circ\text{C}$  for a hole array with pitch of  $1200\text{nm}$  and diameter of  $1000\text{nm}$ . This type of non-uniformity was seen repeatedly in the hole arrays with larger feature sizes. One possible reason for this behavior is non-uniform heat conduction as these regions of lower migration rate are always at the center of the membranes where vacuum gap resulting from the released buried oxide and as opposed to the continuous solid material at the boundaries of the membranes. Also in Figure 8, there are local migration defects that can be seen. While significant care was taken with the cleanliness of these samples it is possible these defects arise from particulate contamination or as a possible by-product of silicon evaporation on the sample.



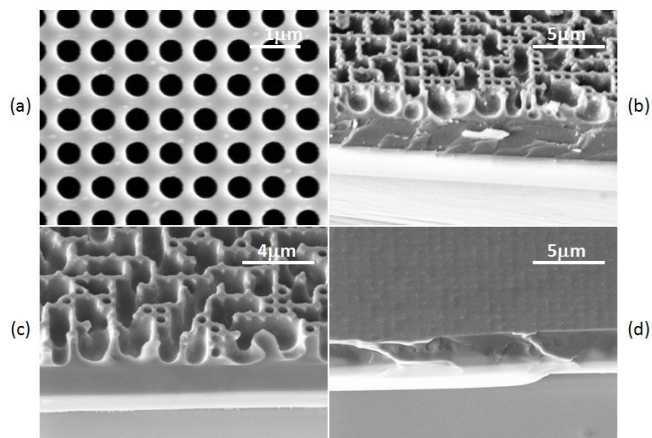
**Figure 8:** SEM showing a hole array with initial condition of  $1200\text{nm}$  pitch and  $1000\text{nm}$  diameter after 96 minutes of vacuum anneal at  $1100^\circ\text{C}$ . Both a large region of reduced migration rate at the center of the membrane and some localized migration defects are highlighted.

Figure 9 indicates another type of consistently observed non-uniformity in migration, namely incomplete membrane formation. A hole array with initial lithographically defined dimensions of a pitch of  $800\text{nm}$  and diameter  $600\text{nm}$  was not sufficiently etched to reach the buried oxide. After a vacuum anneal of  $1000^\circ\text{C}$  for 96 minutes the device layer silicon has migrated into a double layer (Figure 9a) over much of the lateral dimension of the hole array. But only a few microns away from the region of Figure 9a, this migration process is still ongoing and regions where the two silicon layers are still connected is observed (Figure 9b). Further, the number of “unit cells” joined in the migration step is non-uniform even in consecutive cells.



**Figure 9:** SEM of two neighboring regions in a membrane formed from a hole array of initial dimensions 800nm pitch and 600nm diameter. The anneal conditions were 1000 °C for 96 minutes. The double silicon layer is caused by an etch that did not penetrate to the buried oxide. The formation of the double silicon layer can be seen to be different in even neighboring cells.

Finally, Figure 10 reveals a striking case of non-uniformity that could be thought of as the combination of the phenomena shown in Figures 8 and 9. Upon observation of the original sample (Figure 10a) the hole array appears to be comprised of many identical unit cells. However, migration under different temperature and time steps produce a collection of shapes formed from highly non-uniform migration rates for neighboring unit cells. It should be noted that the mechanism for such non-uniformity is not fully understood currently. However, it is clear that in systems without perceptible non-uniformity at a given imaging scale, massive non-uniformity can arise during silicon migration.



**Figure 10:** SEMs of a hole array with 700nm pitch and 500nm diameter at various stages of migration. a) no migration, b) 32 minutes at 1100C, c) 64 minutes at 1000C, and d) 64 minutes at 1100C. At intermediate steps the progression of the migration is highly non-uniform laterally, but the final membrane is fully formed and continuous.

## CONCLUSION & FUTURE WORK

Through the production of a large sample set of similar structures, we were able to undertake a systematic evaluation of silicon migration on the micron scale. All of the hole array designs eventually migrated to form continuous membranes of solid silicon. The time evolution of the migration was observed through electron microscopy. The membranes were observed to seal first at the bottom and approach an asymptotic, smooth membrane by first reducing sharp local features that larger scale curved features.

We measured small deviations in volume of the original hole array and the final membrane. This change in volume is on the order of 2% and may fall within experimental error. An additional factor indicating non-conservation of device layer volume is the observed nanostructuring from silicon surface evaporation.

Additionally, highly non-uniform migration behavior was

observed on both a large (several 10s of microns) and small scale (less than 1 micron). The large scale difference could be attributed to deviations in temperature due to thermal conductivity. The cause of the small scale non-uniformity is more difficult to account for as systems that appear uniform at a certain imaging scale become massively non-uniform at that same scale during migration, with even neighboring unit cells deviating significantly.

Further work to understand the interaction between migration and evaporation at these pressure and temperatures will be essential to determining the long-term usefulness of silicon migration as a tunable fabrication technique. In addition, we have begun to perform surface analysis of the migrated samples to determine various material properties after migration such as crystallinity, film stress, and material composition.

## ACKNOWLEDGEMENTS

This work was supported by DARPA MTO Center on Interfacial Engineering in Microelectromechanical Systems (CIEMS) (HR 0011-06-1-0049; Dr. Dennis Polla, Program Manager).

## REFERENCES

1. T. Sato, *et al*, *Micro-structure Transformation of Silicon: A Newly Developed Transformation Technology for Patterning Silicon Surfaces using the Surface Migration of Silicon Atoms by Hydrogen Annealing*, Jpn. J. Appl. Phys. Vol 39 (2000), pp 5033-5038.
2. S. Kim, *et al*, "Interface Quality Control of Monolithic Photonic Crystals by Hydrogen Annealing," Conference on Lasers and Electro-Optics (CLEO) 2008, San Jose, CA.
3. T. A. Zangle, *et al*, "Microfluidic device with integrated nanopores for protein detection," to be presented at the 13<sup>th</sup> Int. Conf. on Miniaturized Systems for Chemistry and Life Sciences (mTAS 2009), Jeju, Korea, Nov. 1-5, 2009.
4. R. Kant, *et al*, "Micro-scale silicon migration in high temperature, low pressure, inert ambient", *Electrochemical and Solid-State Letters* 12 (2009), H437-H440.
5. R. Kant, *et al*, "Suspended microstructures made using silicon microstructures," 15<sup>th</sup> Int. Conf. on Solid-State Sensors, Actuators and Microsystems, Denver, Colorado, June 21-25, 2009.
6. L. Zhong, *et al*, "Determination of Silicon Evaporation Rate at 1200°C in Hydrogen," *Applied Physics Letter*, 67 (26), December 1995.

## CONTACT

\*J Provine, tel: +1-650-644-04-3; jprovine@stanford.edu

# VERY-HIGH-ASPECT-RATIO MICRO METAL STRUCTURES OF NON-STRAIGHT PATTERNS

Guangyi Sun<sup>1,2\*</sup>, Xin Zhao<sup>2</sup>, and Chang-Jin “CJ” Kim<sup>1</sup>

<sup>1</sup>University of California, Los Angeles (UCLA), California, U.S.A.

<sup>2</sup>Nankai University, Tianjin, China

## ABSTRACT

A fabrication of a periodic array of very-high-aspect-ratio (VHAR) freestanding micro metal structures of regular (non-straight) patterns is presented. By combining a recently reported surfactant-added TMAH process, which creates the sharp pits in non-straight line patterns on a silicon surface, with a recently developed high-yield fabrication of VHAR micro metal structures, which was enabled by the vacuum-assisted electroplating into the electrochemically etched VHAR silicon mold, a new family of metal structures, e.g., VHAR plates in a zigzag and a spiral-like pattern with an aspect ratio and height up to 60:1 and 250  $\mu\text{m}$ , respectively, have been demonstrated for the first time.

## INTRODUCTION

The fabrication of high-aspect-ratio (HAR) micro metal structures is of central interest for many applications of microelectromechanical systems (MEMS). For example, a dense array of HAR metal posts was fabricated to serve as the three dimensional (3-D) electrodes [1] for 3-D micro batteries, which produce more energy and power than what traditional two dimensional 2-D planar electrodes do on a given footprint area while sustaining high discharge rates [2]. Recently, a high yield fabrication of a dense array of very-high-aspect-ratio VHAR (higher than 10) metal posts of aspect ratio up to 85:1, freestanding 425  $\mu\text{m}$  tall, has been achieved by using improved photo-electrochemical etching of silicon and vacuum degassing-assisted electroplating [3]. However, the reported fabrication technique for VHAR metal posts in [3] is limited to either square or straight-line patterns in  $\langle 110 \rangle$  directions on a (100) silicon wafer. Any other patterns off  $\langle 110 \rangle$  (especially convex corners) suffer from being undercut during the sharp-pit etching, which is needed to initiate the photo-electrochemical etching for silicon mold fabrication. This crystal-direction-dependent undercut has been considered universal with all  $\{111\}$ -bounded wet anisotropic etching methods that use KOH or TMAH etchant. Although attempts have been made to overcome this restriction of pattern directions by creating the initial pits in an arbitrary pattern using an isotropic wet etchant (e.g., HNA) or reactive ion etching (RIE) [4, 5], the subsequent photo-electrochemical etching tended to result in branches due to the lack of sharp pits, limiting the aspect ratio far below (no report larger than 20:1) than what a photo-electrochemical etching can produce for square patterns (i.e.,  $> 100:1$ ).

In the meantime, a surfactant-added TMAH process [6, 7] has shown that the addition of small amounts of surfactant (e.g., Triton X-100 ( $\text{C}_{14}\text{H}_{22}\text{O}(\text{C}_2\text{H}_4\text{O})_n$ ,  $n=9-10$ )) in TMAH can significantly suppress the undercut in all non- $\langle 110 \rangle$  directions. Without the undercut, the modified anisotropic etchant can etch arbitrary patterns with a minimal distortion. More importantly for our interest in photo-electrochemical etching, the etched pits by this method are equally as sharp along any patterns.

We hereby propose to fabricate VHAR micro metal structures of non-straight patterns by combining the above two recently developed techniques. We will first define the initial sharp pits of arbitrary directions using the above-referenced surfactant-added TMAH solution [6, 7]. Starting from these sharp pits, we will then exercise the improved photo-electrochemical etching to produce a

VHAR silicon mold [3]. Finally, we will utilize the vacuum degassing-assisted electroplating technique [3], which produces defect-free metal fillings in VHAR trenches, to obtain VHAR micro metal structures with various shapes not bounded by silicon crystal directions.

In this paper, we present the processing steps and details for the sharp pits fabrication, photo-electrochemical etching of silicon mold, and electroplating of nickel. Although this report is not written for any specific application, an important interest of ours is fabricating high-performance electrodes for 3-D micro batteries.

## FABRICATION

The overall fabrication process for HAR and VHAR metal structures of non- $\langle 110 \rangle$  orientation is schematically shown in Figure 1. Four principal steps are involved: sharp pits formation (Figure 1 (a)), photo-electrochemical etching of silicon (Figure 1 (b)), metal filling (Figure 1 (c)), and silicon removal by  $\text{XeF}_2$  etching (Figure 1 (d)).

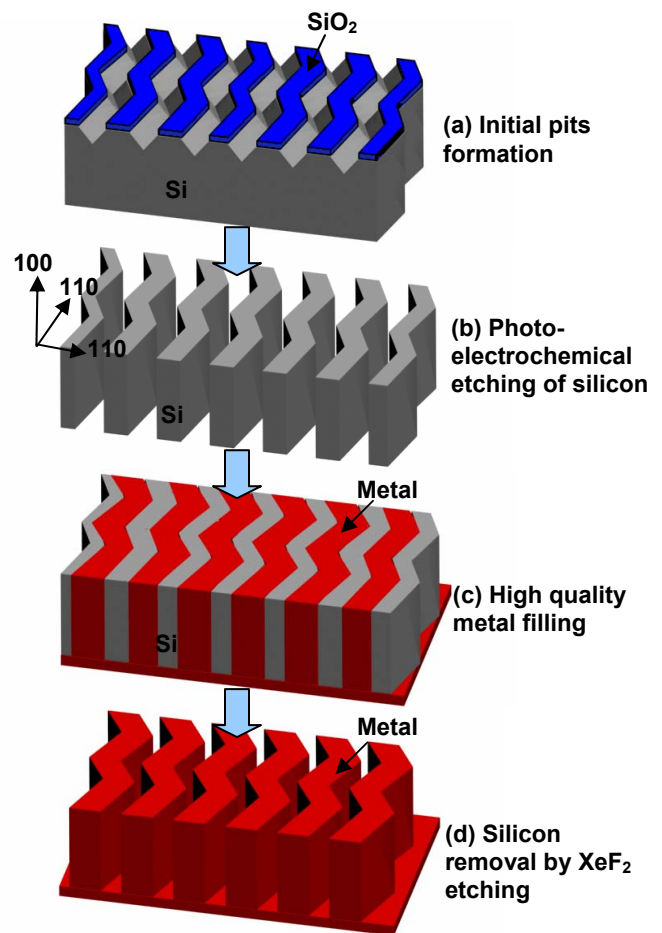


Figure 1: Fabrication procedure of VHAR micro metal structures of non-straight patterns.



The first step is to form the sharp pits on a silicon surface needed to start the subsequent photo-electrochemical etching. An N-type (100) silicon wafer with 40-60  $\Omega\cdot\text{cm}$  resistivity is used and 500 nm  $\text{SiO}_2$  is deposited on the surface by a STS Plasma Enhanced Chemical Vapor Deposition (PECVD) system. An array of various patterns with  $\sim 4$   $\mu\text{m}$  line width and  $\sim 4$   $\mu\text{m}$  spacing is then transferred to the  $\text{SiO}_2$  layer by photolithography and one 90 s dry etching by Ulvac NLD-570 glass etcher, followed by a  $\sim 20$  s BOE wet etching, serving as the etching mask in TMAH. Following the recipe for a moderate etching rate to  $\langle 100 \rangle$  and a minimal undercutting to non- $\langle 110 \rangle$  directions [6, 7], the silicon is then etched in 25 wt% TMAH in water (Sigma-Aldrich) with 0.1% v/v Triton X-100 surfactant (laboratory grade, Sigma-Aldrich) at 60  $^\circ\text{C}$  for 24 min to form the sharp pits, which will serve as the nucleation sites for the subsequent photo-electrochemical etching.

After removing the PECVD  $\text{SiO}_2$  layer in buffered oxide etchant (BOE), the silicon is etched in 4 wt% hydrofluoric acid (HF) in DI water (21 ml of 49% HF in total volume of 300 ml) at room temperature with the backside near-infrared (870 nm wavelength) illumination using a high-power light source (Marubeni America Corporation). A few droplets of a wetting agent (Kodak Foto-Flo) are added to the electrolyte to help remove the hydrogen bubbles generated during the etching, which is very important for VHAR holes etching. The etching current density and bias voltage are independently kept constant at 12  $\text{mA}/\text{cm}^2$  and 3 V, respectively. Next, the holes are opened from the backside using deep reactive ion etching (DRIE), and 2000  $\text{\AA}$  thermal  $\text{SiO}_2$  is grown to electrically isolate the silicon surface during the subsequent metallization and prevent the bulk silicon get electroplated.

Next, to seal the openings on the backside of silicon mold, a Ti/Ni (100  $\text{\AA}$ / 1000  $\text{\AA}$ ) seed layer is evaporated followed by  $\sim 50$   $\mu\text{m}$  nickel electroplating at 5  $\text{mA}/\text{cm}^2$ . This nickel layer then serves as the metal seed layer for the subsequent vacuum degassing-assisted nickel electroplating step to fill up the VHAR silicon mold. Commercially available solution (Technic, Inc.) is used for the nickel electroplating, and nickel sheet is used as the counter electrode. Eventually, the silicon mold is removed by  $\text{XeF}_2$  etching, and the VHAR micro metal structures emerge.

## EXPERIMENTAL RESULTS AND DISCUSSION

### Surfactant-added TMAH etching

Using the Triton-added TMAH etching, we have successfully obtained various patterns of pits to initiate photo-electrochemical etching. Figure 2 shows a spiral-like pattern and a zigzag. Figures 2(a) and 2(b) show the PECVD  $\text{SiO}_2$  patterns with  $\sim 4$   $\mu\text{m}$  line width on silicon surface. Figures 2(c) and 2(d) show the etched grooves (i.e., sharp pits) by using a solution of TMAH + Triton X-100. Figures 2(e) and 2(f) show the high magnification SEM images. Notably, addition of a small amount of surfactant in TMAH significantly reduced the undercutting at convex corners and non- $\langle 110 \rangle$  edges, while maintaining the bottom of the pits apparently as sharp as other wet anisotropic etchings (e.g., KOH) would generate.

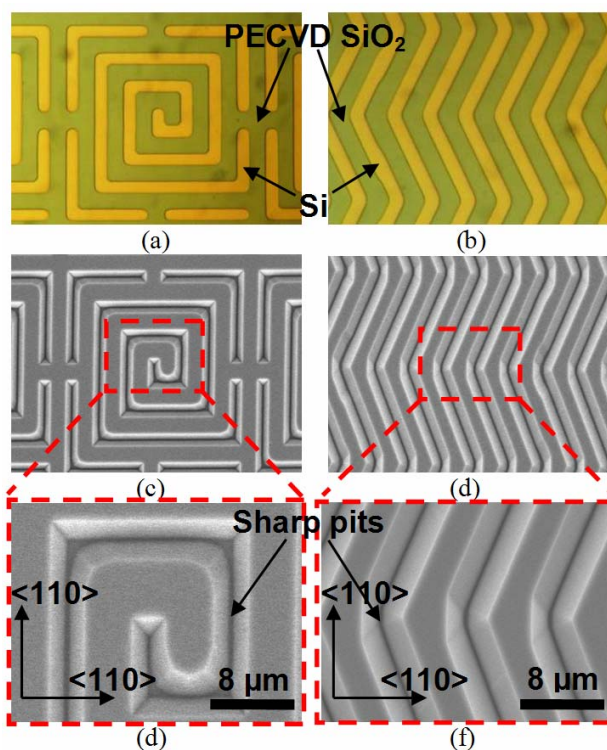


Figure 2: Fabrication of initial sharp pits for photo-electrochemical etching by using a solution of TMAH + Triton X-100. (a) and (b) PECVD  $\text{SiO}_2$  patterns before etching; (c) and (d) pits with sharp tips after etching; (e) and (f) close view of etched pits.

During the surfactant-added TMAH etching, the etching time has to be precisely controlled, as once the mask openings take the V-shape, which is bounded by  $\{111\}$  planes, the reactants start to attack more prominently on sharp convex and rounded concave corners and on the straight edges along the non- $\langle 110 \rangle$  directions. Compared with the reported patterns with several tens of microns line widths [6, 7], the patterns in our application have line width and spacing of only  $\sim 4$   $\mu\text{m}$ , demanding more precise etching control. Another noteworthy issue is that any agitation (e.g., magnetic stir or ultrasonic) during etching should be avoided, as the agitation strongly reduces the effect of surfactant.

### Photo-electrochemical etching

To fabricate VHAR silicon mold using photo-electrochemical etching, we have optimized etching parameters, including HF concentration (4 wt%), current density (12  $\text{mA}/\text{cm}^2$ ), and anodic bias voltage (3 V), succeeding in transferring the patterns of the initial pits (Figures 2(c) and 2(d)) more than 250  $\mu\text{m}$  deep in a highly anisotropic way, as shown in Figure 3, after  $\sim 5$  hours of etching. Uniformity and stability were excellent, as no apparent branching and self-stopping of pores were observed over the entire processing area (0.5  $\text{cm}^2$ ) during the etching. To our knowledge, this is the highest aspect ratio of regular (i.e., not aligned to crystal directions) patterns generated by a photo-electrochemical etching.

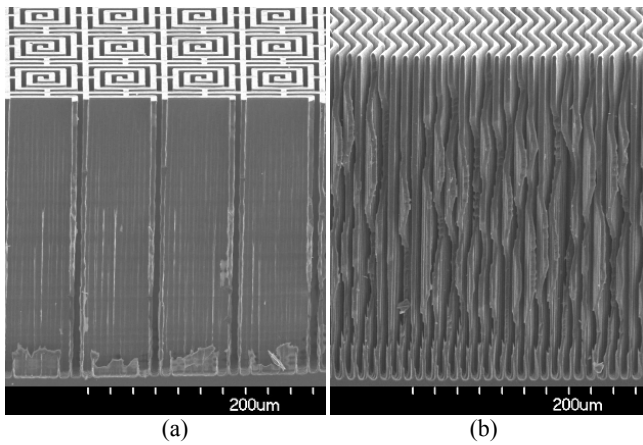


Figure 3: Photo-electrochemically etched very-high-aspect-ratio silicon mold by using TMAH + Triton X-100 etched initial pits. The side walls are straight; they appear irregular because of the way the cross section was made (physical breakage) across the patterned silicon.

#### Vacuum degassing-assisted electroplating

To fill the 250  $\mu\text{m}$ -deep and 4  $\mu\text{m}$ -wide trenches in the silicon mold shown in Figure 3, we needed to use the newly developed intermittent vacuum degassing-assisted electroplating technique [3]. Filling such a VHAR holes by electroplating without a defect throughout the height was not possible before because of the gas bubbles generated during the electroplating.

Usually, molding-based metal microstructures are fabricated by filling the voids in the silicon with electroplating. An issue is the gas trapped in the voids, which would make the resulting metal porous or even block the growth of the metal. Most known electroplating processes use a small amount of surfactant to help remove the gas bubbles in the voids. This simple method works well for relatively low aspect ratio and even HAR voids but unfortunately not for VHAR voids (e.g., 100:1). Vacuum degassing has been found to overcome the problem [3]. In [8], the air space above the electroplating bath was substantially evacuated and maintained at a pressure lower than atmospheric pressure during the electroplating. A smooth and pits-free surface has been reported on a flat surface with no holes. However, the evaporation of water was greatly accelerated due to the vacuum bath, which requires more complex feed-through control. More importantly, for electroplating of VHAR voids, this vacuum-plating method hurts rather than helps, as the vacuum makes even a small amount of gas grow to form bubbles and block the voids. In [9], on the other hand, vacuum and venting were repeated several times before electroplating started, causing the initially trapped bubbles to be drawn out from the cavities and to dislodge from the surface. However, the lack of an effective degassing technique during the electroplating has been keeping it difficult to reduce the accumulation of  $\text{H}_2$  after the plating process started. The solution was surprisingly simple for us yet effective. Unlike all other vacuum electroplating techniques, our technique [3] uses an intermittent degassing mechanism, as schematically shown in Figure 4. To remove the trapped air during the initial wetting of the mold, the pressure was lowered before electroplating started. During the electroplating, on the other hand, the tank was evacuated and vented periodically (e.g., hourly) to remove the hydrogen being accumulated.

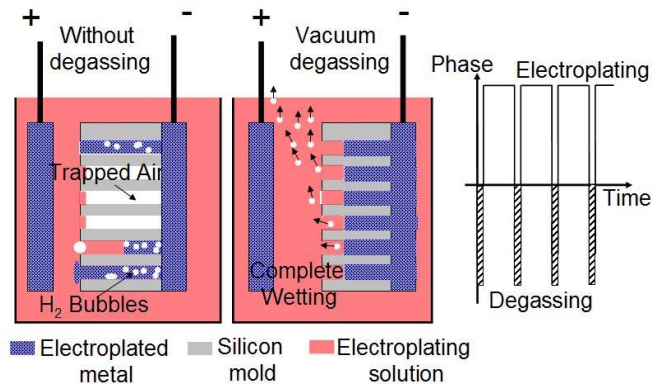


Figure 4: Schematic illustration of intermittent vacuum degassed electroplating [3].

Using the new plating technique described above, a high quality metal filling in VHAR voids in the silicon mold has been achieved. After  $\sim 8$  hours of nickel electroplating using 20  $\text{mA}/\text{cm}^2$  at a temperature of 40°C, the photo-electrochemically etched VHAR silicon molds (Figure 3) were completely filled without any defect (Figure 5).

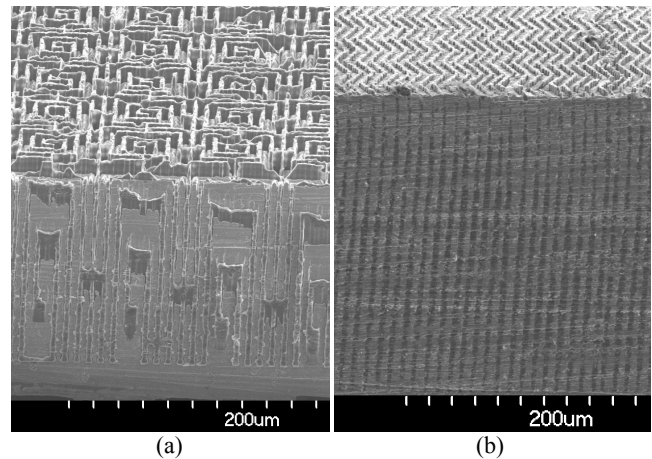


Figure 5: Very-high-aspect-ratio nickel filling inside silicon mold with vacuum degassing-assisted electroplating.

#### Freestanding micro metal structures

To obtain the freestanding micro metal structures, the silicon molds were removed by a  $\text{XeF}_2$  etching at a pressure of 3000 mTorr for  $\sim 1$  hour. Figure 6 shows the final micro metal structures in a spiral-like and a zigzag pattern with an aspect ratio and height up to 60:1 and 250  $\mu\text{m}$ , respectively. The good uniformity and mechanical stability of electroplated structures further proves the efficacy of the intermittent vacuum degassing-assisted electroplating technique [3].

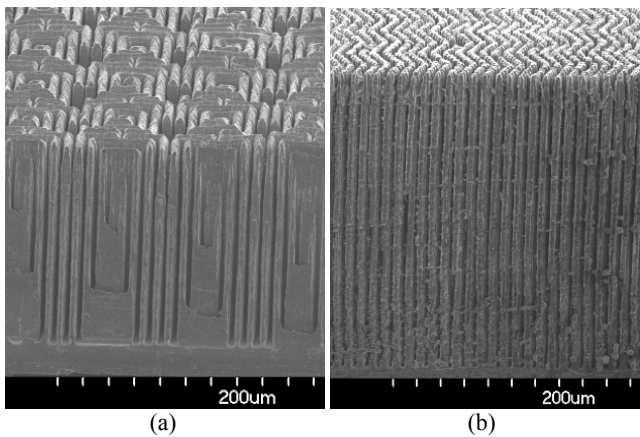


Figure 6: Very-high-aspect-ratio micro metal structures released after  $XeF_2$  etching.

## CONCLUSIONS

By combining surfactant-added TMAH etching, which generates sharp pits in non-straight line patterns, with improved photo-electrochemical etching and vacuum-degassing-assisted electroplating, a dense array of VHAR (up to 60:1) freestanding micro metal structures of regular patterns (e.g. zigzag and spiral-like pattern) has been achieved. Consequently, the restriction of pattern directions in fabricating VHAR micro metal structures has been eliminated, which would expand the versatility of photo-electrochemical etching for micromachining. For our immediate application of 3D microbatteries, we will study the pattern design, the uniformity of photo-electrochemically etched trenches over a relatively large processing area (e.g., over 2 cm by 2 cm), and mechanical stability of the metal structures.

## ACKNOWLEDGEMENTS

The authors thank Prof. K. Sato and Dr. P. Pal for many helpful suggestions on surfactant-added TMAH etching, and Prof. B. Dunn and his group for discussions on 3D battery applications. This work was supported by DARPA through Brewer Science, Inc., DARPA through Science and Technology Center iMINT, UC Discovery Grant, and Hughes Research Lab. G. Sun was partly supported by China Scholarship Council (CSC).

## REFERENCES

- [1] F. Chamran, Y. Yeh, H. Min, B. Dunn, and C.-J. Kim, "Fabrication of High-aspect-Ratio electrode arrays for three-dimensional microbatteries," *J. Microelectromech. Syst.*, vol. 16, 2007, pp. 844-852
- [2] J. W. Long, B. Dunn, D. Rolison, and H. White, "Three-dimensional battery architectures," *Chem. Rev.*, vol. 104, 2004, pp. 4463-4492
- [3] G. Sun, J. Hur, X. Zhao, and C.-J. Kim, "High yield dense array of very-high-aspect-ratio micro metal posts by photo-electrochemical etching of silicon and electroplating with vacuum degassing," *Proc. IEEE Int. Conf. MEMS*, Jan. 2010, Hong Kong, China, pp. 340-343
- [4] G. Barillaro, P. Bruschi, A. Diligenti, and A. Nannini, "Fabrication of regular silicon microstructures by photo-electrochemical etching of silicon," *Phys. Stat. Sol. C*, vol. 2, 2005, pp. 3198-3202

- [5] K. Grigoras, A. J. Niskanen and S. Franssila, "Plasma etched initial pits for electrochemically etched macroporous silicon structures," *J. Micromech. Microeng.*, vol. 11, 2001, pp. 371-375
- [6] P. Pal and K. Sato, "Various shapes of silicon freestanding microfluidic channels and microstructures in one-step lithography," *J. Micromech. Microeng.*, vol. 19, 2009, 055003 (11 pp)
- [7] P. Pal and K. Sato, "Complex three-dimensional structures in  $Si\{100\}$  using wet bulk micromachining," *J. Micromech. Microeng.*, vol. 19, 2009, 105008 (9 pp)
- [8] Apparatus for electroplating metal, U.S. Pat. No. 2,465,747, April 30, 1945
- [9] Removing bubbles from small cavities, U.S. Pat. No. 5,368,634, November 29, 1994

## CONTACT

\*G. Sun, tel: +1-310-825-3977; guangyi@ucla.edu

# 100 NM THICK ALUMINUM NITRIDE BASED PIEZOELECTRIC NANO SWITCHES EXHIBITING 1 MV THRESHOLD VOLTAGE VIA BODY-BIASING

Nipun Sinha<sup>1\*</sup>, Zhijun Guo<sup>1</sup>, Valery V. Felmetzger<sup>2</sup> and Gianluca Piazza<sup>1</sup>

<sup>1</sup>University of Pennsylvania, Philadelphia, Pennsylvania, USA

<sup>2</sup>Tegal Corporation, San Jose, California, USA

## ABSTRACT

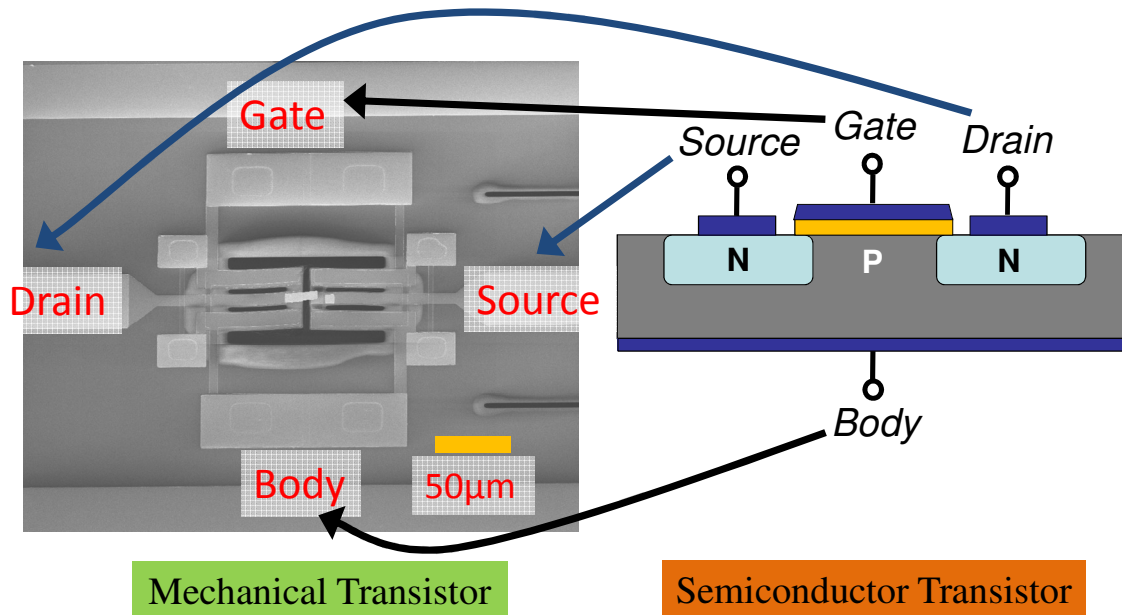
This paper reports on the first demonstration of aluminum nitride (AlN) piezoelectric logic switches that were fabricated with ultra-thin (100nm) AlN films and exhibit a 1 mV threshold voltage via the body-biasing scheme. The application of a relatively low (< 6 V) fixed potential to the body terminal of a 4-terminal switch has resulted in a repeatable threshold voltage of 1 mV. The nano-switch has been cycled to > 10<sup>9</sup> cycles and, although the contact resistance was found to be high (~ 1 MΩ), the nano-films have functioned throughout to show high piezoelectric nano-film reliability.

## INTRODUCTION

With the continuous scaling of the transistor the CMOS industry has recognized the emergence of some key problems that are proving to be serious obstacles to further miniaturization. Some of the major hurdles that need to be overcome involve the source-to-drain leakage in the standby state, the gate leakage because of ultra-thin dielectric layers, the inability to reduce operating power, the variation of threshold voltages over a wafer and the increasing effect of parasitics on the device performance. With miniaturization, transistors have become faster, but the gain in speed has come at a penalty in terms of standby power consumption. Also, with the CMOS transistors already switching in less than few nanoseconds, power is becoming a more relevant aspect to consider than speed. Keeping all these factors in mind the International Technology Roadmap for Semiconductors

(ITRS) [1] has emphasized the need to develop alternate devices, like NEMS switches, that will consume less power in the standby state and will help in minimizing the transistor operating voltages.

Mechanical switches have been a topic of research and investment for few decades. They have nearly zero standby leakage due to the presence of an air gap between the source and the drain terminals. In addition, they are characterized by a very sharp transition between their standby and on states. This transition is not governed, as in a semiconductor, by the modulation of carriers in the channel, but by the actual mating of contacts due to mechanical motion. Therefore, mechanical switches exhibit a subthreshold slope that is orders of magnitude lower than that of CMOS devices. Because of these characteristics they are the ideal candidate to lower power consumption in the standby state and operating voltages. Most of the mechanical switches developed to date have utilized electrostatic [2-3], magnetic [4], thermal [5] or piezoelectric [6-9] actuation mechanisms. These mechanical switches have not been commercialized on a large scale as they are not as reliable and as fast as the semiconductor transistors. Micromechanical switch reliability has been limited by the very stringent requirements on the on-resistance as dictated by radio frequency (RF) applications (*i.e.* few Ohm of contact resistance), which have so far been the most attractive for microswitches. When we consider the same devices for implementation of mechanical computing/logic, the main design challenge resides not in the loss due to the contact resistance but the speed of operation. According to these new guidelines a mechanical switch can operate with contact

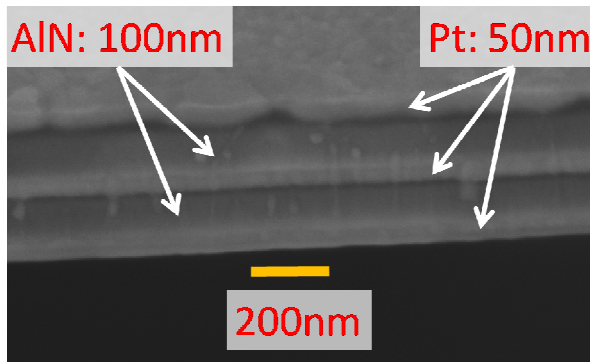


**Figure 1:** SEM of a nano-film based three-finger dual-beam AlN switch illustrating the source, drain, gate and body bias terminals. This nano-switch is being termed as a Mechanical Transistor. The figure above also shows its similarity with a Semiconductor Transistor shown on the right of the figure.

resistances in excess of 10 k $\Omega$ , therefore significantly relaxing the reliability challenges that exist with hot switching of large currents. Nonetheless, significant issues arise in the miniaturization of the mechanical switches to achieve higher frequencies of operation (approaching 100s of MHz).

For these reasons, there has been a renewed interest in the development of fast electrostatic [10-12] and piezoelectric [9, 13-14] nano switches. These implementations have utilized the concept of a 4-terminal device for tuning the threshold voltage of the switch and reducing the dynamic power consumption. Figure 1 shows an SEM of a piezoelectric nano-switch and highlights its similarity with a 4-terminal MOSFET. Though electrostatic actuation has been the most common method of implementing mechanical switches, we have used piezoelectric actuation as it is linear and can easily produce a pull-off force. Amongst the various piezoelectric materials being commonly used for research, Lead Zirconate Titanate (PZT) and AlN have already been employed for fabricating mechanical switches [6-9]. Nonetheless, PZT has the drawback that it is incompatible with present day CMOS foundries. AlN, on the other hand, is post-CMOS compatible, has higher dielectric strength, is amenable to scaling to the nano-dimensions [15] and is easy to process. AlN MEMS switches have already been used to demonstrate logic elements like NOT [13], NAND and NOR [14] gates and prove the concept of body biasing in 4-terminal piezoelectric devices.

The mechanical switches presented in this work have structural AlN layers that have been scaled in thickness to 100 nm, exhibit a low subthreshold slope ( $\sim 0.033$  mV/dec) and the ability to operate at lower supply voltages than CMOS. The use of low supply voltages translates in greatly reduced power consumption with energy per operation in the order of few tens of aJ. The AlN film is an order of magnitude thinner than the films used for making switches in [13], operate with lower body-biasing voltages (6 vs. 20 V), and especially are capable of a threshold voltage of 1 mV (w.r.t. to 30 mV in [13]). The demonstration of these nano-switches represents a significant step forward towards the implementation of ultra-low active power mechanical computing.



**Figure 2:** The zoomed-in SEM of the cross-section of the nano-actuator shows the AlN nano-films (100nm thick) and the sandwiching Pt films (50 nm thick).

### NANO-SWITCH AND BODY BIASING

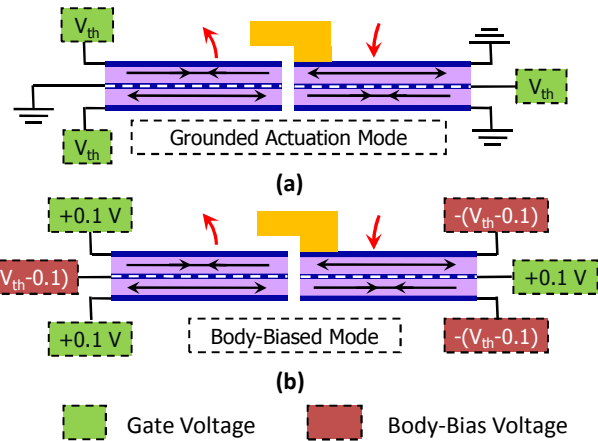
The piezoelectric switch shown in Fig. 1 is a miniaturized version of the switch implemented earlier in [7, 13-14]. It is a three-finger dual beam switch that has been fabricated using two layers of 100 nm thick AlN sandwiched by three layers of 50 nm thick Platinum (Pt) (Fig. 2). The AlN nano-films have been deposited by Tegal Corporation, CA. The authors, in collaboration

with Tegal Corp have already demonstrated that the piezoelectric properties of 100 nm AlN nano-films are comparable to those of thicker AlN films. [15].

The switches presented in this work have been fabricated using an 8-mask process on silicon wafers that is based on the same steps presented in [14].

In this work, the scaling of the AlN films and the consequently improved control over the actuation voltage has enabled us to demonstrate a decrease in the threshold voltage of the switches. This threshold voltage control has been achieved by employing the body-biasing method [13-14]. Figure 3 explains how the body biasing scheme can be used for accurate control of the threshold voltage. In Fig. 3(a), the commonly used grounded actuation mode (body terminal grounded) is shown. In this mode the  $V_{th}$  and the Ground are able to generate the electric field desired for actuation in the piezoelectric film. This same electric field (as shown in Fig. 3(b)) can be obtained by fixing a bias voltage on the set of electrodes that are grounded in Fig. 3(a). By introducing this body-bias the required electric field for actuating the switch is achieved by applying a gate voltage of just +100 mV on the set of electrodes that required a gate voltage of  $V_{th}$  in Fig. 3(a). In this example, the threshold voltage was selected to be 100 mV, but can be adjusted to any arbitrary value by controlling the value of the body-bias, as shown in [13-14].

In this work,  $V_{th}$  was controlled to be 1 mV. Achievement of a 1 mV threshold voltage is greatly attributed to the scaling of the film thickness and the subsequent decrease in the required body-bias voltage. Switches fabricated with 100 nm AlN films need a body bias  $\leq 6$ V whereas the devices made with 1  $\mu$ m AlN needed a bias of  $\leq 20$ V [13] for low threshold voltage actuation. In this specific demonstration, the change in electric field caused by 1 mV is  $\sim 30$  times higher for the 100 nm AlN film based switches than for the switches that use the thicker 1  $\mu$ m AlN [13]. The higher sensitivity of electric field to voltage variations is enabled by the scaling of the film thickness, which simultaneously help in reducing the body bias voltage and increase the degree of control over actuation.



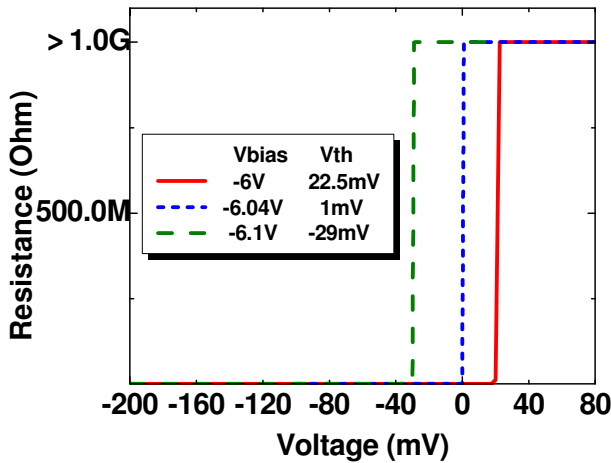
**Figure 3:** Schematic representation of (a) grounded actuation mode and (b) body-biased actuation mode.

### EXPERIMENTAL RESULTS

The device threshold voltage was measured by monitoring the change in contact resistance while varying the gate voltage. An Agilent E3631A DC power supply was used to apply the body-bias voltage. An Agilent 34401A multi-meter and an Agilent 33250A function generator were both controlled using LabView to step

through different voltages so as to study the variation of contact resistance with respect to gate voltage and applied body-bias.

Figure 4 shows the variation of the  $V_{th}$  achieved by changing the body-bias. The plot shows that a threshold voltage of 1 mV has been measured. Switching occurred when the contact resistance suddenly increased to a value that was out of the range of measurement of the multi-meter. The open state value was assumed to be greater than 1 G $\Omega$  according to the specifications of the available multi-meter. From the same experiment, a value of  $< 0.033$  mV/dec can be estimated for the subthreshold slope. This extracted subthreshold slope is comparable to those measured on similar micromechanical switches. The variation of the threshold voltage displayed in Fig. 4 is the first experimental validation that body-biasing functions, as expected, in AlN nano-films.

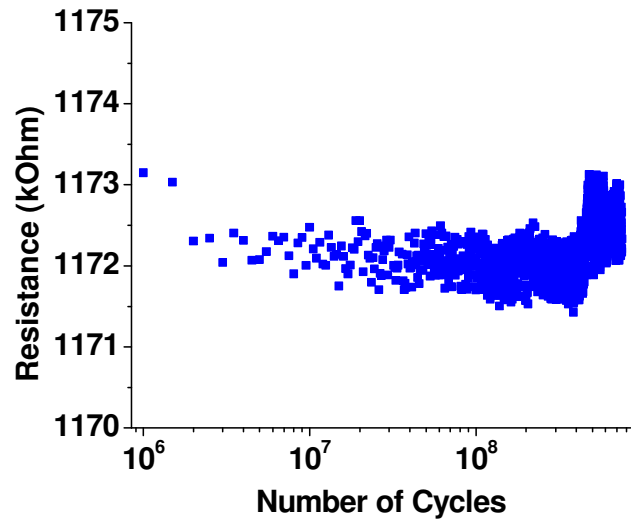


**Figure 4:** The ability to use body-biasing to shift the threshold voltage is demonstrated. 1 mV threshold was measured by stepping through the applied gate voltage at 0.1mV steps.

These nano-film based switches can be actuated with voltages much lower than the breakdown value of the film, which was found to be  $\sim 12$  V. The use of voltages lower than the breakdown is associated with low leakage currents flowing from the gate to the body terminal and assures that low standby power consumption can be attained via the body-biasing technique.

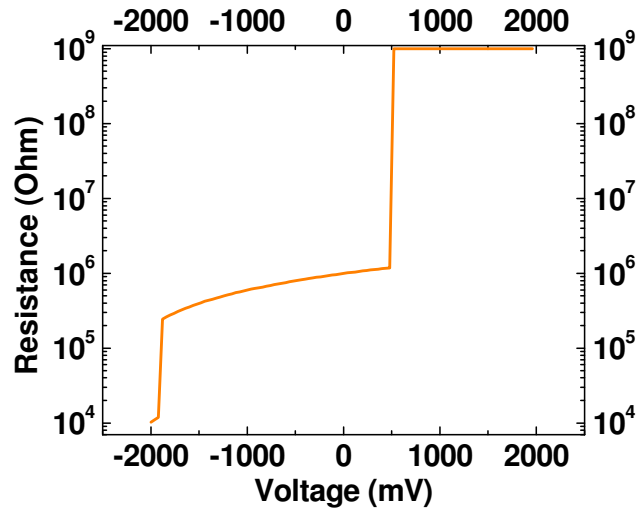
These switches exhibit a contact resistance ( $\sim 1$  M $\Omega$ ) higher than usually expected for metal contact switches [2-8] (Fig. 5). The possible reasons for this high contact resistance are the low force at the contact and the presence of Titanium Oxide (TiO<sub>2</sub>) at the interface. This layer of TiO<sub>2</sub> could have formed by oxidation of the Ti adhesion layer used during the Pt deposition. Figure 6 highlights how the contact resistance varies when the gate voltage is stepped from  $-2$  V to  $+2$  V, *i.e.* when the contact force is varied. From these results it is evident that the resistance is a strong function of the applied force. The contact force is the highest at the beginning of the sweep where the resistance is  $\sim 10$  k $\Omega$ . As the voltage is increased the contact force decreases and there is a sudden increase in contact resistance to  $\sim 200$  k $\Omega$ . The exact phenomenon for this sudden increase in resistance is not known, but it can be likely attributed to the partial breaking of contact bonds between the two mating surfaces. As the voltage is further increased, the resistance rises up to a value of  $\sim 1$  M $\Omega$ . Past 0.52 V the switch completely breaks contact and an open is recorded.

The low subthreshold slope permits operating the switch with very low supply voltages and effectively take advantage of the



**Figure 5:** Experimental results for the reliability testing of the AlN nano-switch up to 750 million cycles. The device has been tested up to 1 billion cycles before if failed closed. The device was tested at a speed of 500 kHz with a body bias of 4.6 V and a square wave of  $\pm 2$  V.

repeatable 1 mV  $V_{th}$  demonstrated with these nanoscaled devices. The high value of the recorded contact resistance ( $\sim 1$  M $\Omega$ ), though, constitute a possible limitation on the maximum frequency of operation of these devices because of both noise and electrical time constant considerations. The use of other contact pairs with different adhesion energies that will provide for values of contact resistance of few 10s of k $\Omega$  are under investigation.



**Figure 6:** Plot of a single voltage sweep, showing the variation of contact resistance as a function of the gate voltage. The contact resistance is a strong function of the applied force.

The nano-switch was also subjected to reliability testing to study the effect of fast and long term cycling on the Pt-Ti-Pt contact and the nano-piezoelectric film. The resonance frequency of the actuator beam was derived to be  $\sim 110$  kHz by means of finite element analysis in COMSOL Multiphysics. For the purpose of rapidly testing for a large number of cycles the beams were

actuated above their resonance frequency, but far from any higher order modes. This was done to minimize the cross-coupling between the intended mode of actuation and other higher order modes of vibration.

Figure 5 shows the results of reliability testing of the switch operated at 500 kHz with a body-bias of 4.6 V and a square wave form of  $\pm 2$  V up to 750 million cycles. Cumulatively, the switch was tested for  $>10^9$  cycles after which it failed in the closed position. This data shows that the piezoelectric nano-film functioned throughout the testing demonstrating very high nano-film reliability. Contact reliability greater than  $10^9$  cycles will have to be demonstrated. Investigations on the contact wearing and its tribological properties are ongoing.

## CONCLUSIONS

In summary, the first AlN piezoelectric switches that employ 100 nm thick AlN films have been demonstrated. These switches validate the use of the body-biasing technique at the nano-scale. As the thickness of the films has been scaled to the nano-dimensions the body bias voltages have been lowered to  $<6$  V and a better control over the actuator motion has been demonstrated. This enhanced control over switching translates into a threshold voltage of  $\sim 1$  mV and the ability to potentially operate with supply voltages of few 10s of mV. Such supply scaling translates in several orders of magnitude reduction in active power consumption. Further scaling of these devices in the lateral dimensions will lead to the development of nanomechanical logic elements that have very low capacitance and reliably operate with extremely low supply voltages.

## ACKNOWLEDGEMENTS

This work was supported by the DARPA NEMS program. The authors would like to acknowledge the help of the staff of the Wolf Nanofabrication Facility at the University of Pennsylvania and the PRISM Micro/Nano Fabrication Laboratory at Princeton University. The authors would also like to thank Mr. T. S. Jones for his help with LabView programming.

## REFERENCES

- [1] International Technology Roadmap for Semiconductors 2007 Edition, Austin, TX, Sematech.
- [2] P. M. Zavracky, S. Majumder and N. E. McGruer, "Micromechanical switches fabricated using nickel surface micromachining," *Jour. of MEMS*, vol.6, no.1, pp.3-9, Mar 1997.
- [3] C. Bozler, R. Drangmeister, S. Duffy, M. Gouker, J. Knecht, L. Kushner, R. Parr, S. Rabe, and L. Travis, "MEMS microswitch arrays for reconfigurable distributed microwave components", *IEEE MTT-S International Microwave Symposium Digest*, Boston, MA (June 2000), pp. 153–156.
- [4] M. Ruan, J. Shen, and C. B. Wheeler, "Latching Micromagnetic Relays", *Journal of MEMS*, 10/2001, pp. 511–517.
- [5] R. D. Streeter, C. A. Hall, R. Wood, and R. Madadevan, "VHF high-power tunable RF bandpass filter using microelectromechanical (MEM) microrelays", *Int. J. RF Microwave CAE*, 11/5/2001, pp. 261–275.
- [6] R. Mahameed, N. Sinha, M. B. Pisani, and G. Piazza, "Dual Beam Actuation of Piezoelectric AlN RF MEMS Switches Monolithically Integrated with AlN Contour-mode Resonators," *Journal of Micromech. Microeng.* 18, 105011, 2008.
- [7] N. Sinha, R. Mahameed, C. Zuo, G. Piazza, "Integration of AlN micromechanical contour-mode technology filters with

three-finger dual beam AlN MEMS switches," *Frequency Control Symposium, 2009 Joint with the 22nd European Frequency and Time forum. IEEE International*, pp.1-4, 20-24 April 2009.

- [8] H. C. Lee, J. H. Park, J. Y. Park, H. J. Nam and J. U. Bu "Design, fabrication and RF performances of two different types of piezoelectrically actuated Ohmic MEMS switches", *Journal of Micromech. Microeng.*, 15(2004), pp. 2098-2104.
- [9] D. C. Judy, J.S. Pulskamp, R. G. Polcawich and L. Curran, "Piezoelectric Nanoswitch" 22<sup>nd</sup> IEEE International Conference on Micro Electro Mechanical Systems, 2009, pp.591-594, 25-29 Jan. 2009.
- [10] R. Nathanael, V. Pott, H. Kam, J. Jeon, and T.-J. King Liu, "4-terminal relay technology for complementary logic," in *IEDM Tech. Dig.*, 2009, pp 223-226.
- [11] H. Kam, V. Pott, R. Nathanael, J. Jeon, E. Alon, and T.-J. King Liu, "Design and reliability of a micro-relay technology for zero-standby-power digital logic applications," in *IEDM Tech. Dig.*, 2009, pp. 809–812.
- [12] H-H Yang, J. O. Lee and J-B Yoon, "Maneuvering Pull-in Voltage of an Electrostatic Micro-switch by Introducing a Pre-charged Electrode," *IEEE IEDM 2007*, Washington DC, USA, pp. 439-442.
- [13] N. Sinha, T. S. Jones, Z. Guo and G. Piazza, "Body-Biased Complementary Logic Implemented Using AlN Piezoelectric MEMS Switches", *2009 IEEE International Electron Devices Meeting (IEDM 2009)*, Baltimore, MD, USA, December 2009, pp. 813-816.
- [14] N. Sinha, T. S. Jones, Z. Guo and G. Piazza, "Demonstration of Low Voltage and Functionally Complete Logic Operations Using Body-Biased Complimentary and Ultra-Thin AlN Piezoelectric Mechanical Switches," *The 23rd IEEE Conference on Micro Electro Mechanical Systems (MEMS 2010)*, Hong Kong, January 2010, pp. 751-754.
- [15] N. Sinha, G. E. Wabiszewski, R. Mahameed, V. V. Felmetzger, S. M. Tanner, R. W. Carpick, and G. Piazza, "Piezoelectric Aluminum Nitride Nanoelectromechanical Actuators," *Appl. Phys. Lett.* 95, 053106 (2009).

## CONTACT

\*Nipun Sinha, tel: +1-215-573-3276; nipun@seas.upenn.edu

# A PLANAR, INTEGRATED TOTAL INTERNAL REFLECTION SENSOR FOR BIOFOULING DETECTION

K. H. Nam<sup>1,2\*</sup>, W. Choi<sup>3</sup>, J. Yeo<sup>4</sup>, S. H. Ko<sup>4</sup> and Liwei Lin<sup>1</sup>

<sup>1</sup>Berkeley Sensor and Actuator Center, University of California, Berkeley, CA USA

<sup>2</sup> Research Center of MEMS Space Telescope, Ewha Womans University, Korea

<sup>3</sup>LG Innotek, Inc., Korea

<sup>4</sup>Department of Mechanical Engineering, Korea Advanced Institute of Science and Technology, Korea

## ABSTRACT

A planar, integrated total internal reflection (TIR) sensor for the characterizations of biofouling has been demonstrated based on angular interrogation of Fraunhofer diffraction. This sensor is made of a two-mask process to have optical prism and built-in waveguides of  $4 \times 0.25 \mu\text{m}^2$  in cross section area. The core and cladding layer of the waveguide are made of silicon nitride and silicon dioxide, respectively and a 780nm in wavelength light source is used in the experiments. Water, ethanol, acetone and glycerol, have all been tested to illustrate the basic refractive index sensing principle of the prototype sensor. Biofouling measurements show that after been immersed into milk as the testing liquid, the surface refractive index of a prototype TIR sensor shifted continuously to as much as 0.0089 for a 9-hour test. As such, this technique could be useful to various biofouling control and monitoring applications, including water desalination, medical, marine and electronic device industries.

## INTRODUCTION

Biofouling is the result of unwanted accumulation of biological substances on surfaces which are constantly exposed in aqueous environments. These include surfaces of pipeline systems, sinks, marine equipments, and even blood vessels in human body. Substances deposited and adhered on these surfaces can form thin films composed of bacteria, algae, fungi, and inorganic matters. Leaving unattended, these biofilms can result in reduced efficiency of aquatic equipment and increased efforts in system maintenance. For example, thick biofilms are hard to remove by using common antimicrobial agents and could dramatically increase the equipment maintenance cost [1]. Today, the mechanisms and control of the biofouling process is still far from full understanding and one fundamental and practical issue is to monitor the growth of biofilms.

The current state-of-art biofouling sensors are bulky and expensive and they utilize different techniques to characterize biofouling such as fiber optics [2], light intensity [3], and bioluminescence [4]. Most of these aforementioned sensors are only operational under laboratory conditions. On the other hand, the sensing technique of total internal reflection principle such as the angular interrogation type (AIT) sensors [5] as illustrated in Figure 1(a), has been proven to be sensitive but has not been applied to the area of biofouling detection probably limited by its large size and the requirement of a rotating light source. Here we propose to use a built-in waveguide with a prism-coupler to replace the moving part of a conventional AIT sensor as shown in Figure 1(b) to take the advantage of Fraunhofer diffraction occurring at the end of the waveguide. As a result, this work presents three distinctive accomplishments for biofouling sensors: (1) microscale devices by batch manufacturing; (2) built-in waveguide coupled with prism; (3) demonstration of total internal reflection as the basic sensing principle. Because the proposed architecture is based on batch microfabrication processes for low-cost manufacturing, we believe that the proposed biofouling sensor could be applicable to various applications, including maintenance and control for water desalination and marine equipments.

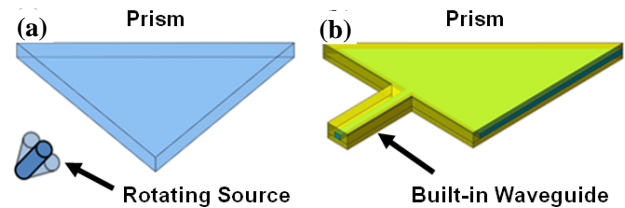


Figure 1: (a) Conventional AIT sensor (with rotating light source), (b) sensor for this work (with built-in waveguide).

## WORKING PRINCIPLE

Figure 2 illustrates the sensing principle of the proposed biofouling sensor which consists of a light source, an integrated waveguide-prism structure and a detector. The waveguide is designed to deliver light from the open-end of the waveguide to the prism-coupler and the reflected light can come out through the side-facet of the prism. The surface of the prism is exposed to the aqueous environment where biofouling occurs. Diffraction occurs at the input edge (interface of the waveguide and prism) to spread light into various directions such that the output signals at the detector side can accomplish measurements of various angles similar to the conventional angular interrogation type sensors without the need to dynamically change the light emitting angles. By observing the movement of the positions of the critical points from total internal reflection due to the formation of biofouling, the shift of refractive index of medium being sensed due to biofouling can be calculated. This design enables (1) the reduction of sensor size without moving parts, (2) the elimination of scanning time, and (3) planar integration of the whole system. Furthermore, small-size sensors further enable possible multi-point local detections for better sensing accuracy.

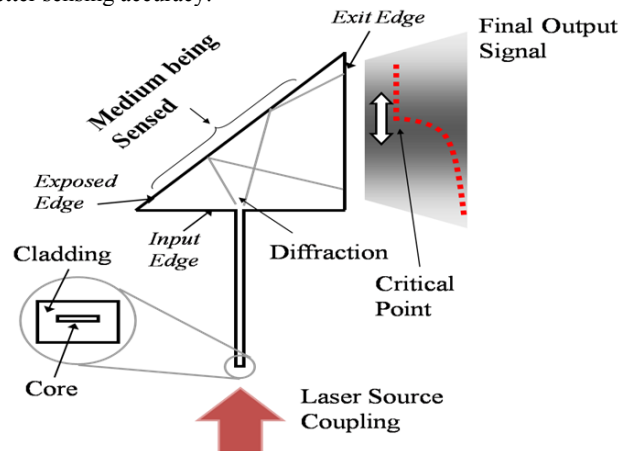


Figure 2: Sensing mechanism. Laser light source passes through the waveguide and diffraction occurs at the waveguide/prism interface. The reflection of laser light due to biofouling is detected at the output and the position of total reflection is recorded.



## THEORETICAL ANALYSIS

The output signals captured by the detector can record the position of the critical point of reflected light as shown in Figure 2, and refractive index of the media is calculated by the derivation based on Fresnel equation as expressed in Equation 1. Figure 3 illustrates the light passing paths. In this illustration,  $L$  represents the distance of total light travel from the input edge of the prism to the CCD, and  $D$  is the distance of light travel after the reflection point.  $\Delta d$  is the shift of critical point on CCD detector. The basic optical Snell's law states:

$$\theta_{critical\ point} = \sin^{-1}(n_2 / n_1), \Delta\theta = \Delta d / L \quad (1)$$

$$\Rightarrow n_{biofouling} = n_{nit} \sin(\theta_{crit\_i} + \Delta\theta)$$

where  $\theta_{crit\_i}$  and  $\Delta\theta$  are the critical angle at initial stage (without biofouling) and the total angle shift of the critical point due to biofouling during the experiment, respectively. Both  $n_{biofouling}$  and  $n_{nit}$  represents the refractive indices of biofouling surfaces and silicon nitride, respectively.

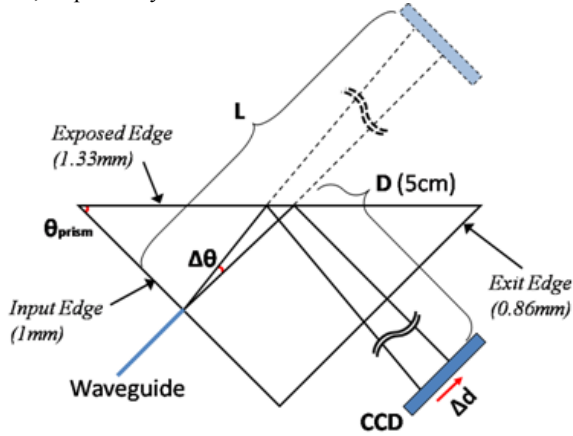


Figure 3: Schematic diagram of light paths where  $L$ ,  $D$ ,  $\Delta\theta$ , and  $\Delta d$  are total distance of light travel, distance between reflection facet of prism and CCD, total angle shift of the critical point due to biofouling, and shift of critical point on CCD, respectively.

$\theta_{prism}$  is a design parameter for the prism and it is selected such that the initial critical point will position appropriately on CCD for easy observation. For this study,  $\theta_{prism}$  was set as  $41^\circ$ , which is close to the incident light angle at total internal reflection from silicon nitride to water without biofouling at  $39.29^\circ$ .

## DESIGN AND FABRICATION

A simple two-mask fabrication process is used as illustrated in Figure 4 to make the built-in waveguide with integrated prism. A  $2.5\mu\text{m}$ -thick silicon dioxide (bottom cladding) layer and  $0.25\mu\text{m}$ -thick silicon nitride (core layer) were deposited on a silicon substrate (Fig. 4a). The body of the prism-coupler and waveguide were defined using the first mask. (Fig. 4b) Additional  $2.5\mu\text{m}$ -thick of oxide (top cladding) was deposited on top of the structure (Fig. 4c), and the final structure was defined using the second mask by RIE (reactive ion etching) to have smooth sidewall surfaces and good aspect ratio (Fig. 4d). Finally, the end of the waveguide is opened by wafer dicing and a polishing process is conducted to reduce the insertion loss of light.

Silicon nitride was used as a core layer due to its higher refractive index than that of silicon oxide. For the core layer, standard stoichiometric silicon nitride was deposited using LPCVD, and its refractive index was measured as 2.10. The cross sectional area of the waveguide is determined by optical simulation as

$4 \times 0.25\mu\text{m}^2$ . Here, we set the thickness of the core layer by using the maximum thickness for a single mode of light under the designed geometry of rectangular waveguide in this study. The cladding layer needs to be thick enough to prevent excessive propagation leakage of light into the silicon substrate. Optical simulations have been preformed and  $2.5\mu\text{m}$ -thick oxide was chosen.

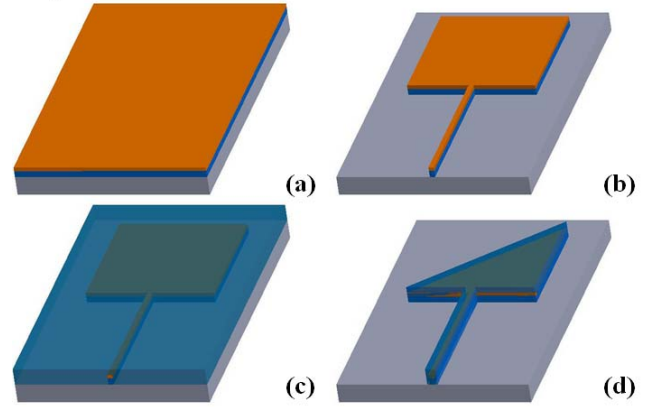


Figure 4: Microfabrication procedure: (a) silicon oxide and silicon nitride are deposited as bottom cladding and core layer of the waveguide, respectively; (b) prism-coupler body and waveguide are defined using first mask; (c) silicon oxide is deposited as a top cladding layer; (d) final structure is defined using the second mask with smooth side-wall surfaces to reduce optical noises.

Figure 5a shows a fabricated device where the cross section of the waveguide has a designed dimension of  $4 \times 0.25\mu\text{m}^2$  and the smallest prism has 1, 0.86 and 1.33mm in length for the exit, input and exposed edges (as illustrated in Fig. 3), respectively. The designed prism angle for the prism is  $41^\circ$ . Two larger sensors have also been fabricated with the same prism angle but larger edges (5 and 10 mm for the input edge, respectively) to characterize the size effects. Diffraction occurs at the end of the waveguide as shown in Figure 5b, as the result of Fraunhofer diffraction. Figure 5c shows reflected light at the interface between prism and aqueous medium.

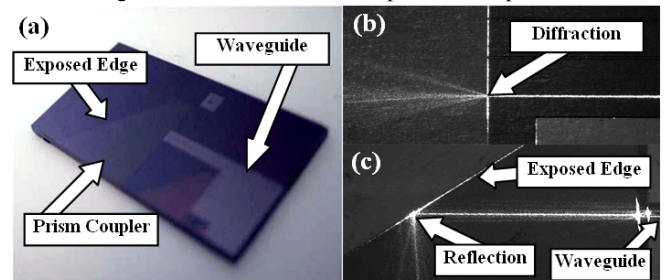


Figure 5: (a) Microscale sensors on a chip, (b) diffraction pattern from waveguide, and (c) reflection pattern.

A Polydimethylsiloxane (PDMS) channel was constructed and placed on the sensor chip as shown in Figure 6 as the interface for liquid media and the sensor in experiments. The size of the channel was determined in accordance with the viscosity of liquid media being measured to prevent leakage. For the prototype experiments, milk was used as the media and microchannel has 200 or 300 $\mu\text{m}$  in height. The height of the channel reduces as biofilms grow thicker during experiments and it is important to have enough initial height cushions to prevent the blocking of liquid supply. Furthermore, liquid media was provided with a flow rate at 0.1–0.5mL/hr to minimize the accumulation of unwanted floating substances. Table 1 summarizes the important parameters during experiments.

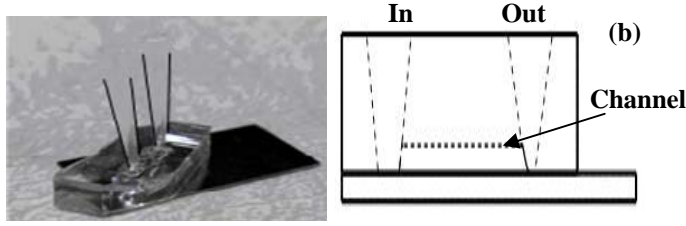


Figure 6: PDMS microchannel on a sensor chip; (a) optical microphoto; (b) cross-sectional view of the PDMS channel.

Table 1: Summary of Total Internal Reflection Sensor for Biofouling

Component	Dimension
Cladding thickness	2.5 $\mu\text{m}$
Core thickness	0.25 $\mu\text{m}$
Width of waveguide	4 $\mu\text{m}$
Input edge (3 sensors)	1, 5, and 10 mm
PDMS channel height	200 and 300 $\mu\text{m}$

## EXPERIMENTAL RESULTS AND DISCUSSIONS

### Calibration

Prototype sensors have been designed to have a critical point without biofouling at about one-eighth of peak-to-peak distance of Fraunhofer diffraction from the 0<sup>th</sup> peak. More than 50% of light intensity concentrated in the region of first one-fourth peak-to-peak Fraunhofer diffraction and that region has been selected as the main observation area. Once the sensor was tested with water, ethanol was tested and results were compared as a mean of calibration.

### Refractive Index

Direct refractive index measurements were conducted for several liquids, including water, ethanol, acetone and glycerol, to illustrate the basic sensing principle as a refractive index sensor. The measured refractive index values were in good agreement with values in literature as illustrated in Figure 7. *Reference Line* in the figure is a line which shows how far each measurement are off from the numbers in literatures. The error range of the measurements for four media with different refractive indices was less than  $\pm 0.002$  Refractive Index Unit (RIU).

### Biofouling Sensing

Biofouling changes the optical properties of biofilms. When the thickness of biofilms increases, their refractive index increases accordingly [6]. The state-of-art biofouling sensors based on optical detection have not been examining the issue of changes in refractive index of biofilms and this could be a source of measurement errors [7, 8]. Here, surface refractive index between the prism-coupler and media is measured and characterized with respect to time to monitor biofouling.

Figure 8a shows the typical output signals captured by CCD and Figure 8b is the intensity profile for the milk tests after 2, 4 and 8 hours into experiments, respectively. It is observed that the critical point gradually moved rightwards and the corresponding refractive index variations can be calculated to quantify biofouling characteristics. The captured signals are the convolution of Fresnel reflection and Fraunhofer diffraction, and Figure 8b shows this convolution on the curve of the 0<sup>th</sup> order of the diffraction pattern. For the convolution, diffraction pattern does not move, while critical point shifts along the diffraction pattern in accordance with

the change of refractive index of medium being measured. This output signals are in good agreement with theoretical derivation:

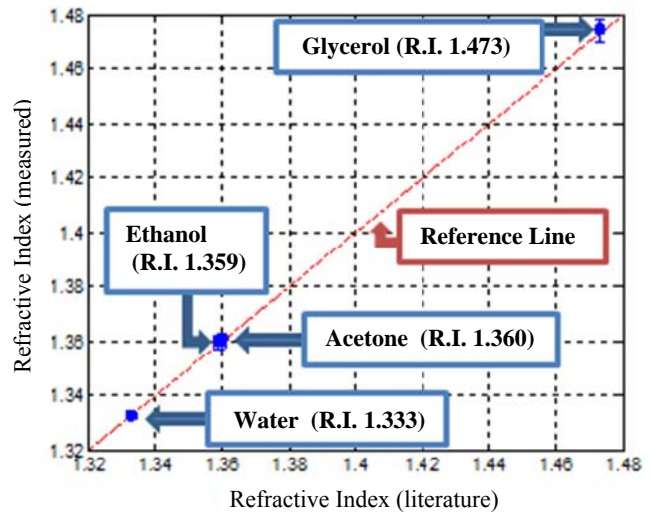


Figure 7: Experiment results for media of known refractive indices, including water, ethanol, acetone, and glycerol, with comparisons to literature values.

$$I(\theta) = I_d(\theta_d) \times R(\theta) \quad (2)$$

$$= I_0 \left[ \sin c \left( \frac{\pi d}{\lambda} \right) \right]^2 \cdot \frac{\left[ n_1 \cos(\theta) - n_2 \sqrt{1 - \left( \frac{n_1}{n_2} \sin(\theta) \right)^2} \right]^2}{\left[ n_1 \cos(\theta) + n_2 \sqrt{1 - \left( \frac{n_1}{n_2} \sin(\theta) \right)^2} \right]^2}$$

where  $I_d$  is the intensity distribution of end-waveguide diffraction, and  $R$  is the reflectance at the facet of prism-coupler.  $\theta_d$  is a design parameter for sensor fabrication, and it determines the position of 0<sup>th</sup> peak of Fraunhofer diffraction. Fraunhofer diffraction is a far-field optical phenomenon; therefore, the minimum size of the geometric dimension of the sensor is hundreds micrometer and the distance of total light traveled is not less than several tens of micrometers.

Output signals were analyzed by using image software, Image-pro Plus (Media Cybernetics, USA), and Figure 8c shows the numerical results which clearly show the detection of critical points. In this figure, the critical point is the point after which intensity of output signal rapidly drops. Flat region comes from light patterns induced by Fraunhofer diffraction, and after the critical point, the output signal drops because of decrease of reflectance.

Figure 9 shows three independent sensor outputs in terms of pixel positions (beginning and end of output profiles) with respect to time during the 9-hour experiment. The downward movements of TIR critical points (top symbols) are results of biofouling and the corresponding refractive index change is as much as 0.0089. Variations between each individual measurement could be mainly due to the random process of biofouling accumulation as well as fabrication variations of different sensors [9]. From the output signals, the position of critical point is extracted as a point of rapidly dropping its intensity using the image software. The bottom curve in the figure represents the measurement points (bottom symbols) of *Reference Point* (most left point of the output signal in the inset), and it barely changed during whole experiment. Since intensity of output signal before the critical point is in the region of total internal reflection, the reference point, as well as all other points in that region, does not shift and change. Therefore, measurement of the unchanging reference point verifies that the shifts of critical point came from the change of refractive index on the sensing surface.

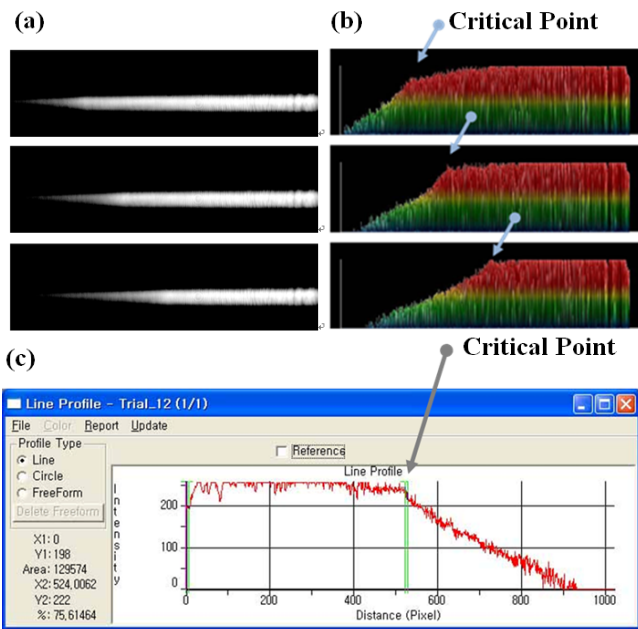


Figure 8: (a) Output light signal captured by CCD; (b) intensity profile clear showing the critical points for each patterns; (c) Analysis of output signals using image software.

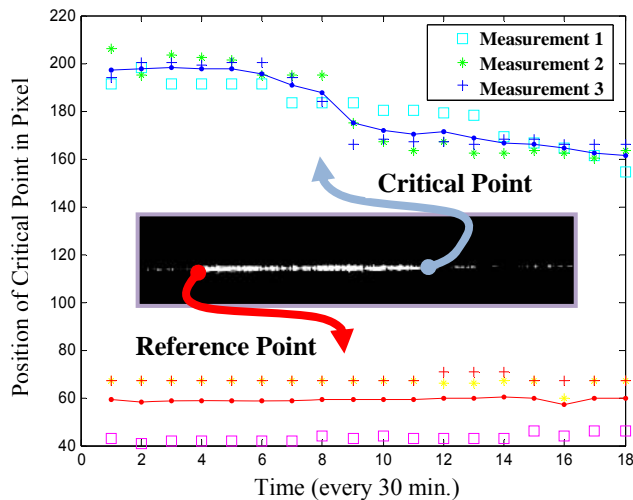


Figure 9: Microscale sensing experiment result for observation of biofouling formation. Average refractive index change for biofouling formation of milk was 0.0089 for 9 hours of experiment.

For sensing experiments, polarized laser source was directly coupled with the opening of the built-in waveguide of the sensor as shown in Figure 10. The wavelength of light source being used was 780nm because biofilms can be extracellular polymeric substances (EPS), sediments and bacteria combinations. They have different optical properties but usually have little absorbance at this and higher wavelength. Furthermore, reflectance is high in the region when the wavelength of light is greater than 700 nm, and this means that the output signal of the sensor is strong in this range.

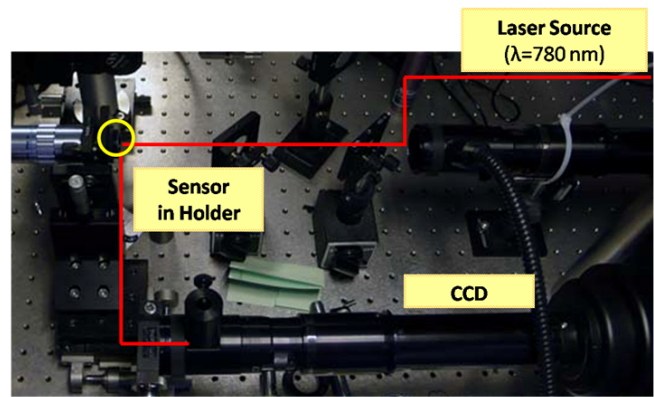


Figure 10: Experimental setup for biofouling sensing experiment. The wavelength of light source is 780 nm at which the absorption of biofouling is minimized (for maximum reflection.)

## CONCLUSION

We have demonstrated the feasibility of utilizing a planar, integrated total internal reflection sensor for characterizing the biofouling process. This work details the working principles of sensing mechanism, design, fabrication and characterizations of the biofouling sensors, including image analysis and experimental verifications. The TIR sensor for this work utilizes a simple optical design with a built-in waveguide as a TIR sensor. Furthermore, the fabrication process is simple by using only two masks for the entire fabrication process. Several liquids have been tested as base-line characterizations for the sensor, and measured refractive index were in good agreement with the values given by manufacturers (literature) with the error range of less than  $\pm 0.002$  Refractive Index Unit. During the biofouling experiments, the sensor measured the change of surface refractive index of a testing liquid (milk) and a shift as much as 0.0089 during a 9-hour test has been measured as the result of biofouling.

## REFERENCES

- [1] J.W. Costerton, P.S. Steward, and E.P. Greenberg, "Bacterial Biofilms: A Common Cause of Persistent Infections", *Science*, Vol. 284, pp. 1318-22 (1999).
- [2] D.F. Merchant, P.J. Scully, and N.F. Schmitt, "Chemical tapering of polymer optical fibre", *Sensors and Actuators A: Physical*, Vol. 76, pp. 365-71 (1999).
- [3] J. Klahre and H-C. Flemming, "Monitoring of biofouling in papermill process waters", *Water Research*, Vol. 34, pp. 3657-65 (2000).
- [4] P. Angell, A.A. Arrage, M.W. Mittelman, and D.C. White, "On line, non-destructive biomass determination of bacterial biofilms by fluorometry", *Journal of Microbiological Methods*, Vol. 18, pp. 317-27 (1993).
- [5] J. Homola, S.S. Yee, and G. Gauglitz, "Surface plasmon resonance sensors: review", *Sensors and Actuators B: Chemical*, Vol. 54, pp. 3-15 (1999).
- [6] M.Leitz, A. Tamachkarow, H. Franke and K.T.V. Grattan, "Monitoring of biofilm growth using ATR-leaky mode spectroscopy", *Journal of Physics D: Applied Physics*, Vol. 35, pp. 55-60 (2002).
- [7] M.G. Trulear and W.G. Characklis, "Dynamics of biofilm processes", *Water Pollution Control Federation*, Vol. 54, pp. 1288-1301 (1982).
- [8] R. Bakke, R. Kommedal and S. Kalvenes, "Quantification of biofilm accumulation by an optical approach", *Journal of Microbiological Methods*, Vol. 44, pp. 13-26 (2001).
- [9] J. Wimpenny, "Ecological determinants of biofilm formation", *Biofouling*, Vol. 10, pp. 43-63 (1996).

## CONTACT

\*K. H. Nam, tel: +1-510-642-8983; koonam@me.berkeley.edu

# AN ALUMINUM NITRIDE PIEZOELECTRIC MICROPHONE FOR AEROACOUSTICS APPLICATIONS

M. D. Williams, B. A. Griffin, A. Ecker, J. Meloy, M. Sheplak\*

Interdisciplinary Microsystems Group, Dept. of Mechanical and Aerospace Engineering,  
University of Florida, Gainesville, Florida, USA

## ABSTRACT

This paper describes an aluminum nitride (AlN)-based piezoelectric MEMS microphone designed to serve as aircraft fuselage instrumentation for full-scale noise characterization flight tests. The optimal microphone design was determined using lumped element modeling and composite plate theory. Measurements of the microphone's frequency response and linearity revealed it to have a higher sensitivity ( $71 \mu\text{V}/\text{Pa}$ ), larger dynamic range (29 – 147 dB) with lower noise floor, and significantly higher resonant frequency (89 kHz) than previous piezoelectric aeroacoustic microphones.

## INTRODUCTION

With the worldwide airline fleet estimated to double in the next 20 years [1], aircraft manufacturers increasingly face regulatory and market driven pressures to reduce aircraft noise. Passenger expectations for a quiet flight experience and concern about long-term noise exposure of flight crews are important drivers in aircraft manufacturers' efforts to reduce cabin noise in flight [2-3]. Treating the noise at its source shows potential for reduction of noise and weight savings compared to alternatives such as insulating panels.

In order to identify noise sources and assess the impact of noise reduction technologies during the design process, aircraft manufacturers require robust, low cost microphones. Measuring primary sources of cabin noise is difficult under simulated cruise conditions in test facilities [2] and establishes the need for microphones that can be used in full-scale tests at altitude. Their use on the fuselage exterior requires extremely small packaged sizes. Important performance metrics include a high maximum sound pressure level (SPL)  $\sim 150$  dB coupled with a noise floor  $< 45$  dB (ref  $20 \mu\text{Pa}/\sqrt{\text{Hz}}$ ) and a flat frequency response in the audio band ( $\sim 20$  Hz – 20 kHz). Microelectromechanical systems (MEMS) microphones show promise for meeting the stringent performance requirements of aircraft manufacturers at reduced size and cost, made possible using batch fabrication technology.

Piezoelectric MEMS microphones, in particular, are a robust and less power-demanding alternative to capacitive or piezoresistive microphones. In the past, piezoelectric materials used in MEMS microphones have largely been lead zirconate titanate (PZT) and zinc oxide (ZnO) [4-10]. In contrast, the microphone presented here makes use of aluminum nitride (AlN), which provides inherent advantages in CMOS compatibility, dielectric loss, and signal-to-noise ratio [11]. Despite these advantages, the difficulty of aluminum nitride fabrication has led to few piezoelectric MEMS microphones using AlN [12-13], and those have not targeted aeroacoustic applications.

In this paper, a batch-fabricated AlN piezoelectric microphone designed to serve as aircraft fuselage instrumentation for full-scale noise characterization flight tests is presented. Microphone design and characterization are both addressed, and its performance is compared to previous piezoelectric MEMS microphones.

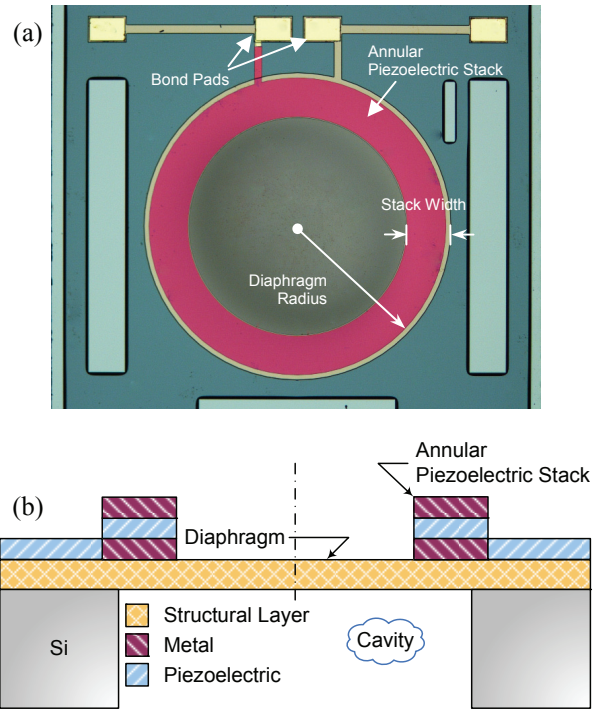


Figure 1. (a) Partial photograph of a piezoelectric microphone die (total die size is  $2 \times 2 \text{ mm}^2$ ); (b) Cross-sectional view of the microphone structure.

## DESIGN Structure

The microphone structure (Figure 1) includes a circular diaphragm composed of a structural layer and an annular piezoelectric/metal film stack, all deposited on a silicon substrate. As the diaphragm deflects under an incident acoustic pressure, strain in the piezoelectric yields an electric field that is sensed as a voltage difference across the metal electrodes. The location of the piezoelectric ring was chosen to take advantage of the high stress boundary region and to avoid the need for metal lines over the diaphragm surface. Diaphragm motion is enabled by an air cavity on the diaphragm backside.

## Modeling

Lumped element modeling [14] is an effective technique for producing system-level transducer models via "lumping" of system components into equivalent mass-spring-damper elements. The use of lumped element modeling requires characteristic length scales of the transducer to be much smaller than the wavelength of associated physical phenomenon; for example, at frequencies of interest, the diaphragm dimensions must be much less than the wavelength of the incident acoustic pressure and the bending wavelength within the diaphragm itself. Using a circuit analogy to represent the lumped element model allows engineers to leverage intuitive understanding of circuit diagrams and available circuit analysis tools. In addition, the equivalent circuit model can be

coupled directly to additional circuitry, providing a true system-level model.

Figure 2(a) shows the microphone structure with associated lumped circuit elements. The diaphragm is modeled as a lumped mass and compliance,  $M_{AD}$  and  $C_{AD}$ , respectively. Damping is included as a resistance,  $R_{AD}$ , and is estimated from prior devices of similar size and shape [10]. Coupling between the diaphragm and the air on the topside is modeled using a radiation mass  $M_{ADrad}$  and resistance  $R_{ADrad}$  estimated from a classical acoustics solution for radiation impedance seen by a piston in an infinite baffle. The cavity is modeled as a mass and compliance,  $M_{AC}$  and  $C_{AC}$ , respectively. The vent (not shown) is presented as a resistance  $R_{AV}$ . The electrical elements associated with the piezoelectric stack are the capacitance,  $C_{EB}$ , piezoelectric leakage path  $R_{EP}$ , and lead resistance  $R_{ES}$ . Each of these elements are connected into an equivalent circuit, shown in Figure 2(b), based on whether they share a common "effort" (pressure/voltage) or "flow" (volume velocity/current). The piezoelectric transduction is represented as a transformer with turns ratio  $\phi_A$  that relates the acoustic and electrical energy domains on the left and right sides, respectively. With expressions for each of the lumped elements known [10,15], the sensitivity of the microphone  $S = v_0/p$  [V/Pa] may be found directly from the circuit diagram of Figure 2(b).

Lumped elements associated with the diaphragm mass/compliance and piezoelectric transduction are the most difficult to compute and are based on a static piezoelectric composite plate model. The model [15,16] is found from the solution of the Kirchhoff plate equations in the inner and outer (annular) regions, with matching conditions on displacements and forces/moments applied at the interface and clamped boundary conditions applied at the exterior. Arbitrary in-plane stresses are included in the linearized governing equations [16]. In addition, a nonlinear version of the model is used to estimate the maximum pressure ( $P_{max}$ ) at which the microphone response remains linear.

The lower end of the microphone's dynamic range, the minimum detectable pressure ( $MDP$ ), is predicted via a circuit noise model (Figure 3) derived from the equivalent circuit model (Figure 2(b)). In this model, thermal noise sources [14] are added at the location of dissipative elements (as voltage sources in series or current sources in parallel with perfect dissipative elements) and the output power spectral density,  $S_o^v$  [V<sup>2</sup>/Hz] may then be found. Note the inclusion of a buffer amplifier and its own noise contributions. The  $MDP$  is then simply the input-referred voltage noise,

$$MDP = \sqrt{\int_{f_1}^{f_2} \frac{S_o^v}{|S|^2} df} \quad [\text{Pa}]. \quad (1)$$

### Optimization

The goal of a microphone design is maximization of its operational range (both in terms of frequency and pressure) while minding the demands of a particular application. The bandwidth requirements of a microphone are usually well known, such as the range of human hearing (20 Hz-20 kHz). Maximum pressure levels of interest are also usually known, but improvement in the  $MDP$ , regardless of requirements, yields improved measurement resolution. As a result, it is natural to state the objective function

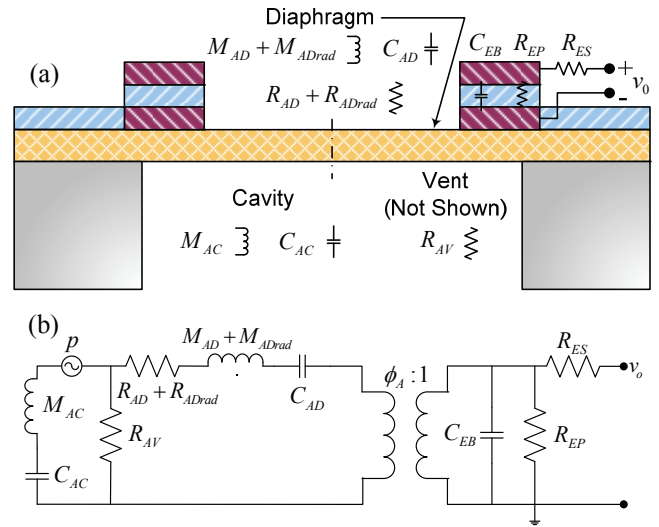


Figure 2. (a) Piezoelectric microphone structure with lumped circuit elements; (b) Equivalent circuit representation of a lumped element model of the piezoelectric microphone.

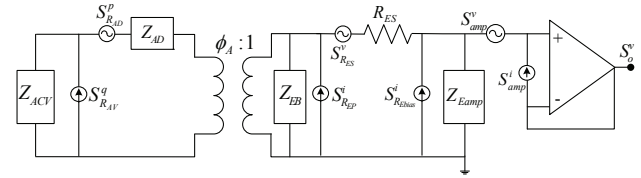


Figure 3. Microphone noise model including buffer amplifier.

for microphone optimization as

$$\min_{\bar{X}} MDP, \quad (2)$$

where the design variables  $\bar{X}$  include film thicknesses and radii. Constraints are placed on the bandwidth and  $P_{max}$ , which are estimated from the equivalent circuit model and nonlinear composite plate model, respectively. Fabrication constraints (i.e. minimum radii, bounds on achievable film thicknesses, etc.) are also applied. The optimization yielded a diaphragm that was 1.3  $\mu\text{m}$  in thickness with an outer diameter of 600  $\mu\text{m}$ , an annular piezoelectric film stack width of 156  $\mu\text{m}$ , and AlN thickness of 1  $\mu\text{m}$ .

### FABRICATION

Fabrication of the microphone was performed by Avago Technologies using a variant of their well-known FBAR process [13]. The proprietary process involves deposition and etching of the AlN and metal films followed by a backside deep reactive ion etch to define the cavity. At this time, sealing of the back cavity is accomplished at the packaging stage.

### EXPERIMENTAL SETUP AND RESULTS

The first step toward characterization of the piezoelectric microphone was selection of the most promising microphone die. The voltage chirp excitation response of several microphones were inspected using a Polytec scanning laser vibrometer system, composed of a Polytec OFV 3001S vibrometer controller and OFV-074 microscope adapter attached to an Olympus BX600 microscope. Two of the microphones with resonant frequencies that compared favorably with the model (80 and 89 kHz, respectively, compared to 84 kHz predicted) were selected for further characterization. These microphones are described

throughout this section and are labeled Mic 1 and Mic 2, respectively.

Measurement of the sensitivity and linearity of both microphones was conducted in a normal incidence plane wave tube (PWT) using the Brüel & Kjær 4138 and PCB Piezotronics 377A12, respectively, as references. The PULSE Multi-analyzer system provided pseudo-random noise and single tone excitation signals for these measurements, which were amplified prior to rendering by a BMS compression driver at one end of the tube. The device under test (DUT) and reference microphone were mounted side-by-side at the end of the tube. The DUT was epoxied into a recess in a printed circuit board (Figure 5), which was clamped into position at the end of the plane wave tube via a slot in the backplate. BNC connections and appropriate electronics, including a buffer amplifier, were also located on this printed circuit board. The measurements were conducted over a 6.4 kHz bandwidth about a center frequency of 3.5 kHz with a 1 Hz bin width using 100 complex spectral averages. The maximum frequency of 6.7 kHz was dictated by the cut-on of higher order modes within the plane wave tube.

The microphone sensitivities are shown in Figure 6 together with the predicted value. The frequency responses were flat to within 1.5 dB and the sensitivity was  $71 \mu\text{V}/\text{Pa}$  ( $-83 \text{ dB ref } 1 \text{ V}/\text{Pa}$ ). The linearity measurement results in terms of total harmonic distortion for Mic 2 are found in Figure 7. Distortion was measured to be less than 2% up to 147 dB ref  $20 \mu\text{Pa}$ . Five harmonics of the fundamental tone  $f_i = 1 \text{ kHz}$  were considered in the calculation, i.e.

$$\text{THD}[\%] = 100\% \times \sum_{n=2}^6 V^2(nf_i) / V^2(f_i). \quad (3)$$

Each of these five harmonics propagate as plane waves in the tube used for testing.

The sensor noise floors were also measured using a Stanford Research Systems SR785 spectrum analyzer, with the packaged microphones placed in a triple Faraday cage for shielding. Figure 8 shows the minimum detectable pressure, here calculated as the voltage noise spectra referred to the sensor input via the measured sensitivity at 1 kHz. Under these conditions, the noise floor for a 1 Hz bin centered at 1 kHz was measured to be 29 dB ref  $20 \mu\text{Pa}$  and the A-weighted noise floor was  $64 \text{ dB ref } 1 \text{ Pa}/\sqrt{\text{Hz}}$ . Note that the  $1/f$  shaped noise due to dielectric leakage in the piezoelectric extends into the audio band and that the sensor thermal noise floor is less than  $20 \text{ dB ref } 1 \text{ Pa}/\sqrt{\text{Hz}}$ .

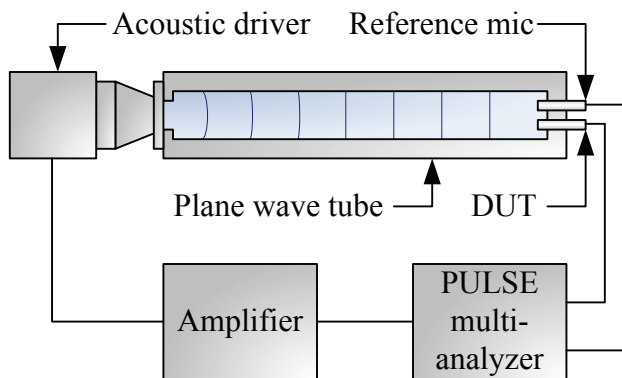


Figure 4. Experimental setup for frequency response measurement in a plane-wave tube.

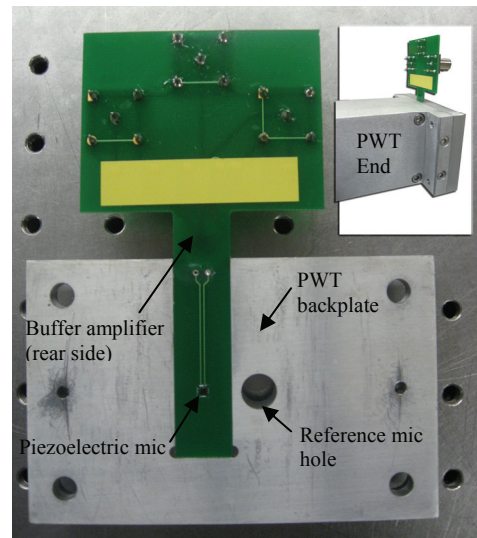


Figure 5. Packaged microphone, also shown mounted in plane wave tube (inset).

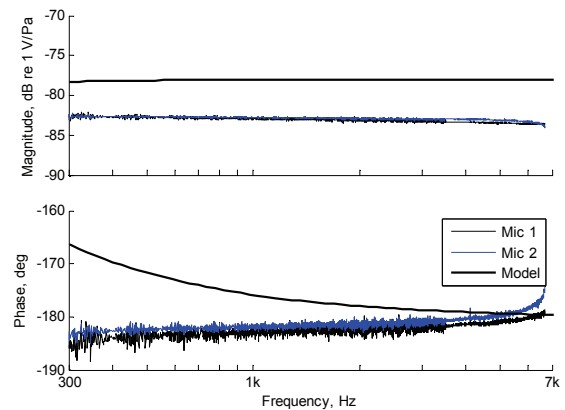


Figure 6. Measured microphone frequency response.

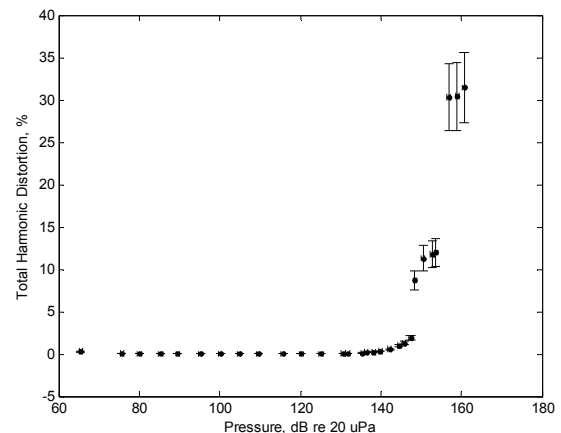


Figure 7. Total harmonic distortion for a 1 kHz tone, considering 5 harmonics.

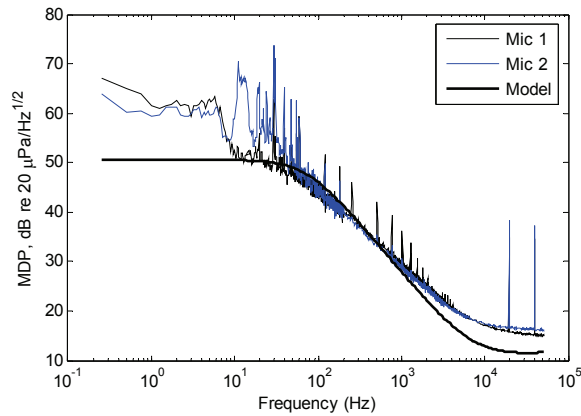


Figure 8. Measured and theoretical minimum detectable pressure (voltage noise referred to input via sensitivity at 1 kHz).

## CONCLUSIONS

The design, optimization, and characterization of an AlN-based piezoelectric MEMS microphone for aeroacoustic measurements were described in this paper. This microphone is among the earliest to use AlN over more common piezoelectrics such as PZT and ZnO, and is the first targeted at aeroacoustic applications. Characterization of two AlN-based microphones yielded a sensitivity of  $71 \mu\text{V}/\text{Pa}$ , dynamic range of 29-147 dB SPL, and resonant frequency of 89 kHz.

A comparison of experimental results with those from prior piezoelectric mics is found in Table 1. The sensitivity of the microphones presented here ( $71 \mu\text{V}/\text{Pa}$ ), though lower than the two prior AlN-based microphones [12-13] ( $180 \mu\text{V}/\text{Pa}$  and  $2 \text{ mV}/\text{Pa}$ ), was more than an order of magnitude better than the most recent piezoelectric aeroacoustic microphone [10]. The noise floor was also improved, and was comparable to that reported in [12]. Finally, the resonant frequency of 89 kHz is the highest reported among piezoelectric microphones, indicating a particularly large useable bandwidth.

Table 1: Summary and comparison with previous work.

Researcher	Material	Sensitivity (mV/Pa)	$f_{\text{res}}$ (kHz)	MDP (dB SPL)	P <sub>MAX</sub> (dB SPL)
Present work	AlN	0.071	89	29 <sup>a</sup> , 64 <sup>b</sup>	147
Littrell et al. [12]	AlN	0.18	11	58 <sup>b</sup>	148
Fazzio et al. [13]	AlN	0.5-2	NR	NR	NR
Horowitz et al. [10]	PZT	0.0017	59	35.7 <sup>a</sup> , 95.3 <sup>b</sup>	169
Kim et al. [5]	ZnO	1	16	50 <sup>b</sup>	NR
Ried et al. [6]	ZnO	0.92	18	57 <sup>b</sup>	NR
Lee et al. [8]	ZnO	30	0.89	NR	NR
Royer et al. [4]	ZnO	0.25	10	66.02 <sup>c</sup>	NR
Schellin et al. [7]	Polyurea	0.030	NR	NR	NR
Ko et al. [9]	ZnO	0.51 <sup>d</sup>	7.3	NR	NR

<sup>a</sup> At 1 kHz w/ 1 Hz bin; <sup>b</sup> A-weighted; <sup>c</sup> Method not reported; <sup>d</sup> At resonance

For future work, agreement between the model and experiment can be improved. The discrepancies are believed to relate to uncertainty in residual stresses and thin film properties, and efforts are currently underway to establish the source of disagreement. Other ongoing efforts involve improving the test package and characterization of a new round of devices. Finally, future microphone designs with lower noise floors may be achievable via careful design of the piezoelectric layer such that  $1/f$  noise is pushed out of the audio band.

## ACKNOWLEDGEMENTS

Fabrication was performed by Avago Technologies of Fort Collins, CO. Financial support for this work was provided by Boeing Corporation and a NSF Graduate Fellowship.

## REFERENCES

- [1] B. Burnett "Sssh, we're flying a plane around here," Boeing Frontiers, vol. 4, 2006.
- [2] V.G. Mingle et. al., "Clocking effects of chevrons with azimuthally-varying immersions on shockcell/cabin noise" 29<sup>th</sup> AIAA Aeroacoustics Conference, #08-3000, Vancouver, British Columbia Canada, 2008.
- [3] I.C. Organization, "Occupational safety and health protections for cabin crew members," 36th Assembly of the International Civil Aviation Organization, A36-WP/208, Montreal, Canada, 2007.
- [4] M. Royer et al., "ZnO on Si integrated acoustic sensor," Sensors and Actuators, vol. 4, 1983, pp. 357-362.
- [5] E.S. Kim, J.R. Kim, and R.S. Muller, "Improved IC-compatible Piezoelectric Microphone and CMOS Process," International Conference on Solid-State Sensors and Actuators, San Francisco, CA, 1991, pp. 270-273.
- [6] R. Ried, D. Hong, and R. Muller, "Piezoelectric microphone with on-chip CMOS circuits," J. Microelectromech. S., vol. 2, 1993, pp. 111-120.
- [7] R. Schellin, G. Hess, R. Kressmann, and P. Wassmuth, "Micromachined silicon subminiature microphones with piezoelectric P(VDF/TRFE)-layers and silicon-nitride-membranes," 8th International Symposium on Electrets, 1994, pp. 1004-1009.
- [8] S.S. Lee, R.P. Reid, and R.M. White, "Piezoelectric Cantilever Microphone and Microspeaker," Journal of Microelectromechanical Systems, vol. 5, 1996, pp. 238-242.
- [9] S.C. Ko, Y.C. Kim, S.S. Lee, S.H. Choi, and S.R. Kim, "Micromachined piezoelectric membrane acoustic device," Sensor. Actuat. A-Phys, vol. 103, 2003, pp. 130-134.
- [10] S. Horowitz, T. Nishida, L. Cattafesta, and M. Sheplak, "Development of a micromachined piezoelectric microphone for aeroacoustics applications," J. Acoust. Soc. Am., vol. 122, 2007, pp. 3428-3436.
- [11] S. Trolier-McKinstry and P. Muralt, "Thin Film Piezoelectrics for MEMS," J. Electroceram., vol. 12, 2004, pp. 7-17.
- [12] R. Littrell and K. Grosh, "Advantages of piezoelectric MEMS microphones," 157th Meeting of the Acoustical Society of America, Portland, OR, 2009.
- [13] R.S. Fazzio et al., "Design and Performance of Aluminum Nitride Piezoelectric Microphones," Solid-State Sensors, Actuators and Microsystems Conference, 2007, pp. 1255-1258.
- [14] S.D. Senturia, "Microsystem Design," Kluwer Academic Publishers, 2001.
- [15] S.A. Prasad et al., "Analytical electroacoustic model of a piezoelectric composite circular plate," AIAA Journal, vol. 44, 2006, pp. 2311-2318.
- [16] G. Wang, B.V. Sankar, L.N. Cattafesta, and M. Sheplak, "Analysis of a composite piezoelectric circular plate with initial stresses for MEMS," ASME International Mechanical Engineering Congress, New Orleans, LO, United States: ASME, 2002, pp. 339-346.

## CONTACT

\*M. Sheplak, tel: +1-352-392-3983; [sheplak@ufl.edu](mailto:sheplak@ufl.edu)

# LOW-COST THERMAL MEMS GYROSCOPE

A.M. Leung

School of Engineering Science, Simon Fraser University, Burnaby, BC, Canada

## ABSTRACT

This paper describes a new MEMS gyroscope (gyro) with a simple device structure. Its operation is based on the Coriolis effect on an oscillatory gas stream. The oscillatory motion is created by two heaters which are activated alternately. The fabrication of the thermal MEMS gyro is not equipment intensive or process critical, making this device a potential contender for the low-cost MEMS gyro market. A rudimentary prototype running at 4mW heater power has shown a linearity of better than 1% with a 360°/s full scale, and a noise density of 1.5°/s/Hz<sup>0.5</sup>.

## INTRODUCTION

With very few exceptions, all commercial MEMS gyros measure Coriolis effects on a moving solid proof mass at resonance to determine angular rate [1, 2]. Tight control of proof mass dimensions is required to achieve good performance, particularly in the capacitance sensing type. The extremely low cost requirement of the large consumer market is a tremendous challenge for manufacturers of this type of MEMS gyroscopes, considering the fact that the design of resonator-based gyroscopes is a mature field. The work reported here explores the possibility of achieving lower cost using a fluidic angular sensing mechanism based on thermal principles.

Angular rate sensors with no vibrating solid proof mass are not new. An apparatus for measuring angular rate was disclosed in 1932 as a “turn indicator” [3]. It was built using traditional machined parts to detect moving fluid path deviation resulted from Coriolis acceleration. Improvements to this type of angular rate sensor include a miniature electric pump for moving fluid and temperature sensors for detecting fluid stream position [4]. While not as active as the vibrating mass MEMS gyro development, research efforts continue in fluidic angular rate sensor based on forced convection produced by a piezoelectric pump [5]. In spite of these efforts, the size, complexity and cost of these research devices have prevented them from becoming mainstream MEMS gyro contenders. Furthermore, these reported fluidic gyros use unidirectional flow which makes it impossible to cancel the linear acceleration effect [2]. The device described in this paper can achieve very low manufacture cost due to its simple device structure, and has a built-in linear acceleration effect cancellation capability to improve device performance.

## PRINCIPLE OF OPERATION

The operating principle of the new thermal MEMS gyroscope is illustrated in Figure 1. In an enclosed space, two miniature filaments  $H_T$  and  $H_B$ , or Top Heater and Bottom Heater, are placed on the line of symmetry between two temperature sensors,  $T_L$  and  $T_R$ , or Left Temperature Sensor and Right Temperature Sensor. The Top Heater and Bottom Heater are activated alternately to move the gas between them. In Phase I of the device operation, shown in Figure 1(a), a current through  $H_B$ 's filament heats it up while  $H_T$  stays at the ambient temperature. As illustrated by the shaded circle, the gas in the vicinity of  $H_B$  heats up and expands. Before thermal equilibrium is reached, this gas expansion creates a moving gas stream, illustrated by the dotted arcs, towards  $H_T$ . With no rotation, i.e. angular rate  $\Omega=0$ , this gas stream moves along a symmetrical path between the two temperature sensors  $T_L$  and  $T_R$ . This is indicated by the thick arrow in Figure 1(a). Due to symmetry, this gas movement produces no differential temperature

$\Delta T$ . In Phase II when  $H_T$  heats up, as shown in Figure 1(b), the direction of gas flow reverses but differential temperature output  $\Delta T$  remains at zero because of symmetry and no rotation.

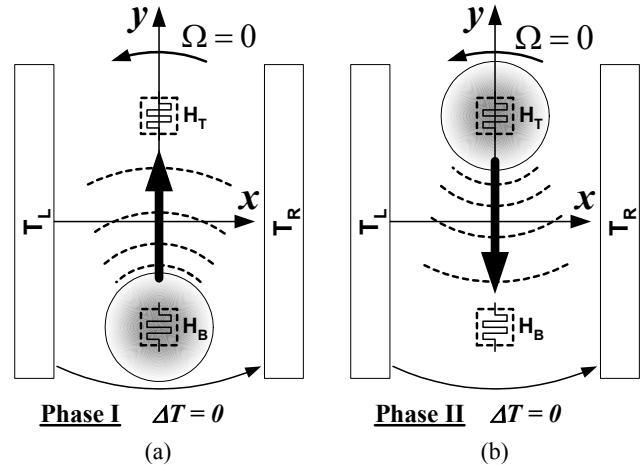


Figure 1: Thermal gyroscope operation with no rotation. Differential temperature output  $\Delta T$  is zero in both Phase I (a) and Phase II (b).

When the device is rotated, Coriolis acceleration acts on the moving gas stream and disturbs its symmetrical path. In Phase I of the device operation, this is illustrated by the thick arrow in Figure 2(a). The higher temperature gas stream moves towards  $T_R$  and generates a time dependent positive  $\Delta T(t)$ . Phase II of the device operation is shown in Figure 2(b). When  $H_T$  is activated instead of  $H_B$ , the direction of the gas movement reverses. This creates a negative  $\Delta T(t)$ . By reversing the polarity of  $\Delta T(t)$  synchronous to the activation of  $H_B$  and  $H_T$ , an output signal proportional to the angular rate and direction can be obtained. This synchronous detection method also suppresses the linear acceleration signal, provided the device is symmetrical.

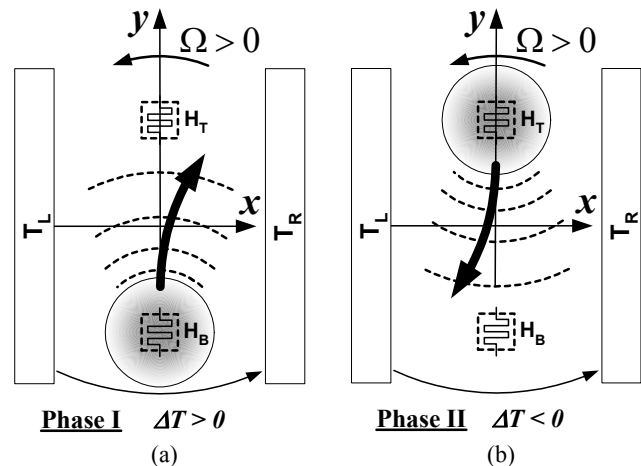


Figure 2: Thermal gyroscope operation with rotation. (a) Differential temperature output  $\Delta T$  is positive in Phase I when  $H_B$  is activated. (b) In Phase II when  $H_T$  is activated, the gas stream reverses direction and produces a negative  $\Delta T$ .



## RESULTS

### Device structure

The construction of the MEMS thermal gyro is illustrated in Figure 3. It is fabricated using a 2-mask process. A  $0.4\mu\text{m}$  thick CVD oxide and a  $0.5\mu\text{m}$  thick aluminum are deposited on the silicon substrate. The aluminum thin film is first patterned to form the bond pads, and the resistors for the heaters and the temperature sensors corresponding to  $H_T$ ,  $H_B$ ,  $T_L$  and  $T_R$  shown in Figure 2. The oxide layer is then patterned to define the widows for silicon etching. Isotropic dry etching using Xenon Difluoride [6] results in a  $300\mu\text{m}$ -deep cavity on the silicon substrate, and creates three suspended oxide bridges for the heaters and temperature sensors shown in Figure 3. The top view of the prototype thermal gyro is shown in Figure 4.

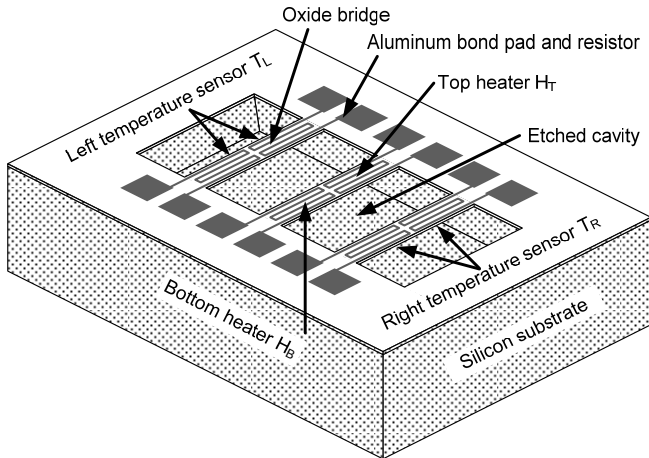


Figure 3: Thermal gyro device structure.

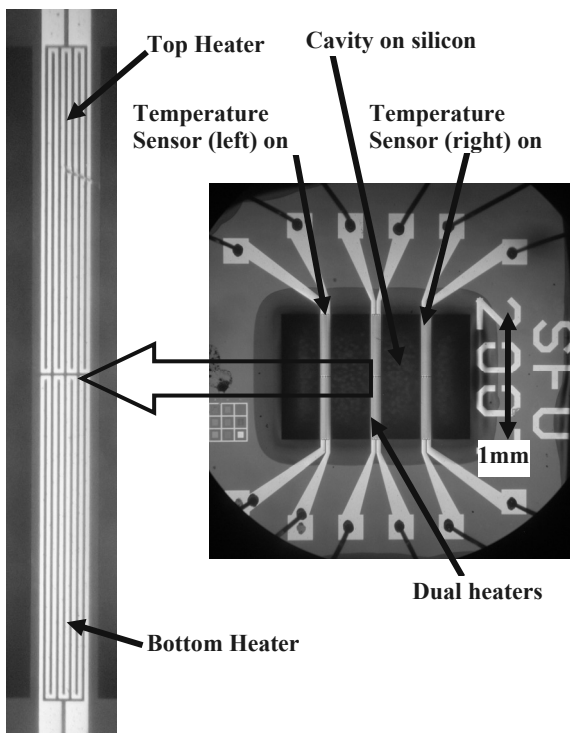


Figure 4: Top view of Thermal Gyro prototype.

To increase sensitivity, the thermal gyro is sealed in a 16-pin dual-in-line package, shown in Figure 5, which is filled with a high density sulfur hexafluoride gas. It is worthwhile to note that this thermal gyro device structure is practically identical to that of the thermal accelerometer reported more than a decade ago [7], except that the heater bridge is electrically divided to form two heaters.

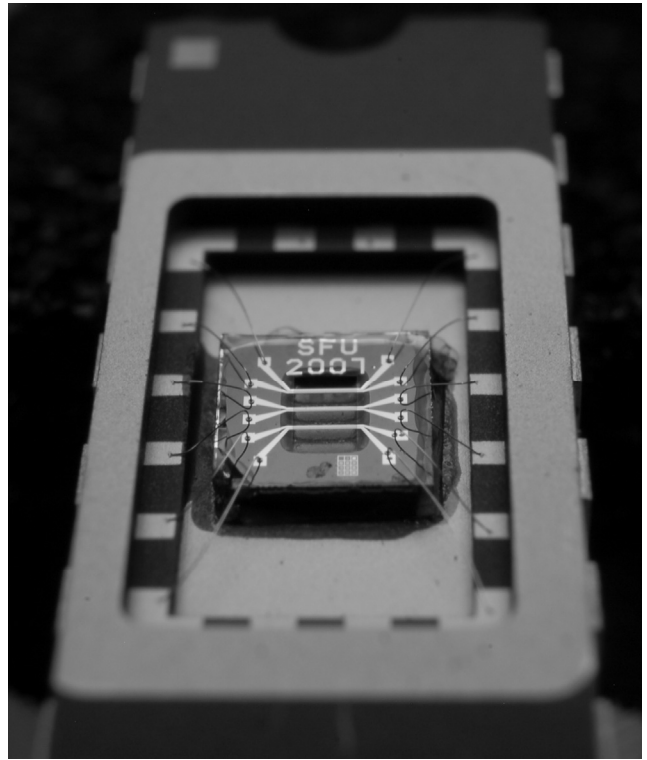


Figure 5: Thermal Gyro in 16-pin ceramic package. Wire bonding and cavity etching completed. It is ready to be sealed in  $\text{SF}_6$ .

### Prototype testing

A simple test setup shown in Figure 6 is used to verify the functionality of the thermal gyro. A rotational platform for testing the thermal gyro is attached directly to the shaft of a servo motor. The thermal MEMS gyro, amplifiers, and signal processing circuits are assembled on a prototype board mounted on the rotational platform. Wire connections to stationary data recording equipment interfere with the platform's rotation. They are replaced by a battery power source and a short-range infrared (IR) data link consists of three IR light emitting diodes. The amplified thermal gyro signal is used to frequency modulate the IR light emitting diode current. A phase lock loop is used in the IR receiver to recover the analog thermal gyro signal.

In characterizing the thermal gyro prototype, the servo motor is programmed to rotate at rates from  $-360^\circ/\text{s}$  to  $+360^\circ/\text{s}$  with  $90^\circ/\text{s}$  step increments. At each rotational rate the thermal gyro output is recorded. The data of the thermal gyro output as a function of angular rate are summarized in Figure 7. The testing setup specifics and measured results are summarized below:

Heater power:	4mW
Heater switching frequency:	33Hz
Signal bandwidth:	3Hz
Device sensitivity:	$24\mu\text{V}/360^\circ/\text{s}$
Noise:	$1.5^\circ/\text{Hz}^{0.5}$

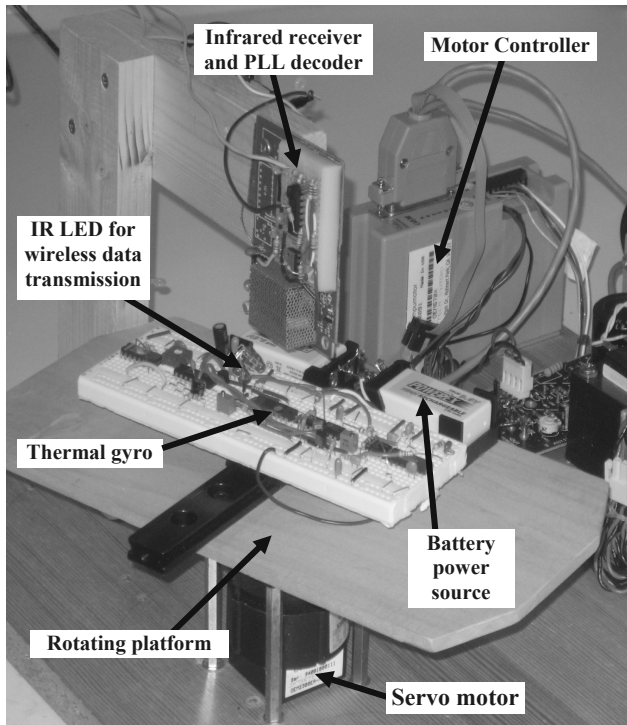


Figure 6: Experimental setup for Thermal Gyro prototype characterization.

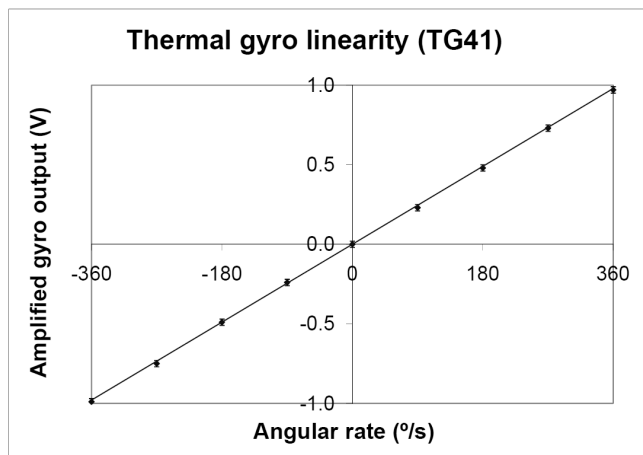


Figure 7: Thermal gyro output as a function of angular rate.

### Discussions

The preliminary data collected from the thermal gyro prototype are surprisingly encouraging. Not only has the operational principal of this new thermal gyro validated by the prototype's functionality, a linearity of better than 1% for a 360°/S full scale input is observed.

It is anticipated that the sensitivity of the thermal gyro can increase as the square of heater power. This can provide significant improvement of device performance. In our prototype, however, the heater power is limited to about 4mW because of low electrical resistance of the aluminum heater resistor, and the limited current carrying capability of the thin aluminum traces

used. Better performance is expected in the next iteration of thermal gyro when better heater material is chosen.

The switching frequency of the heaters is set at its cut off frequency of approximately 33Hz. A third-order 3Hz low pass filter is used to remove the 33Hz modulation signal. While it is conceivable that a well designed heater can achieve a switching frequency of well above 100Hz [8], the required use of a heavier gas such as the sulfur hexafluoride to improve sensitivity will limit this upward increase of heater switching frequency. The practical limit will likely be in the range of 50-100Hz. For this reason, the thermal gyro frequency response is not expected to go much beyond 10Hz. The use of higher order filters can possibly increase the thermal gyro's signal bandwidth.

The new thermal gyro described in this work switches on two heaters alternately to create bi-directional gas motions for angular rate detection. Synchronous detection is used to extract angular rate signals. In this arrangement, unwanted linear acceleration signals, along with other low frequency noise, are up-shifted in frequency and filtered. In testing the thermal gyro prototype, however, we observe very significant linear acceleration effects – up to 100°/s/g. Because Coriolis acceleration is orders of magnitude smaller than the interfering linear acceleration, very large rejection is required. We suspect the XeF<sub>2</sub> etched cavity may be slightly asymmetrical. The residue stresses of the oxide film with metal film resistors on them may also deform the bridges and introduce additional device asymmetry. Fabricating devices with better symmetry will be an important area for future thermal gyro development.

### CONCLUSIONS

A MEMS thermal gyro with unconventional device structure and sensing principle is presented in this paper. This operation of this new device has been successfully demonstrated. Only preliminary performance data have been collected on this device and more research is required to verify the competitiveness of this new technology. In spite of that, some observations can be made. Since the thermal gyroscope's device structure is identical to that of the thermal accelerometer, we can conclude that it has the potential of achieving the same robustness and low manufacture cost in the production environment. The thermal gyro's signal bandwidth will likely be limited to about 10Hz, and its resolution performance will be modest. The very low device cost, however, may allow this new thermal gyro technology to become one possible contender in the cost sensitive consumer market.

### ACKNOWLEDGEMENTS

This work is supported by a Discovery Grant from the Natural Sciences and Engineering Research Council of Canada.

### REFERENCES

- [1] N. Yazdi, F. Ayazi, and K. Najafi, "Micromachined inertial sensors," Proceedings of the IEEE, vol. 86, no. 8, pp. 1640–1659, August 1998.
- [2] W. Zhang et al. "The development of micro-gyroscope technology," J. Micromech. Microeng. 19 (2009) 113001.
- [3] P. Kollsman, "Turn indicator," US Patent 1841607, 1932.
- [4] M. T. Lopiccolo, M. A. Schaffer, and G. A. Jachyra, "Unitary fluidic angular rate sensor," US Patent 4020700, 1977.
- [5] V. T. Dau, D. V. Dao, T. Shiozawa, H. Kumagai, and S. Sugiyama, "Development of a dual-axis thermal convective gas gyroscope," Journal of Micromechanics and Microengineering, vol. 16, no. 7, pp. 1301–1306, July 2006.

- [6] P. B. Chu, J. T. Chen, R. Yeh, G. Lin, J. C. P. Huang, B. A. Warneke and K. S. J. Pister, "Controlled Pulse-etching with Xenon Difluoride," Proceedings of the Ninth International Conference on Solid State Sensors and Actuators, June. 1997.
- [7] A.M. Leung, J.Jones, E. Czyzewska, J.Chen and B. Woods, "Micromachined Accelerometer based on convection heat transfer", Digest, IEEE/ASME MicroElectroMechanical Systems Workshop, Heidelberg, Germany, January 25-29, 1998, pp627-630.
- [8] J. Couteaud et al., "Studies and optimization of the frequency response of a micromachined thermal accelerometer", Sensors and Actuators A 147 (2008) 75-82.

**CONTACT**

\*A.M. Leung, tel: +1-778-782-4296; [aleung@sfu.ca](mailto:aleung@sfu.ca)

# PASSIVE WIRELESS DIRECT SHEAR STRESS MEASUREMENT

Jeremy Sells, Vijay Chandrasekharan, Henry Zmuda, Mark Sheplak and David P. Arnold  
Interdisciplinary Microsystems Group, University of Florida, Gainesville, Florida USA

## ABSTRACT

This paper presents a passive-wireless interrogation strategy for shear stress measurement. The wireless system is realized via a hybrid packaging approach that combines a floating-element-type MEMS capacitive shear stress sensor die flush-mounted in a printed circuit board (PCB) substrate. The sensor die is wire-bonded to a 5-turn inductor on the PCB to form an LC tank circuit with a nominal resonant frequency of 258 MHz and a Q of ~6. A change in input shear leads to a change in the sensor capacitance and a corresponding shift in the resonant frequency. A single-turn loop antenna, fabricated on a second PCB substrate and placed in proximity to the sensor is used for wireless interrogation. The sensor displayed a linear sensitivity of 219 kHz/Pa (849 ppm/Pa) up to the testing limit of 1.6 Pa with a resolution of 45 mPa (limited by instrumentation). The sensor showed superb stability, with drift variations of only  $\pm 0.1\%$  over 3 hrs. A wireless range of 8 mm was also achieved at 3.4 mW RF source power.

## INTRODUCTION

Measurement of shear stress is important for various applications involving aircraft/watercraft/land vehicles and pipe/duct flow problems [1]. These measurements are typically quite challenging because one is trying to measure very small shear forces in a fairly harsh operating environment (high or low mean pressures, high dynamic pressures, elevated temperatures, atmospheric moisture, electromagnetic interference, etc.). This is compounded by the need for high spatial and temporal resolution, thus demanding high-bandwidth sensors with small sensing areas. Additionally, multiple measurements over the surface of a body are often desired, requiring multiple sensors or a distributed sensing mechanism.

The advent of passive-wireless shear stress sensors could dramatically improve future flow testing. First, wireless detection eliminates the challenge of making direct electrical connections to the device, simplifying power, cabling, and machining requirements on the test specimen (e.g. wind-tunnel models). This permits truly flush mounted sensors and the possible installation of shear sensors in hostile environments where wired connections are not possible. Second, passive wireless measurement relies on frequency detection. This mitigates the difficulties of parasitic capacitance and electromagnetic interference that normally hamper direct measurement of capacitive-based sensors. Third, this technology can be extended to arrays utilizing a single antenna to monitor multiple sensors in different frequency bands.

### Passive Wireless Theory

The passive wireless technique used here has been implemented previously to measure pressure [3-6], humidity [7], or various chemical gasses [8]. This work adopts similar passive wireless interrogation strategies to a variable-capacitance shear stress sensor. To detect a change in shear stress, an inductive coil is connected to a variable-capacitor shear stress sensor. This forms a second-order resonant circuit with a characteristic natural frequency given by,

$$f_n(\tau) = (2\pi\sqrt{LC(\tau)})^{-1}, \quad (1)$$

where  $L$  is the inductance of the coil and  $C(\tau)$  is the variable capacitance of the sensor. Input shear  $\tau$ , causes a change in the capacitance and thus changes its natural frequency. This expression is inherently nonlinear but for small changes in capacitance relative to the nominal capacitance, a linear approximation may be used to estimate the resulting change in resonance,

$$\Delta f(\tau) = -\frac{f_o}{2} \frac{\Delta C(\tau)}{C_o}, \quad (2)$$

where  $C(\tau) = C_o + \Delta C(\tau)$  and  $f_n(\tau) = f_o + \Delta f(\tau)$ . Note, this simplified analysis ignores the influence of electrical resistance, but for narrowband resonators, similar frequency shifts occur.

Frequency changes are tracked by interrogating the device with an external antenna attached to a network analyzer. The sensor's resonance shows up as a dip in the magnitude of the scattering parameter  $S_{11}$  (Figure 1). Assuming a constant inductance, any change in frequency will be proportional to a change in capacitance according to Equation 2.

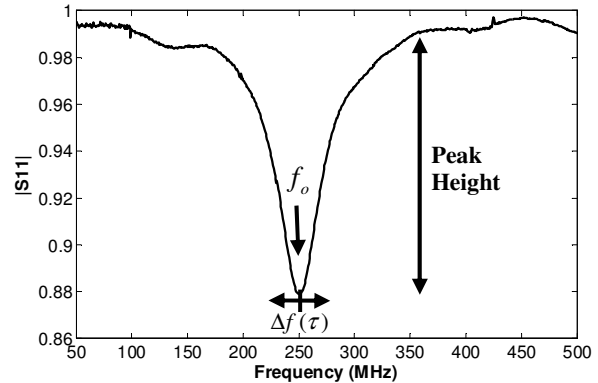


Figure 1: Wireless sensor resonant peak in Network Analyzer output spectrum. The nominal natural frequency is indicated as well as the peak height used to evaluate the wireless range

### Sensor System Design

Our group previously reported a wired capacitive shear stress sensor at Transducers 2009 [2], and a similar design and fabrication approach is used for this wireless device. Figure 2 shows the basic structures that make up the capacitive shear stress sensor. The tethered, floating element (1 mm x 1 mm x 45  $\mu\text{m}$ ) in the center of the die is free to move in response to an input shear force from a fluid flow over the surface. The four tethers (1 mm x 10  $\mu\text{m}$  x 45  $\mu\text{m}$ ) act as restorative springs, and the comb fingers at the edge of the element are used to detect the displacement due to shear. There are 22 comb finger pairs with each finger 170  $\mu\text{m}$  x 10  $\mu\text{m}$  x 45  $\mu\text{m}$  and a gap of 3.5  $\mu\text{m}$ . The sensor has a nominal capacitance of 1.3 pF, including parasitics. The stiffness of the tethers was designed to provide a linear displacement up to at least

180 nm, which corresponds to a 5 Pa input shear, while rejecting pressure forces and transverse shear forces.

The 5-turn inductor coil has a 10 mm outer length and a pitch of 0.5 mm. This gives a simulated inductance of 227 nH and a simulated parasitic capacitance (coil inter-winding capacitance) of 370 fF. The coil trace cross section is  $250\ \mu\text{m} \times 35\ \mu\text{m}$  and has a simulated high frequency resistance of  $1.3\ \Omega$  at 260 MHz. When wired with the capacitive sensor, the LC tank yields a nominal natural frequency of 258 MHz.

The system uses a packaging approach that combines the silicon capacitive sensor with an inductive coil fabricated in a PCB substrate. The silicon die is flush-mounted in a recess in the PCB to provide a smooth surface for exposure to the flow. The sense comb terminals are connected to the inductor coil using the electrical bond sites as indicated (Figure 2). In the current design, this connection is made via gold wire bonds, but future implementations may use other interconnect technologies (e.g. through silicon vias and/or flip-chip approaches) to eliminate the wire bonds and ensure a hydraulically smooth surface.

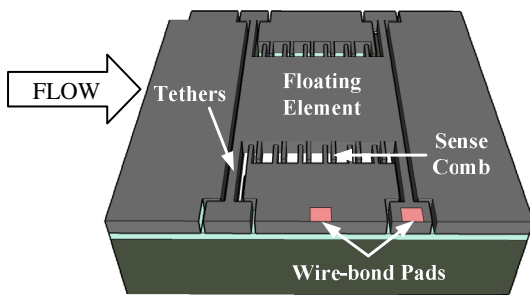


Figure 2: Capacitive shear stress sensor showing mechanical device structures and electrical bond points.

## FABRICATION AND PACKAGING

The fabrication process flow is illustrated in Figure 3, A-C. First a simple 2 mask fabrication process is used to create the sensor. An SOI wafer with a highly doped device layer is etched via deep reactive ion etching (DRIE) to define the sensor structures using a first mask. The silicon is then electroplated with Ni to enable electrical connection and mitigate charge accumulation on the electrode surfaces (associated with the native oxide on the silicon). A front to back alignment is used with the second mask to DRIE the rear cavity directly underneath the floating element. To release the mechanical structures a BOE etch is used to remove the underlying oxide. The 3.5 mm x 3.5 mm sensor die is shown in Figure 4 along with an SEM of the capacitive comb fingers.

A flush mountable PCB substrate package is created as shown in Figure 3, 1-3. Copper-clad FR4 board is milled to create the inductor coil. The coil is electroplated with Ni and Au to enable wire bonding to the sensor die in the final step. A photodefinable solder mask polymer is then applied to reduce the surface roughness due to the Cu traces. Contact window openings are made in the solder mask to facilitate electrical connections to the inductor bond pads. A cavity is then milled in the top surface of the board to snugly accommodate the sensor die. Epoxy is applied to only one corner of the die to affix it in the cavity and avoid mechanical stresses on the die. Gold ball-wedge wire bonding is used to connect the sensor to the inductor. The final device footprint is 10 mm x 10 mm in the center of a 30 mm x 30 mm x 1.5 mm board. The board size allows room for up to a four-sensor array in the future. Figure 5 shows the die packaged in the PCB with a 5-turn coil.

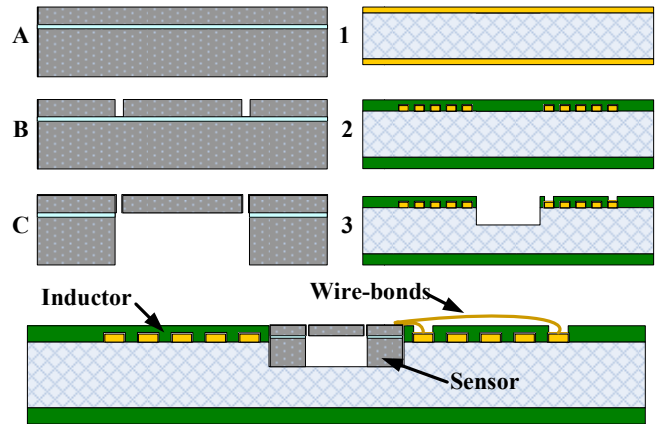


Figure 3: Sensor fabrication and packaging. A) Start with SOI wafer. B) Etch sensor structure. C) Etch cavity and release floating element. 1) Start with copper clad FR4. 2) Mill coil and seal board with solder mask. 3) Open bond points and mill cavity for sensor die. Epoxy die in board and wire-bond.

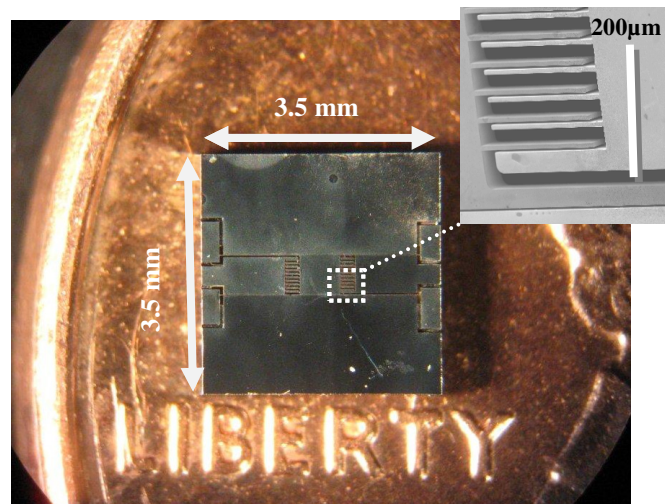


Figure 4: Photograph of capacitive shear stress sensor with SEM close up of comb fingers.

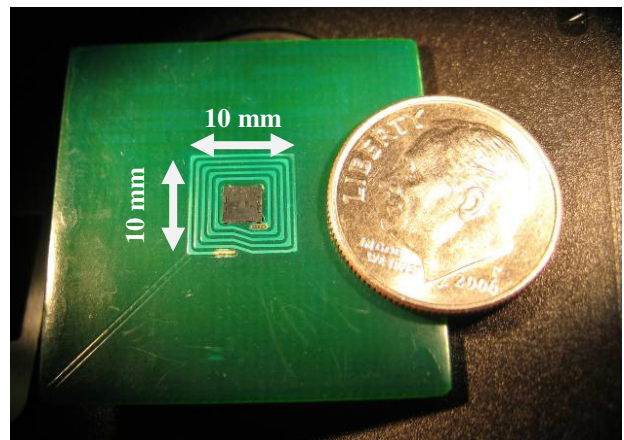


Figure 5: Hybrid packaged sensor integrating PCB coil with MEMS capacitive shear stress sensor. Sensor and coil form second order LC resonator.

## EXPERIMENTAL RESULTS

### Test Setup

The sensor PCB tank was mounted in a Lucite plug fixture and inserted into a laminar flow cell for static shear stress characterization (Figure 6). The test fixture allows for flush mounting of the sensor on the side wall of the flow cell while minimizing sensor induced flow disturbance. A flow controller is used to set a steady flow rate, and the input shear is calculated (assuming 2D fully-developed Poiseuille flow) by,

$$\tau = -\frac{h}{2} \frac{dP}{dx}, \quad (3)$$

where  $\tau$  is shear,  $h = 1$  mm is the height of the chamber, and the differential pressure  $dP$  is measured by two pressure taps located  $x = 76.2$  mm apart. This experimental setup was limited to an input shear up to 1.6 Pa, even though the sensor was designed to operate up to 5 Pa.

A 12-mm-wide single-turn square loop antenna was fabricated on a second PCB. Frequency shifts were tracked by monitoring the reflection coefficient ( $S_{11}$ ) of the antenna with an Agilent 8719D network analyzer. The antenna was placed on the backside of the sensor tank PCB. When mounting the antenna to the test setup, the minimum gap ( $g$ ) between the antenna and the sensor inductor coil was 3 mm. This distance was limited by the 1.5 mm thickness of the FR4 used for both the device and the antenna. For testing, additional shims were added to change this distance between the two PCB's (from 3 mm to 11 mm) to evaluate the wireless range.

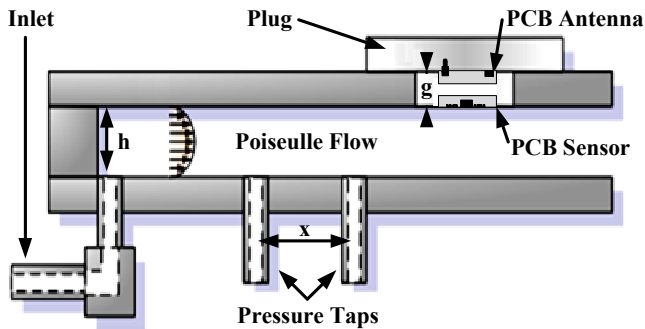


Figure 6: Schematic cross section of flow cell test setup used for calibration. The sensor fits into an acrylic plug for flush mounting.

### Static Shear Calibration

A calibration test was run by monitoring the resonant frequency of the device while incrementing the input shear from 0 to 1.6 Pa in 24 increments. The network analyzer was set to perform a linear sweep of  $S_{11}$  from 247.1 MHz to 261.1 MHz with 1601 frequency points. During the sweep a Heise pressure monitor recorded the differential pressure across the two pressure taps which was averaged and converted to shear using the known flow cell geometry and Equation 2. Ten sweeps were taken at each flow condition and averaged. The results of this test are shown in Figure 7, indicating a linear sensitivity of 219 kHz/Pa. This corresponds to a normalized sensitivity of 849 ppm/Pa, which is nearly an order of magnitude improvement on previous force sensors [3-6]. A large sensitivity is very important for shear stress measurement in air where the shear forces are extremely small, on

the order of 10  $\mu$ N for a typical subsonic test.

The minimum detectable frequency shift is limited by the frequency resolution of the network analyzer. A 16 MHz sweep was taken to capture the resonant dip, and given the 8719D's 1601 point limit, this translates to a frequency resolution of 10 kHz or 45.6 mPa.

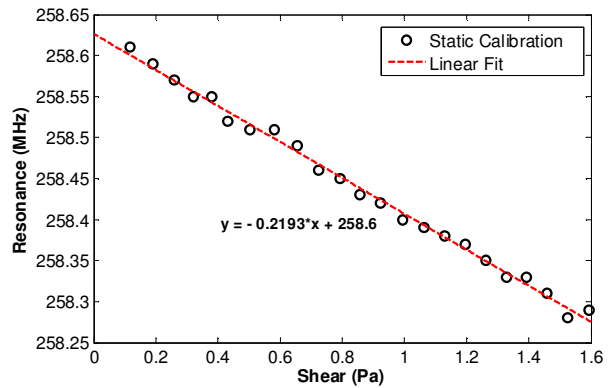


Figure 7: Frequency shift shows a linear response of 219 kHz per Pa input shear.

### Resonant Drift

A common problem with passive wireless sensors is frequency drift. To quantify this effect a three hour drift test was conducted under two flow conditions, as shown in Figure 8. The first test was with the flow turned off (blue data). The zero flow test shows a flat response within  $\pm 0.1\%$  variation for the entire test. Next a constant flow rate was set to maintain the shear level at 0.75 Pa for the entire three hour period (red data). This test showed a noticeable slope pointing to a negative frequency drift with time for the constant flow case. The random variation remained relatively constant indicating a source other than the sensor. Further investigation revealed that the flow controller itself was in fact drifting in time. The input shear for the flow test is plotted (green data) on the secondary axis in Figure 8. Future work will involve including a feedback loop in the flow controller to maintain a constant shear. The stability demonstrated by this sensor is encouraging for use in long tests runs extending for several hours.

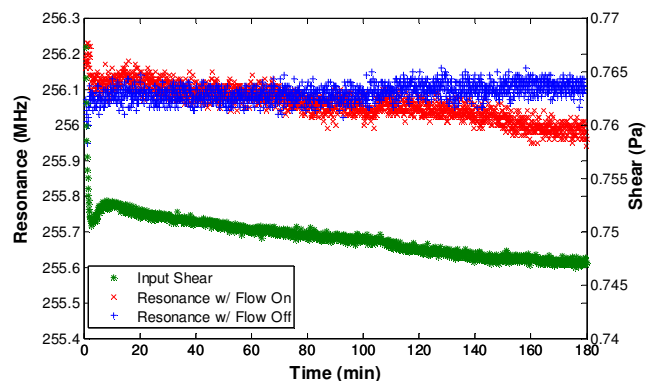


Figure 8: Stability test results show sensor resonant frequency with no input and with constant flow. The input shear for the constant flow test is plotted on the secondary axis.

## Effective Wireless Range

Another metric of interest for a wireless sensor is the effective range of the device. The maximum wireless range has serious implications for the successful implementation of the device in any useful application. To test the range of the sensor, the gap between the coil and the antenna was incremented from the minimum of 3 mm (limited by PCB thickness) to 11 mm where the resonant peak was not discernable. The maximum power of the 8719D, which was limited to 5 dBm or 3.4 mW, was used to perform all measurements.

At each gap height a calibration was performed as described in the wireless calibration section above. The resonant peak magnitude was also measured. The peak height was normalized by the maximum peak height found with the minimum gap of 3 mm (Figure 9). The signal strength decays exponentially with distance as expected for electromagnetic coupling of the sensor to the antenna. Even with proper network analyzer correction performed before each measurement, there is some naturally occurring frequency shaping as seen in Figure 1, above 350 MHz and below 150 MHz. The calibration becomes unreliable when the resonant peak is reduced to the same magnitude as these frequency artifacts. This is defined as the noise floor for the signal strength in the range test and is indicated by the blue line in Figure 9. The effective range for this configuration with this specific network analyzer is around 8 mm, which should be adequate for many test application where the airfoil skin or pipe wall is the limiting factor for sensor to antenna separation. This range requires that any material separating the antenna from the sensor is of a dielectric nature.

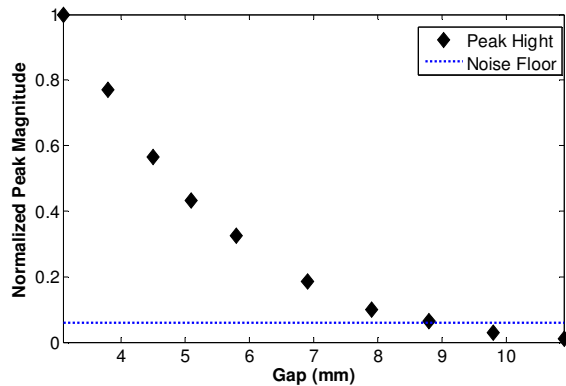


Figure 9: Wireless range test showing exponential decrease in resonant signal level with increasing gap. Maximum range is defined at the crossing of the peak height with the noise floor.

## CONCLUSIONS

This paper presented a wireless shear stress sensor for flow characterization. A summary of the sensor parameters and performance metrics is shown in Table 1 for comparison with previous work on other wireless force sensors. The device was shown to have a linear sensitivity of 219 kHz/Pa at 258 MHz, giving a normalized sensitivity of 849 ppm/Pa, making it one of the most sensitive devices developed. The minimum detectable signal (limited by instrumentation) was found to be 45 mPa. This corresponds to 1.6 nm displacements of the floating element and 45 nN shear forces. Considering the sensor was designed for 5 Pa this gives the sensor 40 dB dynamic range. The stability of the sensor makes it useful for taking mean shear measurements over time periods of at least a few hours.

Table 1: Wireless sensor parameters and performance metrics.

Wireless Sensor	$C_o$ (pF)	$f_o$ (MHz)	$Q$	$S$ (kHz/Pa)	$S_n$ (ppm/Pa)
Reported	1.3	258	6	219	849
Park [3]	3.0	120		15*	125*
Akar [4]	3.7	76	8	0.9	11.9
Fonseca [5]	5 <sup>†</sup>	51	77	0.04	1.2
Chen [6]	3.1	150	5	8.6	57

\*Theoretically predicted, †Estimated from reported geometry

Future work is focused on expanding this measurement approach to multiple sensor arrays. Giving each sensor its own characteristic bandwidth, a single antenna will be able to interrogate the entire array.

## ACKNOWLEDGMENTS

The authors would like to thank the National Aeronautics and Space Administration (NASA) for their financial support. This project was funded under a Subsonic Fixed Wing Project Grant No. NNX07AB27A and a NASA Graduate Student Research Project Fellowship No. NX07AT43H.

## REFERENCES

- [1] J.W. Naughton and M. Sheplak, "Modern Development in Shear Stress Measurement," *Progress in Aerospace Science*, 38, 515-570, (2002).
- [2] V. Chandrasekharan, J. Sells, J. Meloy, D.P. Arnold, and M. Sheplak, "A Metal-on-Silicon Differential Capacitive Shear Stress Sensor," *Solid-State Sensor, Actuator, and Microsystems Workshop*, Denver, OR, (2009), pp. 1537-1540
- [3] E. Park, J. Yoon, and E. Yoon, "Hermetically Sealed Inductor-Capacitor (LC) Resonator for Remote Pressure Monitoring," *Japanese Journal of Applied Physics*, 7124-7128, (1998).
- [4] O. Akar, T. Akin, K. Najafi, "A Wireless Batch Sealed Absolute Capacitive Pressure Sensor," *Sensors and Actuators A: Physical*, 95, 29-38 (2001).
- [5] M. A. Fonseca, J. Kroh, J. White, and M.G. Allen, "Flexible Wireless Passive Pressure Sensors for Biomedical Applications," *Solid-State Sensor, Actuator, and Microsystems Workshop*, Hilton Head Island, SC, (2006), pp. 37-42.
- [6] P. Chen, D.C. Rodger, S. Saati, M.S. Humayun, and T. Chong, "Microfabricated Implantable Parylene-Based Wireless Passive Intraocular Pressure Sensors," *Journal of Microelectromechanical Systems*, 17, 1342-1351, (2008).
- [7] T. J. Harpster, B. Stark, and K. Najafi, "A Passive Wireless Integrated Humidity Sensor," *Sensors and Actuators A: Physical*, 95, 100-107, (2002).
- [8] K.G. Ong, K. Zeng, and C.A. Grimes, "A Wireless, Passive Carbon Nanotube-Based Gas Sensor," *IEEE Sensors Journal*, 2, 82-88, (2002).

## CONTACT

Jeremy Sells, tel: +1-352-392-7653; [jsells@ufl.edu](mailto:jsells@ufl.edu)

# REAL-TIME HERMITICITY DETECTION USING TITANIUM DIOXIDE THIN FILM RESISTOR AS BOTH OXYGEN AND PRESSURE SENSORS

Firas Sammoura\* and Ken Yang

The Micromachined Product Division, Analog Devices, Wilmington, Massachusetts, USA

## ABSTRACT

In-situ hermiticity detection using Titanium dioxide ( $\text{TiO}_2$ ) thin film resistors has been investigated for the first time. Titanium dioxide is widely used as an oxygen sensor, with accurate partial pressure reading at high temperatures. In addition to being oxygen sensitive at room temperature,  $\text{TiO}_2$  thin film resistors were found to be excellent pressure gauges at typical bonding pressures in the range of 1 Torr to 760 Torr. Combining the pressure sensitivity with the oxygen selectivity, Titanium dioxide thin film resistors constitute perfect hermiticity solutions for MEMS devices capped in an oxygen deficient environment at sub-atmospheric pressures. This unprecedented demonstration opens up new opportunities for monitoring real-time hermiticity in packaged MEMS devices, understanding the various failure modes during operation, and implementing the necessary diagnostic solutions.

## INTRODUCTION

Hermiticity constitutes a critical precursor for the reliability of MEMS sensors. Ensuring hermiticity is a mandatory requirement for most encapsulated MEMS devices including automotive-grade sensors. Hermiticity failures emanates from two major sources: (1) Defects in the bonding material and (2) Cracks due to stress. A breach in hermiticity can change the gas content and pressure surrounding the MEMS device which in turns leads to performance shifts. In our previous work [1], we have found that any slight modification in the water content of the capped MEMS devices can lead to failure due to stiction. In addition, it is reported that the performance of RF MEMS switches is deleteriously affected when the devices are non-hermitically sealed due to the effect of humidity and small particles [2].

The state of the art hermiticity detection technique is Helium presence determination using mass spectroscopy [3]. However, this technique is not suitable for micro-cavities due to fast Helium diffusion rate. Several hermiticity detection techniques have been investigated. Elger *et al.* have investigated hermiticity existence optically using a non-contact profilometer with a chromatic confocal sensor. The pressure change inside the sealed cavity due to gas leakage causes a built-in membrane to deflect [4]. Pinter *et al.* have developed the technique of measuring the gas viscosity inside the cavity by the Quality factor (Q) of a vibratory device built inside the sealed MEMS devices [5]. Any breach in hermiticity will cause viscosity to change which is consequently detected by Quality factor shift. In addition, Lellouchi *et al.* adopted a Fourier transform infrared spectroscopy (FTIR) to quantify the concentration and composition of the gases in the sealed cavity [6]. These techniques do not allow for monitoring hermiticity in real-time during use and require expensive analysis equipment.

Titanium dioxide is an intrinsic semiconductor whose conductivity varies with the change in the concentration of the oxygen gas in the surrounding environment when deposited in the Anatastase phase [7]. In this work, Titanium dioxide thin films are used to quantify the pressure and oxygen content of the sealant gas by simple resistance measurement enabling real-time hermiticity checking both during manufacturing and in-operation. In contrast to the previous publications, this is the first paper that investigates

in-situ hermiticity detection of sealed MEMS devices using  $\text{TiO}_2$  thin film resistors integrated inside the MEMS cavity for devices capped in a sub- atmospheric pressure and in an oxygen deficient environment.

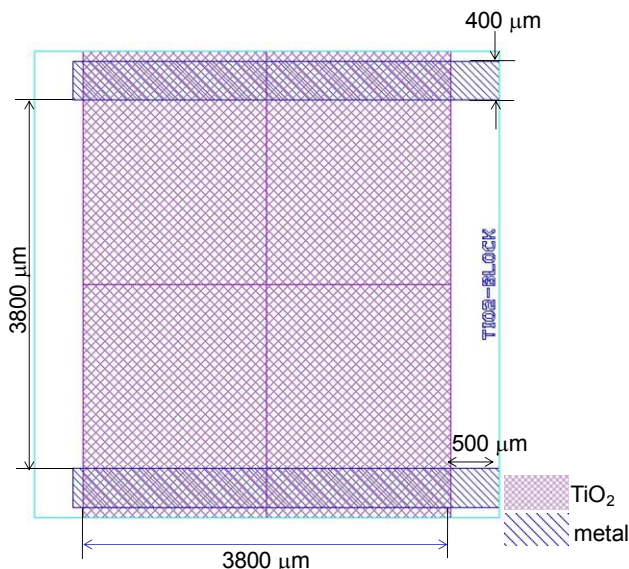


Figure 1: Layout schematic of a  $\text{TiO}_2$  test structure.

## FABRICATION PROCESS

A Titanium dioxide thin film with metal electrodes was built on insulated substrate. The test structure was measured in a sealed pressure chamber that mimics the environment within a sealed MEMS device in order to validate the proposed hermiticity detection concept. Figure 1 shows the layout schematic of a  $3800\mu\text{m} \times 3800\mu\text{m}$   $\text{TiO}_2$  block test structure. The fabrication process starts by thermally growing  $1.47\mu\text{m}$  of oxide followed by the deposition of  $1200\text{\AA}$  of stoichiometric nitride to form the insulation layers. A  $2200\text{\AA}$  thick Titanium dioxide film was then deposited on the wafer using Plasma Enhanced Chemical Vapor Deposition (PECVD), and consequently annealed at  $500^\circ\text{C}$  for 30min in a vacuum environment in order to form the Anatastase phase [8]. The  $\text{TiO}_2$  film was then patterned with a wet etchant composed of 5:1:4  $\text{HNO}_3$ : HF:  $\text{H}_2\text{O}$  at  $70^\circ\text{C}$ . A  $200\text{\AA}/2000\text{\AA}$  of Ti/Au was then deposited and patterned by lift-off to form metal contacts to the  $\text{TiO}_2$  film resistor.

The integration of the  $\text{TiO}_2$  thin film resistors inside a capped MEMS sensor is proposed to be achieved using *Through Silicon Via* (TSV) technology as shown in the process flow outlined in Figure 2. The  $\text{TiO}_2$  thin film is deposited on the cap side of the sealed MEMS devices. The processing of the cap wafer starts by forming front side alignment marks on the front side of the wafer. Vias are then etched on the back side of the wafer up to a depth of two-thirds the total wafer thickness using Deep Reactive Ion Etching (DRIE). Via isolation is achieved by a thin thermally grown oxide of  $250\text{nm}$  in thickness. The cavity is later filled with a thin conductor seed layer followed by copper electroplating. The deposited copper is grinded down to the underlying oxide liner



using Chemical Mechanical Polishing (CMP). Titanium dioxide is deposited on the back side of the wafer and the front side is grinded down using CMP to get access to the copper bond pads. The cap wafer is finally bonded to the device wafer.

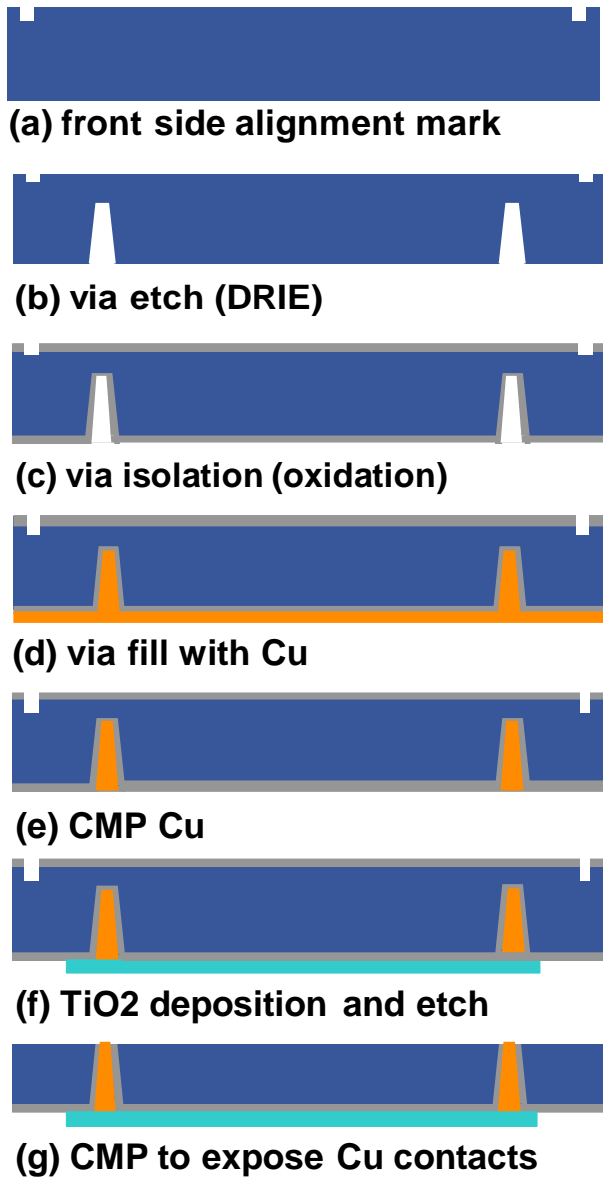


Figure 2: Fabrication Process of TiO<sub>2</sub> thin film resistors on cap side using Through Silicon Via (TSV) technology.

## RESULTS AND DISCUSSION

The thin film resistor were tested in a Lake Shore low temperature probe chamber Model CPX-HF equipped with a temperature controller Model 332 with built-in probes and gas inlets, where both O<sub>2</sub> and N<sub>2</sub> gases can be flown and chamber pressure was monitored as shown in Figure 3. An Agilent B1500A parametric semiconductor analyzer was used to measure the I-V curves necessary to extract the thin film resistivity where the voltage was swept between 0 and 1.5V at an increment of 50mV.

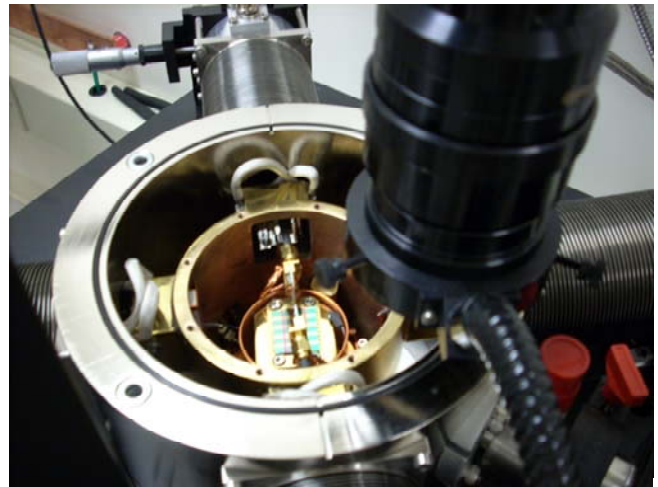


Figure 3: Digital picture showing testing setup of TiO<sub>2</sub> thin film resistors inside an enclosed chamber.

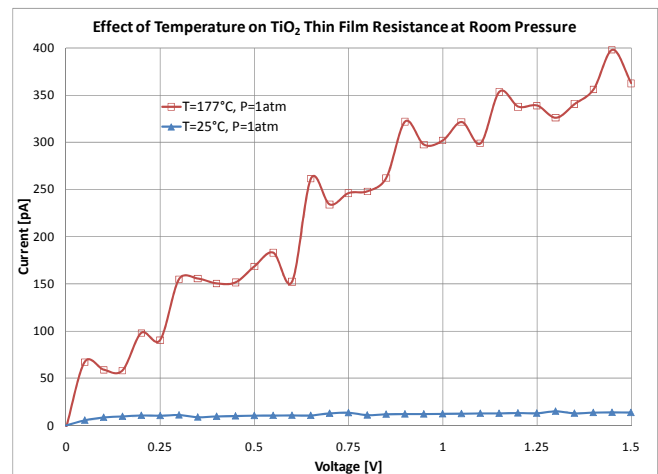


Figure 4: The TiO<sub>2</sub> thin film resistance vs. temperature at atmospheric pressure.

The resistance of the Titanium dioxide thin film resistor was measured at both room temperature (25°C) and 177°C as shown in Figure 4. Both tests were done are normal pressure of 1 atm with the chamber lid open. At room temperature the resistance of the thin film resistor as outlined in the schematic shown in Figure 1 was measured as 200GΩ. The resistivity can be then deduced as follows:

$$R = \frac{\rho W t}{L} \quad (1)$$

where R is the resistance of the thin film resistor, ρ is the film resistivity, W is the width of the resistor with a value 3800 μm for this resistor structure, t is the thickness of the film with a value of 220nm, and L is the resistor length with a value of 3800 μm. As such the resistivity of the Titanium dioxide film at room temperature is calculated as 4.4x10<sup>6</sup> Ω-cm. At 177°C, the resistance is measured 4GΩ, and as such the resistivity is calculated as 88x10<sup>3</sup> Ω-cm. The resistivity decreased 50 times as the chuck temperature increased from room temperature to 177°C

at atmospheric pressure as can be inferred from the I-V curves shown in Figure 4. The resistivity of sputtered thin film of Titanium dioxide has been reported in the literature with values of  $4.95 \times 10^6 \Omega\text{-cm}$  and  $20 \times 10^3 \Omega\text{-cm}$  at  $25^\circ\text{C}$  and  $177^\circ\text{C}$ , respectively [9]. The value measured at room temperature is very close to the value reported in the literature. The discrepancy between the measured value and the value reported in the literature at  $177^\circ\text{C}$  is attributed to the lower equilibrium temperature of the Titanium dioxide thin film due to the silicon substrate and epoxy glue separation between the heated chuck and the tested sample.

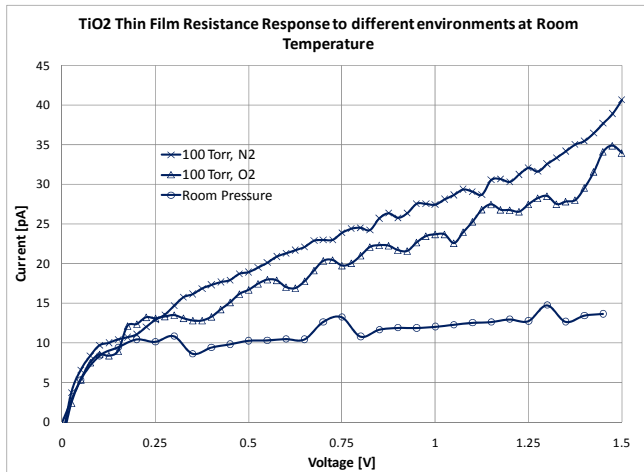


Figure 5: Response of  $\text{TiO}_2$  thin film resistors capped at 100 Torr of pure  $\text{N}_2$ , 100 Torr of pure  $\text{O}_2$ , and normal room pressure at room temperature of  $25^\circ\text{C}$ .

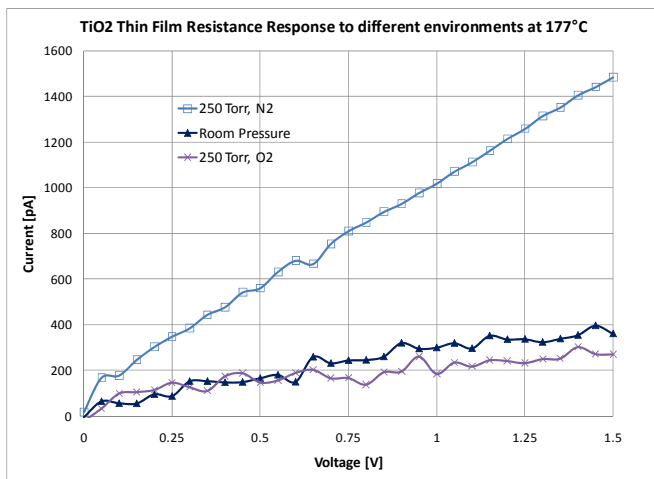


Figure 6: Response of  $\text{TiO}_2$  thin film resistors capped at 250 Torr of pure  $\text{N}_2$ , 250 Torr of pure  $\text{O}_2$ , and room pressure at a temperature of  $177^\circ\text{C}$ .

In order to reproduce micro-cavity gas environment conditions, the chamber was evacuated and then filled with pure nitrogen gas ( $\text{N}_2$ ) up to 100 Torr pressure, a typical gas content and pressure level of many capped MEMS devices. As shown in Figure 5, current flowing through the  $\text{TiO}_2$  thin film at 1.5V DC Bias and room temperature dropped from 40pA when bonding environment to roughly 10pA when the control chamber was opened and exposed to atmospheric pressure. As such the resistance dropped 4 times as hermeticity was breached and sensor

environment changed from pure Nitrogen at 100 Torr to a room temperature and pressure environment. The resistivity of the Titanium dioxide thin film was also measured at 100 Torr of pure Oxygen gas. There is a distinct shift in thin film resistivity as shown in Figure 5 with the Titanium dioxide resistance increasing from  $48\text{G}\Omega$  in a Nitrogen environment to  $58\text{G}\Omega$  in an Oxygen environment. This shows the selectivity of the thin film sensor to oxygen at room temperature.

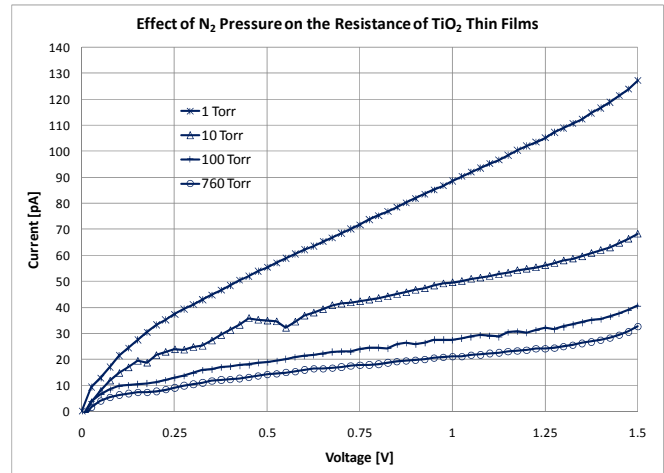


Figure 7:  $\text{TiO}_2$  thin film resistors I-V curves for varying  $\text{N}_2$  pressures showing increase in resistance as  $\text{N}_2$  pressure inside the control chamber increases.

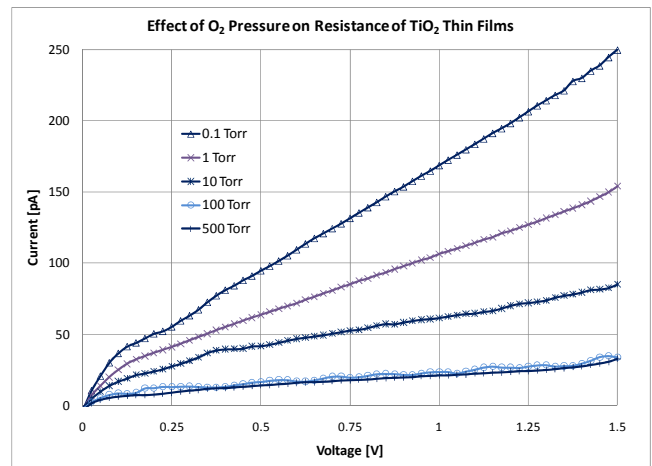


Figure 8:  $\text{TiO}_2$  thin film resistors I-V curves for varying  $\text{O}_2$  pressures showing increase in resistance as  $\text{O}_2$  pressure inside the control chamber increases.

As the temperature increased to  $177^\circ\text{C}$ , the current flowing through the  $\text{TiO}_2$  thin film dropped from 1480pA for a hermetically sealed die capped at 250 Torr of pure Nitrogen to 360pA for a leaky die exposed to atmospheric pressure as shown in Figure 6. This corresponds to a resistance drop from roughly  $4\text{G}\Omega$  to  $1\text{G}\Omega$  as hermeticity is breached. Response of  $\text{TiO}_2$  thin film resistors to pure  $\text{O}_2$  environment with same pressure as pure  $\text{N}_2$  capped devices is also measured. The current flowing through the  $\text{TiO}_2$  thin film resistor was 270pA at 1.5V of bias. This corresponds to a resistance value of  $5.54\text{G}\Omega$ . The higher resistance measured in a pure oxygen environment at a pressure

level of 250 Torr relative to the value measured at normal atmospheric conditions is an indication of sensitivity of the thin film to oxygen content in the surrounding environment.

The variation of  $\text{TiO}_2$  film resistivity to control chamber pressure was studied. As shown in Figure 7,  $\text{TiO}_2$  thin film resistors act as perfect pressure sensors at room temperature and  $\text{N}_2$  pressure varying from 1 Torr to 760 Torr. The resistance increased as the nitrogen pressure increased. The resistance values were 0.313G $\Omega$ , 0.786G $\Omega$ , 1.078G $\Omega$ , and 1.72G $\Omega$ , at a pressure of 1 Torr, 10 Torr, 100 Torr, and 760 Torr, respectively.

In addition,  $\text{TiO}_2$  thin film resistors are sensitive to  $\text{O}_2$  pressure varying from 0.1 Torr to 100 Torr, with signal saturating above 100 Torr indicating sensor selectivity to  $\text{O}_2$  at room temperature. The resistance increased as the oxygen pressure increased. The resistance values were 0.533G $\Omega$ , 2.132G $\Omega$ , and 4.000G $\Omega$ , and 6.993G $\Omega$ , at a pressure of 0.1 Torr, 1 Torr, 10 Torr, and 100 Torr, respectively. After 100 Torr, the measured I-V overlapped indicating saturation in the output signal. It is also observed that the resistance values at the same pressure are higher in the presence of the oxygen gas vs. nitrogen gas.

The transduction phenomenon of Titanium dioxide thin films and their oxygen sensitivity is a surface phenomenon. A structure with parallel  $\text{TiO}_2$  line resistors is proposed in order to maximize open surface area as shown in Figure 9.

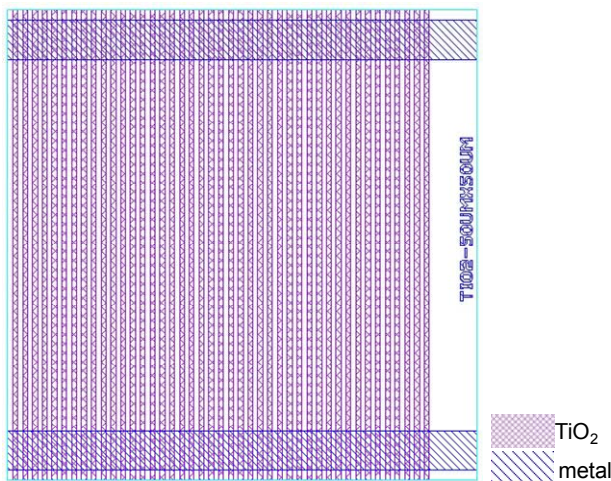


Figure 9: Layout schematic of a proposed  $\text{TiO}_2$  test structure with improved oxygen sensitivity.

## CONCLUSION

A real-time hermeticity solution has been investigated for the first time. The proposed technique is based on the resistance measurement of a thin film Titanium dioxide resistor at a DC bias voltage as small as 1V. Titanium dioxide is an extrinsic semiconductor with some missing oxygen atoms in its crystalline structure. The variation of the oxygen concentration in the surrounding environment will modulate the resistivity of the thin film due to the change in the free carrier concentration. MEMS devices capped at sub-atmospheric pressure in an oxygen deficient environment will experience an abrupt change in built-in Titanium dioxide resistance as the film is exposed to atmospheric pressure and a 21% oxygen concentration. This is a clear indication of hermeticity and it can be used to monitor MEMS devices during operation versus the other techniques which check for hermeticity during manufacturing. Titanium dioxide thin films with metal electrode were built on insulated substrates, and their behavior to varying gas pressures and composition was studied in a control

chamber. The testing results show clear distinction between resistance of Titanium dioxide films at room temperature at pressure versus environments with pure nitrogen gas and sub-atmospheric pressure levels. The thin films were very sensitive to both nitrogen and oxygen gas pressures in the range between 1 Torr to 760 Torr and 0.1 Torr to 100 Torr, respectively. In addition, the thin films were selective to oxygen with higher resistances measured at the same pressure level for oxygen gas as compared to nitrogen gas. A process flow to integrate the Titanium dioxide with the MEMS capping process is proposed using Through Silicon Via (TSV) technology with the thin film built on the cap side of the sensor. It is envisioned that this novel study will resolve many issues related to hermeticity by enabling in-use hermeticity monitoring in order to understand the root-cause of failures in field and part returns.

## ACKNOWLEDGEMENTS

The authors would like to thank Dr. Noah Clay from the Harvard Center for Nanotechnology Systems (CNS) for his help in the fabrication and testing of the samples. The authors would also like to acknowledge Dr. Mehmet Hancer, Dr. Bill Sawyer, Dr. Li Chen, Dr. Christine Tsau, and Mr. Kieran Nunan from the Micromachined Product Division at Analog Devices for their valuable discussion and feedback.

## REFERENCES

- [1] F. Sammoura, A. Sparks, W. Sawyer, M. Bhagavat, M. Judy, and K. Yang, "Stiction in Low Humidity Environment," the Proceedings of 22<sup>nd</sup> IEEE Micro Electro Mechanical Systems Conference, pp. 88-91, Sorrento, Italy, January 25-29, 2009.
- [2] C. Goldsmith, T. H. Lin, W. R. Powers, and B. Norvell, "Micromechanical membrane switches for microwave application," *IEEE MTT-S International Microwave Symposium Digest*, pp. 91-94, Orlando, FL, May 1996.
- [3] R. R. Tummala, *Microelectronics Packaging Handbook*, Van Reinhold, New York, USA, 1989.
- [4] G. Elger, L. Shiv, N. Nikac, F. Mueller, R. Liebe, M. Grigat, and Matthias Heschel, "Optical Leak Detection for Wafer Level Hermeticity Testing," *IEEE/SEMI Int'l Electronics Manufacturing Technology Symposium*, no. 29, pp. 326-331, San Jose, 2004.
- [5] S. Pinter, "Method for Checking the Sealing of a Package and Apparatus for Measuring Viscosity," US Patent No. 5,872,309.
- [6] D. Lellouchi, J. Dhennin, X. Lafontan, D. Veyrie, J. F. Le Neal, and F. Presseccq, "A New Method for the Hermeticity Testing of Wafer-Level Packaging," *Journal of Microelectronics and Microengineering*, vol. 20, no. 2, February 2010.
- [7] E. M. Logothetis and W. J. Kaiser, "TiO<sub>2</sub> Film Oxygen Sensors Made by Chemical Vapor Deposition from Organometallics," *Sensors and Actuators*, vol. 4, pp. 333-340, 1983.
- [8] M. D. Stamme, "On the Dielectric Properties of DC Magnetron TiO<sub>2</sub> Thin Films," *Applied Surface Science*, pp. 317-332, vol. 218, April 2003.
- [9] A. A. Akl, H. Kamal, and K. Abdel-Hady, "Fabrication and Characterization of Sputtered Titanium Dioxide Films," *Applied Surface Science*, pp. 8651-8656, vol. 252, no. 24, October 2006.

## CONTACT

\*Firas Sammoura, 804 Woburn Street, Wilmington, MA 01887; Tel +1-781-937-2244; firas.sammoura@analog.com

# WICKING OPTIMIZATION FOR THERMAL COOLING -WITH A TITANIUM BASED HEAT PIPE SYSTEM

C. Ding<sup>1\*</sup>, P. Bogorzi<sup>2</sup>, M. Sigurdson<sup>2</sup>, C.D. Meinhart<sup>2</sup> and N.C. MacDonald<sup>2</sup>

<sup>1</sup>California Nanosystems Institute, UCSB, Santa Barbara, CA, USA

<sup>2</sup>Department of Mechanical Engineering, UCSB, Santa Barbara, CA, USA

## ABSTRACT

Micromachined titanium pillars with nanoscale titania structures on surfaces are adopted to form wicking material for a proposed flat heat pipe system. This unique bitextured titania structure (BTS) provides a superhydrophilic surface and improves the wicking ability of the titanium based pillar arrays. Experimental studies on optimizing the wicking behaviors of BTS pillar arrays are reported in this work. Oxidization and plating techniques are applied to modify the surface properties and pillar/gap dimensions of the wicks. A titanium based flat heat pipe is proposed to integrate the BTS wicks and study the concept of this titanium based flat heat pipe architecture. A thermal conductivity  $\sim 500\text{W/m-K}$  (with contact resistance included) is achieved at around  $118^\circ\text{C}$ . The chamber of this Ti heat pipe is formed by hermetically welding two substrates together using laser welding technique. The hermiticity performance of the chamber is studied with helium leaking approaches. A leaking rate of  $3.4 \times 10^{-10} \text{ atm.cm}^3/\text{s}$  is achieved for a chamber of  $\sim 170\mu\text{L}$  in volume.

## INTRODUCTION

### Flat Titanium Heat Pipe Architecture

Flat heat pipes adopt a relatively much larger geometry in planar direction than traditional heat pipes to provide a potential for transporting or spreading a large amount of heat. They are finding their ways in the thermal cooling systems for applications such as computer chips, circuit boards, and space based radar systems which consume a high density of power. A flat heat pipe has wicking materials on the interior walls of its chamber to automatically pump the cooling fluids from the heat sink side to the evaporator side when transporting heat. The wicking materials enable heat pipes some unique functions that thermal siphons could not achieve [1]. The flat geometry allows micro/nano-scale machining techniques to be applied for forming unique wicking materials such as carbon nanotubes, sintered copper, micromachined structures, etc..

Besides wicking materials flat heat pipes have two other important components: a hermetically-sealed cavity and a working fluid. The cavity must be hermetically sealed to avoid input of any noncondensable gases by leaking. Ideally, only different phases of a working fluid are allowed in the chamber. The merit number is used to select a working fluid [2] in Anderson's work for heat pipe systems. In this work water is adopted as the working fluid.

During operation, heat is applied to the hot side of a wicking substrate, causing evaporation. The water vapor is transported to a cold region and condensed by rejecting heat with a heat sink. The condensed water is then pumped back to the evaporating region by the wicking material which provides capillary force when contacting with working fluids. This process is continuous forming different steady states during operations. Figure 1 shows the schematic of a laser-welded titanium flat heat pipe architecture. Fabrication of the device will be described in the latter part of this paper. This device is enhanced by adding the Ti posts to support the relatively thin sealing substrate, which avoids the volume changes when chamber pressure is lower than the outside pressure.

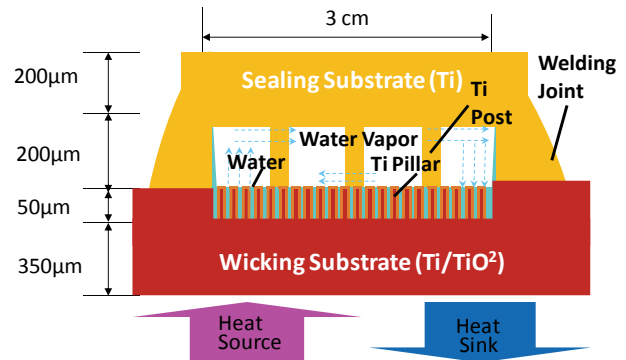


Figure 1: Schematic of the titanium based flat heat pipe. Note that the Ti posts function as supporting structure for the sealing substrate.

### Wetting on Textured Surfaces

The following Wenzel equation [3], predicts that rough surfaces possibly help enhance the wettability of high energy solid surfaces, where  $r$  is the roughness number defined in Figure 2.

$$\cos\theta_e^r = r\cos\theta_e \quad (1)$$

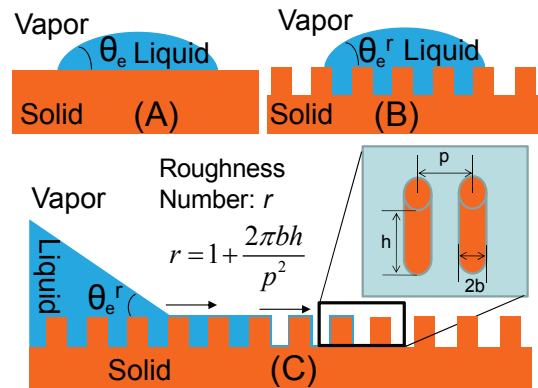


Figure 2: Flow of the impregnating film at the front boundary. Figure A shows the Young's contact angle; Figure B and C show the static and dynamic cases of the wetting on solid surfaces.

However the rough surfaces help with wetting only when the contact angle (shown in Fig. 2A) is less than  $\pi/2$ . For a droplet to sit on a smooth and flat surface, the contact angle is governed by the Young's equation:

$$\cos\theta_e = \frac{\gamma_{SV} - \gamma_{SL}}{\gamma} \quad (2)$$

where  $\theta_e$  is the equilibrium contact angle,  $\gamma_{SV}$ ,  $\gamma_{SL}$ , and  $\gamma$ , are the interface energy at the solid-vapor, solid-liquid, and

liquid-vapor interfaces, respectively. For the hydrophilic case,  $\theta_e < \pi/2$ .

If Young's contact angle is larger than  $\pi/2$ , the roughness will increase the apparent contact angle, leading to superhydrophobic/super-antiwetting case [4]. Since the roughness modifies the value of apparent contact angle superwetting can be achieved by tuning the roughness. For the complete wetting case, the contact angle,  $\theta_e^r$ , will decrease to zero once the fluid fully wets the wick structure. Our idea is to make micromachined pillars to obtain large surface roughness and optimize the wetting by modifying the pillar dimensions. We denote such a mono-textured surface by its pillar density  $\phi_s$  and roughness  $r$ . Provided that the case of wetting as in Fig. 2, the pillars guide water liquid among the arrays and form in a phenomenon similar to wicking but more accurately hemiwicking which is intermediate between spreading and imbibition [5].

The wicking material is usually designed to provide high capillary force on the spreading liquid. The capillary force,  $F=\gamma(r-1)$ , can be derived using virtual energy method where  $\gamma$  is the surface tension of the wicking fluid. Detailed studies and discussions about wicking dynamics of fluid on textured structured can be found in previous works [5-7]. Although capillary can be well defined, the friction force between fluid and solid surfaces is relatively difficult of measure and analytically define for complicated structures.

## FABRICATION

Different kinds of materials such as carbon nanotubes [8], nanowires, sintered copper [9], and micromachined channels have been investigated as wicking materials. In this work, we adopt recently developed titanium bulk micromachining techniques [10] to fabricate titanium pillar arrays as wicking materials, then we modify the micromachined pillars to form micro-&nano-textured (bitextured) titania structures (BTS) (Fig. 3) on all surfaces.

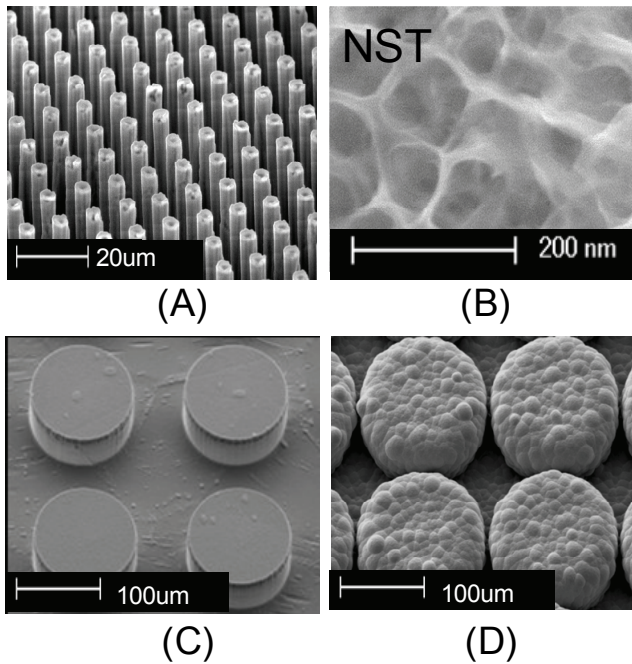


Figure 3: SEM photograph of the  $5\mu\text{m}/5\mu\text{m}$  (Dia./Gap) BTS and  $100\mu\text{m}/50\mu\text{m}$  (Dia./Gap) BTS. All pillars are  $\sim 50\mu\text{m}$  high. The nanostructured titania (NST, Fig. 3B) covers all the pillar surfaces and the bottom floor on Fig. 3A and Figure 3C. Figure 3D shows

the SEM photograph of Figure 3C after gold plating.

Two dimensions were fabricated with radius/gap of  $5\mu\text{m}/5\mu\text{m}$  and  $100\mu\text{m}/50\mu\text{m}$ . Further, we modified the surfaces of both dimensions to form BTS. Then we plated gold (Fig. 3D) on the  $100\mu\text{m}/50\mu\text{m}$  arrays to tune the dimensions and formed  $\sim 145\mu\text{m}/5\mu\text{m}$  surfaces to tune the structure dimensions and their wettabilities. Detailed fabrication about bulk micromachining of the Ti pillar arrays and BTS formation can be found in [11].

## WETTING EXPERIMENTS FOR OPTIMIZATION

The experiments were done by bringing a drop of water ( $\sim 40\mu\text{L}$ ) into contact with our samples. Then the flows were recorded with a camera (Nikon D90). The wetting results show all samples are completely wettable with DI water. The recorded video was decomposed to study the travel distance of the front boundary radial path ( $x$ ) of the spreading water as a function of time ( $t$ ).

$$x^2 = Dt \quad (3)$$

A curve of the form equation 3 inspired by Washburn equation [12], is well fitted to the collected distance-vs-time data shown in Fig. 4, where  $D$  is defined to be dynamic coefficient.

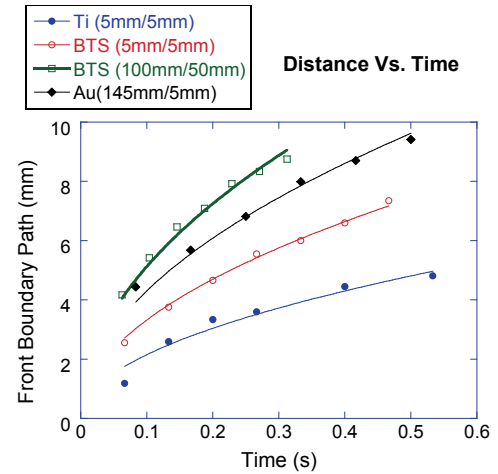


Figure 4: The front boundary flow path vs. time of the four experiments.

The experimental data generate the dynamic coefficients for different wetting experiments listed in Table 1. We proposed to use the velocity profiles as shown in Figure 4 for wicking material performance/design.

Table 1: Dynamic coefficient comparison.

Items	Ti Only $5\mu\text{m}/5\mu\text{m}$	BTS $5\mu\text{m}/5\mu\text{m}$	BTS $100\mu\text{m}/50\mu\text{m}$	BTS/Au $145\mu\text{m}/5\mu\text{m}$
SQRT(D) ( $\text{m}/\text{s}^{1/2}$ )	6.5E-3	1.05E-2	1.62E-2	1.36E-2
D/2 ( $\text{m}^2/\text{s}$ )	2.12E-5	5.50E-5	1.31E-4	9.25E-5

The Velocity-Vs-Distance profile is found by differentiating the fitted curve,  $x^2 = Dt$ , to be:

$$\frac{dx}{dt} = \frac{D}{2x} \quad (3)$$

Equation (3) shows similar diffusive spreading behavior predicted by Washburn equation. Figure 5 shows the compared corresponding velocity profiles by plotting the derived fitting curves from Fig. 4. The super wetting ability of BTS wicking materials not only improve thermal conductivity, but may also help avoid dry-out phenomena of heat pipes.

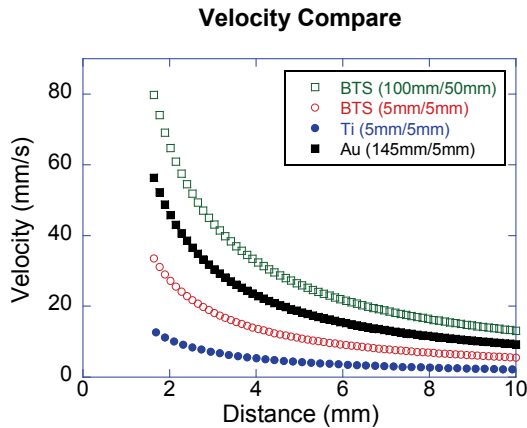


Figure 5: Comparison of the velocity profiles. The wetting (in radius direction) is much faster at the very beginning.

From Fig. 5 it shows that pillar arrays with BTS (100μm/50μm, Dia/Gap) has the fastest traveling speed comparing to all the other three wicking materials. This indicates that wicking materials can be designed and/or modified to provide a broad range of wetting speeds for the wicking needs of micro-fluid based pumping systems. Also these wicking materials provide different capillary limits when heated at elevated temperature. From the experimental studies shown in Fig. 5 we decide to integrate the wicking material shown in Fig. 3C for its fastest wetting speed into the proposed flat titanium heat pipe shown in Fig. 1.

### PACKAGING AND THERMAL PERFORMANCE

To investigate the thermal performance of the proposed heat pipe device we packaged two separate substrates (sealing substrate and wicking substrate) as shown in Fig. 1 using a pulsed wave YAG laser welder (Neodymium-Doped Yttrium Aluminum Garnet, Nd: Y3Al5O12) with a wavelength of 1064nm. The bottom substrate contains the wicking material as shown in Fig. 3C with an area of 3cmx3cm. The top substrate has a cavity (200μmx3cmx3cm) with 16 Ti posts evenly located on it for supporting purposes. The net volume of cavity is 170μL. Two charging tubes were welded onto the device with laser welding techniques. The device is then purged with pressurized water vapor for 15minute to eliminate the air inside the device. Then it was charged with ~40μL water so that the water level is about ~10μm above the pillar top surface. The final packaged device is shown in Fig. 6.

The device was tested with one side (0.5cmx3cm) to contact with heat source (copper block) and the other side (1cmx3cm) to contact with a heat sink (thermal electric cooler) via (copper block). Both copper blocks were brought into contact with the device via a thermal interface material (Arctic Silver 5). And the heat flow was monitored by two thermocouples at each copper block to confirm if the system is at steady state.

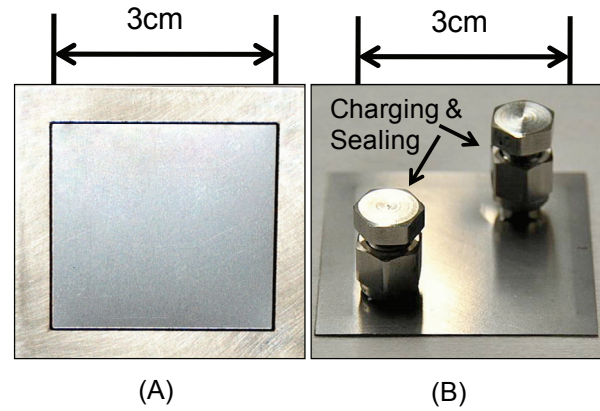


Figure 6: Laser welded Ti heat pipe with Figure (A) as backside and Figure (B) as front side where the two 1/8" charging tubes are sealed with Swagelok end caps.

A copper plane with similar dimensions was used to calibrate the measurement system. A maximum of conductivity 500.085W/m-K (with contact resistance included) was achieved with a steady state heat flow of 8.65W at 118°C on the heat source side of the heat pipe (shown in Fig. 6). Contact area and thermal interface material thickness were measured for calculation of the thermal contact resistances of the interface material. Assuming that the thermal contact resistances at different temperatures are the same then we get the above plot in Fig. 7 as the device thermal conductivity performance which gives a peak performance of ~700W/m-K at 118°C with the heat flow of 8.65W.

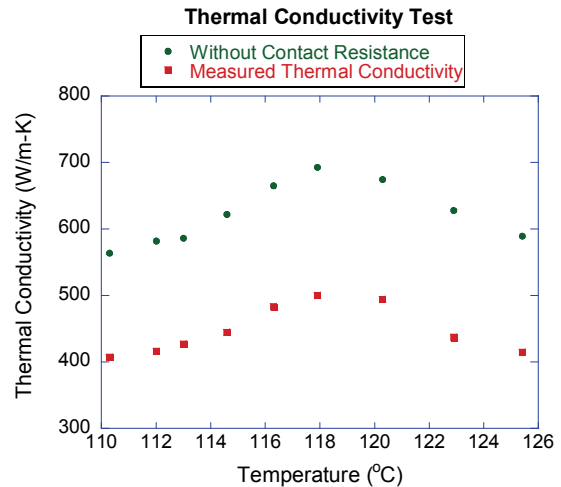


Figure 7: Thermal performance of the flat Ti heat pipe.

### HERMITICITY TEST

The titanium heat pipe architecture not only offers rigid, compatible [13] and light weight [14] building structure, but also provides the convenience of packaging at large scale thanks to the weldability of titanium substrates. The hermeticity research in this work was conducted by helium leaking rate test method based on MIL-STD-883E standard. The helium leak detector was used in this test is ASM 142 with a sniffing unit, and its minimum detectable helium leak rate is  $1 \times 10^{-11}$  atm.cm<sup>3</sup>/s. As shown in the schematic (Fig. 8) the test is conducted at room temperature while the pressure is maintained to be 1atm in the test chamber.

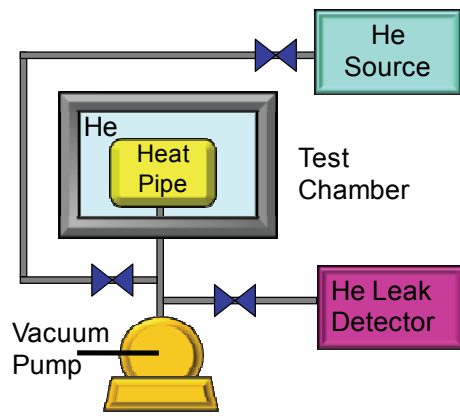


Figure 8: Schematic of hermeticity test with the helium leaking approach.

A device is made (shown in Fig. 9) with the same dimension as Fig. 6 for hermeticity test. The volume under leaking test device is  $\sim 170\mu\text{L}$  with a 1/8 inch outside diameter tube to connect with the adaptors of the test instrument. The device is placed inside of a helium gas chamber with the temperature and pressure inside of the chamber set up to be  $23^\circ\text{C}$  and  $1\text{atm}$ , respectively. The device is pumped down to create a negative pressure in the cavity. A mass spectrometer is connected to the cavity to measure penetrated helium molecules from the outside chamber into the sealed cavity. The response time to detect helium molecules of ASM 142 leak detector machine is less than a second. In this work the pressure inside of the cavity was pumped down to  $0.05\text{ mbar}$ , and the leaking test was carried out three times on same pressure and temperature to investigate consistency of leaking rate. In all three runs after 2 minutes the leaking rate of  $3.4 \times 10^{-10} \text{ atm.cm}^3/\text{s}$  was measured.

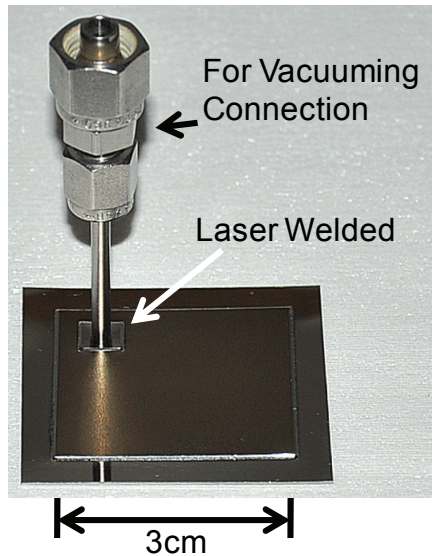


Figure 9: Laser welded device for hermeticity test. The device connects to the testing instrument by a 1/8 inch tube which is laser welded to the heat pipe.

## CONCLUSION

Dimensions and surface nanostructures were found to play critical roles on wetting with bitextured titania structures. The nanostructured titania greatly enhanced the wetting speed for the  $5\mu\text{m}/5\mu\text{m}$  pillar array. However the  $100\mu\text{m}/50\mu\text{m}$  array shows

much higher wicking speed than the former wick. Balancing the driving force with the viscous force, the dynamic behavior of the flow on rough solids is found to be diffusive and follows Washburn relation[15]. A thermal conductivity over  $500\text{W/m-K}$  (with contact resistance included) is achieved at around  $118^\circ\text{C}$ . The chamber of this Ti heat pipe is formed hermetically by welding two substrates together using laser welding technique. The hermeticity performance of the chamber is studied with helium leaking approaches. A leaking rate of  $3.4 \times 10^{-10} \text{ atm.cm}^3/\text{s}$  is achieved for the chamber with a volume of  $\sim 170\mu\text{L}$ .

## REFERENCES

- [1] P. D. Dunn and D. A. Reay, "Heat pipe," Physics in Technology, vol. 4, pp. 187-201, 1973.
- [2] W. G. Anderson, J. H. Rosenfeld, D. Angirasa, and Y. Me, "Evaluation of Heat Pipe Working Fluids in the Temperature Range 450 to 700 K," Space Technology and Applications International Forum (STAIF-04), edited by M. S. El-Genk, American Institute of Physics, Melville, New York, pp. 20-27, 2004.
- [3] R. N. Wenzel, "RESISTANCE OF SOLID SURFACES TO WETTING BY WATER," Industrial & Engineering Chemistry, vol. 28, pp. 988-994, 1936.
- [4] X. Feng and L. Jiang, "Design and creation of superwetting/antiwetting surfaces," Adv. Mater, vol. 18, pp. 3063-78, 2006.
- [5] D. Quéré, "Wetting and Roughness," Annual Review of Materials Research, vol. 38, pp. 71-99, 2008.
- [6] J. Bico, U. Thiele, and D. Quéré, "Wetting of textured surfaces," Colloids and Surfaces A: Physicochemical and Engineering Aspects, vol. 206, pp. 41-46, 2002.
- [7] C. Ding, G. Soni, P. Bozorgi, C. D. Meinhart, and N. C. MacDonald, "Wicking Study of Nanostructured Titania Surfaces for Flat Heat Pipes," in Nanotech Conference & Expo, Houston, TX, 2009.
- [8] U. Vadakkan, G. M. Chrysler, J. Maveety, and M. Tirumala, "A Novel Carbon Nano Tube based Wick Structure for Heat Pipes/Vapor Chambers," in Semiconductor Thermal Measurement and Management Symposium, 2007. SEMI-THERM 2007. Twenty Third Annual IEEE, 2007, pp. 102-104.
- [9] L. Mariana, L. O. Radu, S. Gheorghe, L. Magdalena Valentina, and K. Wilhelm, "Metallic Porous Parts for Electronics Devices Cooling," in Electronics Systemintegration Technology Conference, 2006. 1st, 2006, pp. 343-346.
- [10] M. P. Rao, M. F. Aimi, E. R. Parker, and N. C. MacDonald, "Single-mask, high aspect ratio, 3D micromachining of bulk titanium," 18th IEEE International Conference on MEMS 2005, pp. 64-67, 2005.
- [11] C. Ding, G. Soni, P. Bozorgi, B. Piorek, C. D. Meinhart, and N. C. MacDonald, "A Titanium Based Flat Heat Pipe," in International mechanical engineering congress and exposition, Boston, Massachusetts, 2008.
- [12] E. W. Washburn, "The Dynamics of Capillary Flow," Physical Review, vol. 17, p. 273, 1921.
- [13] W. Anderson, P. Dussinger, R. Bonner, and D. Sarraf, "High temperature titanium-water and Monel-Water heat pipes," 2006, pp. 2006-4113.
- [14] M. Ishizuka, T. Sasaki, and Y. Miyazaki, "Development of Titanium Heat Pipes For Use In Space," 1985, pp. 157-165.

## CONTACT

\*C. Ding. Public, tel: +1-805-893-5341;  
changsong\_ding@yahoo.com

# A WIRELESS-ENABLED RADIATION DETECTOR USING MICROMACHINED STEEL AND GLASS ELEMENTS IN A TO-5 PACKAGE

Christine K. Eun\* and Yogesh B. Gianchandani\*\*

Department of Electrical Engineering and Computer Science, University of Michigan, Ann Arbor, USA

## ABSTRACT

This paper reports a beta/gamma radiation detector that is manufactured by in-package assembly of micromachined stainless steel and glass elements. The detector is hermetically-sealed at 760 Torr with an Ar fill-gas. Gas micro-discharges (between the steel elements) are triggered by the presence of radiation, which can concomitantly transmit a wideband wireless signal. The detector diameter and height are 9 mm and 9.6 mm, respectively, and has a mass of 0.97 g. It has a measured output of >100 cpm when in close proximity to 30  $\mu\text{Ci}$  from  $^{137}\text{Cs}$ . Wireless spectra spanning 1.25 GHz at receiving antenna-to-detector distances >89 cm have been measured, with the device detecting 0.1  $\mu\text{Ci}$  from  $^{90}\text{Sr}$  and operating with a portable high-voltage conversion circuit.

## INTRODUCTION

Sensing beta and gamma radiation is important for many homeland security applications. These forms of radiation have appreciable travel range and are also generated by most radiation sources of interest. Gas  $\mu$ discharge-based radiation detection offers low dark current, temperature insensitivity, avalanche-driven signal amplification, and the ability to detect a wide range of radiation energies [1]. We have previously reported Marconi-based transmission using micromachined test structures [2]. Miniaturized wireless-enabled radiation sensors could someday be used in easily redeployable or mobile network configurations [3,4].

## DEVICE CONCEPTS AND OPERATION

The detector structure includes a stacked pair of steel electrodes, and insulating glass elements, that are hermetically-packaged inside a fill-gas (Fig. 1). The steel elements (Layers 2a and 4a) are perforated and separated by a glass spacer (Layer 3), which defines the anode-cathode gap spacing. The interspacers lie in-plane with the electrode to provide protection against spurious discharges near high-field regions between the steel elements and pins. An applied field generates high-field regions near the perforations. Beta radiation passes through the perforations and directly interacts with the fill-gas, whereas gamma radiation mostly interacts with the steel electrodes to generate photoelectrons. Beta radiation or photoelectrons initiate current-

driven avalanche pulses between the biased electrodes, which transmit wideband wireless signals.

## FABRICATION & ASSEMBLY

The detector elements are manufactured by commercial processes. To fabricate the electrodes (Fig. 2a), dry photoresist is laminated on 125  $\mu\text{m}$ -thick stainless steel (302/304). Following double-sided lithography, the sample is through-etched by a hot etchant spray. In this particular design, 125  $\mu\text{m}$ -diameter circular perforations are formed, with 250  $\mu\text{m}$  center-to-center spacing. The glass spacer elements are fabricated using a micro-abrasive jet process (Fig. 2b). A protective masking layer is lithographically-patterned on a 150  $\mu\text{m}$ -thick borosilicate glass substrate. An abrasive powder mixed with compressed air is sprayed onto the surface, chiseling the desired pattern. The interspacers are machined similarly. A 22° sidewall results from this process. To facilitate assembly, each element (steel or glass) is designed with alignment openings to line up with the package pins.

The package is an 8-pin TO-5 metal can package of 9 mm diameter and 9.6 mm height. It comprises a nickel base and a lid composed of a Kovar body with a 750  $\mu\text{m}$ -thick glass (Corning 7052) window. Electrical feed-throughs are available as pins through the package base. First, a glass spacer is assembled for electrical insulation (Fig. 3a), followed by the anode that is flanked by a pair of interspacers (Fig. 3b). Next, another glass spacer is installed, defining the electrode gap spacing, followed by the

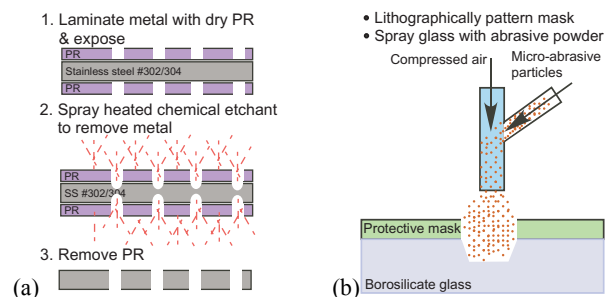


Figure 2: Fabrication process for (a) photochemically-etched electrodes and (b) powder-blasted glass spacers.

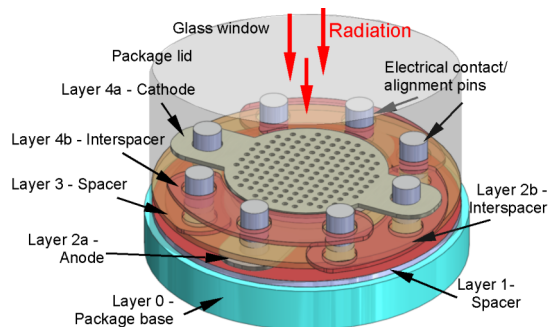


Figure 1: The detector comprises a stacked arrangement of stainless steel electrodes (Layers 2a, 4a) and glass insulators (Layers 1, 3) assembled within a commercial TO-5 package base. Layer 3 defines the electrode gap spacing. Radiation triggers avalanche within the biased gap, which leads to wireless signaling.

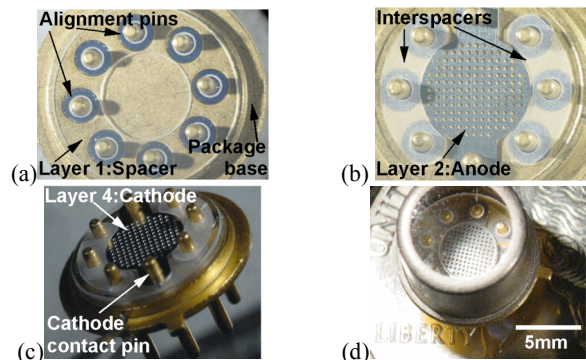


Figure 3: Microassembly of the detector. (a) A glass insulator is positioned onto the base. (b) Followed by the anode and interspacers, (c) Next, the electrode gap defining spacer and then the cathode and interspacers. (d) The hermetically-sealed device.



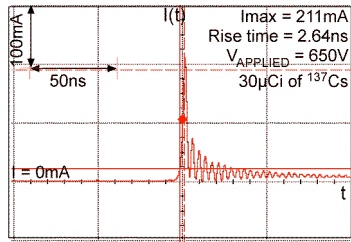


Figure 4: Current pulse measurement (of a “count”) using a high-frequency inductive current probe attached to the cathode shows approximately 200 mA peaks and 50–100 ns duration.

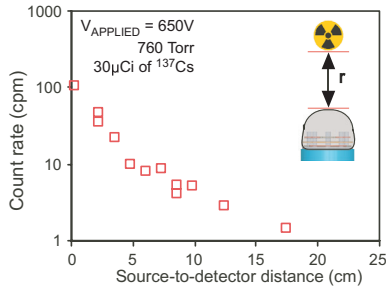


Figure 5: Wired measurement. Count rates decrease logarithmically with increasing source-to-detector distance,  $r$ . The source and detector are axially aligned and moved vertically.

cathode that is flanked by a pair of interspacers (Fig. 3c). After assembly, the package is hermetically-sealed at 760 Torr with an Ar fill-gas, using a commercial resistance projection welding process (Fig. 3d). The overall device weighs <1 g.

## RESULTS AND DISCUSSION

The hermetically-sealed device was characterized using radioisotope sources of  $30 \mu\text{Ci } ^{137}\text{Cs}$  (which emits beta and gamma radiation) and  $0.1 \mu\text{Ci } ^{90}\text{Sr}$  (a pure beta-emitter).

Wired measurements The count rate was measured with a high-frequency inductive current probe. At 650 V bias, current pulses with 50–100 ns duration and up to 100 cpm frequency were observed (Fig.4). Pulse rates were correlated to separation from the radioisotope,  $r$  (Fig. 5). The measured background rates (in the absence of the radiation source) were 1.3 cpm.

Wireless measurements The wireless spectra transmitted by the device were measured inside an anechoic chamber using a 200 MHz–1 GHz log-periodic antenna (EMCO 93146) connected to a spectrum analyzer (HP8563E). In order to increase portability, a high-voltage flash circuit modified from a disposable camera was coupled to the detector (Fig. 6). Additionally, the drive circuit included an RC timing circuit and ballast resistors. During detector operation (in the presence of  $^{90}\text{Sr}$ ), wireless spectra were observed to span 1.25 GHz with peaks at 550 MHz, 750 MHz, and 1.1 GHz. The received signal power decreased with increasing antenna-detector distances,  $d$  (Fig. 7). For these measurements,  $V_{\text{APPLIED}}$  was 2.8 V, leading to 670–680 V at the device.)

## CONCLUSIONS

A wireless-enabled micromachined radiation detector manufactured using in-package assembly methods has been presented. The device generated count rates >100 cpm and transmitted wideband wireless spectra spanning >1.25 GHz. The device is powered using a portable high-voltage conversion circuit. The overall detector and power module (excluding battery) weighs 0.97 g and 7.9 g, respectively, which can enable future portable, reconfigurable networks of wireless radiation sensors.

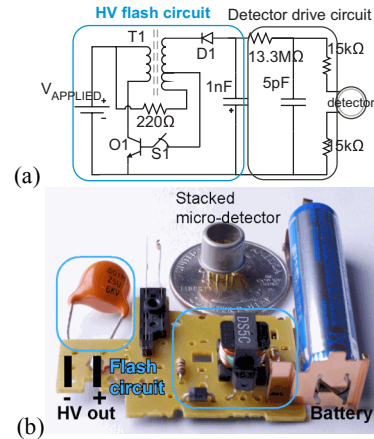


Figure 6: (a) Schematic of the high-voltage flash circuit and the detector drive circuit. (b) Photo of a battery-operated high-voltage supply adapted from the flash circuit board of a disposable camera.

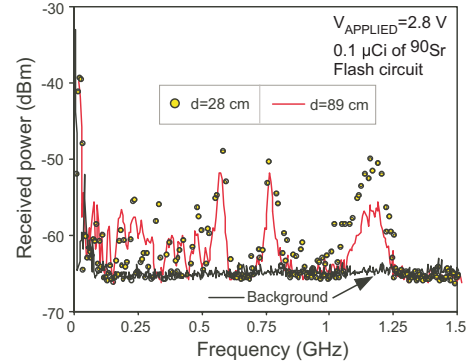


Figure 7: Wireless measurement. Wireless spectra measured inside an anechoic chamber spans 1.25 GHz, with peaks at 550 MHz, 750 MHz, and 1.1 GHz.  $V_{\text{APPLIED}}=2.8 \text{ V}$ . The received wireless power decreases with increasing antenna-detector distance. Strong signaling was observed at distances >89 cm.

## ACKNOWLEDGEMENTS

This work was supported by the Dept. of the Army, Micro Autonomous Systems and Technology (MAST) Collaborative Technology Alliance, Contract No. W911NF-08-2-0004. The authors thank Prof. Sarabandi, Dr. Adib Nashashibi, and Prof. Gharpurey for collaboration on the signaling concept.

## REFERENCES

- [1] G.F. Knoll, *Radiation Detection and Measurement*, John Wiley and Sons, 2000.
- [2] C.K. Eun, Y.B. Gianchandani, “A Micromachined Wireless Gamma Radiation Detector Using Bulk Metal Conversion Layers,” *Solid-State & Actuator Workshop*, Hilton Head Isl, SC, (2008) pp. 308-311.
- [3] R.J. Nemzek et al., “Distributed sensor networks for detection of mobile radioactive sources,” *IEEE Trans. on Nuclear Science*, vol. 51, no. 4, Aug. 2004, pp. 1693-1700.
- [4] R. Kyker et al., “Hybrid Emergency Radiation Detection (HERD), a wireless sensor network application for consequence management of a radiological release,” *Proceedings of SPIE*, vol. 5440, pp. 293-304.

## CONTACT

\*C.K. Eun tel: +1-734-763-6132; [eunc@umich.edu](mailto:eunc@umich.edu)

\*\*Y.B. Gianchandani tel: +1-734-615-6407; [yogesh@umich.edu](mailto:yogesh@umich.edu)

# BIOINSPIRED WATER-ENHANCED ACCELERATION SENSING USING ARTIFICIAL HAIRCELL SENSOR

Huan Hu and Chang Liu

MedX Research Laboratory, Northwestern University, Evanston, IL, USA

## ABSTRACT

This paper presents the first demonstration of water-enhanced acceleration sensing using a new version of artificial haircell sensor (AHC). Mimicking the rotational acceleration-sensing organism of human – semicircular canals, the device consists of a canal chamber with an AHC integrated. Water is filled in the canal to enable larger drag force on the artificial hair in accelerated condition than in air. We show that when the canal is filled with water, the acceleration sensitivity is increased 56 times than that in air in 225Hz. Furthermore, frequency response test showed its unique frequency selectivity that can potentially be used for selectively sensing.

## INTRODUCTION

In Nature, animals own superior sensing capabilities over human engineered sensors in sensitivity, selectivity and robustness. We hope to gain inspiration from nature on developing high-performance sensors. Haircells are widely found in nature for sensing, such as flow sensing in fish lateral line [1], vibration sensing in spiders [2], rotational acceleration sensing in human cochlear [3].

Our group has developed different types of AHC in the past [4-6]. The ultimate goal of this research is to seek an optimized AHC and develop proper methods of modifying it for different sensing purposes. We have successfully demonstrated modifying it into tactile sensing [7]. In this work, we developed a new version AHC integrating inside a canal chamber and demonstrated its unique acceleration sensing capability.

The similarity of the device to the semicircular canal in human is illustrated in Fig. 1

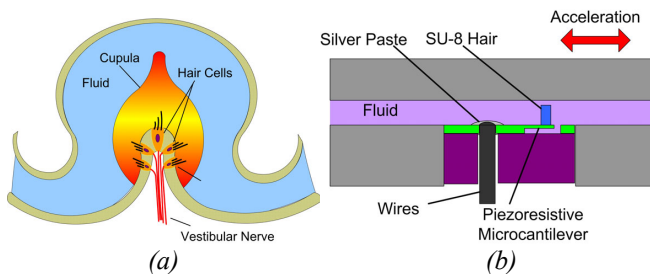


Figure 1: (a) Schematics of the semicircular canal structure in human; when human rotate its head, the cupula will experience force acted by fluid, bending haircells within the cupula, which trigs the neuron (b) Schematics of AHC in canal for acceleration sensing. Upon acceleration in the direction along the canal, water will act upon the SU-8 hair sitting on the piezoresistive cantilever causing the bending of the cantilever. Therefore, the acceleration information will be converted into the resistance change of the piezoresistive cantilever.

## APPROACH

**Fabrication** - The fabrication process of AHC is based on the process of previous AHC developed in our group [1] shown in Fig. 2. Through-wafer vias are fabricated so that metal leads can make contact with the sensor through the bottom of the sensor. This enables convenient integration with a canal chamber and also makes the front surface more flat thus hydrodynamically preferred. A

complete device is shown in Fig. 3(a), the AHC is packaged into a canal chamber with the microcantilever right in the middle of the canal. Fig. 3(b) shows the detailed view of AHC in microscope.

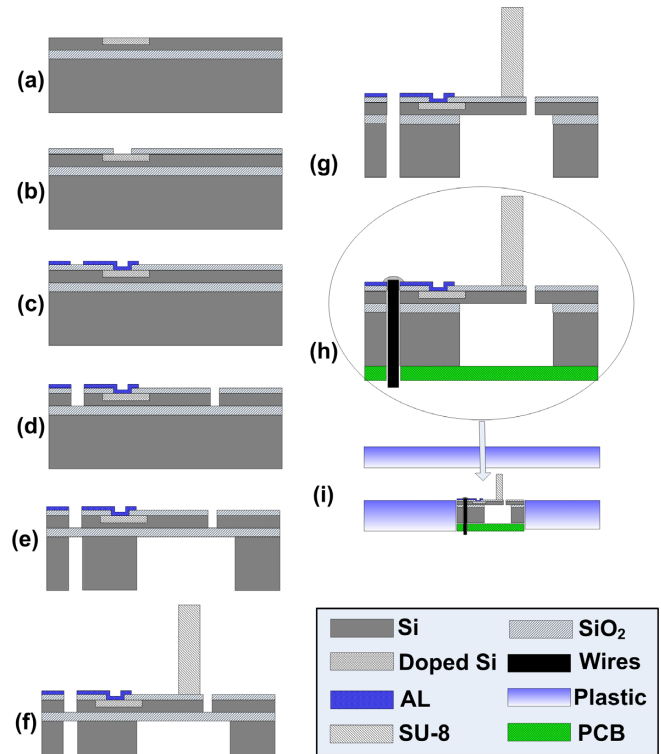


Figure 2: Fabrication Process Flow: (a) Doping; (b) Opening contact spot; (c) AL electrode deposition; (d) Front Etching to define cantilever shape and also shape of vias; (e) Back Etching; (g) SU-8 patterning to form artificial hair; (h) bond on PCB board and make electric connections through the bottom of the wafer. (i) Fit the artificial haircell sensor into the plastic canal chamber.

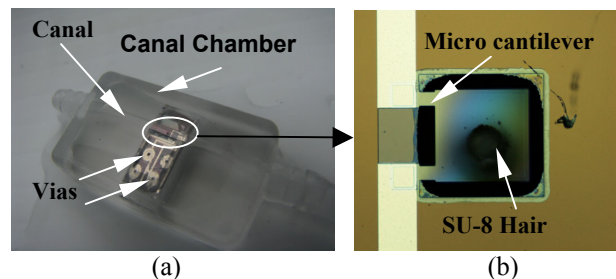


Figure 3: (a) Optical picture of a bio-inspired acceleration sensor with the artificial haircell integrated; (b) Microscopic picture of the artificial haircell sensor.

**Experiment Setup** - A commercial accelerometer is embedded in a rod and the canal chamber with artificial haircell is bonded on the rod, which is vibrated vertically by a shaker as shown in Fig. 4. A

function generator is to generate the waveform, which feeds into the amplifier to actuate the shaker. An oscilloscope is used to record the output of both AHC and the commercial accelerometer. The output of the commercial accelerometer is used to calibrate the acceleration.

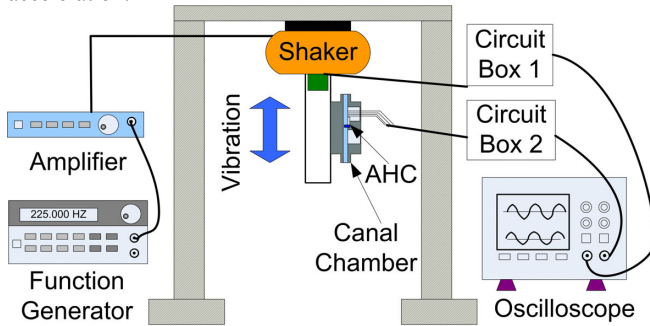


Figure 4: Experiment Setup for testing the acceleration sensing capability of AHC in canal chamber.

## RESULTS AND DISCUSSIONS

Linearity test is performed on the device both in air and in water. The AHC is always in the canal. When tested in air, no water is filled. When tested in water, water is filled. The vibration is kept at 225Hz while the amplitude of the vibration is increased. The results are shown in Fig. 5. Both in air and water, AHC exhibits good linearity. Furthermore, the sensitivity of AHC in water is 16.9mV/g, while the AHC in air is 0.3mV/g. Water has enhanced the sensitivity to 56 times.

Frequency responses of AHC both in air and in water are shown in Fig. 6. Frequency is swept from 35Hz to 305 Hz with 10Hz step. We divide the output of AHC to the output of the commercial accelerometer as the calibrated output. Two peaks are observed for AHC in water at 115Hz and 225Hz. AHC in air shows no resonance within this range.

Upon acceleration, water plays two roles. One is to increase the momentum applied on the hair, this increased the vibration amplitude of the AHC; the other is to increase the damping, which decreases the resonance frequency.

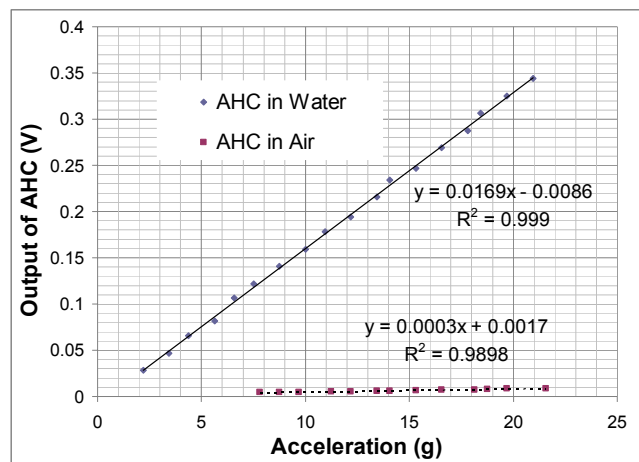


Figure 5. Experimental results of linear sensitivity test of AHC both in air and in water at 225 Hz. Acceleration is measured by the commercial accelerometer.

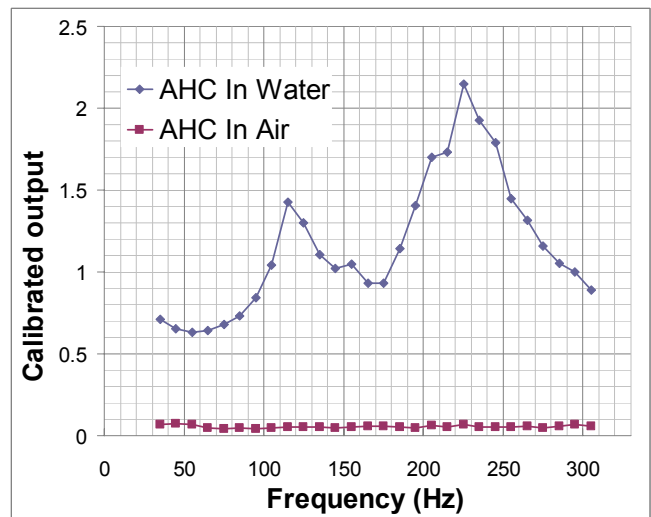


Figure 6: Ratio of output of AHC in water over output of accelerometer and ratio of output of AHC in air over output of accelerometer at vibration frequencies from 35Hz to 305Hz.

## REFERENCES

- [1] J. C. Montgomery and S. Coombs, "Peripheral encoding of moving sources by the lateral line system of a sit-and-wait predator," *Journal of Experimental Biology*, vol. 201, pp. 91-102, 1998.
- [2] F. G. Barth, J. Humphrey, and K. Voss, "The motion sensing hairs of arthropods: Using physics to understand sensory ecology and adaptive evolution," in *Ecology of Sensing*, A. Schmid, Ed. New York, NY: Springer, 2001, pp. 105-125.
- [3] R. D. Rabbitt, B. Boyle, S. M. Highstein, "Mechanical amplification by hair cells in the semicircular canals", *Proceedings of the National Academy of Sciences*, V17 (8), 2010
- [4] N. Chen, C. Tucker, J. Engel, Y. Yang, S. Pandya and C. Liu, "Design and Characterization of Artificial Haircell Sensor for Flow Sensing With Ultrahigh Velocity and Angular Sensitivity", *Journal of Microelectromechanical System*, V16(5), 2009.
- [5] J. Engel, J. Chen, N. Chen and C. Liu, "Development and Characterization of an Artificial Hair Cell Based on Polyurethane Elastomer and Force Sensitive Resistors," *The 4th IEEE International Conference on Sensors*, Irvine, California, 31 Oct- 1 Nov, 2005.
- [6] J. Chen, J. Engel, and C. Liu, "Development of Polymer-Based Artificial Haircell Using Surface Micromachining and 3D Assembly," *The 12th International Conference on Solid-State Sensors, Actuators and Microsystems*, Vol. 2, Boston, MA, 8-12 June 2003.
- [7] H. Hu, N. Chen and C. Liu, "A robust tactile shear stress sensor derived from a bio-inspired artificial haircell sensor", *The 7th IEEE Sensor Conference*, Italy, October, 2008

## CONTACT

Huan Hu, [huanhu@u.northwestern.edu](mailto:huanhu@u.northwestern.edu); 1-847-467-0702

# HETERODYNED ELECTROSTATIC TRANSDUCTION OSCILLATORS EVADE LOW FREQUENCY NOISE ALIASING

Gaurav Bahl, James Salvia<sup>†</sup>, Hyung Kyu Lee, Renata Melamud<sup>‡</sup>, Bongsang Kim<sup>‡</sup>,  
Roger T. Howe, Thomas W. Kenny  
Stanford University, Stanford, California, USA

## ABSTRACT

We recently demonstrated a polarization technique that eliminates the frequency drift due to dielectric charge in MEMS oscillators [1]. In this work we show that these oscillators are also first-order insensitive to low-frequency voltage noise, with potential for significant positive impact on predicted close-to-carrier phase noise performance. Close-to-carrier noise also determines the limits of some resonant sensor applications [2, 3].

## INTRODUCTION

Electrostatic MEMS resonators are typically polarized with dc voltages. By simply changing resonator polarization  $v_p$  to ac (at frequency  $\omega_B$ , Fig. 1), it has been shown that frequency drift due to dielectric charging disappears [1]. Under this scheme, the system electrically oscillates at two frequencies simultaneously ( $\omega_R \pm \omega_B$ ), an effect caused by heterodyning, i.e. frequency mixing, at both the input and output transducers of the device. The mixing of frequencies within the oscillator is summarized in Fig. 2. The polarization  $v_p(t)$  can be generated by frequency division of the oscillator's output as discussed previously in [1].

Kaajakari [4] identifies the inherent force nonlinearity and current nonlinearity to be the primary sources of the aliasing of low frequency noise (Fig. 3(a)) into close-to-carrier current noise in conventional electrostatic MEMS oscillators. This aliased low-frequency noise determines the phase noise performance of the oscillator. In this work we show that although these sources of aliasing still exist under the ac actuation scheme, they cause low-frequency noise (such as  $1/f$  noise) to appear far from the carrier frequencies. Instead, it is the higher frequency noise near the polarization signal at  $\omega_B$  (Fig. 3(b)) that aliases to the carrier sidebands.

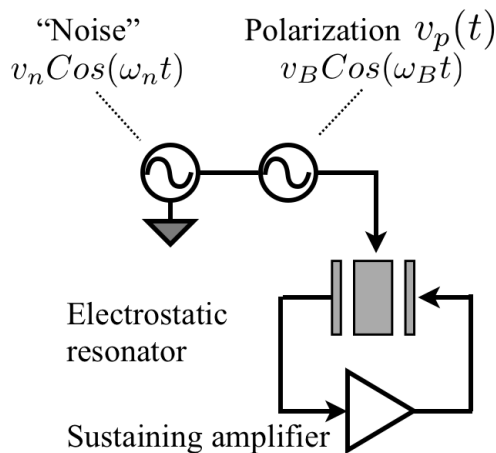


Figure 1: General oscillator representation and test setup with artificial ‘noise’ injection. The polarization source is generalized to frequency  $\omega_B$  and voltage amplitude  $v_B$ . For DC polarization we set  $\omega_B = 0$ .

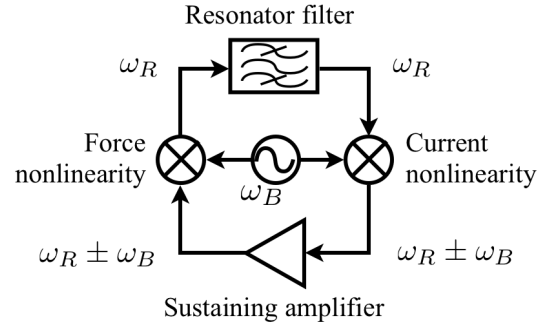


Figure 2: A simplified model of circulating signals in a heterodyned electrostatic transduction oscillator. Here,  $\omega_R$  is the device resonance frequency, and  $\omega_B$  is the polarization frequency. Although the device continues to mechanically resonate at frequency  $\omega_R$ , we can only observe  $\omega_R \pm \omega_B$  in the electrical domain.

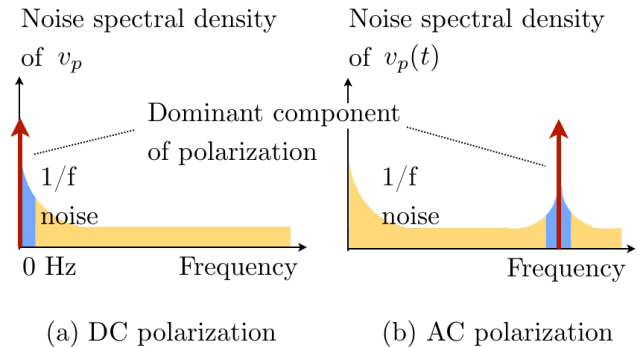


Figure 3: Dominant noise contributions from  $v_p(t)$ . (a) With conventional (DC) polarization, the dominant close-to-carrier noise source in the oscillator output is the aliased  $1/f$  noise near 0 Hz (marked in blue). (b) With AC polarization, the dominant noise source in the oscillator is adjacent to the polarization frequency (marked in blue), and not low frequency noise.

## THEORY

We propose an extended version of Leeson’s phase noise model [5] for ac polarized MEMS oscillators.

$$v_{nj}^2(\Delta\omega) = \frac{R^2}{2} \left( 1 + \left( \frac{\omega_R}{2Q\Delta\omega} \right)^2 \right) \left( i_{n1}^2(\Delta\omega) + i_{n2}^2(\Delta\omega) \right)$$

for  $j = 1, 2$ , where the subscripts 1,2 indicate the two carrier frequencies [1],  $Q$  is quality factor,  $R$  is the device motional impedance,  $\omega_R$  is the device resonance frequency, and  $\Delta\omega$  is the frequency offset. This shows that the total current noise injection in the two carrier sidebands ( $i_{n1}^2, i_{n2}^2$  including all noise sources and aliasing effects) at the amplifier input determines the close-to-carrier noise ( $v_{n1}^2, v_{n2}^2$ ) performance of these oscillators as well. However, since low frequency noise in  $v_p(t)$  no longer aliases to close-to-carrier current

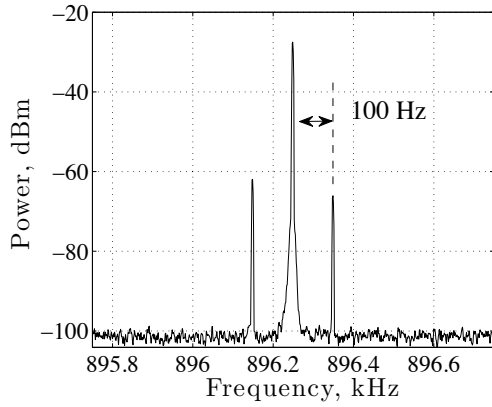


Figure 4: Conventional (DC polarized) oscillator showing injection of low frequency noise to the carrier sidebands. DC Polarization is  $v_B = 7.07$  VDC with frequency  $\omega_B = 0$  Hz (DC). Noise is  $v_n = 100$  mVpp with frequency  $\omega_n = 100$  Hz.

noise  $i_{n1}^2, i_{n2}^2$ , the oscillator phase noise is no longer directly affected by low frequency electrical noise sources. As a result, no sidebands should appear adjacent to the carrier frequency when the noise is at low frequency.

## EXPERIMENT

One can experimentally simulate low frequency noise injection through an additional voltage ‘noise’ source on the polarization terminal (Fig. 1). Noise sidebands appear adjacent to the carrier frequency output from the oscillator, consistent with Kaajakari’s noise aliasing theory [4], when  $v_p$  is dc polarization (Fig. 4). Under the ac polarization scheme, however, the same low frequency noise does not appear near the carriers (Fig. 5(a)), validating the prediction in the previous section. Instead, only close-to-polarization noise appears in the carrier sidebands (Fig. 5(b)).

## CONCLUSION

It has been previously asserted that close-to-carrier phase noise in electrostatic MEMS oscillators is limited by a  $1/f^3$  trend appearing from aliased  $1/f$  voltage noise [4], which is unavoidable in dc sources. By moving the polarization away from dc, the oscillator phase noise is now limited by the quality of the ac source in use. This enables us to have additional engineering capability of the noise trends of the oscillator, as trends other than  $1/f$  (such as  $1/f^2$  or  $1/f^3$ ) can be obtained with ac sources. However, it is unclear whether such ac sources can outperform the  $1/f$  trend available with dc voltage supplies, when given the same resources.

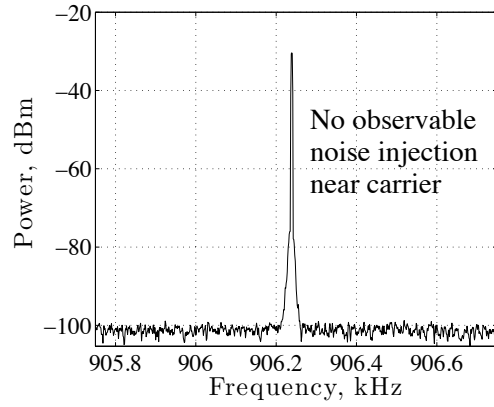
In conclusion, although it has been previously shown that nonlinearities inherent in electrostatic resonant MEMS cause noise aliasing, this work demonstrates that the same nonlinearities can be exploited to evade the low frequency noise aliasing effect.

† currently at SiTime Corporation, Sunnyvale, CA

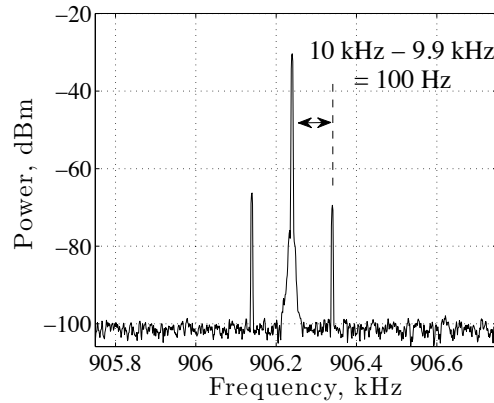
‡ currently at Sandia National Labs, Albuquerque, NM

### Corresponding author:

Gaurav Bahl, bahlg@stanford.edu,  
440 Escondido Mall, 530-224, Stanford, CA - 94305



(a) Noise  $v_n = 200$  mVpp with frequency  $\omega_n = 100$  Hz



(b) Noise  $v_n = 100$  mVpp with frequency  $\omega_n = 9.9$  kHz

Figure 5: Heterodyned oscillator with AC polarized resonator. Here, the  $\omega_R + \omega_B$  carrier is shown. In both sub-figures the polarization is  $v_B = 7.07$  Vrms with frequency  $\omega_B = 10$  kHz. (a) Low frequency noise does not alias near the carriers. FM artifacts appear at very large noise magnitudes (not shown). (b) Only high frequency noise sources, i.e. near  $\omega_B$ , appear near the carriers.

## REFERENCES

- [1] G. Bahl *et al.* “Charge-Drift Elimination in Resonant Electrostatic MEMS”. In *IEEE MEMS 2010*, Hong Kong, China, January 24–28, 2010.
- [2] A. A. Seshia, M. Palaniapan, T. A. Roessig, R. T. Howe, R. W. Gooch, T. R. Schimert, and S. Montague. “A vacuum packaged surface micromachined resonant accelerometer”. *JMEMS*, 11(6):784–793, Jan 2002.
- [3] R. G. Azevedo, D. G. Jones, A. V. Jog, B. J., D. R. Myers, L. Chen, X. Fu, M. Mehregany, M. B. J. Wijesundara, and A. P. Pisano. “A SiC MEMS resonant strain sensor for harsh environment applications”. *IEEE Sensors Journal*, 7(3-4):568–576, Jan 2007.
- [4] V. Kaajakari, J. Koskinen, and T. Mattila. “Phase noise in capacitively coupled micromechanical oscillators”. *IEEE Transactions on Ultrasonics*, Jan 2005.
- [5] D.B Leeson. “A simple model of feedback oscillator noise spectrum”. *Proc. of the IEEE*, 54(2):329–330, 1966.

# HIGH ASPECT RATIO TRANSMISSION LINES MICROMACHINED IN SILICON WITH LARGE THERMAL OXIDE DIELECTRICS

*S. T. Todd<sup>1</sup>, J. E. Bowers<sup>1</sup>, and N. C. MacDonald<sup>2</sup>*

<sup>1</sup>Department of Electrical and Computer Engineering, University of California, Santa Barbara, CA, USA

<sup>2</sup>Department of Mechanical Engineering, University of California, Santa Barbara, CA, USA

## ABSTRACT

A micromachining process has been developed to create high aspect ratio transmission lines on silicon. The transmission lines contain large SiO<sub>2</sub> dielectrics that separate the signal and ground conductors. The large SiO<sub>2</sub> dielectric is fabricated by merging silicon mesa arrays into solid SiO<sub>2</sub> mesas using thermal oxidation. We report measurements of a 40 Ω semi-rectangular coaxial (SERC) line with an effective dielectric constant of 3.7 and attenuation of 1.3 dB/cm at 30 GHz.

## INTRODUCTION

A problem with silicon microwave circuits is that the substrate conductivity causes substantial transmission line loss. Micromachining methods can reduce the substrate loss of silicon. One micromachining approach is to reduce field exposure to the substrate through silicon removal [1]. Micromachining can also be used to lower conductor loss [2, 3]. Problems with these types of micromachined transmission lines include difficult and expensive fabrication methods and non-planar surfaces.

Previously, high aspect ratio coplanar waveguide (HARC) was created with a planar surface on silicon [4]. A problem with this method was that long thermal oxidation times limited the width of the SiO<sub>2</sub> dielectric. In this paper, we introduce high aspect ratio transmission lines with large SiO<sub>2</sub> dielectrics. We have created both HARC and SERC with this method and will summarize the results of SERC transmission lines. A mesa merging thermal oxidation process similar to that reported in [5] is utilized to create large dielectrics. The SERC lines have a ground plane that completely isolates the transmission line from the silicon substrate. Fig. 1 shows a 3-D schematic of SERC.

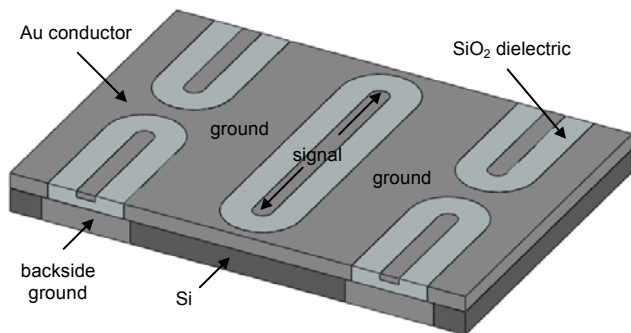


Fig. 1. 3-D schematic of SERC fabricated on silicon.

## FABRICATION

The fabrication method of SERC, shown in Fig. 2, starts with silicon DRIE to create mesas which define the dielectric topology. Next, wet thermal oxidation at 1050 °C transforms the silicon mesas into oxide, creating a low-loss dielectric for the transmission lines. During thermal oxidation, the width of each mesa expands until it merges with an adjacent mesa. Annealing is then performed at 1100 °C for 12 hours to ensure mesa merging. Fig. 3 shows SEM micrographs of cross-sections before and after mesa merging.

The surface is then planarized using CMP. Next, a deep

anisotropic SiO<sub>2</sub> etch forms trenches within the dielectrics that define the center conductor topology. Silicon DRIE follows to define the ground plane trenches. A conformal Ti/Au seed layer is then sputtered. Next, Au electroplating fills both the ground and signal trenches with conductor. The top of the structure is then planarized using lapping and CMP. A backside DRIE follows which removes the silicon underneath the SERC line. Finally, a backside Ti/Au seed layer is sputtered followed by backside electroplating. Fig. 4 shows SEM micrographs of the SERC surface.

Before thermal oxidation, the width of each Si mesa is about 4.7 μm and the trench width between mesas is about 5.3 μm as shown in Fig. 3 (a). Obtaining the correct mesa to trench pitch is important because making the pitch too small results in gaps between the mesas and making the pitch too large results in residual silicon in the center of each mesa. With this mesa to trench width pitch, the mesas contact and merge with no residual silicon left in the center of each mesa. Fig. 3 (b) shows the SiO<sub>2</sub> mesa after thermal oxidation and anneal. Notice that a very large SiO<sub>2</sub> mesa is created without gaps or residual silicon.

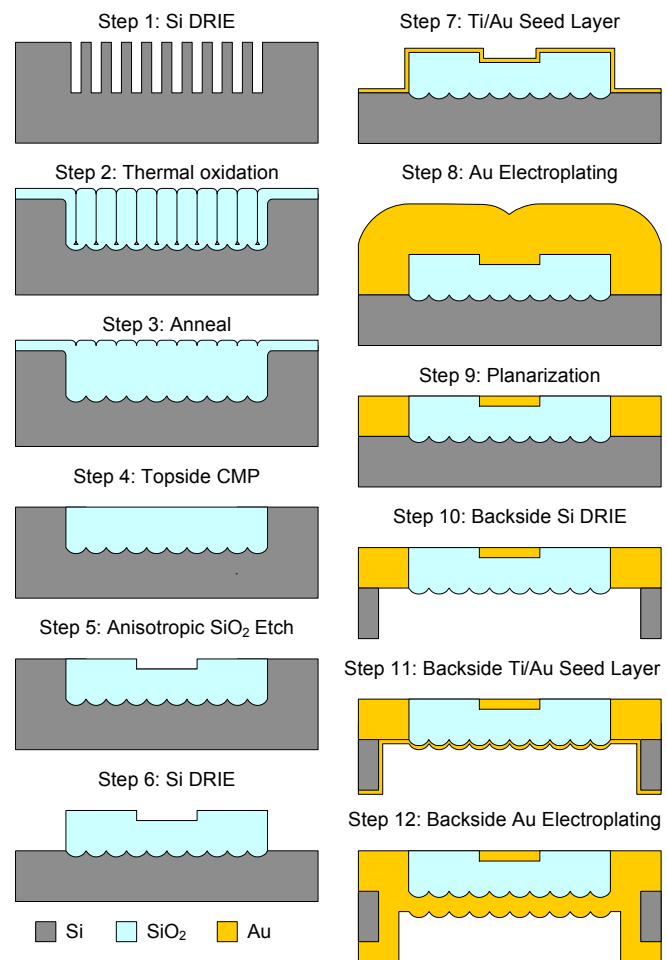


Fig. 2. The process flow for creating SERC.

## EXPERIMENTAL RESULTS

The SERC transmission line characteristics were extracted from S-parameters that were measured after performing short-open-load-thru and thru-reflect-line calibrations. Measurements were compared to analytical models that have been derived for SERC. Fig. 5 shows results of characteristic impedance versus frequency of a 400  $\mu\text{m}$  long line. Fig. 6 shows results of effective dielectric constant versus frequency of a 400  $\mu\text{m}$  long line.

Fig. 7 shows measurements and calculations of attenuation constant versus frequency of a 400  $\mu\text{m}$  long line. Notice that the measured loss is higher than the model predicts. We assumed a loss tangent of zero in the model, so the higher than predicted loss could be due to a finite loss tangent. Fig. 8 shows measurements of the loss due to turns in the serpentine SERC line shown in Fig. 4 (b). Fig. 8 shows that the additional loss is less than 0.0006 dB per  $180^\circ$  turn over a span of 25 GHz. This verifies that turns can be implemented in SERC lines without significant loss.

## REFERENCES

- [1] C. Y. Chi and G. M. Rebeiz, "Planar microwave and millimeter-wavelength elements and coupled-line filters using micromachining techniques," *IEEE Trans. Microwave Theory Tech.*, 43, 4, pp. 730–738, (1995).
- [2] J. R. Reid, E. D. Marsh, and R. T. Webster, "Micromachined rectangular coaxial transmission lines," *IEEE Trans. Microwave Theory Tech.*, 54, 8, pp. 3433–3442 (2006).
- [3] T. L. Willke and S. S. Gearhart, "LIGA micromachined planar transmission lines and filters," *IEEE Trans. Microwave Theory Tech.*, 45, 10, pp. 1681–1688 (1997).
- [4] S. T. Todd, X. T. Huang, J. E. Bowers, and N. C. MacDonald, "High aspect ratio CPW fabricated using silicon bulk micromachining with substrate removal," *In Proc. Asia Pacific Microwave Conference 2009*, Singapore.
- [5] C. Zhang and K. Najafi, "Fabrication of thick silicon dioxide layers for thermal isolation," *Journal of Microeng. Microeng.*, 14, pp. 769–774, (2004).

## CONTACT

S. T. Todd, tel: +1-805-893-5341; stodd@ece.ucsb.edu

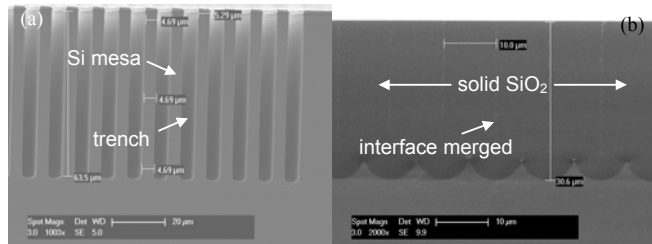


Fig. 3. SEM micrographs of mesa cross sections (a) before thermal oxidation and (b) after oxidation, anneal, and planarization.

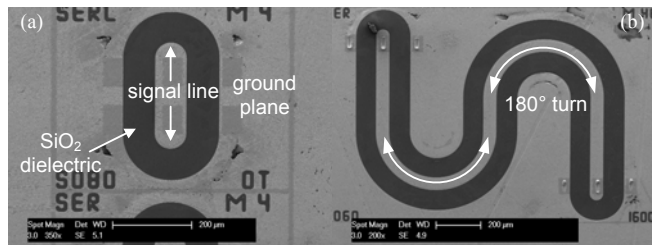


Fig. 4. SEM micrographs of SERC showing (a) a thru line and (b) a serpentine line with two  $180^\circ$  turns.

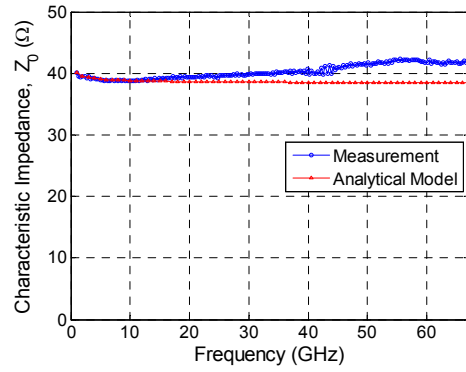


Fig. 5. Measurements/calculations of impedance vs. frequency.

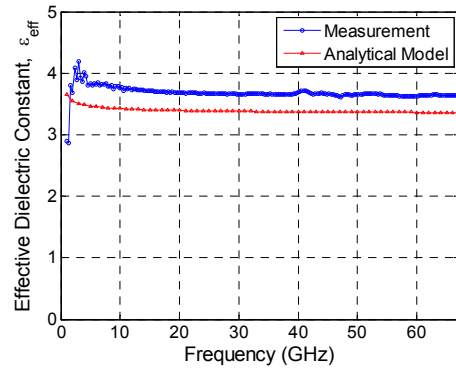


Fig. 6. Measurements/calculations of effective dielectric constant vs. frequency.

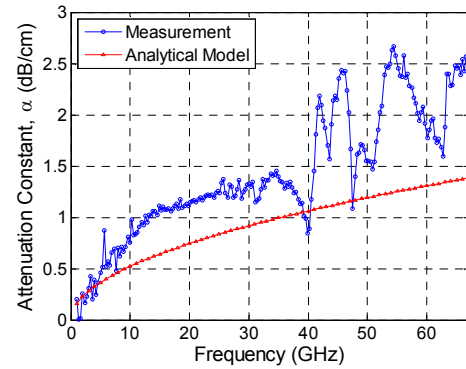


Fig. 7. Measurements/calculations of attenuation vs. frequency.

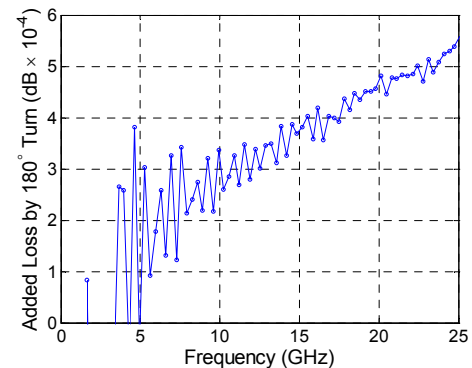


Fig. 8. Measurements of added loss by one  $180^\circ$  turn.

# LOW TEMPERATURE QUALITY FACTOR SCALING OF GHz FREQUENCY SILICON RESONATORS

Eugene Hwang\* and Sunil A. Bhave

OxideMEMS Lab, Cornell University, Ithaca, NY, USA

## ABSTRACT

In this paper, we demonstrate quality factor ( $Q$ ) enhancement of a silicon RF MEMS resonator by cryogenic cooling from room temperature down to liquid nitrogen temperatures (78K). The resulting  $Q$  is approximately 63,000 at a frequency of 3.72 GHz, yielding an  $f$ - $Q$  product of  $2.34 \times 10^{14}$  Hz. This work verifies that the resonator is operating in the Landau-Rumer regime at room temperature, where individual phonon scattering results in a strong dependence of  $Q$  on temperature [1-3]. We find that as the temperature approaches 120K, the  $Q$  converges to a constant value, indicating that intrinsic phonon loss mechanisms are replaced by temperature independent electrical and mechanical anchor losses as the dominant  $Q$  limiting factor.

## INTRODUCTION

Advances in micromechanical resonators have resulted in high quality factor ( $Q$ ) resonators at room temperature with frequencies in the microwave regime, highlighting the possibility of their use in integrated RF systems [4, 5]. Theoretical and experimental studies hypothesize that phonon interactions dominate the intrinsic loss in bulk-mode resonators, making possible even higher  $Q$  at lower temperatures [1-3, 6-12]. Chip-scale micro-cryogenic cooling is not as farfetched as it seems, as integrated microsystems demonstrating cooling to temperatures as low as 76K have already been developed [13]. Recent measurements of  $Q$  in 60-MHz silicon resonators demonstrated  $Q \propto 1/T$ , characteristic of the Akhiezer effect [7-9]. Instead, if we operate at frequencies in the Landau-Rumer regime,  $Q \propto 1/T^4$ , greatly enhancing the gains in  $Q$  due to cooling. We have previously demonstrated a pn-diode transduced, low motional impedance resonator (Fig. 1) at 3.72 GHz, which is operated in the Landau-Rumer regime [14]. This transduction mechanism is used primarily because it allows for efficient transduction at high frequencies in a completely homogeneous resonator, allowing us to carefully study the intrinsic loss mechanisms due to phonon scattering.

## EXPERIMENTAL RESULTS AND DISCUSSION

An acoustic wave in a resonator can be thought of as a highly excited acoustic phonon mode containing a number of phonons much larger than the thermal equilibrium value. Due to various scattering processes, phonons in this highly excited mode will decay

Table 1: Expressions estimating  $Q$  limits due to the two main phonon-phonon scattering mechanisms [1-3, 7-9]

<b>Akhiezer Effect</b>	$Q_{AKE} = \frac{2\pi\rho c_D^2}{c_v \gamma^2} \frac{1 + (\omega\tau_{th})^2}{\tau_{th}} \frac{1}{\omega T}, \quad (1)$ $\tau_{th} = \frac{3\kappa}{c_v c_D^2}$
<b>Landau-Rumer Effect</b>	$Q_{L-R} = \frac{30\rho c_l^5 h^3}{\pi^4 \gamma^2 k_B^4 T^4} \quad (2)$
$\rho$ = density $c_l$ = longitudinal velocity $c_D$ = Debye velocity $c_v$ = volumetric heat capacity	$\gamma$ = Grüneisen parameter $\kappa$ = thermal conductivity $h$ = Planck's constant

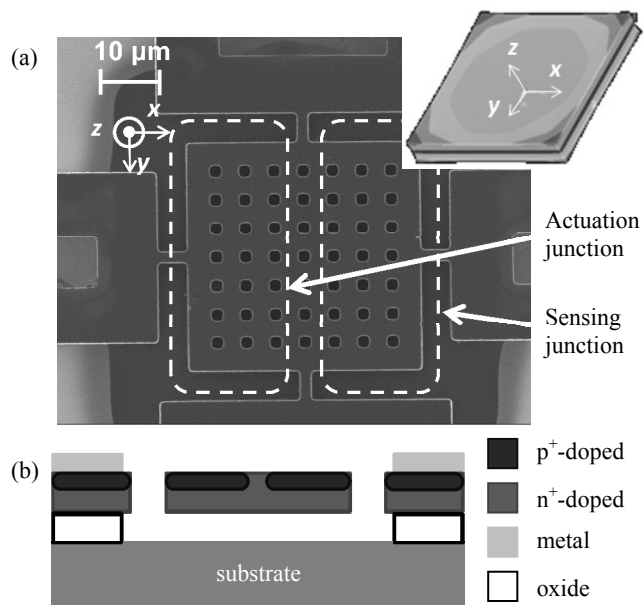


Figure 1. (a) Top-view SEM of the pn-diode transduced 3.7-GHz silicon micromechanical resonator and ANSYS simulation of thickness-stretch (FBAR) mode (inset) [14] (b) resonator cross sectional diagram

into other modes, resulting in attenuation of the acoustic wave. The dominant phonon-phonon scattering mechanisms depend strongly on the relationship between  $\omega$ , the frequency of the acoustic wave, and the thermal phonon lifetime  $\tau_{th}$ . When  $\omega\tau_{th} \ll 1$ , the device is in the Akhiezer regime and when  $\omega\tau_{th} > 1$ , the Landau-Rumer effect

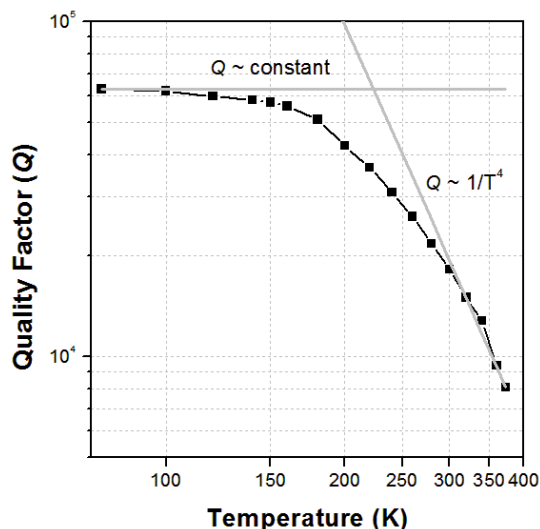


Figure 2. Measured  $Q$  of pn-diode transduced silicon resonator showing  $1/T^4$  dependence at temperatures close to 300K. The  $Q$  eventually tapers off to a constant value at around 120K to a maximum of about 63,000. We believe this is due to anchor losses and routing resistance. All measurements are performed in a Lakeshore vacuum RF probe station.



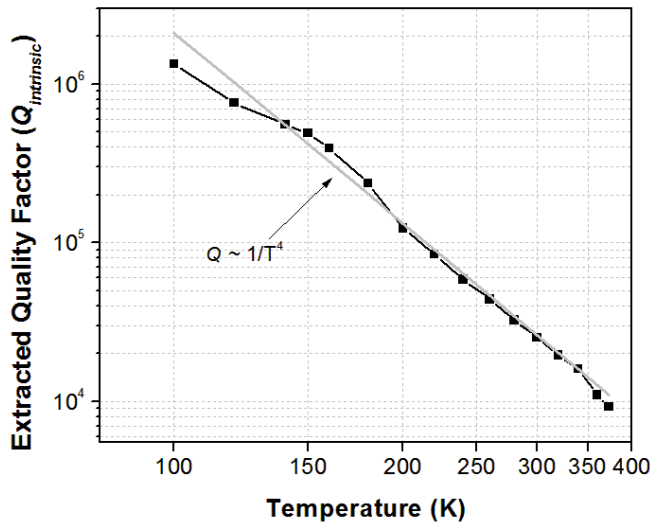


Figure 3. Extracted  $Q$  of pn-diode transduced silicon resonator by removing lumped anchor losses using relationship given by Eq. (3). A near  $1/T^4$  dependence is seen throughout the measured temperature range indicating operation in the Landau-Rumer regime.

must be considered. Acoustic attenuation in both regimes has been studied extensively and theoretical details can be found in the literature [1-3, 7-9]. Expressions for the quality factor in these regimes are shown in Table 1.

Interestingly, it has been shown that for resonators operating in the Landau-Rumer regime,  $Q$  is constant with frequency, a fact which is exploited in the high frequency resonators used in this work [14]. Operation in this regime is beneficial not only in terms of  $fQ$  product scaling with frequency ( $fQ \propto f$ ), but also with temperature due to the strong dependence of  $Q \propto 1/T^4$ , as shown in Eq. (2). Fig. 2 verifies that our device is in this regime by showing such dependence at temperatures close to 300K. However, the  $Q$  approaches a constant value as temperature decreases, which we believe to be a result of both electrical and mechanical losses due to the anchor. Electrical resistive losses, which typically are not considered in electrostatically transduced resonators, are important because of the low motional impedance of these devices.

In order to verify whether the remaining loss is due to the Landau-Rumer effect, we lumped the  $Q$  obtained in the constant- $Q$  region into an equivalent anchor loss term  $Q_{anchor}$  and, assuming that the remaining loss is entirely intrinsic, used the relationship

$$\frac{1}{Q_{total}} = \frac{1}{Q_{anchor}} + \frac{1}{Q_{intrinsic}} \quad (3)$$

to determine  $Q_{intrinsic}$  plotted in Fig. 3. This plot shows a  $1/T^4$  dependence, thus verifying operation in the Landau-Rumer regime. Note that these experiments were repeated with three other similar resonators, all showing similar temperature dependence.

## CONCLUSION

Through this work, we were able to verify operation of the pn-diode transduced micromechanical resonators in the Landau-Rumer regime. We have demonstrated the  $1/T^4$  dependence of  $Q$  and exploited it to demonstrate  $Q \sim 63,000$  and  $fQ$  product of  $2.34 \times 10^{14}$  Hz at 78K. The conclusions drawn from this work are not dependent on the use of pn-diode transduction and are widely applicable to GHz frequency single crystal silicon resonators. With the availability of chip-scale spot cooling, silicon micromechanical

resonators show the potential to be used in high- $Q$  applications such as chip-scale spectrum analysis and narrowband RF applications.

## ACKNOWLEDGEMENTS

This work was funded by the DARPA HI-MEMS project and Army Research Labs (ARL). The devices were fabricated in the Cornell Nanoscale Science and Technology Facility (CNF).

## REFERENCES

- [1] H. J. Maris, "Interaction of sound waves with thermal phonons in dielectric crystals," In W. P. Mason, R. N. Thurston, editors, *Physical Acoustics – Volume VIII*, Academic Press, New York, 1971.
- [2] R. Tabrizian, M. Rais-Zadeh, and F. Ayazi, "Effect of phonon interactions on limiting the  $fQ$  product of micromechanical resonators," *Transducers '09*, Denver, CO, USA, June 21-25, 2009, pp. 2131-2134.
- [3] P. G. Klemens, "Decay of high-frequency longitudinal phonons," *J. Appl. Phys.*, **38**, 12 (1967).
- [4] D. Weinstein and S. A. Bhave, "The resonant body transistor," accepted for publication in *Nano Letters*, 2010.
- [5] M. Rinaldi, C. Zuniga, and G. Piazza, "5-10 GHz AlN contour-mode nanoelectromechanical resonators," *MEMS 2009*, Sorrento, Italy, Jan. 25-29, 2009, pp. 916-919.
- [6] S. A. Chandorkar *et al*, "Limits of quality factor in bulk-mode micromechanical resonators," *MEMS 2008*, Tucson, AZ, USA, Jan. 13-17, 2008, pp. 74-77.
- [7] T. O. Woodruff and H. Ehrenreich, "Absorption of sound in insulators," *Physical Review B*, **123**, 5 (1961).
- [8] W. P. Mason and T. B. Bateman, "Ultrasonic-wave propagation in pure silicon and germanium," *J. Acoust. Soc. Am.*, **36**, 4 (1964).
- [9] A. N. Cleland, *Foundations of Nanomechanics: From Solid-State Theory to Device Applications*, Springer-Verlag, Berlin, 2003.
- [10] A. El Habeti, F. Bastien, "Low temperature limitation on the quality factor of quartz resonators," *IFCS 1992*, May 27-29, 1992, pp. 597-602.
- [11] B. Kim *et al*, "Temperature dependence of quality factor in MEMS resonators," *MEMS 2006*, Istanbul, Turkey, Jan. 22-26, 2006, pp. 590-593.
- [12] W.-C. Li, Y. Lin, B. Kim, Z. Ren, and C. T.-C. Nguyen, "Quality factor enhancement in micromechanical resonators at cryogenic temperatures," *Transducers '09*, Denver, CO, USA, June 21-25, 2009, pp. 1445-1448.
- [13] M.-H. Lin, P. E. Bradley, H.-J. Wu, J. C. Booth, R. Radebaugh, Y. C. Lee, "Design, fabrication, and assembly of a hollow-core fiber-based micro cryogenic cooler," *MEMS 2009*, Sorrento, Italy, Jan. 25-29, 2009, pp. 1114-1117.
- [14] E. Hwang and S. A. Bhave, "PN-diode transduced 3.7-GHz silicon resonator," *MEMS 2010*, Hong Kong SAR, Jan. 24-28, 2010, pp. 208-211.

## CONTACT:

\*E. Hwang, tel: +1-408-515-4132; eoh3@cornell.edu

# TWO DEGREE OF FREEDOM PZT MEMS ACTUATED FLAPPING WINGS WITH INTEGRATED FORCE SENSING

J. S. Pulskamp\*, G. L. Smith, R. G. Polcawich, C. M. Kroninger, and E. D. Wetzel  
US Army Research Laboratory, Adelphi, MD, USA

## ABSTRACT

This paper reports on the demonstration of microfabricated two degree of freedom actuated insect-inspired wings for small-scale robotics. Previous efforts demonstrated the feasibility of achieving insect-like stroke amplitudes in thin-film PZT actuated millimeter-scale wings [1]. Lift production in insect flight depends upon unsteady aerodynamic effects associated with three-dimensional kinematics utilizing both stroke (i.e. flap) and pitch (i.e. wing rotation) degrees of freedom [2]. Incorporation of wing rotation is essential to mimicking insect wing kinematics and hence force production. Closed loop flight control and device characterization have also motivated the development of feedback sensors. Two degree of freedom PZT MEMS actuators, directly controlling both stroke and pitch, have been monolithically integrated with compliant thin film wings and piezoelectric strain sensors.

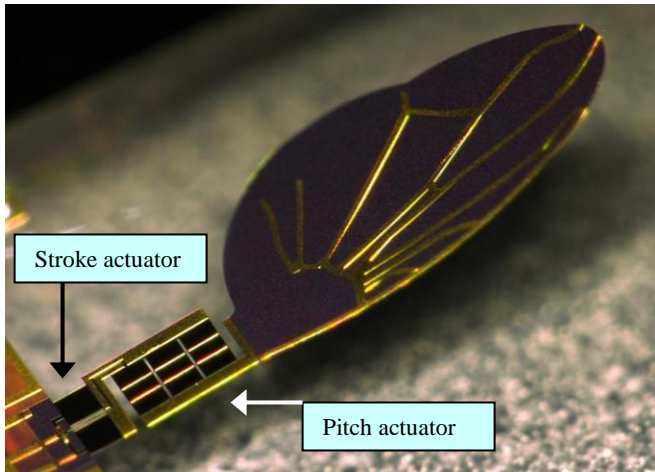


Figure 1: Image of typical design, illustrating PZT MEMS stroke and pitch actuators and thin film wing structure.

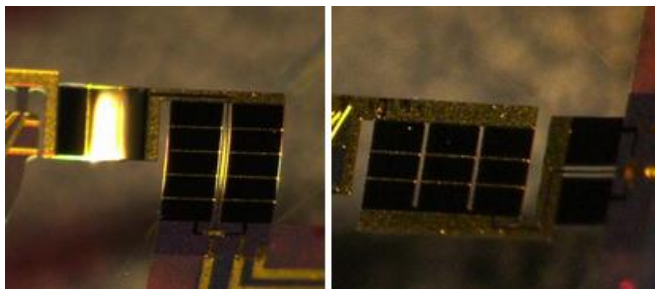


Figure 2: Images of primary designs; left image) the stroke actuator is attached to the wing, right image) the stroke actuator is attached to the substrate.

## DEVICE DESIGN

The primary actuator designs utilize two orthogonal piezoelectric unimorph cantilevered actuators as depicted in Fig. 1. One actuator's plane of bending coincides with the span of the

wing while the other is orthogonal; permitting them to drive the stroke and pitch respectively. Two designs were included that exchange the positions of the stroke and pitch actuators (see Fig. 2). A quasi-steady aerodynamic model informed by empirically determined coefficients, capturing various steady and unsteady force components, estimated the expected flight forces in terms of the wing kinematics. Nonlinear analytical models, utilizing these peak aerodynamic loads, provided actuator displacements and stresses for various wing and actuator configurations. This analysis verified that the necessary dimensions of thin film PZT actuators were reasonable to drive these loads at the desired kinematics and provided the unimorph composite thicknesses and actuator dimensions. Finite element analysis was then employed to fine tune the geometries and to determine if the actuator/wing system response times were adequate for the targeted motion (see Fig. 3). Some designs additionally feature passive or actuated hinge structures located just behind the leading edge of the wing to amplify pitch through passive wing rotation or additional actuation. Analytical models were also employed to design piezoelectric strain sensors integrated at the base of the actuator anchored to the substrate with an expected force resolution of a few nano-newtons. These two orthogonal sensors utilize the same piezoelectric layer and bottom electrode as the actuators but feature separate top electrodes. Each sensor is structured as a high aspect ratio (length to width) clamped-clamped structure to ensure the voltage sensitivities of the respective sensors provide information on the dominant orthogonal strains (see Fig. 4).

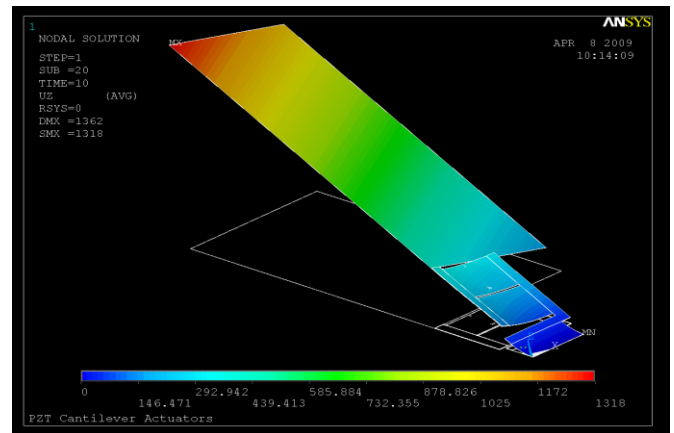


Figure 3: Image of loaded static nonlinear displacement piezoelectric finite element analysis of actuator design and simplified wing structure (precise wing geometry not relevant to analysis).

## FABRICATION

The composite actuators are comprised of silicon dioxide-silicon nitride / titanium-platinum bottom electrode / PZT / top platinum electrode. The composition of the wings vary based on the design but are generally comprised of the same silicon dioxide and nitride layer with either PZT or Ti-Au layers. The venation pattern visible in the images is a thick gold layer. The layer thicknesses used are presented in Table 1. The details of the

fabrication process are similar to those employed in our earlier work [1].

Table 1: PZT Actuator and wing composite thicknesses. The two silicon dioxide and nitride thicknesses are for different designs and wafers.

Layer	Thickness (Å)
Silicon Dioxide/Nitride/Dioxide <sup>1</sup>	19800
Silicon Dioxide/Nitride/Dioxide <sup>2</sup>	10000
Titanium/Platinum	200/850
PZT	4970
Top Platinum	500
Titanium/Gold	200/15000
Gold	20000

## RESULTS

The initial characterization has consisted of driving the individual actuators on a probe station with separate signal generators while being monitored with oscilloscopes. A Keyence high speed microscope was used to measure the wing kinematics. The initial results are plotted in Fig. 5 & 6. In summary, these significantly improved designs have enabled stroke amplitudes in excess of 84 degrees under resonant drive at about 3.4V. Quasi-static displacements of 36 degrees have been measured for pitch.

## CONCLUSION

Our future work will focus on device characterization and addressing proper control. Although lift has yet to be measured with these initial results, the improved designs demonstrate many of the necessary features anticipated to replicate mm-scale flapping insect-inspired flight.

## REFERENCES

- [1] J.R. Bronson, et. al., "PZT MEMS Actuated Flapping Wings for Insect-Inspired Robotics", 22nd IEEE International Conference on MEMS, Sorrento, Italy, Jan 2009.
- [2] M. H. Dickinson, F. O. Lehmann, and S. P. Sane, "Wing Rotation and the Aerodynamic Basis of Insect Flight", Science, 284, 1954-1960, 1999.

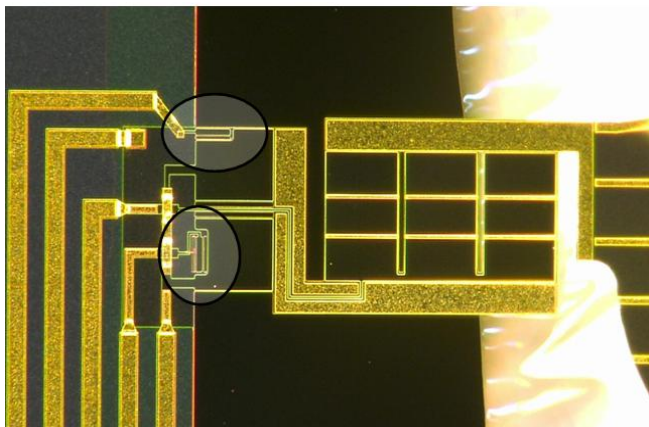


Figure 4: Image device with two integrated piezoelectric strain sensors near the base of the stroke actuator.

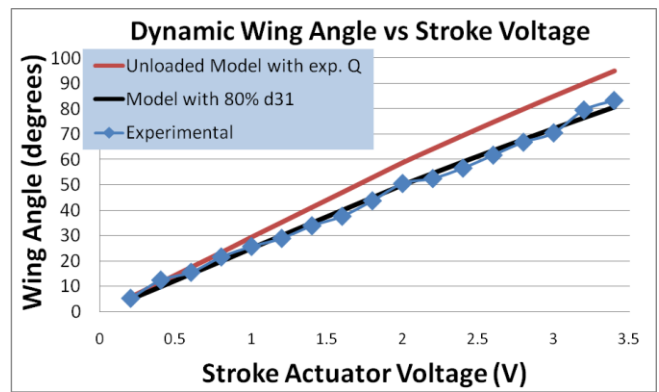


Figure 5: Wing tip angle vs stroke actuator voltage at resonance frequency of 64 Hz. The modeled data utilizes the measured  $Q$  (5.9) and typical thin film piezoelectric coefficients for prediction. The model is also presented with a 20% reduction in  $d_{31}$  for improved agreement.

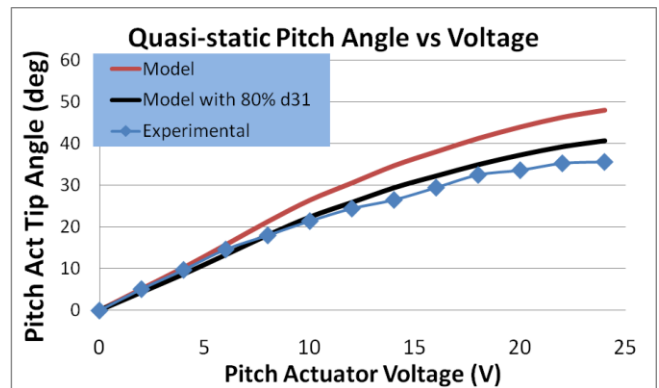


Figure 6: Wing rotation angle vs Pitch actuator voltage at low frequency. The modeled data utilizes typical thin film piezoelectric coefficients for prediction. The model is also presented with a 20% reduction in  $d_{31}$  for improved agreement.

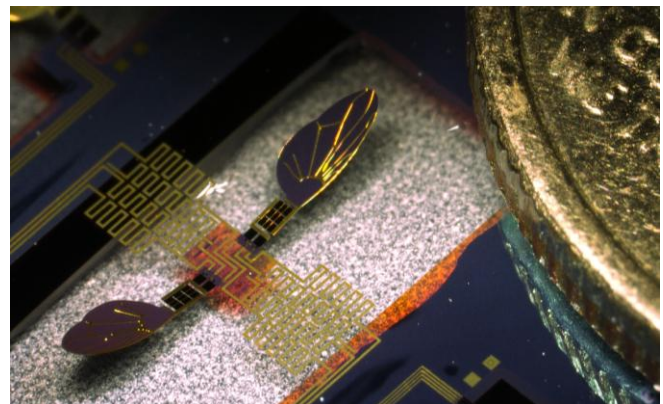


Figure 7: Image of suspended platform with individually controllable wings next to a US dime.

## CONTACT

\*J. S. Pulskamp, tel: (301) 394-0016, jeffrey.pulskamp1@us.army.mil.

# A STUDY OF MICROMACHINED DISPLACEMENT PUMPS FOR VACUUM GENERATION

H. Zhou\*, V. Sharma, H.Q. Li, and M.A. Schmidt

Microsystems Technology Laboratories  
Massachusetts Institute of Technology, Cambridge, Massachusetts, USA

## ABSTRACT

This paper explores the limits of micromachined displacement pumps for vacuum generation. We studied a single stage pump which has a theoretical vacuum level of 406 torr (limited by dead volume), but which experimentally achieves a base pressure of 494 torr. Careful characterization has enabled us to quantitatively understand and measure the various effects that limit the performance for this class of pumps. In particular, we have measured valve leakage under vacuum operation, and correlated this to valve design parameters such as seal ring width.

## INTRODUCTION

Micro vacuum pumps are one of the key components in miniature systems for chemical and biological analysis, e.g. mass spectrometer. Due to their portability, miniature analyzing systems can be deployed in numerous ways, such as in space research and field applications.

Micromachined pumps have been well studied [1, 2], however, only a few have been used for vacuum generation. Examples include Knudsen pumps [3], vapor-jet pumps [4], and displacement pumps [5, 6]. Knudsen pumps have a relatively small flow rate, and vapor-jet pumps involve fluid heating that might lead to high power consumption. Thus, a displacement pump seems very promising in microsystems, provided reasonable vacuum levels can be achieved.

Our vacuum pump was designed to be pneumatically driven for purposes of characterization, but ultimately will be integrated with piezoelectrics, similar to our previous work on high pressure pumps [7]. Silicon-on-insulator (SOI) wafers were chosen to form the displacement membrane due to the high quality device silicon layer. One SOI wafer and one standard silicon wafer were fabricated by deep-reactive ion etching (DRIE) and other standard micromachining techniques. Two pyrex wafers bonded to both the top and bottom sides completed the pump.

## MICROPUMP AND ITS OPERATION

### Micropump Structure

The micromachined vacuum pump is shown in Fig. 1 schematically. The pump includes three pneumatic actuation ports along with inlet and outlet ports. Device layers, L2 and L3, integrate two sealing valves and one pumping piston. Pyrex layers, L1 and L4, provide protection and support.

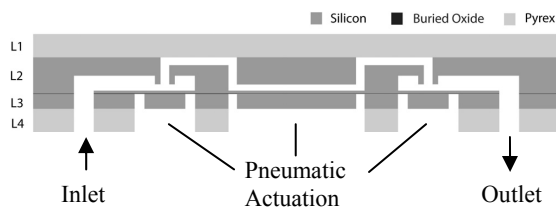


Figure 1: Schematic cross-section view of the micromachined vacuum pump.

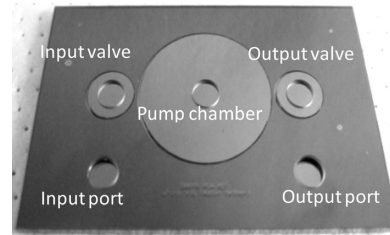


Figure 2: Micromachined vacuum pump (bottom view).

The actual pump is 30mm×50mm×2mm in dimension, as shown in Fig. 2. The two ports labeled as "input valve" and "output valve" are actuation ports for the two valves, one to seal the channel between inlet and the pump chamber, the other to seal the channel between pump chamber and the outlet. "Input port" in the figure connects to the inlet and "Output port" is open to outside. The pump chamber and valves are all designed to permit a 6 micron stroke. The pump chamber is 20 mm in diameter, and the valves are 4 mm in diameter with an approximate seal-ring diameter of 180 microns.

### Fabrication

The critical process is the fabrication of the membranes of the two valves and the pump chamber. To ensure a durable movement, there must not be any stress intensive points on the membranes, and fillets at the corners of the membrane and substrate are the key, as illustrated in [8].

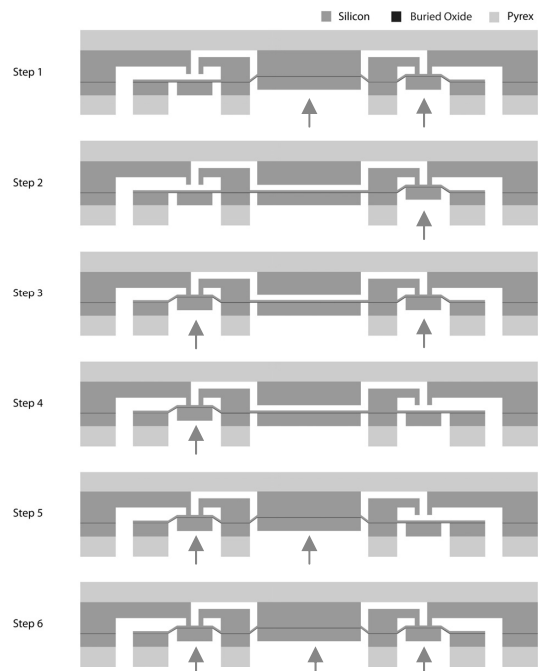


Figure 3: 6-step operation cycle (arrows indicate pushing-up actuation by applying positive pressures).

SOI wafers with a 10 $\mu$ m thick device layer were picked for the L3 layer. A DRIE process was fine tuned to etch the handle layer until the buried oxide layer was reached. A "U" shape etching was desired, with fillets on both ends and without any excess silicon in the middle. A double-side polished silicon wafer was used as the L2 layer, and was etched on both sides multiple times. The L2 and L3 layers were bonded, and then the L1 and L4 layers were bonded afterwards, all at the wafer level.

### Pump Operation

The pump was operated in a reciprocal 6-step cycle (Fig. 3), among which Step 2 and 5 represent gas charging and discharging steps respectively. Gas inside the test volume flows into the pump chamber during Step 2 by pulling the piston down, while gas inside the pump chamber is pushed out through outlet port during Step 5. Arrows in Fig. 3 indicate pushing-up actuation by applying a positive pressure of  $\sim 2$  atm, while pulling-down actuation is applied to the unmarked actuation ports by using a vacuum of  $\sim 100$  torr.

## RESULTS AND DISCUSSION

### Testing Setup

The micromachined vacuum pump was mounted onto a customized testing jig with all ports facing down, as shown in Fig. 4. A vacuum pressure sensor, Parker MPS-V3N-PGA, measured the pressure change inside the test volume. The actuation pressures were connected to testing jig through gas switches, Parker Kuroda VA01PEP34-1U. A microcontroller was used to control the pump operation.

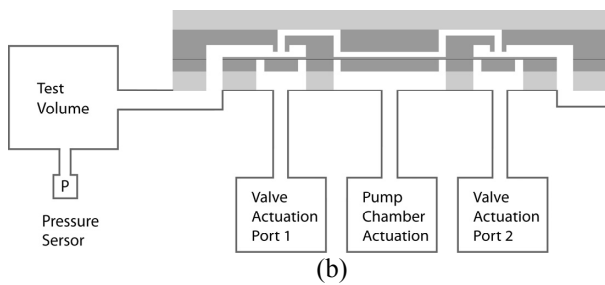
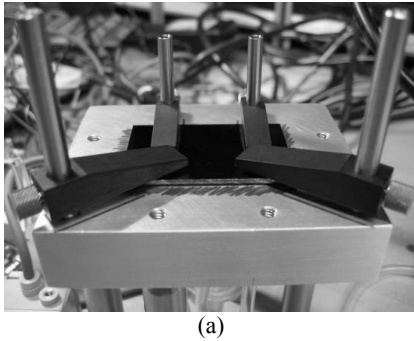


Figure 4: Testing setup for vacuum generation.

### Flow Rate

By connecting the pump outlet to a flow sensor, the flow rate was measured. Below 2 Hz operating frequency, the pumping flow rate increases with frequency as expected. At frequencies higher than 2 Hz, the flow rate remains constant until it reaches 3 Hz, when the pumping speed starts to drop.

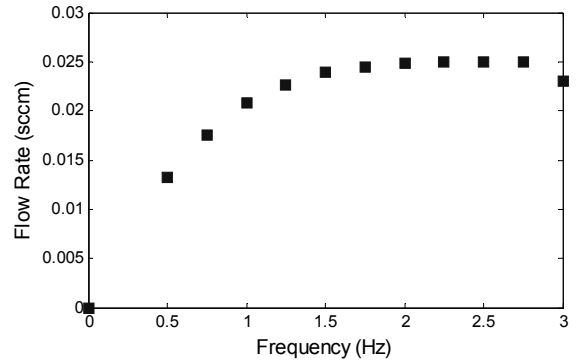


Figure 5: Pump speed at 760 torr.

The plateau in Fig. 5 reflects the delay of pump chamber gas charging and discharging. In order to understand this effect, we can make an approximate estimate of the time constants for charging and discharging the pump chamber. By assuming Poiseuille flow, the fluidic resistances of charging and discharging (refer to Step 2 and 5 in Fig. 3) can be calculated approximately by integrating the resistances for rectangle channels [9] along the diameter of the chamber. For charging, we assume the pump piston is undeflected:

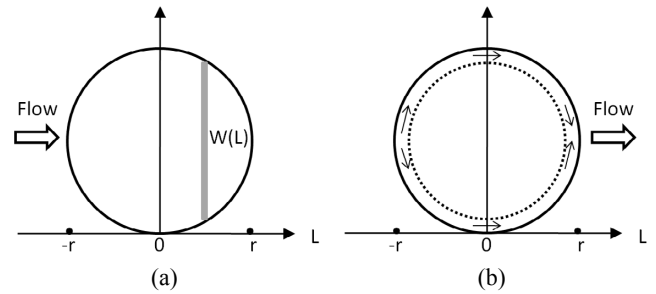


Figure 6: Resistance model for the pump chamber, for a flow along the chamber diameter, (a) for charging and (b) for discharging.

$$R_{\text{charging}} = \int_{-r}^r \frac{12\eta}{W(L)h^3} dL \quad (1-1)$$

where

- $R_{\text{charging}}$ : chamber fluidic resistance
- $\eta$ : viscosity of air
- $W(L), L$ : as labeled in Fig. 6
- $h$ : chamber height, 6  $\mu$ m

Therefore, the fluidic resistance of pump chamber at charging step is

$$R_{\text{charging}} = 1.5 \times 10^{12} \text{ Pa}\cdot\text{s}\cdot\text{m}^{-3} \quad (1-2)$$

During discharging, we assume the central piston is fully pushed to the chamber ceiling with zero gap, and the gas exits from the annular periphery region. The flow path is simplified to two parallel trapezoid channels, and the chamber resistance is calculated as

$$R_{discharging} = 1.25 \times 10^{14} \text{ Pa} \cdot \text{s} \cdot \text{m}^{-3} \quad (1-3)$$

Analogous to electrical circuit, the fluidic capacitances of the pump chamber are derived from the relationship between flow rate and pressure drop

$$Q = C \frac{d\Delta P}{dt} \quad (2-1)$$

and mass conservation equation

$$Q = \frac{V}{\rho} \frac{d\rho}{dt} \quad (2-2)$$

where

- $Q$ : flow rate
- $V$ : chamber volume
- $\Delta P$ : pressure difference
- $\rho$ : density

From Eq. (2-1) and (2-2), we have

$$C = \frac{V}{\rho} \frac{d\rho}{d\Delta P} = \frac{V}{\rho} \frac{d\rho}{dP_{chamber}} = \frac{V}{P_{chamber}} \quad (2-3)$$

The fluidic capacitances for the pump chamber at 760 torr are

$$C_{charging} = 1.9 \times 10^{-14} \text{ Pa}^{-1} \cdot \text{m}^3 \quad (2-4)$$

$$C_{discharging} = 9.3 \times 10^{-16} \text{ Pa}^{-1} \cdot \text{m}^3 \quad (2-5)$$

Thus, the approximate time constants in the fluidic circuit are

$$\tau_{charging} = (R \cdot C)_{charging} = 0.029 \text{ s} \quad (3-1)$$

$$\tau_{discharging} = (R \cdot C)_{discharging} = 0.116 \text{ s} \quad (3-2)$$

The 500ms operating period, corresponding to 2 Hz frequency, is approximately twice the time constants of the charging and discharging steps plus 50ms each for the other four steps. Faster operation than 2 Hz could not improve the pump speed due to the inherent delay, and insufficient charging or discharging time might even degrade the speed, suggested from the flow rate testing.

### Vacuum Generation

Based on the flow rate testing results, we measured the pump vacuum generation performance by leaving sufficient time for pump gas charging and discharging. With an operation frequency of 0.5 Hz, a base pressure of 494 torr was achieved (Fig. 7).

Vacuum performance is limited mostly by dead volume and valve leakage. Dead volume comes from design, e.g. the channel volume, other non-ideal factors such as wafer bow, and also insufficient charging or discharging. An efficiency factor  $\alpha$  is introduced, which represents the fraction the pump chamber is evacuated each cycle during gas discharging ( $0 < \alpha < 1$ ). Valve leakage comes from imperfect contact between the valve seat and valve boss. By taking all factors into account, we developed a model of displacement pumps for vacuum generation:

$$P_{vacuum} = \frac{P_0 \times (V_{channel} + (1 - \alpha) \cdot V_{chamber}) + P_0 \cdot Q \cdot T}{V_{channel} + V_{chamber}} \quad (4)$$

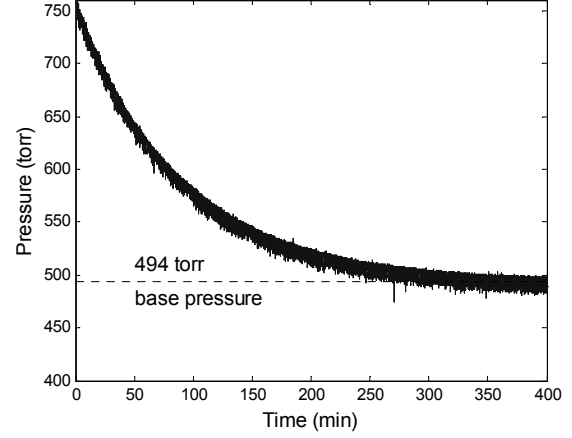


Figure 7: Vacuum generation performance. Speed is limited by the size of the test volume ( $\sim 1 \text{ cm}^3$ ).

where

- $P_{vacuum}$ : ultimate vacuum generated
- $P_0$ : atmosphere pressure
- $\alpha$ : efficiency factor
- $Q$ : leak rate
- $T$ : period
- $V_{channel}$ : pump channel volume
- $V_{chamber}$ : pump chamber volume

Eq. 4 describes the vacuum generation performance of a single-stage pump. It shows clearly by increasing  $\alpha$ , i.e. by reducing dead volume, the pump vacuum performance can be improved. Dead volume of the pump here includes four major parts: (1) channel volume; (2) residue chamber volume when chamber piston is fully pushed up; (3) dead volume caused by non-ideal structure factors like wafer bow; and (4) virtual dead volume caused by insufficient pump chamber gas charging and discharging. (1) & (2) are determined by design, (3) involves with fabrication process, and (4) is controlled by operation.

This model can help to understand better of the displacement pump for vacuum generation. However, before further discussion, another major limiter, leakage, needs to be studied.

### Valve Leak Rate

For a single-ring valve seat, the valve flow is generally limited by the gap between valve seat and valve boss, and at low pressure difference, the fluidic resistance  $R_{valve}$  is as in [10]:

$$R_{valve} = \frac{6\eta}{\pi h^3} \ln\left(\frac{r_1}{r_2}\right) \quad (5)$$

where

- $R_{valve}$ : valve fluidic resistance
- $r_1$ : outer radius of valve seat
- $r_2$ : inner radius of valve seat
- $h$ : gap between valve seat and valve boss

With inner radius of the valve seat as  $50 \mu\text{m}$ , a variety of valves were fabricated and their leak rates were measured. All the valves went through the same fabrication process and the same testing environment, which ensures they have the same gap  $h$ . As can be seen in Fig. 8, the fluidic resistance is proportionally to the

logarithm term and the leak rate results agree with that.

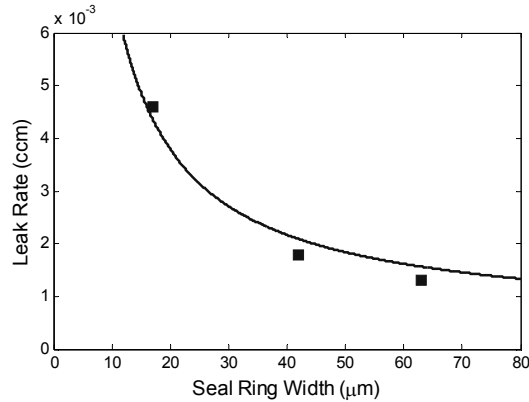


Figure 8: Valve leakage rate versus seal ring width (reproduced from [11]). Solid line is a best fit using Eq. 5.

### Virtual Dead Volume

To explore the effect of virtual dead volume on vacuum performance, we conducted a two-step experiment. The performance is expected to be improved with larger discharging time which reduces the virtual dead volume based on the analysis above. The pumping started with a discharging time of 300ms per cycle. When the vacuum generation reached an equilibrium with a vacuum of ~530 torr, we increased the discharging time to 600ms and the pressure was reduced further to below 500 torr, as shown in Fig. 9.

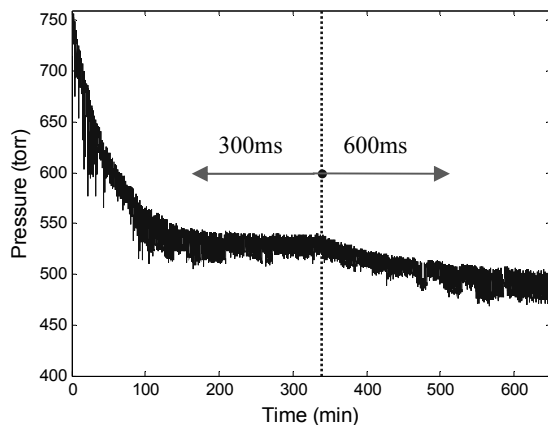


Figure 9: Vacuum generation by tuning discharging time.

### Analysis of Vacuum Generation Performance

With the leak rate,  $Q$  in Eq. 4, we have a better understanding of the vacuum generation performance of this displacement pump. Operation was fine tuned to minimize the virtual dead volume and an efficiency factor of 0.6 was obtained theoretically by neglecting part (3) of the dead volume. Without consideration of the leak term, we get  $P_{vacuum} = 406$  torr from Eq. 4. By incorporating leak rate into the equation, we can have  $P_{vacuum} = 425$  torr. The difference between tested result of 494 torr and calculated 425 torr would be mainly contributed by the imperfect assumption to neglect part (3) in dead volume estimation. Wafer bow may account for as much as 15% of the total pump chamber volume and the difference is right within that range.

### CONCLUSION

We have developed a single stage micromachined

displacement vacuum pump. Its vacuum performance was measured to achieve a base pressure of 494 torr experimentally, and the factors limiting its performance were systematically studied. With all the knowledge we have gained, we built a model that explains the testing results and improves our understanding of displacement pump for vacuum generation. Dead volume and leakage are the two major limiters on vacuum performance. Our immediate next step is to reduce the dead volume with a more compact design and optimized fabrication process, and also to minimize leakage with valve seat redesign.

### ACKNOWLEDGEMENT

This work was partially conducted in Microsystems Technology Laboratories at Massachusetts Institute of Technology. This project is sponsored by DARPA under the Micro Gas Analyzer and Micro Pumps Programs.

### REFERENCES

- [1] P. Woias, "Micropumps—Past, Progress and Future Prospects", *Sensors and Actuators B*, 105, 28 (2005).
- [2] D.J. Laser, and J.G. Santiago, "A Review of Micropumps", *Journal of Micromechanics and Microengineering*, 14, R35 (2004).
- [3] S. McNamara, and Y.B. Gianchandani, "On-chip Vacuum Generated by a Micromachined Knudsen Pump", *Journal of Microelectromechanical Systems*, 14, 741 (2005).
- [4] M. Doms, and J. Muller, "A Micromachined Vapor-jet Vacuum Pump", *Transducers & Eurosensors '07, The 14th International Conference on Solid-State Sensors, Actuators and Microsystems*, Lyon, France, 4C1.1 (2007).
- [5] K.P. Kamper, J. Dopfer, W. Ehrfeld, and S. Oberbeck, "A Self-filling Low-cost Membrane Micropump", *Proc. 11th Annual Int. Workshop on Micro Electro Mechanical Systems*, Heidelberg, Germany, 432 (1998).
- [6] A.A. Astle, H.S. Kim, L.P. Bernal, K. Najafi, and P.D. Washabaugh, "Theoretical and Experimental Performance of a High Frequency Gas Micropump", *Sensors and Actuators A*, 134, 245 (2007).
- [7] D.C. Roberts, H. Li, J.L. Steyn, O. Yaglioglu, S.M. Spearing, M.A. Schmidt, and N.W. Hagood, "A Piezoelectric Microvalves for Compact High-frequency, High Differential Pressure Hydraulic Micropumping Systems", *Journal of Microelectromechanical Systems*, 12, 81 (2003).
- [8] H.Q. Li, D.C. Roberts, J.L. Steyn, K.T. Turner, J. A. Carretero, O. Yaglioglu, Y.-H. Su, L. Saggere, N.W. Hagood, S.M. Spearing, M.A. Schmidt, R. Micak, and K.S. Breuer, "A High Frequency High Flow Rate Piezoelectrically Driven MEMS Micropump", *Technical Digest of the 2000 IEEE Solid State Sensor and Actuator Workshop*, Hilton Head Isl., SC, 6/4-8/00, Transducer Research Foundation, Cleveland (2000), pp. 69-72.
- [9] S.D. Senturia, *Microsystem Design*, Kluwer Academic Publishers, Boston, 2000.
- [10] P. Galambos, C.D. James, J. Lantz, R.C. Givler, J. J. McClain, and R.J. Simonson, "Passive MEMS Valves with Preset Operating Pressures for Microgas Analyzer", *Journal of Microelectromechanical Systems*, 18, 14 (2009).
- [11] V. Sharma, "MEMS Micropump for a Micro Gas Analyzer", Ph.D. Thesis, Massachusetts Institute of Technology, 2009.

### CONTACT

\*Hui Zhou, tel: +1-617-253-0446; zhouhui@MIT.EDU

# A WIRELESSLY CONTROLLED SHAPE-MEMORY-ALLOY MEMS GRIPPER MICROFABRICATED USING AN ELECTROPLATING-BASED BONDING PROCESS

M. S. Mohamed Ali<sup>1, 2\*</sup> and K. Takahata<sup>1</sup>

<sup>1</sup> The University of British Columbia, Vancouver, Canada

<sup>2</sup> Universiti Teknologi Malaysia, Skudai, Johor, Malaysia

## ABSTRACT

This paper reports the wireless control of bulk-micromachined shape-memory-alloy actuators using an external radiofrequency magnetic field and its application to a MEMS gripper. The frequency-sensitive wireless resonant heater to which the gripper actuator is bonded is activated only when the field frequency is tuned to the resonant frequency of the heater. A bonding technique based on photo-defined copper electroplating is developed to mechanically and thermally couple the gripper with the planar heater circuit. The actuation range of 290  $\mu\text{m}$  as the tip opening distance is obtained with normally-closed 4-mm-long grippers at a device temperature of 138  $^{\circ}\text{C}$ . The active frequency range is measured to be  $\sim 6$  MHz. The manipulation of vertically aligned carbon nanotube forests is experimentally demonstrated.

## INTRODUCTION

Bulk-micromachined shape-memory-alloy (SMA) actuators provide attractive features such as very large forces, high mechanical robustness with simple structures, and biocompatibility [1-3]. Various actuation mechanisms for SMA microactuators have been investigated. Joule heating by passing currents through heaters [4, 5] and directly through the SMA parts [6] is among the most widely used method to establish a heat source to the actuators. In this case, however, the mobility of the devices is severely constrained by the need of wired interface to them, limiting the application range for the devices. In order to address this, wirelessly controlled microactuators have been studied. For example, wireless SMA actuators in microrobotic applications were recently reported [7, 8]. However, they require batteries for their operations, resulting in relatively large device sizes and the need of complex control mechanisms. Nitinol, a biocompatible Ti-Ni alloy, has been extensively used in medical fields, enabling a variety of implantable devices and surgical tools [9-13]. Toward the application of SMA microactuators to this type of medical areas, the ability to wireless control is a key to reducing the interface complexity and hence promoting the practicality of the devices. In addition, passive configurations are highly beneficial to enable simple/robust, small, and low-cost products in these fields.

The reversible actuation of SMA has been approached mainly by two mechanisms – one-way memory assisted with external forces provided by cold-state reset layers [14] and two-way memory [15]. The one-way memory has been more commonly utilized for the actuation because of its reliability compared to the two-way memory approach that requires long thermal cycling for the material training and is not very stable. Despite of the favorable features of bulk SMA materials mentioned above, they have not been widely adopted in MEMS largely due to their incompatibility with standard batch microfabrication techniques and difficulties in their wafer-scale assembly. Recently, a wafer-scale integration method for bulk-SMA devices was reported [16]. However, polymer bonding utilized in the method poses issues in bonding quality and effective heat transfer to the SMA components. There are still many challenges in the integration of bulk SMA for MEMS applications.

This research explores a bulk-micromachined SMA-based microactuator that is passively controlled through radiofrequency (RF) power transfer to a wireless heater with which the SMA

actuator is coupled. In order to address the issues related to SMA bonding, a planar assembly technique based on photo-defined selective electroplating is developed and used to bond the SMA actuators to the wireless heater circuits.

## DEVICE PRINCIPLE

The micromachined SMA actuator developed in this effort is operated through an inductor-capacitor (LC) resonant circuit that serves as a frequency-sensitive wireless heater activated by an external RF magnetic field (Figure 1 (a)). An ac current is generated in an LC circuit when the circuit is exposed to an ac magnetic field due to the electromotive force induced by the field. The power consumed in the LC circuit,  $P$ , can be expressed as [17];

$$P(\omega) = \frac{Rv^2}{[R + j(\omega L - 1/\omega C)]^2} \quad (1)$$

where  $v$  is the electromotive force,  $L$  and  $C$  are respectively the inductance and the capacitance of the circuit,  $R$  is the parasitic resistance of the circuit, and  $\omega$  is the angular frequency of the ac current. The reactance in (1) will be eliminated when the frequency of the ac current, or that of the magnetic field matches the resonant frequency of the circuit,  $\omega_r = (LC)^{-1/2}$ . At this condition, the power transfer to the circuit is maximized, resulting in:

$$P(\omega_r) = \frac{v^2}{R}. \quad (2)$$

Thus, the field energy is effectively converted to Joule heat when the field frequency is tuned to the resonant frequency of the LC circuit, i.e., the actuation is controlled with the frequency, rather than the field intensity. The steady state temperature rise of the LC circuit,  $T_{ss}$ , can be theoretically expressed as [18]:

$$T_{ss} = \frac{R_T v^2 / R}{1 + \alpha_R R_T v^2 / R} \quad (3)$$

where  $R_T$  is the thermal resistance to the surrounding of the circuit and  $\alpha_R$  is the temperature coefficient of resistance of the circuit.

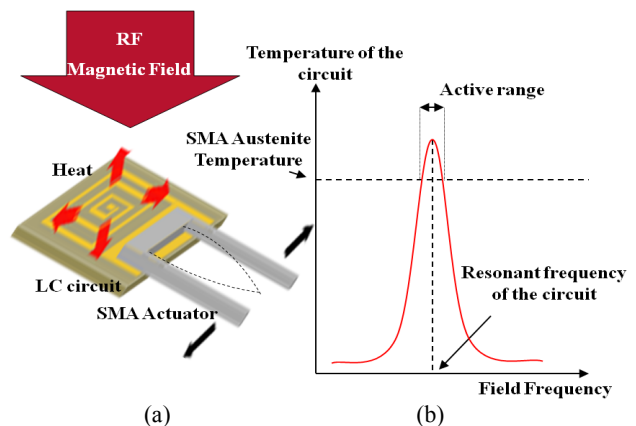


Figure 1: (a) Wirelessly controlled SMA micro-gripper and (b) working principle of the device.



The SMA gripper with two beams that have a rectangle cross section is fabricated so that one of the sidewalls of each of the beams is coated with the cold-state reset layer. When the temperature of the device exceeds the austenite-phase temperature of the SMA, the gripper is actuated as the material returns to its remembered shape (Figure 1(b)). The shape of the gripper will be restored to be the cold-state original shape when heat is removed due to the force provided by the reset layer. The electroplating-based bonding method developed in this study (discussed in the next section) is used to achieve not only high-precision assembly of the micromachined SMA gripper on the wireless heater with high mechanical bonding strength but also high thermal conductance between the two components.

## DESIGN AND FABRICATION

The SMA grippers developed have a normally closed design (Figure 2 (a)). The 4-mm-long gripper structures are formed by micro-electro-discharge machining ( $\mu$ EDM) [19] of 300- $\mu$ m-thick Ti-Ni SMA sheets with an austenitic-phase temperature of 65 °C. The SMA components are designed to have a bonding pad with a cavity and perforations as shown in Figure 2(a). Each of the two gripper beams has a thickness of 62  $\mu$ m and a compressive SiO<sub>2</sub> layer 3- $\mu$ m thickness on the outer sidewall of the beam. This configuration is calculated to bend the beam with a displacement of ~300  $\mu$ m at the tip of the beam. The spacing between the two beams at their bottoms is defined to be 570  $\mu$ m so that the bending is large enough to close the gripper at its cold state. The LC circuit has a planar spiral coil with an overall size of 5 $\times$ 5 mm<sup>2</sup> and the line width and spacing as indicated in Figure 2(b). The SMA component is bonded on one of the capacitor electrodes of the LC circuit that provides heat to the SMA through the bonded region. Figure 3 shows the process flow developed for the device fabrication. The planar LC circuit is fabricated using single-sided copper-clad polyimide (PI) film with 50- $\mu$ m thickness (G2300, Shehdahl Co.). The photolithography for the circuit fabrication is performed with dry-film photoresists (MacDermid SF306 and DuPont PM240). First, one of the capacitor electrodes is formed by wet etching of the copper-clad layer (Figure 3, step 1). This electrode provides the region for the SMA bonding to the circuit. Next, the PI film is etched using a KOH-based solution to create the via contact hole in the film (Figure 3, step 2). After depositing a

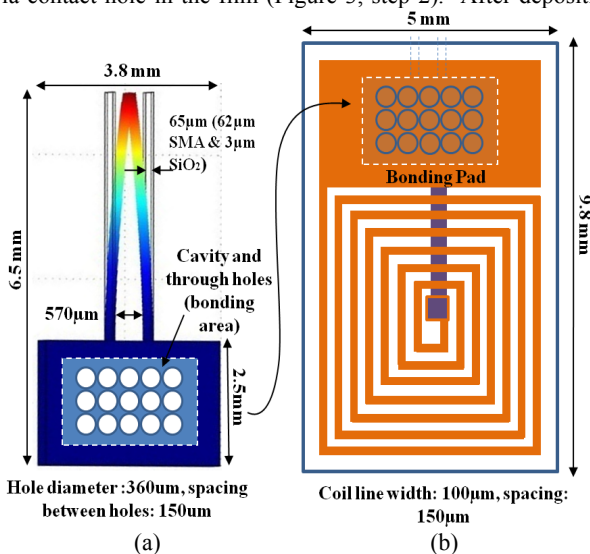


Figure 2: (a) SMA gripper design and (b) LC circuit design.

Ti-Cu seed layer on the PI side, copper electroplating in the patterned dry-film photoresist mold is performed to form the coil and the other capacitor electrode with a thickness of 30-35  $\mu$ m (Figure 3, step 3). Figure 4(a) shows the fabricated LC circuits. For the SMA gripper fabrication, the gripper component is first shaped to have the single beam structure in a piece of the SMA sheet using  $\mu$ EDM. This is followed by the deposition of a 1.5- $\mu$ m-thick SiO<sub>2</sub> layer using PECVD at 350 °C on both sides of the SMA piece so the sidewalls of the beam have ~3- $\mu$ m-thick SiO<sub>2</sub> that serves as the reset layer. The SMA component is then  $\mu$ EDMed to create the bonding pad with the cavity and perforations (Figure 4(b)). This  $\mu$ EDM step removes the SiO<sub>2</sub> layer from the pad region. The bonding pad of the SiO<sub>2</sub>-coated SMA is fixed onto the capacitive electrode on the copper-clad side of the circuit that is coated with photoresist (SPR 220-7, ROHM and HASS) (Figure 3, step 4), followed by the lithography to remove the photoresist in the pad region (Figure 3,

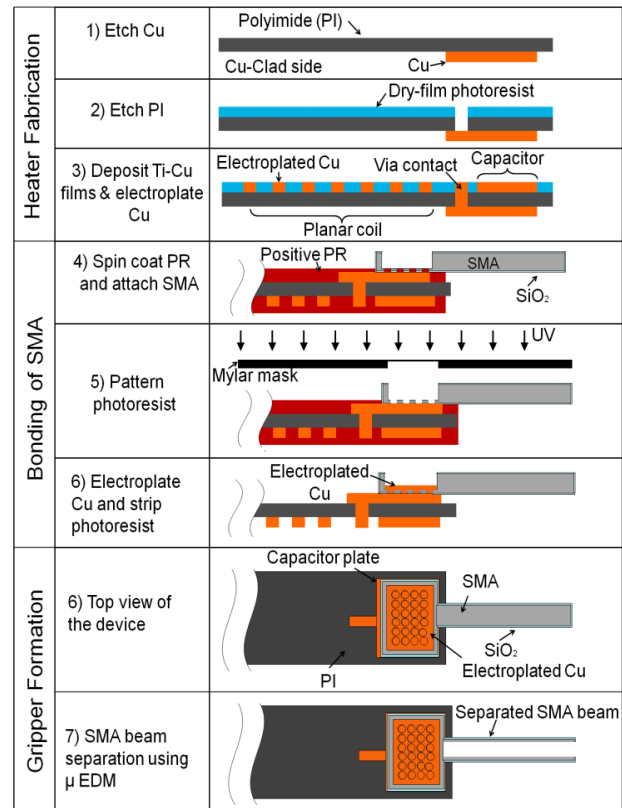


Figure 3: Fabrication process flow (cross-sectional view except steps 6 and 7).

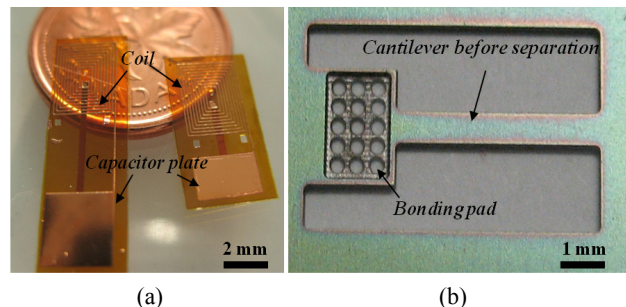


Figure 4: (a) Samples of fabricated LC resonant circuits and (b) an SMA gripper component fabricate with  $\mu$ EDM (prior to separation from the original sheet).

step 5). Copper electroplating is then performed in the pad region (Figure 3, step 6) so that the copper grown from the capacitor electrode through the pad's perforations is over-plated and connected to the portion plated on the pad, mechanical fixing the pad. In this step, the SiO<sub>2</sub> layer on the SMA beam acts as a mask for electroplating so that copper is only deposited on the cavity of the SMA and on the capacitor electrode through the perforations in the cavity. Figure 6(a) shows the pad of the SMA gripper component that was bonded on the circuit with this electroplating process. Finally, the single beam of the SMA is split into two beams using  $\mu$ EDM (Figure 3, step 7) to form the gripper structure with vertical sidewalls (Figure 5). These split beams consequently have inner sidewalls without SiO<sub>2</sub> layers, resulting in bending and closing their tips due to the compressive SiO<sub>2</sub> layer present on the outer sidewalls of the beams. The final form of the device is shown in Figure 6 (b).

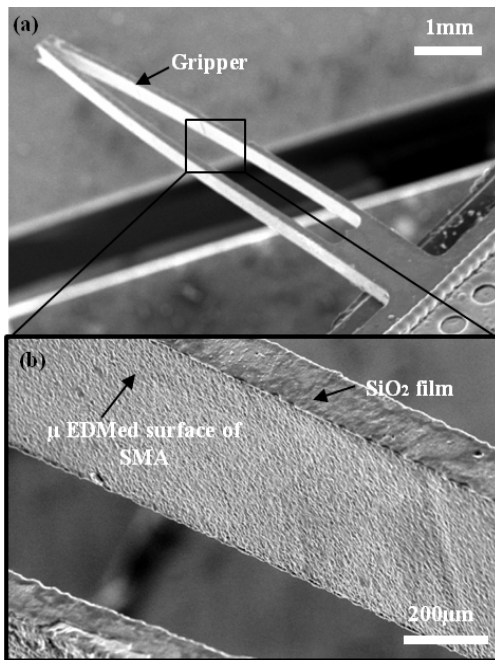


Figure 5: A fabricated SMA gripper: (a) The gripper beams split using  $\mu$ EDM; (b) a close-up of the inner sidewall of the beam.

### EXPERIMENTAL RESULTS

Preliminary wireless tests were performed to characterize the fabricated grippers. The tests were conducted using the set-up illustrated in Figure 7. In this set-up, an amplified RF signal with an output power of up to  $\sim 1$  W is fed to the external coil (diameter  $\sim 4$  mm, 497-nH inductance) to generate an RF magnetic field that excites the LC circuit of the device. The thermo-mechanical behavior of the gripper was characterized using a thermocouple that was attached to the devices (on the capacitor electrode of the circuit located on the opposite side of the electrode bonded with the SMA) as well as a measuring microscope to characterize the displacement of the gripper. It was experimentally verified that the dependence of the thermocouple reading on the presence of the magnetic field with the power level and frequencies used in the tests was minimal or undetectable.

Figure 8 shows a typical thermal response of the fabricated device. The resonant frequency of the LC circuit used in this test was 105 MHz. The device temperature was measured while scanning the field frequency from 93MHz to 113MHz at a constant output power. The result shows a strong peak (of 138 °C) when the

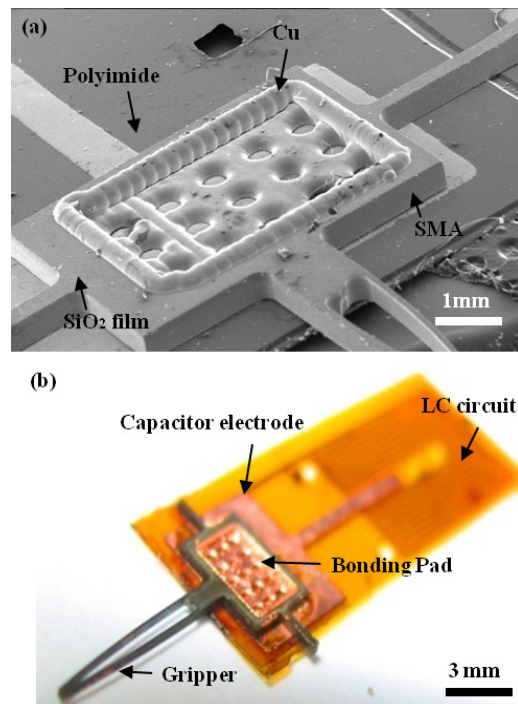


Figure 6: Fabrication results: (a) The SMA pad bonded by electroplated copper; (b) the overall shape of a fabricated device.

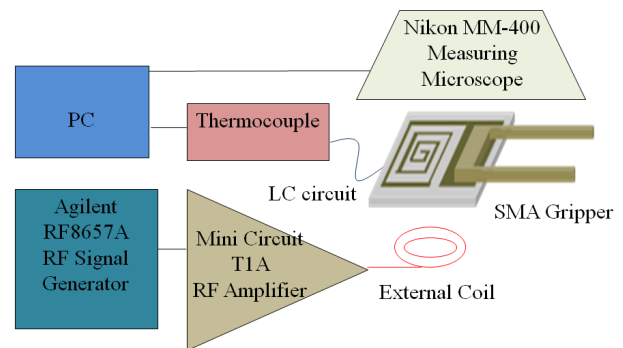


Figure 7: A set-up for wireless tests.

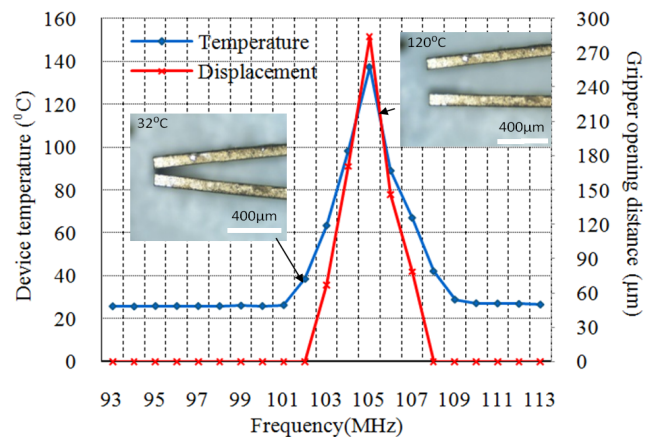


Figure 8: Measured circuit temperature and gripper openings vs. field frequency (inset images show tip opening of the gripper at corresponding temperatures).

field frequency is aligned to the resonant frequency of the circuit. The opening distance of the gripper was also measured and plotted in Figure 8, indicating the maximum opening of 290  $\mu\text{m}$ . It also suggests that the actuation is initiated when the device temperature reaches around 40  $^{\circ}\text{C}$ , and that the active frequency range for the actuation of this device is  $\sim 6$  MHz. The gripping ability of the devices was demonstrated using samples of vertically aligned carbon nanotube (CNT) forests as shown in Figure 9; a part of CNT forests were successfully manipulated by controlling the opening distance of the grippers fabricated in this effort.

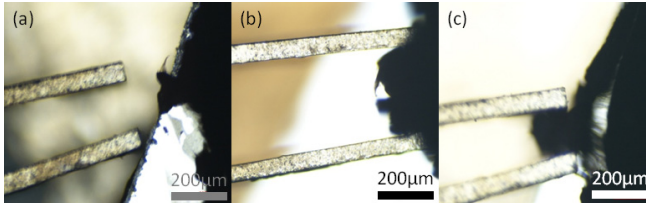


Figure 9: Manipulation of a CNT forest: (a) Approaching the forest (device temperature  $\sim 100$   $^{\circ}\text{C}$ ); (b) making contact ( $\sim 140$   $^{\circ}\text{C}$ ); (c) gripping and manipulating a part of the forest (room temperature).

## CONCLUSIONS

A fully passive, bulk-micromachined SMA gripper that can be controlled using external RF magnetic fields has been investigated. A 4-mm-long SMA gripper with a normally closed design was coupled with a planar resonant wireless heater with a  $5 \times 5$ -mm<sup>2</sup> spiral coil that is activated by tuning the field frequency to the resonant frequency of the heater. An electroplating-based planar bonding technique was developed to achieve mechanical and thermal coupling of the SMA gripper components with the wireless heater circuits. The fabricated grippers exhibited the tip opening of 290  $\mu\text{m}$  at a device temperature of  $\sim 140$   $^{\circ}\text{C}$  that was obtained when the frequency field is at the heater's resonant frequency of 105 MHz with a constant RF power of  $\sim 1$  W. The frequency selectivity of the device provides an opportunity to implement simultaneous control of multiple SMA actuators that are bonded to the wireless heaters with different resonant frequencies. The developed bonding technique based on photo-defined electroplating may be leveraged for the microfabrication of arrayed SMA actuators by scaling up the technique.

## ACKNOWLEDGMENTS

The authors would like to thank Ningyuan Wang for his assistance in fabrication and testing work and also Dr. Alireza Nojeh for our use of CNT forests. This work was partially supported by the Natural Sciences and Engineering Research Council of Canada, the Canada Foundation for Innovation and the British Columbia Knowledge Development Fund. M.S. Mohamed Ali acknowledges financial support from Ministry of Higher Education Malaysia and Universiti Teknologi Malaysia.

## REFERENCES

- [1] N.B. Morgan, "Medical shape memory alloy applications-the market and its products" *Materials Science and Engineering A*, vol. 378 (2004), pp. 16-23.
- [2] H. Kahny, M. A. Huffz, and A. H. Heuery, "The TiNi shape-memory alloy and its applications for MEMS" *J. Micromech. Microeng.*: vol. 8 (1998), pp. 213-221.
- [3] W. Benard, H. Kahn, A. Heuer, M. Huff, "A titanium-nickel shape-memory alloy actuated micropump", *Transducers '97 Chicago*, 1997, pp. 361-364 vol.1.

- [4] N. Sandström, S. Braun, G. Stemme, W. van der Wijngaart, "Full Wafer Integration of Shape Memory Alloy Microactuator using Adhesive Bonding" *Proc. IEEE Transducers*, 2009, pp.845- 848.
- [5] T. Suguwara, K. Hirota, M. Watanabe, T. Mineta, E. Makino, S. Toh and T. Shibata, "Shape memory thin film actuator for holding a fine blood vessel", *Sensors and Actuators A: Physical*, Vol 130-131 (2006), pp 471-467.
- [6] W. M. Huang, J. P. Tan, X. Y. Gao, and J. H. Yeo, "Design, testing, and simulation of NiTi shape-memory-alloy thin-film-based microgrippers" *J. Microlithography, Microfabrication, Microsystems*, Vol. 2 (2003), pp 185-190.
- [7] B. Kim, M.G. Lee, Y.P. Lee, Y. Kim, G. Lee, "An Earthworm-like Micro Robot using Shape Memory Alloy Actuator" *Sensors and Actuators A: Physical*, 125 (2) (2006), pp 429 – 437.
- [8] Y.P Lee, B. Kim, M.G Lee, J.Park, "Locomotive mechanism design and fabrication of biomimetic micro robot using shape memory alloy" *Proc. IEEE Robotics & Automation*, 2004, pp 5007-5012.
- [9] H. Kahn, M.A. Huff, A.H. Heuer, The TiNi shape-memory alloy and its applications for MEMS, *Journal of Micromech. and Microeng.*, Vol 8 (1998), pp 213–221.
- [10] Y.Q. Fu, W.M. Huang, H.J. Du, X. Huang, J.P. Tan, X.Y. Gao, Characterization of TiNi shape-memory alloy thin films for MEMS applications, *Surface Coating and Technology*, Vol 145 (2001), pp 107–112.
- [11] A. Ishida, M. Sato, A. Takei, K. Nomura, S. Miyazaki, Effect of aging on shape memory behavior of Ti–51.3 at.% Ni thin films, *Metall. Mater. Trans. A* 27A (1996) pp 3753–3759.
- [12] D. Reynaerts, J. Peirs and H. Brussel, "An implantable drug-delivery system based on shape memory alloy micro-actuation", *Sensors and Actuators A: Physical*, Volume 61, Issues 1-3 (1997), pp 455-462 .
- [13] Y. Fu, H. Du, W. Huang, S. Zhang and M. Hu, "TiNi-based thin films in MEMS applications: a review", *Sensors and Actuators A: Physical*, vol. 112, May. 2004, *Microsyst.*, Vol. 2, 185 (2003), pp. 395-408.
- [14] Y. Bellouard, R. Clavel, R. Gotthardt, J. E. idaux, T. Sidler, "A new concept of monolithic. Shape Memory Alloys micro-devices used in micro-robotics", *Actuator'98- 6th International Conference on New Actuators*, Bremen, Germany, June 17-19, 1998, P88.
- [15] H. Scherngell and A.C. Kneissl, "Training and stability of the intrinsic two-way Shape memory effect in Ni-Ti alloys" *Scripta Materialia*. Vol 39 (1998), p. 205-212.
- [16] S. Brown N. Sandström, G. Stemme, "Wafer-scale manufacturing of bulk shape-memory-alloy microactuators based on adhesive bonding of titanium-nickel sheets to structured silicon wafers" *Journal of Microelectromechanical Systems*, vol. 18, no 6 (2009), pp. 1309-1317
- [17] E.H. Sarraf, G.K. Wong, K. Takahata, "Frequency-Selectable Wireless Actuation of Hydrogel using Micromachined Resonant Heaters Toward Implantable Drug Delivery Application" *Proc. IEEE Transducers*, 2009, pp 1525-1528.
- [18] S.D. Senturia, *Microsystem Design*, Kluwer Academic Publishers, New York, 2001.
- [19] T. Masaki, K. Kawata, T. Masuzawa, "Micro Electro-Discharge Machining and Its Applications" *Proc. IEEE MEMS*, 1990, pp 21-26.

## CONTACT

\*M.S. Mohamed Ali, tel: +1-604-761-8716;  
mohamedm@ece.ubc.ca

# CMOS-MEMS 8-BIT MEMDAC NANOPositionER WITH INTEGRATED POSITION SENSING AND DIGITAL CONTROL

Neil Sarkar<sup>1\*</sup> and Raafat Mansour<sup>1</sup>

<sup>1</sup>University of Waterloo, Waterloo, Ontario, Canada

## ABSTRACT

An 8-bit MEMDAC (microelectromechanical digital-to-analog converter) with nanometric position sensing and digital control has been implemented in a CMOS-MEMS process. The device is intended for use in scanning probe lithography and requires a closed-loop position resolution of 1 nm. Lateral electrothermal actuators provide a displacement of 8 $\mu$ m to each of the 8 inputs of the compliance network. The step size corresponding to a transition of the least significant bit (LSB) is ~31nm. A piezoresistive sensor integrated in the LSB has an output-referred position resolution of 0.39nm. The design has been extended to 2 dimensions with an integrated cantilever and CMOS electronics to reduce pincount.

## INTRODUCTION

Arrays of MEMS-based nanopositioners are desirable for parallel atomic precision patterning (APP) on Si. [1] The H depassivation lithography process is depicted below in figure 1. The lateral position resolution, stiffness, range of motion, voltage limitations, stability, and vacuum compatibility requirements of the APP process are used as specifications in the design of the MEMDAC positioning unit presented here.

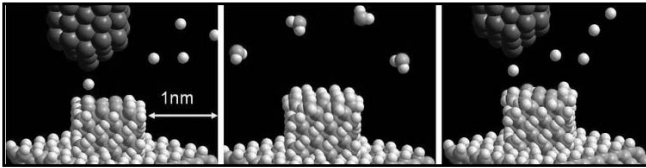


Figure 1: H Depassivation lithography process begins with the removal of H from a Si surface with atomic precision (left). In the deposition phase (center), SiH<sub>2</sub> radicals in the gas phase deposit one Si atom wherever an H atom is removed (patterned Atomic Layer Epitaxy). After the deposition cycle, SiH<sub>2</sub> is evacuated and the pattering step is repeated to create 3D structures.

We report an 8-bit MEMDAC that is fabricated in the ASIMPS (Application-specific integrated MEMS processes) CMOS-MEMS process [2]. The design is based on previously reported MEMDAC architectures [3,4,5] and has been augmented in the following ways:

- 1) The number of bits has been increased to 8 in order to achieve a step-size of 31nm.
- 2) The LSB contains a piezoresistive position sensor for sub-positioning within a bit. The piezoresistive position sensor has an output-referred resolution of < 1 nm.
- 3) A CMOS scan chain and current drivers are integrated with the device in order to control multiple MEMDACs with a 5-wire interface.
- 4) A latch has been placed at the distal end of the positioner for power-off positioning.
- 5) A 2-D positioner with an integrated cantilever has been implemented using four 1-D MEMDACs

## DEVICE DESIGN

### Lateral Actuation

Electrothermal actuation based on the thermal bimorph effect can be implemented in a CMOS-MEMS process by laterally offsetting the internal layers in a structural beam, as shown in figure 2. The details of the actuator's design and optimization have been presented elsewhere [6].

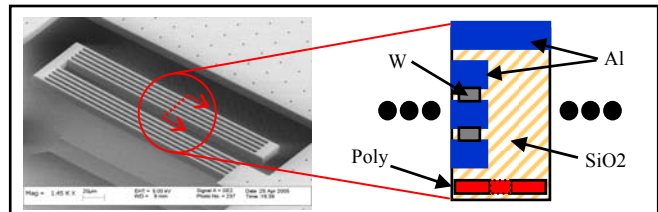


Figure 2: SEM image (left) of a lateral actuator in the ASIMPS CMOS-MEMS process. The parallel arrangement of beams increases the output force. A cross section of one bimorph (right) shows the offset in the internal metal layers used to achieve a lateral thermal moment.

The two constituent materials of the bimorph are aluminum and silicon dioxide, which have a similar young's modulus but a very dissimilar TCE ( $\alpha_{Al}=23.1\mu K^{-1}$  and  $\alpha_{SiO_2}=0.5\mu K^{-1}$ ).

It is advantageous to couple multiple bimorphs together in the actuator in order to increase out-of-plane stiffness and lateral force; however, the bimorph beams cannot simply be coupled to a rigid plate, since this would impose a zero-moment constraint and result in zero-deflection of the beams. Arranging 2 bimorphs (in series within a beam) in a symmetrically opposed fashion eliminates rotation at the distal end of the beam, thus enabling the designer to couple multiple beams together to a plate. Due to the asymmetric cross section of the beam in the out-of-plane (z) direction, a single set of coupled beams experiences parasitic out-of-plane motion. This issue is mitigated by folding and reflecting the first set of beams, resulting in the U-shaped structure of figure 3c.

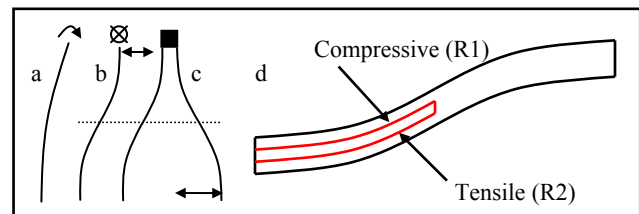


Figure 3: (a) Full-length bimorph beams cannot be coupled in parallel due to the moment that exists at the tip. (b) A pair of symmetrically opposed bimorphs in a beam has parasitic out-of-plane motion. (c) This u-shaped arrangement moves in a purely rectilinear fashion. (d) Piezoresistors are differentially arranged within a beam to sense lateral deflection.

This type of lateral actuator was selected due to its relatively high work/unit volume metric, its capability to produce a large static displacement, and its low driving voltage which is CMOS compatible. In vacuum, this actuator is capable of deflecting 10 $\mu$ m while consuming 1.3mW.

### Lateral Piezoresistive Position Sensing

The gauge factor of the polysilicon available in the ASIMPs process has been extracted using a passive test structure in conjunction with a motion control stage. An FEA model of the passive cantilever used in the experiment is used to predict the strain in the polysilicon layer as a function of deflection. The measured resistance of the piezoresistors is then applied to this FEA model in order to identify the gauge factor. Our measurements indicate a gauge factor of  $\sim 20$  in the high-value-resistor-type polysilicon available in the process. This number is significantly higher than the gauge factors obtained in the silicided and low-value-resistor materials available in the same process.

In order to obtain strain measurements on lateral displacements while mitigating TCR (temperature coefficient of resistivity) effects, we adopt the design pattern shown in figure 3. Within a monolithic beam structure, we place 2 piezoresistors in parallel, on either side of the beam's neutral axis. Upon actuation, one of the resistors experiences compressive stress while the other experiences tensile stress, while they both experience the same temperature distribution. The cross-sectional temperature profile at any plane along the length of the beam is assumed to be equithermal. Thus, this design is insensitive to temperature variations along the length of the beam, since the temperature distribution within the 2 resistors is identical. Measurements on piezoresistors incorporated into an actuator beam are reported elsewhere [7]. Measurements of piezoresistance in the ASIMPs process are also presented in [8]. In this work, we integrate the piezoresistors within the MEMDAC's compliance network, as discussed further below.

### Compliance Network

The MEMDAC design consists of a network of compliant beams that is analogous to the resistive ladder network that is present in an R-2R electronic DAC, as described in [3] and shown in figure 4.

The actuators that provide input displacements into the compliance network are limited by hard-stops in order to provide distinct positions of 0 $\mu$ m and 8 $\mu$ m. A lateral self-assembly displacement occurs in the actuators due to residual stress gradients, so the hard-stops are judiciously shifted to mitigate this effect. In placing the hard-stops, one must also consider thermal coupling from adjacent actuators through the compliance network, substrate, and ground shield. These sources of heat flow result in partial actuation of a bit that is intended to be "off" when adjacent bits are "on." The hard stops must therefore be placed conservatively so that this partial actuation does not displace the actuator from its "off" position.

An additional actuator is placed orthogonally with respect to the output of the MEMDAC, and serves as a latching element. This actuator self-assembles into the engaged position upon release, eliminating power consumption while the device is off.

The LSB in the MEMDAC connects to a load beam with integrated differential piezoresistive strain sensors. This geometry ensures that the resistors are temperature-matched, but they experience opposite stress. An off-chip bridge circuit is used to

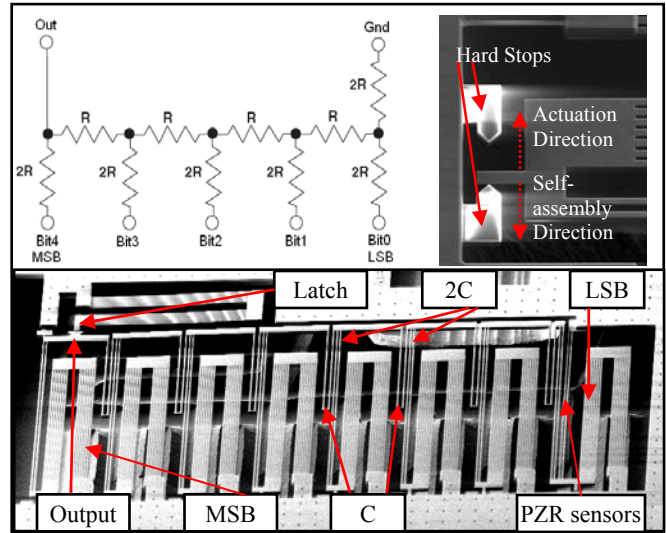


Figure 4: Electronic R-2R DAC (top left) and MEMS implementation (bottom). SEM image shows beams of compliance C and 2C in the network. A latch is present for power-off positioning at the output, and the LSB and MSB are indicated. The piezoresistive strain gauge is located within the load beam near the LSB. Hard stops are used to limit the input position to 2 distinct values (top right).

measure position with a resolution of 100nm. A 100nm position resolution in the LSB corresponds to <0.5nm displacement at the output.

## ANALYSIS

### Electrical Equivalent Circuit

An equivalent circuit of the mechanical system is developed according to the methodology presented in [9] and shown in figure 5. In the simplest case, the beams are considered to be pure springs and are represented as capacitors with a value of:

$$C_e = \frac{1}{k_m} = C_m$$

Where

$C_e$  = capacitance in the electrical domain

$k_m$  = stiffness in the mechanical domain

$C_m$  = compliance in the mechanical domain

In this analogy (the e $\rightarrow$ V convention), the input and output displacements of beams are replaced by input and output charges on capacitors; the output voltage is calculated after charge sharing has occurred, and represents the output force. The output force is applied to the load beam, resulting in an output displacement that is equivalent to the charge that is obtained with:

$$Q_{net} = C * V_{out}$$

Where

$Q_{net}$  is the net charge across the network

C is the capacitance looking into the network (this value remains constant regardless of the number of bits in the network)

$V_{out}$  is the voltage at the output of the circuit, and is analogous to the force at the output of the mechanical system.

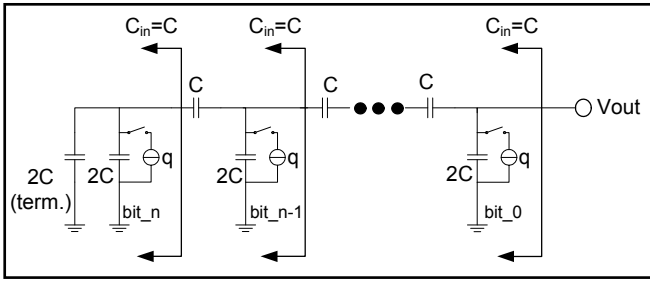


Figure 5: Mechanical equivalent circuit of the compliance network. Input displacements are represented by charge sources  $q$ . Spring constants of beams are replaced with capacitances  $C$  and  $2C$ . The capacitance looking into the network is always  $C$ , regardless of the number of bits in the system.

Note that this convention captures the fact that the operation of the MEMDAC is non-dissipative in the mechanical domain, since it uses capacitances to represent stiffness, as opposed to resistances that would represent dampers.

### Geometric Advantage

The MEMDAC's compliance network provides a geometric advantage of  $1/256$  between the LSB and the output, as calculated by applying a charge of  $q$  to the LSB and obtaining an output charge of  $q/256$ . This is an attractive feature and is indeed the reason why such an architecture was considered for the atomically precise patterning application. Several sources of noise limit our position resolution in the piezoresistive sensor to  $\sim 100\text{nm}$ . This resolution is effectively scaled down by a factor of 256 in the compliance network. Thus, we obtain superior output-referred resolution by including the sensor in the LSB of the device.

The total achievable output displacement is sensitive to the number of bits, and can be obtained with the following relation that is easily calculated from the R-2R ladder circuit:

$$D_{\max} = D_{\text{act}} * \sum_{i=1}^N \frac{1}{2^i}$$

Where

$D_{\max}$  is the maximum output displacement

$D_{\text{act}}$  is the deflection of each bit ( $8\mu\text{m}$ )

$N$  is the number of bits

### Mechanical Advantage

The output stiffness of the MEMDAC, represented by the capacitance looking into the network, remains constant regardless of the number of bits as illustrated in figure 5. Each bit in the compliance network experiences a binary weighted mechanical advantage equivalent to the reciprocal of its geometric advantage.

The mechanical and geometric advantage features can also be implemented by connecting a single actuator to its load through a pair of springs (connected similarly to a single unit in the C-2C ladder), but with a stiffness ratio of  $1/256$ . This would result in a more compact design than the MEMDAC. Such a design pattern would result in improved output-referred sensor resolution and enhanced stiffness at the expense of reduced deflection.

### Thermomechanical Noise

The thermomechanical noise that is introduced by the network between the LSB and the output is lower than the desired resolution. In order to calculate this, a damping term must be included in the beam model. The full model of the beam as a mass-spring-damper system is replaced as in [9] with an equivalent

RLC circuit. Thermomechanical noise is the mechanical equivalent of electrical Johnson noise, and can be calculated with the following expression from [10]:

$$|Z_n(f)| = \sqrt{4k_bTB/k}$$

Where

$Z_n(f)$  is the noise displacement

$k_b$  is boltzmann's constant

$T$  is temperature

$B$  is damping

$k$  is the stiffness of the beam

The methodology for calculating Johnson noise in the resistive ladder of an electronic R-2R DAC can be used to calculate the output-referred thermomechanical noise in the compliance network. The damping terms in the compliance network are not binary weighted, in fact they are similar for both the  $C_m$  and  $2C_m$  beams. The stiffness term does affect the calculation, making it similar to the R-2R case. The schematic below contains only the damping symbol but the expression for noise is scaled according to the beam stiffness. We replace the resistors with a series combination of a resistor and a voltage noise source, and calculate the equivalent voltage noise for the 8-bit DAC as shown in figure 6. Assuming a bandwidth limited to 10 kHz by the tunneling amplifier in our system, a typical value for  $B$  of  $1E-5$ , and room temperature operation, this calculation yields a value of  $\sim 0.13\text{nm}$ , which is below the output-referred position resolution of the piezoresistive sensor placed in the LSB.

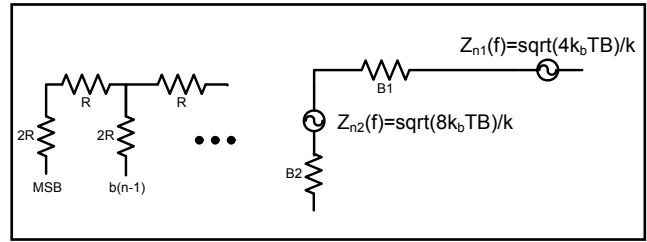


Figure 6: Calculation of Johnson noise in a resistive ladder is similar to calculation of thermomechanical noise in a compliance network where the beams have damping terms  $B$ .

### FEM and LEM

A finite element model of the compliance network was developed using Coventorware in order to predict the integral and differential nonlinearity error (INL and DNL), (figure 7). This model assumed no mismatch in the beam stiffness. A lumped element model in the electrical domain was implemented using Cadence. This model accounts for stiffness mismatches. Results of both models are included with experimental results, and are shown to capture the nonlinearities that were measured.

It is possible to operate the LSB using an analog input to scan within a step while all other bits are fixed to a specific binary input value. This operation has been modeled, and our FEM and predicts excellent linearity. The position resolution required to characterize this behaviour is beyond the capability of our motion capture system; however, tunneling measurements may confirm this in the future.

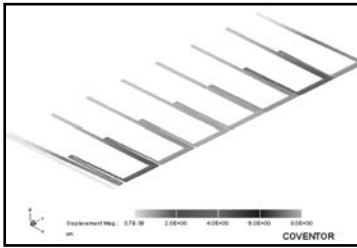


Figure 7: Coventor simulation of the compliance network in a state corresponding to input [01111110]. The MSB is the right-most bit connected to the output shuttle, and the LSB is the left-most bit.

## RESULTS

### 1-D MEMDAC

Data was taken using a stroboscopic motion capture system (Umech) using an off-chip 8-bit binary counter to drive the actuators in a bitwise incrementing pattern. The results of this test are compared to the LEM and FEM outputs in figure 8.

The maximum measured DNL is 2.3 LSB and the INL was measured at 1.9 LSB.

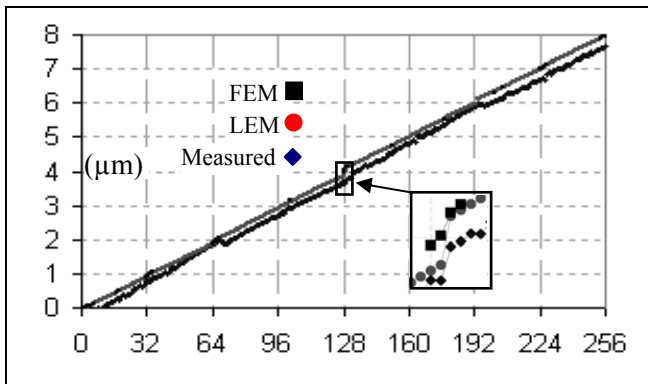


Figure 8: Finite Element Model, Lumped Element Model and measurement results. Note the significant DNL error that occurs at the transition from 127 to 128.

### Sources of Error

Several processing and design aspects of the device contribute to the observed positioning error. Structural bloat that occurs during the post-CMOS release process reduces the range of motion of the actuators. The asymmetry in the C and 2C beams contributes to a compliance mismatch that results from a difference in loading effects during etching. Thermal coupling through the ground plane, substrate and compliance network results in parasitic actuation. This effect is most noticeable in the transition from input value 127 to 128, since these are the two adjacent values with the largest difference in power consumption and temperature.

### 2-D MEMDAC

An orthogonal arrangement of four 1-D MEMDACs was used to position a centrally mounted cantilever in 2-D (figure 9). The device can be reliably positioned on a 2-D grid with a 32nm step size, and exhibits similar INL and DNL. The rationale behind this device is to position a tip on a 2-D grid quickly with only digital inputs, and scan within each cell in an analog fashion (figure 9).

Two versions of the device were designed, one with integrated CMOS electronics to reduce pincount, and one with 32 bond-wires. The CMOS electronics include a scan chain which serially loads data into electronic R-2R DACs. The DACs are used to set an input voltage to a source follower, which in turn drives the bits of the MEMDAC. The CMOS electronics occupy approximately the same area as the 2-D MEMDAC, but can be reduced significantly with the omission of the DAC circuits for all

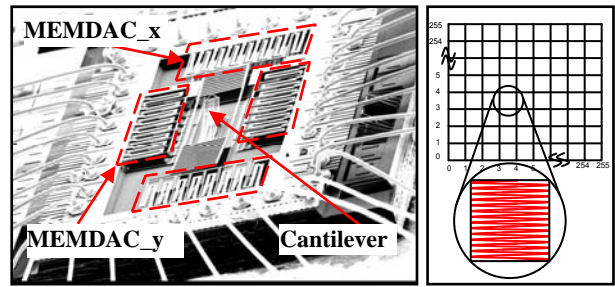


Figure 9: 2-D MEMDAC composed of 4 orthogonally arranged 1-D MEMDAC's. The device addresses a grid and can scan within a cell in closed loop using the LSB positioner.

## CONCLUSION

An 8-bit MEMDAC based on the R-2R electronic DAC architecture was fabricated using a CMOS-MEMS process. The step size achievable with this design is 32nm, which is smaller than the resolution attainable with a lateral differential piezoresistive position sensing scheme. By placing a strain gauge at the LSB of the device, sub-nanometer position resolution was obtained with measurement levels above the thermal noise floor. Although sub-step positioning operation exhibits good linearity, significant error is observed during transitions in which a large number of bits are toggling and significantly changing the power consumption and heat generation from the device.

## ACKNOWLEDGEMENTS

This material is based upon work supported by the Defense Advanced Research Project Agency (DARPA) and Space and Naval Warfare Center, San Diego (SPAWARSYSCEN-SD) under contract N66001-08-C-2040, and the Emerging Technology Fund of the State of Texas. The authors would also like to thank Mr. Kyle Trainor for his assistance in the characterization of CMOS electronics.

## REFERENCES

- [1] J. N. Randall et. al., "Atomic precision patterning on Si: An opportunity for a digitized process", *Microelectronic Engineering*, vol. 87, pp. 955-958, Dec. 2009.
- [2] Fedder, G. K., et. al., Invited Paper, *Proc. IEEE*, Vol. 96, No. 2, pp. 306 – 322, Feb. 2008.
- [3] Toshiyoshi, H. et. al., *JMEMS*, Vol. 9-2, pp. 218–225, June 2000.
- [4] R.Yeh, R.Conant, K.S.J.Pister, "Mechanical Digital-to-Analog Converter," *Transducers '99*, pp. 998-1001.
- [5] N. Sarkar, R. Mansour, "CMOS-MEMS Nanopositioners with Integrated Position Sensors and Digital Control," presented at *CWMEMS 2007*.
- [5] N. Sarkar, R. Mansour, "CMOS-MEMS Nanopositioners with Integrated Position Sensors and Digital Control," presented at *CWMEMS 2007*.
- [6] Gilgunn, P.J. et. al., "CMOS-MEMS Lateral electrothermal actuators," *JMEMS*, Vol. 17, No. 1, pp. 103-114.
- [7] Sarkar, N. et. al., "Modular MEMS experimental platform for TEM," *Proc. MEMS 2006*.
- [8] Liu, J. et. al, "Polysilicon Sensors for CMOS-MEMS Electrothermal Probes," *Proc. Transducers 2009*, pp.2425-2428, June 2009.
- [9] Senturia, S.D., "Microsystem Design," Kluwer Academic Publishing, 2001.
- [10] T. B. Gabrielson, *IEEE Electron Devices*, 40, 903 (1993).

## CONTACT

\*N. Sarkar, nsarkar@uwaterloo.ca

# HIGH-SPEED AXIAL-FLUX PERMANENT MAGNET MICROMOTORS WITH ELECTROPLATED WINDINGS

Florian Herrault, Preston Galle, and Mark G. Allen

School of Electrical and Computer Engineering,  
Georgia Institute of Technology, Atlanta, Georgia, USA

## ABSTRACT

This paper reports the design and microfabrication of electroplated multi-phase stator windings and their use in a high-speed permanent magnet micromotor. As the stator windings of an axial-flux micromotor, both single-plated folded coils, and two-layer double-plated interleaved coils are demonstrated. These stators, combined with a 10 mm-diameter permanent magnet rotor and an all-CMOS drive circuit, enabled speeds in excess of 50,000 RPM and 200,000 RPM, respectively, establishing a trade-off between performance and fabrication simplicity. At these speeds, the dissipated power in the microfabricated coils was approximately 1.81 W and 1.80 W for the folded and double-plated coils, respectively.

## INTRODUCTION

Microscale electromagnetic energy conversion is a key component of many high-performance MEMS electromechanical actuators such as micro-relays, micro-pumps, and micromotors. The small size of a microscale electromechanical system puts limits on its throughput, in terms of electrical power as well as generalized application capacity. Operating electromechanical systems at faster speeds is a fitting way to increase throughput without losing size and integration advantages.

Miniaturized rotary machines are particularly apt for high-speed operation. The small mass and size of the rotors give very small imbalance moments, naturally allowing faster rotation within a given bearing load rating. Also many rotary applications, such as fluidic pumping, machining, and electricity generation, scale very well to high speeds.

However, fabrication simplicity must be a key requirement to further expand the development of MEMS-based electromechanical systems and potentially commercialize these devices. With regards to the research in permanent-magnet micromotors, achieving high performance and high rotational speeds with complex motor designs and fabrication has often been favored over commercially-viable designs. More specifically, sequential plated layers with interleaved conductors, as used in [1-6] for micro-coil fabrication, have enabled the demonstration of MEMS motors/generators. Recently, microcoils on printed circuit boards (PCBs) have been used in micromotors [7], but rotational speeds and overall performance were inferior to the previously-mentioned devices.

In this paper, we present two micromotors that attain high rotational speeds. One micromotor uses a complex coil stator fabrication with interleaved windings, and demonstrates rotational speeds higher than that of previously-reported permanent magnet micromotors. The second micromotor, which presents the same coil parameters, is constructed with an eye towards mass-manufacturability, using a simpler approach based on folding coil phases one atop the other.

The folded-coil stator fabrication process is detailed, followed by the motor driver topology. Experimental characterization is presented and includes maximum rotational speed measurements, and power dissipated in the coils.

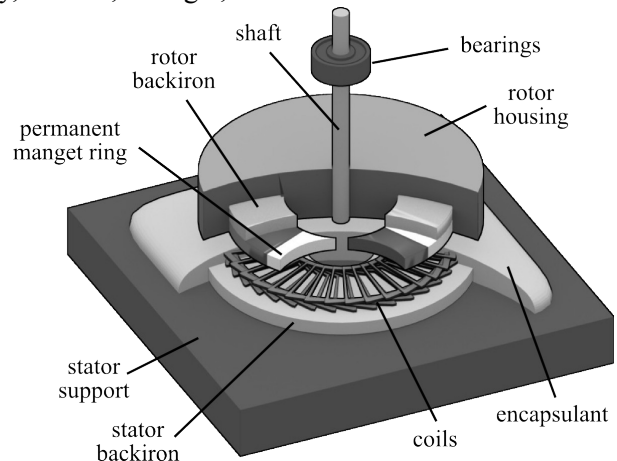


Figure 1: Cutaway view of generalized axial-flux motor

## Motor Design

The motors presented in this research are largely identical to the generator presented in [1]. The axial-flux micromotors consist of an eight-pole permanent magnet rotor and a three-phase, three turns-per-phase stator with electroplated windings. A rendering of the device is shown in Figure 1. The 10 mm-diameter rotor includes a 0.5 mm thick SmCo permanent magnet ring and a 0.5 mm thick FeCoV backiron encased in a titanium housing. A

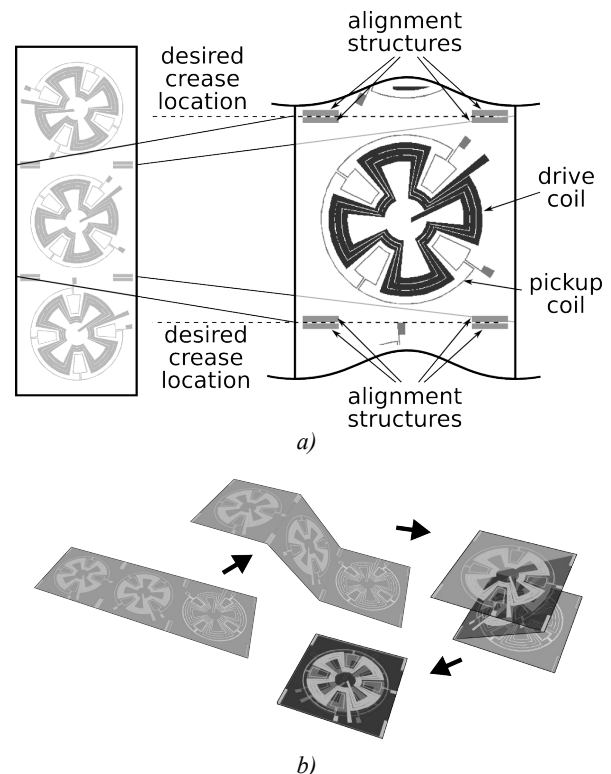


Figure 2: Folded-coil a) stator design and b) folding process



1.6 mm diameter shaft connects the rotor to the turbine bearings for experimental characterization.

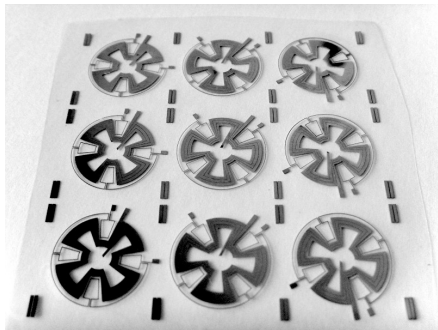
Two stator designs, denominated as folded-coil and double-plated stators, were fabricated and tested, as reported in this paper. The fabrication of previously-reported windings, including the double-plated stator characterized in this work, requires multiple electroplating steps as well as patterning of intervening insulation layers, with careful attention to alignment and planarity as the layers accumulate [1-7]. While these multi-layer microfabrication techniques are now part of standard MEMS processes, they are still time-consuming and also very challenging to transfer to mass-production because of yield requirements. In contrast, the presented folding-based approach only requires a single electroplating step and blanket insulator depositions, while a folding step achieves excellent interlayer alignment. The three folded stator coils possess the same geometry as those in the double-plated stator: eight poles, three turns per phase, three phases, identical conductor widths, and inner and outer diameters of approximately 3mm and 15mm, respectively.

## STATOR FABRICATION

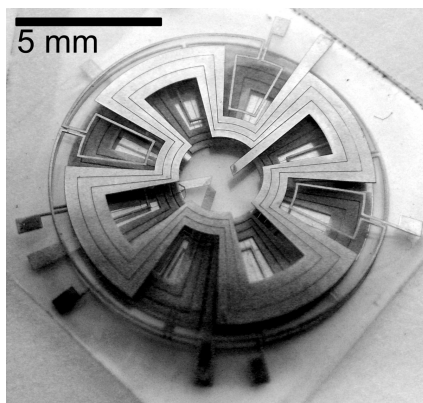
### Folded-coil stator

The folded-coil stator was formed in three primary steps. First was the fabrication of a parylene sheet with embedded, single-layer electroplated copper structures. Second was the folding of this parylene sheet to form the multilayer stator. Finally, the folded structure, along with a 0.5 mm thick ferromagnetic back-iron, were affixed into a stator housing with epoxy.

The plating mask for the folded coils is shown in Figure 2a,



a)



b)

Figure 3: Folded-coil fabrication results. a) shows an uncut, unfolded parylene sheet containing coils for 3 stators; b) shows a finished 3-layer folded coil

and the folding process is illustrated in Figure 2b. Along each intended fold line there are four oblong rectangles. These are fold alignment structures and are electroplated along with the coils. They are essential to obtaining desired interlayer alignment, but after folding, they also provide substantial detent about the fold line, passively helping the stator maintain its fully folded state.

When folded, the three copper coils, which have similar geometries, are mechanically oriented at  $30^\circ$  between one another. This is a design requirement in eight-pole machines to obtain an electrical angle of  $120^\circ$  between the three phases. It should also be noted that pickup coils were designed and integrated within the coil stator topology, as pointed out in Figure 2a. These pickup coils will eventually provide position feedback for closed-loop control.

Conductors were fabricated by through-resist electrodeposition of copper onto an oxidized silicon substrate with a titanium-copper-titanium seed layer. Futurrex NR-2 was used to construct the plating mold through which  $80\ \mu\text{m}$  of copper was electrodeposited from an aqueous bath. After photoresist and seed layer removal,  $6\ \mu\text{m}$  of parylene was deposited. The parylene-coated coils were then fully released by under-etching the oxide layer of the silicon substrate with an extended hydrofluoric acid etch (HF). Next, another  $6\ \mu\text{m}$  parylene layer was deposited onto the newly exposed backside of the coils, rendering the structure fully passivated and ready for folding.

Figure 3a shows a finished parylene sheet containing three sets of coils, and Figure 3b presents a finished three-layer winding. The coils exhibited an average resistance of  $119\ \text{m}\Omega$  and an average self-inductance of  $0.56\ \mu\text{H}$ .

### Double-plated stator

The fabrication process for the double-plated stator was as in [1]. Two  $80\ \mu\text{m}$  conductor layers, separated by a  $40\ \mu\text{m}$  via layer, are electroplated atop a polyimide-coated high-permeability ferromagnetic (NiFeMo) substrate. The areal coincidence of interlayer vias with top conductor is exploited to combine these structures' depositions into a single electroplating step. In each electroplating step, copper is deposited onto a sputtered titanium-copper-titanium seed layer from an aqueous bath through a photoresist mold (Futurrex NR-9). The photosensitive epoxy SU-8 (Microchem) is used to fixate the plated copper after the plating mold and seed layer have been removed. The outcome, shown in Figure 4, is a stator

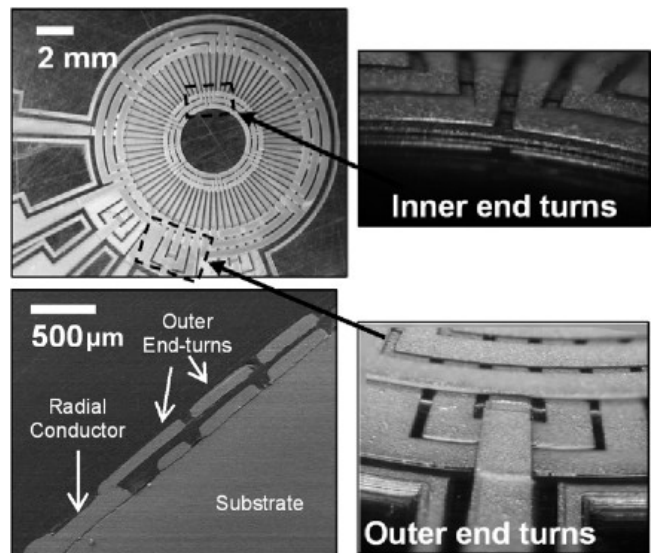


Figure 4: Double-plated stator (from [1])

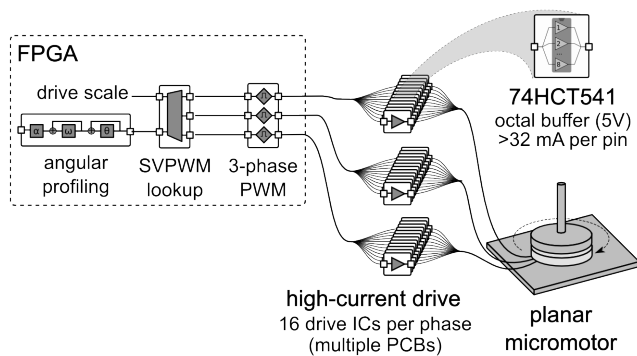


Figure 5: Motor driver system

structure consisting entirely of SU-8 and thick copper layers, with per-phase resistance of approximately 100 mΩ and per-phase inductance of approximately 140 nH.

### MOTOR DRIVER DESIGN

The motors were driven by the custom, all-CMOS system illustrated in Figure 5. Permanent magnet synchronous machines, such as the presented motors, are typically operated in a closed-loop mode, relying on position feedback to drive electrical commutation. However, for this preliminary work, an open-loop control scheme was sufficient. The expected dominant mechanical loads, such as bearing friction and fluidic drag, present near-constant torque, and thus a minimal risk of sharp perturbations that would require dynamic correction. As well, the output drive amplitude could simply be temporarily increased, manually, during acceleration to ensure maximal immunity to perturbations.

Octal buffer ICs (Philips SN74HCT541) were chosen as output drivers. These fit the motor's need for very high drive frequencies, high drive currents and low drive voltages, but their built-in output current limiting also protects the microfabricated stators from overheating hazards. This implementation choice also clearly establishes the feasibility of driving the motor with conventional CMOS-based ASICs or full-custom ICs.

An open-loop space vector pulse width modulation (SVPWM) inverter was selected to generate the control signals for the output drivers. While allowing straightforward implementation in hardware, SVPWM provides compatibility with vector-based control, if closed-loop control is desired, and also minimizes the number of output switches. The controller was implemented in an Altera Cyclone III FPGA installed on a general-purpose development board (Terasic DE0). The output switching frequency and the commutation update rate was 1 MHz, nominally allowing rotation at well over one million RPM. The controller's governing parameters were exposed over an asynchronous serial port interface. A terminal communication program running on a PC served as the motor controller's user interface. A constant-acceleration angular profiler, with user-set parameters for speed and acceleration, generated the SVPWM's command angle. The SVPWM drive magnitude, or maximum duty cycle setting, was presented as a single user-set parameter.

To expedite characterization, an RL filter, not shown in Figure 5, consisting of a 100 mΩ resistor and a 5 μH inductor, was placed in series with each motor phase. Phase currents were measured across the resistors. The inductors suppressed SVPWM switching currents, which were responsible for critical levels of both parasitic power dissipation in the stator and electrical noise in the current measurements.

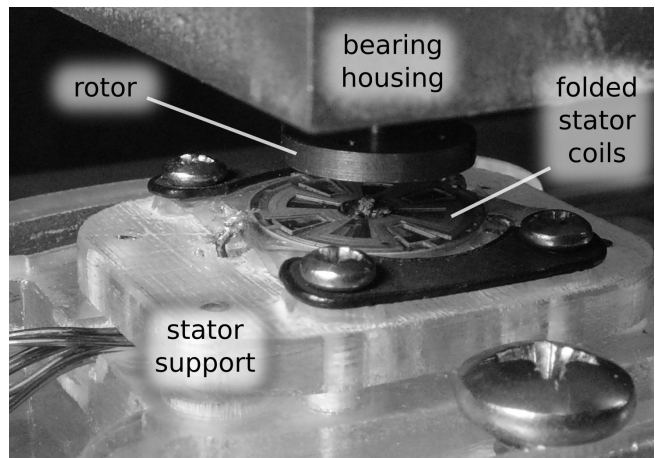


Figure 6: Photograph of micromotor with folded-coil stator

### CHARACTERIZATION

#### Folded-coil stator

The folded-coil stator was first tested in generator mode, with compressed air driving a turbine attached to the rotor shaft. The stator housing was clamped onto x-y-z micro-positioners to ensure proper alignment between the stator and the rotor. A photograph of the assembled micromotor with folded coils is shown in Figure 6. The output waveforms for the three phases are shown in Figure 7. They exhibit excellent symmetry in both angle and magnitude, confirming proper coil alignment. The 10% discrepancy in magnitude is inherent to the design of the folded-coil stator. Because each phase is folded onto the others, the distance between each phase's coil and the stator ferromagnetic back iron varies. This introduces significant geometrical differences between the phases' magnetic circuits, naturally resulting in a variation in amplitude of their open-circuit voltages.

The stator was then characterized in motor mode. Maximum attainable speed was observed for a number of drive currents. During motor start-up and acceleration, the parameters for angular acceleration and drive magnitude were varied as needed. But at near-terminal speeds, the drive magnitude is held constant and the angular acceleration is set to very low value, under 500 RPM/s. A reflective photoemitter-photodetector pair generated the tachometer signal used to measure the motor's speed.

These results are shown in Figure 8. The relationship clearly exhibits two plateaus. Below approximately 2 A per phase, the

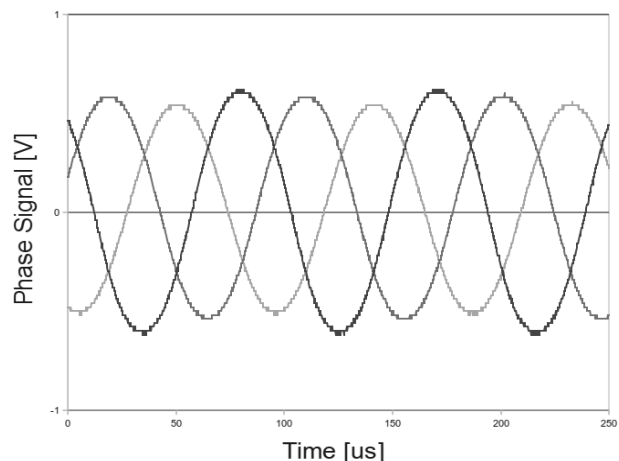


Figure 7: Folded-coil stator generator-mode waveforms

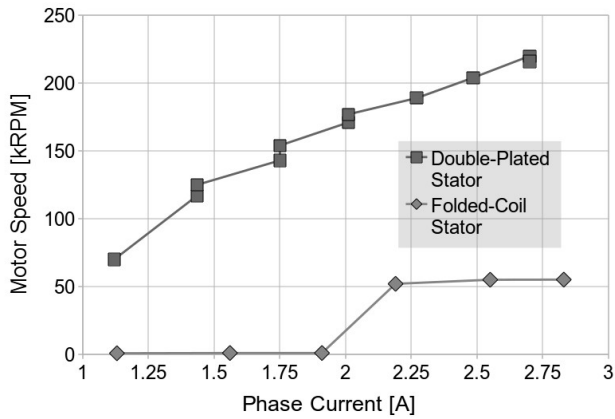


Figure 8: Maximum micromotor speeds for both stator types, for various drive currents.

motor rotated under 3000 RPM. At higher currents, the motor speed remains at approximately 50,000 RPM, reaching 52,000 RPM at a drive current of  $2.83 A_{RMS}$ .

Although the nonlinearity in the speed-current graph was not investigated in detail, a likely cause is the high-speed bearings used. They are optimized for operation above 100,000 RPM, and exhibit several resonances at lower speeds.

#### Double-plated stator

The double-plated stator, having been characterized in generator mode in [1], was operated in motor mode. The experimental setup and procedure was identical to that used for the folded-coil stator. The results are also shown in Figure 8 for comparison. A speed of 204,000 RPM at  $2.49 A_{RMS}$  per phase was attained. Under these operating conditions, the power dissipation in the coils was 1.86 W.

The double-plated stator's performance was also measured as a function of stator-rotor gap. As exhibited in Figure 9, the micro-motor operated best at a  $400 \mu m$  air gap. For smaller gaps, the magnetic pull-in force between the stator back iron and the magnetic rotor increased the axial load on the bearings, leading to higher bearing torque; larger gaps resulted in lowered magnetic interaction, producing less drive torque. Both phenomena result in lower maximum rotational speeds

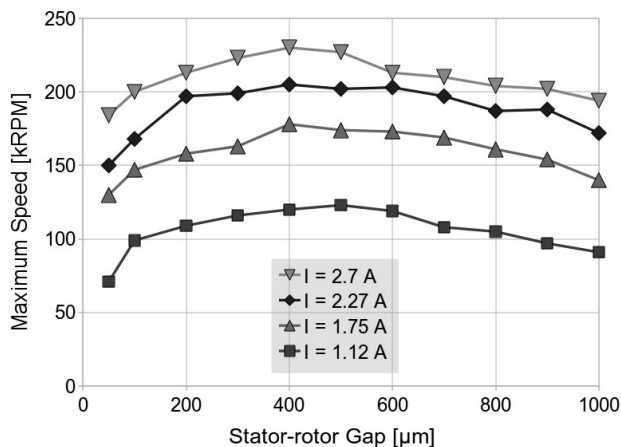


Figure 9: Influence of stator-rotor gap on performance of micro-motor with double-plated stator

Heat accumulation imposed a major constraint on the achievable drive currents. The double-plated stator exhibited far better power dissipation capability than the folded-coil stator. This can be attributed to the double-plated stator's tighter vertical construction and thinner conductor to substrate insulation thickness, providing a lower thermal resistance for heat dissipation.

## CONCLUSIONS

High-speed micromotors driven by an all-CMOS driver were presented in this paper, with an emphasis on two stator designs. Both of them had similar coil parameters (numbers of turns, poles, and phases), but one required an elaborate fabrication sequence using multiple electroplating steps, while the other one singled itself out by one electrodeposition and a folding technique. The two devices demonstrated high rotational speeds, indicating that folded micro-coils are suitable for efficient magnetic actuation at MEMS scales.

## ACKNOWLEDGEMENTS

This project was supported by the DARPA MACE program and Raytheon Space & Airborne Systems.

## REFERENCES

- [1] D. P. Arnold, F. Herrault, I. Zana, P. Galle, J.-W. Park, S. Das, J. H. Lang, and M. G. Allen, "Design Optimization of an 8 W, Microscale, Axial-flux, Permanent-magnet Generator," *Journal of Micromechanics and Microengineering*, 16, 9 (2006), pp. S290-6.
- [2] F. Herrault, B. C. Yen, C.-H. Ji, Z. S. Spakovszky, J. H. Lang, and M. G. Allen, "Fabrication and Performance of Silicon-embedded Permanent-magnet Microgenerators," *Journal of Microelectromechanical Systems*, 19, 1 (2010), pp. 4-13.
- [3] C. H. Ahn, Y. J. Kim, and M. G. Allen, "A Planar Variable Reluctance Magnetic Micromotor with Fully Integrated Stator and Coils," *Journal of Microelectromechanical Systems*, 2, 4 (1993), pp. 165-173.
- [4] A. Waldschik and S. Büttgenbach, "Fabrication of Internal Driven Micro Centrifugal Force Pump Based on Synchronous Micro Motors with Polymer Magnet Rotors," 2009 Symposium on Design, Test, Integration & Packaging of MEMS/MOEMS (2009 DTIP), Rome, Italy, 4/1-3/09, IEEE, Piscataway (2009), 4 pp.
- [5] S. Merzaghi, C. Koechli, and Y. Perriard, "Development of a Hybrid MEMS BLDC Micromotor," *Proceedings of the 2009 IEEE Energy Conversion Congress and Exposition (ECCE 2009)*, San Jose, CA, 9/20-24/09, IEEE, Piscataway (2009), pp. 3595-3601.
- [6] N. Achotte, P.-A. Giles, O. Cugat, J. Delamare, P. Gaud, and C. Dieppedale, "Planar Brushless Magnetic Micromotors," *Journal of Microelectromechanical Systems*, 15, 4 (2006), pp. 1001-1014.
- [7] D. Gambetta and A. Ahfock, "Designing Printed Circuit Stators for Brushless Permanent Magnet Motors," *IET Electric Power Applications*, 3, 5, (2009), pp. 482-90.

## CONTACT

Corresponding author: Florian Herrault – 791 Atlantic Drive, Atlanta GA 30332 – (404-385-0273, fh59@mail.gatech.edu)

# SINGLE-LAYER ELASTOMERIC OUT-OF-PLANE ACTUATOR WITH ASYMMETRIC SURFACE PROFILE

T. Maleki<sup>1,3</sup>, G. Chitnis<sup>2,3</sup>, A. Panja<sup>1,3</sup>, B. Ziaie<sup>1,3</sup>

<sup>1</sup>School of Electrical and Computer Engineering

<sup>2</sup>School of Mechanical Engineering

<sup>3</sup>Birck Nanotechnology Center,  
Purdue University, West Lafayette, IN, USA

## ABSTRACT

In this paper, we report on the first batch-fabricated single-layer elastomeric out-of-plane actuator using an asymmetric surface profile. The cantilever actuator is composed of a single polydimethylsiloxane (PDMS) layer and soft-lithographically patterned conductive carbon grease electrodes. Low actuation voltage and large out-of-plane displacement are achieved using a flat surface on one side and a corrugated one on the opposite side. An actuator 5mm in length, 1mm in width, and 80 $\mu$ m in thickness can produce up to 650 $\mu$ m out of plane displacement. The same actuator consumes 20 $\mu$ W of static power and generates 4 $\mu$ N of force.

## INTRODUCTION

Out-of-plane actuators are essential elements in micropumps, micromirrors, and many other MEMS devices. Many actuation mechanisms (electrostatic, magnetic, piezoelectric, etc.) have been used to implement such structures, each with its unique advantages and disadvantages. Elastomeric actuators (or dielectric elastomer DE actuators) are an emerging class of electromechanical transducers having the ability to emulate biological muscle in achieving high fracture toughness, large strain, and inherent vibration damping [1]. Major efforts in this area have been devoted towards reducing the actuating voltage and increasing the strain through various mechanical modifications. Although some out-of-plane actuators using dielectric elastomers have been reported, they are mostly hand-made, require several elastomeric layers, and have complicated fabrication processes involving stretch-frames and pre-patterned dome-shape elastomers [2, 3]. These complicated fabrication processes are not batch-compatible which increases their cost and makes their integration into a MEMS system very cumbersome. In this paper, we report on the first batch-fabricated single-layer elastomeric out-of-plane actuator using an asymmetric surface profile. The actuator uses a geometric design to achieve a single layer configuration. In addition, soft lithography and laser-micromachining are used to batch fabricate the actuators.

## DESIGN AND SIMULATION

Figure 1 shows 3D schematic and cross-section of a single-layer elastomeric cantilever actuator with an asymmetric surface profile, i.e., the top surface is corrugated while the bottom one is flat. As can be seen in the Figure 1b, the thickness ( $d$ ) of the actuator is not constant. It can be modeled as two components, a constant ( $t$ ) and a square wave (magnitude  $A$  and frequency  $\omega$ ) representing the corrugation. Upon actuation, the elastomer undergoes a transverse contraction given by

$$\frac{\Delta d}{d} = -\frac{1}{2E} \epsilon \epsilon_0 \frac{V^2}{(t \pm A)^2} \quad (1)$$

where  $d$  is the thickness of the elastomer,  $E$  is its Young's modulus,  $\epsilon$  is its dielectric constant,  $\epsilon_0$  is the air permeability, and  $V$  is the applied voltage. Due to the asymmetric surface profile, a non-uniform transverse compression and longitudinal expansion is created, inducing a bending moment in the cantilever.

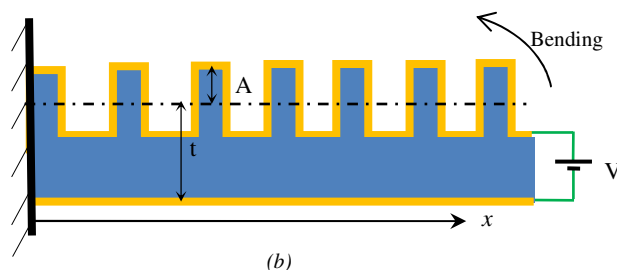
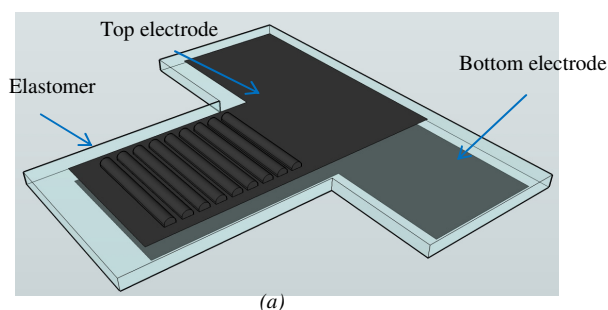


Figure 1: 3D schematic (a) and cross section (b) of a single-layer elastomeric actuator with an asymmetric surface profile.

Figure 2 illustrates a simplified structure in order to better understand the actuation mechanism. This simplified model assumes the induced electrostatic force is perpendicular to the surface of the actuator. Figure 2a represents a single actuator element without any actuation voltage, while similar element after actuation is depicted in Figure 2b. As can be inferred from Equation 1, the induced attraction force is larger in the thinner segment as compared to the thicker segment, resulting in an asymmetric compressive strain in the element. The thicker area of the element can be divided into two distinct parts, Figure 2b. The lower part (darker color) that is connected to the thinner segment experiences higher transverse strain compared to the top part. Since PDMS elastomer has a Poisson's ratio close to 0.5, this transverse strain induces a longitudinal strain, hence expanding the bottom part more than the top. This asymmetric longitudinal expansion creates a unimorph actuator, bending the cantilever beam in the upward direction.

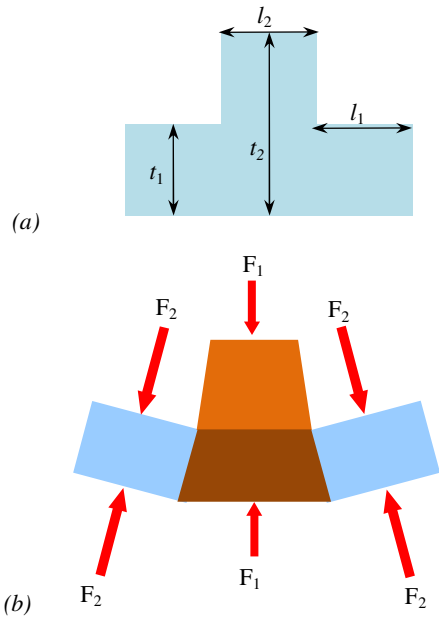


Figure 2: Simplified structure of one element of the asymmetric actuator. (a) without applied voltage, (b) with applied actuation voltage inducing a bending moment in the element

Comsol<sup>®</sup> Multiphysics was used to simulate the stress/strain in an 5mm long, 1mm wide, PDMS ( $E=750\text{kPa}$ ,  $\nu=2.7$ ) actuator having different corrugation structures ( $l_1$ ,  $l_2$ ,  $t_1$ ,  $t_2$ ). Figure 3 shows the simulation result for an actuator with corrugation parameters of  $l_1=60\mu\text{m}$ ,  $l_2=20\mu\text{m}$ ,  $t_1=40\mu\text{m}$ , and  $t_2=100\mu\text{m}$  under 1kV applied voltage (left side is the fixed point). The inset in the figure clearly proves our hypothesis that the induced transverse stress is not uniform through the thicker part of the PDMS element causing a bending moment in the actuator.

Figure 4 represents the deflection simulation results versus thick segment's length ( $l_2$  in figure 2a) for a 5mm long, 1mm wide actuator when 1kV voltage is applied. In this simulation, the thickness of the thin segment ( $t_1$  in figure 2a) and the whole element length ( $l_1+l_2$ ) are assumed to be fixed at  $40\mu\text{m}$  and  $80\mu\text{m}$ , respectively. As can be seen, deflection is increasing with larger  $l_2/l_1$  ratio. This can be explained by the fact that the induced deflection is mostly due to an asymmetric strain in the thicker segment (see the inset of Figure 3), and the length of the thin segment has limited effect on the deflection. Therefore, the longer the thick segment, the higher the deflection. The inset in Figure 4 shows deflection versus thick segment thickness,  $t_2$ , while  $l_1$ ,  $l_2$ , and  $t_1$ , are held constant at  $5\mu\text{m}$ ,  $75\mu\text{m}$ , and  $40\mu\text{m}$ , respectively. As illustrated in the figure, deflection is higher for an actuator with increased thick segment thickness, due to the minimal effect of thin segment width on the asymmetry of the induced longitudinal strain.

Simulation results for deflection versus thick layer length for 5mm long, 1mm wide actuators having different thin segment thickness,  $t_1$ , is depicted in Figure 5. In this simulation, the thickness of the thick segment,  $t_2$ , is assumed to be fixed at  $100\mu\text{m}$ . As shown in the figure, the thinner the thin segment, the higher the deflection. This is because of the higher transverse contraction (see Equation 1) in the thin segment. The inset of the figure represents the deflection versus thin segment thickness,  $t_1$ , while  $l_1$ ,  $l_2$ , and  $t_2$ , are  $5\mu\text{m}$ ,  $75\mu\text{m}$ , and  $100\mu\text{m}$ , respectively.

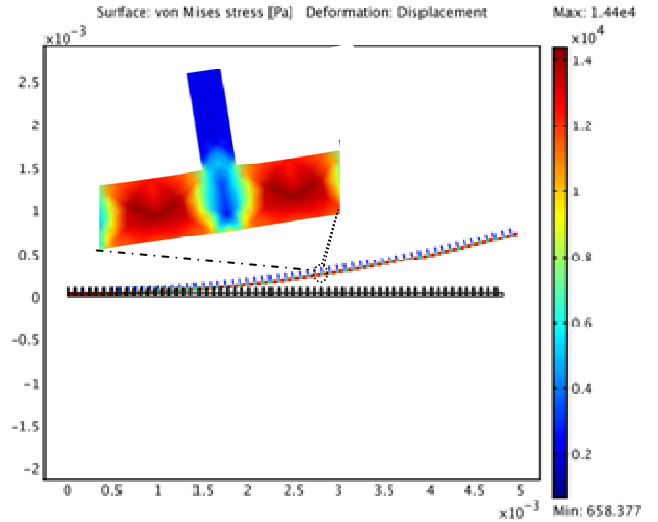


Figure 3: Comsol<sup>®</sup> simulation results for the new asymmetric actuator. Inset clearly shows non-uniform induced stress in the thicker segment.

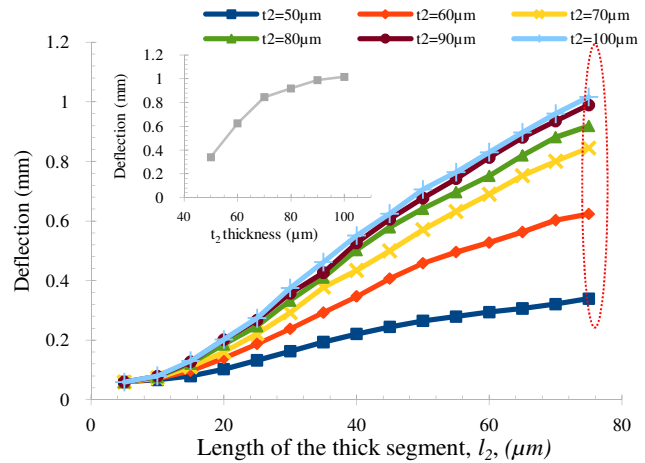


Figure 4: Simulation results for asymmetric actuator having a constant thin segment thickness and various other geometries.

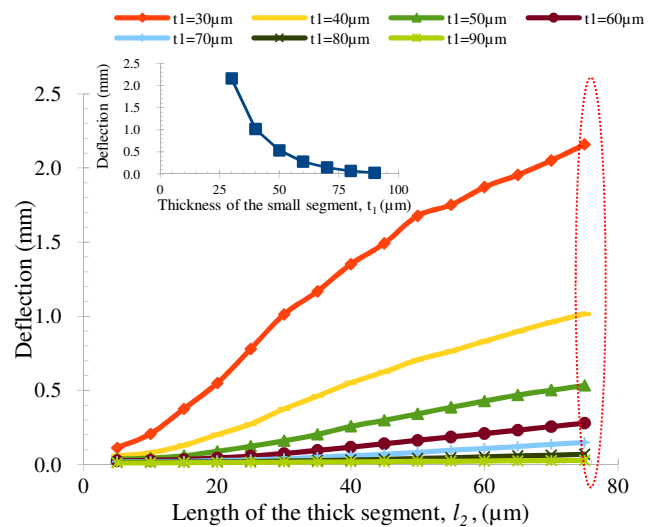


Figure 5: Simulation results for an actuator with constant thick segment thickness and various other geometries.

In another set of simulations, the end point of the actuator with 40 $\mu$ m thin segment and 100 $\mu$ m thick segment was fixed and the reaction force at that point was calculated. The results of this simulation are plotted in Figure 6. As shown in the figure, an actuator with a longer thick segment creates less force. This is due to the fact that longer segment can dissipate nonsymmetrical strain in itself by less amount of force that a short segment.

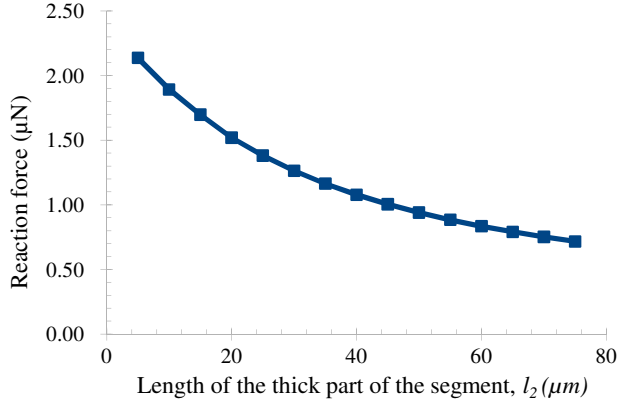


Figure 6: Reaction force at the end of actuator when the end point is fixed.

In conclusion, simulation results suggest that an actuator with a very asymmetric profile creates the maximum deflection. However, such an actuator would generate least amount of force. We should mention that practical limitations might prevent the fabrication of such structures. For example, in an actuator with very narrow and deep surface non-uniformity, achieving a uniform electrode coating is very difficult. Moreover, handling ultra thin PDMS sheets (less than 40 $\mu$ m) is another challenge in fabricating such an actuator. In the following sections, fabrication and experimental results for an actuator with following geometrical parameters is presented,  $l_1=20\mu$ m,  $l_2=70\mu$ m,  $t_1=40\mu$ m, and  $t_2=100\mu$ m.

## FABRICATION PROCESS

Figure 7 shows the fabrication process for an elastomeric actuator using PDMS as the structural material and conductive grease as the electrodes. An advantage of using PDMS is its well known mechanical properties, low cost, and MEMS compatible fabrication process-ability [4]. Conductive carbon grease was chosen as the electrode material due to its good adhesion to PDMS and low deformation resistance.

The process starts with the fabrication of a silicon mold with a corrugated top surface (60 $\mu$ m deep) using HNA (20%wt HF:70%wt HNO<sub>3</sub>:10% wtCH<sub>3</sub>COOH) as the etchant and silicon nitride as mask, Figure 7a. Next, a 70 $\mu$ m thick PDMS (SYLGARD 184, Dow Corning, Midland, MI) is spun coated (1500rpm for 30sec) and cured (at 120 °C for 30min) to form the structural layer, Figure 7b. Subsequently, an electrode stamp is fabricated by casting PDMS against a SU8-on-silicon mold, Figure 7c. The stamp is inked by conductive carbon grease (MG Chemicals, Burlington, Ontario, CA), and is used to deposit the top electrode on the PDMS layer, Figure 7d. The stamped PDMS layer is then separated from the mold and transferred to a parylene-coated silicon wafer. This is followed by the aligned stamping of the top electrode on the corrugated surface, Figure 7e. A slight pressure is applied during this step in order to deform the

corrugations and ensure a uniform coverage. Finally, individual actuators are separated at the wafer level using laser micromachining, (CO<sub>2</sub> laser generated by 2007 Professional Systems from Universal Laser Systems Inc. AZ, USA), Figure 7f.

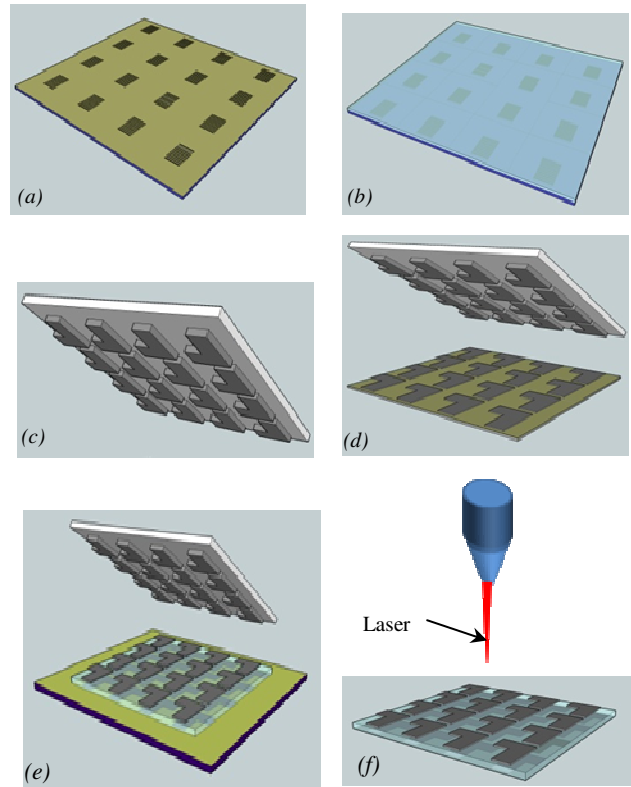


Figure 7: Batch-scale fabrication process of elastomeric actuators.

Figure 8a shows a wafer with batch fabricated actuators prior to separation. SEM picture of the actuator illustrating the uniform coverage of the corrugated surface by carbon grease is depicted in Figure 8b. Figure 8c is a close-up optical photograph of the mounted actuator showing the corrugations. Figure 8d demonstrates the testing setup in which the actuator is mounted on a metal-coated glass slide acting as the backside connection and a needle used as the front contact.

## MEASUREMENT RESULTS

The actuators were tested using a high voltage power supply and their displacement was measured through a video frame-grabber. Figure 9 shows the tip-displacement vs. applied voltage for three different lengths (3, 4, and 5mm). One should notice that the measured displacement for a 5mm actuator is well matched the simulation result (see figure 5,  $t_1=40\mu$ m, and  $l_2=70\mu$ m). As can be seen, mm scale actuation was achieved for voltages of less than 1kV. The maximum power for a 5mm long actuator with 900V actuation voltage was 20 $\mu$ W.

In another experiment, the required force to bend the un-actuated cantilevers is measure and results are plotted in Figure 10. As depicted in the figure,  $\mu$ N force is required to generate mm bending in the cantilever. By comparing figures 9 and 10, one can calculate the zero-deflection force of the actuators.

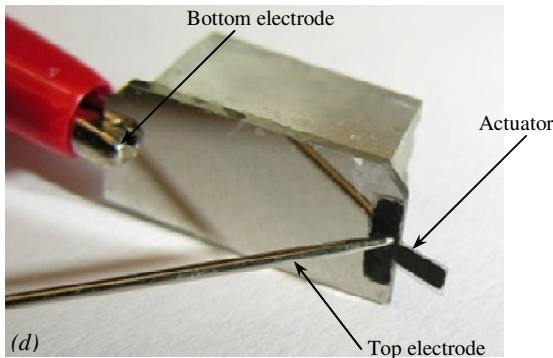
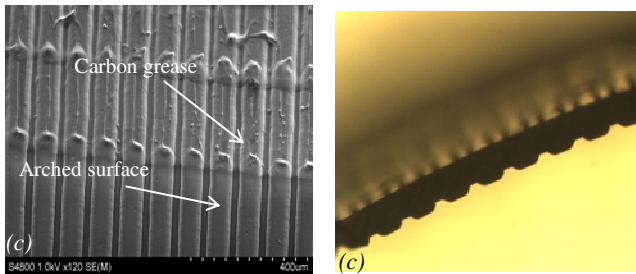
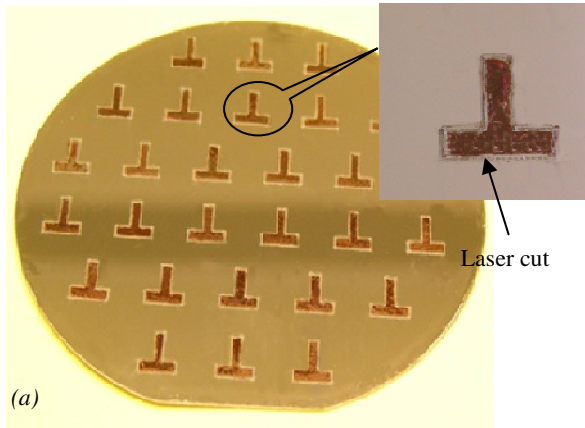


Figure 8: Batch fabricated actuators, b) SEM picture of the single layer actuator, c) cross sectional photograph of the actuator, d) a mounted actuator.

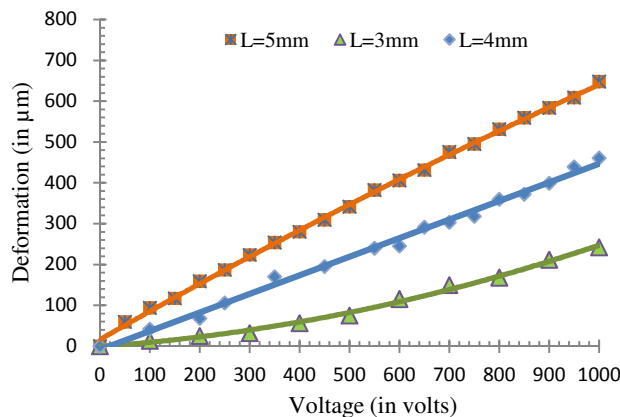


Figure 9: Microactuator displacement vs. voltage ( $l_1=20\mu\text{m}$ ,  $l_2=70\mu\text{m}$ ,  $t_1=40\mu\text{m}$ , and  $t_2=100\mu\text{m}$ ).

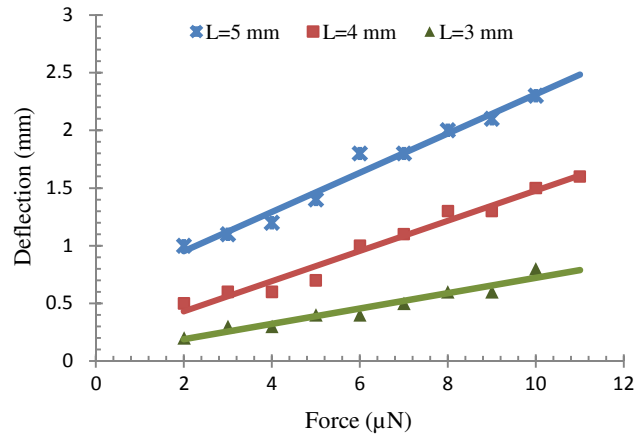


Figure 10: Deflection vs. applied force for 1mm wide actuators with different length ( $l_1=20\mu\text{m}$ ,  $l_2=70\mu\text{m}$ ,  $t_1=40\mu\text{m}$ , and  $t_2=100\mu\text{m}$ ).

## CONCLUSIONS

In this paper, we presented a batch fabrication process for the first single layer elastomeric actuator based on asymmetric surface profile that can achieve large out-of-plane deflections with a low actuation voltage. Comsol<sup>®</sup> simulation results showed that actuators with highest non-uniform profile creates the maximum deflection. However practical limitations prevented fabrication of such structures. Three different size actuators with optimized geometry for maximum out-of-plane deflection were successfully fabricated and characterized. Their measured performances showed a good agreement with the Comsol<sup>®</sup> simulation results. Millimeter scale out of plane displacement was achieved using a fairly low voltage (less than 1kV). A 5mm long actuator was capable of generating 5μN force when actuated with 1kV voltage and consumed less than 20μw power.

## REFERENCES

- [1] A. O'Halloran, F. O'Malley, P. McHugh, "A review on dielectric elastomer actuators, technology, applications, and challenges", *Journal of Appl. Phys.* (104), 071101, pp. 1-10, 2008.
- [2] R. Kornbluh, R. Pelrine, Q. Pei, R. Heydt, S. Stanford, S. Oh, J. Eckerle, "Electroelastomers: applications of dielectric elastomer transducers for actuation, generation and smart structures" *Proceedings of the SPIE*, (2002), pp. 254-270.
- [3] F. Carpi, G. Frediani, A. Mannini, D. De Rossi "Contractile and buckling actuators based on dielectric elastomers: devices and applications", *Advances in Science and Technology*, 61, pp. 186-191, 2008.
- [4] X. Q. Brown, K. Ookawa, J. Y. Wong, "Evaluation of polydimethylsiloxane scaffolds with physiologically-relevant elastic moduli: interplay of substrate mechanics and surface chemistry effects on vascular smooth muscle cell response" *Biomaterials*, 26 (16), pp 3123-3129, 2005.

## CONTACT

\*B. Ziaie, tel: +1-765-494-0725; bziaie@purdue.edu

# A CHEMOMECHANICAL NANOMACHINE FOR SENSING AND ACTUATION BASED ON A BIASED BROWNIAN RATCHET ARCHITECTURE

G. Lavella<sup>1</sup>, R. Morfino<sup>2</sup>, and M. M. Maharbiz<sup>1</sup>

<sup>1</sup>University of California, Berkeley, Berkeley, California, USA

<sup>2</sup>Polytechnic University of Turin, Turin, Piedmont, Italy

## ABSTRACT

We present the design, fabrication and experimental demonstration of a self-powered transducer that couples molecular sensing and mechanical actuation into a single nanoscale structure. This capability is achieved through a chemomechanical device that uses an antibody based, biased Brownian ratchet architecture. We demonstrate that this new ratchet can directly convert a detection event into mechanical motion. The device can be tailored to specifically detect a broad range of molecules through the choice of antibody and operates in physiologic solutions. This work provides initial experimental evidence that this mechanism of chemomechanical transduction is feasible.

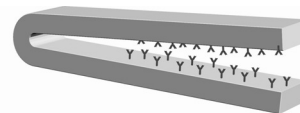
## INTRODUCTION

Nanoscale machines which directly convert chemical energy into mechanical work are ubiquitous in nature and are employed to perform a diverse set of tasks such as transporting molecules, maintaining molecular gradients, and providing motion to organisms [1]. Numerous forms exist, categorized as biological motors, rotors, shuttles, springs and ratchets [1, 2]. By and large, these devices are powered by energy extracted from concentration gradients, the breaking or formation of covalent bonds - most notably ATP, NADH, and NADPH - or in the case of ratchet type mechanisms from polymerization reactions [3]. In their own right, they operate as sensors and actuators, where the sensed molecule and the energy source are one and the same. The extensive study of their operation has provided scientists with empirical demonstrations of the mechanisms by which nanoscale machines can operate. They suggest that in a nanoscale environment where viscous and thermal forces dominate inertia, structures that perform chemomechanical transduction are well served by biasing random thermal movements with asymmetries in the energy landscape. This design strategy, which has been well understood by thermal physicists for decades [4], allows devices to accomplish directed motion against thermal fluctuations. Drawing from these lessons, we have developed a synthetic Brownian ratchet that converts antigenic binding into motion. However, unlike the Brownian machines observed in nature, our device extracts power from binding free energy by tensioning antibody-antigen, host-guest complexes. This shift in strategy enables chemomechanical transduction to be tailored to respond to a broad range of molecules and no longer limits it to a relatively small set of molecules, gradients or polymerization reactions. Throughout this paper we refer to our architecture as an antibody zipper.

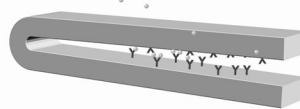
It is instructive to begin by describing the basic structure of an antibody zipper. A schematic of the device used in our experiments can be seen in Figure 1. The structure is relatively simple; a precisely patterned backbone conjugated with a high density layer of active antibodies. It should be noted that the entire device is covered with antibodies; however, only antibodies in the region relevant to zippering are shown. Within a range of geometries, the operation of the device proceeds as follows. In solution, the structure experiences small vibrations in

each arm from thermal fluctuations and ambient noise. When no antigen is present, no closing is observed (State 1 in Figure 1). As antigenic molecules are encountered, the antibodies on the top and bottom arms begin to bind antigen until a critical threshold is reached. We believe this threshold is determined by numerous kinetic, geometric and mechanical factors. Nevertheless, for this threshold to be reached it is necessary that a sufficient number of complexes (antibody-antigen) are created to enable sandwich bond (antibody-antigen-antibody) formation with vacant paratopes on an opposing arm (State 2 in Figure 1). The motion required to bring the two species into contact is supplied by thermal and ambient vibrations. In order to prevent saturation of antibodies with ligand before sandwich bonds can be formed, the kinetics associated with zippering must be faster than the antibody-antigen reaction kinetics. The resultant sandwich bonds that form across the arms prevent the device from relaxing back to its original unbound equilibrium state. This process repeats itself and the device zippers progressively from the hinge side towards the open end of the device, essentially zippering the device closed (State 3 in Figure 1).

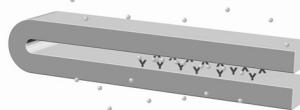
State 1: Open  
(no antigen)



State 2: Zippering begins  
(antigen detection and loading)



State 3: Closed  
(zippering complete)



Detected Antigen: ● Antibody (IgG): Y

Figure 1. Operational schematic for an antibody based Brownian Ratchet. Note the IgG layer covers the entire device.

## THEORY

Brownian ratchet mechanisms are an area of active interest in the physics community. The detailed mechanisms by which they operate are diverse, however in all such devices, a random input (which need not be thermal), a source of energy and an asymmetry in the potential must be present. Tailoring these components such that the movement of a Brownian particle is statistically favored in one direction is critical to Brownian ratchet design. The potential energy surface of device reflects the design of system and can be used to understand which parameters must be altered in order to achieve a working device. The barrier heights dictate the amount of random input energy



required for a Brownian particle to proceed, while the shape of the curve reflects both the asymmetry in the system and the energy input. The exact nature of this surface for our device as constructed is still under investigation.

Thermal and ambient vibrations act as the required randomization element and supply the necessary displacement of the Brownian particle. In our system this particle can be chosen arbitrarily as any point along the structural backbone. As thermal vibrations provide motion, sandwich bonds can form across the arms of the device. At this point, no energy has been transferred to the system. As the arms relax back to their equilibrium state, the sandwich bond is placed in tension and work is performed on the system. This work arises from the free energy change associated with the product of force and displacement along the reaction coordinate [5].

## RESULTS

In this study, the devices used were bound to a substrate bound anchor with a small metal bridge. The devices are suspended ~350 nm above the substrate. The interior angles at the hinge region ranged from 4° to 6.9°. Both the arms and hinge were patterned to be approximately 50 nm in width and 30 nm thick. Device sets with arm lengths of 1µm and 2µm were used.

Figure 2 shows micrographs of devices functionalized to detect streptavidin both before and after the introduction of the sensed molecule (0.5 mg/ml streptavidin). The structural change is clearly noticeable in the active devices (Figure 2.a) and is not seen in the controls (Figure 2.b). Experiments for both active devices (n=21) and controls (n=23) were performed in parallel under identical conditions (immersed in phosphate buffered saline pH 7.4, 25°C).

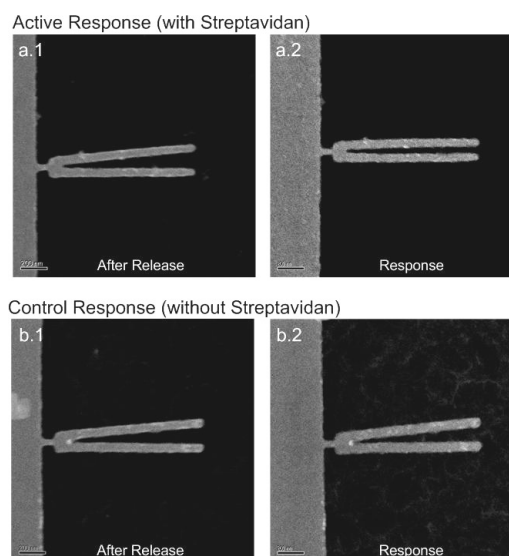


Figure 2. SEM images of anchored device response; a.1) freely suspended device before functionalization and introduction of streptavidin; a.2) response after functionalization and introduction of streptavidin into solution; b.1) control, freely suspended device before functionalization; b.2) control device, response after functionalization, no streptavidin was introduced into the solution.

Figure 3 shows a statistical distribution for the degree of closing in terms of 'percent closed' for the controls and active devices. Percent closed is computed by dividing the total

deflection between tips of each arm by the deflection required to reach a closed state. We define a closed state as a distance between arms of 40 nm – the aggregated length of the sandwich bond and protein A stack.

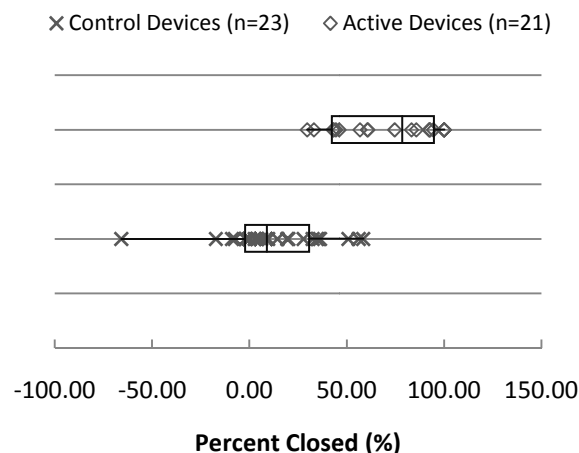


Figure 3. Antibody based, Brownian Ratchet response. Figure shows the statistical distribution of closing in active (median = 83.5%) and control (median = 9.72%) devices.

## METHODS

Devices were fabricated on silicon wafers. The wafers were first coated with poly-germanium layer via sputtering (350 nm,  $R_{rms} < 2nm$ ). A resist bilayer (PMMA A2-950k/A3-50k, 40nm/70nm, Microchem) was then deposited by spin coating and patterned using electron beam lithography (Crestec CABL-9510CC High Resolution Electron Beam Lithography System) and developed (MIBK/IPA 1:3, Microchem) for 60s at room temperature. Subsequently, a Cr/Au (5nm/30nm) metal layer was directionally deposited by electron beam evaporation. Metal liftoff was then performed in acetone at room temperature. This resulted in devices anchored to the poly-germanium layer. The devices were then released by under-etching the poly-germanium layer in 10%  $H_2O_2$  for ten minutes at room temperature. Devices used in these studies were prepared freely suspended over the substrates (as seen in Figure 2).

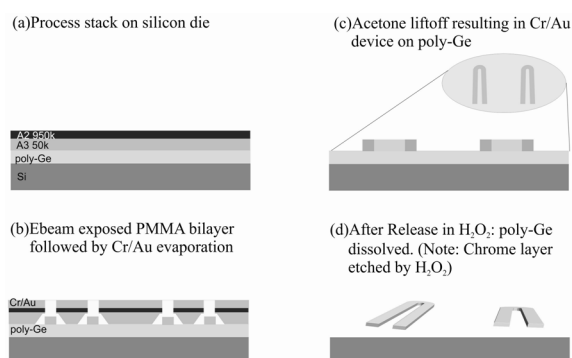


Figure 4. Process sequence for fabrication of gold structural backbone

After creating the gold structural backbone, the devices were washed in acetone (3x, 5min) then in DI (3x, 5 min). The DI was then replaced by the organic solvent Dimethyl sulfoxide

(DMSO) though a series of three washing steps. A 0.002M Dithio-bis(Succinimidyl Propionate) (DSP) in DMSO solution was prepared. DSP is a homobifunctional crosslinker molecule which binds to Protein A (Recombinant Staphylococcal) via the amine residues – at neutral pH or higher – and to the gold surface via the sulfide exposed during cleaving in DMSO. The solution containing the devices was then combined with a DSP solution and incubated for 2 hrs at room temperature. Unbound DSP was removed from the solution by washing (3x, 5min) in phosphate buffered saline pH 7.4 (PBS 7.4). A solution containing 0.1 mg/ml to 0.5 mg/ml of polyclonal IgG (rabbit anti-streptavidin, GenScript Corporation) was prepared, and added to the solution containing the devices and incubated for 1 hr at room temperature. Unbound IgG was removed through a series of three washing steps in PBS. BSA (1% in PBS) was then added to the solution to block residual reactive sites and incubated for 1 hr. This method produced an oriented and densely packed polyclonal IgG layer. A high active IgG density was critical to proper device function. Two conjugation methods were explored, the first method directly cross-linked the IgG to the DSP monolayer, while the second method made use of Protein A (Pr A) intermediate layer to orient the antibodies, as describe in the method above. The results quantifying the active IgG density for both methods (Table 1) were obtained using Immuno-SEM and verified using quartz crystal microbalance (QCM).

*Table 1. Comparison of active IgG functional densities measured on evaporated Cr/Au substrates using amine crosslinked and Protein A conjugation*

Conjugation Method	Functionalization Molecules	Density [particles/cm <sup>2</sup> ]	Spacing between active antibodies [nm]
Amine Crosslinked	DSP(0.002 M), IgG (0.1mg/ml)	690	57.4
Protein A conjugated	DSP (0.002 M), PrA (0.5mg/ml), IgG (0.1mg/ml)	1156	44.3

After preparation, the device response to the antigenic biomolecule was measured. In parallel, a set of controls and active devices were prepared. All experiments were performed at room temperature. A PBS 7.4 solution containing 0.5mg/ml streptavidin was introduced to solution containing the active devices, while in the controls only PBS 7.4 was introduced. The

device sets were then incubated for 30 minutes. Following incubation, both device sets were washed in DI (3x). Both active and control device sets were then fixed in a 2% solution of glutaraldehyde for 30 minutes. The fixation agent was then removed in a series of washing steps, first in PBS 7.4 (3x, 5min), then in DI (3x, 5min). The devices were then suspended in methanol and critically point dried (Tousimis 915B Critical Point Dryer). Micrographs of dry devices were then captured and analyzed.

## CONCLUSIONS

Given the large set of molecules against which antibodies can be raised, and the innately high specificity of antibody binding, we believe this work could have broad applications in biological sensing and transduction. Specifically, we envision a class of nanodevices which can elute drugs and construct synthetic chemical signaling cascades through the coupling of a chemically-triggered mechanical event with the release of sequestered compounds in conjugated capsules. We believe mesoscale devices based on these architectures offer a paradigm shift for sensing and actuation inherent in the architecture which leverages mechanochemical phenomena across multiple size scales and that this will lead to the creation of new families of sensors, actuators and nanomachines.

## REFERENCES

- [1] L. Mahadevan and P. Matsudaira, "Motility Powered by Supramolecular Springs and Ratchets", *Science*, 288, 95 (2000)
- [2] E.R. Kay, D. A. Leigh, and F. Zerbetto, "Synthetic Molecular Motors and Mechanical Machines", *Angew. Chem. Int. Ed.*, 46, 72-191 (2007)
- [3] M.Muller, A. Engel, U. Aebi, "Structural and Physicochemical Analysis of the Contractile MM Phage Tail and Comparison with the Bacteriophage T4 Tail", *J. Struct. Biol.*, 112, 1 (1994)
- [4] R. Feynman, *The Feynman Lectures on Physics*
- [5] C. Bustamante, Y. R. Chemla, N. R. Forde, and D. Izhaky, "Mechanical Processes in Biochemistry", *Annu. Rev. Biochem.*, 73, 705-48 (2004)

# DISPOSABLE IMMUNOASSAY CHIPS FOR HIV MONITORING IN RESOURCE-CONSTRAINED ENVIRONMENTS

Chien-Fu Chen,<sup>1,2</sup> Jikun Liu,<sup>1</sup> Eric Wong,<sup>3</sup> Chien-Cheng Chang,<sup>2</sup> Indira Hewlett,<sup>3</sup> Don L. DeVoe<sup>1\*</sup>

<sup>1</sup>University of Maryland, USA

<sup>2</sup>National Taiwan University, Taiwan

<sup>3</sup>U.S. Food and Drug Administration, USA

## ABSTRACT

Here we describe the microfluidic components enabling disposable immunoassay chips for HIV diagnosis in resource-constrained environments. The thermoplastic chip monitors the conserved viral capsid protein, p24 antigen. It combines blood sampling and plasma separation together with zero-power on-chip pumps and burst valves for manual flow control of sample and buffers. To enable sensitive p24 detection we have realized a polymer monolith porous support together with a novel anchoring chemistry allowing efficient covalent antibody immobilization. Using IgG as a model antigen to monolith-immobilized anti-IgG, an detection limit below 0.1 ng/mL has been achieved with an assay time of only 10 min.

## INTRODUCTION

Accurate, portable, and robust platforms for monitoring infectious diseases are critically needed to improve the quality of life for millions of people living in high-risk areas around the world. In particular, The HIV pandemic continues to be a significant worldwide public-health problem. The HIV virus is highly infective, rapidly mutates, and has no cure. Early diagnosis is critical for effective management. While most diagnostic assays detect HIV antibodies, the time for a host to produce these antibodies is up to six months after exposure, and newborns under 18 months of age cannot be tested with these methods due to masking by maternal antibodies. As an alternative, PCR-based nucleic acid testing (NAT) is highly sensitive, but labor-intensive and not suitable for resource-poor settings where simple, rapid, and inexpensive assays are required. Diagnostic tests targeting host antibodies or viral nucleic acids are also susceptible to false or discordant results due to viral variations.

Rather than detecting host antibody response, the thermoplastic chip described here is designed to directly monitor the conserved viral capsid protein, p24 antigen. While p24 detection provides exceptional specificity for monitoring early-stage infection, existing assays are not appropriate for use in resource-constrained environments where infrastructure, environmental, personnel, and financial resources can be highly limited [1]. To overcome these challenges we are developing a thermoplastic chip that combines blood sampling and plasma separation together with zero-power on-chip pumps and burst valves for manual flow control of sample and buffers. These functionalities are made possible by low-cost surface modifications based on UV-ozone exposure, enabling simple lithographic patterning of “microgap” channels and control over bond strength across different regions of the chip. To enable sensitive p24 detection we have realized a polymer monolith porous support together with a novel anchoring chemistry allowing efficient covalent antibody immobilization. The monolith sensors are shown to offer higher sensitivity than open-tubular flow-through sensors, with significantly shorter assay times. The chip also provides for on-chip reagent and buffer storage, and safe storage of assay waste.

## RESULTS AND DISCUSSION

A schematic of an integrated immunoassay chip is shown in Fig. 1. Whole blood from a finger prick is introduced into an inlet chamber, which is capped using a screw threaded into the thermoplastic substrate. The screw is manually actuated to flow ~50  $\mu$ L of whole blood past a plasma extraction element to prevent fouling of the downstream detection elements by red blood cells. Manual pumps are also used to deliver rinse buffers and immunoassay reagents within the chip.

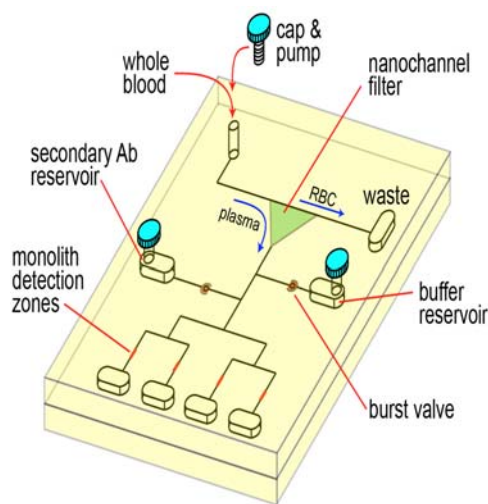


Figure 1: Schematic of the disposable thermoplastic HIV immunoassay chip.

A schematic of a manual screw pump is shown in Fig. 2, together with burst valves used to seal reagents on-chip. The valves are fabricated by controlling the thermoplastic bond strength through UV-ozone surface modifications.

A similar technique is used to fabricate the microgap plasma extraction element shown in Fig. 3. Details of this novel method for bond strength control and micro/nanochannel fabrication will be fully described. Detection of viral protein is achieved using antibodies immobilized on an array of porous epoxide monolith segments modified using a heterobifunctional crosslinking reagent (Fig. 4), ensuring high bioavailability of the antibodies. Detection may be performed using a direct or sandwich (Fig. 5) immunoassay format. Using IgG as a model antigen to monolith-immobilized anti-IgG in a direct assay, an excellent detection limit well below 0.1 ng/mL has been achieved with an assay time of only 10 min in a fully-manual format (Fig. 6).

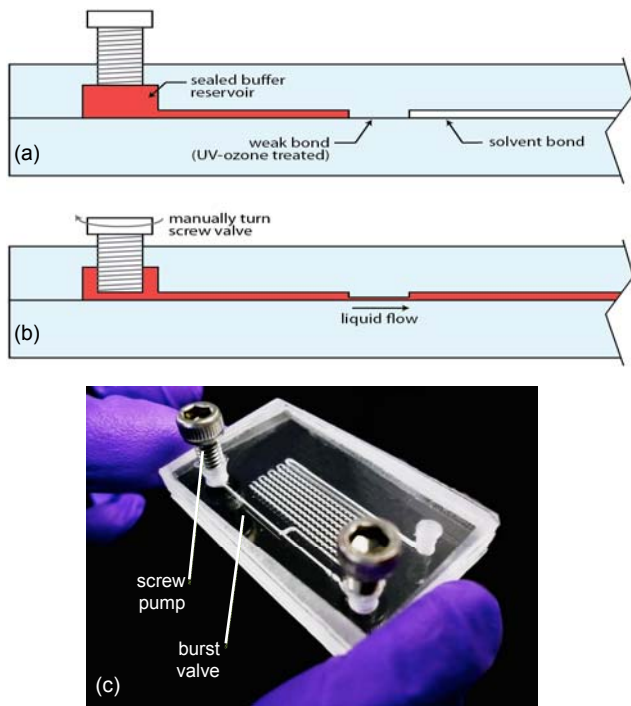


Figure 2: Buffer packet with integrated screw pump and burst valve (a) before and (b) after valve actuation, and (c) fabricated chip with 2 pumps and valves (actuated valve shown inset).

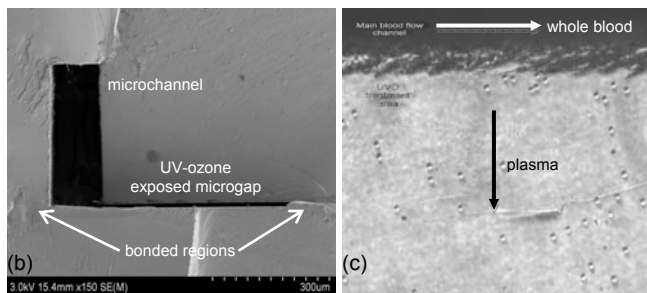
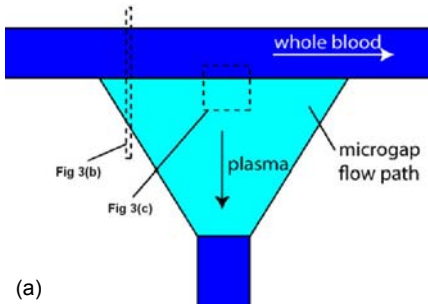


Figure 3: (a) schematic of a microgap plasma extraction element, (b) cross-sectional SEM image showing the sample injection microchannel seamlessly interfaced to a  $\sim 4 \mu\text{m}$  deep microgap fabricated by UV-ozone exposure and solvent bonding, and (c) isolation of plasma from whole blood using the microgap filter, with extraction efficiency above 95% achieved in this example. The regions depicted in (b-c) are noted in (a).

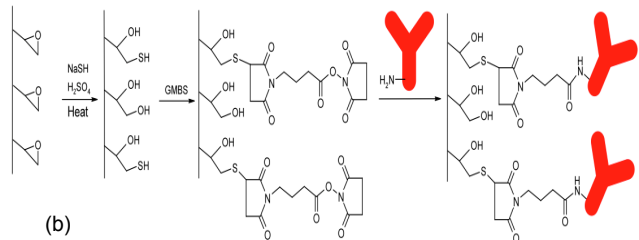
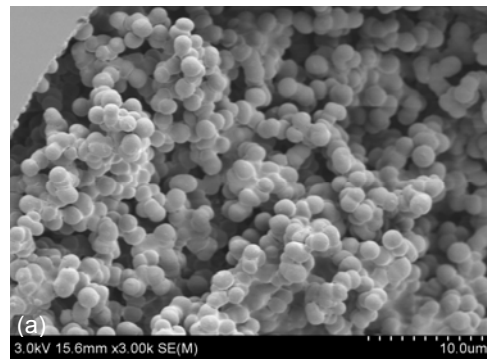


Figure 4: (a) SEM image of a porous monolith, and (b) antibody immobilization process using a heterobifunctional crosslinker.

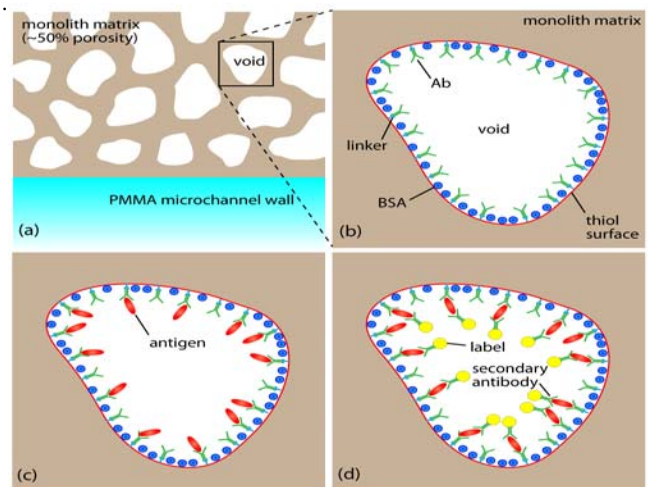


Figure 5: Sandwich assay steps performed within the porous monolith support matrix.

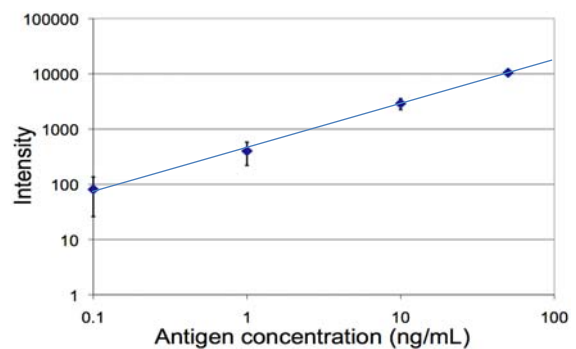


Figure 6: Dilution curve for rabbit IgG as a model antigen to monolith-immobilized anti-rabbit IgG. A limit of detection below 0.1 ng/mL is observed.

## **REFERENCES**

- [1] B. Ledergerber, M. Flepp, J. Boni, Z. Tomasik, R. W. Cone, R. Luthy and J. Schupbach, "Human immunodeficiency virus type 1 p24 concentration measured by boosted ELISA of heat-denatured plasma correlates with decline in CD4 cells, progression to AIDS, and survival: comparison with viral RNA measurement". *The Journal of Infectious Diseases*. 181, 1280 (2000).

## **CONTACT**

\*Don L. DeVoe, tel: +1-301-405-8125; ddev@umd.edu

# FAST AND MINIMALLY-INVASIVE TUMOR MARGIN DETECTION USING A NOVEL MICROMACHINED “SIDE-VIEWING” OIDRS SENSOR PROBE

C-C. Chang<sup>1</sup>, A. Garcia-Uribe<sup>2,1</sup>, J. Zou<sup>1</sup>, L. V. Wang<sup>2</sup>, B. Banerjee<sup>3</sup>, and J. Kuczynski<sup>3</sup>

<sup>1</sup>Department of Electrical and Computer Engineering, Texas A&M University, College Station, Texas, USA

<sup>2</sup>Department of Biomedical Engineering, Washington University in St. Louis, St. Louis, Missouri, USA

<sup>3</sup>Department of Gastroenterology, University of Arizona College of Medicine, Tucson, Arizona, USA

## ABSTRACT

In this paper, we report the design, fabrication and testing of a novel miniaturized optical sensor probe with “side-viewing” capability. Its unprecedented small size, unique “side-viewing” capability and high optical transmission efficiency enable the agile maneuvering and efficient data collection even in the narrow cavities inside the human body. The sensor probe consists of four micromachined substrates with optical fibers for oblique light incidence and collection of spatially resolved diffuse reflectance from the contacted tissues. The optical sensor probe has been used to conduct the oblique incidence diffuse reflectance spectroscopy (OIDRS) on a human pancreatic specimen. Based on the measurement results, the margin of the malignant tumor has been successfully determined optically, which matches well with the histological results.

## INTRODUCTION

The American Cancer Society estimated that there were about 42,470 new cases of pancreas cancers with about 35,240 deaths in the U.S. in 2009 [1]. The survival rate of the pancreatic cancer is relatively low compared with many other types of cancers. The low survival rate is due to the fact that early detection of pancreatic cancer is very difficult. This is because the pancreas is deep inside the body and so far there are no tests or physical exam can detect the pancreatic cancer in its early stage. Currently clinical methods for diagnosing pancreas cancers include laparoscopy and biopsy. However, for the follow-up treatments, these detection methods lack the ability to quickly and precisely determine a safe margin for removing the malignant pancreatic tissues. Usually, the tissue in a suspicious region is removed and histologically analyzed. Based on the results, another suspicious cite for tissue removal is planned and performed. Multiple rounds of cut-and-analyze procedure are required to complete the tumor removal, which would end up with an extremely time-consuming surgical procedure. To address this issue, new techniques that can enable simple, fast, accurate and reliable tumor margin detection are necessary.

Recent studies have shown that the change in the optical absorption and scattering properties of human tissues are closely related to their states of the malignancy [2, 3]. Several different optical methodologies have been investigated for determining the malignancy of tumors [4, 5]. Among them, oblique incidence diffuse reflectance spectroscopy (OIDRS) is a unique approach, which utilizes a special fiber optic sensor probe to measure the diffuse reflectance of the tissue in contact [6]. The diffuse reflectance spectra can be further used to extract optical absorption and scattering properties of the tissue [7]. In our previous studies, a remarkably high accuracy of 95% in differentiating (pre)cancerous human skin lesions from benign ones with automated OIDRS data processing and classification [6]. However, to extend the application of OIDRS from skin to pancreas cancer which is inside the body, miniaturized fiber optic probes suitable for inner-body measurements are needed.

In this paper, we report the design, fabrication and testing of the first 2-mm OIDRS probe with side-viewing capability using micromachining technology. This miniaturized, high optical

transmission efficiency, and “side-viewing” configuration makes it compatible with medical endoscopes for effective and efficient *in-vivo* measurements even in the narrow cavities inside human body. The new OIDRS probe has been used to conduct diffuse-reflectance measurement on a human pancreas specimen. Based on the measurement and classification, the margin between the malignant tissues and the benign ones has been successfully identified, which matches well with the histological results.

## THEORY

As shown in Fig. 1, when light is incident on the surface of an inhomogeneous medium (e.g. biological tissue), some of the incident light will be directly reflected (specular reflectance) and the remaining light will transmit into and interacts with the medium through scattering and absorption. After undergoing multiples times of interactions, part of the transmitted light will be scattered back to the surface and escape from the medium to form the diffuse reflectance.

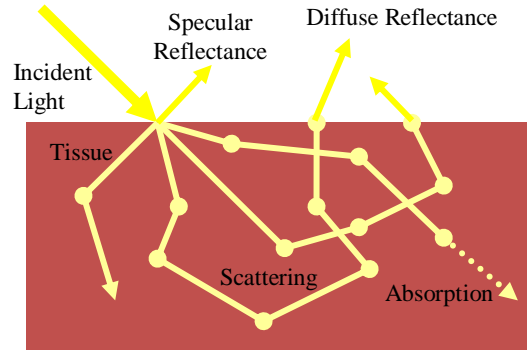


Figure 1: Illustration of light absorption and scattering in an inhomogeneous medium.

The spatially resolved steady-state diffuse reflectance for a particular wavelength can be calculated by diffusion theory [8].

$$R(x) = \frac{1}{4\pi} \left[ \frac{\Delta z(1 + \mu_{eff} \rho_1) \exp(-\mu_{eff} \rho_1)}{\rho_1^3} + \frac{(\Delta z + 2z_b)(1 + \mu_{eff} \rho_2) \exp(-\mu_{eff} \rho_2)}{\rho_2^3} \right] \quad (1)$$

where  $\rho_1$  and  $\rho_2$  are the distances between the positive and negative source points and the observation point on the medium surface (Fig. 2).  $\Delta z$  is the distance between the virtual boundary and the tissue depth, and  $z_b$  is the distance between the virtual boundary and the surface of the sample (Fig. 2). The distance from the point of incidence to the positive point source  $d_s$  is equal to  $3D$ . For oblique incidence, the diffusion coefficient is  $D = (3(0.35\mu_a + \mu_s'))^{-1}$ , where  $\mu_a$  is the absorption coefficient and  $\mu_s'$  is the reduced scattering coefficient. The effective attenuation coefficient  $\mu_{eff} = (\mu_a/D)^{1/2}$ . The shift of the point sources in the  $x$  direction  $\Delta x = \sin(\alpha_t)/(3(0.35\mu_a + \mu_s'))$ , and  $\alpha_t$  is the angle of light transmission into

the medium. The absorption and reduced scattering coefficients can be calculated by [9]

$$\mu_a = \frac{\mu_{eff}^2 \Delta x}{3 \sin(\alpha_i)} \quad (2)$$

$$\mu_s' = \frac{\sin(\alpha_i)}{\Delta x} - 0.35 \mu_a \quad (3)$$

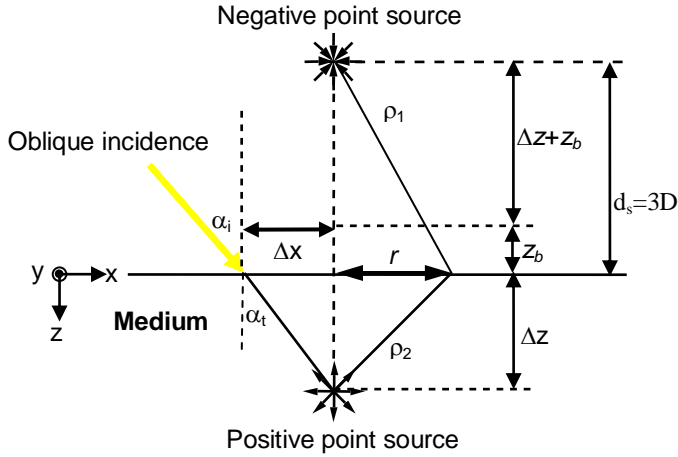


Figure 2: Schematic of the diffusion theory model for oblique incidence.

The assumption of the diffusion theory is that the reduced scattering coefficient is much larger than the absorption. The source and detector must also be separated in space so that the light is diffuse reflectance instead of specular reflectance. When the distance between the source and the detectors is comparable to the transport mean free path ( $\sim 1$  mm), diffusion theory does not apply. In this case, Monte Carlo simulation can be applied to extract optical properties from the diffuse reflectance [10].

The optical absorption of the human tissue is mostly related to the concentration of hemoglobin and its oxygen saturation. These parameters are believed to have close relationship with the disease state of lesions [11, 12]. On the other hand, the cell nuclei of the tissue can be considered as the major contributor for the scattering properties. Research has shown the diameter of the nuclei would increase with the degree of dysplasia in different lesions [13]. Therefore, the close relationship between the optical absorption and scattering properties can be used to differentiate the state of the malignancy of human tissue, which forms the physiological foundation for applying OIDRS for the cancer detection.

## PROBE DESIGN AND FABRICATION

In the OIDRS measurements, light with particular wavelengths is delivered at a desirable oblique incidence angle on the tissue surface and the one-dimensional linear distribution of the diffuse reflectance  $R(x)$  is collected. While this can be achieved by using a conventional front-viewing probe that consists of straight optical fiber bundles (Fig. 3(a)), it will not be convenient and feasible to conduct *in-vivo* OIDRS measurements inside the human body. This is due to the fact that internal organs mostly consist of long and narrow tubular cavities. To address this issue, we have investigated the idea of building a miniaturized side-viewing fiber optic probe suitable for measurements inside the human body (Fig. 3b). However, the side-viewing capability requires all the collection fibers to undergo a sharp  $90^\circ$  turn within a radius of curvature less than 2.5 mm. This inevitably would cause significant light loss and leakage and also possible mechanical fracture of the collection

fibers.

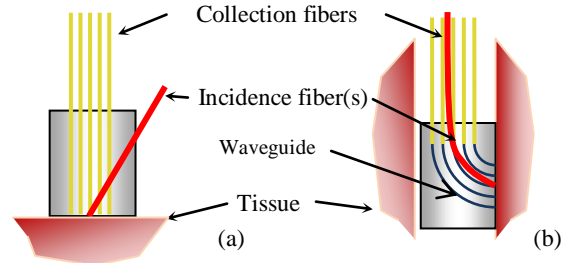


Figure 3: Schematic of micro OIDRS probes for *in-vivo* optical characterization of human tissues: (a) front-viewing configuration and (b) side-viewing configuration.

To solve this problem, we came up with a new probe design using optical-epoxy-filled waveguides. The probe consists of two micromachined devices assembled together. The first device functions as collectors of the diffuse reflection and contains five epoxy-filled waveguides with a  $90^\circ$  turn for side viewing, which are coupled to  $100 \mu\text{m}$  diameter optical fibers (Fig. 4(a)). The waveguides are filled with optically transparent epoxy (Epotek 301) to increase the coupling efficiency with the fibers and protect them from possible contamination from the body fluids (e.g. blood). In the second device, two chips are assembled to hold and position one source fiber ( $200 \mu\text{m}$  in diameter) which delivers light precisely at an oblique angle to the tissue of interest (Fig. 4(b)).

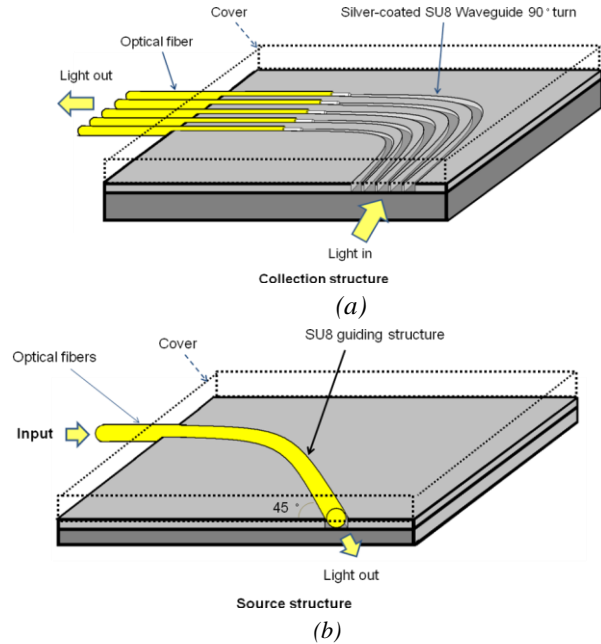


Figure 4: Schematic design of the new "side-viewing" OIDRS probe: (a) Collection device and (b) Source device.

The detail of the probe fabrication process is described below. Four silicon substrates with patterned SU-8 channel are used. SU-8 is chosen as the structural material because it can easily form patterned thick layers with high aspect ratio. The fabrication of SU-8 structure fabrication is based on the recipe from the material provider [14]. The first and second substrates have five curved SU-8 channel ( $\sim 75 \mu\text{m}$  deep,  $\sim 150 \mu\text{m}$  wide) on each of them and their patterns are mirror-flipped. When the two substrates are stacked together, tightly closed channels with cross section  $150 \mu\text{m} \times 150 \mu\text{m}$  can be formed and serve as the waveguide and positioning

device for the connection fibers. Similarly, the third and fourth substrates each have one open channel (~125  $\mu\text{m}$  deep, 250  $\mu\text{m}$  wide) and mirror flipped patterns. When being stacked together, a close channel with 250  $\mu\text{m} \times 250 \mu\text{m}$  cross section can be created as a position structure for source fiber.

To form the optical waveguides, all channels were coated with a thin layer of silver (~300 nm thick) uniformly using electron-beam evaporation. Transparent optical epoxy is applied to fill the collection waveguides and the fibers are placed inside all the aligning SU-8 channels. The assembly of the probe was essentially stacking and aligning the four substrates and glued together. The proximal ends of the fibers are connected to the OIDRS system and the light source via SMA connectors. The completely assembled probe is shown in Fig. 5. The probe has one 45° oblique incidence channel and five collection channels with an overall dimension of 8  $\times$  2.5  $\times$  2 mm<sup>3</sup>. This small size provides the possibilities for endoscopic applications in the pancreatic duct.

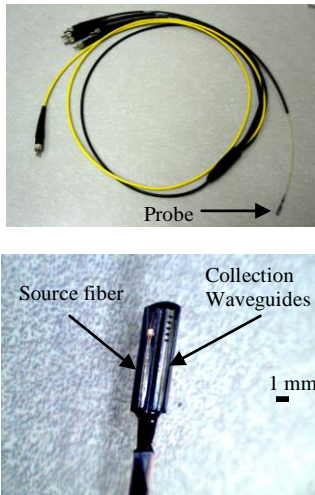


Figure 5: Complete OIDRS probe.

## TESTING AND RESULTS

The OIDRS measurement setup is shown in Fig. 6. It consists of a white light source, a fiber optic probe, an imaging spectrograph coupled with a CCD camera, and a personal computer. The source fiber of the optical probe is connected to the light source, while the collection fibers are connected to the spectrograph. During the OIDRS measurement, the probe is gently placed on the surface of the tissue. The incident light is delivered at an oblique angle through the source fiber, and the spatial distribution of the diffuse reflectance ( $R(x)$ ) is acquired by the collection waveguides and transmitted through the collection fibers to the spectrograph. The CCD camera captures the diffuse reflectance spectra (from 455 to 765 nm) from all the collection channels within about one second, which are then stored in the personal computer for future analysis. Before the OIDRS measurement, the whole experimental setup was calibrated using a standard liquid phantom with trypan blue dye as the absorbers and polystyrene microspheres as the scattering elements [15]. After calibration, the OIDRS probe was used to conduct *ex-vivo* measurements on a freshly excised human pancreas specimen with malignant tumors (Fig. 7). It should be noted that due to the extensive bleeding caused by the surgical excision, the entire pancreatic specimen appears in the same bloody color, which makes it almost impossible to visually differentiate the normal and malignant regions.

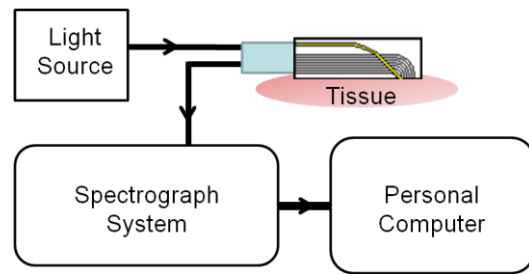


Figure 6: Experimental setup for OIDRS measurement.

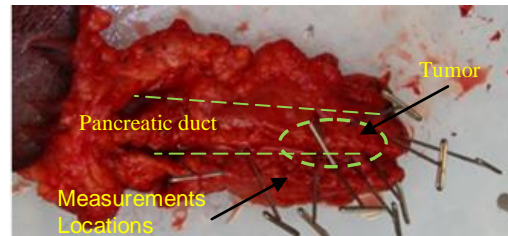


Figure 7: A human pancreas specimen with malignant tumors.

Fig. 8a and 8b show the representative diffuse reflectance spectra (five channels) measured from both the normal and the malignant regions in the pancreas specimen, which clearly show the difference in their optical signatures. To achieve a better understanding of the physiological origin of these differences, the absorption and scattering parameters were extracted from the measured diffuse reflectance spectra. In human tissues, hemoglobin is the major absorber within the visible spectrum.

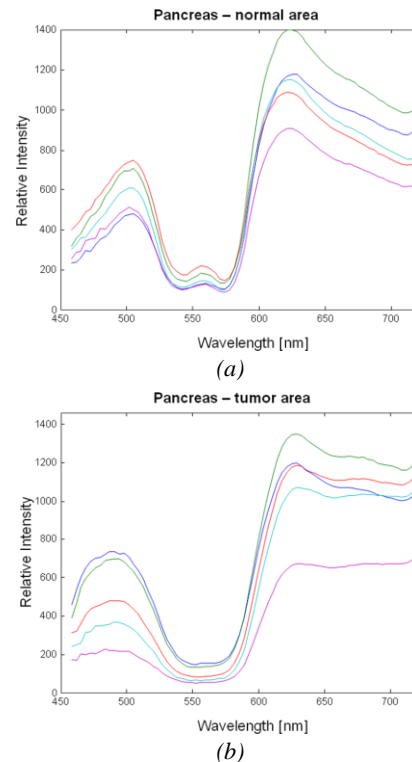


Figure 8: Diffuse reflectance spectra of human pancreas tissue from *ex-vivo* OIDRS measurement: (a) Normal tissue; and (b) Cancer tissue.



As shown in Fig. 7, due to the extensive bleeding caused by the surgical excision, the concentration of the hemoglobin and thus the absorption parameters of both the normal and malignant regions in the pancreatic specimen must have changed significantly from their original values. However, the scattering parameter, which is mainly due to the cell density and the size of the cell nuclei, will not be affected by the bleeding. Previous studies have shown that malignant tissues usually manifest higher optical scattering due to increased cell density and enlarged cell nuclei. Therefore, the relative value of the scattering parameter could serve as a good indicator to differentiate the malignant tissues from the normal ones. To test the feasibility of using OIDRS for malignant tumor margin detection, we made a series of measurements along the opened pancreatic duct (where the pancreatic cancers usually start to develop). Fig. 9 shows the extracted scattering parameters for different locations along the pancreatic duct, which clearly indicate the existence and location of the tumor region. This result matches well with the histological reading of the pancreas specimen.

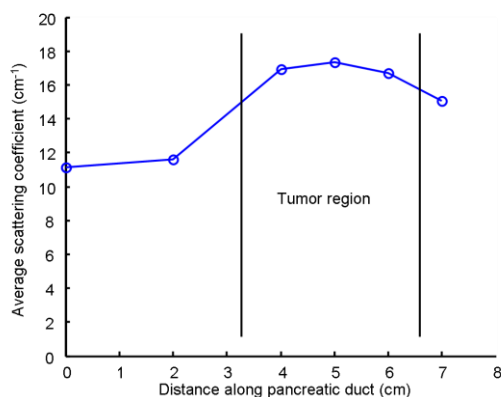


Figure 9: Average scattering coefficient along the pancreatic duct

## CONCLUSIONS

A new miniaturized OIDRS optical sensor probe with side-viewing capability has been successfully developed utilizing micromachining technology. Our preliminary results show that the probe, combined with OIDRS can provide both functional and structural information of tissue malignancy and thus can be a useful tool for rapidly determining a safe margin for the surgical treatment of cancers. The micromachining technology plays a critical role in enabling probe miniaturization and performance enhancement for the clinical application of OIDRS.

## ACKNOWLEDGMENTS

This project is partially supported by National Institutes of Health grant R01 CA106728.

## REFERENCES

- [1] American Cancer Society website. <http://www.cancer.org>. (Accessed Feb 2010).
- [2] P. R. Bargo, S. A. Pral., T. T. Goodell, R. A. Slevin, G. Koval, G. Blair, and S. L. Jacques, "In vivo determination of optical properties of normal and tumor tissue with white light reflectance and an empirical light transport model during endoscopy", *Journal of Biomedical Optics* 10(3) 034018 (2005).
- [3] T. C. Zhu, J. C. Finlay, and S. M. Hahn, "Determination of the distribution of light, optical properties, drug concentration, and tissue oxygenation in-vivo in human prostate during motexafin

- lutetium-mediated photodynamic therapy", *Journal of Photochemistry and Photobiology B* 79(3), pp. 231-241 (2005).
- [4] S. Brand, J. M. Poneros, B. E. Bouma, G. J. Tearney, C. C. Compton, and N. S. Nishioka, "Optical Coherence Tomography in the Gastrointestinal Tract", *Endoscopy* 32, pp. 796-803 (2000).
- [5] H. Messmann, R. Knüchel, W. Bäuml, A. Holstege, and J. Schölmerich, "Endoscopic fluorescence detection of dysplasia in patients with Barrett's esophagus, ulcerative colitis, or adenomatous polyps after 5-aminolevulinic acid-induced protoporphyrin IX sensitization", *Gastrointestinal Endoscopy*, 49(1), pp. 97-101 (1999).
- [6] A. Garcia-Urbe, N. Kehtarnavaz, G. Marquez, V. Prieto, M. Duvic, and L. V. Wang, "Skin Cancer Detection by Spectroscopic Oblique-Incidence Reflectometry: Classification and Physiological Origins", *Applied Optics* 43 (13), pp. 2643-2650 (2004).
- [7] A. Garcia-Urbe, K. C. Balareddy, J. Zou, and L. V. Wang, "Micromachined Fiber Optical Sensor for In-Vivo Measurement of Optical Properties of Human Skin", *IEEE Sensors Journal* 8(10), pp. 1698-1703 (2008).
- [8] L. -H. Wang and S. L. Jacques, "Use of a laser beam with an oblique angle of incidence to measure the reduced scattering coefficient of a turbid medium", *Applied Optics* 34, pp. 2362-2366 (1995).
- [9] S. -P. Lin, L. -H. Wang, S. L. Jacques, and F. K. Tittel, "Measurement of tissue optical properties using oblique incidence optical fiber reflectometry", *Applied Optics* 36, pp. 136-143 (1997).
- [10] T. J. Farrell and M. S. Patterson, "A diffusion theory model of spatially resolved, steady-state diffuse reflectance for the noninvasive determination of tissue optical properties in vivo", *Medical Physics* 19, pp. 879-888 (1992).
- [11] H. B. Stone, J. M. Brown, T. L. Phillips, and R. M. Sutherland, "Oxygen in human tumors: correlations between methods of measurement and response to therapy", *Radiation Research* 136, pp.422-434 (1993).
- [12] S. Thomsen and D. Tatum, "Physiological and Pathological Factors of Human Breast Disease That Can Influence Optical Diagnosis: Proc", *New York Academy of Science*. 838:337-343 (1998).
- [13] L. T. Perelman, V. Backman, M. Wallace, G. Zonios, R. Manoharan, A. Nusrat, S. Shields, M. Seiler, C. Lima, T. Hamano, I. Itzkan, J. Vandam, J. M. Crawford, and M. S. Feld, "Observation of periodic fine structure in reflectance from biological tissue - a new technique for measuring nuclear size distribution", *Physical Review Letters* 80, pp. 627-630 (1998).
- [14] Microchem Corp. website. <http://www.microchem.com>. (Accessed Sep 2009).
- [15] G. Marquez and L.-H. Wang, "White light oblique incidence reflectometer for measuring absorption and reduced scattering spectra of tissue-like turbid media", *Optics Express* 1, pp. 454-460 (1997).

# HUMAN TEAR FLUID DIAGNOSTIC ASSESSMENT ENABLED BY MICROFLUIDIC PROTEIN ELECTROPHORESIS

Kelly Karns, Aleksandra Denisin and Amy E. Herr

Department of Bioengineering, University of California, Berkeley, CA 94720, USA

## ABSTRACT

Human tear film fluid offers tremendous potential as a non-invasive diagnostic fluid. However, the use of tear fluid in diagnostic medicine is limited owing to non-standardized collection methodologies and low volume availability. We present a first-reported microfluidic tear fluid biomarker assay which will serve as a foundation for both rapid biomarker validation and point-of-care ocular diagnostics. Furthermore, we detail important advances in tear fluid preparation for high fidelity protein collection.

## INTRODUCTION

Human tear film fluid contains numerous proteins that are specific to the eye and others that are indicative of systemic protein levels [1]. Importantly, several eye-specific tear proteins have been shown to be putative biomarkers for diseases ranging from autoimmune diseases (e.g., Sjogren's syndrome) to ocular bacterial infections rampant in the developing world (e.g. trachoma) [2,3]. Furthermore, other proteins such as albumin exist in tear fluid at levels equal to those in serum, offering the potential to use tear fluid to monitor and track systemic protein expression levels. As a result, human tear fluid has significant potential as a non-invasive diagnostic fluid [1]. Despite the promise it offers, the use of tear fluid in diagnostic medicine is limited [4].

Major technological hurdles hinder routine clinical assessment of tear film fluid proteins. These gaps include: low throughput (>5 hours for analysis), lack of automation potential, consumption of large sample volumes, and limited sensitivity levels for clinical assessment. Taken together, these gaps make current assays (i.e., sizing, ELISA) unsuitable for point-of-care diagnostics and rapid endogenous protein quantification in clinically relevant ranges. Furthermore, tear collection methodologies are poorly characterized and highly variable, yielding widely disparate starting sample compositions which confound research findings and limit biomarker-based diagnostic measurements. Consequently, efficient, reliable

sample preparation and rapid, quantitative, highly specific assays for endogenous tear proteins would impact a spectrum of needs: from our basic understanding of ocular disease to the possibility of point-of-care diagnosis and treatment.

In particular, a rapid biomarker-based assay for the diagnosis of Sjogren's syndrome (SS) would provide tremendous clinical benefit. SS is a severe form of keratoconjunctivitis sicca (KCS or dry eye disorder) and is a systemic autoimmune disease that is estimated to impact 1-2% of the general population [5]. It causes severe dry eye and xerostomia (dry mouth arising from reduced saliva production) and is associated with vision threatening complications including scleritis (a serious inflammatory disease that affects the white outer coating of the eye), corneal ulceration and secondary bacterial infection [6]. Early diagnosis is important for timely disease management and the prevention of permanent tissue damage. However, current diagnostics are complicated by the absence of universal diagnostic criteria, the requirement of an invasive salivary gland biopsy and the similarity of symptoms with those of other common disorders. Consequently, average time to diagnosis after the onset of symptoms is over 6 years [7].

Lactoferrin (Lf) stands out as a high-abundance tear-specific protein which is down-regulated in the tears of patients with KCS and SS when compared with healthy controls and down-regulated in tears of patients with SS when compared with non-SS KCS patients [8]. Importantly, the development of a biomarker-based assay for the differential diagnosis of SS and severe KCS would have real clinical benefit by eliminating the need for salivary gland biopsy and promoting timely treatment of glandular and extraglandular manifestations of SS. It would also open up the possibility of presymptomatic diagnosis of autoimmune diseases such as rheumatoid arthritis, which occur in 60% of SS patients [6]. Owing to the clinical benefits of such a test as well as the identification of Lf as a possible biomarker for SS, Lf was chosen as a biomarker to validate the technology platform performance.

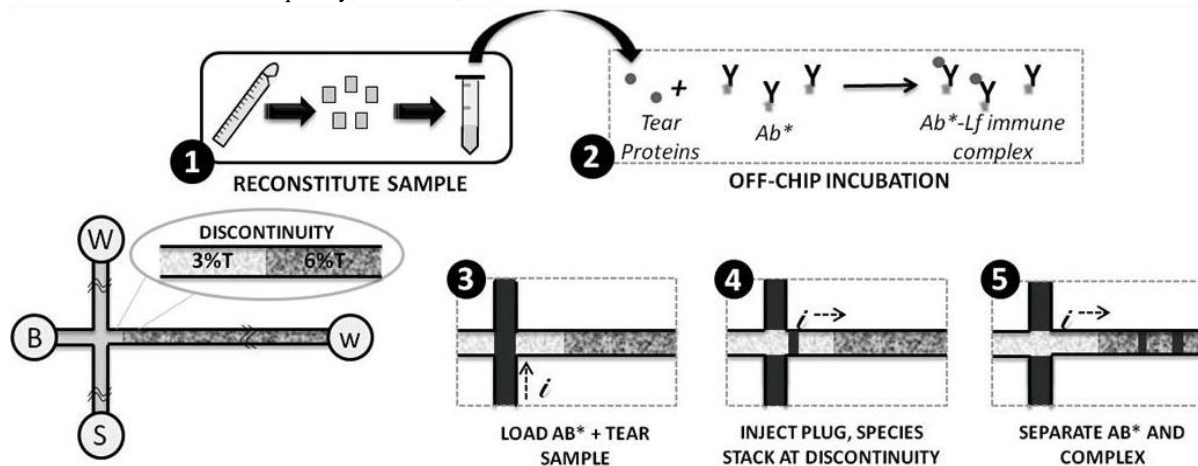


Figure 1: Microfluidic protein electrophoresis enables the rapid quantification of endogenous volume-limited tear fluid proteins. (1) Tear proteins are reconstituted from Schirmer strips. (2) Lf-containing tear fluid is incubated with labeled antibody (Ab\*) and loaded on chip (well S). (3) Sample is electrophoretically loaded into loading channel. (4) Finite plug is injected into separation channel and stacked at discontinuity (5) Ab\* and complex peaks are resolved. Ab\*-Lf complex formation detects presence of targeted proteins in tear sample.

This paper presents important advances in tear fluid preparation for high fidelity protein collection and a first-in-kind rapid microfluidic tear fluid biomarker assay (Lf). Importantly, while the focus in the present study is measurement of Lf, other important protein markers of disease are amenable to measurement using the approach. To our knowledge, no similar efforts exist. The following sections present theory and device design followed by fabrication technique, experimental results and finally the relevant discussion and conclusions.

## THEORY AND DEVICE DESIGN

Microfluidic electrophoretic immunoassays are uniquely suited to rapidly quantify endogenous proteins in volume-limited tear samples. The approach takes advantage of the high specificity of antibody-antigen interactions to separate fluorescently labeled free antibody from bound antibody-antigen immune complex for a quantitative measure of antigen concentration in a complex sample. These immunoassays offers numerous advantages over current techniques including rapid species resolution (seconds), high analytical specificity, low sample volume requirements (nL to  $\mu$ L), the potential for facile multiplexing to assess multiple proteins in a single sample, and a small form factor for point-of-care, automated use.

For use as a differential diagnostic for SS and KCS, the assay was optimized to ensure detection of clinically relevant Lf concentrations. Previous reports have shown the mean concentration of Lf in SS tears to be  $1\mu\text{M}$  Lf, while non-SS KCS tears have a mean Lf concentration of  $8\mu\text{M}$  [8]. Allowing for a 10x dilution factor in sample preparation, this suggests 100nM Lf as a starting diagnostic threshold on which to center the detectable assay range.

A polyacrylamide gel was used within the channels as shown previously [9] and the gel pore size was tuned in order to enhance sensitivity. Photopatterned discontinuous gel architectures in particular have recently been shown by our group to enhance sensitivity levels and allow for ultra short separation distances, opening the possibility for point-of-care, battery powered devices that employ analytical grade electrophoresis [10]. Sample stacking occurs at the pore discontinuity and is proportional to the extent of pore size change as given in Equation 1

$$\log\left(\frac{C_1}{C_2}\right) = -k_r(T_2 - T_1) \quad (1)$$

where  $C_1$  and  $C_2$  are the average plug concentrations before and after the discontinuity respectively,  $k_r$  is the retardation coefficient of the analyte and  $T_1$  and  $T_2$  are the total acrylamide concentrations before and after the discontinuity respectively. The change in total acrylamide concentration was therefore maximized to achieve the greatest possible sample stacking and enhanced sensitivity. A discontinuous gel architecture of 3-6%T was experimentally determined to allow for maximal sample stacking and resolution while still allowing for the migration of both free antibody and complex.

Figure 1 presents a schematic overview of the final assay concept. Key design features include: (i) large pore-size loading gel for non-biased sample loading, (ii) pore-size discontinuity for sample stacking and enhanced resolution and sensitivity and (iii) smaller pore-size separation gel for rapid species resolution.

## FABRICATION

A 3-6%T discontinuous polyacrylamide gel architecture was fabricated and optimized to separate fluorescently-labeled

anti-human Lf antibody ( $\text{Ab}^*$ ) from the Lf immune complex. Figure 2 shows the two step photopolymerization protocol as described previously [10]. Briefly, 6%T precursor solution was loaded onto a standard T-channel networked glass microfluidic chip. A small region immediately after the injection junction was polymerized using a photomask and UV objective for 3 min at  $5.8\text{mW}/\text{cm}^2$ . The precursor solution in the loading channels were then replaced with a 3%T precursor solution and the chip was flood exposed on a UV lamp for 7 min at  $12\text{mW}/\text{cm}^2$ . The result was a sharp discontinuity in pore size  $600\mu\text{m}$  after the injection junction.

## RESULTS AND DISCUSSION

### Microfluidic Immunoassay

Using this new approach, we have demonstrated the ability to detect and quantify endogenous Lf in  $<1\mu\text{L}$  of healthy and SS tears using a 3-6%T discontinuous gel architecture. Figure 3 shows time-based montages of the electrophoretic separation of  $\text{Ab}^*$  in dilute healthy tears and dilute SS tears compared to buffer. In both the healthy and SS tear samples, the unbound antibody is clearly separated from the  $\text{Ab}^*$ -Lf immune complexes which are retarded at the discontinuity, indicating the detection of endogenous Lf in healthy and SS tears. In Figure 4A, fluorescence intensity along the channel is plotted at 19s for three samples:  $\text{Ab}^*$  in buffer,  $\text{Ab}^*$  in healthy tears, and  $\text{Ab}^*$  in

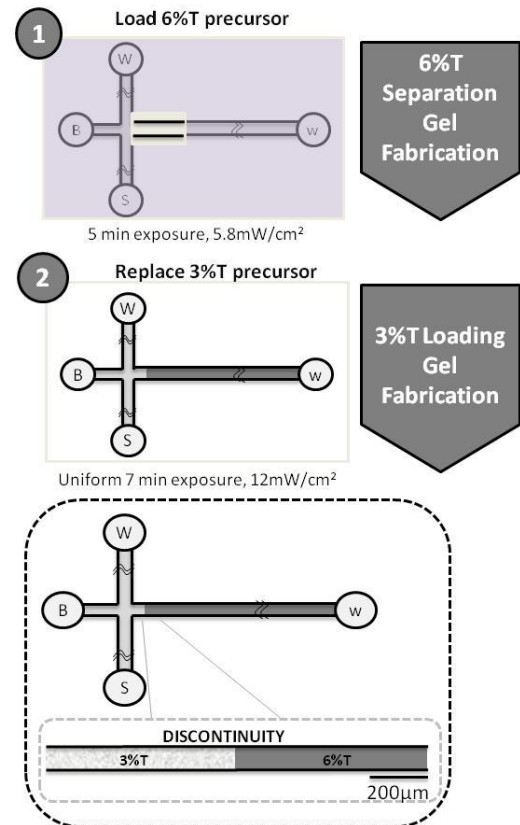


Figure 2: Two step photopatterning polymerization fabrication protocol yields sharp pore size discontinuity that enhances assay sensitivity and resolution efficiency. 6%T precursor is loaded into chip and small region is exposed on a UV objective for 3 min at  $5.8\text{mW}/\text{cm}^2$ . Solution in loading channels was then replaced with a 3%T precursor and the whole chip flood exposed for 7 min at  $12\text{mW}/\text{cm}^2$ .

SS tears. When Ab\* binds to endogenous Lf in tear fluid, there is a decrease in free antibody in solution and an immune complex peak appears, yielding a quantitative measure of Lf. Importantly, we note the following: (i) a complex peak emerges in both SS and healthy tears when compared to Ab\* in buffer, indicating the detection of endogenous Lf in both SS and healthy tears, (ii) the complex peak in SS tears is lower than that of healthy tears, demonstrating a decrease in endogenous Lf in SS tears compared to healthy tears and validating the clinical observation that Lf is down-regulated in SS tears, and (iii) unlike in conventional slab gel measurements (data not shown), multiple complex bands can be resolved in the assay, providing additional information about tear composition and binding configurations. Gold-standard ELISA measurements confirm the data observed in the immunoassay assessment. Critical for point-of-care diagnostics, the Lf immunoassay completes in <20s.

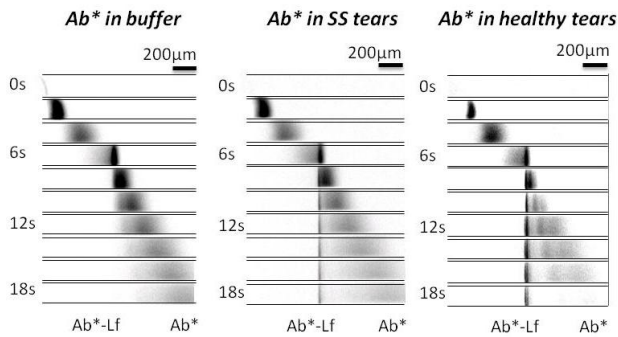


Figure 3: Endogenous Lf is detected in healthy and diseased tears in <20 s with a 700µm separation distance. Ab\* is incubated in buffer, dilute SS tears and dilute healthy tears and electrophoretically separated. Time-evolving fluorescence images are shown for the first 18s. Ab\* and Ab\*-Lf complexes are resolved in 700µm.

To provide an accurate quantitative measure of Lf in solution, increasing amounts of Lf were spiked into diluted SS tears and separated on-chip. Complex peak heights were extracted from the fluorescence images as shown in Figure 4B and a nonlinear least-squares fit with a 3-parameter model was used to establish the relationship between Lf concentration and complex peak height ( $\beta_1 = 882.8$ ,  $\beta_2 = 69.6$ ,  $\beta_3 = 30.2$ ). The model is predictive to within 12% in the clinically relevant range of 15-230nM Lf. Quantification of endogenous Lf in SS tears is confirmed to within 8% of gold-standard ELISA measurements.

Assay specificity is also crucial for a diagnostic measurement. Especially due to the complexity and relative unknown composition of tear fluid, efforts must be made to control for any non-specific interaction of anti-human Lf Ab\* with other components of tears. Samples of Ab\* and a protein ladder containing known proteins trypsin inhibitor, parvalbumin and anti-human IgG antibody were separated independently on chip and then incubated together and separated simultaneously. A lack of additional peaks in the simultaneous separation gives a preliminary indication that nonspecific binding is not occurring between Ab\* and these proteins (Figure 5) while incubation of Ab\* with Lf has shown binding both in on-chip and bench-top studies.

Further work will include incubation of Ab\* in Lf-depleted tear fluid to probe for nonspecific binding interactions.

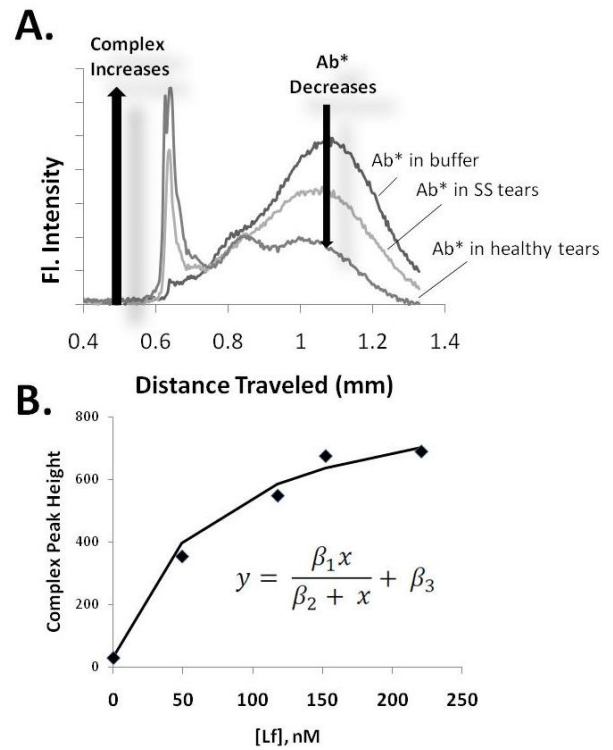


Figure 4: The Lf immunoassay is quantitative. (A) Fluorescence intensity in the channel is plotted at 19s for three samples: Ab\* in buffer, Ab\* in healthy tears, and Ab\* in SS tears. A complex appears in tear fluid, yielding a quantitative measure of endogenous Lf in SS and healthy tears. (B) Lf immunoassay is quantitative for endogenous Lf in tear fluid to within 12%. Lf dose response curve generated by on-chip immunoassay with 3-parameter model fit given by equation.

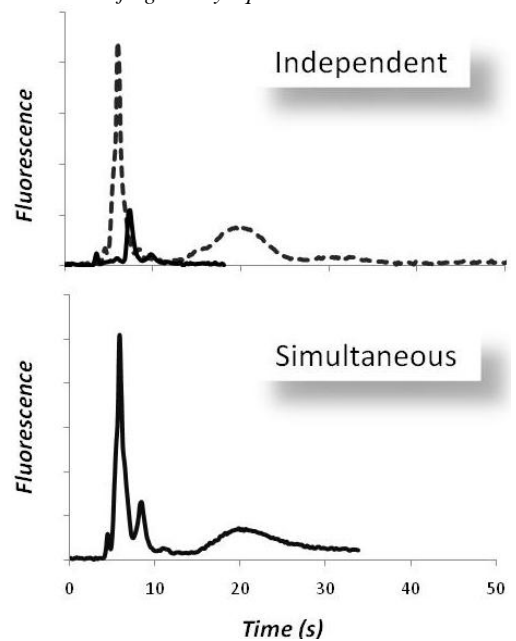


Figure 5: Preliminary results indicate assay specificity. Labeled protein ladder (dashed line) and Ab\* (solid) are separated independently and then incubated and separated simultaneously. A lack of added peaks shows preliminary indication of assay specificity.

## Sample Preparation

For a biomarker-based immunoassay to yield meaningful clinical results it must utilize a standardized sample preparation methodology. Currently, novel tear-based diagnostic assays are complicated by the difficulties of collecting tear fluid in sufficient volumes and standardized composition. The clinical standard for tear collection and storage in large patient registries (e.g. UCSF) is the Schirmer strip; yet these strips are intended for volumetric measurements of tear production for diagnostic purposes and not for protein collection and extraction. Since assay reliability is only as good as upstream sample preparation, an efficient method of reconstituting tear proteins from Schirmer strips is paramount to a successful diagnostic assay. Key reconstitution metrics include: i) minimal sample dilution, ii) high efficiency extraction and iii) comparison of efficiencies across different proteins and concentrations.

To optimize and characterize the reconstitution protocol, we used BSA as a model protein to establish the reconstitution efficiency of protocols found in the literature [11,12,13,4]. Tested variables included altered buffer conditions, elution times and centrifugation vs. diffusion-based extraction. The optimized protocol involves incubating the strips in phosphate-buffered saline (PBS) for 3 hours at room temperature while shaking. Using this protocol, we have been able to demonstrate 78-100% extraction efficiencies across a concentration range of 0.75-2mg/mL with a 2x dilution factor during reconstitution (Figure 6). Results are on par with most efficient reported extraction protocols to date [14]. Future work in this area will include expanding this study to other proteins, complex samples and lower concentrations, closer to the protein levels found in tear fluid.

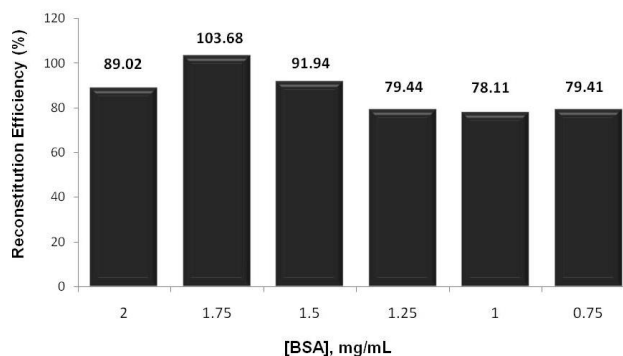


Figure 6: Optimized sample reconstitution protocol yields 78-100% efficiencies with minimal (2x) dilution.

To our knowledge, this study represents the first use of tear fluid to diagnose systemic disease and opens up the possibility of an entirely new non-invasive diagnostic sample matrix. The technology platform can be expanded to other diseases by changing the biomarker or multiplexing. As such, we anticipate that it will have a large impact on the research and clinical community by advancing our basic understanding of ocular and systemic disease as well as opening the possibility of point-of-care diagnosis and treatment.

## CONCLUSIONS

For the first time, we demonstrate technologies critically needed for non-invasive tear-based diagnostics. Namely, we report on improved sample preparation for protein extraction and the first known endogenous microfluidic immunoassay for protein biomarker detection and quantitation in human tears.

Importantly, the microfluidic protein assay requires seconds to complete and microliter sample volumes, providing the foundation for first-in-kind, highly specific, rapid clinical diagnostics relevant to ocular and systemic diseases.

## ACKNOWLEDGEMENTS

The authors thank Ms. Chenlu Hou (UC Berkeley) and Dr. Nancy McNamara (UCSF Proctor Eye Foundation) for technical assistance. Financial support provided by the DARPA Young Faculty Award (AEH) and an NSF GRF (KK).

## REFERENCES

- [1] Mann A.M, Tighe B.J., "Tear Analysis and Lens-Tear Interactions Pt.1: Protein Fingerprinting with Microfluidic Technology." *Cont Lens Anterior Eye*. **30**, 163 (2007).
- [2] Wu K., Zhang Y., "Clinical Application of Tear Proteomics: present and future prospects", *Proteomics Clin. Appl.* **1**, 972 (2007).
- [3] Dean D., Kandel R.P., Adhikari H.K., Hessel T., "Multiple Chlamydiaceae Species in Trachoma – Implications for Disease Pathogenesis and Control", *PLOS Med.* **5**, 57 (2008).
- [4] Zhou L., Beuerman R.W., Chan C.M., Zhao S.Z., Li X.R., Yang H., Tong L., Liu S., Stern M.E., Tan D., "Identification of Tear Fluid Biomarkers in Dry Eye Syndrome Using iTRAQ Quantitative Proteomics", *J. Proteome Res.* **8**, 4889 (2009).
- [5] Asbell P.A., Lemp M.A., *Dry Eye Disease: The Clinician's Guide to Diagnosis and Treatment*. Thieme Medical Publishers, NY (2006)
- [6] Lemp M.A., "Epidemiology and Classification of Dry Eye", *Technical Digest of the 2<sup>nd</sup> International Conference on the Lacrimal Gland, Tear Film, and Dry Eye Syndromes*, Southampton Princess Resort, Bermuda (1996) pp. 791-803
- [7] Sjogren's Syndrome Foundation. "Diagnosis" <http://www.sjogrens.org/home/about-sjogrens-syndrome/diagnosis>
- [8] Ohashi Y, Ishida R, Kojima T, Goto E, Matsumoto Y, Watanabe K, Ishida N, Nakata K, Takeuchi T, Tsubota K, "Abnormal Protein Profiles in Tears with Dry Eye Syndrome", *AJO*, **136**, 291 (2003)
- [9] Herr A.E., Sing, A.K. "Photopolymerized Cross-Linked Polyacrylamide Gels for On-Chip Protein Sizing", *Anal Chem*, **76**, 4727 (2004)
- [10] Hou. C., Herr A.E. "Ultrashort Separation Length Homogeneous Electrophoretic Immunoassays Using On-Chip Discontinuous Polyacrylamide Gels", *Anal Chem*, *accepted* (2010)
- [11] Li K, Chen Z, Duan F, Liang K.W. "Quantification of tear proteins by SDS-PAGE with an internal standard protein: A new method with special reference to small volume tears", *Graefes Arch Clin Exp Ophthalmol*, **10**, 107 (2009)
- [12] Mackie I.A., Seal D.V. "Diagnostic Implications of Tear Protein Profiles", *British Journal of Ophthalmology*, **68**, 321 (1984)
- [13] Remington S.G., Crow J.M., Nelson J.D., "Autoantibodies to Endogenous Tear Protein in Normal Human Tears", *Current Eye Research*, **34**, 819 (2009)
- [14] A. Kijlstra, S.H.M. Jeurissen, K.M. Koning, "Lactoferrin Levels in Normal Human Tears", *BJO*. **67**, 199 (1983).

# ISOELECTRIC FOCUSING – MULTIPLEXED REVERSED PHASE LIQUID CHROMATOGRAPHY – MALDI-TOF MASS SPECTROMETRY IN A MICROVALVE-INTEGRATED POLYMER CHIP

J. Liu<sup>1</sup>, C.-F. Chen<sup>1</sup>, C.-C. Chang<sup>2</sup> and D. DeVoe<sup>1\*</sup>

<sup>1</sup> Department of Mechanical Engineering, University of Maryland, College Park, USA

<sup>2</sup> Institute of Applied Mechanics, National Taiwan University, Taipei, Taiwan

## ABSTRACT

A cycloolefin polymer chip supporting isoelectric focusing (IEF) and reversed-phase liquid chromatography (RPLC) is demonstrated for two dimensional peptide separations, with IEF as the first electrokinetic enrichment stage for effective fractionation of sample components prior to RPLC. The thermoplastic chip contains integrated high pressure microvalves, enabling uniform sample transfer from the IEF channel to parallel RPLC channels in gradient elution and hydrodynamic isolation between the separation dimensions. The reusable system is shown to provide efficient and rapid 2-D separations together with facile interfacing with MALDI-MS, suggesting a new route towards effective peptide analysis from complex sample matrixes.

## INTRODUCTION

While mass spectrometry is a highly successful technique for proteomic identification and quantification, effective front-end separation methods is necessary to greatly enhance its analytical capability to cope with the complexity and dynamic range of proteins within biological samples. Peak capacity is an important criterion to select a proper separation method. While relatively high peak capacities can be achieved with single dimensional separation methods [1], multidimensional separations generally offer greater resolving power according to the theoretical prediction of Giddings [2].

Two dimensional polyacrylamide gel electrophoresis (2-D PAGE) is a standard multidimensional separation technique used in proteomic analysis. To overcome the intrinsic disadvantages of 2-D PAGE, including poor reproducibility, low analysis speed, and difficult automation, a variety of liquid-phase multidimensional separation techniques were demonstrated in either on-line or off-line modes. In these techniques, resolved species eluted from the first separation dimension are collected in multiple fractions and sequentially loaded into the second dimension, thus reducing analytical throughput and enhancing instrument complexity. To overcome the shortcoming of current liquid-phase multidimensional separation techniques and leverage potential benefits including small sample and reagent consumption, high analysis speed, and high levels of integration, we used microfluidic technology to develop a cycloolefin polymer (COP) chip supporting on-line isoelectric focusing (IEF) and multiplexed reversed-phase liquid chromatography (mRPLC) for high throughput two dimensional peptide separations, with IEF acting as a highly concentrating CE separation mode for effective isolation of sample components prior to mRPLC.

## CHIP FABRICATION

An IEF-mRPLC chip is depicted in Fig. 1. The channel pattern was fabricated by direct micromilling of COP plaques using a computer numerical control machining system and sealed with COP cover plates in a solvent-bonding process [3]. The integrated thermoplastic chip contains two novel microvalves (Fig. 1) with maximum pressure resistance up to 24 MPa, enabling uniform sample transfer and gradient elution from each RPLC column, and ensuring hydrodynamic isolation between the

separation dimensions. Fluidic connection between the IEF-mRPLC chip and the off-chip LC pump and capillary flow splitter (Fig. 1) were established using a high pressure and low dead volume needle interface shown to withstand pressures above (40 MPa), well above the delamination limit (24 MPa) of solvent-bonded COP substrates [3] and exceeding the typical pressure limits required for efficient RPLC. Multiplexed RPLC columns were prepared by packing 5  $\mu\text{m}$  C18 silica particles to each RPLC channel, with porous polymer frits photosynthesized at column end.

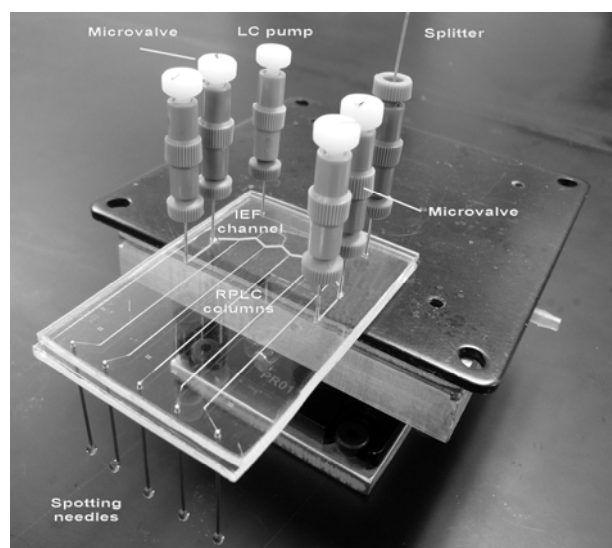


Figure 1: IEF-mRPLC chip with spotting needles for MALDI-TOF MS analysis.

## RESULTS AND DISCUSSION

A chip IEF and the following mRPLC separations of a fluorescein-labeled BSA digest are shown Fig. 2 and Fig. 3 respectively.

During early chip tests, the strongly hydrophobic COP channel surface was found to provide multiple non-specific

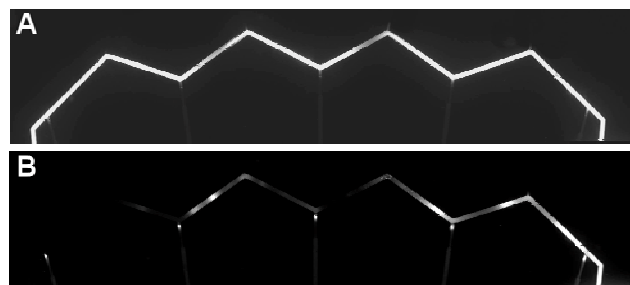


Figure 2: Focusing of Fluorescein-BSA digest in the IEF channel. (A) Sample introduction; (B) 30 min IEF of the digest.

adsorption sites for focused peptides, causing sample loss and significant decreasing IEF resolution, capacity and reproducibility. We found that HPMC can deactivate the hydrophobic surface without significantly affecting the following RPLC separations. By doping sample with 0.4% HPMC, focused peptide bands were repeatedly generated during IEF, as shown in Fig. 2 for the case of BSA digest. This figure also reveals limited dispersion of analyte into the constrained channels linking the RPLC columns, presumably due to electrokinetic mobilization from fringing fields at the channel junctions. However, the amount of the trapped samples was much smaller than that of the focused analytes in the IEF channel, and significant carryover of peptides between the LC fractions was not observed.

In comparison to the 1-D  $\mu$ RPLC separation, the free dye peak does not appear in the RPLC stage of the 2-D separation since the dye is not zwitterionic but negatively charged, and migrates out of the sampling region toward the anode during IEF. About 25 components can be recognized in 1D  $\mu$ RPLC separation, compared with 66 in the IEF-mRPLC separation, corresponding to a 2.6-fold improvement in overall peak yield within the same separation time frame. Using unlabeled BSA digest as a model system, MALDI-MS analysis was performed on a set of 6 sequential fractions collected from the spotting needles inserted at each end of the LC channels (Fig. 1). Comparing the results obtained with and without the front-end separation, 48 unique digest peptides were identified following IEF-mRPLC separations, while only 18 unique peptides were identified by direct MALDI-MS detection of the whole digest.

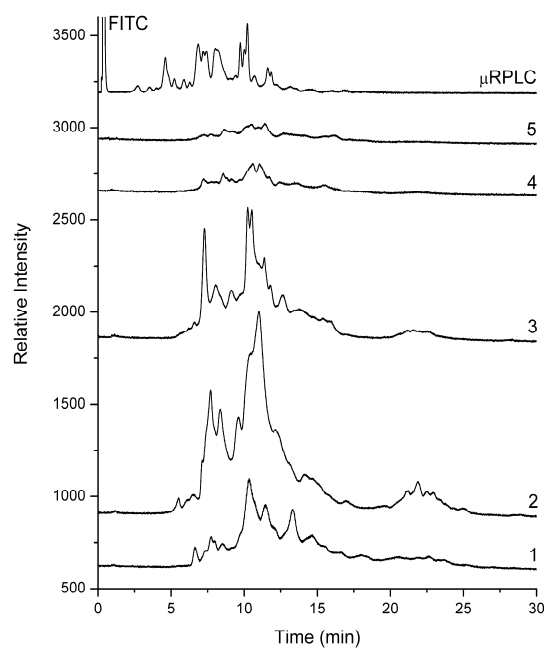


Figure 3:  $\mu$ RPLC and  $\mu$ IEF-mRPLC of 0.25 mg/mL Fluorescein-BSA digest. Identical RPLC conditions were used in both separations.

Data obtained from the IEF-mRPLC fractions were converted to a set of 2-D cluster maps to show the distribution of the 30 highest intensity peptides (Fig. 4). The cluster maps reveal that the majority of peptides were confined to specific channels and fractions, with little overlap across multiple MALDI target spots. For several peptides which appear in multiple target spots, these

peptides generally exhibit discrete patterns across adjacent spots, suggesting the presence of isomers for these peptides. These results reveal that the IEF-mRPLC separations are effective at isolating peptides to specific fractions defined by their pI and hydrophobicity, thereby simplifying the content of each individual fraction while preventing unwanted overlap of peptides across multiple fractions.

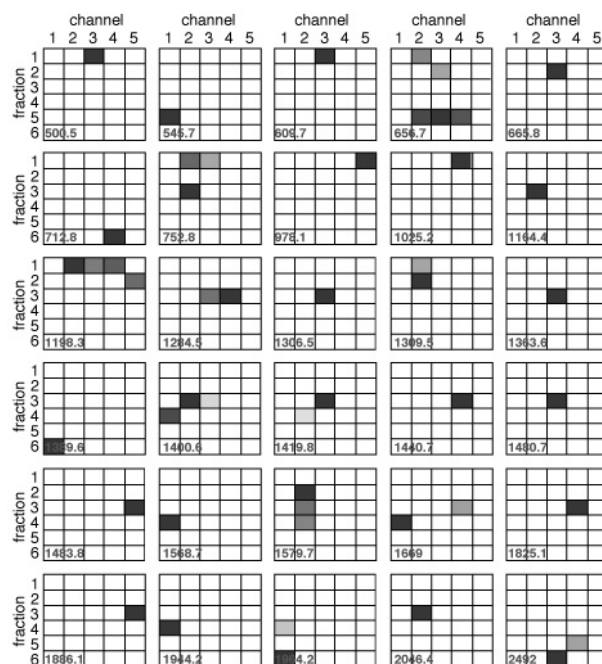


Figure 4: Locations of top 30 peptides identified from BSA digest by mRPLC fraction and channel. Sequential fractions were collected every 6 min over a 36 min period. Peptide  $m/z$  values are shown in the lower left of each panel. Increasing color saturation represents higher signal intensity. Mass tolerance:  $\pm 1$  Da,  $m/z$  cut-off: 500 Da.

## REFERENCES

- [1] "High-Efficiency Nanoscale Liquid Chromatography Coupled On-Line with Mass Spectrometry Using Nanoelectrospray ionization for Proteomics," Y. Shen, R. Zhao, S. J. Berger, G. A. Anderson, N. Rodriguez, and R. D. Smith, *Analytical Chemistry*, 74, 4235 (2002).
- [2] J. C. Giddings, *Unified Separation Science*, John Wiley & Sons, New York, 1991.
- [3] "Polymer Microchips Integrating Solid-Phase Extraction and High-Performance Liquid Chromatography Using Reversed-Phase Polymethacrylate Monoliths," J. Liu, C.-F. Chen, C.-C. Chang, C.-C. Chu, and D. L. DeVoe, *Analytical Chemistry*, 81, 2545 (2009).

## CONTACT

\*D. DeVoe, tel: +1-301-405-8125; ddev@umd.edu

# MICROFABRICATED SUBSTRATES FOR THE REMOTE GENERATION OF PRECISION FORCES ON SINGLE CELLS VIA INTRACELLULAR MAGNETIC FLUORESCENT NANOPARTICLES

P. Tseng<sup>1\*</sup>, J. W. Judy<sup>1,2</sup>, and D. Di Carlo<sup>1,2,3</sup>

<sup>1</sup>Electrical Engineering Department

<sup>2</sup>Biomedical Engineering, IDP

<sup>3</sup>Bioengineering Department

University of California, Los Angeles, Los Angeles, California, USA

## ABSTRACT

A microfabrication process has been investigated and developed for the precision alignment of electroplated ferromagnetic elements with biological cells that are shaped by patterned fibronectin on transparent slides. In addition, we investigate one technique enabled by this process, which is the massively parallel generation of forces on single cells via internalized magnetic-fluorescent nanoparticles. Large magnetic field gradients generated by magnetizing the elements in close proximity to the cells allows the remote generation of large forces on single cells via intracellular localization of nanoparticles, which are capable of polarizing cell shape and activity.

## INTRODUCTION

### Microfabrication-based force application

Cellular mechanotransduction, or the method by which cells respond and react to externally and internally generated forces and stresses, plays critical roles in a large number of biological processes, including, but not limited to: mitotic division, cell shape, contractility, polarity, and mobility. Traditionally, researchers attempt to simulate these forces in unwieldy methods, including pipette and AFM tips, however, these lack bulk handling capabilities and tend to significantly perturb cellular systems.<sup>1</sup>

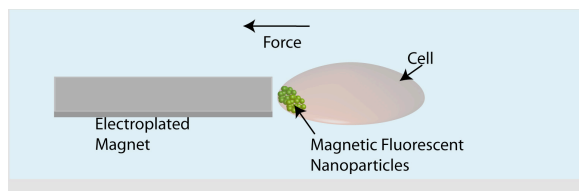


Figure 1: Schematic of the various elements in our system: microfabricated magnets localize and generate forces on magnetic nanoparticles that are internalized within cells.

Magnetic forces have been used to apply simple downward torques and forces on magnetic beads resting above cells,<sup>2</sup> however this method is limited as the location of the force is entirely random, and these techniques cannot follow moving cells, as well as apply planar forces and shear stresses, which are far more useful in terms effecting cellular response. In an ideal system, large planar forces and shears could be generated and be applied over long periods of time to track cellular response over complicated processes, like through cell division and cell motion. In this work, we combine microfabrication techniques<sup>3,4,5</sup> and cell-patterning techniques to align force-generating elements in precision proximity to shaped cells.<sup>6</sup> The cells are loaded with magnetic-fluorescent nanoparticles, which are then localized within the cell using large fields.<sup>7,8,9</sup> The small size allows efficient loading and

translation of particles within the cells (larger particles are immobilized in the cytoskeletal network), and the limitations on force becomes the particle saturation magnetization and loading densities.

## FABRICATION

### Connecting Magnetism and Cells

Our substrates can be separated into three primary components: the magnet layer that focuses external permanent magnetic fields, a planarization layer to generate a flat substrate, and finally surface modification to allow cells to adhere, pattern, and polarize on the substrate.

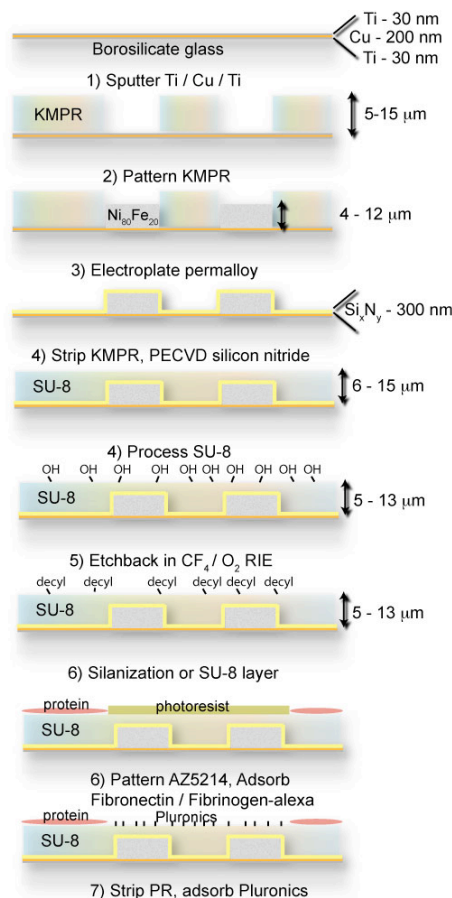


Figure 2: Process flow for our microfabricated, magneto-active slides. Traditional magnetic fabrication and modern cell-patterning techniques are modified to connect cells and magnets for our application.



Substrate fabrication begins on borosilicate glass (Figure 2). The wafers are cleaned in Piranha, and evaporated with a Ti/Cu/Ti (30-250-30 nm), and patterned with KMPR photoresist. Permalloy is electrodeposited using a custom-designed setup, and the KMPR is stripped. The thickness of the permalloy plated is dependent to a certain extent on our desired force. Thicker layers have a larger effective reach, and are able to manipulate more particles more efficiently, however are more difficult to planarize. The thickness typically varies from 4 micron to 12 micron in thickness. For the planarization step, SU-8 is spun on, and selectively etched back in CF<sub>4</sub> / O<sub>2</sub> RIE. The SU-8 surface is then prepared for surface modification.

Cell patterning is adapted from previous methods<sup>9</sup>, and requires a hydrophobic surface to adsorb protein and surfactant. The required surface hydrophobicity of the SU-8 is recovered in two approaches: 1) the additional spinning of a thin layer of SU-8 diluted in PGMEA, or 2) silanization of the oxidized surface in octadecyl trichlorosilane. AZ5214 resist is then spun onto the substrate, and various patterns are defined in proximity to the elements, including X, I, and square outline patterns. These shapes generate a variety of “square” cell shapes with polarized actin substructure. At this point, these substrates can be stored in this state indefinitely.

In preparation for cell tests, adhesive protein fibronectin is adsorbed, in addition to fibrinogen-alexa fluor conjugates in order to visualize the protein pattern. The photoresist is stripped, and the substrate is immersed in a Pluronic F127 solution to selectively deposit dense polyethylene glycol chains on the surface. Cells can then be patterned onto the substrate.

Magnetic fluorescent nanoparticles are prepared by direct chemical modification of dextran-covered magnetic nanoparticles (nanomag-D, micromod, Germany). The particles are initially cross-linked with the chemical epichlorohydrin, and then subsequently reacted with ammonium hydroxide to generate primary amines on the nanoparticle surface. These are then subsequently conjugated with a selection of fluorophores, depending on the required situation (Texas-Red, RBITC, FITC, alexa-fluor).

## SIMULATION

Magnetic response of the substrate is simulated in both ANSYS and COMSOL (Figure 3). The magnetic element is modeled with our nonlinear ferromagnet BH loop, and the resultant fields are solved around the element. Extracting the magnetic flux density, we can discern the gradients, and estimate forces on our particles according to the simple equation:

$$F = \Sigma (m * \nabla B), \quad (1)$$

where  $m$  is the saturation magnetization of an individual nanoparticle, and the summation is over all localized nanoparticles. This equation can be modified to:

$$F = V * B_{sat} * \nabla B / \mu_0, \quad (2)$$

where  $V$  is an estimate of the volume of the nanoparticle cluster.

Depending on the planarization layer thickness, simulations estimate that we are able to achieve magnetic flux density gradients from 1000 T/m to 1000000 T/m close to the element. We approximate these gradients to generate forces on cells up to and well exceeding those generated during cell motion (10 to 100 pN), dependent on the loading density of magnetic nanoparticles inside of cells.

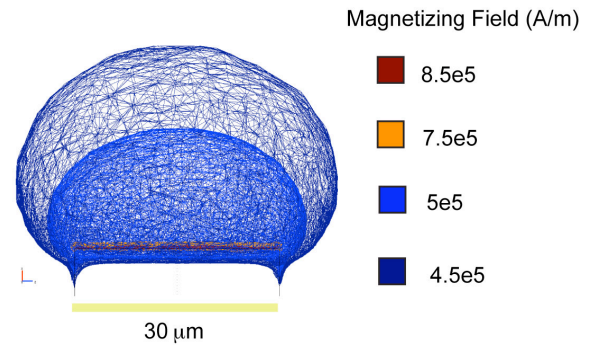


Figure 3: Curves of equal magnetizing fields as simulated in COMSOL. Magnetic particles are localized to areas of large field directly adjacent to the magnetic element.

## RESULTS AND DISCUSSION

### Experimental Setup

Details of our protocol are given elsewhere. In general, cells are seeded onto our substrate, and given 30 minutes to adhere, and then the substrate subsequently washed and inverted above the objective of an inverted fluorescent microscope. Once cells are properly patterned, a magnet is applied to the substrate, and time-lapse images are recorded to investigate the response of the cells to the magnetic force.

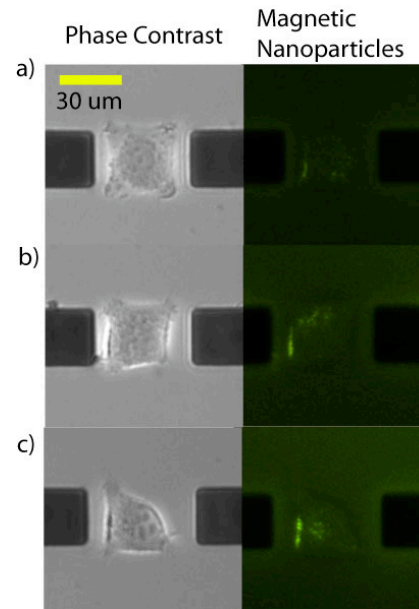
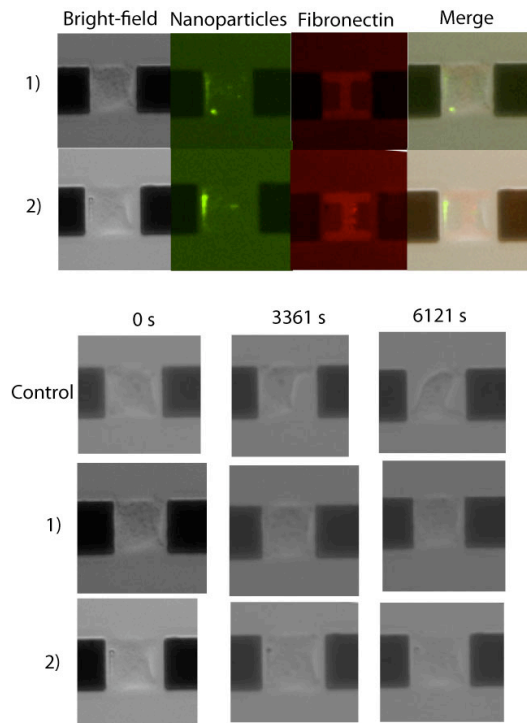


Figure 4: Cells patterned above X fibronectin patterns. Row a) displays the standard cell shape above these particular patterns, as the loaded nanoparticle quantity was low. These cells have characteristically 4 concave sides. Row b) sees a cell with modified shape due to a large density of magnetic nanoparticles, and generates noticeable polarization in cell shape on both the side of the nanoparticles and the other side of the nanoparticles. Row c) sees a cell with even higher nanoparticles, however because these particles are a larger distance from the elements, this yields a lower magnetic field gradient, and thus a lower force. Parameters such as cell distance from element, element size, and fibronectin pattern were all varied on our test chip.

## Results

Our results indicate the ability to properly shape and control cell localization in close proximity to our magnetic elements. Shown in Figure 4 are merged images of cells, protein patterns, and localized magnetic nanoparticles.

Early results also indicate that the application of forces modifies certain aspects of cell shape stability and polarize the cell shape (Figure 5). Shown in Figure 5 are images of polarized cell structures maintaining their shape over long times, as compared to cells with few to no nanoparticles that commonly destabilize. From these results, we anticipate that these structures can additionally be used to study and influence cell motion.



*Figure 5: Stability of polarized cell structures under magnetic force influence. Rows 1) and 2) display various channel and merged images of cells strongly polarized by magnetic force. The bottom rows display the differences in stability of these structures against a control structure with no magnetic nanoparticles. The control cells commonly bounced around the pattern, and displayed structural instability. This was not the case of particles under influence of magnetic force, that saw a continuous polarized structure until mitosis.*

## CONCLUSION

We have demonstrated precisely aligned, remotely controlled force application on cells within minimal additional perturbation to cellular systems, which should open up avenues in both short term and long term study and actuation of cellular response to chemo-mechanical signals. The method of force application should allow simple application and deapplication of force, and additionally can track the effect on cells as they are free to move around the top of the substrate.

## REFERENCES

- [1] A.J. Maniotis, C.S. Chen, and D.E. Ingber, "Demonstration of mechanical connections between integrins, cytoskeletal filaments, and nucleoplasm that stabilize nuclear structure," *Proc Nat Acad Sci USA*, 94, 849 (1997).
- [2] M. Srboljub, M. Mijailovich, M. Kojic, M. Zivkovic, B. Fabry, and J. J. Fredberg, "A finite element model of cell deformation during magnetic bead twisting," *J Appl Physiol* 93, 1429 (2002).
- [3] M. Zborowski, L. Sun, R. Lee, P. Williams, and J. Chalmers, "Continuous cell separation using novel magnetic quadrupole flow sorter," *Journal of Magnetism and Magnetic Materials*, 194, 224 (1999).
- [4] H. Lee, A.M. Purdon, R.M. Westervelt, "Manipulation of biological cells using a microelectromagnet matrix," *Appl. Phys. Lett.* 85, 1063 (2004).
- [5] C. Ahn, M. Allen, W. Trimmer, Y-N. Jun, and S. Erramilli, "A Fully Integrated Micromachined Magnetic Particle Separator," *J. MEMS*, 5, 151 (1996).
- [6] H. Guillou, A. Depraz-Depland, E. Planus, B. Vianay, J. Chaussy, A. Grinchine, C. Albiges-Rizo, M. R. Block, "Lamellipodia nucleation by filopodia depends on integrin occupancy and downstream Rac1 signalling," *Experimental Cell Research*, 314, 478 (2008).
- [7] J. Gao, W. Zhang, P. Huang, B. Zhang, X. Zhang, and B.J. Xu, "Intracellular control of fluorescent magnetic nanoparticles," *J. Amer. Chem. Soc.*, 130, 3710 (2009).
- [8] A. de Vries, B. Krenn, R. Driel, and J. Kanger, "Micro Magnetic tweezers for nanomanipulation inside live cells," *Biophysical Journal*, 88, 2137 (2005).
- [9] P. Tseng, D. Di Carlo, and J.W. Judy, "Rapid and dynamic intracellular patterning of cell-internalized magnetic fluorescent nanoparticles," *Nano Lett.*, 9 (2009), pp. 3053–3059.

# ON-CHIP PCR WITH FREE-STANDING PARYLENE CHANNEL

*P. Satsanarukkit, H. Lo, Q. Quach, and Y.C. Tai*  
California Institute of Technology, Pasadena, CA, USA

## ABSTRACT

We present an on-chip PCR using a free-standing parylene channel with an integrated platinum heater for on-chip temperature cycling. The PCR chip reduces the reagent amount from tens of  $\mu\text{L}$  (as required by convention qPCRs) to 550 nL. The on-chip PCR has a higher thermal efficiency than conventional PCR because of its smaller thermal capacity and good heat transfer. The demonstrated chip's free-standing channel structure reduces the thermal capacitance to  $3.25 \text{ mJ}/^\circ\text{C}$  and shortens the duration of PCR cycles with a thermal time constant of 3 seconds. The transparent parylene channel in visible light range enables direct optical detection. The impermeable parylene channel also prevents solution evaporation. It is shown that the pin-hole free, chemically and biologically inert parylene allows efficient PCR amplification and no additional surface treatment is required. The PCR chip can facilitate the further development of a fully-integrated, portable PCR system.

## INTRODUCTION

After the discovery of PCR technique by Karis Mullis in 1986 [1], the PCR technique has become a widely-used, powerful technology for various molecular biological applications such as disease diagnosis and detection, forensic, etc.

On-chip PCR technology is particularly useful in single-cell analysis. This technology is capable of fast and easy cell loading and precise cell alignment, two critical steps in single-cell analysis. The free-standing on-chip heater and sensor reduces the system's thermal mass and increases the heating and cooling rates [1, 2].

Researchers have been investigating many materials for on-chip PCR chambers [2]. Among inorganic materials, opaque silicon inhibits PCR amplification and bars optical detection. Though transparent, glass possibly impedes PCR reactions. Besides the less-than-satisfactory inorganic materials, researchers have looked to polymers and many have examined PDMS. However PDMS is not ideal, either. PDMS is porous and permeable, and it causes bubbles and loss of PCR samples during PCR reactions [2, 3]. We then investigate parylene-C as the material for PCR reaction chambers and channels. Parylene is biocompatible and chemically inert. When thicker than fifteen angstroms, parylene is pin-hole free [4]. Pin-hole free parylene may reduce PCR reagent evaporation and bubble formation [2, 3]. Furthermore, parylene technology allows easy integration of other components: sample loaders, cell capturing filters, waste disposal parts, and DNA detectors [5]. A parylene-based PCR system may have less thermal mass than a PDMS-based system. In this work, we examined a PCR reaction system based on parylene-C, and we intentionally avoided any surface treatment on parylene.

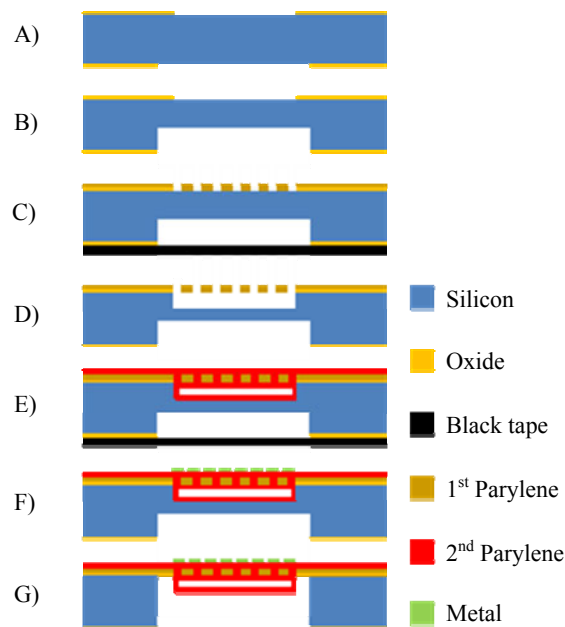
For on-chip PCR amplification detection, we used a fluorescence-based detection technique. This technique includes a TaqMan® probe, which consists of a fluorophore, a quencher and a 20-40 bp DNA single strand. In practice, the probe first binds to the amplified target DNA fragment. When DNA polymerization occurs and the polymerase cleaves the 5' end of the probe, the probe releases the fluorophore. Then, the released, unquenched fluorophore emits fluorescence. Because

of the probe's specific binding capability, the measured fluorescence intensity is proportional to the number of the amplified target DNA fragments.

## FABRICATION

The chip fabrication (Figure 1) started with DRIE etching of silicon on the back of an oxide wafer. Next, we deposited and patterned the first layer of parylene. Next, we etched the front side silicon with DRIE and  $\text{XeF}_2$  and deposited the second layer of parylene to form the channel. For the resistive heating element, a  $2000 \text{ \AA}$  platinum layer was deposited on the second layer of parylene and patterned using a lift off process. Then the free-standing channel was made by etching the backside of silicon wafer with DRIE and  $\text{XeF}_2$ .

Figure 2 and 3 show the finished PCR chip and the final testing assembly. The parylene channel had an approximate total volume of 550 nL. The platinum heater had a resistance of 2.9 kOhms at room temperature. A CNC-machined acrylic jig coupled the PCR chip to the loading microfluidic components.



*Figure 1: Chip fabrication process: A) Oxide growing and patterning; B) Backside DRIE; C) 1<sup>st</sup> layer of parylene deposition and patterning; D) Frontside DRIE and  $\text{XeF}_2$  etching; E) 2<sup>nd</sup> layer of parylene deposition; F) Platinum deposition and lift-off patterning; and G) Backside DRIE and  $\text{XeF}_2$  etching*

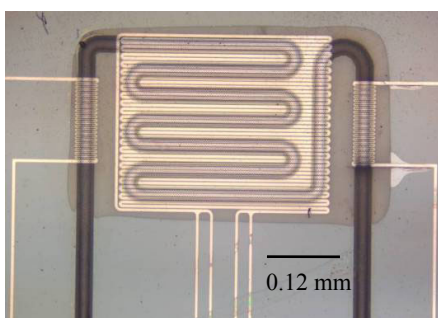


Figure 2: On-chip PCR device

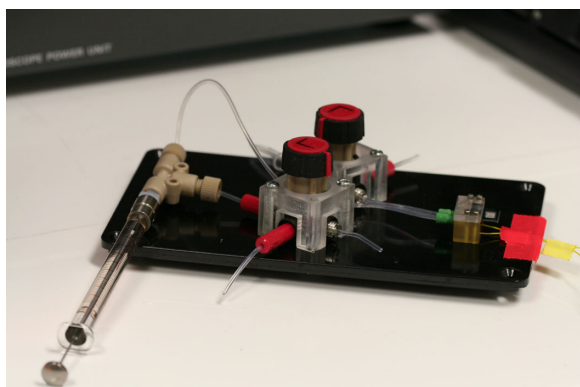


Figure 3: Loading technique using a gas-tight microsyringe manually

## CHIP CHARACTERIZATION

### Thermal Time Constant Measurement

To measure the heating time constant, a pulse of input power was applied, and we measured the time when the chip temperature reached 63.2% of its steady state temperature. Figure 4 shows the input power and the chip temperature profile. The chip's heating time constant is 3 seconds.

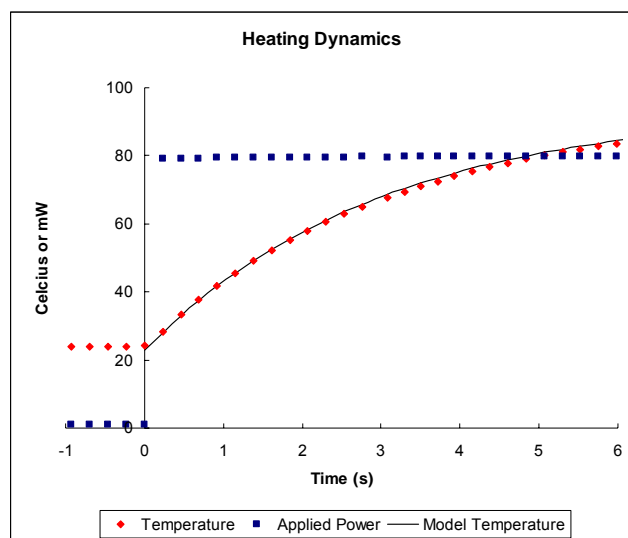


Figure 4: Chip heating time constant

To measure the cooling time constant, we first heated the chip to a certain temperature. Once the chip reached the steady state, we turned off the applied power. We measured the time when the temperature reached at 36.8% of the steady state temperature. The chip's cooling time constant is also around 3 seconds.

### Temperature Coefficient of Resistance

Equation 1 shows the relation between resistance ( $R$ ) and temperature ( $T$ ):

$$\frac{R(T) - R(T_0)}{R(T_0)} = \alpha(T - T_0) \quad (1)$$

where  $T_0$  is the reference temperature, and  $\alpha$  is the temperature coefficient of resistance.

To obtain the TCR, we measured the sensor's resistances at different temperatures, all of which are within the PCR's operational range. The resistance and temperature are plotted in Figure 5. The sensor's TCR is  $2.0 \times 10^{-3}/^\circ\text{C}$ .

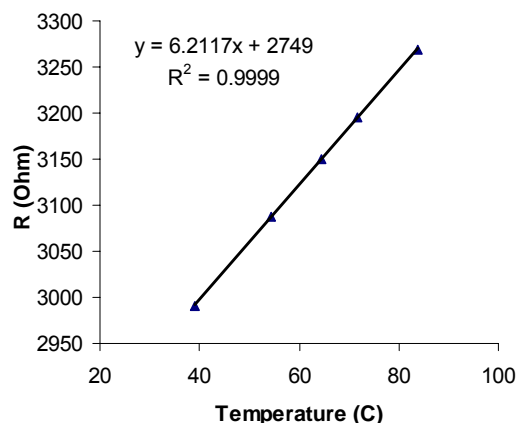


Figure 5: Temperature coefficient of resistance of the on-chip platinum sensor

## MATERIALS

Parylene-C is the most commonly used among the polyethylene polymers in microfluidics due to its high mechanical strength, and fast deposition rate. Parylene-C has an USP class VI biocompatible rating. It uses chemical vapor deposition technique which operates at room temperature. The deposition first starts from dimer powder (Specialty Coating Systems) vaporizing. Then the sublimed parylene vapor is pyrolyzed in the pyrolysis tube at  $680^\circ\text{C}$ . The obtained monomers next enter the deposition chamber and are polymerized on the surface of the substrate.

The PCR solution consists of 1X Quanta PerfeCTa™ MultiPlex qPCR SuperMix (Quanta Biosciences); 200 nM of forward primer 5'-TGGAGAGGCTATTCGGCTATGACTG-3'; 200 nM of reverse primer 5'-ATACTTCTCGGCAGGAGCAAGGTG-3'; 200 nM of probe 5'-FAM-TAGCAGCCAGTCCC TTCCCGCTTCAGTGA-BHQ-3'(IDT), kindly designed by Arbel D. Tadmor; 1X ROX; and 6 and 90 pg of high copy plasmid bearing the ColE1 origin of replication and the kanamycin resistance gene pZS25O1+11-YFP, kindly provided by Hernan G. Garcia. The amplicon fragment is 294 bp.

## EXPERIMENTAL

First, we studied the effect of parylene on PCR efficiency. We conducted the PCR experiment with a standard thermal cycler and evaluated the results by gel electrophoresis. We compared the samples using the standard polypropylene tubes and the standard polypropylene coated with 15  $\mu\text{m}$  of parylene-C. In addition, we investigated the possible minimum volume of PCR reagent because we wanted to compare the effects of parylene channels and parylene-coated tube with similar SA/V ratios.

Secondly, the PCR reaction was verified with the standard qPCR machine (Stratagene Mx3000). The initial template copies varied from 10 to  $10^7$  copies with tenfold increment. The total volume is limited to 20  $\mu\text{L}$  each tube because of the machine's specifications.

Then, we conducted the on-chip PCR reaction. We first cleaned the parylene channel with DNA decontamination solution (Ambion) and rinsed with DEPC-treated and sterile filtered water (Sigma Aldrich). We manually injected the fluids with a micro syringe (Hamilton), as shown in Figure 3. All of the loading procedures do not need any bulky external pumping system, leading to feasibility to be the portable device. Then the device was filled with the PCR solution described above. Approximately 550 nl of PCR mixture was injected.

For thermal cycling, the on-chip platinum resistor was used as both the heater and temperature sensor. The voltage was supplied from Universal Source (HP 3245A) to the chip and the current was measured with a precision multimeter (Agilent 34401A). The close-loop temperature control for PCR thermal cycling was done with a LabView PID feedback control program. The PCR thermal cycling started with 95°C for 3 minutes, followed by 50 cycles of 95°C for 15 seconds (denaturation) and 60°C for 90 seconds (annealing/extension) respectively. Figure 6 and Figure 7 show the first 3 cycles of input power and temperature profiles.

To measure fluorescence, fluorescent images were taken after each thermal cycle using a Nikon Eclipse E800 fluorescence microscope. The E800 microscope has a Nikon super high pressure mercury lamp power supply (Nikon Inc.), and an integrated CCD camera. Figure 8 shows the testing assembly and the fluorescent microscope. The fluorescence picture was then analyzed with image processing software, Image J (National Institutes of Health). To reduce the noise from fluctuation of light source and autofluorescence of the chip during the measurement, the obtained fluorescence intensity was normalized against the parylene background on the base of the chip.

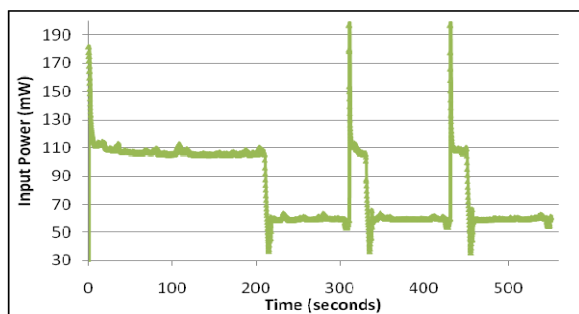


Figure 6: Input power of the initiation and the first 3 thermal cycles

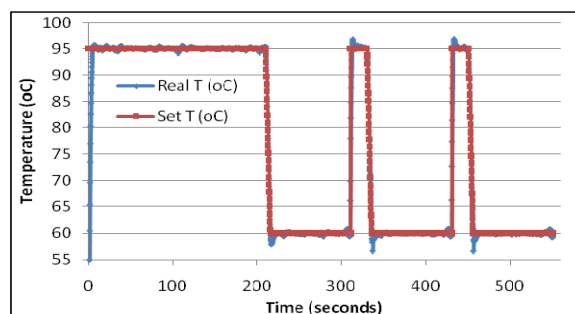


Figure 7: Temperature profiles of the initiation and the first 3 thermal cycles

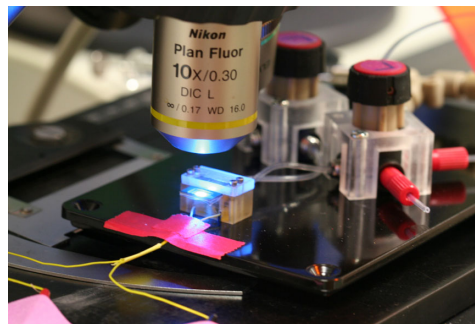


Figure 8: Fluorescence image taking at the end of each thermal cycle

## RESULTS AND DISCUSSIONS

Figure 9 shows the gel electrophoresis images of the PCR experiments using a standard thermal cycler. In Figure 9, the amplicon fragments of 294 bp were shown with the 100 bp DNA ladder on the left. The minimum volume for distinguishable bands was 2  $\mu\text{L}$ . No primer-dimer was observed. Also, the parylene coated tubes gave good amplification results. The no-template-control (NTC) tube shows no amplification band.

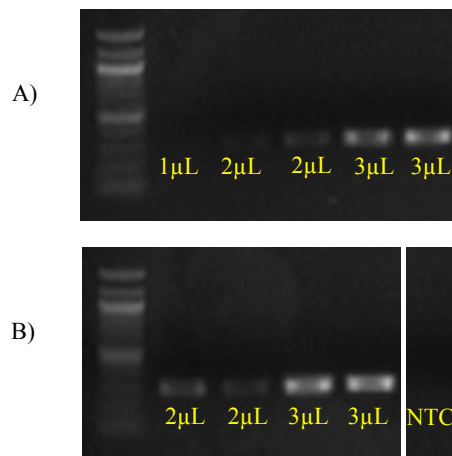


Figure 9: Gel electrophoresis images: A) Standard polypropylene tubes of volume 1, 2, 2, 3, and 3  $\mu\text{L}$ ; and B) Standard polypropylene coated with 15  $\mu\text{m}$  of parylene-C of volume 2, 2, 3, 3  $\mu\text{L}$  and No Template Control (NTC) using a standard thermal cycler

Figure 10 shows the normalized amplification plots from the standard qPCR machine (Stratagene Mx3000). The resulting plot has the same curves as standard plots. The results also show that the probe and other PCR reagent were working well.

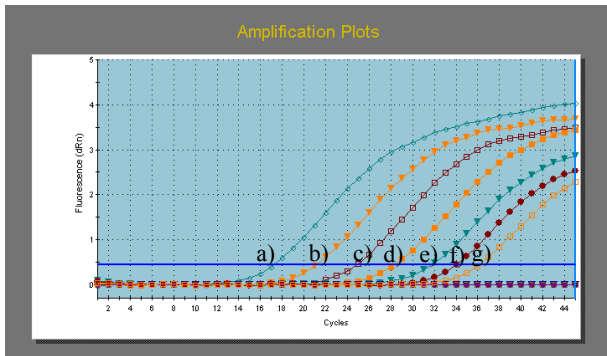


Figure 10: Normalized amplification plots of initial copies of templates of a-f: a)  $10^7$ ; b)  $10^6$ ; c)  $10^5$ ; d)  $10^4$ ; e)  $10^3$ ; f)  $10^2$ ; and g) 10 using a standard qPCR machine

For the on-chip PCR results, Figure 11 shows the channel fluorescence pictures of 90 pg initial template after the thermal cycles 0<sup>th</sup>, 10<sup>th</sup>, 20<sup>th</sup>, 30<sup>th</sup>, 40<sup>th</sup> and 50<sup>th</sup> respectively. The intensity successfully increases over the cycles. Figure 12 shows the comparison of amplification plots of fluorescence (dRn) of 6 and 90 pg initial templates, and the no primer control (NPC). These results show that the templates were significantly amplified within the first few PCR cycles. In addition, the curves clearly show the differences of different initial template amounts respectively. This device can differentiate different starting template quantities.

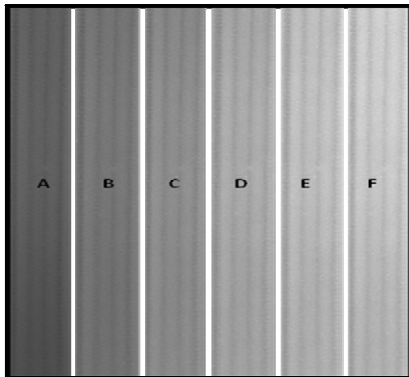


Figure 11: On-chip fluorescence images of the 90 pg initial template after cycle: A) 0<sup>th</sup> B) 10<sup>th</sup> C) 20<sup>th</sup> D) 30<sup>th</sup> E) 40<sup>th</sup> F) 50<sup>th</sup>

We are improving device designs. The presented chip cannot achieve uniform temperature distribution across the chip. Sporadically, bubbles appear in the channel and impede PCR efficiency. Future chips will incorporate heaters with optimized geometry that improves on-chip heat distribution. Changing PCR preparation protocols may reduce bubble generation. More work is underway.

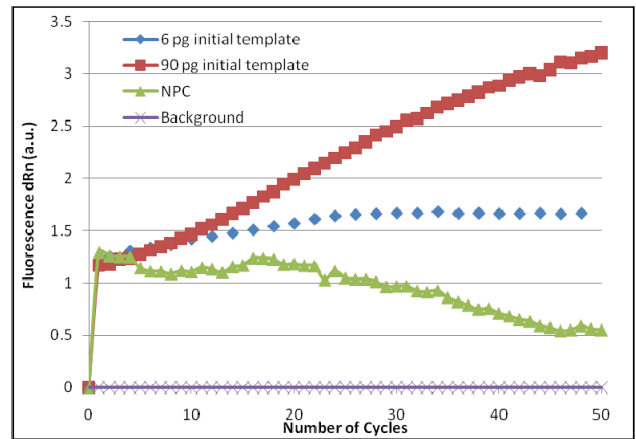


Figure 12: On-chip fluorescence intensities: 1) 6 pg initial template 2) 90 pg initial template 3) No Primer Control

## CONCLUSIONS

In conclusion, a free-standing parylene-C PCR channel with an on-chip Pt heater/sensor for fast thermal cycling was demonstrated. Fast cycling and efficient PCR amplification were observed. The device can distinguish different initial amount of templates. This work validates that parylene-C is an adequate material for on-chip PCR and further downsizing of the device to reduce its volume and integrating necessary microfluidic components are also possible. However, the heating uniformity and bubble suppression should still be improved.

## ACKNOWLEDGEMENTS

This work was supported by The Royal Thai Government scholarship and The Boeing Company. The authors would like to thank Dr. Franz M. Weinert, Peera Jaru-Ampornpan, Kuang Shen, Arbel D. Tadmor, and Hernan G. Garcia for all the PCR trainings, sample preparations and valuable technical support. The authors appreciate all generous help and precious advice from the members of Caltech Micromachining Laboratory.

## REFERENCES

- [1] A. J. Mello, "DNA Amplification: Does 'Small' Really Mean 'Efficient'?", *Lab On a Chip*, 1 (2001), pp. 24N-29N.
- [2] C. Zhang and D. Xing, "Miniaturized PCR Chips for Nucleic Acid Amplification and Analysis: Latest Advances and Future Trends", *Nucleic Acids Research*, 35, 13 (2007), pp. 4223-4237.
- [3] Y. S. Shin, K. Cho, S. H. Lim, S. Chung, S. J. Park, C. Chung, D. C. Han and J. K. Chang, "PDMS-based Micro PCR Chip with Parylene Coating", *J. Micromech. Microeng.* 13 (2003), pp. 768-774.
- [4] J. J. Senkevich and P. I. Wang, "Molecular Layer Chemistry via Parylenes", *Chemical Vapor Deposition*, 15 (2009), pp. 91-94.
- [5] S. Sukas, A. E. Erson, C. Sert, and H. Kulah, "A Parylene-based Dual Channel Micro-Electrophoresis System for Rapid Mutation Detection via Heteroduplex Analysis", *Electrophoresis*, 29 (2008), pp. 3752-3758.

## CONTACT

\*P. Satsanurukit, tel: +1-626-395-3885;  
penvipha@mems.caltech.edu

# STRETCHABLE TACTILE SENSING SKIN FOR INTELLIGENT PROSTHETIC LIMBS

Shenshen Zhao, Huan Hu and Chang Liu  
NU MedX Lab, Northwestern University  
2145 Sheridan Road, Evanston, Illinois, 60208, USA

## ABSTRACT

In this work, we report for a first time a stretchable tactile sensing skin that senses distributed contact force and is capable of conforming to curved surfaces, such as those of prosthetic limbs. The sensor comprises of three elements – substrates, force transduction elements and electric leads. All these elements are stretchable. The 2D force sensing array consists of 14 nodes spreading over an area of  $4\text{cm} \times 7\text{cm}$ . We demonstrate here that the sensor skin can endure up to 8% of tensile strain repeatedly while the metal conductors are fully functioning, and with a detection limit of 1.57 mN normal force. The initial feasibility study shows promise for integrating such skin with a prosthetic limb part.

## INTRODUCTION

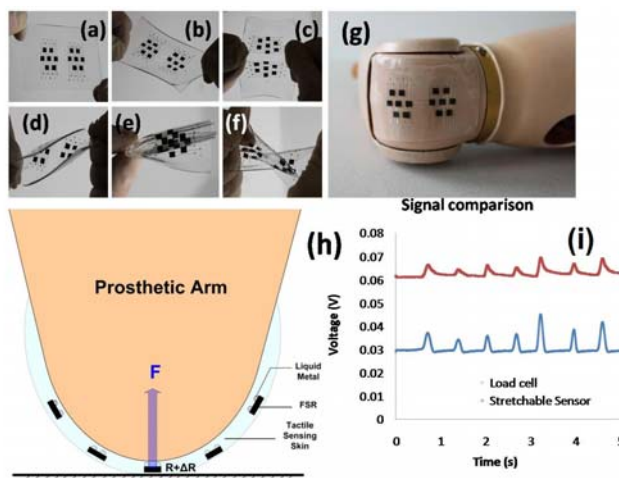
Tactile sensor is defined as a device or system that can measure a given property of an object or contact event through physical contact between the sensor and the object [7]. The measured properties can include shapes, texture, temperatures, hardness, as well as normal contact force. Tactile sensing plays a key role in the fields where physical manipulation and tactile exploration are involved, such as surgeries [8] [9] [10], robotics [11], and entertainment, etc.

Tactile sensors integrated with prosthetic limbs that measure normal contact promise to restore the touch sensation to the disabled, allowing enhanced dexterity and manipulation capabilities. One premise for such application is that the sensors should be able to conform to the 3D-flexed surfaces while functioning. This criterion not only requires stretchable materials or structures for the carrier skin, but all transducers and electrical conductors to be made stretchable. Existing MEMS tactile sensors, mostly silicon based, do not meet such need.

One conceptual architecture was proposed by Wagner, et. al. [13], that an electronic tactile skin ideally should incorporate subunits of tactile sensors and actuators arranged in array configuration and deformable conductive leads running in lines and columns inside a stretchable continuous substrate. Here we adopted a similar configuration where each unit contains one sensing node and two stretchable electric leads. Adjacent leads are shared in order to minimize wiring complexity.

The stretchable sensing skin in this work consists of three stretchable components – the polydimethylsiloxane (PDMS) thin film substrate, the nanocomposite force sensing resistors (FSR) made of carbon nanofiber suspension in PDMS, and the electric conductors made of micro fluid channels filled with liquid metal alloy. Figures 1(a) – (f) are photos of the sensing skin undergoing various deformation modes. Figure 1(g) is a photo of the sensing skin conforming to the curved surface of a limb part. Figure 1(h) illustrates the conceptual design, construction and function of the sensing skin. Figure 1(i) shows representative experimentally recorded time traces when such skin and a commercial load cell are subject to the same normal contact force – impulses in this case. The lower trace is the output from the load cell and

the upper trace is that from the sensing skin, demonstrating the skin's ability of capturing contact events in real time.



**Figure 1:** Conceptual design and function of the sensing skin. (a)-(f) Sensing skin under various deformation modes. (g) Sensing skin conformal to the curved end of a prosthetic limb part. (h) Conceptual illustration of design and function of sensing skin. (i) Signal comparison between sensing skin (upper) and a commercial load cell (lower) when subject to the same contact event

In this paper, the important characteristics and of single stretchable elements – FSRs and conductors are investigated separately, followed by discussion of the fabrication process flow, and concluded by the characterization results of the device as a whole.

## MATERIAL OPTIONS AND DESIGN

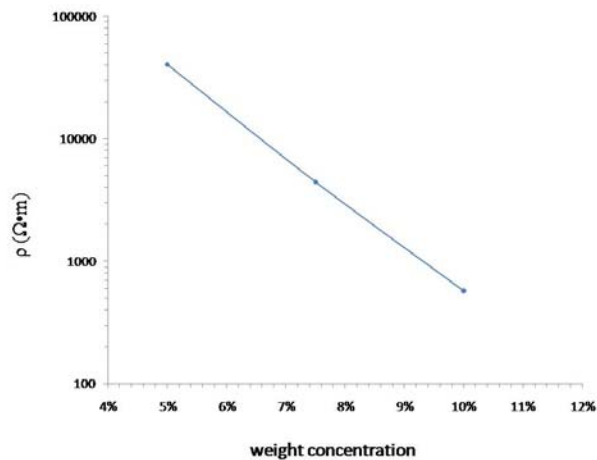
### Nanocomposite FSRs as embedded force sensors

It has been reported that force sensing resistors (FSR) can be made by doping polymers with conductive or semi-conductive particles or fibers, like carbon nanotubes or carbon nanofibers. The resistivity of the composite is extremely sensitive to the change of volume fraction of the nanofiller at the so-called percolation region. An external strain can change the volume fraction due to the difference in the stiffness between the filler and matrix materials thus can change the apparent resistivity of the mixture. This is the basic underlying mechanism for FSR's resistive strain sensitivity.

Strain-sensitive nanocomposite made of carbon nanofibers dispersed in polydimethylsiloxane (PDMS) matrix is used as force sensing resistors (FSR) in this work. It is chosen as embedded force sensors for its compatibility with the PDMS substrate. The FSR's resistive sensitivity to normal contact force has been characterized and utilized in our previous work [1].

In this work, we demonstrate that FSR's baseline

resistivity follows a linear relationship with the weight concentration of the nanofillers of the mixture on the semi-log plane, as shown in Figure 2. With this chart, the mixing ratio can be tuned in order to achieve desired resistance of the FSRs. In this work, 10% weight ratio is chosen for an ultimate resistivity of 1000  $\Omega\cdot\text{m}$ .



**Figure 2:** FSR base-line resistivity as a function of wt.% concentration of carbon nanofibers on a semi-log plane

#### Micro liquid metal channel as conductors

Various approaches to make stretchable conductors on polymeric substrates have been investigated by researchers [2] [3] [4]. However, due to debonding failure and large resistivity, none have yet achieved ideal and robust conductors that endure repeating tensile loading on stretchable substrate.

Our group has pioneered the use of liquid metal alloy as conductors. In this work, it is experimentally proved that micro fluid channels filled with liquid metal alloy are ideal conductors for the stretchable sensors.

Test samples with liquid metal filled channels are prepared and four different widths are explored (See Figure 4). The liquid metal alloy used here is formed by using 3 metals – gallium, indium and tin. The melting point can range from room temperature to as low as  $-20^\circ\text{C}$ , depending on the mixing ratio of the compound. Some additional advantages of such liquid metal alloys include good conductivity, wettability (due to gallium oxide formation), and non-toxicity [6].

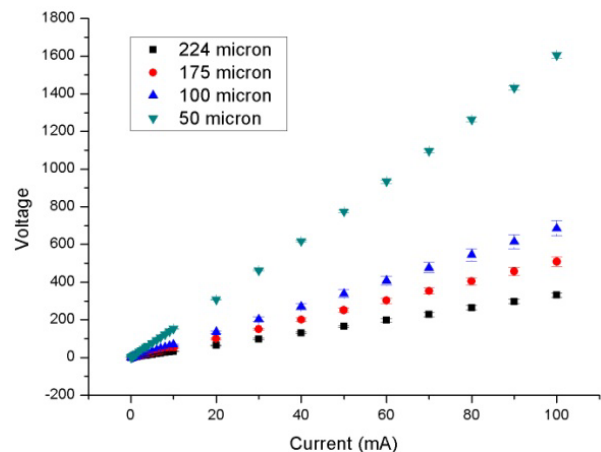
Figure 3 shows the I-V characteristics of the liquid metal conductors of various widths. The straight lines on the I-V plane are strong indicators that the liquid metal channels are ideal Ohmic conductors. Figure 4 shows the measured resistance increases with applied tensile strain in a linear fashion. The conductors function repetitively when undergoing up to 8% tensile strain with a maximum resistance of 6.2  $\Omega$ .

We have also demonstrated in our previous work [5] that by introducing liquid metal as conductive enhancement, the contact resistance between nanocomposite FSRs and metal electrodes is dramatically reduced. This is another reason why liquid metal conductors are preferred.

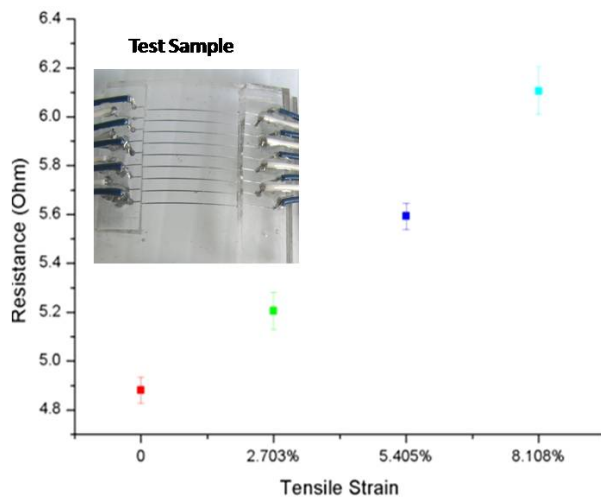
#### FABRICATION

The fabrication involves two parallel processes followed by an assembly step, as is illustrated in Figure 5 and Figure 6. The FSR layer (Figure 5) and the micro channel layer (Figure

6) are prepared separately, and then bonded together (Figure 6).



**Figure 3:** I-V characteristics of liquid metal conductors of difference widths – 50, 100, 175 and 224 microns.



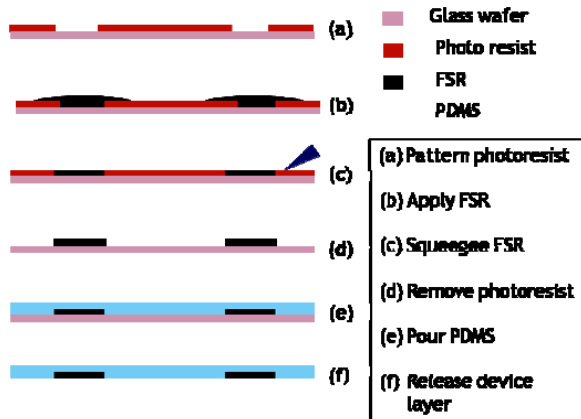
**Figure 4:** A plot of the resistance values of liquid metal leads as a function of applied longitudinal strain, with photo of the test sample.

The patterning of FSR starts with photolithography on a glass wafer. After exposure of the photoresist, nanocomposites are applied. A soft blade is used to squeegee the excess of nanocomposites, leaving only those inside the recess regions created by the photoresist. After baking at  $90^\circ\text{C}$  in the convection oven for hardening, the photoresist is dissolved in acetone. A thin layer of PDMS is either poured over or spin-coated on top of the FSRs, and the resulted thickness of PDMS coating can be controlled by the volume or the rate of spinning. After baking, PDMS and FSRs will bond firmly due to covalent bonding, thus can be peeled off from the glass substrate easily.

The patterning of micro channels starts with photolithography on a glass wafer, where the height of the channels is defined by the thickness of the photoresist. An

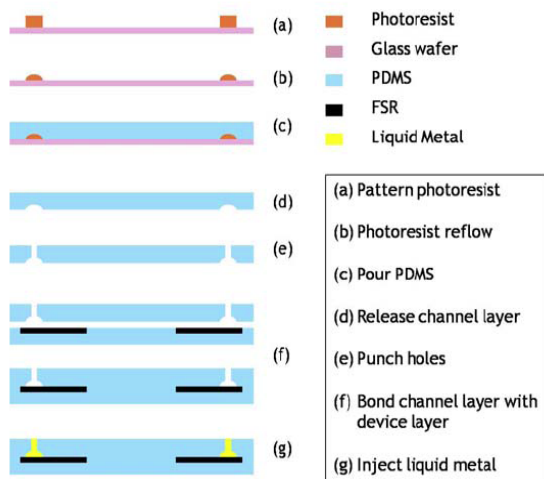


annealing step involving maintaining the samples at an elevated temperature is introduced. After annealing, the sharp corners of the channels are rounded and flow resistance during the injection process of the liquid metal can be reduced. PDMS is either poured over or spin-coated on top of the channels to form a thin film, the thickness of which can be controlled by volume or the rate of spinning. Injection holes are punched after the PDMS film is released from the glass substrate.



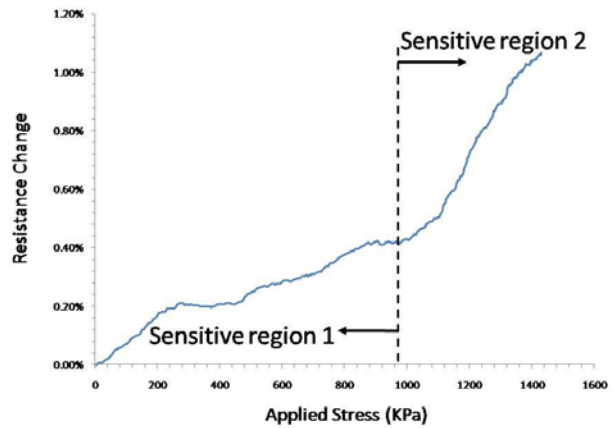
**Figure 5:** The process flow for patterned FSR layer. (a) Pattern photoresist to define the geometries of FSRs. (b) Apply carbon nanofiber / PDMS composites to the recessed regions (c) Squeegee with a soft blade to remove excess composites and shape FSR. (d) Bake FSR and remove photoresist (e) Pour or spin-on PDMS to a desired thickness. (f) Bake and release.

The FSR layer and the channel layer are bonded at 90°C in the convection oven after oxygen plasma treatment. Afterwards, liquid metal alloy is injected at a pressure of 20 psi using a home-built injection pump. The injection holes can be sealed with epoxy after external wiring is completed.



**Figure 6:** The process flow for micro channel layer and assembly. (a) Pattern photoresist to define the geometry of the

micro channels. (b) Anneal at 115 °C for photoresist reflow. (c) Pour or spin-on PDMS to a desired thickness. (d) Peel PDMS from the glass substrate. (e) Punch holes for liquid metal injection. (f) Bond FSR layer and channel layer after oxygen plasma treatment. (g) Inject liquid metal and seal with epoxy.



**Figure 7:** Resistance changes of the device as a function of the magnitude of the normal loading stress

## DEVICE CHARACTERIZATION

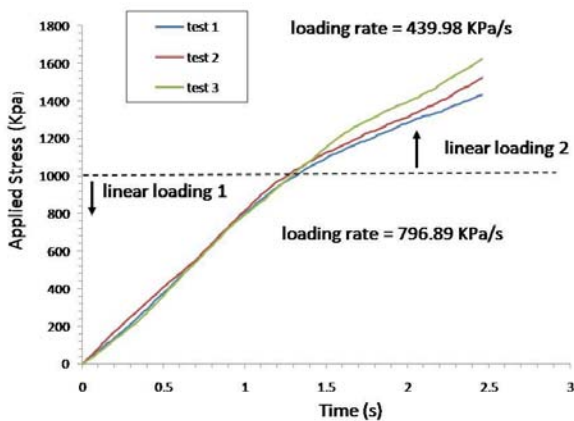
The sensor’s performance is characterized on a home-built automated system. A 1KG commercial load cell is used to monitor the applied force while a motorized stage is driving it at the velocity of 1mm/s towards the sensing skin. Two sets of data from both the reading of load cell and the output of the sensing skin are collected at a sampling rate of 200 Hz simultaneously.

Figure 7 shows measurement of the sensor skin’s response to normal stress at a single detection node. The measured resistance, i.e. the output of the sensing skin, increases monotonously with the normal contact pressure which can be inferred from the reading of the load cell, with a detection limit of 1.7mN.

Interestingly, the curve exhibits two distinct linear regions – The sensitivity above 1000KPa point is about 6 times bigger than below that. This deviation is presumably due to the viscoelastic behavior of the polymers – the strain is not only a function of the stress  $\sigma$ , but also a function of the time derivative of the stress  $d\sigma/dt$ .

Figure 8 shows the history of loading recorded in three separate tests. On the plot, all the curves exhibit two different slopes under and above the dashed line, indicating different time derivatives  $d\sigma/dt$  – 796.89KPa/s and 439.98KPa/s for before and after the 1000KPa point, respectively. The difference in the rate of applied stress can be used to explain the distinct sensitivities in Figure 7 for lower and higher ranges.

While viscoelasticity is universal to polymeric materials, it is one property of the human skin too – the touch sensation is a function of both the magnitude and the rate of the stress. However, a verifiable model is yet to be developed for this complex mechanical – electrical coupling system to achieve a close form analytical solution for describing the complete stress response of the sensing skin.



**Figure 8:** The history of loading indicating two distinct zones where the rates of stress are different

## CONCLUSIONS

We have demonstrated the concept, design, fabrication process and characterization results of a tactile sensing skin which is constructed by all-stretchable constituents. The sensing skin capable of capturing the contact events has distributed detection nodes, and is able to conform to the curved surface of a prosthetic limb part.

Major unique contributions of this work are summarized below:

- (1) Construction of a flexible touch sensing skin consisting of multiple stretchable constituents;
- (2) Initial feasibility studies for integrating such sensing skin on prosthetic limb parts;
- (3) Systematic characterization results of stretchable elements under loading conditions.

Future improvement includes complete integration with prosthetic limbs and comprehensive device characterization, contact imaging, analytical modeling and verification of the viscoelastic behavior of the sensing skin, etc.

## ACKNOWLEDGEMENTS

This work is supported by the National Science Foundation Emerging Frontier in Research and Innovation (EFRI) program (EFRI COPN and EFRI-BSBA).

The author would like to thank Northwestern University NUFAB clean room for providing processing facilities, and Laura Miller at the Rehabilitation Institute of Chicago for providing prosthetic parts for experiments.

The student authors wish to thank the Transducers Research Foundation for travel support.

## REFERENCES

- [1] Jonathan M. Engel, Jack Chen, Chang Liu, and David Bullen, 'Polyurethane Rubber All-Polymer Artificial Hair Cell Sensor', Journal of MEMS, 2006
- [2] Z. Suo, Sigurd Wagner, et al., 'Stretchable gold conductors on elastomeric substrate', Applied Physics Letters, 2003
- [3] John A. Rogers, Yonggang Huang, et al., 'Biaxially stretchable "wavy" silicon nanomembranes', Nano Letters, 2007
- [4] Tsuyoshi Sekitani, Takao Someya, et al. 'A Rubberlike Stretchable Active Matrix Using Elastic Conductors', Science, 2009
- [5] Hu, et al., 'Characterization and Optimization of Electric Contact Between nanocomposite Elastomer and Metal', Transducers'09, 2009
- [6] [http://scitoys.com/scitoys/scitoys/thermo/liquid\\_metal/liquid\\_metal.html](http://scitoys.com/scitoys/scitoys/thermo/liquid_metal/liquid_metal.html)
- [7] M.H.Lee and H.R.Nicholls, 'Tactile sensing for mechatronics – a state of the art survey', Mechatronics, 1998
- [8] Voges, 'Technology in Laparoscopy – what to expect in the future', 1996
- [9] Howe, Peine, et al. 'Remote palpation technology', IEEE Engineering in Medicine and Biology, 1995
- [10] Fischer, Heilig, et al. 'Tactile optical sensor for use in minimally invasive surgery', Langenbecks Archiv Fur Chirurgie, 1996
- [11] Stone, Brett, 'A sensing technique for the measurement of tactile forces in the gripping of dough-like materials', Proc. of the Institute of Mechanical Engineers, 1996

## CORRESPONDENCE INFORMATION

Shenshen Zhao  
 Phone: 1-847-467-0702  
 Email: shenshen@u.northwestern.edu

# THE CAPTURE AND 3-D CULTURE OF VIABLE CIRCULATING TUMOR CELLS USING HIGH OPEN-FACTOR PARYLENE-C/HT MEMBRANE FILTERS

B. Lu<sup>1\*</sup>, T. Xu<sup>2</sup>, A. Goldkorn<sup>2</sup>, and Y. C. Tai<sup>1</sup>

<sup>1</sup>California Institute of Technology, Pasadena, California, USA

<sup>2</sup>University of Southern California, Los Angeles, California, USA

## ABSTRACT

This paper presents an improved method of capturing viable circulating tumor cells (CTC) from human blood using low-constant-pressure filtration through a high open-factor parylene-C membrane filter with parylene-HT surface coating. More than 90% viable CTCs can be captured on the filter, with minimal blood cells left. For the first time, we demonstrated the feasibility of on-filter 3D culture (with significant cell proliferation) from captured cancer cells. This work is one-step closer to the final goal of capturing and culturing CTCs directly from cancer patient blood to enable cancer analysis and management.

## INTRODUCTION

Cancer metastasis is still the main cause of death for patients having solid-tumor cancers. Circulating tumor cells (CTC) are tumor cells disseminated from the primary tumor into blood stream. The presence of CTC in peripheral blood has important clinical significance for patients with various types of cancers. Study of CTC will also provide valuable insight into the mechanism of tumor metastasis.

Most current CTC assays are used either for the enumeration of CTCs by immunostaining [1-5], or for specific molecular analysis by quantitative PCR (qPCR) [2,3]. For both applications, the main challenge is the extremely low concentration of CTC (e.g.  $\sim 1/\text{mL}$ ) in the patient blood. Therefore, an enrichment step of rare CTCs from a large volume (e.g. in the milliliter range) of patient blood sample is crucial for successful CTC study. So far, the reported CTC enrichment techniques include the density gradient centrifugation [3], immunomagnetic separation [3], microfluidic devices combined with immunoaffinity based selection [4,5] and size based filtration [1-3]. Immunoaffinity based methods capture CTCs by using cancer specific markers [3-5]. Non-cancer blood cells can be efficiently removed, resulting in high CTC enrichment. However, the CTC capture efficiency greatly depends on the biomarkers selected, and the throughput is usually low because of the incubation time required. Size based filtration has been explored for solid-tumor cancers because the herein epithelial CTCs (15-30 $\mu\text{m}$  in diameter) are generally larger and less deformable than normal blood cells [1-3]. Among various filter designs, membrane filters have the advantage of short operation time (i.e. high throughput). Previously, we reported parylene-C based dual-layer [1] and single-layer [2] membrane filters, which could capture viable CTCs with high capture efficiency and viability. However, the CTC enrichment was not good enough because too many blood cells were also captured after filtration.

Further analyses of CTCs after capture can enable the characterization of the original tumor and greatly benefit future genetic and chemotherapy studies. However, these studies are usually restricted by the rarity of available CTCs after capture. Therefore, a CTC culture step after capture is highly desirable. Current CTC culture methods focus on conventional 2D culture, where cells are cultured as a monolayer on a substrate [2,5]. Recently, researchers are recognizing the limitations of 2D culture, given that it cannot fully reproduce the *in vivo* cellular microenvironment with cell-cell and cell-matrix interactions [6,7]. To better recapitulate the morphology and features the *in vivo* cells

have, 3D culture models, which provide more *in vivo*-like conditions and realize the original growth characteristics of the tumors, are attracting increasingly more attentions [6,7].

In this work, we present the use of a netlike high open-factor (i.e., area of openings/total area) parylene-C slot filter (coated with parylene-HT) with a low-constant-pressure filtration system to capture viable CTCs from blood. More than 90% viable cancer cells were consistently recovered from whole blood, with minimal blood cells remaining on filter. The CTC enrichment was 1 and 2 order(s) of magnitude higher than our previously reported single-layer [2] and dual-layer filters [1], respectively. More excitingly, for the first time, we demonstrated the feasibility of on-filter 3D culture (with significant cell proliferation) from captured cancer cells.

## EXPERIMENTAL

### Filter Design and Fabrication

Parylene-C was chosen as the filter material because of its unique properties [1]. It is mechanically strong (Young's modulus  $\sim 4\text{GPa}$ , and tensile strength  $\sim 70\text{MPa}$ ) while malleable (elongation to break  $\sim 200\%$ ). It is optically transparent in the visible range, which facilitates direct pathological observation of stained cells under microscope. It is inert to most of the chemicals and solvents used in standard chemical and biological laboratories. Moreover, its biocompatibility makes parylene-C based devices suitable for cell culture applications. Finally, high quality pin-hole free parylene-C thin film can be obtained with room-temperature chemical vapor deposition (CVD), and further patterned with lithography and oxygen plasma by reactive ion etching (RIE).

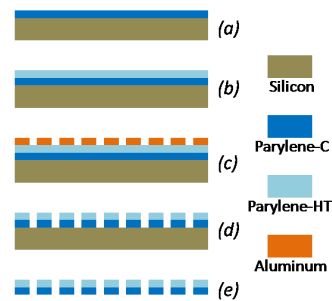


Figure 1: Filter fabrication process. (a) 9 $\mu\text{m}$  parylene-C deposition; (b) 0.5 $\mu\text{m}$  parylene-HT deposition; (c) Aluminum deposition and wet-etching patterning; (d) Pattern parylene layers by RIE, with Al mask; (e) Release parylene filter from Si substrate.

Parylene-C and parylene-HT dimers were purchased from Specialty Coating Systems. The fabrication process started with a 9 $\mu\text{m}$  parylene-C film deposition on silicon wafer (Fig. 1). A 0.5 $\mu\text{m}$  parylene-HT (chemical structure shown in Fig. 2) was then coated on parylene-C surface. This inert and hydrophobic parylene-HT coating could efficiently prevent cancer cell adhesion on the filter surface, which was important for 3D tumor culture application. Aluminum was deposited using a thermal evaporator, followed by lithography and wet-etching patterning. For each filter, slot arrays were etched through the parylene-C film by RIE in a 6mm $\times$ 6mm

square region. Each slot size was  $6\mu\text{m}\times 30\mu\text{m}$ , which was optimal according to our previous publication [2]. The patterned parylene membrane was peeled off from the silicon substrate. The fabricated filter looked like a net, with a high open-factor of 42% (Fig. 3).

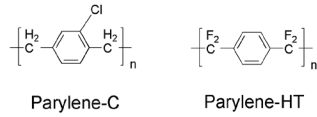


Figure 2: Chemical structures of parylene-C and parylene-HT film.

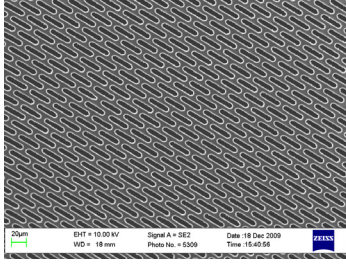


Figure 3: SEM picture of the fabricated membrane filter.

### Filtration Procedure

Four pieces of PDMS sheets were used to sandwich the parylene filter, and form a top and bottom chambers (Fig. 4(b)). The top chamber had the dimension of  $6\text{mm}\times 6\text{mm}\times 1.5\text{mm}$ . Two acrylic sheets with central holes were also used. The assembly was clamped to ensure good sealing and prevent leakage.

The CTC filtration was carried out with a low-constant-pressure fluid delivery system (Fig. 4(a)), which was connected to the filter assembly. During filtration, sample was driven into the filter assembly by  $\text{N}_2$  with low drive pressure  $P$ . Low drive pressure ensured a low pressure drop  $\Delta P$  across the filter, which was crucial for the high viability of captured CTCs. In previous filtration approaches, sample was driven by direct hand-push or syringe pump [1,3]. Although a near-constant flow rate could be achieved,  $\Delta P$  increased when the filter was gradually and partially clogged. In contrast, the low-constant-pressure fluid delivery system could keep a near-constant low  $\Delta P$  during filtration.

We used non-small-cell prostate cancer PC-3 cells for device testing. PC-3 cell line was cultured in RPMI 1640 culture medium (Mediatech, Inc.) supplemented with 10% fetal bovine serum (RPMI complete medium) at 5%  $\text{CO}_2$  and  $37^\circ\text{C}$ . PC-3 cells were pre-labeled with calcein-AM fluorescent dye (Invitrogen), centrifuged and then re-suspended in phosphate buffered saline (PBS). A model system was constructed by spiking PC-3 cells at  $100\text{ cells mL}^{-1}$  into 1mL human whole blood obtained from a healthy donor. We used 0.1psi low pressure to drive the sample during filtration. Filtration of 1mL whole blood took about 5min. After filtration, capture efficiency (Eq. (1)) was measured by counting the captured cancer cells under epifluorescence microscope. The viability (Eq. (2)) of captured cancer cells was evaluated by on-filter staining with Propidium Iodide (PI) (Invitrogen). Enrichment (Eq. (3)) was determined by staining white blood cells (WBCs) remaining on filter with the nucleus dye Acridine Orange (AO) (Invitrogen) followed by WBC counting.

$$\text{Capture Efficiency} = \frac{\# \text{ of captured cancer cells}}{\# \text{ of spiked cancer cells}} \quad (1)$$

$$\text{Viability} = \frac{\# \text{ of viable cancer cells}}{\# \text{ of captured cancer cells}} \quad (2)$$

$$\text{CTC enrichment (fold)} = \frac{\# \text{ cancer cells} / \# \text{ WBCs on filter after filtration}}{\# \text{ cancer cells} / \# \text{ WBCs in original sample}} \quad (3)$$

### Cell-substrate adhesion assay

To examine cancer cell adhesion on parylene-C with different surface conditions, four types of surfaces were used in this study, including untreated parylene-C film,  $\text{O}_2$  plasma treated parylene-C film, parylene-C film with parylene-HT coating and polystyrene substrate. Plasma treated parylene-C sample was prepared by treating parylene-C film in a plasma etching machine for 1min (100W, 200mtorr). Parylene-HT coating was obtained by depositing  $0.5\mu\text{m}$  parylene-HT on parylene-C film. Polystyrene substrate is widely used in cell culture and was used here as a control for cell adhesion assay. Each substrate was sterilized in 70% ethanol and PBS before experiments. Contact angle measurements were performed by measuring the contact angles of deionized water drops on different substrates by using a NRL Contact Angle Goniometer (Ramé-Hart instrument co.). To determine the cell adhesion, PC-3 cells were counted and loaded onto each substrate. After 10 hours of incubation, the substrates were washed twice with PBS. Cells remaining on the substrates were then counted to determine the percentage of adhering cells.

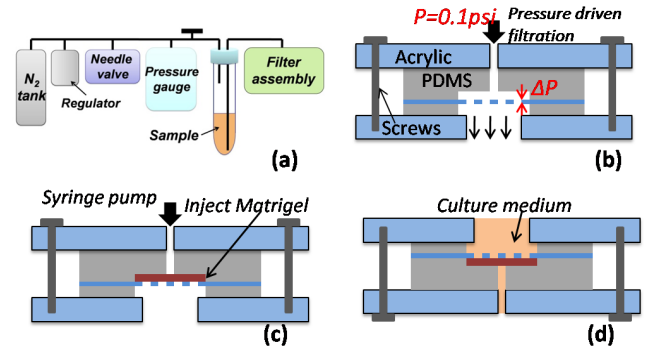


Figure 4: Operation procedure. (a) Schematic of the low-constant-pressure filtration system; (b) Filter assembly and filtration process; (c) Matrigel injection after filtration; (d) Schematic of 3D on-filter tumor culture.

### 3D tumor culture

To demonstrate the feasibility of on-filter 3D culture of the captured cancer cells after filtration, we spiked about 30 unlabeled PC-3 cancer cells into 1mL PBS. The sample was filtrated and cancer cells were captured on the filter. Matrigel was selected as the 3D scaffold material. A 1:1 mixture of Matrigel (BD Biosciences) and RPMI complete medium was carefully injected into the filter top chamber by a syringe pump, to prevent the cell damage and undesirable bubble appearance. Gelation was allowed to occur at  $37^\circ\text{C}$  for 30min. Then the filter assembly was placed invertedly and covered with RPMI complete medium. The whole setup was left in a petri-dish and placed in an incubator. Culture medium was refreshed every day. Calcein-AM and PI live/dead cell staining was used again to determine the cellular viability of the 3D tumor.

2D monolayer cancer cell culture without Matrigel injection was used as a control. For 2D on-filter culture, membrane filter was disassembled after filtration and soaked in the culture medium.

### Immunofluorescence and image acquisition

Immunofluorescence staining was performed on the 3D tumor after 8 days of culture. FITC-conjugated anti-EpCAM antibody

(BioLegend) and PE-conjugated anti-CD49b antibody (BD Biosciences) were used to immunostain the cancer cell membranes. After staining, images were taken by a Nikon E800 epifluorescence microscope (Nikon Inc.), equipped with a CCD camera.

## SIMULATION

In order to estimate the shear stress and tension exerted on the captured cancer cells during filtration, we used finite-element simulation tool COMSOL Multiphysics. 2D incompressible Navier-Stokes steady-state analysis model was selected. The dynamic viscosity of blood was set as 0.003Pa·s. Drive pressure  $P = 0.1$ psi. Simulated 2D flow velocity profile in the filter chambers was shown in Fig. 5. A nearly uniform flow field was achieved in the filter region. Based on this velocity profile, we calculated the maximum shear stress and surface tension on the cancer cells captured at different locations (Fig. 6). Due to the low trans-filter pressure drop  $\Delta P$ , the shear stress and tension were also low, ensuring the high viability of the cancer cells [8].

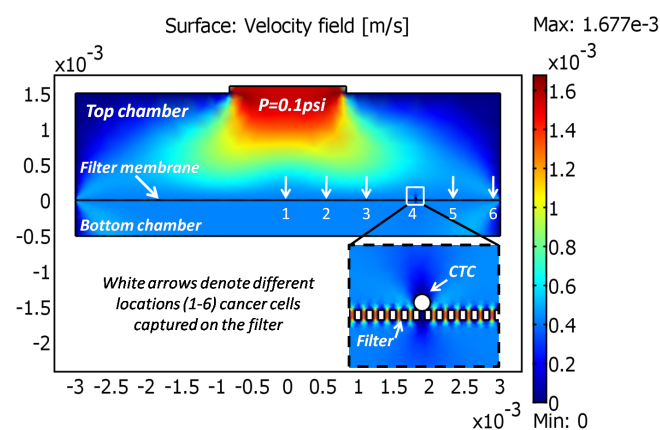


Figure 5: FEM simulation result of the flow velocity field during filtration. The inset shows an example of captured CTC.

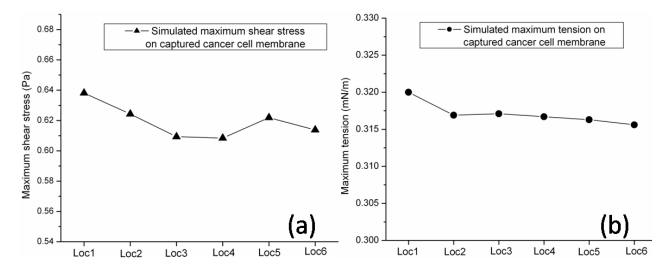


Figure 6: Simulated maximum shear stress (a) and tension (b) on CTC membrane captured at different locations (Location 1-6 were labeled in Fig. 5).

## RESULTS AND DISCUSSION

The large open-factor contributed in two aspects to the improved filter performance. Firstly, the large open-factor decreased the flow resistance during filtration. Reduced flow resistance lowered the drive pressure required for successful sample processing and the trans-filter pressure drop  $\Delta P$ , which ensured the high viability of captured cancer cells. Filter testing with the model system showed that the capture efficiency was 92.4% (SD=7.4%), and the viability was measured to be 93.8% (SD=3.4%). Fig. 7 shows the examples of live and dead cancer cells using calcein-AM and PI live/dead staining assay.

Secondly, the large open-factor also decreased the filter surface area. Because of their smaller size and larger deformability, most blood cells can deform and pass through the slots during filtration. However, some blood cells may remain on the filter top surface, resulting in a non-ideal CTC enrichment. Reduced filter surface area greatly lowers the chance of blood cell retention on filter surface, thus improving the enrichment. Compared to the ~200-fold enrichment of our previously reported filter (open-factor 18%) [2], this new filter (open-factor 42%) achieved a 2149-fold (SD=1120) enrichment. Fig. 7(c) shows that there were still minimal amount of blood cells remaining on the filter, possibly due to the friction between the cell and slot side walls.

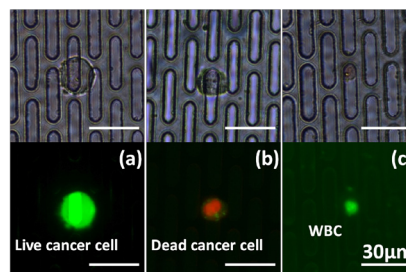


Figure 7: Live/dead staining assay of captured cancer cells. (a) live cancer cell retained calcein-AM; (b) dead cancer cell was stained with PI; (c) later on, remaining WBC was stained with the nucleus dye AO. (scale bars: 30µm)

For on-chip 3D cell culture, cell-cell and cell-extracellular matrix (ECM) interactions should dominate over cell-substrate interaction. Therefore, we needed to treat the filter surface to be resistant to cancer cell adhesion. Surface property and cancer cell adhesion evaluations of untreated parylene-C,  $O_2$  plasma treated parylene-C, parylene-C with parylene-HT coating, and polystyrene are shown in Fig. 8(a) & (b). Untreated parylene-C surface was hydrophobic. While plasma treatment could turn it to be hydrophilic, parylene-HT coating rendered the surface to be even more hydrophobic. After 10 hours of incubation, about 30% PC-3 cancer cells remained adhering on the untreated parylene-C surface. Although untreated parylene-C surface could be considered as cell resistant compared to the tissue culture polystyrene control, it was still not suitable for 3D tumor culture. Fig. 8(c) shows that during 3D tumor culture, some cancer cells adhered and proliferated two-dimensionally on the untreated parylene-C filter, which was undesirable. It was noticed that plasma treated parylene-C surface displayed enhanced adhesion. In comparison, parylene-HT coated surface heavily repelled cancer cell adhesion, reducing the cell adhesiveness to be only one-third of the original level.

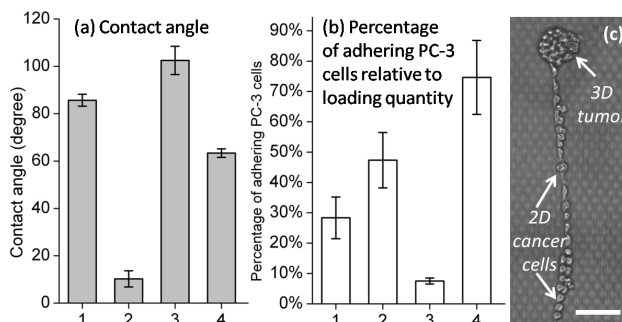


Figure 8: Parylene surface treatment. 1: untreated parylene-C surface; 2:  $O_2$  plasma treated parylene-C; 3: parylene-C with

parylene-HT coating; 4: tissue culture polystyrene substrate. (a) contact angle measurement; (b) evaluation of cancer cell adhesiveness; (c) without parylene-HT coating, some cancer cells adhered and proliferated on untreated parylene-C filter surface during 3D tumor culture with Matrigel. (scale bar: 100 $\mu$ m)

Therefore, parylene-HT coated parylene-C filter was selected for 3D culture after filtration. Captured PC-3 cancer cells proliferated three-dimensionally into the Matrigel, and gradually formed a spherical tumor. Matrigel is a biomatrix hydrogel containing many essential components of the ECM such as collagen, laminin, entactin and other important growth factors, which can support cellular proliferation and induce cellular differentiation [6,7]. The cellular proliferation rate was monitored in Fig. 9(a). On the 6<sup>th</sup> day, live/dead staining was used to evaluate the cellular viability inside the tumor (Fig. 9(b)-(e)). Over 90% cells kept viable during the tumor formation. To further investigate the structure of the tumor, after 8 days of culture, we stained the cell membranes with cancer specific immunofluorescence surface markers (Fig. 10). The images indicated that separate cells were adhering to form a combined structure. Cell-cell and cell-ECM interactions were clearly observed. In comparison, 2D on-filter culture was used as a control (Fig. 10). Cells attached to parylene-C filter, and formed a confluent 2D monolayer after 8 days of culture.

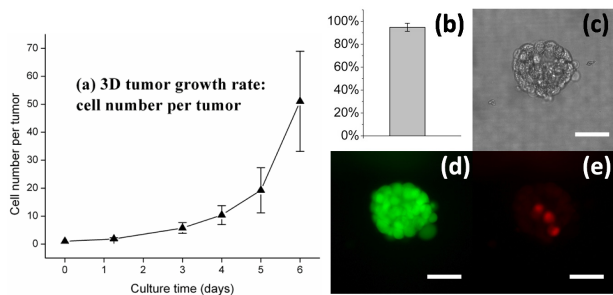


Figure 9: 3D on-filter cultured tumor growth rate and viability. (a) growth rate; (b) viability on the 6<sup>th</sup> day; (c)-(e) bright field and fluorescence images of calcein-AM & PI stained tumor. (all scale bars: 40 $\mu$ m)

## CONCLUSION

In this paper we report the use of a high open-factor parylene-C/HT filter for the capture of CTCs from whole blood, with high capture efficiency, viability, enrichment and throughput. Due to the large open-factor, CTC enrichment was much higher than our previous filters. Moreover, for the first time, we

demonstrated the feasibility of 3D tumor culture after filtration. Captured cancer cells were cultured on-filter, and proliferated into Matrigel three-dimensionally. Live/dead staining assay and immunofluorescence staining verified the cellular viability and the morphology of the 3D tumor. Our ongoing work includes the capture and culture of CTCs directly from clinical patient blood sample, which can enable the characterization of the original tumor and greatly benefits the future genetic and chemotherapy studies.

## ACKNOWLEDGEMENT

This work is supported by the Caltech CI2 I-Grant Award.

## REFERENCES

- [1] S. Zheng, H. Lin, R. J. Cote and Y. -C. Tai, "A novel 3D micro membrane filtration device for capture viable rare circulating tumor cells from whole blood", *Proc. of Hilton Head 2008*, Hilton Head Island, SC, USA, 2008, pp. 134-137.
- [2] B. Lu, T. Xu, S. Zheng, A. Goldkorn and Y. -C. Tai, "Parylene membrane slot filter for the capture, analysis and culture of viable circulating tumor cells", *Proc. of MEMS 2010*, Hong Kong, China, 2010, pp. 935-938.
- [3] P. Paterlini-Brechot and N. L. Benali, "Circulating tumor cells (CTC) detection: Clinical impact and future directions", *Cancer Letters*, vol. 253, pp. 180-204, 2007.
- [4] S. Nagrath, L. V. Sequist, S. Maheswaran, et al. "Isolation of rare circulating tumor cells in cancer patients by microchip technology", *Nature*, vol. 450, pp. 1235-1239, 2007.
- [5] K. T. Helzer, H. E. Barnes, L. Day, et al. "Circulating tumor cells are transcriptionally similar to the primary tumor in a murine prostate model", *Cancer Research*, vol. 69, pp. 7860-7866, 2009.
- [6] Y. Torisawa, H. Shiku, T. Yasukawa, et al. "Multi-channel 3-D cell culture device integrated on a silicon chip for anticancer drug sensitivity test", *Biomaterials*, vol. 26, pp. 2165-2172, 2005.
- [7] T. R. Sodunke, K. K. Turner, S. A. Caldwell, et al. "Micropatterns of Matrigel for three-dimensional epithelial cultures", *Biomaterials*, vol. 28, pp. 4006-4016, 2007.
- [8] L. Weiss and G. W. Schmid-Schonbein, "Biomechanical interactions of cancer cells with the microvasculature during metastasis", *Cell Biochemistry and Biophysics*, vol. 14, pp. 187-215, 1989.

## CONTACT

\* B. Lu, tel: +1-626-802-0898; lubo@mems.caltech.edu

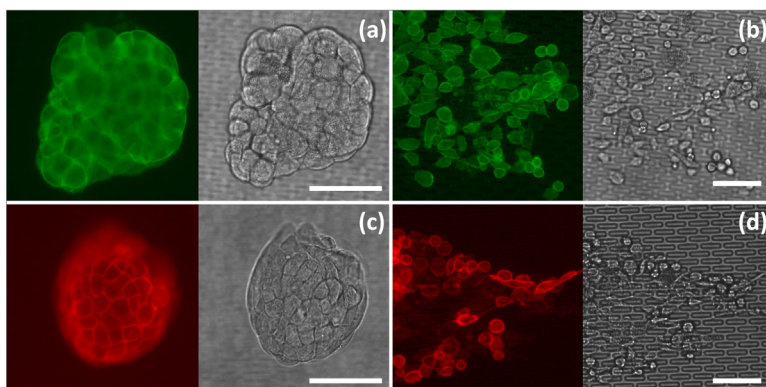


Figure 10: Immuno-staining of cultured 3D tumor. (a) 3D tumor stained with FITC-conjugated anti-EpCAM antibody. (c) 3D tumor stained with PE-conjugated anti-human CD49b antibody. The 2D on-filter (without parylene-HT coating) culture controls are shown in (b)&(d), respectively. (all scale bars: 100 $\mu$ m)

# ALL-SOLID-STATE 3-D RECHARGEABLE LITHIUM BATTERIES WITH SILICON ROD STRUCTURED ELECTRODE

Jian Wang, James E. Trevey, Se-Hee Lee, and Victor M. Bright\*  
University of Colorado, Boulder, Colorado, USA

## ABSTRACT

This paper presents 3-D MEMS-fabricated lithium rechargeable batteries relying on structured silicon rods as anodes in order to increase the effective electrode area. A new method of fabricating silicon micro/nano rod arrays with controllable diameters in the range of 300 nm-8  $\mu\text{m}$  is proposed. 2  $\mu\text{m}$  silicon rods as anodes were successfully incorporated into an all-solid-state battery construction. The structured architecture of the silicon electrodes allowed for a heightened surface area as well as improvement in cycle life and capacity over comparable planar electrodes. Structured rod array electrodes showed a first cycle coulombic efficiency over 80% which is more than double that of conventional powder composite silicon electrodes. Galvanostatic cycling of structured silicon rod electrodes showed highly reversible capacity for high current densities.

## INTRODUCTION

Mounting electric energy sources on semiconductor chips is highly attractive due to rapid growth of electrical and mechanical integration technologies such as wireless telecommunications and emerging integrated optoelectronic circuits. Planar solid-state thin film batteries are widely used as an energy source in current MEMS and CMOS devices but are incapable of meeting growing power demands [1]. Recent technological advancements have realized improved battery performance by reconfiguring electrode materials from the typical 1-D battery design of commercial technology into 3-D architectures [2]. Such battery configurations more effectively utilize the highly limited space on board of MEMS and CMOS devices by increasing the power capabilities of batteries without increasing their footprint.

The binary silicon-lithium material system shows the highest specific capacities up to 4,200 mAh  $\text{g}^{-1}$  (which corresponds to 4.4 mol of Li per mol of Si) [3]. Unfortunately, the reversibility of conventional Si material at room temperature is poor, due to the expansion and contraction of lithium silicide during the charge-discharge process that results in the pulverization of the Si material [4-6]. As a consequence, the electrical contact between the current collector and the Si material fails, leading to a rapid decrease in the system capacity after several cycles. Many reports have focused on reducing such volume change via conductive additives that act as an electron conductor between pulverized particles. This approach however, requires that a high percent of the electrode be a non-contributing material, thereby largely reducing the maximum attainable capacity of the battery [7]. In principle, a reduction in the size of the Si material (i.e. from micro- to nano-sized crystals) should mitigate the reversibility problem, since a smaller Si crystallite will have greater surface to volume ratio and more surface area in contact the current collector, even after lattice expansion and contraction during cycling. To this end, the binary Li-Si system has been previously investigated to a limited extent, with initial work demonstrating superior discharge capacity for micro- and nano-sized Si materials [8]. In general, this approach offers initial evidence for the improved performance of small-scale Si materials for the Li-Si anode system over conventional battery materials [4]. Here, we show that silicon rod structured battery electrodes circumvent the pulverization issues as they can accommodate large strain with minimal pulverization, providing

good cycle life and relatively high coulombic efficiency.

## DESIGN AND ROD ARRAY FABRICATION

In this work we investigate the fabrication and use of 3-D integrated all-solid-state lithium batteries with structured Si rod electrodes and powder solid-state electrolyte (figure 1). Using a n-type (Sb doped) single side polished, 3 inch diameter silicon wafer (<100> cut, 350  $\mu\text{m}$  thick, 0.008-0.02  $\Omega\text{cm}$ ), Si micro-rods are

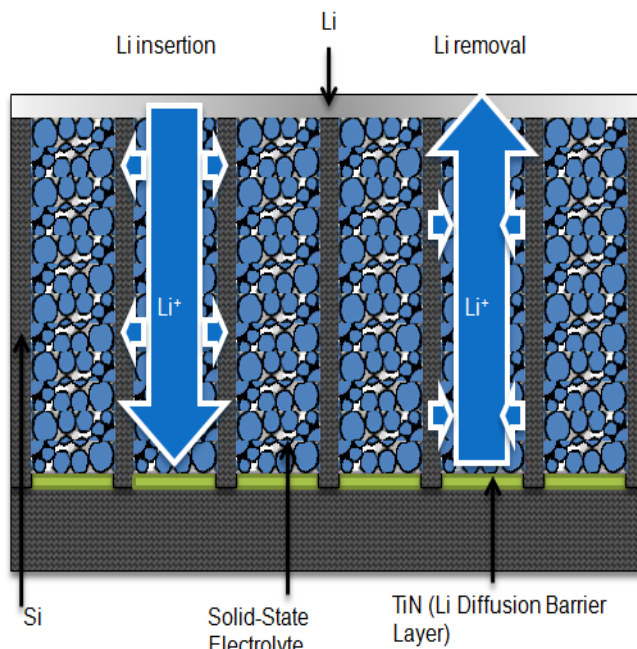


Figure 1: Cross-section view of our 3D integrated all-solid-state battery.

obtained by deep reactive ion etching (DRIE: STS Pegasus DRIE system), and made thinner by subsequent RIE (Plasmatherm 540/540 Dual Chamber RIE system). The fabrication process of the rod array is shown in figure 2. After spin coating and photo lithography, the photoresist (AZ 4210) is hard baked in a vacuum oven for 10 minutes before using DRIE to obtain the Si rod array. The diameter of the rods can be controlled to within the range of 3  $\mu\text{m}$ -8  $\mu\text{m}$  by using different masks. Following DRIE, rods are made thinner by subsequent  $\text{SF}_6$  RIE at an etching rate of 400-600 nm/min. At this step, 400 nm copper is thermally evaporated (3\_L-TEC MED 020 Coating System) onto the sample as a metallic mask layer for the RIE process. After RIE, the copper layer is removed by copper etchant and then a 70 nm layer of Ti is evaporated on top of the Si substrate and the rods. Ti is turned into a TiN barrier layer by heating the sample in  $\text{N}_2$  for 1 minute at 800  $^\circ\text{C}$ . Due to the high aspect ratio of the gap, the TiN barrier will only cover the substrate and the top of the rods but not the side wall as proved by figure 3. A TiN Li diffusion barrier layer is formed on the Si substrate for the purpose of preventing the lithiation of Si substrate, in order to avoid mechanical failure of the bulk Si substrate during the cycling [9]. After the TiN barrier layer is coated,  $\text{SF}_6$  RIE is used again to obtain the desired dimension of

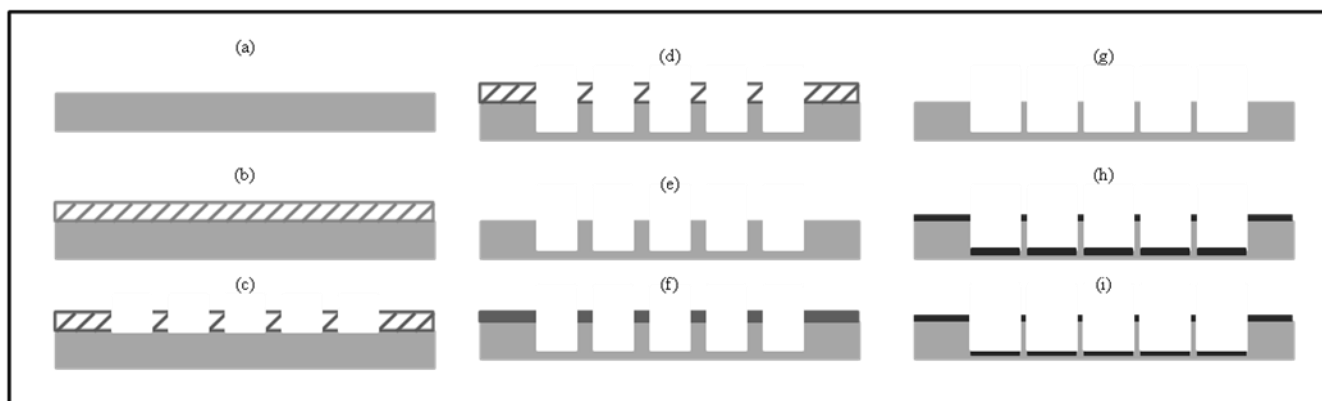


Figure 2. Fabrication process for creating Si rod array. (a) Silicon wafer (n-type, Sb-doped, 100 cut, 350  $\mu\text{m}$  thick 0.008~0.02  $\text{ohm-cm}$ ) (b) Spin coating 2.5  $\mu\text{m}$  Photoresist (AZ 4210) on Silicon wafer (c) Photo lithography and PR hard baking (d) DRIE for 8 mins (etching rate 3  $\mu\text{m}/\text{min}$ ) (e) Remove PR and clean the sample (Acetone, API clean first, then Plasma clean) (f) Thermal evaporate metallic mask (Copper) (g)  $\text{SF}_6$  RIE and remove Copper (h) Thermal evaporate Ti and heat the sample in  $\text{N}_2$  atmosphere (i)  $\text{SF}_6$  RIE

the rods. The diameter of the rods is controlled by the etching time of RIE. Figure 4 shows the final result of a fabricated rod array. From (a) to (d), the diameters of the rods are respectively 300 nm, 750 nm, 2000 nm and 8000 nm. The gap between the rods can also be controlled by using different mask in the lithography process. Here, we choose the rod array with the diameter of 2  $\mu\text{m}$ , height of 20  $\mu\text{m}$  and gap of 10  $\mu\text{m}$  for battery demonstration.

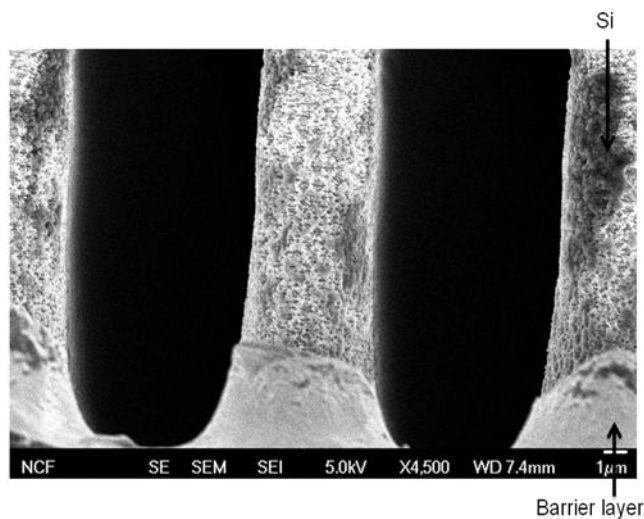
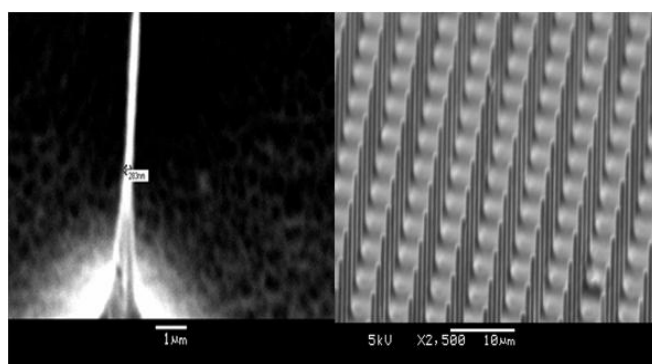


Figure 3. SEM image of Si rods with TiN barrier layer coated on the substrate but not the side wall of the rod

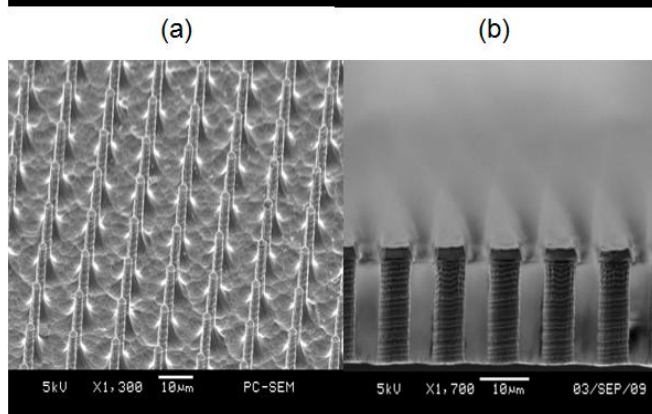
## MATERIALS AND CHEMISTRY

### Solid Electrolyte

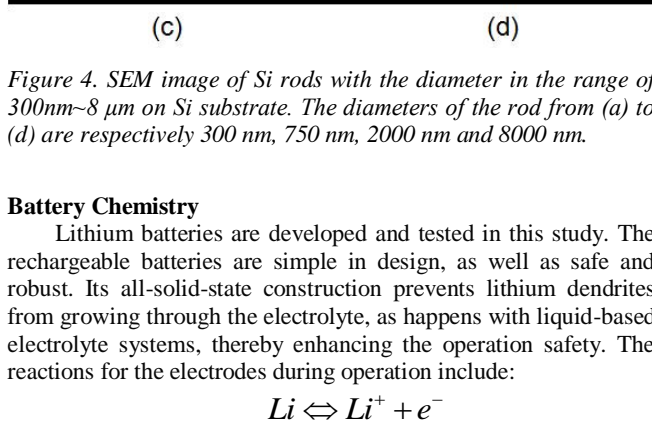
Reagent-grade powders of  $\text{Li}_2\text{S}$  (Aldrich, 99.999%) and  $\text{P}_2\text{S}_5$  (Aldrich, 99%) were used as starting materials for mechanical ball milling. We produce 77.5 $\text{Li}_2\text{S}$ -22.5 $\text{P}_2\text{S}_5$  (mol%) by the single step ball milling (SSBM) process [10]. Appropriate concentrations of materials are deposited into a zirconia vial (Spex) at a net weight of one gram with 2 zirconia balls (1x 12mm, 1x15mm in diameter) for grinding. High energy ball milling (Spex2000) took place for 20 continuous hours in an Ar filled glove box at 55  $^\circ\text{C}$ . The resulting powder is recovered and used without further alterations for solid state batteries.



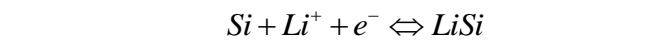
(a)



(b)



(c)

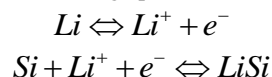


(d)

Figure 4. SEM image of Si rods with the diameter in the range of 300nm~8  $\mu\text{m}$  on Si substrate. The diameters of the rod from (a) to (d) are respectively 300 nm, 750 nm, 2000 nm and 8000 nm.

### Battery Chemistry

Lithium batteries are developed and tested in this study. The rechargeable batteries are simple in design, as well as safe and robust. Its all-solid-state construction prevents lithium dendrites from growing through the electrolyte, as happens with liquid-based electrolyte systems, thereby enhancing the operation safety. The reactions for the electrodes during operation include:





## BATTERY ASSEMBLY AND TESTING

### Assembly

A cross sectional schematic of the battery assembly process composed of two electrodes separated by an electrolyte cavity can be seen in Fig. 5. In the lithium battery, the bottom electrode is comprised of just the silicon wafer and rod array while the top electrode is simply lithium metal, both in contact with titanium current collectors.

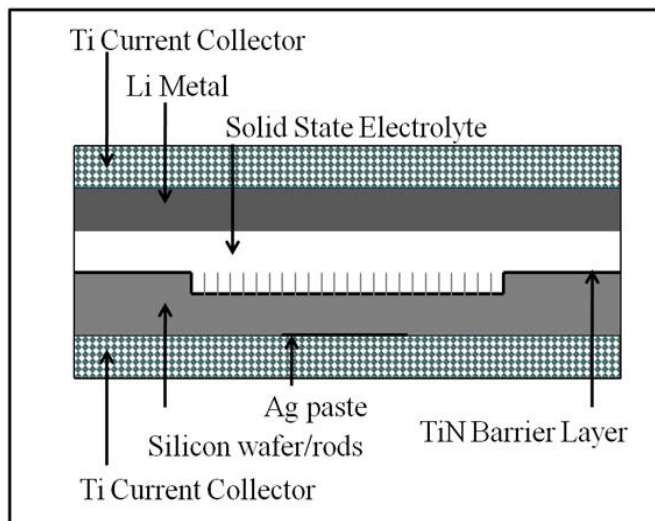


Figure 5: Schematic of battery construction. The lithium battery employing the silicon wafer/rods in a cathode design

The lithium batteries are formed by first attaching the silicon substrate to a titanium current collector with a conductive silver paste to ensure good contact. After the conductive paste has cured, solid electrolyte is weighed and poured into the die. The silicon wafer/solid electrolyte are pressed together in the die at 5 metric tons for approximately 5 minutes. A lithium foil is then attached to the solid state electrolyte at a pressure of 1 metric ton.

### Testing

Batteries were characterized by using galvanostatic cycling to observe their charge-discharge behavior. Batteries were cycled at varying current densities to observe performance and degradation at high rates. Most commonly, batteries are charged and discharged between preset voltage limits, called constant voltage cycling. We employed constant capacity cycling limits so that structured silicon rods were lithiated to a capacity correlating to approximately  $3600 \text{ mAh g}^{-1}$ , which is the room temperature capacity limit for silicon as an electrode material in all solid state batteries. In general, constant capacity cycling is used to determine materials' potential limits for the first few cycles and will be followed by constant voltage cycling to observe degradation. Our experiments, using continued constant capacity cycling perform the same task but allow for closer observation of structural transformations of materials.

## RESULTS

### Columbic efficiency

Figure 6 shows the electrochemical data for our 3D integrated all-solid-state lithium battery for the first 20 cycles and data for a comparable state-of-the-art 1D battery for comparison [10]. The columbic efficiencies of the first cycle of structured 3D batteries are 70% and 82% at an applied current of  $1250 \mu\text{Ah}/\text{cm}^2$  and  $250 \mu\text{Ah}/\text{cm}^2$

$\mu\text{Ah}/\text{cm}^2$  respectively (Fig. 6A). The high value of the columbic efficiency of the first cycle is most fascinating because the generally accepted value for the columbic efficiency of batteries with Si based electrodes is closer to 35% due to the excessive pulverization of electrode material. Columbic efficiency is a reading of how well a battery is transporting lithium. 100% columbic efficiency implies that all of the lithium that was transported from the lithium metal to the silicon electrode is transported back to the lithium metal. In the case of low columbic efficiency, some lithium is being trapped in the electrode. Continued cycling revealed a relatively stable columbic efficiency that indicates lithium trapping and degradation in the  $\text{Li}_x\text{Si}$  electrode is minimal during cycling.

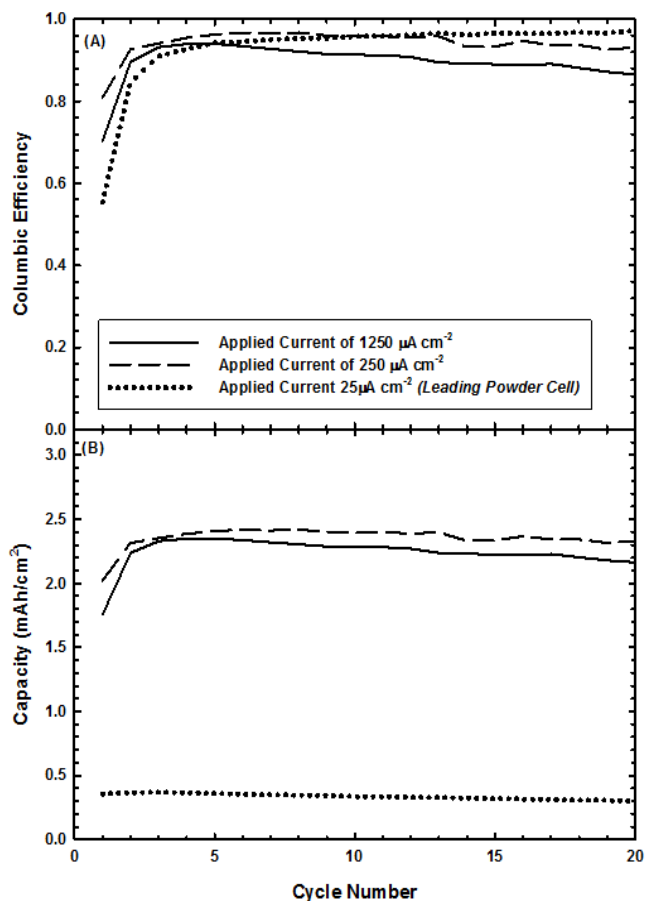


Figure 6. (A) Electrochemical data for our 3D integrated all-solid-state battery and comparison with state-of-the-art battery, columbic efficiency versus cycle number at different applied currents. (B) Electrochemical data for our 3D integrated all-solid-state battery and comparison state-of-the-art battery, capacity versus cycle number at different applied currents.

### Capacity

Figure 6B shows again a comparison of our all-solid-state lithium batteries versus a current state-of-the-art battery, except for capacity at various applied currents instead of columbic efficiency. An approximate 8 fold improvement in capacity is observed for our rod structured battery over the leading technology. We have shown significant improvement of not only the overall capacity of potential on-board batteries but we have achieved high columbic efficiency on the first cycle of a Si based electrode.

### Cycle life

Si Micro/Nano rod structures were found to exhibit a longer cycle life than bulk Si [4]. Our rod-structured battery displays constant capacity with minimal degradation for over 20 cycles. As lithium trapping and pulverization isolate Si upon cycling, lithium diffuses deeper into the rods for conducting Si with which to react. As more Si becomes isolated, a larger resistance is observed. Figure 7 shows this trend of increasing resistance with a decreasing low cut-off voltage of each cycle. The structured nature of the rod array electrodes allows for minimal resistance layer build-up, as the rods can accommodate large strain with minimal pulverization.

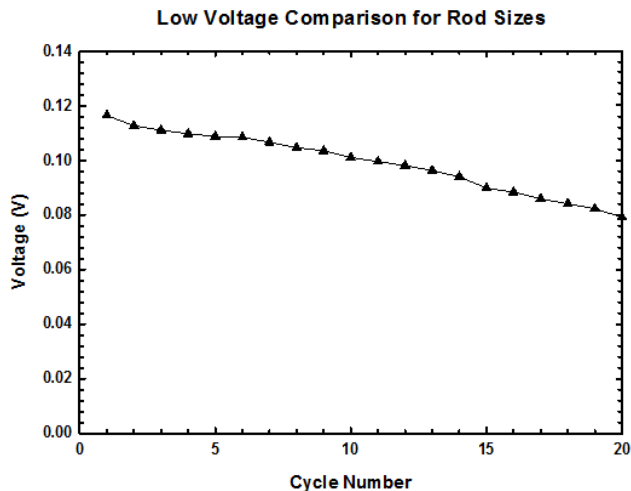


Figure 7. The low cut-off voltage of each discharge cycle.

### DISCUSSION

Rechargeable lithium batteries were produced and tested in this work with a fair degree of repeatability. Inconsistencies arose with imperfections in our method manufacturing rod arrays as well as battery assembly. Rod array dimensions were difficult to fabricate precisely with accuracy within 100 nm of the target dimension, solid electrolyte filling of rod cavity for perfect contact was not verified, and TiN coating effectiveness were all areas in need of further investigation. Future work will focus on repeatability of size dimensioning of rod arrays and of battery assembly, as well as TiN coating effectiveness.

### CONCLUSION

In this work, 3-D MEMS-fabricated lithium batteries incorporating structured silicon rods are designed, fabricated and tested. A simple, quick, and repeatable micro/nano rod array fabrication process for the battery anodes is developed by our group using traditional MEMS technology. The testing results of the 3-D lithium battery showed a fair degree of repeatability and revealed that structured silicon rod arrays achieve a high first cycle as well as high continued cycling columbic efficiency. High capacity with high reversibility was observed for lithium batteries. Long cycle life with little fading was achieved by using rod-structured electrodes.

### ACKNOWLEDGEMENTS

This work was supported by the Semiconductor Research Corporation (SRC). Special thanks to Dr. Ann Li at NIST for assistance with DRIE. Partial support by DARPA Center on Nanoscale Science and Technology for Integrated Micro/Nano-Electromechanical Transducers (iMINT) funded by DARPA

N/MEMS S&T Fundamentals Program (HR0011-06-1-0048)(Dr. D. L. Polla, Program Manager) is also acknowledged.

### REFERENCES

- [1] L. Baggetto, R. A. H. Niessen, F. Roozeboom, and P. H. L. Notten, "High Energy Density All-Solid-State Batteries: A Challenging Concept Towards 3D Integration", *Adv. Funct. Mater.*, 18, 1057 (2008).
- [2] J. W. Long, B. Dunn, D. R. Rolison, and H. S. White, "Three-Dimensional Battery Architectures". *Chem. Rev.*, 104, 4463 (2004).
- [3] M. Green, E. Fielder, B. Scrosati, M. Wachtler, J. S. Moreno, "Structured Silicon Anodes for Lithium Battery Applications", *Electrochemical and Solid-State Letters*, 6 A75 (2003).
- [4] C. K. Chan, H. Peng, G. Liu, K. McIlwraith, X. F. Zhang, R. A. Huggins, and Y. Cui, "High-performance Lithium Battery Anodes Using Silicon Nanowires", *Nature Nanotechnology*, 3, 31 (2008).
- [5] M. H. Park, M. G. Kim, J. Joo, K. Kim, J. Kim, S. Ahn, Y. Cui, and J. Cho, "Silicon Nanotube Battery Anodes", *Nano. Letter*, 9 3844 (2009).
- [6] K. Peng, J. Jie, W. Zhang, and S. T. Lee "Silicon Nanowires for Rechargeable Lithium-ion Battery Anodes", *App. Phys. Lett.*, 93, 033105 (2008).
- [7] H. Kim and J. Cho "Superior Lithium Electroactive Mesoporous Si@Carbon Core-Shell Nanowires for Lithium Battery Anode Material ", 8, 3688 (2008).
- [8] H. Kim, B. Han, J. Choo, and J. Cho "Three-Dimensional Porous Silicon Particles for Use in High-Performance Lithium Secondary Batteries", 47, 10151 (2008).
- [9] US patent, # 5,236,868, Date Aug. 17, 1993
- [10] J. E. Trevey, Y. S. Jung, S. H. Lee, "Glass-ceramic  $\text{Li}_2\text{S-P}_2\text{S}_5$  Electrolytes Prepared by a Single Step Ball Milling Process and Their Application for All-solid-state Lithium-ion Batteries", *Electrochem. Comm.*, 11, 1830 (2009).

### CONTACT

\*Victor M. Bright, Victor.Bright@Colorado.EDU Tel: (303) 735-1734

# HIGHLY EFFICIENT IONIC WIND-BASED COOLING MICROFABRICATED DEVICE FOR MICROCHIP COOLING APPLICATIONS

A. Ongkodjojo<sup>1\*</sup>, R. C. Roberts<sup>1</sup>, A. Abramson<sup>2</sup>, and N. C. Tien<sup>1</sup>

<sup>1</sup>Department of Electrical Engineering and Computer Science, Case Western Reserve University, Cleveland, USA

<sup>2</sup>Department of Mechanical and Aerospace Engineering, Case Western Reserve University, Cleveland, USA

## ABSTRACT

This work explores an innovative and advanced thermal management solution using a microfabricated air-cooling technology that employs an electrohydrodynamic corona discharge (i.e. ionic wind pump) to stimulate forced convection for efficient heat removal from electronic components and devices. The device provides a high COP (coefficient of performance) of 20.5. In fact, the grid structures used in its design enhance the overall heat transfer coefficient and facilitate a batch and IC compatible process. ANSYS<sup>TM</sup> was used to computationally simulate the jet impingement phenomenon and resulting cooling effects of the device. COMSOL Multiphysics<sup>TM</sup> was additionally employed to computationally explore the effects of collector-emitter configuration. For a larger-scale application, performance can be appreciably enhanced by using an array of these microscale devices.

## INTRODUCTION

As microelectronics continue to be miniaturized and their performance improves, power density increases substantially, and currently exceeds 10 W/cm<sup>2</sup> [1]. Consequently, the need for novel and innovative thermal management solutions is becoming critical. This is largely because the performance of these sensitive electronic components depends on temperature, and even a small increase in temperature can lead to issues relating to device lifetime and performance.

Conventional forced-air cooling technologies (i.e. fans) are largely impractical as next generation solutions due to their large volume and high power consumption. For example, the large volume and weight associated with fin-array heat sinks and high power consumption associated with the attached fans make them impractical. Alternative technologies such as liquid microjet cooling [2] are attractive since they do offer significant heat removal, but concerns regarding their cost, weight, reliability, stability, pumping and refrigeration requirements, in addition to the fact that there is hesitation regarding exposing a microelectronics system to liquid, complicate their use [1]. Alternatively, finding a technologically feasible solution that meets the requirements of large heat removal effectiveness; low weight, volume and cost; zero noise generation; no moving parts; but with the use of comparatively simple technologies would certainly be attractive. This work explores ionic wind devices, which can provide enhanced convection solutions for applications that would have otherwise been cooled by natural convection/radiation or an alternative forced air cooling solution with all of these benefits.

The innovative microfabricated ionic wind pump employs an electrohydrodynamic corona discharge for efficient heat removal due to the convective effects induced by the device. The purpose of the work described herein was to test a single ionic wind pump, which could then be employed in an array for use in larger-scale applications. Conceptually, the cooling device, placed in contact with a hot microelectronics device, functions by applying a sufficiently high voltage between a single high-curvature tip and two parallel electrodes. Consequently, a jet of ambient air impinges on the hot, oppositely charged plates, thereby removing heat and acting as an “active heat sink” device.

## THEORY, MATHEMATICAL MODELS, AND IONIC WIND PUMP DEVICE

The ionic wind pump device works by applying a sufficiently high voltage (with corresponding low current, so therefore low power) between a high curvature emitting electrode and a low curvature collecting electrode, which results in a high electric field that ionizes nearby air molecules. The ionized air molecules, through subsequent collisions, transfer their momentum to the nearby neutral air molecules as they are propelled from the emitter and towards the collector electrode due to the presence of the high electric field. In other words, the resulting electric force creates a jet of air with substantial velocity termed an ionic or corona wind that impinges on the collecting electrodes. Figure 1 demonstrates the phenomenon schematically for a single emitter in a specific parallel arrangement of collector electrodes (more commonly, a single point-to-plane configuration is employed [3]). If the collecting electrode is at a relatively higher temperature, then this impinging air stream can be used for forced convective cooling. While the charged molecules effectively stick to the collector plate, there is a net bulk flow of neutral molecules away from the emitters, which behaves more like “plug flow” rather than being fully developed. Consequently, boundary layer effects that may otherwise minimize cooling effectiveness are mitigated, and performance is enhanced.

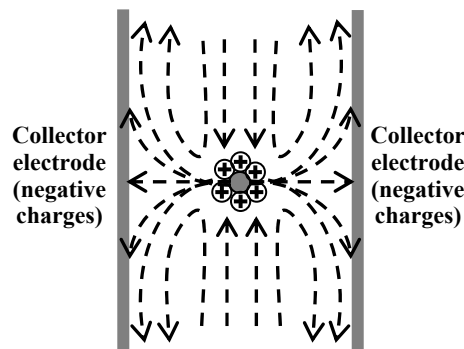


Figure 1: Schematic of the corona discharge/ionic wind pump. A perspective of a simple arrangement of a single emitter electrode (positive charges) located at the midpoint between two parallel collector electrodes (negative charges) with a subsequent flow pattern. The emitter electrode ionizes surrounding air molecules, which are forced towards the collector electrodes. The collected charged molecules may stick to these electrodes, but the neutral molecules with which they collide and exchange momentum are propelled, thereby creating an “ionic wind”.

Since the average flow velocity critically influences the achievable cooling rate of the device, the key parameters affect its magnitude. Electrohydrodynamic theory reveals that the induced air velocity due to the ionic wind is a function of the corona discharge current ( $I_{corona}$ ), the gap between the emitting electrode and the collecting electrode ( $d$ ), and the effective surface area of the collecting electrode ( $A$ ). This average velocity due to the ionic wind ( $\bar{v}$ ) is given by [4]:

$$\bar{v} = \left(\frac{2}{f}\right)^{1/2} \left[\frac{I_{corona} d}{\rho_{air} \mu A}\right]^{-1/2} \quad (1)$$

where  $f$  is the aerodynamic loss factor of the device,  $\mu$  is ion mobility in air, and  $\rho_{air}$  is air density at ambient temperature. Therefore to enhance velocity, the collecting surface area must be small, the gap size large, and the corona current high. However, if the current is too high, power consumption and corresponding Joule heating/ resistive heating will be too large. If the gap size is too large, the very high voltage and power consumption are also required. Therefore, these parameters must be optimized accordingly.

The Townsend expression to analyze the voltage and current requirements is given by:

$$I_{corona} = BV(V - V_0) \quad (2)$$

where  $B$  is a coefficient (related to the emitting electrode radius, ion mobility, electrode gap, and other geometrical factors such as tip shape, tip surface, etc.),  $V$  is the applied voltage, and  $V_0$  is the corona onset voltage (inception voltage) at which the corona discharge is initiated. So obviously to increase  $B$ , the design parameters of the emitter tip and other geometrical factors are accordingly adjusted. Additionally, the applied voltage must be sufficiently high, and certainly greater than the inception voltage, which can be analyzed using Peek's breakdown criterion, which is also employed to calculate the electrical field as expressed by equation (3).

$$E_{critical} = af_0 \delta (1 + b \sqrt{\frac{\delta}{r}}) \quad (3)$$

where  $a = 30 \text{ kV/cm}$ ,  $b = 0.3 \text{ cm}^{1/2}$ ,  $f_0 = 1$  (for smooth surfaces),  $\delta$  is relative air density, and  $r$  is the tip curvature radius; and which relates to voltage by Paschen's law as represented by:

$$E(x) = \frac{2V}{\left(\frac{2x}{r} + 1\right)r \ln\left(\frac{2d}{r} + 1\right)} \quad (4)$$

where  $x$  is the position of the electric field from an emitter surface. Thus, reducing the size of the sharp electrode will produce higher electric field strengths than a larger one for the same applied voltages. This is one of the reasons that an effective ionic wind pump device must be microfabricated such that its components are of microscale dimensions.

As described previously, the ionic wind pump device acts as an "active heat sink"; and the planar collector electrodes act as conventional cooling fins, but in addition the presence of the emitter tip enables forced convection without the use of a fan. The total amount of power dissipated,  $Q_{total}$ , from this "active heat sink" is then given by Newton's law of cooling:

$$Q_{total} = \eta_0 h_{avg} A \Delta T \quad (5)$$

where  $\eta_0$  is the overall efficiency of the cooling device,  $h_{avg}$  is the average heat transfer coefficient,  $A$  is the total surface area available for heat transfer, and  $\Delta T$  is the temperature drop between the cooled surface and surrounding air (ambient temperature).

## MICROFABRICATION PROCESS

The manufacturing process developed for the device uses glass wafers, a single photolithographic mask and a low cost copper-based electroplating process as previously reported [3]. Various design configurations were tested experimentally and modeled computationally to maximize the cooling effect, and a prototype device with an effective surface area of  $0.77 \text{ mm}^2$ , a thickness of  $\sim 17 \text{ }\mu\text{m}$ , and an emitter tip-to-collector plate gap of  $\sim 1 \text{ mm}$  was studied. In fact, the grid structures used in its design (Figure 2) enhance the overall heat transfer coefficient and facilitate

a batch and IC compatible process.

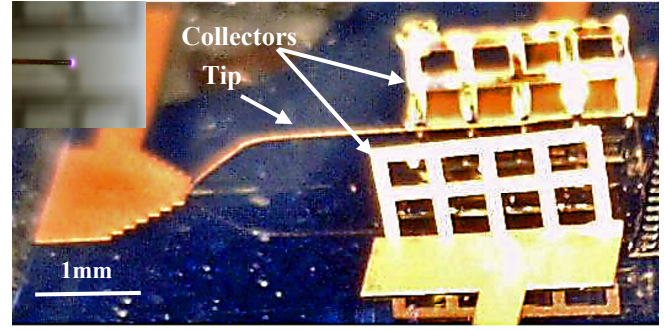


Figure 2: Image of a single microfabricated ionic wind pump device. Two parallel grid-structured collector plates and a single emitter tip are shown. When a certain high voltage is applied between the emitter tip and the collector electrodes, the corona discharge (ionization of air molecules) results in a visible purple haze around the emitter (inset).

## MODELING AND EXPERIMENTAL RESULTS

The performance of the microfabricated ionic wind pump device was experimentally investigated by building the experimental setup as demonstrated in Figure 3. Additionally, characterization experiments such as  $I-V$  (current-voltage) characteristics of the corona discharge-based device were conducted as shown in Figure 4. To measure corona current, the collecting electrode was placed in series with a small resistor to the ground. The corona current was observed from the measurement of the voltage drop across the resistor by the multimeter. A large resistance was also placed in series between the emitter and high voltage terminal to avoid damage to the device.

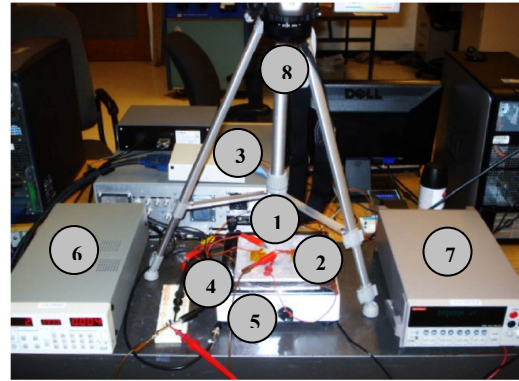


Figure 3: Picture of the experimental setup for the temperature testing. (1) Microfabricated ionic wind pump device; (2) two thermocouple sensors with high thermal conducting paste and Kapton tape covering the ends of the sensors; (3) National Instruments data acquisition (DAQ) board with a cold-junction compensation temperature sensor; (4) thermal spreader; (5) hot plate; (6) high voltage power supply; (7) multimeter; and (8) infrared thermography.

To test the cooling effects due to the ionic wind, the thermocouple was positioned in thermal contact with the backside of the vertical collector plate, the entire device was placed on a hot plate, and temperature was measured as a function of applied voltage and corona discharge current. Temperature was recorded by

using a National Instruments data acquisition (DAQ) board with a cold-junction compensation temperature sensor. The total size of thermocouple including the Kapton tape (required for electrical insulation from the high voltage) and thermal paste is approximately half of the height of the collector plate. In this setup, the heat transfer between the hot collector plate and the cooler air environment was also measured. As shown in Figure 5, the single device achieves a maximum temperature drop of  $4.1^{\circ}\text{C}$  with an applied voltage of  $-1.35\text{ kV}$ . The electrically induced thermal effects (Joule heating) starts occurring at a corona current larger than  $\sim 7\ \mu\text{A}$  or an applied voltage greater than  $1.35\text{ kV}$ . Using the experimental results for a single device, a 2-D array of the microfabricated ionic wind pumps covering approximately  $2''$  square should be able to dissipate greater than  $2\text{ W}$  of heat using about  $1/5$  the power input as a conventional fan.

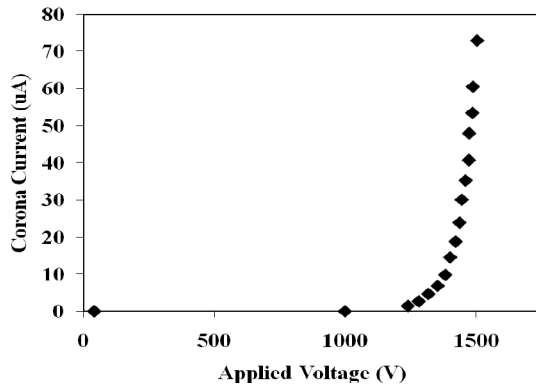


Figure 4: Experiments-based I-V curve for the microfabricated ionic wind pump device.

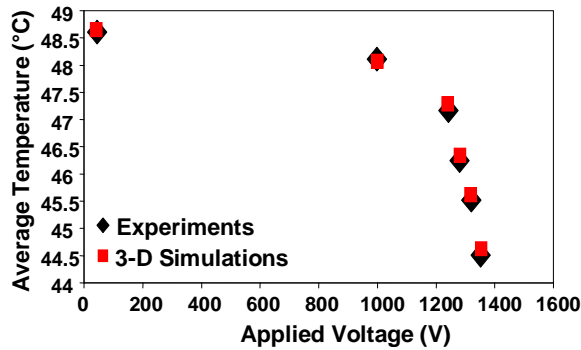


Figure 5: Average temperatures on the collector vs. applied voltage due to the ionic wind.

Infrared thermography (TVS-200EX) was also employed to record the temperature distribution around and on the surface of the device both before and after a voltage was applied to the electrodes. An infrared thermography image (Figure 6) exhibits a drop in temperature of approximately  $\sim 4^{\circ}\text{C}$  at the edge of the collector plate, similar to that observed by direct temperature measurement. The resulting current density for this device was  $8.9\text{ A/m}^2$ , and its electrical power consumption was less than  $9.3\text{ mW}$ , which is significantly lower than previously reported studies [5], [6].

FLOTAN CFD ANSYS™ was used to computationally simulate the jet impingement phenomenon of air from emitter to collector and resulting cooling effects of the device. First to verify the finite element model, a single element device using input

parameters and a design configuration as reported in [5] was simulated. For this structure, an emitting tip was located above one collecting electrode. Their experiments revealed an average heat transfer coefficient of  $63.7\text{ W/m}^2\text{K}$  (considering a natural convection coefficient of  $\sim 10\text{ W/m}^2\text{K}$ ), and an experimentally derived total heat removal rate of  $\sim 1.54\text{ W}$  ( $Q$  is low since only a single element was tested). Using the same design parameters, the simulation presented herein revealed a heat transfer coefficient of  $63.5\text{ W/m}^2\text{K}$  and a calculated heat removal rate using equation (5) of  $1.57\text{ W}$ . Clearly, the simulation results match the published data closely, providing confidence in the modeling efforts.

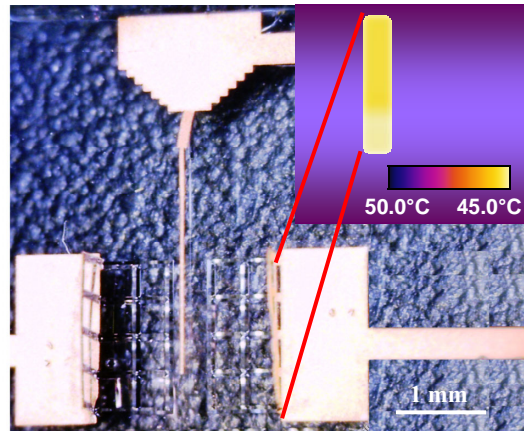


Figure 6: Microscope and corresponding infrared images (inset) of a single element ionic wind pump device. The purple hue suggests the surrounding area is approximately  $50^{\circ}\text{C}$  while the edge of the collector plate is cooled by approximately  $4 - 5$  degrees during operation of the device.

Figure 5 shows the simulation results for the device described herein and characterized experimentally. The simulated average collector plate temperature compares favorably to the temperature obtained from the thermocouple measurement. As an example, the temperature distribution on a single collector determined from these simulations is shown in Figure 7. Using the average heat transfer coefficient on this collector as outputted by the simulation software ( $3.1075 \times 10^3\text{ W/m}^2\text{-K}$ ), the total heat removal was calculated to be  $\sim 190\text{ mW}$  by applying Newton's law of cooling, corresponding to a COP of 20.5. For a comparable simulation in which a solid collector plate was modeled (i.e. no grid structure), the total heat removal was only  $134\text{ mW}$ , demonstrating the enhancement obtained using a grid configuration.

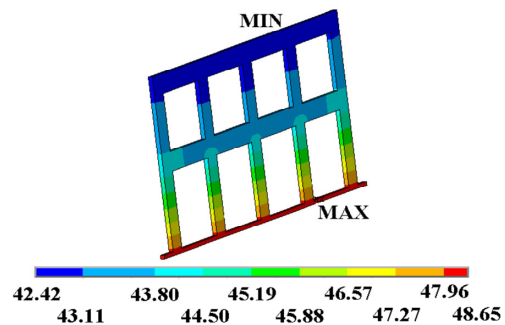


Figure 7: Temperature profile (in  $^{\circ}\text{C}$ ) of a single collector plate on which a jet of air is impinging (corresponding to an applied voltage

of 1.35 kV) using a 3-D ANSYS<sup>TM</sup> thermal/fluids simulation. The bottom boundary of the collector plate is set at the measured temperature, and ambient air impinges on all sides, leading to a cooling effect.

COMSOL Multiphysics<sup>TM</sup> was additionally employed to computationally explore the effects of a two-dimensional collector-emitter configuration on the electrohydrodynamic phenomenon, the flow field and resulting cooling effects. Note that the effect of the grid structure was not investigated. Figure 8 illustrates the velocity vectors in the flow field (shown as arrows); and the temperature field for four cases: a) no ionic wind; b) emitter located along the midline of the collector; c) emitter located one-quarter of the distance between boundaries; and d) emitter located one-eighth of the distance between boundaries. Jet impingement from emitter to collector is clearly demonstrated.

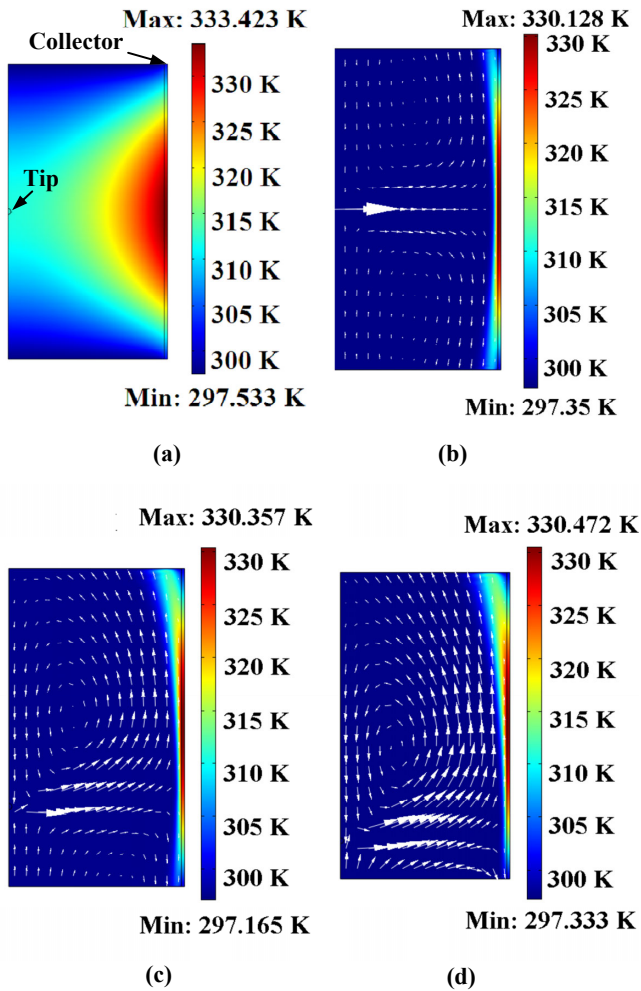


Figure 8: COMSOL Multiphysics<sup>TM</sup>-based 2-dimensional (2D) electrohydrodynamic simulations (top view) demonstrating different temperature distributions and velocity flow fields. (a) Ionic wind is turned off. (b) Emitter location is in the middle of the left boundary. (c) Emitter location is located at one-quarter of the length of the left boundary. (d) Emitter location is located at one-eighth of the length of the left boundary.

Moreover, the flow field and resulting heat transfer are significantly influenced by the location of the emitter tip. The temperature reduction due to ionic cooling demonstrated in Figures 8.b, 8.c and 8.d are relatively equal (approximately 3°C maximum). However, there is an increasing average  $y$ -velocity for the arrangements depicted in Figures 8.b (zero  $y$ -velocity), 8.c and 8.d. Thus, the un-symmetric emitter position will generate higher velocities in  $y$ -direction, which is particularly important once an array structure is employed to avoid recirculation of warmed air. The discrepancy between the temperature drops exhibited by the simulation (less than 3°C) and experimental (greater than 4°C) results is likely due to the fact cooling is enhanced by the presence of the collector grid structure studied experimentally but which was not modeled for this particular computational investigation.

## CONCLUSIONS AND FUTURE WORK

This work demonstrates an innovative and advanced microfabricated air-cooling technology that employs an electrohydrodynamic corona discharge (i.e. ionic wind pump) for efficient heat removal from electronic components and for thermal management applications. The microfabricated ionic wind pump-based cooling device also generates zero noise; contains no moving parts; boasts a low weight, volume and cost; and uses comparatively simple technologies. Moreover, this “active heat sink” can be scaled for either highly localized hot-spot cooling or integrated onto a larger thermal-exchange surface to enhance heat transfer. Using optimized designs with different configurations, a microfabricated ionic wind pump device could then be employed in a three-dimensional array for use in larger-scale microchip cooling applications and enhanced thermal spreaders, which are typically found in mobile cell phones and ultrathin laptops. Experimental and computational work is ongoing to further optimize designs.

## REFERENCES

- [1] A. Majumdar, “Thermoelectric Devices – Helping Chips to Keep Their Cool”, *Nature Nanotechnology*, 4, pp. 214 – 215 (2009).
- [2] E. N. Wang, L. Zhang, L. Jiang, J.-M. Koo, J. G. Maveety, E. A. Sanchez, K. E. Goodson, and T. W. Kenny, “Micromachined Jets for Liquid Impingement Cooling of VLSI Chips”, *Journal of Microelectromechanical Systems*, 13-5, pp. 833 – 842 (2004).
- [3] A. Ongkodjojo, D. Li, R. C. Roberts, Q. Liu, and N. C. Tien, “Modeling and Measurement of Microfabricated Corona Discharge Structures”, *Proceedings of the 3<sup>rd</sup> IEEE International Conference on Nano/Micro Engineered and Molecular Systems*, Sanya, China, 1/6-9/08 (2008), pp. 932 – 937.
- [4] M. Robinson, “Movement of Air in the Electronic Wind of Corona Discharge”, *AIEE Transactions*, 80, pp. 143 – 150 (1961).
- [5] C.-P. Hsu, N. E. Jewell-Larsen, I. A. Krichtafovitch, and A. V. Mamishev, “Heat-Transfer-Enhancement Measurement for Microfabricated Electrostatic Fluid Accelerators”, *Journal of Microelectromechanical Systems*, 18-1, pp. 111 – 118 (2009).
- [6] R.-T. Huang, W.-J. Sheu, and C.-C. Wang, “Heat Transfer Enhancement by Needle-Arrayed Electrodes – An EHD Integrated Cooling System”, *Energy Conversion and Management*, 50, pp. 1789 – 1796 (2009).

## CONTACT

\*A. Ongkodjojo, tel: +1-216-368-6775; axo50@case.edu

# MATERIAL DISTRIBUTION DESIGN FOR A PIEZOELECTRIC ENERGY HARVESTER DISPLAYING GEOMETRIC NONLINEARITY

M.A. Philippine<sup>1\*</sup>, C.-F. Chiang, J. Salvia, C.M. Jha, S. Yoneoka, T.W. Kenny

<sup>1</sup>Stanford University, Stanford, California, USA

## ABSTRACT

The optimal use of the piezoelectric for a cantilevered vibrational piezoelectric energy harvester is achieved if the stress is uniform, which can be approached by departing from a simple rectangular-shaped beam. A material distribution algorithm (BESO) is implemented in ANSYS to obtain designs providing a 20% theoretical increase in power output while maintaining the same maximum stress and less than 5% change in resonant frequency compared to a rectangular beam. Geometric nonlinearities are included in the finite element model of the MEMS-based energy scavenger. This need is backed by experimental observations of spring hardening. The importance of including nonlinearities in the model is reinforced by the obtention of different structures when BESO is applied with the linear and nonlinear models. The focus of this paper is on the energy harvester design, but there are applications of this method to many MEMS designs.

## INTRODUCTION

Simple mechanical structures are commonly employed by MEMS designers; however, these shapes often perform suboptimally. For example, rectangular suspensions [1] and folded beam springs [2] allow for simple device design but may suffer from stress or current concentrations which can limit performance. In this paper, a computational material distribution algorithm is used for the mechanical design of a piezoelectric vibrational energy harvester.

As will be shown in the second section of the theory, this cantilevered device has higher power output levels when the stress in the piezoelectric layer is uniformly distributed. This can be achieved by redesigning the in-plane beam topology using the BESO (Bidirectional Evolutionary Structural Optimization) material distribution algorithm. The algorithm depends on the finite element modeling of the structure, which can take into account the device's stress stiffening behavior.

## THEORY

### Harvester Power Output

The piezoelectric energy scavengers shown in Fig. 1 are intended to respond to vibrations of a car engine near 100 Hz. The power output of a piezoelectric vibrational harvester with a resistive load is given by the following expression [3]:

$$P = \frac{RC_b^2}{2k_2^2\omega^2} \frac{\left(\frac{2c_p d_{31} t_p}{a\epsilon}\right) A_m^2}{(4\zeta^2 + k_{31}^2)(RC_b\omega)^2 + (4\zeta k_{31}^2)(RC_b\omega) + 4\zeta^2} \quad (1)$$

The elasticity constant  $c_p$ , the piezoelectric coefficient  $d_{31}$  and the electrical permittivity  $\epsilon$  are material parameters. The damping ratio  $\zeta$ , the coupling coefficient  $k_{31}$ , the wiring  $a$ , the Laplace transform of input vibrations in terms of acceleration  $A_m$ , and the beam thickness  $t_p$  are system properties, and are relatively unaffected by in-plane geometric design changes. The optimal resistance of the circuit element  $R_{opt}$ , the capacitance across the piezoelectric layer  $C_b$ , the resonant frequency of the device  $\omega$ , the average strain in the piezoelectric layer  $S_{avg}$ , and the ratio  $k_2$  of the

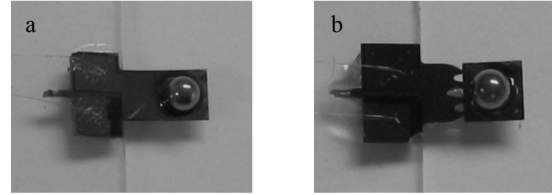


Figure 1: Picture of a) a typical rectangular structure and of b) a structure designed using the BESO material distribution method and a linear finite element model. Dimensions close to those shown in Figure 2 were used for both devices.

Table 1: Material Properties

Parameter	Symbol	Value
elasticity constant	$c_p$	170 GPa
piezoelectric coefficient	$d_{31}$	2 pC/N
electrical permittivity	$\epsilon$	$10 \times 8.85$ pF/m

Table 2: System Properties

Parameter	Symbol	Value
damping ratio	$\zeta$	.02
coupling coefficient	$k_{31}$	.1221
wiring	$a$	1
acceleration	$A_m$	4.905 m/s <sup>2</sup>
beam thickness	$t_p$	20 $\mu$ m

Table 3: System Parameters

Parameter	Symbol
optimal circuit element resistance	$R_{opt}$
capacitance across piezoelectric layer	$C_b$
resonant frequency	$\omega$
average strain in piezoelectric layer	$S_{avg}$
ratio of beam's end displacement to $S_{avg}$	$k_2$
beam surface area	$SA$

beam's end displacement to  $S_{avg}$ , are parameters that are direct functions of changes in the geometric design. These parameters and their values are summarized in Tables 1, 2, and 3.

The optimal resistance can be calculated from:

$$R_{opt} = \frac{2\zeta}{C_b\omega\sqrt{4\zeta^2 + k_{31}^2}} \quad (2)$$

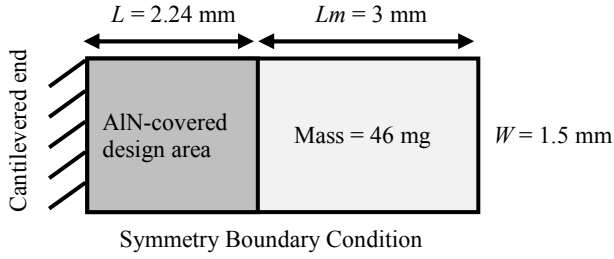


Figure 2: Drawing with dimensions and boundary conditions of sample device used throughout. Thickness of Si beam is 20  $\mu\text{m}$ , thickness of AlN is 1  $\mu\text{m}$ . Subject to out-of-plane accelerations.

The capacitance across the piezoelectric layer is:

$$C_b = \frac{a^2 \varepsilon^* SA}{t_p} \quad (3)$$

where  $SA$  is the surface area of the design area, which is coincident with the area covered by the piezoelectric film.

In S. Roundy (2003) [3], the resonant frequency, the average strain, and the beam's end displacement are calculated using standard beam theory, which does not capture the nonlinear behavior of these devices. Here, these parameters are obtained from a finite element model that will be described in detail in a later section.

### Geometry-dependent power output

In the past, optimizations have been conducted on circuit design, piezoelectric configurations, relative device dimensions, and electromechanical coupling properties [3] [4] for example. The focus here is on mechanical design. In particular, as shown in Fig. 2, the design area consists of the area cantilevered on the left and attached to the mass on the right. The thicknesses of the structural and piezoelectric layers remain unchanged after redesign. From an initial rectangular area, topology design consists of the introduction of holes in the structure, as well as the determination of the shape and dimensions of those holes and of the structure's boundaries.

The material properties are not dependent on topology design, and it is assumed that the system properties have a relatively weak dependence on topology. In addition, if linear beam theory is used as a first approximation for this derivation, the average strain to vertical displacement parameter  $k_2$  is given by:

$$k_2 = \frac{1}{\omega^2 S_{avg}} \frac{F_{mass}}{m} \quad (4)$$

Where  $F_{mass}$  is the force on the beam due to the end mass, and  $m$  the mass itself.

The power output is then roughly proportional to the device frequency, the piezoelectric surface area, and the square of the average strain in the piezoelectric layer:

$$P \propto (\omega_n)(SA)(S_{avg})^2 \quad (5)$$

Thus, given an operating frequency, and assuming that the effect from increasing the average strain dominates the effect from

decreasing the surface area, the problem of increasing the power output is roughly equivalent to that of increasing the average strain in the piezoelectric layer. The maximum stress in that layer should have the same value for all devices being compared, and is set by material strength considerations. An optimal power output is therefore achieved for a uniform stress distribution across the piezoelectric layer.

### Geometric Nonlinearities

Geometric nonlinear behavior is expected from thin plates subjected to large displacements [5]. The in-plane strains cause an out-of plane spring hardening, resulting in nonlinear kinematic relations.

### The Material Distribution Algorithm

The BESO [6] material distribution algorithm has been implemented using the ANSYS parametric design language (APDL). The method distributes material in a design area such that as the algorithm advances, stress is increasingly uniform throughout that area. BESO requires an initial guess structure, which is the simple rectangle in this case. The guess structure is discretized, and its response to an input acceleration is found using the finite element method. In general, the elements within the design area with the lowest strain energies are deactivated, yielding a new structure. The stiffness matrix multiplier for deactivated elements is  $10^{-6}$ . Deactivated elements contribute no mass to the structure. In later iterations, the response to the same input acceleration is found for the structure obtained in the previous iteration. Elements with the lowest strain energies are deactivated, while previously deactivated elements around those with the highest strain energies are reactivated. In addition, the algorithm has been implemented to prevent checker-boarding, and to enhance convergence based on previous iterations.

## RESULTS

### Piezoelectric Energy Scavenger

The energy scavenger shown in Fig. 1a and Fig. 2 is a cantilevered silicon beam, with an area covered with a 1  $\mu\text{m}$  AlN piezoelectric film, and an area covered by a mass. The scavenger is designed to operate around 100 Hz, and dimensions are shown in Fig. 2.

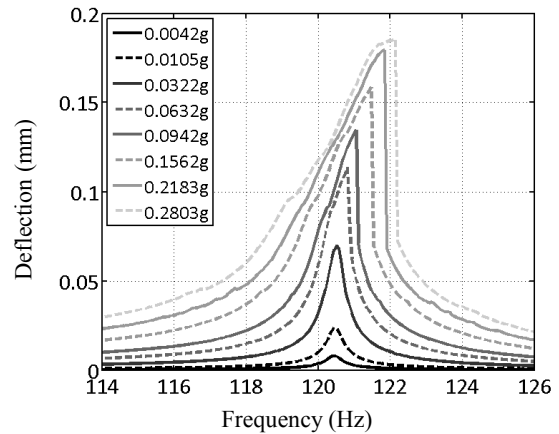


Figure 3: Experimental nonlinear frequency response of a typical device for a range of accelerations. Deflection is measured at center of width, at  $x = 2.24$  mm using laser Doppler velocimetry (LDV).



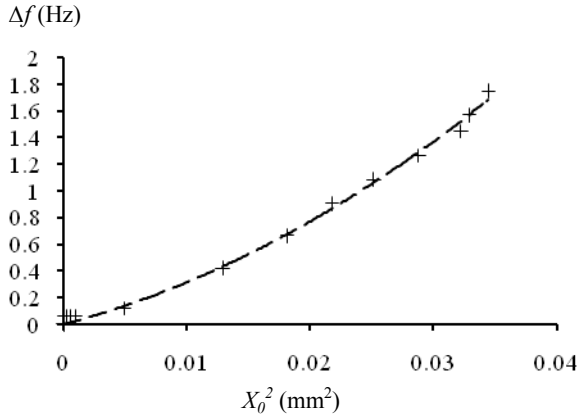


Figure 4: Measured frequency shift plotted against the square of the maximum amplitude at the peak oscillation frequency. The dotted line is the quadratic fit to the experimental data such that  $\Delta f = 713 (X_0^2)^2 + 24 (X_0^2)$ , where  $\Delta f = \Delta\omega/2\pi$ , and  $X_0$  is in millimeters.

### Device Nonlinearities

Figure 3 shows the experimental nonlinear frequency response of a typical device. The spring hardening observed is typical for thin beams subjected to large displacements [5]. These deformations are typical of many vibration-based scavenging devices. Stresses obtained from a linear model are artificially high. For example, if the structure considered in this paper is subjected to 0.5 g of acceleration, and a quality factor of  $Q = 250$  is assumed, the linear theory would predict the average stress in the piezoelectric layer to be 23% higher than the one obtained using a more accurate nonlinear model. In addition, the stress distributions due to linear deformations differ from those created from nonlinear deformations; a nonlinear model should be used for stress-based design.

### Modeling nonlinearities

An attempt was made to model the device nonlinearities using the theory presented by V. Kaajakari [7]. In that theory, it is assumed that the following relationship holds:

$$\Delta\omega = \omega_0' - \omega_0 = \kappa \omega_0 X_0^2 \quad (6)$$

where  $\omega_0'$  is the peak nonlinear oscillation frequency for a given input acceleration,  $\omega_0$  is the linear resonant frequency,  $\Delta\omega$  is the peak frequency shift,  $\kappa$  is a proportionality factor, and  $X_0$  is the maximum amplitude at the peak oscillation frequency. However, as shown in Fig. 4, the harvester peak frequency shift varies quadratically with  $X_0^2$ , not linearly. This may indicate that in addition to typical stress stiffening there may also be a more complex quality factor dependence on oscillation amplitude.

Although a complete model of the nonlinear response of the harvester has not yet been achieved, the frequency shift can easily be attributed to a stress stiffening effect. A finite element model of the harvester was implemented using 4-noded shell elements with a 0.05 mm size, and silicon material properties. As shown in Fig. 2, a clamped boundary condition is applied on the left edge, a symmetry boundary condition on the bottom edge, and mass elements are added in the mass area. The geometric nonlinearities

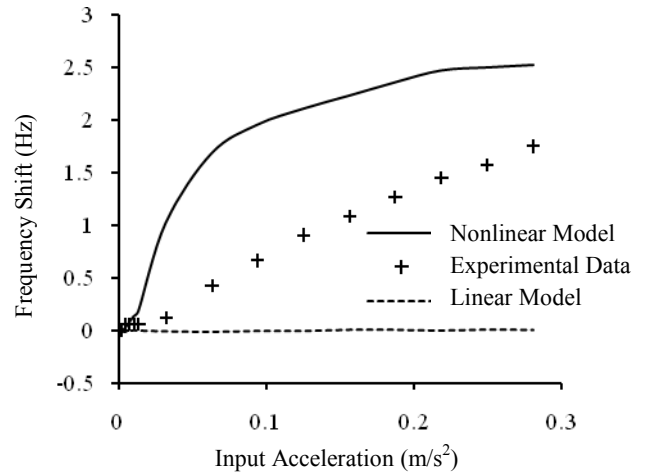


Figure 5: Estimated modeled frequency shifts and experimentally measured frequency shifts plotted against input acceleration. Estimated modeled frequency shifts are based on an equivalent stiffness and on equation 7. The model that includes geometric nonlinearities supplies a frequency shift of the correct order of magnitude but does not model the acceleration dependence well.

are modeled by turning on the NLGEOM option in ANSYS and by applying the load incrementally using approximately 300 substeps.

An equivalent stiffness is defined as the ratio of the input forcing to the maximum static deflection at the in-plane center of the mass. The input forcing is defined as  $F = maQ$  where the mass  $m = 26.4$  mg is an effective mass such that the resonant frequency found from a linear eigenfrequency analysis corresponds to the experimentally measured small displacement frequency. The effective mass compensates for the fabrication uncertainties and for the fact that although the mass is modeled as being distributed over the entire mass area, it is actually a sphere glued to a smaller area. The quality factors were chosen such that both models would predict that the deflection at  $L = 2.24$  mm be equal to the experimental deflection at that same location. As a result, the models provide information regarding the amount of forcing required to deflect the device by a certain amount; they provide an equivalent stiffness.

A precise peak oscillation frequency cannot be found from an equivalent stiffness since the stiffness is a function of amplitude during the oscillation. However, a rough estimate of the shift in peak oscillation frequency due to the stiffening can be obtained by using the following expression:

$$\Delta f = \frac{1}{2\pi} \frac{1}{\sqrt{m}} (\sqrt{k_1} - \sqrt{k_2}) \quad (7)$$

where  $\Delta f$  is the frequency shift over the acceleration range considered, and  $k_1$  and  $k_2$  are the equivalent stiffness values at the beginning and end of the acceleration range respectively. Figure 5 compares the frequency shifts found from the equivalent stiffness values obtained with both the linear and nonlinear finite element models and the experimentally measured frequency shifts. As expected, the frequency shift predicted by the linear model is null since the equivalent stiffness is independent of input forcing, while stiffening is predicted in the nonlinear case. The nonlinear model

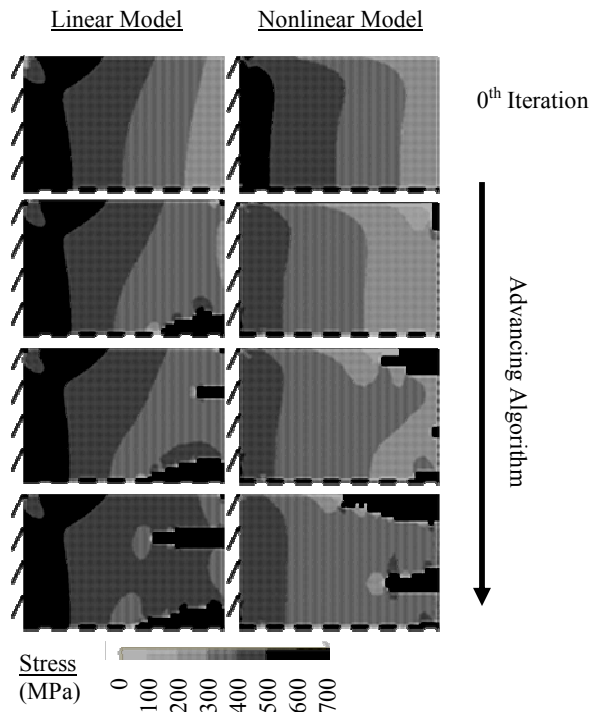


Figure 6: Description of the BESO material distribution algorithm. Stress distribution plots for AlN-covered design areas as the algorithm advances. Results from both linear and nonlinear models are shown. Cantilevered ends on left side and symmetry lines at bottom are shown on each plot. Mass areas are not included. Dark areas are those where material has been removed. Results demonstrate how difference between linear and nonlinear solutions is related to differences in stress distributions.

predicts a maximum frequency shift of 2.5 Hz at an input acceleration of  $0.2803 \text{ m/s}^2$ , which is on the same order of magnitude as the experimentally observed 1.7 Hz shift at that same acceleration. The stress stiffening phenomenon can therefore be considered to be the major cause of the nonlinear behavior observed, although a full model has not yet been achieved.

### BESO Material Distribution

The BESO material distribution algorithm has been implemented for both the linear and nonlinear finite element mechanical models described previously. When nonlinear modeling is used, the resulting structure converges towards a trapezoidal shape with a small central hole. In contrast, if linear modeling is used, the algorithm favors central holes. This is a direct consequence of the differences in stress distributions shown in Fig. 6, and of the logic of the algorithm, removing material from the lowest stressed areas. Preliminary implementations of the BESO algorithm result in a 20% theoretical increase in power output for an unchanged maximum stress and a frequency that

remains within 5% of the original one.

### CONCLUSIONS

A material distribution algorithm has been applied to a piezoelectric vibrational energy scavenger. By departing from the default rectangular beam structure, and allowing the algorithm to add holes of various shapes and sizes in the structure, a more uniformly distributed stress is obtained in the piezoelectric layer. This results in a device that theoretically has a higher power output than a rectangular structure with an equivalent footprint and maximum stress value.

Geometric nonlinearities have been observed experimentally, and are explained in part by the large deformations being imposed by a large mass on a thin beam. Nonlinear finite element modeling has partially captured this phenomenon. The nonlinearities were shown to have a significant effect on the BESO material distribution algorithm since the stress distribution is different than that in a linear model. Obtaining an accurate nonlinear model will be essential in designing a high-performance mechanical structure.

### REFERENCES

- [1] C.M. Jha, M.A. Hopcroft, S.A. Chandorkar, J. Salvia, M. Agarwal, R.N. Candler, R. Melamud, B. Kim, T.W. Kenny, "Thermal Isolation of Encapsulated MEMS Resonators". *Journal of Microelectromechanical Systems*, Vol. 17, No. 1, (2008).
- [2] R. Legtenberg, A.W. Groeneveld, M. Elwenspoek, "Comb-drive Actuators for Large Displacements", *J. Micromech. MicroEng.*, 6, pp. 320-329, (1996).
- [3] S. Roundy, "A Piezoelectric Vibration Based Generator for Wireless Electronics", *Smart Materials and Structures*, 13, pp. 1131-1142 (2003).
- [4] S.R. Anton and H.A. Sodano, "A Review of power harvesting using piezoelectric materials (2003-2006)", *Smart Materials and Structures*, 16, R1-R21, (2007).
- [5] P. Malatkar, *Nonlinear Vibrations of Cantilever Beams and Plates*, PhD thesis, Virginia Polytechnic Institute (2003)
- [6] O.M. Querin and G.P. Steven, "Evolutionary Structural Optimization (ESO) using a Bidirectional Algorithm", *Eng. Computations*. Vol. 15 No. 8, (1998), pp. 1031-1048
- [7] V. Kaajakari, T. Mattila, A. Oja, and H. Seppä, "Nonlinear limits for single-crystal silicon microresonators", *IEEE Journal of Microelectromechanical Systems*, Vol. 13, No. 5, pp. 715-724, (2004)

### ACKNOWLEDGEMENTS

This material is based upon work supported under a National Science Foundation Graduate Research Fellowship. The project was also funded by Audi, a premium brand of Volkswagen Group and by the Electronics Research Laboratory, the R&D division of Volkswagen Group of America.

### CONTACT INFORMATION

\*M.A. Philippine, tel: +1-650-823-3811; mandyp@stanford.edu

# MICROMACHINED THICK-FILM COPPER POWER INDUCTORS AND TRANSFORMERS FOR INTEGRATED POWER CONVERTERS

C.D. Meyer<sup>1,2\*</sup>, S.S. Bedair<sup>1</sup>, B.C. Morgan<sup>1</sup>, and D.P. Arnold<sup>2</sup>

<sup>1</sup>U.S. Army Research Laboratory, Adelphi, Maryland, USA

<sup>2</sup>Interdisciplinary Microsystems Group, Gainesville, Florida, USA

## ABSTRACT

This work presents surface-micromachined, air-core, power inductors and transformers for next-generation, integrated, high-frequency switching power converters operating in the 50–500 MHz frequency range. The high-performance devices are realized by a multilayer, copper electroforming process that enables low resistance, three-dimensional, free-standing structures for high mutual inductance coupling and low parasitic capacitance. Three fabricated inductor designs are presented with areas 1–4 mm<sup>2</sup>, inductance densities > 100 nH/mm<sup>2</sup>, and quality factors up to 21. Three transformer designs are also presented, all with areas 2.25 mm<sup>2</sup> and primary inductances of 47 nH but with variable secondary inductances to yield voltage gains from 1:1 up to 1:3.5.

## INTRODUCTION

Power converters will have an essential role in empowering mobile microsystems by providing efficient interoperation of various subsystems—batteries, energy harvesters, actuators, and sensors—but must do so within diminishing size and weight constraints [1]. The miniaturization of today's power converters is typically limited by the requirement for high-efficiency passives, e.g. inductors with high quality factors [2], which often entails the use of large external components. Newer conversion architectures have pushed switching frequencies up into the multimegahertz realm and have reduced the passive size requirement [3]. For instance, a 233 MHz buck dc-dc converter has demonstrated 80–87% efficiency utilizing four 4 nH off-chip air-core inductors [2]. However, many magnetic materials exhibit prohibitively large magnetic core losses above several MHz [4], while air-core GHz RF passives typically have inductances and quality factors that are still too low for efficient conversion [2].

In [5] we presented batch-fabricated, micromachined air-core inductors and transformers to bridge this frequency gap with high quality factors and efficiencies in the 100–500 MHz frequency range. The surface-micromachined, multilevel metallization process enabled 10- $\mu$ m-thick copper windings for low resistance and enabled two-layer stacking of windings for enhanced mutual coupling and higher inductance density. The low temperature of all the processing steps makes it feasible to consider post-CMOS integration of the inductors on silicon power electronic circuits.

We now extend the study of these devices by introducing 1) the patterning of the interlayer dielectric into support posts for reduction of parasitic capacitance, resulting in up to ~20% improvement in quality factors and operating frequencies, and 2) the design of transformers of various turns ratios using the same fabrication process. The image of one such fabricated inductor in Fig. 1 highlights the freestanding, stacked spiral structure that is common to both the inductors and transformers of this work. Each transformer, such as that shown in Fig. 2, is comprised of two air-core inductors with windings that are nested and interleaved for strong mutual magnetic flux coupling. Primary and secondary coils are each stacked for increased inductance densities (>300 nH/mm<sup>2</sup>) in voltage-gain configurations. All devices were fabricated on Pyrex substrates for characterization without substrate losses. Planar contact with a 10  $\Omega$ -cm silicon wafer is expected to decrease quality factors and efficiencies by 10–20% [5].

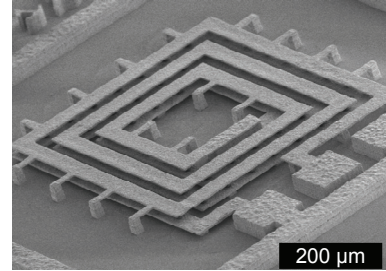


Figure 1: SEM image of a surface-micromachined, stacked, copper spiral inductor.

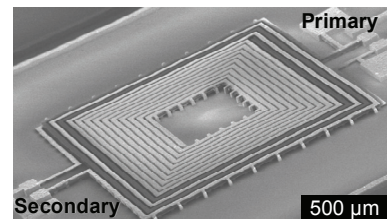


Figure 2: SEM view of a step-up transformer. Secondary winding is charged to display a lighter shade than the dark-shaded primary winding.

## DESIGN CONSIDERATIONS

### Inductors

The inductors of this work were designed with an emphasis on yielding maximum quality factor, defined as the frequency-dependent ratio of reactance to resistance,  $Q = \text{Im}\{Z\}/\text{Re}\{Z\}$ . The quality factor of an inductor provides a figure of merit that quantifies the efficiency of magnetic energy storage available to the circuit [6].

In order to roughly optimize inductor geometry, analytic expressions [7] were used to estimate the ratio of dc inductance to resistance,  $L_{dc}/R_{dc}$ , which at low frequencies is proportional to  $Q$ . From inspection of trends for inductors with ~100 nH and area ~1 mm<sup>2</sup>, maximum  $L_{dc}/R_{dc}$  was found to occur with a trace width of ~50  $\mu$ m and with minimum lateral spacing between traces, which for the process presented here was set at 10  $\mu$ m. With a given fixed outer dimension,  $L_{dc}/R_{dc}$  generally increased with the number of inner turns but reached its maximum value in all test cases when the number of turns was ~80% of the space-constrained limit due to the reduced coupling of the smaller inner turns. For this reason, the number of turns was not maximized, and the central 10–20% area of each inductor was left empty.

FastHenry inductance simulation software was used to determine the effect of vertical spacing between upper and lower winding layers on the mutual inductance of the inductors. Simulations indicated that the inductance asymptotically approached perfect vertical coupling (4x the single layer value) with a gap less than 1% of the outer dimension of the device. The devices of this work—with outer dimensions  $\geq$  1 mm—therefore used an interlayer spacing of 10  $\mu$ m since a shorter gap would not significantly improve the inductance of the devices but would detrimentally increase parasitic capacitance.

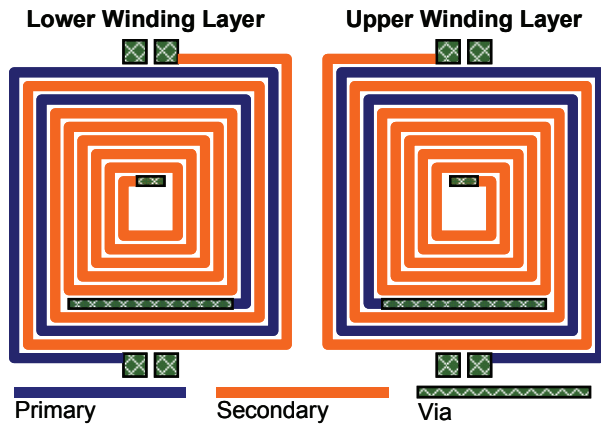


Figure 3: Layout of step-up transformer showing interleaved and nested wiring of primary and secondary coils for mutual coupling.

### Transformers

The design of the transformers was primarily focused on enabling a non-unity turns ratio, which required maximizing inductance density. Since a turns ratio of  $1:n$  requires an inductance ratio of  $L_2 = n^2 L_1$ , the maximum achievable turns ratio can be severely limited by size constraints if some minimum primary side inductance is required. A narrower trace width of  $30\ \mu\text{m}$  was chosen to allow more turns and to increase the inductance density of these transformers compared to the inductors at the expense of greater dc resistance.

The transformer layout—shown in Fig. 3 for a step-up transformer—employed a hybrid winding scheme in which the outer two turns of the primary and the secondary were interleaved on both the upper and lower winding layers while the remainder of the secondary was nested in the inner turns. This arrangement allowed transformers with non-unity turns ratios to leverage the strong vertical magnetic flux coupling for increased primary, secondary, and mutual inductances. The turns ratio was set by the number of inner turns. A unity-gain isolation transformer was obtained by omitting any inner turns; a 1:2.5 ratio was obtained with five inner secondary turns on each of the two layers; and a 1:3.5 ratio was obtained with nine inner secondary turns per layer.

### FABRICATION

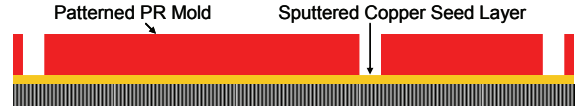
The devices were fabricated on Pyrex wafers using a thick-film copper electroforming process capable of producing three-dimensional structures. This process consisted of two stages: 1) the layer-by-layer building up of the structure by consecutively electroplating copper through  $10\text{-}\mu\text{m}$ -thick, patterned photoresist molds, as in Figs. 4a & 4b; and 2) the release of the structure by removal of the photoresist molds and seed layers, as in Fig. 4c.

While much of the photoresist mold was removed as sacrificial material during the release stage, the use of photoresist developer as the etchant enabled portions of the mold to remain as structural elements in the final, released devices. This photoresist was used to physically and electrically separate the upper from the lower winding layers. Compared to the continuous interlayer photoresist used previously in [5] (Fig. 5a), the devices in this work featured patterned photoresist support posts (Fig. 5b) for decreased parasitic capacitance. The posts were placed  $40\text{--}100\ \mu\text{m}$  apart with  $20\ \mu\text{m} \times 20\ \mu\text{m}$  footprints, corresponding to approximately 90% removal of the interlayer photoresist.

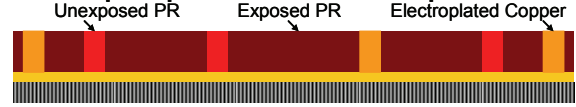
In building up each layer, as illustrated in Fig. 4a, AZ9245 positive-tone photoresist was spun and patterned over a thin, sputtered copper seed to create an electroplating mold. After

### a) Per-Layer Steps

#### 1. Deposit thin seed and pattern mold.



#### 2. Re-expose photoresist and electroplate.



### b) Built-Up Structure



### c) Released Structure

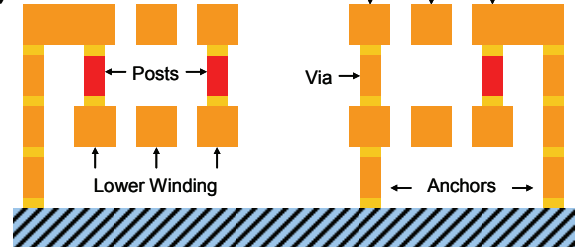


Figure 4: Fabrication process consisting of a) electroplating copper through photoresist molds to construct each layer of b) the four-layer built-up structure, c) which is then released in alternations of photoresist developer and copper etchant.

patterning, the mold was UV-exposed a second time with the support post areas masked from exposure. The mold was then filled with copper using timed electroplating in a copper sulfate bath. These molding and electroplating steps were repeated four times to obtain a layered structure, depicted in Fig. 4b, with each successive copper seed sputtered directly on top of the previous layer.

In the release stage, the exposed photoresist and copper seed layers were then consecutively removed in AZ 400K KOH-based photoresist developer and copper etchant, respectively. After four etch cycles, the final released structures were obtained as shown in Fig. 4c with two copper winding layers suspended in air above the wafer surface.

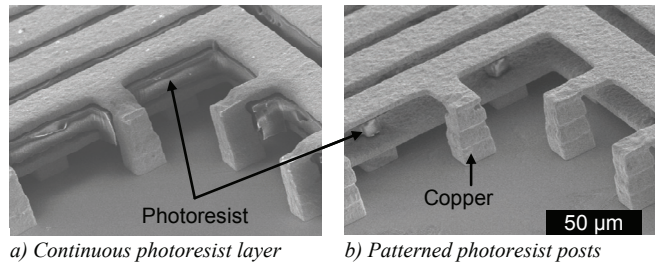


Figure 5: SEM images of device scaffolding consisting of copper anchors and photoresist support layers.

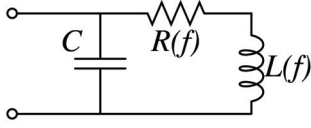


Figure 6: Frequency-dependent inductor model with shunt capacitance.

Table 1: Comparison of circuit-model shunt capacitance with patterned photoresist support posts vs. continuous interlayer photoresist.

Inductor Geometry	Model Shunt Capacitance	
	Continuous Photoresist	Patterned Posts
1.00 mm <sup>2</sup>	0.55 pF	0.39 pF
2.25 mm <sup>2</sup>	0.90 pF	0.63 pF
4.00 mm <sup>2</sup>	2.15 pF	1.34 pF

## PARASITIC CAPACITANCE MITIGATION

An inductor model was required in this work to quantify the parasitic capacitance of the inductors and to determine the performance improvement associated with the patterning of the interlayer photoresist into support posts. The inductors were modeled by a series  $RL$  circuit with parallel, shunt capacitance as shown in Fig. 6. Additionally, the  $R$  and  $L$  values were functions of frequency,  $f$ , to account for the effects of eddy current generation within the traces. The resistive and inductive elements maintain their dc values up to a certain frequency  $f_k$ , past which the value of the resistive element increases with frequency while that of the inductive element conversely decreases [8]. The frequency-dependence of the resistive elements was found to follow the form,

$$X(f) = X_{dc} \left[ 1 + \left( \frac{f}{f_k} \right)^{s_x} \right]^{o_x}, \quad (1)$$

with each occurrence of ‘ $X$ ’ replaced by ‘ $L$ ’ or ‘ $R$ ’ for inductive and resistive elements, respectively. The parameters used in Eq. (1) were obtained by a best fit of the model to the data for all three measured inductor designs:  $f_k=37.7$  MHz,  $s_R=1.24$ ,  $o_R=0.554$ ,  $s_L=2.18$ , and  $o_L=-0.0225$ .

The shunt capacitance values were extracted by fitting the circuit model to the measured data both for inductors with support posts and for those with continuous photoresist layers. As listed in Table 1, inductors with patterned support posts exhibited a 27–38% reduction in this parasitic capacitance—with the greatest reduction occurring in the largest-sized inductor. The benefit of parasitic capacitance mitigation is illustrated by the plots of inductor performance measurements in Fig. 7; a 4 mm<sup>2</sup> inductor having intermittent support posts is shown to have 26% higher self-resonant frequency and 21% higher peak quality factor than another inductor of identical dimensions except having a contiguous photoresist separation layer. All other results presented in this paper are for devices with patterned photoresist posts.

## MEASUREMENT AND CHARACTERIZATION

One- and two-port scattering parameters of the inductors and transformers, respectively, were measured through an Agilent E8361A Network Analyzer with frequency sweeps from 10 MHz to 8 GHz. The scattering parameters were then converted to impedance parameters in order to extract the measured inductances,  $\text{Im}\{Z\}/2\pi f$ , and resistances,  $\text{Re}\{Z\}$ .

### Inductors

The inductance, resistance, and quality factor were measured for each of the inductors. A summary of these performance

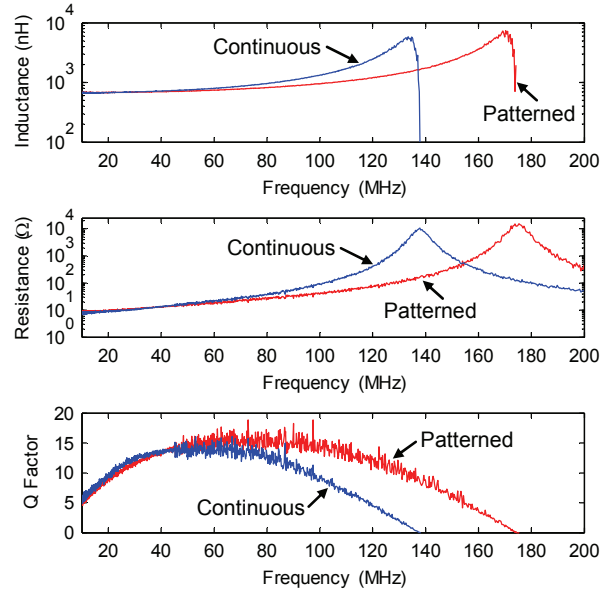


Figure 7: Plots of frequency-dependent performance characteristics of 4 mm<sup>2</sup> inductors, comparing effect of patterned vs. continuous interlayer photoresist support.

Table 2: Performance comparison of power inductors.

Inductor Comparison	Performance Characteristics					
	Area (mm <sup>2</sup> )	$L_{dc}$ (nH)	$L/Area$ (nH/mm <sup>2</sup> )	$Q_{max}$	$f@Q_{max}$ (MHz)	$R_{dc}$ ( $\Omega$ )
<i>This work, air</i>	1.00	90	90	21	400	1.6
<i>This work, air</i>	2.25	200	89	21	200	3.2
<i>This work, air</i>	4.00	675	169	16	75	8.5
<i>Park, air [9]</i>	1.69	36	21	44	1200	2.8
<i>Fukuda, NiZn [10]</i>	36	1400	39	40	5	0.67
<i>Wang, NiFe [11]</i>	5.69	160	28	6	4	0.26
<i>Sato, FeCoBN [12]</i>	21.9	370	17	15	7	-

characteristics is found in Table 2 along with results from several other works for comparison. Even without the use of magnetic materials, these inductors have significantly higher (2-8x) inductance densities and operate at higher frequencies than comparable ferromagnetic-core devices [10-12].

### Transformers

Although the low-frequency transformer inductances and resistances are readily obtained through the two-port impedance parameters [5], performance characterization requires accounting for the load. For this reason, the measured scattering parameters are transformed into  $ABCD$  parameters for modeling the effect of attaching a load to the secondary port.

While optimal efficiency can be found using only the measured scattering parameters and the expression for maximum available gain in [13], such calculation does not yield the associated voltage gains and load impedances. The matched load with which the transformer operates at maximum efficiency at each frequency is found as a function of the  $ABCD$  parameters by solving for  $Z_L$ ,

$$\left( \overline{AC} + \overline{AC} \right) \overline{Z_L}^2 + \left( \overline{BC} - \overline{BC} + \overline{AD} - \overline{AD} \right) \overline{Z_L} - \left( \overline{BD} + \overline{BD} \right) = 0. \quad (2)$$

Efficiency, defined as the real power delivered to the load in proportion to the real power input to the transformer, is then calculated as a function of  $Z_L$ :

$$Eff = \frac{\text{Re}\{Z_L\}}{\text{Re}\{(AZ_L + B)(CZ_L + D)\}}, \quad (3)$$

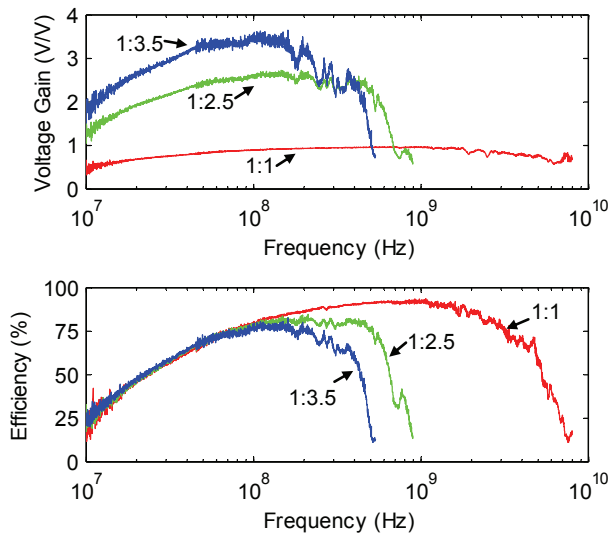


Figure 8: Predicted matched-load performance characteristics of transformers of different turns ratios.

Table 3: Performance comparison of microtransformers.

Transformer Comparison	Performance Characteristics							
	Area (mm <sup>2</sup> )	L <sub>1,dc</sub> (nH)	R <sub>1,dc</sub> (Ω)	L <sub>2,dc</sub> (nH)	R <sub>2,dc</sub> (Ω)	k	Eff (max)	Eff (50 Ω)
This work, air, 1:1	2.25	47	2.1	47	2.1	0.85	91%	84%
This work, air, 1:2.5	2.25	47	2.1	309	7.0	0.71	82%	48%
This work, air, 1:3.5	2.25	47	2.1	492	9.0	0.62	78%	35%
Yamaguchi, air [14]	7.44	70	-	65	-	0.35	67%	-
Kurata, CoFeSiB [15]	1.38	50	-	50	-	0.92	-	54%
Wang, NiFe [16]	23.73	400	0.5	400	0.5	0.93	72%	63%

which is equivalent to the expression in [13] when  $Z_L$  satisfies Eq. 2. With  $Z_L$  identified the voltage gain of the loaded transformer can be calculated from

$$G_v = \left| \frac{Z_L}{AZ_L + B} \right|. \quad (4)$$

Using the measured  $ABCD$  parameters and the values of  $Z_L$  solved from Eq. 2, the voltage gains and efficiencies of the three transformer designs were plotted in Fig. 8 for the case of maximum efficiency. While voltage gain is approximately equal to the turns ratio for the case of matched loading, it is important to note that significantly higher or lower voltage gains can be attained on the same transformer with different loads. For instance, voltage gains  $>15$  could be obtained from the 1:3.5 transformer with capacitive loads of 1–6 pF, albeit with efficiencies  $<10\%$ .

The low-frequency resistances and inductances measured from each of the transformers are summarized in Table 3 along with the maximum efficiencies, both as measured with 50-Ω loading and as projected from Eqs. 2 and 3 with matched loading. Compared to other air-core transformers [14], the devices here have demonstrated greater inductance densities, coupling coefficients, and efficiencies. Although the coupling coefficients are less, the efficiencies of these air-core transformers are also competitive with those of magnetic film devices [15, 16].

## CONCLUSION

The use of thick-film micromachining enabled air-core inductors and transformers with high performance for next-generation switched power conversion architectures operating in

the frequency range of 50–500 MHz. Strong vertical mutual coupling provided inductance densities rivaling those of thin-film magnetic devices, while dielectric removal was shown to reduce parasitic capacitance and to increase quality factors and operating frequencies.

## ACKNOWLEDGEMENTS

This work was supported in part by the US Army Research Lab Collaborative Agreement W911NF-08-2-0035.

## REFERENCES

- [1] B.C. Morgan, *et al.*, “Power Considerations for MAST Platforms,” in *Proceedings of SPIE Defense, Security, and Sensing*, to be published.
- [2] P. Hazucha, *et al.*, “A 233-MHz 80%-87% Efficient Four-Phase DC-DC Converter Utilizing Air-Core Inductors on Package,” *IEEE JSSC*, vol. 40, no. 4, pp. 838-845, 2005.
- [3] S. C. O. Mathuna, *et al.*, “Magnetics on Silicon: An Enabling Technology for Power Supply on Chip,” *IEEE TPE*, vol. 20, no. 3, pp. 585-592, 2005.
- [4] D. Flynn, *et al.*, “Characterization of Core Materials for Microscale Magnetic Components Operating in the Megahertz Frequency Range,” *IEEE TMAG*, vol. 43, no. 7, pp. 3171-3180, 2007.
- [5] C.D. Meyer, *et al.*, “High-Inductance-Density, Air-Core, Power Inductors and Transformers Designed for Operation at 100-500 MHz,” *IEEE TMAG*, to be published.
- [6] C.P. Yue and S.S. Wong, “On-Chip Spiral Inductors with Patterned Ground Shields for Si-Based RF IC’s,” *IEEE JSSC*, vol. 33, no. 5, pp. 743-752, 1998.
- [7] S.S. Mohan, *et al.*, “Simple Accurate Expressions for Planar Spiral Inductances,” *IEEE JSSC*, vol. 34, no. 10, pp. 1419-1424, 1999.
- [8] G. Antonini, *et al.*, “Internal Impedance of Conductors of Rectangular Cross Section,” *IEEE TMTT*, vol. 47, no. 7, pp. 979-985, 1999.
- [9] J.Y. Park and M.G. Allen, “Packaging-Compatible High Q Microinductors and Microfilters for Wireless Applications,” *IEEE TAP*, vol. 22, no. 2, pp. 207-213, 1999.
- [10] Y. Fukuda, *et al.*, “Planar Inductor With Ferrite Layers for DC-DC Converter,” *IEEE TMAG*, vol. 39, no. 4, pp. 2057-2061, 2003.
- [11] N. Wang, *et al.*, “High-frequency Micro-Machined Power Inductors,” *JMMM*, vol. 290-291, pp. 1347-1350, 2005.
- [12] T. Sato, *et al.*, “FeCoBN Magnetic Thin Film Inductor for MHz Switching Micro DC-DC Converters,” *T. IEE Japan*, vol. 121-D, no. 1, pp. 84-89, 2001.
- [13] K.T. Ng, *et al.*, “Substrate Effects in Monolithic RF Transformers on Silicon,” *IEEE TMTT*, vol. 50, no. 1, pp. 377-383, 2002.
- [14] K. Yamaguchi, *et al.*, “Load Characteristics of a Spiral Coil Type Thin Film Microtransformer,” *IEEE TMAG*, vol. 29, no. 6, pp. 3207-3209, 1993.
- [15] H. Kurata, *et al.*, “Study of Thin Film Micro Transformer with High Operating Frequency and Coupling Coefficient,” *IEEE TMAG Japan*, vol. 9, no. 3, pp. 90-94, 1994.
- [16] N. Wang, *et al.*, “Thin Film Microtransformer Integrated on Silicon for Signal Isolation,” *IEEE TMAG*, vol. 43, no. 6, pp. 2719-2721, 2007.

## CONTACT

\*C.D. Meyer, tel: +1-352-392-7657; toph@ufl.edu

# ACOUSTIC RESONANCE IN AN INDEPENDENT-GATE FINFET

Dana Weinstein<sup>1\*</sup> and Sunil A. Bhave<sup>2</sup>

<sup>1</sup>Massachusetts Institute of Technology, Cambridge, Massachusetts, USA

<sup>2</sup>Cornell University, Ithaca, New York, USA

## ABSTRACT

This paper demonstrates the acoustic resonance of an Independent-Gate (IG) FinFET driven with internal dielectric transduction and sensed by piezoresistive modulation of the drain current through the transistor. An acoustic resonance at 37.1 GHz is obtained with a quality factor of 560, corresponding to an  $fQ$  product of  $2.1 \times 10^{13}$ . The demonstrated hybrid NEMS-CMOS technology can provide RF CMOS circuit designers with high- $Q$  active devices operating up to mm-wave frequencies and beyond.

## INTRODUCTION

As we scale to deep sub-micron (DSM) technology, transistor unity gain frequencies increase, enabling the design of CMOS circuits for RF and mm-wave applications up to 95 GHz. However, such high-frequency CMOS transistors have limited gain, resulting in poor output power efficiency. Successful implementation of DSM CMOS in mm-wave applications therefore requires high- $Q$ , low-power components operating at high frequencies.

Another challenge facing DSM circuits is the increasing density of devices, projected to reach  $10^{11}$  devices/cm<sup>2</sup>. At such densities, clock distribution and the power consumption associated with it necessitate implementation of low-power local clocks with the potential for global synchronization. The Resonant Body Transistor (RBT) presented in this work is a fundamental building block that addresses both these challenges.

Field effect transistors (FETs) were first used for sensing mechanical motion in one of the earliest Micro Electromechanical (MEM) devices. In 1967, Nathanson et al. demonstrated the Resonant Gate Transistor (RGT), driving resonance in a gold cantilever with an air-gap capacitive electrode [1]. The RGT cantilever functioned as the gate of an air-gap transistor, with output drain current modulated by the cantilever resonant motion. This device achieved a resonance frequency of 30 kHz with quality factor of  $\sim 70$  despite the limited processing capabilities of the time. Fabrication limitations prevented the proliferation of these and other MEMS devices until the advent of silicon-based surface micromachining.

FET sensing has only recently regained momentum as a means of mechanical detection, and has been implemented in a variety of micromechanical devices. Resonant Gate Transistors similar to Nathanson's device have been demonstrated in silicon air-gap resonators up to 14 MHz [2,3]. Mechanical resonators sensed through direct elastic modulation of a transistor channel have also been demonstrated. Such devices include air gap resonators with FETs embedded in the resonator body up to 71 MHz [4], mechanical mixing in single electron transistors up to 245 MHz [5], and piezoelectric high electron mobility transistor (HEMT) channel modulation in GaN resonators up to 2 MHz [6].

## Internal Dielectric Transduction

To improve electrostatic transduction efficiency and scale MEM resonators into the GHz domain, we previously demonstrated longitudinal silicon bar resonators using a novel method to drive and sense acoustic waves in the bar. This mechanism, termed 'internal dielectric transduction' [7], incorporates thin dielectric film transducers inside the resonator body for capacitive transduction. Internal dielectrically transduced resonators have yielded acoustic resonance frequencies up to 6.2

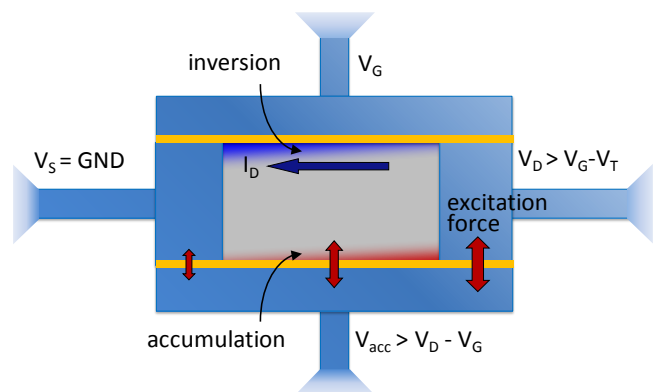
GHz [8] and frequency-quality factor products ( $fQ$ ) up to  $5.1 \times 10^{13}$  [9]. Moreover, these dielectrically transduced resonators demonstrate improved efficiency as resonance frequency increases, providing a means of scaling MEM resonators to previously unattainable frequencies. However, at multi-GHz frequencies capacitive feed-through becomes significant and prevents capacitive detection of MEM resonance without three-port mixing measurements.

Unlike capacitive sensing employed in these resonators, FET sensing can amplify the mechanical signal prior to any feed-through parasitics. Combining the benefits of FET sensing with the frequency scaling and high- $Q$  capabilities of internal dielectrically transduced resonators, the authors recently demonstrated a Resonant Body Transistor (RBT) [10] operating at 11.7 GHz with  $Q$  of over 1800. This device incorporates a field-effect transistor into the resonator body for internal amplification of the resonant signal. The best RBT geometry for optimal dielectric transduction at high frequencies is an internal dielectrically transduced longitudinal-mode resonator, with dielectric films positioned at points of maximum strain. As we scale to higher frequency, the width of the resonator decreases, eventually converging to a geometry very similar to that of Independent-Gate FinFETs [11].

## THE RESONANT BODY TRANSISTOR

### Theory

The principle of operation of the internal dielectrically transduced RBT is shown in Fig. 1. The region in light grey represents the active region of the resonator, while the blue region is highly doped. The active region near the drive gate is biased into accumulation (red), so that a large capacitive force acts across the thin dielectric film (yellow), driving longitudinal vibrations in the body. A gate voltage is applied to the opposing gate, generating an inversion channel (blue) which results in a DC drain current. At resonance, elastic waves formed in the resonator modulate the drain current both by physically changing the gate capacitance and by piezoresistive modulation of carrier mobility. The internally amplified RBT has significantly lower output impedance than capacitive detection mechanisms, simplifying impedance matching with active circuits.



**Fig. 1.** Top-view schematic showing principle of operation of a bulk-mode dielectrically transduced Resonant Body Transistor. The RBT geometry, similar to that of an IG-FinFET, incorporates FET sensing with a dielectrically transduced bar resonator.

The amplitude of vibrations of the internal dielectrically transduced RBT  $U_0|_{RBT}$  can be found in an analysis similar to [7] and has been investigated in [10]. The strain induced in the resonator piezoresistively modulates the drain current running through the inversion layer. Assuming a piezoresistive coefficient of  $\pi_{110}$  for current traveling perpendicular to the normal of elastic wave fronts along  $\langle 110 \rangle$ , the change in mobility is given by

$$\frac{d\mu_n}{\mu_n} = \pi_{110} Y \frac{\partial u}{\partial x} \Big|_{inversion} = \pi_{110} Y k_n U_0|_{RBT} \cos\left(\frac{1}{2} k_n g\right). \quad (1)$$

where  $g$  is the dielectric thickness,  $Y$  is the Young's modulus and  $k_n$  is the wave number of the  $n^{\text{th}}$  harmonic. The piezoresistive mobility modulation of Eqn. 1 generates an AC current linearly dependent on the drain current:

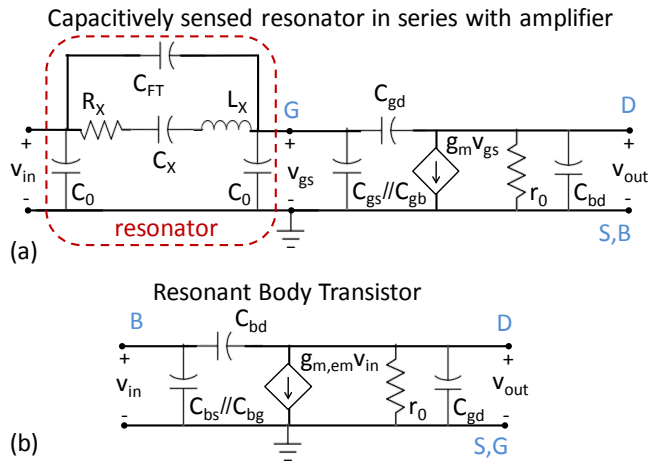
$$i_{out}|_{RBT} \approx I_D \frac{\partial \mu_n}{\mu_n} \quad (2)$$

The electromechanical transconductance is defined by

$$g_{m,em} \equiv i_{out}|_{RBT} / v_{in}. \quad (3)$$

One of the fundamental obstacles of scaling MEMS resonators to multi-GHz frequencies is the need for a sense transducer that overcomes feed-through and parasitic capacitance and provides adequate sensitivity to measure mechanical motion at those frequencies. Fig. 2(a) shows a standard Butterworth-Van Dyke (BVD) model of a capacitively transduced resonator whose output is fed into a common source amplifier. As electrostatically transduced resonators shrink in size to scale to GHz frequencies, the feed-through capacitance  $C_{FT}$  limits the minimum detectable electromechanical signal through the device. In Fig. 2(a), both the feed-through current and electromechanical current are amplified in the amplifier following the resonator, making 2-port detection impossible at high frequencies.

The linear equivalent circuit (LEC) of a dielectrically driven RBT is given in Fig. 2(b). This model differs from that of a standard MOSFET in two ways. First, the AC electrical signal is applied to the back gate (B) biased in accumulation, leaving the inversion gate (G) at a constant bias voltage. This biasing prevents the input signal from electrically modulating the inversion channel. Second, the small signal current source is not a constant function of frequency. In this model, the electromechanical transconductance  $g_{m,em}$  has a Lorentzian frequency dependence with peak amplitude defined by Eqn. 3 and a mechanical quality factor  $Q_m = 1/R_X \sqrt{L_X/C_X}$  as in the case of the standard BVD model. The capacitive feed-through in the RBT is just the parasitic



**Fig. 2.** Small signal model of (a) a capacitively sensed resonator with an external single-stage amplifier, and (b) a Resonant Body Transistor, with resonance incorporated into  $g_{m,em}$ .

$C_{bg}$ ,  $C_{bs}$ , and  $C_{bd}$ . Due to the symmetry of the RBT,  $C_{bs}$  and  $C_{bd}$  are equivalent to  $C_{gs}$  and  $C_{gd}$  found in the amplifier of Fig. 2(a). Moreover, the feed-through component  $C_{bg}$  in the fully depleted RBT, equal in magnitude to  $C_{FT}$ , is not amplified in any way. Therefore, integration of FET sensing into the acoustic resonator enables amplification of the electromechanical signal without amplification of electrical feed-through.

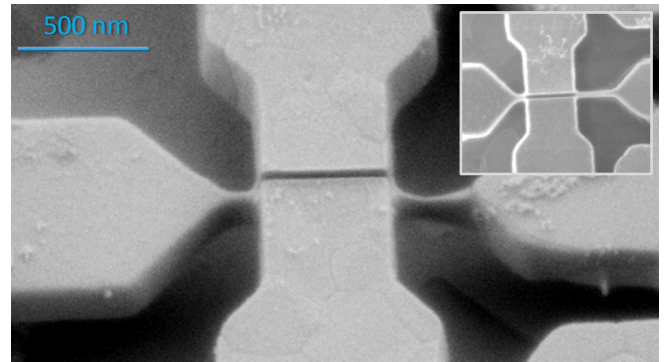
### Independent-Gate FinFET Resonance

Many three-dimensional transistors such as nanowire FET and tri-gate and independent gate FinFETs are currently under development for future CMOS nodes. As the RBT realized in [10] scales to higher frequencies, the length direction (perpendicular to the drain current in device) decreases resulting in a structure very similar to an Independent-Gate (IG) FinFET. However, resonant transistors are not limited to this topology; the drive and sense mechanisms in the RBT can be extended to acoustically resonate transistors of various geometries and materials.

In this paper, we demonstrate the acoustic resonance of the released IG-FinFET similar to that shown in Fig. 3, with a single-crystal silicon fin of 114 nm width and 220 nm thickness and two polysilicon gates. The gate dielectrics are composed of 15 nm silicon nitride on either side of the fin. As in the case of the RBT, one gate of the IG-FinFET is biased into accumulation to drive acoustic waves in the device. The other gate biases the fin into inversion to generate a drain current for FET sensing of the elastic waves. The active area of this n-type device is lightly p-doped ( $N_A = 10^{14} \text{ cm}^{-3}$ ) while gates, source, and drain are highly doped with As ( $N_D \sim 10^{18} \text{ cm}^{-3}$ ).

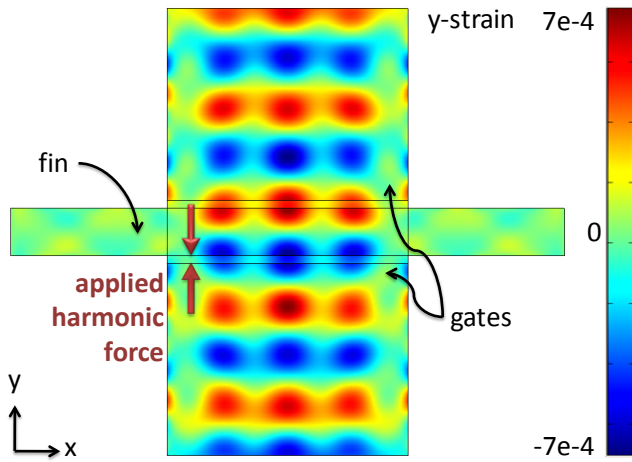
After the HF release of the device, both fin and gates are freely suspended and can resonate in contour plate modes defined by the composite geometry of the gates and fin. Each gate of the demonstrated device measured 500 nm (gate length along the fin) by 400 nm. While many plate modes may be possible in this structure, the longitudinal waves generated perpendicular to the dielectric film reduces the number of modes excited by dielectric transduction of the device. Moreover, the FET sensing averages the distributed piezoresistive contribution of strain to the total AC drain current along a small region of the device (along the FET channel) resulting in a further reduction of undesired modes detected at the output.

A harmonic analysis of the IG-FinFET was performed in COMSOL Multiphysics to determine the resonance modes which could be both excited and detected in the device. A harmonic force of  $2.7 \times 10^5 \text{ N/m}^2$  was applied along both interfaces of one dielectric film to simulate the electrostatic force on the accumulation side of the fin. This corresponds to an accumulation gate voltage  $V_{ACC} = -1 \text{ V}$ , a drain voltage  $V_D = 4 \text{ V}$ , a grounded source, and an AC



**Fig. 3.** Scanning electron micrograph of a suspended independent-gate FinFET. The devices have a gate length of 500 nm.





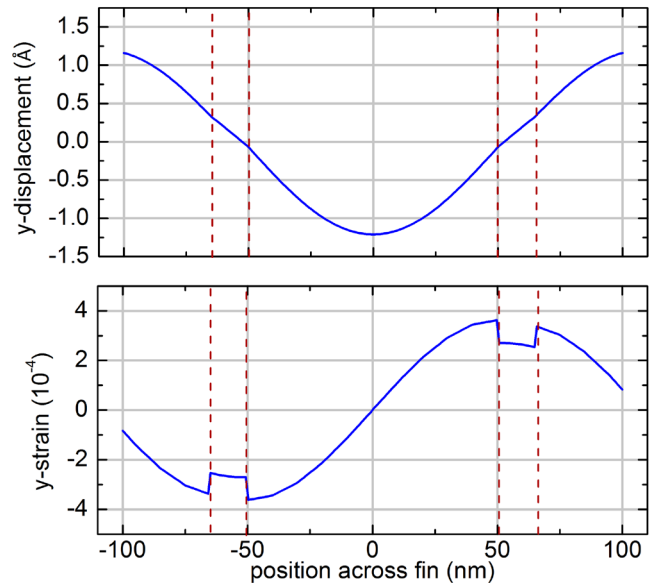
**Fig. 4.** COMSOL harmonic analysis of released IG-FinFET structure. Simulation shows the y-axis strain due to harmonic force applied across the lower dielectric film at the resonance frequency. Due to symmetry of the mode, the x-axis strain does not contribute to the piezoresistive signal. This mode corresponds to the half-wavelength resonance of the fin width (width-extensional mode).

excitation at the accumulation gate of  $v_{in} = 0.4 V$ . There is a roughly linear voltage drop from drain to source along the fin, resulting in an electrostatic force gradient along the dielectric. In the harmonic analysis, this is approximated as an averaged voltage evenly distributed along the length of the capacitor. The direction of the harmonic forces applied is shown in Fig. 4.

A frequency sweep from 30 to 50 GHz resulted in about 8 resonance modes excited from the force on the dielectric film. To determine the subset of these modes that would be detected with piezoresistive FET sensing, the strain was integrated along the fin at the region of inversion. As illustrated in Fig. 1, the inversion region exists inside the fin at the interface to the second dielectric film not used for driving resonance. Integration along this interface reduced the number of detectable eigenmodes to three in the simulation range of 20 GHz. Fig. 4 shows a contour plot of the y-axis strain of a contour mode resonance with acoustic half-wavelength corresponding to the width of the fin.

This simulated contour mode of the IG-FinFET at 35 GHz in Fig. 4 shows a  $10^{\text{th}}$  harmonic longitudinal mode in the y-direction coupled to a  $7^{\text{th}}$  harmonic in the x-direction. Fig. 5 provides displacement and strain plots extracted from this mode across the fin. An AC drain current through the fin can result from both transverse (y-direction) and longitudinal (x-direction) strain acting piezoresistively on the drain current flowing in the x-direction. The simulated mode exhibits both positive and negative strain in the x-direction, resulting in cancellation of piezoresistive contribution to the drain current from longitudinal strain. The transverse strain inside the fin generated by its  $\lambda/2$  resonance is both tensile and compressive. However, the current flowing through the fin is confined to the inversion region near one of the dielectrics, where the transverse strain is largely uniform along the length of the fin. This contributes to a net piezoresistive change in drain current at the resonance frequency.

In accordance with the theory of internal dielectric transduction, the harmonic response of the structure results in maximum strain and corresponding displacement nodes at the dielectric transducers. This configuration of drive (capacitive) and sense (piezoresistive) transducers yields the highest efficiency conversion from the electrical to mechanical domain and back into an electrical signal.

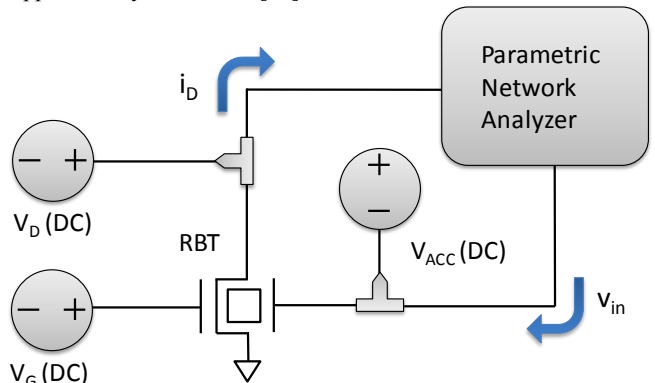


**Fig. 5.** COMSOL simulation of displacement and strain in y-direction across the 100 nm fin ( $\pm 50$  nm). Dashed lines indicate position of 15 nm dielectric films, extending into the gate silicon beyond  $\pm 65$  nm.

## MEASUREMENT

The devices were tested in a two-port configuration at room temperature in a vacuum probe station, as shown in Fig. 6. The resonating IG-FinFET is represented by a new RBT symbol. This symbol of the 4-terminal device illustrates the contribution of mechanical resonance from the back gate to the characteristics of the transistor channel.

The devices were tested in vacuum to prevent ionization of air in the fringe fields near the dielectric, where up to 5 V were applied across a 15 nm gap. The vacuum also prevented adsorption of molecules onto the surface of the resonator over time, which can degrade the quality factor. After de-embedding the device from the probe pads and routing, the transconductance is obtained from the Y-parameters,  $g_m = Y_{21} - Y_{12}$ , as in the case of conventional transistor measurements. A detailed explanation of the de-embedding structures and algorithm is provided in the supplementary material of [10].



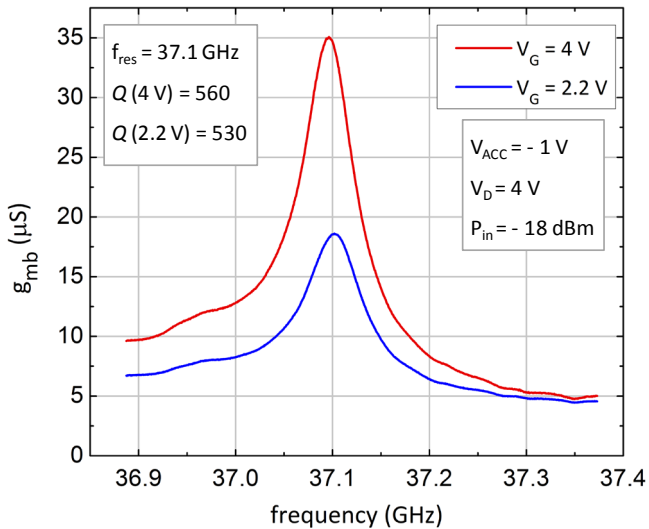
**Fig. 6.** Schematic of 2-port measurement for frequency characterization of RBT. The drive and sense gates of the RBT were biased into accumulation and inversion, respectively. An AC excitation was superimposed on the drive gate using a parametric network analyzer.

## EXPERIMENTAL RESULTS

IG-FinFETs were fabricated side-by-side with bar RBTs demonstrated in [10] in an SOI process similar to that used in standard CMOS processing. While the bar-geometry RBTs have polysilicon gates patterned to define the resonance frequency, the poly gates of the IG-FinFETs extend uniformly to the metal contacts, as seen in Fig. 3. The resonance frequency of the IG-FinFET corresponds to the width-extensional mode of the transistor fin. All IG-FinFETs have a gate length of 500 nm and a device thickness of 220 nm. The active area of the FETs is lightly p-doped ( $N_A = 10^{14} \text{ cm}^{-3}$ ), resulting in fully-depleted devices.

The measured frequency response of one IG-FinFET is shown in Fig. 7, applying an accumulation gate voltage  $V_{ACC} = -1 \text{ V}$ , a drain voltage  $V_D = 4 \text{ V}$ , and an AC excitation at the accumulation gate of -18 dBm or  $v_{in} = 0.4 \text{ V}$ . The measured response is given in terms of the back gate transconductance  $g_{mb}$ , highlighting the fact that the excitation is applied to the back gate. This is done in order to isolate the electrical input signal from the output. The resonance peak is attributed to the frequency-dependent electromechanical transconductance  $g_{m,em}$  due to piezoresistive modulation of the drain current. The signal floor in Fig. 7 corresponds to direct electrical modulation of the channel from the back gate.

An electromechanical transconductance of the IG-FinFET is measured at 35  $\mu\text{S}$  (or 159  $\mu\text{S}/\mu\text{m}$ ) for a transistor gate length of 500 nm and gate dielectric of 15 nm silicon nitride, with a gate voltage of 4 V.



**Fig. 7.** Measured frequency response of the IG-FinFET applying gate voltages of 2.2 V and 4 V. The resonance frequency of 37.1 GHz corresponds to the 1<sup>st</sup> harmonic width-extensional mode of the 114 nm fin. The excitation on the back gate of the IG-FinFET isolates the electrical input and output signals.

The IG-FinFET exhibits a resonance at 37.1 GHz with a quality factor of  $Q = 560$  at a gate voltage of 4 V and  $Q = 530$  at a gate voltage of 2.2 V. The resulting  $fQ$  product of  $2.1 \times 10^{13}$  is on par with the high  $fQ$  products seen in all internal dielectrically transduced longitudinal-mode bar resonators, in spite of the IG-FinFET's unpatterned gate. The limiting dissipation mechanisms in this device are the acoustic losses due to misalignment of the fin and gate masks as well as the electrical losses through the resistive ungated segment of the fin at the source and drain.

An atomic force microscopy (AFM) scan of the IG-FinFET revealed a fin width of 114 nm, in excellent agreement with 1<sup>st</sup> harmonic width extensional mode of the fin at 37 GHz.

## CONCLUSION

The electromechanical resonance of transistors enables internal amplification of the desired mechanical signal, greatly improving the dynamic range of GHz-frequency MEMS devices above the parasitic capacitance floor. This sensing mechanism allows for detection of acoustic resonance at previously inaccessible frequencies. A freely-suspended IG-FinFET was implemented as a Resonant Body Transistor, demonstrating an acoustic resonance frequency of 37.1 GHz and quality factor of 560. The hybrid NEMS-CMOS RBT will provide a small-footprint, low-power, high sensitivity building block for many RF and mm-wave applications.

## ACKNOWLEDGMENTS

This work was funded by Army Research Labs. The authors thank Wentao Wang of MIT for providing COMSOL simulations of the device. Devices were fabricated at the Cornell Nanoscale Science and Technology Facility (CNF), a member of the NNIN.

## REFERENCES

- [1] H.C. Nathanson, W.E. Newell, R.A. Wickstrom, J.R. Davis Jr., "The resonant gate transistor," *IEEE Transactions on Electron Devices* **1967**, 14 (3), 117-133.
- [2] C. Durand, F. Casset, P. Renaux, N. Abele, B. Legrand, D. Renaud, E. Ollier, P. Ancey, A.M. Ionescu, L. Buchaillet, "In-plane silicon-on-nothing nanometer-scale resonant suspended gate MOSFET for in-IC integration perspectives," *Electron Device Letters* **2008**, 29 (5), 494-496.
- [3] E. Colinet, C. Durand, L. Duraffourg, P. Audebert, G. Dumas, F. Casset, E. Ollier, P. Ancey, J.-F. Carpentier, L. Buchaillet, A.M. Ionescu, "Ultra-sensitive capacitive detection based on SGMOSFET compatible with front-end CMOS process," *Journal of Solid-State Circuits* **2009**, 44 (1), 247-257.
- [4] D. Grogg, M. Mazza, D. Tsamados, A.M. Ionescu, "Multi-gate vibrating-body field-effect transistors (VB-FETs)," *IEEE IEDM* **2008**, 1-4.
- [5] Kim, H.S.; Qin, H.; Blick, R.H., "Direct mechanical mixing in a nanoelectromechanical diode," *Applied Physics Letters* **2007**, 91, 143101.
- [6] M. Faucher, B. Grimbirt, Y. Cordier, N. Baron, A. Wilk, H. Lahreche, P. Bove, M. François, P. Tilmant, T. Gehin, C. Legrand, M. Werquin, L. Buchaillet, C. Gaquière, D. Théron, "Amplified piezoelectric transduction of nanoscale motion in gallium nitride electromechanical resonators," *Applied Physics Letters* **2009**, 94, 233506.
- [7] D. Weinstein, S.A. Bhawe, "Internal dielectric transduction: optimal position and frequency scaling," *IEEE TUFFC* **2007**, 54(12), pp. 2696-98.
- [8] D. Weinstein, S.A. Bhawe, S. Morita, S. Mitarai, K. Ikeda, "Frequency scaling and transducer efficiency in internal dielectrically transduced silicon bar resonators," *Transducers* **2009**, pp. 708-711.
- [9] D. Weinstein, S.A. Bhawe, "Internal dielectric transduction of a 4.5 GHz silicon bar resonator," *IEEE IEDM* **2007**, pp.415-418.
- [10] D. Weinstein, S.A. Bhawe, "The resonant body transistor" *Nano Letters ASAP* **2010**. DOI: 10.1021/nl9037517
- [11] D.M. Fried, J.S. Duster, K.T. Kornegay, "High-performance p-type independent-gate FinFETs," *IEEE Electron Device Letters* **2004**, 25(4), pp. 199-201.

## CONTACT

\*D. Weinstein, tel: +1-617-253-8930; dana@mtl.mit.edu

# CAPACITIVE-PIEZO TRANSDUCERS FOR HIGHER $Q$ CONTOUR-MODE ALN RESONATORS AT 1.2GHZ

Li-Wen Hung and Clark T.-C. Nguyen

Department of Electrical Engineering and Computer Science  
University of California at Berkeley, Berkeley, CA 94720-1774, U.S.A.

## ABSTRACT

A “capacitive-piezo” transducer that combines the strengths of capacitive and piezoelectric mechanisms to achieve an impedance and  $Q$  simultaneously lower and higher, respectively, than otherwise attainable by either mechanism separately, has allowed demonstration of a 1.2-GHz contour-mode ALN ring resonator with a motional resistance of 889  $\Omega$  and  $Q=3,073$  higher than so far measured for any other  $d_{31}$ -transduced piezoelectric resonator at this frequency. Here, the key innovation is to separate the piezoelectric resonator from its metal electrodes by tiny gaps to eliminate metal material and metal-to-piezoelectric interface losses thought to limit thin-film piezoelectric resonator  $Q$ 's, while also maintaining high electric field strength to preserve a strong piezoelectric effect. In addition, this capacitive-piezo transducer concept does not require dc-bias voltages and allows for much thicker electrodes that then lower series resistance without mass loading the resonant structure. The latter is especially important as resonators and their supports continue to scale towards even higher frequencies.

## INTRODUCTION

The ever-increasing appetite for wireless interconnectivity is beginning to drive new functions, like frequency gating spectrum analysis [1], that in turn drive a need for GHz resonators with simultaneous high  $Q$  ( $>30,000$ ) and low impedance ( $<200 \Omega$ ). Unfortunately, no single on-chip resonator device can deliver such performance in this frequency range. Indeed, among popular resonator choices, thin-film piezoelectric (e.g., ALN) resonators post lower electrical impedances, but also lower mechanical  $Q$ 's (e.g.,  $R_x=125 \Omega$  and  $Q=2,100$  [2]), than capacitive counterparts (e.g.,  $R_x=12.8 \text{ k}\Omega$  and  $Q=48,048$  [3]) at comparable ( $\sim 60 \text{ MHz}$ ) frequencies. To achieve simultaneous high  $Q$  and low impedance, either the impedance of capacitive resonators must be lowered [4][5], or the  $Q$ 's of piezoelectric resonators must be raised.

This work focuses on the latter and specifically introduces a new “capacitive-piezo” transducer, shown in Fig.1(b), that combines the strengths of capacitive and piezoelectric mechanisms to achieve an impedance and  $Q$  simultaneously lower and higher, respectively, than otherwise attainable by either mechanism separately. Using this new transducer, a 1.2-GHz contour-mode ALN ring resonator achieves a motional resistance of 889  $\Omega$  and a  $Q=3,073$  higher than so far measured for any other  $d_{31}$ -transduced piezoelectric resonator at this frequency. The key innovation here is to separate the piezoelectric resonator from its metal electrodes by tiny gaps to eliminate metal material and metal-to-piezoelectric interface losses thought to limit thin-film piezoelectric resonator  $Q$ 's, while also maintaining high electric field strength to preserve a strong piezoelectric effect. To understand the logic behind this approach, the next section starts off with some discussion of previous attempts to raise piezoelectric resonator  $Q$ 's.

## RAISING PIEZOELECTRIC RESONATOR $Q$

Indeed, plenty of researchers have sought to raise the  $Q$ 's of thin-film piezoelectric resonators, with approaches that span from reducing electrode roughness [6], to optimizing the electrode material [7], to carefully balancing the ALN-to-electrode thickness ratio [8], to use of a Bragg reflector to prevent energy loss [9]. Unfortunately, none of the above methods raises the  $Q$ 's of on-chip

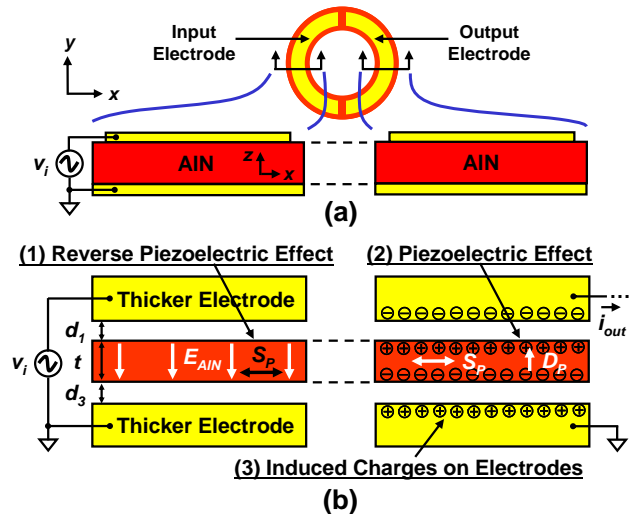


Fig.1: (a) Conventional piezoelectric transducers employing electrodes that directly contact the piezoelectric structure; and (b) working principles behind a capacitive-piezo resonator for which electrodes are separated from the piezoelectric structure via tiny air gaps.

piezoelectric resonators anywhere near the  $>30,000$  values needed for RF channel-selection and frequency gating spectrum analyzers.

Yet, polysilicon resonators easily achieve such  $Q$  values (but with higher than-desired impedances). To date, the measured  $Q$ 's of polysilicon resonators are on the order of 20 times larger than that of sputtered ALN resonators at similar frequencies. Interestingly, material loss theory [10][11][12] predicts that the  $(fQ)$  product limit due to (dominant) phonon-phonon interactions in the ALN material itself is only four times lower than that of silicon. This suggests that the ALN material itself might not be the principal culprit among  $Q$ -limiting losses, but rather the metal electrodes or the electrode-to-resonator interface strain might be more responsible. In fact, experimental data shows that as the thickness of a piezoelectric resonator's electrode increases, both the resonance frequency and  $Q$  of the resonator drop due to mass loading and electrode loss, respectively [13]. Electrode-derived energy loss perhaps also contributes to the lower  $Q$ 's measured in  $d_{31}$ -transduced resonators, where the electrodes often cover locations with the maximum strain, versus the  $Q$ 's of  $d_{33}$ -transduced thickness-mode resonators, where electrodes are placed very close to the nodes of the acoustic standing waves. Of course, despite their lower  $Q$ 's,  $d_{31}$ -transduced resonators are arguably more attractive than  $d_{33}$ , since their frequencies are set by CAD-definable lateral dimensions, so are more suitable for on-chip integration of multiple frequencies.

Whether a resonator uses  $d_{31}$  or  $d_{33}$ , both share the common problem that  $Q$  gets worse as dimensions scale to achieve larger coupling and/or higher frequencies. In particular, while a piezoelectric structure can be scaled, its electrode thickness often cannot scale as aggressively, since doing so incurs excessive electrical loss derived from increased electrode and interconnect electrical resistance. If a designer attempts to compensate for this by using thinner, but wider, metal traces, then the beams supporting the resonator would need to be wider to accommodate the wider metal traces, and wider beams incur more energy loss through supports

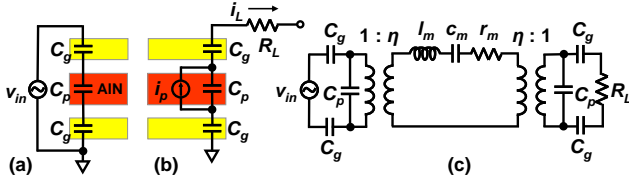


Fig. 2: Equivalent electrical circuit at (a) input and (b) output, modeling the effect of gap spacing on the electromechanical coupling coefficient; (c) equivalent circuit of a capacitive-piezo resonator. Here,  $\eta$  is the coupling coefficient with gap spacing  $d_{Total}=0$ .

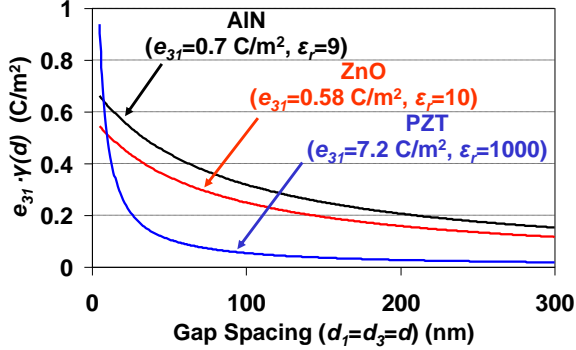


Fig. 3: The effective  $e_{31}$  on the drive side decreases as the gap spacing increases. The gap spacing affects the coupling of PZT the most due to its much larger relative permittivity  $\epsilon_r$ .

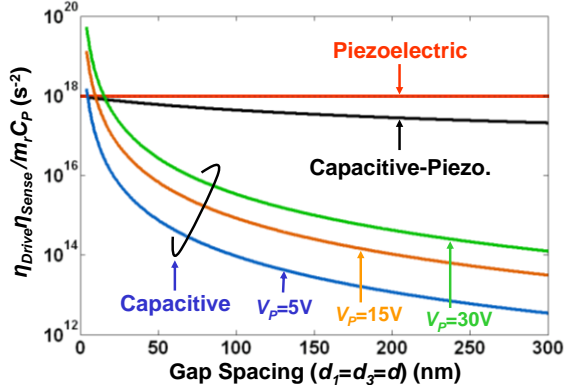


Fig. 4: Comparison of filter FOM of different transducers as a function of gap spacing, given the same filter bandwidth and type.

and anchors, hence lower  $Q$ . If the width of the support beams are decreased in order to lower anchor losses and raise  $Q$ , the width of the metal traces must also be decreased, which then increases their resistance, again, lowering  $Q$  and negating the gains.

### CAPACITIVE-PIEZO TRANSDUCERS

From the above discussion, it seems that  $Q$  degradation cannot be avoided as long as the electrode is in physical contact with the piezoelectric structure (which generates loss through strain coupling) and as long as the piezoelectric structure governs the size and thickness of the electrode (which governs electrical loss). Interestingly, all of these issues can be circumvented by mechanically decoupling the electrodes from the resonating body by simply separating the electrodes from the vibrating structure so that they are no longer in contact, as shown in Fig.1(b). The resulting transducer, dubbed the “capacitive-piezo” transducer, should not only raise the  $Q$  of the piezoelectric film, but should also allow much thicker (and thus much less resistive) electrodes without the electrode loss and mass loading penalties that would otherwise result if the electrode is contacted as in Fig.1(a). Thicker electrodes should

also further increase the  $Q$ , since the electrode parasitic series resistance would be smaller.

Although not a well known technique, the use of contactless electrodes on piezoelectric resonators is actually not new. This strategy had in fact been demonstrated on 5- and 10-MHz quartz crystal resonators, called BVA resonators, as far back as 1977 [14]. Since the piezoelectric-to-electrode thickness ratio of these devices was on the order of  $100\mu\text{m}$ -to- $100\text{nm}$ , or 1000, separating the electrode from the piezoelectric did little to increase the  $Q$  of the device. It did, however, allow for a more stable device against drift, since it eliminates electrode-to-resonator stress variations. This was the main reason for investigating such devices in the past.

For micromechanical resonators, on the other hand, the piezoelectric-to-electrode thickness ratio is much smaller, on the order of 10. Thus, the case for using a “capacitive-piezo” transducer is much stronger on the micro-scale. In addition, the ease with which tiny electrode-to-resonator gaps can be achieved via MEMS technologies further encourages the use of contactless electrodes. In effect, capacitive-piezo transducers stand to improve the  $Q$  and drift stability of micro-scale thin-film piezoelectric resonators with very little increase in fabrication cost.

### ANALYTICAL MODELING

Electrical models for AIN contour-mode resonators with contacting electrodes, such as described in [1], are abundant in the literature. The present approach to modeling the capacitive-piezo resonator focuses on how electrode-to-resonator air gaps influence the electrical model parameters. Pursuant to this, Fig.1(b) presents the cross-section of a contour-mode resonator with capacitive-piezo transducers under a typical excitation configuration. When the input signal is applied across the top and bottom electrodes, mechanical strain,  $S_p$ , is induced on the AIN film via the reverse piezoelectric effect. The induced strain is linearly proportional to both the piezoelectric stress constant,  $e_{31}$  ( $e_{31}\sim 0.7\text{ C/m}^2$  for sputtered AIN), and the electric field established within the AIN film,  $E_{AIN}$ , regardless of the mode shape of the resonator. The gap-AIN-gap stack can be modeled by three capacitors in series, as shown in Fig. 2(a), from which  $E_{AIN}$  can be written as

$$E_{AIN} = \frac{v_{in}}{t + \epsilon_r d_{Total}} \quad (1)$$

where  $\epsilon_r$  ( $\sim 9$ ) and  $t$  are the relative permittivity in the c-axis direction and thickness of AIN, respectively; and  $d_{Total}$  is the total gap spacing ( $d_{Total}=d_1+d_3$ ). When the input frequency matches the resonance frequency, the lateral force  $F_p$  induced by  $E_{AIN}$  via the reverse piezoelectric effect excites the resonator into lateral-mode vibration with an electromechanical coupling coefficient on the drive side given by

$$\eta_{Drive} = \frac{F_p}{v_{in}} = \alpha \cdot e_{31} \cdot \frac{t}{t + \epsilon_r d_{Total}} = \alpha \cdot e_{31} \cdot \gamma(d_{Total}) \quad (2)$$

where the value of  $\alpha$  depends on the electrode coverage area and placement, and on the resonator mode shape; and where  $\gamma(d_{Total})$  is a function gauging how much the coupling coefficient degrades with increasing air gap spacing. Fig. 3 plots the  $(e_{31} \cdot \gamma(d_{Total}))$  product for different piezoelectric materials. In general, small gap spacing is preferred to maintain a high coupling coefficient. It should be noted that a large  $e_{31}$  does not guarantee a large coupling coefficient. As shown in Fig. 3, even though PZT has a larger  $e_{31}$  than AIN and ZnO, its capacitive-piezo coupling is weaker at most gap spacings due to its much higher relative permittivity.

On the sense side, vibration-induced strain polarizes the AIN film via the piezoelectric effect, and the resulting electric displacement can be expressed as

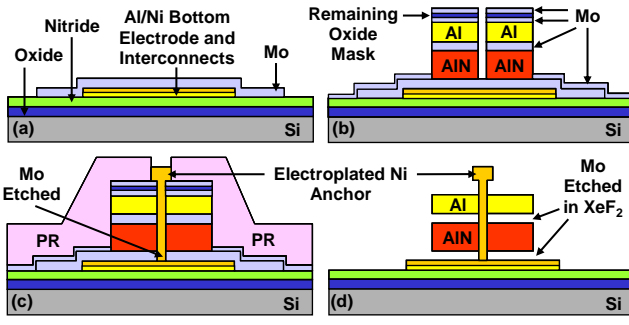


Fig. 5: Fabrication process flow of capacitive-piezo AlN resonator with electroplated Ni anchor and Mo sacrificial material dry released in XeF<sub>2</sub>.

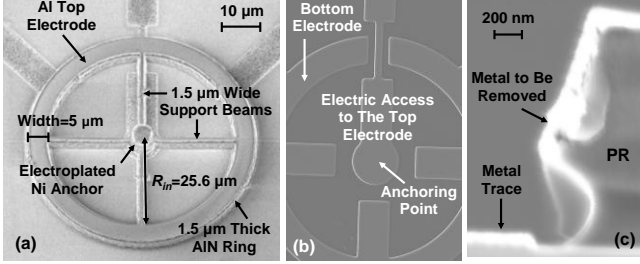


Fig. 6: (a) Fabricated 1.2-GHz capacitive-piezo AlN ring resonator; (b) bottom electrode and interconnect configuration, showing anchoring at the very center; (c) cross sectional SEM showing the double-layer lift-off process that ensures smooth metal trace edges.

$$D_p = e_{31} S_p = e_{31} \left[ \frac{\partial u_x}{\partial x} + \frac{\partial u_y}{\partial y} \right] \quad (3)$$

where  $u_x$  and  $u_y$  are the mechanical displacements in the  $x$  and  $y$  directions, respectively. Assuming a perfectly aligned AlN film and no spurious modes, AlN is uniformly polarized (i.e., with only bound surface charges and no bound body charges),  $D_p$  is purely along the vertical direction, and the integral of  $D_p$  over the entire electrode area equates to the total amount of induced charge  $Q_p$ , the time derivative of which becomes the current  $i_p$ . The piezoelectric effect on the sense side can thus be modeled by a current source with magnitude  $i_p = \omega \cdot Q_p$  as shown in Fig. 2(b), and the output current, i.e., the current flowing through  $R_L$  ( $R_L = 50 \Omega$  for measurement with a network analyzer), becomes

$$i_{out} = i_p \cdot \frac{Z_p}{Z_p + Z_g + Z_g + R_L} \approx i_p \cdot \frac{t}{t + \epsilon_r d_{total}} = i_p \cdot \gamma \quad (4)$$

From (4), the electromechanical coupling coefficient on the sense side,  $\eta_{sense}$ , is also a function of the gap spacing through  $\gamma(d_{total})$ . Although air gaps degrade  $k_r^2$  by a factor of  $\gamma^2$ , the higher  $Q$  provided by non-contacting electrodes together with sufficiently small gap spacings actually make it possible to achieve higher  $Q \cdot k_r^2$  than piezoelectric resonators with contacting electrodes.

Perhaps the best way to compare different transducers is via the filter  $FOM$  defined in [4], given by

$$FOM = \frac{1}{R_Q C_o} \propto \frac{\eta_{Drive} \eta_{Sense}}{m_r C_o} \quad (5)$$

where  $R_Q$  is the filter termination resistor,  $C_o$  the physical input capacitance, and  $m_r$  the motional mass of a constituent resonator in the filter. The right most form delineates parameters in the expanded equation most relevant to resonator design.

Fig. 4 compares simulated plots of  $(\eta_{Drive} \eta_{Sense} / m_r C_o)$  in the filter  $FOM$  for three different transducers (i.e. piezoelectric, capacitive-piezo, and capacitive alone) versus gap spacing  $d$  ( $d = d_1 = d_3$ ) at the same frequency. The simulation uses a ring inner radius and

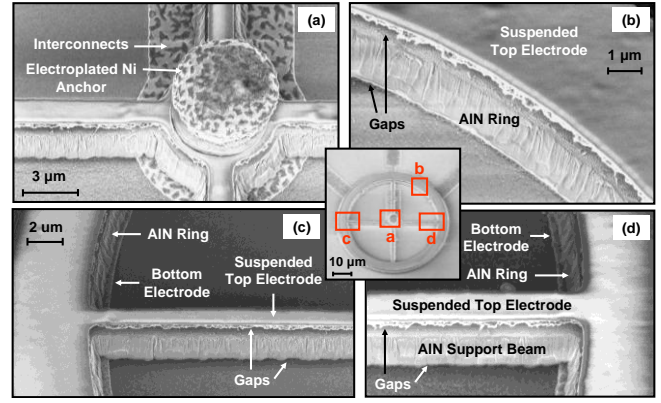


Fig. 7: SEM's at different parts of the same resonator confirming that the entire top electrode and the AlN ring resonator are suspended via the electroplated nickel anchor at the center.

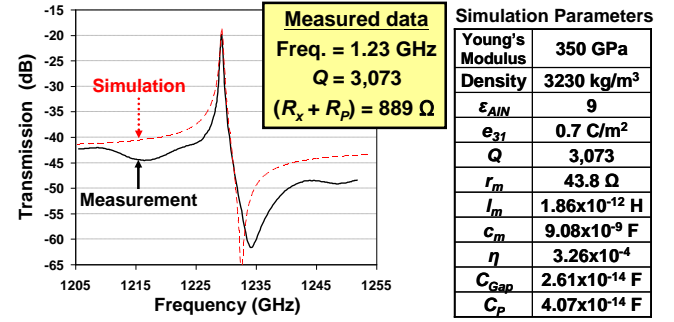


Fig. 8: Measured frequency characteristic for a 1.2-GHz AlN ring resonator with dimensions as shown in Fig. 6 and equivalent circuit of Fig. 2(c).

thickness of 25.6  $\mu\text{m}$  and 1.5  $\mu\text{m}$ , respectively; and ring widths of 5  $\mu\text{m}$  for AlN and 4.3  $\mu\text{m}$  for polysilicon, both chosen to achieve a 1.2-GHz resonance frequency for both materials under the same mode shape, neglecting DC bias-induced electrical spring softening inherent to capacitive resonators. In addition, the electrodes for the polysilicon resonator are assumed to be placed both inside and outside the ring, similar to [3]. As expected, the  $FOM$  of the capacitive-piezo transducer depends on gap spacing, but not as strongly as one might think, mainly because  $C_o$  drops by the same ratio  $\gamma$  as the electromechanical coupling coefficient when the gap spacing increases. Even so, a capacitive-piezo transducer with a 200 nm gap spacing achieves  $(\eta_{Drive} \eta_{Sense} / m_r C_o)$  of  $2.7 \times 10^{17} \text{ s}^{-2}$ , for which a capacitive (alone) transducer would require a much smaller gap spacing of 23 nm. Needless to say, this relaxed gap spacing is a distinct advantage of capacitive-piezo transducers over capacitive.

## FABRICATION

AlN resonators employing capacitive-piezo transducers were fabricated using a newly-developed 4-mask low-temperature CMOS-compatible process briefly summarized in Fig. 5. Here, aluminum top and Al/Ni bottom electrodes are temporarily separated from the AlN structure by a sputtered molybdenum (Mo) sacrificial material. Molybdenum is used as a sacrificial material instead of the oxide, silicon, or germanium, more commonly used in surface-micromachining processes, mainly to attain better c-axis orientation when sputtering the AlN film. Anchoring for all suspended structures, including the AlN and top electrode, is realized by a single electroplated nickel peg that contacts the top electrode. The device is released via a gaseous XeF<sub>2</sub>/N<sub>2</sub> etchant.

Fig. 6(a) presents the wide-view SEM of a completed 1.2-GHz contour-mode  $d_{31}$ -capacitive-piezo-transduced ring resonator. Fig. 7 presents SEM's of different parts of the same ring resonator

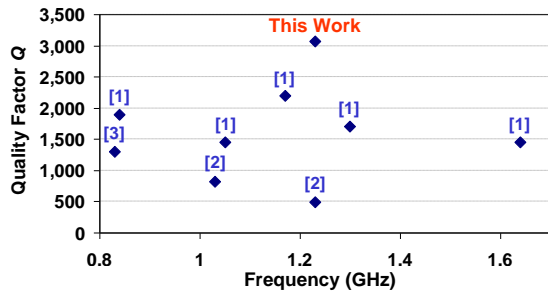


Fig. 9: Comparison of  $Q$ 's achieved via the capacitive-piezo AlN ring resonator of this work versus other  $\sim 1$  GHz lateral-mode AlN resonators.

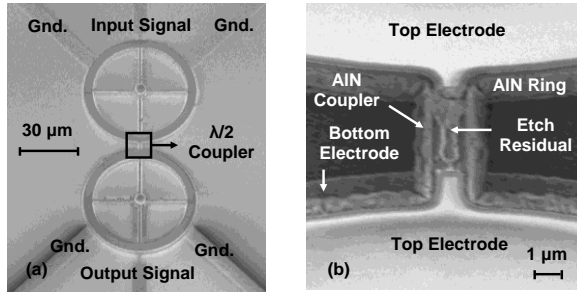


Fig. 10: (a) SEM of a capacitive-piezo ring resonator array with  $\lambda/2$  coupler; and (b) top-view SEMS showing how the electrode is removed from the coupler to electrically isolate the output from the input.

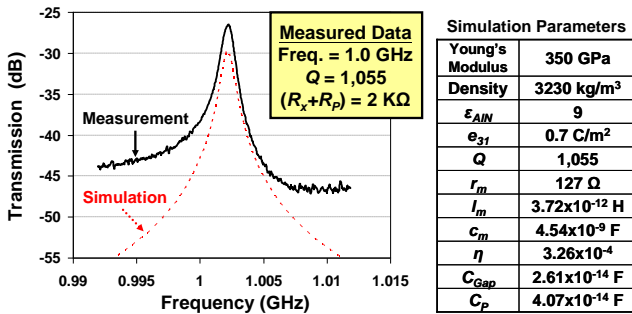


Fig. 11: Measured frequency characteristic for the resonator of Fig. 10, confirming suppression of the parallel resonance peak.

delineating the gaps between the top/bottom electrode and the resonator. For this device, to reduce electrode resistance, 400 nm thick Al is used as the top electrode—something that otherwise would not be permissible in a conventional AlN resonator, since its attached electrode would mass load the resonant structure.

## MEASUREMENTS

Fig. 8 presents the measured frequency response characteristics for the AlN ring resonator of Fig. 6(a), showing  $f_s=1.23$  GHz,  $Q=3,073$ , and  $R_x=889 \Omega$  at 3 mTorr. Both the input and output are DC grounded via bias-tee's to avoid electrostatic forces that might pull the top and bottom electrodes together and into the AlN resonator. Although the measured  $Q$  is still less than predicted by material loss theory, it is still substantially higher than any other measured contour-mode AlN resonator at similar frequencies, as plotted in Fig. 9 [15][16][17]. The etch residuals observed in the gaps after release, as shown in Fig. 7, may have affected the measured  $Q$ . Moreover, it has been confirmed experimentally that electroplated Ni anchors are mechanically weaker and more poorly attached to the substrate than the PECVD polysilicon anchors used in previous capacitive resonators. This may induce more anchor loss, especially at high frequencies. Finally, due to process difficulties, the supports of the final fabricated resonators deviated from quarter-wavelength dimensions, and this further lowers  $Q$ .

It should be noted that the 260 nm gap spacing used in this device is a rather conservative design. In fact, if the gap spacing were reduced from 260 nm to the 100 nm commonly used in capacitive (only) resonators, the impedance could be lowered to 250  $\Omega$ .

To evaluate the efficacy of building mechanical circuits using capacitive-piezo transducers, mechanically coupled two-resonator arrays, shown in Fig. 10, were also fabricated and tested. Here, the top electrode on the coupling beam is removed to electrically isolate the output from the input. The measured frequency response, shown in Fig. 11, exhibits much less feedthrough than seen in single-electrode devices. However, the  $Q$  is lower for this mechanical circuit than for a single resonator, which might be caused by etch residuals atop the coupling beam formed after dry etching the top electrode. Fixes to this problem are underway.

## CONCLUSIONS

This paper demonstrated a 1.2-GHz contour-mode AlN ring resonator with a motional resistance of 889  $\Omega$  and  $Q=3,073$ , confirming that resonators equipped with “capacitive-piezo” transducers can achieve higher  $Q$  than so far measured for any other  $d_{31}$ -transduced piezoelectric resonator at this frequency and at the same time maintain high electromechanical coupling. Although the demonstrated  $Q$  is higher than other piezoelectric resonators, it is probably far from what is achievable using this technology. In particular, it is not unreasonable to expect that future capacitive-piezo equipped resonators with better defined quarter-wave length supports and stiffer anchors might eventually achieve the  $Q$ 's in the tens of thousands predicted by the theory.

**ACKNOWLEDGEMENTS:** This work is supported by DARPA. The authors would like to thank Berkeley Microlab staff and members, especially Dr. X. Meng, Dr. J. Black, Dr. P. Stephanou, and J. Donnelly, for their assistance and advice on fabrication.

## REFERENCES

- [1] C. T.-C. Nguyen, “Integrated micromechanical RF...,” *26<sup>th</sup> Sym. on Sensors, Micromachines, and App. Sys.*, pp. 1-5, 2009.
- [2] G. Piazza, *et. al.*, “Piezoelectric aluminum nitride...,” *J. IEEE/ASME Microelectromech. Syst.*, vol. 15, pp. 1406-1418, 2006.
- [3] S.-S. Li, *et. al.*, “Micromechanical “hollow-disk” ring...,” *MEMS'04*.
- [4] L.-W. Hung, *et. al.*, “Capacitive transducers...,” *Hilton Head*, 2008.
- [5] T. J. Cheng and S. Bhave, “High- $Q$ , low impedance polysilicon resonators with 10nm air gaps,” *MEMS'10*, pp. 695-698, 2010.
- [6] S.-H. Lee, *et. al.*, “Influence of electrode configurations on the quality factor...,” *J. Appl. Phys.*, vol. 92, pp. 4062-4069, 2002.
- [7] C.-L. Huang, *et. al.*, “Effect of AlN film thickness and top electrode materials...,” *J. Appl. Phys.*, vol. 44, pp. 1397-1402, 2005.
- [8] M. Ueda, *et. al.*, “High- $Q$  resonators using FBAR/SAW technology...,” *Digest, IEEE Inter. Microwave Symp.*, pp. 209-212, 2005.
- [9] L. Mai, *et. al.*, “ZnO-based film bulk acoustic resonator devices on a specially...,” *J. Applied Physics*, vol. 95, pp. 667-671, 2009.
- [10] S. K. Kor, *et. al.*, “Ultrasonic attenuation in pure and doped n-type silicon,” *J. Physical Review B*, vol. 10, pp. 775-778, 1974.
- [11] D. K. Pandey, *et. al.*, “Ultrasonic wave propagation in III<sup>d</sup> group nitrides,” *Applied Acoustics*, vol. 68, pp. 766-777, 2007.
- [12] R. Tabrizian, *et. al.*, “Effect of phonon interactions on limiting the  $fQ$  product of micromechanical...,” *Transducers'09*, pp. 2131-2134.
- [13] C. G. Courcimault and M. G. Allen, “High- $Q$  mechanical tuning of MEMS resonators using a metal...,” *Transducers'05*, pp. 875-878.
- [14] R. Besson, “A new ‘electrodeless’ resonator design,” *Freq. Control Symp.* pp. 147-152, 1976.
- [15] C. Zuo, *et. al.*, “1.05GHz MEMS oscillator based on lateral-field-excited piezoelectric...,” *Freq. Control Symp.*, pp. 381-384, 2009.
- [16] P. J. Stephanou and A. P. Pisano, “GHz higher order contour mode AlN annular resonators,” *MEMS'07*, pp. 787-790.
- [17] G. Piazza, *et. al.*, “One and two port piezoelectric higher order contour-mode MEMS...,” *Solid-State Electronics*, pp. 1596-1608, 2007.

**CONTACT:** Li-Wen Hung; lwhung@eecs.berkeley.edu

# CAPACITIVELY TRANSDUCED MICROMECHANICAL RESONATORS WITH SIMULTANEOUS LOW MOTIONAL RESISTANCE AND $Q > 70,000$

Mehmet Akgul\*, Bongsang Kim, Zeying Ren and Clark T.-C. Nguyen

Department of Electrical Engineering and Computer Science  
University of California at Berkeley, CA 94720, U.S.A

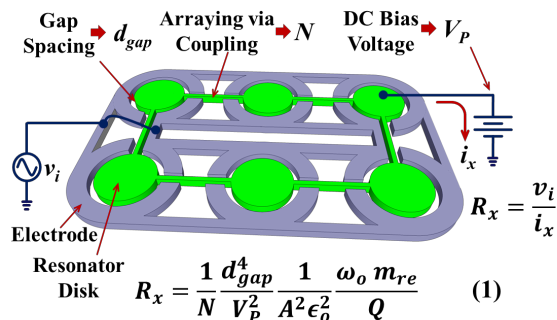
## ABSTRACT

Capacitively transduced micromechanical disk resonators that exhibit simultaneous low motional resistance ( $< 130 \Omega$ ) and high  $Q$  ( $> 70,000$ ) at 61 MHz are demonstrated using an improved ALD-partial electrode-to-resonator gap filling technique that reduces the  $Q$ -limiting surface losses of previous renditions by adding an alumina pre-coating before ALD of the gap-filling high-k dielectric. This work increases the  $Q$  over the  $\sim 10,000$  of previous renditions by more than  $6\times$  towards demonstration of the first VHF micromechanical resonators in any material, piezoelectric or not, to meet the simultaneous high  $Q$  ( $> 50,000$ ) and low motional resistance  $R_x$  ( $< 200\Omega$ ) specs highly desired for front-end frequency channelizer requirements in cognitive and software-defined radio architectures. This work finally overcomes the high impedance bottleneck that has plagued capacitively transduced micromechanical resonators over the past decade.

## INTRODUCTION

Capacitively transduced micromechanical resonators have historically achieved the highest  $Q$ 's among micro-scale counterparts using other technologies [1][2][3], reaching  $Q$ 's past 200,000 at VHF and 14,600 at 1.2 GHz [4]. Such  $Q$ 's are highly desired for a myriad of applications, from very narrow band low insertion loss filters for co-site interference suppression [5]; to low phase noise, low power oscillators for radar and communications [6]; to frequency gating spectrum analyzer functions for true software-defined cognitive radio [5]. Additional advantages, like zero DC power consumption and the ability to self-switch, further bolster the argument for using these devices [7].

Still, adaptation of capacitive micromechanical resonators in these applications has so far been slowed by their higher than conventional impedances, which makes them difficult to interface with widely used  $50\Omega$  RF components. Theoretically, there is actually no good reason why the impedances of such resonators must be high. In particular, just a quick glance at Eq. (1) governing the motional resistance  $R_x$  of the disk array-composite resonator shown



$m_{re}$  : Equivalent dynamic mass       $Q$  : Resonator quality factor  
 $\omega_0$  : Resonance frequency in radians     $\epsilon_0$  : Permittivity of vacuum  
 $A$  : Overlap area between the electrode and resonator

Fig. 1: Schematic of an array-composite disk resonator, showing a one-port excitation/readout scheme, identifying important variables, and providing the expression for the effective motional resistance  $R_x$  of the device.

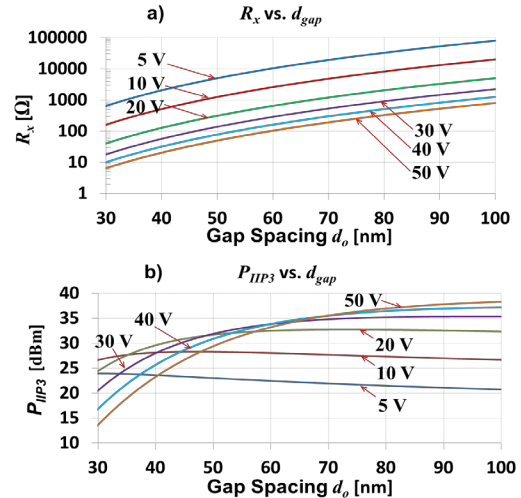


Fig. 2: Simulated plots of (a) motional resistance and (b)  $IIP_3$  versus dc-bias voltage and electrode-to-resonator gap spacing for a 61-MHz wineglass disk resonator with  $Q = 70,000$ .

in Fig. 1 reveals that there are many knobs to turn that allow a designer to achieve a very wide range of motional resistances. Fig. 2(a) presents curves of  $R_x$  versus gap spacing and dc-bias that illustrate the wide range of values attainable by capacitively transduced resonators. Although all the variables in (1) can (and have been) used as knobs to tailor  $R_x$ , the 4<sup>th</sup> power dependence on electrode-to-resonator gap spacing  $d_{gap}$  makes it the most effective of the bunch [8]. Furthermore, as detailed in [8], reducing gap spacing is the most effective knob by which to maximize the  $\omega_{FOM} = 1/(R_x C_o)$  figure of merit that governs the efficacy of a given resonator for filter construction. And contrary to popular belief, shrinking  $d_{gap}$  does not necessarily reduce resonator linearity, as clearly shown by the  $IIP_3$  versus gap spacing and dc-bias curves of Fig. 2(b), generated using the theory of [9]. Here, for a dc-bias voltage of 20V, the  $IIP_3$  remains above 25 dBm at a gap spacing of 30 nm. For lower dc-bias voltages, e.g., 5V, the  $IIP_3$  remains high for gap spacings well below 30 nm.

Of the approaches to reducing gap spacing towards lower impedance [8][10][11], the partial atomic layer deposition (ALD)-filled gap spacing method described in [8] combines the advantages of better yield relative to brute force gap-release approaches [10][12], and demonstrated application to a lateral disk resonator, to which the silicide gap method of [11] has not yet been applied. Unfortunately, the work of [8] lowered the  $Q$  of resonator devices from starting values over 150,000 without partial ALD-gap filling down to only  $\sim 10,000$  with ALD, supposedly due to surface losses introduced by the  $HfO_2$  high-k dielectric film used to partially fill the gap and coat the resonator.

Pursuant to restoring  $Q$ 's to over 50,000 while simultaneously achieving impedances less than  $200\Omega$ , this work employs an alumina ( $Al_2O_3$ ) pre-coating layer to improve the material quality of partial gap-filling ALD dielectric material, thereby greatly reducing surface losses towards a more than  $6\times$  increase in  $Q$ . The measured simultaneous  $Q$  of 73,173 and motional resistance of

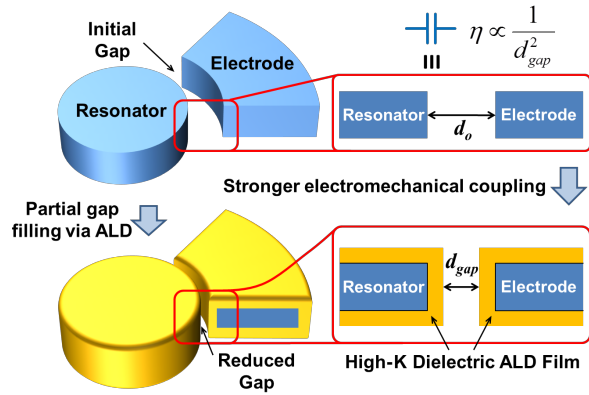


Fig. 3: Schematics summarizing the partial gap-filling gap reduction method of [8], where ALD of a high-k dielectric film effectively reduces the gap distance between the electrode and the disk.

130Ω achieved by this work at 61 MHz further bolster the notion that there are very few limits to the impedance- $Q$  combinations achievable by capacitively transduced micromechanical resonators.

### PARTIAL ALD ELECTRODE-TO-RESONATOR GAP FILLING

Partial ALD gap-filling, first demonstrated in [8], comprises a clever way to achieve tiny sub-30nm electrode-to-resonator gaps without the need to etch tiny sacrificial spacer layers, and thus, without the associated yield losses. As described in Fig. 3, the method involves first fabricating and releasing a micromechanical resonator, e.g., a disk resonator, with relatively wide initial electrode-to-resonator gap-spacings that permit good device yield; then coating the resonator and its electrodes with a conformal high-k dielectric ALD film. If the dielectric constant of the dielectric material is sufficiently high, i.e., if it is a “high-k” material, the effective electrode-to-resonator gap spacing of the coated device will be much smaller than the original spacing, and very close to the physical spacing between the dielectric surfaces, as shown in Fig. 3. Since ALD [13] provides a very uniform and conformal film deposition with <1nm thickness accuracy controlled simply by the number of reaction half cycles used, one can tune the final gap spacing to any desired value very accurately, provided the initial gap spacing is well known. This equates to an ability to achieve virtually any low motional resistance in accordance with (1), while simultaneously improving  $\omega_{FOM}$  and avoiding the excessive chip area (for arraying) and high bias voltage that would otherwise be needed if large gaps are used.

As mentioned, although the work of [8] successfully reduced the gap spacing of a 61-MHz wineglass mode disk resonator from 94 nm to 32 nm by coating the released resonator with a 30.7 nm HfO<sub>2</sub> ALD film, it did so with a penalty amounting to a 20x reduction in resonator  $Q$ , from the original uncoated  $Q$  of 150,527 to a much lower value of 7,368. Needless to say, if not mitigated in some way, such a reduction in  $Q$  renders the described partial-gap filling approach quite ineffectual, since  $Q$ 's less than 30,000 are not sufficient for the RF channel-selection or low phase noise applications targeted by MEMS-based vibrating resonators [5]. With all other parameters that influence energy loss (e.g., pressure, temperature, device geometry, anchor size) held constant before and after the HfO<sub>2</sub> ALD coating, the most probable explanation for the reduction in resonator  $Q$  is added surface loss arising from poor HfO<sub>2</sub> ALD film quality, and this was indeed postulated in [8].

If surface losses are the main culprit here, then methods for improving ALD film quality are required. Indeed, the need to mitigate surface-film-based losses becomes even more urgent as devices

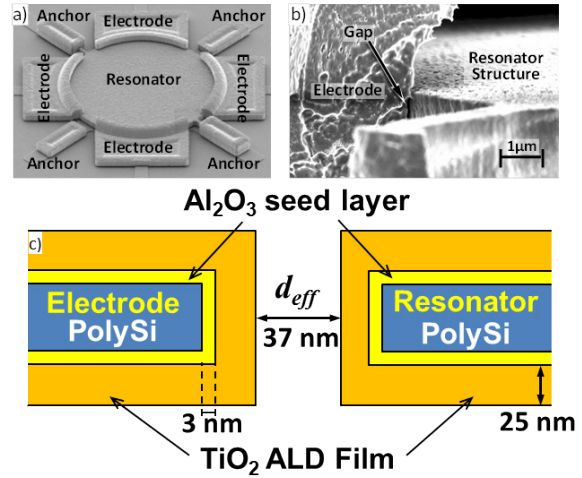


Fig. 4: SEM images of a) a polysilicon micromachined wine-glass mode disk resonator before gap tuning and b) cross-section after conformal ALD of 3nm Al<sub>2</sub>O<sub>3</sub> + 25nm TiO<sub>2</sub>. c) Schematic showing reduction of the resonator-to-electrode gap size from 87nm to 37nm via ALD partial-gap filling.

are scaled towards higher frequency, since scaling raises the surface-to-volume ratio, making surface-derived loss mechanisms even more prominent.

### IMPROVING ALD FILM QUALITY

Pursuant to reducing surface-derived losses, this work attempts to improve the ALD film quality by more properly nucleating the high-k dielectric ALD as it grows. In particular, the key to the order of magnitude  $Q$  boost in this work is the introduction of an interfacial 3nm Al<sub>2</sub>O<sub>3</sub> ALD pre-coating before ALD of the much higher-k gap-filling dielectric film—in this case, 25nm of TiO<sub>2</sub>—shown in Fig. 4(c). The need for such a pre-coating is governed by the ALD deposition chemistry of TiO<sub>2</sub>, which requires a healthy forest of dangling OH bonds over the starting surface to achieve a conformal and high quality film [14]. Without the pre-coating of Al<sub>2</sub>O<sub>3</sub>, the number of free OH bonds on the silicon surface is comparatively sparse, resulting in nucleation problems for the TiO<sub>2</sub> film that in turn lead to  $Q$ -reducing surface defects and losses (Fig. 5(a)). Al<sub>2</sub>O<sub>3</sub> is an excellent choice for the pre-coating, because it depends less on a perfectly hydroxylated surface; i.e., it

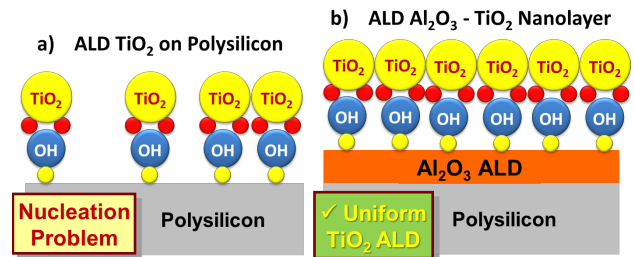


Fig. 5: a) Good quality TiO<sub>2</sub> ALD film requires good surface hydroxylation, i.e. a rich and uniform OH (hydroxyl) layer, which silicon lacks, leading to a nucleation problem and resultant surface loss mechanism that reduces the resonator  $Q$ . b) Al<sub>2</sub>O<sub>3</sub> grows good quality films on various substrates, even without good hydroxylation, and also provides a dense and uniform forest of AlOH hydroxyl group. This then leads to a uniform subsequent TiO<sub>2</sub> ALD, eliminating surface loss mechanisms that otherwise limit the resonator  $Q$ .



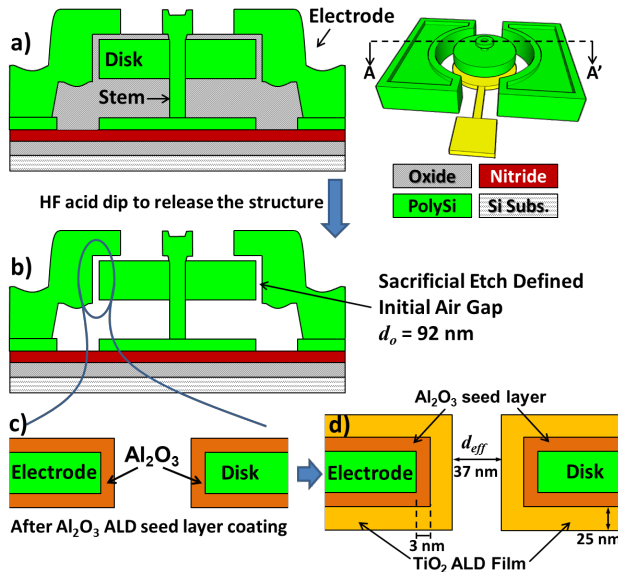


Fig. 6: Cross-sections describing the process flow for  $\text{Al}_2\text{O}_3$ - $\text{TiO}_2$  nanolayer ALD partial-gap filling.

ALDs into good quality films on various substrates, including silicon, whether or not the starting OH forest is sparse [15].

Of course,  $\text{Al}_2\text{O}_3$ 's dielectric constant ( $k=9$ ) is too low to serve as the primary gap-filling material, so the thickness of the  $\text{Al}_2\text{O}_3$  film should be kept small: for this work, on the order of 3 nm. Although very thin, this  $\text{Al}_2\text{O}_3$  film still provides the desired OH surface for the much higher- $k$  ( $k=80$ )  $\text{TiO}_2$  film to follow [16], as described in Fig. 5(b). Now, with  $\text{Al}_2\text{O}_3$  present, the  $\text{TiO}_2$  film can be deposited free of nucleation defects, hence, with much better quality and fewer sites for defect-derived energy loss. As a result, this  $\text{Al}_2\text{O}_3$ - $\text{TiO}_2$  bilayer approach achieves an optimal solution that provides simultaneous narrow gaps for low motional resistance and low surface losses for high  $Q$ .

### ALD PARTIAL GAP FILLING PROCESS FLOW

Fig. 6 summarizes the process flow for the ALD partial gap filling process, with the new measures described above to pre-coat structure surfaces with an  $\text{Al}_2\text{O}_3$  seed layer prior to ALD of the main partial gap filling high- $k$  dielectric  $\text{TiO}_2$ . The process starts with conventional steps [17] to achieve an unreleased 61-MHz wineglass mode disk resonator in polysilicon with 87 nm lateral electrode-to-resonator gaps temporarily filled with sacrificial high temperature oxide (HTO), as shown in Fig. 6(a). The resonator is then dipped in a 49% HF acid bath for 30 minutes to etch the sacrificial oxide and release the structure, yielding the cross-section of Fig. 6(b). Because the gaps are 87 nm, and not smaller, the yield of the release etch can be quite high, in excess of ~95%.

Next, the released resonator is coated with a 3nm  $\text{Al}_2\text{O}_3$  ALD to achieve the cross-section of Fig. 6(c). This  $\text{Al}_2\text{O}_3$  layer is quite conformal over the polysilicon surface, which is necessary if it is to serve as a seed layer providing a uniform and dense AIOH hydroxylated surface for a subsequent ALD of 25 nm thick  $\text{TiO}_2$ . Fig. 6(d) presents the final cross-section of the device, for which the final effective gap spacing is 37 nm. For comparative purposes, versions of the process were also run without the  $\text{Al}_2\text{O}_3$  pre-coating and just ALD'ing 25 nm  $\text{TiO}_2$  directly over the polysilicon resonator surfaces.

To allow for electrical connection to bond pads, a final lithography step is performed to cover all released devices and expose their bond pads, after which a very short HF dip removes ALD

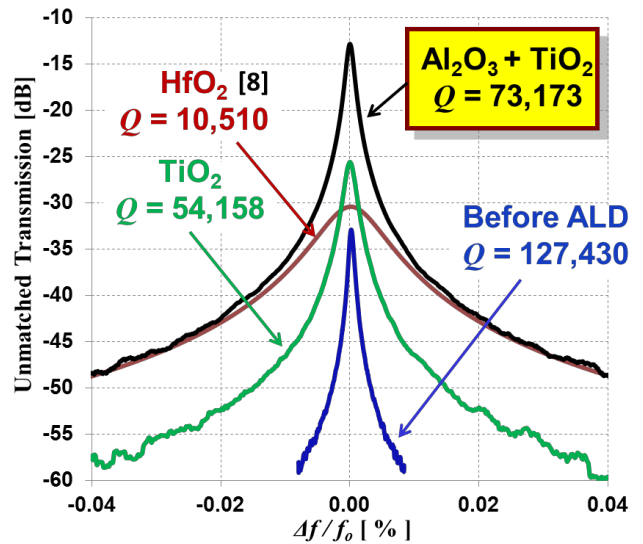


Fig. 7: Comparison of measured frequency characteristics under vacuum with dc-bias voltage of 9V for 61-MHz wine-glass disk resonators treated with various ALD partial gap filling recipes.

material over the bondpads. Photoresist is then removed via acetone, and critical point drying applied to clean devices.

### EXPERIMENTAL RESULTS

To verify the efficacy of  $\text{Al}_2\text{O}_3$  pre-coating as a method for reducing surface losses, the frequency characteristics of 61-MHz wine-glass disk resonators treated with various ALD-coating recipes were measured under 1  $\mu\text{Torr}$  vacuum in direct two-port configurations using an HP 5070B network analyzer. All tested devices were identical prior to ALD-coating, and all were measured under the exact same electrical connection and vacuum conditions. Fig. 7 compares measured frequency characteristics for 61-MHz wine-glass disk resonators with electrode-to-resonator gaps partially filled with 25nm of  $\text{TiO}_2$  only, without the  $\text{Al}_2\text{O}_3$  seed layer; and 3nm  $\text{Al}_2\text{O}_3$ +25nm  $\text{TiO}_2$ ; showing  $Q$ 's of 54,158 and 73,173, respectively, which clearly indicates the benefits of  $\text{Al}_2\text{O}_3$  pre-coating. Comparison of these results with data from [8] (included in the plot) also makes clear the importance of the high- $k$  dielectric film type and quality, since the  $Q$  of 54,158 achieved via the  $\text{TiO}_2$ -only case is still much higher than the  $\text{HfO}_2$ -only case of [8], which used an inferior ALD tool to deposit  $\text{HfO}_2$ .

It should be noted that ALD film coating does change the resonance frequency of each disk, most likely due to a combination of mass loading and an equivalent stiffness change caused by ALD film stress. Therefore, to better compare resonator  $Q$ 's and peak heights for different ALD coating experiments, the data in Fig. 7 is normalized to a common frequency axis by applying to all data points the expression

$$\% f_{Norm} = \frac{f - f_0}{f_0} \times 100 \quad (2)$$

where  $f_0$  is the center frequency of each disk and  $f$  is the measurement frequency of the data point. Table 1 provides a summary and comparison of all measured results.

### Effect of Parasitic Resistance on Resonator $Q$

Parasitic resistance  $R_p$  can significantly degrade resonator  $Q$  when the impedance of the resonator is on the order of or lower than that of the parasite. Fig. 8 explains how various parasitic elements like interconnect traces and bond-pad contacts can modify the electrical equivalent  $LCR$  circuit of the resonator and load the

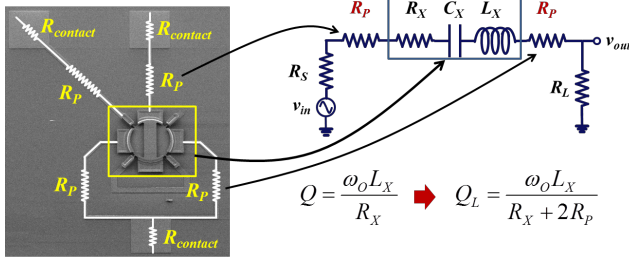


Fig. 8: (Left) SEM of the 61-MHz wineglass disk resonator used in this work. The polysilicon traces and bond-pad contacts create parasitic resistance that then load the (right) electrical equivalent LCR circuit of the resonator, lowering its  $Q$  via the indicated expression.

Table 1: Summary and comparison of measurement results for wineglass disk resonators treated with various ALD recipes.

	Before ALD	HfO <sub>2</sub> [8]	TiO <sub>2</sub>	Al <sub>2</sub> O <sub>3</sub> + TiO <sub>2</sub>
$Q$	127,430	10,510	54,158	73,173
$R_x$	10,180 $\Omega$	6,500 $\Omega$	512 $\Omega$	130 $\Omega$
$d_o$	92 nm	32 nm	35 nm	37 nm
$V_p$	9V	5V	9V	17 V

resonator  $Q$  via the expression shown. This work uses 400 nm-thick doped polysilicon traces as interconnect, as shown in Fig. 8, for which the measured parasitic resistance is  $R_p = 1.2$  k $\Omega$ . Compared to the motional resistance  $R_x = 130$   $\Omega$  achieved by the Al<sub>2</sub>O<sub>3</sub>-TiO<sub>2</sub>-coated device of this work, such a large parasitic resistance leads to a loaded  $Q$  that is 10.2x smaller than the actual  $Q$  of the device alone (without interconnects), and this is what is actually measured. Since the focus here is on the  $Q$  and  $R_x$  of the resonator device alone, sans the effect of interconnects, the data plotted in Fig. 7 represents the actual  $Q$  of each device after extracting out loading by parasitic resistance using the expression in Fig. 8.

#### Extraction of the gap spacing $d_{gap}$

As described in [8], the effective gap spacing of any capacitively transduced micromechanical resonator can be conveniently extracted by utilizing the electrical-stiffness-derived dependence of resonance frequency  $\omega_o$  on the applied bias voltage  $V_p$  and the gap spacing  $d_{gap}$ . Fig. 9 presents measured curves of frequency and motional resistance vs. bias voltage for the Al<sub>2</sub>O<sub>3</sub>+TiO<sub>2</sub>-coated resonator, all of which can be curve fitted simultaneously to reveal an effective gap spacing of 37nm; nominal zero-bias resonance frequency and  $Q$ 's of 60.68 MHz and 73,173, respectively; and a motional resistance (with series interconnect resistance removed) of only 130  $\Omega$ , as advertised.

#### CONCLUSION

This work demonstrates the first VHF micromechanical resonators in any material, piezoelectric or not, to meet the simultaneous high  $Q$  (>50,000) and low motional resistance (<200 $\Omega$ ) commonly desired in many RF and frequency control applications. In doing so, it disproves to a large extent the common misconception that capacitively transduced resonators always exhibit high impedance. Interestingly, however, even as this work confirms the low impedance prowess of capacitive micromechanical resonators, other research begins to question the need for such low impedance in RF and other applications, and actually makes a case that higher impedance is preferred when a system can be fully integrated onto a single chip [18]. Whether or not low impedance is actually needed in the end, one can at least rest assured that capacitive resonators can provide it, while also simultaneously delivering  $Q$ 's in

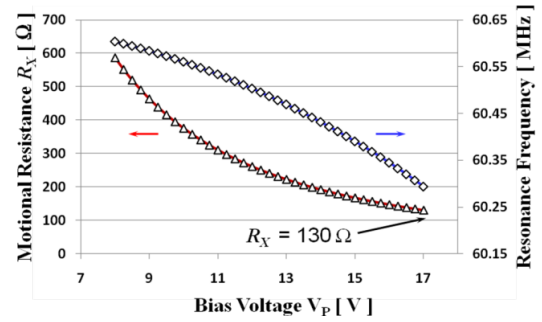


Fig. 9: Measured curves of motional resistance (bottom curve) and resonance frequency (top curve) versus dc-bias. The electrical stiffness effect observed in the latter is used to extract the effective electrode-to-resonator gap spacing of a given device [8].

the tens of thousands.

#### REFERENCES

- [1] Ruby R.C., et al., "Thin Film Bulk Wave Acoustic Resonators for Wireless...", Ultrasonic Sym., 2001 IEEE, Vol.1, pp. 813-821
- [2] G. Piazza, "Integrated Aluminum Nitride Piezoelectric MEMS...", J. of Vac. Sci. Technol. A, 2009, Vol. 27, No. 4, pp 776-784
- [3] Yue C.P., et al., "On-chip spiral inductors with patterned ground...", IEEE J. of Solid-State Cir., 1998, Vol.33, no 5, pp. 743-752
- [4] S.-S. Li, et al., "Micromechanical Hollow-Disk...", Proceedings, 17<sup>th</sup> Int. IEEE MEMS Conf., Jan. 25-29, 2004, pp. 821-824.
- [5] C. T.-C. Nguyen, "Integrated micromechanical RF...", 26<sup>th</sup> Sym. on Sensors, Micromachines & App. Sys., Tokyo, 2009, pp. 1-5.
- [6] Y.-W. Lin, et al., "Series-resonant VHF micromechanical res...", IEEE J. Solid-State Cir., vol. 39, no. 12, pp. 2477-2491, 2004.
- [7] S.-S. Li, et al., "Self-switching vibrating micro...", IEEE Int. Freq. Cont./Pre. T. & T. Int. Sym., Canada, 2005, pp. 135-141.
- [8] Hung L.-W., et al., "Capacitive Transducer Strengthening Via ALD-Enabled Partial-Gap Filling", Hilton-Head'08.
- [9] Y.-W. Lin, et al., "Third-order intermodulation distortion in capacitively...", IEEE Int. Ultrasonics Sym., 2005, pp. 1592-1595.
- [10] Tiffany J. Cheng, Sunil Bhawe, "High- $Q$ , low impedance polysilicon resonators with 10nm air gaps", MEMS'10, pp. 695-698.
- [11] Hung L.-W., et al., "Silicide-Based Release of High Aspect-Ratio Microstructures", MEMS 2010, Hong Kong, pp. 120-123
- [12] Y.-W. Lin, et al., "Vibrating micromechanical resonators...", IEEE Int. Freq. Cont./Prec. T. & T. Int. Sym., 2005, pp. 128-134.
- [13] Markku Leskela, Mikko Ritala, "Atomic layer deposition (ALD): from precursors...", Thin Solid Films, 2002, pp.138-146.
- [14] H. Cheng, et al., "Substrate Materials and Deposition Temperature Dependent...", Jou. of The Electrochem. Soc., v.156, 2009.
- [15] A.C. Dillon, S.M. George, et al., "Surface chemistry of Al<sub>2</sub>O<sub>3</sub> deposition using Al(CH<sub>3</sub>)<sub>3</sub>...", Surface Sci., vol. 322, Jan. 1995.
- [16] M.D. Groner, S.M. George, et al., "Electrical characterization of thin Al<sub>2</sub>O<sub>3</sub> films...", Thin Solid Films, vol. 413, Jun. 2002.
- [17] M. A. Abdelmoneum, et al., "Stemless wine-glass-mode disk micromechanical reson.", MEMS'03, Kyoto, Japan, pp. 698-701.
- [18] Y. Xie, et al., "UHF Micromechanical Extensional Wine-Glass Mode Ring Resonators", IEDM 2003, Washington, pp. 953-956.

#### ACKNOWLEDGMENTS

This work was supported by DARPA.

#### CONTACT

\* Mehmet Akgul, tel: +1-510-684-2166; akgul@berkeley.edu

# GHZ RANGE NANOSCALED ALN CONTOUR-MODE RESONANT SENSORS (CMR-S) WITH SELF-SUSTAINED CMOS OSCILLATOR

M. Rinaldi\*, C. Zuniga, C. Zuo and G. Piazza  
University of Pennsylvania, Philadelphia, USA

## ABSTRACT

This paper reports on the design and experimental verification of a new class of nanoscaled AlN Contour-Mode Resonant Sensors (CMR-S) for the detection of volatile organic chemicals (VOC) operating at frequencies above 1 GHz and connected to a chip-based CMOS oscillator circuit for direct frequency read-out. This work shows that by scaling the CMR-S to 250 nm in thickness and by operating at high frequencies (1 GHz) a limit of detection of  $\sim 35 \text{ zg}/\mu\text{m}^2$  and a fast response time ( $< 1 \text{ ms}$ ) can be attained. In addition, the capability to detect concentrations of volatile organic compounds such as 2,6 dinitrofluorene (DNF) as low as 1.5 ppb ( $4.7 \text{ ag}/\mu\text{m}^2$ ) is experimentally verified.

## INTRODUCTION

In recent years the demand of highly miniaturized sensor arrays capable of selectively detecting extremely small concentrations (part per trillion, ppt) of multiple gaseous analytes has steadily grown. The necessity to detect such small concentrations requires reliably measuring extremely small variations in the sensor output signal. In this perspective, gravimetric sensors, such as Quartz Crystal Microbalances (QCMs), have a significant advantage over other sensor technologies (conductance-based sensors, Chem-FET, or optical sensors) since they use frequency as the output variable, which is one of the physical quantities that can be monitored with the highest accuracy [1].

Nevertheless, smart, compact, portable and low cost electronic noses for multiple gas detection cannot be implemented with bulky and unintegrable QCMs. Even if QCMs have been successfully employed as gravimetric sensors thanks to their extremely high quality factors, which permit to obtain limits of mass detection in the order of few nanograms, their relatively large volume and their inability to be directly integrated on silicon render them unattractive for the fabrication of sensor arrays composed of a large number of mechanical elements.

In response to this growing demand for miniaturization, the use of micro and nano electromechanical (MEMS/NEMS) resonators for sensing applications has been extensively explored. The scaling of the device dimensions enables the fabrication of ultra-sensitive nanomechanical gravimetric sensors that can be arranged in single-chip arrays capable of selectively detecting extremely small concentrations (ppb-ppt) of multiple gaseous analytes.

Different MEMS/NEMS resonator technologies based on electrostatic or piezoelectric transduction [2,3] or piezoresistive displacement transduction [4] have been proposed. In particular, NEMS resonators have been exploited as transducers for the realization of extremely sensitive gravimetric sensors. Sub-attogram mass resolution has been demonstrated in NEMS cantilevers [4] thanks to the minuscule mass and the relatively high quality factor ( $Q$ ). Nevertheless the greatly reduced dimensions of these devices render their transduction extremely difficult and require the use of cumbersome, complex and power inefficient read-out techniques. In this perspective, the employment of large surface area devices with nanoscaled thickness (such as flexural membranes [5] or laterally vibrating contour-mode resonators [6]),

instead of beams, is advantageous in the making of gravimetric sensors since it enables the fabrication of extremely low mass devices with power efficient transduction and readout.

In addition, the scaling of micro/nanoelectromechanical resonators to GHz frequencies, hence higher sensitivity to mass loading, has been a significant challenge because the device transduction tends to become inefficient and its performance is generally accompanied by a reduction in quality factor,  $Q$ . These issues have prevented connecting high frequency nanoelectromechanical resonators to self-sustaining oscillators, therefore rendering real-time VOC sensing measurements impossible.

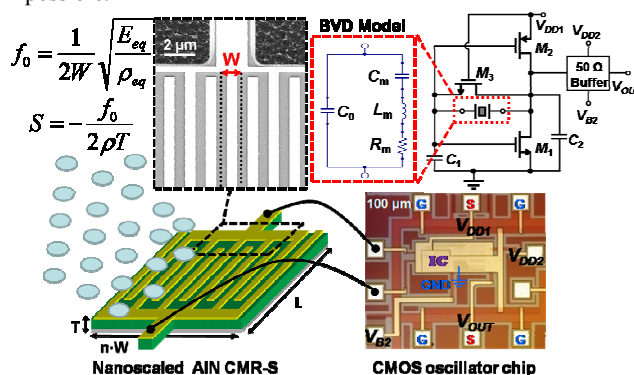


Figure 1: Schematic representation of the fabricated nanoscaled AlN CMR-S connected to a self-sustained CMOS oscillator circuit. A number,  $n$ , of subresonators (width,  $W$ ) are mechanically coupled in order to excite a higher mode of vibration in the AlN plate ( $f_0$  is set by  $W$ ). The butterworth van dyke (BVD) model is used to describe the resonator behavior.

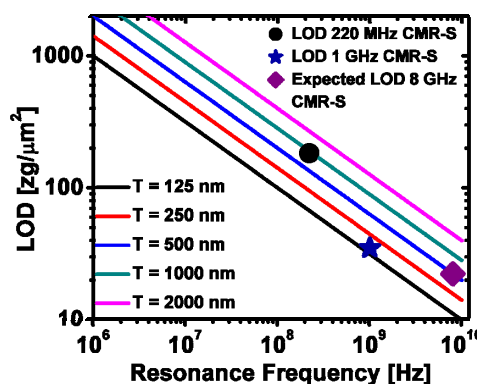


Figure 2: Limit of detection as function of the CMR-S resonance frequency and thickness. The device surface area is assumed to be constant over frequency and the input power is assumed to be the device critical power (maximum power before non-linear behavior). The measured data points follow the predicted trend.

In this work, fundamental transduction problems in NEMS resonators were solved by using on-chip piezoelectric actuation and sensing of an ultra-thin (250 nm) AlN plate (equivalent to a membrane) formed of AlN nanostructures mechanically coupled

and forced to simultaneously vibrate at the same frequency (GHz range) in the contour-extensional mode (Fig. 1). A low frequency (~220 MHz) ultra-thin-film AlN CMR-S for VOC detection was previously demonstrated by our group [6]. In this work, the sensor performance in terms of LOD (Fig.2), or measurement speed for a given LOD (Fig.3), were improved by scaling the device to higher frequencies of operation.

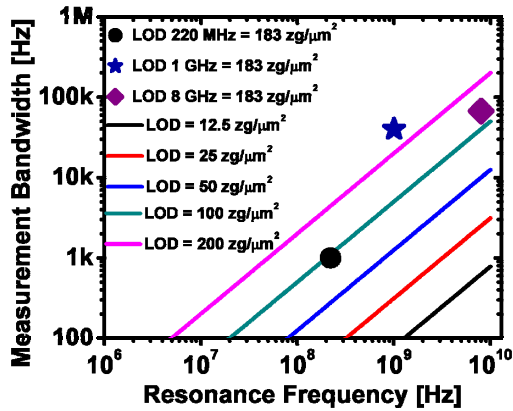


Figure 3: Measurement bandwidth (i.e. speed) as a function of the CMR-S resonance frequency for a given LOD. Note that the experimental data are in line with theoretical predictions.

Ultra-thin-film (250-500 nm) AlN CMR-S operating at frequencies as high as 8 GHz with figure of merit ( $FOM = k_t^2 \cdot Q$ , product of the electromechanical coupling and resonator  $Q$ ) in excess of 10 and impedances below 100  $\Omega$  were experimentally demonstrated. High values of sensitivity to mass loading (~290  $\text{KHz} \cdot \mu\text{m}^2 / \text{fg}$  at 1 GHz) were attained thanks to the nanoscaled thickness of the AlN resonators and their high frequency of operation. Because of the large value of the resonator FOM, direct wire-bonding of nano-CMR-S, operating up to 1 GHz, to a Pierce oscillator fabricated in the ON-Semiconductor 0.5  $\mu\text{m}$  CMOS process was made possible (Fig. 1). The insertion of the 1 GHz CMR-S in the oscillator loop permitted to measure a minimum Allan Variance of 10 Hz, which translates in an ultimate LOD of 35  $\text{zg}/\mu\text{m}^2$  with a measurement bandwidth of solely 1 ms.

These unprecedented results have not been demonstrated by any other micro/nanoscale resonant sensor [5,7,8]. By operating the CMR-S technology at high frequency, which is associated with an increase in CMR-S mass sensitivity and power handling (i.e. better phase noise performance) [9], a lower LOD and a higher measurement speed for a given LOD (Fig. 2-3) were attained.

In order to test the sensing properties of one of the fabricated devices, its top metal electrode was made out of gold, given its known ability to adsorb organic molecules in vapor phase and its capability to be eventually functionalized with thiol terminated self assembled monolayers for selective affinity enhancement towards specific analytes [10]. The device was exposed to different concentrations of 2,6 dinitrotoluene (DNT) and, despite the lack of an affinity enhancing functionalization layer, the ability to detect concentrations as low as 1.5 ppb (4.7  $\text{ag}/\mu\text{m}^2$ ) was demonstrated. This constitutes a ~10X improvement in mass per unit area detection capability compared to the one previously demonstrated by the same group with lower frequency nano-CMR-S [6].

## DESIGN

A CMR is composed of an AlN film sandwiched between two patterned metal electrodes (Fig. 1). When an AC voltage is applied across the thickness ( $T$ ) of the device a contour-extensional

mode of vibration is excited through the equivalent  $d_{31}$  piezoelectric coefficient of AlN. Given the equivalent mass density,  $\rho_{eq}$ , and Young's modulus,  $E_{eq}$ , of the material stack (AlN and metal electrodes) that forms the resonator, the center frequency,  $f_0$ , of this laterally vibrating mechanical structure, is set by the period,  $W$ , of the metal electrode patterned on the AlN plate and can be approximately expressed as in Eq. (1).

$$(1) \quad f_0 = \frac{1}{2W} \sqrt{\frac{E_{eq}}{\rho_{eq}}}$$

The other two geometrical dimensions, thickness,  $T$ , and length,  $L$ , set the equivalent electrical impedance of the resonator [3] and can be designed independently of the desired resonance frequency.

The sensitivity to mass per unit area of a CMR-S loaded on its top surface can be expressed as in Eq. (2) [11, 12].

$$(2) \quad S_{CMR-S} = -\frac{f_0}{2\rho_{eq}T}$$

It is worth noting that the resonance frequency,  $f_0$ , and the thickness,  $T$ , of the CMR-S can be set independently so as to achieve the desired value of sensitivity. In particular, the device sensitivity can be improved by scaling the thickness,  $T$ , of the AlN film and by increasing the device resonance frequency,  $f_0$ .

Nevertheless, the mass per unit area sensitivity of the device cannot be considered the only important parameter for the design of a high performance gas sensor. In fact, the limit of detection, LOD, of the sensor (smallest amount of adsorbed mass per unit area that can be resolved) needs to be taken in to account:

$$(3) \quad LOD = \frac{\Delta f_{min}}{S_{CMR-S}}$$

where  $\Delta f_{min}$  indicates the minimum frequency shift detectable by the sensor read-out. When the resonant sensor is connected to a self-sustained oscillator loop for direct frequency readout, the minimum detectable frequency shift,  $\Delta f_{min}$ , is determined by the phase noise of the oscillator. Therefore, the performance of the sensor can be improved by reducing the thickness,  $T$ , of the AlN layer and by increasing the device resonance frequency,  $f_0$  (i.e. improving the device sensitivity) up to the limit at which good phase noise is preserved.

According to these guidelines, the CMR-S of this work were scaled both in the vertical ( $T$ ) and lateral ( $W$ ) directions and a lateral field excitation scheme (LFE) was employed to excite a higher order contour-extensional mode of vibration in the nanoscaled AlN structures. Despite the volume reduction and the increase in the resonance frequency, high  $Q$  (~700 in air at 8 GHz) and high  $k_t^2$  (>1.5 %) were still attained. Such high values of the device figure of merit,  $k_t^2 \cdot Q$ , enable the direct connection of the CMR-S to a compact and low power self-sustained oscillator circuit for direct frequency read-out. In fact, the primary power loss in this oscillator circuit is due to the motional resistance,  $R_m$ , of the resonator [13], whose value is inversely proportional to the device figure of merit,  $k_t^2 \cdot Q$  [14].

The oscillator circuit topology used as read-out for the CMR-S of this work is described in [13]. Briefly, the circuit (Fig. 1) consists of a Pierce oscillator implemented by means of a CMOS inverter biased in its active region. Transistors M1 and M2 form the CMOS inverter while transistor M3 acts as a large resistor to provide biasing in the active region of M1 and M2.

### 1 GHz nano-CMR-S design

In order to improve the device sensitivity to mass loading according to equation 2 the frequency setting dimension,  $W$ , was

set to 4  $\mu\text{m}$  (frequency of operation of  $\sim 1$  GHz) and the thickness of the AlN film was scaled to 250 nm. The very thin AlN film (composing the body of the resonator) was deposited on top of a floating bottom Platinum (Pt) electrode which acts to confine the electric field across the thickness of the device and provides for a high  $k_t^2$  (1.7 % in this work).

### 8 GHz nano-CMR-S design

The capability to fabricate nanoscaled CMR-S operating in the Super High Frequency (SHF) band ( $> 3\text{GHz}$ ) has been previously demonstrated by our group [15]. Nevertheless, the motional impedance,  $R_m$ , of that device was considerably high ( $\sim 1$  K $\Omega$ ) and not suitable for the implementation of compact and low power self-sustained oscillators for direct sensor frequency readout. In this work a substantial step forward towards the implementations of such sensor system has been made by designing a nano-CMR-S operating at 8 GHz with a value of motional resistance,  $R_m$ , of  $\sim 70 \Omega$ .

To operate at  $\sim 8$  GHz, the frequency setting dimension,  $W$ , was scaled into the nanodomain ( $W=600$  nm) and no bottom electrode was employed in order to maintain extremely high quality AlN. The nano AlN film was directly deposited on top of a Si substrate and its thickness set to 500 nm in order to maximize the electromechanical coupling,  $k_t^2$ , given a resonance frequency of 8 GHz [16].

## EXPERIMENTAL RESULTS

A 4 mask fabrication process, analogue to the one reported in [12], was employed to fabricate the devices presented in this work.

The electrical response of the fabricated ultra-thin-film AlN CMR-S was characterized in ambient conditions in an RF probe station and the admittance curve measured by an Agilent® N5230A Network Analyzer after performing a short-open-load (SOL) calibration on a reference substrate.

Both the experimental and fitted admittance curves of the fabricated high frequency CMR devices are shown in Figures 4 and 5.

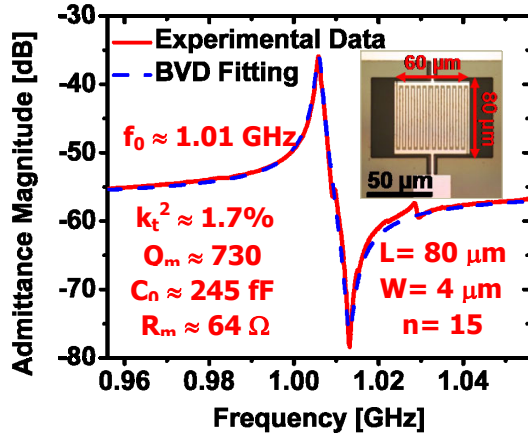


Figure 4: Experimental and BVD fitted admittance curves of the fabricated 1 GHz nano CMR-S (70 nm thick top Al electrode).

Despite the device volume reduction,  $k_t^2 \cdot Q$  products as high as 12.4 and 5.6 were attained at 1 GHz and 8 GHz, respectively.

These characteristics enabled the demonstration of the first GHz range oscillator based on nanoscaled AlN CMR-S. The 1 GHz device was directly wire-bonded to the oscillator circuit chip fabricated in the ON Semiconductor 0.5  $\mu\text{m}$  CMOS process. In order to estimate the noise limited minimum frequency shift

detectable by the sensor read-out ( $\Delta f_{min}$ ), the short term frequency stability of the oscillator output signal was characterized by its phase-noise derived Allan variance,  $\sigma_y(\tau)$ . An equivalent value of Allan variance of  $\sim 10$  Hz was derived for a measurement time of 1 ms (Fig.6). Therefore, considering a mass sensitivity of  $\sim 290$  KHz $\cdot\mu\text{m}^2/\text{fg}$  (extracted according to [12]) and a minimum detectable frequency shift of 10 Hz, a LOD of mass per unit area of  $\sim 35$  zg/ $\mu\text{m}^2$  can be estimated. The experimentally derived values of LOD and measurement bandwidth confirm that resonant sensor performances are significantly improved by scaling the CMR-S device thickness and moving from megahertz to gigahertz frequencies.

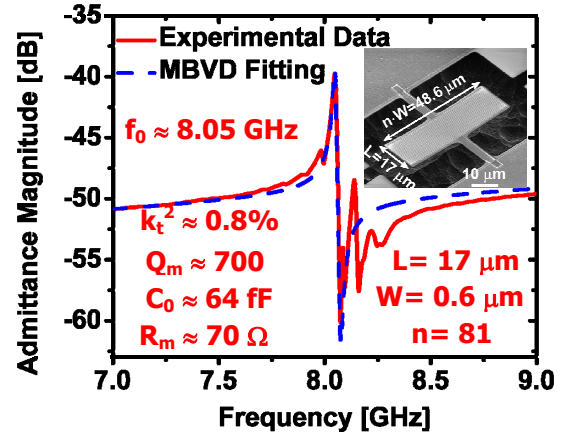


Figure 5: Experimental and MBVD fitted admittance curves of the fabricated 8 GHz nano CMR-S.

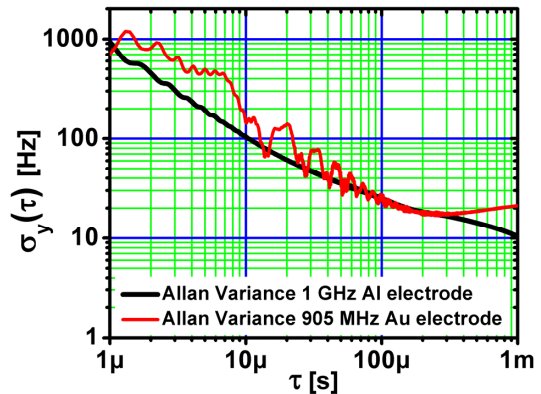


Figure 6: Allan variances for different values of integration time,  $\tau$ , calculated from the measured phase noise of the fabricated 1 GHz oscillator (using an Agilent® 8562EC spectrum analyzer) and of the 905 MHz oscillator (using an Agilent® E5052B Signal Source Analyzer).

In order to test the sensing properties of one of the fabricated devices, its top metal electrode was made out of gold (40 nm), given its known ability to adsorb organic molecules in vapor phase [10]. The geometry of the device is the same of the one reported in Fig. 4 but its measured resonance frequency is lower ( $\sim 905$  MHz) because of the difference in thickness and mass density between the gold and the aluminum electrodes.

Both the resonator die and the CMOS chip were attached to a custom designed PCB, which served as the lid for the testing chamber [12]. The phase-noise of the gold electrode nano-CMR-S oscillator was measured with an Agilent® E5052B Signal Source Analyzer (Fig. 6-7) and found to be comparable to the one observed in the lower frequency nano-CMR-S oscillator (Fig. 7).

The sensor was exposed to DNT vapor (generated by bubbling method [12]) and the frequency shift due to the adsorption of the analyte on the Au electrode (without any functionalization layer) was monitored with the spectrum analyzer functionality of an Agilent® E5052B Signal Source Analyzer (Fig. 8). The sensor was exposed to different concentrations of DNT ranging between 0.2% and 1% (Table 1) of the saturated vapor pressure and a minimum frequency shift of ~1 KHz was detected in correspondence of the 0.2% of the DNT saturated vapor pressure (Table 1). Considering that the DNT saturated vapor pressure at room temperature is equal to  $5.67 \cdot 10^{-4}$  Torr [17], a concentration of DNT as low as 1.5 ppb was detected by the fabricated nanoenabled CMR-S prototype. Given the device sensitivity of  $\sim 210 \text{ KHz} \cdot \mu\text{m}^2/\text{fg}$  (extracted according to [12]) and the minimum frequency shift of ~1 KHz a LOD of mass per unit area of  $4.7 \text{ ag}/\mu\text{m}^2$  was experimentally verified.

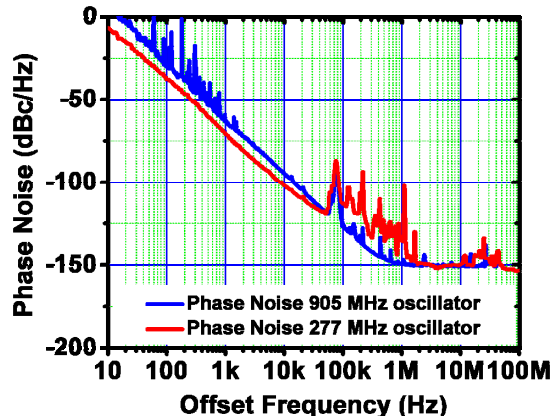


Figure 7: Measured phase noises of a 905 MHz and 277 MHz oscillators based on nano-CMR-S. A phase noise of 71.3 dBc/Hz at 1 KHz frequency offset from the carrier is recorded for the 905 MHz oscillator.

Table 1: Sensor response to different concentrations of DNT.

DNT Vapor Pressure Percentage (%)	DNT Concentration (ppb)	Frequency Shift (KHz)
1	7.46	6.5
0.5	3.73	3.4
0.25	1.86	1.7
0.2	1.49	1

Despite the lack of an affinity enhancing functionalization layer an extremely low concentration of DNT (1.5 ppb) was detected. This LOD of DNT concentration is expected to reduce by about 8X (~190 ppt) when a nano-bio coating layer such as the one reported in [6] is employed.

## CONCLUSION

In this paper, the design and the experimental verification of nanoscale GHz range gravimetric sensors based on ultra-thin film AlN CMR-S connected to a chip-based self-sustaining oscillator loop for direct frequency read-out was demonstrated. Devices operating up to 8 GHz with values of FOM within 5.6 and 12.4 were experimentally demonstrated. An ultimate LOD of mass per unit area of  $\sim 35 \text{ zg}/\mu\text{m}^2$  for a 1 GHz sensor was estimated thanks to the high frequency stability of the oscillator signal (minimum Allan variance of 10 Hz for 1 ms bandwidth). Concentrations of DNT as low as 1.5 ppb were experimentally detected and

correspond to a value of adsorbed mass per unit area of  $4.7 \text{ ag}/\mu\text{m}^2$ . These results constitute a ~10X improvement in mass per unit area limit of detection compared to previously demonstrated low frequency nano-CMR-S and confirm that resonant sensor performances are significantly enhanced by scaling the CMR-S device thickness and moving from megahertz to gigahertz frequencies.

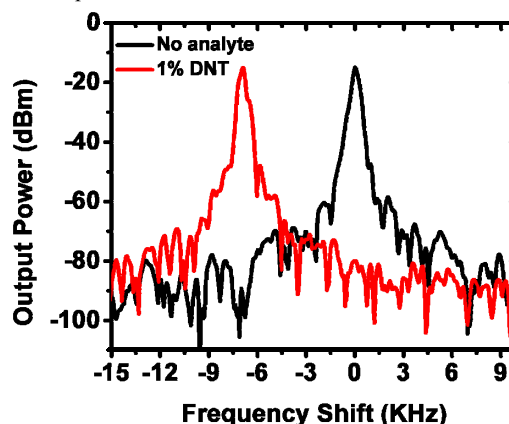


Figure 8: Shift of the oscillator spectrum corresponding to exposure to 1% DNT saturated vapor pressure. The detection of smaller shifts, corresponding to lower concentrations, was attained by averaging over various measurements.

## REFERENCES

- [1] J. R. Vig, L. Filler, Y. Kim, *J. Microelectromech. Syst.*, vol. 5, no. 2, pp. 131-137, 1996.
- [2] K. Wang, A.-C. Wong and C. T.-C. Nguyen, *J. Microelectromech. Syst.*, vol. 9, no. 3, pp. 347-360, 2000.
- [3] G. Piazza, P.J. Stephanou, A.P. Pisano, *J. Microelectromech. Syst.*, vol. 15, no.6, pp. 1406-1418, 2006.
- [4] M. Li, H. X. Tang, M.L. Roukes, *Nature Nanotechnology*, vol. 2, pp. 114-120, 2007.
- [5] H. J. Lee, K. K. Park, P. Cristman, Ö. Oralkan, M. Kupnik, and B. T. Khuri-Yakub, *Proc. IEEE MEMS 2009*, Jan. 2009, pp. 761-764.
- [6] M. Rinaldi, B. Duick, C. Zuniga, C. Zuo and G. Piazza, *Proc. IEEE MEMS 2010*, Jan. 2010, pp. 132-135.
- [7] Feng, X.L., White, C.J., Hajimiri, A. and Roukes, M.L, *Nature Nanotechnology*, 3, 342-346, 2008.
- [8] M. Penza et al, *IEEE Trans. Electron Device*, 55, 1237, 2008.
- [9] C. Zuo, M. Rinaldi and G. Piazza, *Proc. IEEE International Ultrasonics Symposium 2009*, Sep. 2009, pp. 1187-1190.
- [10] T. M. Herne and M. J. Tarlov, *J. Am. Chem. Soc.*, 119, pp. 8916-8920, 1997.
- [11] C. Zuniga, M. Rinaldi, S. M. Khamis, A. T. Johnson, and G. Piazza, *Applied Physics Letters*, vol. 94, 223122, 2009.
- [12] M. Rinaldi, C. Zuniga, and G. Piazza, *Proc. IEEE International Ultrasonics Symposium*, Sept. 2009, pp. 714-717.
- [13] C. Zuo, J. Van der Spiegel, and G. Piazza. *Proceedings IEEE EFTF-IFCS 2009*, April 2009, pp. 381-384.
- [14] K.M. Lakin, *Proc. IEEE MTT-S Int. Microwave Symp. Dig.*, June 1992, pp. 149-152.
- [15] M. Rinaldi, C. Zuniga, and G. Piazza, *Proc. IEEE MEMS 2009*, Jan. 2009, pp. 916-919.
- [16] M. Benetti, D. Cannata, F. Di Pietroantonio, and E. Verona, *Proc. IEEE IUS 2007*, Sept. 2007, pp. 1673-1676.
- [17] Regulatory Determinations Support Document for Selected Contaminants from the Second Drinking Water Contaminant Candidate List (CCL 2), United States Environmental Protection Agency, Chapter 7, June 2008.

## CONTACT

\*M. Rinaldi, tel: +1-215-573-3276; rinaldim@seas.upenn.edu

# $Q$ AMPLIFICATION IN GALLIUM NITRIDE THICKNESS MODE FILTERS USING ACOUSTOELECTRIC EFFECT

Vikrant J. Gokhale\*, Yonghyun Shim, Vikram A. Thakar, and Mina Rais-Zadeh  
University of Michigan, Ann Arbor, USA

## ABSTRACT

We report, for the first time, on the observation of the acoustoelectric amplification of the quality factor in thickness-mode gallium nitride micromechanical filters. Acoustoelectric amplification, which is most effective in piezoelectric semiconductors, occurs when charge carriers drift under the influence of an applied electric field with a velocity higher than that of the acoustic wave, thus transferring energy to lower velocity phonons. We demonstrate  $Q$  amplification of more than 300% by applying an electric field in the direction of acoustic propagation in a 2.2  $\mu\text{m}$  thick gallium nitride filter operating at 1.5 GHz. The power handling of the filter is measured by applying RF powers up to +20 dBm. No significant distortion is observed in the frequency response at elevated input powers.

## INTRODUCTION

Gallium nitride (GaN) based devices have gained interest in recent years mainly because of their large band gap, high electron mobility and high power handling. There is also great potential for GaN-based resonators in sensor applications and sensing systems. In addition, high quality factor ( $Q$ ) GaN resonators are envisioned to have far-reaching applications in frequency synthesizers and high-performance filters integrated with GaN electronics.

GaN thin-film bulk acoustic resonators (FBAR) have recently been demonstrated at gigahertz regime [1]. However, because of fabrication complexities and imperfections, the quality factor of the reported GaN resonators has not been sufficiently high for use as frequency references. In this paper, we demonstrate that the  $Q$  of GaN bulk acoustic filters can be electronically amplified using the acoustoelectric effect. Acoustoelectric  $Q$  amplification can be observed in semiconductors when an applied electric field accelerates electrons in the direction of acoustic wave propagation with a velocity higher than that of the acoustic phonons. Using the acoustoelectric effect, phonon-electron interactions may reduce (or can even cancel) the loss due to phonon-phonon interactions [2]. Therefore,  $fQ$  values greater than the limit set by phonon-phonon interactions can be achieved. GaN, unlike other piezoelectric materials, possesses a high electron mobility ( $>900 \text{ cm}^2/\text{Vs}$ ) [3] and a high intrinsic carrier concentration, which makes it a great material for observation of the acoustoelectric effect. However, till date, due to the poor quality of GaN layers grown on silicon or non-silicon substrates and fabrication limitations in sandwiching a high quality film between metal layers, this interesting phenomenon was not experimentally verified in GaN. In this paper, we report on the first experimental verification of acoustoelectric effect in GaN bulk acoustic filters. Acoustoelectric phenomenon is manifested as an amplification of the  $Q$ , improvement of the insertion loss, and increase in the out-of-band rejection of filters upon application of a DC bias between the input and output RF ports, as shown schematically in Fig. 1.

Another benefit of using GaN is its superior power handling capability. GaN switches have been shown to work reliably at power levels of up to +20 dBm, and up to operating temperatures of 300  $^\circ\text{C}$  [4]. Similarly, GaN filters reported herein are shown to operate at power levels of up to +20 dBm without observing any distortion in the frequency response.

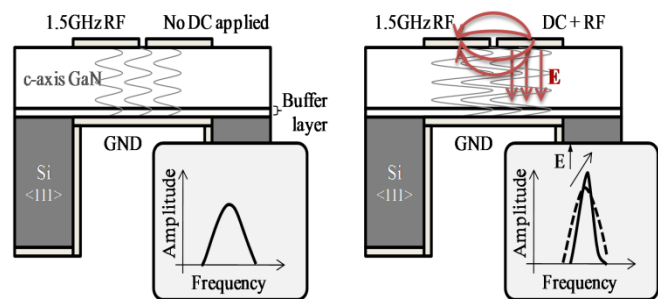


Figure 1: Cross-sectional schematic of the GaN filters showing the concept of the acoustoelectric effect and placement of the RF and DC electrodes.

## ACOUSTOELECTRIC AMPLIFICATION

The theory of acoustoelectric effect was first suggested by Shaposhnikov in 1941 who discussed the absorption of acoustic wave energy by electrons [5]. Later in 1953 Parmenter substantiated this theory by observing that a DC electric current appeared in the direction of the acoustic wave propagation in piezoelectric semiconductors and concluded that this was due to the transfer of momentum between the phonon stream and the electron gas [6]. The reverse effect (i.e., the transfer of energy from electrons to the acoustic wave) was reported by Hutson in 1961 [7]. Hutson demonstrated the amplification of acoustic waves in a crystal of photoconductive CdS upon application of an external electric field. The energy transfer was analytically treated by Spector [8] for interaction of electrons and acoustic waves in the presence of a DC electric field with the material considered as a free electron gas. The two regimes under discussion included the cases where the acoustic wavelength is larger or smaller than the mean free path of the electrons. This treatment yields an analytical expression for electronic current produced solely by acoustic energy transfer. This current is in addition to the component of the current due to the DC field itself. The analytical expression for longitudinal waves yields the simple criterion that the acoustic wave will be amplified when the electron drift velocity exceeds the acoustic velocity, causing crossover from acoustic energy loss to energy gain.

One practical problem faced by investigators was the low mobility of electrons in CdS ( $\sim 200 \text{ cm}^2/\text{Vs}$ ), which would necessitate the use of very high bias voltages (on the order of kilovolts) for good amplification [5]. A DC voltage in this range is not practical due to heating effects that would damage the crystalline structure. This problem was circumvented ingeniously by using the surface interactions of the piezoelectric semiconductor with a highly conductive metal, thus removing the high voltage requirements and making the DC operation regime practical [5]. This led to the development and successful implementation of  $Q$  amplification in surface acoustic wave (SAW) resonators.

On the other hand, there has not been much research reported on the acoustoelectric effect in bulk materials. Research on this topic has been revived recently due to the growing interest in GaN as an emerging material for use in high power and high-electron mobility transistors (HEMT) and circuits. Efforts have been made

to evaluate the viability of achieving acoustoelectric amplification in bulk GaN. Significant among these recent analyses is the work by Abdelraheem et al [9] and Mensah et al [10] who analytically demonstrated that GaN is a suitable material for the observation of acoustoelectric gain.

One of the significant advantages of GaN is its high electron mobility. While theoretical models estimate mobility as high as  $1500 \text{ cm}^2/\text{Vs}$ , a maximum value of  $950 \text{ cm}^2/\text{Vs}$  has been measured [3] for GaN electron mobility at room temperature. Combined with the large piezoelectric coefficients, these values indicate that there would be strong interactions between electrons and acoustic phonons in GaN.

## FABRICATION & CHARACTERIZATION

We designed and fabricated thickness mode GaN filters using GaN on  $\langle 111 \rangle$  silicon epiwafers obtained from SOITEC [11]. Fig. 2 shows a cross section of the GaN epitaxial wafer. The wafer stack consists of  $600 \mu\text{m}$  high-resistivity silicon ( $>10 \text{ k}\Omega\cdot\text{cm}$ ),  $500 \text{ nm}$  thick buffer layer to reduce the strain mismatch of GaN epitaxy on silicon, and  $1.8 \mu\text{m}$  wurtzite GaN grown by molecular beam epitaxy (MBE). A  $30 \text{ nm}$  thick AlGaIn-GaN caps the GaN layer. This layer is primarily used to generate a planar high conductivity region known as a 2D electron gas (2DEG) required for operation of HEMTs.

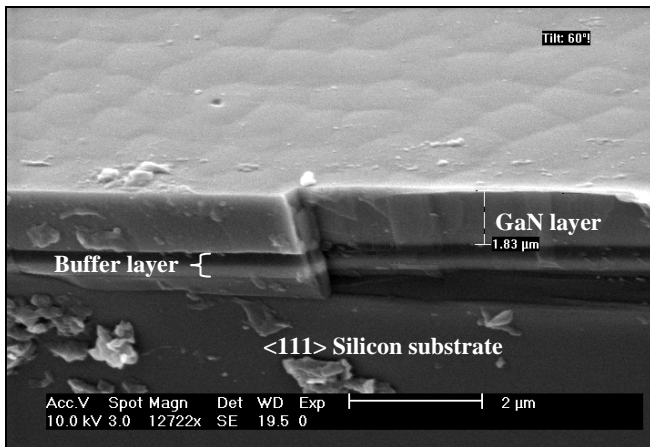


Figure 2: SEM cross section of the original wafer indicating the  $1.8 \mu\text{m}$  GaN layer, the  $0.5 \mu\text{m}$  buffer layer and the handle layer comprising of  $\langle 111 \rangle$  high resistivity silicon.

The fabrication starts with deposition of a  $50 \text{ nm}$  thick PECVD silicon dioxide layer on the wafer to act as a barrier against the conductive GaN layer. Next, the GaN/silicon dioxide stack was patterned and etched down to create the individual GaN devices. The GaN etching was done in inductively coupled plasma etch (ICP) using chlorine as the primary etching chemistry. The top electrodes consisted of  $10 \text{ nm}$  Ti and  $100 \text{ nm}$  Au and were patterned using evaporation and lift-off. Devices were released by selectively removing the silicon substrate from the backside using Deep Reactive Ion Etching (DRIE). The DRIE step was deliberately designed to give a small non-vertical sidewall angle to facilitate the proper contact of the sputtered bottom electrode to the ground plane. Finally, the Ti/Au bottom electrode ( $10 \text{ nm}/100 \text{ nm}$ ) was sputtered from the backside.

Fig. 3 (a) and Fig. 3 (b) show optical microscope and scanning electron microscope (SEM) images of two different filters with varying electrode dimensions. In Fig. 3(a), the bottom electrode is clearly seen through the transparent GaN/silicon dioxide stack.

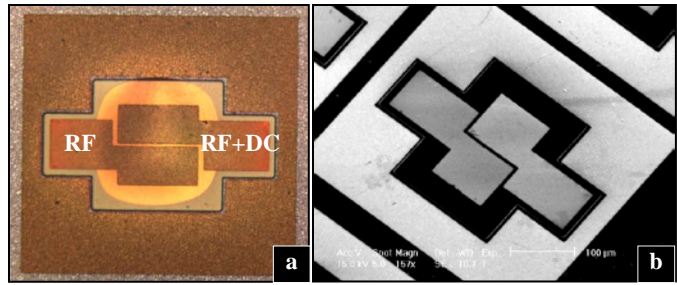


Figure 3: (a) Optical microscope and (b) SEM images of two fabricated filters. The DRIE back-etch release is seen in (a).

X-ray diffraction spectroscopy (XRD) analysis was carried out to verify the crystalline orientation and quality of the GaN film. Fig. 4 shows a clear peak resulting from the  $[0002]$  GaN centered at a detector angle (2-theta) of  $34.5^\circ$ . We believe that the smaller peak at  $35.35^\circ$  belongs to the AlN layer present in the buffer layer. The Full Width at Half Maximum (FWHM) of the  $[0002]$  GaN is measured to be  $0.088^\circ$ , indicating a highly oriented crystalline structure.

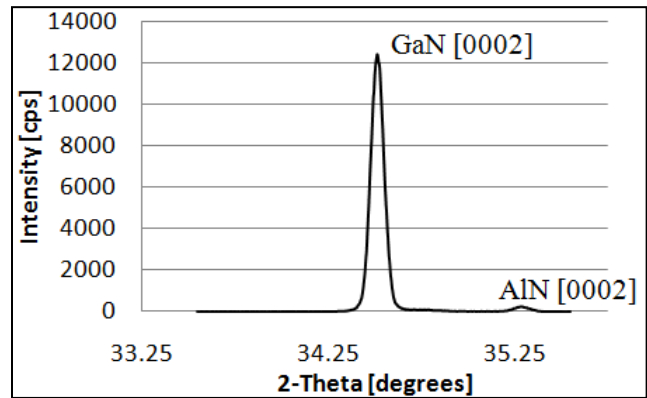


Figure 4: XRD analysis indicates that the peak for  $[0002]$  GaN is found at a detector angle of  $34.51^\circ$ . The FWHM for this peak is found to be  $0.088^\circ$  or  $316.8$  arc seconds.

## EXPERIMENTAL DATA

The scattering parameters of the filters were measured in an air ambient using a Suss Microtek PM5 probe station and an Agilent N5241A PNA. All measurements were taken with GSG Z-probes from Cascade Microtech. Fig. 5 shows the frequency response of a thickness-mode GaN filter with effective electrode area of  $90 \mu\text{m} \times 180 \mu\text{m}$  (Device 1). The center frequency of the filter agrees with ANSYS finite element simulations (Fig. 6). The mode shape shown in Fig. 6 confirms the presence of a standing wave in the film.

The equivalent electrical model of the filter is shown in Fig. 7. We modified the Butterworth Van Dyke model to accurately simulate the performance of the fabricated GaN micromechanical filters. The center frequency and pass-band response of the filters modeled using the modified BVD configuration is in good agreement with the measured results (see Fig. 7(right)). The poor out-of-band response of the filter is due to the feed-through resistance through the conductive GaN layer. Due to fabrication limitations, the electrical connectivity to the bottom sputtered electrode is not very good. This causes a relatively large resistance from the bottom electrode to ground. By reducing the ground contact resistance using alternative fabrication processes, the performance of the filters can be significantly improved.



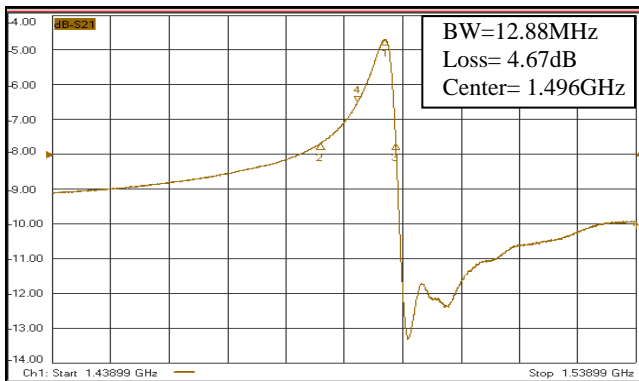


Figure 5: Measured frequency response of a 2.2  $\mu\text{m}$  thick GaN micromechanical bulk mode filter.

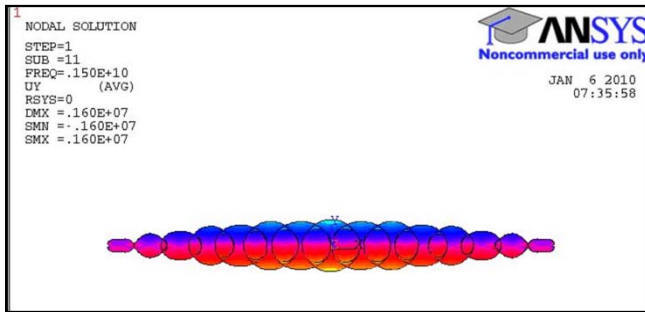


Figure 6: 2D simulation of the mode shape showing the thickness mode resonance at 1.5 GHz.

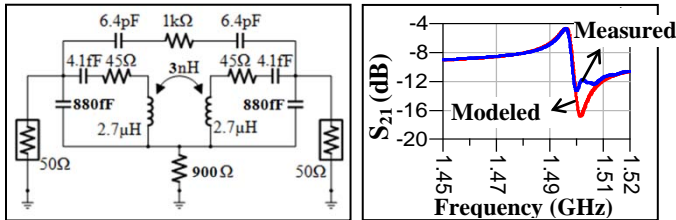


Figure 7: (left) Equivalent electrical model and (right) modeled and measured response of the filter for Device 1.

### Q Amplification

The acoustoelectric effect can be used to improve the characteristics of the filters. To achieve acoustoelectric amplification in the GaN filters, DC bias was superimposed to the RF input signal using a Bias Tee from Picosecond Pulse Labs [12]. The frequency response of two filters with different electrode dimensions with increasing DC bias is shown in Figs. 8 and 9, respectively.

As shown in Fig. 8 the insertion loss of Device 1 improves up to 30 V DC, but saturates beyond this point. This trend in insertion loss could be due to the fact that the ohmic loss of the contacts and electrodes dominates the motional impedance and impedes further improvement of the loss. With an increasing electric field, the resonance frequency of the device changes slightly (by 0.057%) because of the piezoelectric effect. The maximum value of  $Q$  achieved for this particular device, after amplification, is 225. Similar trends in insertion loss and  $Q$  are observed for Device 2, as shown in Fig. 9.

The  $Q$  as a function of DC bias for both filters is compared in Fig. 10, indicating  $Q$  amplification by a value as large as 300%. For both devices,  $Q$  increases with the application of a DC voltage as low as 5 V (i.e., an electric field as small as 5 V/2.2  $\mu\text{m}$ ). There

is a maximum value for the DC bias beyond which the  $Q$  saturates. This maximum DC value is dependent on the size of the device and the electrode geometry.

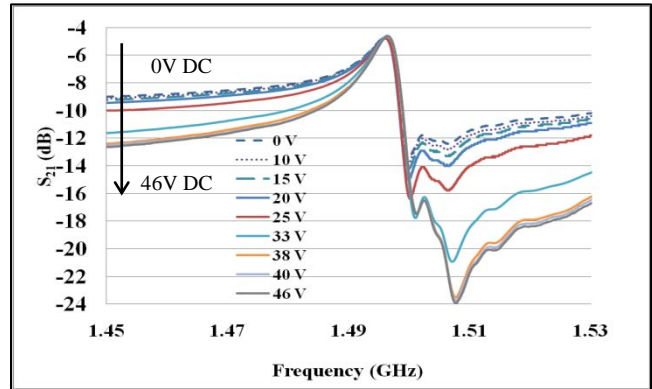


Figure 8: The acoustoelectric amplification of the filter  $Q$  for Device 1.

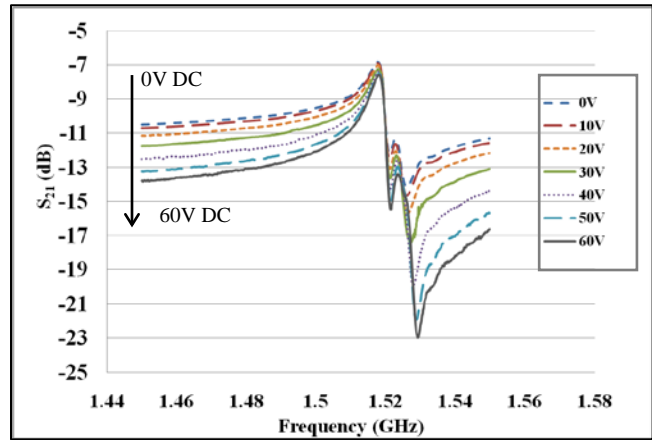


Figure 9: The acoustoelectric  $Q$  amplification for Device 2 with larger electrodes. The  $Q$  tends to saturate after 60 V DC.

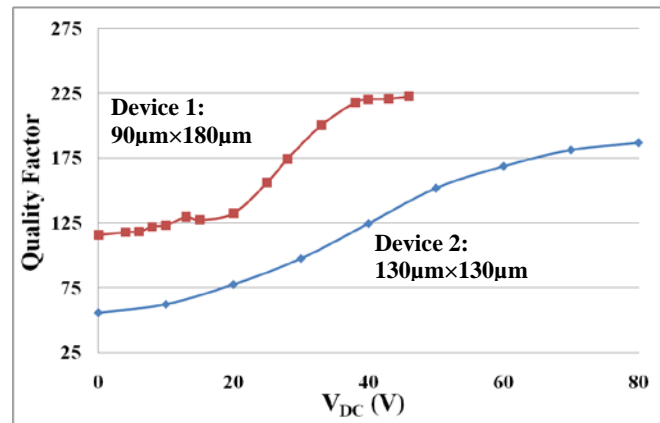


Figure 10: Trends for acoustoelectric  $Q$  amplification of Devices 1 and 2 as a function of applied DC voltage.

### Repeatability

To ensure that the acoustoelectric  $Q$  amplification is repeatable, the response of filters is measured when DC level is switched between 0 V and 50 V over 100 times. Fig. 11 shows the  $Q$  of Device 2 versus switching iteration number. The  $Q$  value at

0V remains within 0.91% of its nominal value and the amplified  $Q$  remains within 0.32% of its nominal value over 100 cycles.

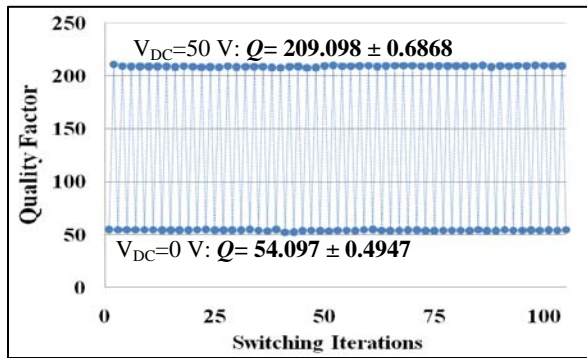


Figure 11: Measured  $Q$  at 0 V DC and 50 V DC switched over 100 cycles. The filter response switches reliably between the two values.

### Power Handling

In general, micromachined piezoelectric resonators suffer from a low power handling capability due to the small form factor of the device and intrinsic material constraints and tend to show a distorted response at high power levels. The use of configurations involving piezoelectric materials on silicon improves the power handling [13]. However, thin film piezoelectric resonator and filters (such as AlN, PZT, or ZnO) have suffered from significant distortion. GaN on the other hand is known to possess good power handling capability. It has been shown that GaN MESFET switches can reliably handle up to +20 dBm of RF power without significant distortion to the response [4].

To characterize the power handling of GaN micromechanical filters, the frequency response of the fabricated filters was measured at varying power levels from -15 dBm to +20 dBm. As shown in Fig. 12, the response did not suffer any significant distortion at elevated power levels. The maximum change in center frequency and insertion loss was measured to be 0.018% and 0.7%, respectively. Fig. 12 also compares the filter characteristics at power levels of -15 dBm and +20 dBm when a DC voltage of 50 V is applied between the input and output ports. As shown, at higher DC levels the  $Q$  improves due to the acoustoelectric effect but the response does not get distorted with increasing RF power.

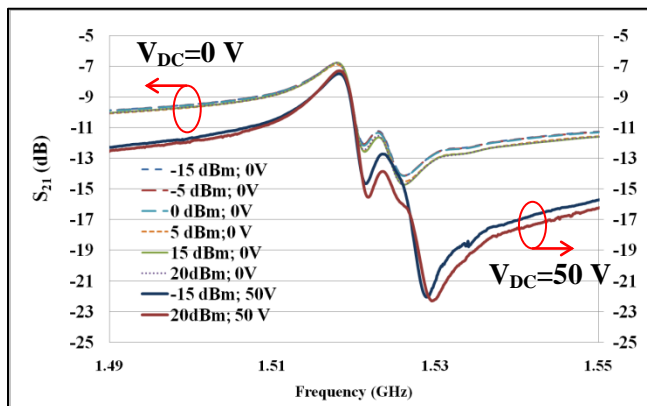


Figure 12: Response of Device 2 with RF input powers ranging from -15 dBm to +20 dBm at two different DC voltages. The pass-band response does not change or distort over the power range for either DC value.

## CONCLUSION

In this paper, we reported on the observation of the acoustoelectric effect in GaN bulk acoustic filters for the first time. Using this effect, we could amplify the quality factor and improve the out-of-band rejection of the filters by applying a DC electric field in the direction of acoustic wave propagation. We believe this is a significant development in the field of acoustoelectronics since it opens up opportunities to use this effect in practical devices. The power handling of the GaN bulk acoustic filters was verified by applying RF powers as high as 20 dBm (the maximum output power of the PNA) and no distortion was observed in the frequency response. Repeatable results have been measured for a number of filters.

## ACKNOWLEDGEMENT

Authors would like to thank the staff at the Michigan Nanofabrication Facilities (LNF) for their assistance.

## REFERENCES

- [1] A. Muller et al, "6.3-GHz Film bulk acoustic resonator structures based on a GaN/silicon thin membrane," *IEEE Electron Device Letters*, Vol.30, No.8, pp.799-801, 2009.
- [2] R. Tabrizian, M. Rais-Zadeh and F. Ayazi, "Effect of phonon interactions on limiting the  $fQ$  product of micromechanical resonators", *Solid-State Sensors, Actuators and Microsystems Conference*, Denver, pp 2131-2134, 2009.
- [3] J. H. Edgar, S. Strite, I. Aksaki, H. Amano and C. Wetzel, "Properties, Processing and Applications of Gallium Nitride and Related Semiconductors", INSPEC, IEE, 1999.
- [4] M. Kameche and N. Drozdovski, "High-temperature distortion and power-handling properties of GaAs-, 4H-SiC-, GaN MESFET's switches", *IEEE MELECON*, Benalmadena, pp. 169-172, 2006.
- [5] Y. Gulyaev and F. S. Hickernell, "Acoustoelectronics: history, present state, and new ideas for a new era" *Acoustical Physics*, Vol.5, No.1, pp. 81-88, 2005.
- [6] R. H. Parmenter, "The acousto-electric effect", *Physical Review*, Vol.89, No.5, pp.990-998, 1953.
- [7] A. R. Hutson, "Acousto-electric explanation of non-ohmic behavior in piezoelectric semiconductors and Bismuth," *Physical Review Letters*, Vol. 9, No.7, pp.296-298, 1962.
- [8] H. N. Spector, "Amplification of acoustic waves through interaction with conduction electrons" *Physical Review*, Vol.127, No.4, pp. 1084-1090, 1962.
- [9] S. K. Abdelraheem, D. P. Blyth and N. Balkan, "Amplification of ultrasonic waves in bulk GaN and GaAlN/GaN heterostructures", *Physica Status Solidi. (a)*, Vol.185, No.2, pp. 247-256, 200.
- [10] S. Y. Mensah, N. G. Mensah, V. W. Elloh, G. K. Banini, F. Sam and F. K. A. Allotey, "Propagation of ultrasonic waves in bulk gallium nitride (GaN) semiconductor in the presence of high-frequency electric field", *Physica E*, Vol.28, pp. 500-506, 2005.
- [11] <http://www.soitec.com/picogiga>
- [12] [www.picosecond.com](http://www.picosecond.com)
- [13] R. Abdolvand and F. Ayazi, "Enhanced power handling and quality factor in thin-film piezoelectric-on-substrate resonators," *IEEE International Ultrasonics Symposium*, New York, pp. 608-611, 2007.

## CONTACT

\*V.J. Gokhale, Tel: +1-734-945-5732; vikrantg@umich.edu  
M. Rais-Zadeh, Tel: +1-734-764-4249; minar@umich.edu

# QUALITY FACTOR SENSITIVITY TO CRYSTALLOGRAPHIC AXIS MISALIGNMENT IN SILICON MICROMECHANICAL RESONATORS

A. K. Samarao and F. Ayazi

Georgia Institute of Technology, Atlanta, Georgia, USA

## ABSTRACT

We study the sensitivity of quality factor in single crystal silicon (SCS) micromechanical resonators to crystallographic axis misalignments that are present due to fabrication non-idealities. Our experimental results, being reported for the first time here, unveil that very small angular misalignment from [110] axis of transduction adversely affects the high  $Q$  of a bulk acoustic wave SCS resonator by more than 50%, unlike the misalignment errors about the [100] axis of transduction. Interestingly, when the axis of transduction is intentionally offset by a large angle from either [100] or [110], multiple peaks with comparable relative strength are observed from a single resonator.

## INTRODUCTION

Single crystal silicon (SCS) micromechanical resonators have shown high frequencies ( $>100$  MHz) and high quality factors ( $Q > 50,000$ ), surpassing those of commercially available quartz resonators [1]. Insertion of such high frequency silicon resonators into low phase-noise frequency references requires stable and reproducible  $Q$ . However, the observed  $Q$  variation across various batches of simultaneously processed devices under very similar processing conditions suggests that there might be a possible influence from a non-systematic non-ideality in the fabrication process that might be adversely affecting the  $Q$ . While many studies have been conducted on determining the various energy loss mechanisms limiting the  $Q$  of a SCS resonator [2], the sensitivity of  $Q$  to crystallographic misalignment has not yet been systematically studied.

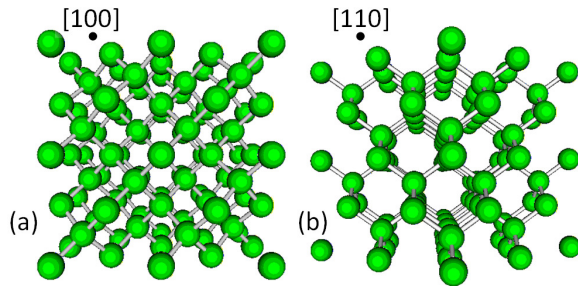


Fig. 1: Schematic showing the arrangement of atoms in the silicon crystal lattice as seen along the (a) [100] and (b) [110] directions.

Every atom in silicon has a linear chain of atoms aligned along the [100] or [110] direction which facilitates efficient transmission of the compressional and dilational forces of an acoustic wave (Figure 1). Hence, SCS microresonators are typically transduced along either of these axes. However, any angular misalignment from these two axes of transduction disrupts the atomic linearity which might lead to acoustic losses at the atomic level, the ensemble of which might reflect on the  $Q$  of the resonator. As will be revealed from this work, the amount of angular misalignment needed to adversely affect the  $Q$  of the resonator is imperceptible to the human eye and are beyond the tolerance limits of automated lithography systems as well.

A rectangular silicon bulk acoustic resonator (or SiBAR) (Figure 2(a)) that involves a capacitive air-gap based transduction along a very specific crystallographic axis in SCS is the best

candidate to study variations in  $Q$  with very small angular offsets from the intended axes of transduction. The SiBAR is placed between the drive and sense electrodes separated by a very high aspect-ratio air-gap realized using the HARPSS process [3]. A DC polarization voltage ( $V_p$ ) applied to the resonator generates an electrostatic field in these capacitive gaps. When an AC voltage is applied to the drive electrode, the resulting time-varying electrostatic force applied to the corresponding face of the resonator induces an acoustic wave that propagates through the bar, resulting in a width-extensional resonance mode (Figure 2(b)) whose frequency is primarily defined by the width of the SiBAR. Small changes in the air gap on the other side of the device induce a voltage on the sense electrode whose amplitude peaks at the mechanical resonance frequency.

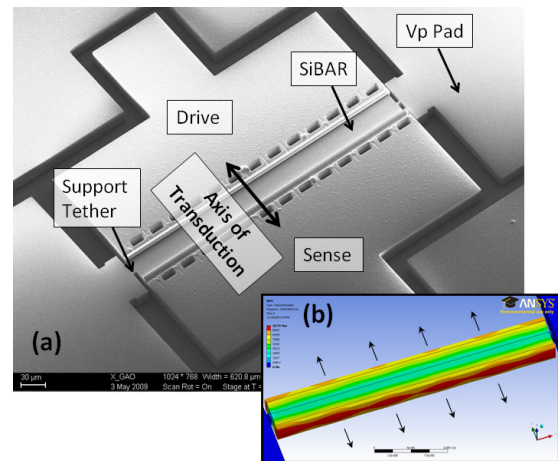
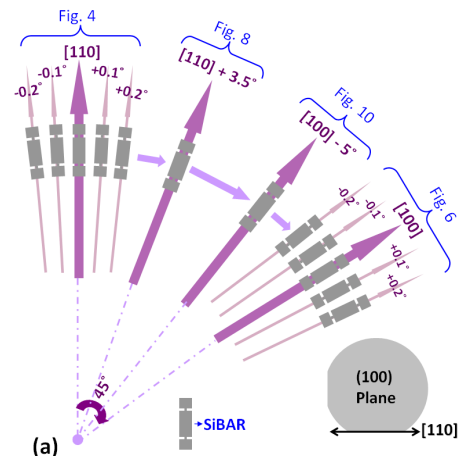


Fig. 2: (a) SEM and (b) Simulated width-extensional mode (WEM) shape of the SiBAR.

## Experimental platform to study $Q$ sensitivity to angular offset

A batch of 100 MHz SiBARs (width = 40  $\mu\text{m}$ , thickness = 20  $\mu\text{m}$  and length = 10  $\times$  width) were fabricated about both the [110] and [100] axes of transduction with intentionally created negative and positive angular offsets in steps of 0.1 degrees as illustrated in Figure 3.



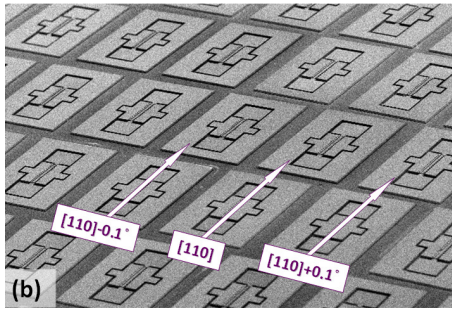


Fig. 3: (a) Schematic and (b) SEM of the intentionally angular offset 100 MHz SiBARs for studying the  $Q$  variation with angular misalignment.

The variation in  $Q$  with the doping level of the SCS substrate and the size of support tethers needs to be taken into account to attribute any variation in  $Q$  solely to the angular misalignment. Hence, these SiBARs were fabricated across various batches of wafers that spanned different levels of boron doping (0.01~0.02  $\Omega\text{-cm}$  [moderately-doped], 0.001~0.002  $\Omega\text{-cm}$  [highly-doped] & <0.001  $\Omega\text{-cm}$  [ultra-highly-doped]) as purchased from the vendor for different widths of the support tethers (3  $\mu\text{m}$  & 1.5  $\mu\text{m}$ ). Any pattern in  $Q$  variation observed across all these batches of devices can be safely concluded to stem from the angular misalignment in the axis of transduction.

### $Q$ VARIATION ABOUT [110] AXIS OF TRANSDUCTION

Among the SiBARs fabricated about the [110] axis, the SiBAR that offers the highest  $Q$  is assumed to be transduced exactly along [110]. This assumption is reasonable as the atomic arrangement favoring minimum loss for acoustic transduction would exist only for the [110] axis of transduction. The SiBARs that are angularly offset clockwise from the [110] device are assumed to have a positive offset and vice versa (Figure 3). A very interesting symmetric pattern in the  $Q$  variation with angular offsets has been observed in these devices about [110] as shown in Figure 4. These results correspond to moderately doped substrate with a supporting tether width of 3  $\mu\text{m}$ . The  $Q$  values were measured in vacuum at an input power of -10 dBm at a  $V_p$  of 10 V, and a capacitive air-gap of  $\sim 100$  nm. Except for a minor variation in each  $Q$  value by  $\pm 3k$ , this exact pattern repeats in highly doped and ultra-highly-doped substrates as well, thus confirming the pattern to be a result of angular misalignment.

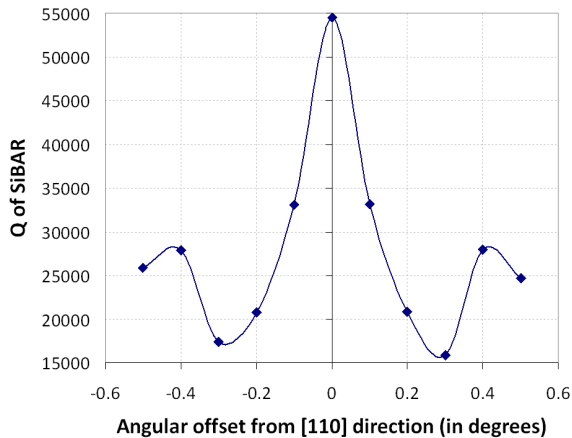


Fig. 4: Measured pattern of  $Q$  variation in SiBARs with angular offsets from [110] axis of transduction.

The most important conclusion from this study is that the  $Q$  drops by  $\sim 50\%$  when offset from the [110] axis of transduction by just 0.1 degree. This calls for additional efforts to alleviate misalignment sensitivity when  $Q$  is of utmost importance. A  $180^\circ$  phase difference has been measured across all the resonance peaks to confirm that the lower- $Q$  is not due to a coupling of adjacent resonant modes of the SiBAR. When these devices were fabricated with a 1.5  $\mu\text{m}$  wide supporting tether to further reduce the support loss, the unloaded  $Q$  (i.e.,  $Q$  at the turn-ON  $V_p$  of 1 V) along the [110] direction almost matches the maximum possible  $fQ$  in SCS (Figure 5(a)) [4]. Figure 5(b) illustrates that other than the expected  $\sim 50\%$  drop with a 0.1 degree angular offset, spurious modes start appearing within a span of 1 MHz from the main resonance peak. One or more of such spurs have been observed in all the devices about the [110] axis except for the one aligned exactly long [110]. Thus, the observation of such spurs can serve to be a good indicator of the existence of an angular misalignment from the fabrication process. A vacuum measurement setup and careful *SOLT* calibration have been found to be necessary in the case of some devices to observe the spurs.

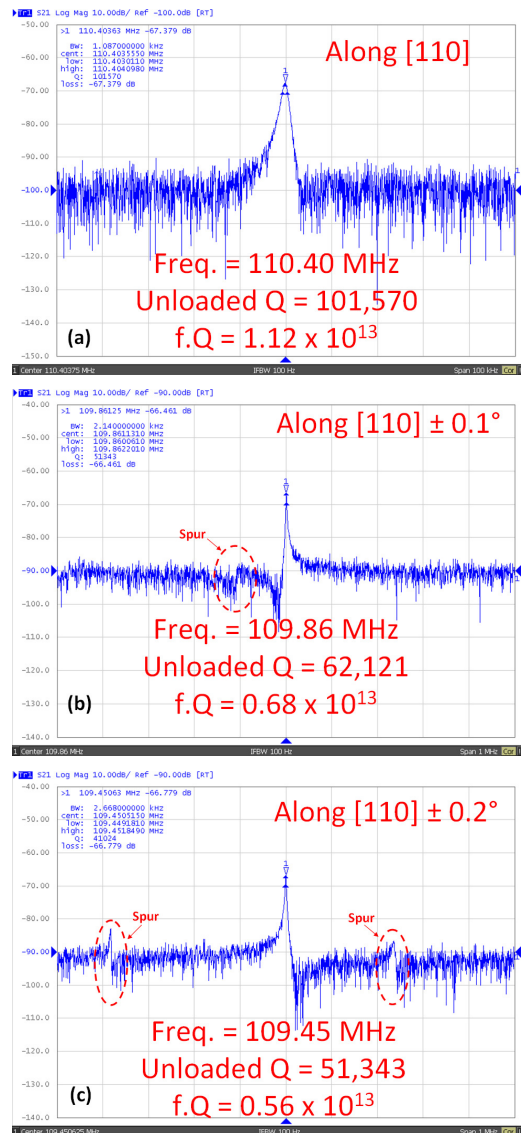


Fig. 5: Measured responses from the SiBARs transduced (a) along [110] direction, and along (b)  $\pm 0.1^\circ$  and (c)  $\pm 0.2^\circ$  angular offset.

## Q VARIATION ABOUT [100] AXIS OF TRANSDUCTION

Unlike [110], the SiBARs about [100] were not observed to show any pattern in  $Q$  variation with angular offsets from the [100] axis of transduction (Figure 6). The data in Figure 6 corresponds to the devices about [100] but are from the same wafer and under the same measurement conditions as that of Figure 4. A random variation about 10% in the  $Q$  value was observed in these devices making [100] axis of transduction the best option when repeatability of  $Q$  across various batches of fabrication is of prime importance. Such a random  $Q$  variation of  $\sim 10\%$  in the devices about [100] was observed across the highly-doped and ultra-highly doped substrates as well. The absence of a pattern in  $Q$  variation about [100] unlike [110] can be attributed to the comparatively high atomic density along the (100) plane over the (110) plane (Figure 1). As a result, the disruption of atomic periodicity with angular offsets in the case of [110] axis of transduction is more drastic compared to [100], which might be leading to sharper patterns in  $Q$  variations.

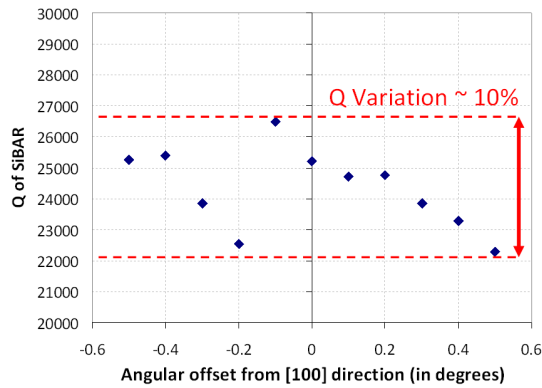


Fig. 6: Measured random  $Q$  variation of  $\sim 10\%$  in SiBARs with angular offsets from [100] axis of transduction.

Figure 7 shows a typical SiBAR fabricated with a  $1.5\ \mu\text{m}$  wide supporting tether (same wafer as Figure 5) and transduced about [100] at a  $V_p$  of 10 V. The unloaded  $Q$  for such devices randomly varies between 60k~70k. Spurs are observed in a span of 5 MHz in all the devices about [100] except for the one aligned exactly along [100]. In both the devices about [110] and [100], the spurs become more prominent with increasing  $V_p$  similar to the main resonance peak. The  $Q$  value observed exactly along [100] axis of transduction ( $\sim 65\text{k}$ ) is smaller in comparison to [110] ( $\sim 101\text{k}$ ) which is in agreement with the Akheiser regime of the silicon  $fQ$  product [4].

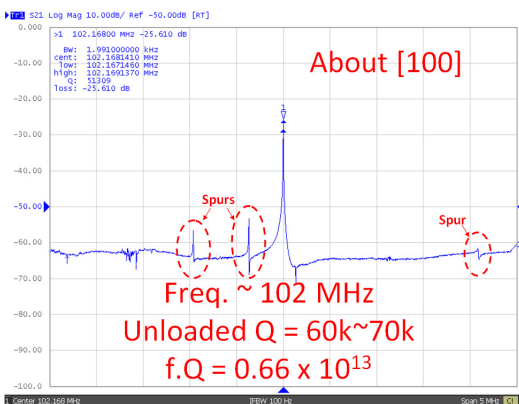


Fig. 7: Typical measured response from the SiBARs transduced about [100] axis of transduction.

## SPURIOUS MODES BETWEEN [110] AND [100] AXES OF TRANSDUCTION

The geometry of the SiBAR and the configuration of its drive/sense electrodes do not favor the excitation of out-of-plane or torsional modes of resonance. Hence, the spurious resonance modes also need to be predominantly confined to those similar to the primary width-extensional mode ( $WEM$ ) (Figure 2(b)). However, the effective width as seen by the acoustic wave may differ, albeit slightly, depending on the chain of atoms favored for propagation. As a result, they give rise to spurious width-extension-like resonance modes very near the main resonance peak when transduced at an angular offset from [110] or [100]. However, the acoustic impedance for these spurious modes are typically very large compared to the primary  $WEM$  along [110] and [100] which usually makes them very weak in comparison (i.e., larger insertion loss). Interestingly, there exist certain axes of transduction between [110] and [100] where two or more such  $WEM$ -like resonance modes can be equally or comparably favored, giving rise to multiple strong peaks from a single SiBAR.

For example, at an angular offset of  $+3.5^\circ$  from [110] axis of transduction (Figure 8), four comparable peaks can be seen in a span of 1 MHz at a  $V_p$  of 10 V, each varying considerably in  $Q$  and insertion loss ( $IL$ ). No regular patterns have been observed in the relative strength or spectral spacing of these multiple peaks with increasing angular offsets from [110] or [100]. The temperature coefficient of frequency ( $TCF$ ) of the multiple peaks are found to vary only within  $\pm 2\ \text{ppm}/^\circ\text{C}$  across all such measured angular offset devices and correspond to the range of  $TCF$  expected from the respective doping level of the substrates [5]. However, the same multiple peak responses are repeatable across batches of fabrication varying in doping levels and tether widths.

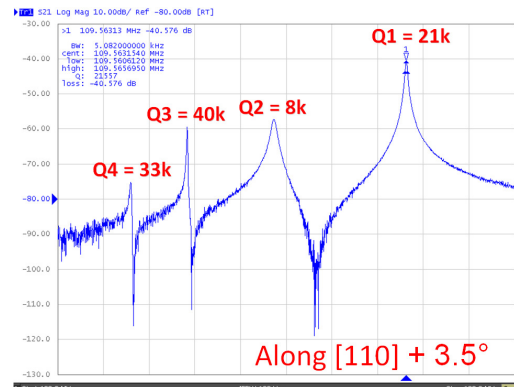


Fig. 8: Measured response from a SiBAR transduced along [110] +  $3.5^\circ$  axis of transduction.

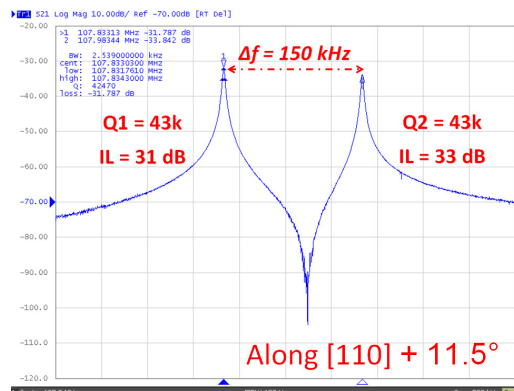


Fig. 9: Measured response from a SiBAR transduced along [110] +  $11.5^\circ$  axis of transduction.

Two equally strong peaks ( $IL \sim 31$  dB) separated by 150 kHz with the same  $Q$  of 43k has been observed from a single SiBAR transduced at an offset of  $+11.5^\circ$  from [110] axis of transduction and at a  $V_p$  of 10 V (Figure 9). It is worth noting that achieving such small frequency separations with the same  $Q$  from an array of two micromechanical resonators is challenging otherwise due to the tolerance limits of microfabrication processes [6].

Another interesting observation from SiBARs that are  $5^\circ$  and  $5.1^\circ$  offset respectively from the [100] axis of transduction is shown in Figure 10. Transduction along  $5^\circ$  offset from [100] shows two very prominent, equally strong peaks ( $IL \sim 30$  dB) at a  $V_p$  of 10 V separated by 486 kHz as shown in Figure 10(a), among other minor spurs. One of the peaks exhibits a  $Q$  of 74k which is more than twice that of the other strong peak with a  $Q$  of 35k. Interestingly, the SiBAR that is transduced at  $5.1^\circ$  offset from [100] has only one strong peak at the same  $V_p$  of 10 V as shown in Figure 10(b) among other minor spurs. The  $Q$  of this single strong peak is an average of the  $Q$ s of the two peaks in the  $5^\circ$  offset device, and its  $IL$  of 24 dB is 6 dB better. Also, the resonance frequency at  $5.1^\circ$  offset approximates to be in the middle of the two peaks from the  $5^\circ$  offset device. These reflect that a transitional acoustic path of transduction might be favored in the  $5.1^\circ$  offset device wherein the larger  $Q$  from the  $5^\circ$  offset device has decreased while the smaller  $Q$  has increased. However, such a transitional acoustic path seems to half the motional impedance, leading to twice a voltage gain at the sense electrode which reflects as a 6 dB improvement in  $IL$ . Such observations hold the key to understanding the transduction along non-conventional axes which might hold possible to a new type of coupling at the atomic level that offers low-loss SCS electromechanical resonators and resonator-array functionalities within a very small footprint.

## DISCUSSIONS

The study of  $Q$  variation with angular misalignment can have a high risk of error due to the non-idealities of the silicon wafer manufacturing processes, even prior to the fabrication of the SiBARs. The tolerances involved in the thickness and planarity of the sliced wafers from the silicon ingot and the subsequent manufacturing of the SOI layers introduce unpredictability in precisely determining the axis of transduction in these SiBARs. Hence, all reported trends in  $Q$  variation in this work have been cross-checked across multiple fabrication batches. The systematic variations from the DRIE and photolithography processes and their effects on the dimensions of the resonator and the support tether have been minimized to the extent that trends in  $Q$  variations reported from adjacent devices with  $\leq \pm 0.5^\circ$  angular offset become independent of process tolerances. Other dissipative mechanisms that limit the  $Q$  (i.e., thermo-elastic damping, support loss, etc.) are assumed to be identical for the SiBARs positioned across minor angular offsets.

## CONCLUSION

Three major conclusions can be drawn from this work. First, among the SCS resonators transduced about the [110] direction, the maximum achievable  $Q$  is observed only while transduced exactly along the [110] direction. A 50% reduction in  $Q$  occurs even when the axis of transduction is angularly offset by  $0.1^\circ$ , which calls for additional efforts to alleviate misalignment sensitivity when  $Q$  is of utmost importance. Second, no such observable pattern has been observed in resonators transduced about the [100] direction. The variation in  $Q$  is random and is smaller than 10%, suggesting [100] direction to be a better choice of transduction axis when  $Q$  reproducibility across various batches of fabrication is desirable. Finally, two or more dominant peaks

have been observed from a single SiBAR when offset by a relatively larger angle from either [110] or [100] axis of transduction. It may be possible to choose a particular axis of transduction that might offer a new type of electromechanical coupling at the atomic level for the realization of low-loss resonators and resonator-array type of functionalities.

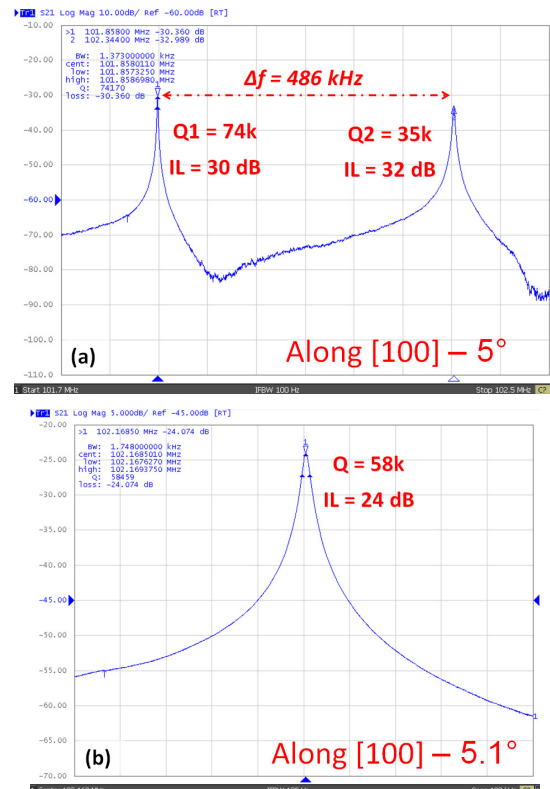


Fig. 10: Measured response from SiBARs transduced along (a) [100] -  $5^\circ$  and (b) [100] -  $5.1^\circ$  axis of transduction.

## ACKNOWLEDGEMENTS

This work was supported by Integrated Device Technology (IDT).

## REFERENCES

- [1] F. Ayazi, "MEMS for Integrated Timing and Spectral Processing," *Invited Paper, Proc. IEEE Custom Integrated Circuits Conference (CICC 2009)*, pp. 65-72.
- [2] R. N. Candler, H. Li, M. Lutz, W. T. Park, A. Partridge, G. Yama, and T. W. Kenny, "Investigation of Energy Loss Mechanisms in Micromechanical Resonators," *Transducers 2003*, pp. 332-335.
- [3] S. Pourkamali, G. K. Ho, and F. Ayazi, "Low-Impedance VHF and UHF Capacitive Silicon Bulk Acoustic Wave Resonators - Part I: Concept and Fabrication," *IEEE Transactions on Electron Devices*, vol. 54, no. 8, Aug. 2007, pp. 2017-2023.
- [4] R. Tabrizian, M. Rais-Zadeh, and F. Ayazi, "Effect of Phonon Interactions on Limiting the  $fQ$  Product of Micromechanical Resonators," *Transducers 2009*, pp. 2131-2134.
- [5] A. K. Samarao and F. Ayazi, "Temperature Compensation of Silicon Micromechanical Resonators via Degenerate Doping," *IEEE International Electron Devices Meeting (IEDM 2009)*, pp. 789-792.
- [6] A. K. Samarao and F. Ayazi, "Post Fabrication Electrical Trimming of Silicon Bulk Acoustic Resonators using Joule Heating," *IEEE International Conference on Micro Electro Mechanical Systems (MEMS 2009)*, pp. 892-895.

## CONTACT

A. K. Samarao, tel: +1-404-385-3291; [ashwins@ece.gatech.edu](mailto:ashwins@ece.gatech.edu)

# SENSITIVITY ENHANCEMENT USING PARAMETRIC AMPLIFICATION IN A RESONANT SENSING ARRAY

Z. Yie<sup>1\*</sup>, K.L. Turner<sup>1</sup>, N.J. Miller<sup>2</sup>, and S.W. Shaw<sup>2</sup>

<sup>1</sup>University of California-Santa Barbara, Santa Barbara, California, USA

<sup>2</sup>Michigan State University, East Lansing, Michigan, USA

## ABSTRACT

In this work we describe the parametric amplification of a multi-degree of freedom resonant chemical mass sensing array. We experimentally demonstrate that parametric forcing can be employed to increase the effective resonant quality factor of the array structure via an applied base motion containing the appropriate frequency content. Applying parametric forcing in this manner is simple and aligns naturally with the vibrational properties of the sensing structure. Our effort to increase the effective quality factor is motivated by the desire to enhance the sensitivity of the device.

## INTRODUCTION

Resonant chemical mass sensing using N/MEMS has received a great deal of attention over recent years [1]. The fundamental factors limiting sensitivity have largely been identified [2] and the question remains how best to manipulate them. In the pursuit of higher mass sensitivity, in this work we experimentally demonstrate parametric amplification, first demonstrated in MEMS in [3], as a means to improve the resonant quality factors,  $Q$ , of multiple resonances in a sensor array.

It has been shown that minimum detectable mass scales with the quality factor according to  $Q^{-1/2}$  [4]. Thus, increasing  $Q$  can be an effective way of reducing the minimum detectable mass and hence increase device sensitivity. However, in many environments, and for typical systems,  $Q$  is limited by intrinsic dissipation. Numerous researchers have employed various techniques to reduce dissipation effects. Some have inverted the sensor by placing the dissipative environment inside microchannels embedded in the device while leaving vacuum outside [5]. Although this method is effective, the device fabrication complexity is significantly increased. Others have used feedback control methods to reduce the effect of dissipation, for example in [6, 7], where feedback was used to boost the effective quality factor of a single MEMS resonator. However, in order to apply feedback control, a means of detecting the device behavior is necessary. For a sensor array, this means that the behavior of each sensor element in the array must be known, a requirement that also increases device complexity.

Parametric amplification, an example of vibrational control [8], is an open-loop control strategy that can be easily implemented on an entire MEMS sensor array without the need for any feedback to monitor the device behavior. The only thing required is to develop a method for parametrically forcing the array. Moreover, it can be implemented in cooperation with a concurrent frequency sweep [9] to increase the quality factor of any resonance encountered by the frequency sweep without prior knowledge of the resonance location. This makes parametric amplification an approach worth consideration for quality factor control in swept systems. This is also of particular importance in this work because our sensor array is a multi-degree of freedom resonator and, as such, lacks the guaranteed 90 degrees phase lag at resonance found in single-degree of freedom resonators. Accordingly our device employs a frequency sweep for resonance tracking. The primary deficiency of this method, however, is that it is not effective for devices with significant inherent damping. Consequently, we have

yet to demonstrate the effect at atmospheric pressure.

The sensor array of interest is the single-input-single-output scheme proposed in [10] for the simultaneous detection of multiple analytes. The device is shown in Fig. 1 and composed of four slightly detuned microcantilevers  $M_1$ ,  $M_2$ ,  $M_3$ , and  $M_4$ , attached to a common oscillator comprised of a cantilever plate SM. The sensor is forced via base motion applied to the entire structure and the response is monitored at a single point (labeled L) on the shuttle cantilever.

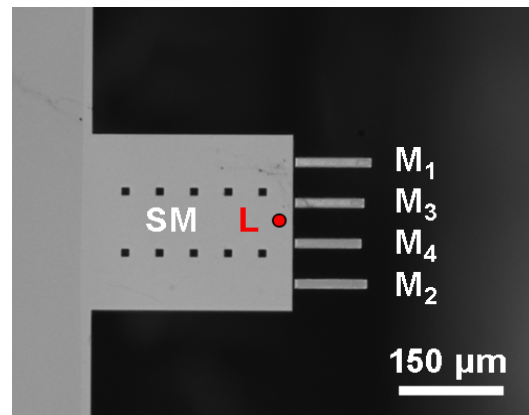


Figure 1: Microscope image depicting the sensor array with labeled shuttle cantilever SM, microcantilevers  $M_1$  through  $M_4$ , and detection location L.

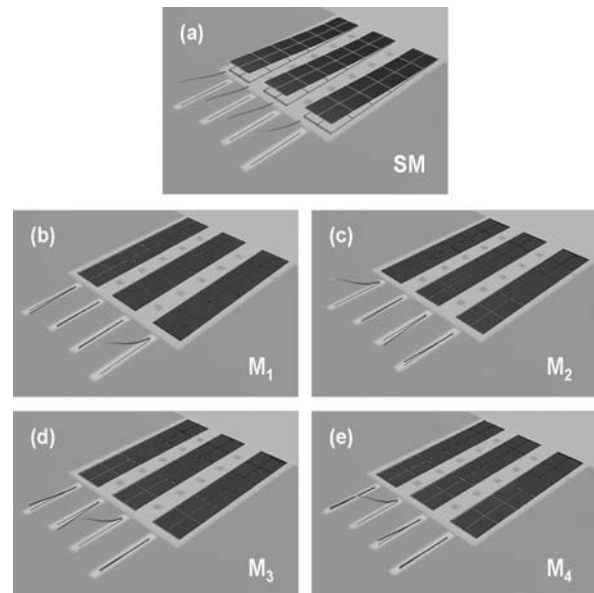


Figure 2: Experimentally measured mode shapes of the device. The mode shape in (a) corresponds to the shuttle cantilever SM. The mode shapes in (b)–(e) correspond to microcantilevers  $M_1$  through  $M_4$ , and are physically localized.

The modes of interest for this device are physically localized in the individual microcantilevers (see Fig. 2). These are intentionally designed to correlate frequency response features, specifically, the location of resonance peaks, with mass attachment sites in the array. The attachment sites are the tips of the microcantilevers. A frequency sweep is used to monitor the level of attached mass at each site. By piggybacking parametric excitation, also known as parametric pumping, on the frequency sweep, at twice the basic sweep frequency and with a fixed relative phase, we can effectively amplify the important resonances of the sensing structure. This can be done simply by altering the direction of the base motion relative to the plane of the device and adding a second harmonic term to the base motion signal with an appropriate phase [9, 11].

## THEORY

In principle, the vibrations of the device are described by a partial differential equation. By projecting onto the four modes of interest, we can describe the system with a lumped parameter model

$$\ddot{x} + Z\dot{x} + \Omega x + \Delta(t)x = F(t), \quad (1)$$

where  $x$  is a 4-vector describing the component of vibration in each of the four modes of interest,  $\Omega$  is a diagonal matrix whose elements are the squared natural frequencies for each mode,  $Z$  is the modal dissipation matrix,  $F(t)$  is the forcing vector, and  $\Delta(t)$  is the parametric forcing matrix.  $Z$  is assumed to be small and diagonal, while  $F(t)$  and  $\Delta(t)$  are also assumed to be small and periodic in time.

Equation (1) describes four linear vibration modes coupled through parametric forcing. In our system, the parametric forcing arises from the base motion-induced inertial force along the axis of the device. In cantilevered structures, this force has been shown to result in parametric excitation [11]. For our analysis, we assume that  $F(t)$  and  $\Delta(t)$  take the form

$$F(t) = f \cos(\omega t + \phi), \quad \Delta(t) = \delta \cos(2\omega t), \quad (2)$$

where  $f$  and  $\delta$  are a vector and constant matrix, respectively. In principle,  $F(t)$  and  $\Delta(t)$  should contain both harmonics since they both arise from the same base motion. However, we have only kept the terms that produce resonant responses. The phase difference  $\phi$  between  $F(t)$  and  $\Delta(t)$  can be chosen to produce the maximum quality factor amplification. The quality factor can also be attenuated if the phase relationship is chosen differently [11].

In order to have a clean parametric amplification of the modes of interest, it is necessary for them to have a degree of frequency isolation from other modes. In particular, if the modes of interest span a frequency band of  $[\omega_l, \omega_h]$ , then there can be no resonances in the frequency bands  $[2\omega_l, 2\omega_h]$  or  $[3\omega_l, 3\omega_h]$ . Moreover, the condition for two modes with frequencies  $\omega_i$  and  $\omega_j$  to couple through parametric forcing is

$$\omega \approx \left| \omega_i \pm \omega_j \right| \quad \text{or} \quad 2\omega \approx \left| \omega_i \pm \omega_j \right|, \quad (3)$$

and so the device should have  $2\omega_l > \omega_h$ . If these conditions hold, then the pump-strength/pump-frequency parameter space will have several Arnold tongues corresponding to the resonances,  $\omega = \omega_i$ , and combination resonances  $2\omega = \omega_i + \omega_j$ . Inside these tongues, the linear system will become unstable and exhibit parametric resonance. However, if we maintain the pump strength below

these tongues and sweep the direct and parametric forcing frequencies together (i.e. sweep  $\omega$ ), then the system will remain stable and the quality factor of the resonances encountered during the sweep will be increased [9]. Furthermore, the combination resonances will not show up in the response because they will not be simultaneously forced directly and parametrically with resonant forcing [9]. This is because of the locked frequency relationship between the direct and parametric forcing. The stability requirement is given by [12]

$$\delta_{ij}\delta_{ji} < 4Z_{ii}Z_{jj}\omega_i\omega_j \quad \forall i, j. \quad (4)$$

The maximal effective quality factor for a resonance, at frequency  $\omega_i$ , encountered during the sweep is

$$Q_{eff} = \frac{\omega_i^2}{\sigma_{1/2}}, \quad (5)$$

where  $\sigma_{1/2}$  is the frequency detuning at half power, given by

$$\sigma_{1/2} = \frac{1}{2} \sqrt{(\alpha - 1)(-2 + \sqrt{4 + (\alpha + 1)^2})}, \quad (6)$$

$$\alpha = \frac{2Z_{ii}\omega_i}{\delta_{ii}}. \quad (7)$$

The quality factor can be increased as  $\alpha$  approaches 1 so long as the amplitude of the response remains sufficiently small so that nonlinear effects do not come into play. When this happens, the gain in resonance quality is limited [13].

## RESULTS

In experiment, the base motion is provided by an externally mounted shear-type piezo-actuator (P-121.01, Physik Instrumente). The frequency response of each microcantilever is captured from a single point measurement on the shuttle cantilever using a laser vibrometer (see Fig. 1). The shuttle cantilever has a measured resonant frequency of 50.55 kHz, while the resonant frequencies of the microcantilevers range from 71–93 kHz. For all experiments, the device was operated in a test chamber at 50 mTorr.

Depending on the applied driving signal, the shear piezo provides movements in both the out-of-plane and in-plane directions, which can be used to realize both direct and parametric forcing. By applying a small driving voltage, enough out-of-plane motions can be created to achieve direct forcing. Applying a larger driving voltage allows the shear piezo to generate strong in-plane motions and achieve parametric forcing. To implement parametric amplification, we set the piezo-forcing function to be

$$A_d \cos(\omega t + \phi) + A_p \cos(2\omega t), \quad (8)$$

where  $A_d$  represents the peak voltage amplitude for the effective direct forcing and  $A_p$  presents the peak voltage amplitude for the effective parametric forcing. The phase difference  $\phi$  between the two forcing terms was set to 90° for a first run. The theoretical optimal phase is 45°, but due to experimental difficulties we were unable to vary the phase.

In order to determine the appropriate values for  $A_p$ , we first map the Arnold tongues for each microcantilever. Fig. 3 depicts the experimental curves. These plots were obtained by setting the piezo-driving frequency  $\omega$  to be close to twice the resonant frequencies of the microcantilevers and then gradually increasing the driving voltage until a significant response was observed at half the driving frequency. From these plots, the minimum threshold



voltage  $V_{th}$  necessary for parametric resonance for each microcantilever can be obtained. Note that we were unable to locate the combination resonances because the effective pump strength at the combination resonances is extremely weak. This implies that the matrix  $\delta$  is approximately diagonal. While this is not generally true, the localized modes of our device make this possible. This arises because the inner product of any two non-identical modes with respect to the differential operator in the governing partial differential equation of this system is approximately zero as a result of the localization. Accordingly, parametric amplification not only allows for the increase in the effective quality factor, but does so without introducing spurious frequency response features such as combination resonances.

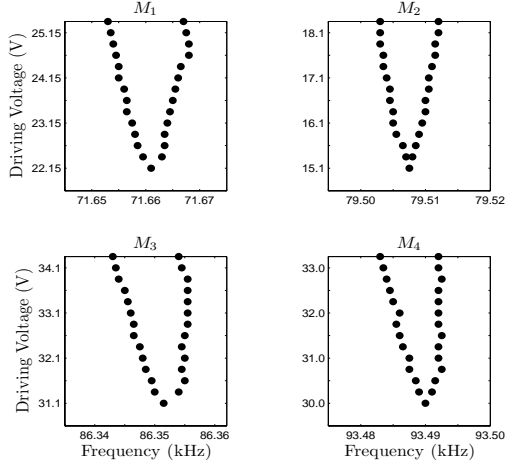


Figure 3: Experimental mapping of the Arnold tongues for microcantilevers  $M_1$  through  $M_4$ .

Table 1 shows the value of  $A_p$  for each microcantilever which was selected to be below the corresponding threshold voltage. The value of  $A_d$  was set to 0.05 V, which is small enough in amplitude to ensure that neither parametric resonance nor nonlinearity effects can be induced.

Table 1: Resonant frequency  $\omega_0$ , threshold voltage  $V_{th}$ , and parametric forcing amplitude  $A_p$  for microcantilevers  $M_1$  through  $M_4$ .

	$\omega_0$ (kHz)	$V_{th}$ (V)	$A_p$ (V)
$M_1$	71.66	22.15	21.3
$M_2$	79.50	15.1	14.25
$M_3$	86.35	31.1	30.25
$M_4$	93.49	30.0	27.5

To show parametric amplification and to characterize the parametric gain, we first perform direct forcing on each of the microcantilevers by actuating the shear piezo with a 0.05 V sinusoidal driving signal around their resonant frequencies. We then add the parametric forcing term by implementing the input given in equation (8). The plots in Fig. 4 show the frequency response of the microcantilevers with and without parametric forcing. The resonances clearly exhibit an enhancement of the effective resonant quality factor values.

All the frequency responses were curve-fitted to obtain the effective resonant quality factor values before and after parametric amplification. A parametric gain of two or more was calculated for all the microcantilevers as summarized in Table 2.

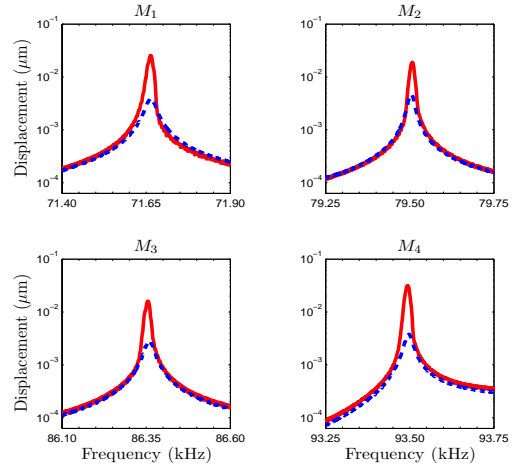


Figure 4: Frequency response of microcantilevers  $M_1$  through  $M_4$ . The blue dashed line plots indicate direct forcing only, while the red solid line plots indicate the addition of parametric forcing.

As an illustration of the practical operation of the sensor, a full range frequency sweep was performed between 71 and 94 kHz with and without parametric amplification. This is shown in Fig. 5, where the value of  $A_p$  was set to 14.25 V to give  $M_2$  the maximum amplification without inducing instability.

Table 2: Effective  $Q$  values for microcantilevers  $M_1$  through  $M_4$  before and after parametric amplification.

	Effective $Q$		Gain
	Parametric Amplification <b>off</b> $Q_{off}$	Parametric Amplification <b>on</b> $Q_{on}$	
$M_1$	1409	3751	2.6
$M_2$	2539	5080	2.0
$M_3$	1894	4944	2.6
$M_4$	2407	5604	2.3

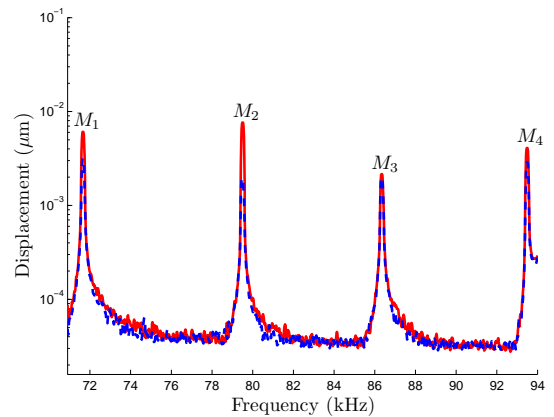


Figure 5: Full range frequency sweep with (red solid line) and without (blue dashed line) parametric amplification. The value of  $A_d$  was set to 0.05 V, while the value of  $A_p$  was set to 14.25 V to give maximum amplification for  $M_2$  without inducing any instabilities.

## CONCLUSIONS

In this work, we have demonstrated that parametric amplification extended to the case of multiple resonances is a simple and effectual method of controlling the effective resonant quality factor in a multi-degree of freedom resonant chemical mass sensor array. By increasing the effective quality factor, the minimum detectable mass can be reduced which leads to an increase in device sensitivity. Since the minimum detectable mass scales with the quality factor according to  $Q^{-1/2}$ , the gain in sensitivity can be expressed as  $G_s = \sqrt{Q_{on}/Q_{off}}$ . From the experiments, the sensitivity gains for microcantilevers  $M_1$  through  $M_4$  were calculated to be 1.63, 1.41, 1.61, and 1.52, respectively. The limitation of our technique is that a sufficiently small damping is required initially. As well, the gain in effective quality factor can also be limited by nonlinearities. Nevertheless, by supplementing the usual frequency sweep with a properly selected parametric pump one can effectively amplify the important resonances of the sensing structure. This results in higher effective quality factors in the sweep response and can be used to enhance the sensitivity of swept MEMS devices that rely on resonance location for measurement.

## ACKNOWLEDGEMENTS

This work was supported by NSF Sensors and Sensor Systems Program Grants [0758419](#) and [0800753](#), and by ICB Sensors Grant [W911NF-09-D-0001](#). The authors would like to thank Dr. Barry DeMartini for fabricating the device and providing preliminary data on the device characteristics.

## REFERENCES

- [1] P.S. Waggoner and H.G. Craighead, "Micro- and nanomechanical sensors for environmental, chemical, and biological detection", *Lab on a Chip*, 7, 1238 (2007).
- [2] A.N. Cleland, "Thermomechanical noise limits on parametric sensing with nanomechanical resonators", *New Journal of Physics*, 7, 235 (2005).
- [3] D. Rugar and P. Grütter, "Mechanical parametric amplification and thermomechanical noise squeezing", *Physical Review Letters*, 67, 699 (1991).
- [4] J.F. Vignola, J.A. Judge, J. Jarzynski, M. Zalalutnov, B.H. Houston, and J.W. Baldwin, "Effect of viscous loss on mechanical resonators designed for mass detection", *Applied Physics Letters*, 88, 041921 (2006).

- [5] T.P. Burg, A.R. Mirza, N. Milovic, C.H. Tsau, G.A. Popescu, J.S. Foster, and S.R. Manalis, "Vacuum-packaged suspended microchannel resonant mass sensor for biomolecular detection", *Journal of Microelectromechanical Systems*, 15, 1466 (2006).
- [6] J. Tamayo, A.D.L. Humphris, A.M. Malloy, and M.J. Miles, "Chemical sensors and biosensors in liquid environment based on microcantilevers with amplified quality factor", *Ultramicroscopy*, 86, 167 (2001).
- [7] J. Mertz, O. Marti, and J. Mlynek, "Regulation of a microcantilever response by force feedback", *Applied Physics Letters*, 62, 2344 (1993).
- [8] S. Meerkov, "Principle of vibrational control: Theory and applications", *IEEE Transaction on Automatic Control*, 25, 755 (1980).
- [9] N.J. Miller and S.W. Shaw, "Frequency sweeping with concurrent parametric amplification", *Proceedings of the 1<sup>st</sup> ASME Dynamic systems and Control Conference*, Ann Arbor, MI, 10/20-22/08, American Society of Mechanical Engineers (2008), DSC2008-118.
- [10] B.E. DeMartini, J.F. Rhoads, M.A. Zielke, K.G. Owen, S.W. Shaw, and K.L. Turner, "A single input-single output coupled microresonator array for the detection and identification of multiple analytes", *Applied Physics Letters*, 93, 054102 (2008).
- [11] J.F. Rhoads, N.J. Miller, S.W. Shaw, and B.F. Feeny, "Mechanical domain parametric amplification", *Journal of Vibration and Acoustics*, 130, 061006 (2008).
- [12] N.J. Miller, "Mechanical domain parametric amplification in multiple-degree-of-freedom systems," M.S. thesis, Michigan State University, East Lansing, MI, 2007.
- [13] J.F. Rhoads and S.W. Shaw, "The Effects of nonlinearity on parametric amplifiers", *Proceedings of the ASME 2008 International Design Engineering Technical Conferences & Computers and Information in Engineering Conference*, Brooklyn, NY, 08/03-06/08, American Society of Mechanical Engineers (2008), DETC2008-49594.

## CONTACT

\*Z. Yie, tel: +1-805-893-7849; [yie@engineering.ucsb.edu](mailto:yie@engineering.ucsb.edu)

# VACUUM ENCAPSULATED RESONATORS FOR HUMIDITY MEASUREMENT

Robert G. Hennessy<sup>1</sup>, Max M. Shulaker<sup>1</sup>, Renata Melamud<sup>1\*</sup>, Nathan Klejwa<sup>1</sup>, Saurabh Chandorkar<sup>1</sup>,  
Bong sang Kim<sup>1\*</sup>, J. Provine<sup>1</sup>, Thomas W. Kenny<sup>1</sup> and Roger T. Howe<sup>1</sup>

<sup>1</sup>Stanford University, Stanford, CA, USA

## ABSTRACT

This paper demonstrates using charge-biased vacuum encapsulated single-anchored double-ended tuning fork (DETF) resonators for humidity sensing. We charge-bias the DETF resonators and measure the change in the stored charge by observing the resonant frequency. Environmental humidity modifies the discharge characteristic of the resonator by varying the resistance between the bias bondpad and the surface silicon dioxide. Using this variation, we demonstrate a sensor that can determine relative humidity from <1 % to 60% with an absolute measurement uncertainty of less than  $\pm 0.8\%$  RH.

## INTRODUCTION

The resonant frequency of unencapsulated MEMS resonators is sensitive to environmental variables such as ambient temperature, pressure, and humidity, making direct sensing of any single environmental variable difficult. Li, *et al.* observed changes in the discharge characteristics of a contour mode disk resonator in vacuum and air [1]. Additionally, operating the resonator in atmosphere leads to a significant reduction in the quality factor of the device. Siwak, *et al.* used a cantilever resonator coated with pentacene to detect IPA and ethanol vapors in nitrogen. The resonant frequency shifted due to absorption, which caused a change in mass. When these devices were operated in air, the resonators possessed a quality factor of less than 80 [2]. In order to improve the quality factor of their resonant mass sensor, Berg, *et al.*, placed a fluidic channel inside their resonator and then operated their resonator in a gaseous environment or vacuum [3].

In this paper, we use perturbation of the charge decay of a charge biased, high quality factor ( $Q \sim 10,000 - 15,000$ ), vacuum encapsulated resonator to measure the relative humidity of the environment. Humidity modifies the surface resistance of the unencapsulated bias bondpad-oxide interface. This changes the discharge characteristics of the resonator. We track the charge stored on the resonator by observing the electrostatic spring softening term.

## THEORY

### Device Description

The fabrication process for these hermetically encapsulated, temperature compensated resonators has been discussed by Melamud, *et al.* [4]. The resonators have a beam length of 400  $\mu\text{m}$  and width of 8  $\mu\text{m}$ . The buried oxide layer is 2  $\mu\text{m}$  thick and the device layer has a resistivity of 0.3-0.7  $\Omega\text{-cm}$ . The aluminum bond pads are 100  $\mu\text{m} \times 100 \mu\text{m}$ . They are on top of 3.2 - 3.3  $\mu\text{m}$  of LTO deposited at 450° C. The oxide between the cap and the device layer is 2.6  $\mu\text{m}$  of TEOS that consisted of 4 depositions. After each deposition, the wafers are annealed at 1100° C for 1 hour.

### Device Operation

Under small resonant amplitude, the resonant frequency of the resonator is given by

$$f \approx f_0 \left( 1 - \frac{k_e}{2k_m} \right) \quad (1)$$

where  $k_m$  is the mechanical spring constant and  $k_e$  is the electrostatic spring softening term. The charge relaxation time of a

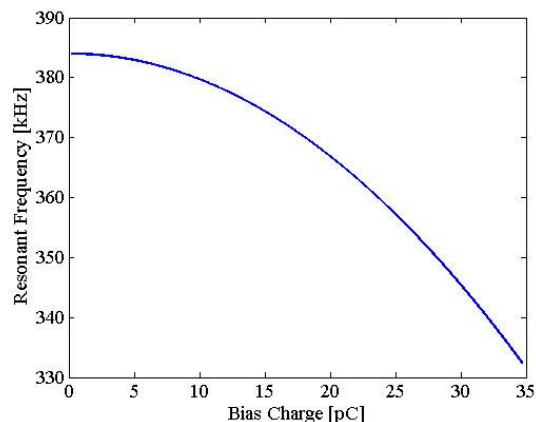


Figure 1: Resonant frequency versus charge stored on the resonator. The charge corresponds to bias voltage of 0 – 50 V.

uniform conductor is given by

$$\tau_e = \frac{\epsilon}{\sigma} \quad (2)$$

where  $\epsilon$  is the dielectric constant of the material and  $\sigma$  is the conductivity of the material. For our resonators, the relaxation time is  $3.1 - 7.25 \cdot 10^{-13} \text{ s}$ . This is significantly less than the period of oscillation ( $\sim 3 \mu\text{s}$ ) so we can assume equipotential on the resonator beam. Assuming also the voltage on the sense and drive is much less than the effective voltage on the resonator, the electrostatic spring softening term,  $k_e$ , is given by

$$k_e = \frac{2A\epsilon_0 Q_{er}^2}{g(gC_3 + 2A\epsilon_0)^2} + \frac{A\epsilon_0 C_3 V_d^2 (gC_3 + A\epsilon_0)}{2g(gC_3 + 2A\epsilon_0)^2} \quad (3)$$

where  $g$  is the gap between the resonant beam and the electrodes,  $C_3$  is the parasitic capacitance between the resonator and ground,  $Q_{er}$  is the charge stored on the resonator, and  $A$  is the area of the electrode. However, since the first term dominates for our devices, the spring softening term reduces to

$$k_e \approx \frac{2A\epsilon_0 Q_{er}^2}{g(gC_3 + 2A\epsilon_0)^2} = \frac{2A\epsilon_0 V_{er}^2}{g^3} \quad (4)$$

where  $V_{er}$  is the effective voltage on the floating electrode resonator. Figure 1 shows the resonant frequency versus the charge stored on the DETF. As the charge decays, the resonant frequency will increase because electrostatic spring softening decreases. Additionally, the sense current produced at resonance is given by

$$I_s = \frac{A\epsilon_0 V_d}{g^2} \frac{Q\omega_o}{k} \frac{A\epsilon_0}{g^2} \frac{Q_e^2}{(C_3 + 2A\epsilon_0/g)^2} = \frac{A\epsilon_0 V_d}{g^2} \frac{Q\omega_o}{k} \frac{A\epsilon_0}{g^2} V_{er}^2 \quad (5)$$

where  $Q$  is the mechanical quality factor,  $\omega_o$  is the resonant frequency, and  $V_d$  is the amplitude of the drive voltage. For both the current and the spring softening, the equations are similar to the case of dc biasing the resonator. Additionally, both the amplitude of the signal and the resonant frequency depend on the stored charge squared.

### Leakage Mechanisms

Leakage changes the amount of charge stored on the resonator. The primary leakage mechanisms for a floating electrode resonator are surface conduction from the aluminum

bond pads and conduction through the internal oxide layers (Fig. 2). Surface conduction depends on the relative humidity of the external environment.

Expanding on Ho, *et al.*, Fig. 3 shows a circuit model for the leakage from the resonator. The bias electrode voltage is modeled by

$$\frac{\partial V}{\partial t} = \frac{1}{R_s C_s} \frac{\partial^2 V}{\partial x^2} - \frac{V}{R_b C_s}, \quad (6)$$

$$-C_d \frac{\partial V_d}{\partial t} = \frac{V_d}{R_d} - \frac{S}{R_s} \frac{\partial V}{\partial x} \Big|_{x=0}, \quad (7)$$

$$V_d = V(x=0) = \frac{Q_{er}}{2A \epsilon_0 \sqrt{g + C_3}} \quad (8)$$

where  $R_s$  is the surface resistance,  $C_s$  is the capacitance between the surface and ground,  $R_b$  is the resistance between surface and ground,  $C_d$  is the device capacitance,  $R_d$  is the resistance between the device and ground,  $V_d$  is the voltage on the device, and  $S$  is the bond pad perimeter [5].

Equations 6, 7 and 8 were numerically solved in MatLab using the finite difference method. The device charge decay was fitted to a single exponential function to determine the charge decay time constant,  $\tau$ . Figure 4 shows the case where the resistivity of  $R_d$  equals the resistivity of  $R_b$ . Figure 5 uses the experimentally determined value for  $R_d$ .

The simulations show that at high surface resistivity ( $R_s \rightarrow \infty$ ),  $\tau \rightarrow R_d C_d$  because surface conduction becomes negligible. At low surface resistivity ( $R_s \rightarrow 0$ ),  $\tau \propto R_s$  because the leakage is similar to constant dose diffusion or a distributed RC line. From these simulations, we can determine the change in surface resistance from the change in the charge decay time constant.

Surface conduction on insulators,  $R_s$ , is determined by electrons hopping between adsorbed spots of water on the surface. Using B.E.T. theory for surface adsorption, the surface coverage ratio can be determined. From that, the surface resistance of silicon dioxide is given by

$$R_s = R_{s0} \exp\left(\alpha \left(\frac{1-h}{Ch}\right)^{1/2}\right), \quad (9)$$

$$C \approx \exp\left(\frac{E_1 - E_L}{RT}\right) \quad (10)$$

where  $h$  is the relative humidity (RH),  $R_s$  is the resistance at 100% RH,  $\alpha$  is a constant that depends on the electron mass, diameter of adsorbed spots and the energy of electrons on the surface,  $E_1$  is the heat of adsorption for the 1<sup>st</sup> adsorbed water monolayer and  $E_L$  is the heat of adsorption for the subsequent monolayers [6].

At low electric fields, through-oxide current in low temperature oxide is produced by charge hopping between states in the forbidden zone. For this hopping conduction, the resistivity for

$$R_d \text{ is given by } \rho = \rho_0 \exp\left(\frac{E}{kT}\right) \quad (11)$$

where  $E$  is the activation energy,  $k$  is the Boltzmann constant and  $T$  is the temperature [7].

### Experimental setup

A resonator chip is mounted on a PCB and placed in a custom humidity and temperature controlled chamber. The relative humidity is measured using a HIH-4021 humidity sensor, which has an accuracy of 3% RH. By adjusting the flow of wet and dry nitrogen, the chamber can reach RH from <1% to >99%. To change the temperature of the chip, a peltier thermoelectric

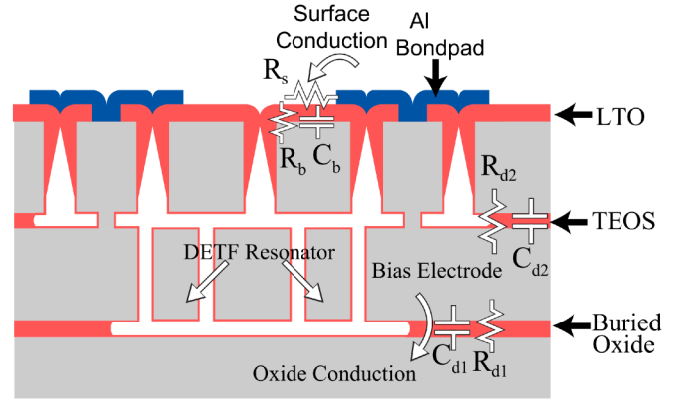


Figure 2: DETF cross-section showing primary leakage paths and locations of parasitic capacitances and resistances. Figure is not to scale.

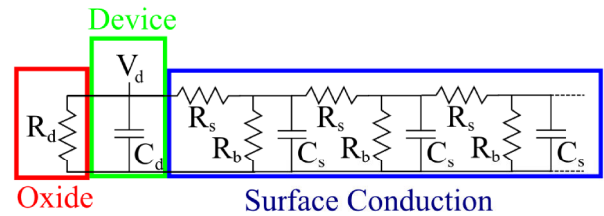


Figure 3: Equivalent circuit for the discharge of the DETF.

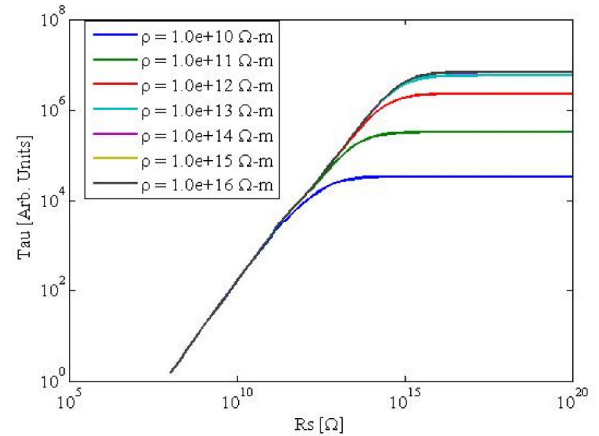


Figure 4: Finite difference model showing  $\tau$  for different  $R_s$  and  $\rho$ . Assumes  $\rho_b = \rho_d = \rho$ .

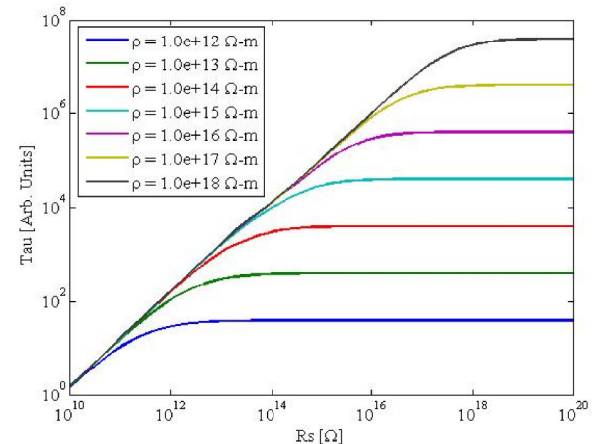


Figure 5: Finite difference model showing  $\tau$  for different  $R_s$  and  $\rho$ . Assumes  $\rho_b = \rho$  and  $R_d = 7 \cdot 10^{13} \Omega$ .

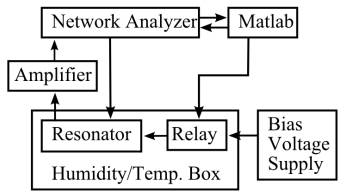


Figure 6: Measurement test setup (Block Diagram).

heater/cooler is placed between a heat sink and the PCB. The temperature is monitored using National Semiconductor LM34CZ (accuracy = 0.56° C at 25° C) and a feedback network is used to control the temperature.

The resonator is biased through the anchor for 10 seconds using a relay inside the humidity box and a HP 3631A voltage supply outside of the box. An AC signal is applied to the two outside drive electrodes and the signal is sensed from the inside sense electrode. While performing a humidity sweep, the humidity is allowed to stabilize for 10 minutes before performing the measurement. Additionally, we wait five minutes after complete decay before performing another measurement. This is to ensure that the initial charge distribution on the surface oxide is the same for all measurements. The signal from the resonator is amplified with a transimpedance amplifier. The resonant frequency, amplitude, and quality factor of the resonator were measured in approximately 7 second intervals using a HP 3577a network analyzer (Fig. 6). A measurement span of 60kHz is used to ensure successful peak tracking during the decay, and the peak frequency is measured with a resolution of 150 Hz.

## RESULTS

The charge decay constant  $\tau$  is defined as the time required for electrostatic spring softening to decrease by a factor of  $e$ . To determine  $\tau$ , the data is fit to a single exponential using the Curve Fitting Toolbox in MatLab. Fig. 7 shows a typical change in resonant frequency as the charge decays over time and the single exponential fitting function. As seen in the analytical model, as the charge decays, spring softening reduces, and the resonant frequency increases. After 300s, the signal level becomes equal to the noise level.

For one resonator, three trials were performed by ramping the relative humidity from <1% to >99% with a step size of 10% RH. Figure 8 shows the fitted  $\tau$  for the different relative humidities. For relative humidities above 60%, the decay occurs in less than 7 seconds, which is too fast to be captured by the current test setup. Figure 9 shows the absolute measurement uncertainty for these measurements. This uncertainty was calculated by multiplying the standard deviation with the sensitivity of the measurements. For all measured relative humidities, the measurement uncertainty is less than the 3% relative humidity accuracy for the humidity sensor that is used to control the humidity in the box. Additionally, removing the single outlier from the 50% RH values, the relative humidity error for 50% becomes 0.754% RH. For that case, the relativity humidity error is less than 0.81%.

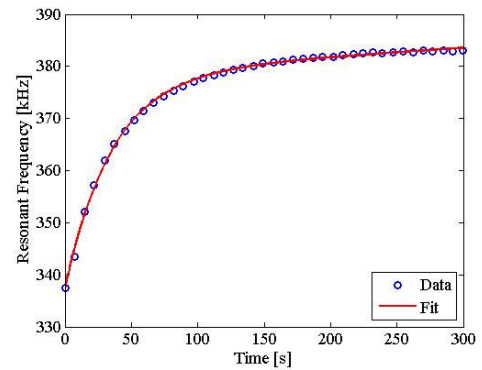


Figure 7: Change in resonant frequency as charge decays at <1% RH. Dots are the data points and the line is the fitted function using a single exponential fit.

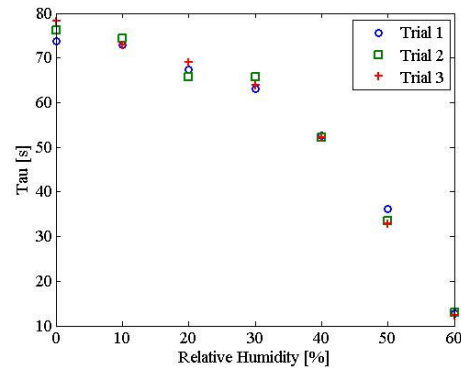


Figure 8: Charge decay for relative humidities from <1% to >99% RH. Test performed three times using the same resonator.

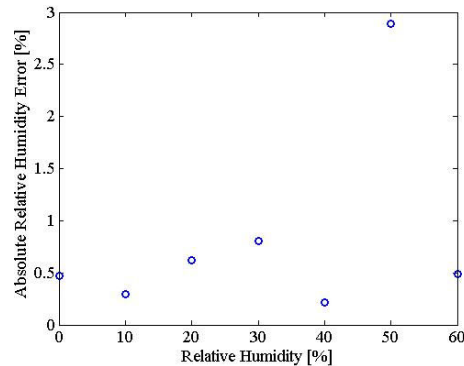


Figure 9: Absolute measurement error for relative humidities from <1% to >99% RH. Test performed three times using the same resonator.

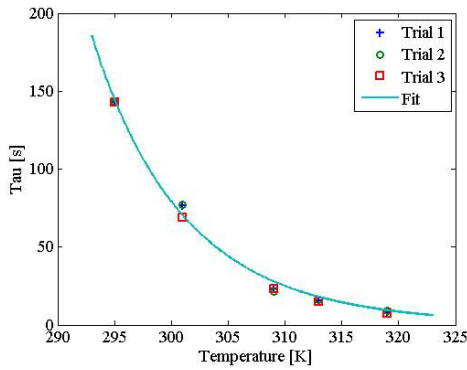


Figure 10: Charge decay for <1% relative humidity at 22°C, 28°C, 36°C, 40°C and 46°C. Test performed three times using the same resonator.

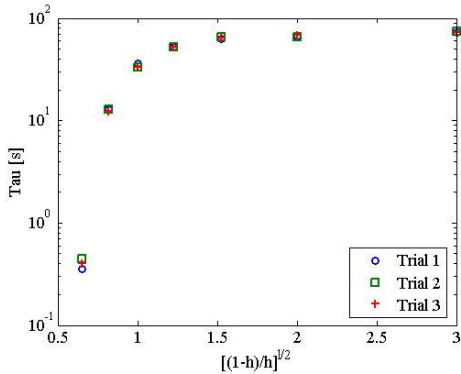


Figure 11: Charge decay for relative humidities from <1% to >99% RH. Test performed three times using the same resonator.

Fig. 10 shows  $\tau$  versus temperature with <1% relative humidity for a resonator. Using MatLab, the average of the three sweeps were fitted to equation 11 and the resulting r-squared value is 0.99. The fitted activation energy is 0.92 eV which is close to the values observed by Belousov, *et al.* for conduction in low temperature silicon dioxide [8]. Therefore, at <1% relative humidity, the dominating charge loss mechanism is hopping conduction through the oxide. Assuming that  $\tau = R_d C_d$  at 0% RH,  $R_d = 7.14 \cdot 10^{13} \Omega$  at 295 K.

Unfortunately, the low  $R_d$  resistance severely limits the sensitivity of the device to humidity because for most of the humidity range this resistance dominates the discharge mechanism. Ho, *et al.*, measured surface resistance of untreated thermal oxide between  $10^{20} - 3 \cdot 10^{15} \Omega$  for relative humidities between 0% and 80% and assuming that  $R_b = \infty$ . Fig. 11 also shows that the device resistance is contributing to the decay of the charge. If surface resistance was dominating, the line in the figure would be linear because of equation 9.

To improve the device performance, the resistance between device and ground ( $R_d$ ) must be significantly larger than the surface resistance. This could be accomplished by growing thermal oxide before depositing LTO or TEOS. Additionally, another surface material could be used that possesses a lower surface resistance.

## CONCLUSIONS

We have demonstrated that charge-biased microshell-encapsulated single-anchored double-ended tuning fork (DETF)

resonators can be used for precision humidity sensing. These sensors electrically sense the change in resonant frequency as the charge decays from the resonator through an external metal-oxide interface. Additionally, vacuum encapsulation protects the resonator from the environment and we achieve a quality factor of 10,000-15,000.

Currently, we are fabricating devices that use a combination of fusion wafer bonding and epitaxial reactor sealing [9]. These devices should have significantly higher  $R_d$  because the oxide between the device and cap will be thermal oxide instead of TEOS. We are examining how to perform humidity sweeps at different temperatures by using a recirculator to heat the nitrogen and the bubbler. Additionally, self assembled monolayers, including HMDS, can be used to change the surface conduction properties.

## ACKNOWLEDGEMENTS

This work was supported by DARPA Center on Interfacial Engineering in Microelectromechanical Systems (CIEMS) (HR 0011-06-1-0049), Analog Devices, and the National Nanofabrication Users Network facilities funded by the National Science Foundation.

\* - The present address for Renata Melamud is SiTime Corporation, Sunnyvale, CA. The present address for Bongsam Kim is Sandia National Laboratories, Albuquerque, NM.

## REFERENCES

- [1] S.-S. Li, Y.-W. Lin, Y. Xie, Z. Ren, and C. T.-C. Nguyen, "Charge-biased vibrating micromechanical resonators", Proceedings, IEEE Int. Ultra-sonics Symposium, Rotterdam, The Netherlands, Sept. 18-21, 2005, pp. 1596-1599.
- [2] Siwak, N., X. Z. Fan, D. Hines, S. Kanakaraju, N. Goldsman and R. Ghodssi, "Indium Phosphide MEMS Cantilever Resonator Sensors Utilizing a Pentacene Absorption Layer", J. Microelectromech. Syst., 18, pp.103-110, (2009).
- [3] Burg, T. P., and S. R. Manalis, "Suspended microchannel resonators for biomolecular detection", Appl. Phys. Lett. 83, 2698 (2003)
- [4] Melamud, R., S. A. Chandorkar, B. Kim, H. K. Lee, J. C. Salvia, G. Bahl, M. A. Hopcroft, and T.W. Kenny, "Temperature-insensitive composite micromechanical resonators", J. Microelectromech. Syst., 8, 1409 (2009).
- [5] Ho, P., K. Lehovc and L. Fedotowsky, "Charge Motion on Silicon Oxide Surfaces", Surface Science, 440 (1967).
- [6] J.A. Voorthuizen, K. Keskin, and P. Bergveld, "Investigations of the surface conductivity of silicon dioxide and methods to reduce it", Surface Science, 187, 202 (1987).
- [7] Dearnaley, G., A. M. Soneham, and D. V. Morgan, "Electrical phenomena in amorphous oxide films", Reports on Progress in Physics, 33, 1129 (1970).
- [8] Belousov, I. I., V. M. Efimov, S. P. Sinita, V. V. Vorontsov, and A. A. Shklyayev, "Charge Transport in MOS-Structures with Low-Temperature Silicon Dioxide Films", Physica Status Solidi, 125, 387 (1991).
- [9] Messana, M. W., A.B. Graham, S. Yoneoka, R. T. Howe, and T.W. Kenny, "Packaging of large lateral deflection MEMS using a combination of fusion bonding and epitaxial reactor sealing", Technical Digest of the 2010 Solid-State Sensor and Actuator Workshop, Hilton Head Isl., SC, 6/6-10/10, Transducer Research Foundation, Cleveland (2010), (in press).

# Author Index

Scroll to the author and select a [Blue](#) link to open a paper. After viewing the paper, use the bookmarks to the left to return to the beginning of the Author Index.

## A

Abbaspour-Tamijani, A. ....	258
Abramson, A. ....	447
Adams, G.G. ....	190
Agah, M. ....	166
Agasid, E. ....	110
Ahn, H.C. ....	202
Akarvardar, K. ....	7
Akgul, M. ....	467
Alf, M.E. ....	41
Alfeeli, B. ....	166
Allen, M.G. ....	404
Allendorf, M.D. ....	146
Almeida, R. ....	282
Amsden, J. ....	138
Araz, M.K. ....	286
Arnold, D.P. ....	118, 238, 368, 455
Averitt, R.D. ....	138
Ayazi, F. ....	100, 479
Azevedo, R. ....	260

## B

Bahl, G. ....	70, 384
Banerjee, B. ....	418
Bashir, R. ....	250
Beach, K. ....	78
Beardslee, L.A. ....	23
Beasley, C. ....	110
Bedair, S.S. ....	455
Beheymer, E.M. ....	226
Bergbreiter, S. ....	126, 340
Bhatia, B. ....	94
Bhave, S.A. ....	388, 459
Block, B. ....	78
Bogorzi, P. ....	308, 376
Bohn, P.W. ....	30
Bohrer, F. ....	278
Bohringer, K.F. ....	206
Bond, T.C. ....	226
Boniche, I. ....	118
Bora, M. ....	226
Bowers, J.E. ....	386
Branagan, S.P. ....	30
Brand, O. ....	23
Branda, C.S. ....	154

Bright, V.M. ....	443
Britten, J.A. ....	226
Burgner, C.B. ....	130, 308

## C

Candler, R.N. ....	150
Carlisle, J.A. ....	250
Carmo, M. ....	90
Carraro, C. ....	214
Carson, B.D. ....	154
Casinovi, G. ....	100
Chae, J. ....	82, 162, 258
Chandorkar, S.A. ....	70, 487
Chandrasekharan, V. ....	368
Chang, A.S.-P. ....	226
Chang, C.-C. ....	415, 426
Chang, C.-C. ....	418
Chang, H.W. ....	278
Chattopadhyay, G. ....	264
Chen, C.C. ....	96
Chen, C.-F. ....	415, 426
Chen, H. ....	294
Chen, J. ....	266
Chen, L. ....	190
Chen, L. ....	320
Chen, S. ....	37
Chen, S.-J. ....	234
Chen, Y.C. ....	96
Cheng, B. ....	206
Cheng, X. ....	202
Cheng, Y. T. ....	96
Chiang, C.-F. ....	451
Chiappetta, M. ....	290
Chiou, P.Y. ....	15
Chitnis, G. ....	408
Choe, Y.K. ....	234
Choi, S. ....	82
Choi, W. ....	356
Chong, S. ....	7
Choo, H. ....	262
Chow, A. ....	206
Chow, E.M. ....	206
Chu, K.-H. ....	41
Chu, M. ....	266
Chung, S.E. ....	218
Churaman, W.A. ....	126
Colombini, M. ....	302
Conley Jr., J.F. ....	194
Contento, N. ....	30
Costello, B. ....	260
Culver, J.N. ....	86
Cunningham, J. ....	206
Currano, L.J. ....	126



## D

Dam van, R.M. ....	37
DeBruyker, D. ....	206
Demirci, K.S. ....	23
Denisin, A. ....	422
DeVoe, D.L. ....	302, 415, 426
Di Carlo, D. ....	428
Diaz-Aguado, M. ....	110
Ding, C. ....	308, 376
Ding, H. ....	37
Ding, S. ....	90
Dueck, M. ....	19

## E

Ecker, A. ....	360
Eid, H. ....	190
Elata, D. ....	7
Enright, R. ....	86
Eun, C.K. ....	380

## F

Fachin, F. ....	312
Fan, K. ....	138
Fasenfest, B.J. ....	226
Fedder, G.K. ....	242
Felmetsger, V.V. ....	324, 352
Ferralis, N. ....	344
Fletcher, P. ....	94
Frank, J. ....	260
Friedericks, C. ....	110
Furlani, E.P. ....	170

## G

Gaitan, M. ....	298
Galle, P. ....	404
Gao, F. ....	150
Garcia-Uribe, A. ....	418
Geist, J. ....	298
Gerasopoulos, K. ....	86
Gerratt, A. ....	340
Ghodssi, R. ....	86
Giacchino, L. ....	122
Gianchandani, Y.B. ....	53, 182, 380
Gilmour, R.F. ....	270
Gleason, K.K. ....	41
Glickman, M. ....	328
Gokhale, V.J. ....	475
Goldberg, I.B. ....	328
Goldkorn, A. ....	439
Gordijo, C.R. ....	266
Graham, A.B. ....	336, 344
Greathouse, J.A. ....	146

Griere, M. ....	206
Griffin, B.A. ....	360
Guo, Z.J. ....	190, 352
Gutierrez, C.A. ....	57

## H

Haque, R.M. ....	49
Harrison, J. ....	328
Hartwell, P.G. ....	198
He, M. ....	114
Heinrich, S. ....	23
Hennessy, R.G. ....	487
Henschke, M. ....	110
Herr, A.E. ....	106, 114, 422
Herrault, F. ....	404
Hesketh, P.J. ....	146
Hess, A. ....	142
Hettiarachchi, K. ....	102
Hewlett, I. ....	415
Hines, J.W. ....	110
Hong, L.F. ....	33
Hopcroft, M.A. ....	70, 324
Horsley, D.A. ....	45, 254
Hou, C. ....	106
Houk, R.J. ....	146
Howe, R.T. ....	7, 336, 344, 384, 487
Hsia, B. ....	214
Hsieh, A.T.-H. ....	102
Hu, H. ....	382, 435
Hung, L.-W. ....	463
Hwang, E. ....	388
Hwang, Y. ....	150

## I

Iwai, K. ....	19
Izhar, U. ....	230

## J

James, C.D. ....	154
Jensen, M. ....	260
Jha, C.M. ....	451
John, J. ....	134
Joo, J. ....	154
Joshi, N. ....	190
Josse, F. ....	23
Judy, J.W. ....	328, 428
Jung, C. ....	264

## K

Kaanta, B.C. ....	294
Kant, R. ....	262, 344

Kaplan, D.L. ....	138
Karacor, M.B. ....	174
Karns, K. ....	422
Kenny, T.W. ....	70, 198, 336, 344, 384, 451, 487
Khuri-Yakub, B.T. ....	316
Kim, B. ....	467
Kim, B.S. ....	70, 384, 487
Kim, C.-J. ....	37, 158, 348
Kim, E.S. ....	234
Kim, G.-H. ....	202, 210
Kim, G.J. ....	210
Kim, J. ....	218
Kim, J.K. ....	202
Kim, K. ....	98
Kim, K.-T. ....	202
Kim, L.N. ....	218
Kim, S. ....	162
Kim, S.-J. ....	78
Kim, S.K. ....	278
King, W.P. ....	94, 250
Kitts, C. ....	110
Klejwa, N. ....	487
Ko, S.H. ....	356
Kotovskiy, J. ....	254
Kroninger, C.M. ....	390
Kuczynski, J. ....	418
Kudlicki, A. ....	110
Kumar, G. ....	90
Kupnik, M. ....	316
Kurabayashi, K. ....	78
Kwon, J.W. ....	282
Kwon, S. ....	218

## L

Laermer, F. ....	1
Lal, A. ....	222, 270, 286, 332
Lantz, J. ....	154
Larson, C.C. ....	226
Lavella, G. ....	412
Lazarus, N. ....	242
Lee, A.P. ....	102
Lee, C. ....	264
Lee, D. ....	7
Lee, H.-S. ....	82
Lee, H.K. ....	70, 384
Lee, J. ....	27
Lee, J.-H. ....	146
Lee, L.P. ....	19
Lee, S.H. ....	443
Lee, T. ....	320
Leung, A.M. ....	364
Leung, R. ....	110
Li, H. ....	392
Li, Y. ....	134

Lien, W.-C. ....	324
Lim, M. ....	61
Lin, C.-M. ....	324
Lin, D. ....	186
Lin, K.-Y. ....	96
Lin, L. ....	19, 356
Lin, R. ....	264
Liu, C. ....	382, 435
Liu, F. ....	214
Liu, J. ....	415, 426
Lo, H. ....	431
Loeb, J.A. ....	134
Lu, B. ....	439
Lu, Y. ....	222
Lüthi, B. ....	19
Luzinova, Y. ....	23
Luzzi, E. ....	110
Ly, D. ....	110

## **M**

Maboudian, R. ....	214, 344
MacDonald, N.C. ....	308, 376, 386
Maharbiz, M.M. ....	412
Maleki, T. ....	408
Manalis, S.R. ....	27
Manginell, R.P. ....	154
Mansour, R. ....	400
Martin, H.B. ....	142
Martino, A. ....	154
Mas, I. ....	110
Mateti, K. ....	246
McCarthy, M. ....	86
McGinnis, M. ....	110
McGruer, N.E. ....	190
McIntyre, M. ....	110
Mehdi, I. ....	264
Mehregany, M. ....	320
Meinhart, C.D. ....	376
Melamud, R. ....	70, 384, 487
Meloy, J. ....	360
Meng, E. ....	57
Menon, C. ....	304
Messana, M.W. ....	336, 344
Meyer, C.D. ....	455
Miller, N.J. ....	130, 483
Miller, T. ....	186
Min, S. ....	218
Mitra, S. ....	7
Mizaikoff, B. ....	23
Mohamed Ali, M.S. ....	396
Mojarrad, M. ....	290
Moorman, M.W. ....	154
Morfino, R. ....	412

Morgan, B.C. ....	455
Morris, C.J. ....	126

## N

Nam, K.H. ....	356
Nasiri, S. ....	61
Nelson, W.C. ....	158
Nguyen, C.T.-C. ....	463, 467
Nguyen, H.T. ....	226
Niblock, T. ....	328
Niesel, D. ....	110
Nikles, S.A. ....	312
Nunan, K. ....	320

## O

Olsson III, R.H. ....	65
Omenetto, F.G. ....	138
Ongkodjojo, A. ....	447
Ooi, B.S. ....	230
Ozkeskin, F.M. ....	182

## P

Pan, T.R. ....	33
Panchawagh, H.V. ....	170
Panja, A. ....	408
Parra, M. ....	110
Parsa, R. ....	7
Patil, N. ....	7
Pennathur, S. ....	178
Penskiy, I. ....	340
Peralta, A. ....	264
Philippine, M.A. ....	451
Piazza, G. ....	352, 471
Piccini, M. ....	110
Pisano, A.P. ....	214, 324
Polcawich, R.G. ....	194, 390
Pollock, C.R. ....	332
Pourkamali, S. ....	74
Prakash, S. ....	174
Prikhodko, I.P. ....	11
Privorotskaya, N.L. ....	250
Provine, J. ....	7, 344, 487
Pruitt, B.L. ....	98
Pulskamp, J.S. ....	194, 390

## Q

Qu, Y.Q. ....	70
Quach, Q. ....	431

## R

Rahafrooz, A. ....	74
Rahn, C.D. ....	246

Rais-Zadeh, M. ....	475
Rajkowski, J. ....	126
Ramkumar, A. ....	270
Rao, M.P. ....	290
Rasay, R. ....	110
Regan, C. ....	320
Reidy, S. ....	78
Ren, Z. ....	467
Renzi, R. ....	154
Ricco, A.J. ....	110
Ricks, R. ....	110
Rinaldi, M. ....	471
Rittmann, B.E. ....	82
Roberts, R.C. ....	447
Ronzano, K. ....	110

## S

Sabens, D. ....	142
Salvia, J.C. ....	70, 384, 451
Samarao, A.K. ....	479
Sameoto, D.E. ....	304
Sammoura, F. ....	320, 372
Sarkar, N. ....	400
Satsanarukkit, P. ....	431
Schmidt, M.A. ....	392
Schroers, J. ....	90
Schwerdt, H.N. ....	258
Seeger, J. ....	61
Sells, J. ....	368
Senesky, D.G. ....	214, 324
Shah, G.J. ....	37
Shannon, M.A. ....	92, 94
Shao, C. ....	302
Sharma, V. ....	392
Shaw, S.W. ....	130, 483
Shekhar, S. ....	258
Shen, C.J. ....	270
Sheplak, M. ....	360, 368
Shi, J. ....	206
Shim, Y. ....	475
Shkel, A.M. ....	11
Shubin, I. ....	206
Shulaker, M.M. ....	487
Sigurdson, M. ....	376
Sing, A.K. ....	154
Sinha, N. ....	352
Smith, C.T. ....	290
Smith, G.L. ....	194, 390
Smith, W.S. ....	198
Sochol, R.D. ....	19
Sounart, T.L. ....	170
Squires, D. ....	110
Stavis, S.M. ....	298
Strikwerda, A. ....	138

Su, J.J. ....	23
Sukaew, T. ....	278
Sun, G. ....	348
Sun, K. ....	90
Sun, Y. ....	266
Surks, H. ....	274
Suryanarayanan, K. ....	186

## T

Tabrizian, R. ....	100
Tadigadapa, S. ....	246
Tai, Y.-C. ....	122, 431, 439
Takahata, K. ....	396
Tao, H. ....	138
Tatic-Lucic, S. ....	230
Taylor, A.D. ....	90
Taylor, R.E. ....	98
Thakar, V.A. ....	475
Thomas, B. ....	264
Thompson, M.J. ....	45
Thompson, T. ....	260
Tien, N.C. ....	447
Timucin, L. ....	110
Todd, S.T. ....	386
Tooker, A.C. ....	254
Tovar, A. ....	102
Towe, B.C. ....	258
Trevey, J.E. ....	443
Trusov, A.A. ....	11
Tsau, C. ....	320
Tseng, P. ....	328, 428
Turner, K.L. ....	130, 308, 483

## U

Urban, A. ....	1
----------------	---

## V

Varghese, M. ....	312
-------------------	-----

## W

Waggoner, T. ....	194
Walmsley, R.G. ....	198
Wang, E.N. ....	41, 86
Wang, J. ....	443
Wang, L.V. ....	418
Wardle, B.L. ....	312
Wei, P. ....	290
Weinstein, D. ....	459
Wetzel, E.D. ....	390
Williams, M.D. ....	360
Wise, K.D. ....	49, 78
Wojciechowski, K.E. ....	65

Wong, E. ....	415
Wong, H.-S.P. ....	7
Wright, S.A. ....	53
Wu, T.H. ....	15
Wu, X.Y. ....	266
Wu, Y. ....	94
Wygant, I.O. ....	316
Wynne, T.M. ....	178

## X

Xiao, F. ....	15
Xiao, R. ....	41
Xu, T. ....	439
Xu, W. ....	258
Xu., Y. ....	134

## Y

Yang, K. ....	320, 372
Yang, Y. ....	82, 162
Yen, T.-T. ....	324
Yeo, J. ....	356
Yeom, J. ....	92
Yie, Z. ....	308, 483
Yoneoka, S. ....	70, 336, 451
Yoon, Y.-K. ....	202, 210
Yoshimizu, N. ....	332
Yost, B. ....	110

## Z

Zdeblick, M. ....	260
Zellers, E.T. ....	78, 278
Zeng, H. ....	250
Zhang, J. ....	134
Zhang, X. ....	134
Zhang, X. ....	138, 274, 294
Zhang, Z. ....	246
Zhao, S. ....	435
Zhao, X. ....	348
Zheng, X.Y. ....	274
Zhou, H. ....	392
Ziaie, B. ....	290, 408
Zipperian, H.A. ....	53
Zito, J.C. ....	238
Zmuda, H. ....	368
Zorman, C.A. ....	142
Zotov, S.A. ....	11
Zou, J. ....	418
Zuniga, C. ....	471
Zuo, C. ....	471



# Keyword Index

Scroll to the keyword and select a [Blue](#) link to open a paper. After viewing the paper, use the bookmarks to the left to return to the beginning of the Keyword Index.

---

---

## A

AC Polarization .....	<a href="#">384</a>
Acceleration Sensing .....	<a href="#">382</a>
Acoustic Actuator .....	<a href="#">286</a>
Acoustic Transducers .....	<a href="#">360</a>
Acoustoelectric Effect .....	<a href="#">475</a>
Aeroacoustics .....	<a href="#">360</a>
Air-Liquid Cavity Transducers .....	<a href="#">102</a>
Airborne Ultrasound .....	<a href="#">316</a>
ALD Partial Electrode-to-Resonator Gap Filling .....	<a href="#">467</a>
All-Solid-State .....	<a href="#">443</a>
AlN-on-Silicon Resonators .....	<a href="#">100</a>
Aluminum Nitride .....	<a href="#">65</a> , <a href="#">324</a>
Aluminum Nitride (AlN) Contour-Mode Resonant Sensors (CMR-S) .....	<a href="#">471</a>
Amorphous Silicon Carbide .....	<a href="#">320</a>
Analytical Solution .....	<a href="#">312</a>
Angular Misalignment .....	<a href="#">479</a>
Angular Rate .....	<a href="#">364</a>
Antibody Zipper .....	<a href="#">412</a>
Artificial Haircell .....	<a href="#">382</a>
Asymmetric Surface Profile .....	<a href="#">408</a>
Asymmetry .....	<a href="#">41</a>
Atomic Layer Deposition .....	<a href="#">194</a> , <a href="#">467</a>
Automation .....	<a href="#">114</a>

## B

Back-to-Back Diodes .....	<a href="#">94</a>
Backscattering .....	<a href="#">258</a>
Bano-Switch .....	<a href="#">352</a>
Batch-Fabricated .....	<a href="#">408</a>
Beta/Gamma Radiation .....	<a href="#">380</a>
Bifurcation .....	<a href="#">130</a>
Biofouling Detection .....	<a href="#">356</a>
Bioinspired .....	<a href="#">382</a>
Biomimetic .....	<a href="#">304</a>
Biomimetic Microphone .....	<a href="#">96</a>
Brownian Ratchet .....	<a href="#">412</a>
Bulk Metallic Glass Nanowires .....	<a href="#">90</a>

## C

Cantilever (s) .....	<a href="#">23</a> , <a href="#">94</a> , <a href="#">400</a>
Capacitive Micromachined Ultrasonic Transducer .....	<a href="#">316</a>
Capacitive Micromechanical Resonators .....	<a href="#">467</a>
Capacitive Sensors .....	<a href="#">368</a>

Cell Contractility .....	274
Cell Force Transducer .....	274
Cell Manipulation .....	428
Charge Biased Resonator .....	487
Chemical Analysis .....	166
Chemical Sensors .....	23
Chemomechanical .....	412
Circulating Tumor Cell .....	439
Clover Stalk .....	96
CMOS .....	242
CMOS Chip Protection .....	260
Colloidal Stability .....	286
Compliant Interconnect .....	206
Composite .....	7
Contact Materials .....	190
Contact Printing .....	92
Contact-Stress .....	254
Controlled Drug Delivery .....	266
Cubic Silicon Carbide .....	324
Cycloolefin Polymer .....	426

## D

Deep Reactive Ion Etching .....	194
Diamond .....	142, 250
Dielectric .....	320
Dielectric Barrier Discharge .....	238
Diffraction .....	332
Digital Microfluidic .....	158
Direct Alcohol Fuel Cell .....	90
DRIE-Tools .....	1
Droplet .....	158
Droplet Microfluidics .....	102
Drug Reservoir .....	290
Dry Adhesives .....	304

## E

Eigenmode .....	27
Elastomer .....	340
Elastomeric Actuator .....	408
Electrocatalysis .....	90
Electrochemical Impedance Sensing .....	57
Electrode .....	142
Electrode Loss .....	463
Electrohydrodynamics Modeling .....	447
Electrolysis .....	122
Electromagnetic Actuators .....	404
Electrophoretic Immunoassay .....	106
Electroplating .....	328
Electroplating Bonding .....	396
Electrospinning .....	210
Electrostatic Resonators .....	384
Electrothermal .....	94
Electrowetting .....	37, 41

Encapsulation .....	336, 487
Energy Harvester .....	118
Energy Storage .....	340
Escherichia Coli .....	162
Etch Stop .....	320
EWOD .....	158

## **F**

Fabrication .....	344
Filtration .....	439
Flapping .....	390
Flexible Boundaries .....	312
Flight .....	390
Flip Chip Packaging .....	206
Flow Rate Insensitive .....	294
Fluidic Interface .....	33
Fluidic Sensor .....	364
Fluorescence Detection .....	431
Folded Coils .....	404
Frequency Sweep .....	483
Friction .....	198
Fully-Passive .....	258

## **G**

Gallium Nitride Filters .....	475
Gas Chromatography .....	78
Gas Detection .....	146
Geobacteraceae-Enriched Mixed Bacterial Cultures .....	82
Geometric Nonlinearity .....	451
GHz NEMS Oscillator .....	471
Glass Reflow .....	49
Glucose-Responsive Membranes .....	266
Graphitization .....	214
Gyroscope .....	61, 364

## **H**

Harsh Environment .....	53, 324
Heat Pipe .....	376
Heater .....	94
Hermiticity .....	372
High Aspect Ratio .....	1, 348, 386
High Current/Power .....	206
High Frequency Resonator .....	74
High Performance Catalyst .....	90
High Power .....	182
High Power Density .....	82
High Pressure Microvalve .....	426
High Q .....	100, 463
High Temperature Stability .....	214
Humidity Sensor .....	242, 487
Hydrogel Printing .....	282

<b>I</b>	
Imaging .....	230
Immunoassay .....	422
Immunoassay Chip .....	415
Immunoblotting .....	114
In-Package Assembly .....	380
Inchworm .....	122
Inductors .....	455
Inertial Sensors .....	1
Inkjet Printing .....	170
Insect-Inspired .....	390
Integrated Microchannels .....	134
Integrated Microsystem .....	110
Integration .....	30
Intelligent .....	126
Interface Load .....	254
Internal Dielectric Transduction .....	459
Intraocular .....	49
Ion Channel .....	302
Ion Gauge .....	222
Ion Pump .....	222
Ionic Wind Pump .....	447

<b>J</b>	
Jump .....	126

<b>K</b>	
Kinetic Study .....	302

<b>L</b>	
Lactoferrin .....	422
Lap-on-a-Chip Device .....	162
Lateral .....	7
Lattice Filter .....	65
Leaky Dielectrics .....	170
Liquid Chromatography .....	426
Liquid Measurement .....	23
Lithium Batteries .....	443
Lorentz Force .....	45
Low Impedance .....	463

<b>M</b>	
Magnetic Actuators .....	218
Magnetic Nanoparticles .....	218, 428
Magnetometer .....	45
Manduca Sexta .....	270
Marconi Transmission .....	380
Maskless Lithography .....	218
Mass Sensing .....	27
Material Distribution Design .....	451
Mechanical Logic .....	352
Mechanobiology .....	98

MEMDAC .....	400
MEMS .....	246, 254, 308
MEMS Acoustic Transducer .....	234
MEMS Switches .....	190
Metal Organic Framework .....	146
Metal Structures .....	348
Metal-Dielectric-Metal Waveguides .....	226
Metallization .....	214
Metamaterials .....	138
Metrology .....	298
Micro Devices .....	266
Micro Gas Chromatography .....	166
Micro GC .....	278
Micro Total Analytical Systems .....	166
Micro-Channel .....	294
Micro-Discharge .....	380
Micro-Motors .....	404
Micro-Relays .....	182
Microactuator .....	396
Microbeads .....	19
Microbial Fuel Cell .....	82
Microbubble Transducer .....	57
Microcantilever .....	146, 250
Microchip Cooling .....	447
Microcontacts .....	190
Microdischarge (s) .....	53, 238
Microelectricalmechanical System .....	451
Microelectromechanical .....	400
Microfabricated Air-Cooling Technology .....	447
Microfabrication .....	455
Microfluidic (s) .....	19, 170, 174, 218, 286, 302, 422
Microfluidic Isolation .....	154
Microfluidic Valve .....	282
Microgravity .....	110
Micromachining .....	264, 336, 386
Micromechanical Resonators .....	475
Micromirror .....	230
Microparticles .....	19
Microphones .....	360
Microposts .....	98
Microspheres .....	19
Microthruster .....	126
Migration .....	262
Modeling .....	74
Molding .....	304
Monolithic .....	158
Motion Processing .....	61
Multifunctional Transducer .....	246
Multiple Height Microprobes .....	202

## N

Nanobead Characterization .....	286
Nanoelectromechanical (NEMS) Sensors .....	471
Nanofluidic (s) .....	30, 174, 178, 298

Nanomachine .....	412
Nanomaterials .....	92
Nanometrology .....	332
Nanoparticle .....	298
Nanostructure .....	41
Nanostructuring .....	344
Nanotemplates .....	86
Nanowires .....	226
Nasiri-Fabrication .....	61
Near Field Photothermal Printing .....	15
Neural Interface .....	142, 270
Neural Microsystem .....	258
Neural Probes .....	134
Neuropotential acquisition .....	258
NF-KB Oscillation .....	154
Ni-63 .....	222
NiFe .....	328
Noise .....	130
Nonlinear Dynamics .....	186
Nonlinear Oscillation .....	70
Nonlinear Post-Buckling .....	312

## O

Olfactory Sensor .....	270
On-Chip Gel Electrophoresis .....	106
On-Chip PCR .....	431
Optical Coherence Tomography .....	230
Optical Probe .....	418
Oscillator (s) .....	70, 384
Out of Plane Actuator .....	408
Overload .....	186
Oxide Pillars .....	100
Oxygen Sensing .....	372

## P

Packaging .....	308, 336
Parametric Amplification .....	45, 483
Parasitoid Fly .....	96
Parylene .....	431, 439
Parylene C .....	57
Passive Wireless .....	368
PDMS .....	290
Permalloy .....	328
Permanent Magnet .....	404
pH-Responsive Hydrogel Nano Particles .....	266
Phase Noise .....	384
Photo-Electrochemical Etching .....	348
Piezo-Resistive Sensing .....	74
Piezoelectric .....	194, 234, 246
Piezoelectric AlN Resonator .....	463
Piezoelectric Harvester .....	451
Piezoelectric Transducers .....	360
Piezoresistive .....	250, 382

Piezoresistor .....	250, 400
Planar Phospholipid Membrane .....	302
Plasma .....	238
Plasmonics .....	30
Plasmons .....	226
Plastic Deformation .....	11
Platinum .....	7
pn-Diode Transduction .....	388
Point-of-Care Diagnostic .....	106
Polydimethylsiloxane .....	98, 340
Polyimide .....	118, 254
Polymer MEMS .....	435
Polyurethane .....	304
Porous Silicon .....	150
Positron Emission Tomography .....	37
Power Converters .....	455
Power Handling .....	475
Pressure Gauge .....	372
Pressure Sensing .....	57
Pressure Sensor .....	49, 53
Probe Arrays .....	198
Prosthetic .....	435
Protein Array Diagnostics .....	102
Protein Assay .....	114
Protein Biomarker .....	106
Pt-Rh .....	182
Pulse Laser .....	308
PZT MEMS .....	390

## Q

Quality Factor .....	388, 459, 479
Quantum Dots .....	178
Quasiperiodic .....	332

## R

Radio Frequency Microelectromechanical Systems (RF MEMS) .....	324, 388, 459
Receiver .....	264
Reduced Order Modeling .....	186
Refractive Index Sensor .....	356
Relays .....	7
Release-Hole .....	262
Resonant Body Transistor .....	459
Resonant Cavities .....	226
Resonator (s) .....	11, 70, 130, 150, 388, 483
Robot .....	126

## S

Scanning .....	230
Scanning Probe Microscopes .....	332
Scattering .....	418
Seal .....	262
Self-Assembled Cantilever .....	206
Self-Cleaning .....	86

Self-Powered .....	222
Senser Array .....	278
Sensing .....	130
Sensing Array .....	483
Sensitivity .....	479
Sensor .....	146
Separation .....	298
Shape Memory Alloy (SMA) .....	396
Shear Stress Sensor .....	368
Silicon .....	118
Silicon Carbide .....	214
Silicon Micromechanical Resonator .....	479
Silicon on Insulator .....	194
Silicon Rod Structured .....	443
Silicon Surface Migration .....	344
Silicone .....	122
Silk .....	138
Simultaneous High-Q and Low Impedance .....	467
Single Cell Capture .....	154
Small Satellite .....	110
Soft Lithography .....	92
SOI .....	340
Sound Source Localization .....	96
Space Biology .....	110
Spectroscopy .....	418
Spreading .....	41
Stability .....	70
Stem Cells .....	98
Stretchable Sensing Skin .....	435
SU-8 .....	210
Submillimeter .....	264
Superhydrophobic .....	86
Surface Microfluidics .....	33
Surface Modification .....	174
Surface Resistance .....	487
Suspended Microchannel Resonator .....	27
Switch .....	182, 352
System Development .....	78

## **T**

T-Beam .....	246
Tactile Sensor .....	435
TaqMan Probe .....	431
Targeted Therapeutic Hybrid Particles .....	102
Tear .....	422
Temperature Compensation .....	100
Terahertz .....	138
Thermal .....	364
Thermal Actuation .....	74
Thermal Conductivity Detector .....	294
Thermal Cooling .....	376
Thermal Desorption .....	166
Thermal Oxidation .....	386
Thermoelectric Generator .....	118



Three-Dimensional .....	30, 33
Three-Dimensional Culture .....	439
Three-Dimensional Electrode Arrays .....	134
Three-Dimensional Etches .....	1
Three-Dimensional MEMS .....	11
Three-Dimensional microstructures .....	92
Timed Development and Thermal Reflow .....	202
Titanium .....	376
Titanium Dioxide .....	372
Tobacco Mosaic Virus .....	86
Toll-Like Receptor Signaling .....	154
Total Internal Reflection .....	356
Total Internal Reflection Fluorescence .....	178
Touch-Mode .....	49
Tracer .....	37
Transdermal Drug Delivery .....	290
Transformers .....	455
Transmission Lines .....	386
Two-Dimensional Microfluidic Technology .....	114
Two-Dimensional Separation .....	426

## U

Urinary Tract Infection .....	162
-------------------------------	-----

## V

Vacuum Degassing-Assisted Electroplating .....	348
Vacuum Pump .....	392
Valveless .....	174
Vapor HF Release .....	320
Vapor Intrusion .....	278
Vapor Micro System .....	278
Vapor Sensor .....	150
Volatile Organic Chemical (VOC) Detection .....	471

## W

Wafer .....	308
Wafer Bonding .....	336
Wafer-Level Bonding .....	61
Waveguide .....	264
Wear .....	198
Wicking .....	376
Wireless Flow Sensor .....	368
Wireless Power .....	396

# 2010

## Solid-State Sensors, Actuators, and Microsystems Workshop

Hilton Head Island, South Carolina • June 6 - 10, 2010

All opinions expressed in this digest are those of the authors and are not binding on Transducer Research Foundation, Inc.

Copies of available volumes of this digest may be obtained from the Transducer Research Foundation, Inc., c/o 307 Laurel Street, San Diego, California 92101-1630 USA (+1-619-232-9499)

Copyright and Reprint Permission: Abstracting is permitted with credit to the source. Libraries are permitted to photocopy beyond the limit of U.S. copyright law for private use of patrons those articles in this volume that carry a code at the bottom of the first page, provided the per-copy fee indicated in the code is paid through Copyright Clearance Center, 222 Rosewood Drive, Danvers, MA 01923. For other copying, reprint or republication permission, contact Transducer Research Foundation, Inc., c/o 307 Laurel Street, San Diego, California 92101-1630 USA, [info@transducer-research-foundation.org](mailto:info@transducer-research-foundation.org). All rights reserved. Copyright ©2010 by the Transducer Research Foundation, Inc. Personal use of this material is permitted. However, permission to reprint/republish this material for advertising or promotional purposes or for creating new collective works for resale or redistribution to servers or lists, or to reuse any copyrighted component of this work in other works must be obtained from the Transducer Research Foundation, Inc.

TRF Catalog Number: IOTRF-0001

Library of Congress Control Number: 2010926577

ISBN Number: 0-9640024-8-5

ISSN: 1539-2058 (Print) ISSN: 1539-204X (Electronic)

DOI 10.31438/trf.hh2010.0

This product contains Adobe Acrobat software. Copying this product's instructions and/or designs for use on future CD-ROMs or digital products is prohibited without written permission from The Printing House and Adobe Systems Incorporated. The Printing House or its suppliers are not liable for any direct, indirect, special, incidental, or consequential damages to your hardware or other software arising out of the use—or the inability to use—the material on this CD-ROM. This includes, but is not limited to, the loss of data or loss of profit. Adobe, Acrobat and the Acrobat logo are trademarks of Adobe Systems Incorporated or its subsidiaries and may be registered in certain jurisdictions.

If you have questions regarding the installation, please contact:



The Printing House, Inc.

Phone: +1-608-873-4500

Fax: +1-608-873-4558

Hours: Monday through Friday, 8 am - 5 pm CST

E-mail: [graphics@printinghouseinc.com](mailto:graphics@printinghouseinc.com)